Transactions of the ASME®

Transactions of the ASME, Journal of Heat Transfer (ISSN 0022-1481) is published quarterly (Feb., May, Aug., Nov.) for $160.00 per year by The American Society of Mechanical Engineers, 345 East 47th Street, New York, NY 10017. Second class postage paid at New York, NY and additional mailing offices. POSTMASTER: Send address changes to Transactions of the ASME, Journal of Heat Transfer, c/o THE AMERICAN SOCIETY OF MECHANICAL ENGINEERS, 22 Law Drive, Box 2300, Fairfield, NJ 07007-2300.

CHANGES OF ADDRESS must be received at Society headquarters seven weeks before they are to be effective. Please send old label and new address.

PRICES: To members, $36.00, annually: to nonmembers, $160.00. Add $15.00 for postage to countries outside the United States and Canada.

INDEXED by Applied Mechanics Reviews and Engineering Information, Inc.

Journal of Heat Transfer

Published Quarterly by The American Society of Mechanical Engineers

VOLUME 113 • NUMBER 1 • FEBRUARY 1991

ANNOUNCEMENTS

TECHNICAL PAPERS

(Contents Continued)

TECHNICAL NOTES

Analytical Solutions and Sinc Function Approximations in Thermal Conduction With Nonlinear Heat Generation

A. Lippke
Fachbereich Mathematik,
Technische Universität Berlin,
Berlin, Federal Republic of Germany

This paper is concerned with the numerical and analytical evaluation of multiple solutions of the steady-state radial temperature distribution in a solid m*-dimensional sphere, which is caused by nonlinear heat generation. To achieve highly accurate solutions a Sinc function approximation of the differential operator is introduced.*

1 Introduction

In some technical applications the heat production in a solid satisfies a nonlinear relation between heat and temperature. For example, consider the heat production in solid dielectrics as by Copple et al. (1935).

We know about similar thermal behavior in some chemical reactions of higher order. In these cases it has been found experimentally that an exponential law for nonlinear heat generation holds. In this context Rice (1940) dealt with the role of heat conduction in thermal explosions. He stated that if a certain parameter exceeds a critical value, no steady-state solution of the describing equations exists and that such a condition must result in explosion.

The analytical investigation of Wacker (1986) for the one-dimensional problem and the numerical ones of Lippke (1988) for one- and two-dimensional spheres showed that the critical value of the leading parameter for the one-dimensional problem is 2.0, which is a turning point for the continuum of solutions.

In the present paper this thermal problem is solved analytically and this solution is used to investigate the benefits of Sinc function approximations. The decision to use this nonlinear problem as a numerical test is justified by the following.

The problem is nonlinear with a singularity in one of the coefficients at the endpoint of the interval and Neumann and Dirichlet boundary conditions have to be satisfied. This ensures that the problem is difficult enough to give valuable information on the numerical applicability of Sinc function approximations.

On the other hand analytical solutions for the one- and two-dimensional problems are given in section three and the turning points for the three-dimensional problem are calculated from an initial value problem using a Runge–Kutta method.

2 Formulation of the Problem

Let us consider the temperature distribution in the radial direction of the m-dimensional sphere. For the sake of simplicity let us assume the sphere to be a homogeneous isotropic solid, with its thermal conductivity independent of temperature. If the rate of heat loss can become as great as the rate of heat generation, the process can become independent of time and hence a stationary solution may exist.

Under the additional assumption that the nonlinear heat generation follows an exponential law such as $f(T') = e^{\gamma' T'}$, the temperature field can be described by the following ordinary differential equation:

$$k' \frac{d^2T'}{dr'^2} + k' \frac{m}{r'} \frac{dT'}{dr'} + \alpha' f(T') = 0, \qquad 0 < r' < R' \tag{1}$$

R' denotes the radius, r' is the radial coordinate and T' the temperature of the sphere, k' is the thermal conductivity, and α' and γ' are heat generation constants. Adequate boundary conditions are that the surface is kept at a constant temperature and that the temperature gradient is zero at the center.

$$\left.\frac{dT'}{dr'}\right|_{r'=0} = 0 \text{ and } T'(R') = 0 \tag{2}$$

By scaling with the natural parameters we introduce the dimensionless variables

$$r = \frac{r'}{R'}, \quad T = \gamma' T', \text{ and } \beta = \frac{\alpha' \gamma' R'^2}{k'} \tag{3}$$

According to physical considerations β must be positive. This parameter expresses the ratio of heat generation to heat conduction. Its magnitude is a measure of the intensity of inner heat generation. Equations (1) and (2) then become

$$\frac{d^2T}{dr^2} + \frac{m}{r} \frac{dT}{dr} + \beta e^T = 0, \qquad 0 < r < 1 \tag{4}$$

$$\left.\frac{dT}{dr}\right|_{r=0} = 0 \text{ and } T(1) = 0 \tag{5}$$

Wacker (1986) solved equations (4) and (5) analytically for the one-dimensional sphere ($m = 1$, a cylinder) by using a coupled transformation $s = e^r$ and $T = U + as + b$ for the dependent and independent variables r and T, respectively. The requirements of the solution yield an upper limit for the parameter β at the value of $\beta_0 = 2$.

3 Analytical Solutions

To obtain analytical solutions with $m = 0$ and $m = 1$ we will follow the ideas of Gel'fand (1963). For convenience we rescale equation (4) to

$$\frac{d^2u}{dr^2} + \frac{m}{r} \frac{du}{dr} + \kappa e^u = 0, \qquad 0 < r < \sqrt{\lambda} \tag{6}$$

with the boundary conditions

Contributed by the Heat Transfer Division for publication in the JOURNAL OF HEAT TRANSFER. Manuscript received by the Heat Transfer Division September 12, 1988; revision received October 10, 1989. Keywords: Conduction, Numerical Methods.

$$\frac{d}{dr}u\Big|_{r=0}=0 \text{ and } u(\sqrt{\lambda})=0 \tag{7}$$

We note that $\beta = \kappa\lambda$ and introduce the boundary conditions

$$\frac{d}{dr}u\Big|_{r=0}=0 \text{ and } u(0)=\alpha \tag{8}$$

where α must be chosen to satisfy the second of conditions (7).

Let $u_0(r)$ denote a solution of equation (6) with respect to the boundary conditions (8) using $\alpha=0$. We note that differential equation (6) is invariant with respect to a group of transformations defined by

$$u(r,\ \alpha)=\alpha+u_0(re^{\alpha/2}) \tag{9}$$

and every solution of this type satisfies the boundary conditions (8).

The family of functions (9) represents all solutions of equation (6) satisfying conditions (8), and it fills only part of the u, $re^{\alpha/2}$ space, which is easily seen if we calculate the envelopes of the family. Differentiating equation (9) with respect to α and putting $u' = \partial u/\partial\alpha = 0$ (because for all fixed values of r we find the extremal points for u as a function of α and hence the envelope) gives

$$1+u_0'(re^{\alpha/2})\frac{1}{2}re^{\alpha/2}=0 \tag{10}$$

so that the envelopes are given by

$$\hat{u}(r)=u_0(R_i)+2\ln\left(\frac{R_i}{r}\right), \tag{11}$$

where R_i are the roots of the equation

$$2+u_0'(R_i)R_i=0 \tag{12}$$

3.1 Case: $m=0$. Assuming $m=0$ we achieve a solution

$$u_0(r)=-2\ln(\cosh(r)) \tag{13}$$

of equation (6) with respect to the boundary conditions (8) using $\kappa=2$.

Equation (12) assumes the form

$$1-R_i\tanh(R_i)=0 \tag{14}$$

and admits only one root $R_0 = 1.199679$. If we look for a solution of the differential equation (6) with the boundary conditions (7) we have to satisfy $u(\sqrt{\lambda_0},\ \alpha_0) = 0$ and $\hat{u}(\sqrt{\lambda_0}) = 0$, respectively; the latter condition yields $\sqrt{\lambda_0} = 0.6627434$, and the condition

$$\alpha_0=u(0,\ \alpha_0)=2\ln\left(\frac{R_0}{\sqrt{\lambda_0}}\right) \tag{15}$$

gives $u(0,\ \alpha_0) = 1.186842$. Recalling $\beta = \lambda\kappa$ we obtain $\beta_0 = 0.8784576$.

We see that no solution exists for $\beta > \beta_0$, one for $\beta = \beta_0$, and two for every $\beta < \beta_0$. To parametrize the solutions with α we remark that condition (7) gives

$$u(\sqrt{\lambda_\alpha},\ \alpha)=\alpha+u_0(\sqrt{\lambda_\alpha}e^{\alpha/2})=0 \tag{16}$$

Thus we obtain with the abbreviation $e^{\alpha/2} = C_\alpha$

$$\sqrt{\lambda_\alpha}=\frac{1}{C_\alpha}\operatorname{arccosh}(C_\alpha) \tag{17}$$

and hence

$$u(r,\ \alpha)=\alpha-2\ln\left(\cosh\left(\frac{C_\alpha}{r}\operatorname{arccosh}(C_\alpha)\right)\right) \tag{18}$$

Proposition 1 ($m=0$): *There exists a positive real number β_0 such that the differential equation (4) with the boundary conditions (5) and $m=0$ has no solution if $\beta > \beta_0$, one if $\beta = \beta_0$, and two solutions for every $0 < \beta < \beta_0$. Let $C = e^{u(0)/2}$, then*

$$u(r,\ u(0))=u(0)-2\ln\left(\cosh\left(\frac{C}{r}\operatorname{arccosh}(C)\right)\right),\qquad r\in(0,\ 1)$$

is the solution.

3.2 Case: $m=1$. We can turn now to the case $m=1$, which was investigated by Wacker (1986). We find

$$u_0(r)=-2\ln(1+r^2) \tag{19}$$

is a solution of equation (6) with the boundary conditions (8) and $\kappa = 8$. Equation (12) reads

$$2-\frac{4R_i^2}{1+R_i^2}=0 \tag{20}$$

which yields only one solution $R_0 = 1$. In a very similar way to the previous case we obtain $\sqrt{\lambda_0} = 0.5$ and $\alpha_0 = 2\ln(2)$. First of all we note that $\beta_0 = \lambda_0\kappa$ is found to be 2 and hence α_0 and β_0 take the values previously found by Wacker (1986), respectively.

In the next step we obtain an analytical representation of the continuum of solution of (4). We choose a parametrization with respect to λ to verify the analytic solution found by Wacker (1986) for the lower branch of solutions ($\alpha < 2\ln(2)$) although this cannot lead to a parametrization of the whole continuum due to the turning point at λ_0.

We define $\alpha=2\ln(1-C)$ and obtain from equation (9)

$$\begin{aligned}\hat{u}(r,\ \alpha)&=2\ln(1-C)+u_0(r(1-C))\\&=2\ln\left(\frac{1-C}{1+r^2(1-C)^2}\right)\end{aligned} \tag{21}$$

Using

$$\begin{aligned}\lambda&=e^{-\alpha}(e^{\alpha/2}-1)\\&=-\frac{C}{(1-C)^2}\end{aligned} \tag{22}$$

gives

$$C=\frac{\pm\sqrt{1-4\lambda}-1}{\pm\sqrt{1-4\lambda}+1} \tag{23}$$

and the solution as

$$\hat{u}(r,\ \alpha)=2\ln\left(\frac{1-C}{1-Cr^2/\lambda}\right),\qquad r\in(0,\ \sqrt{\lambda}). \tag{24}$$

Proposition 2 ($m=1$): *The differential equation (4) with the boundary conditions (5) and $m=1$ has no solution if $\beta > 2$, one if $\beta = 2$, and two solutions for every $0 < \beta < 2$. Let*

$$C_+=\frac{+\sqrt{1-\beta/2}-1}{+\sqrt{1-\beta/2}+1}$$

$$C_-=\frac{-\sqrt{1-\beta/2}-1}{-\sqrt{1-\beta/2}+1}$$

then

$$u(r,\ \beta)=2\ln\left(\frac{1-C_+}{1-C_+r^2}\right),\qquad r\in(0,\ 1)$$

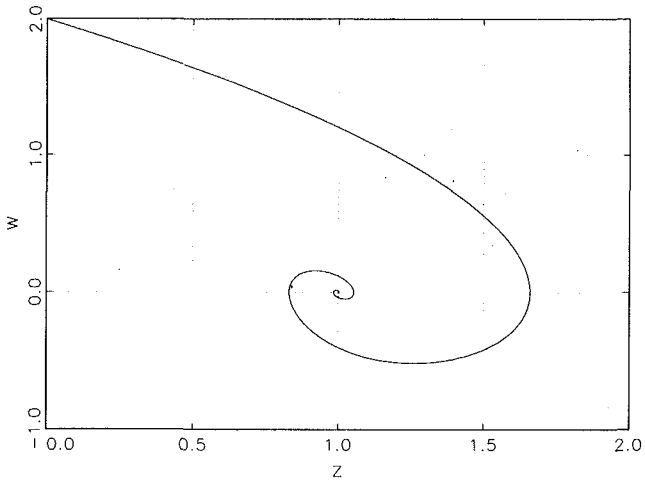

Fig. 1 Solution of equation (30), $m=2$

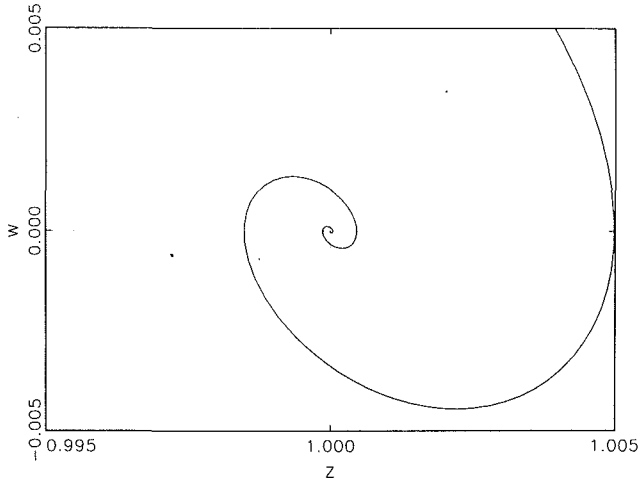

Fig. 2 Partial view of Fig. 1

is a solution on the lower branch and

$$u(r, \beta)=2\ln\left(\frac{1-C_-}{1-C_-r^2}\right), \qquad r\in(0, 1)$$

on the upper one.

3.3 Case: $m=2$, $m=3$. Let us assume $m=2$ or $m=3$. Although we do not know of an analytical solution of equation (6) with respect to the boundary conditions (8) we can obtain some information about the structure of the solution for these cases.

Applying a coupled transformation to equation (4) we put $\zeta = re^{\alpha/2}$ and get

$$\frac{d^2T}{d\zeta^2}+\frac{m}{\zeta}\frac{dT}{d\zeta}+\beta e^{T-\alpha}=0 \tag{25}$$

Defining $u = T-\alpha$ and $\xi = \sqrt{\lambda}\zeta$ gives (see equation (6))

$$\frac{d^2u}{d\xi^2}+\frac{m}{\xi}\frac{du}{d\xi}+2e^u=0 \tag{26}$$

With

$$u(\xi)=v(\xi)-2\ln(\xi) \text{ and } \eta=\ln(\xi) \tag{27}$$

we obtain

$$\frac{d^2v}{d\eta^2}+(m-1)\frac{dv}{d\eta}-2(m-1)+2e^v=0 \tag{28}$$

Introducing

$$z = \frac{1}{m-1}e^v \text{ and } w = \frac{dv}{d\eta} \tag{29}$$

yields

$$\frac{dw}{dz} = (m-1)\frac{2(1-z)-w}{zw} \tag{30}$$

We immediately see that the trajectory leaving the singular point $(z, w) = (0, 2)$ ends at the other singular point $(1, 0)$ and the trajectory circles infinitely often around this limit point. For the details on the transformation see Gel'fand (1963).

Solving equation (30) with a fourth-order Runge–Kutta method using a step size control mechanism (see Stoer and Bulirsch, 1980) we find the following trajectory (Fig. 1). The curve crosses the abscissa axis many times near the singular point (0, 1). At each point of intersection we have $w = dv/d\eta = 0$, from which the first of equations (27)

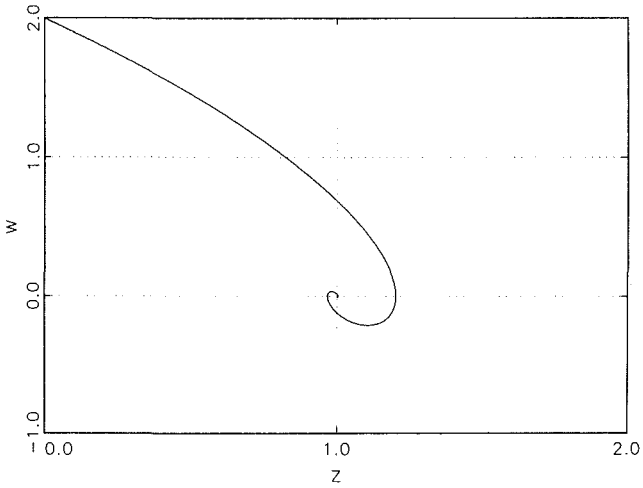

Fig. 3 Solution of equation (30), $m=3$

Table 1	
Turning point β	$\|u\|_\infty$
3.321993	1.607458
1.664160	6.740794
2.108548	11.37651
1.967469	16.16116
2.009984	20.90015

Table 2	
Turning point β	$\|u\|_\infty$
4.814696	1.861047
3.871452	5.586143
4.021075	9.197612
3.996571	12.82783
4.000570	20.08267

$$\frac{du}{d\eta}+2=0 \Rightarrow \xi\frac{du}{d\xi}+2=0 \tag{31}$$

Hence for each point of intersection equation (12) is satisfied. The family of curves (9) has an infinite number of parallel envelopes. Tracing back the transformations and using equations (11) and (9) yields a bifurcation from infinity at $\beta_\infty = 2(m-1)$. A partial plot of the trajectory for $m=2$ (Fig. 2) and one for $m=3$ (Fig. 3) are given in the subsequent figures.

The numerical calculations yield the following first turning points in the case $m=2$ (Table 1) and $m=3$ (Table 2), respectively; note that $\|u\|_\infty$ is the maximum norm defined as $\|u\|_\infty = \max_{i=1,\ldots,n}(|u_i|)$.

Proposition 3 ($m=2$, $m=3$): *There exists a positive real number β_0, such that the differential equation (4) with the boundary conditions (5) and $m=2$ or $m=3$ has no solution*

if $\beta > \beta_0$ and one solution if $\beta = \beta_0$. For every sequence u_i of solutions with $u_i(0) \to \infty$ $(i \to \infty)$ the corresponding parameters $\beta_i \to 2(m-1)$ $(i \to \infty)$.

4 Sinc Galerkin Method

All analytic function f on the real line, or on an interval, can be approximated by its Sinc function expansion

$$C(f, h)(x) = \sum_{k=-\infty}^{\infty} f(kh) S_{k,h}(x) \tag{32}$$

whenever this series converges, where $h>0$ is the step size and

$$S_{k,h}(x) = \frac{\sin[(\pi/h)(x-kh)]}{(\pi/h)(x-kh)} \tag{33}$$

In the survey papers of Stenger (1981, 1989) many remarkably accurate approximations based on Sinc function expansions can be found. Stenger reports on $(2n+1)$-point approximations of integral equations with convergence rates of $O(e^{-\alpha n^{1/2}})$, $\alpha>0$ even if the function f has singularities at the endpoints of the interval. The most important ones, especially for approximations of differential equations via Galerkin methods, are the trapezoidal rule and the approximation of derivatives.

Let $\mathfrak{D}$ be a simply connected domain with the boundary $\partial\mathfrak{D}$, a and $b \neq a$ be points of $\partial\mathfrak{D}$ and let $\mathfrak{D}_d$ be the strip $\{z \in C: -d \leq Im(z) \leq d\}$. Let $\phi(x)$ be a conformal map of $\mathfrak{D}$ onto $\mathfrak{D}_d$ such that $\phi(a) = -\infty$, $\phi(b) = \infty$. Let $\psi = \phi^{-1}$ denote the inverse map, and set $\Gamma = \{\psi(x): -\infty \leq x \leq \infty\}$.

Let $B(\mathfrak{D})$ denote the family of all analytic functions F with the property

$$\int_{\psi(u+L)} |F(z)dz| \to 0 \text{ as } u \to \pm\infty, \tag{34}$$

where

$$L = \{z \in C: -d \leq Im(z) \leq d\} \tag{35}$$

and

$$N(F, \mathfrak{D}) = \lim_{C_1 \to \delta\mathfrak{D}} \inf_{C_1 \subset \mathfrak{D}} \int_{C_1} |F(z)dz| < \infty \tag{36}$$

With the abbreviations $\phi_k = \phi(x_k)$ and $\psi_k = \psi(kh)$ the following theorems can be proved.

Theorem 1 (Stenger, 1980): *Let $F \in B(\mathfrak{D})$ and $|F(x)/\phi'(x)| \leq Ce^{-\alpha|\phi(x)|}$, $\forall x \in \Gamma$ with positive constants C and α. Using $h = [2\pi/(\alpha N)]^{1/2}$ we get*

$$\left| \int_\Gamma F(x)dx - h \sum_{k=-N}^{N} \frac{F(\psi_k)}{\phi'(\psi_k)} \right| \leq C_1 e^{-(2\pi d\alpha N)^{1/2}},$$

where C_1 depends only on F, d, and α.

Introducing a "nullifier" function g with the property that

$$\left(\frac{d}{dx}\right)^n (g(x) S_{k,h}(\phi(x))) \tag{37}$$

is bounded on Γ, for $n=0, \ldots, m$ the following statement is true.

Theorem 2 (Stenger, 1980): *Let $F\phi'/g \in B(\mathfrak{D})$ and $|F(x)/g(x)| \leq Ce^{-\alpha|\phi(x)|}$, $\forall x \in \Gamma$ with positive constants C and α. Using $h = [\pi/(\alpha N)]^{1/2}$, for all $x \in \Gamma$ we have*

$$\left| F^{(n)}(x) - \left(\frac{d}{dx}\right) \sum_{k=-N}^{N} \frac{F(\psi_k)}{g(\psi_k)} g(x) S_{k,h}(\phi(x)) \right| \leq C_2 N^{(n+1)/2} e^{-(\pi d\alpha N)^{1/2}},$$

$n=0, \ldots, m$ where C_2 depends only on m, g, d, F, and α.

To discretize a nonlinear second-order ordinary differential equation

$$D(u) = \frac{d^2u}{dr^2} + \mu(r)\frac{du}{dr} + \nu(r)u + \sigma(r, u) = 0, \qquad r \in (a, b) \tag{38}$$

with the boundary conditions

$$u(a) = \alpha \text{ and } \beta u(b) + \gamma u'(b) = \delta \tag{39}$$

we apply a Galerkin method with the approximation

$$\mathfrak{U}_N(r) = a\frac{b-r}{b-a} + \frac{\gamma\alpha + (b-a)\delta}{\beta(b-a)^3 + 2\gamma(b-a)^2} + c_{n+1}w(r) + \mathfrak{S}_N(r) \tag{40}$$

with

$$\mathfrak{S}_N(r) = \sum_{k=-N}^{N} c_j \frac{b-r}{b-a} S_{k,h}(\phi(r)), \qquad h>0 \tag{41}$$

$$\phi(x) = \ln\left(\frac{x-a}{b-x}\right) \tag{42}$$

and

$$w(r) = (r-a)\left[1 - \frac{\{\beta(b-a)+\gamma\}(r-a)}{\beta(b-a)^2 + 2\gamma(b-a)}\right] \tag{43}$$

The evaluation of the Galerkin equations for the differential equation (38) with the test functions $(b-r)/(b-a)S_{k,h}(\phi(r))$, $k = -N, \ldots, N$, and the scalar product

$$(\psi, \varphi) = \int_a^b \psi(x)\varphi(x)(x-a)dx \tag{44}$$

yields

$$\begin{aligned}
&\int_a^b D(\mathfrak{U}_N(r)) \left(\frac{b-r}{b-a}\right) S_{k,h}(\phi(r))(r-a)dr \\
&= \frac{1}{b-a}\int_a^b D(\mathfrak{U}_N(r))(b-r)S_{k,h}(\phi(r))(r-a)dr \\
&= c_{n+1}\int_a^b [w''(r) + \mu(r)w'(r) + \nu(r)w(r)]S_{k,h}(\phi(r))\frac{dr}{\phi'(r)} \\
&\quad + \int_a^b \mathfrak{S}_N(r)\frac{d^2}{d\tau^2}\left[\frac{1}{\phi'(\tau)} S_{k,h}(\phi(\tau))\right]_{\tau=r} dr \\
&\quad - \int_a^b \mathfrak{S}_N(r)\frac{d}{d\tau}\left[\frac{\mu(\tau)}{\phi'(\tau)} S_{k,h}(\phi(\tau))\right]_{\tau=r} dr \\
&\quad + \int_a^b \mathfrak{S}_N(r)\nu(r)S_{k,h}(\phi(r))dr \\
&\quad + \int_a^b \sigma(r, \mathfrak{U}_N(r))S_{k,h}(\phi(r))dr
\end{aligned} \tag{45}$$

By applying the trapezoidal rule we derive the approximation

$$\begin{aligned}
&\int_a^b D(\mathfrak{U}_N(r)) \left(\frac{b-r}{b-a}\right) S_{k,h}(\phi(r))(r-a)dr \\
&= \frac{1}{b-a}\int_a^b D(\mathfrak{U}_N(r))(b-r)S_{k,h}(\phi(r))(r-a)dr \\
&\approx c_{n+1}h\,[w_k'' + \mu_k w_k' + \nu_k w_k]\left(\frac{1}{\phi_k'}\right)^2 \\
&\quad + h\sum_{j=-N}^{N} c_j \frac{b-r_j}{b-a}\frac{1}{\phi_j'}\left[\left(\frac{d^2}{d\tau^2} - \frac{d}{d\tau}\mu(\tau) + \nu(\tau)\right)\left(\frac{1}{\phi'(\tau)} S_{k,h}(\phi(\tau))\right)\right]_{\tau=r_j} \\
&\quad + h\frac{\sigma(r_k, \mathfrak{U}_N(r_k))}{\phi_k'^2}
\end{aligned} \tag{46}$$

With the test function $w(r)$ we obtain

$$
\begin{aligned}
&(D(\mathfrak{U}_N),\ w)\\
&= \int_a^b D(\mathfrak{U}_N(r))\, w(r)\,(r-a)\,dr\\
&= c_{n+1}\int_a^b [w''(r)+\mu(r)w'(r)+\nu(r)w(r)]w(r)\,(r-a)\,dr\\
&+ \int_a^b \mathcal{S}_N(r)\,\frac{d^2}{d\tau^2}\,[w(\tau)\,(\tau-a)]_{\tau=r}\,dr\\
&- \int_a^b \mathcal{S}_N(r)\,\frac{d}{d\tau}\,[\mu(\tau)w(\tau)\,(\tau-a)]_{\tau=r}\,dr\\
&+ \int_a^b \mathcal{S}_N(r)\nu(r)w(r)\,(r-a)\,dr\\
&+ \int_a^b \sigma(r,\ \mathfrak{U}_N(r))\,w(r)\,(r-a)\,dr\\
&\approx c_{n+1}\int_a^b [w''(r)+\mu(r)w'(r)+\nu(r)w(r)]w(r)\,(r-a)\,dr\\
&+ h\sum_{j=-N}^{N} c_j\,\frac{b-r_1}{b-a}\,\frac{1}{\phi_j'}\left[\left(\frac{d^2}{d\tau^2}-\frac{d}{d\tau}\,\mu(\tau)\right.\right.\\
&\qquad\left.\left.+\nu(\tau)\right)(w(\tau)\,(\tau-a))\right]_{\tau=r_j}\\
&+ \int_a^b \sigma(r,\ \mathfrak{U}_N(r))\,w(r)\,(r-a)\,dr \qquad (47)
\end{aligned}
$$

We introduce the abbreviations $r_j = \psi(jh)$, $w_j = w(r_j)$, and

$$\delta_{jk}^{(n)} = S_{j,1}^{(n)}(k) = \frac{d^n}{dx^n}\,S_{j,1}(x)\,|_{x=k} \qquad (48)$$

in particular

$$\delta_{jk}^{(0)} = \begin{cases} 1 & \text{if } j=k \\ 0 & \text{if } j\neq k \end{cases} \qquad (49)$$

$$\delta_{jk}^{(1)} = \begin{cases} 0 & \text{if } j=k \\ \dfrac{(-1)^{k-j}}{\mathrm{k-j}} & \text{if } j\neq k \end{cases} \qquad (50)$$

$$\delta_{jk}^{(2)} = \begin{cases} -\pi^2/3 & \text{if } j=k \\ -\dfrac{2(-1)^{k-j}}{(k-j)^2} & \text{if } j\neq k \end{cases} \qquad (51)$$

and define the functions

$$
\begin{aligned}
\zeta_k(r_j) &= \frac{b-r_i}{b-a}\,\frac{1}{\phi_j'}\left[\left(\frac{1}{\phi_j'}\right)'' - \left(\frac{\mu_j}{\phi_j'}\right)' + \frac{\nu_j}{\phi_j'}\right]\delta_{jk}^{(0)}\\
&+ \left[\left(\frac{1}{\phi_j'}\right)' - \frac{\mu_j}{\phi_j'}\right]\frac{\delta_{jk}^{(1)}}{h} + \frac{\delta_{jk}^{(2)}}{h^2}, \qquad k=-N,\ \ldots,\ N \qquad (52)
\end{aligned}
$$

$$
\begin{aligned}
\eta(r_j) = \frac{b-r_i}{b-a}\,\frac{1}{\phi_j'}\,&[w_j''\ (r_j-a)+2w_j'\\
&-\mu_j' w_j(r_j-a)-\mu_j w_j'(r_j-a)-\mu_j w_j+\nu_j w_j(r_j-a)] \qquad (53)
\end{aligned}
$$

to obtain

$$
\begin{aligned}
&\int_a^b D(\mathfrak{U}_N(r))\left(\frac{b-r}{b-a}\right)S_{k,h}(\phi(r))\,(r-a)\,dr\\
&\qquad \approx c_{n+1}h[w_k''+\mu_k w_k'+\nu_k w_k]\left(\frac{1}{\phi_k'}\right)^2\\
&\qquad + h\sum_{j=-N}^{N} c_j\zeta_k(r_j) + h\,\frac{\sigma(r_k,\ \mathfrak{U}_N(r_k))}{\phi_k'^2} \qquad (54)
\end{aligned}
$$

and

$$
\begin{aligned}
&\int_a^b D(\mathfrak{U}_N(r))\,w(r)\,(r-a)\,dr\\
&\approx c_{n+1}\int_a^b [w''(r)+\mu(r)w'(r)+\nu(r)w(r)]w(r)\,(r-a)\,dr\\
&\quad + h\sum_{j=-N}^{N} c_j\eta(r_j) + \int_a^b \sigma(r,\ \mathfrak{U}_N(r))\,w(r)\,(r-a)\,dr \qquad (55)
\end{aligned}
$$

Equations (54) and (55) are the Sinc Galerkin equations for the differential equation (38) with the boundary conditions (39). This system of nonlinear equations for the unknowns $c_{-N}, \ldots, c_{N+1}$ defines the approximate solution of the nonlinear second-order differential equation given by equation (38). The numerical method used to solve the system of nonlinear equations will be briefly described in the next section.

5 Following the Path

To obtain solutions on the whole arc we apply a multiple-continuation procedure (Lippke, 1985, 1989). The proposed algorithm (*MultiCon*) solves the nonlinear equation $F(\mathbf{x},\ \mu) = 0$, $\mathbf{x} \in \mathbb{R}^n$, $\mu \in \mathbb{R}^m$, $F{:}\mathbb{R}^n \times \mathbb{R}^m \to \mathbb{R}^n$ with multiple parameters μ by a combination of Newton's method and a piecewise linear continuation algorithm to achieve a fast and reliable procedure. The *MultiCon* program has been developed especially for problems with turning points and bifurcation points of odd multiplicity.

The application of Newton methods is common and leads to reliable procedures if the continuum of solutions is sufficiently smooth and the different arcs are well separated. Difficulties arise at turning and bifurcations points due to singular Jacobian matrices and special care has to be taken to prevent the algorithm from falling back on the wrong arc at turning points. These problems can be solved by combination with a piecewise linear algorithm.

Piecewise linear solvers (Peitgen and Prüfer, 1978) were introduced to numerical mathematics by a constructive proof of the Brouwer fixed point theorem. To derive a numerical procedure the domain of the function F is triangulated by simplices and the function approximated by a piecewise linear approximation. If the mesh size of the triangulation is sufficiently small the completely labeled simplices carry the solution continuum of F.

To overcome the poor performance and limitations of fixed piecewise linear algorithm, predictor-corrected techniques were applied by Saupe (1982). The resulting procedure is superior to all piecewise linear algorithms and the performance on highly curved arcs is of the same magnitude as Newton pathfollowing techniques.

The *MultiCon* algorithm combines the benefits of both algorithms. A predictor-corrector piecewise linear algorithm is applied in highly curved regions and adjacent to turning or bifurcation points. If the predictor step falls under a certain limit a piecewise linear procedure with a fixed K-type triangulation is applied. In regions of moderate incline the Newton-continuation method is adopted and a Newton-corrector is applied as a post-processor to achieve high accuracy if convergence is obtained.

By this efficient combination of the very stable but slow piecewise linear algorithm with Newton procedures a highly stable, efficient, and reliable procedure is established.

6 Numerical Solution of the Two-Point Boundary Value Problem

Applying the approximation (40) to equations (4) and (5) yields

$$\mathfrak{U}_N(r) = c_{n+1}\,\frac{1}{2}\,(r^2-1) + \mathcal{S}_N(r) \qquad (56)$$

with

$$S_N(r) = \sum_{k=-N}^{N} c_j r S_{k,h}(\phi(r)), \qquad h>0 \tag{57}$$

$$\phi(r) = \ln\left(\frac{r-1}{r}\right) \tag{58}$$

and equations (54) and (55) imply

$$\int_a^b D(\mathfrak{U}_N(r)) S_{k,h}(\phi(r)) r dr$$

$$\approx c_{n+1} h(1+m)\left(\frac{1}{\phi_k'}\right)^2 + h\sum_{j=-N}^{N} c_j r_j$$

$$\left[r_j(r_j-1)(2-m)\delta_{jk}^{(0)} + (2r_j - 1 - m(r_j-1))\frac{\delta_{jk}^{(1)}}{h} + \frac{\delta_{jk}^{(2)}}{h^2}\right]$$

$$+ h\frac{\sigma(r_k, \mathfrak{U}_N(r_k))}{\phi_k'^2}, \qquad k=-N, \ldots, N, \tag{59}$$

and

$$\int_a^b D(\mathfrak{U}_N(r)) w(r) r dr$$

$$\approx c_{n+1}\frac{(1+m)}{2}\int_1^0 (r^2-1)(r-1)dr$$

$$+ h\sum_{j=-N}^{N} c_j\left[r_j^2(r_j-1)^2 + 2r_j^3(r_j-1) + \frac{m}{2}(r_j^2-1)(r_j-1)^2\right.$$

$$\left. - m r_j^2(r_j-1)^2 - \frac{m}{2} r_j(r_j^2-1)(r_j-1)\right]$$

$$+ \int_1^0 \sigma(r, \mathfrak{U}_N(r)) w(r)(r-1)dr \tag{60}$$

Evaluation of the nonlinear term with the test functions $rS_{k,h}(\phi(r))$, $k = -N, \ldots, N$ in the scalar product (44) yields

$$\int_a^b e^{\mathfrak{U}_N(r)} S_{k,h}(\phi(r)) r dr \approx h e^{\mathfrak{U}_N(r_k)}\left(\frac{1}{\phi_k'}\right)^2 \tag{61}$$

To integrate the product of the nonlinear term and the test function $\frac{1}{2}(r^2-1)$ we apply a Gauss integration formula with nine points.

7 Results

The discrete equations (59)–(61) have been solved as a two parameter problem $F(\mathbf{u}, \beta, h) = 0$ for various numbers of unknowns ($N = 3, \ldots, 24$). The discrete residuals in maximum norm are of magnitude 10^{-12} if the Newton post-processor converges and of magnitude 10^{-8} if this is not achieved. To show the dependence of the approximation accuracy on the control parameter h, mentioned above, we plotted the maximum difference between the analytic solution and the numerical solution for $m = 1$ and $\beta = 1$ (Fig. 4). In this special case the optimal value of h is easily calculated from the analytic solution and is found to be in good agreement to the numerically determined one.

All solutions are calculated using $N = 12$ and $h = 0.875$. The norm diagram given in Fig. 5 for the one-dimensional sphere (cylinder) $m = 1$ is in good agreement with the analytical solution found in Proposition 2. It additionally shows the absolute error enlarged by a factor of 10^3 (marked with ∇). Table 3 gives the numerical and the analytical values at the turning point for the one-dimensional problem.

Figure 6 gives the norm diagram for the two-dimensional sphere using the same number of unknowns and the same value of the parameter h. In addition, Table 4 gives the numerical values of the turning points. Here we can only compare the numerical results with those found in Section 3.3.

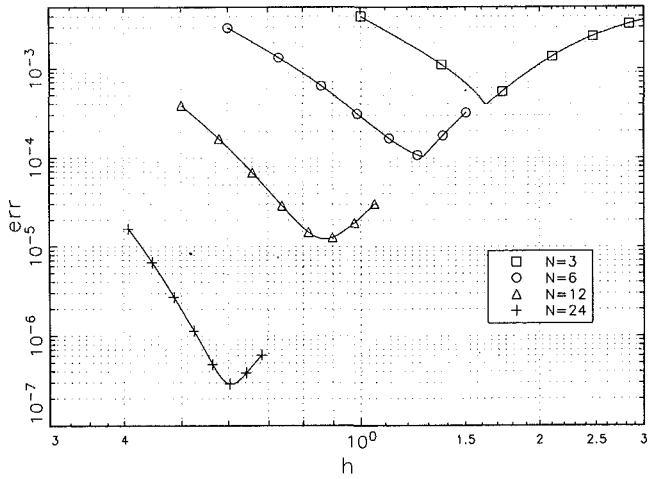

Fig. 4 Absolute error versus control parameter h, $m=1$

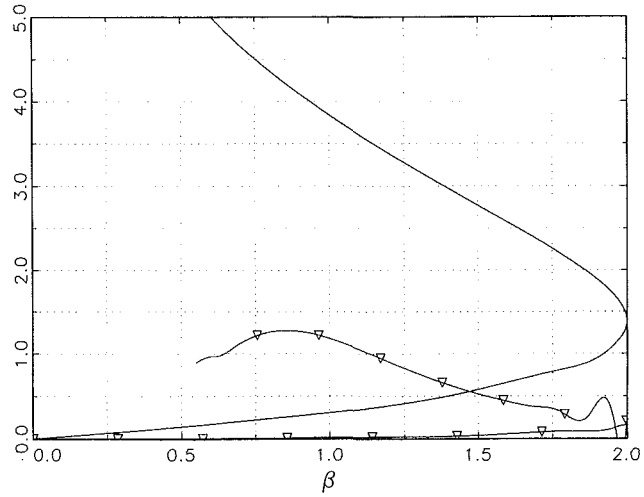

Fig. 5 Maximum norm of the solution versus β, $m=1$

Table 3			
	Numerical value	Analytical value	Relative accuracy
β_0	2.000000	2.0	$\approx 10^{-7}$
$\|u\|_\infty$	1.384340	2.0ln(2.0)	1.4E−3

All numerical work has been carried out on an IBM-AT personal computer and a Norsk Data ND-540 at the Technische Universität Berlin with the PC and the Mainframe version of the MultiCon procedure using a double precision arithmetic (Lippke, 1985).

8 Summary

In the first part of the paper analytical solutions of the nonlinear heat conduction with exponential heat generation are calculated. These analytic solutions include those which are not stable and hence not observed in the laboratories.

The second part gives a Sinc function approximation of the solution of a more general nonlinear second-order differential equation that includes, e.g., various nonlinearities and coefficient functions. The approximation is highly accurate with

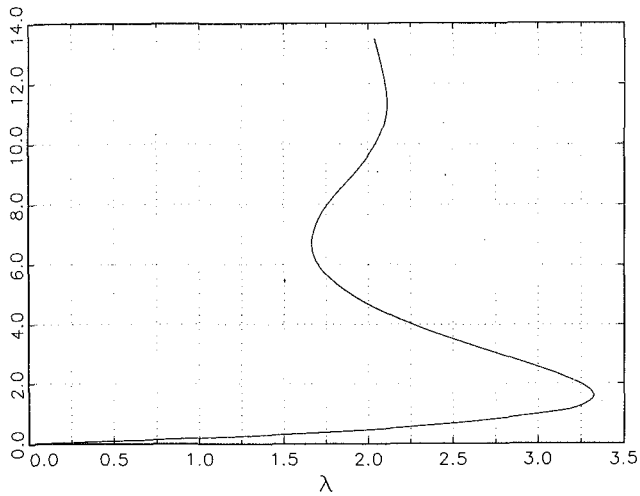

Fig. 6 Maximum norm of solution versus β, $m=2$

a discretization error of order $Ne^{\sqrt{N}}$ for a number of $2N+2$ unknowns. Therefore the discretization error is close to the best possible one and especially much better than the polynomial error expansions of the standard methods.

In the last part of the paper the approximation is applied to the problem mentioned above and solutions are calculated numerically with a continuation method for the whole arc, including the unstable solutions. The numerically determined solutions are compared with the analytical ones, derived in the first part, to verify the high accuracy of the approximation. The maximum of the difference between the analytical and the numerical solution is approximately 2.0E−7, using 50 unknowns in the calculation.

9 Conclusions

The Sinc function approximation proposed and applied in this paper leads to very accurate solutions of the nonlinear second-order differential equation for the thermal conduction with exponential heat generation. With the method all solutions of the problem are calculated and compared with the analytical solutions. The numerical method is applicable to a wide class of nonlinear second-order differential equations including those coefficient functions with singularities at the endpoints of the interval.

Table 4

	Numerical value	Section (3.3)	Relative accuracy
β_0	3.322042	3.321993	4.7E−4
$\|u\|_\infty$	1.607755	1.607458	1.9E−4
β_1	1.664782	1.664160	3.7E−4
$\|u\|_\infty$	6.689171	6.740794	7.6E−3
β_2	2.109319	2.108548	3.7E−4
$\|u\|_\infty$	11.31217	11.37651	5.7E−3

References

Copple, C., Hartrée, D. R., Porter, A., and Tyson, H., 1935, "The Evaluation of Transient Temperature Distribution in a Dieletric in an Alternating Field," *J. Inst. of Elec. Engs.*, Vol. 85, pp. 56–66.

Gel'fand, I. M, 1963, "Some Problems in the Theory of Quasilinear Equations," *Trans. AMS*, Vol. 29, pp. 295–381.

Lippke, A., 1985, "Kontinuitätsmethoden und schnelle elliptische Löser bei zähen Strömungen," Dissertation, Technische Universität Berlin, Federal Republic of Germany.

Lippke, A., 1988, "Multiple Solutions for Nonlinear, One- and Two-Dimensional Thermal Conduction With Exponential Heat Generation," *Z. angew. Math. Mech.*, Vol. 68, pp. 252–255.

Lippke, A., 1989, "An Efficient Continuation Algorithm," Preprint 194, Technische Universität Berlin, Federal Republic of Germany.

Na, T. Y., and Tang, S. C., 1969, "A Method for the Solution of Conducting Heat Transfer With Nonlinear Heat Generation," *Z. angew. Math. Mech.*, Vol. 49, pp. 45–52.

Peitgen, H.-O., and Prüfer, M., 1978, "The Leray-Schauder Continuation Method Is a Constructive Element in the Numerical Study of Nonlinear Eigenvalue and Bifurcation Problems," *Approximation of Fixed Points*, H.-O. Peitgen and H.-O. Walther, eds., Springer-Verlag, Bonn, Federal Republic of Germany.

Rice, J., 1940, "The Role of Heat Conduction in Thermal Gaseous Explosions," *J. Chem. Phys.*, Vol. 8, pp. 727–733.

Saupe, D., 1982, "On Accelerating PL Continuation Algorithms by Predictor-Corrector Methods," *Math. Progr.*, Vol. 23, pp. 87–110.

Stenger, F., 1981, "Numerical Methods Based on Whittaker Cardinal, or Sinc Functions," *SIAM Review*, Vol. 23, pp. 165–224.

Stenger, F., Lund, J., and Bowers, K. L., 1989, "Development and Direction of the Sinc-Galerkin Method for Differential Equations," to be published.

Stoer, J., and Bulirsch, R., 1980, *Introduction to Numerical Analysis*, Springer-Verlag, Berlin.

Wacker, D., 1986, "A Contribution for Nonlinear, One-Dimensional Thermal Conduction With Exponential Heat Generation," *Z. angew. Math. Mech.*, Vol. 66, pp. 378–379.

Laser-Induced Heating of a Multilayered Medium Resting on a Half-Space: Part II—Moving Source

R. Kant

K. L. Deckert

IBM Research Division,
Almaden Research Center,
San Jose, CA 95120-6099

Direct access storage devices (DASDs) are widely used in the computer industry to store and manage data. In conventional magnetic recording, an induction head flying very close to the disk surface alters the polarization of the magnetic field of the disk surface to erase and/or write the information on the disk. However, a new technology known as magneto-optical recording or optical recording has considerable promise to increase data densities and reliability of data storage. In magneto-optical storage, magnetic fields are altered by a laser source, which heats the magnetic medium beyond its Curie point, a temperature at which the magnetic medium loses its magnetization. This domain with zero magnetization is subsequently reversed by using an induction magnet. All these processes take place when the disk is rotating at a very high speed with respect to the laser source. An optical disk is a multilayered medium consisting of a thick glass disk on which many layers of different materials are sputtered, only one layer of which serves as a magnetic medium. Therefore, in this paper, a problem of laser-induced heating of a multilayered medium resting on a half-space is considered when the laser is translating with respect to it. The transient heat conduction equation is solved by employing the Laplace transform in the time domain and the Fourier Transform in the x, y dimensions. The resulting ordinary differential equation is solved and the inversion of the Laplace transform is obtained by a technique developed by Crump. The Fourier inversion is obtained by using a Fast Fourier Transform. The technique developed here is then applied to calculate domain size for recorded bits for a given disk, laser power, source characteristics, and rotational velocity.

Introduction

Current DASDs (Direct Access Storage Devices) or disk drives, as they are commonly known, record data by changing the magnetic state of disks coated with some magnetic material. Technologies involved in magnetic recording technology require high precision in manufacturing. Even though the areal densities can be significantly increased from their present values, it would require that the slider be flown at very low flying heights (a few nanometers above the disk surface). However, lower flying heights require a near-perfect surface finish and hold extremely tight tolerances on the slider. Disk drives with magneto-optical storage technology have a storage density of up to 2000 megabits per square inch of the disk surface as opposed to about 300 megabits per square inch for the current magnetic storage drives. Magneto-optical drives are more forgiving in the area of head disk interface. Designers have more room to work with and these drives are very compact.

In magneto-optical recording, an optical disk is initially magnetized in one direction. To write on such a disk, a laser (650 to 1000 nanometer in wavelength) spot heats it to its Curie point, the temperature at which the medium loses its magnetization. The disk consists of a multilayered medium sputtered on a glass substrate. As the spot cools, it is magnetized in the direction opposite to the rest of the medium (Fig. 1).

To read the recorded bits, the same laser, now operating at diminished power, bounces a polarized beam off of the disk surface, through an objective lens, into a photo-detector. The reversal of the magnetization in the recorded bit causes the plane of polarization of the reflected light to rotate slightly, a phenomenon known as the Kerr effect (Fig. 2). This change is detected and the recorded bit is identified. These spots with changed magnetic properties spaced between segments of a track with unchanged magnetic properties provide a basis for binary code (Ohr, 1985). Erasure is a duplication of the writing process, except the applied field is reversed to obtain uniform magnetization. All these processes take place while the disk is rotating at a very high speed with respect to the laser.

Apart from reading and writing processes in the magneto-optical recording, the problem considered here is also important from the heat conduction in composites viewpoint. Numerous approaches have been taken to study heat conduction problems in composites, such as the sophisticated continuum mixture theory (Nayfeh, 1978) on one hand, to simple procedures that approximate a heterogeneous medium to an "equivalent" medium (Christensen, 1979), on the other. These theories, although useful in some applications, impose enough constraints to preclude their application to the problems of practical interest. Some of these problems are discussed here. In a previous paper, the author (Kant, 1988) has presented a solution of a similar problem when the source was stationary.

The computer industry has long been known for pioneering the use of thin films. Current computer products such as memory chips, magnetic disks, magneto-optical disks, optical disks

Contributed by the Heat Transfer Division for publication in the JOURNAL OF HEAT TRANSFER. Manuscript received by the Heat Transfer Division December 13, 1988; revision received May 29, 1990. Keywords: Laser Processing, Transient and Unsteady Heat Transfer.

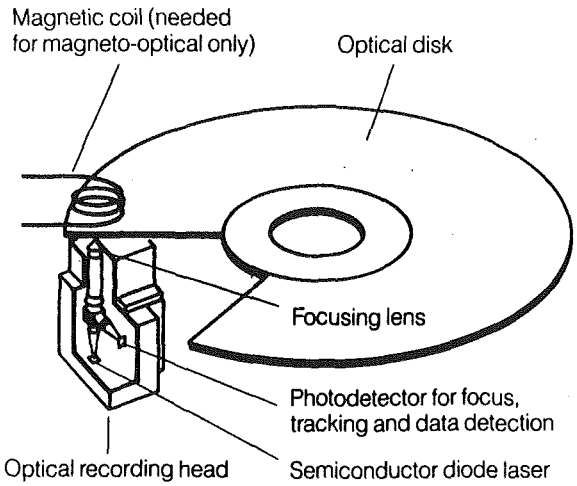

Fig. 1 Schematic of the magneto-optical disk drive

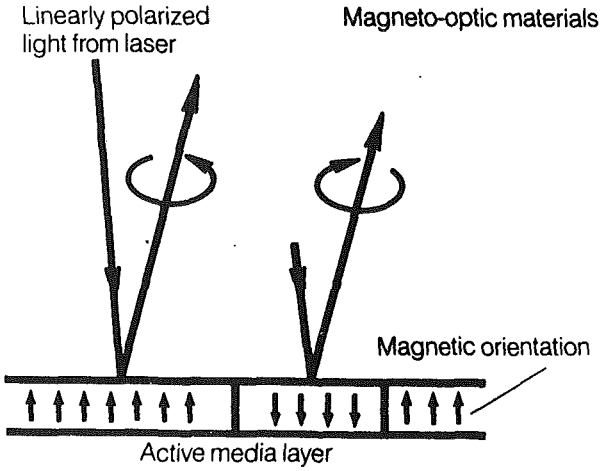

Fig. 2 The Kerr effect

(used in a type of recording process based on the phase change at selected spots), magnetic recording heads, etc., contain thin films. With the increase of the use of thin films in commercial products, it has become extremely important to obtain information on their physical properties. Very little, if any, reliable information exists for numerically verifying the data gathered by the experimentalists. Many of these methods are based on the solution of the heat conduction equation in one dimension and some of these methods are extremely crude. Rosencwaig et al. (1980) have solved one-dimensional heat equation in a three-layered composite and their method remains the standard method in pyroelectric calorimetry. Other than the fact that this solution is one-dimensional, this method is sound. Mandelis et al. (1985) have repeated the above method almost entirely. Skumanich et al. (1987) have considered the same one-dimensional approach and concluded that the substrate effects are not important.

This problem is also attempted by Iravani and Wickramsinghe (1985). In a nearly similar treatment (Kant, 1988), Iravani and Wickramsinghe assume that the source term is harmonic in time and consequently the temperature at any plane parallel to $z=0$ is harmonic. This simplifies the problem considerably. It is difficult to comment on the applicability of their method to the problem under consideration. However, it can be pointed out that the frequency of the material response to a harmonic thermal excitation will necessarily be different, depending upon the material characteristics and configuration. Therefore, in the opinion of the present authors, the assumption is restrictive and has been removed. Furthermore, the results of Iravani and Wickramsinghe (1986), especially Fig. 10, indicate that the cooling process after the source is turned off is discontinuous in the sense that it is slower in the beginning and faster later on. It can be argued on physical grounds that (by Newton's law of cooling) the initial cooling rate must be faster than the later. Results presented here do not indicate such behavior.

The importance of numerical solutions of this problem must also be pointed out. Tsai and Rubinsky (1984), Shin (1986), and Salcudean et al. (1986) have attempted these problems. Salcudean et al. use explicit and implicit finite difference methods and Rubinsky uses a so-called "front tracking," finite element method. Shin has used explicit finite-difference technique to solve this problem numerically. These solutions are very useful. As a word of caution, we might add that due to the very fine layered structure of the medium used in optical recording, these methods consume excessive cpu times even on very fast machines. As mentioned earlier, the purpose of this paper is to design operating parameters for magneto-optical recording; that is, to calculate the bit size given the medium, relative velocity of the laser with respect to the medium, and the laser power. It is also important to determine how close the laser pulses can be and still have two distinct regions, with changed magnetization at the desired separation.

In this paper, we discuss two pulse sequences for a medium typically used in the magneto-optical recording and show that one pulse produces spots that are merged and the other produces distinct spots. In addition, to be able to produce two distinct regions on the same track, it is also important to achieve desired track separation. Depending upon the code to be written, sometimes it is necessary to write long bits of data on the same track. If these bits are written with one long pulse, the net effect is that the bits so produced have variable size in the track width direction. This causes an intertrack cross-talk (as opposed to on-track cross-talk, which is produced when two bits are merged or not sufficiently far apart on the same track). To achieve this desired track separation, one must modulate the laser power during the period in which one long sequence of bits is written. This can be accomplished either by contin-

Nomenclature

x, y, z = Cartesian coordinates
$u_i(x, y, z, t)$ = temperature in ith layer at time t
κ_i, c_i, ρ_i = Fourier coefficient of heat conduction, specific heat, and density of ith layer
h_i = thickness of ith layer
α_i = diffusivity of ith layer
q = source strength
ρ_N = reflectance at the Nth interface
a_N = absorptance of Nth active layer
c_x, c_y = relative velocity of disk with respect to source
v_x, v_y = parameters characterizing Gaussian profile of laser
$\hat{\epsilon}$ = complex dielectric tensor of active layer
κ = extinction coefficient
$\hat{n}$ = complex refractive index of the active layer

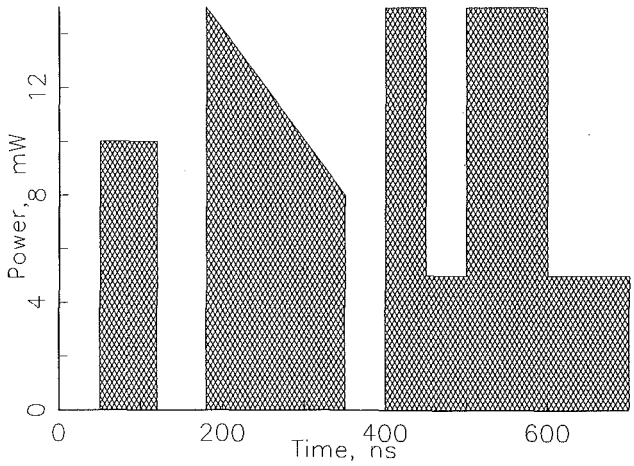

Fig. 3 Typical laser pulses used in optical recording

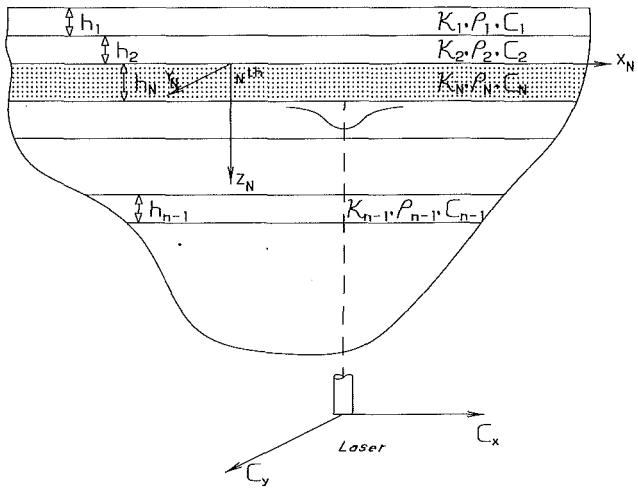

Fig. 4 Geometry of the problem and the coordinate system

uously varying the power or adjusting the power in steps (see t_3–t_4 or t_5–t_9 in Fig. 3). The former is difficult to achieve with the present hardware. Using the approach discussed here, we determine a pulse that writes a sequence that does not produce intertrack cross-talk.

Statement of the Problem

As we have mentioned earlier, optical disks consist of a layered medium sputtered on a thick glass substrate. Only one of these layers, the M-O or the so-called active layer actually contains the recorded data. We assume that all the other layers besides the active layer are optically transparent. A moving laser of Gaussian profile illuminates the optical disk from the substrate direction and is perpendicular to the disk. With this configuration, we further assume that the ith layer has its own coordinate system, embedded in it in such a way that the positive z_i-direction points into the substrate and the plane formed by the x_i, y_i directions coincides with the surface whose z_i coordinate is assigned the value $z_i=0$. Within each layer the value of $z_i \geq 0$ (see Fig. 4).

With the coordinate systems defined above, we consider a medium consisting of $(n-1)$ layers resting on a half-space. One of these layers, say the Nth, is designated to be the active layer. In view of the comment above on the coordinate system used in the problem, it is assumed that the temperature and flux boundary conditions are evaluated at appropriate values of the z coordinate. A moving laser pulse of varying intensity produces a flux of heat energy across the planes $z_N=0$ and $z_N=h_N$. The problem is to find the temperature field $u_i(x, y, z, t)$ that satisfies the equation

$$\frac{\partial^2 u_i}{\partial x^2}+\frac{\partial^2 u_i}{\partial y^2}+\frac{\partial^2 u_i}{\partial z^2}=\frac{1}{\alpha_i}\frac{\partial u_i}{\partial t} \tag{1}$$

where

$$\alpha_i=\frac{\kappa_i}{\rho_i c_i} \qquad i=1, \ldots, n$$

and the following initial, regularity, boundary, and continuity conditions

$$u_i(x, y, z, 0) \text{ and } u_i(x, y, z, t) = 0 \text{ as } |r| \to \infty \quad i=1, \ldots, n \tag{2}$$

$$\kappa_1 \frac{\partial u_1}{\partial z}=0 \text{ at } z_1=0 \tag{3}$$

Equation (3) implies that the top layer also acts as an insulator and no heat escapes from the top surface. This assumption is made for simplicity; however, the mathematical analysis presented here can accommodate any given heat flux at the boundary.

$$u_i=u_{i+1} \qquad i=1, \ldots, n-1$$

$$\kappa_i \frac{\partial u_i}{\partial z}=\kappa_{i+1}\frac{\partial u_{i+1}}{\partial z} \qquad i=1, \ldots, n-1,\ i\neq N \tag{4}$$

When $i=N$, the following conditions hold:

$$\left.\begin{aligned}\kappa_{N-1}\frac{\partial u_{N-1}}{\partial z}-\kappa_N\frac{\partial u_N}{\partial z}&=0\\ \kappa_N\frac{\partial u_N}{\partial z}-\kappa_{N+1}\frac{\partial u_{N+1}}{\partial z}-(1-\rho_{N+1})a_N q&=0\end{aligned}\right\} \tag{5}$$

$N-1$, N, and $N+1$ correspond to the layer immediately above the active layer, the active layer, and the layer immediately below the active layer. The quantity ρ_{N+1} represents coefficient of reflectance for the surface $N+1$ while a_N is the coefficient of absorptance for the active layer. In optical recording, Tb_xFe_{1-x} is commonly used as a recording medium. The intensity absorptance in a layer depends on the optical properties of the metal film and its configuration in the layered structure (Born and Wolf, 1980). Allen and Connell (1982) have evaluated the optical properties of amorphous terbium-iron ($x=0.21$) compound. By using ellipsometry, these authors have reported values of the complex dielectric tensor, $\hat{\epsilon}=Re\hat{\epsilon}+Im\hat{\epsilon}$, as a function of wavelength of incident light. From these values, the complex refractive index $\hat{n}=n(1+i\kappa)$, in which κ is the extinction coefficient, are evaluated by the relations (Born and Wolf, 1980, Chap. 13):

$$n^2-n^2\kappa^2=Re\hat{\epsilon} \tag{6}$$

$$n^2\kappa=Im\hat{\epsilon}$$

Next, we calculate the intensity transmittance for a terbium-iron layer as a function of its thickness when it is situated between two dielectric media, a configuration often used in optical recording. The intensity transmittance denotes the percentage of light transmitted into the final medium. In Fig. 5, we show the transmittance for the case used in this paper (see Table 2). Here the active layer is sandwiched between two layers of sputtered SiO_2 and a glass substrate. Since refractive indices of the glass and sputtered SiO_2 are roughly equal and both are nonabsorbing media, we have used a trilayer model (Gray, 1963, Chap. 6) to evaluate the transmittance. In Fig. 5, it is

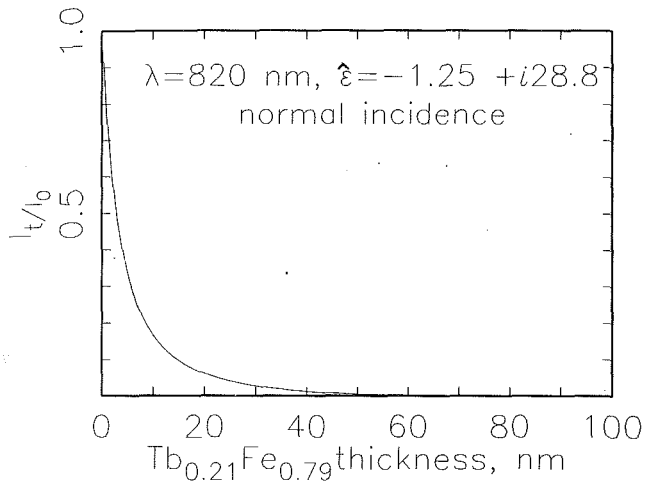

Fig. 5 Intensity transmittance for terbium-iron at normal incidence

seen that the intensity is extinguished to $\frac{1}{e}$ in the first 4 nm of the medium which is typically 5 percent of the total thickness of the active layer. Furthermore, Fig. 5 also shows that the transmittance of the terbium-iron layer approaches zero at about 40 nm, which is less than the thickness of the active layer for the example presented in this paper; thus the coefficient absorptance a_N is taken to be 1. Therefore, in equation (5) we have assumed that the entire heat energy absorbed in the active layer is expressed as the flux at the interface of the active layer. Other authors have also used this assumption (see for example, Burgner and Reedy, 1982). The reflectance ρ_{N+1} can similarly be evaluated by using expressions given by Gray (1963). Bell (1986) has experimentally evaluated the reflectance for a terbium-iron layer and has found that it is about 20 percent for a configuration typically used in optical recording. In equation (5), it is further assumed that the light is incident on the $N+1$th interface of the layered medium. In equation (5), the source is characterized by the equation

$$q = p(t)\exp-\left\{\frac{(x-c_x t)^2}{v_x^2} + \frac{(y-c_y t)^2}{v_y^2}\right\} \tag{7}$$

where c_x and c_y are the components of the local velocity of laser beam in the x and y directions, respectively; v_x and v_y characterize the laser profile.

For the analysis in this paper, all functions are assumed to belong to the class $L^2(-\infty, \infty)$ of functions whose squares are integrable in the sense of Lebegue. With this assumption, the transforms and integrals discussed are known to exist (Miles, 1971; Sneddon, 1951).

The time-dependent amplitude, $p(t)$. of the source q, can be quite general; however, in the optical recording q is usually a pulsating laser that can be represented by taking a sequence of step functions of varying amplitude. Suppose t_j for $j=1, 2, \ldots$ is a sequence of successive on-off times, then

$$p(t) = \begin{cases} p_k & t_{2k-1} \le t < t_{2k} \\ 0 & t_{2k} \le t < t_{2k+1} \end{cases} \tag{8}$$

for $k=1, 2, \ldots$ (see Fig. 3). In equations (1)–(6), the subscript i on the variables x, y, z referring to the coordinate system attached to each layer is dropped for simplicity. Equations (4) are continuity conditions for the temperature and the flux, respectively, at layer interfaces. Finally, equation (5) describes the conditions at the surfaces of the active layer. These express the flux continuity at these interfaces and also account for the amount of heat added per unit area.

The Method

Application of integral transforms reduces the boundary and initial value problems governed by partial differential equations to ordinary differential equations. We apply the Laplace transform (Miles, 1971) in the t variable and the two-dimensional Fourier transform in the x and y variables (Sneddon, 1951). These pairs are defined by

$$\left.\begin{aligned} \mathcal{L}\{f(t)\} = F(s) &= \int_0^\infty f(t)e^{-st}dt \\ \mathcal{L}^{-1}\{F(s)\} = f(t) &= \frac{1}{2\pi i}\int_{c-i\infty}^{c+i\infty} F(s)e^{st}ds \end{aligned}\right\} \tag{9}$$

where c is chosen such that all the singularities, if any, are to the left of c, and

$$\left.\begin{aligned} \mathcal{F}\{f(x, y)\} = F(\xi, \eta) &= \int_{-\infty}^{\infty}\int_{-\infty}^{\infty} f(x, y)e^{-i2\pi(\xi x+\eta y)}dxdy \\ \mathcal{F}^{-1}\{F(\xi, \eta)\} = f(x, y) &= \int_{-\infty}^{\infty}\int_{-\infty}^{\infty} F(\xi, \eta)e^{i2\pi(\xi x+\eta y)}d\xi d\eta \end{aligned}\right\} \tag{10}$$

We also define by $\bar{u}_i(\xi, \eta, z, t)$ and $U_i(\xi, \eta, z, s)$ the quantities

$$\left.\begin{aligned} \bar{u}_i(\xi, \eta, z, t) &= \mathcal{F}\{u_i(x, y, z, t)\} \\ U_i(\xi, \eta, z, s) &= \mathcal{L}\{\bar{u}_i(\xi, \eta, z, t)\} \end{aligned}\right\} \tag{11}$$

Application of the abovementioned transform procedures to equation (1) in conjunction with the initial condition (2) yields

$$\frac{d^2U_i}{dz^2} - \lambda_i^2 U_i = 0 \tag{12}$$

where

$$\lambda_i^2 = 4\pi^2(\xi^2+\eta^2) + \alpha_i^{-1}s \tag{13}$$

In equations (3)–(5), u_i is replaced by U_i. The quantity q in equation (5) is replaced by

$$Q(\xi, \eta, s) = \pi v_x v_y e^{-\pi^2(v_x^2\xi^2+v_y^2\eta^2)} \times \int_0^\infty P(t)e^{-2\pi i(\xi c_x+\eta c_y)t}e^{-st}dt \tag{14}$$

Solution

The solution of equation (12) is

$$U_i(\xi, \eta, s, z) = A_i(\xi, \eta, s)e^{-\lambda_i z} + B_i(\xi, \eta, s)e^{\lambda_i z} \quad i=1, 2, \ldots, n \tag{15}$$

Equation (15) represents the temperature in the ith layer in the transformed domain. For a medium consisting of $n-1$ layers resting on a half-space, there are n such solutions and they involve $2n-1$ unknown coefficients. Equations (2)–(6) represent $2n$ conditions for $2n$ unknowns A_i, B_i. Application of these conditions results in the following $2n-1$ algebraic equations for the functions A_i, B_i ($B_n=0$):

$$
\begin{bmatrix}
1 & -1 & 0 & 0 & & & & & & & & & & & \\
(e^{-\lambda_0 h})_1 & (e^{\lambda_0 h})_1 & -1 & -1 & & & & & & & & & & & \\
(\kappa\lambda e^{-\lambda_0 h})_1 & (\kappa\lambda e^{\lambda_0 h})_1 & (\kappa\lambda)_2 & -(\kappa\lambda)_2 & & & & & & & & & & & \\
 & & (e^{-\lambda_1 h})_1 & (e^{\lambda_1 h})_1 & -1 & -1 & & & & & & & & & \\
 & & (\kappa\lambda e^{-\lambda_1 h})_1 & (\kappa\lambda e^{\lambda_1 h})_1 & (\kappa\lambda)_2 & -(\kappa\lambda)_2 & & & & & & & & & \\
 & & & & \cdot & \cdot & \cdot & \cdot & & & & & & & \\
 & & & & & & & & & & & & & & \\
 & & & & & & (e^{-\lambda_{N-1} h})_{N-1} & (e^{\lambda_{N-1} h})_{N-1} & -1 & -1 & & & & & \\
 & & & & & & (\kappa\lambda e^{-\lambda_{N-1} h})_{N-1} & (\kappa\lambda e^{\lambda_{N-1} h})_{N-1} & (\kappa\lambda)_N & -(\kappa\lambda)_N & & & & & \\
 & & & & & & & & (e^{-\lambda_N h})_N & (e^{\lambda_N h})_N & -1 & -1 & & & \\
 & & & & & & & & (\kappa\lambda e^{-\lambda_N h})_N & (\kappa\lambda e^{\lambda_N h})_N & (\kappa\lambda)_{N+1} & -(\kappa\lambda)_{N+1} & & & \\
 & & & & & & & & & & \cdot & \cdot & \cdot & & \\
 & & & & & & & & & & & & & & \\
 & & & & & & & & & & (e^{-\lambda_{n-1} h})_{n-1} & (e^{\lambda_{n-1} h})_{n-1} & -1 & -1 & \\
 & & & & & & & & & & & & & & \\
\end{bmatrix}
\begin{Bmatrix}
A_1 \\ B_1 \\ A_2 \\ \cdot \\ \cdot \\ \cdot \\ A_{N-1} \\ B_{N-1} \\ A_N \\ B_N \\ A_{N+1} \\ B_{N+1} \\ \cdot \\ \cdot \\ \cdot \\ A_n
\end{Bmatrix}
=
\begin{Bmatrix}
0 \\ 0 \\ 0 \\ 0 \\ 0 \\ 0 \\ a_N(1-\rho_{N+1}) \\ 0 \\ 0 \\ 0 \\ 0
\end{Bmatrix}
Q(\xi, \eta, s) \qquad (16)
$$

Note: $(\kappa\lambda e^{-\lambda_1 h})_1 = \kappa_1\lambda_1 e^{-\lambda_1 h_1}$

For later reference, we write equation (16) in the symbolic form

$$[W_{ij}(\xi, \eta, s)]\{\epsilon_j(\xi, \eta, s)\} = Q(\xi, \eta, s)\{f_i\} \qquad (17)$$

The matrix $[W_{ij}]$ is a banded complex matrix. The solution to equation (18) can also be expressed in symbolic form as

$$\{\epsilon_j\} = Q(\xi, \eta, s)[W_{ij}]^{-1}\{f_i\} \qquad (18)$$

In this equation

$$\{\epsilon_j\} = \{A_0, B_0. \ldots .A_j, B_j. \ldots\}^T \qquad (19)$$

Substituting $\{\epsilon_j\}$ from equation (18) into equation (15), we get

$$U_i(\xi, \eta, s, z) = L_i(\xi, \eta, s)Q(\xi, \eta, s) \qquad (20)$$

$$L_i(\xi, \eta, s) = [E_{ik}][W_{kj}]^{-1}\{f_j\} \qquad (21)$$

where

$$[E_{ik}] = \begin{bmatrix} e^{-\lambda_0 z} & e^{\lambda_0 z} & 0 & 0 & 0 & 0 & 0 \\ 0 & 0 & e^{-\lambda_1 z} & e^{\lambda_1 z} & 0 & 0 & 0 \\ 0 & 0 & 0 & 0 & e^{-\lambda_2 z} & e^{\lambda_2 z} & 0 \end{bmatrix} \qquad (22)$$

The solutions (20) are in the transformed domain and have to be inverted to get the temperature fields. The Laplace transform of equation (21) is given by (see Miles, 1971, and Kant, 1988)

$$\bar{u}(\xi, \eta, z, t) = \int_0^t \bar{q}(\xi, \eta, u)l_i(\xi, \eta, z, t-u)du \qquad (23)$$

where

$$\bar{q}(\xi, \eta, u) = \pi v_x v_y e^{-\pi^2(v_x^2\xi^2 + v_y^2\eta^2)}e^{-2\pi i(\xi c_x + \eta c_y)u}p(u) \qquad (24)$$

and

$$l_i = \frac{1}{2\pi i}\int_{c-i\infty}^{c+i\infty} L_i e^{st}ds \qquad (25)$$

Evaluation of the integral (25) is not an easy task. Therefore, we employ a technique developed by Crump (1979). According to this method, $l_i(\xi, \eta, t)$ is given by

$$l_i(\xi, \eta, z, t) = \frac{e^{at}}{\tau}\left[\sum_{k=0}^{\infty}\left\{\frac{1}{(1+\delta_{0k})}ReL_i(\xi, \eta, z, k\pi i + a)\cos\frac{k\pi t}{\tau} - ImL_i(\xi, \eta, z, k\pi i + 1)\sin\frac{k\pi t}{\tau}\right\}\right] \qquad (26)$$

where in equation (26), *Re* and *Im* respectively represent real and imaginary parts. This expression is valid for the time interval $0 \le \tau \le t$. The accuracy of the inversion is determined by the expression $e^{-a\tau} = \epsilon$; ϵ is any desired number. Substituting equations (24) and (26) into equation (23), we get

$$\bar{u}_i(\xi, \eta, z, t) = \frac{\pi}{\tau}v_x v_y e^{-\pi^2(v_x^2\xi^2 + v_y^2\eta^2)^2} \cdot \sum_{k=0}^{\infty}\sum_{q=1}^{m}\frac{p_q}{(1+\delta_{0k})} \cdot \frac{e^{(a-\theta_0)t}}{(\theta_0^2+\beta^2)}[ReL_iC(t, \theta_0, k, T_q) - ImL_iS(t, \theta_0, k, T_q)] \qquad (27)$$

where

$\theta_0 = 2\pi i(\xi c_x + \eta c_y)$

$\beta = \dfrac{k\pi}{\tau}$

p_q = sequence of step functions approximating

$p(t)$ on time interval T_q $\{T_q$: T_{q1} to $T_{q2}\}$

$$\begin{Bmatrix} C \\ S \end{Bmatrix}(t, \theta_0, k, T_q) = \begin{Bmatrix} C_1 \\ S_1 \end{Bmatrix}(t, \theta_0, k, T_{q2}) - \begin{Bmatrix} C_1 \\ S_1 \end{Bmatrix}(t, \theta_0, k, T_{q1})$$

$$C_1(t, \theta_0, k, T_{q_m}) = e^{\theta_0(t-T_{q_m})} \times \{\theta_0 \cos \beta(t-T_{q_m}) + \beta \sin \beta(t-T_{q_m})\}$$

and

$$S_1(t, \theta_0, k, T_{q_m}) = e^{\theta_0(t-T_{q_m})} \times \{\theta_0 \sin \beta(t-T_{q_m}) - \beta \cos \beta(t-T_{q_m})\}$$

Equation (27) represents temperatures in the "frequency" domain. To obtain temperatures in the space ($x-y$ domain), we must evaluate the inverse Fourier transform of $\bar{u}_i(\xi, \eta, z, t)$ according to expression:

$$U_i(x, y, z, t) = \int_{-\infty}^{\infty}\left[\int_{-\infty}^{\infty} \bar{u}_i(\xi, \eta, z, t) e^{2\pi i \xi x} d\xi\right] e^{2\pi i \eta y} d\eta \tag{28}$$

In evaluating equation (27), we use the so-called Fast Fourier Transform method of Cooley et al.

Discussion of Results

In this section, we present results for a medium typically used in optical recording. The values of the material parameters are given in Table 1. All results presented here are for layer number 2, which is the active layer. The temperature is plotted for the bottom surface of the active layer. The laser beam illuminates the medium from the half-space side. The reflection at the surface of the active layer is taken to be 20 percent. It is assumed that the laser beam moves along the line $x=0$ with a prescribed velocity of 10 m/s and the coefficient of absorptance is taken to be 1.0. Further, it is also assumed that there is no reflecting layer on top of the active layer. For the case when the velocity of the source is $v=0$, results obtained in the present investigation were in agreement with those reported by Kant (1988). To avoid duplication, we omit presentation of the case when the laser is stationary and proceed directly to the more interesting case when the laser is translating, i.e., the case when bits are being written on the disk.

As stated previously, the laser pulse is used to change the magnetic properties of the medium. If two pulses of laser beam are sufficiently close, then it is likely that the regions with changed magnetic properties are very close and may be merged together, whereas if two pulses of laser beam are far apart then the two regions may be farther apart than is necessary, resulting in a loss of bit density.

In this sample problem, we show results for the pulses described in Table 2. In Fig. 6, we show the temperature distribution, for pulse number 2, at the center of the laser beam at the bottom surface of the active layer on the line along which the source moves with a prescribed velocity of 10 m/s. The temperature distributions after 150, 200, 450, 500, and 650 ns are shown by curves 1–5, respectively. Curve 1 shows the temperature after 150 ns, which also is the time duration for which the laser remains on. It can be seen that peak temperature nearly follows the laser beam. Curves 2–4 show temperature distribution while the laser is off but continues to move along the line. When the laser is turned off, the peak temperature begins to decrease and some adjustment in the distribution takes place. The temperature continues to decrease until 500 ns (Curve 4), at which time the laser is turned on once again.

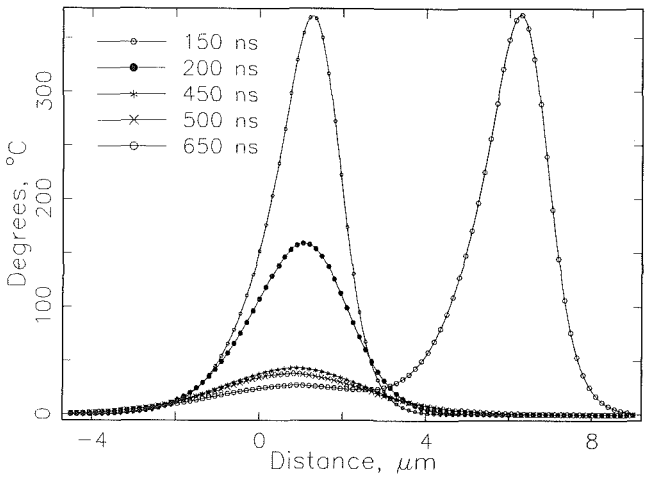

Fig. 6 Temperature at the bottom surface of the active layer along the line of laser travel at various times, pulse 2

Table 1 Material parameters

Layer No.	$\kappa\left(\frac{\text{cal}}{\text{s°C cm}}\right)$	$\rho\left(\frac{\text{g}}{\text{cm}^3}\right)$	$c\left(\frac{\text{cal}}{\text{g°C}}\right)$	h(Å)
1	0.0033	2.2	0.18	710
2	0.095	7.87	0.097	800
3	0.0033	2.2	0.18	710
4	0.0025	2.76	0.20	∞

Notes: No reflecting layer present.
Absorptance coefficient for the active layer (#2) = 1.0.
Reflectance for the bottom surface of the active layer = 50 percent.

Table 2 Pulse characteristics

Pulse number	Power (mW)	Laser on from (ns)	to (ns)	v_r (ηm)
1	20	0	150	0.6005
		230	380	
2	20	0	150	0.6005
		500	650	

Note: $v_r = v_x = v_y$.

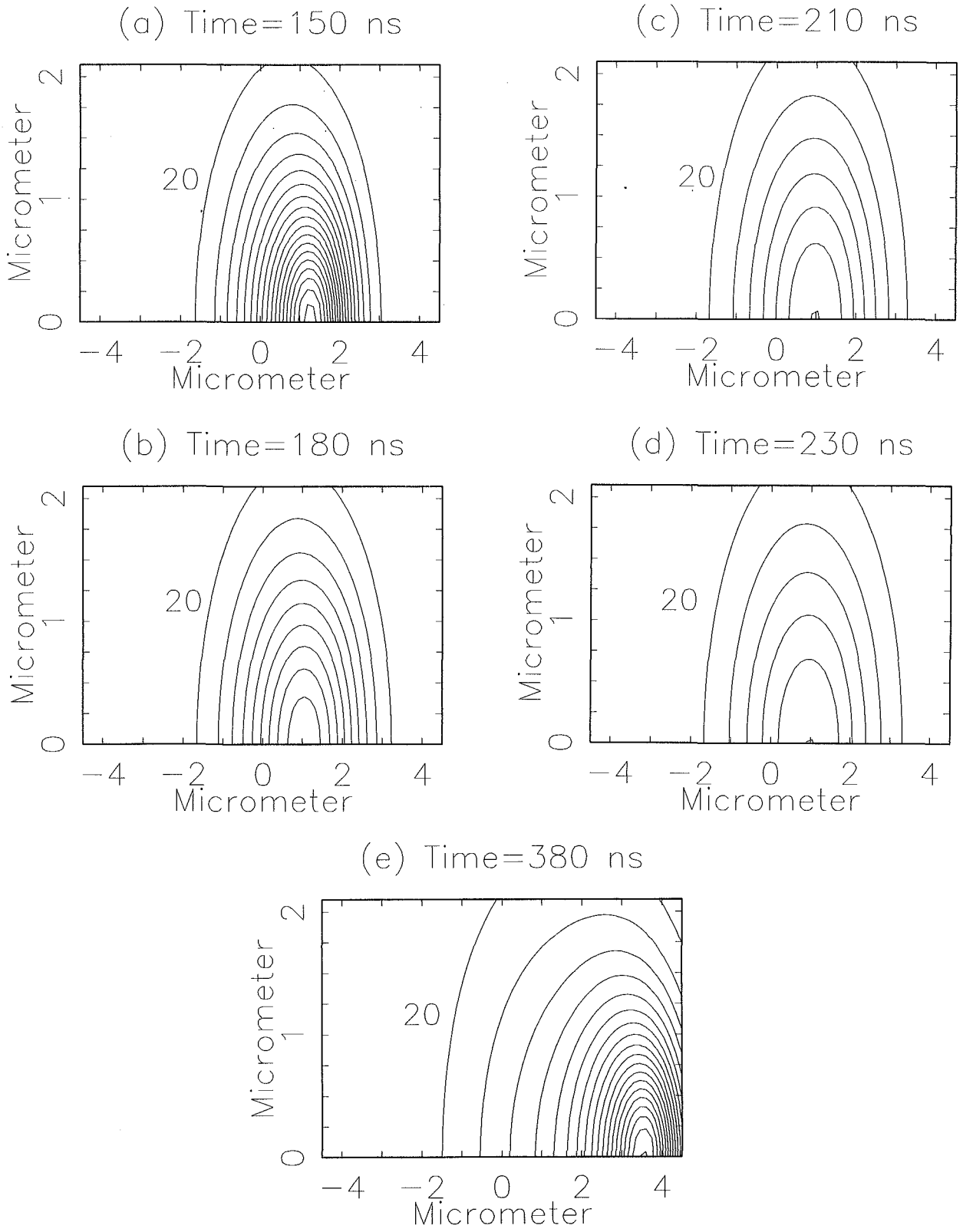

Fig. 7 Isotherms for temperature distribution, pulse 1

The temperature then begins to rise again. Curve 5 shows the temperature after 650 ns at which time the laser is turned off again. We can see that at this time there is a different peak near 6.5 μm, which is the location of the laser beam.

We next consider the temperature distribution in the x-y plane of the layer. In this investigation, we wish to calculate the domain where the magnetic properties have changed, i.e., the "spot size." The area enclosed within the Curie temperature (temperature at which the magnetic properties of the material change) is the size of the spot. In Figs. 7(a–e), we show isotherms at intervals of 20°C. Figure 7(a) shows the isotherms at 150 ns at which time the laser is turned off. In

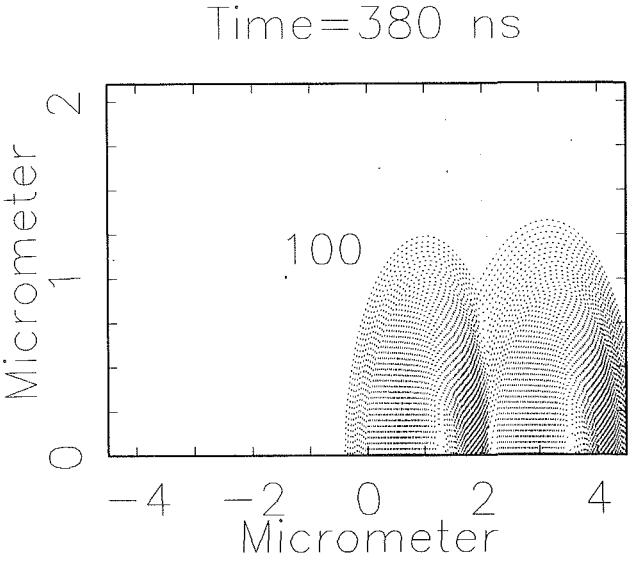

Fig. 8 Spot size, pulse 1

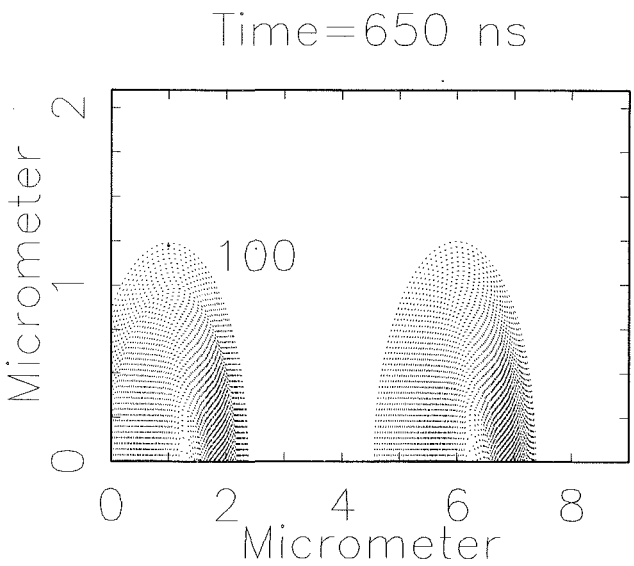

Fig. 10 Spot size, pulse 2

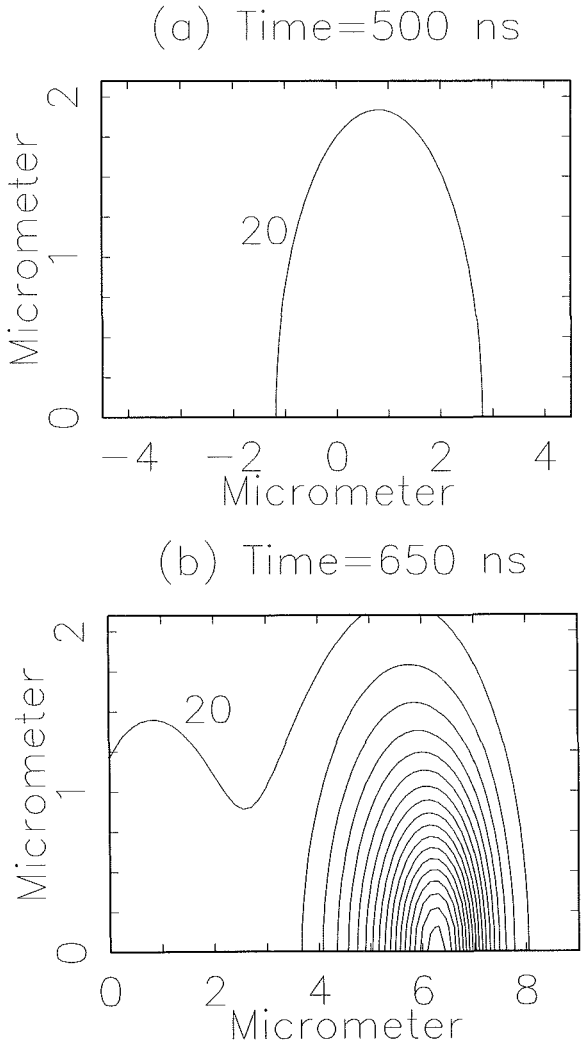

Fig. 9 Isotherms for temperature distribution, pulse 2

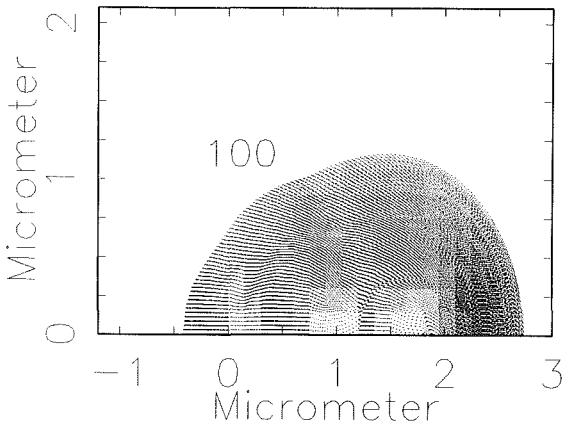

Fig. 11(*a*) Spot size, uniform pulse

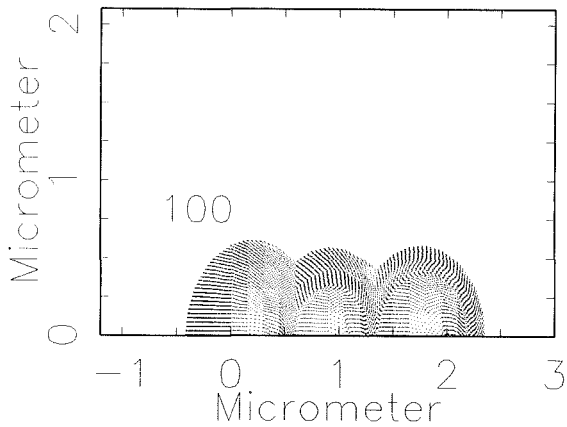

Fig. 11(*b*) Spot size, modulated pulse

Figs. 7(*b–d*), we show isotherms at 180, 210, and 230 ns. Note that the laser is off during this period, and we see that the active layer cools down considerably. At 230 ns, the laser turned on again for 150 ns for writing the second spot. Figure 7(*e*) shows isotherms at 380 ns, at which time the laser is once again turned off after being on for 150 ns. Once again temperature isotherms similar to Fig. 7(*a*) are produced but at a different location. In order to determine the spot size, we must know the area within which the temperature was equal to or higher than the Curie temperature of the material during the entire course of a pulse. We do this by updating the records of maximum temperatures on the x, y plane at various time intervals. We show this record for pulse number 1 (0→150, 230→380 on) in Fig. 8. For the material of the active layer under consideration the Curie temperature is 100°C. The shaded

area enclosed within the 100°C isotherm has been demagnetized and, therefore, represents the spot size. It is seen from Fig. 8 that the two spots written by pulse number 1 are merged and cross-talk exists. The recording is not good.

Figures 9(*a*, *b*) show isotherms at 500 and 650 ns for pulse number 2 (0→150, 500→650 on). These two figures are a continuation of the series of Figs. 7(*a–d*). We see (Fig. 9(*a*)) that the temperature continues to decrease to almost initial conditions. At 500 ns, the temperature at the center of the "spot" is less than 40°C. In Fig. 8(*b*), we show isotherms after 650 ns. At this time, the laser is turned off once again after being turned on for 150 ns (for comparison with pulse number 1, see Fig. 7(*a*)). This "spot" is similar to the "spot" shown in Fig. 7(*a*). In Fig. 10, we show the record of maximum temperature for pulse number 2. In this case, the shaded areas enclosed within the 100°C isotherms are separated from each other by approximately 2 μm and there is no cross-talk. The recording is good.

We next consider the inverse problem of determining the pulse-sequence to produce a long spot with no intertrack cross-talk. In Fig. 11(*a*), we show the spot produced by a long pulse {6 mW (0→320), $v_r = v_x = v_y = 0.54$ μm, $c_x = 5.9$ m/s, $c_y = 0$}. As we can see, the spot dimension increases in the direction perpendicular to the track. In this case, in order to prevent intertrack cross-talk, the tracks have to be separated by at least 1.3μm. To increase the track density, it is desirable to produce a spot as straight as possible. This can be accomplished by modulating the power in the beam with time. After a few iterations, we arrived at a pulse with the following history: {6 mW (0→50), 5.5 mW (142→177), and 4.75 mW (270→320); $v_r = v_x = v_y = 0.54$ μm, $c_x = 5.9$ m/s, $c_y = 0$}. The spot produced by this pulse history is straight (Fig. 11(*b*)). Consequently, the track separation can be reduced to achieve higher track density.

Acknowledgments

The authors are thankful to their colleagues: Vic Jipson, who suggested this problem; Martin Chen, James Suits, and Kurt Rubin for their helpful discussions, suggestions, and for various test problems. Thanks are also due to Ms. Lorraine Rodriquez, IBM Research Publications, for producing this report.

References

Allen, R., and Connell, G. A. N., 1982, "Magento-optic Properties of Amorphous Terbium-Iron," *Journal of Applied Physics*, Vol. 53, No. 3.

Bell, A., Personal Communication.

Born, M., and Wolfe, E., 1980, *Principles of Optics*, Pergamon Press, New York.

Burgner, M. L., and Reedy, R. E., 1982, "Temperature Distributions Produced in a Two-Layer Structure by a Scanning CW Laser of Electron Beam," *Journal of Applied Physics*, Vol. 53, No. 6.

Cooley, J. W., Lewis, P. A. W., and Welch, P. D., 1967, "The Fast Fourier Transform and Its Applications," IBM Research Publication, RC-1743, Yorktown Heights, NY.

Christensen, R. M., 1978, *Mechanics of Composite Materials*, Wiley, New York.

Crump, K. S., 1976, "Numerical Inversion of Laplace Transform Using a Fourier Series Approximation," *J. Assoc. for Computing Industry*, Vol. 23, No. 1.

Gray, D. E., 1963, *American Institute of Physics Handbook*, McGraw-Hill, New York.

Iravani, M. V., and Wickramsingle, H. K., 1985, "Scattering Matrix Approach to Thermal Wave Propagation in Layered Structures," *Journal of Applied Physics*, Vol. 58, No. 1.

Kant, R., 1988, "Laser Induced Heating of a Multilayered Medium Resting on a Half-Space. Part I: Stationary Source," ASME *Journal of Applied Mechanics*, Vol. 55, pp. 93–97.

Mandelis, A., and Zver, M. M., 1985, "Theory of Photopyroelectric Spectroscopy of Solids," *Journal of Applied Physics*, Vol. 57, No. 9.

Miles, J., 1971, *Integral Transforms in Applied Mathematics*, Cambridge University Press, United Kingdom.

Nayfeh, A. H., 1978, "Continuum Mixture Theory of Heat Transfer for Layered Medium," ASME *Journal of Applied Mechanics*, Vol. 45.

Ohr, S., 1985, "Magneto-optics Combines Erasability and High Density Storage," *Electronic Design*, July.

Rosencwaig, A., and Greshko, A., 1976, "Theory of the Photoacoustic Effects With Solids," *Journal of Applied Physics*, Vol. 47, No. 1.

Sneddon, I. N., 1951, *Fourier Transforms*, McGraw-Hill, New York.

Salcudean, M., Choi, M., and Greif, R., 1986, "A Study of Heat Transfer During Arc Welding," *International Journal of Heat and Mass Transfer*, Vol. 29, No. 2.

Shin, S. C., 1986, "Thermal Analysis of Magneto-Optical Thin Films Under Laser Irradiation," *Journal of Magnetism and Magnetic Materials*, Vol. 61.

Skumanich, A., et al., 1987, "A Contactless Method for Investigating the Thermal Properties of Thin-Films," *Applied Physics A*, Vol. 43.

Tsai, H. L., and Rubinsky, B., 1984, "A Front Tracking Finite Element Study of Change of Phase Interface Stability During Solidification Processes in Liquids," *J. Crystal Growth*, Vol. 70.

C. P. Grigoropoulos[1]

W. E. Dutcher, Jr.

A. F. Emery

Department of Mechanical Engineering,
University of Washington,
Seattle, WA 98195

Experimental and Computational Analysis of Laser Melting of Thin Silicon Films

Recrystallization of thin semiconductor films can yield improved electrical and crystalline properties. The recrystallization is often effected by using a laser source to melt the semiconductor that has been deposited on an amorphous insulating substrate. This paper describes detailed experimental observations of the associated phase-change process. A computational conductive heat transfer model is presented. The numerical predictions are compared to the experimental results and good agreement is obtained.

I Introduction

A technique oriented toward the fabrication of high-performance electronic devices is the recrystallization of thin semiconductor films deposited on amorphous substrates. The use of light sources and, in particular, lasers to melt and subsequently recrystallize thin semiconductor layers on insulators (SOI structures) has shown good potential for applications to commercial VLSI technology (Tsaur, 1986). Despite the significant progress that has been made toward improving the crystal growth in thin silicon films, it has not been possible consistently to eliminate the formation of grain boundaries in the recrystallized material. These grain boundaries are detrimental (Celler, 1983; Fan et al., 1983) to the use of the material as an active component in electronic devices. The silicon film melting and recyrstallization is controlled by (1) the laser beam total power, (2) the shape of the laser beam intensity distribution, and (3) the material translation speed. To optimize these parameters, it is necessary to model the heat transfer associated with the melting process. Experimental studies (Kawamura et al., 1982; Stultz and Gibbons, 1981) have shown some success in controlling crystal growth by modifying the laser beam shape, and thus the induced temperature field. Accurate theoretical modeling of thin film laser annealing is essential for material processing improvements.

The steady-state temperature distribution in the melting of a thick silicon slab by a stationary laser light source has been obtained by Kokorowski et al. (1981). Schvan and Thomas (1985) used the enthalpy formulation of phase-change problems along with simplifying assumptions to obtain the transient temperature distribution for a nonmoving thick silicon slab irradiated with a stationary light source. One-dimensional phase-change finite difference models (Kubota et al., 1986; Miaoulis and Mikic, 1986) have been developed to study the effects of the laser beam scanning rates and the encapsulating structural configurations. Approximate solutions for the temperature field distribution in melting of thin silicon layers by scanning laser beams of elliptical or circular symmetry have been given by Waechter et al. (1986) and Willems et al. (1987).

A three-dimensional transient numerical algorithm for thin silicon film laser melting and recrystallization based on the enthalpy formulation (Atthey, 1974; Shamsundar and Sparrow, 1975, 1976) has been presented by Grigoropoulos et al. (1986). The sensitivity of the melt zone to the different material properties and laser beam parameters has been analyzed when melted by infinitely wide laser beams (Grigoropoulos et al., 1990); the results were compared to a limited set of experimental data of monochromatic CW Argon ion laser beam melting of thin silicon films (Grigoropoulos et al., 1988) and reasonable agreement was obtained.

In this work, sufficient experimental data are obtained to validate a three-dimensional transient heat transfer algorithm for predicting the phase-change process. The experimental uncertainty is reduced by direct measurement of the laser beam parameters. It is therefore possible to compare the heat transfer solutions to the experimental results. To the knowledge of these authors, such a detailed comparison has not been reported.

II Experimental Procedure and Results

A sketch of the laser annealing experimental apparatus is shown in Fig. 1. A Spectra Physics 164-08 4W CW Argon ion laser is used as the annealing source. This laser operates in the fundamental mode, TEM_{00}, with a Gaussian intensity distribution across the multiline laser beam. The laser beam line centers, λ_i, and the corresponding power fractions $f_p(i)$ have been measured using a monochromator system and are given in Table 1. This table shows that most of the laser beam power

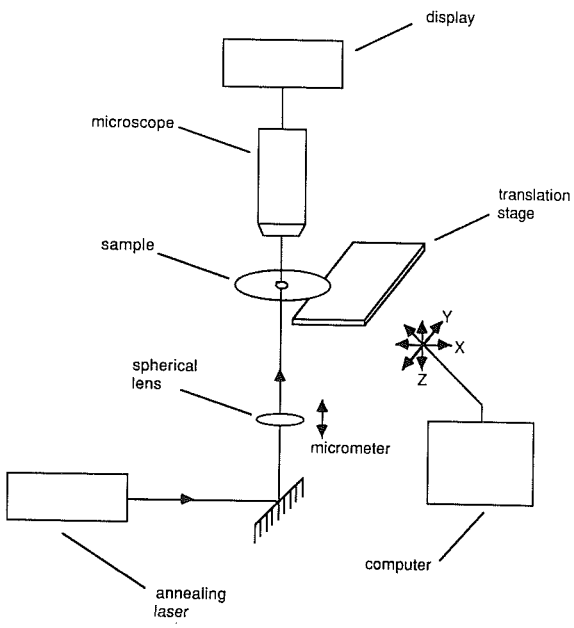

Fig. 1 Schematic of the laser annealing experimental apparatus

[1]Present address: Department of Mechanical Engineering, University of California, Berkeley, CA 94720.

Contributed by the Heat Transfer Division and presented at the National Heat Transfer Conference, Philadelphia, PA, August 6-9, 1989. Manuscript received by the Heat Transfer Division August 23, 1989; revision April 4, 1990. Keywords: Laser Processing, Materials Processing and Manufacturing Processes, Phase-Change Phenomena.

is centered around the $\lambda = 488$ nm (blue) and $\lambda = 514.5$ nm (green) wavelengths. The description of the laser beam absorption by the silicon layer requires a knowledge of the material radiative property spectral properties and estimates of the laser beam intensity distribution.

The laser beam is focused by a spherical lens of $f = 10$ cm focal length on the silicon sample, which is mounted on a precision translation stage. The repeatable positioning accuracy is 1 μm and the maximum constant speed is 2 mm/s. The experiments were performed on 0.5-μm-thick polysilicon layer deposited on bulk, fused silica wafers of 7.6-cm diameter and 0.5-mm thickness. The silicon layer is encapsulated by a 0.5-μm-thick SiO_2 layer. This encapsulating layer prevents the generation of thermocapillary-driven flows and mass transport in the molten silicon pool.

The laser beam passes through the transparent (in the visible spectrum) glass substrate and is partially absorbed in the film. The transmitted light passes through the transparent encapsulating layer and is observed by using an optical microscope. The different experiments were conducted by placing the sample at different locations along the z_f axis, thus changing the intensity of the beam. In order to define this intensity, it is necessary to measure the laser beam dimensions as a function of z_f. The laser beam dimensions are measured using a variable frequency rotating blade chopper, which is traversed along the propagation axis of the laser beam (Fig. 2). An interference filter is used to isolate the blue ($\lambda_b = 488$ nm) component of the laser beam. This Gaussian beam is chopped and the chopped light is focused on the silicon photodiode to give a waveform profile that is captured by a 11402 Tektronix digitizing oscilloscope. A least-squares analysis is used to fit the Gaussian profile of the laser beam intensity radius, $w_{\lambda b}$, to this waveform. Figure 3 shows the $1/e$ irradiance radius, $w_{\lambda b}$, in the vicinity of the focal waist.

$$w_{\lambda b}(z_f) = 33.67 - 0.149 z_f + 0.457 z_f^2 - 0.013 z_f^3 \qquad (1)$$

A standard expression for the calculation of the laser beam $1/e$ irradiance radius at the focal waist, w_f, is

$$w_f = \frac{2 \cdot \lambda \cdot f}{\pi w_{\text{lens}}} \qquad (2)$$

The theoretically minimum laser beam $1/e$ radius, predicted by equation (2), is $w_f = 19$ μm, in contrast with the measured minimum $1/e$ radius of about 30 μm. The difference is attributed to focusing lens aberrations. In practice, a correction factor of about 1.5 is suggested for equation (2) by the lens manufacturer. The distance z_f along the laser beam axis can be directly related to the spherical lens travel, with an error

Table 1 Power fractions for the laser beam components; laser beam total power $P_T = 2.0$ W

wavelength, λ_i (nm)	Power fractions, f_p
457.9	0.03
476.5	0.10
488.0	0.32
496.5	0.11
501.7	0.08
514.5	0.36

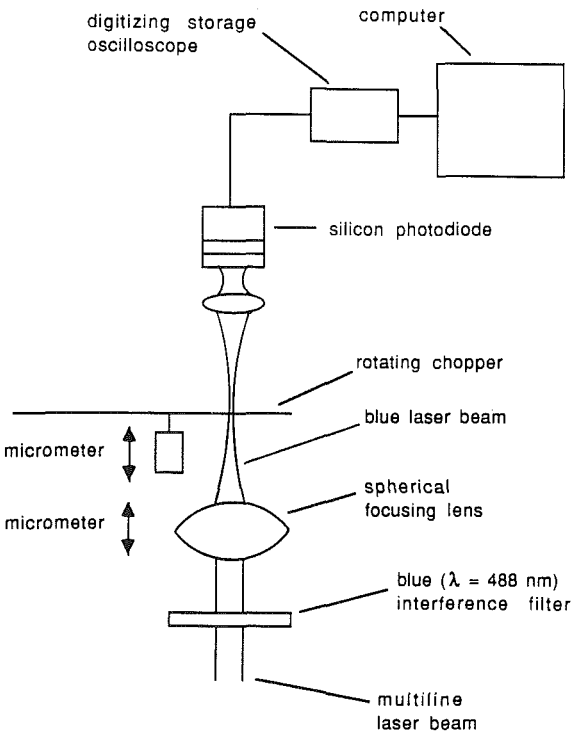

Fig. 2 Schematic of experimental arrangement of measurement of laser beam parameters

Nomenclature

a_n = linear coefficient of temperature dependence of the real part of the silicon refractive index
c_p = specific heat
d_{enc} = encapsulating layer thickness
d_{si} = semiconductor layer thickness
d_{ss} = substrate thickness
f = focal length of spherical focusing lens
f_l = liquid silicon volume fraction $= 1 - f_s$
$f_p(i)$ = fraction of laser power for the λ_i laser light wavelength line
f_s = solid silicon volume fraction
h_l = heat transfer coefficient at the bottom substrate surface
h_u = heat transfer coefficient at the surface of the top encapsulating layer
H = enthalpy
j = imaginary unit
k = thermal conductivity
k^{ext} = extinction coefficient
k_{si}^o = extinction coefficient of silicon at 300 K
L = latent heat of fusion
M = transmission characteristic matrix
n_{si} = real part of the silicon refractive index
n_{si}^o = real part of the silicon refractive index at 300 K
n_w = number of laser beam peak wavelengths
$\hat{n}$ = complex refractive index
$\hat{p}$ = complex characteristic matrix coefficient
P_T = laser beam total power
Q_{ab} = power absorbed by the thin silicon layer
Q^{ext} = laser light source irradiance distribution
Q^o = peak power intensity of the laser beam
Q_{rad} = radiative loss from the silicon layer through the capping layer and the glass substrate
R = reflectivity
r = reflective coefficient
r_f = iterative convergence criterion
s_x = molten pool size in the direction of motion
s_y = molten pool size in the direction transverse to the translating motion
t = time
t_r = transmission coefficient

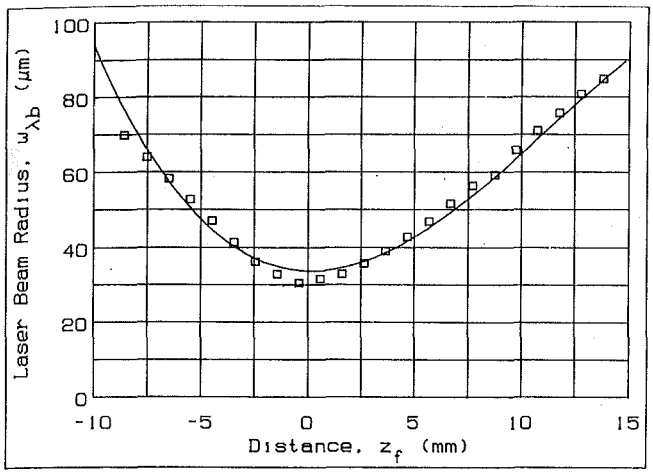

Fig. 3 Graph of the 1/*e* laser beam irradiance radius, $w_{\lambda b}$, as a function of the distance along the beam axis

of about 1 percent. The total error in the measurement of the laser beam diameter was estimated to be 7 percent. The location of the laser beam focal waist and the measured laser beam profiles were independently verified by scanning a knife-edge attached to the sample translation stage. Thin lens optics analysis (Yariv, 1976) indicates that the laser beam 1/*e* radius for the wavelength λ_i at the focal waist is given by.

$$w_{\lambda i}(z_f) = w_{\lambda b}(z_f)\sqrt{\frac{\lambda_i}{\lambda_b}} \tag{3}$$

The laser beam total power incident on the sample was measured by using both a thermopile detector and a calibrated silicon photodiode-attenuator device. These systems have a measurement accuracy of 5 percent. The laser beam peak power density for any position z_f is given by

$$Q^o(z_f) = P_T \sum_{i=1}^{n_w} \frac{f_p(i)}{\pi w_{\lambda i}(z_f)^2} \tag{4}$$

In the experiments, the power level, the distance z_f, and the material translation speed were varied. The experimental observations show that the molten zone is nearly circular and there is no phase boundary distortion due to the material translation speed. Part of the experimental results are represented in Table 2. As expected by an order of magnitude analysis and verified by the computational results, the effects of the material

Table 2 Experimentally measured molten pool diameters in μm; partial melting conditions are indicated by "mushy" and absence of phase change to liquid is marked by "solid"

$w_{\lambda b}$(μm)	P_T(W)	V (mm/s)			
		0.0	0.5	1.0	2.0
90	1.0	solid	solid	solid	solid
	1.4	solid	solid	solid	solid
	1.8	mushy	mushy	mushy	mushy
84	1.0	solid	solid	solid	solid
	1.4	mushy	solid	solid	mushy
	1.8	mushy	mushy	mushy	mushy
78	1.0	solid	solid	solid	solid
	1.4	mushy	mushy	mushy	mushy
	1.8	131	133	131	125
73	1.0	solid	solid	solid	solid
	1.4	mushy	mushy	mushy	mushy
	1.8	133	131	131	125
68	1.0	solid	solid	solid	solid
	1.4	94	97	mushy	mushy
	1.8	136	139	133	131
62	1.0	mushy	mushy	mushy	solid
	1.4	100	100	94	97
	1.8	133	133	133	128
57	1.0	mushy	67	mushy	mushy
	1.4	100	100	97	100
	1.8	133	133	133	131
53	1.0	78	72	75	mushy
	1.4	103	106	97	94
	1.8	128	125	128	119
48	1.0	75	75	75	69
	1.4	100	100	97	103
	1.8	128	122	125	119
44	1.0	81	75	72	69
	1.4	94	94	92	94
	1.8	119	119	117	114
41	1.0	81	75	72	67
	1.4	92	89	89	92
	1.8	114	114	111	111
38	1.0	72	69	72	67
	1.4	89	86	83	92
	1.8	keyhole	keyhole	100	keyhole
36	1.0	72	67	64	67
	1.4	78	83	72	83
	1.8	keyhole	keyhole	100	keyhole
34.2	1.0	67	64	61	62
	1.4	72	81	75	81
	1.8	keyhole	keyhole	keyhole	keyhole
33.7	1.0	64	61	58	61
	1.4	keyhole	78	75	75
	1.8	keyhole	keyhole	keyhole	keyhole

Nomenclature (cont.)

T = temperature
T_m = melting temperature
T_∞ = ambient temperature
V = material translation speed
w = distance from the laser beam center to the point where the laser beam irradiance intensity drops to 1/*e* of its peak value
$w_{\lambda b}$ = distance from the laser beam center to the point where the irradiance intensity of the blue ($\lambda = 488$ nm) component of the laser beam drops to 1/*e* of its peak value
$w_{\lambda i}$ = distance from the laser beam center to the point where the irradiance of the λ_i wavelength component of the laser beam drops to 1/*e* of its peak value
x = coordinate in the scanning direction (Fig. 5)
y = coordinate in the transverse direction (Fig. 5)
z = coordinate normal to the sample surface (Fig. 5)
z_f = distance along the laser beam axis from the beam focal waist
Δ = computational grid spacing
ϵ = emissivity
θ_o = incidence angle with respect to the outward normal to the surface
θ_i = complex angle of refraction in an absorbing film
λ = laser light wavelength
λ_i = wavelength of laser line center ($i = 1, \ldots, n_w$)
λ_b = blue ($\lambda = 488$ nm) laser light wavelength
ρ = density
σ = Stefan–Boltzmann constant
τ = transmissivity

Subscipts

enc = encapsulating layer
f = laser beam focal waist
l = liquid silicon
s = solid silicon
si = silicon
ss = substrate

Superscripts

m = iteration level
$+$ = emissive loss through the top encapsulating layer surface
$-$ = emissive loss through the bottom substrate surface

translation speed are small compared to the conductive heat transfer. In general, speeds in this low range (0–3 mm/s) have been found effective in the zone melting and recrystallization of semiconductor layers on insulators (Pfeiffer et al., 1987). The change in the molten pool size is small as the laser beam size is increased for $w_{\lambda b} > 50$ μm.

Figure 4(*a*) corresponds to the maximum laser power density that is incident on the silicon layer when the laser beam is intercepted at its focal waist. It is seen that the silicon solidification edge is pulled into a "keyhole" leaving a narrow strip of bare substrate behind its center. As the laser beam size is increased, a uniform molten zone is observed (Fig. 4*b*). Upon further increase of the laser beam size, partial melting occurs (Fig. 4*c*). The partially molten zone is recrystallized into a chaotic structure as it moves through the polysilicon layer.

III Computational Analysis

A sketch of the basic structure is shown in Fig. 5. A polysilicon film of thickness d_{si} is deposited on a fused silica substrate of thickness d_{ss} and encapsulated by a SiO_2 layer of thickness d_{enc}. A laser beam of Gaussian intensity distribution passes through the substrate, and is partially absorbed in the silicon film. Heat is lost from the upper and bottom surfaces of the structure by convection and radiation. The silicon film and the capping layer are thin (of 0.5 μm thickness each); hence, the heat transfer in each of these films can be represented by the heat conduction equation integrated across their respective layer thicknesses. For temperatures below the melting temperature, the heat transfer in the silicon film is given by

$$\rho_{si}(T_{si})c_{p;si}(T_{si})\left(\frac{\partial T_{si}}{\partial t} + V\frac{\partial T_{si}}{\partial x}\right) = \frac{\partial}{\partial x}\left(k_{si}(T_{si})\frac{\partial T_{si}}{\partial x}\right) + \frac{\partial}{\partial y}\left(k_{si}(T_{si})\frac{\partial T_{si}}{\partial y}\right) + \frac{Q_{ab}(x, y, T_{si}) - Q_{\text{rad, }si}(T_{si})}{d_{si}} + \frac{k_{si}(T_{si})\left[\left.\frac{\partial T_{si}}{\partial z}\right|_{z=d_{si}+d_{\text{enc}}} - \left.\frac{\partial T_{si}}{\partial z}\right|_{z=d_{\text{enc}}}\right]}{d_{si}} \quad (5)$$

In the top capping layer

$$\rho_{\text{enc}}(T_{ss})_{p;\text{enc}}(T_{\text{enc}})\left(\frac{\partial T_{\text{enc}}}{\partial t} + V\frac{\partial T_{\text{enc}}}{\partial x}\right) = \frac{\partial}{\partial x}\left(k_{\text{enc}}(T_{\text{enc}})\frac{\partial T_{\text{enc}}}{\partial x}\right) + \frac{\partial}{\partial y}\left(k_{\text{enc}}(T_{\text{enc}})\frac{\partial T_{\text{enc}}}{\partial y}\right) - \frac{h_u(T_{\text{enc}} - T_\infty) - k_{\text{enc}}(T_{\text{enc}})\left.\frac{\partial T_{\text{enc}}}{\partial z}\right|_{z=d_{\text{enc}}} - Q_{\text{rad,enc}}}{d_{\text{enc}}} \quad (6)$$

The heat conduction equation in the substrate is

$$\rho_{ss}(T_{ss})c_{p;ss}(T_{ss})\left(\frac{\partial T_{ss}}{\partial t} + V\frac{\partial T_{ss}}{\partial x}\right) = \frac{\partial}{\partial x}\left(k_{ss}(T_{ss})\frac{\partial T_{ss}}{\partial x}\right) + \frac{\partial}{\partial y}\left(k_{ss}(T_{ss})\frac{\partial T_{ss}}{\partial y}\right) + \frac{\partial}{\partial z}\left(k_{ss}(T_{ss})\frac{\partial T_{ss}}{\partial z}\right) \quad (7)$$

The laser beam energy that is absorbed by the silicon layer is given by

$$Q_{ab}(x, y, T_{si}) = \sum_{i=1}^{n_w}[1 - R_{\lambda i}(T_{si}) - \tau_{\lambda i}(T_{si})]Q_{\lambda i}^{\text{ext}}(x, y) \quad (8)$$

The radiative flux balance and the thin film reflectivity and transmissivity are calculated using thin film optics that take into account wave interference effects (Appendix A). The material optical properties used in these calculations are given in Appendix B. Figure 6 shows the film reflectivity, transmissivity, and absorptivity as functions of the solid silicon film temperature for the $\lambda_b = 488$ nm wavelength. When liquid, the silicon film is opaque and its reflectivity at the same wavelength is $R_l = 0.527$. The laser beam intensity distribution is assumed to be Gaussian and circular.

$$Q_{\lambda i}^{\text{ext}}(x, y) = Q_{\lambda i}^{o}\exp\left[-\frac{x^2 + y^2}{w_{\lambda i}^2}\right] \quad (9)$$

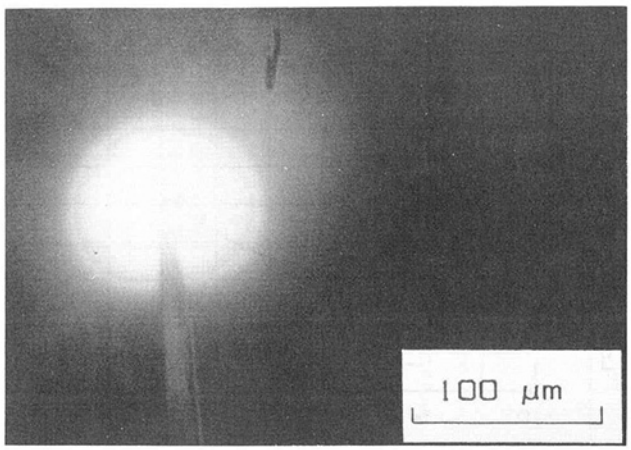

Fig. 4(*a*) Micrograph of light transmitted through the silicon layer: laser beam power $P_T = 1.8$ W; material translation speed $V = 2$ mm/s; and 1/*e* irradiance radius $w_{\lambda b} = 34$ μm

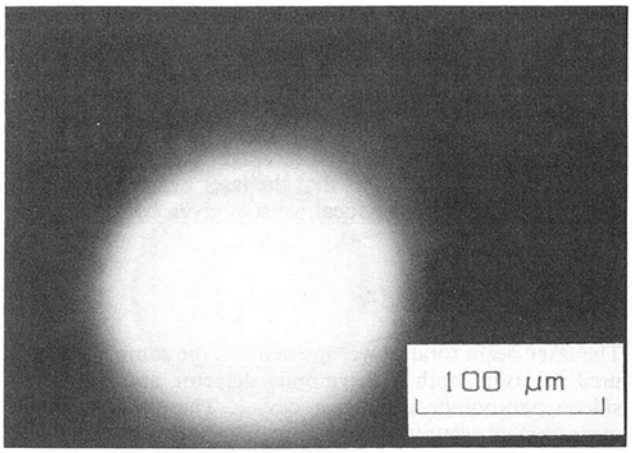

Fig. 4(*b*) Micrograph of light transmitted through the silicon layer: laser beam power $P_T = 1.8$ W; material translation speed $V = 2$ mm/s; and 1/*e* irradiance radius $w_{\lambda b} = 48$ μm

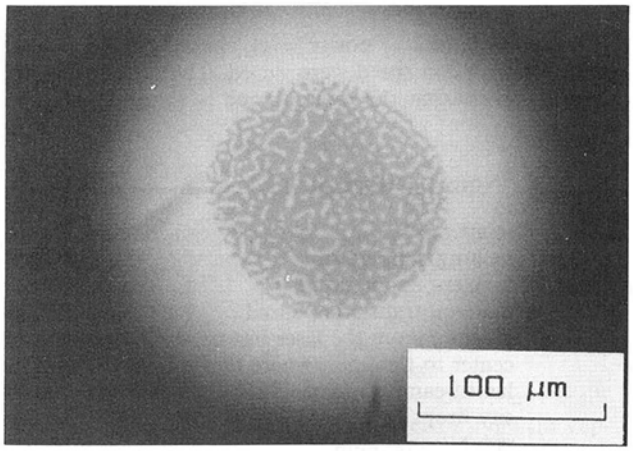

Fig. 4(*c*) Micrograph of light transmitted through the silicon layer: laser beam power $P_T = 1.8$ W; the silicon layer is not moving; and 1/*e* irradiance radius $w_{\lambda b} = 90$ μm

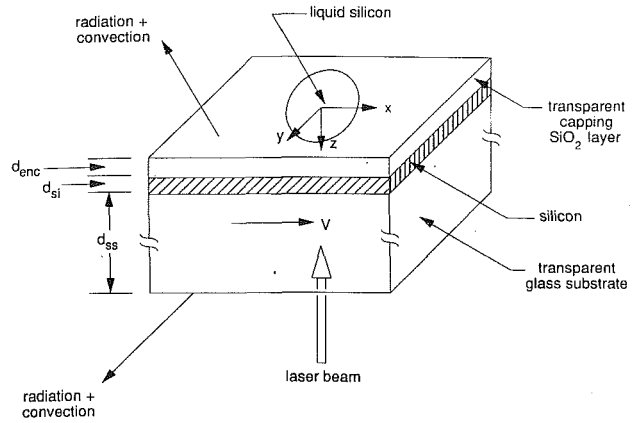

Fig. 5 Sketch of a silicon layer of thickness d_{si}, deposited on a glass substrate of thickness d_{ss}, and encapsulated by a glass layer of thickness d_{enc}

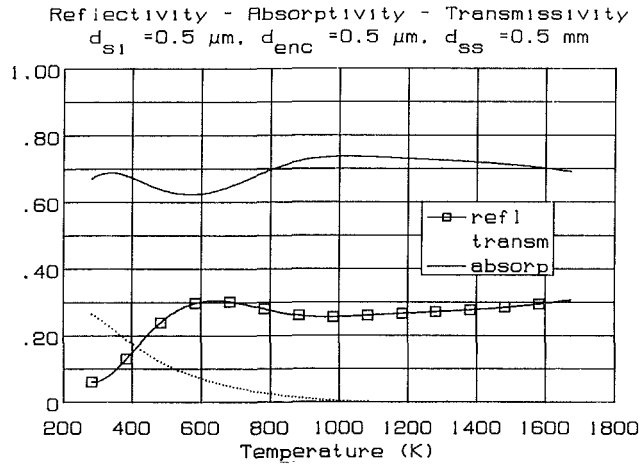

Fig. 6 Thin film reflectivity, transmissivity, and absorptivity as functions of the silicon layer temperature for the $\lambda_b = 488$ nm wavelength

To evaluate the radiative thermal emission losses an isothermal structure was considered as subjected to unpolarized irradiation. The directional spectral absorptivities were calculated by analyzing the electromagnetic wave propagation through the stratified structure (Appendix A). The hemispherical total emissivities $\epsilon^{\pm}_{enc}$, $\epsilon^{\pm}_{si,s}$, $\epsilon^{\pm}_{ss}$ were then evaluated by integrating, first with respect to direction and then over the wavelength spectrum, using Planck's spectral distribution of emissive power. These emissivities are shown in Fig. 7, as functions of temperature. Upon melting of the silicon layer, its emissivities are $\epsilon^{+}_{si,l} = 0.132$, $\epsilon^{-}_{si,l} = 0.113$, and the emissivity from the bottom substrate surface, $\epsilon^{-}_{ss} = 0.128$.

The radiative loss from the silicon layer is

$$Q_{\text{rad},si} = \sigma(\epsilon^{+}_{si} + \epsilon^{-}_{si}) \cdot (T^4_{si} - T^4_{\infty}) \tag{10}$$

The emissive loss through the substrate $\epsilon^{-}_{si,s} \approx O(10^{-3})$, since the solid silicon film is optically thin in the infrared range, as compared to the substrate.

The term $h_u(T_{enc} - T_{\infty})$ in equation (6) represents the energy convected from the silicon layer surface to the surroundings. The radiative loss from the encapsulating layer is

$$Q_{\text{rad, enc}} = \sigma(\epsilon^{+}_{enc} + \epsilon^{-}_{enc})(T^4_{enc} - T^4_{\infty}) \tag{11}$$

The emissive loss through the substrate is negligible, $\epsilon^{-}_{enc} \approx O(10^{-4})$.

It was assumed that thermal contact between adjacent layers is perfect. Throughout these calculations bulk properties were assumed. The silicon layer thermal and optical properties may depart from the bulk values. Additional experiments are needed to measure these departures. The boundary condition at the bottom substrate surface is

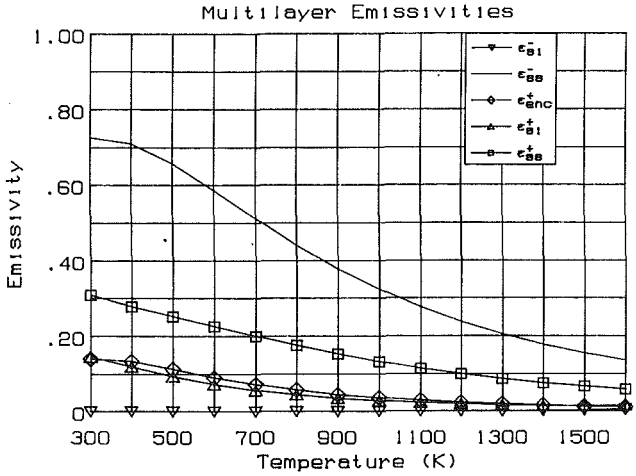

Fig. 7 Predicted emissivities as functions of temperature

$$-k_{ss}\frac{\partial T_{ss}}{\partial z}\bigg|_{z=d_{\text{enc}}+d_{si}+d_{ss}} = h_l[T_{ss}(x, y, d_{\text{enc}}+d_{si}+d_{ss}) - T_{\infty}] + \epsilon^{-}_{ss}\sigma[T_{ss}(x, y, d_{\text{enc}}+d_{si}+d_{ss})^4 - T_{\infty}{}^4] \tag{12}$$

The coefficients h_u and h_l are estimated using expressions for free convection from horizontal surfaces. The thermal emission losses are small compared to the absorbed laser power flux. The computations for a laser power $P_T = 1.8$ W, $w_{\lambda b} = 40$ μm predict silicon melting and maximum temperature in the neighborhood of 2500 K. The absorbed peak power flux by the silicon film is approximately $Q_{ab} \cong 1.4 \times 10^8$ W/m^2. The emissive loss from the silicon layer is $Q_{\text{rad, }si} \cong 5 \times 10^5$ W/m^2. The heat transfer is conduction dominated and there is no need for solving the complete equation of radiative transfer in semitransparent materials. This would be the case in processing with a CO_2 laser ($\lambda = 10.6$ μm) where both the encapsulating layer and the substrate must be treated as participating media.

The enthalpy function is used to account for phase change in the silicon layer.

$$H_{si}(T) = \int_0^T \rho_{si}(T) c_{p;si}(T) dT, \qquad T < T_m \tag{13}$$

$$H_{si}(T) = \int_0^T \rho_{si}(T) c_{p;si}(T) dT + L, \qquad T > T_m \tag{14}$$

where the density ρ_{si} and the specific heat vary differently with temperature in the solid and liquid phases. For $T = T_m$ the enthalpy function assumes values between $H_{s,si}$ and $H_{l,si}$

$$H_{s,si}(T) = \int_0^{T_m} \rho_{si}(T) c_{p;si}(T) dT \tag{15}$$

$$H_{l,si}(T) = \int_0^{T_m} \rho_{si}(T) c_{p;si}(T) dT + L \tag{16}$$

The enthalpy value $H = H_{s,si}$ is assigned to solid material at the melting temperature, while $H = H_{l,si}$ corresponds to pure liquid at the same temperature. Thus, there exists a region in which the melting is partial, and is defined by

$$H_{s,si} < H_{si} < H_{l,si}; \qquad T = T_m \tag{17}$$

Each point within this region can be assigned a solid fraction $f_s(x, y, t)$ and a liquid fraction $f_l(x, y, t)$ for which

$$f_s(x, y, t) + f_l(x, y, t) = 1 \tag{18}$$

Thus, the enthalpy function during melting at $T = T_m$ is given by

$$H_{si} = H_{s,si} + f_l L \tag{19}$$

The enthalpy function in the glass substrate and the encapsulating layer is

$$H(T) = \int_0^T \rho(T) c_p(T) dT \tag{20}$$

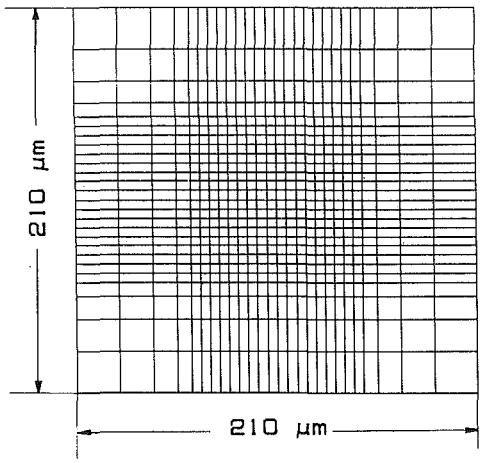

Fig. 8 Grid spacing in the x-y plane, toward the center of the laser beam

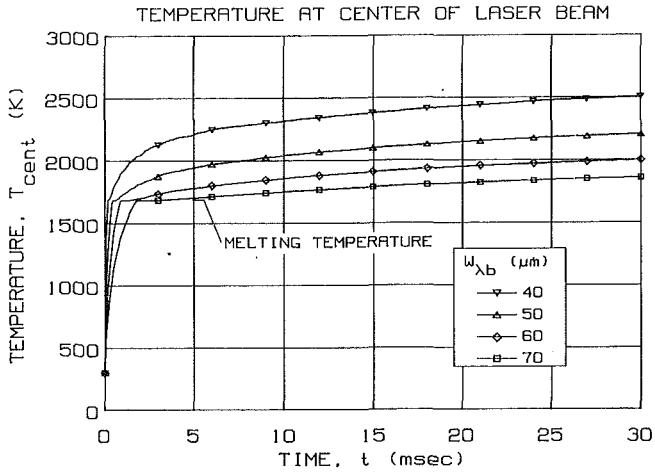

Fig. 9 Predicted temperature history of silicon layer at the laser beam center

Using the enthalpy as dependent variable, along with the temperature, equation (5) is written

$$\frac{\partial H_{si}(T_{si})}{\partial t} + V\cdot\frac{\partial H_{si}(T_{si})}{\partial x} = \frac{\partial}{\partial x}\left(k_{si}(T_{si})\frac{\partial T_{si}}{\partial x}\right) + \frac{\partial}{\partial y}\left(k_{si}(T_{si})\frac{\partial T_{si}}{\partial y}\right) + \frac{Q_{ab}(x, y, T_{si}) - Q_{\text{rad}}(T_{si})}{d_{si}} + \frac{k_{si}(T_{si})\left[\left.\frac{\partial T_{si}}{\partial z}\right|_{z=d_{si}+d_{\text{enc}}} - \left.\frac{\partial T_{si}}{\partial z}\right|_{z=d_{\text{enc}}}\right]}{d_{si}} \quad (21)$$

The initial temperature is assumed to be the ambient temperature T_∞. The conductive heat transfer equations and boundary conditions were discretized by using a control volume finite difference approach. For short times, when the temperature in the silicon layer is below the melting temperature, the heat conduction is solved by a three-step ADI finite difference algorithm. When the temperature in the silicon layer reaches the melting temperature at any location, equation (21) is solved by using a modified Gauss-Seidel iteration scheme for the liquid fraction, f_l and the temperature T_{si}. Microscopic observations of cross sections through recrystallized silicon layers have shown that melting occurs uniformly through the thickness of the film. The dendritic formations observed in partial melting also extend through the silicon layer. Accordingly, the computational scheme assumes that the silicon melting occurs uniformly through the thickness of the film, so that f_l may be assigned to the local melted area fraction. Thus, for the computational nodes that are found to be at T_m, the absorbed power density, Q_{ab}, and the radiation loss, Q_{rad}, scale with the phase fraction, f_l. Vaporization effects that occur when the film temperature reaches the boiling point have not been incorporated into this model.

The computational domain was discretized by using an orthogonal mesh of nonuniform grid spacing, which was scaled with the incident laser beam $1/e$ radius, $w_{\lambda b}$, in the x and y directions. The grid spacing was kept at $\Delta = w_{\lambda b}/10$, toward the center of the laser beam. This grid spacing was sufficient to capture accurately the temperature field variation in the liquid pool and across the phase boundary. The mesh was also variable in the z direction, with the first points placed close to the film to obtain the heat flux penetration into the substrate. Because of the symmetry of the problem, the temperature distribution was solved in one half of the physical domain, with the x-z plane considered adiabatic. In the computations a 51 × 26 × 20 mesh was used. Figure 8 shows the x-y mesh distribution toward the center of the laser beam. The temperature field solution did not noticeably change when the mesh was refined by a factor of two.

The criterion used for the iterative convergence of the temperature field at each time step was

$$\max_{i,j,k}[|T^{m+1}_{i,j,k} - T^{m}_{i,j,k}|] < r_f \quad (22)$$

No appreciable changes in the calculated maximum temperature were observed when r_f was changed from 0.01 K to 0.2 K. In the calculations presented in this paper, r_f was set at 0.1 K. The same criterion was applied to determine the convergence of the temperature field to the quasi-steady, fixed with respect to the xyz system of coordinates, temperature distribution.

IV Numerical Results and Comparisons to Experimental Data

The calculations were carried out for a range of parameters that corresponds to the experiments. It was assumed that the laser beam is turned on instantaneously and that it is focused on the moving silicon layer. Results are presented for a laser beam total power, $P_T = 1.8$ W and material translation speed, $V = 2$ mm/s. Figure 9 shows the silicon temperature rise of the silicon film at the center of the laser beam for $1/e$ laser beam intensity radii, $w_{\lambda b}$, of 40, 50, 60, and 70 μm. It is seen that after an elapsed time of about 20 ms, a quasi-steady temperature distribution is virtually established.

Figure 10(a) shows a contour plot of the temperature field in the silicon layer, for $w_{\lambda b} = 50$ μm. In accordance with the experimental evidence, it is seen that the speed effect is small, in that the molten pool shape, defined by the $T = 1685$ K isotherm, is almost perfectly circular. Figure 10(b) shows the corresponding temperature distribution on the x-z plane cross section through the substrate. Due to the relatively poor thermal conductivity of the substrate, the distortion of the temperature field isotherms due to material motion is more pronounced in the substrate. The computations for $w_{\lambda b} = 30$ μm, $P_T = 1.8$ W, and $V = 2$ mm/s show that the maximum temperature in the silicon layer rises to the boiling point, $T_{bp} = 2628$ K, within 3 ms. This is related to the "keyhole" formation observed in the experiments for the above parameters. For $w_{\lambda b} = 40$ μm, $P_T = 1.8$ W and $V = 2$ mm/s the calculations predict a uniformly liquid molten pool. The corresponding experimental results are not conclusive, since for $w_{\lambda b} = 41$ μm a uniformly liquid pool is observed, but for $w_{\lambda b} = 38$ μm, a keyhole is formed (Table 2). These differences are attributed in part to the experimental uncertainty, although this factor has been reduced by repeated experimental measurements.

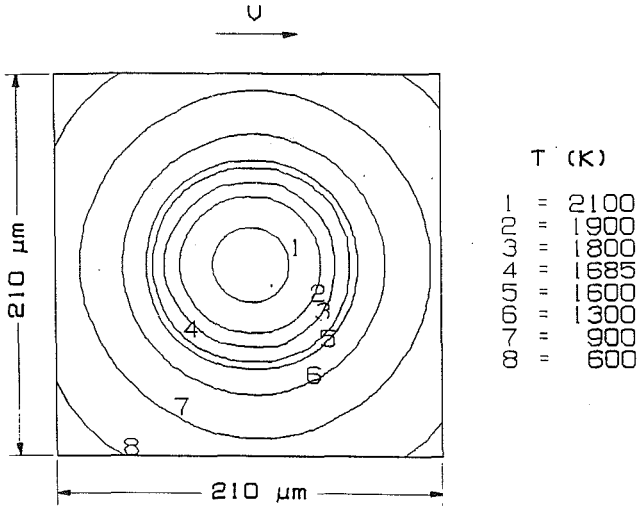

Fig. 10(*a*) Predicted temperature distribution in the silicon layer at $t = 20$ ms: laser beam power $P_T = 1.8$ W, $1/e$ irradiance radius $w_{\lambda b} = 40$ μm, and material translation speed $V = 2$ mm/s

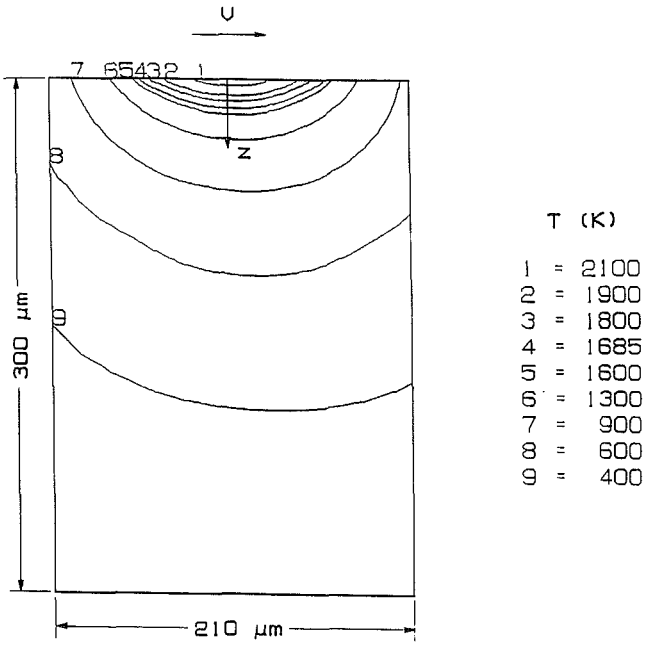

Fig. 10(*b*) Predicted temperature distribution on a x-z cross section through the glass substrate, corresponding to Fig. 9(*a*)

Based on Table 3, it can be stated that the numerical model captures the experimental trends. In accordance with the experiment, computations for $P_T = 1.8$ W show that the molten pool size remains virtually constant as $w_{\lambda b}$ is increased from 50 to 70 μm. For $P_T = 1.4$ W, the predicted molten pool temperatures are lower, and for $w_{\lambda b} = 70$ μm, numerical convergence is achieved when the results show a partially molten pool at the temperature T_m. The calculated liquid phase fraction, f_l, in this case is decreased toward the edge of the partially molten zone. This dependence is not exhibited in the dendritic phase coexistence formations observed experimentally.

The laser beam irradiance distribution can be shaped to be elliptical

$$Q_{\lambda i}^{\text{ext}}(x, y) = Q_{\lambda i}^{o} \exp\left\{-\left[\left(\frac{x}{w_{\lambda ix}}\right)^2 + \left(\frac{y}{w_{\lambda iy}}\right)^2\right]\right\} \quad (23)$$

Such laser beam shapes can be obtained by using a spherical lens of 7 cm focal length and a cylindrical lens of 8 cm focal length in the experimental apparatus. Table 4 shows the experimentally measured molten spot sizes as the laser beam is stretched in the y direction. Figure 11 shows the calculated temperature distribution in the silicon layer for a laser beam of $w_{\lambda bx} = 22$ μm and $w_{\lambda by} = 150$ μm. The predicted molten pool size is $s_x = 38$ μm and $s_y = 200$ μm as compared to the experimentally measured $s_x = 31$ μm and $s_y = 259$ μm. The estimated experimental uncertainty for $w_{\lambda bx}$ is 2 μm and for $w_{\lambda by}$ is 16 μm.

As mentioned in the introduction, it has been found that concave solidification fronts may yield nearly defect-free recrystallized films. The doughnut-shaped laser beams used by Kawamura et al. (1982) result from a linear combination of

Table 3 Comparison between the experimental and numerical results; material translation speed $V = 2$ mm/s

Molten Spot Diameter (μm)				
$w_{\lambda b}$ (μm)	$P_T = 1.8$W		$P_T = 1.4$W	
	Experiment	Computation	Experiment	Computation
40	108	89	91	86
50	118	107	95	87
60	120	106	100	90
70	126	102	partial melting	partial melting

Table 4 Experimentally measured molten pool size in μm for melting with laser beams of elliptical intensity distribution; total laser beam power $P_T = 1.8$ W

		V (mm/sec)								
		V = 0.5		V = 1.0		V = 1.5		V = 2.0		
$w_{\lambda bx}$ (μm)	$w_{\lambda by}$ (μm)	s_x	s_y	s_x	s_y	s_x	s_y	s_x	s_y	
22	100	53	213	53	219	50	209	44	219	
	107	47	222	50	225	47	228	47	219	
	115	44	228	47	234	44	234	47	234	
	124	41	238	47	234	38	241	47	244	
	132	34	244	41	241	38	253	41	250	
	141	31	256	38	250	34	259	38	256	
	150	31	266	47	266	31	266	31	259	
	160	28	272	47	266	28	269	28	266	
	169	25	281	31	275	31	281	27	266	
	179	25	281	31	281	25	281	25	281	
	190	19	281	31	281	25	291	25	281	
	201	25	291	25	281	22	291	22	281	
	212	17	295	25	281	16	300	19	281	
	223	20	292	25	281	16	300	16	266	
	234	16	300	16	281	13	291	16	266	mushy
	246	16	286	16	266	9	281	9	234	mushy
	258			9	281	9	266	9	234	mushy
	271					6	250	6	219	mushy
	284							3	188	mushy
	297							-	-	solid

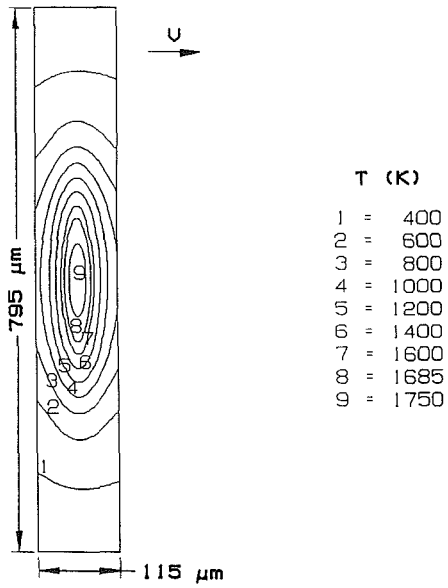

Fig. 11 Predicted temperature distribution in the silicon layer at $t = 20$ ms: laser beam $1/e$ irradiance half-span $w_{\lambda bx} = 22$ μm, $w_{\lambda by} = 150$ μm, and material translation speed $V = 2$ mm/s

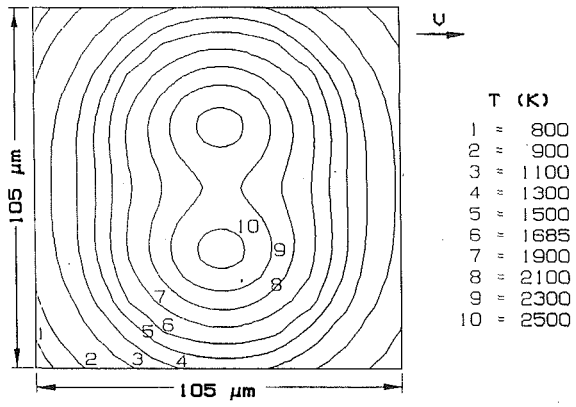

Fig. 12 Predicted temperature field in the silicon layer at $t = 20$ ms; laser beam operates on the TEM_{01} mode; total power $P_T = 8$ W; radius $w_{\lambda b} = 20$ μm, material translation speed $V = 2$ mm/s

low-order rectangular Hermite-Gaussian modes, the TEM_{01} and TEM_{10} modes. Operation on the TEM_{01} mode yields the following external laser beam irradiance distribution (Carter, 1980):

$$Q_{\lambda i}^{\text{ext}}(x, y) = Q_{\lambda i}^{o} \frac{y^2}{3w_{\lambda i}^2} \exp\left\{ -\left[\frac{x^2}{w_{\lambda i}^2} + \frac{y^2}{3w_{\lambda i}^2} \right] \right\} \qquad (24)$$

Figure 12 shows the calculated temperature field distribution in the silicon layer for a laser beam of total power, $Q_T = 8$ W, $w_{\lambda b} = 20$ μm, and material translation speed, $V = 2$ mm/s with spatial distribution given by equation (24). It can indeed be seen that the predicted solidification trailing edge is curved inward. One factor that limits the practical implementation of this finding is that the higher order modes are unstable. It is however possible to use lithographically patterned films to shape the laser beam to the desired irradiance distribution (Zorabedian et al., 1983).

V Conclusions

This paper studied laser melting of thin silicon films effected by a 4-W, multiline CW Argon ion laser beam. The experiments measured the molten pool size as a function of the laser beam parameters and the material translation speed. A three-dimensional conductive heat transfer algorithm was constructed. The numerical predictions were compared to the experimental data and reasonable agreement was obtained. The numerical model was applied to the analysis of the heat transfer induced by shaped laser beam profiles. Such distributions may yield modified solidification fronts and potential semiconductor crystal growth improvements.

Acknowledgments

Support to the first two authors by the National Science Foundation, Division of Mechanics, Structures and Materials under Grant No. MSM-8708757 is gratefully acknowledged. The authors also wish to thank Dr. David K. Biegelsen of Xerox, Palo Alto Research Center for providing the samples for the experiments. The help of Mr. Kenneth E. Barclay in conducting the experiments is acknowledged.

References

Atthey, D. R., 1974, "A Finite Difference Scheme for Melting Problems," *J. Inst. Math Applics.*, Vol. 13, pp. 353–365.

Born, M., and Wolf, E., 1970, *Principles of Optics*, 6th ed., Pergamon, United Kingdom, pp. 55–60, 611–624.

Carter, W. H., 1980, "Spot Size and Divergence for Hermite-Gaussian Beams of Any Order," *Applied Optics*, Vol. 19, No. 7, pp. 1027–1029.

Celler, G. K., 1983, "Laser Recrystallization of Thin Si Films on Amorphous Insulating Substrates," *J. Cryst. Growth*, Vol. 63, pp. 429–444.

Fan, J. C. C., Tsaur, B. Y., and Geis, M. W., 1983, "Graphite-Strip-Heater Zone Melting Recrystallization of Si Films," *J. Cryst. Growth*, Vol. 63, pp. 453–483.

Grigoropoulos, C. P., Buckholz, R. H., and Domoto, G. A., 1986, "A Heat Transfer Algorithm for the Laser-Induced Melting and Recrystallization of Thin Silicon Layers," *J. Appl. Phys.*, Vol. 60, No. 7, pp. 2304–2309.

Grigoropoulos, C. P., Buckholz, R. H., and Domoto, G. A., 1988, "An Experimental Study on Laser Annealing of Thin Silicon Layers," ASME JOURNAL OF HEAT TRANSFER, Vol. 110, pp. 416–423.

Grigoropoulos, C. P., Emery, A. F., and Wipf, E. P., 1990, "Heat Transfer in Thin Silicon Film Melting by Laser Line Sources," *Int. J. Heat Mass Transfer*, Vol. 33, No. 5, pp. 797–803.

Heavens, A. S., 1955, *Optical Properties of Thin Films*, Butterworths, London, pp. 66–74.

Jellison, G. E., Jr., 1984, "Optical and Electrical Properties of Pulsed Laser-Annealed Silicon," in *Semiconductors and Semimetals*, Vol. 23, R. F. Wood, C. W. White, and R. T., Young, eds., Academic Press, Orlando, FL, pp. 95–164.

Jellison, G. E., Jr., and Burke, H. H., 1986, "The Temperature Dependence of the Refractive Index of Silicon at Elevated Temperatures at Several Laser Wavelengths," *J. Appl. Phys.*, Vol. 60, No. 2, pp. 841–843.

Kawamura, S., et al., 1982, "Recrystallization of Si on Amorphous Substrates by Doughnut-Shaped CW Ar Laser Beams," *Appl. Phys. Lett.*, Vol. 40, No. 5, pp. 394–395.

Knittl, Z., 1976, *Optics of Thin Films*, Wiley, Prague, Czechoslovakia, pp. 240–282.

Kokorowski, S. A., Olson, G. L., and Hess, L. D., 1981, "Thermal Analysis of CW Laser Annealing Beyond the Melt Temperature," *Proceedings, Materials Research Society*, J. F. Gibbons et al., eds., North-Holland, New York, Vol. 1, pp. 139–146.

Kubota, K., Hunt, C. E., and Frey, J., 1986. "Thermal Profiles During Recrystallization of Silicon Insulator with Scanning Incoherent Light Line Sources," *Appl. Phys. Lett.*, Vol. 46, No. 12, pp. 1153–1155.

Miaoulis, I. N., and Mikic, B. B., 1986, "Heat Source Power Requirements for High-Quality Recrystallization of Thin Silicon Films for Electronic Devices," *J. Appl. Phys.*, Vol. 59, No. 5, pp. 1658–1666.

Palik, E. D., 1985, *Handbook of Optical Constants of Solids*, Academic Press, Orlando, FL, p. 760.

Pfeiffer, L., Gelman, A. E., Jackson, K. A., and West, K. A., 1987, "Growth Mechanisms During Thin Film Crystallization From the Melt," *Proceedings, Materials Research Society*, M.O. Thompson et al., eds., MRS, Pittsburgh, PA, Vol. 74, pp. 543–553.

Schvan, P., and Thomas, R. E., 1985, "Time Dependent Heat Flow Calculation of CW Laser-Induced Melting of Silicon," *J. Appl. Phys.*, Vol. 57, No. 10, pp. 4738–4741.

Shamsundar, N., and Sparrow, E. M., 1975, "Analysis of Multidimensional Conduction Phase Change Via the Enthalpy Model," ASME JOURNAL OF HEAT TRANSFER, Vol. 97, pp. 333–340.

Shamsundar, N., and Sparrow, E. M., 1976, "Effects of Density Change on Multidimensional Conduction Phase Change," ASME JOURNAL OF HEAT TRANSFER, Vol. 98, pp. 551–557.

Shvarev, K. M., Baum, B. A., and Gel'd, P. V., 1975, "Optical Properties of Liquid Silicon," *Sov. Phys. Solid State*, Vol. 16, No. 11, pp. 2111–2112.

Stultz, T. J., and Gibbons, J. F., 1981, "The Use of Beam Shaping to Achieve Large-Grain CW Laser-Recrystallized Polysilicon on Amorphous Substrates," *Appl. Phys. Lett.*, Vol. 39, No. 6, pp. 498–500.

Touloukian, Y. S., 1970, *Thermophysical Properties of Matter, Thermal Conductivity*, IFI/Plenum, New York.

Tsaur, B. Y., 1986. "Assessment of Silicon on Insulator Technologies for VLSI," *Proceedings, Materials Research Society*, A. Chiang et al., eds., MRS, Pittsburgh, PA, Vol. 53, pp. 365–373.

Waechter, D., Schvan, P., Thomas, R. E., and Tarr, N. G., 1986, "Modeling of Heat Flow in Multilayer CW Laser-Annealed Structures," *J. Appl. Phys.*, Vol. 59, No. 10, pp. 3371–3374.

Willems, G. J., Poortmans, J. J., and Maes, H. E., 1987, "A Semiempirical Model for the Laser-Induced Molten Zone in the Recrystallization Process," *J. Appl. Phys.*, Vol. 62, No. 8, pp. 3408–3415.

Yariv, A., 1976, *Introduction to Optical Electronics*, 2nd ed., Holt, Rinehart, and Winston, New York, pp. 36–39.

Zorabedian, P., Drowley, C. I., Kamins, T. I., and Cass, T. R., 1983, "Beam Shaping for CW Laser Recrystallization for Polysilicon Films," *Proceedings, Materials Research Society*, J. Narayan et al., eds., North-Holland, New York, Vol. 13, pp. 523–528.

APPENDIX A

The encapsulated silicon layer structure is treated as a stratified, multilayer medium (Born and Wolf, 1970; Knittl, 1976; Heavens, 1955). A plane wave of light of wavelength λ is incident on the multilayer structure through the substrate or through the encapsulating layer. The wave propagation direction forms an angle θ_o with the outward normal on the boundary surface of the structure. The characteristic transmission matrix M_i, representing an absorbing layer of thickness d_i and having complex refractive index $\hat{n}_i$, is given by

$$M_i = \begin{pmatrix} \cos\left(\frac{2\pi}{\lambda}\hat{n}_i d_i \cos\theta_i\right) & -\frac{j}{\hat{p}_i}\cos\theta_i \sin\left(\frac{2\pi}{\lambda}\hat{n}_i d_i \cos\theta_i\right) \\ -j\hat{p}_i \sin\left(\frac{2\pi}{\lambda}\hat{n}_i d_i \cos\theta_i\right) & \cos\left(\frac{2\pi}{\lambda}\hat{n}_i d_i \cos\theta_i\right) \end{pmatrix} \quad (24)$$

The coefficient $\hat{p}_i$ is given by $\hat{p}_i = \hat{n}_i \cos\theta_i$ for the TE (transverse electrical) wave, and by $\hat{p}_i = \cos\theta_i/\hat{n}_i$ for a TM (transverse magnetic) wave. The angles θ_i are complex for absorbing films and they are defined by the generalized Snell's law, $\hat{n}_i \sin\theta_i = \sin\theta_o$.

The system transmission matrix M for illumination through the substrate is

$$M = M_{ss} \times M_{si} \times M_{\text{enc}} \quad (25)$$

The system reflection and transmission coefficients r and t_r are

$$r = \frac{(M(1,1) + M(1,2)\cos\theta_o)\cos\theta_o - (M(2,1) + M(2,2)\cos\theta_o)}{(M(1,1) + M(1,2)\cos\theta_o)\cos\theta_o + (M(2,1) + M(2,2)\cos\theta_o)} \quad (26)$$

$$t_r = \frac{2\cos\theta_o}{(M(1,1) + M(1,2)\cos\theta_o)\cos\theta_o + (M(2,1) + M(2,2)\cos\theta_o)} \quad (27)$$

The above equations are valid for both TE and TM wave propagation. For normal incidence, $\theta_o = 0$, the results are identical for the two polarizations.

The film reflectivity and transmissivity in terms of r and t_r are

$$R = |r|^2 \quad (28)$$

$$\tau = |t_r|^2 \quad (29)$$

The local energy flux through the structure and thus the light absorption in the encapsulating layer, the polysilicon film, and the substrate are readily evaluated.

APPENDIX B

B.1 Optical Properties

The real part of the silicon refractive index is a linear function of temperature between approximately 300 and 1000 K (Jellison and Burke, 1986; Jellison, 1984)

$$n_{si}(\lambda, T) = n_{si}^o(\lambda) + a_n(\lambda)(T - 300) \quad (30)$$

The coefficient $a_n(\lambda)$ is a fifth-order polynomial of wavelength λ. The extinction coefficient k_{si}^{ext} is given by the following expression:

$$k_{si}^{\text{ext}}(\lambda, T) = k_{si}^o(\lambda)\exp(T - 273/430) \quad (31)$$

The liquid silicon complex refractive index has been measured by Shvarev et al. 1975) as

$$\hat{n}_l = 2.2 + j4.4 \quad (32)$$

B.2 Thermal Properties

The silicon thermal conductivity varies with temperature (Touloukian, 1970) as

$$k_{si}(T) = 2.99 \times 10^4/(T - 99) \quad \text{(W/m/K)} \quad (33)$$

The solid silicon volumetric specific heat is given by

$$\rho_{si}(T)c_{p;si}(T) = 1.45 \times 10^6 + 86500 \times (T - 270)^{0.23} \quad \text{(J/m}^3\text{/K)} \quad (34)$$

The fused silica substrate thermal conductivity was assumed to be constant, $k_{ss} = 1.4$ W/mK.

The substrate thermal conductivity at high temperatures is not well known. Previous computational work (Grigoropoulos et al., 1990) for one-dimensional laser line source melting of thin silicon layers has shown this to be a second-order effect.

Thermal Rectification in Similar and Dissimilar Metal Contacts

P. F. Stevenson
Research Assistant.
Student Mem. ASME

G. P. Peterson
Professor of Mechanical Engineering.
Mem. ASME

L. S. Fletcher
Dietz Professor of Mechanical Engineering.
Fellow ASME

Department of Mechanical Engineering,
Texas A&M University,
College Station, TX 77843

An investigation was conducted to verify experimentally the existence of thermal rectification and to determine the effect of surface roughness and material type. Four pairs of test specimens were evaluated: one with a smooth Nickel 200 surface in contact with a rough Nickel 200 surface, one with a smooth Stainless Steel 304 surface in contact with a rough Stainless Steel 304 surface, one with a smooth Nickel 200 surface in contact with a rough Stainless Steel 304 surface, and finally, one with a smooth Stainless Steel 304 surface in contact with a rough Nickel 200 surface. The thermal contact conductance was measured for heat flow from both the smooth to rough and rough to smooth configurations for all four pairs. The results indicate that thermal rectification is a function of surface characteristics, material type, and heat flow direction. For similar materials in contact, some thermal rectification was observed with heat flow from the rough surface to the smooth surface resulting in a higher value of contact conductance. For dissimilar materials, the thermal contact conductance was highest when the heat flow was from the Stainless Steel 304 to Nickel 200. In these cases, the surface roughness was shown to be of secondary importance.

Introduction

Although many of the factors that affect the transfer of heat across metallic interfaces are reasonably well understood, the directional dependence of the thermal contact conductance has not yet been completely explained. This phenomenon, referred to as thermal rectification, is of significant importance in the design of heat exchangers and spacecraft thermal control systems, and has potential applications in the thermal control of electronic equipment as a thermal rectifier.

Typical experimental contact conductance configurations consist of two right coaxial cylinders in contact. In this physical arrangement, convective and radiative heat transfer from the outside of the test specimens can be controlled and one-dimensional heat flow can be approximated. For these conditions, three mechanisms of heat transfer exist at the interface: (*i*) conduction through the actual contact area, (*ii*) conduction through any interstitial media, and (*iii*) radiation across the gap between the surfaces. In vacuum environments of 10^{-5} Torr or less, the contribution of interstitial gases is negligible. Also for low temperatures, such as those of interest in this investigation, radiation can be neglected (Madhusudana and Fletcher, 1986) making conduction across the actual contact area the most significant of the three.

Steady-state heat flow in one dimension through a material may be described by Fourier's law of heat conduction:

$$q = -kA\,\partial T/\partial Z \tag{1}$$

where q is the heat transfer, k is the thermal conductivity of the materials, and $\partial T/\partial Z$ is the one-dimensional temperature gradient. Assuming the thermal conductivity is constant, $\partial T/\partial Z$ can be approximated by $\Delta T/\Delta Z$, yielding the area dependent resistance to heat flow as

$$R_F = \frac{\Delta T}{q} = \frac{T_1 - T_2}{q} = \frac{\Delta Z}{k} = \frac{Z_1 - Z_2}{k} \tag{2}$$

Figure 1(*a*) shows a graphic representation of this concept for dissimilar metals in contact with no interfacial resistance. Equation (2) may also be written

$$R_F = \frac{T_1 - T_i}{q} + \frac{T_i - T_2}{2} \tag{3}$$

where T_i is the temperature of the interface. If a thermal contact resistance R_c, is present at the interface, then the total resistance R_T can be written:

$$R_T = R_F + R_c = \frac{T_1 - T_2}{q} \tag{4}$$

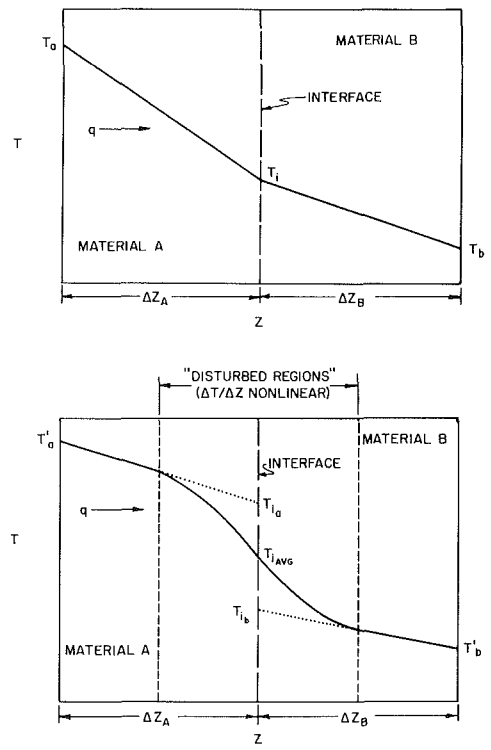

Fig. 1 Graphic representation of heat flow through a metallic joint

Contributed by the Heat Transfer Division and presented at the ASME Winter Annual Meeting, San Francisco, California, December 10-15, 1989. Manuscript received by the Heat Transfer Division August 21, 1989; revision received June 11, 1990. Keywords: Conduction, Measurement Techniques, Modeling and Scaling.

or

$$R_c = R_T - R_F = \frac{T_1 - T_2}{q} - \left(\frac{\Delta A_1}{k_1} + \frac{\Delta Z_2}{k_2}\right) \tag{5}$$

The thermal contact resistance R_c may also be written in terms of the interface temperatures as

$$R_c = \frac{T_{i1} - T_{i2}}{q} \tag{6}$$

where T_{i1} and T_{i2} are the temperatures that would exist at the contact interface if only one resistance to heat flow were present. Figure 1(*b*) illustrates the effect of this contact resistance very clearly.

The thermal contact conductance is defined as the reciprocal of the area-independent contact resistance and can be written as

$$h_c = \frac{q/A}{\Delta T_i} = \frac{q/A}{T_{i1} - T_{i2}} = \frac{1}{AR_c} \tag{7}$$

This definition of thermal contact conductance is independent of the direction of the heat flow through the interface and includes the effects of any oxides or films present on the contacting surfaces.

Thermal Rectification. An idealized model can be used to understand the basic physical phenomenon of thermal rectification. This model consists of two elastic spheres with radii of R_1 and R_2, respectively, in contact. These spheres are located mechanically with a force F, normal to the contact, as shown in Fig. 2(*a*) (Somers and Fletcher, 1983). This contact geometry is analogous to the microscopic contact points between two right coaxial cylinders, i.e., the contact may be assumed to be comprised of individual asperities, which are spherically shaped. Using a Hertzian analysis, this contact point may be shown to be circular in shape with radius r_o where

$$r_o = \left(\frac{(3\pi F(K_1 + K_2)R_1R_2)}{4(R_1 + R_2)}\right)^{1/3} \tag{8}$$

and

$$K_1 = \frac{(1 - \nu_1^2)}{\pi E_1} \text{ and } K_2 = \frac{(1 - \nu_2^2)}{\pi E_2} \tag{9}$$

If the thermal properties of the two materials remain constant with respect to temperature, equation (8) will remain valid for any given heat flow. For a known temperature drop across the interface, the contact radius may be used to calculate the actual thermal contact area and hence, the thermal resistance of the contact.

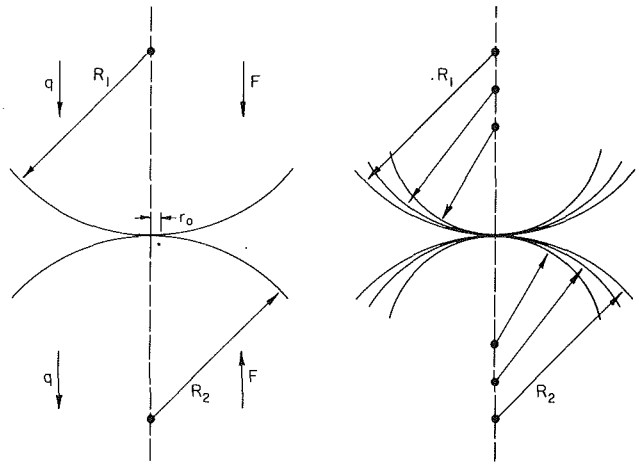

Fig. 2 (*a*) Hertzian spherical contact; (*b*) thermal distortion of contacting spheres

Since a majority of the physical and thermophysical properties are a function of temperature, changes in the magnitude of the heat flow can result in thermomechanical changes in one or both of the materials and thermal distortion of the contact area, as shown in Fig. 2(*b*). If a frictionless contact is assumed, the thermomechanical movement of each contacting surface can be analyzed separately and equation (8) can be used to determine the actual contact area of the interface. The relative change in the contact area due to changes in the heat flow may be found by taking the partial derivative of the contact area with respect to the heat flow. Differentiating equation (8) and simplifying yields

$$\frac{\partial r_o}{\partial q} = \left(\frac{K}{3}\right)\left(\frac{R_1R_2}{R_1 + R_2}\right)^{-2/3}\left(\frac{1}{(R_1 + R_2)^2}\right)\left(R_2^2\frac{dR_1}{dq} + R_1^2\frac{dR_1}{dq}\right) \tag{10}$$

where

$$K = \left(\frac{3\pi}{4}F(K_1 + K_2)\right)^{1/3} \tag{11}$$

The last term in equation (10) is the only term that may have a negative value; therefore, this is the term that controls the sign of $\partial r/\partial q$ and hence, influences the thermal rectification (i.e., heat flowing out of surface 1 will cause the material to contract due to thermal distortion and become more convex, decreasing R_1). Therefore, for heat flow out of a surface, dR/dq will be negative. The sign of the last term in equation (10)

Nomenclature

A = cross-sectional area of specimen
b = specimen radius
c = Vickers microhardness coefficient
d_v = indentation diagonal
d = gap roughness parameter = $(FD + 2\sigma)_r - 0.5(FD + 2\sigma)_s$
E = modulus of elasticity
F = force
FD = flatness deviation
h_c = thermal contact conductance
H = microhardness
k = thermal conductivity
K = parameter (defined in equation (9))
m = mean absolute asperity slope
M = effective flow pressure of the softer material
P = contact pressure
q = thermal power
r_o = radius of Hertzian contact point
R = thermal resistance
T = temperature
W = flatness deviation from centerline
δ_o^* = δ_o/b
ν = Poisson ratio
σ = roughness of the contacting materials

Subscripts

a = arithmetic mean
c = contact
F = area dependent
i = interface
m = harmonic mean value
q = rms value
t = maximum peak to valley
T = total
v = Vickers
1 = surface one
2 = surface two

Superscripts

* = dimensionless

therefore will depend on which material has the greater thermal strain and/or largest radius of curvature. This implies that the thermal rectification is dependent upon both the material properties and the surface characteristics.

Literature Review

There are many independent parameters that influence the conduction of heat at metallic interfaces, such as the roughness and/or waviness of the contacting surfaces, the mean slope of the individual roughness asperities, the mean interface temperature, the apparent contact pressure, the mechanical and physical properties of the contacting materials, the heat flux magnitude and direction, the loading history, the physical geometries of the asperity contacts, and hysteresis effects associated with heat flux reversals. Many of these parameters have been studied in previous investigations, the results of which are summarized below.

Experimental Investigations. Starr (1936) was the first to report a directional effect of heat flow through an interface in copper–copper oxide contacts, but subsequent studies yielded conflicting results. Several investigations that dealt with aluminum/stainless steel contacts in an air environment resulted in disagreement as to which direction of heat flow showed the highest thermal rectification effects, stainless steel to aluminum or aluminum to stainless steel, and several researchers have observed no thermal rectification effects. This conflict led to a number of studies in the late 1960s, a majority of which were conducted in vacuum environments.

Clausing (1966) presented data resulting from aluminum to stainless steel and magnesium to stainless steel contacts. The resulting data showed that the highest thermal rectification effect occurred in contacts in which the heat flow was from stainless steel to aluminum. This was contrary to a majority of the earlier studies. Shortly after this investigation, Lewis and Perkins (1968) performed similar experiments with aluminum to stainless steel contacts, and noted that the thermal rectification direction was related to the physical characteristics of the interface. The results indicated that for flat to rough contacts, where microscopic resistance dominated, the greater directional effect occurred in the aluminum to stainless steel direction. However, for spherically shaped contacts where macroscopic resistance was dominant, the direction of greatest effect was reversed. In addition, data were presented that indicated that increases in the interfacial contact pressure resulted in corresponding increases in the thermal rectification.

In examining the effect of the heat flux magnitude, Thomas and Probert (1970) obtained results that contradicted those obtained by Clausing (1966), whereas other researchers, such as Somers et al. (1978), found no effect from the magnitude of heat flux. Jones et al. (1974) conducted experiments in which the directional effect at low contact pressures was greater for stainless steel to aluminum, but was reversed at higher contact pressures.

Experiments conducted by Somers and Fletcher (1983) consisted of five dissimilar pairs of materials with contact pressures ranging from 234.1 to 5618.4 kPa (33.9 to 813.7 psi), mean interface temperatures from 301.88 to 484.8 K (84 to 413.2°F), and heat flux magnitudes of 74.04 to 14.81 MW/m^2 (77 to 15.4 MBTU/hr-ft^2). Thermal rectification was observed in all five pairs. It was hypothesized that the directional effect was due partly to the presence of variations in surface curvature and microscopic asperities.

More recently, Yovanovich and Nho (1989) conducted an experimental investigation of three ground/lapped Stainless Steel 304 interfaces and compared the results with anisotropic and isotropic models. The data and theory of both models were in good agreement, provided the contact microhardness was corrected for temperature.

Analytical Investigations. Analytical investigations of the thermal contact conductance can be grouped into three major classifications: (*i*) electronic solid state models, (*ii*) microscopic contact models, and (*iii*) macroscopic contact models. The first classification, the electronic solid state models, were initially investigated by Moon and Keeler (1962) and later endorsed by Thomas and Probert (1970). A difficulty with this approach is that the derived expression contains the work potential of the contacting materials as variables. This makes the relation hard to use because of the limited information available on work potentials. This theory does, however, predict the thermal rectification effect.

The second classification, those that utilize the microscopic contact model, deal with the conductance of heat at individual asperities. Two fundamental approaches have been developed in recent years: one by Thomas and Probert (1970) and the other by Dundurs and Panek (1976). Both of these approaches yield mathematical expressions for the contact conductance that indicate the presence of a directional bias.

The third classification, those that use a macroscopic model, consider the effect of the overall constriction resistance due to a reduction in the interfacial contact areas. These models emphasize the influence of the different interfacial thermal strains in producing the thermal rectification effects. The first such analysis was presented by Veziroglu (1967), followed by the Veziroglu and Chandra (1970) model and the Barber (1971) model.

A computer analysis performed by Somers and Fletcher (1983) on existing experimental data determined that none of the published theoretical models are capable of accurately predicting the magnitude of the thermal conductance or the direction of the thermal rectification for dissimilar metal contacts.

Although the results of past investigations of thermal rectification are contradictory, some of the differences can be explained by examining the differences in the surface characteristics of the contacting metals and/or the thermophysical properties. The existing data, however, are not adequate to determine the extent to which variations in the surface characteristics and/or the material type affect the magnitude of the thermal contact conductance. In addition, in a majority of the previous investigations only minor precautions were taken to ensure that the effect of heat transfer reversal was actually being measured and not the effects of variations in heat flux level, surface finish, or loading cycle.

Experimental Program

The objective of this investigation was to verify experimentally the existence of thermal rectification; to separate it from the effects of variation in heat flux level, surface finish, and loading cycle; and to compare the resulting data with existing analytical and empirical models.

The experimental procedure was divided into three steps: step 1 was to prepare all of the samples in a similar manner to ensure repeatable results; step 2 was to test similar metal pairs to determine the effect of variations in surface roughness; and step 3 was to test dissimilar materials to determine the effect of variations in the physical and thermophysical properties.

Surface Analysis. For this investigation, a total of eight test specimens were used, four each of Stainless Steel 304 and Nickel 200. These materials were selected because the behaviors of Nickel 200 to Nickel 200 and Stainless Steel 304 to Stainless 304 interfaces have been previously tested and the results are well documented in the literature (Song and Yovanovich, 1988). All eight specimens were machined on a lathe to a nominal size of 2.54 cm (1.0 in.) diameter and 8.89 cm (3.5 in.) in length, and three thermocouple holes were drilled at 1.27 cm (0.5 in.) intervals along the centerline of each. Two of the

Table 1 Test specimen characteristics

SPECIMEN #	σ_a (μm)	σ_b (μm)	σ (μm)	m_{da}	m_{dq}	V_a (μm)	V_b (μm)
*SS 3	3.06	-----	3.91	-----	0.16	-----	0.58
SS 5	0.17	1.76	0.22	0.06	0.08	0.08	0.58
Composite			3.92		0.18		
*Ni 3	4.97	-----	6.59	-----	0.24	-----	-----
Ni 8	0.36	2.69	0.47	0.08	0.11	0.10	0.76
Composite			6.61		0.26		
*Ni 4	1.96	-----	2.41	-----	0.13	-----	-----
SS 8	0.23	2.49	0.32	0.06	0.08	0.13	0.74
Composite			2.43		0.16		
*SS 4	0.98	-----	1.22	-----	0.08	-----	-----
Ni 7	0.30	3.20	0.39	0.07	0.10	0.38	2.14
Composite			1.28		0.13		

* Samples prepared and characterized at the University of Waterloo

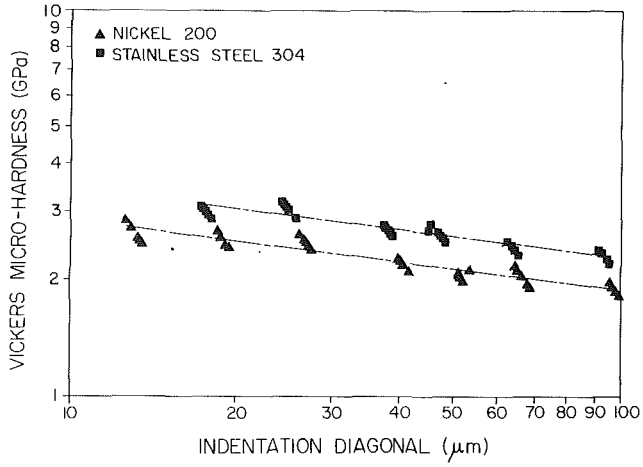

Fig. 3 Vickers microhardness as a function of indentation diagonal for Nickel 200 and Stainless Steel 304

stainless steel and two of the nickel samples were sent to the University of Waterloo, Ontario, Canada, for bead blasting of the surfaces and subsequent surface analysis. A Talysurf V surface analyzer was used to define the surface characteristics of the specimens. The remaining four samples were surface ground and sent to Sheffield Measurement Services in Dayton, OH where the surface characteristics were measured using an optical profilometer. The surface parameters for each specimen are listed in Table 1.

Microhardness. If a material deforms under loading, the thermal joint resistance, R_c, will be affected by changes in the contact radius. For this reason it is important to know the deformation characteristics of a given material. The plastic deformation of materials under static loading may be quantified by the "microhardness" of the material and can be measured with a Vickers microhardness tester. The Vickers microhardness value, H_v, is obtained by indenting the material with a diamond braille indenter and measuring the resulting projected diagonal length. The results can then be used in the following equation to predict the thermal conductance (Mikic, 1974):

$$h_c = \frac{k}{\sigma} 1.13 \tan\theta \left(\frac{P}{H_v}\right)^{0.94} \tag{12}$$

Song and Yovanovich (1988) developed an explicit expression for the relative contact pressure P/H_c for use in the prediction of the thermal contact conductance

$$\frac{P}{H_c} = \left(\frac{P}{c_1\left(\frac{1.62 \times 10^6\,\sigma}{m}\right)^{c_2}}\right)^{\frac{1}{1+0.071c_2}} \tag{13}$$

where

$$H_v = c_1 d_v^{c_2} \tag{14}$$

is used to find the constants c_1, which indicated the value of H_v at d_v equal to 1 μm, and c_2 which is the slope of the line on a log-log plot of the data.

Samples of Nickel 200 and Stainless Steel 304, prepared in the same manner as the thermal test specimens, were tested for hardness prior to measuring the thermal contact conductance. The results of these measurements are shown graphically in Fig. 3.

Thermal Conductivity Calibration. In addition to knowing the microhardness, it was necessary to determine the thermal conductivity of the specimens. Two smooth stainless steel samples, prepared in the same manner as the contact conductance test specimens, were placed in a high-quality vacuum test apparatus along with an electrolytic iron sample constructed from standard NBS reference material. The contact surfaces were coated with heat sink compound to assure minimal thermal contact resistance between the specimens and the reference sample. Using the known thermal conductivity of the electrolytic iron and Fourier's law of heat conduction, the temperature-dependent thermal conductivity of the stainless steel material was determined.

Thermal Contact Resistance. The stainless steel and nickel samples were grouped to make four pairs of specimens: one stainless steel pair, one nickel pair, one stainless steel to nickel (smooth to rough), and one stainless steel to nickel (rough to smooth). The sample pairs were then placed into the test apparatus and axially loaded in 40 N increments to a maximum load of 900 N using a gas bellows mechanism. The mean interface temperature was held constant at 300 K ±2 K and allowed to reach steady state between successive data readings.

The uncertainties associated with these types of measurement have been presented in detail by Kapischke (1987) and are comprised of the uncertainty in the location of the thermocouple wells, the measurement of the temperature, and the determination of the axial heat flux. Using the method outlined by Kline and McClintock (1953), the overall experimental uncertainty was estimated to be ± 6 percent at the highest heat flux and ± 10 percent for the lowest heat flux.

Results and Discussion

In order to ensure that the experimental technique employed was repeatable, the thermal contact conductance was measured for one test pair. The two samples in this test pair were then separated and rotated slightly and retested. This procedure was repeated a total of four times. The data obtained from this series of tests were all within ±2 percent of each other with the highest deviation occurring at light loads between the first and second consecutive tests.

Once the experimental procedure had been verified, the first pair, stainless steel to stainless steel, was tested and thermal contact conductance of the interface measured over a pressure range from approximately 20 kPa to 1400 kPa with the heat flow from the ground surface to the bead blasted surface (smooth to rough). At the conclusion of this test, the samples were separated and rotated slightly, and the measurements repeated with the heat flow direction reversed. This procedure was repeated with each of the other three sample pairs. As shown in Fig. 4(*a*), stainless steel to stainless steel, some thermal rectification was observed with heat flow from the rough surface to the smooth surface having the higher value of conductance by 11.8 percent at 4 MPa and 9.8 percent at 14 MPa. Although as shown in Fig. 4(*b*) (nickel to nickel) the same

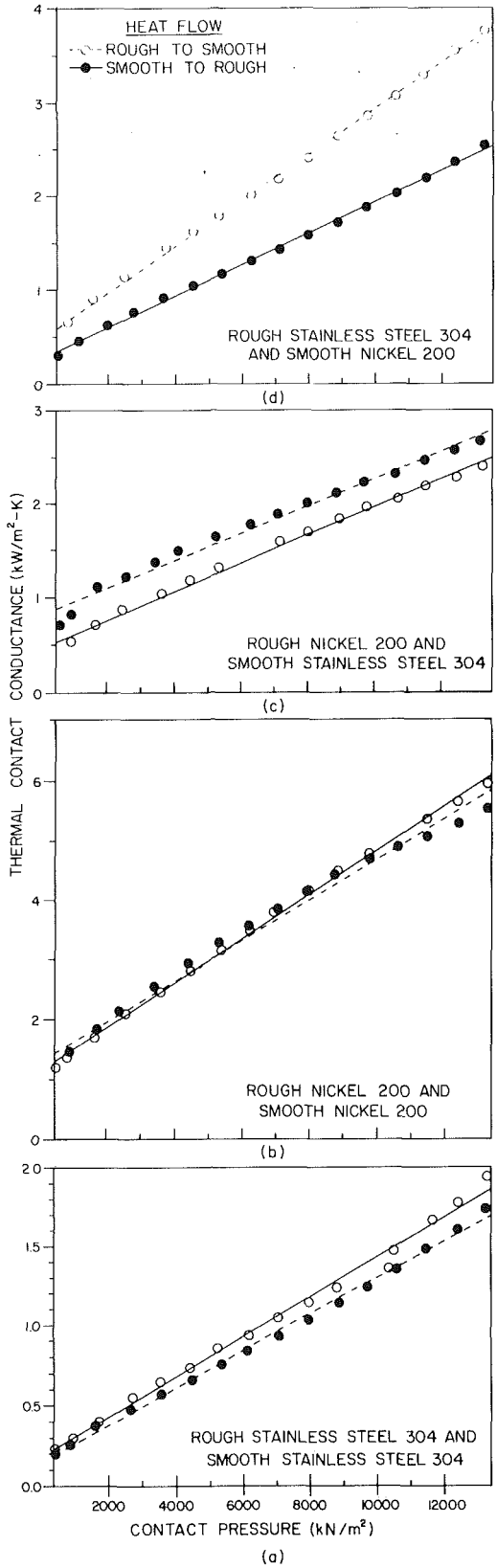

Fig. 4 (*a*) Thermal contact conductance as a function of pressure for similar Stainless Steel 304 specimens; (*b*) thermal contact conductance as a function of pressure for similar Nickel 200 specimens; (*c*) thermal contact conductance as a function of pressure for rough Nickel 200 and rough Stainless Steel 304 specimens

trend is apparent at higher pressures, the difference between the two measured values at 4 MPa is only 1.21 percent and at 14 MPa only 4.5 percent. Because these values are within the experimental error, no clear correlations may be drawn for this case.

Both of the experiments using nickel to stainless steel contacts show some evidence of thermal rectification, as noted in Figs. 4(*c*) and 4(*d*). For both cases, the thermal contact conductance was highest when the heat was flowing from stainless steel to nickel, 31.5 percent at 4 MPa and 10.95 percent at 14 MPa (Fig. 4*c*) and 55.2 percent at 4 MPa and 49.7 percent at 14 MPa (Fig. 4*d*). Further analysis of the data indicates that where nickel is the rough surface, the value of conductance is higher when heat flows from stainless steel to nickel, but is not as high in magnitude as in Fig. 4(*d*) where stainless steel is the rougher surface.

Comparison of Results With Theories. A comparison between the results of this experimental program and several analytical, empirical, and semiempirical modeling techniques may be seen in Figs. 5–8. The first theoretical technique used for comparison was that of Yovanovich et al. (1983):

$$h_c = \frac{mk_m}{\sigma} 1.25 \left(\frac{P}{H_v}\right)^{0.95} \tag{15}$$

where

$$1.0 \times 10^{-6} \leq \frac{P}{H_v} \leq 2.3 \times 10^{-2} \tag{16}$$

This expression was developed for optically flat surfaces and does not consider directional effects. As shown in Figs. 5–8, it results in an overprediction of the measured experimental thermal contact conductance for all four pairs of materials. These findings are consistent with those of Kapischke (1987), whose samples were polished. Kapischke (1987) attributed the difference to rounding of the contact surface during polishing; however, the samples in this investigation were surface ground and thus Kapischke's hypothesis may be only partially correct.

The empirical correlation of Madhusudana and Fletcher (1983) for the solid spot conductance of Zircaloy-2/uranium

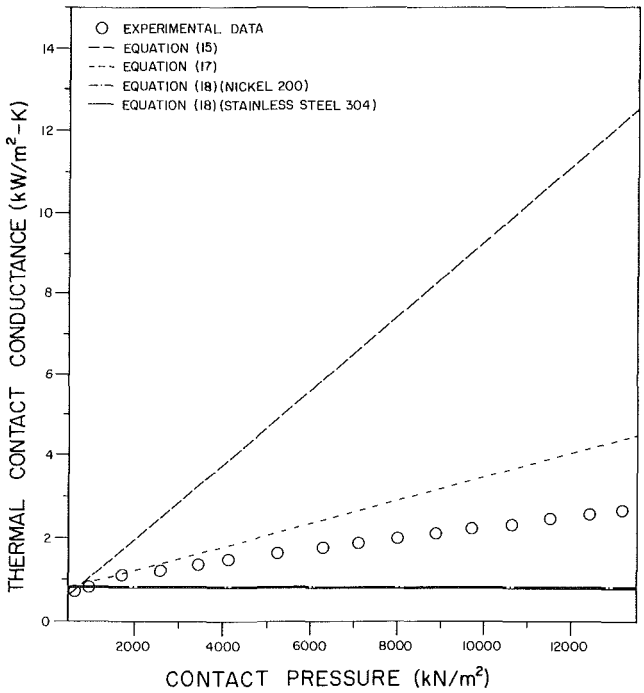

Fig. 5 Comparison of theoretical and experimental data for smooth Stainless Steel 304 to rough Nickel 200 specimens

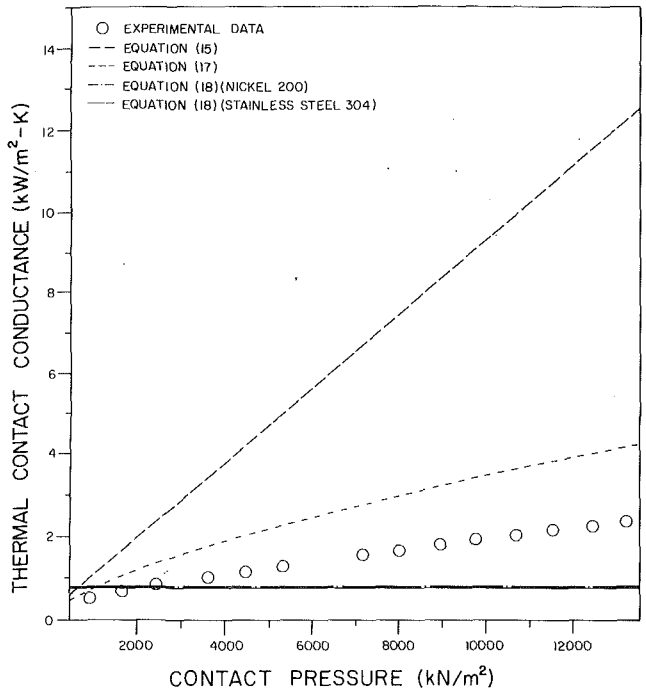

Fig. 6 Comparison of theoretical and experimental data for rough Nickel 200 specimens to smooth Stainless 304

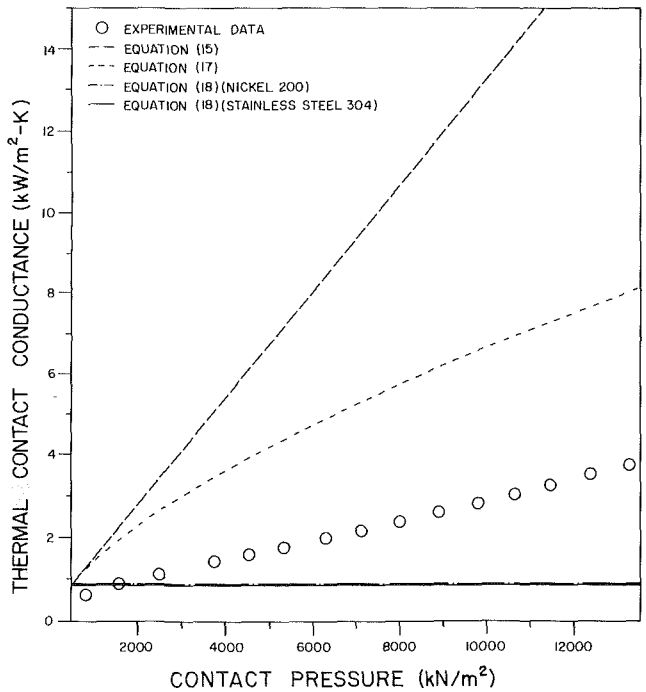

Fig. 7 Comparison of theoretical and experimental data for rough Stainless Steel 304 to smooth Nickel 200 specimens

dioxide contacts was also used for comparative purposes. This model utilized the microscopic approach and has been shown to be accurate for several different combinations of materials. It can be expressed as

$$h_c = \frac{k_m}{\sigma} 12.29 \times 10^{-3} \left(\frac{P}{M}\right)^{0.66} \tag{17}$$

As can be seen in Figs. 5–8, this relationship also overpredicts the experimental values, although not nearly as much. The empirical curves were nonlinear in the low loading ranges, but

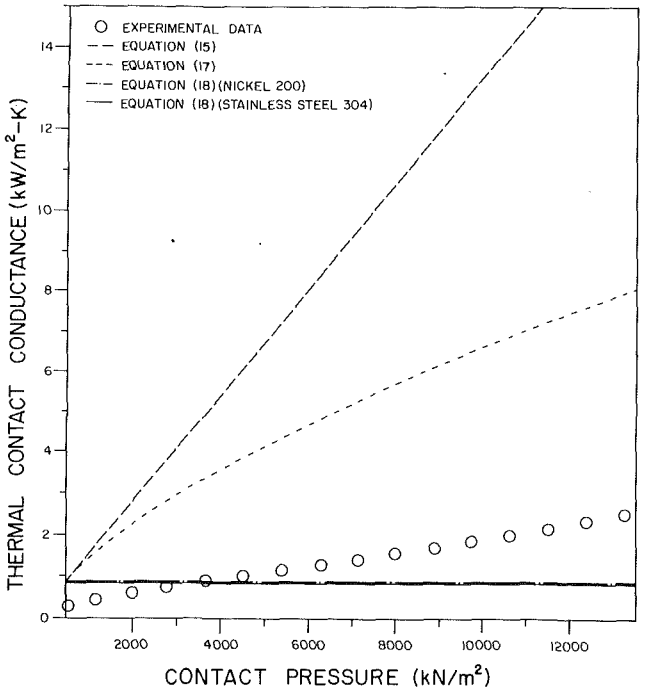

Fig. 8 Comparison of theoretical and experimental data for smooth Nickel 200 to rough Stainless Steel 304 specimens

obtained a slope similar to that of the experimental data for the higher loading range. In the original model of Madhusudana and Fletcher (1983), the effective flow pressure, M, was directly correlated with the hardness of the material. The hardness of Zircaloy-2 was shown to decrease rapidly with temperature, thus influencing the contact conductance. However, neither the hardness of Stainless Steel 304 nor that of Nickel 200 is significantly affected by temperature in the range of interest in this investigation. This may partially explain the deviation of the correlated values from those obtained experimentally.

Fletcher and Gyorog (1971) presented an empirical correlation based on experimental results from an investigation of aluminum, brass, stainless steel, and magnesium over a range of test variables, including surface conditions, loading parameters, and test temperatures. This model utilized a macroscopic approach to contact conductance. The correlation proposed by Fletcher and Gyorog (1971) for similar metals in contact made use of three parameters not seen in previous investigations: the mean junction temperature, T_m, a gap roughness parameter relating the rms roughness, σ, the flatness deviation, FD, and the effect of pressure variations on the previous parameter. The modulus of elasticity was used in lieu of the microhardness to nondimensionalize the pressure.

The correlating equation was

$$h_c = \frac{k_m}{\delta_o} e^{\frac{170 P^* T^*}{\delta_o}} \left(5.22 \times 10^{-6} \delta_o^* + 0.036 P^* T^*\right)^{0.56} \left(\frac{\text{Btu}}{\text{hr-ft}^2\text{°F}}\right) \tag{18}$$

where

$$\delta_o = 20.45 + (8.06 \times 10^{-2} d) - (1.58 \times 10^{-5} d^2) + (1.36 \times 10^{-9} d^3) \quad [\mu\text{in.}]$$

As shown in Figs. 5–8, the correlated values appear slightly higher than the experimental values in the low loading range

and lower in the high load range. The linear, nonsloping nature of the curve for the empirical values makes it appear as if this correlation is relatively unaffected by changes in load for the temperature range of interest here. The data presented in the literature (Fletcher and Gyorog, 1971) correlate well with data published by other investigators. Although the loading range was similar, the mean interfacial contact temperature was approximately 470 K, whereas the mean interface temperature in the present investigation was approximately 300 K.

Because the surface characteristics of the rough specimens were random due to bead-blasting, the surface analysis did not provide a representative value for the flatness deviation, *FD;* therefore, the value used was the flatness deviation of the smooth surface only.

Conclusions

Based on the findings of this investigation, it is apparent that current analytical and empirical models do not accurately predict the thermal contact conductance of metallic surfaces with surface characteristics similar to those tested in this investigation, for either similar or dissimilar pairs of Nickel 200 and Stainless Steel 304. In addition, thermal rectification has been shown to be a strong function of both the material properties and the surface characteristics.

For stainless steel to stainless steel contacts, some thermal rectification was observed with the heat flow from the rough surface to the smooth surface having the higher value of contact conductance. At higher pressures the nickel to nickel tests showed similar results; however, the magnitude of these differences is somewhat less than the experimental uncertainty. For both of the experiments using nickel to stainless steel contacts, evidence of thermal rectification was observed. When the heat was flowing from stainless steel to nickel, the value of conductance was highest. In the dissimilar metal contacts where nickel was the rough surface, the value of conductance was higher when heat was flowing from stainless steel to nickel, but the percent difference was not as great as in the other dissimilar metal contact where stainless steel was rough.

In summary, it is apparent that for the materials tested, thermal rectification is a function of both the material properties and the surface characteristics. For similar materials in contact, some thermal rectification occurred with heat flow from the rough surface to the smooth surface resulting in a higher value of contact conductance. For dissimilar materials, the thermal contact conductance was higher when the heat flow was from stainless steel to nickel. In all cases, the surface roughness was found to be of secondary importance.

Acknowledgments

This work was sponsored in part by the Texas Higher Education Coordinating Board Advanced Technology Program. The authors would like to thank Professor M. M. Yovanovich for his assistance in preparing and characterizing the test specimens.

References

Barber, J. R., 1971, "The Effect of Thermal Distortion on Constriction Resistance," *Int. J. Heat Mass Transfer,* Vol. 14, pp. 751–766.

Clausing, A. M., 1966, "Heat Transfer at the Interface of Dissimilar Metals—The Influence of Thermal Strain," *Int. J. Heat Mass Transfer,* Vol. 9, pp. 791–801.

Dundurs, J., and Panek, C., 1976, "Heat Conduction Between Bodies With Wavy Surfaces," *Int. J. Heat Mass Transfer,* Vol. 19, No. 7, pp.731–735.

Fletcher, L. S., and Gyorog, D. A., 1971, "Prediction of Thermal Contact Conductance Between Similar Metal Surfaces," in: J. W. Lucas, ed., *Progress in Astronautics and Aeronautics: Heat Transfer and Spacecraft Thermal Control,* Vol. 24, MIT Press, Cambridge, MA, pp. 273–288.

Jones, A. M., O'Callaghan, P. W., and Probert, S. D., 1974, "Effect Interfacial Distortions on the Thermal Resistance of the Contact Between Coaxially Mating Radially Symmetrical Cylinders," in: M. M. Yovanovich, ed., *Progress in Astronautics and Aeronautics: Heat Transfer With Thermal Applications,* Vol. 39, MIT Press, Cambridge, MA, pp. 21–45.

Kapischke, J. W., 1987, "Thermal Contact Conductance at Smooth-Rough Metallic Interfaces," Report No. ME-CHTL-90690-2, Texas A&M University Mechanical Engineering Department, College Station, TX.

Kline, S. J., and McClintock, F. A., 1953, "Describing Uncertainties in Single Sample Experiments," *Mechanical Engineering,* Vol. 5, pp. 37–43.

Lewis, D. V, and Perkins, H. C., 1968, "Heat Transfer at the Interface of Stainless Steel and Aluminum—the Influence of Surface Conditions on the Directional Effect," *Int. J. Heat Mass Transfer,* Vol. 11, pp. 1371–1383.

Madhusudana, C. V., and Fletcher, L. S., 1986, "Contact Heat Transfer—The Last Decade," *AIAA Journal,* Vol. 24, No. 3, pp. 510–523.

Mikic, B. B., 1974, "Thermal Contact Conductance: Theoretical Considerations," *Int. J. Heat Mass Transfer,* Vol. 17, No. 2, pp. 205–214.

Moon, J. S., and Keeler, R. N., 1962, "A Theoretical Consideration of Directional Effects in Heat Flow at the Interface of Dissimilar Metals," *Int. J. Heat Mass Transfer,* Vol. 5, pp. 731–735.

Somers, R. R., Fletcher, L. S., and Miller, J. W., 1978, "An Experimental Investigation of the Thermal Contact Conductance of Dissimilar Metal Contacts," *Proc. 14th Southeastern Seminar of Thermal Sciences,* Raleigh, NC.

Somers, R. R., Fletcher, L. S., 1983, "The Thermal Conductance of Dissimilar Metals," Technical Report TEES-4547-83, Texas Engineering Experiment Station, Texas A&M University, College Station, TX.

Song, S., and Yovanovich, M. M., 1988, "Relative Contact Pressure: Dependence on Surface Roughness and Vickers Microhardness," *AIAA J. Thermophysics and Heat Transfer,* Vol. 2, No. 1.

Starr, C., 1936, "Copper Oxide Rectifier," *J. Applied Physics,* Vol. 7, pp. 15–19.

Thomas, T. R., and Probert, S. D., 1970, "Thermal Contact Resistance: the Directional Effect and Other Problems," *Int. J. Heat Mass Transfer,* Vol. 13, No. 5, pp. 789–807.

Veziroglu, T. N., 1967, "Correlation of Thermal Contact Conductance Experimental Results," *Progress in Astronautics and Aeronautics: Thermophysics of Spacecraft and Planetary Bodies,* Vol. 20, pp. 879–907.

Veziroglu, T. N., and Chandra, S., 1970, "Direction Effect in Thermal Contact Conductance," *Proc. Fourth Int. Heat Transfer Conference,* Paris, pp. 3–10.

Yovanovich, M. M., DeVaal, J., and Hegazy, A. A., 1983, "A Statistical Model to Predict Thermal Gap Conductance Between Conforming Rough Surfaces," AIAA Paper No. 83-0888, presented at the AIAA/ASME 3rd Joint Thermophysics, Fluids, Plasma and Heat Transfer Conference, St. Louis, MO.

Yovanovich, M. M., and Nho, K., 1989, "Experimental Investigation of Heat Flow Rate and Direction on Contact Resistance of Ground/Lapped Stainless Steel Interfaces," AIAA Paper No. 89-1657, presented at the 24th AIAA Thermophysics Conference, Buffalo, NY, June.

Y. Cao

A. Faghri

Department of Mechanical and Materials Engineering,
Wright State University,
Dayton, OH 45435

A. Juhasz

NASA Lewis Research Center,
Cleveland, OH 44135

A PCM/Forced Convection Conjugate Transient Analysis of Energy Storage Systems With Annular and Countercurrent Flows

Latent heat energy storage systems with both annular and countercurrent flows are modeled numerically. The change of phase of the phase-change material (PCM) and the transient forced convective heat transfer for the transfer fluid are solved simultaneously as a conjugate problem. A parametric study and a system optimization are conducted. It is found that the energy storage system with the countercurrent flow is an efficient way to absorb heat energy in a short period for pulsed power load space applications.

Introduction

Phase-change thermal energy storage systems can store heat energy at a high temperature during the time period when the system is subjected to heat input and release it to the environment over a long period of time. Therefore, they are especially suitable for space applications involving pulsed power loads, such as a large amount of heat rejection from a power cycle in a short period of time.

The use of a hollow cylinder of PCM for a solar latent energy storage system was modeled by Soloman et al. (1986), where the heat transport fluid is pumped through the interior tube. A finite difference formulation with the Kirchhoff temperature was used to calculate the internal energy, temperature, and the position of the phase-change front. Stovall and Arimilli (1988) studied a thermal energy storage system consisting of a cylindrical tube filled with a phase-change material. The tube is surrounded by an annular region containing the liquid metal transfer fluid for pulsed power load applications. Recently, Yimer and Adami (1989) studied a phase-change thermal energy storage system similar to that of Solomon et al. with one-dimensional modeling.

All of the numerical studies above were focused on the diffusion-controlled heat transfer in the PCM. The heat transfer between the transfer fluid and the PCM was calculated by using empirical correlations without solving the flow and temperature fields of the transfer fluid as a conjugate problem. Since the temperature field of the transfer fluid continues to change as the melting interface progresses, the use of steady fully developed empirical heat transfer correlations and the assumption of a constant fluid temperature may result in a significant error for the evaluation of the system performance. Also, for all the system configurations studied above, it was found that some PCM downstream remains unmelted. This will surely reduce the efficiency of the system.

In this paper, the two-dimensional change of phase for the PCM and the transient forced convection entrance region for the transfer fluid with low Prandtl numbers are solved simultaneously as a conjugate problem. The numerical calculation is first made with the annular system configuration similar to that of Stovall and Arimilli, as shown in Fig. 1, and then the numerical results of energy storage systems with countercurrent flows as shown in Fig. 2 are elaborated. A parametric study and system optimization are also conducted.

Mathematical Modeling

The continuity, momentum, and energy equations governing two-dimensional transient incompressible laminar flows with no viscous dissipation in the cylindrical coordinates are (Ganic et al., 1985)

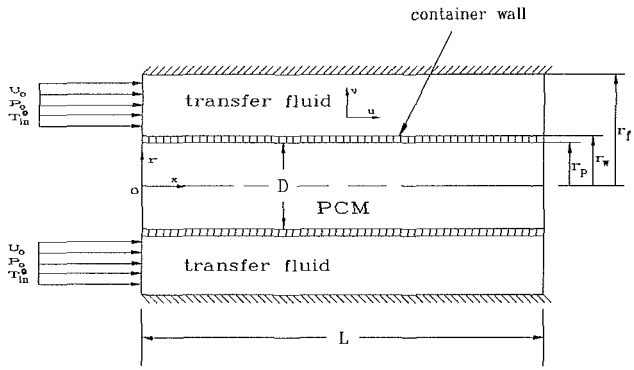

Fig. 1 Schematic of latent heat storage system with annular flow

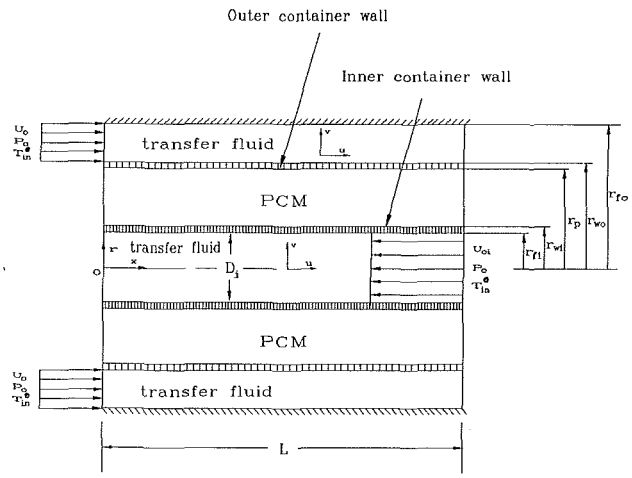

Fig. 2 Schematic of latent heat storage system with countercurrent flows

Contributed by the Heat Transfer Division and presented at the Joint AIAA/ASME Thermophysics and Heat Transfer Conference, Seattle, Washington, June 18–20, 1990. Manuscript received by the Heat Transfer Division January 30, 1990; revision received July 25, 1990. Keywords: Conjugate Heat Transfer, Phase-Change Phenomena, Thermal Energy Storage.

$$\frac{1}{r}\frac{\partial}{\partial r}(rv)+\frac{\partial u}{\partial x}=0 \tag{1}$$

$$\frac{\partial v}{\partial t}+v\frac{\partial v}{\partial r}+u\frac{\partial v}{\partial x}=-\frac{1}{\rho_f}\frac{\partial p}{\partial r}+\nu_f\left[\frac{1}{r}\frac{\partial}{\partial r}\left(r\frac{\partial v}{\partial r}\right)-\frac{v}{r^2}+\frac{\partial^2 v}{\partial x^2}\right] \tag{2}$$

$$\frac{\partial u}{\partial t}+v\frac{\partial u}{\partial r}+u\frac{\partial u}{\partial x}=-\frac{1}{\rho_f}\frac{\partial p}{\partial x}+\nu_f\left[\frac{1}{r}\frac{\partial}{\partial r}\left(r\frac{\partial u}{\partial r}\right)+\frac{\partial^2 u}{\partial x^2}\right] \tag{3}$$

$$\rho_f c_f\left(\frac{\partial T^o}{\partial t}+v\frac{\partial T^o}{\partial r}+u\frac{\partial T^o}{\partial x}\right)=k_f\left[\frac{1}{r}\frac{\partial}{\partial r}\left(r\frac{\partial T^o}{\partial r}\right)+\frac{\partial^2 T^o}{\partial x^2}\right] \tag{4}$$

For the PCM, the temperature transforming model (Cao and Faghri, 1990) is used. The energy equation is written as

$$\frac{\partial(\rho C^o T^*)}{\partial t}=\frac{1}{r}\frac{\partial}{\partial r}\left(kr\frac{\partial T^*}{\partial r}\right)+\frac{\partial}{\partial x}\left(k\frac{\partial T^*}{\partial x}\right)-\frac{\partial(\rho S^o)}{\partial t} \tag{5}$$

where $T^*=T^o-T^o_m$.

$$C^o=C^o(T^*)=\begin{cases} c_s & (T^*<-\delta T^o) \quad \text{(solid phase)} \\ c_m+\dfrac{H}{2\delta T^o} & (-\delta T^o\le T^*\le\delta T^o) \quad \text{(mushy phase)} \\ c_l & (T^*>\delta T^o) \quad \text{(liquid phase)} \end{cases} \tag{6}$$

$$S^o=S^o(T^*)=\begin{cases} c_s\,\delta T^o & (T^*<-\delta T^o) \quad \text{(solid phase)} \\ c_m\,\delta T^o+\dfrac{H}{2} & (-\delta T^o\le T^*\le\delta T^o) \quad \text{(mushy phase)} \\ c_s\,\delta T^o+H & (T^*>\delta T^o) \quad \text{(liquid phase)} \end{cases} \tag{7}$$

$$k(T^*)=\begin{cases} k_s & (T^*<-\delta T^o) \quad \text{(solid phase)} \\ k_s+(k_l-k_s)(T^*+\delta T^o)/2\delta T^o & (-\delta T^o\le T^*\le\delta T^o) \quad \text{(mushy phase)} \\ k_l & (T^*>\delta T^o) \quad \text{(liquid phase)} \end{cases} \tag{8}$$

The use of the temperature transforming model of Cao and Faghri (1990) has two advantages. First, equations (5)–(8) form a set of closed-group equations, so an explicit treatment of the phase-change interface is not needed. Secondly, the time step and grid size limitations are eliminated, which are normally encountered for other fixed-grid methods. It should be pointed out that due to the space application the natural convection in the liquid PCM has been ignored.

For the pipe wall, the energy equation is

$$\rho_w c_w\frac{\partial T^o}{\partial t}=k_w\left[\frac{1}{r}\frac{\partial}{\partial r}\left(r\frac{\partial T^o}{\partial r}\right)+\frac{\partial^2 T^o}{\partial x^2}\right] \tag{9}$$

The initial and boundary conditions for the system configuration in Fig. 1 for the case of uniform inlet conditions are defined as follows:

Nomenclature

c = specific heat, J/(kg-K)
c_m = specific heat of mushy phase = 1/2 (c_s+c_l), J/(kg-K)
c_p = specific heat of PCM, J/(kg-K)
C^o = coefficient in equation (5), J/(kg-K)
C = C^o/c_l
C_{sl} = c_s/c_l
D = diameter of the circular cylinder in Fig. 1, m
D_f = reference diameter, m
D_i = inside diameter of the circular pipe in Fig. 2, m
D_h = hydraulic diameter, m
H = latent heat, J/kg
k = thermal conductivity, W/(m-K)
K = dimensionless thermal conductivity = k/k_l
K_{sl} = k_s/k_l
L = length of pipe, m
M = total mass of PCM, kg
m_i = flow rate through interior tube, kg/s
m_o = flow rate through outer annulus, kg/s
Nu_x = Nusselt number = $q_w D/k(T^o_w-T^o_{av})$
p = pressure, N/m^2
p_o = inlet pressure, N/m^2
P = dimensionless pressure = $(p-p_o)/\rho_f U_o^2$
Pr_f = fluid Prandtl number = ν_f/α_f
Q = heat energy, J
Q_l = total latent energy stored, J
Q_t = total energy stored, J
Q_m = energy storage density, J/kg
q_w = wall heat flux, W/m^2
Re_f = fluid Reynolds number = $U_f D_f/\nu_f$
S^o = term in equation (5), J/kg
S = $S^o/c_l\,(T^o_{in}-T^o_m)$
St = Stefan number = $c_l(T^o_{in}-T^o_m)/H$
T^o = temperature, K
T^o_{av} = mixed mean temperature, K
T^o_m = melting temperature, K
T = dimensionless temperature = $(T^o-T^o_m)/(T^o_{in}-T^o_m)$
T^* = scaled temperature = $T^o-T^o_m$, K
t = time, s
U_f = reference velocity of transfer fluid, m/s
U_o = inlet velocity, m/s
U_{oi} = inlet velocity for the interior tube, m/s
U, V = dimensionless velocities = u/U_o, v/U_o
u, v = velocities, m/s
X, R = dimensionless coordinate directions = x/D, r/D, or x/D_i, r/D_i
x, r = coordinate directions
α = thermal diffusivity, m^2/s
$2\delta T^o$ = phase-change temperature range or mushy phase range, K
δT^* = $\delta T^o/(T^o_{in}-T^o_m)$
δ_w = wall thickness, m
ν = kinematic viscosity, m^2/s
ρ = density, kg/m^3
τ = dimensionless time = $U_f t/D$ or $U_f t/D_i$

Subscripts

f = transfer fluid
fi = inner transfer fluid
fo = outer transfer fluid
i = initial condition, or inside radius of the pipe
in = inlet
s = solid PCM
l = liquid PCM or latent heat
m = mass or mushy phase
o = outer surface of the PCM module
p = PCM
w = container wall
wi = inner container wall
wo = outer container wall

Initial conditions: $t=0$

Entire domain: $0\le x\le L,\ 0<r<r_f$

$$T^o=T_i^o,\ u=v=0 \tag{10a}$$

Boundary conditions: $t>0$

Inlet plane: $x=0$

$$\begin{aligned} &r_w\le r\le r_f\text{:}\quad u=U_o,\quad T^o=T_{in}^o,\quad v=0\\ &0\le r\le r_w\text{:}\quad \frac{\partial T^o}{\partial x}=0 \end{aligned} \tag{10b}$$

Outer adiabatic boundary: $0\le x\le L,\quad r=r_f$

$$\frac{\partial T^o}{\partial r}=0 \tag{10c}$$

PCM/wall interface: $0\le x\le L,\ r=r_p$

$$k_p\frac{\partial T^o}{\partial r}\bigg|_{r=r_p^-}=k_w\frac{\partial T^o}{\partial r}\bigg|_{r=r_p^+} \tag{10d}$$

Wall/fluid interface: $0\le x\le L,\ r=r_w$

$$k_w\frac{\partial T^o}{\partial r}\bigg|_{r=r_w^-}=k_f\frac{\partial T^o}{\partial r}\bigg|_{r=r_w^+} \tag{10e}$$

Outlet plane: $x=L$

$$\begin{aligned} &0<r<r_f\text{:}\quad \frac{\partial T^o}{\partial x}=0\\ &r_w<r<r_f\text{:}\quad \frac{\partial u}{\partial x}=0 \end{aligned} \tag{10f}$$

The initial and boundary conditions for the system configuration in Fig. 2 and for the case of uniform inlet conditions are defined as follows:

Initial conditions: $t=0$

Entire domain: $0\le x\le L,\quad 0\le r\le r_{fo}$

$$T^o=T_i^o,\quad u=v=0 \tag{11a}$$

Boundary conditions: $t>0$

Inlet plane: $x=0$:

$$\begin{aligned} &0\le r\le r_{fi}\text{:}\quad \frac{\partial u}{\partial x}=0\\ &r_{wo}\le r\le r_{fo}\text{:}\quad u=U_o,\quad v=0,\quad T^o=T_{in}^o\\ &0\le r\le r_{wo}\text{:}\quad \frac{\partial T^o}{\partial x}=0 \end{aligned} \tag{11b}$$

Outlet plane: $x=L$:

$$\begin{aligned} &0\le r\le r_{fi}\text{:}\quad u=-U_{oi},\quad v=0,\quad T^o=T_{in}^o\\ &r_{wo}\le r\le r_{fo}\text{:}\quad \frac{\partial u}{\partial x}=0\\ &r_{fi}\le r\le r_{fo}\text{:}\quad \frac{\partial T}{\partial x}=0 \end{aligned} \tag{11c}$$

Fluid/inner wall interface: $0\le x\le L,\quad r=r_{fi}$

$$k_f\frac{\partial T^o}{\partial r}\bigg|_{r=r_{fi}^-}=k_w\frac{\partial T^o}{\partial r}\bigg|_{r=r_{fi}^+} \tag{11d}$$

Inner wall/PCM interface: $0\le x\le L,\ r=r_{wi}$

$$k_w\frac{\partial T^o}{\partial r}\bigg|_{r=r_{wi}^-}=k_p\frac{\partial T^o}{\partial r}\bigg|_{r=r_{wi}^+} \tag{11e}$$

PCM/outer wall interface: $0\le x\le L,\ r=r_p$

$$k_p\frac{\partial T^o}{\partial r}\bigg|_{r=r_p^-}=k_w\frac{\partial T^o}{\partial r}\bigg|_{r=r_p^+} \tag{11f}$$

Outer wall/fluid interface: $0\le x\le L,\quad r=r_{wo}$

$$k_w\frac{\partial T^o}{\partial r}\bigg|_{r=r_{wo}^-}=k_f\frac{\partial T^o}{\partial r}\bigg|_{r=r_{wo}^+} \tag{11g}$$

Outer adiabatic boundary: $0\le x\le L,\quad r=r_{fo}$

$$\frac{\partial T^o}{\partial r}=0 \tag{11h}$$

The following nondimensional variables are introduced:

$$\begin{aligned} &R=\frac{r}{D},\quad X=\frac{x}{D},\quad U=\frac{u}{U_f},\quad V=\frac{v}{U_f},\\ &\mathrm{Re}_f=\frac{U_fD_f}{\nu_f},\quad T=\frac{T^o-T_m^o}{T_{in}^o-T_m^o},\quad \tau=\frac{U_f}{D}t,\quad P=\frac{p-p_o}{\rho_fU_f^2},\\ &C=\frac{C^o}{c_l},\quad K=\frac{k}{k_l},\quad S=S^o/c_l(T_{in}^o-T_m^o),\\ &\mathrm{St}=c_l(T_{in}^o-T_m^o)/H,\quad \delta T^*=\delta T^o/(T_{in}^o-T_m^o) \end{aligned} \tag{12}$$

The dimensionless continuity, momentum, and energy equations for the transfer fluid are as follows:

$$\frac{1}{R}\frac{\partial}{\partial R}(RV)+\frac{\partial U}{\partial X}=0 \tag{13}$$

$$\frac{\partial U}{\partial\tau}+V\frac{\partial U}{\partial R}+U\frac{\partial U}{\partial X}=-\frac{\partial P}{\partial X}+\frac{1}{\mathrm{Re}_f}\frac{D_f}{D}\left[\frac{1}{R}\frac{\partial}{\partial R}\left(R\frac{\partial U}{\partial R}\right)+\frac{\partial^2U}{\partial X^2}\right] \tag{14}$$

$$\frac{\partial V}{\partial\tau}+V\frac{\partial V}{\partial R}+U\frac{\partial V}{\partial X}=-\frac{\partial P}{\partial R}+\frac{1}{\mathrm{Re}_f}\frac{D_f}{D}\left[\frac{1}{R}\frac{\partial}{\partial R}\left(R\frac{\partial V}{\partial R}\right)+\frac{\partial^2V}{\partial X^2}-\frac{V}{R^2}\right] \tag{15}$$

$$\frac{\partial T}{\partial\tau}+V\frac{\partial T}{\partial R}+U\frac{\partial T}{\partial X}=\frac{1}{\mathrm{Re}_f\mathrm{Pr}_f}\frac{D_f}{D}\left[\frac{1}{R}\frac{\partial}{\partial R}\left(R\frac{\partial T}{\partial R}\right)+\frac{\partial^2T}{\partial X^2}\right] \tag{16}$$

For the system in Fig. 1, $U_f=U_o$ and $D_f=D_h=2(r_f-r_w)$, where D_h is the hydraulic diameter. For the system in Fig. 2, $U_f=U_o$ and $D_f=D_i=\mathrm{D}$. The dimensionless energy equation for the PCM is

$$\frac{\partial(CT)}{\partial\tau}=\frac{1}{\mathrm{Re}_f\mathrm{Pr}_f}\frac{\alpha_l}{\alpha_f}\frac{D_f}{D}\left[\frac{1}{R}\frac{\partial}{\partial R}\left(KR\frac{\partial T}{\partial R}\right)+\frac{\partial}{\partial X}\left(K\frac{\partial T}{\partial X}\right)\right]-\frac{\partial S}{\partial\tau} \tag{17}$$

where

$$C(T)=\begin{cases} C_{sl} & (T<-\delta T^*)\\ \dfrac{1}{2}(1+\mathrm{C}_{sl})+\dfrac{1}{2\mathrm{St}\delta T^*} & (-\delta T^*\le T\le\delta T^*)\\ 1 & (T>\delta T^*) \end{cases}$$

$$S(T)=\begin{cases} C_{sl}\delta T^* & (T<-\delta T^*)\\ \dfrac{1}{2}\delta\mathrm{T}^*(1+C_{sl})+\dfrac{1}{2\mathrm{St}} & (-\delta T^*\le T\le\delta T^*)\\ C_{sl}\delta T^*+\dfrac{1}{\mathrm{St}} & (T>\delta T^*) \end{cases}$$

$$K(T)=\begin{cases} K_{sl} & (T<-\delta T^*) \\ K_{sl}+(1-K_{sl})\,(T+\delta T^*)/2\delta T^* & (-\delta T^*\le T\le \delta T^*) \\ 1 & (T>\delta T^*) \end{cases}$$

The dimensionless energy equation for the container walls is

$$\frac{\partial T}{\partial \tau}=\frac{1}{\mathrm{Re}_f \mathrm{Pr}_f}\frac{\alpha_w}{\alpha_f}\frac{D_f}{D}\left[\frac{1}{R}\frac{\partial}{\partial R}\left(R\frac{\partial T}{\partial R}\right)+\frac{\partial^2 T}{\partial X^2}\right] \quad (18)$$

The temperature field for the system configuration in Fig. 1 can be expressed as

$$T=T(\tau,\ R,\ X,\ \mathrm{Re}_f,\ \mathrm{Pr}_f,\ \alpha_l/\alpha_f,\ \alpha_w/\alpha_f,\ \mathrm{St},\ C_{sl},\ \delta T^*,\ K_{sl},\ k_f/k_w,\ k_p/k_w,\ r_w/D,\ r_f/D,\ L/D) \quad (19)$$

The temperature field for the system configuration in Fig. 2 can be expressed as

$$T=T(\tau,\ R,\ X,\ \mathrm{Re}_f,\ m_i/m_o,\ \mathrm{Pr}_f,\ \alpha_l/\alpha_f,\ \alpha_w/\alpha_f,\ \mathrm{St},\ C_{sl},\ \delta T^*,\ K_{sl},\ k_f/k_w,\ k_p/k_w,\ r_{wi}/D_i,\ r_p/D_i,\ r_{wo}/D_i,\ r_{fo}/D_i,\ L/D_i) \quad (20)$$

Numerical Procedure

The problem has been specified mathematically by equations (1)-(11). The solution procedure used for solving these equations is the control-volume finite-difference approach described by Patankar (1980, 1988). In this methodology, the discretization equations are obtained by applying the conservation laws over a finite control volume surrounding the grid node and integrating over the control volume. The velocities and pressure are solved by using the SIMPLE scheme (Patankar, 1980). At the PCM/wall and the wall/fluid interfaces, the harmonic mean of the thermal conductivity is used. For example, with a uniform grid size

$$k_p\frac{\partial T^o}{\partial r}\bigg|_{r=r_p^-}=k_w\frac{\partial T^o}{\partial r}\bigg|_{r=r_p^+}=\frac{2k_pk_w}{k_p+k_w}\frac{\partial T^o}{\partial r}\bigg|_{r=r_p}$$

The discretization equations are solved by using the tridiagonal matrix algorithm (TDMA or Thomas algorithm). During each time step, iterations are needed. The converged results were assumed to be reached when the maximum relative change of all variables between consecutive iterations was less than 0.1 percent. The residual of the continuity equation was also checked. The iteration was continued until the sum of the residuals was less 10^{-5}. Different grid sizes and time steps for the same problem have been tested and it has been proven that both the PCM model and the numerical scheme used for the transfer fluid are essentially independent of the grid sizes and time steps for the numerical results presented in the next section. A variation of the grid size from 32×40 to 44×70 resulted in a change of the numerical values of Q_t and Q_m of less than 1.5 percent. A further refinement of the grid size to 56×90 resulted in a change of 0.7 percent in Q_t and Q_m. Doubling the dimensionless time step $\Delta\tau=3$ to 6 changed Q_t and Q_m less than 1 percent. The space grid and time step specifications are given in the next section for the cases presented.

Numerical Results and Discussion

Before presenting the numerical results for the energy storage system, the computer code for the liquid metal flow was tested against other numerical results in the literature. Consider the heat transfer in a laminar pipe flow in the developing thermal and velocity (DTV) region with constant wall heat flux. Figure 3 shows the prediction of the DTV regions in the form of Nu_x versus $\mathrm{Pr}_f\mathrm{Re}_f/(x/D)$ for $\mathrm{Pr}_f=0.02$ and $\mathrm{Re}_f=2000$. Also shown in the figure is the numerical result from Chen and Chiou (1981). It can be seen that the agreement between the two

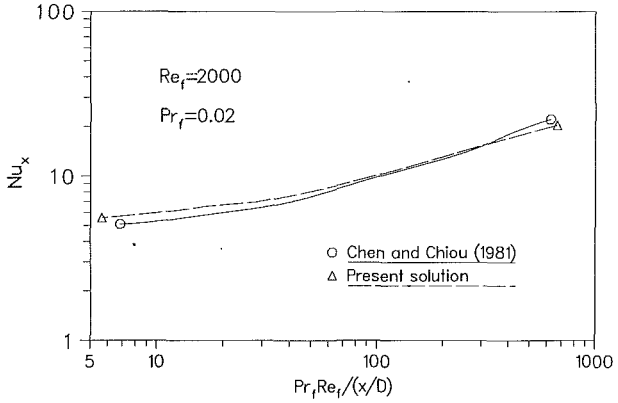

Fig. 3 Heat transfer in the developing thermal and velocity region with constant wall heat flux

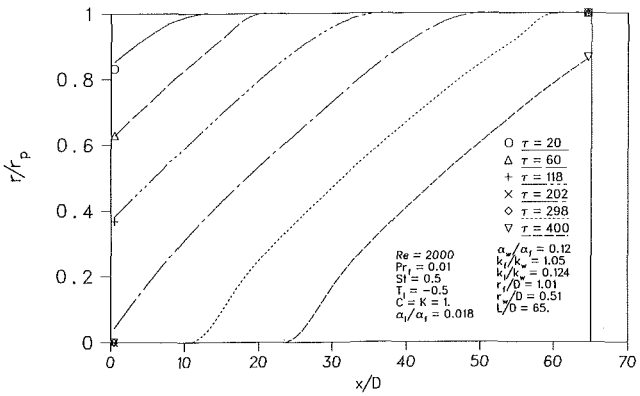

Fig. 4 Melting fronts along axial direction for different time periods for the system with annular flow

results is generally good. The small difference between the two may be attributable to the governing equations employed in the two numerical calculations. For the numerical result of Chen and Chiou (1981), the boundary layer approximation has been applied, while for the present numerical result, no such approximation is involved.

The numerical calculations for the thermal energy storage system were first conducted with the configuration in Fig. 1. The system is initially at a temperature $T_i<0$. The hotter fluid enters the circular annulus surrounding the PCM cylinder and heats the system, which absorbs the energy from the fluid and stores it as both latent and sensible heat. The grid size used for the calculation was 70 (axial) × [15 (radial PCM) + 5 (radial container wall) + 10 (radial transfer fluid)] and a dimensionless time step $\tau=6$. The phase-change material used in the calculation is LiH, which is one of the most promising candidates for space-based energy storage systems. In order to simulate the phase-change at a single temperature using equation (17), the dimensionless phase change temperature range δT^* is taken to be 0.005. A moderately small δT^* is enough to simulate the phase-change problem occurring at a single temperature (Cao and Faghri, 1990).

Figure 4 shows the melting interface along the axial direction at different times. The melting interface progresses from the upper left corner to the lower right corner with time. At about $\tau=200$, the melting interface has reached the core of the PCM cylinder at $x=0$, while much of PCM remains unmelted on the right side. The reason is that since the Prandtl number of the transfer fluid is very small (the thermal conductivity is very large), a large amount of heat is transferred directly to the PCM upstream while a relatively small amount of heat is carried downstream. The heat transfer in the PCM is not uniform

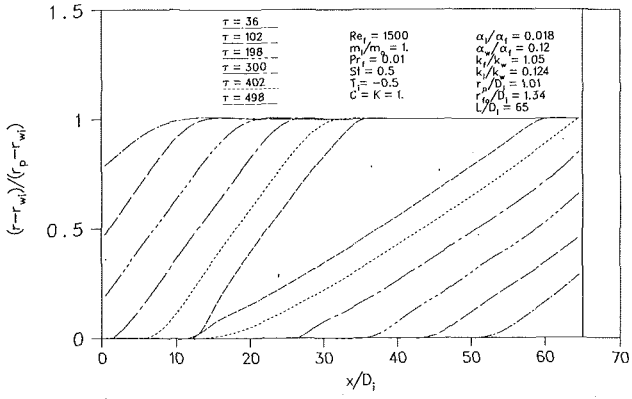

Fig. 5 Melting fronts along axial direction for different time periods for the system with countercurrent flows

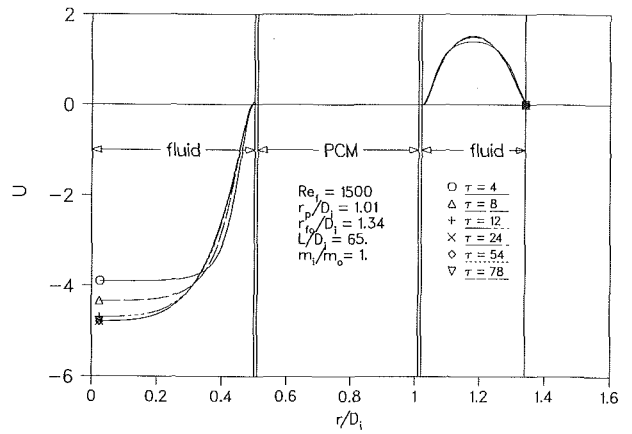

Fig. 6 Axial velocity distribution of transfer fluids at $X=32$ for different time periods

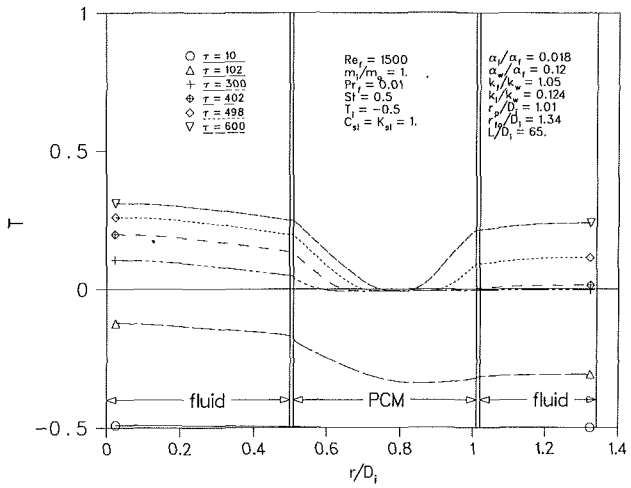

Fig. 7 Radial temperature distribution at $X=32$ for different time periods

along the axial direction. This will surely reduce the efficiency of the energy storage system.

The calculation is then conducted with the system in Fig. 2. In this system, countercurrent transfer fluids are employed. The thermal energy system module consists of a concentric annulus of PCM and countercurrent flows through the interior tube and along the outer cylinder boundary. The grid size used in the calculation was 70 (axial) × [10 (radial interior flow) + 4 (radial inner container wall) + 15 (radial PCM) + 4 (radial outer container wall) + 10 (radial outer annular flow)] and a dimensionless time step $\Delta\tau=4$. The dimensionless wall thickness of both the inner container wall and the outer container wall was taken to be $\delta_w/D_i=0.01$. The phase-change material used in the calculation was LiH.

Figure 5 shows the melting interfaces along the axial direction at different times for the system with countercurrent flows. Unlike those in Fig. 4, the melting interfaces progress from the upper left corner to the right and from the lower right corner to the left at the same time, and meet at about $\tau=U_o t/D_i=500$. This will surely increase the efficiency of the system. Note that the dimensionless time $\tau=U_o t/D_i$ is different from that in Fig. 4 due to the different geometric configuration and the dimensional inlet fluid velocity.

Figure 6 shows axial velocity distribution in the radial direction at $X=32$ for different time periods with the countercurrent flow configuration. It can be seen that the velocity reaches steady state quickly. After about $\tau=12$, the velocity profile remains unchanged, but the temperature distribution is different. Figure 7 shows the radial temperature distribution at $X=32$ for different time periods. The five regions in the radial direction (the inner transfer fluid, the inner container wall, the PCM, the outer container wall, and the outer transfer fluid) are also indicated in the figure. The melting interfaces at different times are the intersections of $T=0$ and the corresponding temperature curves. It can be seen that as the melting interface progresses, the temperature curve moves upward accordingly. Although the velocity field of the transfer fluid quickly reaches the steady state, its temperature counterpart cannot reach steady state before the PCM is totally melted. This clearly demonstrates that the use of steady fully developed empirical heat transfer correlations and a constant temperature for the transfer fluid may result in a significant error for the evaluation of the system performance.

It is important to evaluate the overall performance of the system and optimize the system design with different flow parameters. The important system parameters used to evaluate a thermal energy storage system are the energy storage capacity or total energy stored, Q_t (J), the energy storage density, $Q_m=Q_t/M$ (J/kg), the total latent energy stored, Q_l (J), and the ratio of the latent to the total energy stored, Q_l/Q_t. The first two parameters, Q_t and Q_m, are most important to an energy storage system. In many cases, the energy storage capacity is the primary parameter one would be concerned with, while for a space application, the energy storage density is equally important.

Figures 8 and 9 show the total energy storage and energy storage density variations with time and mass flow ratios between the interior tube and outer annulus, respectively. The dimensional parameters used to calculate Q_t and Q_m are $H=2.9\times10^6$ J/kg, $\rho_p=690$ kg/m^3, $c_p=7420$ J/(kg-K), $T_{in}^o-T_m^o=195.4$ K, and $D_i=0.1$ m. Both Q_t and Q_m follow the trend of increasing with larger m_i/m_o and dimensionless time τ.

The optimization of the system geometry at a specific design operation time is important. Figure 10 presents the numerical results for the system optimization analysis for different L/D_i at an operation time $\tau=500$. The dimensional parameters used in the calculation are the same as those used for the results in Figs. 8 and 9. The energy storage capacity Q_t initially follows the trend of increasing with larger L/D_i and then remains almost constant after L/D_i greater than 50. The trend of the energy storage density Q_m is opposite to that of Q_t. It drops sharply with the increase in L/D_i. In this situation, a trade-off needs to be reached when designing a thermal energy storage system.

Figure 11 shows the comparison of the energy storage capacities and the energy storage densities between the two systems. The system with the annular flow in Fig. 1 is denoted by 1, while that with the countercurrent flows in Fig. 2 is denoted by 2. The comparison has been made under the con-

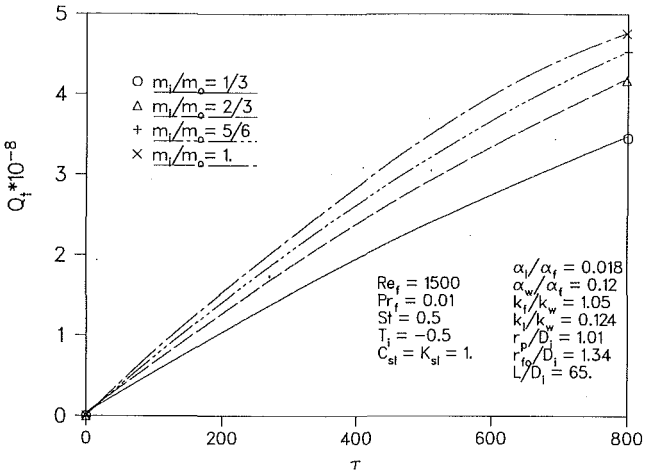

Fig. 8 Total energy storage with different τ and flow ratios

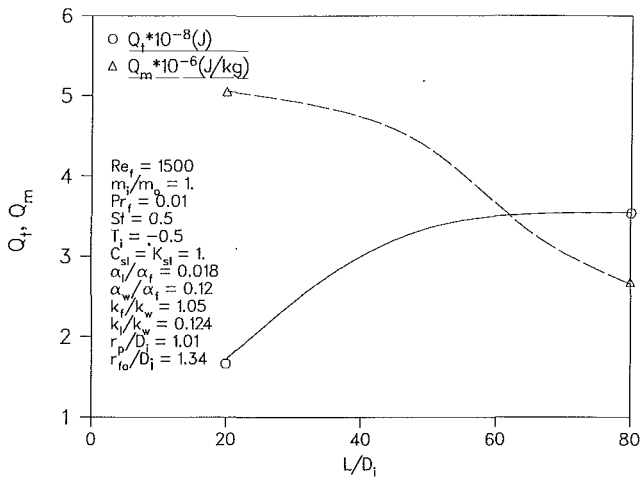

Fig. 10 System optimization analysis for different L/D_i at $\tau = 500$

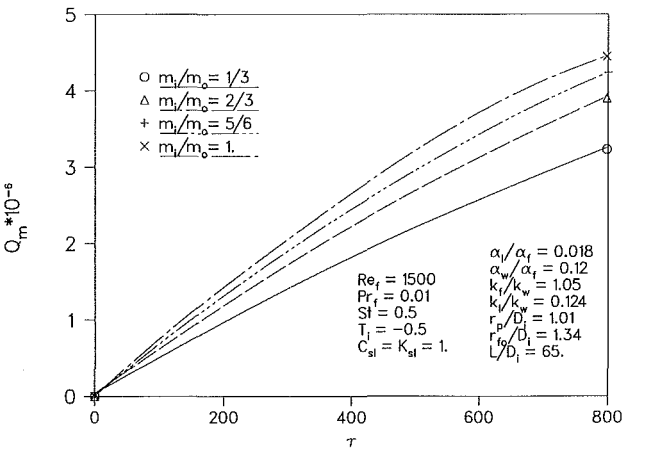

Fig. 9 Energy storage density with different τ and flow ratios

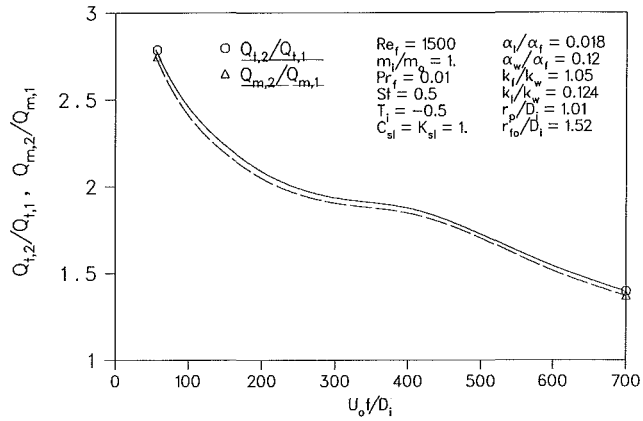

Fig. 11 Comparison between the two systems for Q_t and Q_m at different times

ditions that both systems have the same amount of PCM, and that the flow rate in system 1 is equal to that of the outer annulus in Fig. 2. Since the dimensionless time in the two systems is different, the comparison is also made at the corresponding real time. The system parameters in Fig. 11 are those of system 2. It can be seen that the system with countercurrent flows improved the operation performance significantly. When the dimensionless time τ is comparatively small, both ratios $Q_{t,2}/Q_{t,1}$ and $Q_{m,2}/Q_{m,1}$ exceed 2; with a larger τ, the ratios reduce to about 1.5. Therefore, the system design with countercurrent flows is especially suitable for the energy storage system involving pulsed power loads within a short period.

Conclusions

The system with an annular flow in Fig. 1 and that with countercurrent flows in Fig. 2 have been studied numerically. The results indicated that the transfer fluid velocities both in the inner pipe and in the outer annulus reach steady state quickly, while the temperature field continues to change as the phase change interface in the PCM progresses. Therefore, it is very important to solve the change of phase for the PCM and the transient forced convection for the transfer fluid as a conjugate problem. The numerical results also show that the energy storage system with the countercurrent flows increases both energy storage capacity and energy storage density significantly.

Acknowledgments

Funding for this work was provided by a joint effort of the NASA Lewis Research Center and the Thermal Energy Group of the Aero Propulsion Laboratory of the U.S. Air Force under contract No. F33615-88-C-2820.

References

Cao, Y., and Faghri, A., 1990, "A Numerical Analysis of Phase-Change Problems Including Natural Convection," ASME JOURNAL OF HEAT TRANSFER, Vol. 112, pp. 812–816.

Cao, Y., Faghri, A., and Chang, W. S., 1989, "A Numerical Analysis of Stefan Problems for Generalized Multi-dimensional Phase-Change Structures Using the Enthalpy Transforming Model," *Int. J. Heat Mass Transfer,* Vol. 32, No. 7, pp. 1289–1298.

Chen, C.-J., and Chiou, J. S., 1981, "Laminar and Turbulent Heat Transfer in the Pipe Entrance Region for Liquid Metals," *Int. J. Heat Mass Transfer,* Vol. 24, pp. 1179–1189.

Ganic, E. N., Hartnett, J. P., and Rohsenow, W. M., 1985, "Basic Concepts of Heat Transfer," in: *Handbook of Heat Transfer Fundamentals,* W. M. Rohsenow et al., pp. 15–25.

Patankar, S. V., 1980, *Numerical Heat Transfer and Fluid Flow,* McGraw-Hill, New York.

Patankar, S. V., 1988, "Elliptic Systems: Finite-Difference Method I," in: *Handbook of Numerical Heat Transfer,* W. J. Minkowycz et al., eds., pp. 215–290.

Solomon, A. D., Morris, M. D., Martin, J., and Olszewski, M., 1986, "The Development of a Simulation Code for a Latent Heat Thermal Energy Storage System in a Space Station," Technical Report ORNL-6213.

Stovall, T. K., and Arimilli, R. V., 1988, "Transient Thermal Analysis of Three Fast-Changing Latent Heat Storage Configurations for a Space-Based Power System," *Proc. 23rd Intersociety Energy Conversion Engineering Conference,* pp. 171–177.

Yimer, B., and Adami, M., 1989, "Parametric Study and Optimization of Phase Change Thermal Energy Storage Systems," *Proc. ASME National Heat Transfer Conf.,* ASME HTD-Vol. 109, pp. 1–8.

Bounds on Heat Transfer in a Periodic Graetz Problem

A. K. Cousins
Spectra Technology Inc.,
Bellevue, WA 98004-1495

It is proven that the heat transfer coefficient and rate of decay of temperature with distance in a fully developed Graetz problem with temporally periodic inlet temperature are greater than or equal to the corresponding quantities in the corresponding steady Graetz problem. The proof is valid for arbitrary duct cross-sectional shapes and for either constant temperature, constant heat flux, or linearized radiation boundary conditions. A numerical solution of the energy equation demonstrates the validity of the theorem. The utility of the result is discussed in the context of heat exchanger design for pulsed gas lasers.

Introduction

The present investigation is motivated by an application to unsteady heat transfer in compact heat exchangers used in pulsed laser applications. Further detail on laser heat exchangers is available from Cousins (1990) and Cassady (1985); a brief description of this application will be given here to motivate the following discussion.

In a pulsed gas laser the laser gas circulates through the discharge cavity in a flow loop containing a fan and a compact gas-to-liquid heat exchanger. The heat exchanger serves to remove thermal energy generated in the gas by the succession of discharge pulses; these pulses generate a train of alternating hot and cold gas regions. The heat exchanger must remove the mean energy of the heated gas and also reduce the amplitude of thermal oscillations due to the hot/cold alternation by several orders of magnitude.

Standard heat exchanger design methods in conjunction with manufacturers' data on the performance of heat exchanger cores enable the laser designer to ensure that the mean thermal energy in the gas can be removed effectively. It is also essential to understand the response of the heat exchanger to unsteady thermal loading in the form of temporally periodic inlet temperatures; this behavior has been characterized in previous work (Cousins, 1990).

An implicit assumption in this work was that the heat transfer coefficient is identical for both steady and unsteady periodic inlet temperature conditions. In fact, the heat transfer coefficients can be expected to be different in these two cases, and it is important to know how they differ. In laser applications, where the heat exchanger is designed to minimize thermal oscillations in the outlet gas stream, it is useful to know whether the error made by assuming that the steady heat transfer coefficient applies to the unsteady case is conservative or nonconservative. The present work focuses on this question.

Statement of the Problem

The heat transfer in the fin passages of pulsed gas laser heat exchangers is characterized by relatively low values of the Reynolds and Peclet numbers (on the order of 20–50) and large length-to-diameter ratios of the heat transfer passage, so that the mean flow is hydrodynamically and thermally developed over most of the region of interest (Kays and Crawford, 1980). The small values of the Reynolds and Peclet numbers are due to the small transverse length scales in the heat exchanger passages, not to small characteristic velocities; thus free convection is negligible compared to forced convection.

The model studied here assumes that the velocity profile is independent of distance along the axis of the channel, i.e., it is fully developed by the time it reaches the heat transfer section of the exchanger. This is quite reasonable, given the presence of uncooled flanges upstream of the heat exchanger. This idealized model does not take into account streamwise velocity variations produced by flow around tubes in crossflow, etc., but the qualitative features of the analysis should not be drastically altered by the idealization.

The mathematical problem consists of the transient laminar energy equation:

$$\frac{\partial \theta}{\partial t} + v(y, z)\frac{\partial \theta}{\partial x} = \kappa \nabla^2_{yz}\,\theta \tag{1}$$

The Laplacian is in the transverse coordinates y and z; these subscripts will be suppressed below with this understanding. Equation (1) contains the implicit assumption that axial conduction is negligible compared to transverse conduction, and that viscous heat generation is negligible (Kays and Crawford, 1980).

The boundary condition at the channel inlet is

$$\theta(0, y, z) = \theta_0 e^{i\Omega t} \tag{2}$$

i.e., a temporally periodic, spatially uniform inlet temperature. On the channel walls, the boundary conditions are

$$\alpha\theta + \beta\frac{\partial \theta}{\partial n} = 0 \tag{3}$$

where n indicates the normal to the wall surface and α and β are arbitrary constants. Note that the constant-heat flux or constant-temperature boundary conditions (the constant can be taken to be zero without loss of generality) are obtained by setting either α or β to zero, respectively.

In steady Graetz flow the neglect of the axial conduction terms in equation (1) is justified by scaling arguments: The transverse length scales for conduction, corresponding to the duct width, are much shorter than the axial length scales. In order to neglect axial conduction in the periodic case, it is also necessary to consider the axial length scale consisting of the wavelength of the inlet temperature waves. This wavelength must be long compared to the duct width in order to neglect the axial conduction terms; in the applications of interest, this requirement is always satisfied.

A temporally periodic solution of the problem will be sought by assuming that

$$\theta(x, y, z, t) = \theta(x, y, z)e^{i\Omega t} \tag{4}$$

Substitution of equation (4) into equations (1)–(3) and nondimensionalization leads to the following system:

$$i\omega T + u(\eta, \zeta)\frac{\partial T}{\partial \xi} = \nabla^2 T \tag{5}$$

Contributed by the Heat Transfer Division and presented at the AIAA/ASME 5th Thermophysics and Heat Transfer Conference, Seattle, Washington, June 1990. Manuscript received by the Heat Transfer Division September 13, 1989; revision received July 15, 1990. Keywords: Forced Convection, Heat Exchangers, Transient and Unsteady Heat Transfer.

$$T(0, \eta, \zeta) = 1 \tag{6}$$

$$\alpha T(\xi, \eta, \zeta) + \beta \frac{\partial T}{\partial n} = 0 \quad \text{at the wall} \tag{7}$$

For $\omega = 0$, the system above reduces to the usual steady Graetz problem.

The problem is separable, and if a solution of the form $f(\eta, \zeta)g(\xi)$ is assumed for equations (5)–(7), the solution to equation (1) can be written as

$$T(\xi, \eta, \zeta) = e^{i\omega\tau} \sum_{n=1}^{\infty} A_n e^{-\lambda_n \xi} f_n(\eta, \zeta) \tag{8}$$

The function f_n satisfies the eigenvalue problem

$$\nabla^2 f_n - i\omega f_n + \lambda_n u f_n = 0 \tag{9}$$

$$\alpha f + \beta \frac{\partial f}{\partial n} = 0 \quad \text{on the boundary} \tag{10}$$

$$\text{where } \lambda_n = \sigma_n + ik_n \tag{11}$$

Note from equation (11) that σ_n and k_n are, respectively, the real and imaginary parts of the eigenvalue; the middle term in equation (9) causes the eigenvalues and eigenfunctions to become complex for $\omega \neq 0$. In the next section some properties of this eigenvalue problem will be established.

Properties of the Solution

It will be convenient to define the following integral over the cross-sectional area of the duct at this point:

$$\langle p(\eta, \zeta) \rangle \equiv \int p(\eta, \zeta)\, d\eta\, d\zeta \tag{12}$$

where the integral is taken over the duct cross-sectional area. It is also convenient to define the following integral:

$$[p] \equiv \int p(s) \cdot ds \tag{13}$$

where ds is a differential element of path length around the contour bounding the cross-sectional area of the duct; the integral is taken around this bounding contour.

In the one-dimensional case, when $\omega = 0$, equations (9)–(10) represent a Sturm–Liouville eigenvalue problem, for which it is known that there exists a complete set of orthogonal eigenfunctions and an infinite number of real eigenvalues. Although the problem is no longer of the Sturm–Liouville type when $\omega \neq 0$, analogous properties can be demonstrated.

Orthogonality of the eigenfunctions is easily proven. For any two eigenfunction f_i and f_j, equation (9) implies that

$$\begin{aligned} f_j \nabla^2 f_i - i\omega f_j f_i + \lambda_i u f_j f_i &= 0 \\ f_i \nabla^2 f_j - i\omega f_i f_j + \lambda_j u f_i f_j &= 0 \end{aligned} \tag{14}$$

Subtracting one of these equations from the other and integrating the result over the duct cross-sectional area yields

$$\begin{aligned} (\lambda_i - \lambda_j)\langle u f_i f_j \rangle &= -\langle f_i \nabla^2 f_j \rangle + \langle f_i \nabla^2 f_j \rangle \\ &= -\langle \nabla \cdot f_i \nabla f_j \rangle + \langle \nabla f_i \cdot \nabla f_j \rangle \\ &\quad + \langle \nabla \cdot f_j \nabla f_i \rangle - \langle \nabla f_j \cdot \nabla f_i \rangle \\ &= -[f_i(\partial f_j/\partial n)] + [f_j(\partial f_i/\partial n)] \\ &= 0 \end{aligned} \tag{15}$$

The third step follows by the divergence theorem. If either $\alpha = 0$ or $\beta = 0$ the last step follows trivially from boundary condition (10). If $\alpha \neq 0$ and $\beta \neq 0$ then

$$-[f_i(\partial f_j/\partial n)] + [f_j(\partial f_i/\partial n)] =$$

$$-[f_i(\partial f_j/\partial n + \frac{\alpha}{\beta} f_j)] + [f_j(\partial f_i/\partial n + \frac{\alpha}{\beta} f_i)] = 0$$

again by equation (10). Thus

$$\text{for } i \neq j \quad \langle u f_i f_j \rangle = 0 \tag{16}$$

which is the desired orthogonality relationship.

The eigenvalues of the problem are complex, and some qualitative information about them may be gained as follows. From equation (9)

$$f_n^* \nabla^2 f_n - i\omega f_n^* f_n + \lambda_n u f_n^* f_n = 0 \tag{17}$$

Integrating over the duct cross section and using the divergence theorem and the boundary conditions as before yields the following two equations:

$$\sigma_n = \mathrm{Re}(\lambda_n) = \frac{\langle \nabla f_n \cdot \nabla f_n^* \rangle + (\beta/\alpha)[(\partial f_n/\partial n)(\partial f_n^*/\partial n)]}{\langle u f_n f_n^* \rangle}, \quad \alpha \neq 0$$

$$= \frac{\langle \nabla f_n \cdot \nabla f_n^* \rangle}{\langle u f_n f_n^* \rangle}, \quad \alpha = 0 \tag{18}$$

$$k_n = \mathrm{Im}(\lambda_n) = \omega \frac{\langle f_n f_n^* \rangle}{\langle u f_n f_n^* \rangle} \tag{19}$$

Equation (18) reveals that for $\frac{\beta}{\alpha} \geq 0$ and $u \geq 0$ everywhere, σ_n is positive, leading to a decay of the temperature with downstream distance, as expected. Equation (19) indicates that $k_n > 0$ and $k_n \neq 1$ in general unless $u \equiv 1$, the "plug flow" case. Reference to equation (8) then indicates that the channel temperature can be written as a superposition of damped traveling

Nomenclature

d = characteristic transverse length scale (width) of the duct
k_n = imaginary part of λ_n (wavenumber)
Pe = Peclet number $= u_m d/\kappa$
t = time
T = dimensionless temperature amplitude $= \theta(\xi, \eta, \zeta)/\theta_0$
T_{mm} = mixed mean temperature
u = dimensionless axial velocity $= v/u_m$
u_m = bulk (mean) velocity
v = axial velocity
x = axial coordinate
y = transverse coordinate
z = transverse coordinate
α = see equation (7)
β = see equation (7)
ζ = dimensionless transverse coordinate $= z/d$
η = dimensionless transverse coordinate $= y/d$
θ = temperature
κ = thermal diffusivity
λ_n = nth eigenvalue of equations (9)–(11)
ξ = dimensionless axial coordinate $= x/(d \cdot \mathrm{Pe})$
σ_n = real part of λ_n (decay constant)
τ = dimensionless time $= t/(\mathrm{Pe} \cdot d/u_m)$
Ω = angular frequency of input temperature oscillation
ω = dimensionless angular frequency $= \Omega \cdot \mathrm{Pe} \cdot d/u_m$
$*$ = indicates the complex conjugate

waves originating at the channel entrance. In the plug flow case, the waves travel in phase; however, the presence of a nonuniform velocity profile produces dispersion, since equation (19) shows that in general the different wavenumber components travel at differing speeds.

Bounds on the Eigenvalues

It is possible to establish a lower bound on the real part of the fundamental eigenvalue of the problem (9)–(11) by comparing it to the corresponding eigenvalue of the steady ($\omega = 0$) problem. In order to do this, a minimum principle for the eigenvalues of the steady problem will be established. This minimum principle is an extension of well-known extremum principles and comparison theorems for self-adjoint problems with real eigenvalues (Courant and Hilbert, 1953) to the present non-self-adjoint problem with complex-valued eigenfunctions and eigenvalues.

The minimum statement that will be demonstrated is that the successive minima of the functional defined below occur when the functions g_n are solutions of the steady Graetz eigenvalue problem. The functional σ_n is defined by

$$\sigma_n = \frac{\langle \nabla g_n \cdot \nabla g_n^* \rangle + (\beta/\alpha)[(\partial g_n/\partial n)(\partial g_n^*/\partial n)]}{\langle u g_n g_n^* \rangle}, \quad \alpha \neq 0$$
$$= \frac{\langle \nabla g_n \cdot \nabla g_n^* \rangle}{\langle u g_n g_n^* \rangle}, \quad \alpha = 0 \tag{20}$$

Note that when the g_n are the solutions of equations (9)–(11), this functional corresponds to the real part of the eigenvalue λ_n; since there is no explicit dependence on ω, this holds for the eigenvalues of both the steady and unsteady problems.

The admissible class of functions g_n is required to satisfy boundary condition (10) of the problem and to be smooth. In addition, each successive function g_n is required to be orthogonal (with weighting function u) to all the preceding functions g_i, i.e.,

$$\langle u g_n g_i \rangle = 0, \qquad i = 1, \ldots, n-1 \tag{21}$$

If σ_n is the minimum value of the functional above, then

$$I \equiv \langle \nabla g_n \cdot \nabla g_n^* \rangle + (\beta/\alpha)[(\partial g_n/\partial n)(\partial g_n^*/\partial n)] - \sigma_n \langle u g_n g_n^* \rangle \geq 0 \quad \text{for } \alpha \neq 0$$
$$\equiv \langle \nabla g_n \cdot \nabla g_n^* \rangle - \sigma_n \langle u g_n g_n^* \rangle \geq 0 \quad \text{for } \alpha = 0 \tag{22}$$

and minimizing I is equivalent to minimizing the functional of equation (20). A necessary condition for a minimum of I is that its first variation be zero, or

$$\lim_{\epsilon \to 0} \frac{\partial I(g + \epsilon\phi)}{\partial \epsilon} = 0 \tag{23}$$

Thus

$$\left[\langle \nabla g_n \cdot \nabla \phi^* \rangle - \sigma_n \langle u g \phi^* \rangle + \frac{\beta}{\alpha} \frac{\partial g_n}{\partial n} \frac{\partial g_n^*}{\partial n} \right] + \text{c.c.} = 0, \quad \alpha \neq 0$$
$$\text{and } [\langle \nabla g_n \cdot \nabla \phi^* \rangle - \sigma_n \langle u g \phi^* \rangle] + \text{c.c.} = 0, \quad \alpha = 0 \tag{24}$$

where "c.c." denotes the complex conjugate of the expression in square brackets. Integration by parts and use of boundary conditions (10) leads to

$$[-\langle \phi^* \nabla^2 g_n \rangle - \sigma_n \langle u g_n \phi^* \rangle] + \text{c.c.} = 0 \tag{25}$$

In order for the above statement to hold for an arbitrary complex-valued function ϕ, it is necessary that

$$\nabla^2 \text{Re}(g_n) + \sigma_n u \cdot \text{Re}(g_n) = 0 \tag{26}$$

and

$$\nabla^2 \text{Im}(g_n) + \sigma_n u \cdot \text{Im}(g_n) = 0 \tag{27}$$

or, more compactly,

$$\nabla^2 g_n + \sigma_n u \cdot g_n = 0 \tag{28}$$

which is the eigenvalue equation for the steady Graetz problem. Thus a necessary requirement for the function that minimizes the functional (20) is that it satisfy the steady Graetz equation (28).

Now the real part σ_1 of the fundamental eigenvalue of the unsteady problem (9)–(11) is given by equation (20), and the fundamental eigenfunction of the unsteady problem satisfies admissibility and orthogonality conditions identical to those of the steady problem. Since the fundamental eigenfunction of the steady problem gives the minimum value of the functional (20), and since the class of solutions of the steady problem is a subset of the class of solutions of the general unsteady problem, the real part of the fundamental eigenvalue of the unsteady problem is greater than the corresponding eigenvalue of the steady problem (see Courant and Hilbert, 1953). This leads directly to the conclusion that the heat transfer coefficient in the periodic case must be larger than in the steady case.

Dependence of the Eigenvalues on ω

One further observation about the eigenvalues of (9)–(11) is useful in applications; namely, that the real part of the eigenvalue changes slowly with increases in ω. This point can be proven by examining the first term in a perturbation solution of the eigenvalue problem. The eigenvalues and eigenfunctions are expanded in powers of $\delta\omega$, a small perturbation of ω:

$$\omega = \omega^{(0)} + \delta\omega + O(\delta\omega^2) \tag{29}$$

$$\lambda = \lambda^{(0)} + \lambda^{(1)}\delta\omega + O(\delta\omega^2) \tag{30}$$

$$f = f^{(0)} + f^{(1)}\delta\omega + O(\delta\omega^2) \tag{31}$$

After substitution of these expansions into equations (9)–(11), the first-order correction to the problem is found to satisfy the equation

$$\nabla^2 f^{(1)} - i\omega f^{(1)} + \lambda^{(0)} u f^{(1)} = i f^{(0)} - \lambda^{(1)} u f^{(0)} \tag{32}$$

If this equation is multiplied by $f^{(0)*}$ and integrated over the duct cross section (making use of integration by parts and the boundary conditions of the problem), the left side vanishes because $f^{(0)}$ satisfies the zero-order equation, and the final result is

$$\lambda^{(1)} = i \frac{\langle f^{(0)} f^{(0)*} \rangle}{\langle u f^{(0)} f^{(0)*} \rangle} \tag{33}$$

Therefore the first-order change in the eigenvalue is purely imaginary for a small perturbation of the frequency ω. This suggests that the real part of the eigenvalues will vary relatively slowly with changes in frequency, and in fact this will be evident in the numerical solution described below.

A Numerical Example

In order to illustrate the preceding argument, a finite-difference solution of the energy equation for a parallel-plate geometry has been performed. This geometry is representative of the parallel-plate fins typically found in laser heat exchangers.

The governing equations are equations (5)–(7) specialized to the parallel-plate case, with the zero wall temperature boundary condition:

$$i\omega T + u(\eta)\frac{\partial T}{\partial \xi} = \frac{\partial^2 T}{\partial \eta^2} \tag{34}$$

where

$$u(\eta) = 1 - \eta^2 \tag{35}$$

$$T(0, \eta) = 1 \tag{36}$$

$$T(\xi, \pm 1) = 0 \tag{37}$$

The computations are performed across the half-width of the

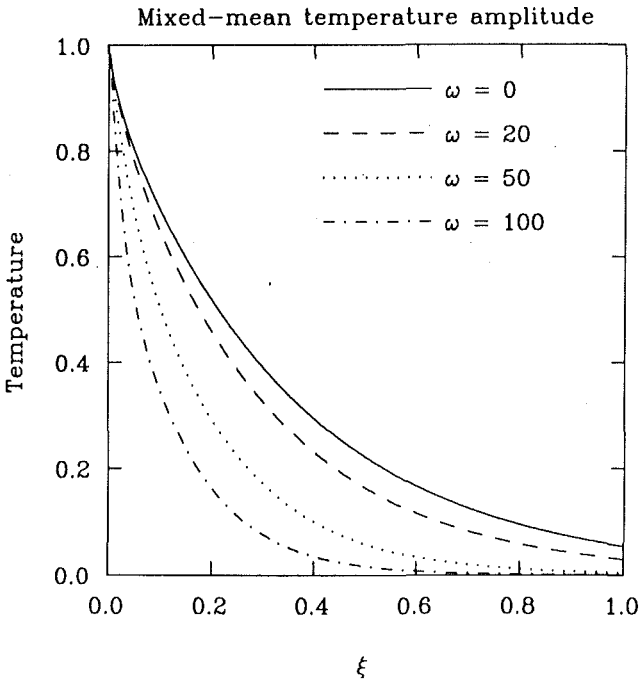

Fig. 1 Decay of the mixed-mean temperature amplitude with downstream distance

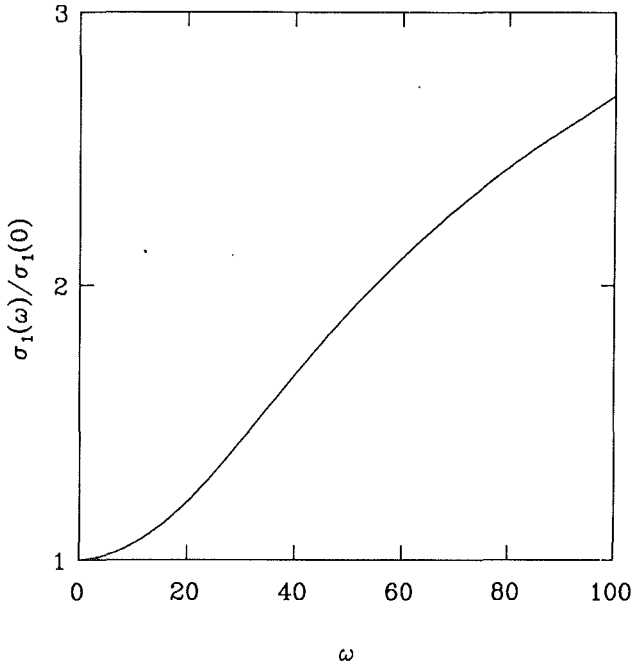

Fig. 2 Dependence of the fundamental eigenvalue on frequency in the flat-plate problem

channel since the problem is symmetric across the channel centerline, and the temperature gradient in the η direction is set to zero at the centerline.

Due to the parabolic nature of the problem, a finite-difference scheme that is implicit in the η direction and marches in the ξ direction has been chosen. The implicit scheme, a modified Crank-Nicolson algorithm, is not subject to numerical stability restrictions and has second-order truncation errors in both spatial directions (Richtmyer and Morton, 1967).

The computational domain is discretized on a mesh with spacings $\Delta\xi$ and $\Delta\eta$ between grid points in the two directions. The following definitions are useful:

$$T_j^i \equiv T(i\Delta\xi,\ j\Delta\eta) \tag{38}$$

$$\delta_\eta^2\, T_j^i \equiv T_{j+1}^i - 2T_j^i + T_{j-1}^i \tag{39}$$

$$u_j \equiv u(j\Delta\eta) \tag{40}$$

Equation (34) is discretized as follows:

$$i\omega\frac{T_j^i + T_j^{i+1}}{2} + u_j\frac{T_j^{i+1} - T_j^i}{\Delta\xi} = \frac{\delta_\eta^2 T_j^i + \delta_\eta^2 T_j^{i+1}}{2\Delta\eta^2} \tag{41}$$

This discretization leads to the following system of equations:

$$T_{j-1}^{i+1} - \left[2 + i\omega(\Delta\eta)^2 + 2u_j\frac{(\Delta\eta)^2}{\Delta\xi}\right] T_j^{i+1} + T_{j+1}^{i+1} =$$

$$-T_{j-1}^i + \left[2 + i\omega(\Delta\eta)^2 - 2u_j\frac{(\Delta\eta)^2}{\Delta\xi}\right] T_j^i - T_{j+1}^i \tag{42}$$

Although this scheme is unconditionally stable, a poor choice of step sizes can lead to physically unrealistic solutions. The necessary condition for a realistic solution is that (Patankar, 1980)

$$\Delta\xi \le u_j(\Delta\eta)^2 \tag{43}$$

and since the minimum value of u_j occurs at the grid point closest to the wall, where $u^j \simeq 2\Delta\eta$, the necessary condition becomes

$$\Delta\xi \le 2(\Delta\eta)^3 \tag{44}$$

The results presented here were obtained with $\Delta\xi = 5 \times 10^{-5}$ and $\Delta\eta = 4 \times 10^{-2}$. The accuracy of the code was verified by checking the asymptotic heat transfer coefficient for the steady problem ($\omega = 0$) against its published value (Shah and London, 1978).

Figure 1 shows the decay of the amplitude of the mixed-mean temperature with downstream distance. The mixed-mean temperature is defined by

$$T_{mm} \equiv \langle uT\rangle / \langle u\rangle \tag{45}$$

and the quantity plotted in Fig. 1 is $|T_{mm}|$, the amplitude of the complex mixed-mean temperature. The numerical results verify the prediction that the decay becomes more rapid as the inlet temperature oscillation frequency increases. In addition, the decay constant is not a strong function of the frequency; even for $\omega = 20$, the mixed-mean temperature amplitude is quite close to that for $\omega = 0$.

Discussion

In fully developed flow, by definition, all the higher modes in equation (8) have decayed to negligible amplitudes, and the dominant term is the fundamental mode ($n = 1$). The heat transfer coefficient is then proportional (Kays and Crawford, 1980) to the real part σ_1 of the fundamental eigenvalue λ_1, whose value can be calculated via

$$\sigma_1 = \lim_{\xi\to\infty} \frac{-1}{|T_{mm}|}\frac{\partial}{\partial x}\left|T_{mm}\right| \tag{46}$$

This relation for σ_1 follows directly from equation (8).

σ_1 has been calculated numerically from the simulation described above, and Fig. 2 illustrates the variation of σ_1 with ω. Note that as predicted above, σ_1 (and therefore the heat transfer coefficient) is always greater than its steady value, and is a weak function of ω.

At this point it is useful to summarize the results developed above. It has been shown that the real part of the fundamental eigenvalue of the laminar energy equation (5) with a temporally periodic input temperature field is greater than or equal to the corresponding (real) eigenvalue in the temporally steady case. This conclusion is valid for a fully developed velocity profile, arbitrary duct cross-sectional shape and either constant heat flux, constant wall temperature, or linearized radiation boundary conditions at the walls.

In the thermally developed region of the flow, all eigenmodes except the first have decayed to zero, and the heat transfer coefficient is given by equation (46). As a consequence of the above result on the eigenvalues, the heat transfer coefficient in the thermally developed region of the flow is greater in the unsteady case than in the steady case (unless the velocity profile is uniform, in which case the heat transfer coefficient is a constant).

Finally, the perturbation argument presented above suggests that the real parts σ_n of the eigenvalues should exhibit a fairly weak dependence on the frequency ω, and this is borne out by the flat-plate results of Fig. 2.

The practical implications of this result for the design of laser heat exchangers are clear. In general, the gas-side heat transfer is the dominant thermal resistance in a laser heat exchanger. The heat exchanger may be designed assuming the gas-side heat transfer coefficient to be constant at its steady value, which is generally known to the manufacturer or can be calculated readily. The unsteady response may be predicted, with this assumption, using the methods of Cousins (1990). The results of the present work then indicate that the actual amplitude of the outlet gas temperature oscillations will be lower than the predicted value, since the actual heat transfer coefficient is slightly higher than its steady value. Thus the error made in assuming the heat transfer coefficient to be constant is conservative.

Acknowledgments

This work was supported by internal research funds from Spectra Technology Inc.

References

Cassady, P. E., 1985, "Fluid Dynamics in Closed-Cycle Pulsed Lasers," *AIAA Journal,* Vol. 23, pp. 1922–1936.

Courant, R., and Hilbert, D., 1953, *Methods of Mathematical Physics, Volume I,* first English ed., Interscience Publishers Inc., New York.

Cousins, A. K., 1990, "Response of Laser Heat Exchangers to Unsteady Spatially Varying Inputs," *Journal of Thermophysics and Heat Transfer,* in press.

Kays, W. M., and Crawford, M. E., 1980, *Convective Heat and Mass Transfer,* 2nd ed., McGraw-Hill, New York.

Patankar, S. V., 1980, *Numerical Heat Transfer and Fluid Flow,* Hemisphere Publishing Corporation, New York.

Richtmyer, R. D., and Morton, K. W., 1967, *Difference Methods for Initial Value Problems,* 2nd ed., Wiley Interscience, New York.

Shah, R. K., and London, A. L., 1978, *Laminar Flow Forced Convection in Ducts,* Academic Press, New York.

Forced Laminar Convection in a Curved Isothermal Square Duct

G. J. Hwang
Professor.
Mem. ASME

Chung-Hsing Chao
Ph.D. Candidate.

Department of Power Mechanical Engineering,
National Tsing Hua University,
Hsinchu, Taiwan, 30043

A numerical study is made to investigate the forced laminar convection in the hydrodynamically and thermally fully developed region of a curved isothermal square duct. Solutions with one and two pairs of vortices superimposed on the main flow are obtained. In the thermally fully developed region, a three-dimensional energy equation of elliptic type is reduced to a two-dimensional one with an eigenvalue, and the axial diffusion term is considered for a small value of the Peclet number. Flow characteristics for cases of dimensionless radius of curvature $\beta = \infty$, 50, 10, and 5 with the square of the Dean number ranging from 0 to 10^6 in a square duct are studied. In addition, heat transfer characteristics for large dimensionless radii of curvature, $Pr = 0.7$ and 7.0, and Peclet number $Pe = \infty$, 10, 5, and 1 are also examined.

Introduction

Curved ducts are extensively employed in many heat and mass transfer devices such as the passages of turbomachinery components, inlet diffusers of rocket engines, and other industrial apparatus. An important feature distinguishing curved-duct flows from straight-duct flows is the secondary flow induced in the cross planes of the curved duct due to the centrifugal forces, which may cause an extra pressure loss, distortions of the axial velocity and temperature profiles, and an enhancement of the heat transfer rate.

Using a perturbation technique, the earliest theoretical studies on the motion of fluid in a curved pipe were made by Dean (1927, 1928). He predicted the characteristics of the twin-vortex secondary flow and pointed out that the dynamic similarity of such flow depends on a dimensionless parameter K [$K = \mathrm{Re}(D_e/R)^{0.5}$] called the Dean number in the scientific community. The solution obtained by using the perturbation technique is limited to a small value of K. A comprehensive review of the analytic studies on flow in curved pipes can be found from Berger et al. (1983).

The laminar forced convection heat transfer in curved rectangular channels was first studied by Cheng and Akiyama (1970) by using a numerical technique. Only one pair of counterrotating vortices was found in the square channel for $K < 130$. For the curved square duct, numerical calculations such as these described by Joseph et al. (1975) and Cheng et al. (1976) revealed that for K larger than a certain critical value, an additional pair of counterrotating vortices occurs near the concave wall. But the friction factor, which is an important overall flow characteristic, did not show the presence of the onset of the four-vortex crossflow at the critical Dean number. For experimental observations by Cheng et al. (1977) the onset of the four-vortex crossflow pattern known as Dean's instability appears at $K = 176.1$. This was the first time the phenomenon was shown photographically, and it confirmed the previous theoretical prediction (Joseph et al., 1975, Cheng et al., 1976). Similarly, the four-vortex crossflow patterns were also found by Dennis and Ng (1982), and Nandakumar and Masliyah (1982) for curved circular pipes.

According to the bifurcation phenomenon reported by Benjamin (1978), both two-vortex and four-vortex crossflow patterns constitute the dual solutions, which are attained depending on the initial condition used to start the numerical computation of nonlinear governing equations. Recently, Winters (1987) showed that for a square cross section the transition is a result of a complex structure of multiple, symmetric, and asymmetric solutions. The singular value of K for the transition of the two- and four-vortex flow patterns is between 113 and 191.

With the appearance of single or multiple pairs of vortices, the heat transfer rate will be enhanced regardless of the thermal boundary conditions and flow cross sections as described by Cheng and Akiyama (1970) and Mori et al. (1971) for rectangular channels with axially uniform wall heat flux and peripherally uniform wall temperature, by Cheng et al. (1975) for curved square channels with uniform wall temperature and constant wall heat flux, by Akiyama and Cheng (1971), Dravid et al. (1971), and Kalb and Seader (1974) for circular tubes with thermal boundary conditions of constant wall heat flux and/or uniform wall temperature.

There are many engineering applications for low Peclet number fluid flows: for instance, when low Prandtl number liquid metals are utilized in solidification and casting processes, in high-temperature heat exchangers, and in low Reynolds number fluid flows in low flow rate heat exchangers designed for food processing, battery cooling, constant temperature baths, electronic cooling, and solar collectors. All the papers in curved ducts reviewed here are analyzed without considering the effect of axial conduction in the thermally fully developed region for a small Peclet number.

An attempt is made in the present paper to analyze the forced laminar convection in the hydrodynamically and thermally fully developed region of a curved isothermal square duct. In the thermally fully developed region, the temperature distribution varies exponentially in the axial flow direction. Therefore a two-dimensional eigenvalue problem is reduced. The axial conduction term is also considered for a small value of Pe. Detailed computation in the region near the critical value marking the onset of the four-vortex flow will be made to give a clear understanding of the flow pattern and the behavior of the friction factor in the vicinity of the critical value.

Theoretical Analysis

Consider forced laminar convection in the hydrodynamically fully developed region of a curved square duct heated isothermally. The fluid temperature will increase exponentially along the main flow direction in the thermally fully developed region. The physical configuration and coordinate system are shown in Fig. 1. An unbalanced centrifugal force is introduced in the X direction. A pair or pairs (Joseph et al., 1975; Cheng et al., 1976) of counterrotating symmetric or asymmetric (Winters, 1987) vortices will be generated and superimposed on the main

Contributed by the Heat Transfer Division for publication in the JOURNAL OF HEAT TRANSFER. Manuscript received by the Heat Transfer Division July 10, 1989; revision received May 18, 1990. Keywords: Forced Convection, Heat Exchangers, Numerical Methods.

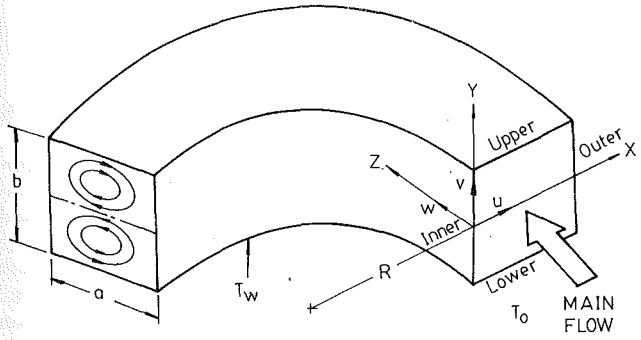

Fig. 1 Coordinates and physical configuration

flow. By transforming cylindrical coordinates (r, θ, z) to a coordinate system (X, Y, Z) on the cross section of the curved duct

$$r = R + X \qquad \theta = Z/R \qquad z = Y \tag{1}$$

and assuming a steady, incompressible, and hydrodynamically fully developed flow, and constant physical properties, we have the continuity and momentum equations as follows:

Continuity equation:

$$\frac{1}{(R+X)}\frac{\partial}{\partial X}[(R+X)U] + \frac{\partial V}{\partial Y} = 0 \tag{2}$$

X-momentum equation:

$$U\frac{\partial U}{\partial X} + V\frac{\partial U}{\partial Y} = -\frac{1}{\rho}\frac{\partial P}{\partial X} + \nu\left[\nabla^2 U - \frac{U}{(R+X)^2}\right] + \frac{W^2}{(R+X)} \tag{3}$$

Y-momentum equation:

$$U\frac{\partial V}{\partial X} + V\frac{\partial V}{\partial Y} = -\frac{1}{\rho}\frac{\partial P}{\partial Y} + \nu\nabla^2 V \tag{4}$$

Z-momentum equation:

$$U\frac{\partial W}{\partial X} + V\frac{\partial W}{\partial Y} + \frac{UW}{(R+X)} = -\frac{R}{\rho(R+X)}\frac{\partial P}{\partial Z} + \nu\left[\nabla^2 W - \frac{W}{(R+X)^2}\right] \tag{5}$$

where $\nabla^2 = \frac{1}{(R+X)}\left[\frac{\partial}{\partial X}(R+X)\frac{\partial}{\partial X}\right] + \frac{\partial^2}{\partial Y^2}$.

The term $W^2/(R+X)$ on the right-hand side of equation (3) is the centrifugal force driving the flow in the X direction; $UW/(R+X)$, the third term on the left-hand side of equation (5), is the Coriolis force acting in the main flow direction; and the terms $\nu U/(R+X)^2$ and $\nu W/(R+X)^2$ on the right-hand sides of equations (3) and (5), respectively, are the viscous forces due to the coordinate transformation.

Furthermore, the channel wall is heated and kept at a uniform wall temperature T_w; the fluid with a uniform entrance temperature T_0 will be heated. After a sufficient heating length, the temperature distribution of fluid along the channel will be thermally fully developed. By assuming no viscous dissipation, the energy equation is

$$U\frac{\partial T}{\partial X} + V\frac{\partial T}{\partial Y} + \frac{R}{(R+X)}W\frac{\partial T}{\partial Z} = \alpha\left[\nabla^2 T + \frac{R^2}{(R+X)^2}\frac{\partial^2 T}{\partial Z^2}\right] \tag{6}$$

It is noted that the axial viscous terms in equations (3)–(5) are neglected because the flow is hydrodynamically fully developed, but the axial conduction term in the energy equation (6) is kept in the present thermally fully developed region. The reason for this formulation will be explained later.

In order to obtain governing parameters in the present problem, the following dimensionless transformations for the independent and dependent variables are introduced:

$$X = D_e x, \qquad Y = D_e y, \qquad Z = Lz$$

$$U = K^2\left(\frac{\nu}{D_e}\right)u, \qquad V = K^2\left(\frac{\nu}{D_e}\right)v, \qquad W = \overline{W}w \tag{7}$$

$$P = P_z(Z) + \rho K^2\left(\frac{\nu}{D_e}\right)^2 \cdot P$$

Nomenclature

A = cross-sectional area
a = channel width
b = channel height
C = constant $= -(\partial P_z/\partial Z)D_e^2/\mu\overline{W}$
D_e = hydraulic diameter $= 4A/S$
f = friction factor $= 2\bar{\tau}_w/\rho\overline{W}^2$
h = heat transfer coefficient $= \bar{q}_w/(T_b - T_w)$
K = Dean number $= \mathrm{Re}(D_e/R)^{0.5}$
k = thermal conductivity of fluid
L = Z-direction characteristic length
Nu = Nusselt number $= hD_e/k$
n = dimensionless normal direction coordinate
P, p = pressure and dimensionless pressure
Pe = Peclet number $= \overline{W}D_e/\alpha$
Pr = Prandtl number $= \nu/\alpha$
q_w = wall heat flux
r, θ, z = cylindrical coordinate system
R = radius of curvature
Re = Reynolds number $= \overline{W}D_e/\nu$
S = perimeter
T = temperature
U, V, W = velocity components in X, Y, and Z directions, respectively
u, v, w = dimensionless velocity components in x, y, and z directions, respectively
X, Y, Z = Cartesian coordinate system
x, y, z = dimensionless Cartesian coordinate system
∇^2 = Laplace operator $= \frac{1}{(R+X)}\left[\frac{\partial}{\partial X}(R+X)\frac{\partial}{\partial X}\right] + \frac{\partial^2}{\partial Y^2}$
α = thermal diffusivity of fluid
β = dimensionless radius of curvature $= R/D_e$
γ = height-to-width aspect ratio $= b/a$
θ = dimensionless temperature difference $= (T - T_w)/(T_b - T_w)$
λ = eigenvalue
μ = viscosity
ν = kinematic viscosity
ξ = vorticity
ρ = density
τ_w = wall shear stress
ψ = stream function

Subscripts

b = bulk quantity
c = characteristic quantity
i, j = nodal point
o = condition at $Z = 0$, or values for straight channel
w = condition at wall
z = in z direction

Superscripts

$\bar{}$ = average value
k, m = number of iteration

where D_e is the hydraulic diameter, L is the curved heating length along the channel, $K = \mathrm{Re}\,(D_e/R)^{0.5} = (\overline{W}D_e/\nu)\ (D_e/R)^{0.5}$ is the Dean number, $\overline{W}$ is the average axial velocity, and $P_z(Z)$ is the hydrodynamically fully developed pressure distribution. In the present problem, the case for $L/D_e >> 1$ is considered. It is noted that the characteristic values of U, V, and P are obtained by considering that the order of magnitude of the centrifugal force W^2/R is equal to those of the viscous terms and the pressure term in equation (3).

By substituting the dimensionless transformations (7) into equations (2)–(6), the continuity and momentum equations become

$$\frac{1}{(\beta+x)}\frac{\partial}{\partial x}[(\beta+x)u]+\frac{\partial v}{\partial y}=0 \tag{8}$$

$$K^2\left(u\frac{\partial u}{\partial x}+v\frac{\partial u}{\partial y}\right)=-\frac{\partial p}{\partial x}+\frac{1}{(\beta+x)}\frac{\partial}{\partial x}\left[(\beta+x)\frac{\partial u}{\partial x}\right]+\frac{\partial^2 u}{\partial y^2}-\frac{u}{(\beta+x)^2}+\frac{\beta}{(\beta+x)}w^2 \tag{9}$$

$$K^2\left(u\frac{\partial v}{\partial x}+v\frac{\partial v}{\partial y}\right)=-\frac{\partial p}{\partial y}+\frac{1}{(\beta+x)}\frac{\partial}{\partial x}\left[(\beta+x)\frac{\partial y}{\partial x}\right]+\frac{\partial^2 v}{\partial y^2} \tag{10}$$

$$K^2\left(u\frac{\partial w}{\partial x}+v\frac{\partial w}{\partial y}\right)=\frac{\beta C}{(\beta+x)}+\frac{1}{(\beta+x)}\frac{\partial}{\partial x}\left[(\beta+x)\frac{\partial w}{\partial x}\right]+\frac{\partial^2 w}{\partial y^2}-\frac{w}{(\beta+x)^2}-K^2\frac{uw}{(\beta+x)} \tag{11}$$

where $\beta = R/D_e$ is the dimensionless radius of curvature; $C = -D_e^2\ (\partial P_z/\partial Z)/\mu\overline{W}$ is a constant, which will be determined by considering the global continuity condition, i.e., $\overline{w} = \iint((\beta+x)w/\beta)\ dxdy = 1$ in each cross section. Equations (8)–(11) represent a two-dimensional flow in a sufficient long curved channel. The parameter $K^2 = (\overline{W}D_e/\nu)^2 \cdot (D_e/R)$, the square of the Dean number, represents the effect of centrifugal force and will be used throughout the present study.

In the thermally fully developed region of a long duct with a uniform wall heat flux or with a linearly varying wall temperature, the fluid temperature will change linearly along the channel. But in the present problem the fluid with temperature T_0 is heated in a curved isothermal channel with a constant wall temperature T_w. The fluid temperature can be expressed as (Shah and London, 1978)

$$T - T_w = (T_0 - T_w)\sum_{n=0}^{\infty} C_n\theta_n(X, Y)\ \exp\ (-\lambda_n Z/\mathrm{Pe}D_e) \tag{12}$$

where λ_n are the eigenvalues and $\mathrm{Pe} = \overline{W}\mathrm{D}_e/\alpha$ is the Peclet number. Because the velocity components U, V, and W in equation (6) are functions of X and Y only, the exponential functions in equation (12) can be separated from the functions in X and Y. Although the process may be tedious and time consuming, the eigenfunctions θ_n, in principle, can be determined with each corresponding λ_n. Since $0 < \lambda_0 < \lambda_1 < \lambda_2 < \ldots$, we may find $\exp\ (-\lambda_0 Z/\mathrm{Pe}D_e) >> \exp\ (-\lambda_1 Z/\mathrm{Pe}D_e) >> \ldots$ at a sufficiently large value of Z, i.e., in the thermally fully developed region of an isothermal duct. Therefore we may neglect the higher order terms in equation (12) and rewrite it by setting $\lambda_0 = \lambda$ and $C_0\theta_0 = \theta$. Equation (12) becomes

$$T - T_w = (T_0 - T_w)\ \exp\ (-\lambda Z/\mathrm{Pe}D_e)\theta(x, y) \tag{13}$$

In expression (13), the condition $\iint\left[\frac{\beta+x}{\beta}\right]w\theta dxdy = 1$ should be satisfied for the solution of $\theta(x, y)$.

By substituting equations (7) and (13) into energy equation (6), the dimensionless energy equation can be written as

$$\mathrm{Pr}K^2\left(u\frac{\partial\theta}{\partial x}+v\frac{\partial\theta}{\partial y}\right)-\left[\frac{1}{(\beta+x)}\frac{\partial}{\partial x}\left[(\beta+x)\frac{\partial\theta}{\partial x}\right]+\frac{\partial^2\theta}{\partial y^2}\right]=\left[\frac{\beta}{\beta+x}\lambda w+\frac{\beta^2}{(\beta+x)^2}\frac{\lambda^2}{\mathrm{Pe}^2}\right]\theta \tag{14}$$

where the eigenvalue λ should be positive to ensure a monotonically decreasing exponential value. With the help of equation (13), the energy equation reduces from a three-dimensional boundary value problem to a two-dimensional eigenvalue problem. The effect of centrifugal force on the temperature distribution is represented by the product of Pr and K^2. One important fact must be pointed out clearly in energy equation (14), that the effect of axial conduction term on the heat transfer characteristics in the thermally fully developed region of a channel with a uniform wall temperature is frequently overlooked in the literature. We can see that the second term $\frac{\beta^2}{(\beta+x)^2}\frac{\lambda^2}{\mathrm{Pe}^2}\theta$ on the right-hand side of equation (14) representing the axial conduction term is nonlinear and cannot be neglected for a small value of Pe, in comparison with the term $\frac{\beta}{(\beta+x)}\lambda w\theta$ representing the axial convection term. This means that the exponent in equation (13) will not be small with a second differentiation for a small Pe. It is noted that the two-dimensional eigenvalue problem described in equation (14) and its solution have not been reported in the literature.

In the computation of the present two-dimensional equations, the vorticity transport equation is employed. By a cross-differentiation of the X- and Y- momentum equations (9) and (10), and eliminating the pressure terms, one has

$$K^2\left(u\frac{\partial\xi}{\partial x}+v\frac{\partial\xi}{\partial y}\right)=\frac{1}{(\beta+x)}\frac{\partial}{\partial x}\left[(\beta+x)\frac{\partial\xi}{\partial x}\right]+\frac{\partial^2\xi}{\partial y^2}+\frac{2}{\beta+x}\frac{\partial\xi}{\partial x}-2\left(\frac{\beta}{\beta+x}\right)^2 w\frac{\partial w}{\partial y} \tag{15}$$

where

$$\left(\frac{\beta+x}{\beta}\right)^2\xi = -\left(\frac{\partial^2\psi}{\partial x^2}+\frac{\partial^2\psi}{\partial y^2}\right)+\frac{1}{\beta+x}\frac{\partial\psi}{\partial x}$$

$$u = \frac{\beta}{\beta+x}\frac{\partial\psi}{\partial y} \text{ and } v = -\frac{\beta}{\beta+x}\frac{\partial\psi}{\partial x}$$

The associated boundary conditions for equations (11), (14), and (15) are

$$\psi = \xi = \frac{\partial w}{\partial y} = \frac{\partial\theta}{\partial y} = 0 \text{ along the horizontal center plane } y = 0$$

$$\psi = \frac{\partial\psi}{\partial n} = w = \theta = 0 \text{ on the channel wall} \tag{16}$$

where n is a coordinate normal to the channel wall. It is noted that because asymmetric vortices are not considered, only half of the channel is used in the present study.

Flow and Heat Transfer Characteristics

The important overall flow and heat transfer characteristics of forced laminar convection in a channel flow are indicated by the friction factor and the Nusselt number, respectively. Following the conventional definitions, the friction factor and the Nusselt number are written as

$$f = 2\frac{\bar{\tau}_w}{\rho\overline{W}^2}, \qquad \mathrm{Nu} = \frac{hD_e}{k} = \frac{\bar{q}_w D_e}{(T_b - T_w)k} \tag{17}$$

where $\bar{\tau}_w$ is the mean wall shear stress, and the $\bar{q}_w$ is the mean wall heat flux. Both $\bar{\tau}_w$ and $\bar{q}_w$ can be derived from the averages

(a) **Table 1 Numerical experiments for grid size**

fRe / Grid size / K^2	21×11	41×21	61×31	81×41	101×51	Vortex numbers	CPU,**s
0	14.26	14.23	14.23	14.23	14.23*	0	32
10^4	21.27	20.11	19.50	19.50	19.50*	2	218
10^5	33.21	30.50	29.62	29.41	29.40*	4	305

Exact value $fRe = 14.23$ for $K^2 = 0$.

(b)

fRe / Grid size / K^2	21×11	41×21	61×31	81×41	101×51	Vortex numbers	CPU,**s
$K^2 = 10^4$, Pr = 0.7	6.14	5.97	5.93	5.93	5.93*	2	101.0
$K^2 = 10^4$, Pr = 7.0	10.34	8.55	8.14	7.96	7.89*	2	59.6
$K^2 = 10^5$, Pr = 0.7	11.21	10.59	10.11	10.06	10.04*	4	82.2
$K^2 = 10^5$, Pr = 7.0	32.95	21.05	18.59	17.45	16.82*	4	48.5

* Present analysis.
** IBM Model 3090.

of local derivatives. The friction factor and the Nusselt number become

$$f\cdot \mathrm{Re} = 2\cdot\overline{\frac{\beta+x}{\beta}}\cdot\overline{\frac{\partial w}{\partial n}}$$
$$\mathrm{Nu} = \overline{\frac{\beta+x}{\beta}}\cdot\overline{\frac{\partial \theta}{\partial n}} \tag{18}$$

On the other hand, the friction factor and the Nusselt number can be also derived from the overall force and energy balances, and the results are

$$f\cdot \mathrm{Re} = \frac{C}{2} - \frac{1}{2\beta}\iint w\left(\frac{1}{\beta+x} + K^2 u\right) dxdy$$
$$\mathrm{Nu} = \frac{\lambda}{4} + \frac{\beta\lambda^2}{4Pe^2}\iint \frac{\theta}{\beta+x} dxdy \tag{19}$$

From equations (19), $f\cdot \mathrm{Re} = C/2$ can be obtained readily as the dimensionless radius of curvature approaches infinity. In this case the effect of secondary flow on the friction factor comes from the inertia terms $K^2\left(u\frac{\partial w}{\partial x} + v\frac{\partial w}{\partial y}\right)$ on the left-hand side of equation (11) only. Similarly, $\mathrm{Nu} = \lambda/4$ is derived as $\mathrm{Pe}\to\infty$ without the effect of axial conduction. In the present study equations (19) are used for computations of the $f\cdot \mathrm{Re}$ and Nu.

Method of Solution

The solution for the unknown variables, u, v, w, ψ, ξ, and θ in equations (11), (14), and (15) with unknown constant C and eigenvalue λ satisfying boundary conditions (16) is a matter of considerable mathematical difficulty. A nonuniform strongly implicit scheme of finite-difference approximation is used to ensure a convergent solution at higher values of parameters K^2 and $\mathrm{Pr}K^2$ in equations (11) and (14). One technique to improve the efficiency and to make it more robust is to use the strongly implicit scheme of Stone (1968). The nonuniform grid system used in this study is generated through the following simple algebraic relation: $\overline{P_l P_I} = \overline{P_1 P_N}\left(\frac{I-l}{N-l}\right)^m$, for $l < I < N$, where P_l, P_N are the end points and P_I is the position of an intermediate point. The value $m = 1.2$ is used throughout the present study for nonuniform grid size. The numerical procedure is:

1 Assign initial values for the unknowns u, v, w, ψ, ξ, and θ and values for the parameters K^2, $\mathrm{Pr}K^2$, Pe, and β.

2 The vorticity transport equation (15) is solved for ξ with the associated boundary vorticity evaluated from the stream function in step (1).

3 The relation for ξ and ψ in equation (15) is solved for ψ.

4 Compute the values u and v from the obtained ψ.

5 Give an initial value for the constant C and solve equation (11) for w. The value C is adjusted by considering the relation

$$\iint \frac{\beta+x}{\beta} w\, dxdy = 1 \tag{20}$$

6 Repeat steps (2) to (5), until the criterion of convergence for ξ, ψ, and w is satisfied

$$\mathrm{Max}\,|F_{i,j}^{(K+1)} - F_{i,j}^{(K)}| / Max|F_{i,j}^{(K+1)}| < 10^{-5} \tag{21}$$

where k stands for the kth outer iteration.

7 Calculate the friction factor from equation (19).

8 With the obtained solution u, v, and w and an initial guess for θ and the eigenvalue λ, energy equation (14) is solved for θ. Considering the relation

$$\iint \frac{\beta+x}{\beta} w\theta dxdy = 1 \tag{22}$$

the eigenvalue is adjusted. This step is repeated until the criterion of equation (21) is satisfied.

9 Compute the value for Nusselt number by using equation (18) with the obtained λ.

As shown in Table 1, a numerical experiment was conducted to establish the mesh size for various Dean numbers. A convergence study of the numerical solution can also be made by comparing the data with the known exact solution for the limiting case of straight square duct $K^2 = 0$. Comparing the data obtained by using an 81 × 41 mesh and a 101 × 51 mesh, one can find that the largest differences are 0.03 percent in fRe for $K^2 = 10^5$, 0.2 percent in Nu for $\mathrm{Pr} = 0.7$, $K^2 = 10^5$, and 3.8 percent in Nu for $\mathrm{Pr} = 7$, $K^2 = 10^5$. The differences in fRe and Nu for $\mathrm{Pr} = 0.7$ are quite satisfactory. The error for $\mathrm{Pr} = 7$ should be taken into account in the applications of these data. In order to obtain accurate solutions and understand the step changes in the flow patterns, the mesh size of 101 × 51 is used throughout the present study.

Results and Discussion

As pointed out by Benjamin (1978), both two-vortex and four-vortex crossflow patterns constitute the dual solutions, which are attained depend on the initial condition used to start the numerical computation of nonlinear governing equations. This statement is verified in the present study for 12,940 ≤

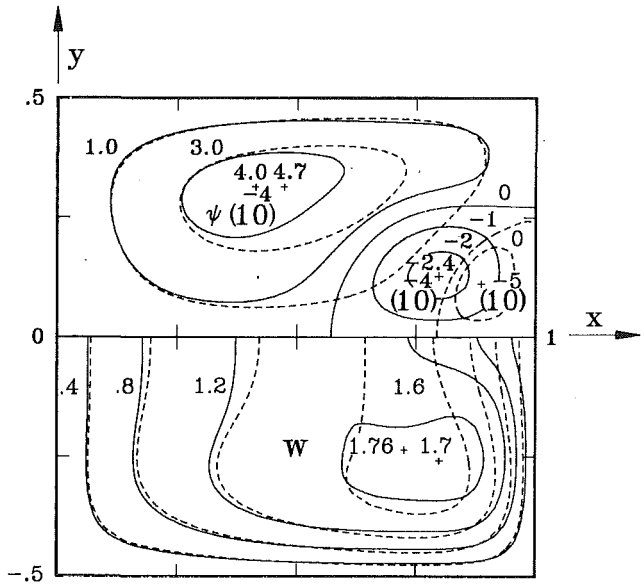

$\beta >> 1, K^2 = 20505$ ---- $K^2 = 20510$ ----

(a)

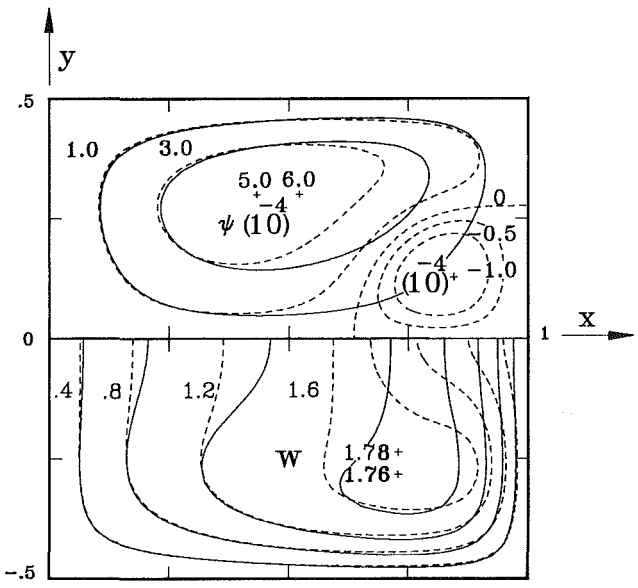

$\beta >> 1, K^2 = 12935$ —— $K^2 = 12940$ -----

(b)

Fig. 2 Streamlines and constant axial velocities

$K^2 \leq 20{,}510$ and $\gamma = 1$. But for $K^2 > 20{,}510$, a four-vortex crossflow pattern is obtained with an initial two-vortex flow pattern. On the other hand, for $K^2 < 12{,}940$ the flow attained is two-vortex even with an initial four-vortex flow pattern.

Secondary Flow Field. The dashed lines in Fig. 2(*a*) show the crossflow stream lines and constant axial velocity lines in a square channel for $K^2 = 20{,}505$. This two-vortex flow pattern is attained step by step from the flow pattern at $K^2 = 0$. Due to the secondary flow, the centrifugal force is higher near

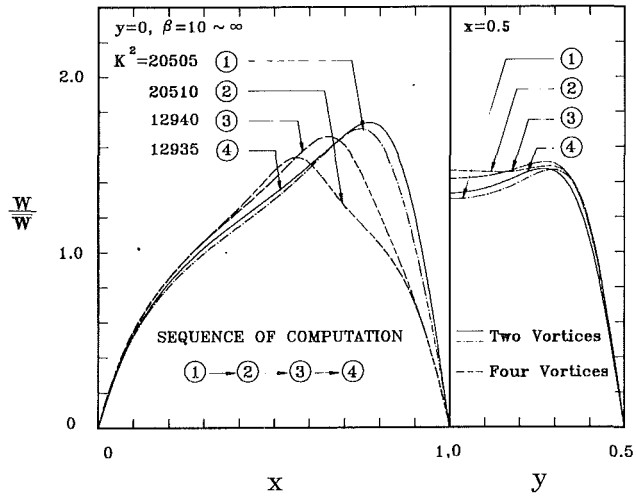

Fig. 3 Dimensionless axial velocity distributions

$x = 0.75$ than that near the right-hand concave wall ($x = 1.0$). Finally the flow pattern breaks into four-vortex type: An additional vortex pair is formed near the right-hand concave wall when the value of K^2 is increased from 20,505 to 20,510. The four-vortex flow pattern is shown by solid lines. Due to the additional vortices, the constant axial velocity lines are moved toward the central region of the channel. For $K^2 > 20{,}510$, once the four-vortex crossflow pattern is established, the flow pattern will remain the same as the Dean number increases.

Using the four-vortex crossflow pattern as the initial one for computation and decreasing the Dean number, the flow pattern remains the same for the value of K^2 down to 12,940 as shown by the dashed lines in Fig. 2(*b*). This computation confirms the statement of Benjamin (1978). Using the four-vortex flow pattern for $K^2 = 12{,}940$ and further decreasing the value of K^2, a two-vortex flow pattern is attained. The solid lines in Fig. 2(*b*) show the two-vortex streamlines and the corresponding constant axial velocities for $K^2 = 12{,}935$ with an initial four-vortex flow pattern. The "hysteresis behavior" with critical values at both ends is clearly demonstrated in the present numerical study. It is noted that the dependence of the mesh size and the relaxation factor on the critical value is examined. A 1.9 percent difference is observed for mesh sizes 81 × 41 and 101 × 51 and the relaxation factor 0.1 and 0.05.

Velocity Distribution. Two-vortex and four-vortex crossflow patterns will drastically affect the axial velocity distribution. Figures 3(*a*) and 3(*b*) show the axial velocity distributions along $y = 0$ and $x = 0.5$, respectively, for values of K^2 near the critical values $K^2 = 20{,}505$ and 12,940. The sequence of computation is also shown. Curve one is the axial velocity with a two-vortex crossflow pattern for $K^2 = 20{,}505$. When the value of K^2 increases to 20,510, the two-vortex flow breaks into a four-vortex flow pattern. As shown in Fig. 3(*a*), the maximum value of the axial velocity along $y = 0$ moves toward $x = 0.5$ and decreases in magnitude, and the value of axial velocity along $x = 0.5$ shown in Fig. 3(*b*) increases. When the value of K^2 decreases to 12,940, the four-vortex crossflow is weakened and the maximum axial velocity increases and moves back to $x = 1$ as shown in Fig. 3(*a*). Finally, when $K^2 = 12{,}935$, the crossflow pattern becomes two-vortex again and the maximum value in the axial velocity along $y = 0$ moves further back to $x = 1$.

Figure 4 shows the comparison between the present numerical data and the previous numerical and experimental results. The computations were carried out for the same parameters as the previous ones. By taking the same value of $W/\overline{W}$ at $x = 0.5$, $y = 0$, the agreements between the present numerical data and the previous results are quite reasonable

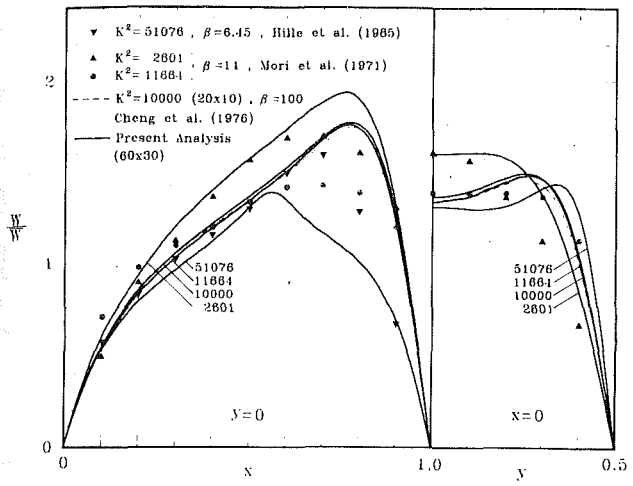

Fig. 4 Comparison for $W/\bar{W}$

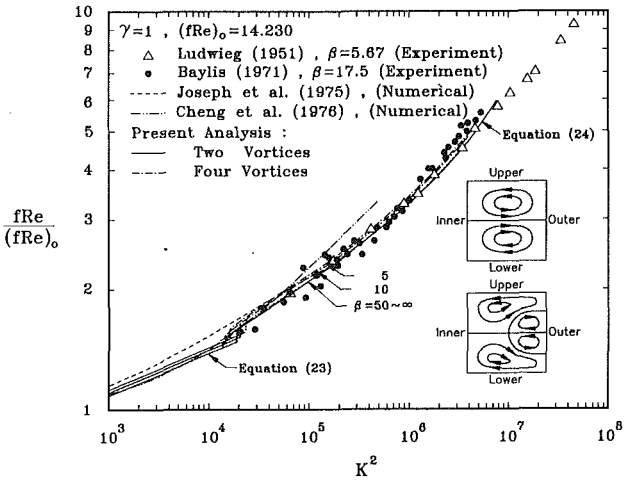

Fig. 6 $fRe/(fRe)_o$ versus K^2

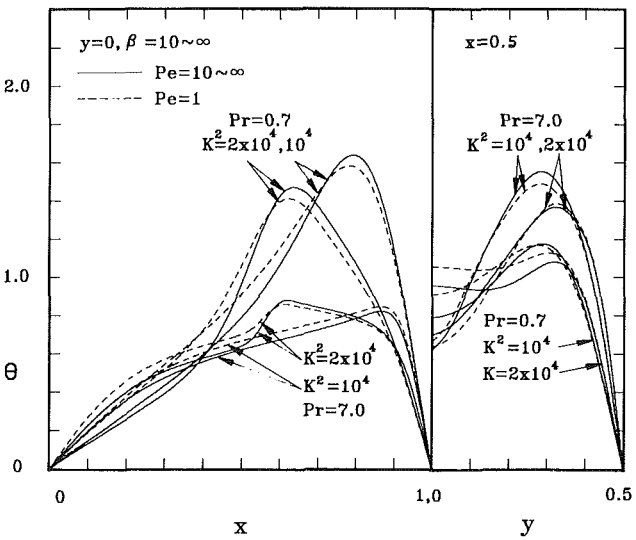

Fig. 5 Dimensionless temperature distributions

except in the regions $y=0$, $x=0.7$–0.8 and $x=0.5$, $y=0.2$–0.3 with large velocity gradients. This may be due to the coarse mesh size (20×10) used previously by Cheng et al. (1976) and possible velocity fluctuations and entrance effects in the experimental measurements. It is noted that the data of Hille et al. (1985) were measured at an axial position of $Z/(D_e\mathrm{Re})=0.031$, which is in the entrance region of the curved channel. The comparison of the results of Mori and Uchida (1967) also shows a similar trend as pointed out by Cheng et al. (1976).

Temperature Distribution. The temperature distribution in the channel is affected not only by the crossflow patterns but also by the Prandtl number and the Peclet number. Figures 5(*a*) and 5(*b*) show the temperature distributions along $y=0$ and $x=0.5$, respectively, for values of $K^2=10{,}000$ and 20,000, $\mathrm{Pr}=0.7$ and 7.0, and $\mathrm{Pe}=1\sim\infty$. The curves with $K^2=10{,}000$ and 20,000 represent the profiles with two-vortex and four-vortex crossflow patterns, respectively. One can see that the additional vortex pair moves the maximum value of θ along $y=0$ toward $x=0.5$ and decreases the magnitudes of θ along $y=0$ and $x=0.5$. The thermal convection is magnified by the value of the Prandtl number. The curves for $\mathrm{Pr}=7.0$ are more uniform than those for $\mathrm{Pr}=0.7$ with the corresponding values of K^2 and Pe. One can also see that the curves are more uniform with the effect of axial conduction. This phenomenon can also be justified physically.

Friction Factor. Similar to the axial velocity, the friction factor will be greatly affected by the appearance of the two-vortex or four-vortex crossflow pattern. The transition critical points of these two flow patterns were not clearly depicted in the literature (Cheng and Akiyama, 1970; Cheng et al., 1976). Figure 6 shows $f\mathrm{Re}/(f\mathrm{Re})_o$ versus K^2 with dimensionless radius of curvature β as a parameter. For $\beta=5$, 10, and $50\sim\infty$, step jumps at $K^2=23{,}200$, 21,900, and 20,505 and step drops at $K^2=16{,}200$, 14,500, and 12,940 in the value of $f\mathrm{Re}/(f\mathrm{Re})_o$ are observed. The values of critical K^2 will be increased with a small value of β. A smaller value of β predicts a larger value of $f\mathrm{Re}$. This confirms the observation by Soh and Berger (1987). Different crossflow patterns show not only the difference in the value of $f\mathrm{Re}$ but also the difference in the slope of $f\mathrm{Re}$. The curves of Cheng et al. (1976) for $\beta=100$ and Joseph et al. (1975) are also plotted for comparison. The experimental work of Ludweig (1951) is also shown in this figure. Good agreement with the present data is observed.

For engineering application, the numerical results may be correlated by using

$$f\mathrm{Re}/(f\mathrm{Re})_o=0.513K^{0.216} \tag{23}$$

For $K^2<12{,}900$, and by

$$f\mathrm{Re}/(f\mathrm{Re})_o=0.318K^{0.326}(1+C_1K^{0.5}+C_2K+C_3K^{1.5}) \tag{24}$$

for $K^2>20{,}500$, where $C_1=-6.13\times10^{4}$, $C_2=1.08\times10^{-5}$, and $C_3=2.82\times10^{-6}$ with an error of less than 2.4 percent.

Heat Transfer. Figure 7 shows $\mathrm{Nu}/\mathrm{Nu}_o$ versus $\mathrm{Pr}K^2$ with $\mathrm{Pr}=0.7$ and 7.0, and $\mathrm{Pe}=1\sim\infty$ for the case of large β and $\gamma=1$. Although $\mathrm{Pr}=0.7$ and 7.0 are not large enough, the Nu is already well correlated with the product of Pr and K^2. Similar to the phenomena in Fig. 6, the crossflow patterns change not only the magnitude of Nu but also the slope of Nu. It is seen that the value of Nu will be decreased with the increase in Pe and a difference of about 11 percent is observed between the curves for $\mathrm{Pe}=1$ and ∞ at $\mathrm{Pr}=0.7$, $\mathrm{Pr}K^2=10^4$ and $\mathrm{Pr}=7$, $\mathrm{Pr}K^2=10^7$. The data of Cheng et al. (1975) are plotted from the asymptotic values of solution in thermal entrance region. They agree quite well with the present solution. The dashed curve of Kalb and Seader (1974) is for the isothermal circular tube. It shows about the same slope as the present solution. Both the existing data of Cheng et al. (1975) and Kalb and Seader (1974) did not show the transition of flow patterns in the Nu data. It is noted that the Nusselt number data for the other values of Prandtl number can be easily computed using the present approach.

The Nusselt number ratio may be also correlated by

$$\mathrm{Nu}/\mathrm{Nu}_o=0.518(\mathrm{Pr}K^2)^{0.147} \tag{25}$$

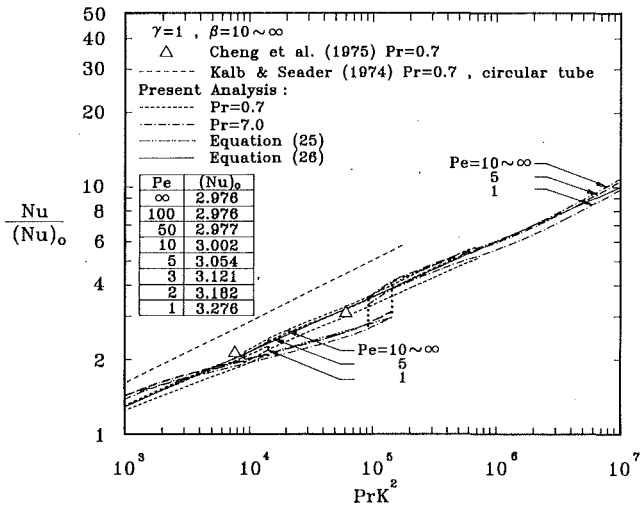

Fig. 7 Nu/Nu_0 versus PrK^2

for $Pr = 7$ and $PrK^2 < 1.44 \times 10^5$ with an error of 6.6 percent, and correlated by

$$Nu/Nu_o = 0.278\ (PrK^2)^{0.222} \tag{26}$$

for $Pr = 7$, $1.44 \times 10^5 < PrK^2 < 10^7$, and $Pr = 0.7$, $PrK^2 < 8 \times 10^5$ with an error of 7.9 percent.

Table 2 summarizes the numerical data for the case of large β and $r = 1$. The constant C and the eigenvalue λ are tabulated. The step changes in the values near critical points $K^2 = 12{,}940$ and 20,505 are also listed. With the accuracy of the present numerical data shown in Table 1, the step changes in the values of fRe and Nu are one or two orders of magnitude higher than the numerical error.

Finally, the region of validity of the present solution is discussed. In the present study, the forced laminar convection in the thermally fully developed region of a curved isothermal duct is examined. One may ask what is the length of the thermal entrance region in a curved isothermal duct. It is well understood that the criterion for the length of thermal entrance region with $Pe \to \infty$ in a straight duct ($K^2 = 0$) is found to be

Table 2 Numerical data for $\beta \to \infty$ and $\gamma = 1$

K^2	C	fRe	Pe	Pr = 0.7		Pr = 7.0		Vortex number
				λ	Nu	λ	Nu	
0	28.460	14.230	10∼∞	11.894	2.976	11.894	2.976	2
			5	9.668	3.054	9.668	3.054	
			1	3.696	3.276	3.696	3.276	
500	29.329	14.665	10∼∞	12.790	3.200	21.042	5.269	2
			5	10.233	3.275	14.883	5.386	
			1	3.816	3.472	4.814	5.583	
1000	30.749	15.374	10∼∞	14.350	3.591	23.087	5.782	2
			5	11.179	3.657	15.914	5.906	
			1	4.014	3.813	5.032	6.100	
5000	36.220	18.110	10∼∞	20.596	5.157	28.017	7.020	2
			5	14.591	5.187	18.262	7.187	
			1	4.718	5.232	5.528	7.413	
10,000	39.000	19.500	10∼∞	23.667	5.927	31.459	7.885	2
			5	16.096	5.938	19.732	8.064	
			1	5.024	5.947	5.819	8.283	
12,935	40.514	20.257	10∼∞	24.784	6.208	33.149	8.310	2
			5	16.595	6.205	19.732	8.487	
			1	5.116	6.194	5.947	8.695	
12,940	41.422	20.711	10∼∞	25.521	6.392	42.315	10.616	4
			5	16.926	6.384	23.946	10.778	
			1	5.180	6.365	6.655	10.934	
20,000	42.566	21.283	10∼∞	27.687	6.936	37.092	9.302	2
			5	17.917	6.910	21.941	9.473	
			1	5.387	6.869	6.247	9.657	
20,000	45.040	22.520	10∼∞	28.774	7.212	49.160	12.341	4
			5	18.441	7.193	26.359	12.482	
			1	5.502	7.161	7.132	12.601	
20,505	42.881	21.440	10∼∞	27.890	6.987	38.749	9.718	2
			5	18.021	6.951	22.617	9.894	
			1	5.411	6.896	6.390	10.074	
20,510	45.319	22.659	10∼∞	29.090	7.289	49.369	12.394	4
			5	18.573	7.270	26.430	12.531	
			1	5.526	7.234	7.149	12.653	
50,000	52.923	26.461	10∼∞	35.008	8.775	59.244	14.886	4
			5	21.310	8.791	29.757	15.073	
			1	6.136	8.787	7.825	15.215	
100,000	58.796	29.398	10∼∞	40.084	10.044	66.167	16.821	4
			5	23.405	10.085	31.796	16.999	
			1	6.579	10.092	8.226	17.113	
200,000	65.569	32.785	10∼∞	47.128	11.825	75.903	19.104	4
			5	26.098	11.811	34.478	19.212	
			1	7.130	11.756	8.750	19.290	
500,000	76.817	38.409	10∼∞	58.790	14.764	94.927	23.935	4
			5	30.090	14.613	39.459	23.953	
			1	7.929	14.430	9.749	23.975	
1,000,000	88.010	44.000	10∼∞	67.950	17.077	114.794	28.998	4
			5	33.209	16.968	44.309	29.001	
			1	8.584	16.799	10.732	29.012	

reasonably expressed by $L = 0.05 \cdot \mathrm{Pe} \cdot D_e$. It was clearly indicated by Cheng et al. (1975), and Tan and Hsu (1972) that the thermal entrance length decreases with the increase in the Dean number and the decrease in the Peclet number. Therefore the thermal entrance length in the curved isothermal duct with the effect of axial conduction will be less than $0.05 \cdot \mathrm{Pe} \cdot D_e$ and the present solution will be valid in the region where the length of the curved duct exceeds $0.05 \cdot \mathrm{Pe} \cdot D_e$.

Conclusions

1 A study has been made to investigate the forced laminar convection in the hydrodynamically and thermally fully developed region of a curved isothermal duct. A three-dimensional energy equation of elliptic type is reduced to a two-dimensional one with an eigenvalue. The problem described in equation (14) and its solution have not heretofore been reported in the literature.

2 For $12{,}940 \le K^2 \le 20{,}510$, $\gamma = 1$ and $\beta = \infty$ both two-vortex and four-vortex flow patterns can be obtained depending on the initial flow pattern used to start the computation. But for $K^2 > 20{,}505$ a four-vortex flow pattern is obtained with an initial two-vortex flow pattern. On the other hand, for $K^2 < 12{,}940$, the flow obtained is two-vortex even with an initial four-vortex flow pattern. the "hysteresis behavior" with critical values at both ends is clearly demonstrated in the present numerical study.

3 For large β and $\gamma = 1$, a step jump at $K^2 = 20{,}505$ and a step drop at $K^2 = 12{,}940$ in the value of $f\mathrm{Re}/(f\mathrm{Re})_o$ is observed. Different crossflow patterns show not only the difference in the value of $f\mathrm{Re}$ but also the difference in the slope of $f\mathrm{Re}$.

4 The crossflow patterns change not only the magnitude of Nu but also the slope of Nu. The temperature distribution will become more uniform and the value of Nu will be decreased with a small value of Pe.

Acknowledgments

The authors would like to acknowledge the National Science Council, R.O.C., for its support of the present work through project No. NSC 79-0404-E007-07.

References

Akiyama, M., and Cheng, K. C., 1971, "Boundary Vorticity Method on Laminar Forced Convection Heat Transfer in Curved Pipes," *Int. J. Heat Mass Transfer,* Vol. 14, pp. 1659–1675.

Baylis, J. A., 1971, "Experiments on Laminar Flow in Curved Channels of Square Section," *J. Fluid Mech.,* Vol. 48, pp. 417–422.

Benjamin, T. B., 1978, "Bifurcation Phenomena in Steady Flows of a Viscous Fluid," *Proceedings of Royal Society of London, A,* Vol. 359, pp. 1–43.

Berger, S. A., Talbot, L. and Yao, L. S., 1983, "Flow in Curved Pipes," *Ann. Rev. Fluid Mech.,* Vol. 15, pp. 461–512.

Cheng, K. C., and Akiyama, M., 1970, "Laminar Forced Convection Heat Transfer in Curved Rectangular Channels," *Int. J. Heat Mass Transfer,* Vol. 13, pp. 471–490.

Cheng, K. C., Lin, R. C., and Ou, J. W., 1975, "Graetz Problem in Curved Square Channels," ASME JOURNAL OF HEAT TRANSFER, Vol. 97, pp. 244–248.

Cheng, K. C., Lin, R. C, and Ou, J. W., 1976, "Fully Developed Laminar Flow in Curved Rectangular Channels," ASME *Journal of Fluids Engineering,* Vol. 98, pp. 41–48.

Cheng, K. C., Nakayama, J., and Akiyama, M., 1977, "Effect of Finite and Infinite Aspect Ratios on Flow Patterns is Curved Rectangular Channels," in: *Flow Visualization* Tokyo, Japan, pp. 181–186.

Dean, W. R., 1927, "Note on the Motion of Fluid in a Curved Pipe," *Philosophical Magazine,* Vol. 4, pp. 208–223.

Dean, W. R., 1928, "The Stream-Line Motion of Fluid in a Curved Pipe," *Philosophical Magazine,* Vol. 5, pp. 673–695.

Dennis, S. C. R., and Ng, M., 1982, "Dual Solutions for Steady Laminar Flow Through a Curved Tube," *Quarterly Journal of Mechanics and Applied Mathematics,* Vol. 35, Part 3, pp. 305–324.

Dravid, A. N., Smith, K. A., Merrill, E. W., and Brian, L. T., 1971, "Effect of Secondary Fluid Motion on Laminar Flow Heat Transfer in Helically Coiled Tubes," *AIChE Journal,* Vol. 17, pp. 1114-1122.

Hille, P. Vehrenkamp, R., and Schulz-Dubois, E. O., 1985, "The Development and Structure of Primary and Secondary Flow in a Curved Square Duct," *J. Fluid Mech.,* Vol. 151, pp. 219–241.

Joseph, B., Smith, E. P., and Adler, R. J., 1975, "Numerical Treatment of Laminar Flow in Helically Coiled Tubes of Square Cross-Section," *AIChE Journal,* Vol. 21, pp. 965–973.

Kalb, C. E., and Seader, J. D., 1974, "Fully Developed Viscous—Flow Heat Transfer in Curved Circular Tubes With Uniform Wall Temperature," *AIChE Journal,* Vol. 20, pp. 340–346.

Ludwieg, H., 1951, "Die Ausgebildete Kanalstromung in einem Rotierenden System," *Ingenieur-Archiv,* Vol. 19, pp. 296–308.

Mori, Y., and Uchida, Y., 1967, "Study on Forced Convective Heat Transfer in a Curved Square Channel," *Trans. Japan Society of Mechanical Engineers,* Vol. 33, pp. 1836–1846.

Mori, Y., Uchida, Y., and Ukon, T., 1971, "Forced Convective Heat Transfer in a Curved Channel With a Square Cross Section," *Int. J. Heat Mass Transfer,* Vol. 14, pp. 1787–1805.

Nandakumar, K., and Masliyah, J. H., 1982, "Bifurcation in Steady Laminar Flow Through Curved Tubes," *Journal of Fluid Mechanics,* Vol. 119, pp. 475–490.

Shah, R. K., and London, A. L., 1978, *Laminar Flow Forced Convection in Ducts,* Academic Press, New York.

Soh, W. Y., and Berger, S. A., 1987, "Fully Developed Flow for a Curved Pipe of Arbitrary Curvature Ratio," *Int. J. Num. Methods in Fluids,* Vol. 7, pp. 733–755.

Stone, H. L, 1968, "Iterative Solution of Implicit Approximations of Multidimensional Partial Differential Equations," *SIAM Journal of Numerical Analysis,* Vol. 5, pp. 530–558.

Tan, C. W., and Hsu, C. J., 1972, "Low Peclet Number Mass Transfer in Laminar Flow Through Circular Tubes," *Int. J. Heat Mass Transfer,* Vol. 15, pp. 2187–2201.

Winters, K. H., 1987, "A Bifurcation Study of Laminar Flow in a Curved Tube of Rectangular Cross-Section," *Journal of Fluid Mechanics,* Vol. 180, pp. 343–369.

Direct Air Cooling of Electronic Components: Reducing Component Temperatures by Controlled Thermal Mixing

A. M. Anderson[1]

R. J. Moffat

Department of Mechanical Engineering,
Stanford University,
Stanford, CA 94305

This paper discusses forced convection heat transfer in a channel populated with discrete components similar to those found in electronics cooling situations. The temperature rise of each component is expressed as the sum of two parts; its adiabatic *temperature rise, $T_{ad} - T_{in}$, due to the thermal wakes of upstream components; and its* self-heating *temperature rise, $T_e - T_{ad}$ due to its own power dissipation. A component's temperature can be reduced either by reducing the adiabatic temperature rise or the self-heating temperature rise, or both. This investigation concentrates on the former: reducing the adiabatic temperature rise through increased thermal mixing in the coolant flow. The temperature of the air near the components exceeds the mean temperature of the cooling fluid, often by a large amount. In the present work, small scoops were installed in regions of high temperature but low velocity fluid (i.e., in between rows of components rather than in the free stream) to augment thermal mixing and reduce the nonuniformity. This approach does not induce as large a pressure drop as some conventional "turbulators," for a given decrease in operating temperature. In the present work, the scoops reduced the adiabatic temperature rises by 10 to 55 percent, resulting in up to 19 percent reduction in the overall temperature rise. The test section pressure drop increased 11 percent.*

Foreword

Increases in the required power density on a typical printed circuit board have led to the need for improved cooling methods. Recent developments include vigorous forms of cooling such as liquid cooling or conduction enhancement; however, many computer manufacturers prefer air as a coolant because of its ready availability and the mechanical simplicity of the systems. The present work is part of a continuing program to understand better the limits of air cooling, and to develop methods for extending its usable range.

Figure 1 shows a typical printed circuit board with an in-line array of quasi-regular components. Circuit board packages form channels with one smooth wall and one rough wall (the component side). A bypass flow region exists above the components in the channel when the channel spacing (board to board) exceeds the component height. When the channel spacing is large, most of the cooling air flows in the bypass region and a smaller portion (depending on the channel-to-component height ratio) flows between the components. This results in temperature stratification in the channel: hot air near the components and cooler air in the bypass region. Diverting this hot air away from the components and into the bypass region will bring cooler air to the components, increase the thermal mixing in the channel, and decrease the component temperatures. This approach can yield a smaller increase in pressure drop than the usual approach of enhancing the heat transfer coefficient by increasing either the Reynolds number or the turbulence intensity because thermal mixing devices can be designed to act on low-momentum fluid.

Several investigators have attempted to increase heat transfer in a circuit board channel. Sparrow et al. (1982) studied the heat transfer enhancement effect of placing long barriers behind components. They used naphthalene sublimation to measure the effects of these barriers on the mass transfer coefficient and related this to the heat transfer coefficient. The barriers enhanced heat transfer, with the greatest effect (about a factor of two) in the second row downstream of the barrier. The barriers induced a pressure drop 10 to 150 times that for a barrier-free row of components.

Sparrow et al. (1983) looked at the effectiveness of varying the number and height of the barriers. Again they saw large increases in the heat transfer coefficient, up to a factor of two, with the use of fence-like barriers. The heat transfer coefficient in the presence of multiple barriers correlates well with those for a single barrier. The barrier related pressure drop for a multibarrier system was less than the corresponding multiple of the pressure drop for a single barrier up to barrier separations of six rows.

Chou and Lee (1987) performed an investigation to study the possibility of reducing flow nonuniformities in large-scale integrated packages by vortex generators. Their test configuration consisted of two cubic integrated circuits mounted on a simulated printed circuit board. They attached a rectangular plate to the front face of the downstream cube. The vortex generators reduced both the integrated circuit surface temperature and the temperature nonuniformities in the integrated circuit itself. The vortex generator had an optimum height beyond which its effectiveness died off. They studied only the effects of the vortex generator on the upstream component.

Ratts et al. (1987) conducted an experimental study on internal flow modulation induced by vortex shedding from cylinders perpendicular to an air flow and its effect on cooling an array of chips. They found enhancement effects up to 82 percent in the heat transfer coefficient for cylinders periodically positioned above the back edge of each row of chips. They studied the effects of cylinder position, diameter, length, and number of cylinders on the heat transfer enhancement.

[1] Current address: Dept. C71, Bldg. 701, IBM Corporation, P.O. Box 950, Poughkeepsie, NY 12602.

Contributed by the Heat Transfer Division and presented at the ASME Winter Annual Meeting, Chicago, Illinois, November 28–December 2, 1988. Manuscript received by the Heat Transfer Division February 21, 1989; revision received June 21, 1990. Keywords: Electronic Equipment, Forced Convection, Thermal Packaging.

Our investigation differs from the above studies because it emphasizes increasing thermal mixing, without necessarily attempting to augment the heat transfer coefficient. Other investigators have concentrated on augmenting the heat transfer coefficient without regard for whether the benefit comes from altering the fluid mechanics or altering the temperature distribution. We believe that this is the first study to use thermal mixing explicitly as distinct from "increasing turbulence" as a means to decrease component temperatures in electronics cooling applications.

Analysis

The superposition method is used to calculate component temperatures. The effect of the array temperature distribution on heat transfer must be accounted for whenever the array heating is arbitrary. Superposition accounts for this effect. We followed the same line of reasoning used in the early analytical works dealing with nonuniform heating and that literature provided the form in which to express the present experimental results. Sellars et al. (1956) presented a solution for the wall temperature distribution in a tube whose wall heat flux varied arbitrarily with length, while remaining peripherally uniform. They took advantage of the linearity of the energy equation and based their method on the superposition principle. Their solution for the wall temperature is

$$T_w(x^+) - T_{in} = \frac{r_o}{k} \int_0^{x^+} g(x^+ - \xi)\, \dot{q}_w(\xi)\, d\xi \tag{1}$$

$$g(x^+) = 4 + \sum_m \frac{\exp\{-\gamma_m^2 x^+\}}{\gamma_m^2 A_m} \tag{2}$$

In these equations T_w is the wall temperature, T_{in} is the tube inlet temperature, x^+ is the nondimensional downstream distance, r_o is the tube radius, k is the thermal conductivity, $\dot{q}_w$ is the wall heat transfer rate, g is the superposition kernel function (SKF), and γ_m and A_m are eigenvalues and constants of the original differential equation.

This general form was chosen to describe the present results. Discretizing equation (1) for a two-dimensional array of components, where the heat flux varies from component to component, yields the following equation for the temperature rise of a module $(T_e - T_{in})_{n,m}$ located in the nth row and mth column:

$$(T_e - T_{in})_{n,m} = \sum_{j=1}^{M} \sum_{i=1}^{n} \frac{\dot{q}_{i,j}}{\dot{m} c_p}\, g^*(n-i,\, m-j) \tag{3}$$

In this equation, T_e is the module temperature, T_{in} is the channel inlet temperature, j is the column counter, M is the number of columns in the array, i is the row counter, $\dot{q}_{i,j}$ is the heat transfer rate at module i, j, $\dot{m}$ is the mass flow rate of air through the channel, c_p is the specific heat of the air, and $g^*(n-i, m-j)$ is the superposition kernel function for discrete systems. It is the ratio of the temperature rise experienced on module, n, m due to heating module i, j, to the mean fluid temperature rise experienced in the fluid due to heating module, i, j.

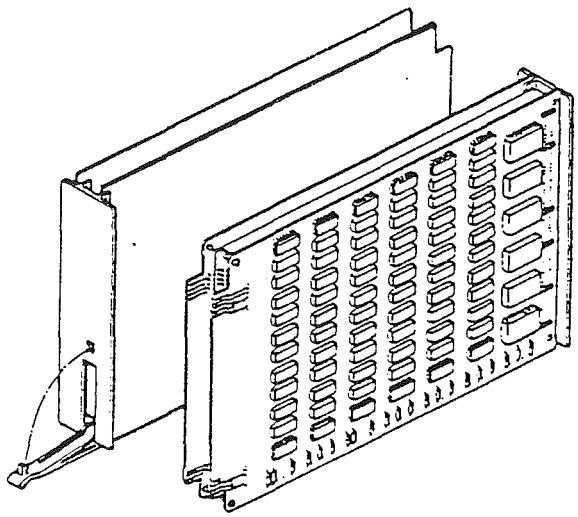

Fig. 1 Typical printed circuit board with an in-line array of semiregular components

The module temperature rise can be broken into the *adiabatic temperature rise* (due to upstream heated modules) and the local or *self-heated temperature rise* (due to the power dissipation at module n, m). The adiabatic temperature is the temperature that a component would achieve if there was no heat transfer to it by any mode. The rest of the system may or may not be powered.

$$(T_e - T_{in})_{n,m} = \sum_{j=1}^{M} \sum_{i=1}^{n-1} \frac{\dot{q}_{ij}}{\dot{m} c_p}\, g^*(n-i,\, m-j) + \frac{\dot{q}_{ij}}{\dot{m} c_p}\, g^*(0,\, 0)^1$$

$$= \underbrace{(T_{ad} - T_{in})_{n,m}}_{\text{adiabatic temperature rise}} + \underbrace{(T_e - T_{ad})_{n,m}}_{\text{self-heated temperature rise}} \tag{4}$$

[1] $g^*(0, m-j) = 0$ for $j = 1, M$, with $j \neq m$, i.e., modules in the same row but different column do not affect the module of interest for convective heat transfer.

Nomenclature

A_{lane} = channel area of one column = HS
B = cube dimension
c_p = specific heat
C_p = pressure coefficient
$g(x^+)$ = integrating kernel of Sellars et al.
g^* = two-dimensional superposition kernel function
h = heat transfer coefficient
H = channel height
i, j = row and column counters
k = thermal conductivity
$\dot{m}$ = mass flow rate
m, n = column and row number
M = total number of columns
Nu = Nusselt number = hB/k
P = pressure
$\dot{q}$ = heat transfer rate
$\dot{q}''$ = heat transfer rate per unit area
S = center-to-center spacing of cubes
T = temperature
V = channel inlet velocity
x^+ = dimensionless distance of Sellars et al.
$\Delta T_{ad,\,o}$ = adiabatic temperature rise above inlet temperature without mixing device = $T_{ad,o} - T_{in}$
$\Delta T_{ad,mix}$ = adiabatic temperature rise above inlet temperature with mixing device = $T_{ad,mix} - T_{in}$
ΔT_{mean} = mean temperature rise above inlet temperature
η_{mix} = thermal mixing efficiency
ρ = density

Subscripts

ad = adiabatic
conv = convective
e = element or module
in = inlet
mean = bulk mean
w = wall

The general definition of the heat transfer coefficient is

$$h = \frac{\dot{q}''_{\text{conv}}}{(T_e - T_{\text{ref}})} \tag{5}$$

In this equation $\dot{q}''_{\text{conv}}$ is the convective heat transfer rate per unit area, T_e is the component temperature, and T_{ref} is some reference temperature. There are several options for T_{ref}. Two commonly used values for T_{ref} in channel flows are the bulk mean temperature, T_{mean}, and the adiabatic surface temperature, T_{ad}. The adiabatic temperature has been used to account for viscous dissipation heating in high-velocity heat transfer, and in boundary layers with film cooling, and other "three-temperature" situations. Use of the adiabatic component temperature results in a considerable simplification of the heat transfer description of those situations. For the present situation the adiabatic heat transfer coefficient is defined as

$$h_{ad} = \frac{\dot{q}''_{\text{conv}}}{(T_e - T_{ad})} \tag{6}$$

Investigators who publish heat transfer coefficient data in the electronics cooling literature almost always report values of the adiabatic heat transfer coefficient without specifying it as the adiabatic heat transfer coefficient. Any experiment that heats only one component at a time implicitly measures the adiabatic heat transfer coefficient. In such experiments, the inlet, mean, and adiabatic temperatures are the same so there is no question as to the value of the reference temperature. Similarly, an experiment that coats one component at a time with naphthalene also measures the adiabatic heat transfer coefficient since the flow approaching the naphthalene specimen is uniform in composition. For components in the first row of an array, the adiabatic heat transfer coefficient and the mean heat transfer coefficient are the same so long as no heat conduction or radiation acts between the components and its surroundings and the inlet air temperature is uniform (see Moffat and Anderson, 1990, for further discussion of the adiabatic heat transfer coefficient).

One might ask, why not use a heat transfer coefficient based on a mean temperature? The answer is that h_{mean} is a function of the heat transfer distribution. Its value changes when the array thermal distribution changes. The adiabatic heat transfer coefficient is the only heat transfer descriptor that is independent of the thermal distribution because it is a local heat transfer descriptor. It may seem easier to use h_{mean} because the reference temperature is easy to deduce, but the value of h_{mean} is dependent on the thermal distribution. The adiabatic heat transfer coefficient, h_{ad}, is not dependent on the upstream heating pattern or on the local heat transfer rate. Those effects are taken into account by the adiabatic temperature. (For further discussion of this issue see Anderson and Moffat, 1990, or Moffat and Anderson, 1990.)

Returning now to equation (4), to calculate the temperature rise on a module, the adiabatic heat transfer coefficient can be used to calculate the local temperature rise, $(T_e - T_{ad})_{n,m}$, and the superposition kernel function can be used to calculate the adiabatic temperature rise, $(T_{ad} - T_{in})_{n,m}$.

The SKF, $g^*(n-i, m-j)$, can be determined from equation (4). It is the ratio of the adiabatic temperature rise to the mean temperature rise at component (n, m), due to heating component (i, j)

$$g^*(n-i, m-j) = \frac{(T_{ad} - T_{in})_{n-i,\, m-j}}{(T_{\text{mean}} - T_{in})_{n-i,m-j}} \tag{7}$$

Figure 2 shows superposition kernel functions measured in the same column as the heated module, i.e., $g^*(n-i, 0)$, versus row number for several typical configurations. In these cases, the centermost module in the first row (i.e., $i = 1$) was heated and the adiabatic temperature was measured on the centermost

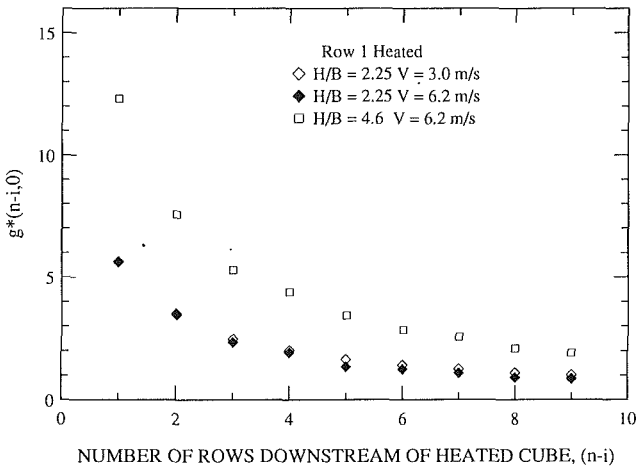

Fig. 2 Superposition kernel function in a typical electronics cooling situation

module in each downstream row (i.e., $n = 2$–9). The mean temperature was calculated from a global energy balance:

$$T_{\text{mean}} = T_{in} + \frac{\dot{q}_{\text{tot, upstream}}}{\dot{m}c_p} \tag{8}$$

In this equation $\dot{q}_{\text{tot, upstream}}$ is the total upstream convective heat transfer rate (in this case only one module was heated so the total upstream heat transfer rate is equal to that released on that module), $\dot{m}$ is the mass flow rate in the channel and c_p is the specific heat of air. The value of $g^*(n-i, 0)$ was calculated from equation (7) using the measured values of T_{ad} and T_{in}, and the calculated value of T_{mean}.

The figure shows $g^*(n-i, 0)$ for three different configurations: (1) $H/B = 4.6$, $V = 6.2$ m/s; (2) $H/B = 2.25$, $V = 6.2$ m/s; and (3) $H/B = 2.25$, $V = 3.0$ m/s. The value of $g^*(n-i, 0)$ peaks in the first row downstream of the heated component and then decreases exponentially. The small amount of thermal mixing immediately downstream of the heated module leads to an adiabatic temperature rise greater than the mean temperature rise and results in a large value of $g^*(n-i, 0)$. More mixing occurs downstream, due to the wakes of the components, and the adiabatic temperature decreases.

Changing the channel spacing has a greater effect on the superposition kernel function than changing the velocity. The figure shows that $g^*(n-i, 0)$ is independent of velocity for the range tested, but $g^*(n-i, 0)$ changes significantly with channel spacing. For a large channel spacing (with fixed cube height) a significant bypass region exists and the bulk of the inlet flow bypasses the array of components. This results in a large value of $g^*(n-i, 0)$.

Returning to the calculation of the overall temperature rise, the overall component temperature rise can be written in terms of the adiabatic heat transfer coefficient and the SKF

$$(T_e - T_{in})_{n,m} = (T_{ad} - T_{in})_{n,\,m} + (T_e - T_{ad})_{n,\,m} = \sum_{j=1}^{M} \sum_{i=1}^{n-1} \frac{\dot{q}_{i,j}}{\dot{m}c_p} g^*(n-i, m-j) + \frac{\dot{q}_{n,m}}{h_{ad,n,m}A} \tag{9}$$

This equation can be compared to the equations for the temperature rise in terms of a heat transfer coefficient based on the mean temperature

$$(T_e - T_{in})_{n,m} = (T_{\text{mean}} - T_{in})_{n,\,m} + (T_e - T_{\text{mean}})_{n,\,m} = \sum_{j=1}^{M} \sum_{i=1}^{n-1} \frac{\dot{q}_{i,j}}{\dot{m}c_p} + \frac{\dot{q}_{n,m}}{h_{\text{mean},n,m}A} \tag{10}$$

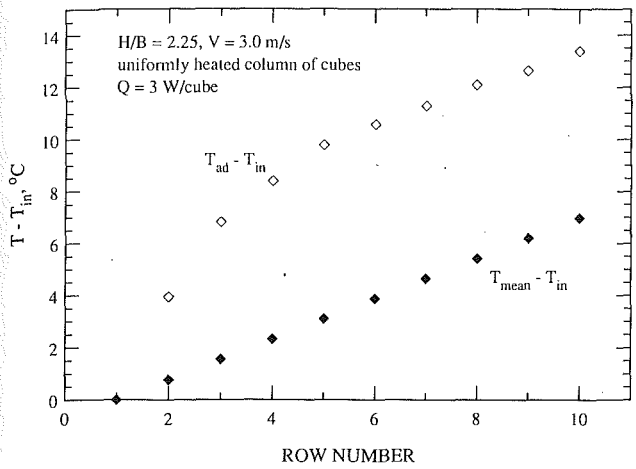

Fig. 3 Adiabatic temperature rise compared to the mean temperature rise in a typical electronics cooling situation

The difference between equations (9) and (10) is important. Equation (10) indicates that the only way to decrease the overall temperature rise, for fixed $\dot{q}_{i,j}$, is to increase h_{mean}. The usual approach to increasing the heat transfer coefficient is to promote turbulence or increase the Reynolds number. From equation (9) it is clear that there are actually two ways to decrease the overall temperature. Increasing the adiabatic heat transfer coefficient will reduce the component temperature as will decreasing the superposition kernel function (i.e., bring the adiabatic component temperature closer to the mean temperature).

Equation (10) conceals the fact that two mechanisms act to set the component temperature and provides no guidance as to the best way to reduce the operating temperature. Separating the two terms as in equation (9) allows a more precise description of the heat transfer process. The first term characterizes the performance of the individual component, and the second term represents the cumulative effects of upstream components. Reducing these upstream effects with low pressure drop thermal mixing devices will result in a lower overall temperature rise.

Figure 3 compares the adiabatic temperature rise to the mean temperature rise for a uniformly heated column of components. The channel spacing to block height ratio H/B is 2.25, the inlet velocity is 3.0 m/s, and the convective heat transfer rate is 3.0 W per component. This situation was used to test the ideal of using thermal mixing to decrease the adiabatic temperature rise. The adiabatic temperature rise is 13.5°C in the last row, while the mean temperature rise is only 7°C. If the air were perfectly mixed, the overall temperature rise would drop 6.5°C.

A perfect mixing device would reduce the adiabatic temperature to the same value as the mean temperature. The mixing efficiency, η_{mix}, is defined as

$$\eta_{\text{mix}} = \frac{\Delta T_{ad,\,o} - \Delta T_{ad,\,\text{mix}}}{\Delta T_{ad,\,o} - \Delta T_{\text{mean}}} \tag{11}$$

where $\Delta T_{ad,\,o} = T_{ad,\,o} - T_{in}$ is the adiabatic temperature rise with no mixing device and $\Delta T_{ad,\,\text{mix}} = T_{ad,\,\text{mix}} - T_{in}$ is the adiabatic temperature rise when the mixing device is in place. The mixing device decreases $T_{ad} - T_{in}$. A perfect mixing device would lower the ΔT_{ad} to ΔT_{mean}, yielding a mixing efficiency of 1.0.

To investigate this mechanism, a set of "scoops" was installed behind the components in the first row (see Fig. 4) and the resulting heat transfer performance was compared to the unscooped case. The scoops were attached to the base board between rows one and two and extended approximately 0.25 cm beyond the component sides and top.

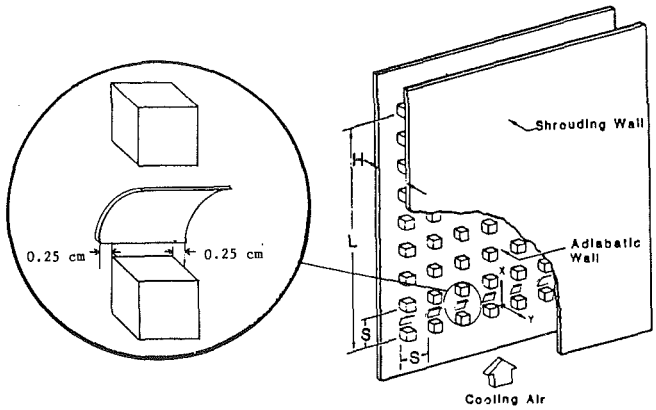

Fig. 4 Schematic of test plate

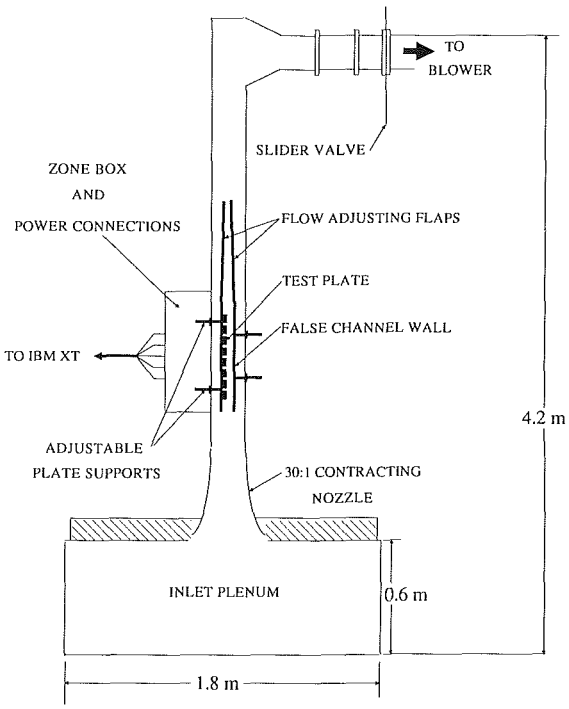

Fig. 5 Schematic of overall test facility

Experimental Apparatus

Figures 4 and 5 illustrate the test channel and the overall test facility. The test plate was a smooth, adiabatic surface, 35 cm wide by 45 cm long, made of 0.95-cm-thick planks of balsa wood epoxied on a 0.44-cm-thick piece of plexiglass. The test array consisted of eighty 1.27 cm aluminum cubes mounted on the balsa wood surface in a regular in-line pattern (ten rows of eight components). The center-to-center spacing of the cubes was 3.81 cm, for a spacing to block-height ratio, S/B, of 3. The upstream edge of the first row of components was 10.2 cm from the leading edge of the plate. Each cube contained a 100 ohm resistance heater and a type-K thermocouple for temperature sensing. A blower operating in suction mode provided air flow with a turbulence level of 1–1.5 percent at the channel inlet.

The experiment was controlled and data acquired with a DEC-MINC PDP-11/03 based computer system interfaced to HP-3497 based peripherals. For a more detailed description of the apparatus and the data-acquisition and control system see Ortega and Moffat (1986).

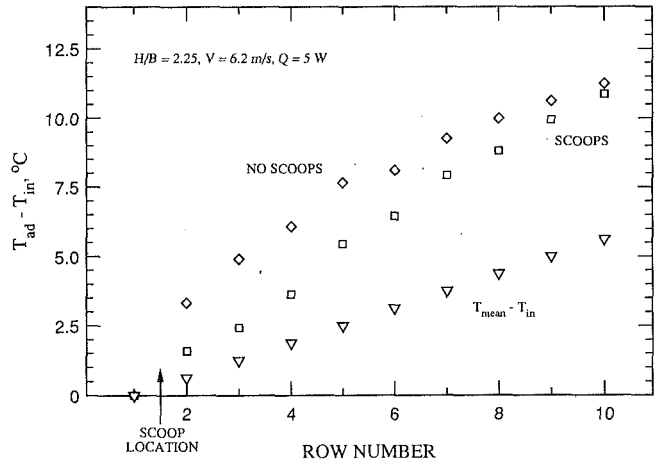

Fig. 6 Comparison of the adiabatic temperature rise with and without mixing devices for H/B = 2.25 and V = 6.2 m/s

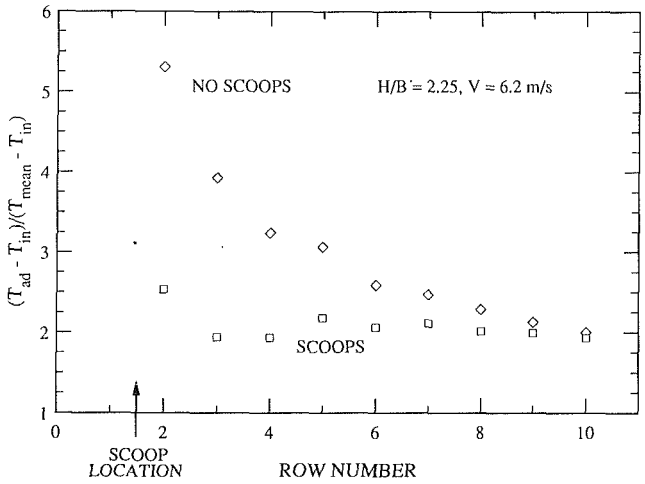

Fig. 8 Comparison of the cumulative two-dimensional superposition kernel function with and without mixing devices for H/B = 2.25, V = 6.2 m/s

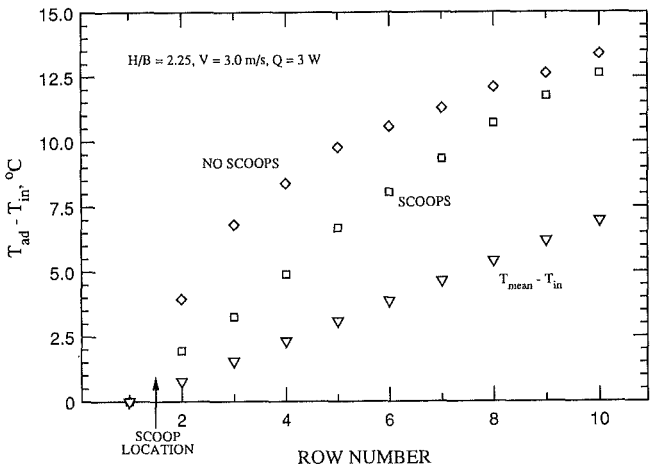

Fig. 7 Comparison of the adiabatic temperature rise with and without mixing devices for H/B = 2.25 and V = 3.0 m/s

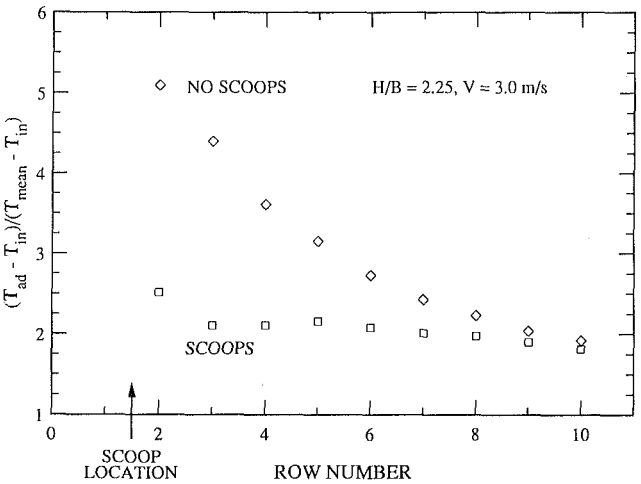

Fig. 9 Comparison of the cumulative two-dimensional superposition kernel function with and without mixing devices for H/B = 2.25, V = 3.0 m/s

Procedure

The thermal mixing effect of the scoops was studied for two channel velocities (V = 3.0 and 6.7 m/s) and a channel to cube height ratio, H/B, of 2.25. For each of the ten rows in turn, the centermost component was heated and the downstream component temperatures measured. The two-dimensional kernel functions, g^*, calculated from these measured temperatures, constitute the direct data from the experiment. To compare the results with and without scoops, the measured g^* were used to calculate the temperatures for a uniformly heated column of components.

The mean temperature was calculated from the convective heat transfer and the mass flow rate in the component lane (i.e., $\dot{m} = \rho V A_{lane}$, where $A_{lane} = HS$, and S is the cube center-to-center spacing). The velocity was measured at the channel center line 5 cm upstream of the first row of components. The flow entering the array was "laminar" in its general features with a free-stream turbulence intensity of 0.5–1.5 percent.

The convective heat transfer rate was determined from the measured power input, corrected for radiation and conduction losses. Uncertainty analysis showed that the nth-order uncertainty (Moffat, 1982) in the superposition kernel function varied from about ±5 percent, one row downstream of the heated component, to ±15 percent, nine rows downstream. The uncertainty in the adiabatic temperature rise was ±0.2 to ±0.7°C (under ±5 percent). The uncertainty in the overall temperature rise was less than ±2 °C (under ±3 percent) and the uncertainty in the adiabatic heat transfer coefficient is less than ±3.5 percent. The uncertainties are quoted at 20 to 1 odds. The uncertainty in the calculated temperatures is higher than the directly measured temperature, which had uncertainties of about ±0.1 °C. (For more information about the uncertainty analysis, see Anderson and Moffat, 1990.)

Results and Discussion

Figures 6 and 7 shows the adiabatic temperature rise versus row number for H/B = 2.25 and two velocities, V = 6.2 (Fig. 6), and V = 3.0 m/s (Fig. 7) for a uniformly heated column of components (Q_{conv} = 5.0 W/module for the higher velocity and Q_{conv} 3.0 W/module for the lower velocity). These data represent that part of the component temperature rise due to upstream effects. Examining Fig. 6, we see that on row 2, the adiabatic temperature rise with no mixing enhancement is about 3.5°C, due to the thermal wake from the component in row one. The adiabatic temperature rise on the tenth row is about 11.5°C and is the sum of the effects of the thermal wakes from the components in rows 1–9.

The figures compare the adiabatic temperature rise with and

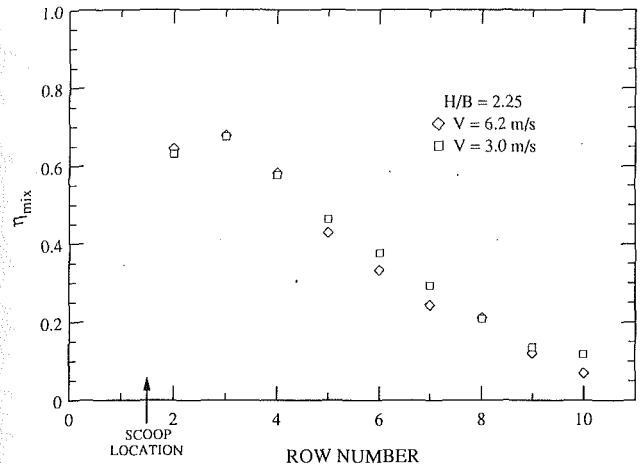

Fig. 10 Thermal mixing efficiency of scoops for $H/B = 2.25$

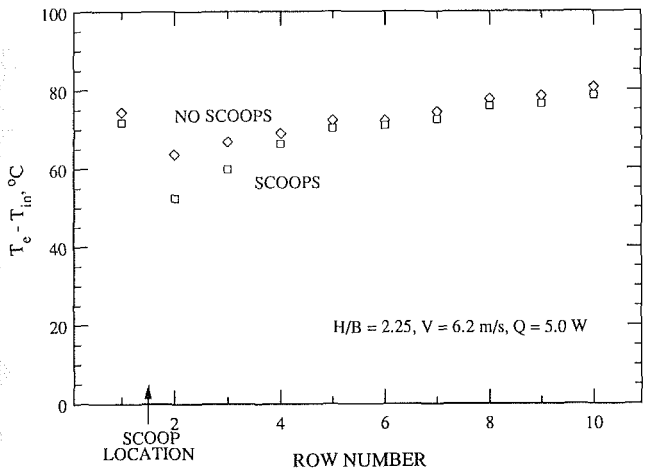

Fig. 11 Comparison of the component temperature rise with and without mixing devices for $H/B = 2.25$ and $V = 6.2$ m/s

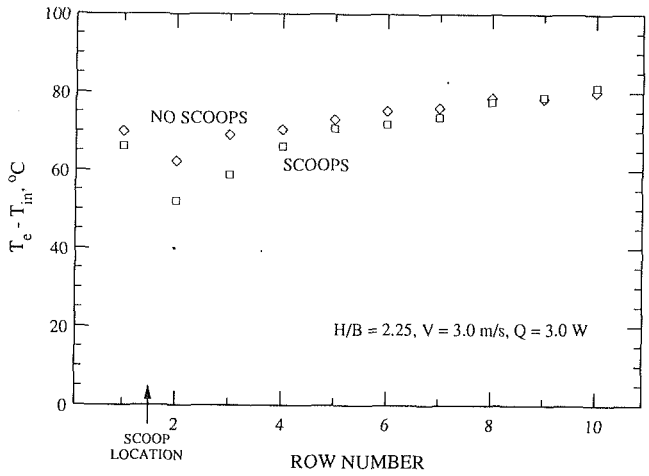

Fig. 12 Comparison of the component temperature rise with and without mixing devices for $H/B = 2.25$ and $V = 3.0$ m/s

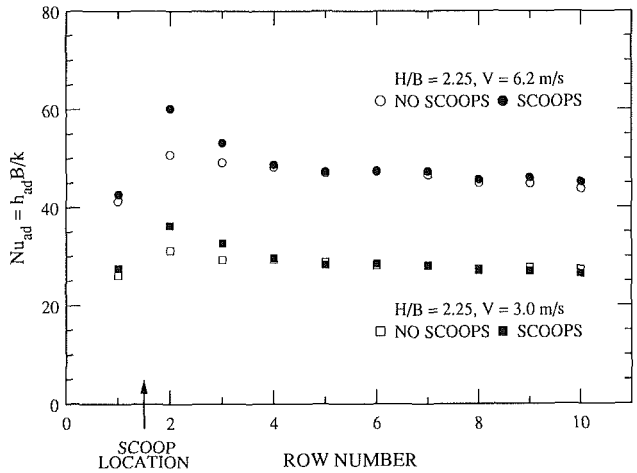

Fig. 13 Comparison of the adiabatic heat transfer coefficient with and without scoops for $H/B = 2.25$

without scoops. It is important to keep in mind that scoops were placed *only* behind row one as indicated by the arrow and only one component in each row was heated. For both velocities shown, the scoops reduced the adiabatic temperature rise about 50 percent one row downstream of the scoop location and as much as 55 percent two rows downstream of the scoop. Figure 7 shows that on the second row downstream of the scoops (row 3) the adiabatic temperature rise drops from 7.5°C to 3°C. After eight or nine rows downstream of the scoop, the reduction effects drops to 10 percent. The figures also show the mean temperature rise as calculated from equation (8). For constant heat flux, the mean temperature rises linearly, and represents the limiting value of the adiabatic temperature for perfect mixing.

Figures 8 and 9 show the ratio of the adiabatic temperature rise to the mean temperature rise in the center column when the center component in each upstream row is heated. In this situation, the scoops have increased mixing and decreased the cumulative g^* by up to 50 percent (this is described as the cumulative g^* because the center component in *each and every* upstream row was heated). Figure 10 shows the thermal mixing efficiency as defined in equation (11). For the particular type of mixing device used, the maximum efficiency is about 67 percent two rows downstream of the scoops. The downstream decay in η_{mix} is approximately 9 percent per row.

The decrease in the adiabatic temperature rise of about 50 percent results in a reduction in overall temperature rise. Figures 11 ($V = 6.2$ m/s) and 12 ($V = 3.0$ m/s) show the reduction in component temperature rise caused by the scoops. As a consequence of placing the scoops in the channel the adiabatic heat transfer coefficient (see Fig. 13) also increased somewhat. The adiabatic heat transfer coefficient increased slightly on row 1 due to changes in the flow field on the back face of the cube caused by the scoop. The scoops increase h_{ad} for a few rows but the effect dies out by the fourth row. The cumulative effect of increasing h_{ad} and decreasing g^* decreases the total component temperature rise by 19 percent in the row just downstream of the scoops.

We determined the pressure drop penalty incurred by the presence of the scoops by measuring the pressure coefficient defined as

$$C_p = \frac{P_{\text{tot, upstream}} - P_{\text{sta, downstream}}}{1/2\rho V^2} \tag{12}$$

The inlet pressure was measured approximately 5 cm upstream of the first row of modules, and the static downstream pressure was measured after the sixth row of modules. The test section pressure coefficient increased 11 percent when the scoops were in place. The scoops were not optimized for minimum pressure drop, so these results are judged quite promising. The drag coefficient is less important when scoops are used for thermal mixing than when they are used to increase the turbulence level, since the thermal scoops work mainly on low-momentum fluid.

Conclusion

Use of the adiabatic heat transfer coefficient allows the temperature rise of a component to be described as the sum of two terms; the self-heating temperature rise due to internal heating, and the adiabatic temperature rise due to the thermal wake effect of upstream heated components. This separation opens the way for a new approach to temperature control, since the adiabatic temperature rise often comprises a significant portion of the overall temperature rise. Thermal mixing can reduce the adiabatic temperature rise for a lower pressure drop penalty than would be incurred by increasing the heat transfer coefficient with turbulence promoters. This study demonstrates that thermal mixing enhancement aimed at decreasing the temperature nonuniformities in the channel can significantly reduce component temperatures. A demonstration experiment yielded a 50 percent reduction in the adiabatic temperature rise, which contributed to a 19 percent reduction in the overall temperature rise of electronic components in forced convection.

Acknowledgments

This research was supported by IBM Corporation. The authors appreciate the interest and assistance of Richard C. Chu, IBM Fellow.

References

Anderson, A. M., and Moffat, R. J., 1990, "Convective Heat Transfer From Arrays of Modules With Non-Uniform Heating: Experiments and Models," Ph.D. Thesis, Rept. No. HMT-43, Thermosciences Division, Department of Mechanical Engineering, Stanford University, Stanford, CA.

Chou, J., and Lee, J., 1987, "Reducing Flow Non-uniformities in LSI Packages by Vortex Generators," *Proceedings of the International Symposium on Cooling Technologies for Electronic Equipment*, Honolulu, HI, pp. 583–594.

Moffat, R. J., 1982, "Contributions to the Theory of Single-Sample Uncertainty Analysis," ASME *Journal of Fluids Engineering*, Vol. 104, pp. 250–260.

Moffat, R. J., and Anderson, A. M., 1990, "Applying Heat Transfer Coefficient Data to Electronics Cooling," ASME JOURNAL OF HEAT TRANSFER, Vol. 112, pp. 882–890.

Ortega, A., and Moffat, R. J., 1986, "Experiments on Buoyancy-Induced Convection Heat Transfer From an Array of Cubical Components on a Vertical Channel Wall," Ph.D. Thesis, Rept. No. HMT-38, Thermosciences Division, Department of Mechanical Engineering, Stanford University, Stanford, CA.

Ratts, E., Amon, C. H., Mikic, B. B., and Patera, A. T., 1987, "Cooling Enhancement of Forced Convection Air Cooled Chip Array Through Flow Modulation Induced by Vortex-Shedding Cylinders in Cross-Flow," *Proceedings of the International Symposium on Cooling Technologies for Electronic Equipment*, Honolulu, HI, pp. 651–662.

Sellars, J. R., Tribus, M., and Klein, J. S., 1956, "Heat Transfer to Laminar Flow in a Round Tube or Flat Conduit—The Graetz Problem Extended," *Trans.* ASME, Vol. 78, pp. 441–448.

Sparrow, E. M., Niethammer, J. E., and Chaboki, A., 1982, "Heat Transfer and Pressure Drop Characteristics of Arrays of Rectangular Modules Encountered in Electronic Equipment," *International Journal of Heat and Mass Transfer*, Vol. 25, No. 7, pp. 961–973.

Sparrow, E. M., Vemur, S. B., and Kadle, D. S., 1983, "Enhanced and Local Heat Transfer, Pressure Drop, and Flow Visualization for Arrays of Block-Like Electronic Components," *International Journal of Heat and Mass Transfer*, Vol. 26, No. 5, pp. 689–699.

Regional Heat Transfer in Two-Pass and Three-Pass Passages With 180-deg Sharp Turns

M. K. Chyu
Department of Mechanical Engineering,
Carnegie Mellon University,
Pittsburgh, PA 15213

The heat transfer distributions for flow passing through two-pass (one-turn) and three-pass (two-turn) passages with 180-deg sharp turns are studied by using the analogous naphthalene mass transfer technique. Both passages have square cross section and length-to-height ratio of 8. The passage surface, including top wall, side walls, and partition walls, is divided into 26 segments for the two-pass passage and 40 segments for the three-pass passage. Mass transfer results are presented for each segment along with regional and overall averages. The very nonuniform mass transfer coefficients measured around a sharp 180-deg turn exhibit the effects of flow separation, reattachment, and impingement, in addition to secondary flows. Results for the three-pass passage indicate that heat transfer characteristics around the second turn are virtually the same as those around the first turn. This may imply that, in a multiple-pass passage, heat transfer at the first turn has already reached the thermally developed (periodic) condition. Over the entire two-pass passage, the heat transfer enhancement induced by the single-turn is about 45 to 65 percent of the fully developed values in a straight channel. Such a heat transfer enhancement decreases with an increase in Reynolds number. In addition, overall heat transfer of the three-pass passage is approximately 15 percent higher than that of the two-pass one. This 15 percent increase appears to be Reynolds number independent. The pressure loss induced by the sharp turns is found to be very significant. Within the present testing range, the pressure loss coefficient for both passages is Reynolds number dependent.

Introduction

In current and advanced turbine engines, to accommodate higher turbine inlet temperatures and still maintain the metal temperatures below acceptable limits, cooling of turbine blades and vanes becomes essential. One cooling method, the so-called internal cooling or convective cooling, is to introduce the coolant air from the compressor through the hub section into the blade interior, and then discharge it out of the blade trailing edge. Inside the blade, the coolant often flows through a complicated serpentine passage that comprises several channels aligned with the airfoil spanwise direction and is connected by a 180-deg bend between any two adjacent channels. Figure 1 shows a schematic view of a typical internally cooled blade. Frequently, the passage surface is roughened with ribs to enhance the convective heat transfer.

As can be seen from the bend geometry shown in Fig. 1, the main coolant flow turns sharply with an extremely small radius of curvature at the bend. The inner-turn radius is determined by the thickness of the thin partition wall that divides two neighboring channels. As a result of this sharp turn, flow separates from the tip region of the partition wall followed by a recirculating region immediately adjacent to the partition wall after the turn. The fundamental aspects of such a flow separation phenomenon are very complex. This, in part, is because the aspect ratios of channel cross sections are generally small, typically on the order of unity. Moreover, as is always the case, the passage cross section differs between channels (along the chordwise direction). Depending on blading geometry, the cross section may even vary along the mainstream flow (radial) direction. It is also possible that strong interactions between two consecutive turns exist for short channels.

Turning flow and heat transfer in different channel cross-sectional geometries have been actively investigated in the past (Mori and Nakayama, 1967, 1971; Cheng and Akiyama, 1970; Patankar et al., 1975; Humphrey et al., 1981). These investigations studied the turning-induced secondary flow fields and their effects on heat transfer and head loss. As a contrast to the sharp 180-deg bends, most of the studies focused on geometries with constant curvature, and the radii of curvature are large compared to the hydraulic diameter of the channel. For these geometries, the effects of flow separation, if any, are insignificant. Results obtained from these studies can only provide little information and are often inadequate for turbine designs.

Research efforts for sharp 180-deg turning flow and heat transfer with direct applications to blade internal cooling began in 1984. Geometrically, all studies used a two-pass model (see Fig. 2) having two straight rectangular channels connected by a 180-deg turn in between. Metzger and coworkers (Metzger et al., 1984, 1988; Metzger and Sahm, 1986; Fan and Metzger, 1987) have published a series of studies on flow visualizations, pressure measurements, and "regionally local" heat transfer characteristics for a large family of smooth and rough channels. The geometric parameters investigated are the passage aspect ratios both before and after the turn, the gap size between the tip of the partition wall and the outer wall at the turn, the two outer-corner radii, and the rib roughness arrangement. Boyle (1984) reported the distribution of heat transfer coefficient along the centerline of channel span for both rough and smooth surfaces. Han et al. (1988) presented a study similar to Boyle's work (1984), with more detailed local measurements but only for rectangular turns. Murthy and Chyu (1987) numerically modeled the laminar

Contributed by the the Heat Transfer Division and presented at the 34th International Gas Turbine and Aeroengine Congress and Exhibition, Toronto, Ontario, Canada, June 4–8, 1989. Paper No. 89-GT-191. Manuscript received by the Heat Transfer Division April 3, 1989; revision received February 27, 1990. Keywords: Analog Techniques, Forced Convection, Turbines.

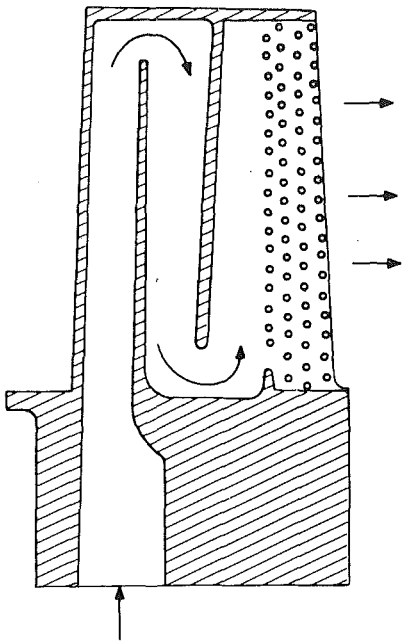

Fig. 1 Blade cooling passage

flow and heat transfer with passage rotation. Wagner et al. (1986) experimentally investigated the rotational effects on regional heat transfer in an engine-scale passage.

As mentioned earlier, all previous studies have used test models to simulate the two-pass (one-turn) cooling passages. However, as shown in Fig. 1, the cooling passage in an actual turbine blade may have more than one single bend ahead of the pedestal section near the blade trailing edge. As the coolant proceeds to the downstream channels, the flow bulk temperature increases and the rate of heat transfer decreases accordingly. In the limiting case, the heat transfer characteristics approach the thermally developed (periodic) condition somewhere downstream provided that the passage is long enough and/or consists of a sufficient number of channels and bends. Under this condition, the heat transfer coefficient, as usually defined for channel flow, is expected to repeat its value at the corresponding locations between coolant passes. With this general concept in mind, it is valuable to observe the variation of heat transfer coefficient for a cooling passage involving more than just one turn. The primary objective of the present study is to investigate the distributions of heat transfer coefficient experimentally for turbulent flow through two-pass and three-pass square channels.

The experimental method used in this study is the naphthalene mass transfer technique. The entire passage surface is divided into a predetermined number of small regions and segments. The locally regional transfer coefficient is determined by individually weighing the sublimed mass loss of each segment before and after a test run. Results obtained from the mass transfer experiment can be transformed into their heat transfer counterparts by invoking a well-developed analogy between heat transfer and mass transfer (Eckert, 1976). The advantage of using a mass transfer technique is twofold. First, it offers an extremely high degree of data accuracy; this, in part, is achieved by utilizing a high-precision, electronic weighing device. Second, the boundary is analogous to an ideal isothermal condition, and a perfect "mass insulation" between any two adjacent surfaces can be managed easily.

Experimental Methods and Apparatus

The primary design requirement of the test rig is that the entire channel inner-wall must be a continuous mass transfer active surface and have easy accessibility for the mass transfer measurements. Figure 2 shows schematic sketches of both two-pass and three-pass test channels (with top wall removed). The test channels for both cases are 203.2 mm long and 25.4 mm square in cross section. This gives a channel length-to-height ratio of 8. The partition tip-to-outer wall clearance is maintained constant for all cases at 25.4 mm, equal to the channel height or width.

The test channel walls are assembled from a number of aluminum-plate segments with naphthalene coated on one of the surfaces of each segment. There are 26 plate segments for the two-pass model, and 40 for the three-pass one. These plates are grouped into eight regions for the two-pass and 12 for the three-pass model, respectively. Figure 3 shows the labeling order of the plate segments for both models. The orientation of "left" and "right" is chosen as one follows the mainstream direction passing through the entire passage. The plate segments having the same labeling number form a region, and the region is labeled by the same number as that of the constituent plates. An additional plate is assigned in each of the turning regions, and it is labeled using a "T" (meaning turning) preceded by the corresponding region number, e.g., 4T, 5T, 8T, etc. Note that for both passage models, only the

Nomenclature

D = passage height = 25.4 mm in present study
$\mathfrak{D}$ = diffusion coefficient for naphthalene-to-air mass transfer
f = pressure drop coefficient, see equation (9)
f_o = friction factor for fully developed turbulent duct flow
h = heat transfer coefficient
h_m = naphthalene mass transfer coefficient
k = thermal conductivity of fluid
L = passage length = 203.2 mm in present study
L_s = passage-centerline total length
m_j = mass transfer per unit time per unit area from segment j
M_j = mass transfer per unit time from region j
Nu = heat transfer Nusselt number
Nu_o = fully developed heat transfer Nusselt number
p = pressure
Pr = Prandtl number
Q = volumetric air flow rate
q = heat flux from wall
Re = Reynolds number based on passage width and mean velocity
Sc = Schmidt number = 2.5 for naphthalene-to-air mass transfer
Sh = segment mass transfer Sherwood number
$\overline{\mathrm{Sh}}$ = regional average mass transfer Sherwood number
Sh_o = fully developed mass transfer Sherwood number
T_w = wall temperature
T_b = bulk mean-flow temperature
U = average air velocity
W = passage width = 25.4 mm in present study
ν = kinematic viscosity
ρ = fluid density
$\rho_{v,w}$ = vapor mass concentration or density of naphthalene at wall
$\rho_{b,j}$ = vapor mass concentration or density of naphthalene in bulk mean flow for region j

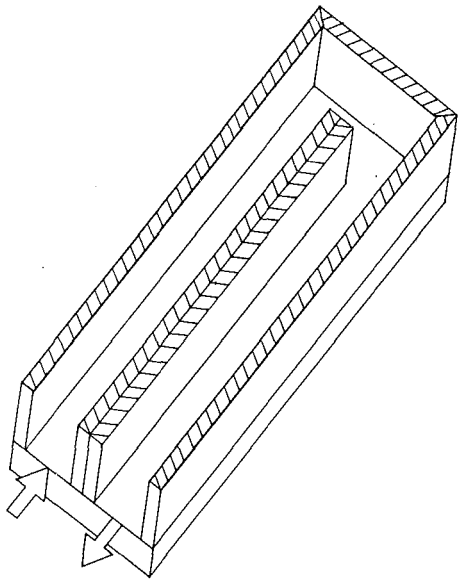

Fig. 2(*a*) Two-pass model

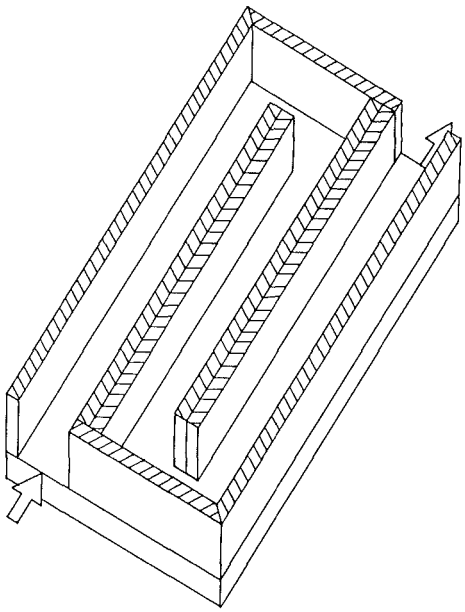

Fig. 2(*b*) Three-pass model

Fig. 2 Test models

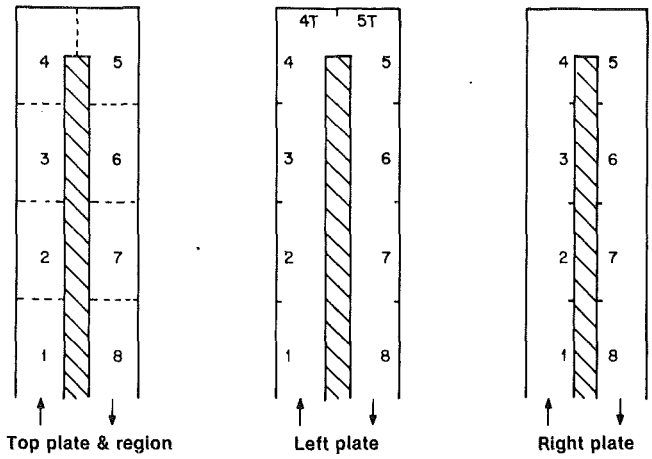

Fig. 3(*a*) Two-pass model

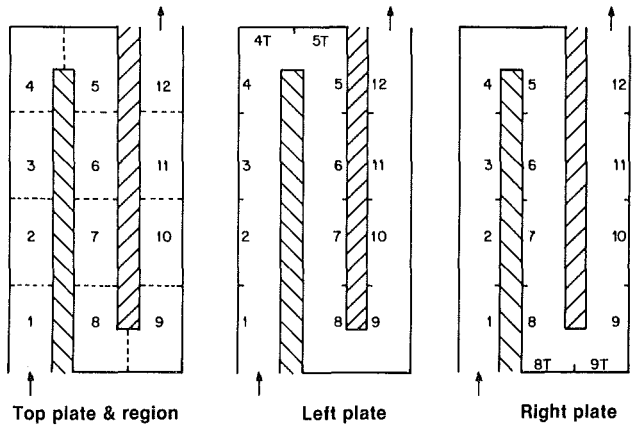

Fig. 3(*b*) Three-pass model

Fig. 3 Segment and region labeling

top and all the side walls (including partition walls) are assembled by the separate segments. The bottom wall is a single, inseparable plate coated with naphthalene. Assuming that the mass transfer from the top and bottom walls is the same, only the mass transfer on the top wall is measured.

The bottom wall, a 114.3-mm-wide, 215.9-mm-long, and 12.7-mm-thick aluminum plate, is the base for test channel construction. All the side-wall segments (18 for two-pass and 28 for three-pass) are screw-mounted vertically to the bottom wall; then the top-wall segments are attached atop the side walls. These plate segments are all 6.35 mm thick and 25.4 mm wide, and their spans of active mass transfer vary slightly depending on location. Except for the segments near partition tip and turning outer walls, the size of mass transfer active region for the side-wall segments is 50.8 mm long. Segments forming the partition tip regions (e.g., right plate 4 and 5) are one-half this size, 25.4 mm in length. Of the outer-wall segments, the ones at a turn (e.g., 4T and 5T), are longer than those of the partition tip but shorter than the straight sections, 31.75 mm. Except for those at a turn, the top-plate segments have mass transfer area identical to that of the side walls. At-turn top segments, e.g., plates 4 and 5, are slightly larger because of additional area involved at a turning region, as Fig. 3 shows. Each partition wall is assembled by attaching two side-wall segments back-to-back, and thus its thickness is 12.7 mm.

An experiment starts with the preparation of mass transfer surfaces. A naphthalene surface is made by casting nearly boiling, molten naphthalene into an approximately 2 mm recession on one of the surfaces of an aluminum test plate. After casting, the naphthalene-coated plates are stored in a tightly sealed plastic box in the testing room for at least 15 hours before an actual test run. This ensures an attainment of thermal equilibrium with the surrounding air. The vapor concentration of naphthalene, which is the primary driving potential of the present mass transfer process, is very sensitive to the temperature variation. Thus, an isothermal system throughout the entire test is highly desirable. The present experiment is performed in a very well air-conditioned laboratory.

Before a test run, all segments are separately weighed and assembled to form the passage. Two aluminum-made extension ducts, having the same cross section as the passage, are connected to the inlet and outlet of the assembled passage, respectively. The length of the extension channel upstream to the assembled passage is 15 times the passage height, and the downstream one is relatively shorter, only 5 times. To settle the flow prior to its entry to the test section, a plenum, which contains a series of screens, is located immediately ahead of the extension duct upstream. The weighing device used is an

electronic balance having an accuracy of 10^{-2} mg and a 166 g range (Sartorius 2004MP). Having completed the passage assembly, a compressed airstream is induced to flow through the passage for approximately 30 minutes. Naphthalene coated on the passage walls sublimes as it is exposed to the air. Measurements of the air flow rate use an ASME standard orifice meter installed far upstream to the test section. The flow rate is varied by a control valve located farther upstream from the orifice. This, in turn, gives the desired Reynolds numbers. The Reynolds number, ranging from 2×10^4 to 7.4×10^4 in the present study, is defined as $\mathrm{Re}=UD/\nu$, where U is the mean velocity in the passage.

During the test run, temperature on the passage walls is recorded every 2 minutes by readings from three thermocouples embedded in the naphthalene layer of the bottom plate. The differences among these three thermocouple readings are within 0.1°C for all the tests. The average of these three temperatures is used as the value to evaluate the at-wall naphthalene vapor concentration for the entire passage. After the test, the passage is disassembled and each plate is weighed again. As aluminum is inert to the mass transfer process, the weight difference for each individual plate segment gives the amount of naphthalene mass sublimed during the test period. The mean loss of each segment is approximately 30 mg.

As an auxiliary study, pressure loss across the entire passage is determined by the difference of static pressure between the passage inlet and exit. At both ends of the test channel, a flush pressure tap is installed at the center of the channel top wall. An inclined manometer connected to these two pressure taps gives the readings of static pressure differential across the entire channel.

Data Reduction and Heat/Mass Transfer Analogy

The mass transfer coefficient h_m and its dimensionless counterpart, the Sherwood number Sh, are evaluated at each segment in the passage. Thus, h_m in this case representing the per-segment, area-averaged mass transfer coefficient, is defined as

$$h_m = m_j/(\rho_{v,w}-\rho_{b,j}) \tag{1}$$

where m_j is the mass of naphthalene sublimed per unit area per unit time from a particular segment j, $\rho_{v,w}$ is naphthalene vapor concentration at the wall, and $\rho_{b,j}$ is the bulk concentration of naphthalene vapor at segment j. Equation (1) corresponds to the conventional definition of heat transfer coefficient h

$$h = q/(T_w - T_b) \tag{2}$$

where q is the heat transfer per unit area per unit time, T_w and T_b are the wall temperature and bulk mean-flow temperature, respectively.

The mass transfer is driven by the difference between the naphthalene vapor concentrations at the wall and in the bulk, analogous to the wall-to-bulk temperature difference for heat transfer. The value of $\rho_{v,w}$ is determined from the measured surface temperature by using the relation between the vapor pressure and temperature for naphthalene (Ambrose et al., 1975) in conjunction with the perfect gas law. Note that $\rho_{v,w}$ is the same for all segments in the present study. Detailed calculation of $\rho_{v,w}$ is given by Chyu (1986). To evaluate $\rho_{b,j}$ it is necessary to note the increase in bulk concentration of naphthalene vapor between the inlet and outlet of a region j

$$\Delta\rho_{b,j} = M_j/Q \tag{3}$$

where M_j is the mass transfer per unit time from all surfaces surrounding this region, and Q is volumetric air flow rate. Since the air at the inlet of the passage is free of naphthalene, it leads to

$$\rho_{b,j} = \sum_{1}^{j-1} M_j/Q \tag{4}$$

The dimensionless per-segment mass transfer coefficient, Sherwood number (Sh), is defined as

$$\mathrm{Sh} = h_m D/\mathfrak{D} \tag{5}$$

The diffusion coefficient $\mathfrak{D}$ for the naphthalene-to-air mass transfer system is evaluated from the Schmidt number $\mathrm{Sc}=\nu/\mathfrak{D}\approx 2.5$, where ν is the kinematic viscosity of air. By analogy, the Sherwood number corresponds to the Nusselt number $\mathrm{Nu}=hD/k$ for heat transfer, where k is the flow thermal conductivity. The experimental uncertainty of Sh, using the method of Kline and McKlintock (1953), is estimated at 4 percent, and the repeatability is about the same magnitude.

Results and Discussion

The mass transfer results presented here use the ratio $\mathrm{Sh}/\mathrm{Sh}_o$, where Sh_o is the value of Sherwood number under the fully developed condition in a straight channel without bends. The ratio represents the mass transfer enhancement caused by flow turning. The value of Sh_o is obtained from its heat transfer counterpart—the Nusselt number for turbulent flow in a thermally developed straight channel (Kays and Crawford, 1980), Nu_o; i.e.,

$$\mathrm{Nu}_o = 0.023\ \mathrm{Re}^{0.8}\mathrm{Pr}^{0.4} \tag{6}$$

By analogy,

$$\mathrm{Sh}_o = 0.023\ \mathrm{Re}^{0.8}\mathrm{Sc}^{0.4} \tag{7}$$

where $\mathrm{Sc}=2.5$ as previously mentioned. In addition, it is reasonable to assume that the turning effects on heat and mass transfer are exclusively hydrodynamic; this implies

$$\mathrm{Sh}/\mathrm{Sh}_o = \mathrm{Nu}/\mathrm{Nu}_o \tag{8}$$

Hence, the ordinates of Figs. 4–6 have a dual label, i.e., $\mathrm{Sh}/\mathrm{Sh}_o$ and $\mathrm{Nu}/\mathrm{Nu}_o$.

Figure 4 shows the segment-by-segment mass transfer results for the two-pass, one-turn passage. Figure 5 shows the corresponding regional mass transfer results. The regional mass transfer Sherwood number, $\overline{\mathrm{Sh}}$, is the area-averaged Sh for all the constituent segments in the region (see Fig. 3). For comparison, the corresponding heat transfer results reported by Fan and Metzger (1987) are also shown in Fig. 5. Note that the passage geometry and the segment (region) arrangement in their study are considerably different from the present setup. Their passage has a shorter passage length ($L/D\approx 5$), a rectangular cross section (i.e., $W/D\neq 1$), and an unheated partitioned wall. Moreover, the entire two-pass passage is divided into five regions, while the current study is divided into eight regions. Thus, to facilitate a sensible comparison, the region numbers for their data are approximately scaled and transformed to the present labeling system. The comparison in Fig. 5, particularly in the regions before and at the turn, shows a very favorable agreement between the two studies. The deviation in the post-turn region is largely attributable to the difference in the passage geometry.

For three different Reynolds numbers $\mathrm{Re}=2\times10^4$, 3.3×10^4, and 7.4×10^4, $\mathrm{Sh}/\mathrm{Sh}_o$ shown in Fig. 4 displays a nearly identical distribution, and its magnitudes among the corresponding segments are very comparable. The values of Sh for the first three segments are all above the corresponding fully developed values, with side-wall and top-wall values nearly equal. $\mathrm{Sh}/\mathrm{Sh}_o$ decreases as flow proceeds downstream—a clear indication of thermally developing regime existing in this part of the passage, as expected. The proximity of segment 3 values to fully developed counterparts, within approximately 10 percent, implies that the flow is close

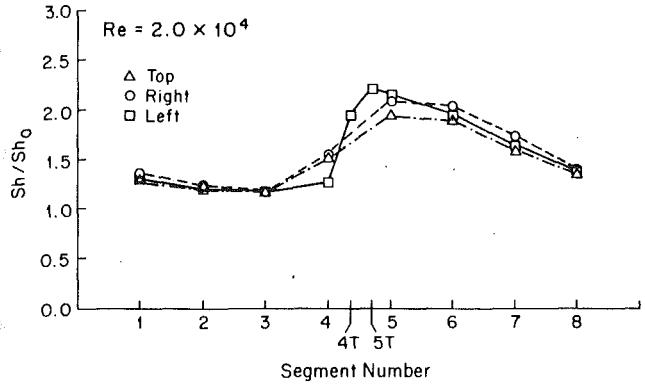

Fig. 4(a) Re = 2.0 × 10⁴

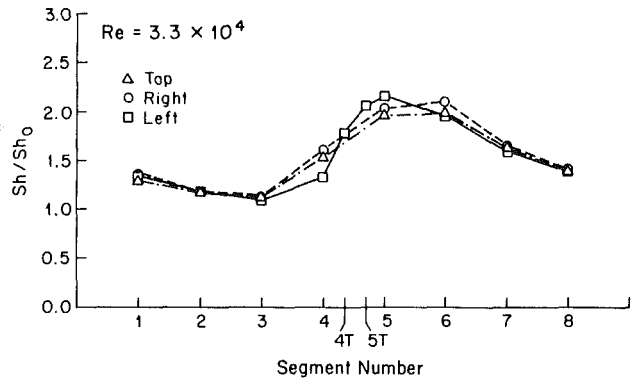

Fig. 4(b) Re = 3.3 × 10⁴

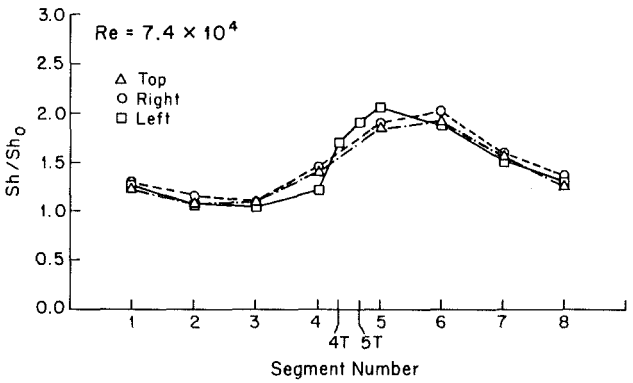

Fig. 4(c) Re = 7.4 × 10⁴

Fig. 4 Segment-by-segment mass transfer for two-pass passage

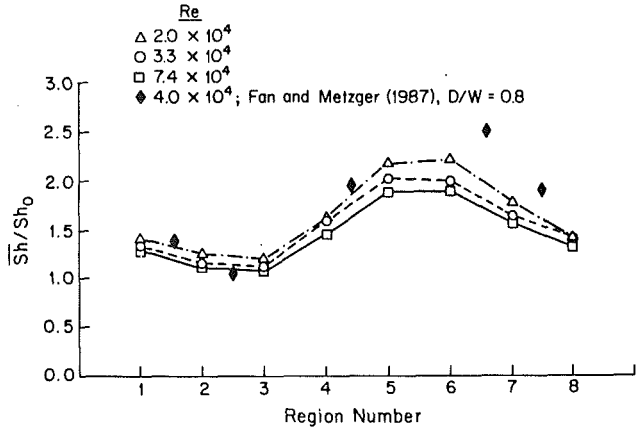

Fig. 5 Regional average mass transfer for two-pass passage

to thermally developed condition near the end of region 3.

Significant turning effects on the mass transfer begin to show in region 4; regional $\overline{Sh}/Sh_o$ is about 30 percent higher than that of region 3, as Fig. 5 shows. Nevertheless, the degrees of increase among different plate segments are different. In Fig. 4, for all the Reynolds numbers tested, Sh/Sh_o of segment 4 has the lowest value on the left (outer) plate and the highest on the right (inner) plate. Sh/Sh_o on the top plates is quite close to, but always slightly higher than, that of the left plate. The low heat transfer on the outer wall near a bend inlet has also been reported in earlier studies (Metzger and Sahm, 1986; Fan and Metzger, 1987). As flow proceeds farther into the turn region (plates 4T, 5T, and 5 in Fig. 4), segment Sh on the left wall rises sharply, about twice as much as the fully developed values. This is virtually the case for the right and top walls in region 5; nevertheless, their Sh/Sh_o values are always lower than those on the left walls. In general, region 5 has the highest value of regional $\overline{Sh}/Sh_o$, as shown in Fig. 5. However, the corresponding Sh/Sh_o values in region 6 are very comparable or even higher. Flow patterns in region 6 considered to be in the "post-turn" regime are very complex and strongly geometry dependent (Metzger et al., 1984). These also produce very nonuniform variations of Sh/Sh_o among segments constituting this region. An interesting observation is that while the left-wall Sh/Sh_o declines significantly from region 5 to region 6, the corresponding Sh/Sh_o on the right wall either increases slightly or remains constant. Mass transfer on the top plate generally behaves similarly to that of the right plate. The post-sharp-turn flow separation and reattachment are largely responsible for the mass transfer behavior in these regions. Downstream from region 6, where the turn effect diminishes, Sh/Sh_o decreases progressively along the streamwise direction, as does the circumferential Sh/Sh_o difference. The value of Sh/Sh_o on the last segment, segment 8, of the present two-pass model is approximately 1.5. If the overall mass/heat transfer of the entire passage is of concern, an integration of regional data shown in Fig. 5 gives an augmentation measure with the bend as compared to the fully developed conditions. The integrated Sh/Sh_o results are 1.64, 1.54, and 1.46 for $Re = 2 \times 10^4$, 3.3×10^4, and 7.4×10^4, respectively. The augmentation effect decreases as the Reynolds number increases.

The increase as well as the nonuniform regional distributions in mass transfer, in part, is attributable to the secondary flow induced by the bend. The flow structure in a curved channel is primarily controlled by local imbalance between centrifugal forces and pressure gradients. For cases with relatively large radii of curvature and without flow separation, the secondary flow is commonly seen in a double-cellular pattern, which consists of a radially inward flow both near the top and the bottom walls, and a radially outward flow along the channel center plan (Mori and Nakayama, 1971; Humphrey et al., 1981). The migration of relatively low-momentum fluid caused by this secondary flow distorts the main (axial) flow field; the velocity maximum shifts to the outside of the bend. The degree of main flow distortion is largely determined by the Reynolds number and radii of curvature. With a higher near-wall velocity gradient, the outer wall thus produces a higher shear stress than the inner wall. In addition, the streamwise turbulence intensity near the outer wall is also higher than that near the inner wall. Accordingly, heat transfer is higher on the outer wall than on the inner wall.

Flow fields associated with the present sharp-bend geometry are expected to be more complex than that described above.

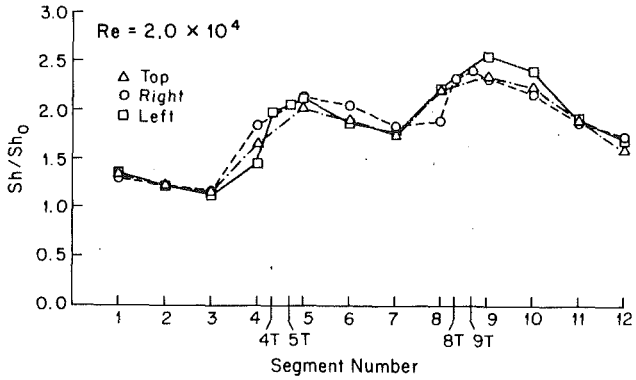

Fig. 6(a) Re = 2.0 × 10⁴

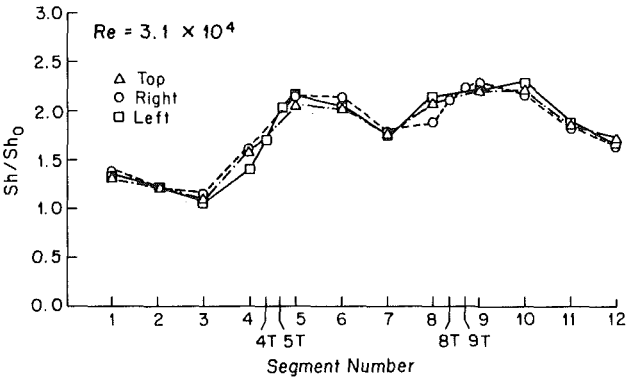

Fig. 6(b) Re = 3.1 × 10⁴

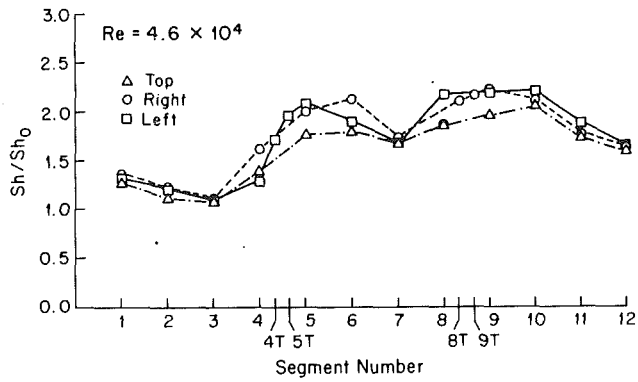

Fig. 6(c) Re = 4.6 × 10⁴

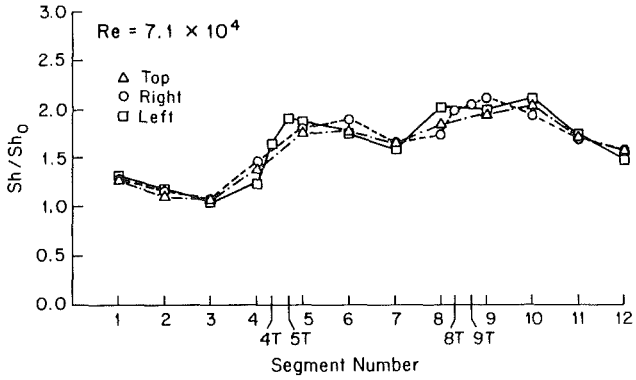

Fig. 6(d) Re = 7.1 × 10⁴

Fig. 6 Segment-by-segment mass transfer for three-pass passage

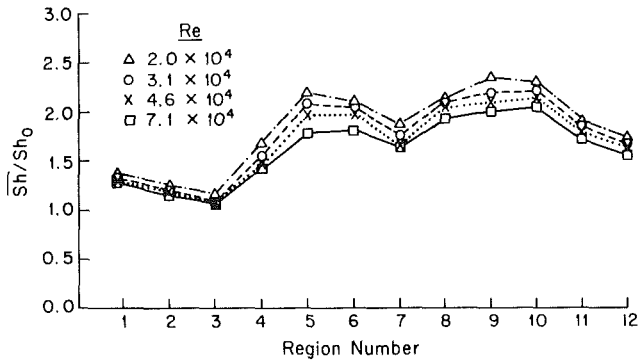

Fig. 7 Regional average mass transfer for three-pass passage

The complexity is mainly due to the combined effects of extremely small inner-wall radius of curvatures, sharp-turn enveloped outer wall, and separated flow regions existing in the bend. In region 4 where the bend begins, the main flow is expected to separate from the outer wall in order to proceed the turning. As a result, a recirculating region exists in the far corner of the outer wall. This is considered to be responsible for the relatively lower mass transfer shown on the left plate 4 in Fig. 4. As for the inner (right) plate near the tip region of partition wall, the detailed physics causing a high mass transfer is rather obscure. From the inviscid consideration, the inner flow accelerates near the partition tip before the strong turning, and the velocity peak shifts toward the inside. However, according to earlier studies with a mildly curved 180-deg, U-shaped turn (Johnson and Launder, 1985), a reduction of heat transfer as well as turbulence intensity on the inner wall is expected. Thus, a general concept to describe inner-wall heat transfer behavior such as this appears to be unsuitable for the present case. This is also true for the heat transfer near the tip region on the other side of partition wall (right-plate 5).

The high values of Sh/Sh_o existing on plates 4T, 5T, and left-plate 5 are typical representatives of the outer-wall characteristics for a well-developed curved flow. According to Metzger and Sahm (1986), among many parameters, the gap size between the partition tip and the outer wall has the greatest influence on the heat transfer characteristics in this region. This is particularly true for left plate 5. The gap size associated with the main flow Reynolds number determines the strength of the jetlike flow initiated at the gap, and such a flow impinges on the upstream portion of left plate 5. The high pressure present in this jet-impinged, stagnation region then pushes the fluid toward thinner wall and further downstream. To a certain extent, a narrower gap results in a stronger jet impingement which, in turn, produces a higher heat transfer on the impinged plate. The present study uses a fixed gap size which is equal to the channel width for all test runs.

One important aspect of the present sharp-turn geometry is the separated flow existing immediately adjacent to the partition wall after the bend. Mainly due to the small channel aspect ratio and the residual turning effects, this separated flow is expected to be highly three dimensional. Typically, the partition wall and a highly turbulent shear layer initiated at the tip of the partition wall form the envelop of a recirculating region. A degraded heat transfer occurs on the surface immediately adjacent to the recirculation. The heat transfer coefficient increases progressively downstream until it reaches a maximum where the separated shear layer reattaches on the partition wall. Metzger et al. (1984) used the ink-dot flow visualization technique and determined the location of the shear layer reattachment—approximately twice the channel width downstream to the partition tip. The present mass

Table 1 Correlations for two-pass passage

Region	Re x 10^{-4}				
	2.0	3.3	7.4	A	- B
1	1.39	1.32	1.26	2.660	0.067
2	1.23	1.17	1.10	2.980	0.089
3	1.19	1.11	1.07	2.460	0.075
4	1.62	1.57	1.44	4.000	0.090
5	2.17	2.01	1.87	6.230	0.108
6	2.20	1.98	1.88	6.694	0.114
7	1.76	1.62	1.55	4.290	0.092
8	1.41	1.40	1.31	2.512	0.058

Table 2 Correlation for three-pass passage

Region	Re x 10^{-4}					
	2.0	3.1	4.6	7.1	A	- B
1	1.38	1.33	1.31	1.28	2.370	0.055
2	1.25	1.21	1.19	1.15	2.380	0.065
3	1.12	1.09	1.08	1.06	1.690	0.042
4	1.68	1.56	1.48	1.43	5.940	0.128
5	2.19	2.09	1.97	1.78	6.906	0.118
6	2.11	2.05	1.98	1.81	5.136	0.103
7	1.87	1.76	1.67	1.64	4.650	0.078
8	2.14	2.09	2.06	1.93	7.050	0.111
9	2.35	2.21	2.11	2.01	6.516	0.103
10	2.31	2.22	2.16	2.06	5.957	0.096
11	1.91	1.86	1.81	1.73	4.136	0.078
12	1.74	1.68	1.64	1.56	4.016	0.084

transfer results, shown in Fig. 4, as the inner-wall Sh/Sh_o rises in region 6 agree well with this finding. Both the bend and the shear-layer development are expected to raise the turbulence levels in the post-turn section of the passage. This, in part, is responsible for the slowly declined Sh/Sh_o in regions 7 and 8.

Mass transfer results for the three-pass, two-turn passage are presented in Figs. 6 and 7. Figure 6 shows the segment-to-segment Sh/Sh_o, and Fig. 7 gives the regional $\overline{Sh}/Sh_o$ distribution. Referring to the segment and region labeling in Fig. 3, the second bend starts at region 8, which is equivalent to region 4 for the first bend. As a contrast to the first turn, the right segments form the outer wall of the second turn and the left segments constitute the inner wall (or the second partition wall). A comparison between Figs. 4 and 6 (or 5 and 7) yields an important finding, i.e., the mass transfer at the first turn is virtually uninfluenced by the presence of the second turn downstream. Furthermore, the general characteristic of mass transfer at the second turn is a repeat of the first turn. This implies that present turning flow establishes its thermally developed condition at the first turn; the only developing region is the first pass. In fact, according to the study by Johnson and Launder (1985), the flow and heat transfer behavior at a turn is rather insensitive to the length of inlet section before the turn. This further supports the notion that the flow in a bend is largely a local phenomenon; whatever exists further upstream and downstream has little effect. The periodicity appears to be stronger for cases with higher Reynolds number. For $Re = 2 \times 10^4$, Sh/Sh_o shows a moderate increase at the second turn as compared to the corresponding value at the first turn. However, this variation diminishes completely for $Re \geq 3.1 \times 10^4$.

The average Sh/Sh_o values over the entire three-pass passage are 1.88, 1.80, 1.74, and 1.65 for $Re = 2 \times 10^4$, 3.1×10^4, 4.6×10^4, and 7.1×10^4, respectively. The three-pass passage produces higher mass/heat transfer augmentation than the two-pass, by approximately 15 percent. Note that this 15 percent increase is virtually Reynolds number independent, at least within the present testing range. However, the actual degree of heat transfer augmentation, for both two-pass and three-pass models, is expected to vary with passage geometries.

The regional mass transfer results are correlated using the least-square-fitted power form $\overline{Sh}/Sh_o = A \cdot Re^B$. Tables 1 and 2 tabulate the correlation coefficients A and B for two-pass and three-pass passages, respectively. For comparison purposes, also included in the tables are the regional results, which are presented graphically in Figs. 5 and 7. From the tabulated coefficients, the distribution of regional mass/heat transfer coefficients can be calculated at any desired Reynolds number. Of particular note here is the distribution of power index B, which represents the measure of Reynolds number dependence of Sh relative to that of Sh_o. A negative-valued B implies that Sh has a weaker dependency than Sh_o on Re; the latter has a 0.8 power index as equation (7) shows. As seen from both tables, all the values of B are negative, although

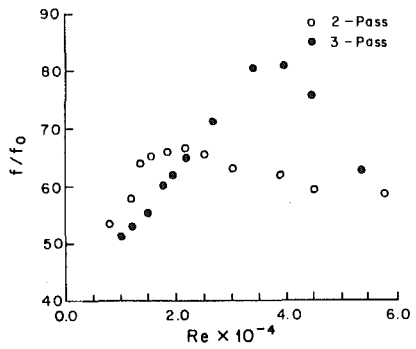

Fig. 8 Pressure loss coefficient

most of the magnitudes are quite small, especially in straight sections. Near or at a turn, the magnitudes of B are larger than those away from a turn. This can be explained by considering the nature of flow in the present turning passages. As discussed earlier, one of the primary features dominating heat/mass transfer characteristics in the present passages is flow separation. Nusselt number with a separated flow region generally has a lower power index on Re than without flow separation. Although regions are divided differently, the present two-pass coefficients agree well with those correlations presented by Metzger and Sahm (1986) and Fan and Metzger (1987). Here, the values of power index B are also negatively larger at a turn than in the straight section. Han et al. (1988), however, have recently reported a constant $B = -0.06$ for the entire region around a turn.

Accompanying the bend-induced heat transfer augmentation are two undesirable aspects that need to be addressed for design of cooling passages. First is the nonuniform cooling effect caused by the high spatial distribution of the heat transfer coefficients shown in the present study. The nonuniform cooling further produces thermal stress in the blade, which is detrimental to its component life. The second concern is the excessive pressure loss incurred with the flow passing additional bends and channels—a direct penalty related to pumping power consumed. Figure 8 shows the characteristics of pressure loss for both passages. The pressure loss coefficient, f, is defined as

$$f = (2\Delta p/\rho U^2) \cdot (D/L_s) \tag{9}$$

where Δp is the pressure drop across the entire passage and L_s is the length of the actually bent passage centerline stretched along the streamwise direction. Note that f represents the conventional definition of friction factor for flow in a straight duct without turns. The inclusion of D/L_s in f provides a comparison basis of pressure loss characteristics between the two passages. Considering the present turning geometry, L_s/D is 16.5 and 25 for the two-pass and three-pass passages, respec-

tively. Shown in the ordinate of Fig. 8, f is further normalized by the corresponding friction factor of the fully developed, turbulent flow in a straight channel, f_o. The value of f_o is calculated from the Blasius Power Law (Kays and Crawford, 1980); i.e.,

$$f_o = 0.078\ \mathrm{Re}^{-0.25} \tag{10}$$

f/f_o thus represents a rational measure of the pressure losses inherited in the present turning passages relative to their limiting counterparts.

The results shown in Fig. 8 indicate that the value of f is approximately one to two order of magnitude greater than that of f_o. Moreover, the distributions of f/f_o are Reynolds number dependent. For both passages, f/f_o increases initially with an increase in Re, reaches a maximum, and then decreases with Re. This implies that, at least within the present testing range, a single power correlation between f and Re for flow through passages with 180-deg sharp turns appears to be nonexistent. The maximum occurs at Re equal approximately to 2.0×10^4 and 4.0×10^4 for the two-pass and three-pass passages, respectively. The magnitude of such a maximum is about 20 percent higher for the three-pass passage than for the two-pass passage. Using a two-passage model and a different definition of pressure loss coefficient (D/L_s excluded), Metzger et al. (1984) have reported the pressure loss data just across the turning region, not the entire passage. With proper data transformation, the present pressure loss across the entire two-pass passage is nearly twice as large as that reported in their study. The difference is considered to be due to the excessive friction loss incurred in the straight sections before and after the turn.

Conclusions

The regional and segment-by-segment heat transfer in both two-pass and three-pass cooling passages with 180-deg turns are studied using the naphthalene mass transfer technique. For the two-pass model, the present results agree well with those of heat transfer reported by Metzger and Sahm (1986) and Fan and Metzger (1987). Except for sections tangent to the main flow direction, heat transfer on the outer wall at a turn shows the characteristics of a developed curve flow. The dominating feature here appears to be the convective transport induced by the secondary flow fields. Near the turn inlet and outlet, heat transfer is largely determined by the flow separation in the regions. Elevated heat transfer is observed near the tip region of the partition wall; this does not agree with the general behavior of inner-wall heat transfer with a mild turn. For the three-pass model, heat transfer characteristics at the second turn are found to be a repeat of the first turn. This implies that the present turning flow and heat transfer are largely a local phenomenon, and heat transfer at the first turn has virtually reached the thermally periodic condition. Evaluations of the average heat transfer over entire passages reveal that, within the present testing range, flow passing through the two-pass (one-turn) passage produces an approximately 45 to 65 percent higher heat transfer as compared to the corresponding straight channel, fully developed conditions. Such a heat transfer augmentation decreases with an increase of Reynolds number. In addition, overall heat transfer for the three-pass passage is approximately 15 percent higher than that of the two-pass one. This 15 percent increase is found to be Reynolds number independent. Accompanying the heat transfer augmentation is the excessive pressure loss induced by the sharp turns. The pressure loss coefficient varies significantly with the Reynolds number.

References

Ambrose, D., Lawenson, I. J., and Sprake, C. H. S., 1975, "The Vapor Pressure of Naphthalene," *J. Chem. Thermo.*, Vol. 7, pp. 1173–1176.

Boyle, R. J., 1984, "Heat Transfer in Serpentine Passages With Turbulence Promoters," ASME Paper No. 84-HT-24.

Cheng, K. C., and Akiyama, M., 1970, "Laminar Forced Convection Heat Transfer in Curved Rectangular Channels," *Int. J. Heat Mass Transfer*, Vol. 13, pp. 1787–1806.

Chyu, M. K., 1986, "Influence of Roughness Element on Local Mass Transfer From a Flat Plate," Ph.D. Thesis, University of Minnesota, Minneapolis, MN.

Eckert, E. R. G., 1976, "Analogies to Heat Transfer Processes," *Measurements in Heat Transfer*, E. R. G. Eckert and R. J. Goldstein, eds., Hemisphere Pub. Co., Washington, DC.

Fan, C. S., and Metzger, D. E., 1987, "Effects of Channel Aspect Ratio on Heat Transfer in Rectangular Passage Sharp 180-Deg Turns," ASME Paper No. 87-GT-113.

Han, J. C., Chandra, P. R., and Lau, S. C., 1988, "Local Heat/Mass Transfer Distributions Around Sharp 180 deg Turns in Two-Pass Smooth and Rib-Roughened Channels," ASME JOURNAL OF HEAT TRANSFER, Vol. 110, pp. 91–98.

Humphrey, J. A. C., Whitelaw, J. H., and Yee, G., 1981, "Turbulent Flow in a Square Duct With Strong Curvature," *J. Fluid Mech.*, Vol. 74, pp. 443–463.

Johnson, R. W., and Launder, B. E., 1985, "Local Nusselt Number and Temperature Field in Turbulent Flow Through a Heated Square-Sectioned U-Bend," *Int. J. Heat Fluid Flow*, Vol. 6, pp. 171–180.

Kays, W. M., and Crawford, M. E., 1980, *Convective Heat and Mass Transfer*, McGraw-Hill, New York.

Kline, S. J., and McKlintock, F. A., 1953, "Describing Uncertainties in Single Sample Experiments," *Mechanical Engineering*, Vol. 75, Jan.

Metzger, D. E., Plevich, C. W., and Fan, C. S., 1984, "Pressure Loss Through Sharp 180 Degree Turns in Smooth Rectangular Channels," ASME *Journal of Engineering for Gas Turbines and Power*, Vol. 106, pp. 677–681.

Metzger, D. E., and Sahm, M. K., 1986, "Heat Transfer Around Sharp 180-deg Turns in Smooth Rectangular Channels," ASME JOURNAL OF HEAT TRANSFER, Vol. 108, pp. 500–506.

Metzger, D. E., Fan, C. S., and Plevich, C. W., 1988, "Effects of Transverse Rib Roughness on Heat Transfer and Pressure Losses in Rectangular Ducts With Sharp 180 Degree Turns," Paper No. AIAA-88-0166, presented at the AIAA 26th Aerospace Sciences Meeting, Jan. 11–14, Reno, NV.

Mori, Y., and Nakayama, W., 1967, "Study on Forced Convective Transfer in Curved Pipes (2nd Report, Turbulent Region)," *Int. J. Heat Mass Transfer*, Vol. 10, pp. 37–59.

Mori, Y., and Nakayama, W., 1971, "Study on Forced Convection Transfer in a Curved Channel With a Square Cross Section," *Int. J. Heat Mass Transfer*, Vol. 14, pp. 1787–1805.

Murthy, J. Y., and Chyu, M. K., 1987, "A Numerical Study of Laminar Flow and Heat Transfer in a Channel With a 180-Deg Bend," ASME Paper No. 87-HT-7.

Patankar, S. V., Pratap, V. S., and Spalding, D. B., 1975, "Prediction of Turbulent Flow in Curved Pipes," *J. Fluid Mech.*, Vol. 67, pp. 583–595.

Wagner, J. H., Kim, J. C., and Johnson, B. V., 1986, "Rotating Heat Transfer Experiments With Turbine Airfoil Internal Flow Passages," ASME Paper No. 86-GT-133.

Local Heat Transfer Coefficients Under an Axisymmetric, Single-Phase Liquid Jet

J. Stevens
Research Assistant.

B. W. Webb
Assistant Professor.
Mem. ASME

Department of Mechanical Engineering,
Brigham Young University,
Provo, UT 84602

The purpose of this investigation was to characterize local heat transfer coefficients for round, single-phase free liquid jets impinging normally against a flat uniform heat flux surface. The problem parameters investigated were jet Reynolds number Re, nozzle-to-plate spacing z, and jet diameter d. A region of near-constant Nusselt number was observed for the region bounded by $0 \le r/d \le 0.75$, where r is the radial distance from the impingement point. The local Nusselt number profiles exhibited a sharp drop for $r/d > 0.75$, followed by an inflection and a slower decrease thereafter. Increasing the nozzle-to-plate spacing generally decreased the heat transfer slightly. The local Nusselt number characteristics were found to be dependent on nozzle diameter. This was explained by the influence of the free-stream velocity gradient on local heat transfer, as predicted in the classical analysis of infinite jet stagnation flow and heat transfer. Correlations for local and average Nusselt numbers reveal an approximate Nusselt number dependence on $Re^{1/3}$.

Introduction

Impinging jets are widely used in industrial heat and mass transfer applications. Due to their high transfer coefficients, air jets have been widely used in the paper and textile industries for drying, while water jets have been used for controlled cooling in the glass and metal industries. Recently, there has also been interest in using the high heat transfer coefficients under impinging jets to deal with the escalating heat fluxes found in advanced technology VLSI circuits (Kiper, 1984; Yamamoto et al., 1987).

Impinging jets can be grouped according to several broad characteristics. In general, a jet is called a submerged jet if it is a gas jet issuing into a gas, or a liquid jet issuing into a liquid, and will be termed a free jet if it is a liquid jet issuing into a gas. In addition, impinging jets can be classified by their shape, their temperature relative to the surface against which they are impinging, whether the jet is oriented normally or obliquely with respect to the impingement surface, and whether the impingement surface is flat or curved.

The purpose of this investigation was to characterize local heat transfer coefficients for round, single-phase free liquid jets impinging normally against a flat, constant-heat-flux surface. The problem parameters investigated were jet Reynolds number, nozzle-to-plate spacing, and jet diameter.

A significant amount of research has been published on various forms of jet impingement heat transfer. Only a representative sample of studies involving single-phase impinging liquid jets issuing into gas surroundings will be cited here.

Theoretical studies include work by Watson (1964) who used boundary layer theory to examine the fluid mechanics of an impinging liquid jet, and Chaudhry (1964) who treated the heat transfer aspect of the same problem and presented solutions for an isothermal impingement surface. In addition, Miyazaki and Silberman (1972) provided an analytical solution to a planar laminar jet striking a flat plate. A theoretical and experimental treatment of local heat transfer coefficients under a planar laminar water jet was offered by Inada et al. (1981). More recently, Wang et al. (1989a, 1989b) provided a theoretical treatment of the heat transfer under a laminar, axisymmetric, free liquid jet with nonuniform temperature or heat flux thermal boundary conditions.

Experimental studies were carried out by Jiji and Dagan (1987) for single jets and arrays of jets using water and FC-77 coolant for various heat source configurations. Average heat transfer data were reported. McMurray et al. (1966) investigated local heat transfer characteristics of a planar liquid jet striking a uniform heat flux plate at various impingement angles. Local heat transfer data were gathered by moving the instrumented heater relative to the jet stagnation plane. Metzger et al. (1974) examined experimentally the effect of Prandtl number on heat transfer for axisymmetric liquid jets. Average

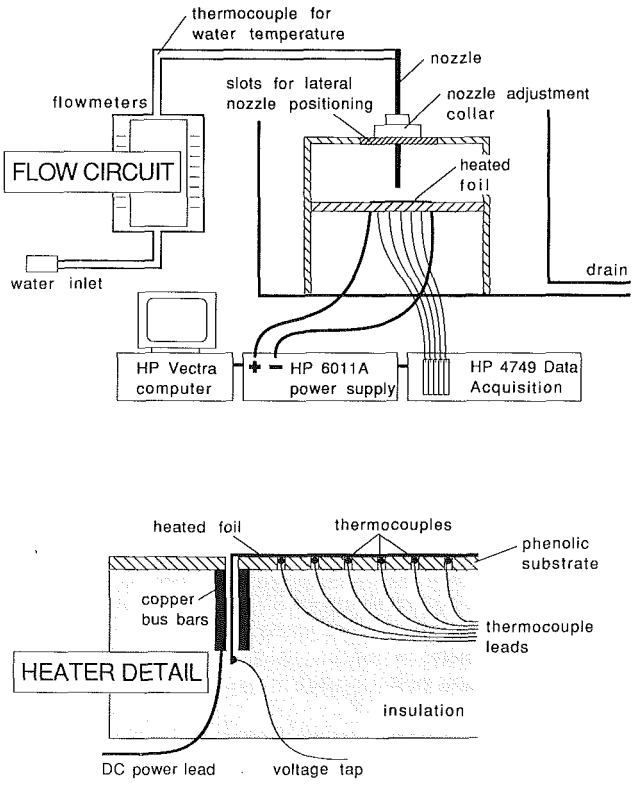

Fig. 1 Schematic of experimental apparatus

Contributed by the Heat Transfer Division and presented at the National Heat Transfer Conference, Philadelphia, Pennsylvania, August 6-9, 1989. Manuscript received by the Heat Transfer Division April 21, 1989; revision received May 14, 1990. Keywords: Electronics Equipment, Forced Convection, Jets.

heat transfer coefficient measurements were made for various heat source and nozzle diameter combinations using water and lubricating oil as the working fluids. The effects of Reynolds number, fluid Prandtl number, and ratio of heat source target to jet nozzle diameters on average heat transfer were correlated using the equation

$$\overline{\mathrm{Nu}} = 2.74\mathrm{Re}^{0.348}\mathrm{Pr}^{0.487}(2r/d)^{-0.774}(\mu_o/\mu_{aw})^{-0.37} \quad (1)$$

where μ_o and μ_{aw} are the fluid dynamic viscosities at the wall and free stream, respectively. Recently, the heat transfer characteristics of a single-phase, planar impinging jet were studied (Vader, 1988; Vader et al., 1990). Local heat transfer correlations were presented for various jet Reynolds numbers for a single nozzle size. Ma and Bergles (1988) examined experimentally the local heat transfer under a circular, submerged jet of R-113. Some measurements of free jet impingement were included for comparison with the submerged jet data.

The brief literature survey presented in the foregoing reveals no studies documenting the local heat transfer behavior of impinging, axisymmetric liquid jets. This paper reports on experimental work whose objective was to fill this critical gap in the jet impingement heat transfer data base. Local heat transfer coefficients under axisymmetric, single-phase liquid jets have been measured for a broad range of experimental parameters.

Experiments

An instrumented heated foil and metered flow delivery system were designed and constructed to permit determination of local heat transfer coefficients under a single-phase impinging water jet. The local heat transfer coefficient was calculated from measurements of the local electrical power dissipated at the heating element, and local heated surface and free-stream liquid temperature measurements. The apparatus and experimental method used in the study are described in more detail in sections to follow.

Experimental Apparatus. Figure 1 illustrates schematically the experimental apparatus used in this research. Water from a laboratory outlet passed through two flow meters, which provided a combined measurement range of 0.0063 to 0.76 L/s with accuracy of ±0.0006 L/s. A thermocouple in the pipe immediately downstream from the flow meters was used to measure the water temperature. The water was then directed into a glass tube, which served as a nozzle. The exit of the tube was carefully ground so as to be perpendicular to the tube axis. Glass tubes of inside diameter 2.2, 4.1, 5.8, and 8.9 mm were used as nozzles. All tubes were 38 cm long. This length was chosen in order to insure fully developed flow at the nozzle outlet (over 50 diameters for three of the nozzles, and 43 diameters for the other) since previous studies with air have indicated that the velocity profile at the jet exit may have a significant effect on the heat transfer results (Hrycak, 1984; Gardon and Akfirat, 1965). Test Reynolds numbers were chosen such that turbulent flow prevailed in all tests. The nozzle was secured in an aluminum collar mounted on a Lexan and steel frame (see Fig. 1). This insured that the jet impinged normally aginst the heated surface and permitted adjustment of the nozzle-to-plate spacing. The collar was attached to the top plate with screws, which passed through slots milled in the Lexan. This arrangement allowed the jet to be moved in a horizontal plane parallel to the heater. However, the horizontal movement was only intended for rough jet positioning. Hence, local heat transfer measurements were determined only from the thermocouple array mounted to the underside of the foil without utilizing the coarse movement capability of the nozzle to increase temperature measurement resolution. The second level of the frame held the heating plate.

A schematic cross section of the instrumented heating plate is illustrated in Fig. 1. The heating element consisted of a rectangular section of 0.0508-mm-thick stainless steel (type 302) shim stock. The shim stock was 1.5 cm wide, with 8.0 cm of length exposed to the jet. It was secured to a 20.3 × 20.3 cm piece of 1.59-mm-thick phenolic (printed circuit board material) using Dow Corning silicone rubber sealant. The silicone rubber was used in order to provide flexible adhesion in case of thermal expansion of the heating foil. The phenolic backing was prepared by using a numerically controlled mill to cut two slots, exactly 8.0 cm apart, through which the shim stock was passed. Twenty-eight holes, 1.5 mm in diameter on 2.5 mm centers, were drilled in the phenolic substrate for thermocouple placement. The mill was used in order to allow precise positioning of the thermocouple holes. After the shim stock was cemented in place, thermocouples (fabricated from 0.127-mm-dia Cu-Co wire) were inserted through the holes in the phenolic sheet and were attached directly to the shim stock with Loctite QM-50 epoxy. Intimate thermal contact between thermocouple beads and the heater strip was guaranteed by insuring electrical continuity between the heated foil and the thermocouple leads.

Possible electrical interaction between the d-c power employed in the Ohmic heating and the thermocouple beads affixed directly to the foil was considered in the apparatus checkout. Tests were conducted in a typical experimenal flow situation to insure that the d-c voltage gradient in the foil did not influence the thermocouple measurements. It was found that reversing the polarity of the d-c power supply (thus, reversing the direction of voltage gradient) resulted in less than 3 percent change in local Nusselt number near the stagnation point, with approximately 5 percent elsewhere. The variation is attributed to slightly different conduction losses in the bus bars due to transient heatup of the apparatus. In spite of the expected high heat transfer coefficients, the shim stock was characterized by a low local Biot number (typically 0.017–0.1) making it reasonable to assume that the temperature of the back surface of the shim stock was identical to the surface exposed to the fluid.

The water jet impinged against the center of the heating element and flowed radially off the sides of the lower Lexan plate where it was collected and directed to a drain. The heated foil was clamped firmly between 2.5 × 10 cm copper bus bars, which were connected with heavy copper wire leads to a 20-V, 120-A d-c power supply. Voltage and current measurements

Nomenclature

d = jet diameter
h = local heat transfer coefficient $= q_w/(T_s - T_\infty)$
k = thermal conductivity
Nu = local Nusselt number based on jet diameter $= hd/k$
Nu_o = stagnation point Nusselt number $= h_o d/k$
$\overline{\mathrm{Nu}}$ = average Nusselt number from stagnation point to radial distance $r = q_w d/k\overline{\Delta T}$
Pr = fluid Prandtl number $= \nu/\alpha$
q_w = wall heat flux imposed at the heating plate
Q = volume flow rate
r = radial distance from stagnation point
r_{hj} = radial distance to location of hydraulic jump
Re = Reynolds number based on jet diameter $= 4Q/\pi d\nu$
T_s = local surface temperature of the plate
T_∞ = jet exit temperature
U = infinite jet free-stream velocity, equation (4)
v = mean jet velocity at nozzle exit
z = nozzle-to-plate spacing
ν = kinematic viscosity

were made with remote sensing leads soldered to heating foil tabs extending through the bus bars, and were accurate to ±0.1 V and ±0.1 A. All thermocouples were read with an HP model 3497A data acquisition system with thermocouple compensation. The accuracy in temperature differences was estimated to be ±0.25°C.

Experimental Method. In determining appropriate power supply settings, it was found that 5 V produced approximately 50 A, and that this power rate provided temperature differences large enough to be accurately resolvable (minimum temperature differences typically greater than 4°C) without overheating the plate for most flow rates. The data acquisition system ran continuously during the test and recorded temperature scans at 15-s intervals. These continuous data sets provided a means for determining when a steady-state condition was reached after a change in operating conditions. At the beginning of each test run, the jet was centered over one thermocouple by moving the jet collar manually in the upper Lexan sheet until the temperatures were radially symmetric on both sides of a single thermocouple.

The data acquisition system collected temperature measurements continuously in time, so for each configuration, the beginning and ending scan numbers were recorded along with the water flow rate (read from the rotameters), nozzle-to-plate spacing (measured with a scale), power supply readings, and nozzle size (measured with precision calipers). After the test run was completed, the extraneous output gathered by the data acquisition system was eliminated so as to include only the scans between each starting and ending scan number. As stated previously, the system was allowed to reach steady state before each set of scans was begun. Hence, each set of multiple scans included only steady-state data. Temporally averaged temperature differences, jet Reynolds numbers, local heat transfer coefficients, local Nusselt numbers, and local average Nusselt numbers were then calculated from the experimental heat flux and local heated surface temperature data.

The temporally averaged temperature difference used in the determination of heat transfer coefficients was calculated by computing the mean difference between water temperature and local plate temperature for the set of scans corresponding to each test configuration. All water properties were evaluated at the jet inlet temperature. This approximation was valid near the stagnation point where temperature differences were small (of order 5°C), and less valid in the jet wings where temperature differences were as high as 30°C. It will be shown that the correlations presented here present only a lower bound for the local heat transfer in the jet wings. A temperature measurement was taken on the back of the phenolic plate in order to assess the heat loss through the plate. That loss was determined to be insignificant (less than 0.5 percent) and no correction was used. Thermocouple leads were drawn from the test apparatus along expected isotherms to minimize conduction losses there. Heat transfer coefficients were so high that conduction losses in the electrical bus bars were minimal.

When an axisymmetric free liquid jet impinges against a flat plate, a hydraulic jump forms in the liquid layer as it spreads over the plate. This is due to the deceleration of the fluid as it expands radially in an ever-thinning liquid layer. This hydraulic jump phenomenon was observed in this study, and with it a substantial decrease in local heat transfer coefficient (Stevens, 1988). However, all heat transfer data reported here were collected with the hydraulic jump located well beyond the edge of the heated plate. Because the hydraulic jump is an important issue in liquid jet impingement heat transfer, the location of the hydraulic jump was correlated and is characterized in a section to follow.

The maximum uncertainty in the local Nusselt numbers was determined to be approximately 8 percent using the method of Kline and McClintock (1953). A similar uncertainty should be applied to the local average data since they were derived by integrating the local data. The maximum uncertainty for Reynolds number values was calculated to be 6.8 percent. In light of these uncertainties, variations in Nu or $\overline{\text{Nu}}$ of less than 8 percent, and variations dependent on changes in Re of less than 7 percent, are not meaningful. The maximum uncertainty in radial position of the local temperature measurements was estimated to range from 4 percent of the nozzle diameter for the $d = 8.9$ mm nozzle, to 17 percent of the nozzle diameter for the $d = 2.2$ mm nozzle.

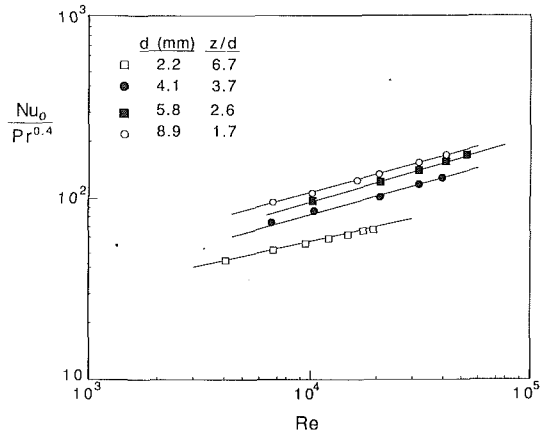

Fig. 2 Dependence of stagnation Nusselt number on Reynolds number for the four nozzle diameters studied

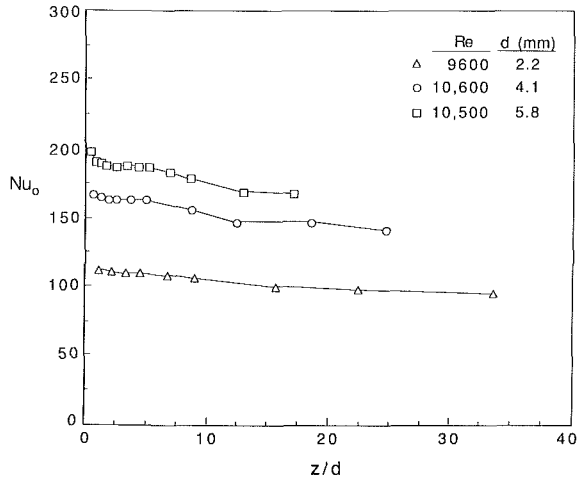

Fig. 3 Dependence of stagnation Nusselt number on nozzle-to-plate spacing, *z/d*

Results and Discussion

Local temperature data were collected using the experimental apparatus and reduced as described in the foregoing for nozzle sizes ranging from 2.2 to 8.9 mm and nominal jet Reynolds numbers ranging from 4000 to 52,000. Experimental results are presented in the sections that follow.

Stagnation Point Nusselt Number. Stagnation point Nusselt number data were collected and correlated over the full range of jet diameter, nozzle-to-plate spacing, and Reynolds number investigated. For the set of experimental data corresponding to each nozzle diameter, it was found that the Nu_o data correlated well with an equation of the form

$$\text{Nu}_o = A\text{Re}^q(z/d)^s\text{Pr}^{0.4} \tag{2}$$

where a multivariate least-squares curve fit was performed to determine the parameters A, q, and s. The Prandtl number

Table 1 Correlation coefficients for stagnation Nusselt number, equation (2)

Nozzle size (mm)		2.2	4.1	5.8	8.9
A		5.36	3.75	3.62	5.08
q		0.27	0.33	0.35	0.33
s		−0.052	−0.035	−0.032	−0.023

dependence for liquid jet impingement has been characterized with exponents ranging from 0.33 to 0.487 (Jiji and Dagan, 1987; Ma and Bergles, 1983; Metzger et al., 1974; Vader et al., 1990). A value of 0.4 was chosen for this study. Table 1 shows the values of the coefficients A, q, and s in equation (2) for the four nozzle diameters investigated.

Figure 2 shows a sample of the stagnation point Nusselt number dependence on Reynolds number for several data sets, along with the correlation for each given by equation (2). As observed by the exponent q in Table 1, the stagnation Nusselt number is described quite well by a power-law dependence on Reynolds number, $Re^{1/3}$. This compares favorably with the $Re^{0.348}$ relationship observed by Metzger et al. (1974). Although the Metzger correlation is for average Nusselt number, the Reynolds number dependence comparison for Nu_o as defined here is valid inasmuch as average Nusselt number scales directly with stagnation Nusselt number. While previous investigations of liquid jet impingement generally correlate as $Nu_o \propto Re^{1/2}$ (Wang et al., 1989a, 1989b; Ma and Bergles, 1988; Miyazaki and Silberman, 1972; Sitharamayya and Raju, 1969; McMurray et al., 1966), only the study by Metzger, et al., uses round, free liquid jets for the basis of the correlation, and none have investigated such a broad range in nozzle diameters as used in this study.

As reflected by the small exponent of z/d in Table 1, the effect of the nozzle-to-plate spacing on Nusselt number is slight. Figure 3 shows Nu_o plotted as a function of z/d for three nozzle sizes at a nominal Reynolds number of 10,000. The general trend is that of a slight decrease in Nu_o with increasing nozzle-to-plate spacing, z/d. This agrees qualitatively with the free jet Nu_o dependence on z/d of Ma and Bergles (1988), which is significantly less than for a submerged jet. There is no distinctive peak in the Nu_o versus z/d curves as reported for circular air jets by Hrycak (1983), and for plane air jets by Gardon and Akfirat (1966) and others. This can be explained by noting that those peaks were attributed to the formation of a potential core due to the effect of entrainment on the submerged jets. Such shear layer interaction and entrainment would be much less important for a free liquid jet. The z/d dependence may be characterized generally for all nozzle diameters using an exponent of $s = -0.0336$ with little loss of correlation accuracy.

Noting the small exponent on z/d in Table 1, and examining the data of Figs. 2 and 3, one observes a distinct dependence of heat transfer on nozzle size. The Nusselt numbers rise consistently with nozzle diameter. The use of dimensionless parameters (Nu, Re, r/d, z/d) based on nozzle diameter does not eliminate dependence on d in the results. Previous work (Vader et al., 1990; Donaldson, 1971) indicates that the velocity gradient exercises a significant influence on the local heat transfer. This is further justified by the analytical solution for rotationally symmetric, laminar stagnation flow from an infinite jet (Burmeister, 1983). Theory reveals that the heat transfer coefficient is independent of r, and is given by

$$h = 1.013k(3C/\nu)^{1/2} \tag{3}$$

where the constant 1.013 is for $Pr = 10$ fluids, and the free-stream velocity distribution is assumed to be given $U = Cr$. The value of the velocity gradient is then given by

$$C = dU/dr \tag{4}$$

Although equation (3) is derived for the case of a constant-temperature surface with impingement by a normally impinging, laminar flow of infinite extent, it does demonstrate that the velocity gradient is an important parameter in stagnation flow. It may be postulated that the stagnation velocity gradient would still be important for the case of a turbulent, finite, free liquid jet under consideration here. Hence, it is not surprising that the stagnation heat transfer characteristics for the four nozzle sizes studied here differ, since the velocity gradient at the stagnation point is nozzle diameter dependent. Such a pronounced nozzle size dependence on the stagnation Nusselt number has not previously been reported in the literature. However, as explained previously, no other work has investigated *local* heat transfer over such a broad diameter range of free, turbulent liquid jets.

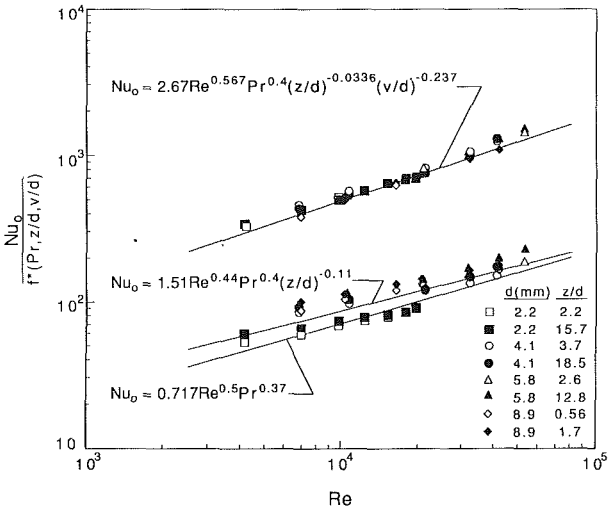

Fig. 4 Correlation of stagnation Nusselt number data using equations (6) and (7), and comparison with the laminar flow analysis of Wang et al. (1989a), equation (8)

The constant C is shown to represent the velocity gradient by White (1974), and is evaluated for a circular liquid jet as $0.88\,(v/d)$ by Wang et al. (1989a) and Nakoryakov et al. (1978) using a laminar flow field. Substitution of this expression into equation (3) yields the result that Nu is proportional to $Re^{1/2}$. This is also Wang's finding (1989a), and is identical to Sibulkin's solution (1952) in the stagnation region for constant heat flux or constant temperature thermal boundary conditions

$$Nu_o = 0.938Re^{1/2} / \int_0^\infty \exp\left[-2Pr\int_0^\eta \phi d\eta\right] d\eta \tag{5}$$

where ϕ is the similarity function describing the flow field. While the Reynolds number dependence may differ, it seems reasonable to assume that the parameter v/d would also describe functionally the stagnation velocity gradient in a turbulent, finite jet. It is recognized that the influence of turbulence may result in a nonlinear dependence of the velocity gradient, dU/dr, on the term v/d. In addition, a consideration of mass and momentum near the stagnation point supports the use of v/d as a velocity gradient scaling parameter. The disadvantage is that v/d is a dimensional quantity of units s^{-1} and there is no obvious reference time scale for use in its normalization.

Inclusion of the velocity gradient as an important parameter leads to $(dU/dr)(d/v)$ as the obvious nondimensional velocity gradient. Unfortunately, no independent method for measuring dU/dr was available in this investigation, leaving only the dimensional term v/d to estimate dU/dr as discussed above. Inasmuch as the proposed velocity gradient effect was originally manifest as a nozzle diameter dependence, and since both turbulence and the finite nature of the jet are presumed to be important, an alternative approach would be to use a dimensionless turbulence characterization parameter of the form $d/$

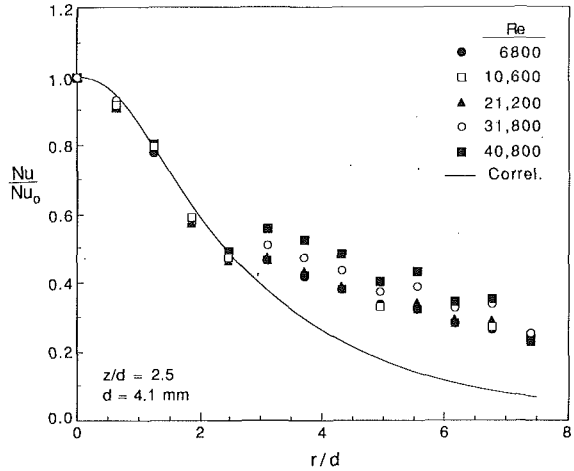

Fig. 5 Normalized local Nusselt number profiles and correlation equation (10) for all Reynolds numbers studied, $z/d = 2.5$, $d = 4.1$ mm

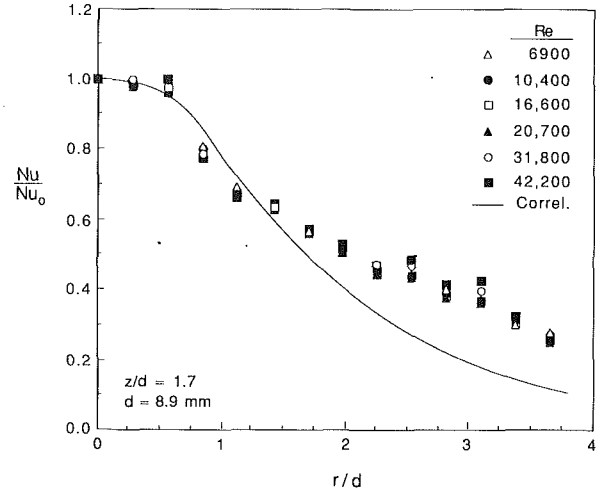

Fig. 6 Normalized local Nusselt number profiles and correlation equation (10) for all Reynolds numbers studied, $z/d = 1.7$, $d = 8.9$ mm

l, where l is the turbulent length scale of the flow. Unfortunately, this approach breaks down since l is proportional to d for fully developed pipe flow (Schlichting, 1968). However, if v/d is employed as a correlating parameter, the dependence of Nu_o on nozzle diameter vanishes and the four correlations of equation (2) and Table 1 collapse to a single expression

$$Nu_o = 2.67Re^{0.567}Pr^{0.4}(z/d)^{-0.0336}(v/d)^{-0.237} \quad (6)$$

where v is expressed in m/s and d in m. Experimental data representing the full range of z/d studied are plotted in Fig. 4 along with equation (6) in the form $Nu_o/f^*(Pr, z/d, v/d)$ where $f^*(Pr, z/d, v/d)$ is the relationship describing the functional dependence on Pr, z/d, and v/d appropriate to the correlation. Also included in Fig. 4 are the same set of experimental stagnation Nusselt number data and the corresponding correlation of all data *without* employing v/d as a correlating parameter. That empirical relation is given by

$$Nu_o = 1.51Re^{0.44}Pr^{0.4}(z/d)^{-0.11} \quad (7)$$

Equation (6) predicts the experimental data with an average and maximum error of 5 and 14 percent, respectively, for all nozzle sizes, jet-plate spacings, and jet Reynolds numbers investigated, a total of 228 tests representing different nozzle diameters and geometric and flow conditions. By contrast, the average and maximum error in equation (7) are 15 and 60 percent, respectively. Also shown in Fig. 4 is Wang's laminar flow solution (1989a) to equation (5), which has been solved over the range of Prandtl number $0.5 \le Pr \le 50$, and which is correlated very well by the equation

$$Nu_o = 0.717Re^{0.5}Pr^{0.37} \quad (8)$$

The significantly better accuracy of correlating equation (6) lends support to the idea that the (stagnation) heat transfer is dependent on the local velocity gradient, and hence, will be strongly affected by the nozzle diameter. As is expected, the experimental data generally exhibit higher heat transfer than the laminar analysis, equation (8), due to the influence of jet turbulence on the heat transfer.

Local Nusselt Number. Figures 5 and 6 show plots of the local Nusselt number normalized by Nu_o for the $d = 4.1$ and 8.9-mm-dia nozzles, respectively. Correlations for Nu/Nu_o to be developed in subsequent sections are also included in the figures. Since the data were symmetric about the stagnation point to within 5 percent, only half-profiles were plotted. Examination of local Nusselt number plots yielded several interesting observations.

First, in the region corresponding approximately to $r/d < 2$–3, it is seen that Nu/Nu_o is nearly independent of Reynolds number, with all curves collapsing to a single profile. Since the dependence on z/d is slight, Nu/Nu_o can be considered to be a function only of r/d in this region. At points far from the stagnation point, a Reynolds number dependence appears in the Nu/Nu_o profiles and the curves diverge. This Re dependence is believed due to a transition to turbulent flow and heat transfer in the flow along the plate, and is discussed in more detail in a section to follow.

Second, the local heat transfer profiles exhibit a region of constant Nu from the stagnation point out to a distance of approximately $r/d = 0.75$, seen most clearly for the largest nozzle (Fig. 6). This is consistent with the classical analytical result for rotationally symmetric stagnation flow of an infinite jet referred to in the foregoing, where the heat transfer coefficient is predicted to be independent of radial position (Burmeister, 1983). Since the flow of a finite liquid jet such as those used in this study would approximate an infinite jet flow very near the stagnation point, one would expect that the Nusselt number would be constant in that region. The near-constant Nu profile observed near the stagnation point for the largest nozzle is evidence of this effect. The absence of such a constant-Nu region for the smaller nozzles can be explained by noting that the thermocouples were located at fixed radial positions, so for the smaller nozzles the spatial resolution of heated surface temperature measurements was insufficient to show the constant-Nu region. Presumably, more finely resolved measurements on the smallest nozzle would show a flat region around the stagnation point similar to the profiles for the largest nozzle.

Third, a sharp knee appears in all local data profiles beyond which the Nu/Nu_o profiles separate and a dependence on Reynolds number surfaces. This knee was located at approximately $r/d = 5.0$, 2.5, 1.75, and 0.9 in the 2.2, 4.1, 5.8, and 8.9-mm-dia nozzle data, respectively (Stevens, 1988). In all cases, Nu/Nu_o drops off rapidly until it reaches the knee, then either flattens out and decreases more slowly thereafter, or rises briefly to a secondary maximum in the profile. These secondary peaks were found to appear at higher Re for the two smaller nozzles. When such a peak occurs, its beginning always coincides with the knee discussed above, and it becomes more pronounced with increasing Re. For the smallest nozzle the peak occurred at $r/d \approx 5.5$ and was evident for $Re > 12{,}400$ in all but the smallest nozzle-to-plate spacing. For the $d = 4.1$ mm nozzle, the secondary peak appears at $r/d \approx 3$ and occurs for $Re > 21{,}000$ (see Fig. 5). The secondary peaks were less prominent in the two largest nozzles. Examination of the profiles for the $d = 4.1$ mm diameter nozzle (Fig. 5) shows that the

Table 2 Correlation coefficients for local Nusselt number, equations (9) and (10)

Nozzle size (mm)		2.2	4.1	5.8	8.9
a		1.15	1.34	1.48	1.57
b		−0.23	−0.41	−0.56	−0.70

knee discussed above becomes more pronounced with increasing Re until, first, a region of constant Nu develops, then a secondary peak appears for the highest Reynolds numbers. This suggests that flat regions in the profiles with higher Re for the larger nozzles might be precursors to secondary peaks, which could have been observed had even higher Re been measured.

Similar secondary peaks were observed for circular air jets by Hrycak (1983) for $z/d > 6$, and in slot air jets for very small nozzle-to-plate spacings by Korger and Krizek (1966), and Gardon and Akfirat (1966), and were attributed to the transition from a laminar to turbulent boundary layer. In addition, similar peaks were observed in plane water jets (Inada et al., 1981; Vader et al., 1990). In this study, both the knee and the secondary peak in the profiles are attributed to the transition from a laminar to turbulent boundary layer in the parallel flow region along the plate.

Correlation of Local Nusselt Number. The development of an empirical correlation for the local Nusselt number behavior was influenced by two observations. First, as discussed in the foregoing, upstream of the transition point, Nu/Nu_o is a function only of r/d. Second, the presence of the near-constant-Nu section in the profile at small r/d suggested the use of two asymptotes: a constant heat transfer coefficient asymptote for $r/d < 0.75$ (motivated by the constant Nu result of the analytical solution for an infinite jet), and an exponential asymptote between $r/d = 0.75$ and the transition point. In all cases, the knee in the profile was taken to be the location of the transition point.

In consideration of the first point, it was decided to formulate correlations for the local Nusselt number profiles based on the normalized curves (Nu/Nu_o), with independent correlations for Nu_o as outlined in equation (6).

From the general shape of the normalized curves, a correlation was chosen of the form

$$f(r/d) = ae^{b(r/d)} \tag{9}$$

(where a and b are constants determined for each nozzle) for the region between $r/d = 0.75$ and the transition point. In order to make an appropriate transition between the constant-Nu ($r/d < 0.75$) and exponential-Nu ($r/d > 0.75$) regimes, a procedure suggested by Churchill and Usagi (1972) was used. This consists of using a correlation equation of the form:

$$Nu/Nu_o = [C^{-P} + f(r/d)^{-P}]^{-1/P} \tag{10}$$

where C is the small r/d asymptote, $f(r/d)$ [from equation (9)] is the exponential asymptote, and P is an exponent to be determined. Since the local Nusselt numbers were normalized by the stagnation Nusselt number, $C = 1$. For each nozzle, the normalized data between $r/d = 0.75$ and the transition point were fit with least-squares regression to determine the coefficients for the exponential function. Then, the parameter P from equation (10) was determined by using a least-squares fit of all of the normalized data, and was found to be relatively insensitive to nozzle diameter. A value of $P = 9.0$ may be used with good accuracy in the correlation equation (10). Table 2 shows the other correlation coefficients used.

Figures 5 and 6 include samples of the local Nusselt number correlation given by equations (9) and (10). This correlation applies only to the region before transition occurs at approximate r/d locations of 5.0, 2.5, 1.5, and 1.0 for the 2.2, 4.1, 5.8, and 8.9 mm diameter nozzles, respectively. Beyond that point, the correlation serves as a lower bound on the local heat transfer, but does not accurately predict the Nu/Nu_o data. In the spatial region prior to transition to turbulent flow, equation (10) represents 87 percent of the data within ±15 percent, and 96 percent of the data within ± 20 percent.

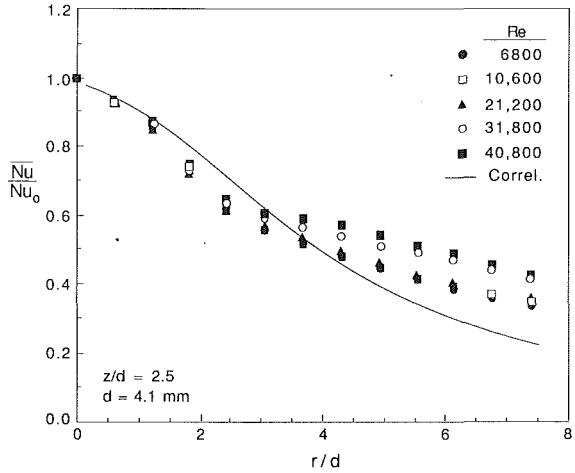

Fig. 7 Normalized local average Nusselt number profiles and correlation equation (13) for all Reynolds numbers studied, $z/d = 2.5$, $d = 4.1$ mm

Average Nusselt Number. The local average Nusselt number was calculated by integrating the experimental local Nusselt number data using the usual definition for isoflux heating

$$\overline{Nu}/Nu_o = (r/d)^2/2 \int_0^{r/d} \frac{(r'/d)d(r'/d)}{(Nu/Nu_o)} \tag{11}$$

where $\overline{Nu}$ is the average Nusselt number over the circular region from the stagnation point to r/d. The definition of equation (11) indicates that the average Nusselt number is based on the average temperature difference, $\overline{Nu} = q_w d/k\Delta\overline{T}$. Hence, for a given and spatially constant heat flux, the average temperature difference may be determined with a correlation for $\overline{Nu}$. In practice, the integration for the local Nusselt number in equation (11) was performed using the trapezoidal rule. Figure 7 is a plot of the normalized local average Nusselt number, $\overline{Nu}/Nu_o$, calculated according to equation (11) for the experimental data of Fig. 5. The local average Nusselt number profiles show Re and r/d dependence similar to the local results discussed above, except that the averaging tends to smooth the curves. Consequently, the secondary maxima observed in Fig. 5, attributed to transition from a laminar to a turbulent boundary layer, are not evident in the average heat transfer data of Fig. 7.

Since the local average Nusselt numbers were derived by numerically integrating the local Nusselt number data, the correlation for $\overline{Nu}/Nu_o$ may, in theory, be determined by substituting the expansion for Nu/Nu_o from equation (10) into equation (11), and performing the integration. The integration, however, is intractable. A new correlation for $\overline{Nu}/Nu_o$ was developed by integrating equation (9) with respect to r/d, yielding

$$g(r/d) = \frac{2}{(r/d)^2}\left\{\frac{f(r/d)}{b}\left[r/d - \frac{1}{b}\right] + \frac{a}{b^2}\right\} \tag{12}$$

The correlating procedure of Churchill and Usagi was used again with the new function $g(r/d)$ used as the high-r/d asymptote. The final form of the $\overline{Nu}/Nu_o$ correlation is

$$\overline{Nu}/Nu_o = [1 + g(r/d)^{-P'}]^{-1/P'} \tag{13}$$

The values for P' were determined by a new least-squares curve fit. As with the correlating parameter P in equation (10), the parameter P' of equation (13) was found to be relatively in-

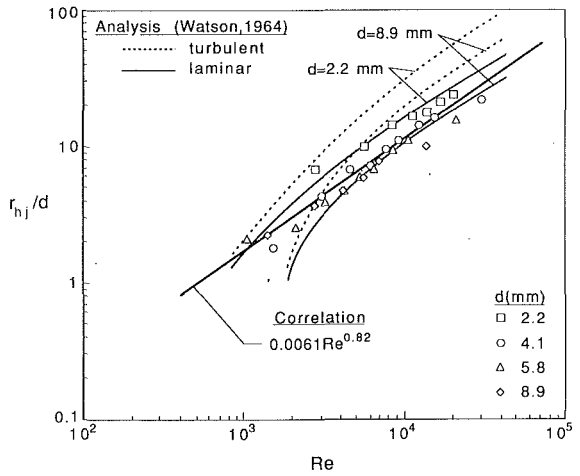

Fig. 8 Correlated location of the hydraulic jump as a function of jet Reynolds number

sensitive to nozzle diameter; a value of $P' = 7.0$ predicts the $\overline{Nu}/Nu_o$ data quite well. Again, considering only the spatial region prior to the transition to turbulent flow, equation (13) represents 89 percent of the data within ±10 percent and 99.7 percent of the data within ±15 percent. The correlation of the average Nusselt number is compared to the experimental data in Fig. 7.

Hydraulic Jump. As mentioned in the foregoing, an interesting effect that occurs when a liquid jet impinges vertically against a flat plate is the formation of a hydraulic jump as the fluid decelerates and spreads in a thin layer over the plate (Watson, 1964). As would be expected, a sharp decrease in the local heat transfer coefficient associated with the hydraulic jump was observed experimentally (Stevens, 1988).

Some coarse measurements of the dependence of the radial location of the hydraulic jump on Reynolds number were carried out. It should be noted that the location of the hydraulic jump oscillated in an unsteady manner, and could only be measured with an estimated accuracy of ±0.5 cm. Hence, the r_{hj}/d data exhibit considerable scatter. The jump location was correlated with Reynolds number using an equation of the form

$$r_{hj}/d = m\mathrm{Re}^n \tag{14}$$

Figure 9 illustrates the measured r_{hj}/d data along with the correlation. The correlation parameters $m = 0.0061$ and $n = 0.82$ predict the r_{hj}/d location with an average error of 15 percent. Watson's theoretical prediction (1964) for the location of the hydraulic jump for the two nozzle diameter extremes studied experimentally is also shown. The Reynolds number dependence for both laminar and turbulent flow is illustrated. The analysis requires knowledge of the liquid layer thickness downstream of the hydraulic jump, and a value of 3 mm was used based on crude measurements. Although the analysis shows rather poor quantitative agreement with the experimental data, the correct trends are predicted. For a given Reynolds number the diameter-normalized hydraulic jump location is smaller for the larger nozzles. Additionally, the analysis shows relatively good agreement in slope of the r_{hj}–Re relationship for $\mathrm{Re} > 4000$. Although the nozzle diameter clearly influences the location of the hydraulic jump in the experimental data, no attempt was made to quantify the relationship due to the obvious uncertainty in the data.

Conclusions

This investigation characterized local heat transfer coefficients for an axisymmetric water jet impinging normally against a flat, constant heat flux plate. It was found that Nusselt number varied with $\mathrm{Re}^{1/3}$ for a given jet diameter. A region of constant local heat transfer coefficient was discovered to prevail in the region bounded by $0 \le r/d \le 0.75$. Beyond there, local Nusselt number profiles exhibited a sharp drop, a bend in the profile, and a slower decrease thereafter. In some cases, a secondary peak occurred after the initial decrease. Where it appeared, this secondary peak was more pronounced with increasing Re. These secondary maxima were attributed to transition to a turbulent boundary layer. Nozzle-to-plate spacing was found to have only a minor effect on the magnitude of the local heat transfer. It was determined that the local heat transfer coefficient was clearly influenced by nozzle size, and this was explained in terms of the dependence on the free-stream velocity gradient. When this dependence was accounted for by including the velocity gradient scaling parameter v/d in the correlation, the nozzle size dependence vanished. A brief consideration of the hydraulic jump quantified its location as a function of jet Reynolds number.

Acknolwedgments

This work was supported by the National Science Foundation under Grant No. CBT-8552493.

References

Burmeister, L. C., 1983, *Convective Heat Transfer*, Wiley, New York.

Chaudhry, Z. H., 1964, "Heat Transfer in a Radial Liquid Jet," *Journal of Fluid Mechanics*, Vol. 20, pp. 501–511.

Churchill, S. W., and Usagi, R., 1972, "A General Expression for the Correlation of Rates of Transfer and Other Phenomenon," *AIChE Journal*, Vol. 18, No. 6, pp. 1121–1128.

Donaldson, C. D., Snedeker, R. S., and Margolis, D. P., 1971, "A Study of Free Jet Impingement, Part 2: Free Jet Turbulent Structure and Impingement Heat Transfer, *Journal of Fluid Mechanics*, Vol. 45, pp. 477–512.

Gardon, R., and Akfirat, J. C., 1965, "The Role of Turbulence in Determining the Heat Transfer Characteristics of Impinging Jets," *International Journal of Heat and Mass Transfer*, Vol. 8, pp. 1261–1272.

Gardon, R., and Akfirat, J. C., 1966, "Heat Transfer Characteristics of Impinging Two-Dimensional Air Jets," ASME JOURNAL OF HEAT TRANSFER, Vol. 88, pp. 101–108.

Hrycak, P., 1983, "Heat Transfer From Impinging Jets to a Flat Plate," *International Journal of Heat and Mass Transfer*, Vol. 26, pp. 1857–1865.

Hrycak, P., 1984, "Heat Transfer From Impinging Jets to a Flat Plate With Conical and Ring Protuberances," *International Journal of Heat and Mass Transfer*, Vol. 27, pp. 2145–2154.

Inada, S., Miyasaka, Y., and Izumi, R., 1981, "A Study on the Laminar-Flow Heat Transfer Between a Two-Dimensional Water Jet and a Flat Surface," *Bulletin of the JSME*, Vol. 24, pp. 1803–1810.

Jiji, L. M., and Dagan, Z., 1987, "Experimental Investigation of Single Phase Multi-Jet Impingement Cooling of an Array of Microelectronic Heat Sources," *Proceedings of the International Symposium on Cooling Technology for Electronic Equipment*, Pacific Institute for Thermal Engineering, HI, pp. 265–283.

Kiper, A. M., 1984, "Impinging Water Jet Cooling of VLSI Circuits," *International Communications in Heat and Mass Transfer*, Vol. 11, pp. 517–526.

Kline, S. J., and McClintock, F. A., 1953, "Describing Uncertainties in Single-Sample Experiments," *Mechanical Engineering*, Jan., pp. 3–12.

Korger, M., and Krizek, F., 1966, "Mass-Transfer Coefficient in Impingement Flow From Slotted Nozzles," *International Journal of Heat and Mass Transfer*, Vol. 9, pp. 337–344.

Ma, C. F., and Bergles, A. E., 1983, "Boiling Jet Impingement Cooling of Simulated Microelectronic Chips," in: *Heat Transfer in Electronic Equipment*, S. Oktay and A. Bar-Cohen, eds., ASME, New York, pp. 5–12.

Ma, C. F., and Bergles, A. E., 1988, "Convective Heat Transfer on a Small Vertical Heated Surface in an Impinging Circular Liquid Jet," *The Second International Symposium on Heat Transfer*, Vol. I, Beijing, China, pp. 248–255.

McMurray, D. C., Myers, P. S., and Uyehara, O. A., 1966, "Influence of Impinging Jet Variables on Local Heat Transfer Coefficients Along a Flat Surface With Constant Heat Flux," *Proceedings of the 3rd International Heat Transfer Conference*, Vol. 2, pp. 292–299.

Metzger, D. E., Cummings, K. N., and Ruby, W. A., 1974, "Effects of Prandtl Number on Heat Transfer Characteristics of Impinging Liquid Jets," *Proceedings of the 5th International Heat Transfer Conference*, Vol. II, pp. 20–24.

Miyazaki, H., and Silberman, E., 1972, "Flow and Heat Transfer on a Flat Plate Normal to a Two-Dimensional Laminar Jet Issuing From a Nozzle of Finite Height," *International Journal of Heat and Mass Transfer*, Vol. 15, pp. 2097–2107.

Nakoryakov, V. W., Pokusaev, B. G., and Troyan, E. N., 1978, "Impingement of an Axisymmetric Liquid Jet on a Barrier," *International Journal of Heat and Mass Transfer*, Vol. 21, pp. 1175–1184.

Schlichting, H., 1968, *Boundary Layer Theory*, McGraw-Hill, New York.

Sibulkin, M., 1952, "Heat Transfer Near the Forward Stagnation Point of a Body of Revolution, *Journal of Aeronautical Sciences*, Vol. 19, pp. 570–571.

Sitharamayya, S., and Raju, K. S., 1969, "Heat Transfer Between an Axisymmetric Jet and a Plate Held Normal to the Flow," *The Canadian Journal of Chemical Engineering*, Vol. 47, pp. 365–368.

Stevens, J. W., 1988, "Measurements of Local Heat Transfer Coefficients: Results for an Axisymmetric, Single-Phase Water Jet Impinging Normally on a Flat Plate With Uniform Heat Flux," M.S. Thesis, Brigham Young University, Provo, UT.

Vader, D. T., 1988, "Convective and Boiling Heat Transfer From a Heated Surface to an Impinging, Planar Jet of Water," Ph.D. Thesis, Purdue University, West Lafayette, IN.

Vader, D. T., Incropera, F. P., and Viskanta, R., 1990, "Local Convective Heat Transfer From a Heated Surface to an Impinging Planar Jet of Water," *International Journal of Heat and Mass Transfer*, in press.

Wang, X. S., Dagan, Z., and Jiji, L. M., 1989a, "Heat Transfer Between a Circular Free Impinging Jet and a Solid Surface With Nonuniform Wall Temperature or Heat Flux—1. Solution for the Stagnation Region," *International Journal of Heat and Mass Transfer*, Vol. 32, pp. 1351–1360.

Wang, X. S., Dagan, Z., and Jiji, L. M., 1989b, "Heat Transfer Between a Circular Free Impinging Jet and a Solid Surface With Nonuniform Wall Temperature or Heat Flux—2. Solution for the Boundary Layer Region," *International Journal of Heat and Mass Transfer*, Vol. 32, pp. 1361–1371.

Watson, E. J., 1964, "The Radial Spread of a Liquid Jet Over a Horizontal Plane," *Journal of Fluid Mechanics*, Vol. 20, pp. 481–499.

White, F. M., 1974, *Viscous Fluid Flow*, McGraw-Hill, New York.

Yamamoto, H., Udagawa, Y., and Suzuki, M., 1987, "Cooling System for FACOM M-780 Large-Scale Computer," *Proceedings of the International Symposium on Cooling Technology for Electronic Equipment*, Pacific Institute for Thermal Engineering, Honolulu, HI, pp. 96–109.

Effects of Vortices With Different Circulations on Heat Transfer and Injectant Downstream of a Row of Film-Cooling Holes in a Turbulent Boundary Layer

P. M. Ligrani
Associate Professor.

C. S. Subramanian
Adjunct Research Professor.

D. W. Craig
Graduate Student.

P. Kaisuwan
Graduate Student.

Department of Mechanical Engineering,
Naval Postgraduate School,
Monterey, CA 93943-5000

Results are presented that illustrate the effects of single embedded longitudinal vortices on heat transfer and injectant downstream of a row of film-cooling holes in a turbulent boundary layer. Attention is focused on the changes resulting as circulation magnitudes of the vortices are varied from 0.0 to 0.15 m^2/s. Mean temperature results are presented that show how injectant is distorted and redistributed by vortices, along with heat transfer measurements and mean velocity surveys. Injection hole diameter is 0.952 cm to give a ratio of vortex core diameter to hole diameter of about 1.5–1.6. The free-stream velocity is maintained at 10 m/s, and the blowing ratio is approximately 0.5. Film-cooling holes are oriented 30 deg with respect to the test surface. Stanton numbers are measured on a constant heat flux surface with a nondimensional temperature parameter of about 1.5. Two different situations are studied: one where the middle injection hole is beneath the vortex downwash, and one where the middle injection hole is beneath the vortex upwash. For both cases, vortex centers pass within 2.9–3.4 vortex core diameters of the centerline of the middle injection hole. To quantify the influences of the vortices on the injectant, two new parameters are introduced. S is defined as the ratio of vortex circulation to injection hole diameter times mean injection velocity. S1 is similarly defined except vortex core diameter replaces injection hole diameter. The perturbation to film injectant and local heat transfer is determined by the magnitudes of S and S1. When S is greater than 1–1.5 or when S1 is greater than 0.7–1.0, injectant is swept into the vortex upwash and above the vortex core by secondary flows, and Stanton number data show evidence of injectant beneath the vortex core and downwash near the wall for x/d only up to about 17.5. For larger x/d, local hot spots are present, and the vortices cause local Stanton numbers to be augmented by as much as 25 percent in the film-cooled boundary layers. When S and S1 are less than these values, some injectant remains near the wall beneath the vortex core and downwash where it continues to provide some thermal protection. In some cases, the protection provided by film cooling is augmented because of vortex secondary flows, which cause extra injectant to accumulate near upwash regions.

Introduction

In order to devise improved film cooling schemes to protect surfaces of components in high-temperature engines from the thermal loading that results from exposure to hot gases, designers must be able to account for the detrimental effects resulting from the presence of embedded longitudinal vortices. This is because, first, embedded vortices are abundant in many such components. Secondly, embedded vortices cause significant perturbations to local wall heat transfer distributions (Eibeck and Eaton, 1987), as well as to distributions of film coolant along with the accompanying thermal protection (Ligrani et al., 1989a; Ligrani and Williams, 1990). Of importance are the magnitudes of perturbations to wall heat transfer and injectant distributions as well as the spatial extents of these perturbations on high-temperature engine component surfaces. To determine such perturbations and extents, the designer must have knowledge of the effects of vortex strength, vortex size, and vortex location relative to a vast array of film cooling injection rates, hole sizes, geometries, and configurations.

The sizes and strengths of embedded longitudinal vortices are particularly varied in turbine blade passages of gas turbine engines. This is illustrated by the schematic of turbine passage flow shown in Fig. 1, which is a slightly modified version of a drawing that originally appeared in Ongoren (1981). At the intersection of the blade leading edge and end wall, a horseshoe or leading edge vortex develops as a result of the intense local pressure gradient, which forces fluid toward the end wall. The horeshoe vortex then splits into a suction side leg and a pressure side leg. As the pressure side leg further develops, it becomes the passage vortex and is influenced by the cross-passage static pressure gradient. Depending on the amount of blade loading, the suction side leg may reside at the intersection of the suction side and the endwall, or it may be pushed away from the endwall by the passage vortex from an adjacent blade, as shown. Corner vortices also develop at many locations, along with Taylor-Goertler vortices, which form near concave surfaces of turbine blades as a result of centrifugal instabilities. Several film injection hole configurations are also included in Fig. 1. Because of the complexity and variety of

Contributed by the Heat Transfer Division for publication in the JOURNAL OF HEAT TRANSFER. Manuscript received by the Heat Transfer Division September 11, 1989; revision received June 19, 1990. Keywords: Forced Convection, Turbines, Turbulence.

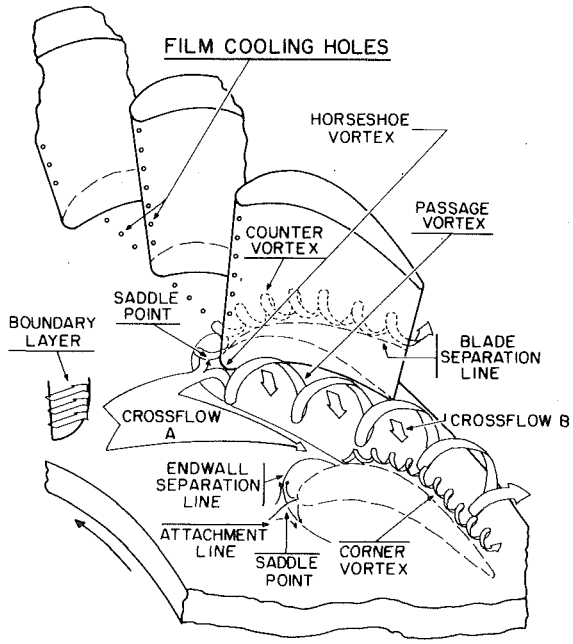

Fig. 1 Schematic of vortices in turbine blade passage

fluid/theral interactions between film injectant from such holes and the different embedded vortices, numerical modeling and prediction of these flows are not presently practical and experiments are needed to clarify physical behavior.

However, in spite of this, experimental studies of the interactions of embedded vortices and film cooling are relatively scarce. One of the earliest is reported by Blair (1974), who measured heat transfer on an endwall film-cooled using a slot inclined at a 30-deg angle. The large vortex located in the corner between the endwall and the suction surface of their cascade was believed to cause significant variations of measured heat transfer and film cooling effectiveness. Goldstein and Chen (1985, 1987) studied the influence of flows originating near the endwall on blade film cooling from one and two rows of holes. A triangular region was found on the convex side of the blade where coolant was swept away from the surface by the passage vortex.

Ligrani et al. (1989a) examined the influences of embedded longitudinal vortices on film cooling from a single row of film cooling holes in turbulent boundary layers. Each hole was inclined at an angle of 30 deg with respect to the test surface, and spaced three hole diameters from neighboring holes. Blowing ratios ranged from 0.47 to 0.98, and free-stream velocities were 10 m/s and 15 m/s. Surface heat transfer distributions, mean velocities, and mean temperatures are presented in this paper, which show that film coolant is greatly disturbed and local Stanton numbers are altered significantly by the secondary flows within vortices. Because characteristics of these secondary flows change around the vortex, the spanwise position of the vortex with respect to film cooling holes is very important. Secondary heat transfer peaks are also present that are associated with regions of high streamwise velocity (Ligrani, et al., 1988). These peaks become higher in magnitude and more persistent with downstream distance as the blowing ratio increases from 0.47 to 1.26.

To clarify the interactions between vortices and wall jets further, Ligrani and Williams (1990) then examined the effects of an embedded vortex on injectant from a single film-cooling hole in a turbulent boundary layer. Attention was focused on the effect of spanwise position of the vortices with respect to film injection holes. The ratio of vortex circulation to injection velocity times hole diameter was 3.16, and the ratio of vortex core size to injection hole diameter was 1.58. The main conclusion of this study is that injection hole centerlines must be at least 2.9–3.4 vortex core diameters away from the vortex center in the lateral direction to avoid significant alterations to wall heat transfer and distributions of film coolant.

Of studies on the effects of longitudinal embedded vortices (without wall injection), the reader is referred to Cutler and Bradshaw (1986), Eibeck and Eaton (1987), Mehta et al. (1983), Shabaka et al. (1985), and Westphal et al. (1987). Information on film cooling (without interactions with embedded vortices) is given by Subramanian et al. (1990) and Goldstein (1971).

The present study is different from these last seven citations because interactions between vortices and wall jets are considered. The present study extends results presented by Ligrani et al. (1989a) and Ligrani and Williams (1990) by focusing on the changes that result as vortex circulation is altered. Heat transfer, mean velocity components, and injection distributions are measured downstream of a row of injection holes inclined at 30 deg with a blowing ratio of 0.5. Two different situations are considered, both of which satisfy the Ligrani and Williams (1990) criteria for spanwise vortex locations that result in the most important interactions. For the first, the vortex upwash passes above the centerline of the middle injection hole such that the vortex center passes 0.87 vortex core diameters away in the positive spanwise direction. For the second, the vortex downwash passes above the centerline injection hole such that the vortex center passes 1.67 vortex core diameters away in the negative spanwise direction. Vortices are generated using a half-delta wing placed on the wind tunnel test surface, and vortex circulation is varied by changing the angle of attack of the delta wing.

With these results, additional physical understanding of the convective heat transfer processes as a result of an extremely complex shear layer interaction are provided. Such design information will lead to improved film-cooling configurations, which minimize the detrimental effects of vortex secondary flows on film-cooling protection. These results will ultimately result in lower thermal stress distributions, giving higher turbine inlet temperatures, more efficient engines, and improved power-to-weight ratios.

Nomenclature

A = vortex generator delta wing angle of attack
c = average vortex core radius
d = injection hole diameter
m = blowing ratio $= \rho_c U_c / \rho_\infty U_\infty$
S = nondimensional circulation $= \Gamma / U_c * d$
$S1$ = nondimensional circulation $= \Gamma / U_c * 2\ c$
St = Stanton number with vortex and film injection
St_o = baseline Stanton number, no vortex, no film injection
St_f = Stanton number with film injection and no vortex
T = static temperature
X, x = streamwise distance
Y = distance normal to the surface
Z = spanwise distance from test surface centerline
Γ = circulation of streamwise vorticity
θ = nondimensional injection temperature $= (T_{rc} - T_{r\infty}) / (T_w - T_{r\infty})$
ξ = unheated starting length
ρ = density

Subscripts

c = injectant at exits of injection holes
r = recovery condition
w = wall
∞ = free-stream

Table 1 Vortex generator spanwise positions for different vortex strengths

Vortex	Vortex generator angle A (deg)	Spanwise Z locations of the generator base edge for vortex spanwise position e	Spanwise Z locations of the generator base edge for vortex spanwise position h
r	18	0.00	+3.80
w	15	−0.51	+3.29
x	12	−1.53	+2.27
y	8	−3.56	+0.24
z	4	−4.07	−0.27

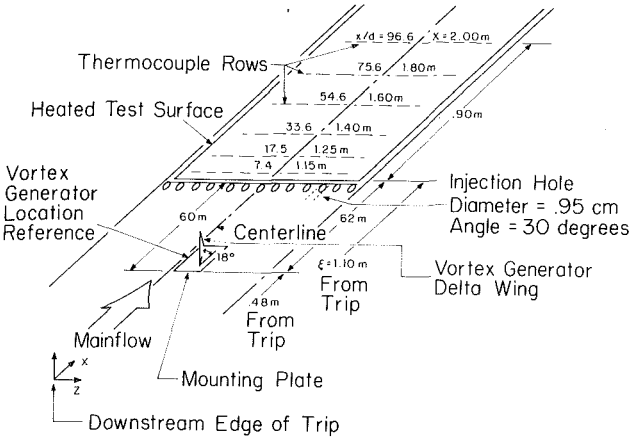

Fig. 2 Coordinate system and schematic of wind tunnel test section

Experimental Apparatus and Procedures

Wind Tunnel and Coordinate System. The wind tunnel is the same one used in the experiments of Ligrani et al. (1989a) and Ligrani and Williams (1990). The facility is open-circuit, subsonic, and located in the laboratories of the Department of Mechanical Engineering of the Naval Postgraduate School. A centrifugal blower is located at the upstream end, followed by a diffuser, a header containing a honeycomb and three screens, and then a 16-to-1 contraction ratio nozzle. The nozzle leads to the test section, which is a rectangular duct 3.05 m long and 0.61 m wide, with a topwall having adjustable height to permit changes in the streamwise pressure gradient.

A schematic showing the test section and coordinate system is presented in Fig. 2. The vortex generator base plate is shown to be located 0.48 m downstream of the boundary layer trip. The left edge of this base plate (looking downstream) is the base edge referred to in Table 1 as a location reference. The downstream edge of the row of 13 injection holes is then 0.60 m further downstream from this base plate. The surface used for heat transfer measurements is then located a short distance farther downstream. With this surface at elevated temperature, an unheated starting length of 1.10 m exists, and the direction of heat transfer is then from the wall to the gas. Thermocouple row locations along the test surface are also labeled in Fig. 2. In regard to the coordinate system, Z is the spanwise coordinate measured from the test section centerline, X is measured from the upstream edge of the boundary layer tip, and Y is measured normal to the test surface. x is measured from the downstream edge of the injection holes and generally presented as x/d.

Injection System. The injection system is described by Ligrani et al. (1989a) and Ligrani and Williams (1990). Of the thirteen injection holes, the one referred to as the middle hole is located on the spanwise centerline ($Z=0.0$ cm) of the test surface. Each hole has a diameter of 0.952 cm, is inclined at an angle of 30 deg with respect to the test surface, and is spaced 3 diameters from neighboring holes. Air for the injection system originates in a 1.5 h-p DR513 Rotron Blower capable of producing 30 cfm at 2.5 psig. From the blower, air flows through a regulating valve, a Fisher and Porter rotometer, a diffuser, and finally into the injection heat exchanger and plenum chamber. The exchanger provides means to heat the injectant above ambient temperature. With this system and test plate heating, the nondimensional injection temperature parameter θ was maintained at about 1.5 for all tests to maintain conditions similar to ones existing in gas turbine components. The plenum connects to 13 plexigless tubes, each 8 cm long with a length/diameter ratio of 8.4. With no vortex present, boundary layer displacement thickness at the injection location is $0.28d$.

Injection system performance was checked by measuring discharge coefficients, which compared favorably with earlier measurements. Procedures to measure discharge coefficients and blowing ratios are described by Ligrani et al. (1989a).

Experimental Approach. In order to isolate the interactions between film injectant and the vortices embedded in turbulent boundary layers, measurements are made on a flat plate in a zero pressure gradient. Wind tunnel speed is 10 m/s, and temperature differences are maintained at levels less than 30°C so that viscous dissipation is negligible and fluid properties are maintained approximately constant. With this approach, many of the other effects present in high-temperature engines are not present (curvature, high free-stream turbulence, variable properties, stator/blade wake interactions, shock waves, compressibility, rotation, etc.) since these may obscure and complicate the interaction of interest.

Detailed measurements are made in spanwise planes at different streamwise locations in order to elucidate the development and evolution of flow behavior. In order to match the experimental conditions found in many practical applications, the boundary layer, embedded vortex, and wall jet are all turbulent.

Mean Velocity Components. Three mean velocity components were measured using a five-hole pressure probe with a conical tip manufactured by United Sensors Corporation. Celesco transducers and Carrier Demodulators are used to sense pressures when connected to probe output ports. Following Ligrani et al. (1989b), corrections were made to account for spatial resolution and downwash velocity effects. The same automated traverse used for injectant surveys was used to obtain surveys of secondary flow vectors, from which mean streamwise vorticity contours were calculated. These devices, measurement procedures employed, as well as data acquisition equipment and procedures used are further detailed by Ligrani et al. (1989a, 1989c).

Stanton Number Measurements. Details on measurement of local Stanton numbers are given by Craig (1989), Kaisuwan (1989), Ligrani et al. (1989a), and Ligrani and Williams (1990). An overview of these procedures is repeated here for completeness.

The heat transfer surface is designed to provide a constant heat flux over its area. The surface next to the airstream is stainless steel foil painted flat black. Immediately beneath this is a liner containing 126 thermocouples, which is just above an Electrofilm Corp. etched foil heater rated at 120 V and 1500 W. Located below the heater are several layers of insulating

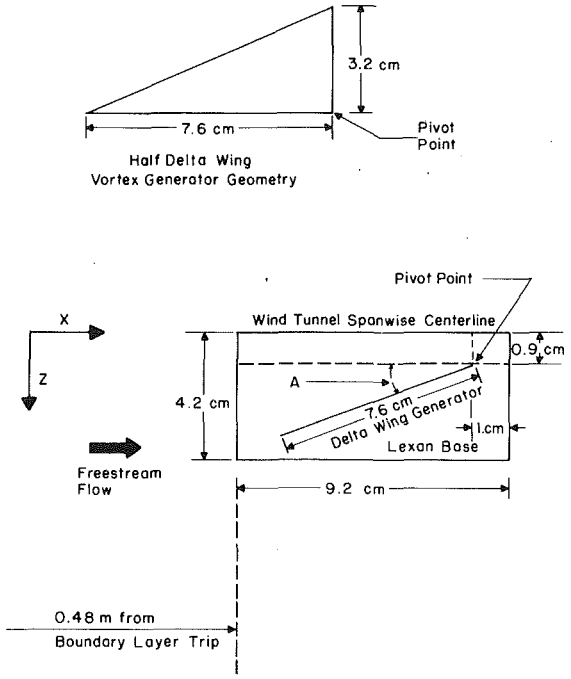

Fig. 3 Vortex generator geometry and orientations in the X-Z plane to produce vortices of different strength. Orientations given for vortex *r* (generator angle $A = 18$ deg) at spanwise position *e*: vortex downwash passes above the film-cooling hole.

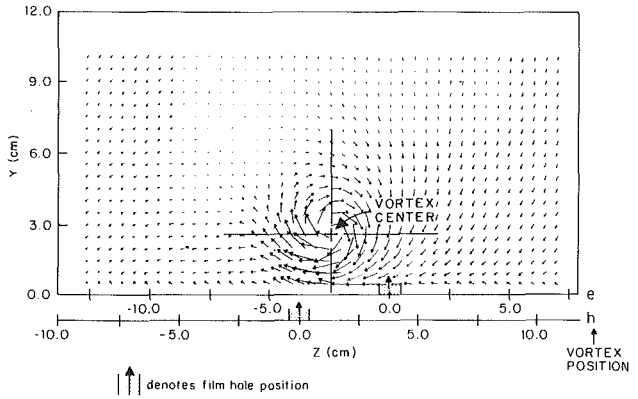

Fig. 4 Film-cooling injection locations with respect to vortex center and secondary flow vectors ($x/d = 0.0$) for vortex positions *e* and *h*. Each horizontal scale corresponds to a different vortex position where $Z = 0$ corresponds to the centerline of the injection hole located on the wind tunnel centerline.

materials including Lexan sheets, foam insulation, styrofoam, and balsa wood. Surface temperature levels and convective heat transfer rates are controlled by adjusting power into the heater using a Standard Electric Co. Variac, type 3000B. To determine the heat loss by conduction, an energy balance was performed. Radiation losses from the top of the test surface were analytically estimated. The thermal contact resistance between thermocouples and the foil top surface was estimated on the basis of outputs of the thermocouples and measurements from calibrated liquid crystals on the surface of the foil. This difference was then correlated as a function of heat flux through the foil.

After the surface was completed, a variety of qualification tests were conducted to check its performance. These are described in detail by Ortiz (1987).

Mean Temperature Measurements. Copper-constantan thermocouples were used to measure temperatures along the surface of the test plate, the free-stream temperature, as well as temperature distributions that are correlated to injection distributions. For the distributions, a thermocouple was traversed over spanwise/normal planes (800 probe locations) using an automated two-dimensional traversing system that could be placed at different streamwise locations. Ligrani et al. (1989a) and Ligrani and Williams (1990) give additional details including procedures used for calibration.

Baseline Data Checks. Baseline data with no film injection already exist for similar test conditions (Ligrani et al., 1989a). Repeated measurements of spanwise-averaged Stanton numbers show good agreement (maximum deviation is 5 percent) with the correlation from Kays and Crawford (1980) for turbulent heat transfer to a flat plate with unheated starting length and constant heat flux boundary condition. Local and spanwise-averaged Stanton numbers with injection at a blowing ratio of 0.5 (and no vortex) also show agreement with earlier results (Ligrani et al., 1989a). Further checks on measurement apparatus and procedures were made by measuring spatial variations of Stanton numbers along the test surface with different strength vortices (and no injection). These data are also consistent with other results in the literature (Eibeck and Eaton, 1987; Ligrani et al., 1989a) and are discussed later in the paper.

Experimental Uncertainties: Uncertainty analysis details are given by Schwartz (1988). Uncertainty estimates are based upon 95 percent confidence levels, and determined following procedures described by Kline and McClintock (1953) and Moffat (1982). Typical nominal values of free-stream recovery temperature and wall temperature are 18.0 and 40.0°C, with respective uncertainties of 0.13 and 0.21°C. The free-stream density, free-stream velocity, and specific heat uncertainties are 0.009 kg/m^3 (1.23 kg/m^3), 0.06 m/s (10.0 m/s), and 1J/kgK (1006 J/kgK), where typical nominal values are given in parentheses. For convective heat transfer, heat transfer coefficient, and heat transfer area, 10.5 W (270 W), 1.03 W/m^2 K (24.2 W/m^{2}K), and 0.0065 m^2 (0.558 m^2) are typical uncertainties. The uncertainties of St, St/St$_o$, m, and x/d are 0.000086 (0.00196), 0.058 (1.05), 0.025 (0.50), and 0.36 (41.9).

In percentages, uncertainties of these quantites are as follows: free-stream recovery temperature: 0.7; wall temperature: 0.5; free-stream density: 0.7; free-stream velocity: 0.6; specific heat: 0.1; convective heat transfer: 3.9; heat transfer coefficient: 4.3; heat transfer area; 1.2; St: 4.4; St/St$_o$: 5.5; m: 5.0; and x/d: 0.9.

Generation and Control of Vortex Characteristics

The device used to generate the vortices is shown in Fig. 3. The generator is a half-delta wing with 3.2 cm height and 7.6 cm base. The wing is attached to a base plate and rotated about the pivot point to give different generator angles, which in turn result in different vortex circulation magnitudes.

With half-delta wing generators, vortices are produced with secondary flow vectors such as the ones shown in Fig. 4. Here, as in Shabaka et al. (1985), regions of negative vorticity are observed around the main vortex, especially near $Z = -5.0$ cm for vortex position *e*. As vortex circulation becomes larger, secondary flow velocities between the main vortex center and the wall increase, and amounts of spanwise vortex drift increase as the vortices are convected downstream. Thus, if the pivot point is maintained at the same location, increasing angle A produces stronger vortices, which are located at more negative Z locations along the test surface.

In order to obtain systematic results as circulation is changed, the present study requires that the same portion of the vortex be located over the middle injection hole as the vortex passes. In other words, the distance between the centerline of the middle injection hole and vortex centers (located at local vorticity maxima) must be maintained con-

Table 2 Characteristics of embedded vortices (spanwise vortex position *e*): symbols for Fig. 7

Symbol	Vortex	Generator angle A (deg)	Maximum streamwise vorticity (1/s)	Circulation (m^2/s)	$2c/d$
●	*r*	18	760.	0.150	1.62
△	*w*	15	626.	0.116	1.52
◆	*x*	12	522.	0.085	1.49
◇	*y*	8	278.	0.041	1.42
▲	*z*	4	179.	0.019	1.51
○	no vortex	0	000.	0.000	—

Table 3 Characteristics of embedded vortices (spanwise vortex position *e*): labels for Figs. 6 and 8; symbols for Fig. 10

Fig. 10 symbols	Figs. 6 & 8 labels	Generator angle A (deg)	Maximum streamwise vorticity (1/s)	Circulation (m^2/s)	S	$2c/d$	$S1$
●	*r*	18	717.	0.134	2.81	1.61	1.75
△	*w*	15	694.	0.111	2.33	1.52	1.53
◆	*x*	12	556.	0.088	1.86	1.48	1.26
◇	*y*	8	328.	0.042	0.89	1.49	0.60
▲	*z*	4	127.	0.008	0.17	1.55	0.11
○	no vortex	0	000.	0.000	0.00	—	0.00

Table 4 Characteristics of embedded vortices (spanwise vortex position *h*): labels for Fig. 9; symbols for Fig. 11

Fig. 11 symbols	Fig. 9 labels	Generator angle A (deg)	Maximum streamwise vorticity (1/s)	Circulation (m^2/s)	S	$2c/d$	$S1$
●	*r*	18	763.	0.134	2.82	1.58	1.78
△	*w*	15	663.	0.108	2.28	1.53	1.49
◆	*x*	12	593.	0.079	1.67	1.50	1.11
◇	*y*	8	339.	0.043	0.91	1.45	0.63
▲	*z*	4	155.	0.010	0.26	1.49	0.17
○	no vortex	0	000.	0.000	0.00	—	0.00

stant. To accomplish this, spanwise locations of the vortices must be altered by changing positions of the generator mounting plate in the spanwise direction, as listed in Table 1.

The first step in determining the spanwise locations in Table 1 was to measure spanwise locations of local vorticity maxima as the delta wing angle A was changed, while maintaining constant the location of the generator pivot point (Fig. 3). The Z locations of these maxima at $x/d=0.0$ gave amounts of spanwise drift of the vortices at the streamwise location of the injection holes. The amount of required baseplate adjustment was then determined from these Z locations. Positions in Table 1 are then the ones that maintain constant vortex center locations with respect to the middle injection hole centerline, as the vortices pass this injection hole. Two sets of spanwise positions are then used, labeled *e* and *h* in Table 1 and Fig. 4.

The two sets of vortices produced, each with a different spanwise position, follow the same labeling scheme used by Ligrani and Williams (1990). Spanwise position *e* is the label for the first set. As shown in Fig. 4, the vortex *downwash* passes over the injection hole, and the vortex center is at -2.5 cm relative to the centerline of the test section. The second set of vortices are located at spanwise position *h*. In this case, the injection emerges beneath the vortex *upwash* and the vortex center is located $+1.3$ cm relative to the centerline of the centerline injection hole. For both cases, $Z=0.0$ locates the centerline of the middle injection hole and the centerline of the test surface. Secondary flow vectors in Fig. 4 were measured just downstream of the injection hole with the vortex at position *e* (Ligrani and Williams, 1990). The horizontal axis is then shifted in the figure so that the centerline of the middle hole is appropriately oriented with respect to the vortex center for both vortex spanwise positions.

Vortices with different circulation magnitudes are labeled *r*, *w*, *x*, *y*, and *z* in Tables 1, 2, 3, and 4, where a particular label

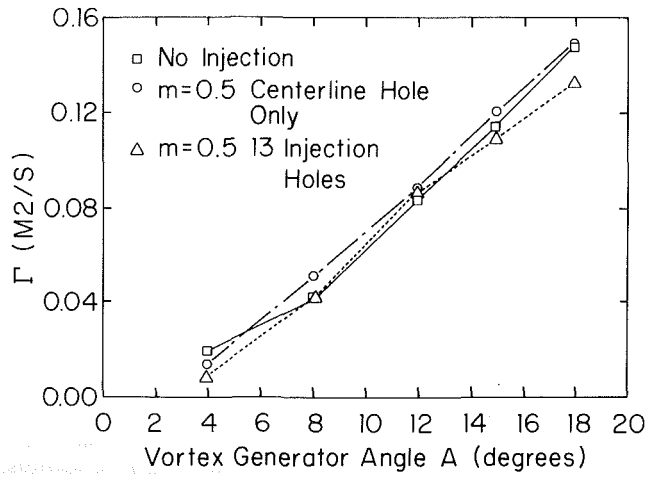

Fig. 5 Vortex circulation as dependent upon vortex generator angle as measured at $x/d=41.9$

applies to a particular generator delta wing angle. The same vortex labels are then used for both vortex spanwise positions (*e* and *h*) and whether or not injection is employed, which is important because vortex characteristics are often altered slightly by injectant. Table 2 gives characteristics of vortices *r*, *w*, *x*, *y*, and *z* with no injection when the vortices are located at spanwise position *e*. Tables 3 and 4 give characteristics of these vortices with $m=0.5$ injection for spanwise vortex positions *e* and *h*, respectively. All of these data were obtained from measurements at $x/d=41.9$. In these tables, *c* is the vortex core radius, determined as one half of the sum of average core radii in the Y and Z directions (as measured from vortex centers). These radii are determined for the area that

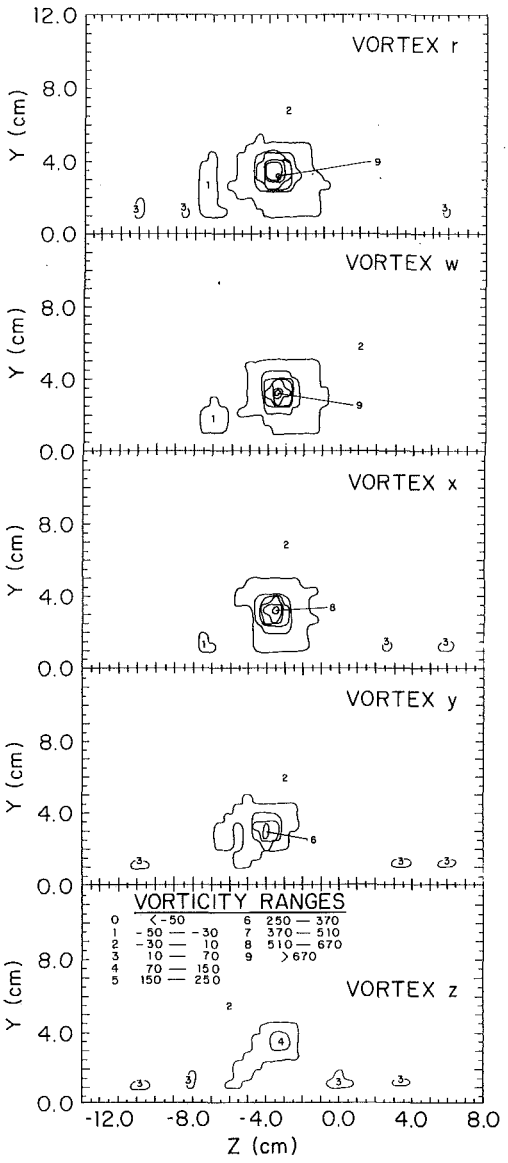

Fig. 6 Vorticity distributions for different vortex generator angles *A* at *x/d* = 41.9, *m* = 0.5, free-stream velocity = 10. m/s. Spanwise vortex position *e*: vortex downwash passes over the centerline injection hole. Labels given in Table 3.

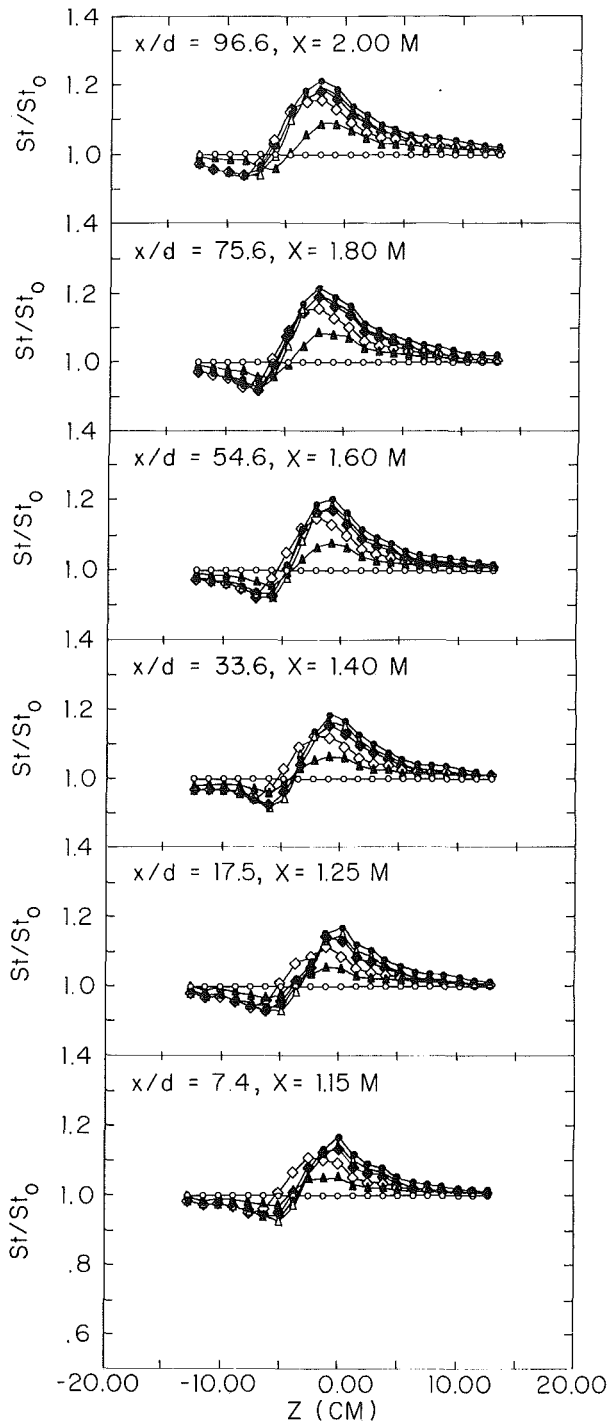

Fig. 7 Streamwise development of Stanton number ratios for different vortex strengths with no film cooling. Free-stream velocity = 10 m/s. Vortex properties measured at *x/d* = 41.9. Spanwise vortex position *e*: vortex downwash passes over the centerline injection hole. Symbols given in Table 2.

encompasses all vorticity values greater than or equal to 40 percent of peak vorticity (at the center) for a particular vortex. The choice of 40 percent was made to give a good match to core radii determined at the locations of maximum secondary flow vectors (Craig, 1989). The area enclosed by secondary flow maxima is important, because for ideal Rankine vortices, it corresponds to the ideal core, which contains *all* vorticity. Secondary flow vector maxima are not used to determine core size as this gives results that are less accurate than the 40 percent threshold approach (Craig, 1989). $2c/d$ then gives the ratio of vortex core diameter to injection hole diameter. Core sizes are about the same even though peak vorticity varies. $2c/d$ is then about 1.5–1.6 for vortices *r*, *w*, *x*, *y*, and *z* in Tables 2–4. Also contained in the latter two tables are parameters *S* and *S*1, which are discussed later in the paper.

Some of the data contained in Tables 2 and 3, as well as other data from Craig (1989), are plotted in Fig. 5, which shows that vortex circulation increases almost linearly with vortex generator angle *A*. Data are given for no injection, for injection from the centerline injection hole only, and for injection from all 13 injection holes in the row. Because of the similarities of these three sets of results, it is apparent that the injectant has little effect on vortex properties for a blowing ratio of 0.5. Circulation magnitudes are calculated assuming that all vorticity values less than a threshold are equal to zero. The same numerical threshold of 76. (1/s) is then used throughout this paper, chosen as the value equal to 10 percent of the maximum vorticity of vortex *r* with no injection (Table 2). Other studies to investigate the influences of vortex generator angle of attack on vortex properties include Eibeck and Eaton (1987) and Westphal et al. (1987). Westphal et al. (1987) employ criteria similar to the ones used in the present

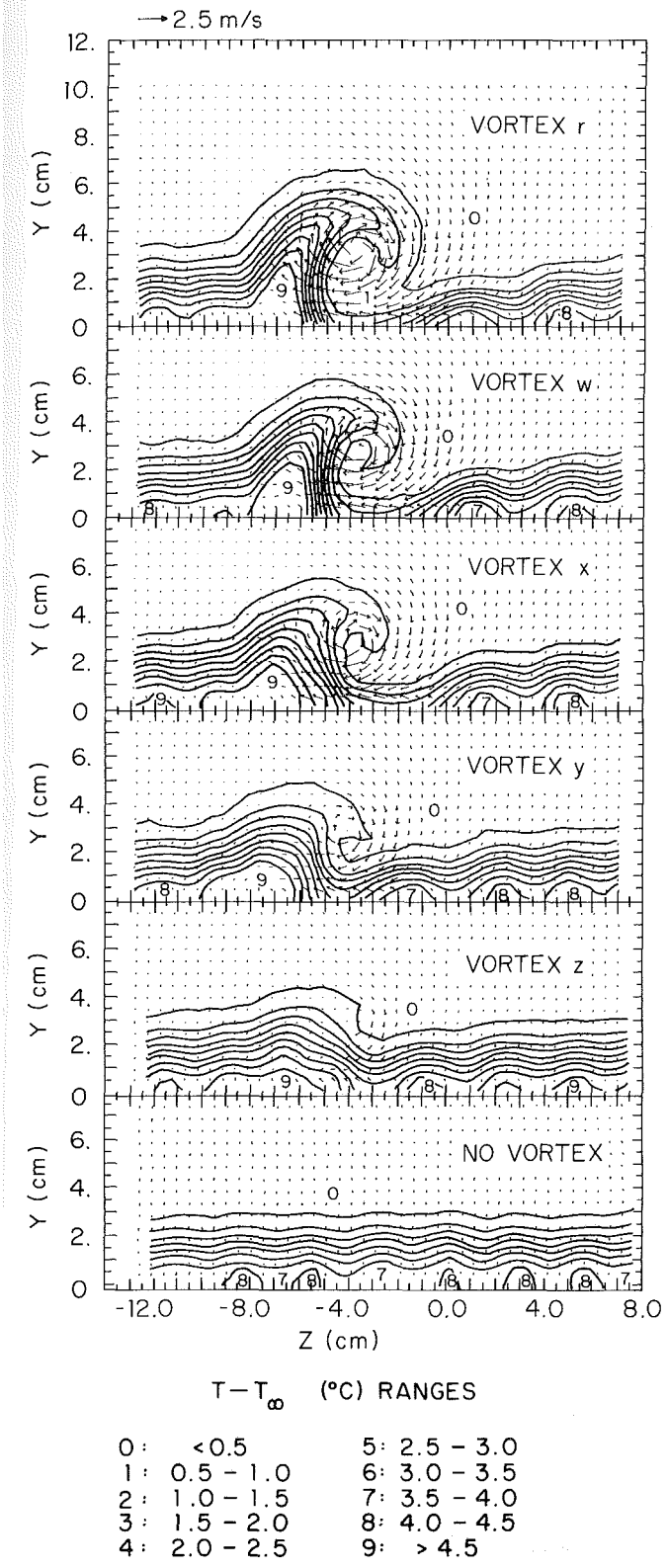

Fig. 8 Mean temperature field showing distributions of film injectant with secondary flow vectors at $x/d = 41.9$, $m = 0.5$, free-stream velocity = 10 m/s. Spanwise vortex position *e*: vortex downwash passes over the centerline injection hole. Labels given in Table 3.

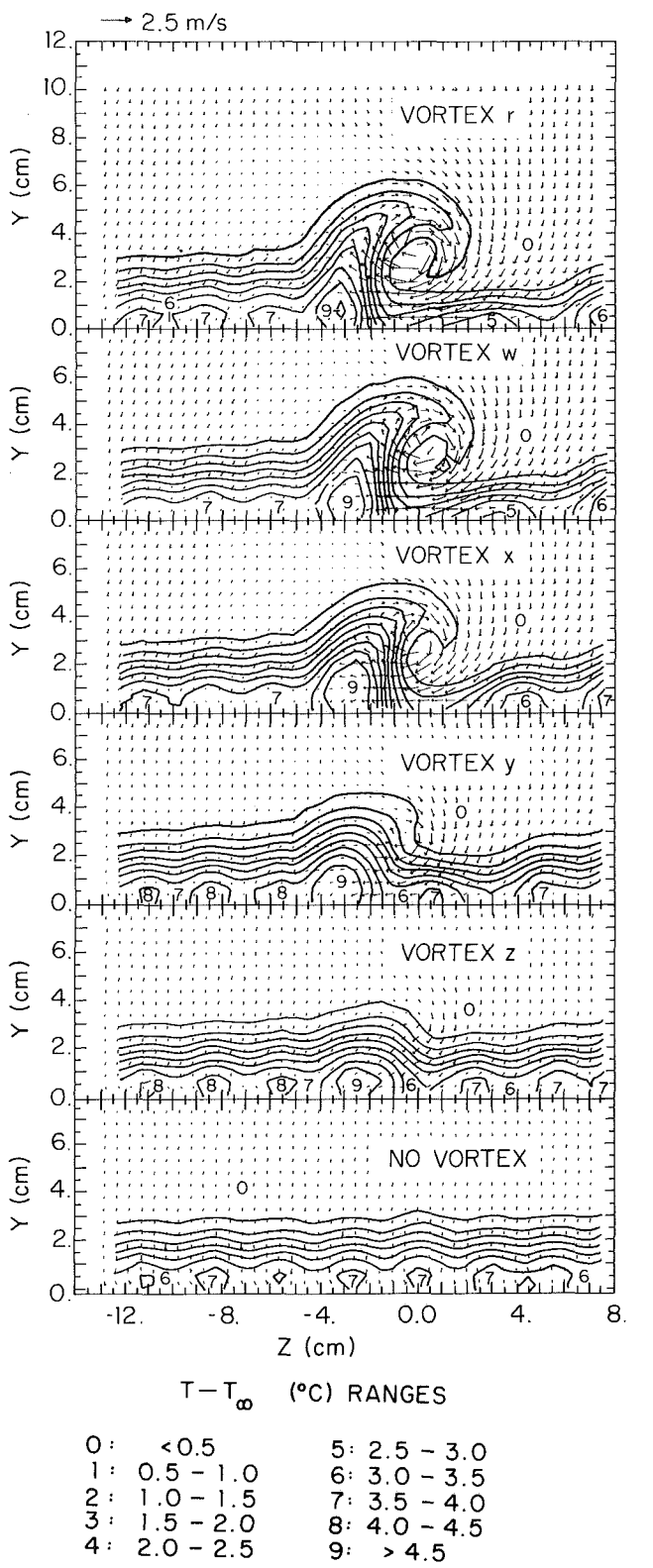

Fig. 9 Mean temperature field showing distributions of film injectant with secondary flow vectors at $x/d = 41.9$, $m = 0.5$, free-stream velocity = 10 m/s. Spanwise vortex position *h*: vortex upwash passes over the centerline injection hole. Labels given in Table 4.

study to determine circulations, center locations, and sizes of vortices, except vortex core length scales are based on vorticity levels that are 50 percent of maximum values.

In Fig. 6, mean streamwise vorticity distributions measured at $x/d = 41.9$ for $m = 0.5$ are presented for different vortex generator angles. Figure labels are given in Table 3. Sizes of the vortices and magnitudes of vorticity both increase as vortex generator angle increases from 0 to 18 deg. Higher levels of vorticity evidence larger gradients of secondary flow vectors as one moves away from the vortex center. Because the

vortex generators were oriented at spanwise vortex position *e*, as listed in Table 1, the centers of the different vortices are all at about the same location, i.e., $Y = 3.0$ cm ± 0.1 cm and $Z = -3.6$ cm ± 0.5 cm.

Heat Transfer and Injectant Distributions

In this section, experimental results are first presented, which illustrate the influences of embedded vortices on turbulent boundary layers with no film injection. The discussion then focuses on the interactions of the vortices with injectant from a single row of film cooling holes. For this part, addressed are the influences of the vortices on: (1) injectant distributions, and (2) local heat transfer variations. Here, data are presented for two different situations: one where the vortex centers are located at $Z = -2.5$ cm (spanwise position *e*), and one where vortex centers are located at $Z = +1.3$ cm (spanwise position *h*).

Heat Transfer Distributions as Dependent Upon Vortex Circulation for No Film Injection. In Fig. 7, Stanton number ratios are presented to illustrate the variations in heat transfer that result as the magnitude of vortex circulation is changed. Data are presented for x/d ranging from 7.4 to 96.6 to show streamwise development. Spanwise locations of the vortices are maintained at position *e*, and symbols used in Fig. 7 are given in Table 2 along with vortex characteristics for no injection.

If the vortices have no effect on heat transfer, St/St_o ratios in Fig. 7 are 1.0. Examination of results at any streamwise location for any magnitude of circulation indicates that ratios are greater than 1.0 on the right-hand sides of the figure as a result of vortex downwash regions, and less than 1.0 on left-hand sides due to upwash regions. Between these two regions, St/St_o gradients exist along the length of the test section. With the exception of data near the gradient for $x/d \leq 54.6$, St/St_o then increases with circulation in the downwash region and decreases with circulation in the upwash region. The largest changes occur as circulation increases from 0.0 m^2/s (no vortex) to 0.019 m^2/s (vortex *z*), and as circulation increases from 0.019 m^2/s to 0.041 m^2/s (vortex *y*). As circulation becomes greater than 0.085 m^2/s, St/St_o data are very similar qualitatively and quantitatively for vortices *r*, *w*, and *x*.

The streamwise coherence of the vortices is evident because ratio magnitudes are significantly different from 1.0 along the entire length of the test plate. In fact, in the downwash region, St/St_o increases with x/d until $x/d = 36.6$. After this, only very small changes with streamwise distance occur. With these characteristics, these data show agreement with qualitative trends and quantitative magnitudes reported by Eibeck and Eaton (1987) and Ligrani et al. (1989a).

Effects of Vortices on Distributions of Film Injection. Figures 8 and 9 quantify the distortion and rearrangement of injectant by different strength vortices. These data are given for a blowing ratio *m* of 0.5 at $x/d = 41.9$. Figure 8 is for spanwise vortex position *e*, where the vortex downwash passes over the middle injection hole, and Fig. 9 is for spanwise vortex position *h*, where the vortex upwash passes over the middle injection hole. Thus, data in Figs. 8 and 9 were obtained with the vortices passing within 2.9–3.4 core diameters of the injection hole; a situation chosen because it results in the greatest disturbance to injectant by vortices (Ligrani and Williams, 1990). In each figure, data are presented for vortices *r*, *w*, *x*, *y*, *z*, and for no vortex, where vortex properties and figure labels are given in Tables 3 and 4. As for the situation with no injection, the ratio of vortex core diameter to injection hole diameter, $2c/d$, is 1.5–1.6.

To quantify the influences of the vortex circulation on injectant, *S* is used, which is defined as

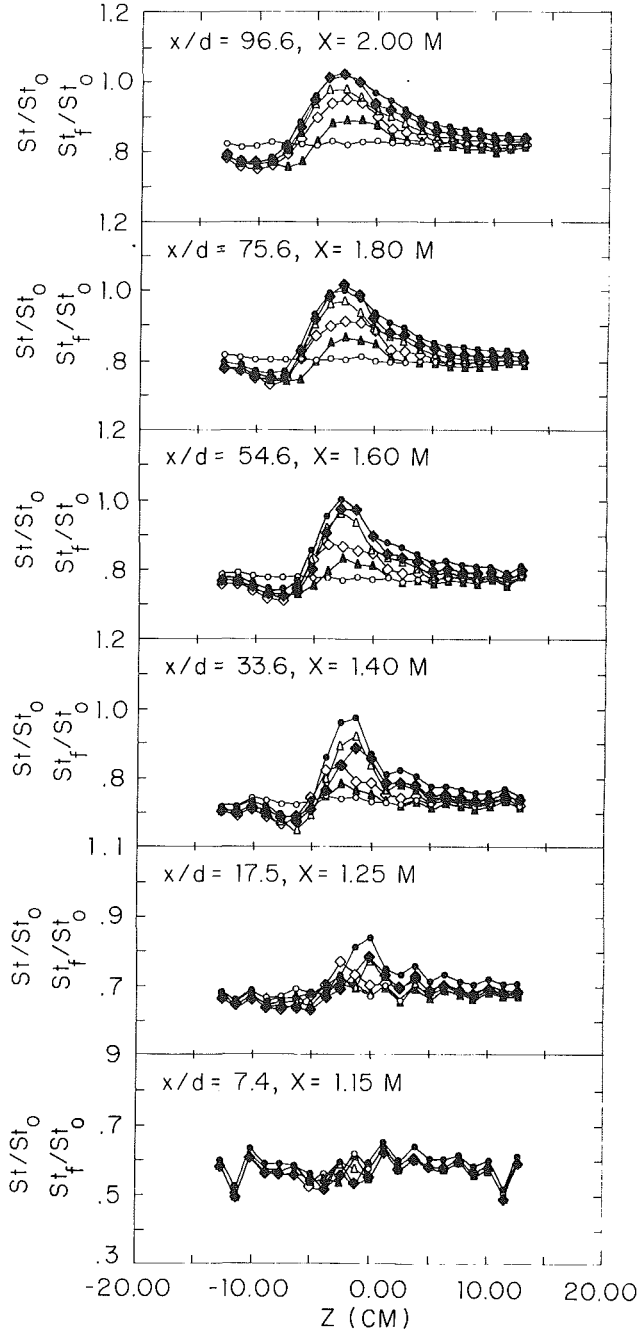

Fig. 10 Streamwise development of Stanton number ratios with film cooling for different vortex strengths. Spanwise vortex position *e*: vortex downwash passes above injection hole. Free-stream velocity = 10 m/s, vortex properties measured at $x/d = 41.9$. Symbols given in Table 3.

$$S = \Gamma / U_c^* d$$

As such, *S* quantifies vortex strength relative to injection jet strength. For all cases of the present study, U_c and *d* are not changed as the blowing ratio *m* is maintained constant and injection geometry is not altered. If *S* is multiplied by $d/2c$, the parameter $S1$ is obtained to account for vortex size

$$S1 = \Gamma / U_c^* 2c$$

For data in Figs. 8 and 9, *S* then ranges from 0.0 to 2.81 and $S1$ ranges from 0.0 to 1.78, where values for individual vortices are listed in Tables 3 and 4.

Measured secondary flow vectors are superimposed on each part of Figs. 8 and 9 to illustrate how their magnitudes and distributions relate to the reorganization of injectant by the

different vortices. The same scaling for secondary flow vectors is used throughout all parts of Figs. 8 and 9. Procedures to determine injectant distributions were developed by Ligrani et al. (1989a) and later also used by Ligrani and Williams (1990). In these studies and the present one, injectant distributions are qualitatively correlated to mean temperature distributions. To do this, injectant is heated to 50°C without providing any heat to the test plate. Thus, because the injectant is the only source of thermal energy (relative to free-stream flow), higher temperatures (relative to free-stream temperature) generally indicate greater amounts of injectant. The temperature field is therefore given as $(T-T_\infty)$, and as such, shows how injectant accumulates and is rearranged mostly as a result of convective processes from the boundary layer and vortex secondary flows. Diffusion of injectant heat accounts for some of the temperature variations observed between injection hole exits and measuring stations, but compared to convection, this is of secondary importance. Because the vortices of the present study are generated in the boundary layer, such levels of diffusion are higher than if vortices were generated in the free-stream by placing vortex generators in the settling chamber upstream of the nozzle (Shabaka et al., 1985).

The data in Fig. 8 were obtained with a vortex whose center passes -2.5 cm or -1.67 core diameters from the centerline of the middle injection hole (spanwise position *e*). Significantly different injectant distribtions are present for the different vortices. If no vortex is present, concentrations of injectant are present in the boundary layer near the wall spaced about 3.0 cm apart at the same interval as injection hole spacing ($3d$). With vortex *z*, which is relatively very weak, S equals 0.17 and $S1$ equals 0.11. Some distortion of the outer portion of the boundary layer is evident from $Z=-2$ cm to -6 cm where secondary flow vectors are largest. Little disturbance to the injectant occurs near the wall, except that small extra amounts of injectant accumulate from $Z=-5.0$ cm to -10.0 cm. A similar situation qualitatively is present for vortex *y* even though S is significantly greater, equal to 0.89 ($S1=0.60$). Added distortion of the film-cooled boundary layer is apparent, although the secondary flows in the vortex are still not strong enough to significantly disrupt injectant coverage near the wall. The boundary layer is thinned slightly near $Z=-4.0$ cm and some redistribution of injectant from the middle hole seems to occur since less injectant is present near $Z=0.0$ cm than at other locations where injectant nominally accumulates near the wall. As for vortex *z* data, extra accumulation of injectant is evident with vortex *y* from $Z=-6.0$ cm to -10.0 cm as a result of convection of injectant by secondary flows.

Significant distortion of injectant distributions and rearrangement of boundary layer fluid is evident with vortex *x* where S equals 1.86 and $S1$ equals 1.26. The data in Fig. 8 indicate that secondary flow vectors of vortex *x* are larger than ones for vortices *y* and *z*. For Z from 0.0 cm to -6.0 cm, significant boundary layer thinning with little evidence of injectant results with vortex *x*. Injectant, which is nominally present near $Z=3.0$ cm, is also partially depleted from secondary flow convection. These locations correspond to a high heat transfer region since the protection nominally provided by the injectant is significantly reduced. This situation results because the vortex *downwash* passes over the middle injection hole, and the vortex center passes above the injection hole just to the left of the middle hole (looking downstream). According to Ligrani et al. (1989a), with this situation, injectant is swept to the side of the vortex in a very efficient manner.

The disruption and rearrangement of injectant is even more severe for vortices *w* and *r* with respective S values of 2.33 and 2.81 ($S1=1.53$ and 1.75). As with vortex *x*, significant amounts of injectant are swept into the vortex upwash and above the vortex core by secondary flows, which increase in strength with S and $S1$. However, secondary flows for vortices

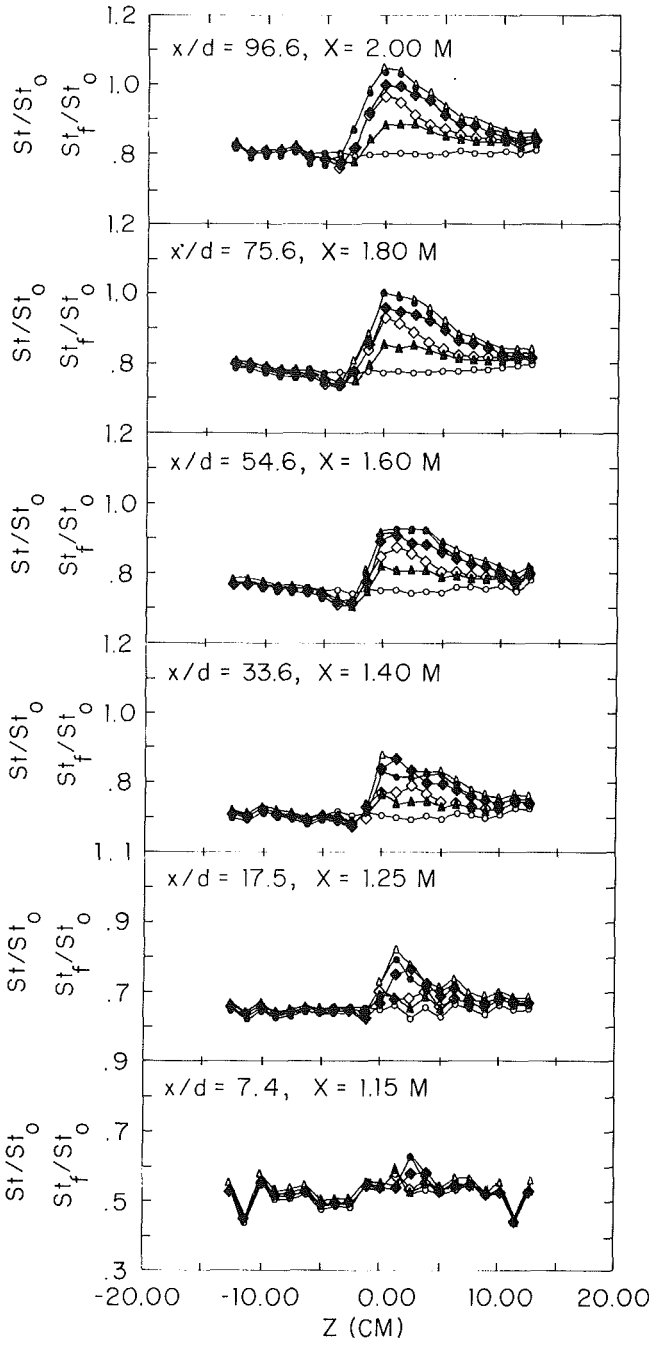

Fig. 11 Streamwise development of Stanton number ratios with film cooling for different vortex strengths. Spanwise vortex position *h*: vortex upwash passes above injection hole. Free-stream velocity = 10 m/s, vortex properties measured at *x/d* = 41.9. Symbols given in Table 4.

w and *r* are so intense that portions of injectant are also swept around the entire circumferences of the vortex cores. The disturbance is greatest when S equals 2.81 (vortex *r*). Here, the protection provided by injectant is minimized near the wall for Z ranging from -6.0 cm to 4.0 cm. As for other cases presented in Fig. 8, a large accumulation of injectant is evident for $Z<-6.0$ cm where low-velocity injectant collects, having initially emanated from injection holes located at $Z=0.0$ cm and $Z=-3.0$ cm. With vortex *r*, this injectant is then crowded into the same region where injectant nominally collects from holes located near $Z=-6.0$ cm and -9.0 cm.

Injectant distributions in Fig. 9 were obtained for spanwise vortex position *h*, a situation where the vortex *upwash* passes over the middle injection hole. In this case, the vortex center

passes only +1.3 cm or 0.87 core diameters away from the middle injection hole centerline, and the vortex center passes between two injection holes at $x/d = 0.0$. Ample evidence of injectant near the wall beneath downwash regions is apparent for vortices y and z. Values of S and $S1$ corresponding to these two vortices are 0.91 and 0.26, and 0.63 and 0.17, respectively, as presented in Table 4 along with other vortex properties. As S reaches 1.67 and $S1$ reaches 1.11 (vortex x), the distribution of injectant near the wall is disrupted significantly, a conclusion consistent with results in Fig. 8. The disruption then intensifies for S equal to 2.28 (vortex w) and 2.82 (vortex r), as expected. These results are different from the ones obtained with the middle hole beneath the downwash (Fig. 8) because: (1) Smaller amounts of injectant accumulate near the upwash side of the vortex as a result of secondary flow convection, and (2) regions where film cooling protection is minimized are smaller and contain more injectant, extending from $Z = 2.0$ cm to $Z = 6.0$ cm for vortex r. Thus, general qualitative trends are similar to the ones in Fig. 8, except the disruptions and distortions imposed on the injectant distributions are somewhat less. This trend is consistent with Ligrani et al. (1989a), whose main conclusion is that the spanwise location of the vortex with respect to injection holes is very important.

Viewing overall trends in Figs. 8 and 9, it is evident that secondary flows are responsible for depletion of injectant near the wall beneath the core and downwash, where local hot spots may develop. The perturbation to film injectant is quantified by the magnitudes of S and $S1$. When S is greater than 1–1.5 and $S1$ is greater than 0.7–1.0, a significant portion of injectant is swept into the vortex upwash and above the vortex core by secondary flows, and enough injectant is depleted near the wall beneath the core and downwash to significantly reduce the protection nominally provided by film cooling. With this situation, injectant distributions show qualitative trends similar to the thermal profiles of Eibeck and Eaton (1987) obtained with a heated wall and no injection. When S is less than 1.0–1.5 and $S1$ is less than 0.7–1.0, some injectant remains near the wall beneath vortex core and downwash regions where it continues to provide some thermal protection.

Heat Transfer Distributions With Film Injection as Dependent Upon Nondimensional Vortex Circulation. Figures 10 and 11 present Stanton number ratios illustrating the influences of the different strength vortices on heat transfer in boundary layers film cooled using a row of holes. Symbols are listed in Tables 3 and 4, respectively, along with vortex characteristics including circulation magnitudes and values of S and $S1$. Results in Fig. 10 were obtained for vortex spanwise position e and those in Fig. 11 were obtained using spanwise position h. To show streamwise development, each figure has six separate parts for x/d of 7.4, 17.5, 33.6, 54.6, 75.6, and 96.6. In each part, St/St_o data are given for vortices r, w, x, y, and z, along with St_f/St_o data for no vortex. Comparison of these data shows how St/St_o change with vortex strength relative to St_f/St_o. Here, St is the Stanton number with film injection and a vortex, St_f is the Stanton number with film cooling only (no vortex), and St_o is the baseline Stanton number (no vortex and no film cooling).

One of the most striking aspects of data in Figs. 10 and 11 is evident if they are compared with data in Fig. 7 for no injection. For smaller x/d, St/St_o with injection differ markedly from cases without injection. Initially, at $x/d = 7.4$, the influence of the vortices is minimal if film injection is present. As x/d increases to 17.5 and 33.6, perturbations from the vortices gradually become more apparent in Figs. 10 and 11, until $x/d = 54.6$, when disturbances with injectant are qualitatively very similar to the perturbations that result without injectant (Eibeck and Eaton, 1987). Although quantitative details are different, data at this and larger x/d also show some qualitative similarity to the local skin friction measurements of Mehta et al. (1983) also obtained without injection and with a single vortex.

Thus, initially downstream of injection locations, the film rather than the vortices is most responsible for the spanwise variations of heat transfer. This is because local heat transfer variations are strongly affected by behavior in the near-wall portions of boundary layers where injectant initially accumulates. In addition, the injectant is believed to push the vortices slightly away from the wall (Ligrani et al., 1989a). Some downstream development is thus required before enough injectant is disturbed and swept away from the wall by vortex secondary flows to cause high St/St_o (even though circulation decreases with streamwise development).

When the vortices influence local St/St_o, qualitative trends in 10 and 11 are similar to those in Fig. 7 for no injection even though the mechanisms that result in changes to wall heat transfer are more complicated. In Figs. 10 and 11, St/St_o are higher than St_f/St_o near vortex downwash regions at larger Z. Because of the downwash and other nearby secondary flows, injectant is depleted, the local boundary layer is thinned, and free-stream fluid is convected very near the wall. St/St_o are lower than St_f/St_o at smaller Z in the vicinity of vortex upwash regions. The upwash and nearby secondary flows serve to sweep extra injectant into these regions giving added thermal protection. In addition, boundary layer fluid and injectant are convected away from the wall, resulting in a thicker local boundary layer. Once the vortices begin to influence local near-wall boundary layer behavior, St/St_o gradients exist along the remaining length of the test surface.

Referring to Fig. 10 for spanwise vortex position e, only minimal St/St_o changes with S occur for $x/d = 7.4$. For larger x/d, St/St_o values generally increase with S and $S1$ in the downwash region, where the most significant St/St_o changes result as S increases from 0.89 to 1.86 and $S1$ increases from 0.60 to 1.26. One exception to this St/St_o trend with S and $S1$ is evident for vortex w data where $S = 2.33$ and $S1 = 1.53$. This data set is somewhat suspect, since its values are slightly inconsistent with $S = 1.86$ and $S = 2.81$ data at $x/d = 75.6$ and 96.6. All other data show consistent trends. When S increases from 0 to 0.17, or from 0.17 to 0.89, St/St_o increases noticeably only when $x/d \geq 33.6$. For x/d greater than 75.6, changes with streamwise distance are quite small. The largest St/St_o values are observed with $S = 2.81$ and $S1 = 1.75$. Here, maximum ratios are about 1.03, which amounts to a 25 percent increase over ratios with film cooling only.

In upwash regions, St/St_o data are noticeably lower than St_f/St_o, data on the left-hand portions of Fig. 10 when $x/d \geq 33.6$. For these locations, different data sets follow the same qualitative trends (relative to St_f/St_o data for $S = 0.0$) with about the same quantitative magnitudes regardless of the values of S or $S1$. Because of this, these results are different from upwash region data in Fig. 7 where St/St_o show some decrease with increasing S and $S1$.

Stanton number ratio variations for $x/d = 33.6$ and $x/d = 54.6$ in Fig. 10 correlate well with injection distributions presented in Fig. 8 for $x/d = 41.9$. For each vortex, high St/St_o correspond to regions where injectant is depleted. The right-hand extents of these depleted regions range from $Z = -2.0$ cm to $Z = 4.0$ cm, depending upon S and streamwise location. For $x/d \geq 33.6$, the left-hand extents of these regions end somewhat abruptly near $Z = -6.0$ cm for the vortices r, w, x, and y. This location corresponds to significant spanwise gradients in the concentration of injectant near the wall, as well as to spanwise St/St_o gradients between high and low St/St_o regions (relative to St_f/St_o). The location does not vary significantly for the different vortices because distances between vortex centers and the middle injection hole centerline are maintained about constant. Regions of significant injec-

tant accumulation at Z smaller than -6.0 cm are then at the same locations where $St/St_o < St_f/St_o$.

Although significant quantitative differences exist, Stanton number ratios in Fig. 11 for spanwise position h show qualitative similarity to distributions in Fig. 10 for position e. At $x/d = 7.4$, the vortices have little influence on the spanwise variations of St/St_o. For larger x/d, St/St_o increases with S and $S1$ in the downwash region. The most significant changes occur as S increases from 0.91 (vortex y) to 1.67 (vortex x). Noticeable changes also occur as S increases from 0.0 (no vortex) to 0.26 (vortex z), and from 0.26 to 0.91. Spanwise variations of St/St_o are very similar for $S = 2.28$ (vortex w) and $S = 2.82$ (vortex r) for all x/d.

St/St_o in upwash regions shown on the left-hand sides of plots in Fig. 11 show almost no variation with S and $S1$ at particular x/d and Z. In addition, the differences between the St/St_o data with vortex and St_f/St_o film-cooling data without a vortex are very small. Thus, for spanwise position h, the vortex has less influence on injectant distributions than for position e. According to Ligrani et al. (1989a), this is because with position h, injectant is swept to the side of the vortex less vigorously than with position e. The spanwise position of the vortex with respect to film injection locations is very important and with position h, the vortex *upwash* passes over the middle injection hole such that the vortex center passes between two injection holes at $x/d = 0.0$. Injectant distributions in Fig. 9 for $x/d = 41.9$ are consistent as they indicate little extra accumulation of injectant in upwash regions compared to distributions in Fig. 8.

As for results in Fig. 10, significant spanwise gradients of injectant near upwash regions are partially responsible for the spanwise gradients of St/St_o shown in Fig. 11 for position h. For h, spanwise gradients are approximately located at $Z = -2.0$ cm, and persist for all x/d greater than 17.5. The spanwise extents of high St/St_o regions to the right of these gradients seem to have larger spanwise extents, and in some cases, slightly smaller peaks than distributions in Fig. 10 for position e. These differences are mostly due to the ways in which injectant is swept away from and depleted from these regions of high heat transfer.

Generally, these trends are consistent with results for different vortex positions given by Ligrani et al. (1989a). Vortex positions A and C from that study are about the same with respect to injection holes as vortex position e. Vortex position B in Ligrani et al. (1989a) is then about the same as location h in the present work. However, because different blowing ratios are used ($m = 1.0$ there) and because the ways in which vortices are located in the two works are slightly different, direct quantitative comparison of results between the two studies is not possible.

The most important general conclusion from the present Stanton number results is that the magnitudes of parameters S and $S1$ determine whether perturbations to local heat transfer are significant. This is consistent with the injection distribution results discussed earlier. When S is greater than 1–1.5 and $S1$ is greater than 0.7–1.0, injectant is swept into vortex upwash regions and above vortex cores by secondary flows. Stanton number ratios indicate that injectant is present near the wall beneath the vortex core and downwash for x/d up to 7.4, and in some cases, 17.5. For larger x/d, local hot spots are present as indicated by Stanton numbers that are locally greater than in film-cooled boundary layers without vortices. When $S < 1.0$–1.5 and $S1 < 0.7$–1.0, some injectant remains near the wall beneath the vortex core and downwash where it continues to provide some thermal protection. For $S = 0.17$–0.26, Stanton number ratios substantially less than 1.0 indicate that thermal protection is provided for x/d values at least up to 96.6. For $S = 0.89$–0.91, Stanton number ratios substantially less than 1.0 indicate that thermal protection is provided for x/d values up to about 54.6.

Summary and Conclusions

Results are presented that illustrate the effects of single embedded longitudinal vortices on heat transfer and injectant downstream of a row of film-cooling holes in a turbulent boundary layer. Attention is focused on the changes resulting as circulation magnitudes of the vortices are varied from 0.0 to 0.15 m^2/s. The ratio of vortex core diameter to hole diameter is about 1.5–1.6, and the blowing ratio is approximately 0.5. Film-cooling holes are oriented 30 deg with respect to the test surface. Stanton numbers are measured on a constant heat flux surface with a nondimensional temperature parameter θ of about 1.5. Two different situations are studied: one where the middle injection hole is beneath the vortex downwash, and one where the middle injection hole is beneath the vortex upwash. For both cases, vortices pass well within 2.9 vortex core diameters of the centerline of the middle injection hole.

To quantify the influences of the vortices on the injectant, two new parameters are introduced. S is defined as the ratio of vortex circulation to injection hole diameter times mean injection velocity. $S1$ is defined as the ratio of vortex circulation to vortex core diameter times mean injection velocity. The most important conclusion is that the perturbation to film injectant and local heat transfer is determined by the magnitudes of S and $S1$, where S is varied from 0 to 2.82 and $S1$ is varied from 0.0 to 1.78. When $S > 1$–1.5 or $S1 > 0.7$–1.0, injectant is swept into the vortex upwash and above the vortex core by secondary flows, and St/St_o data show evidence of injectant beneath the vortex core and downwash near the wall for x/d up to 7.4 and in some cases, 17.5. For larger x/d with such situations, local hot spots are present, and the vortices cause local Stanton numbers in the film-cooled boundary layers to be augmented by as much as 25 percent relative to film-cooled layers with no vortices.

When $S < 1$–1.5 or when $S1 < 0.7$–1.0, some injectant remains near the wall beneath the vortex core and downwash where it continues to provide some thermal protection. For $S1 = 0.11$–0.17, Stanton number ratios substantially less than 1.0 indicate that thermal protection is provided for x/d values at least up to 96.6. For $S1 = 0.60$–0.63, Stanton number ratios substantially less than 1.0 indicate that thermal protection is provided for x/d values up to about 54.6.

In some cases, the protection provided by film cooling is augmented because of the vortex when secondary flows cause extra injectant to accumulate in one area. This occurs near upwash regions when the vortex center passes directly above an injection hole such that the downwash is above the middle injection hole (vortex spanwise position e). S values must be greater than about 0.17 ($S1 > 0.11$) and $x/d >= 33.6$.

Acknowledgments

This study was supported, in part, by the Aero-Propulsion Laboratory of Wright Patterson Air Force Base, MIPR Number FY 1455-88-N0608. Dr. Dick Rivir was program monitor. Some of the facilities used were purchased using funds from the Naval Postgraduate School Foundation Research Program.

References

Blair, M. F., 1974, "An Experimental Study of Heat Transfer and Film Cooling on Large-Scale Turbine Endwalls," ASME JOURNAL OF HEAT TRANSFER, Vol. 96, pp. 524–529.

Craig, D. W., 1989, "Effects of Vortex Circulation on Injectant From a Single Film-Cooling Hole and a Row of Film-Cooling Holes in a Turbulent Boundary Layer, Part 1: Injection Beneath Vortex Downwash," M.S. Thesis, Department of Mechanical Engineering, Naval Postgraduate School, Monterey, CA.

Cutler, A. D., and Bradshaw, P., 1986, "The Interaction Between a Strong

Longitudinal Vortex and a Turbulent Boundary Layer," AIAA Paper No. AIAA-86-1071, presented at the AIAA/ASME Fourth Fluid Dynamics, Plasma Dynamics, and Lasers Conference, Atlanta, GA.

Eibeck, P. A., and Eaton, J. K., 1987, "Heat Transfer Effects of a Longitudinal Vortex Embedded in a Turbulent Boundary Layer," ASME JOURNAL OF HEAT TRANSFER, Vol. 109, pp. 16–24.

Goldstein, R. J., 1971, "Film Cooling," *Advances in Heat Transfer*, Vol. 7, Academic Press, pp. 321–379.

Goldstein, R. J., and Chen, H. P., 1985, "Film Cooling on a Gas Turbine Blade Near the Endwall," ASME *Journal of Engineering for Gas Turbines and Power*, Vol. 107, pp. 117–122.

Goldstein, R. J., and Chen, H. P., 1987, "Film Cooling of a Turbine Blade With Injection Through Two Rows of Holes in the Near-Endwall Region," ASME *Journal of Turbomachinery*, Vol. 109, pp. 588–593.

Kaisuwan, P., 1989, "Effect of Vortex Circulation on Injectant From a Single Film Cooling Hole and a Row of Film Cooling Holes in a Turbulent Boundary Layer, Part 2: Injection Beneath Vortex Upwash," M.S. Thesis, Department of Mechanical Engineering, Naval Postgraduate School, Monterey, CA.

Kays, W. M., and Crawford, M. E., 1980, *Convective Heat and Mass Transfer*, 2nd ed., McGraw-Hill, New York.

Kline, S. J., and McClintock, F. A., 1953, "Describing Uncertainties in Single-Sample Experiments," *Mechanical Engineering*, Jan., pp. 3–8.

Ligrani, P. M., Joseph, S. L., Ortiz, A., and Evans, D. L., 1988, "Heat Transfer in Film-Cooled Turbulent Boundary Layers at Different Blowing Ratios as Affected by Longitudinal Vortices," *Experimental Thermal and Fluid Science*, Vol. 1, pp. 347–362.

Ligrani, P. M., Ortiz, A., Joseph, S. L., and Evans, D. L., 1989a, "Effects of Embedded Vortices on Film-Cooled Turbulent Boundary Layers," ASME *Journal of Turbomachinery*, Vol. 111, No. 1, pp. 71–77.

Ligrani, P. M., Singer, B. A., and Baun, L. R., 1989b, "Spatial Resolution and Downwash Velocity Corrections for Multiple-Hole Pressure Probes in Complex Flows," *Experiments in Fluids*, Vol. 7, No. 6, pp. 424–426.

Ligrani, P. M., Singer, B. A., and Baun, L. R., 1989c, "Miniature Five-Hole Pressure Probe for Measurement of Mean Velocity Components in Low Speed Flows," *Journal of Physics E—Scientific Instruments*, Vol. 22, No. 10, pp. 868–876.

Ligrani, P. M., and Williams, W. W., 1990, "Effects of an Embedded Vortex on Injectant From a Single Film-Cooling Hole in a Turbulent Boundary Layer," ASME *Journal of Turbomachinery*, Vol. 112, pp. 428–436.

Mehta, R. D., Shabaka, I. M. M. A., Shibl, A., and Bradshaw, P., 1983, "Longitudinal Vortices Imbedded in Turbulent Boundary Layers," AIAA Paper No. AIAA-83-0378, presented at the AIAA Twenty-First Aerospace Sciences Meeting, Reno, NV.

Moffat, R. J., 1982, "Contributions to the Theory of Single-Sample Uncertainty Analysis," ASME *Journal of Fluids Engineering*, Vol. 104, pp. 250–260.

Ongoren, A., 1981, "Heat Transfer on the Endwall of a Turbine Cascade With Film Cooling," (Supervisors: P. M. Ligrani and C. Camci), Von Karman Institute for Fluid Dynamics, Project Report 1981-19, Rhode-St-Genese, Belgium.

Ortiz, A., 1987, "The Thermal Behavior of Film Cooled Turbulent Boundary Layers as Affected by Longitudinal Vortices," M.E. Thesis, Department of Mechanical Engineering, Naval Postgraduate School, Monterey, CA.

Schwartz, G. E., 1988, "Control of Embedded Vortices Using Wall Jets," M.S. Thesis, Department of Mechanical Engineering, Naval Postgraduate School, Monterey, CA.

Shabaka, I. M. M. A., Mehta, R. D., and Bradshaw, P., 1985, "Longitudinal Vortices Imbedded in Turbulent Boundary Layers. Part 1. Single Vortex," *Journal of Fluid Mechanics*, Vol. 155, pp. 37–57.

Subramanian, C. S., Ligrani, P. M., Green, J. G., and Doner, W. D., 1990, "Development and Structure of a Film-Cooling Jet in a Turbulent Boundary Layer With Heat Transfer," *Third International Symposium on Transport Phenomena and Dynamics of Rotating Machinery (ISROMAC-3), Vol. 1: Transport Phenomena*, pp. 49–64, Honolulu, HI.

Westphal, R. V., Pauley, W. R., and Eaton, J. K., 1987, "Interaction Between a Vortex and a Turbulent Boundary Layer. Part 1: Mean Flow Evolution and Turbulence Properties," NASA TM88361.

Laminar Natural Convection Heat Transfer From a Horizontal Circular Cylinder to Liquid Metals

K. Sugiyama
Associate Professor.

Y. Ma
Graduate Student.

R. Ishiguro
Professor.

Department of Nuclear Engineering,
Hokkaido University,
Sapporo, Japan

The objective of the present study is to clarify the heat transfer characteristics of natural convection around a horizontal circular cylinder immersed in liquid metals. Experimental work concerning liquid metals sometimes involves such a degree of error that it is impossible to understand the observed characteristics in a measurement. Numerical analysis is a powerful means to overcome this experimental disadvantage. In the present paper we first show that the Boussinesq approximation is more applicable to liquid metals than to ordinary fluids and that the present analysis gives accurate heat transfer rates, even for a cylinder with a relatively large temperature difference (>100 K) between the heat transfer surface and fluid. It is found from a comparison of the present results with previous work that the correlation equations that have already been proposed predict values lower than the present ones.

Introduction

Although the heat transfer by natural convection from a horizontal circular cylinder immersed in an infinite medium has been extensively studied, little information is available concerning liquid metal media. A survey of the literature indicated that there have been three experimental studies (Hyman et al., 1953; Fedinskii, 1958; Kovalev and Zhukov, 1973) that reported mutually different results, the highest Nusselt number of which was approximately twice as large as the lowest. In the case of liquid metal, it is generally recognized that results among different workers mutually differ owing to various experimental difficulties. This result shows that the same problem occurs in natural convection about a horizontal cylinder.

In many types of engineering application in which heat is removed by means of forced-circulation of the coolant, it sometimes becomes very important to understand the thermal behavior of the system when forced flow is suddenly lost. The liquid-sodium-cooled, fast breeder reactor is a typical case; even when the reactor is shut down, a low level of heat generation continues due to the decay of fission products. Thus, in an extreme situation during a loss of the power supply to all coolant pumps, including their emergency backup systems, the only means of removing decay heat from the reactor is by natural convection.

From those practical viewpoints, we must have sufficient knowledge concerning heat transfer by natural convection from liquid metals. However, as mentioned above, even the heat transfer characteristics of natural convection around a horizontal circular cylinder, which is one of the most fundamental configurations, is not sufficiently understood. Therefore, as a first step for obtaining practically needed knowledge, heat transfer by natural convection from a horizontal circular cylinder to a liquid metal must be studied by means of numerical analysis.

From the viewpoint of safety analysis in a fast breeder reactor, heat transfer at that time when a relatively large temperature difference between the cylinder surface and liquid metal occurs is important, since a required amount of heat must be removed by a limited number of tubes arranged within a restricted space. Therefore, we first examine the adaptability of the governing equations used here for this purpose and then report on the heat transfer characteristics of liquid metals in this system.

Examination of Governing Equations

The continuity, momentum, and energy equations for a fluid of variable properties can be written as follows:

$$v_i \frac{\partial \rho}{\partial x_i} + \rho \frac{\partial v_i}{\partial x_i} = 0 \tag{1}$$

$$\rho v_j \frac{\partial v_i}{\partial x_j} = -\frac{\partial P}{\partial x_i} - \rho g_i + \mu \frac{\partial \gamma_{ij}}{\partial x_j} + \gamma_{ij} \frac{\partial \mu}{\partial x_j} \tag{2}$$

and

$$\rho C_p v_j \frac{\partial T}{\partial x_j} = \lambda \frac{\partial^2 T}{\partial x^2_j} + \frac{\partial \lambda}{\partial x_j} \frac{\partial T}{\partial x_j} \tag{3}$$

where

$$\gamma_{ij} = \frac{\partial v_i}{\partial x_j} + \frac{\partial v_j}{\partial x_i} - \frac{2}{3} \frac{\partial v_k}{\partial x_k} \delta_{ij}$$

Since the physical properties of liquid metals vary almost linearly over a large temperature range, 200 K or more, there is no problem in assuming linearized Taylor expansions. Hence, equations for the physical properties can be written as

$$\rho = \rho_0[1 - \alpha_0(T - T_0)] \tag{4}$$

$$\mu = \mu_0[1 + \beta_0(T - T_0)] \tag{5}$$

$$C_p = C_{p0}[1 + \gamma_0(T - T_0)] \tag{6}$$

and

$$\lambda = \lambda_0[1 + \delta_0(T - T_0)] \tag{7}$$

where

$$\alpha = -\frac{1}{\rho} \frac{\partial \rho}{\partial T}, \quad \beta = \frac{1}{\mu} \frac{\partial \mu}{\partial T}, \quad \gamma = \frac{1}{C_p} \frac{\partial C_p}{\partial T}, \quad \delta = \frac{1}{\lambda} \frac{\partial \lambda}{\partial T}$$

The linearized property equations, (4)–(7), are substituted into equations (1)–(3); then the equations are nondimensionalized. The resulting equations are

$$-\epsilon_1 V_i \frac{\partial \theta}{\partial X_i} + \{1 - \epsilon_1(\theta - \theta_0)\} \frac{\partial V_i}{\partial X_i} = 0 \tag{8}$$

Contributed by the Heat Transfer Division for publication in the JOURNAL OF HEAT TRANSFER. Manuscript received by the Heat Transfer Division September 10, 1987; revision received January 24, 1990. Keywords: Liquid Metals, Natural Convection, Numerical Methods.

Table 1 Fluid property coefficients of typical liquid metals and air

	Air (293 ~ 373 K)	Na (550 ~ 1050 K)	K (550 ~ 950 K)
$\epsilon_1/\Delta T$	$3.43 \sim 2.70 \times 10^{-3}$	$2.71 \sim 3.14 \times 10^{-4}$	$2.95 \sim 3.66 \times 10^{-4}$
$\epsilon_2/\Delta T$	$2.55 \sim 2.02 \times 10^{-3}$	$-2.32 \sim -1.03 \times 10^{-3}$	$-2.17 \sim -1.13 \times 10^{-3}$
$\epsilon_3/\Delta T$	$1.04 \sim 1.04 \times 10^{-4}$	$-1.48 \sim 0.00 \times 10^{-4}$	$-1.17 \sim 3.12 \times 10^{-4}$
$\epsilon_4/\Delta T$	$3.05 \sim 2.30 \times 10^{-3}$	$-6.27 \sim -9.10 \times 10^{-4}$	$-7.80 \sim -7.90 \times 10^{-4}$
$(\epsilon_1 - \epsilon_3)/\Delta T$	$3.33 \sim 2.60 \times 10^{-3}$	$4.19 \sim 3.14 \times 10^{-4}$	$4.12 \sim 0.54 \times 10^{-4}$

	Li (550 ~ 1450 K)	Hg (300 ~ 500.K)	$NaK_{25\text{-}75}$ (450 ~ 700 K)
$\epsilon_1/\Delta T$	$1.78 \sim 2.41 \times 10^{-4}$	$1.83 \sim 1.72 \times 10^{-4}$	$3.00 \sim 3.18 \times 10^{-4}$
$\epsilon_2/\Delta T$	$-1.63 \sim -1.00 \times 10^{-3}$	$-3.62 \sim -1.08 \times 10^{-3}$	$-2.93 \sim -1.73 \times 10^{-3}$
$\epsilon_3/\Delta T$	$-9.28 \sim 0.00 \times 10^{-5}$	$-21.6 \sim -7.35 \times 10^{-5}$	$-4.43 \sim -3.52 \times 10^{-4}$
$\epsilon_4/\Delta T$	$10.1 \sim 2.00 \times 10^{-4}$	$29.0 \sim -7.87 \times 10^{-4}$	$5.38 \sim 4.74 \times 10^{-4}$
$(\epsilon_1 - \epsilon_3)/\Delta T$	$2.71 \sim 2.41 \times 10^{-4}$	$3.99 \sim 2.46 \times 10^{-4}$	$7.43 \sim 6.70 \times 10^{-4}$

$$\{1-\epsilon_1(\theta-\theta_0)\}V_j\frac{\partial V_i}{\partial X_j} = -\frac{\partial(P-P_s)}{\partial X_i} + (\theta-\theta_s)\mathrm{Pr}^2\mathrm{Gr}_i + \mathrm{Pr}\{1+\epsilon_2(\theta-\theta_0)\}\frac{\partial \Gamma_{ij}}{\partial X_j} + \mathrm{Pr}\,\epsilon_2\Gamma_{ij}\frac{\partial\theta}{\partial X_j} \quad (9)$$

and

$$\{1-(\epsilon_1-\epsilon_3)(\theta-\theta_0)\}V_j\frac{\partial\theta}{\partial X_j} = \{1+\epsilon_4(\theta-\theta_0)\}\frac{\partial^2\theta}{\partial x_j^2} + \epsilon_4\left(\frac{\partial\theta}{\partial X_j}\right)^2 \quad (10)$$

where $\epsilon_1 = \alpha_0\Delta T$, $\epsilon_2 = \beta_0\Delta T$, $\epsilon_3 = \gamma_0\Delta T$, and $\epsilon_4 = \delta_0\Delta T$.

By requiring that all the ϵ_i parameters be small so that the terms they multiply are small, we can obtain simple equations from equations (8)–(10), which are known as the Boussinesq approximation. The matter to be discussed is under what condition the terms multiplied by the ϵ_i parameters are negligible for an evaluation of practical Nusselt numbers. In order to make an examination, ϵ_i parameters of air and typical liquid metals are shown in Table 1. As can be seen, for the same temperature difference, ΔT, parameters ϵ_1 and ϵ_4 of liquid metals are sufficiently smaller than those of air, except ϵ_4 of mercury at the lower temperature region. The parameter ϵ_3 always appears with ϵ_1 in the form of $\epsilon_1 - \epsilon_3$ in equation (10). As shown in the table, $\epsilon_1 - \epsilon_3$ of liquid metals is also sufficiently smaller than that of air. We can also say that the ϵ_2 parameter of liquid metals is slightly smaller than that of air, except those of Hg and NaK at a lower temperature range.

To examine the effect of the terms including parameters ϵ_i, we first look at equation (8). Choosing θ_o as the average of wall and far fluid temperatures, the value of $\epsilon_1|\theta-\theta_o|$ in the second term of the left-hand side is at most $\sim 0.5\,\epsilon_1$. Hence, if $1+\epsilon_1|\theta-\theta_0|$ is approximated as 1, an error of at most $\sim 0.5\alpha_0\Delta T$ would be included in this term. This error is obviously directly proportional to ΔT. We can therefore maintain this term within the desired error level by restricting the value of ΔT. A quantitative evaluation of the first term of equation (8) is difficult. However, it is reasonable to estimate that the first term in the case of liquid metal is sufficiently smaller than that of air when compared with each second term, since the ϵ_1 of metal is about one order smaller than that of air for system with the same ΔT.

In the same manner, an evaluation of terms including ϵ_i in equations (9) and (10) is possible. However, since ϵ_2 of liquid metals is about the same magnitude as that of air, an explanation is necessary for the terms including ϵ_2 in the right-hand side of equation (9). In these terms the magnitude of $\mathrm{Pr}\epsilon_2$ should be compared with that of air. These terms of liquid metal are obviously smaller than those of air because of the small Prandtl number of liquid metal.

From this examination it is clear that in the Boussinesq approximation the terms multiplied by ϵ_i parameters can be neglected in equations (8)–(10); this is more applicable to liquid

Nomenclature

a = thermal diffusivity
C_p = specific heat at constant pressure
d = cylinder diameter
g = acceleration due to gravity
g_i = component of g in the coordinate direction x_i
Gr = Grashof number = $g\alpha\Delta T d^3/\nu^2$
Gr_i = Grashof number in the coordinate direction $x_i = g_i\alpha\Delta T d^3/\nu^2$
h = heat transfer coefficient
Nu = Nusselt number = hd/λ
p = pressure
P = dimensionless pressure = $pd^2/a^2/\rho$
Pr = Prandtl number = ν/a
Ra = Rayleigh number = GrPr
T = temperature
T_w = temperature at cylinder surface
T_∞ = temperature at far region horizontal to cylinder center $\Delta T = T_\infty - T_w$
v_i = velocity component in direction x_i
V_i = dimensionless velocity component in direction $x_i = v_i\, d/a$
x, y = horizontal, vertical coordinates
X, Y = dimensionless horizontal, vertical coordinates = x/d, y/d
x_i = coordinates in tensor notation
$\alpha, \beta, \gamma, \delta$ = fluid property coefficients
γ_{ij} = deformation rate tensor
Γ_{ij} = dimensionless deformation rate tensor = $\gamma_{ij}\, d^2/a$
$\epsilon_1 \sim \epsilon_4$ = dimensionless parameters
η, ξ = dimensionless coordinates defined by equation (14)
θ = dimensionless temperature = $(T - T_\infty)/\Delta T$
λ = thermal conductivity
μ = dynamic viscosity
ν = kinematic viscosity
ρ = density
ψ = dimensionless stream function
ω = dimensionless vorticity

Subscripts

m = mean value
o = value at $(T_w + T_\infty)/2$
s = surrounding value
η = local value

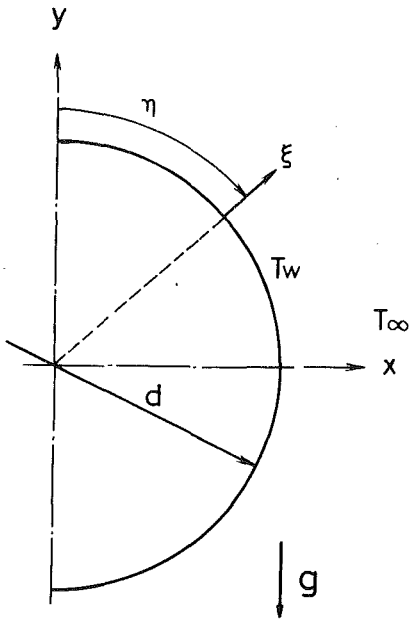

Fig. 1 Coordinate system

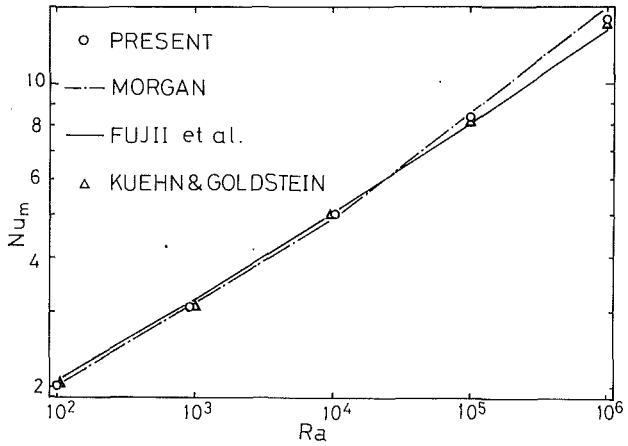

Fig. 2 Comparison of the mean Nusselt numbers for air

metal than to air for the same magnitude of ΔT. Using another expression, if we allow the same tolerance of error for both numerical results of liquid metal and air, the Boussinesq approximated equations would be much more applicable to the natural convection of liquid metal with a temperature difference ΔT significantly larger than that of air.

Governing Equations and Difference Approximation

Using the dimensionless vorticity and stream function for the flow field, the basic equations (8)–(10) in which the terms including ϵ_i are neglected can be written as

$$\frac{\partial}{\partial \xi}\left(\omega \frac{\partial \psi}{\partial \eta}\right) - \frac{\partial}{\partial \eta}\left(\omega \frac{\partial \psi}{\partial \xi}\right) = \mathrm{Pr}\left(\frac{\partial^2 \omega}{\partial \xi^2} + \frac{\partial^2 \omega}{\partial \eta^2}\right) - e^{\xi}\mathrm{GrPr}^2\left(\sin \eta \frac{\partial \theta}{\partial \xi} + \cos \eta \frac{\partial \theta}{\partial \eta}\right) \tag{11}$$

$$\frac{\partial^2 \psi}{\partial \xi^2} + \frac{\partial^2 \psi}{\partial \eta^2} = -e^{2\xi}\omega \tag{12}$$

and

$$\frac{\partial}{\partial \xi}\left(\theta \frac{\partial \psi}{\partial \eta}\right) - \frac{\partial}{\partial \eta}\left(\theta \frac{\partial \psi}{\partial \xi}\right) = \frac{\partial^2 \theta}{\partial \xi^2} + \frac{\partial^2 \theta}{\partial \eta^2} \tag{13}$$

Figure 1 shows the coordinate system. The dimensionless variables ξ and η are related to X and Y as follows:

$$\xi + i(\pi/2 - \eta) = \ln(X + iY) \tag{14}$$

The flow is considered to be symmetric about the vertical plane passing through the center of the cylinder. The boundary conditions on the cylinder surface and the symmetric line are

$$\left.\begin{array}{l} \xi = \ln(1/2);\ \theta = -1,\ \omega = -4\partial^2\psi/\partial\xi^2,\ \psi = 0 \\ \eta = 0,\ \pi;\ \partial\theta/\partial\eta = 0,\ \omega = 0,\ \psi = 0 \end{array}\right\} \tag{15}$$

The outer boundary is divided into two parts: one with fluid coming to the solution domain and the other with fluid leaving it. The fluid is assumed to approach the cylinder radially with the same temperature as that at the far distance in the inflow part and to leave the cylinder radially at the fluid temperature in the outflow part. If the change from inflow to outflow occurs at η_{io}, the outer boundary condition is written as follows:

$$\xi = \xi_\infty (0 \le \eta \le \eta_{io});$$
$$\xi = \xi_\infty (\eta_{io} < \eta \le \pi);$$

$$\left.\begin{array}{l} \theta = 0,\quad \omega = -e^{2\xi_\infty}\partial^2\psi/\partial\eta^2,\quad \partial\psi/\partial\xi = 0 \\ \partial\theta/\partial\xi = 0,\quad \omega = -e^{2\xi_\infty}\partial^2\psi/\partial\eta^2,\quad \partial\psi/\partial\xi = 0 \end{array}\right\} \tag{16}$$

The η_{io} depends on Grashof number. We first confirmed in a preliminary calculation that, if the outer boundary is set far from the cylinder, the change of η_{io} does not influence the temperature and flow fields except for a small region near the η_{io} position. Based on this fact, η_{io} is set at $5\pi/6$ in the present study.

A finite-difference method (Gosman et al., 1969) is used to solve the basic equations numerically. Although a central differencing scheme is used for the diffusion terms, the convection terms are approximated by an upwind difference to preserve the stability of the numerical scheme. The outer boundary is set at a distance of $127(d/2)$. The radial and angular grid numbers are 110 and 73, respectively. These numbers are determined after assuring that there is no substantial difference of calculated results, even when using a double grid number in the ξ and η directions, respectively. The radial grid spacing is basically 0.05 ($=\Delta\xi$), although this is reduced to as low as 0.01 near the cylinder. The angular grids are equally spaced. The iteration is terminated when the current local Nusselt number agrees down to the second decimal place with the previous one. It is confirmed that the temperature and flow fields converge sufficiently when this criterion is used.

Results and Discussion

Before discussing the heat transfer characteristics of liquid metals, we must examine the accuracy of the results obtained in the present analysis. From this viewpoint, we first obtained Nusselt numbers for air; these have been reported sufficiently by many workers. The results are shown in Fig. 2. The correlation equations proposed by Fujii et al. (1982) and Morgan (1975), which are thought to be reliable, are also presented in the same figure. It is obvious that the present results are between the two correlation equations over a range of $10^2 < \mathrm{Ra} < 10^6$. The present results also agree with the numerical results obtained by Kuehn and Goldstein (1980) within 3.5 percent over the range shown in Fig. 2.

A closer comparison between the present results and the experimental results for air is presented in Fig. 3. The experimental data were taken from the paper of Fand et al. (1977). The numerals shown in the figure are the temperature difference between the cylinder surface and far fluid, ΔT. While the

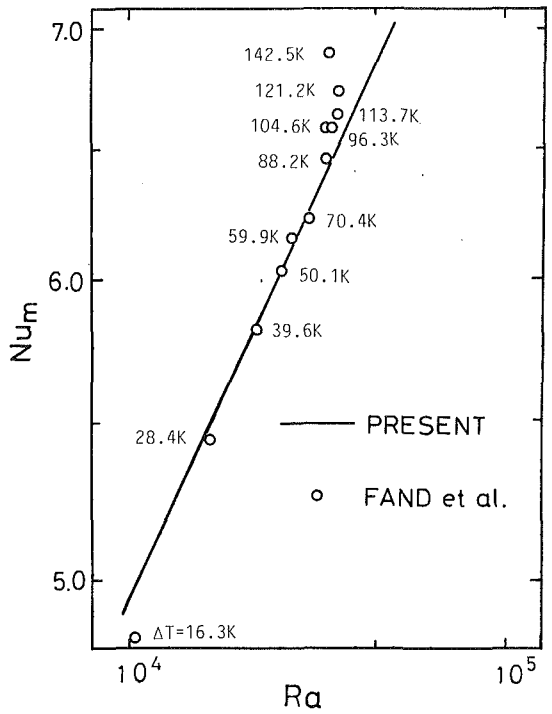

Fig. 3 Comparison of the present result with the air data of Fand et al.

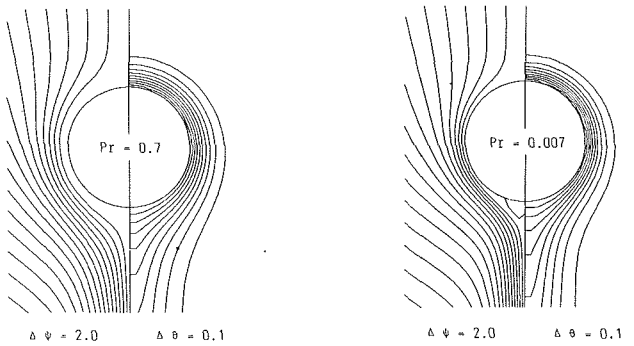

Fig. 4 Streamlines and isotherms of air and liquid metal at $GrPr^2 = 7000$

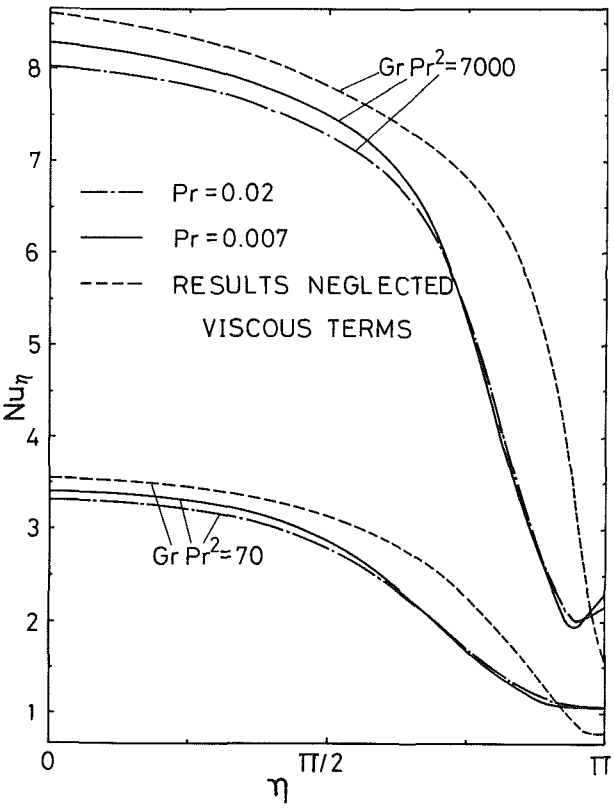

Fig. 5 Local Nusselt numbers of liquid metals

difference between the present result and their data exceeding $\Delta T = 96.3$ K consistently increases with increase in ΔT, a good agreement is obtained for the data with temperature differences less than $\Delta T = 96.3$ K, except for only one with $\Delta T = 16.3$ K. Fand et al. estimated their experimental error to be within 4 percent. Hence we may regard the discrepancy at $\Delta T = 16.3$ K as experimental error. This comparison shows that the Boussinesq approximation is applicable with a good accuracy to the natural convection problem with a temperature difference of about 100 K between the heat transfer surface and the far fluid for the purpose of predicting practical Nusselt numbers.

Since, as shown in Table 1, ϵ_1, $Pr\epsilon_2$, ϵ_4, and $\epsilon_1 - \epsilon_3$ of liquid metals are sufficiently smaller than those of air for practical temperature ranges, if we can tolerate the same magnitude of error as that of air to the natural convection problems of liquid metal, the Boussinesq approximation would be applicable to a temperature difference twice (or more) as large as that of air with a reasonable accuracy. Experiments with liquid metals inevitably give a considerably larger error than that for air. As a result of this experimental difficulty, a numerical analysis of liquid metal is very useful, even if a small amount of error is involved.

To show a distinctive feature of liquid metals, the streamlines and isotherms of both air and a liquid metal for the same $GrPr^2$ number are shown in Fig. 4. Although the Grashof number has a difference of the order of 10^4, the thermal boundary layer thickness of the liquid metal is about the same as that of air owing to the low Prandtl number of liquid metal. Even in this $GrPr^2$ number, which is the highest value calculated in this study, the thermal boundary layer thickness is approximately equal to the cylinder radius. Therefore, it is obvious that curvature effects are always involved in the Nusselt number of liquid metals.

Typical local Nusselt numbers of liquid metals are shown as a function of the angle in Fig. 5. There is no essential difference between the results at $Pr = 0.02$ and $Pr = 0.007$. In the heat transfer process of low Prandtl number fluids, fluid inertia plays a much more important role compared with viscous effects, since the thermal boundary layer spreads much wider than that of ordinary fluids, like air, for the same Grashof number. To confirm this point, results neglecting viscous effects are shown in the same figure. To obtain these results the following equation is used instead of equation (11):

$$\frac{\partial}{\partial \xi}\left(\omega \frac{\partial \psi}{\partial \eta}\right) - \frac{\partial}{\partial \eta}\left(\omega \frac{\partial \psi}{\partial \xi}\right) = -e^{\xi} GrPr^2 \left(\sin \eta \frac{\partial \theta}{\partial \xi} + \cos \eta \frac{\partial \theta}{\partial \eta}\right) \quad (17)$$

The parameter that appears in this equation is only $GrPr^2$. The calculation is made under a slip flow condition at the cylinder surface. The difference between viscous flow and inviscid flow is within 14 percent. From these comparisons we can see that fluid inertia is much more important in low Prandtl number fluids.

The mean Nusselt number for liquid metals is shown in Fig. 6. For the above reason the parameter $GrPr^2$ is used in the abscissa of this figure. The results for Prandtl numbers of 0.004 and 0.02 can be expressed with a tolerance of 3.5 percent as follows:

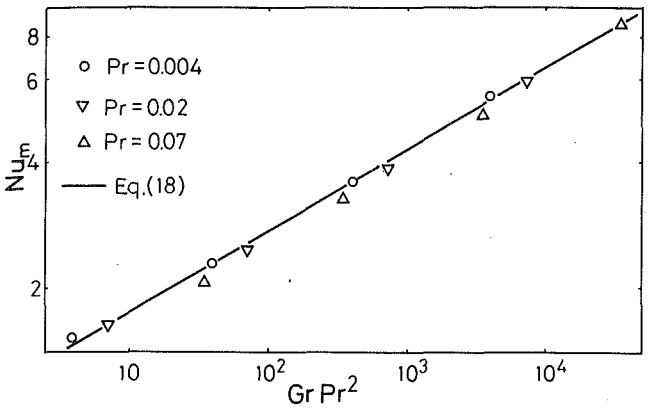

Fig. 6 Mean Nusselt numbers of liquid metals

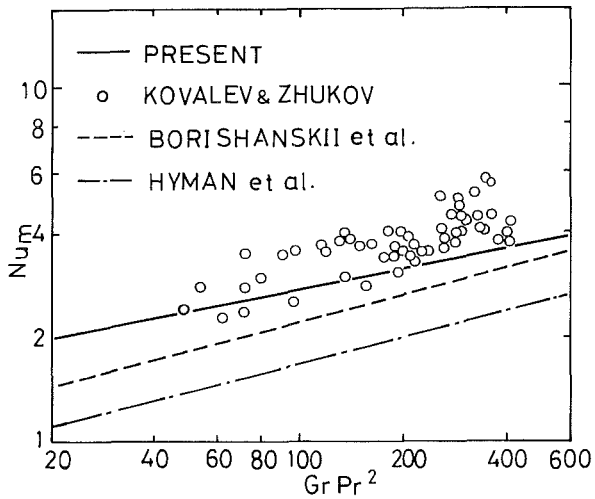

Fig. 7 Comparison of the present result with previous results for liquid metals

$$\mathrm{Nu}_m = 1.11(\mathrm{GrPr}^2)^{0.196} \qquad (4 \le \mathrm{GrPr}^2 \le 7000) \qquad (18)$$

We recommend that this equation be used in the region $\mathrm{Gr} \le 1.5 \times 10^8$ according to Fedinskii's experiments (1958). The Prandtl number range from 0.004 to 0.02 corresponds well to that of liquid metals. A Prandtl number of 0.07, which is especially large for a liquid metal, corresponds to a value near the melting point of lithium. The values of this Prandtl number are about 5 percent different from equation (18). We also confirm that the mean Nusselt numbers in the case of a uniform wall heat flux are 5 to 7 percent higher than those in the present uniform wall temperature. This difference is not large. Therefore, equation (18) is very useful for evaluating practical mean Nusselt numbers of liquid metals.

Here, we must also mention the following point. The exponent of GrPr^2 in equation (18) is 0.196. When curvature effects are negligible, as is well known in ordinary fluids, the exponent of GrPr^2 is 0.25. According to Morgan's equation (1975), the gradient of the curve of the mean Nusselt number for air is 0.188 when $\mathrm{Ra} < 10^4$. This means that a curvature effect is involved when $\mathrm{Ra} < 10^4$. $\mathrm{Ra} = 10^4$ corresponds to $\mathrm{GrPr}^2 = 7000$, since the Prandtl number of air is 0.7. Hence, we can easily suppose that the mean Nusselt numbers of liquid metals involve curvature effects when $\mathrm{GrPr}^2 < 7000$, since the thermal boundary of a liquid metal is as thick as that of air and the velocity of a liquid metal is much higher than that of air near the cylinder, as shown in Fig. 4. From these points the exponent of 0.196 in equation (18) is reasonable.

A comparison of the present result with two empirical equations previously reported is shown in Fig. 7. Hyman et al.

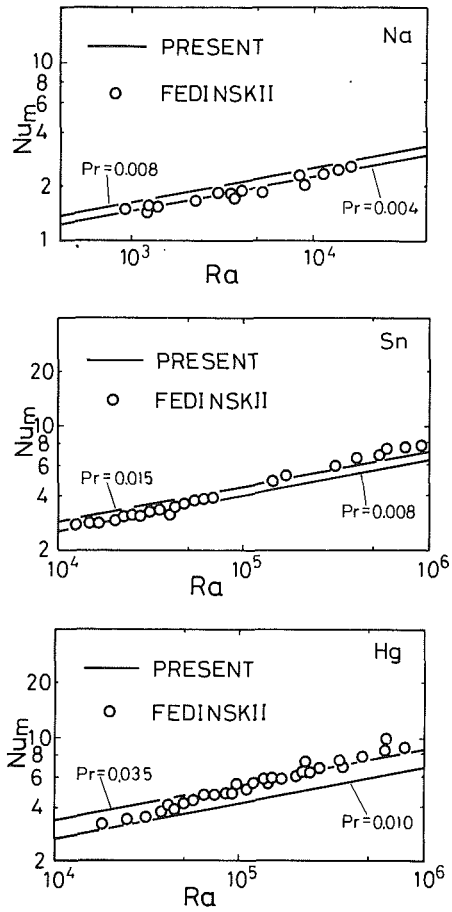

Fig. 8 Comparison of the present result with Fedinskii's experimental results

(1953) proposed the following equation based on their own experiment with liquid metals:

$$\mathrm{Nu}_m = 0.53(\mathrm{GrPr}^2)^{0.25} \qquad (19)$$

Borishanskii et al. (1967) in their book recommended the following correlation for liquid metals:

$$\mathrm{Nu}_m = 0.67(\mathrm{GrPr}^2)^{0.25} \qquad (20)$$

As shown in Fig. 7. both equations show a lower value than the present result.

Hyman et al. conducted their experiment using a relatively small test chamber. Thus, it is obviously supposed in their experiment that a wall effect would be included in their results because of the very thick thermal boundary layer of low Prandtl number fluids. Borishanskii et al. proposed the use of equation (20) for practical purposes, taking Fedinskii's experimental results into account. However, they used an exponent of 0.25 in their equation without any examination. For this reason a discrepancy between the present equation and theirs occurs in the low GrPr^2 number region, which is important for liquid sodium.

We also show the experimental result for liquid sodium found by Kovalev and Zhukov (1973) in Fig. 7. They used a vertical cylinder vessel 840 mm in length and 198 mm in diameter. The cross-sectional area was about three times as large as that of Hyman et al. Thus, errors due to the vessel capacity would be less than those of Hyman et al. The agreement between the present result and theirs is not bad for a liquid metal, but their result for the average gives a somewhat higher value than the present one.

Figure 8 shows a comparison of the present results with those of Fedinski for sodium, tin, and mercury (1958). We cannot find exact Prandtl numbers for these data; thus, the

present results are shown for the maximum and minimum Prandtl number of each liquid metal. For liquid sodium, the present result corresponding to $Pr = 0.004$ is found to be in good agreement with Fedinskii's data. The experimental results for tin almost fall between the present results in a lower Ra number region; however, some points are somewhat above the line, corresponding to $Pr = 0.015$ in a higher Ra number region. It would be possible to explain this tendency from a difference of boundary condition at heat transfer surface between experiment and analysis and some amount of experimental errors. Although the data for mercury are rather scattered, the tendency between the present results and experimental values is about the same as for tin.

Conclusion

In the present study numerical solutions for natural convection from a horizontal circular cylinder immersed in liquid metals have been obtained. We first show that the Boussinesq approximation is more applicable to liquid metals than to gases with a good accuracy. From a comparison of the present result of air with the experimental value of Fand et al., it is confirmed that the Boussinesq approximation is reasonable for predicting practical heat transfer rates of liquid metals, even in a system having a large temperature difference of more than 100 K between the heat transfer surface and the far fluid.

After this examination, we carried out numerical calculations for liquid metals and proposed a new correlation equation for the mean Nusselt number. It was found from a comparison with previous studies that the correlation of Hyman et al. always predicts a lower Nusselt number than the present one and that of Borishanskii et al. predicts a lower value than the present one in the low $GrPr^2$ number region. The present result is also found to be in reasonable agreement with Fedinskii's data.

References

Borishanskii, B. M., Kutateladze, S. S., Novikov, I. I., and Fedinskii, O. S., 1967, *Liquid-Metal Heat Transfer Media*, Atomizdat, Moscow [in Russian].

Fand, R. M., Morris, E. W., and Lum, M., 1977, "Natural Convection Heat Transfer From Horizontal Cylinders to Air, Water and Silicon Oils for Rayleigh Numbers Between 3×10^2 and 2×10^7," *International Journal of Heat and Mass Transfer*, Vol. 20, pp. 1173–1184.

Fedinskii, O. S., 1958, cited by Borishanskii et al.,1967.

Fujii, T., Fujii, M., and Honda, T., 1982, "Theoretical and Experimental Studies of the Free Convection Around a Long Horizontal Thin Wire in Air," *Heat Transfer 1982*, U. Grigull et al., eds., Hemisphere, Washington, DC, Vol. 2, pp. 311–316.

Gosman, A. D., Pun, W. M., Runchal, A. K., Spalding, D. B., and Wolfshtein, M. W., 1969, *Heat and Mass Transfer in Recirculating Flow*, Academic Press, London.

Hyman, S. C., Bonilla, C. F., and Ehrlich, S. W., 1953, "Natural-Convection Transfer Processes: I. Heat Transfer to Liquid Metals and Nonmetals at Horizontal Cylinders," *Chemical Engineering Progress Symposium Series*, Vol. 49, pp. 22–31.

Kovalev, S. A., and Zhukov, V. M., 1973, "Experimental Study of Heat Transfer During Sodium Boiling Under Conditions of Low Pressures and Natural Convection," in: *Progress in Heat and Mass Transfer*, O. E. Dwyer, ed., Pergamon, Oxford, Vol. 7, pp. 347–354.

Kuehn, T. H., and Goldstein, R. J., 1980, "Numerical Solution to the Navier-Stokes Equations for Laminar Natural Convection About a Horizontal Isothermal Circular Cylinder," *International Journal of Heat and Mass Transfer*, Vol. 23, pp. 971–979.

Morgan, V. T., 1975, "The Overall Convection Heat Transfer From Smooth Circular Cylinders," in: *Advances in Heat Transfer*, T. F. Irvine, Jr., and J. P. Hartnett, eds., Academic Press, New York, Vol. 11, pp. 199–264.

Correlations for Natural Convection Between Heated Vertical Plates

S. Ramanathan

R. Kumar

Department of Mechanical Engineering,
Clemson University,
Clemson, SC 29631

This paper presents the numerical results of natural convective flows between two vertical, parallel plates within a large enclosure. A parametric study has been conducted for various Prandtl numbers and channel aspect ratios. The results are in good agreement with the reported results in the literature for air for large aspect ratios. However, for small aspect ratios, the present numerical results do not agree with the correlations given in the literature. The discrepancy is due to the fact that the published results were obtained for channels where the diffusion of thermal energy in the vertical direction is negligible. The results obtained in this paper indicate that vertical conduction should be considered for channel aspect ratios less than 10 for $Pr = 0.7$. Correlations are presented to predict the maximum temperature and the average Nusselt number on the plate as explicit functions of the channel Rayleigh number and the channel aspect ratio for air. The plate temperature is a weak function of Prandtl number for Prandtl numbers greater than 0.7, if the channel Rayleigh number is chosen as the correlating parameter. For Prandtl numbers less than 0.1, the plate temperature is a function of the channel Rayleigh number and the Prandtl number. A correlation for maximum temperature on the plate is presented to include the Prandtl number effect for large aspect ratio channels.

Introduction

The problem of cooling heated, vertical, parallel plates by natural convection has been of considerable interest to the electronics industry. The history of the modeling of such a problem has been a sequence of refinements and successive approximations. The simplest model of heat transfer in such a situation was proposed by Elenbaas (1942) who made heat transfer measurements of natural convective flow between two isothermal vertical plates. He determined that in the limit of small gap width, Nusselt number is proportional to channel Rayleigh number, Ra. His experiments were conducted for a wide range of Rayleigh numbers, $0.2 < \mathrm{Ra} < 10^5$. The similarity solution for a single plate with isoflux boundary condition was obtained by Sparrow and Gregg (1956). They also proposed a correlation for the plate temperatures as a function of the Rayleigh number based on the integral solution. Bodoia and Osterle (1962) studied the problem of parallel isothermal plates numerically, employing boundary layer assumptions and assuming uniform inlet velocity temperature profiles. Their results were in good agreement with Elenbaas' (1942) results. Sobel et al. (1966) solved the same problem numerically for vertical plates subjected to the constant heat flux boundary condition.

The next stage of modeling, i.e., asymmetric heating of the plates, was carried out by Aung (1972) who presented analytical solutions for the temperature and velocity fields for laminar, fully developed flows. His results are independent of any assumptions regarding the entrance temperature and velocity profiles. An important result from these solutions is that the temperature field is fully developed if the velocity field is fully developed. This implies that the development length for the temperature field is at most equal to the development length for the velocity field. A consequence of this result is that the thermal development length is independent of Prandtl number. This result is different from that of forced convective flows where the ratio of the development length for velocity and temperature is a function of Prandtl number.

Aung et al. (1972) solved the asymmetrically heated plates for the developing flow situation computationally. Their assumptions were the same as those made by Bodoia and Osterle (1962). They found that the flow was fully developed for $\mathrm{Ra} \leq 0.14$. They also found that their solutions deviated by about 10 percent from the single plate solution of Sparrow and Gregg (1956) even at $\mathrm{Ra} = 10^5$. Their experimental determination of local heat transfer rate on the plates using the Schlieren method was in good agreement with their numerical predictions.

Wirtz and Stutzman (1982) experimentally studied natural convection between two vertical plates subjected to equal uniform heat fluxes for $18.8 \leq \mathrm{Ra} \leq 2414$. Their results agreed well with the computational results given by Aung et al. (1972) for symmetric heating. They presented a correlation using the method of Churchill and Usagi (1972) for $18.8 \leq \mathrm{Ra} \leq 2414$ as follows:

$$\mathrm{Nu}\left(Y = \frac{L}{b}\right) = \frac{0.144\ \mathrm{Ra}^{0.5}}{(1 + 0.0156\ \mathrm{Ra}^{0.9})^{0.33}} \tag{1}$$

The asymptotic limits used by them were the fully developed solution of Aung (1972) and a correction to the single plate solution of Sparrow and Gregg (1956). Johnson (1986) compared predictions made by the correlation of Wirtz and Stutzman (1982) with recent data and found that the correlation was reliable only for $\mathrm{Ra} \leq 1000$. For $\mathrm{Ra} > 1000$, the correlation equation (1) was found to overpredict the heat transfer. Chung et al. (1981) studied the combined mode of natural convection and forced convection in a channel using the Galerkin principle. They obtained velocity profiles and Nusselt numbers for fluids with low Prandtl number and found that low Prandtl number fluids are more effective in transferring heat by natural convection.

Thus, the literature survey indicates that the maximum temperature is a function of only channel Rayleigh number. The assumptions that were made by earlier researchers in their computational studies were that: (*a*) the inlet temperature and velocity profiles are uniform; (*b*) the only mode of heat

Contributed by the Heat Transfer Division for publication in the JOURNAL OF HEAT TRANSFER. Manuscript received by the Heat Transfer Division August 31, 1988; revision received May 8, 1990. Keywords: Electronic Equipment, Enclosure Flows, Natural Convection.

transfer from the channel is natural convection; and (*c*) the channel aspect ratio is so large that the boundary layer approximations are valid. All of the above computational and experimental work in the literature were carried out in situations where the above assumptions were valid, i.e., in channels of large aspect ratio. Assumptions (*b*) and (*c*) are not valid for channels of moderate aspect ratio. Diffusion of thermal energy in the vertical direction becomes important for low Ra and moderate channel aspect ratios. Aihara (1973) and Nakamura et al. (1982) used boundary layer approximations for flow between isothermal plates; however, they did not make the assumption of uniform inlet temperature and velocity profiles.

Bar-Cohen and Rohsenow (1984) developed an integral formulation for fully developed laminar flow for symmetric as well as asymmetric thermal situations. They also consolidated the experimental data of others and, using the method of Churchill and Usagi (1972), obtained correlations for all the vertical plate situations described earlier. They demonstrated how these correlations may be used with appropriate design criteria to make first-order estimates of temperatures and heat transfer for electronic equipment. Recently, O'Meara and Poulikakos (1987) have experimentally studied the phenomenon of cooling by natural convection of an array of vertical plates with uniform and equal heat fluxes placed in an enclosure. The effect of several factors on the plate temperature distribution was determined. These factors are the spacing of the plates, the effect of the floor, and the effect of the ceiling. Extensive data are not available for correlation or comparison. It was found that the ceiling had the most significant effect on heat transfer. They determined that the ceiling was required to be at least ten times the height of the plate away from the plate if it is not to impede heat transfer from the plate.

The enclosure is postulated so that no assumptions regarding the entrance velocity and temperature profiles are required to be made. The assumptions (*a*), (*b*), and (*c*) listed above are relaxed by solving the two-dimensional problem elliptically. The plate temperatures obtained in this study were compared with the experimental results of Wirtz and Stutzman (1982) for large channel aspect ratios. It must be noted that the smallest aspect ratio presented by Wirtz and Stutzman (1982) was approximately 17. An extensive parametric study has been conducted to include the Prandtl number effect and correlations for maximum temperature and average heat transfer rate are presented in this paper. The correlations are obtained to include the effect of channel aspect ratio for air. The Prandtl number effect is included in the correlations for large aspect ratio channels.

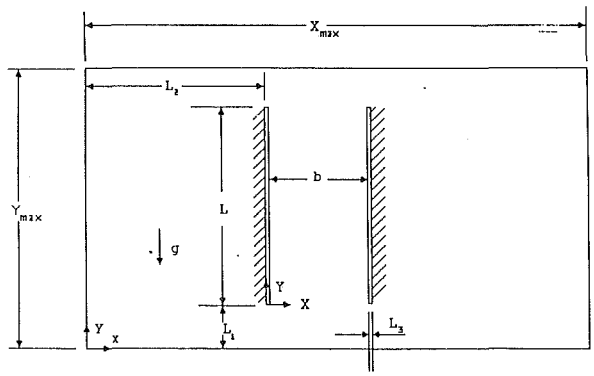

Fig. 1 Geometry of the problem, principal dimensions, and coordinate axes (figure is not to scale)

Mathematical Analysis and Numerical Procedure

The governing equations are derived from the basic laws of conservation of mass, momentum, and energy. The important flow parameters in this natural convection problem between parallel plates kept in a large enclosure are channel Rayleigh number (Ra) and Prandtl number (Pr), and geometric parameters. Referring to Fig. 1, they are the channel aspect ratio, L/b, and x_{max}/b, y_{max}/b, L_1/b, L_2/b, and L_3/b. The channel aspect ratio, L/b, was the only geometric parameter that was varied in this study. The other parameters were maintained at an appropriate value such that the enclosure had no effect on the results. Effectively, the flow between two parallel vertical plates is solved as an elliptic problem as if the plates are positioned in an infinite medium. This is done in order to remove any assumptions that are required to be made on the entrance velocity and temperature profiles, to include the vertical diffusion of energy and to compare our results with those in the literature.

Nomenclature

b = channel width (Fig. 1)
Gr = Grashof number (equation (16))
g = gravitational acceleration
L = channel height (Fig. 1)
L_1, L_2, L_3 = dimensions within the enclosure; see Fig. 1
Nu = local Nusselt number (equation (18))
Nu_a = average Nusselt number (equation (18))
$\mathrm{Nu}_{a,c}$ = correlated value of average Nusselt number (equation (31))
P = nondimensional pressure (equation (11))
Pr = Prandtl number (equation (16))
p' = fluid pressure
p = modified fluid pressure
R = channel aspect ratio
Ra = channel Rayleigh number (equation (18))
T = dimensionless temperature (equation (11))
T_E = centerline entry temperature
T_{max} = maximum nondimensional temperature on the plate
T_o = centerline temperature
$T_{max,c}$ = correlated value of the maximum temperature on the plate (equation (30))
t = fluid temperature
t_w = temperature of the enclosure walls
U = dimensionless fluid velocity in x direction (equation (11))
u = fluid velocity in x direction
V = dimensionless fluid velocity in Y direction (equation (11))
v = velocity of fluid in y direction
X, Y = nondimensional coordinates; see Fig. 1
x, y = dimensional coordinates; see Fig. 1
x_1, y_1, z_1 = arbitrary functions
α = thermal diffusivity of fluid
β = thermal expansion coefficient of fluid (equation (9))
μ = dynamic viscosity of fluid
ν = kinematic viscosity of fluid
ρ = density of fluid

Subscripts

max = maximum value of a coordinate

The assumptions made in this flow situation are that the flow is laminar, incompressible, steady, and two dimensional with no viscous dissipation of thermal energy. The Boussinesq approximation is used, i.e., the buoyancy force term is approximated as $(\rho_o - \rho)g = \beta(t - t_w)\rho_o g$, where β is the coefficient of volumetric expansion and t is the temperature. The governing equations and boundary conditions are given in the following section in both dimensional and nondimensional forms with the appropriate parameters defined. Since the plates are symmetrically heated, only half the enclosure is considered, with boundary conditions on the line of symmetry rewritten as

$$U = \partial V/\partial X = \partial T/\partial X = 0$$

Governing Equations

Continuity:

$$\partial u/\partial x + \partial v/\partial y = 0 \tag{2}$$

x Momentum:

$$u\partial u/\partial x + v\partial u/\partial y = (-1/\rho)\partial p/\partial x + \nu(\partial^2 u/\partial x^2 + \partial^2 u/\partial y^2) \tag{3}$$

y Momentum:

$$u\partial v/\partial x + v\partial v/\partial y = (-1/\rho)\partial p/\partial y + \nu(\partial^2 v/\partial x^2 + \partial^2 v/\partial y^2) + \beta g(t - t_o) \tag{4}$$

Energy:

$$u\partial t/\partial x + v\partial t/\partial y = \alpha(\partial^2 t/\partial x^2 + \partial^2 t/\partial y^2) \tag{5}$$

using

$$\rho = p/(Rt), \tag{6}$$

$$p = p' + \rho_o g y \tag{7}$$

and

$$\rho_o - \rho = \beta(t - t_w)\rho_o \tag{8}$$

where

$$\beta = (-1/\rho)(\partial\rho/\partial t)_p \tag{9}$$

Boundary conditions are (see Fig. 1)

$u, v = 0$	at $y = 0$
	at $y = y_{\max}$
	at $x = 0$
	at $x = x_{\max}$
	at $x = L_2$, $L_1 \le y \le L_1 + L$
	at $x = L_2 + b$, $L_1 \le y \le L_1 + L$
$t = t_w$	at $y = 0$
	at $y = y_{\max}$
	at $x = 0$
	at $x = x_{\max}$
$-k\,\partial t/\partial x = +q$	at channel facing side of left plate
$-k\,\partial t/\partial x = -q$	at channel facing side of right plate
$-k\,\partial t/\partial x = 0$	at wall facing sides of both plates

Nondimensionalizing as

$$\begin{aligned} U &= ub/\nu \\ V &= vb/\nu \\ X &= (x - L_2)/b \\ Y &= (y - L_1)/b \\ P &= pb^2/\rho\nu^2 \\ T &= (t - t_w)/(qb/k) \end{aligned} \tag{11}$$

yields

Continuity: $\partial U/\partial X + \partial V/\partial Y = 0$ (12)

X-Momentum: $U\partial U/\partial X + V\partial U/\partial Y = -\partial P/\partial X + \partial^2 U/\partial X^2 + \partial^2 U/\partial Y^2$ (13)

Y-Momentum: $U\partial V/\partial X + V\partial V/\partial Y = -\partial P/\partial Y + \partial^2 V/\partial X^2 + \partial^2 V/\partial Y^2 + \mathrm{Gr}\,T$ (14)

Energy: $U\partial T/\partial X + V\partial T/\partial Y = (1/\mathrm{Pr})(\partial^2 T/\partial X^2 + \partial^2 T/\partial Y^2)$ (15)

where

$$\mathrm{Pr} = \nu/\alpha \text{ and } \mathrm{Gr} = g\beta q b^4/\nu^2 k \tag{16}$$

are the Prandtl number and the Grashof number, respectively. After nondimensionalization, the boundary conditions become

$U, V = 0$	at $Y = -L_1/b$
	at $Y = (y_{\max} - L_1)/b$
	at $X = -L_2/b$
	at $X = (x_{\max} - L_2)/b$
	at $X = 0$, $0 \le Y \le L/b$
	at $X = 1$, $0 \le Y \le L/b$
$T = 0$	at $Y = -L_1/b$
	at $Y = (y_{\max} - L_1)/b$
	at $X = -L_2/b$
	at $X = (x_{\max} - L_2)/b$
$\partial T/\partial X = -1$	at channel facing side of left plate
$\partial T/\partial X = +1$	at channel facing side of right plate
$\partial T/\partial X = 0$	at wall facing sides of both plates

(17)

Quantities of Interest:

$T_{\max}$, maximum nondimensional temperature on the plate;

Local Nusselt number, $\mathrm{Nu} = 1/(T - T_E)$,

where T_E is the nondimensional centerline entry temperature;

Average Nusselt number

$$\mathrm{Nu}_a = (b/L)\int_0^{L/b} dY/(T - T_E); \tag{18}$$

Channel aspect ratio, L/b;

Channel Rayleigh number, $\mathrm{Ra} = \mathrm{Gr}\,\mathrm{Pr}\,b/L$.

The flow field is subdivided into finite volumes, each of which encloses a grid point. Scalar variables such as pressure and temperature are evaluated at the grid node, while the velocity components are chosen to lie on the control volume faces, where they are used for the mass flow rate computations. The governing differential equations are integrated to yield finite difference equations. These finite difference equations are then solved together with a pressure correction equation to satisfy the continuity equation. The solution procedure follows that given by Patankar (1980).

The validity of the algorithm is documented in the literature for various problems. The errors in the energy balance for the enclosure and between the entry and the exit of the channel have been calculated. The rates of change in the maximum value, the minimum value, and the maximum rates of change from one iteration to the next have been determined for all four variables. The relaxation parameters used for most cases were 0.5, 0.5, 0.8, and 1.0 for U, V, P, and T, respectively. However, for low Prandtl number flows, these parameters were changed to 0.2, 0.2, and 0.3, and 1.0 for faster convergence. An error of 0.2 percent in energy balance in the half-enclosure was obtained. The energy balance within the channel for the flow between the plate and the centerline was determined. The energy transfer at the entrance and the exit occurs

due to the convective and vertical diffusive transport in the energy equation. The transport of energy by the convective terms in the channel is written as

$$q_{\text{flo}} = \left[\int_0^{0.5} VT\,dX\right]_{Y=L/b} - \left[\int_0^{0.5} VT\,dX\right]_{Y=0} \tag{19}$$

The transport of energy by the diffusive terms in the channel is written as

$$q_{\text{dif}} = \frac{1}{\text{Pr}}\left\{\left[\int_0^{0.5} \frac{\partial T}{\partial Y}\,dX\right]_{Y=L/b} - \left[\int_0^{0.5} \frac{\partial T}{\partial Y}\,dX\right]\right\}_{Y=0} \tag{20}$$

An energy balance performed within the channel should yield

$$q_{\text{tot}} = q_{\text{flo}} + q_{\text{dif}} \tag{21}$$

where q_{tot} is the total nondimensional energy supplied to each plate by the imposed uniform heat flux and is given by L/b. When the channel Rayleigh number and channel aspect ratio are large, the vertical diffusion of energy is negligible and $q_{\text{dif}} \approx 0$. In the present study, small and large aspect ratios are considered, and the inclusion of the vertical diffusion terms causes the plate temperatures to be explicitly dependent on the channel aspect ratio. Numerically, an energy balance of less than 5 percent within the channel was tolerated. Also, a mass balance of less than 0.1 percent was obtained in the channel.

Correlating Procedure

With the numerical results obtained for natural convective flows between two vertical plates, correlations for $T_{\max}$ and Nu_a have been obtained to include the effects of channel aspect ratio and Prandtl number. A broad outline of the correlating procedure is given in this section.

Churchill and Usagi (1972) showed that if an arbitrary function y_1 is a function of z_1, and the functional relationships between y_1 and z_1 are characterized by two distinct asymptotic limits for low and high values of z_1, then using the principle of superposition, y_1 may be expressed as follows:

$$y_1 = \{(Az_1^p)^n + (Bz_1^q)^n\}^{1/n}$$

where

$$y_1 \to Az_1^p \text{ as } z_1 \to 0 \qquad y_1 \to Bz_1^q \text{ as } z_1 \to \infty \tag{22}$$

and

$$n > 0, \text{ if } p < q$$

and

$$n < 0, \text{ if } p > q$$

The value of n is evaluated using available data. Wirtz and Stutzman (1982) used this procedure to present their correlation as given in equation (1) for flow between vertical plates. It is demonstrated here that the same procedure can be successfully used if the number of independent variables is two. In the present study, $T_{\max}$ and Nu_a are functions of L/b and Ra. The function, $y_1 = f(x_1, z_1)$ is expected to correlate with x_1 and z_1 as

$$y_1 = \{[(Az_1^p)^n + (Bz_1^q)^n]^{t/n} + [(Cx_1^r)^m + (Dx_1^s)^m]^{t/m}\}^{1/t} \tag{23}$$

In our case, $y_1 = T_{\max}$ or Nu_a, $z_1 = \text{Ra}$, and $x_1 = L/b$. The equation

$$y_2 = \{[(Az_1^p)^n + (Bz_1^q)^n]\}^{1/n} \tag{24}$$

corresponds to the solution when vertical diffusion is negligible, since the exponent t in equation (23) is negative. Vertical diffusion may be ignored when $L/b > 10$ as the present data suggest. Az_1^p corresponds to the fully developed limit of Aung's (1972) solultion and Bz_1^q corresponds to the corrected single plate limit of the solultion of Wirtz and Stutzman (1982). Correlation of the form given in equation (24) was obtained by Wirtz and Stutzman (1982) based on their experimental data. The equation

$$y_3 = \{(Cx_1^r)^m + (Dx_1^s)^m\}^{1/m} \tag{25}$$

corresponds to the solution in the absence of natural convection, i.e., when $\text{Ra} = 0$. Equation (25) is obtained by proposing a conduction model described below.

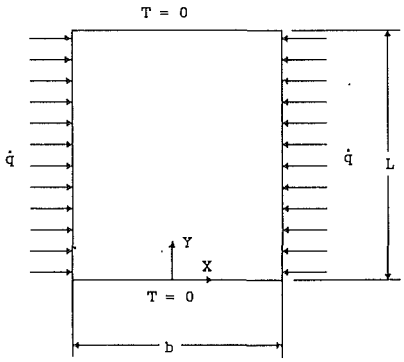

Fig. 2 Conduction model

Conduction Model

In order to obtain the two asymptotic limits of conduction for $L/b \to 0$ and $L/b \to \infty$ for $\text{Ra} \to 0$, a model is proposed as given in Fig. 2. For the new coordinates, the equation and the boundary conditions are given as follows:

$$\begin{gathered} \partial^2 T/\partial X^2 + \partial^2 T/\partial Y^2 = 0 \\ \partial T(0,\ Y)/\partial X = 0 \\ \partial T(0.5,\ Y)/\partial X = 1 \\ T(X,\ 0) = 0 \\ T(X,\ R) = 0 \end{gathered} \tag{26}$$

where $L/b = R$.

The solution to this equation was obtained by separation of variables and is

$$T(X,\ Y) = \left(\frac{2R}{\pi^2}\right)\sum_{m=1}^{\infty} \frac{(1-(-1)^m)}{m^2 \sinh\left(\frac{m\pi}{2R}\right)} \cosh\left(\frac{m\pi X}{R}\right)\sin\left(\frac{m\pi Y}{R}\right) \tag{27}$$

The maximum temperature occurs at the middle of the plates and is given by

$$T_{\max} = \left(\frac{2R}{\pi^2}\right)\sum_{m=1}^{\infty} \frac{(1-(-1)^m)}{m^2 \tanh\left(\frac{m\pi}{2R}\right)} \sin\left(\frac{m\pi}{2}\right) \tag{28}$$

The local temperature on the wall and the average Nusselt number are obtained as

$$T_{\text{wall}} = \left(\frac{2R}{\pi^2}\right)\sum_{m=1}^{\infty} \frac{(1-(-1)^m)}{m^2 \tanh\left(\frac{m\pi}{2R}\right)} \sin\left(\frac{m\pi Y}{R}\right) \tag{29}$$

and

$$\text{Nu}_a = \frac{\pi^2}{2R}\int_0^R \frac{dY}{\sum_{m=1}^{\infty} \frac{(1-(-1)^m)}{m^2 \tanh\left(\frac{m\pi}{2R}\right)} \sin\left(\frac{m\pi Y}{R}\right)}$$

In the case of correlation for T_{max}, the conduction solution has two well-defined asymptotic limits and the series solution given by equation (28) can be approximated in the form given by equation (25). Equation (29) was curve fitted approximately as: $Nu_a = K/R$.

Validation of Results

The validation of the problem simulation was accomplished by comparing with the experimental results of Wirtz and Stutzman (1982). To compare with the experimental data, large values of enclosure size and channel aspect ratios were used. It was found that the heat transfer results were independent of the channel aspect ratio beyond $L/b = 15$. The plates were centrally placed in the x direction. Symmetry was forced and the solution domain was reduced to half its size. All the calculations were carried out on the NAS/XL-60 mainframe computer.

Since the study involves the flow between two parallel plates, the enclosure walls should be ideally kept at infinity. However, for computational purposes, infinity was defined when these walls do not affect the heat transfer between the plates. To this end, 40 different grids were tried to obtain a grid-independent solution. Despite using very tall enclosures (20 times the horizontal width), the heat transfer results were still found to be sensitive to the location of the plates in the vertical direction. This was found to be true for a variety of uniform and nonuniform grids. Hence, the heat transfer from the walls of the enclosure was evaluated. It was found that the top wall was losing more heat than the bottom wall when the plates were centrally placed in the vertical direction. Hence, the plates were moved closer to the bottom wall so that the presence of the enclosure would not affect the solution.

The temperatures within the plates were offset by the entry temperature at the centerline of the plates. This was done to correct for any preheating of the air, as the intention was to quantify the effects of the plates in an infinitely large enclosure. Typically, these nondimensional entry temperatures were of the order 10^{-2}, except when the contribution from conduction was very high. This optimal nonuniform mesh of 56×62 was obtained by comparing the results for different grids and experimental data for $Ra = 2414$. This mesh was then tested for a variety of channel Rayleigh numbers for which experimental data were available. Good agreement of local temperatures along the plate was found throughout the range of the experimental data, as will be discussed later. This mesh was used in all further studies, with the vertical scale just being compressed appropriately, such that the ratios for the nonuniform mesh were preserved. The mesh that was finally used had 12 nodes between the centerline and one plate. For comparison, the temperature at the top edge of the plate was chosen since this was the most sensitive point in the domain of interest. More details of the validation procedures are given by Ramanathan (1988).

Results and Discussion

Natural convection of air between heated vertical plates inside a large enclosure has been studied numerically. The results of heat transfer and fluid motion have been presented using the Boussinesq approximation for a wide range of channel Rayleigh numbers (Ra) and channel aspect ratios (L/b). The effects of the channel aspect ratio and Prandtl number on the heat transfer and fluid motions are discussed. Heat transfer correlations are presented.

Figure 3 shows the local temperature variation along the plate compared with the experimental results of Wirtz and Stutzman (1982) for $Ra = 18.8$, 191, and 2414. A nonuniform mesh was used along the plates to get better accuracy at critical points. The agreement for $Ra = 18.8$ is found to be excellent,

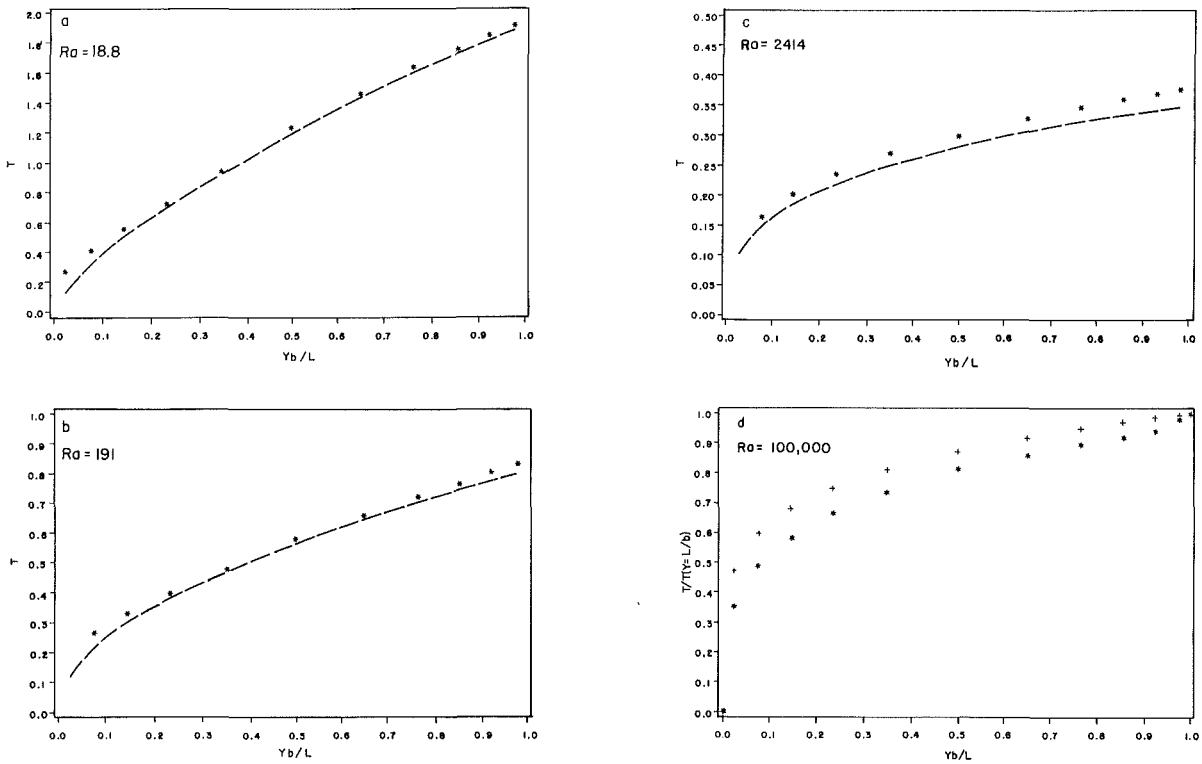

Fig. 3 Nondimensional temperatures along the plate for (*a*) Ra = 18.8, (*b*) Ra = 191, (*c*) Ra = 2414, (*d*) Ra = 100,000; experimental results of Wirtz and Stutzman (1982) (----), present results (*) and similarity solution of Sparrow and Gregg (1956) (+)

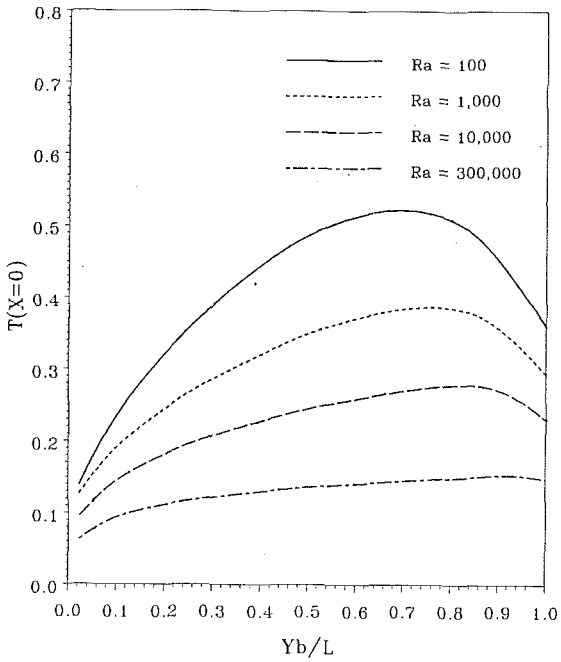

Fig. 4 Nondimensional temperature profiles along the plate for $L/b = 1$

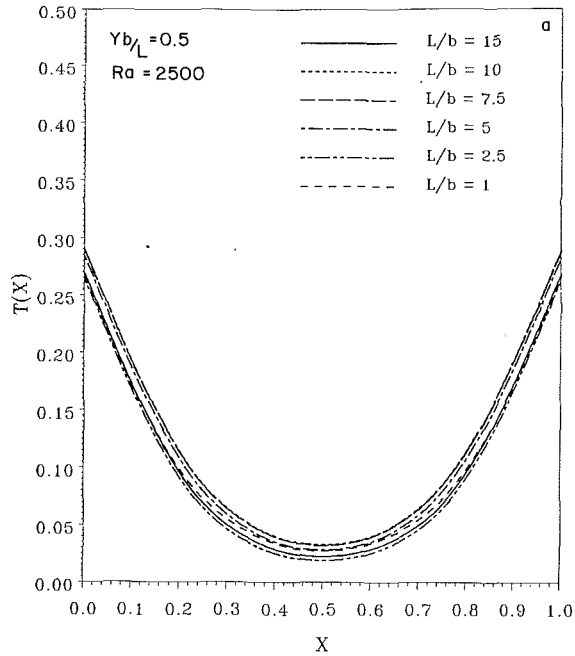

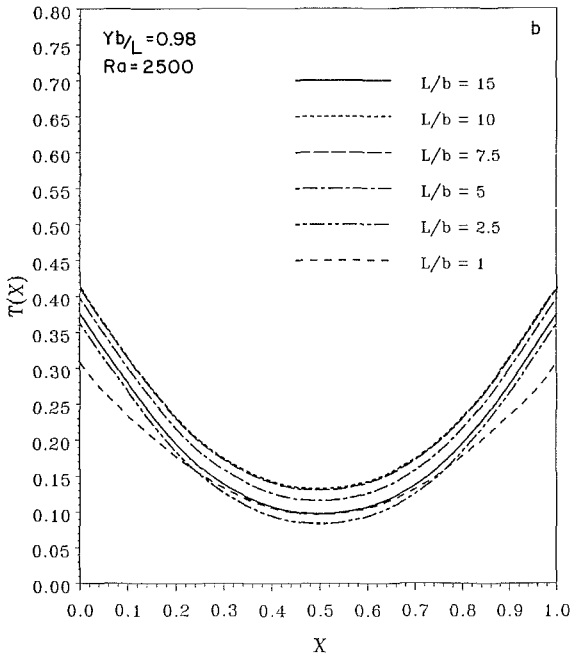

Fig. 5 Nondimensional temperature profiles at Ra = 2500 for different L/b at (a) $Yb/L = 0.5$; (b) $Yb/L = 0.98$

except for $Yb/L \leq 0.2$. It must be emphasized that Wirtz and Stutzman (1982) did not measure the temperatures close to the channel entrance and the exit. Figure 3(b) also shows good agreement except for $Yb/L \leq 0.2$. Figure 3(c), for Ra = 2414, shows a maximum error of about 7 percent. The experimental uncertainties of Wirtz and Stutzman (1982) are 10 percent on Ra and 5 percent on the temperature measurements. The percentage difference between the present results and those of Wirtz and Stutzman (1982) is higher for higher Rayleigh numbers. The error in energy balance between the entrance and the exit of the plates was always less than 5 percent. It must be noted that extremely large computational domains and large variations in mesh spacings are dealt with, and that the full elliptic Navier-Stokes equations are solved, although the primary interest is in a very small portion of the solution. Figure 3(d) shows the normalized temperature profile along the plate at Ra = 100,000 and the single-plate solution of Sparrow and Gregg (1956). The presence of two heated plates causes increased convection and hence increased heat transfer. Thus the single-plate temperature rises at a faster rate than the present results.

Effects of Aspect Ratio for Air. Figure 4 shows the temperature distribution along the plate for $L/b = 1$, for several Rayleigh numbers. This figure shows that for low channel aspect ratios, the maximum temperature occurs close to the midheight of the plate. This is attributed to the significant vertical diffusion occurring at low values of the channel aspect ratio. If the vertical diffusion is significant, the most recessed region on the plate in terms of energy transfer is the midheight of the plate. Thus, the maximum temperature is expected to occur around this region. Further, as the Rayleigh number increases, the convective component of energy transfer becomes more significant. This, in turn, reduces the maximum temperature and moves it higher up the plate.

Figures 5(a) and 5(b) show the temperature distribution across the channel for Pr = 0.7, Ra = 2500, $Yb/L = 0.5$, and $Yb/L = 0.98$, respectively. The differences in temperature levels for different aspect ratios are due to vertical diffusion of energy even for large Rayleigh numbers. The temperature profiles for $L/b \geq 10$ are almost coincident, implying that there are no differences in the heat transfer results for $L/b \geq 10$, if the channel Rayleigh number is chosen as the correlating parameter. Figures 4 and 5 also illustrate the importance of the inclusion of vertical diffusion for moderate aspect ratios.

Velocity and Temperature Fields (Prandtl Number Effect). For a large channel aspect ratio of $L/b = 15$, numerical results were obtained for Pr = 0.01, 0.1, 0.7, 5, 25, and 100. Aung (1972) showed that in natural convection problems, the thermal development length is at most equal to the hydrodynamic development length. His result is independent of entrance profile assumptions for velocity and temperature for large aspect ratios, provided that the vertical diffusion of momentum and energy is negligible. According to Aung's (1972) work, the ratio of the thermal to the hydrodynamic

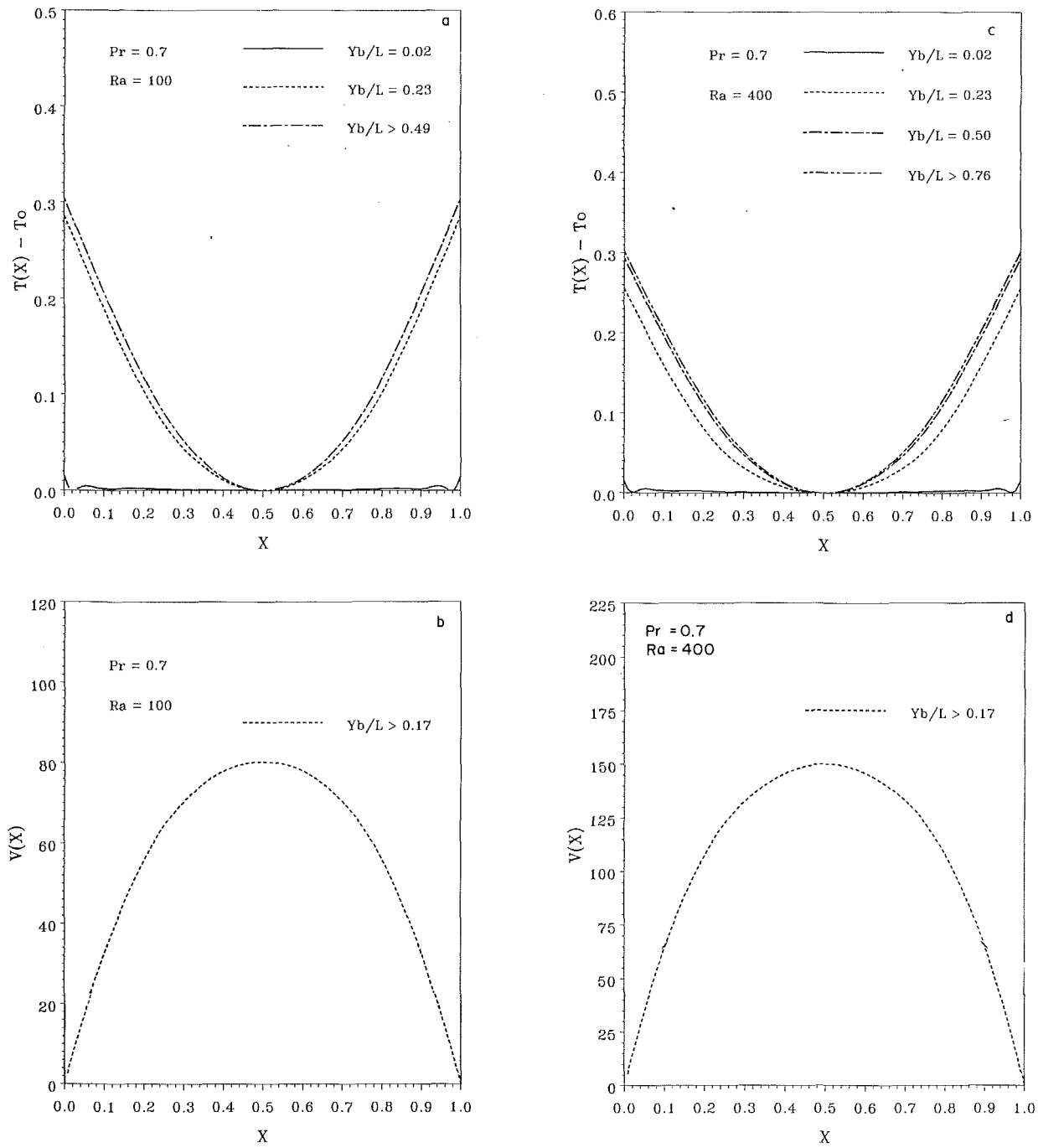

Fig. 6 Nondimensional temperature and velocity profiles at different vertical locations for $L/b = 15$ and Pr = 0.7 for (*a*), (*b*) Ra = 100, (*c*), (*d*) Ra = 400

development length is independent of Prandtl number and is less than or equal to 1.

The velocity and temperature distributions across the channel at different vertical locations along the channel are given in Fig. 6. The temperature at the centerline is subtracted from the temperature profile. Thus, the assumption of uniform entrance temperature in all previous computational studies appears to be correct. It is also seen that the difference between the wall temperature and the centerline temperature is almost the same at different Rayleigh numbers except that the temperatures are scaled down. Figure 6 shows that for Pr = 0.7, Ra = 400, and $L/b = 15$, the velocity profiles are fully developed for $Yb/L > 0.17$. However, the temperature profile $(T - T_o)$ versus X is not fully developed until $Yb/L = 0.76$. This result is contrary to Aung's (1972) results. The inclusion of vertical diffusion of energy seems to contribute to the extension of the thermal development length. Similar results were noted for Ra = 18.8. The present results are also inconsistent with the results of Aung et al. (1972) who determined that only flows with $Ra \leq 0.14$ have a fully developed temperature profile for isoflux plates. This result is attributed to the nonuniformity of the entrance velocity profile. In the present results, there was no change in trend in the fully developed nature of the profiles when the Prandtl number was increased to 5, 25, and 100. Since this is a computational study, the flow field was regarded to be fully developed when the maximum change from one plotted location to the next was less than 1 percent.

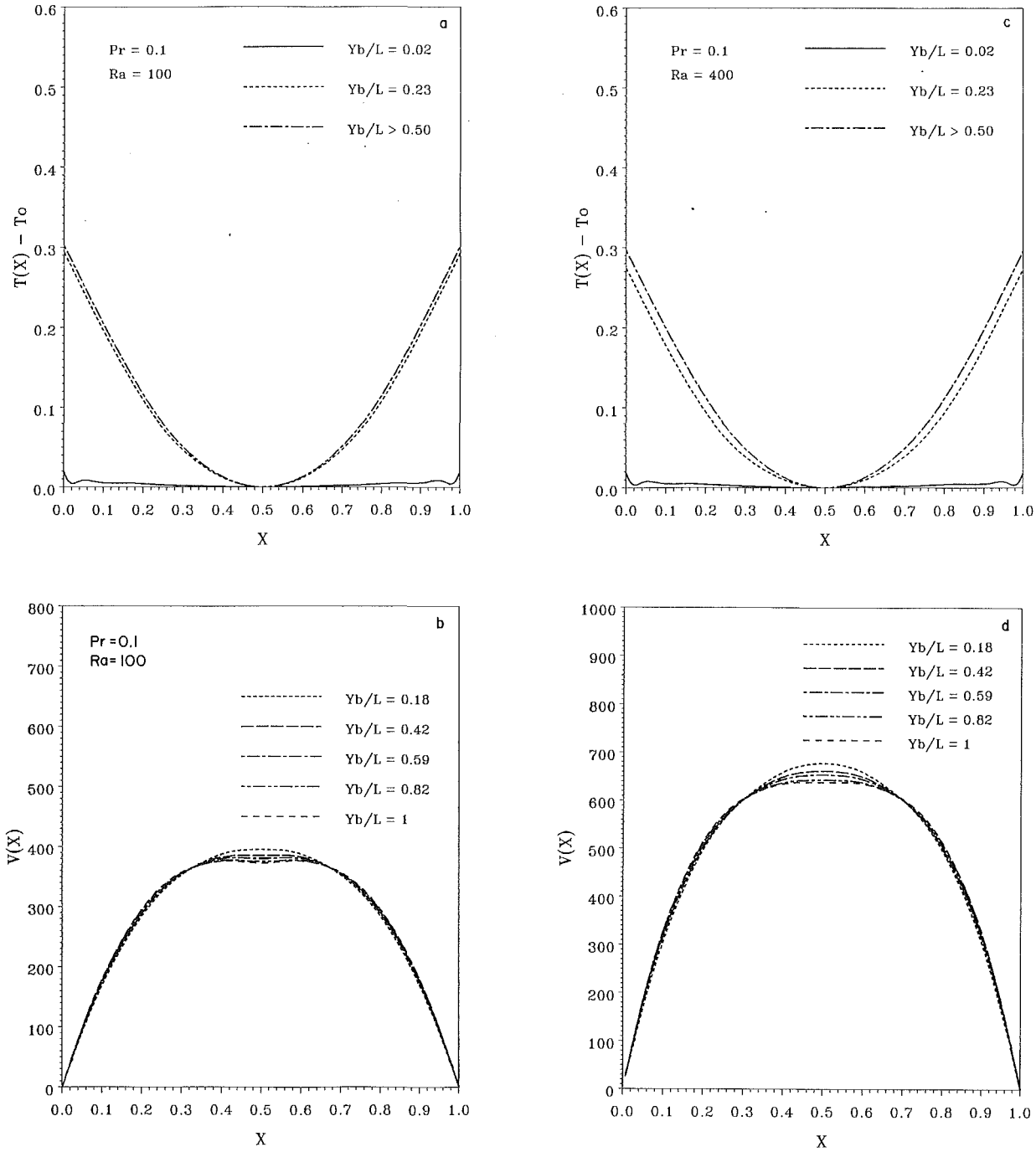

Fig. 7 Nondimensional temperature and velocity profiles at different vertical locations for $L/b = 15$ and Pr = 0.1 for (*a*), (*b*) Ra = 100; (*c*), (*d*) Ra = 400

It is established in the literature that for symmetric and asymmetric isoflux channels, the fully developed local Nusselt numbers are identical to those for forced convection. The results of Aung (1972), Miyatake et al. (1973), and Aihara (1973) demonstrate that there is little difference between buoyancy-induced convection and forced convection for fully developed laminar flow. Also, Aihara (1973) performed a study of the effects of inlet conditions for the isothermal channels. His inlet condition accounts for the pressure drop due to the acceleration of the quiscent fluid to an inlet velocity. He attributed the error in Aung's (1972) result from the theoretical limit to the uniform profile assumption at the channel inlet. The developing flow is predominantly forced channel flow at the inlet for small flow rates (i.e., small Reynolds numbers), which undergoes transition to a predominantly buoyant boundary layer flow at the exit (Bar Cohen and Kraus, 1988). Thus, it is not surprising that a thermally driven flow is hydrodynamically fully developed before it is thermally fully developed.

Figure 7 shows the velocity and temperature profiles for Ra = 100 and 400, when Prandtl number was decreased to 0.1. In this case, the temperature and velocity profiles become fully developed for $Yb/L \geq 0.5$, consistent with Aung's (1972) statement that the thermal development length is less than the hydrodynamic development length. The velocity becomes fully developed at $Yb/L = 1$ for Ra = 100 and Ra = 400 using the

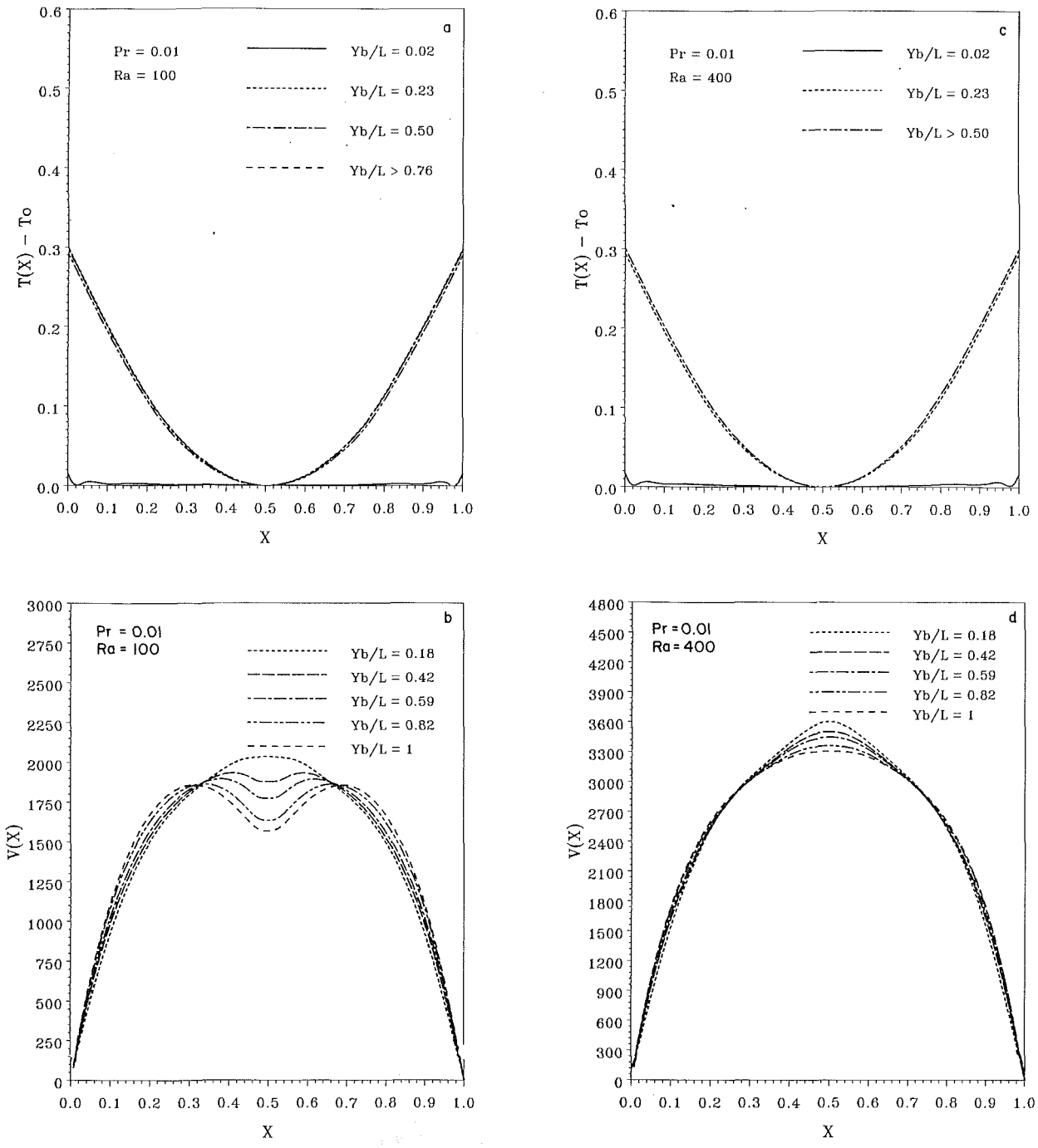

Fig. 8 Nondimensional temperature and velocity profiles at different vertical locations for $L/b = 15$ and $Pr = 0.01$ for (*a*), (*b*) $Ra = 100$; (*c*), (*d*) $Ra = 400$.

abovedescribed criterion. As Prandtl number is decreased to 0.01, it is seen from Fig. 8 that velocity profile is not fully developed for both Ra of 100 and 400, and $(T - T_o)$ increases slightly toward the middle of the channel and decreases again at the top of the channel and never reaches a fully developed state. The contribution due to only conduction was calculated separately and was seen to be nearly 5 times larger (2.5 percent of total heat transfer) for $Pr = 0.01$ when compared with $Pr = 0.7$ for $Ra = 100$. The percentage contribution by conduction dropped when Ra was increased to 400. In the limit as $Pr \to 0$, conduction is the dominant mechanism for transport of heat and the velocity and temperature profiles are not fully developed. Other results for $Pr = 0.01$ suggest the same trend. It is also evident that the channel aspect ratio must be larger than 15 for low Prandtl number fluids if vertical conduction is to be neglected.

Maximum Temperature and Heat Transfer Rates. Figure 9 shows the plot of $Nu(Y = L/b)$ versus Ra. The present numerical data show good agreement with the experimental results of Wirtz and Stutzman (1982) and their correlation, except at large Ra. The data obtained by Wirtz and Stutzman (1982) matched with the computational results of Aung et al. (1972). The disagreement with the correlation at large values of Ra is to be expected as the range of data for which the correlation was presented is $18.8 \leq Ra \leq 2414$. The data for

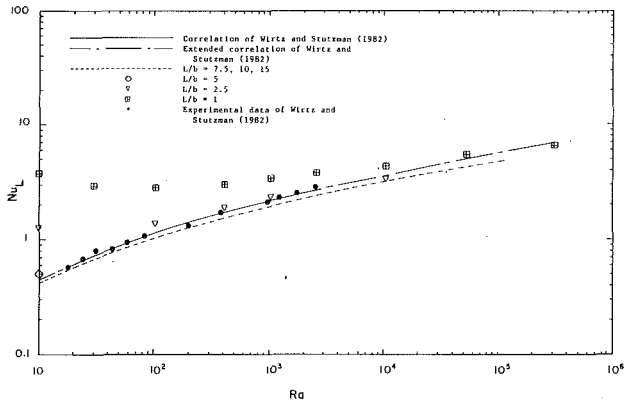

Fig. 9 Nu_L versus Ra

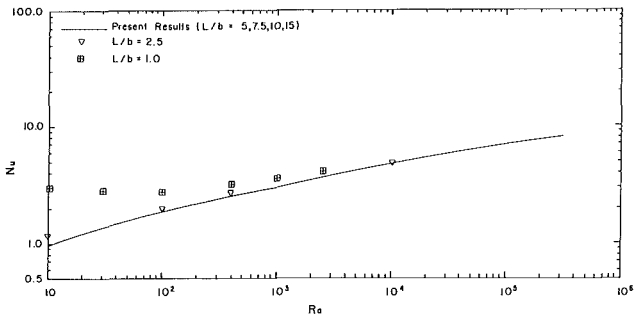

Fig. 10 Nu_a versus Ra

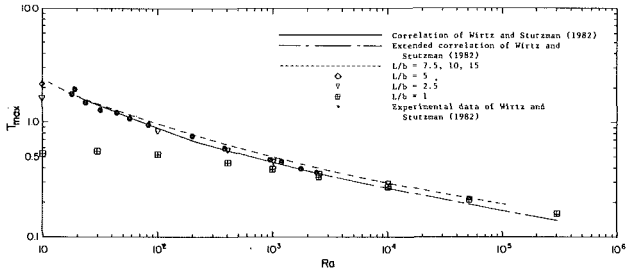

Fig. 11 T_{max} versus Ra

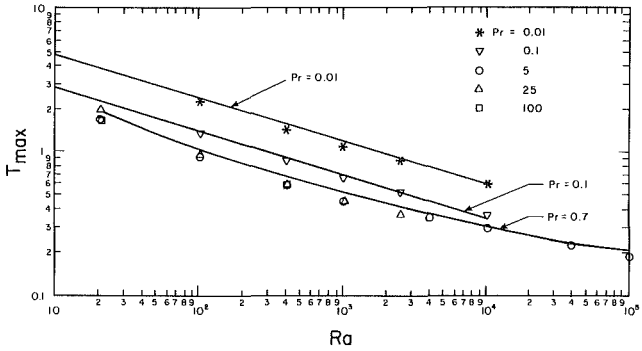

Fig. 12 Maximum temperature on the plate for different Pr and $A = 15$

$L/b \geq 7.5$ are coincident for $Ra \geq 10$ and are represented by a single curve. This implies that the channel aspect ratio is not a separate parameter for $L/b \geq 7.5$. In these situations, the effect of vertical conduction may be ignored, and the currently available correlations may be used. It is seen that for $L/b < 7.5$, there is a deviation from the results for large channel aspect ratio. This deviation decreases as the channel Rayleigh number is increased. These deviations are attributed to the significant vertical conduction that occurs at small and moderate values of the channel aspect ratio, i.e., $L/b \leq 5$. For example, at $Ra = 10$, a difference of 16 percent in $Nu(Y = L/b)$ is noted for $L/b = 5$. Also, Fig. 9 shows that all results tend to the same limit at large Rayleigh numbers. This is due to the fact that conduction in the vertical direction is insignificant and hence the assumptions made by previous analytical studies of the uniform heat flux problem are valid. At low values of the aspect ratio, conduction becomes significant for a wide range of Rayleigh numbers. When vertical conduction is significant, the heat transfer close to the central regions of the plate is the lowest, since these regions are the most recessed. Thus, the top of the plate is significantly cooler than the central regions of the plate. Further, there is a local minimum in the plot of $Nu(Y = L/b)$ versus Ra in Fig. 9, for moderate values of L/b. This can be explained as follows. At low values of Ra, the flow may be characterized as conduction flow regime. This means that the lowest temperature on the plates occurs at $Y = L/b$ and $Y = 0$. Natural convection causes the maximum temperature to move upward without significantly increasing the heat transfer rate. Further increase in Ra results in increased local cooling, which offsets the temperature rise due to the movement of the point of maximum temperature upward. When the conduction heat transfer constitutes about 2 percent or less of the heat transfer from the plates, the maximum temperature occurs at the top of the plate.

It is interesting to note that the average Nusselt number, Nu_a versus Ra, given in Fig. 10, is almost a universal curve except when $L/b \leq 2.5$. Although Fig. 9 shows that the L/b effects are significant when $L/b \leq 5$, Fig. 10 suggests that enhanced heat transfer occurs only for $L/b \leq 2.5$. This means that for $L/b \geq 5$, the inclusion of the vertical conduction terms does not increase the overall heat transfer rate.

Figure 11 is a plot of the maximum temperature on the plate versus the channel Rayleigh number. This again shows the significance of including the vertical conduction heat transfer from the plates in the equations. At $Ra = 10$, low nondimensional temperatures, and thus high Nu, can result for a small channel aspect ratio. This is because the combination of conduction and free convection provides higher heat transfer rates and lower temperatures than when vertical conduction is ignored. Free convection cooling is viable at only moderately large Ra numbers. This may not always be possible, as in the electronic cooling applications where the normal operating range of Ra is between 10 and 300. If the designer does not use an optimum value of channel aspect ratio, he would be forced to use a fan. For example, if the maximum nondimensional temperature specified is 0.5, this could be possible only at $Ra \geq 1000$ without considering the vertical conduction. By utilizing a channel aspect ratio of 1, this may be obtained at $Ra = 10$ if vertical conduction is considered. The disadvantage would be the increased size of the equipment.

Correlations. The importance of vertical diffusion of energy is clearly seen in the plot of T_{max} versus Ra for low channel aspect ratios and $Pr = 0.7$. Maximum temperature decreases for $Ra \leq 2500$ as L/b is decreased. Based on the correlating procedure explained earlier, using purely diffusive transport of energy and negligible vertical, diffusive transport as asymptotes, correlations are presented for T_{max} and Nu_a for $1 \leq L/b \leq 15$ and $10 \leq Ra \leq 3 \times 10^5$ for $Pr = 0.7$ as follows:

$$T_{max,c} = \left\{ \left[\frac{R^2}{5} + \frac{R^4}{15} \right]^{-1.1} + 0.0122 Ra^{1.1} (1 + 0.0156 Ra^{0.9})^{-0.75} \right\}^{-0.4} \quad (30)$$

$$\mathrm{Nu}_{a,c} = \left\{ \frac{185}{R^5} + (23\mathrm{Ra}^{-1.3} + 0.5\mathrm{Ra}^{-0.6})^{-1.25} \right\}^{0.2} \quad (31)$$

where $R = L/b$.

The maximum percentage error between the results obtained in this study and the correlations presented is 10.3 percent for $T_{\max}$ and 7.1 percent for Nu_a.

The effect of Prandtl number on the maximum temperature for $L/b = 15$ is shown in Fig. 12. The change in the maximum temperature for $\mathrm{Pr} \geq 0.7$ is not significant. Higher Prandtl number fluids predict a lower maximum temperature compared to air by less than 14 percent for $\mathrm{Ra} \leq 2500$. For high Ra, the deviation in results is negligible. McGregor and Emery (1969) also found that in rectangular enclosures there was no appreciable change in Nu calculations when Prandtl number was changed from 1 to 100. For $\mathrm{Pr} \leq 0.1$, in the present case, maximum temperatures are higher for all Ra. The data for $\mathrm{Pr} \leq 0.1$ seem to behave as $T_{\max} = C\,\mathrm{Ra}^{-m}\mathrm{Pr}^{-n}$. A correlation could be obtained for $\mathrm{Pr} \leq 0.1$ as

$$T_{\max} = 3.07\ \mathrm{Pr}^{-0.24}\ \mathrm{Ra}^{-0.3} \quad (32)$$

with a maximum error of 7.8 percent. For $\mathrm{Pr} \geq 0.7$, a weak dependence of Prandtl number could be incorporated in the correlation to obtain

$$T_{\max} = 7.521\ \mathrm{Ra}^{-0.5}(1 + 0.0173\mathrm{Ra}^{0.9})^{0.33}\mathrm{Pr}^{-0.007} \quad (33)$$

with a maximum error of 7.4 percent. The standard deviation error in equations (30)–(33) is less than 4 percent.

The integral solution for flow over a single plate given by Sparrow and Gregg (1956) as

$$\frac{\mathrm{Nu}_y}{\mathrm{Gr}_y^{1/5}} = \frac{2}{(360)^{1/5}} \left[\frac{\mathrm{Pr}^2}{0.8 + \mathrm{Pr}} \right]^{1/5} \quad (34)$$

may be reduced to obtain the maximum temperature on the single plate as follows:

$$T_{\max} = 1.6227\ \mathrm{Ra}^{-0.2} \left[1 + \frac{0.8}{\mathrm{Pr}} \right]^{0.2} \quad (35)$$

Using the right-hand side of this equation as guidance, the Prandtl number effect in the present problem may be included in the present correlations in the following form for large L/b and all Prandtl numbers:

$$T_{\max} = 7.521\ \mathrm{Ra}^{-0.5}(1 + 0.0173\ \mathrm{Ra}^{0.9})^{0.33} \left[1 + \frac{0.5}{\mathrm{Pr}} \right]^{0.18} \quad (36)$$

which gives a maximum error of 17 percent.

Summary

Numerical results have been presented for a natural convective flow of fluids ($0.01 \leq \mathrm{Pr} \leq 100$) between two tall vertical plates inside a large enclosure. The physics of the problem has been discussed for small aspect ratios for air.

The results of the present study in air are in close agreement with the finite difference calculations of Aung et al. (1972) and the experimental results of Wirtz and Stutzman (1982) for large aspect ratios.

For fluids with $\mathrm{Pr} \geq 0.7$, the hydrodynamic development length is smaller than the thermal development length for Ra up to 400, contrary to what was reported by Aung (1972). It appears that the vertical diffusion of energy affects the thermal development length, although for high aspect ratios and high Rayleigh numbers, it has no effect on the maximum temperature of the plate. However, the opposite effect is observed for $\mathrm{Pr} \leq 0.1$. For $\mathrm{Pr} = 0.1$, the temperature profile is fully developed around the middle of the plate, whereas the velocity profile becomes fully developed near the exit of the channel. For lower Prandtl numbers ($\mathrm{Pr} \leq 0.01$), the numerical data suggest that the flow should not be assumed to be fully developed. Also, for $\mathrm{Pr} \leq 0.01$, $L/b = 15$ may not be large enough to ignore vertical diffusion of energy.

Vertical conduction has a significant effect on the maximum temperature on the plate for small aspect ratios for air. Correlations have been presented for maximum temperature and average Nusselt number on the plates for $\mathrm{Pr} = 0.7$ to include the aspect ratio effect. Correlations have also been presented to include the effect of Prandtl number for large aspect ratio channels.

References

Aihara, T., 1973, "Effects of Inlet Boundary Conditions on Numerical Solutions of Free Convection Between Vertical Parallel Plates," *Report of the Institute of High Speed Mechanics*, Tohuku University, Japan, Vol. 28, pp. 1–27.

Aung, W., 1972,, "Fully Developed Laminar Free Convection Between Vertical Plates Heated Asymmetrically," *International Journal of Heat and Mass Transfer*, Vol. 15, pp. 1577–1580.

Aung, W., Fletcher, L. S., and Sernas, V., 1972, "Developing Laminar Free Convection Between Vertical Plates With Asymmetric Heating," *International Journal of Heat and Mass Transfer*, Vol. 16, pp. 2293–2308.

Bar-Cohen, A., and Rohsenow, W. M., 1984, "Thermally Optimum Spacing of Vertical Natural Convection Cooled Parallel Plates," ASME JOURNAL OF HEAT TRANSFER, Vol. 106, pp. 116–123.

Bar-Cohen, A., and Kraus, A. D., 1988, *Advances in Thermal Modeling of Electronic Components and Systems*, Vol. 1, Hemisphere Publishing Corporation, Washington, DC.

Bodoia, J. R., and Osterle, J. F., 1962, "The Development of Free Convection Between Heated Vertical Plates," ASME JOURNAL OF HEAT TRANSFER, Vol. 84, pp. 40–44.

Chung, K. S., Bezella, W. A., Thompson, D. H., and Tessier, J. H., 1981, "Analytical and Experimental Simulation of LMFBR Decay Heat Removal by Natural Convection Heat Transfer," *Decay Heat Removal and Natural Convection in Fast Breeder Reactors*, A. K. Agrawal and J. G. Guppy, eds., Hemisphere, Washington, DC, pp. 39–52.

Churchill, S. W., and Usagi, R., 1972, "A General Expression for the Correlation of Rates of Heat Transfer and Other Phenomena," *Journal of American Institute of Chemical Engineers*, Vol. 18, pp. 1121–1138.

Elenbaas, W., 1942, "Heat Dissipation of Parallel Plates by Free Convection," *Physica*, Vol. 9, pp. 1–28.

Johnson, C. E., 1986, "Evaluation of Correlations for Natural Convection Cooling of Electronic Equipment," *Heat Transfer in Electronic Equipment*, A. Bar-Cohen, ed., AIAA/ASME 4th Thermophysics and Heat Transfer Conference, Boston, June 2–4.

McGregor, R. K., and Emery, A. F., 1969, "Free Convection Through Vertical Plane Layers—Moderate and High Prandtl Number Fluids," ASME JOURNAL OF HEAT TRANSFER, Vol. 91, pp. 391–403.

Miyatake, O., Fujii, T., Fujii, M., and Tanaka, H., 1973, "Natural Convective Heat Transfer Between Vertical Parallel Plates—One Plate With a Uniform Heat Flux and the Other Thermally Insulated," *Heat Transfer—Japanese Research*, Vol. 2, pp. 25–33.

Nakamura, H., Asako, Y., and Naitou, T., 1982, "Heat Transfer by Free Convection Between Two Parallel Flat Plates," *Numerical Heat Transfer*, Vol. 5, pp. 95–106.

O'Meara, T., and Poulikakos, D., 1987, "Experiments on the Cooling by Natural Convection of an Array of Vertical Heated Plates With Constant Heat Flux," *The International Journal of Heat and Fluid Flow*, Vol. 8, pp. 313–319.

Ramanathan, S., 1988, "Natural Convection From Heated Plates in Large Enclosures," M.S. Thesis, Clemson University, Clemson, SC, May.

Sobel, N., Landis, F., and Mueller, W., 1966, "Natural Convection Heat Transfer in Short Vertical Channels, Including the Effects of Stagger," *Proceedings, Third International Heat Transfer Conference*, Vol. 2, pp. 121–125.

Sparrow, E. M., and Gregg, J. L., 1956, "Laminar Free Convection From a Vertical Plate With Uniform Surface Heat Flux," *Transactions of the ASME*, Vol. 78, pp. 435–440.

Wirtz, R. A., and Stutzman, R. J., 1982, "Experiments on Free Convection Between Vertical Plates With Symmetric Heating," ASME JOURNAL OF HEAT TRANSFER, Vol. 104, pp. 501–507.

Free Convection Between Series of Vertical Parallel Plates With Embedded Line Heat Sources

S. H. Kim
Graduate Research Assistant.

N. K. Anand
Assistant Professor.
Assoc. Mem. ASME

L. S. Fletcher
Thomas A. Dietz Professor.
Fellow ASME

Department of Mechanical Engineering,
Texas A&M University,
College Station, TX 77843

Laminar free convective heat transfer in channels formed between series of vertical parallel plates with an embedded line heat source was studied numerically. These channels resemble cooling passages in electronic equipment. The effect of a repeated boundary condition and wall conduction on mass flow rate (M), maximum surface temperature ($\theta_{h,max}$ and $\theta_{c,max}$), and average surface Nusselt number ($\overline{Nu}_h$ and $\overline{Nu}_c$) is discussed. Calculations were made for $Gr^* = 10$ to 10^6, $K = 0.1$, 1, 10, and 100, and t/B = 0.1 and 0.3. The effect of a repeated boundary condition decreases the maximum hot surface temperature and increases the maximum cold surface temperature. The effect of a repeated boundary condition with wall conduction increases the mass flow rate. The maximum increase in mass flow rate due to wall conduction is found to be 155 percent. The maximum decrease in average hot surface Nusselt number due to wall conduction (t/B and K) occurs at $Gr^* = 10^6$ and is 18 percent. Channels subjected to a repeated boundary condition approach that of a symmetrically heated channel subjected to uniform wall temperature conditions at $K \geq 100$.

Introduction

Renewed interest in laminar free convection in vertical channels stems from increasing applications in the cooling of electronic circuit boards. Most of the recent work reported in the literature concerns free convection in single channels. In practice, circuit boards with surface-mounted electronic chips are placed parallel to one another (Incropera, 1988) and the circuit boards are separated by the supporting shelves. Heat from electronic chips is dissipated directly to the fluid by convection and to the wall by conduction. Heat conducted to the wall is eventually dissipated by convection to the adjacent channel.

Experimental studies of laminar free convection between parallel heated vertical plates (Elenbaas, 1942; Sparrow and Bahrami, 1980; Wirtz and Stutzman, 1982; Azevedo and Sparrow, 1985; Webb and Hill, 1989) considered both symmetric and asymmetric heating conditions. An implicit finite difference method was used by some investigators (Bodia and Osterle, 1962; Aung and Worku, 1986a, 1986b) to study free convection in vertical channels. These calculations were made by solving boundary layer equations for flow between vertical plates. Some investigators (Aung et al., 1972; Aung, 1972; Carpenter et al., 1976; Sparrow et al., 1984) studied this problem both experimentally and numerically. Burch et al. (1985) numerically studied the effect of wall conduction on free convection between symmetrically heated vertical plates. In this study the external surfaces of the plates were subjected to uniform wall temperature (UWT) conditions. Recently, calculations were made by Anand et al. (1990) and Kim et al. (1990) to examine the effect of wall conduction on free convection in vertical channels under asymmetric heating conditions. Conjugate heat transfer studies (Burch et al., 1985; Anand et al., 1990; Kim et al., 1990) show that wall conduction significantly influences the heat transfer and mass flow rate of air in the vertical channel. Bar-Cohen and Rohsenow (1984) and Johnson (1986) critically reviewed the existing data and correlations for free convection in vertical channels and recommended the most suitable correlations. Incropera (1988) presented a comprehensive review of various convective cooling methods used in electronic equipment. A careful examination of these studies reveals that limited attention has been given to free convection in channels formed between series of parallel plates.

The nature of circuit board arrangement is such that heat dissipation from a heat source is partly by convection to air and partly by conduction to the substrate. Heat conducted to the substrate is eventually removed by convection in the adjacent channel and is repeated in every channel. The temperature and heat flux at any point on the vertical surface are the same at any corresponding point on the vertical surface in the adjacent channel. The temperature distribution on these surfaces is not known a priori but must be determined as a part of the solution. This is the boundary condition used, and it is referred to as the "repeated" boundary condition. Therefore, it is not only important to determine the effect of wall conduction on heat transfer, but also the effect of repeated boundary conditions. The first and last channels, however, are subjected to different boundary conditions and must be treated differently.

The objective of this paper is to study free convection heat transfer in a channel subjected to a "repeated" boundary condition using an implicit finite difference method. As a first step, attention is focused on channel walls with flush-mounted, line heat sources and without considering the support shelves. It should be noted that the simulated heat source is manifested as a line source because consideration is given only to two-dimensional free convective flow in this work. Model development, solution technique, validation of the solution, and discussion of results are presented in the following sections.

Model Development

A schematic of a series of channels considered for the purpose of the present analysis is shown in Fig. 1(*a*). The physical situation that exists in the middle channels is the same and a computational domain can be isolated as shown in Fig. 1(*b*). Note that the temperature and heat flux at any point on surface 1 are the same as the temperature and heat flux at the corresponding point on surface 2. The temperatures on surface 1

Contributed by the Heat Transfer Division and presented at the ASME Winter Annual Meeting, San Francisco, California, December 10-15, 1989. Manuscript received by the Heat Transfer Division August 25, 1989; revision received April 10, 1990. Keywords: Conjugate Heat Transfer, Electronic Equipment, Numerical Methods.

and 2 are not known a priori and must be determined as a part of the solution; however, $T(X, 1) = T(X, 2)$. At a given axial location (X), the transverse velocity and temperature distribution in each of these middle channels are identical and the associated equations in nondimensional form for air can be written as:

Continuity (Air)

$$\frac{\partial U}{\partial X} + \frac{\partial V}{\partial Y} = 0 \tag{1}$$

Axial Momentum (Air)

$$U\frac{\partial U}{\partial X} + V\frac{\partial U}{\partial Y} = -\frac{dP}{dX} + \frac{\partial^2 U}{\partial Y^2} + \theta \tag{2}$$

Energy (Air)

$$U\frac{\partial \theta}{\partial X} + V\frac{\partial \theta}{\partial Y} = \frac{1}{\mathrm{Pr}}\frac{\partial^2 \theta}{\partial Y^2} \tag{3}$$

Consideration is given to steady-state laminar free convective flow of air in a channel, as shown in Fig. 1(*b*). Thermophysical properties of the air and the solid are assumed to remain constant. However, the Boussinesq approximation is invoked to confine the density variation of air to the axial momentum equation. Boundary layer equations are employed and pressure variation in the transverse direction is assumed to be zero. Based on the foregoing assumptions, the conservation of energy equation for the solid is

Energy (Solid Wall)

$$\frac{\partial^2 \theta}{\partial X^2} + \mathrm{Gr}^2\frac{\partial^2 \theta}{\partial Y^2} = 0 \tag{4}$$

where

$$X = \frac{x}{L\mathrm{Gr}^*} \qquad Y = y/B$$

$$\mathrm{Gr} = \frac{q'' g\beta B^4}{k_f \nu^2}, \qquad \mathrm{Gr}^* = \frac{\mathrm{Gr}B}{L}$$

$$U = \frac{uB^2}{L\nu\mathrm{Gr}^*}, \qquad V = \frac{Bv}{\nu}$$

$$P = \frac{(p - p_o)B^4}{\rho L^2 \nu^2 \mathrm{Gr}^{*2}}, \qquad \theta = \frac{(T - T_o)k_f}{q''B} \tag{5}$$

The model equations (1)–(4) form a set of coupled partial differential equations. In order to solve these four coupled equations, a set of boundary conditions must be specified. The velocities U and V will be zero at surface 2 and at the wall surface with the line heat source due to the no-slip condition.

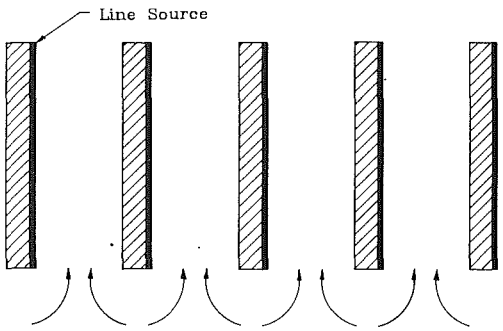

Fig. 1(*a*) Schematic of series of channels

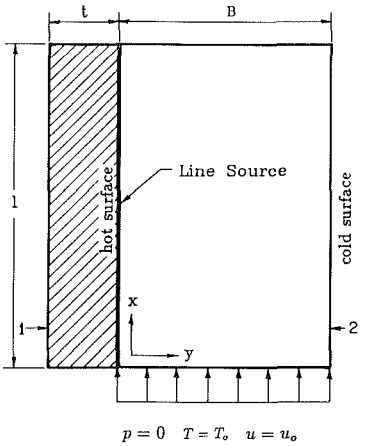

Fig. 1(*b*) Computational domain

Henceforth, the surface with the line heat source and surface 2 will simply be referred to as the hot and cold surfaces, respectively. Pressure at the channel exit will be equal to the ambient pressure (P_o). Air enters the channel at a temperature T_o and with a uniform velocity U_o. In free convection problems the inlet velocity U_o is not known and must be determined as a part of the solution process.

The top and bottom of the solid wall are assumed adiabatic. The "repeated" boundary condition discussed earlier becomes

$$\theta(X, -t/B) = \theta(X, 1) \tag{6}$$

and

$$\left.\frac{\partial \theta}{\partial Y}\right|_{(X, -t/B)} = \left.\frac{\partial \theta}{\partial Y}\right|_{(X,1)} \tag{7}$$

Nomenclature

B = channel width
Gr = Grashof number
Gr* = modified Grashof number
k = thermal conductivity
K = ratio of thermal conductivity of solid wall to thermal conductivity of air
L = channel height
M = mass flow rate of air
Nu = Nusselt number
P = dimensional pressure
p = nondimensional pressure of air
Pr = Prandtl number
q'' = dimensional strength of line heat source
q = nondimensional heat flux
Q = nondimensional total surface heat rate
Ra = Rayleigh number
Ra* = modified Rayleigh number
t = wall thickness
T = dimensional temperature
u = dimensional velocity in the axial direction
v = dimensional velocity in the transverse direction
U, V = nondimensional velocities
x = axial coordinate
y = transverse coordinate
X, Y = nondimensional coordinates
β = thermal expansion coefficient
θ = nondimensional temperature
μ = viscosity
ν = kinematic viscosity
ρ = density

Subscripts

a = air
c = cold surface
h = hot surface
max = maximum value
o = channel inlet
s = single channel

Superscripts

$\bar{}$ = refers to average value

An additional boundary condition is required to determine the temperature at the hot surface. This condition is obtained by applying the heat flux continuity requirement at the hot surface (Zinnes, 1970) as

$$K\frac{\partial\theta}{\partial Y}\bigg|_{(X,0^-)} = \frac{\partial\theta}{\partial Y}\bigg|_{(X,0^+)} + 1 \tag{8}$$

Solution Methodology

The coupled nature of the model equations precludes the possibility of using a closed-form solution technique. In this light an implicit finite difference scheme is used. The axial momentum equation and energy equation for air display parabolic behavior in the axial direction and elliptic behavior in the transverse direction. The first derivative terms in the axial direction (X) are represented by first-order forward difference expressions and second derivative terms in the transverse direction (Y) by second-order central difference terms. The energy equation for the solid (equation (4)) exhibits elliptic behavior in both the X and Y directions. The second derivative terms in equation (4) are represented by the second-order central difference form. The interface condition at the hot surface (equation (8)) is replaced by the second-order difference form. Thus at any given axial location (X), the unknown temperature field displays a cyclic tridiagonal pattern. This cyclic behavior stems from the repeated boundary condition (equation (6)).

The assumption of neglecting the transverse pressure variation has eliminated the transverse momentum equation, which is mathematically essential. To fill this void the integral form of the continuity equation is used

$$\int_0^1 U dY = U_o \tag{9}$$

Equation (9) is converted into a finite difference form by replacing the integral with Simpson's one-third rule.

As stated earlier, the inlet velocity U_o is not known and must be determined as a part of the solution. The pressure at the channel exit ($X = 1/\mathrm{Gr}^*$) is P_o and the pressure at the channel inlet is assumed to be P_o. From potential flow theory it is known that the dimensional pressure at the channel inlet is less than p_o and is equal to $-\rho u_o^2$. However, use of p_o at the channel inlet is a valid assumption based on the fact that the numerical predictions of Aung et al. (1972) using p_o at the channel inlet compares to within 5 percent of the experimental results of Webb and Hill (1989). Only the first derivative term appears in the axial momentum equation, requiring only one boundary condition for pressure at the channel entrance. However, the extra information available for P at the channel exit is used to alleviate the problem of the unknown velocity U_o. An initial value for U_o is estimated and if the calculated value of P at the channel exit is not equal to P_o, then a new estimate of U_o is made and calculations are repeated until the exit pressure is P_o. The computational sequence used in this investigation is similar to that of Anand et al. (1990) and Kim et al. (1990) and is as follows:

1 The value U_o is estimated.

2 Axial momentum and integral forms of the continuity equation (equations (2) and (9)) are solved to obtain U and P by marching in the axial direction. The coupled algebraic equations at each marching station are solved by the Gaussian elimination method.

3 The velocity V is obtained by integrating the differential form of the continuity equation (equation (1)).

4 The energy equation for air (equation (3)) and solid (equation (4)), and the interface condition (equation (8)) are solved to obtain the air and solid temperatures. Note that although solid and air temperature fields are coupled, one is elliptic (equation (4)) and the other is parabolic (equation (3)). The finite difference forms are solved by sweeping alternately in the cross-stream (Y) and axial (X) directions. While sweeping in the axial direction the cyclic tridiagonal matrix algorithm (Anderson et al., 1984) is used to solve for temperatures at each marching station. The tridiagonal matrix algorithm (Peaceman and Rachford, 1955) is used to solve for temperatures in the transverse sweep. The transverse sweep starts at surface 1 and ends at the hot surface.

5 Steps 2–4 are repeated until the maximum difference in temperatures between successive iterative steps at any location is less than 5×10^{-7}.

6 If the calculated value of P at the channel exit is equal to zero, then calculations are terminated. If not, the estimated U_o is altered and steps 2–5 are repeated until $|P_{\min}| < 5\times10^{-5}$.

Validation of the Solution

A series of numerical experiments were conducted to establish grid independence. As a result of this study, 151 uniform grid points were used in the axial direction. In the transverse direction, 40 uniform grid points were used in the solid region and 81 uniform grid points were used in the fluid region. When the number of grid points was increased to 201×141, the change in mass flow rate and average Nusselt number was less than 2 percent.

As a further check, an overall heat balance was examined. The total heat lost by the heat source should be equal to the heat gained by the fluid as it flows through the channel. Mathematically this condition can be represented as

$$\int_0^1 U\theta dY\bigg|_{X=1/\mathrm{Gr}^*} - \int_0^1 U\theta dY\bigg|_{X=0} = 1/\mathrm{Ra}^* \tag{10}$$

For most cases the overall energy balance criteria (equation (10)) were satisfied to within 3 percent. At higher conductivity ratios ($K \geq 100$) and lower Grashof numbers ($\mathrm{Gr}^* \leq 100$), the deviation was higher, with the maximum deviation found to be less than 5.5 percent.

In addition, the analysis was modified to predict heat transfer in a single channel for which experimental data exists in the literature (Aung et al., 1972; Webb and Hill, 1989). Considering the computational domain (Fig. 1*b*) as a single channel, in the absence of wall conduction, the hot surface was subjected to uniform heat flux condition (UHF) and the cold surface represented an insulated surface. This configuration corresponds to heat transfer between two vertical parallel plates subjected to asymmetric heating (Aung et al., 1972; Webb and Hill, 1989) and henceforth will be referred to as the "single channel" solution for simplicity. Conditions representing no wall conduction effects are $t/B = 0$ and a very low conductivity ratio ($K = 0.001$).

In order to make a comparison with other investigations, it was necessary to define a dimensionless mass flow rate (M) as

$$M \equiv \int_0^1 U dY = \frac{U_o B^2}{\nu L \mathrm{Gr}^*} \tag{11}$$

Figure 2(*a*) shows a comparison of the dimensionless mass flow rate of air (M) predicted by the present analysis with those experimentally determined by Aung et al. (1972). The predicted values compared well with the experimental data, with a maximum difference of ± 2 percent.

Figure 2(*b*) shows a comparison of the predicted Nusselt number with those experimentally determined by Aung et al. (1972) and Webb and Hill (1989). The definition of average Nusselt number $\overline{\mathrm{Nu}}_{1/2}$ is given by Aung et al. (1972). The maximum difference between the predicted values and those of

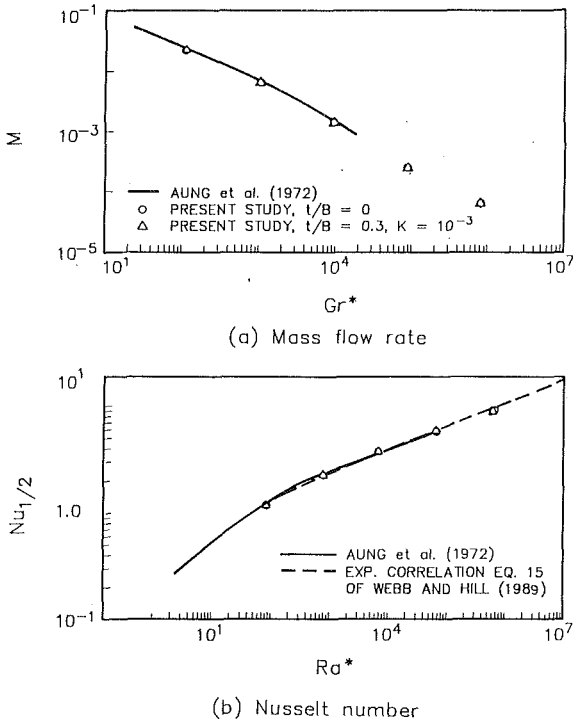

Fig. 2 Validation of the solution technique

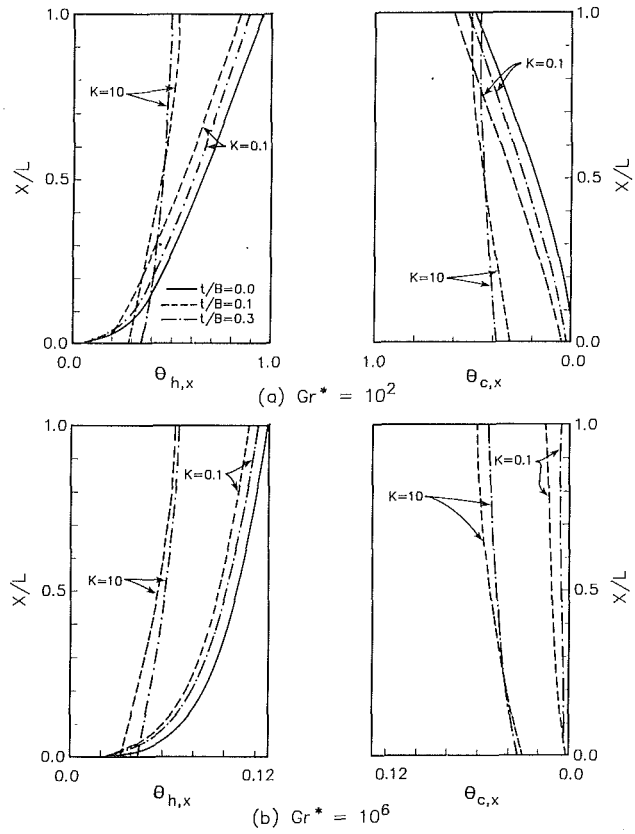

Fig. 3 Interface temperature distribution

Aung et al. (1972) was ±2 percent, and with those of Webb and Hill (1989), ±5 percent.

Results and Discussion

A careful examination of the model equations and associated boundary conditions reveals that the independent parameters are the ratio of wall thickness to channel width (t/B), the ratio of wall thermal conductivity to fluid thermal conductivity (K), modified Grashof number (Gr*), the channel length to channel width ratio (L/B), and the Prandtl number of the fluid (Pr). In this investigation consideration was given only to free convective flow between a series of parallel plates where the Prandtl number was constant at 0.7. The modified Grashof number (Gr*) was defined so that L/B was a part of Gr* and was fixed at unity, and the Gr* was varied from 10^2 to 10^6. Calculations were made for t/B of 0.1 and 0.3, and K of 0.1, 1, 10, and 100, and for various combinations of these independent parameters; however, only results for representative cases were chosen for presentation and discussion.

The effect of wall conduction and the repeated boundary condition on free convection was studied by examining the impact of various independent parameters on the interface temperature distribution ($\theta_{h,X}$ and $\theta_{c,X}$), interface heat flux distribution ($q_{h,X}$ and $q_{c,X}$), transverse velocity distribution (U/U_o), temperature (θ) distribution, maximum interface temperatures ($\theta_{h,\max}$ and $\theta_{c,\max}$), mass flow rate (M), and average surface Nusselt numbers ($\overline{\mathrm{Nu}}_h$ and $\overline{\mathrm{Nu}}_c$).

Interface Temperature Distribution. Figures 3(*a*) and 3(*b*) present interface temperature distributions for $\mathrm{Gr}^* = 10^2$ and $\mathrm{Gr}^* = 10^6$, respectively. In general both surface temperatures increase in the axial direction. This is to be expected, since near the channel entrance the thermal boundary layer is thin, leading to a high heat transfer coefficient. As the channel exit is approached, the thermal boundary layer thickens, leading to a lower heat transfer coefficient. For simplicity the regions closer to the channel entrance and channel exit will be referred to as the upstream and downstream regions, respectively. The existence of wall conduction in the wall lowers the hot surface temperature and leads to a rise in the cold surface temperature, compared to a corresponding single channel. The parameters controlling wall conduction are t/B and K. As shown in Fig. 3(*a*), at low values of K ($K = 0.1$) the temperature of the hot surface decreases with a decrease in t/B, as lower wall resistance facilitates greater heat transport by conduction from the source. For the very same reason the cold surface temperature increases with a decrease in t/B. Similar trends are observed for higher Grashof numbers ($\mathrm{Gr}^* = 10^6$) in Fig. 3(*b*), but are less pronounced because of the higher heat transfer coefficient. However, for higher values of K ($K = 10$) and $\mathrm{Gr}^* = 10^2$ (Fig. 3*a*), $\theta_{h,x}$ and $\theta_{c,x}$ behave differently. In the upstream region, $\theta_{h,x}$ for $t/B = 0.3$ is higher than for $t/B = 0.1$ and this trend is reversed in the downstream region. This change is attributed to the fact that as K increases, conduction heat transfer in the axial direction increases, thus transporting heat from downstream to upstream within the wall. For higher values of Grashof number ($\mathrm{Gr}^* = 10^6$), the temperature crossover occurs near the exit for the hot surface and near the entrance for the cold surface.

At higher conductivity ratios ($K = 100$) the temperature distribution for both hot and cold surfaces is almost uniform and the configuration tends toward that of a UWT condition. The increased conduction heat transfer in both axial and transverse directions is responsible for the uniform surface temperature distribution. The deviation of maximum and minimum surface temperatures from the average surface temperature for both hot and cold surfaces was within 6 percent. The average hot and cold surface temperatures are defined as

$$\bar{\theta}_h = \mathrm{Gr}^* \int_0^{1/\mathrm{Gr}^*} \theta_{h,X} dX$$

$$\bar{\theta}_c = \mathrm{Gr}^* \int_0^{1/\mathrm{Gr}^*} \theta_{c,X} dX \qquad (12)$$

Table 1 Average hot and cold surface temperature; $K = 100$ and $t/B = 0.1$

Gr*	10^2	10^3	10^4	10^5	10^6
$\bar{\theta}_h$	0.429	0.213	0.13	0.0842	0.0549
$\bar{\theta}_c$	0.429	0.213	0.13	0.0837	0.0544

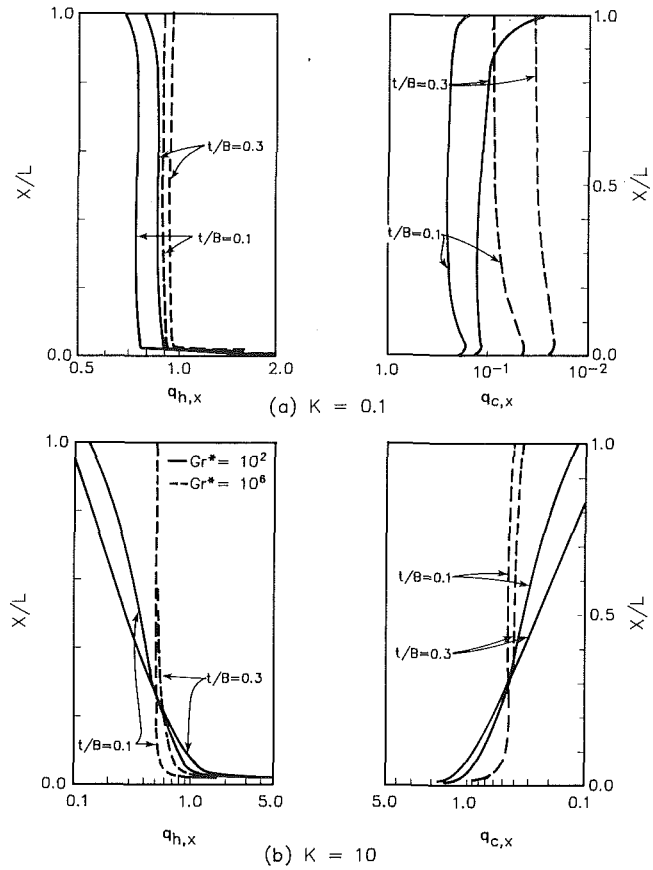

Fig. 4 Axial distribution of surface heat flux

If the conductivity ratio is higher than 100, the computational domain can be viewed as a symmetrically heated single channel subjected to a UWT condition. The average hot and cold surface temperatures for $K = 100$ are given in Table 1.

Interface Heat Flux. The nondimensional surface heat fluxes for the hot and cold surfaces are given by

$$q_{h,X} = -\left.\frac{\partial\theta}{\partial Y}\right|_{Y=0}$$

$$q_{c,X} = \left.\frac{\partial\theta}{\partial Y}\right|_{Y=1} \tag{13}$$

and the axial variations of the surface heat flux for $K = 0.1$ and 10 are shown in Figs. 4(*a*) and 4(*b*), respectively. Note that the heat fluxes are the ratios of convective heat flux at hot and cold surfaces to the strength of the line heat source. At low values of K ($K = 0.1$), the thermal resistance is higher, resulting in a fairly uniform heat flux distribution at both hot and cold surfaces. As the value of K increases, the heat flux at the surfaces becomes nonuniform due to the heat that is transported away from the source by conduction. The axial heat flux gradient is steep in the upstream region compared to the downstream region as the thermal boundary layer thickens in the axial direction. The surface heat flux is nonuniform for lower values of Gr* (Gr* = 10^2) compared to the case for higher value of Gr* (Gr* = 10^6). The higher value of Gr* represents a shorter channel, compared to the lower value of Gr* (Gr* = 10^2), which represents a longer channel. In shorter channels the thermal development is incomplete, while in longer channels the thermal development is complete. This is the reason for the increase in nonuniformity of the heat flux with decrease in Gr. The heat flux distribution for $K = 100$ is similar to that for $K = 10$, and as K increases the effect of t/B diminishes. The heat flux distribution for high K ($K = 100$) and thick wall conditions ($t/B = 0.3$) is very close to the heat flux distribution for the case of a symmetrically heated channel subjected to UWT conditions.

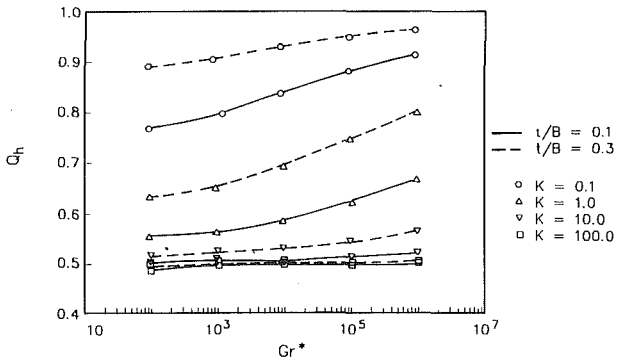

Fig. 5 Total hot surface heat rate

Figure 5 shows the total hot surface heat rate, which is defined as

$$Q_h = \mathrm{Gr}^* \int_0^{1/\mathrm{Gr}^*} q_{h,X}\, dX \tag{14}$$

Note that Q_h is the part of the heat generated by the source that is transferred to the air. The remaining part of the heat, i.e., that which is conducted away from the source (Q_c), is equal to $1 - Q_h$. The maximum value of Q_h will be unity for the case of no wall conduction ($t/B = 0$). The total heat rate at the hot surface decreases with an increase in wall conduction effects (t/B and K).

The value of Q_h increases with an increase in Gr*, but the effect of Gr* diminishes for $K \geq 100$. Also, for $K \geq 100$ the wall conductivity tends to dominate the thermal resistance and the effect of t/B diminishes. For larger values of K ($K = 100$), Q_h is almost equal to one half of the total heat generated by the source.

Transverse Velocity and Temperature Distributions. The transverse velocity distributions (U/U_o) at selected upstream ($X = 0.2$) and downstream ($X = 0.8$) locations are shown in Figs. 6(*a*) and 6(*b*) for a Gr* of 10^2 and 10^6, respectively. The velocity profile indicated by the solid line represents the case of a single channel ($t/B = 0$). For Gr* = 10^2 the velocity profiles do not differ much between the upstream and downstream locations, indicating that the velocity field has fully developed. On the other hand, for a Gr* of 10^6 the development of the velocity profile is not complete (Fig. 6*b*). This behavior is attributed to the fact that a Gr* of 10^2 represents a longer channel, whereas a Gr* of 10^6 represents a shorter channel. In general, velocity profiles are skewed toward the hot wall. The temperature near the hot surface is higher, leading to a higher buoyancy force near the hot surface, and resulting in a higher velocity. The increase in wall conduction tends to lower the hot surface temperature, thus reducing the skewness in the velocity distribution. At higher values of K ($K = 100$) and lower values of t/B ($t/B = 0.1$) the velocity profile is almost symmetric and very similar to the case of a symmetrically heated channel subjected to the UWT condition with no wall conduction. This is because the higher

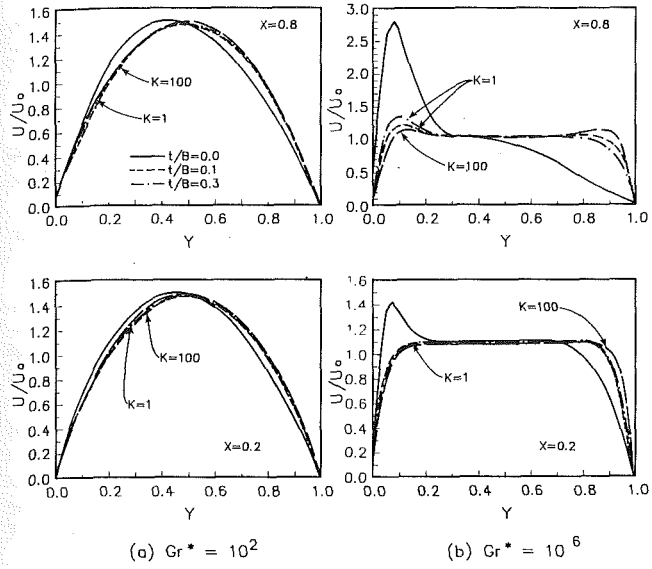

Fig. 6 Transverse velocity distribution

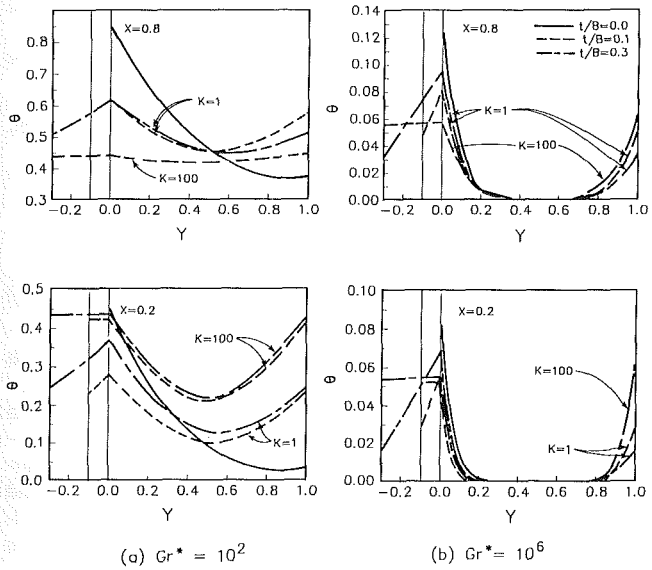

Fig. 7 Transverse temperature distribution

conductivity and lower thickness of the wall reduce the conduction resistance within the wall, resulting in a decrease in the hot surface temperature and an increase in the cold surface temperature. For a Gr* of 10^6, the velocity profile is highly influenced by the wall conduction, a peak in the vicinity of each surface. This profile can be explained by studying the surface temperature distributions (Figs. 3*a* and 3*b*).

Figures 7(*a*) and 7(*b*) show the temperature distribution for $Gr^* = 10^2$ and $Gr^* = 10^6$, respectively. As stated earlier, the requirement for a repeating boundary condition is that a temperature and heat flux on the external surface of the wall (surface without the line heat source) and the cold surface be the same at any given axial location, as shown in Figs. 7(*a*) and 7(*b*). The heat flux at the cold surface is never zero, implying that heat flows from the source to the fluid through the wall. However, for $t/B = 0$, the heat flux is always zero at the cold surface.

In general, the temperature of the solid and the air decreases with an increase in Gr*. This change is because the heat transfer coefficient at the hot and cold surfaces increases with Gr*. It is interesting to note that for $K = 1$, the heat transfer coefficient is lower than the temperature for $K = 100$ in the

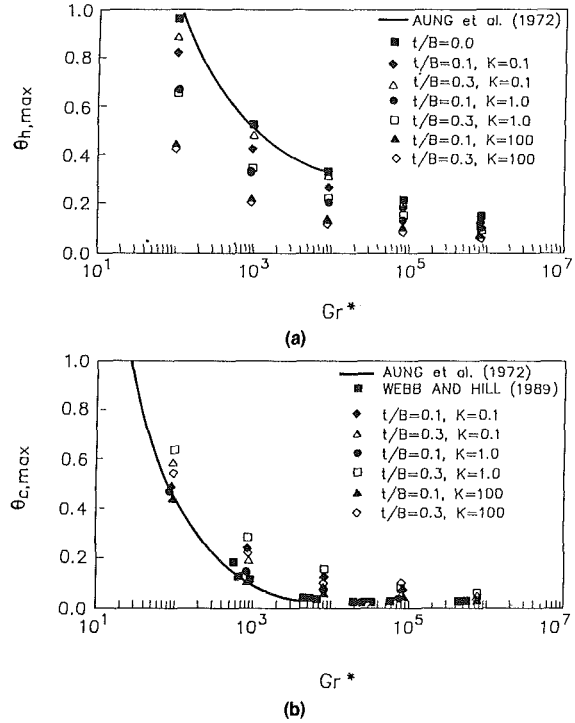

Fig. 8 Maximum surface temperature

upstream region, although this trend reverses in the downstream region. As the conductivity ratio increases, the transport of heat from downstream to upstream within the wall increases, leading to lower temperatures in the downstream region. Both fluid and surface temperatures for the thinner wall ($t/B = 0.1$) are lower than those for a thicker wall ($t/B = 0.3$) in the upstream region, indicating that a thicker wall contributes more toward the axial conduction. This is to be expected because the thicker the wall, the greater the cross-sectional area for conduction. At high Grashof numbers ($Gr^* = 10^6$), the effect of axial conduction within the wall diminishes.

Maximum Surface Temperature. For thermal design engineers in the electronics industry, the prediction of maximum surface temperature is important. The maintenance of a proper operating temperature prolongs the life of many components and enhances their reliability (Johnson, 1986). Based on the simplifying assumptions made in the model development, the maximum temperature will be at the exit of the channel for both hot and cold surfaces. The variation of $\theta_{h,\max}$ with Gr* is shown in Fig. 8(*a*). The predicted values are compared with the results for an asymmetrically heated single channel subjected to a UHF condition by Aung et al. (1972) for the case of $q_2/q_1 = 0$. The case of $t/B = 0$ in the present study corresponds to the situation of an asymmetrically heated single channel subjected to the UHF condition. It is evident from Fig. 8(*a*) that $\theta_{h,\max}$ for $t/B = 0$ compares well with that of Aung et al. (1972). Also, it should be noted that the calculations made by Aung et al. (1972) are for the range up to $Gr^* = 10^4$. It is to be expected that the value for $\theta_{h,\max}$ decreases when a series of walls are placed in parallel, and for this condition $\theta_{h,\max}$ for $t/B = 0$ will be the upper bound. The maximum drop in $\theta_{h,\max}$ due to the repeated boundary condition is maximum for low Gr* ($Gr^* = 10^2$) and high K ($K = 100$). This decrease in $\theta_{h,\max}$ due to the repeated boundary condition decreases with an increase in Gr*. The effect of t/B on $\theta_{h,\max}$ is interesting: For low values of K ($K = 0.1$), $\theta_{h,\max}$ increases with t/B, but for $K \geq 10$ this trend is reversed. This behavior can be explained by examining the surface

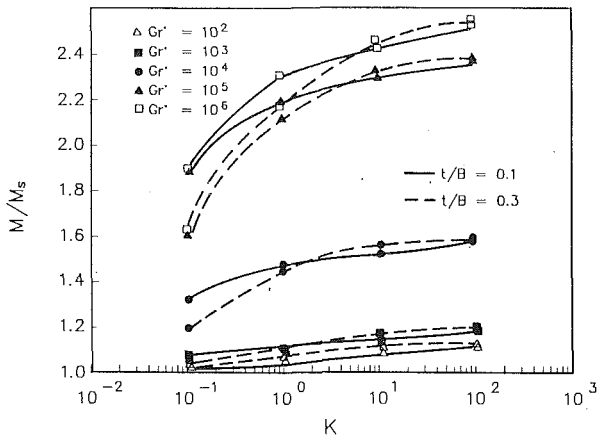

Fig. 9 Ratio of mass flow in a channel with a repeated boundary to mass flow rate in a single channel

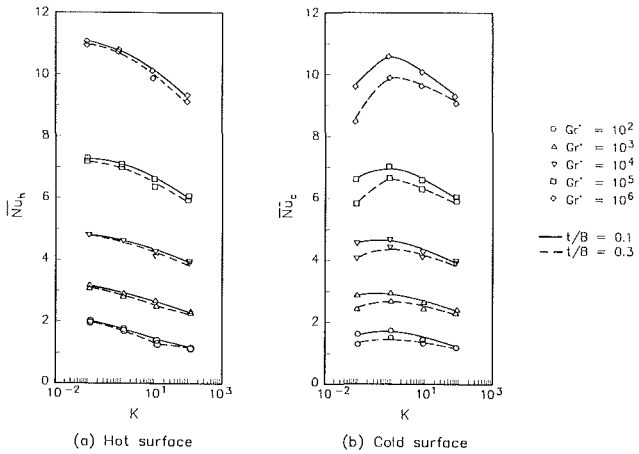

Fig. 10 Average Nusselt number

temperature and heat flux distributions (Figs. 3 and 4). At low values of K ($K=0.1$), only transverse conduction is dominant and the thermal resistance increases with t/B, leading to higher temperatures with minimal effect of the repeated boundary condition. Since higher values of K and the wall thickness increase the axial conduction, the temperature is more uniformly distributed along the channel.

The variation of maximum cold surface temperature ($\theta_{c,\max}$) with Gr* is shown in Fig. 8(*b*). The present results for no wall thickness ($t/B=0$) are compared with the numerical predictions of Aung et al. (1972) and the experimental results of Webb and Hill (1989) for the case of an asymmetrically heated single channel subjected to the UHF condition. In general, $\theta_{c,\max}$ for a single channel is lower than any configuration with a repeated boundary condition. Thus, the $\theta_{c,\max}$ for $t/B=0$ will be the lower bound. The predicted values for $t/B=0$ compare well with those of Aung et al. (1972) and Webb and Hill (1989). The effect of wall thickness on $\theta_{c,\max}$ is opposite to the effect that it has on $\theta_{h,\max}$.

Mass Flow Rate. The mass flow rate (M) for channels considered in this investigation is compared with the mass flow rate (M_s) in single channels between two vertical parallel plates, as shown in Fig. 9. Note that M_s is the mass flow rate in an asymmetrically heated single channel with no wall conduction, where the left wall is subjected to a constant heat flux condition and the right wall is insulated. It is evident that the effect of the repeated boundary condition is to increase the mass flow rate. However, it is not possible to isolate the quantitative contribution of the repeated boundary condition

Table 2 Average hot surface Nusselt number for single channel

Ra*	70	700	7×10^3	7×10^4	7×10^5
Webb and Hill (1989)†	1.8700	2.9200	4.5684	7.141	11.16
Present study ††	2.1351	3.2753	4.7633	6.9164	10.573

† Equation (6) and (10) of Webb and Hill (1989).
†† Equation (15).

towards the increase in mass flow rate. The increase in mass flow rate due to the repeated boundary condition is higher at higher Gr* ($Gr^*=10^6$) and lower at low Gr* ($Gr^*=10^2$). The increase in mass flow rate is higher at higher values of K. At low Gr* ($Gr^*=10^2$), the thick wall ($t/B=0.3$) leads to a greater increase in mass flow rate for all values of K. This behavior changes for Gr* values higher than 10^3. The crossover of M/M_s for $t/B=0.1$ and 0.3 occurs between K values of 1 and 10. A channel with a thin wall has a greater increase in mass flow rate, but this trend is reversed at a higher conductivity ratio. This behavior can be explained by examining surface temperature distribution (Fig. 3). The impact of wall thickness diminishes for $K \geq 100$ and for all values of Gr*. This is due to the fact that the surface temperature tends to be uniform at higher values of K.

Average Surface Nusselt Number. The average Nusselt numbers for the hot and cold surfaces are defined as

$$\overline{\mathrm{Nu}}_h = \mathrm{Gr}^* \int_0^{1/\mathrm{Gr}^*} \frac{1}{\theta_{h,X}} \frac{\partial\theta}{\partial Y}\bigg|_{Y=0} dx$$

$$\overline{\mathrm{Nu}}_c = \mathrm{Gr}^* \int_0^{1/\mathrm{Gr}^*} \frac{1}{\theta_{c,X}} \frac{\partial\theta}{\partial Y}\bigg|_{Y=1} dx \qquad (15)$$

Table 2 shows a comparison of predicted average Nusselt numbers for a single channel with the experimentally obtained correlations of Webb and Hill (1989). The correlation is given by $\overline{\mathrm{Nu}}_b = 0.82(\mathrm{Ra}^*)^{0.194}$ and was obtained by using the properties evaluated at the bulk temperature. The maximum difference between the predicted values and those of Webb and Hill (1989) is within 10 percent. A part of this difference is attributed to the difference in definitions of Nusselt number in these two studies.

Figure 10 shows the variation of average Nusselt numbers for hot and cold surfaces with K for different values of t/B and Gr*. As expected both $\overline{\mathrm{Nu}}_h$ and $\overline{\mathrm{Nu}}_c$ increase with increase in Gr*.

In general, the average hot surface Nusselt number decreases with an increase in the conductivity ratio (K). The effect of K on $\overline{\mathrm{Nu}}_h$ is more pronounced at higher Gr*. As K increases, a greater amount of heat is conducted away from the line heat source, thus reducing both temperature at the hot surface and heat flux to the fluid from the hot surface. The reduction in heat flux to the fluid is greater than the drop in the hot surface temperature (equation (15)) resulting in a lower $\overline{\mathrm{Nu}}_h$. The maximum decrease in $\overline{\mathrm{Nu}}_h$ because of wall conduction effects is 18 percent and occurs at $Gr^*=10^6$. For this same reason, the $\overline{\mathrm{Nu}}_h$ for a thicker wall ($t/B=0.3$) is lower than for a thinner wall ($t/B=0.1$).

The cold surface average Nusselt number ($\overline{\mathrm{Nu}}_c$) for a single channel is zero because the cold surface is adiabatic. As wall conduction effects (K and t/B) come into play, the heat flux at the cold surface is nonzero and begins to increase. The increase in heat flux and the cold surface temperature increases up to $K=1$, resulting in monotonic increase in $\overline{\mathrm{Nu}}_c$ up to $K=1$. For values of K higher than 1 ($K>1$), $\overline{\mathrm{Nu}}_c$ begins to decrease with increase in K. At very high values of K ($K=100$),

channels with repeated boundary conditions approach that of a symmetrically heated single channel subjected to the UWT condition. Thus for $K \geq 100$, the average Nusselt numbers for hot and cold surfaces tend to be equal as shown in Fig. 10. The effect of t/B on $\overline{\mathrm{Nu}}_c$ is the same as the effect of t/B on $\overline{\mathrm{Nu}}_h$. However, the effect of t/B on $\overline{\mathrm{Nu}}_c$ increases with Gr*. The effect of t/B on $\overline{\mathrm{Nu}}_c$ is more pronounced than it was on $\overline{\mathrm{Nu}}_h$.

Summary

Heat transfer and air flow rate in channels formed between series of parallel vertical plates with embedded line heat sources was studied numerically. The model equations were solved by an implicit finite difference scheme. The numerical solution was validated by comparing the resulting analysis with the existing experimental data for single channels (Aung et al., 1972; Webb and Hill, 1989). In addition, calculations were performed for a wide range of independent parameters (t/B, Gr*, and K). The key conclusions are:

1 In general, as the wall conduction increases, the hot surface temperature decreases and the cold surface temperature increases. At higher values of Gr* ($\mathrm{Gr}^* = 10^6$), the wall conduction effects (t/B and K) on surface temperature decrease because of higher heat transfer coefficients. The wall approaches UWT conditions at high values of K ($K = 100$).

2 The surface heat flux is uniform for low values of K ($K = 0.1$). The thermal resistance of the wall decreases with an increase in K resulting in nonuniformity in heat flux.

3 The velocity profile (U/U_o) is skewed toward the hot surface. The skewness decreases with increase in K and Gr* as the temperature of the hot surface decreases with increase in K and Gr*.

4 The maximum surface temperature for both hot and cold surfaces occurs at the channel exit. The effect of a repeated boundary condition is to reduce $\theta_{h,\max}$ and increase $\theta_{c,\max}$. In this light, $\theta_{h,\max}$ for a single channel is the upper bound and $\theta_{c,\max}$ for single channel is the lower bound.

5 The mass flow rate (M) increases with the buoyancy force and the buoyancy force increases with a decrease in Gr*. The conductivity ratio (K) increases with the mass flow rate and the effect of K increases with Gr*. The effect of the repeated boundary condition is to increase the mass flow rate. The maximum increase in mass flow rate due to wall conduction effects (t/B and K) is 13.4 percent for $\mathrm{Gr}^* = 10^2$ and 155 percent for $\mathrm{Gr}^* = 10^6$.

6 The average hot surface Nusselt number decreases monotonically with K and this behavior is more pronounced at high Gr*.

7 The average cold surface Nusselt number increases with K and reaches a maximum at $K = 1$. For $K > 1$, $\overline{\mathrm{Nu}}_c$ decreases with an increase in K.

8 For high values of K ($K \geq 10$), the heat dissipation may be split between adjacent channels.

Acknowledgments

This research was supported in part by Texas A&M University Engineering Excellence funds. Computing facilities were made available by the Texas A&M University Academic Computing Services (ACS). The authors are grateful to Professor B. Webb of Brigham Young University for making his experimental results available prior to publication. The authors would like to acknowledge the valuable input of the reviewers, which have greatly enhanced the quality of this paper.

References

Anand, N. K., Kim, S. H., and Aung, W., 1990, "Effect of Wall Conduction on Free Convection Between Asymmetrically Heated Vertical Plates: Uniform Wall Temperature," *International Journal of Heat and Mass Transfer*, Vol. 33, pp. 1025–1028.

Anderson, D. A., Tannehill, J. C., and Pletcher, R. H., 1984, *Computational Fluid Mechanics and Heat Transfer*, McGraw-Hill, New York.

Aung, W., 1972, "Fully Developed Laminar Free Convection Between Vertical Plates Heated Asymmetrically," *International Journal of Heat and Mass Transfer*, Vol. 15, pp. 1577–1580.

Aung, W., Fletcher, L. S., and Sernas, V., 1972, "Developing Laminar Free Convection Between Vertical Plates with Asymmetric Heating," *International Journal of Heat and Mass Transfer*, Vol. 15, pp. 2293–2308.

Aung, W., and Worku, G., 1986a, "Developing Flow and Flow Reversal in a Vertical Channel With Asymmetric Wall Temperatures," ASME JOURNAL OF HEAT TRANSFER, Vol. 108, pp. 299–304.

Aung, W., and Worku, G., 1986b, "Theory of Fully Developed, Combined Convection Including Flow Reversal," ASME JOURNAL OF HEAT TRANSFER, Vol. 108, pp. 485–488.

Azevedo, L. F., and Sparrow, E. M., 1985, "Natural Convection in Open-Ended Inclined Channels," ASME JOURNAL OF HEAT TRANSFER, Vol. 107, pp. 893–901.

Bar-Cohen, A., and Rohsenow, W. M., 1984, "Thermally Optimum Spacing of Vertical, Natural Convection Cooled, Parallel Plates," ASME JOURNAL OF HEAT TRANSFER, Vol. 106, pp. 116–123.

Bodia, J. R., and Osterle, J. F., 1962, "The Development of Free Convection Between Heated Vertical Plates," ASME JOURNAL OF HEAT TRANSFER, Vol. 84, pp. 40–44.

Burch, T., Rhodes, T., and Acharya, S., 1985, "Laminar Natural Convection Between Finitely Conducting Vertical Plates," *International Journal of Heat and Mass Transfer*, Vol. 28, pp. 1173–1186.

Carpenter, J. R., Briggs, D. G., and Sernas, V., 1976, "Combined Radiation and Developing Laminar Free Convection Between Vertical Flat Plates With Asymmetric Heating," ASME JOURNAL OF HEAT TRANSFER, Vol. 98, pp. 95–100.

Elenbaas, W., 1942, "Heat Dissipation of Parallel Plates by Free Convection," *Physica*, Vol. 9, pp. 1–23.

Incropera, F. P., 1988, "Convection Heat Transfer in Electronic Equipment Cooling," ASME JOURNAL OF HEAT TRANSFER, Vol. 110, pp. 1097–1110.

Johnson, C. E., 1986, "Evaluation of Correlations for Natural Convection Cooling of Electronic Equipment," *Heat Transfer in Electronic Equipment—1986*, ASME HTD-Vol. 57, pp. 103–111.

Kim, S. H., Anand, N. K., and Aung, W., 1990, "Effect of Wall Conduction on Free Convection Between Asymmetrically Heated Vertical Plates: Uniform Wall Heat Flux," *International Journal of Heat and Mass Transfer*, Vol. 33, pp. 1013–1023.

Peaceman, D. W., and Rachford, H. H., 1955, "The Numerical Solution of Parabolic and Elliptic Equations," *J. Soc. Ind. Appl. Math.*, Vol. 3, p. 28.

Sparrow, E. M., and Bahrami, P. A., 1980, "Experiments on Natural Convection From Vertical Parallel Plates With Either Open or Closed Edges," ASME JOURNAL OF HEAT TRANSFER, Vol. 102, pp. 221–227.

Sparrow, E. M., Chrysler, G. M., and Azevedo, L. F., 1984, "Observed Flow Reversals and Measured-Predicted Nusselt Numbers for Natural Convection in a One-Sided Heated Vertical Channel," ASME JOURNAL OF HEAT TRANSFER, Vol. 106, pp. 325–332.

Webb, B. W., and Hill, D. P., 1989, "High Rayleigh Number Laminar Natural Convection in an Asymmetrically Heated Vertical Channel," ASME JOURNAL OF HEAT TRANSFER, Vol. 111, pp. 649–656.

Wirtz, R. A., and Stutzman, R. J., 1982, "Experiments on Free Convection Between Vertical Plates With Symmetric Heating," ASME JOURNAL OF HEAT TRANSFER, Vol. 104, pp. 501–507.

Zinnes, A. E., 1970, "The Coupling of Conduction With Laminar Natural Convection From a Vertical Flat Plate With Arbitrary Surface Heating," ASME JOURNAL OF HEAT TRANSFER, Vol. 92, pp. 528–535.

Experimental Study of Natural Convection Heat Transfer Between a Cylindrical Envelope and an Internal Concentric Heated Octagonal Cylinder With or Without Slots

H. L. Zhang

Q. J. Wu

W. Q. Tao

Department of Power Machinery Engineering,
Xi'an Jiaotong University,
Xi'an Shaanxi 710049
The People's Republic of China

In this paper, the results of an experimental study of laminar natural convection heat transfer and fluid flow in horizontal annuli between a cylindrical envelope and its inner concentric octagonal heated cylinder are presented. Two octagonal cylinders are investigated: one with a complete surface and the other with two horizontal slots on the top and bottom surfaces. The ratio of the slot width W to H is 0.072. Air is used as the working fluid. The range of Rayleigh number is 2.1×10^2–1.58×10^6 *for the unslotted case and* 1.2×10^2–1.5×10^6 *for the slotted case. The average heat transfer correlations for the two cases are provided. The results show that the heat transfer intensity of the unslotted octagon is slightly weaker than that in a cylindrical annulus, while for the slotted case, the overall heat transfer enhancement may be as high as 74 percent. The smoke technique is used to visualize the flow patterns. A series of photographs of the flow patterns are provided, which enhances our understanding of the mechanism of heat transfer enhancement for the slotted octagonal case.*

Introduction

In modern power plants, in order to transmit large electric current from generators to transformers, a variety of isolated-phase buses is used. The hollow, thin-walled octagonal electric bus with two slots in the symmetric vertical plane is one of them. It has some advantages over other bus configurations in heat dissipation, support, and connection. Therefore, it is widely used in large power plants. A schematic view of the cross section is shown in Fig. 1. For the case of natural cooling of the bus, the heat generated in the bus from the Joule heating is first transferred from the bus to the outer cylindrical envelope via natural connection and radiation, and then from the outside surface of the envelope to the ambient. For safety purposes, the bus temperature must be below a certain value when in operation. The radiation heat transfer can be easily determined according to the principles described in textbooks (for example, Sparrow and Cess, 1978). The natural convection between the bus and the envelope, however, is quite complicated. To the authors' knowledge, no experimental work related to this problem has been published to date.

Many studies have been conducted on laminar natural convection between two horizontal concentric cylinders maintained at constant, but different temperatures. Only a few of them will be reviewed here for comparison purposes. In their comprehensive review, Raithby and Hollands (1975) recommended the following average heat transfer correlation in terms of an effective thermal conductivity for the case of radius ratio equal to two:

$$K_{eq}/K = 0.196\ \mathrm{Ra}^{0.25} \qquad (\mathrm{Pr}=0.7) \qquad (1)$$

For the sake of simplicity, the ratio of K_{eq}/K will be written as $\bar{K}_{eq}$ and called relative thermal conductivity hereafter in this paper. In the photographic study conducted by Bishop and Carley (1966), a kidney-shaped eddy was found in the flow pattern. In the investigation of Powe et al. (1969) a crescent eddy flow pattern was observed. As far as the natural convection from an inner isothermal horizontal noncircular cylinder to an outer concentric circular envelope is concerned, a search of the literature has revealed only a limited number of publications. Boyd (1981) proposed a new theory for correlating the data of steady natural convective heat transfer in annuli of arbitrary cross section. By using the similarity transformation and carefully defining the reference temperature and the reference length for the average Nusselt number, he succeeded in correlating the data for two configurations, the circular annulus and the annulus formed by a hexagonal cylinder inside a circular cylinder, into a single line. However, the definition of the characteristic length for Rayleigh number is quite com-

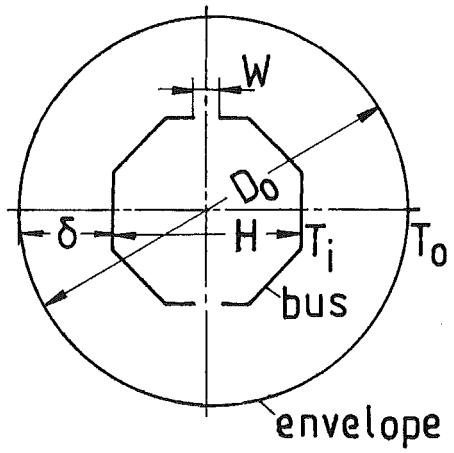

Fig. 1 A schematic diagram of the test configuration

Contributed by the Heat Transfer Division for publication in the JOURNAL OF HEAT TRANSFER. Manuscript received by the Heat Transfer Division July 28, 1989; revision received March 28, 1990. Keywords: Enclosure Flows, Natural Convection.

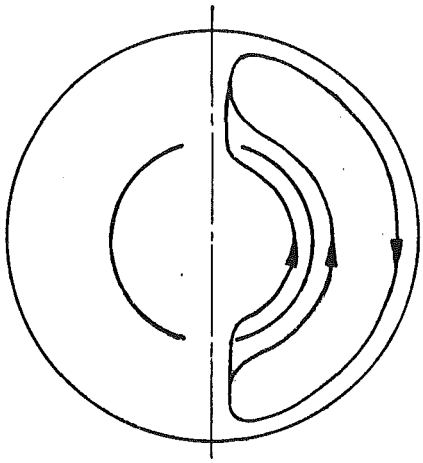

Fig. 2 Suggested flow pattern in an annular space with a slotted inner cylinder (Kuleek, 1964)

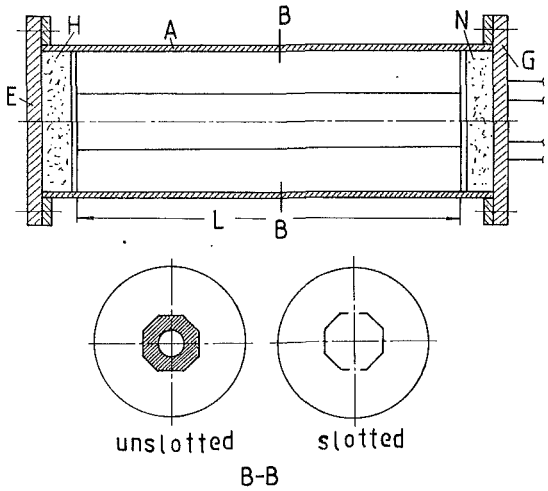

Fig. 3 Sketch of the experimental apparatus

plicated, and for some cases, the agreement between the general correlation and the experimental data is not satisfactory. Chang et al. (1983) performed a numerical analysis for natural convection heat transfer in an irregular two-dimensional enclosure formed by an inner square cylinder and an outer circular cylinder. They used the equivalent thermal conductivity to present their results.

In order to enhance the natural convective heat transfer from the hollow electric bus, Kuleek proposed an efficient configuration for the circular annulus bus early in 1964. The basic feature of his configuration is that two slots are cut out on the inner cylinder, which are situated in the same vertical plane (Fig. 2). Kuleek assumed that the overall heat transfer from the slotted inner cylinder to the outer one was equal to the sum of the following two parts. One part was natural convection heat transfer in the circular annulus with a nonslotted inner cylinder. The other part was heat transfer from the inner surface of the slotted inner cylinder. To calculate this latter part of heat transfer approximately, the correlation for natural convection from a vertical plate was suggested. According to this assumption, the heat transfer rate of an annulus with a slotted inner cylinder might be enhanced 30–40 percent as compared to that of an annulus with unslotted inner cylinder. It is very surprising that for more than twenty years since then no technical papers regarding this problem had been published, and this assumption was widely accepted in many engineering designs. Wang (1986) appears to be the first one to have experimentally studied this problem with air as the working fluid. He found that the heat transfer rate of the slotted annulus could be enhanced by as much as 50 percent, depending on the ratio of the slot width to the diameter of inner cylinder. He also observed that the flow pattern in such a configuration was much more complicated than that schematically shown in Fig. 2, as given by Kuleek.

In the present paper, an experimental study has been made on the natural convection heat transfer between an outer circular envelope and an inner isothermal octagonal cylinder. The outer envelope was placed at a lower but constant temperature water pool. Two cases of the inner octagonal cylinder have been considered: one without slots and the other with slots. The heat transfer characteristics of these two situations have been compared. A smoke visualization technique has been used to reveal the flow patterns in the annuli.

Experimental Apparatus

The experimental apparatus consisted of test section, pressure control, and power supply with associated controls and instruments. A sketch of the test section is shown in Fig. 3. A detailed presentation of the apparatus is available in the thesis of the first author (1988). Only a brief description will be given here.

The envelope A was made of aluminum. Its inner and outer diameters were 130 mm and 170 mm, respectively. Its length was 600 mm. The outer cylinder was closed by two end plates,

Nomenclature

A = area of the unslotted octagonal cylinder surface, m^2
A_i = area of the experimental slotted octagonal cylinder surface, m^2
C_p = specific heat at constant pressure, J/(kg K)
D_i = diameter of the relative circular cylinder whose circumferential area is equal to that of the unslotted octagonal cylinder, m
D_o = diameter of the outer circular envelope, m
g = gravitational acceleration, m/s^2
H = distance between the opposite sides of the octagon, m
K = thermal conductivity, W/(m K)
K_{eq} = equivalent thermal conductivity, W/(m K)
$\bar{K}_{eq}$ = relative thermal conductivity $= K_{eq}/K$
L = axial length of the test section, m
m = ratio of A_i/A
P = pressure in the enclosure, Pa
Q_c = convective heat transfer, W
Q_{cond} = radial heat conduction, W
Q_t = total power applied to the enclosure, W
R = air gas constant, J/(kg K)
Ra = Rayleigh number, equation (3)
T_i = temperature of inner cylinder, K
T_m = mean temperature, K
T_o = temperature of outer cylinder, K
ΔT = temperature difference $= T_i - T_o$, K
δ = maximum gap width of the tested annuli $= (D_o - H)/2$ for the octagonal case, m
μ = dynamic viscosity, kg/(m s)

Superscripts

$'$ = characteristic at lower Rayleigh number, $Ra = 10^3$

E and G. The inner octagonal cylinders (with and without slots) were 65 mm in height (i.e., the distance between the opposite sides of the octagon). They were centered by the end pieces, H and N. The unslotted octagonal cylinder was machined from a copper rod. In the center of the rod there was a hole passing through it. An electric heater was inserted into the hole. The slotted cylinder was made up of two symmetric parts. Each part was composed of three layers, forming a sandwichlike structure. The outside and inside layers were made of 0.8-mm copper plates. In the middle, a thin electric heating layer was placed. Since they were fixed on the two end pieces, the two parts would form an inner octagonal cylinder with two slots on the horizontal planes. The width of the slot was 4.7 mm. In order to reduce radiation heat transfer, the outside surface of the unslotted inner cylinder and the outside and the inside surfaces of the slotted cylinder were all chromium-plated. After all the inner parts had been fixed, the envelope was then put into a large water tank to maintain the constant wall temperature condition. The annular space was filled with air, whose pressure could be regulated from 1.13 kPa to 0.4 MPa to extend the range of the Rayleigh number. Twelve thermocouples were embedded in the outside surface of the inner octagonal cylinder, and eight thermocouples for the outer envelope. The maximum temperature difference for the eight locations of the outer envelope was found to be 2.5 percent of the average value T_o ($\approx 23°C$), while those of the unslotted and slotted octagonal cylinder were 1 and 2.5 percent of the average temperature difference between the inner cylinder and the outer envelope ΔT ($\approx 45°C$), respectively.

To proceed with the flow visualization, the outer aluminum envelope and its two end pieces were all replaced by transparent counterparts, which were made of plexiglass. The outer envelope was made of two concentric plexiglass cylinders with a small gap between them. The diameter of the inside surface of the inner one was 145 mm. Cold water flowed through the gap to maintain an isothermal wall condition. The unslotted octagonal cylinder used in the heat transfer measurement was used again for flow visualization. To visualize the flow patterns in the internal space enclosed by the slotted cylinder, half of the cylinder surface was specially made. In the middle of this half cylinder there was a circumferential slot (width = 2 mm). The slot was covered by transparent tape. It was this transparently covered slot that would allow the beam of light to go through into the internal space enclosed by the octagonal cylinder.

Cigar smoke was used to make flow visual. The smoke was introduced into the annular space via a small pipe positioned at the bottom of the envelope. A vertical optical collimated plane made the light beam pass through the cooled plexiglass envelope and then into the inner octagonal cylinder via the circumferential slot. Through one of the transparent end plates, the flow patterns were photographed using a 35-mm Cannon A-1 camera mounted on a tripod. ASA-400 black and white films were used. The camera lens was set at $f = 5.6$ with a shutter speed of 1–2 seconds.

Data Reduction

The most important work in data reduction is the separation of convective heat transfer from the total power input measured in the experiment. Many previous studies (El-Sherbiny et al., 1982; Keyhani et al., 1983) have shown that when the Rayleigh number is less than 10^3, the heat transfer in an enclosure is dominated by conduction. Therefore, for the case of Rayleigh number less than 10^3, the total heat loss via radiation and end dissipation could be determined by subtracting the calculated radial heat conduction through the air layer (Q'_{cond}) from the total heat input (Q'_t). Since in all cases tested, the difference between the temperatures of the inner octagonal cylinder and the outer envelope was kept almost constant (with maximum deviation of 3°C), it is appropriate to determine the convective heat transfer for any case tested by the following equation:

$$Q_c = Q_t - (Q'_t - Q'_{\text{cond}}) \times \frac{\Delta T}{\Delta T'} \tag{2}$$

where $\Delta T/\Delta T'$ is a modifying factor to account for the effect of a small change in the temperature difference on the heat loss.

The definition of the Rayleigh number is

$$\text{Ra} = \frac{gC_p\delta^3(T_i - T_o)}{R^2K\mu T_m{}^3} P^2 \tag{3}$$

where the law of perfect gas is adopted in order explicitly to include the effect of system pressure, and all the physical properties were evaluated at the mean temperature $T_m = (T_i + T_o)/2$.

To present the results, the relative thermal conductivity $\bar{K}_{eq}$ is used. For the present study it is defined as

$$\bar{K}_{eq} = \frac{mQc}{\dfrac{2\pi Lk\Delta T}{\ln(D_o/D_i)}} \tag{4}$$

In the previous equation, a factor of the heat transfer surface ratio, $m = A_i/A$, is included. Thus, for the case of slotted octagonal cylinder, the value of $\bar{K}_{eq}$ is based on its actual heat transfer surface rather than on the nominal surface of its unslotted counterpart.

Substituting equation (2) into equation (4), we obtain

$$\bar{K}_{eq} = m\left(\frac{Q_t - \dfrac{\Delta T}{\Delta T'} \cdot Q_t}{\dfrac{2\pi LK\Delta T}{\ln(D_o/D_i)}} + \frac{\Delta T}{\Delta T'} \cdot \frac{Q'_{\text{cond}}}{\dfrac{2\pi LK\Delta T}{\ln(D_o/D_i)}}\right) \tag{5}$$

For the case of unslotted inner cylinder, a numerical computation conducted by the present authors has shown that

$$\frac{\Delta T}{\Delta T'} \cdot \frac{Q'_{\text{cond}}}{\dfrac{2\pi LK\Delta T}{\ln(D_o/D_i)}} = \frac{Q'_{\text{cond}}}{\dfrac{2\pi LK\Delta T'}{\ln(D_o/D_i)}} = 0.976 \tag{6}$$

A comparative study has also revealed that for the case of a slotted cylinder the value of Q_{cond} differs very slightly from that of the unslotted case under the same conditions. Thus, for any case tested, $\bar{K}_{eq}$ is calculated by

$$\bar{K}_{eq} = m\left(\frac{Q_t - \dfrac{\Delta T}{\Delta T'} \cdot Q'_t}{\dfrac{2\pi LK\Delta T}{\ln(D_o/D_i)}} + 0.976\right) \tag{7}$$

An uncertainty analysis indicated that the major sources of uncertainty were in measuring the surface temperature and power input. The method used in the data reduction, equations (2) and (3), also brought about some uncertainties in $\bar{K}_{eq}$ and Ra. It is estimated that from all the possible sources of uncertainty considered, the uncertainty in $\bar{K}_{eq}$ is about 5.5 percent and that in Ra is about 4.8 percent.

Results and Discussion

The present experimental results will be presented in two sections: (1) the average heat transfer characteristics, and (2) the flow patterns.

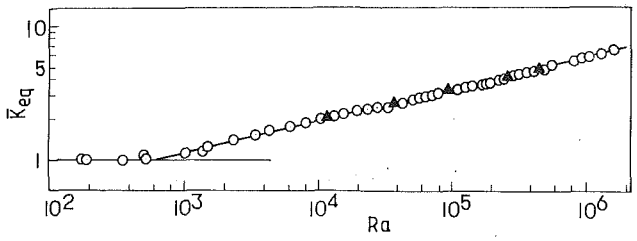

Fig. 4 $\bar{K}_{eq}$ as a function of Ra, unslotted case

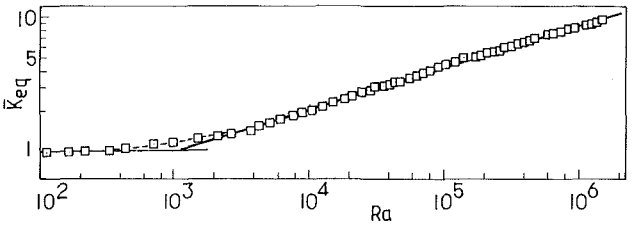

Fig. 5 $\bar{K}_{eq}$ as a function of Ra, slotted case

Average Heat Transfer Correlations. The average relative thermal conductivities obtained for the unslotted case are shown on log-log coordinates in Fig. 4 as a function of Rayleigh number. In the pure conduction region ($Ra \leq 6 \times 10^2$ for the present case), $\bar{K}_{eq} = 1$. In the range of Rayleigh number from 6×10^2 to 1.48×10^3, the convective heat transfer mechanism gradually becomes dominant. For $Ra \geq 1.48 \times 10^3$, all the experimental data can be correlated by the following equation:

$$\bar{K}_{eq} = 0.196 Ra^{0.246} \qquad (Ra \leq 1.59 \times 10^6) \tag{8}$$

The maximum deviation of this correlation from the experimental data is 3.4 percent, and the average deviation is 1.2 percent.

To confirm the reproducible character of the measuring system, an additional measurement was made after the above equation had been correlated. These data are shown in Fig. 4 by the symbol ▲. They agree very well with the above correlation, indicating that the precision of the experimental measurement is excellent.

It is worth noting that both the constant and exponent of equation (8) are equal or very close to their counterparts of equation (1). As mentioned before, equation (1) is for the annular enclosure of radius ratio equal to 2; in the present study the ratio of D/H is also equal to 2.0. With this in mind, it can be concluded that the intensity of natural convection in an annulus with an inner octagonal cylinder is very close to that of an annulus with an inner circular cylinder under the same configuration parameters. In the experimental range of Rayleigh number, the maximum difference in $\bar{K}_{eq}$ is only about 4 percent. This conclusion is expected from the consideration of physical intuition. Actually, with the increasing in the side number of a polygon, its behavior should approach that of its geometric limit—a circular cylinder.

Attention will now be turned to the results for the annulus with slotted inner octagonal cylinder. Figure 5 is presented for this purpose. By comparing with Fig. 4, two features may be noted. First, for the case of a slotted inner cylinder, the transition from pure conduction region to convective dominated region occurs at a lower Rayleigh number, approximately at $Ra = 1.7 \times 10^2$. This may be accounted for by the fact that the existence of the slots eases the air circulation in the enclosed space. Second, the slope of the $\bar{K}_{eq}$ versus Ra curve in the convective regime is larger than that for the unslotted case.

In the convective regime, the results of 48 data runs may be correlated by the following equation:

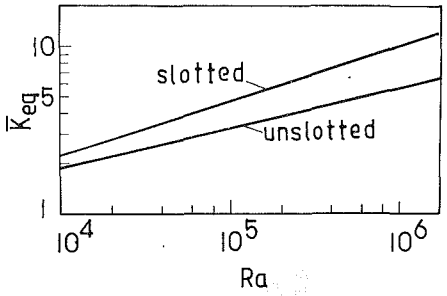

Fig. 6 Comparison of unslotted and slotted cases

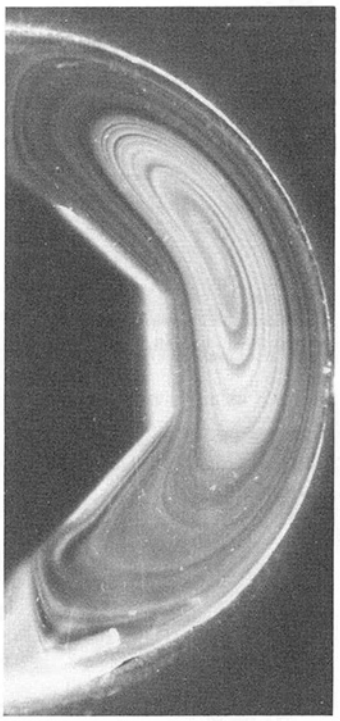

Fig. 7 Smoke streamline visualization, unslotted case, $Re = 4.9 \times 10^4$

$$\bar{K}_{eq} = 0.112 Ra^{0.327} \qquad (1.51 \times 10^3 \leq Ra \leq 1.47 \times 10^6) \tag{9}$$

The average deviation of equation (9) from 48 experimental data is 1.7 percent, with a maximum deviation of 4.9 percent.

To compare the values of $\bar{K}_{eq}$ between the slotted and unslotted cases, the above two equations are plotted in Fig. 6. The value of $\bar{K}_{eq}$ for the slotted case ranges from 21 percent higher than that of the unslotted case at $Ra = 10^4$ to 81 percent higher at $Ra = 1.5 \times 10^6$. Considering that the value of $\bar{K}_{eq}$ for the slotted case is based on the actual heat transfer area, the overall heat transfer enhancement of the slotted case is about 74 percent higher than that of the unslotted one at $Ra = 1.5 \times 10^6$. In engineering practice, the Rayleigh number of large electric buses is mostly higher than 10^6. Therefore, the estimation of heat transfer enhancement given by Kuleek is very conservative.

Flow Visualization Results

We now direct our attention to the detailed flow patterns obtained via the smoke technique. In Fig. 7 the smoke streamlines of the unslotted case are shown for the case of $Ra = 4.9 \times 10^4$. Only the right half of the enclosure was pictured; the other part of the enclosure was shaded because of technical needs. It was observed that the basic flow pattern for this case was a stable crescent-shaped one. This flow pattern is very similar to that in a circular annulus observed by Bishop

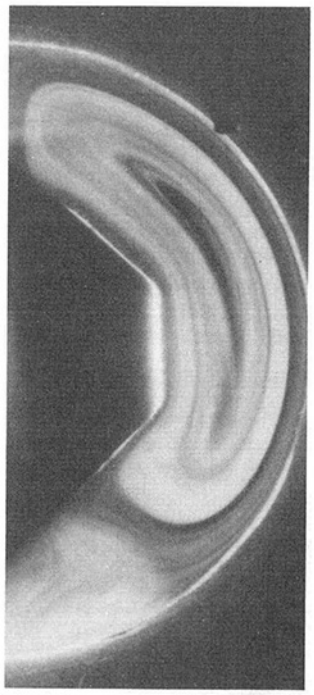

Fig. 8 Smoke streamline visualization, annular space, slotted, $Ra = 5.8 \times 10^4$

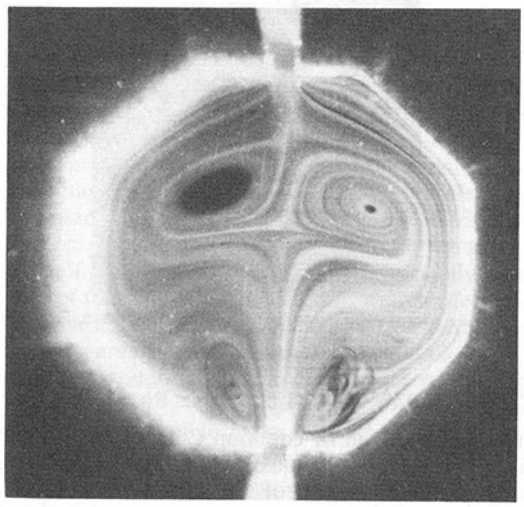

Fig. 9 Smoke streamline visualization, inner space of octagon, slotted case, $Ra = 5.8 \times 10^4$

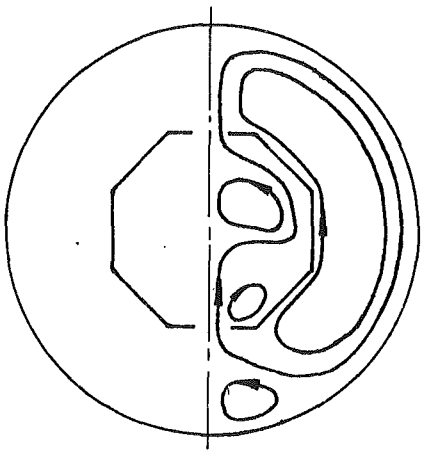

Fig. 10 Schematic diagram of streamline in tested configuration with slotted inner cylinder

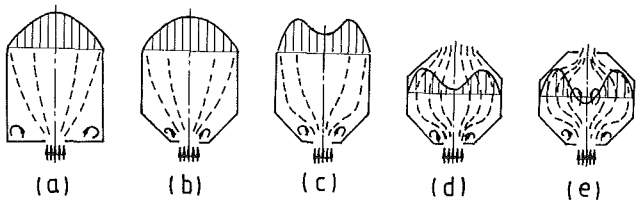

Fig. 11 Schematic diagram for explaining the formation of vortices in the inner space of a slotted octagon

and Carley (1966), except for the minor difference in curvature change near the corners of the octagonal surface. The similarity in flow patterns between the above two configurations may account for the reason that there is only a small difference in the average heat transfer correlations for the two configurations.

Figure 8 shows the flow pattern of the slotted case for $Ra = 5.8 \times 10^4$. It was observed that a stream of fluid was ejected at a rather high speed from the upper slot of the inner octagonal cylinder. The stream meets with the outer envelope, then turns around and goes down along the curved surface of the outer envelope. When the stream is coming near the bottom of the annulus, it turns around again, and goes through the lower slot into the internal space enclosed by the two halves of the inner cylinder, thus completing a closed circulation of the stream. This stream circulation will be called outer circulation. It takes the major part of the heat released from the octagonal cylinder to the outer cooled envelope. Inside this outer circulation, there is an inner stream circulation, which is positioned between the outer envelope and one half of the octagonal cylinder. The heat released from the inner cylinder is transferred via the inner circulation to the stream of the outer circulation adjacent to the outer surface.

At the bottom of the enclosure, it was observed that there was another small cell between the symmetric line and the outer circulation. This cell circulated slowly, and only transferred a small amount of heat from the outer circulation to the cold outer envelope.

Figure 9 shows a very interesting flow pattern, which was found in the internal space enclosed by the two halves of the octagonal cylinder. After coming into the internal space via the lower slot, the cold fluid stream does not turn around immediately to meet the octagonal configuration. Rather, it goes up for a short distance, and then splits into two parts, which turn around and flow to the vicinity of the two vertical sides of the octagon. Hereafter, the two streams go up along the octagonal surface and are gradually heated. They meet at the top of the space and rush out through the top slot. Four additional cells (vortices) are then formed. Two of them are located near the lower slot, counterrotating and symmetrically positioned. The other two were situated in the upper part of the space, also counterrotating, and their positions were approximately symmetric. These two pairs of cells did not make great contributions to the overall heat transfer from the inner cylinder to the outer envelope. It is the circulation of the abovementioned two-fluid streams in the octagonal internal space that greatly enhances the heat transfer from the heated inner cylinder to the cold outer envelope.

The flow patterns presented above are schematically drawn in Fig. 10, which gives a quite different view as compared with the figure suggested by Kuleek (Fig. 2).

A preliminary explanation of the formation of the flow patterns in the internal space of the slotted cylinder is schematically presented in Fig. 11. Figure 11(a) presents a well-known flow pattern of a sudden expansion in a rec-

tangular channel. There are two cells in the regions near the corners. A cut in the two right corners from the flow domain forces the two cells to move toward the flow inlet (Fig. 11*b*). If the fluid is heated by the channel wall, the velocity profile at the outlet of the channel will change. The basic feature of the new velocity profile is the existence of two maxima near the heated wall, leading to a camel-hump-shaped distribution (Fig. 11*c*). The converged shape of the outflow region makes the velocity difference between the maximum and the minimum much larger (Fig. 11*d*). Finally, when only a slot is left at the outflow region, a pair of circulating flows (vortices) will be formed near the center of the internal space.

Conclusions

Natural convective heat transfer and fluid flow in the annuli between unslotted and slotted octagonal cylinder and its concentric circular envelope were investigated experimentally. The average heat transfer correlations for both cases were obtained. The correlation for the unslotted case was very close to that for the circular annulus, with only 4 percent difference in the relative thermal conductivity. The heat transfer enhancement of the slotted case was very significant. For the case investigated ($W/H = 0.072$), the overall heat transfer enhancement of the slotted case ranged from 19 percent at $\mathrm{Ra} = 10^4$ to 74 percent at $\mathrm{Ra} = 1.5 \times 10^6$.

Photographs and written descriptions were presented that gave qualitative information on the flow pattern in the enclosures. It was observed that the flow pattern in the annulus between the unslotted octagonal cylinder and its outer circular envelope was very similar to that in a horizontal circular annulus. It was identified that the flow pattern for the case with slotted inner cylinder was very complicated. There were a total of five circulation regions in one half of the flow domain: the so-called outer circulation, inner circulation, and three small cells. It was the fluid stream coming in and rushing out of the internal space enclosed by the slotted octagonal cylinder that significantly enhanced the heat transfer.

References

Bishop, E. H., and Carley, C. T., 1966, "Photographic Studies of Natural Convection Between Concentric Cylinders," *Proceedings of Heat Transfer & Fluid Mech. Inst.*, pp. 63–78.

Boyd, R. D., 1981, "A New Correlation Theory for Steady Natural Convective Heat Transport Data for Horizontal Annuli," *Proceedings, 20th ASME/AIChE National Heat Transfer Conferencce*, Milwaukee, WI, Aug.

Chang, K. S., Won, Y. H., and Cho, C. H., 1983, "Patterns of Natural Convection Around a Square Cylinder Placed Concentrically in a Horizontal Circular Cylinder," ASME JOURNAL OF HEAT TRANSFER, Vol. 105, pp. 273–280.

El-Sherbiny, S. M., Raithby, G. D., and Hollands, K. S., 1982, "Heat Transfer by Natural Convection Across Vertical and Inclined Layers," ASME JOURNAL OF HEAT TRANSFER, Vol. 104, pp. 77–98.

Keyhani, M., Kulaki, F. A., and Christensen, R. N., 1983, "Free Convection in a Vertical Annulus With Constant Heat Flux on the Inner Wall," ASME JOURNAL OF HEAT TRANSFER, Vol. 105, pp. 445–459.

Kuleek, P. V., 1964, "Heating and Cooling of Busbars for Large Power Generators," *Electric Power Plant* [in Russian], No. 10, pp. 39–43.

Powe, R. E., Carley, C. T., and Bishop, E. H., 1969, "Free Convective Flow Patterns in Cylindrical Annuli," ASME JOURNAL OF HEAT TRANSFER, Vol. 91, pp. 310–314.

Raithby, G. D., and Hollands, K. G. T., 1975, "A General Method of Obtaining Approximate Solutions to Laminar and Turbulent Free Convection Problems," *Adv. in Heat Transfer*, Vol. 11, pp. 265–315.

Sparrow, E. M., and Cess, R. D., 1978, *Radiation Heat Transfer*, augmented ed., Hemisphere, Washington, DC.

Wang, G. X., 1986, "Free Convection in an Horizontal Circular Annulus With the Inner Cylinder Slotted," Thesis, Power Machinery Engineering Department, Xi'an Jiaotong University, Xi'an, People's Republic of China.

Zhang, H. L., 1988, "Natural Convection Heat Transfer Between Cylindrical Surface and Internal Concentric Heated Octagonal Surface With or Without Slotted," Thesis, Power Machinery Engineering Department, Xi'an Jiaotong University, Xi'an, People's Republic of China.

N. Rudraiah

G. N. Sekhar

UGC-DSA Centre in Fluid Mechanics,
Department of Mathematics,
Central College, Bangalore University,
Bangalore, India

Convection in Magnetic Fluids With Internal Heat Generation

The effect of a uniform distribution of heat source on the onset of stationary convection in a horizontal Boussinesq magnetic fluid layer bounded by isothermal nonmagnetic boundaries is investigated. Solutions are obtained using a higher order Galerkin expansion technique, considering different isothermal boundary combinations (rigid–rigid, rigid–free, and free–free). It is found that the effect of internal magnetic number, due to a heat source, is to make the system more unstable. The results obtained, in the limiting cases, compare well with the existing literature.

1 Introduction

In recent years extensive efforts have been put forth to intensify the technological and control-transfer processes in fluid systems that have led to the development of fluids sensitive to magnetic fields. Rosensweig and Kaiser (1967) were the first to synthesize such fluids, called magnetic fluids, successfully by using the method discovered by Papell (1965). Magnetic fluids are a suspension of many tiny particles of a solid ferromagnetic material (e.g., certain iron oxides) dispersed in a carrier liquid such as water, kerosene, hydrocarbon, etc. These magnetic particles are very small and the magnetic fluid behaves as a continuum. Each of these particles is coated with a surfactant like oleic acid to prevent agglomeration. An important property of magnetic fluid is the magnetocaloric effect (Berkovskii and Bashtovoi, 1971), which is considered in the energy balance equation. Magnetic fluids behave as a nonconducting homogeneous continuum and exhibit a variety of surprising phenomena. One such phenomenon is "enhanced convective cooling" having a temperature-dependent magnetic moment due to magnetization of the fluid. This magnetization, in general, is a function of the magnetic field, the temperature, and the density. Any variation of these quantities can induce a change of body force distribution in the fluid. This force gives rise to convection in ferromagnetic fluids in the presence of a gradient of magnetic field (hereafter called ferroconvection). This is analogous to the Rayleigh–Bénard convection in a horizontal layer of fluid heated from below and cooled from above. Ferroconvection is used to increase the efficiency of magnetic fluid seals, loudspeaker coils, energy conversion systems, and also in the cooling of current carrying conductors (Rosensweig, 1985). It is also of interest in diverse fields ranging from aircraft-masking, antiradar paint to magnetic ink printers. In spite of these varied applications, the literature on ferroconvection is very sparse. Finlayson (1970), Lalas and Carmi (1971), Bashtovoi and Berkovskii (1973), and Gotoh and Yamada (1982) have studied the effect of a uniform temperature gradient arising from uniform heating from below and cooling from above on ferroconvection in a horizontal magnetic fluid layer bounded either by rigid–rigid or free–free isothermal boundaries.

However, many of the practical problems cited above require a mechanism to control ferroconvection. One of the mechanisms to control convection is the nonuniform temperature gradient arising due to transient heating or cooling at the boundaries or due to uniform heat sources in the medium. The effect of heat source on Rayleigh–Bénard convection has been investigated experimentally by Tritton and Zarraga (1967) and theoretically by Sparrow et al. (1964) and Roberts (1967). Gasser and Kazimi (1976) and Rudraiah et al. (1982) have studied the effect of heat source on convection in porous media. Later Somerton and Catton (1982) have predicted the conditions for onset of convection in a fluid-saturated porous medium with internal heat generation, heated or cooled from below and overlaid with a finite layer of fluid. No study has been found in the open literature concerning the effect of a heat source on ferroconvection. The object of this paper is, therefore, to show that the nonuniform temperature gradient arising from a uniform heat source (sink) controls ferroconvection. The variation of temperature due to heat source also induces the variation in magnetic field. These variations of temperature and magnetic field can be effectively used to control ferroconvection in the practical problems cited above and particularly in continuous operation refrigerators (Bashtovoi and Berkovskii, 1973).

It is known that boundary conditions play a significant role in the onset of convection (Rudraiah and Chandna, 1985). Therefore, we consider rigid–rigid, free–free, and rigid–free isothermal boundaries. The solution to the stability equation poses a problem because the temperature gradient varies with depth. One way of solving such equations is to use the variational technique (Chandrasekhar, 1961). This technique requires an elaborate numerical computation in the case of rigid–rigid boundaries. Our aim here is to find the smallest critical Rayleigh number by a method that eliminates elaborate numerical computations. For this purpose, the Galerkin method as documented in the book by Finlayson (1972) is used. We note, as in the case of Rudraiah et al. (1982), that the single-term Galerkin expansion does not bring out the heat source effect and we consider the higher order approximation in the Galerkin technique.

The plan of this paper is as follows. The basic equations and the boundary conditions governing the system under consideration are discussed in section 2. In section 3, we obtain the numerical solutions using the Galerkin technique. The last section is devoted to discussing important inferences from this study.

2 Mathematical Formulation

Consider a layer of incompressible Boussinesq ferromagnetic liquid bounded between two horizontal boundaries at $z = -\frac{1}{2}d$ and $\frac{1}{2}d$, in the presence of a transverse applied magnetic field. The lower and upper boundaries are maintained at constant temperature $T_o + \Delta T/2$ and $T_o - \Delta T/2$, respectively. For this configuration the conservation equations (Finlayson, 1970) are

$$\nabla \cdot q = \mathbf{0} \tag{1}$$

$$\rho_o dq/dt = -\nabla p + \rho \mathbf{g} + \mu_o \nabla \cdot (\mathbf{HB}) + \mu \nabla^2 q \tag{2}$$

$$[\rho_o C_{V,H} - \mu_o \mathbf{H} \cdot (\partial \mathbf{M}/\partial T)_{V,H}] dT/dt + \mu_o T (\partial \mathbf{M}/\partial T)_{V,H} \cdot dH/dt = K_1 \nabla^2 T + Q \tag{3}$$

Contributed by the Heat Transfer Division for publication in the JOURNAL OF HEAT TRANSFER. Manuscript received by the Heat Transfer Division November 8, 1988; revision received February 6, 1990. Keywords: Natural Convection, Numerical Methods, Stratified Flows.

$$\rho = \rho_o[1 - \alpha(T - T_o)] \tag{4}$$

Here the third term on the right-hand side of equation (2) represents the ponderomotive force arising due to thermomechanical interaction in the magnetic fluid, and the second term on the left-hand side of equation (3) expresses the heating due to the magnetocaloric effect of magnetic substrate in the presence of a magnetic field. Maxwell's equations, simplified for a nonconducting fluid with no displacement currents, are

$$\nabla \cdot \mathbf{B} = 0 \tag{5a}$$

$$\nabla \times \mathbf{H} = 0 \tag{5b}$$

Equation (5*b*) allows us to write $\mathbf{H} = \nabla\phi$. For ferromagnetic materials, the magnetization is aligned with the magnetic field and is a function of both magnetic field and temperature, represented by

$$\mathbf{M} = \frac{\mathbf{H}}{H} M(H, T) \tag{6}$$

The magnetic equation of state, analogous to the fluid equation of state (4) is

$$M = M_o + \chi(H - H_o) - K(T - T_o) \tag{7}$$

Equations (1)–(7) are the governing equations of the system under consideration.

The basic state of this system is given by

$$p = p_b, \quad \rho = \rho_b, \quad q = 0, \quad \mathbf{H}_b = [0, 0, H_b(z)], \quad \mathbf{M}_b = [0, 0, M_b(z)], \quad T = T_b(z)$$

where T_b satisfies the energy balance equation

$$K_1 \nabla^2 T_b = -Q \tag{8}$$

The solution of equation (8) satisfying the isothermal conditions with a uniform heat source is

$$T_b = T_o - Qz^2/2K_1 - \Delta T z/d + Qd^2/8K_1 \tag{9}$$

Substituting this into equation (7) and simplifying, we get

$$\mathbf{H}_b = \mathbf{k}[H_o - K(Qz^2/2K_1 + \Delta T z/d - Qd^2/8K_1)/(1+\chi)] \tag{10a}$$

and

$$\mathbf{M}_b = \mathbf{k}[M_o + K(Qz^2/2K_1 + \Delta T z/d - Qd^2/8K_1)/(1+\chi)] \tag{10b}$$

Now, we study the stability of this quiescent state using linear theory subject to infinitesimal disturbances. The usual process of linearization leads to

$$M_i' + H_i' = (1 + M_o/H_o)H_i' \qquad (i = 1, 2)$$

$$M_3' + H_3' = (1+\chi)H_3' - KT'$$

with the assumptions $K\Delta T \ll (1+\chi)H_o$ and $KQd^2 \ll (1+\chi)H_o$, where the primes denote the perturbed quantities. Linearizing, eliminating the pressure term from equation (2), assuming all the fields vary in the form

$$f(z, t)\exp(ik_x x + ik_y y)$$

and making the equations dimensionless using d, $K_1/\rho_o C_o d$, $\nu K_1/\rho_o C_o \alpha g d^3$, and $K\nu K_1/\rho_o C_o \alpha g (1+\chi) d^2$ as the scales for length, velocity, temperature, and magnetic potential, respectively, we obtain the following dimensionless equations for the marginal state:

$$(D^2 - a^2)^2 W - [M_1(E) + M_1(I)z + 1]a^2 T + [M_1(E) + M_1(I)z]a^2 D\phi = 0 \tag{12}$$

$$(D^2 - a^2)T + (1 - M_2)[\mathrm{Ra}_I z + \mathrm{Ra}_E]W = 0 \tag{13}$$

$$(D^2 - a^2 M_3)\phi - DT = 0 \tag{14}$$

Here $M_1(E)$ is a ratio of the magnetic force due to the temperature fluctuation to the buoyancy, $M_1(I)$ is a ratio of the magnetic force due to the internal heat source to the buoyancy, and M_3 is a measure of the nonlinearity in magnetization. $M_3 = 1$ corresponds to the linear magnetization. The typical values of M_2 calculated for magnetic fluids with different carrier fluids turn out to be of the order of 10^{-6} (Finlayson, 1970), and hence we neglect this term in the present analysis in comparison with the other nondimensional parameters.

The boundary conditions on velocity are:

$$W = DW = 0 \quad \text{for rigid boundaries at } z = \pm 1/2 \tag{15a}$$

$$W = D^2 W = 0 \quad \text{for free boundaries at } z = \pm 1/2 \tag{15b}$$

Since the boundaries are assumed to be isothermal, the boundary conditions on temperature are

$$T = 0 \text{ at } z = \pm 1/2 \tag{16}$$

Following Finlayson (1970) we can obtain the boundary conditions on magnetic potential as:

$$(1+\chi)D\phi - a\phi = 0 \text{ at } z = -1/2 \tag{17a}$$

Nomenclature

a = dimensionless wave number
$\mathbf{B}$ = $\mu_o(\mathbf{M} + \mathbf{H})$ = magnetic flux density
b = subscript; basic state
$C_{V,H}$ = heat capacity at constant volume and magnetic field
C_o = $[C_{V,H}]_o$
d = thickness of the fluid layer
$\mathbf{g}$ = acceleration due to gravity
$\mathbf{H}$ = magnetic field
H_o = uniform magnetic field
K = $-(\partial \mathbf{M}/\partial_T)_{H_o, T_o}$ = pyromagnetic coefficient
K_1 = thermal conductivity
k_x, k_y = horizontal wave numbers in the directions of x and y axes
k^2 = $(k_x^2 + k_y^2)$
$\mathbf{M}$ = magnetization
$M_1(E)$ = $\mu_o K^2 \Delta T/\rho_o \alpha g (1+\chi) d$ = external magnetization number
$M_1(I)$ = $\mu_o K^2 Q d/\rho_o \alpha g (1+\chi) K_1$ = internal magnetization number
M_2 = $\mu_o K^2 T_o/\rho_o C_o (1+\chi)$
M_3 = $(1 + M_o/H_o)/(1+\chi)$
M_o = constant mean value of magnetization
p = pressure
$\mathbf{q}$ = velocity with components (u, v, w)
Q = uniformly distributed volumetric internal heat source strength
Ra_E = $\rho_o C_o \alpha g \Delta T d^3/\nu K_1$ = external Rayleigh number
Ra_I = $\rho_o C_o \alpha g Q d^5/\nu K_1^2$ = internal Rayleigh number
t = time
T = temperature
T_o = ambient temperature
ΔT = temperature difference between the boundaries
W = w component of velocity, which is a function of z only
α = coefficient of thermal expansion
μ = viscosity of the fluid
μ_o = magnetic permeability of the vacuum
ν = kinematic viscosity
ρ = density
ρ_o = density at the ambient temperature
ϕ = scalar magnetic potential
χ = $(\partial \mathbf{M}/\partial_H)_{H_o, T_o}$ = magnetic susceptibility
$\langle \ldots \rangle$ = $\int_{-1/2}^{1/2} (\ldots) dz$

Table 1 Critical Eigenvalues for different boundary combinations when $M_1(E) = M_1(I) = \mathrm{Ra}_I = 0$

Order of Approximation	Rigid–Rigid		Rigid–Free		Free–Free	
	$(\mathrm{Ra}_E)_c$		$(\mathrm{Ra}_E)_c$		$(\mathrm{Ra}_E)_c$	
1	—	—	—	—	—	—
2	3.1166	1749.98	2.6863	1116.87	2.2271	664.525
3	3.1165	1708.55	2.6832	1101.37	2.2217	657.640
4	3.1165	1708.55	2.6825	1100.84	2.2217	657.640
5	3.1164	1707.76	2.6824	1100.66	2.2215	657.512
Chandrasekhar (1961)	3.1170	1707.762	2.682	1100.65	2.2214	657.511

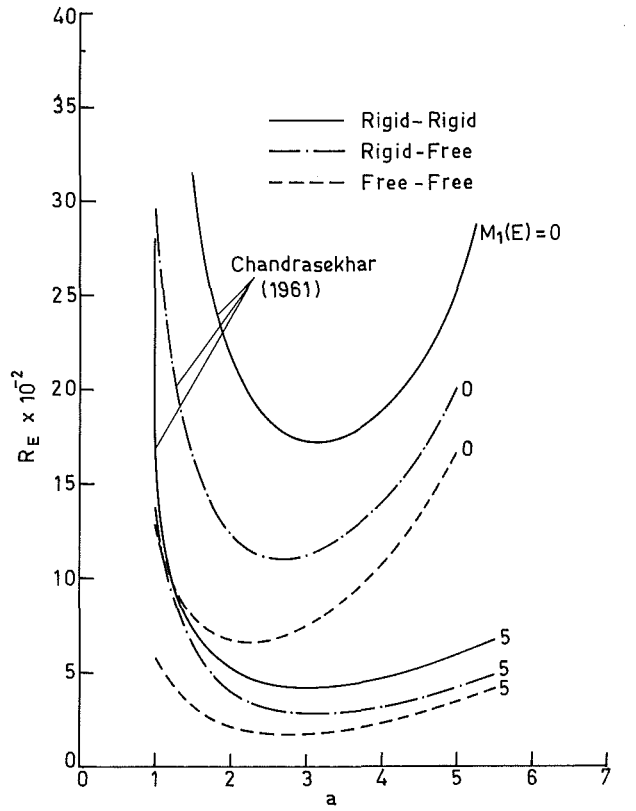

Fig. 1 *a* versus Ra_E for $\mathrm{Ra}_I = M_1(I) = 0$

$$(1+\chi)D\phi + a\phi = 0 \text{ at } z = 1/2 \qquad (17b)$$

These conditions specify that the normal component of the magnetic induction and the tangential component of magnetic field are continuous across the boundaries. We note that for $\chi \to \infty$ we obtain the nonmagnetic boundary conditions $D\phi = 0$, which were used for free–free boundaries by Finlayson (1970). As $a \to \infty$ equations (17*a*) and (17*b*) lead to the simple conditions $\phi = 0$ used by Gotoh and Yamada (1982). In the present analysis we use the general type of boundary conditions (17*a*) and (17*b*).

3 Solution of Stability Equations

The eigenvalue problem composed of equations (12)–(14) and boundary conditions (15)–(17) has been solved analytically using a single-term Galerkin expansion. We found that this expansion failed to predict the heat source effect and we therefore make use of the higher order Galerkin expansion technique. For this purpose, we choose suitable trial functions for velocity, temperature, and magnetic potential perturbations. In the present analysis, the trial function chosen for ϕ does not satisfy the specified boundary condition, and so the boundary residuals are included in the magnetic potential equation. The Galerkin method requires the residual to be orthogonal

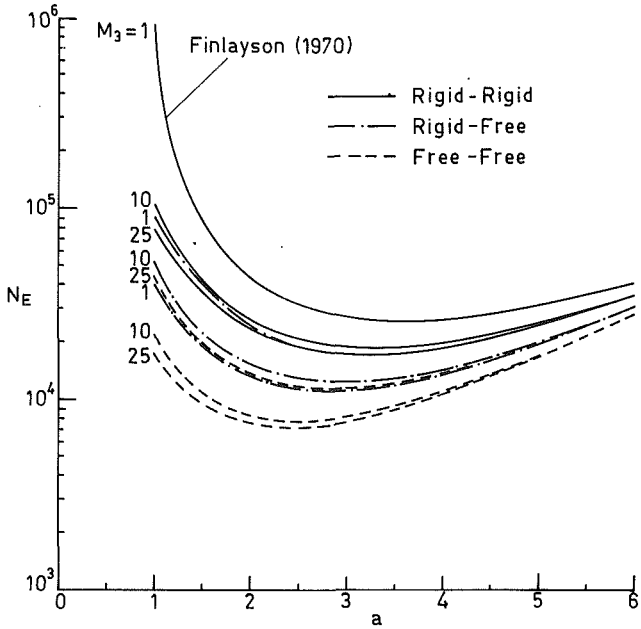

Fig. 2 *a* versus N_E for $M_1(E) = 2500$, $\mathrm{Ra}_I = M_1(I) = 0$ and $\chi = 1.0$

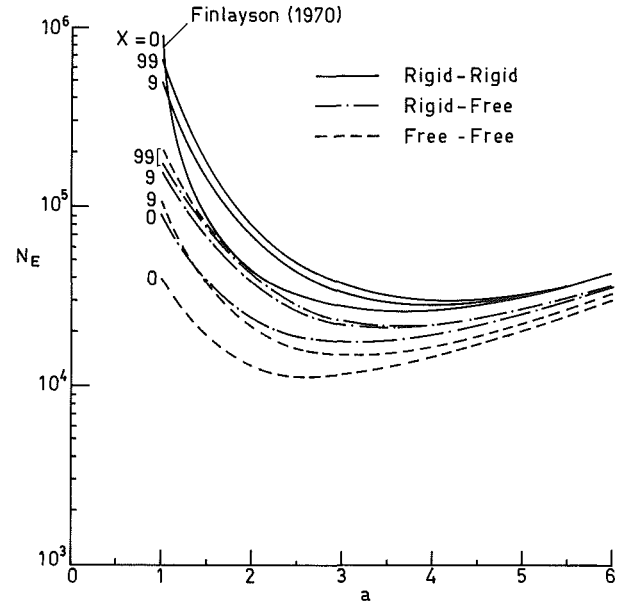

Fig. 3 *a* versus N_E for $M_1(E) = 2500$, $\mathrm{Ra}_I = M_1(I) = 0$ and $M_3 = 1.0$

to each individual trial function. We substitute $W = A_i W_i$, $T = B_i T_i$, and $\phi = C_i \phi_i (i = 1, 2, 3, \ldots)$ in equations (12)–(14) where W_i, T_i, and ϕ_i are the trial functions. Then we multiply the resulting momentum equation by W_j, energy equation by T_j, and magnetic potential equation by ϕ_j and perform the integration by parts from $z = -\frac{1}{2}$ to $\frac{1}{2}$. This procedure leads us to a system of algebraic equations

$$\begin{aligned} A_i D_{ji} + B_i E_{ji} + C_i F_{ji} &= 0 \\ A_i G_{ji} + B_i H_{ji} &= 0 \\ B_i I_{ji} + C_i J_{ji} &= 0 \end{aligned} \qquad (18)$$

where

$$\begin{aligned} D_{ji} &= \langle D^2 W_j D^2 W_i \rangle + 2a^2 \langle DW_j DW_i \rangle + a^4 \langle W_j W_i \rangle \\ E_{ji} &= -a^2 [1 + M_1(E)] \langle W_j T_i \rangle - a^2 M_1(I) \langle W_j T_i z \rangle \\ F_{ji} &= a^2 M_1(E) \langle W_j D\phi_i \rangle + a^2 M_1(I) \langle W_j D\phi_i z \rangle \\ G_{ji} &= (M_2 - 1)[\mathrm{Ra}_I \langle T_j W_i z \rangle + \mathrm{Ra}_E \langle T_j W_i \rangle] \\ H_{ji} &= \langle DT_j DT_i \rangle + a^2 \langle T_j T_i \rangle \end{aligned}$$

$$I_{ji} = \langle \phi_j DT_i \rangle$$
$$J_{ji} = \langle D\phi_j D\phi_i \rangle + a^2 M_3 \langle \phi_j \phi_i \rangle + a[\phi_j(1/2)\phi_i(1/2) + \phi_j(-1/2)\phi_i(-1/2)]/(1+\chi)$$

We compute the eigenvalues by using the condition that for a nontrivial solution of equations (18) the determinant of the coefficients matrix should vanish. This procedure is repeated with the trial functions $W_i = [(z^2 - 1/4)^2]z^{i-1}$, $W_i = (2z^2 - z - 1)(z^2 - 1/4)z^{i-1}$, and $W_i = [(z^2 - 1/4)^2 - (z^2 - 1/4)]z^{i-1}$ with respect to velocity for rigid-rigid, rigid-free, and free-free boundary combinations, respectively. The trial functions chosen for temperature and magnetic potentials are

$$T_i = (z^2 - 1/4)z^{i-1} \text{ and } \phi_i = z^{2i-1}$$

4 Discussion

The condition for the onset of stationary convection in a horizontal magnetic fluid layer in the presence of internal heat sources (sinks) is determined in this paper, using a higher order Galerkin technique. In the absence of magnetization of the fluid and internal heat sources (i.e., $M_1(E) = M_1(I) = \mathrm{Ra}_I = 0$) we recover the classical Rayleigh-Bénard problem. The critical Rayleigh numbers obtained for the Rayleigh Bénard problem, as a limiting case, coincide exactly with those of Chandrasekhar (1961), as shown in Table 1. In some cases an eighth-order Galerkin expansion is required to have plausible convergence of the eigenvalues. However, in this problem, the results converged on using a fifth-order Galerkin expansion and compare well with the exact values. Therefore we present the eigenvalues obtained by using the fifth-order Galerkin expansions as trial functions. In the absence of an internal heat source (i.e., $Q = 0$ and $\Delta T \neq 0$) we obtain the conditions for the onset of convection in a horizontal magnetic fluid layer with uniform temperature distribution. This problem was studied by Finlayson (1970) in the limiting cases of $M_1(E) \to \infty$ for rigid-rigid isothermal boundaries and $\chi \to \infty$ for the free-free isothermal boundaries. The neutral curves for these cases with finite χ are depicted in Figs. 1-3.

In Fig. 1, the eigenvalues are depicted for $M_1(E) = 0$ and 5. The figure reveals that for $M_1(E) = 5$, the external Rayleigh number takes the values 417.073, 282.748, and 184.599 for the rigid-rigid, rigid-free, and free-free boundary combinations, respectively. It is clear that an increase in the magnetization force causes a proportionate decrease in the buoyancy force and it is more pronounced when the layer is bounded by rigid-rigid boundaries. If we eliminate T and ϕ from equations (12)-(14), the resulting single equation, in the absence of heat source, contains Ra_E, $M_1(E)$, and M_3 and the products of these three nondimensional parameters (with χ as a fourth parameter appearing in the magnetic potential boundary conditions). When $M_1(E)$ takes small values (i.e., when both magnetic and buoyancy mechanisms are operative) the stability of the system is dictated by $\mathrm{Ra}_E(1 + M_1(E))$ and when $M_1(E)$ takes large values (i.e., saturated magnetization when the buoyancy forces are turned off and only the magnetic mechanism is operative) the stability of the system is dictated by $N_E (= \mathrm{Ra}_E \cdot M_1(E))$. Therefore, when $M_1(E) = 5.0$, the critical eigenvalues that decide the stability of the system are 2502.438, 1696.488, and 1107.594, which are larger than those obtained for $M_1(E) = 0$, and the effect of magnetization is to stabilize the system in this limit of magnetization. However, when $M_1(E)$ tends to infinity, the number of parameters decreases to three, i.e., N_E, M_3, and χ. Figures 2 and 3 are plots of N_E versus a, for different values

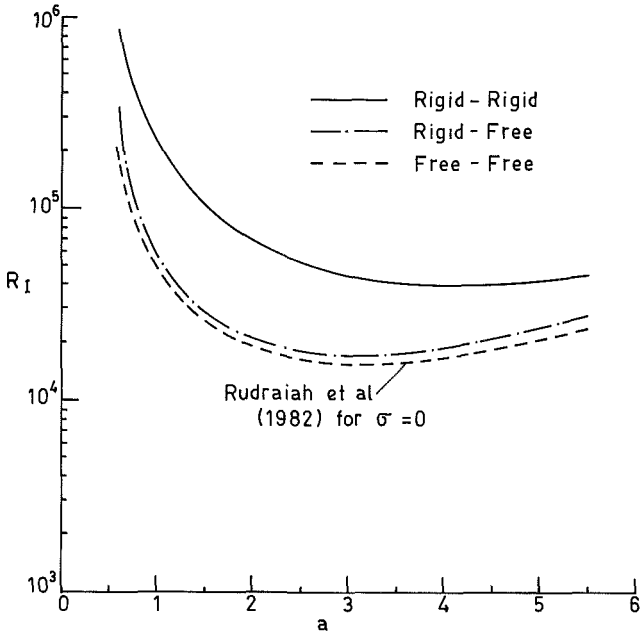

Fig. 4 a versus Ra_I for $M_1(E) = M_1(I) = 0$, $\chi = 10^3$ and $M_3 = 1.0$

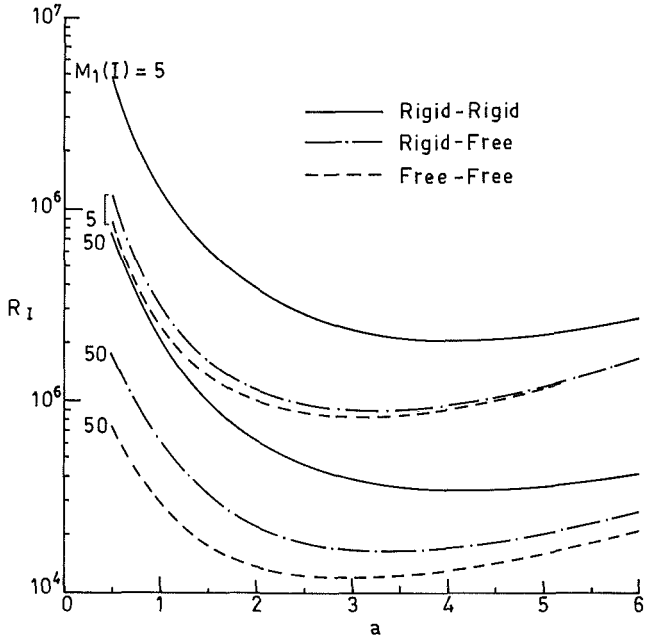

Fig. 5 a versus Ra_I for $\mathrm{Ra}_E = M_1(E) = \chi = 0$ and $M_3 = 1.0$

Table 2 Critical wave numbers and internal Rayleigh numbers for $\mathrm{Ra}_E = M_1(E) = 0$ and $M_1(I) = 5$

χ	M_3	α	Rigid-Rigid	α	Rigid-Free	α	Free-Free
0.00276	1	4.1709	20662.8	3.1438	9010.02	2.9536	8688.02
$HO(NO_3)_3$	2	4.1693	20501.6	3.1421	8938.65	2.9572	8658.46
	3	4.1674	20402.6	3.1403	8890.54	2.9594	8637.91
	4	4.1658	20333.5	3.1388	8854.93	2.9610	8622.40
	5	4.1645	20214.6	3.1375	8827.02	2.9623	8610.05
0.00046	1	4.1708	20662.1	3.1438	9009.51	2.9536	8687.78
$FeCl_3$	2	4.1693	20501.2	3.1421	8938.30	2.9572	8658.29
	3	4.1674	20402.3	3.1403	8890.28	2.9594	8637.78
	4	4.1658	20333.3	3.1388	8854.71	2.9610	8622.29
	5	4.1645	20281.7	3.1375	8826.85	2.9623	8609.96

of M_3 and χ, respectively. Figure 2 reveals that as the magnetic equation of state departs from linearity (i.e., M_3 large) the system is destabilized slightly, showing that the magnetic mechanism suppresses the buoyancy force totally and the magnetization causes convection. As the magnetic susceptibility χ becomes large its influence on the system becomes insignificant (see Fig. 3) as it disappears from the magnetic potential boundary conditions. From Figs. 2 and 3, we also observe that as M_3 and χ tend to infinity, the results of the present problem reduce to those of the classical Rayleigh-Bénard problem.

In the absence of external temperature gradient and magnetization force (i.e,. $\mathrm{Ra}_E = M_1(E) = M_1(I) = 0$) we have the problem of convection induced purely by internal heat source in the usual viscous fluid. The results obtained for this case are presented in Fig. 4 and good agreement is found with the limiting case (i.e., absence of porous parameter) of Rudraiah et al. (1982). For example, in equation (34) of their paper, if we let $\sigma = 0$, we recover $\mathrm{Ra}_I = 1.718504 \times 10^4$, for a layer of viscous fluid bounded by free-free isothermal boundaries.

From Fig. 5, a plot of internal Rayleigh number versus wave number, we see that convection sets in even in the absence of an external temperature gradient caused by magnetization of the fluid due to an internal heat source. Analogous results were obtained by Berkovskii and Bashtovoi (1971) considering the magnetocaloric effect, which is analogous to the heat source effect. When convection sets in purely due to an internal heat source in a horizontal magnetic fluid layer (i.e., $\mathrm{Ra}_E = M_1(E) = 0$) the results obtained are shown in Table 2. The stabilizing effect of χ and the destabilizing effect of M_3 turn out to be qualitatively similar to those of the uniform temperature gradient. From this we infer that the magnetic fluids having larger magnetic susceptibilities (like $HO(NO_3)_3$) are more stable than the fluids with smaller susceptibilities (like $FeCl_3$), because of their dampening effect, due to an increase in magnetic induction.

From Figs. 1-3 and 5 and Table 2, we see that the magnetic parameters $M_1(I)$, $M_1(E)$, M_3, and χ, where the first three are functions of χ, have marginal influence on the critical wave number. This is mainly due to the nature of magnetization. The increase in χ is to increase the size of the suspended magnetic particles. In weak fields, the chief contribution to the magnetization is made by the larger particles, for they are more easily oriented by a magnetic field, whereas the approach to saturation is determined by the fine particles, orientation of which requires large fields as discussed by Rosensweig (1985). The increase in χ obstructs the fluid from getting the saturated magnetization and hence both buoyancy and magnetic mechanisms make opposing contributions to the system. In the present analysis we observe that as $M_1(E)$, $M_1(I)$, and M_3 increase, the critical Rayleigh number decreases. Thus the complementary nature of the buoyancy and magnetic forces is the cause for the observed marginal influence of magnetic parameters on the critical wave number. A similar situation has been observed by Finlayson (1970) in the presence of uniform temperature distribution.

We now look into the possibility or otherwise of oscillatory instability. Most magnetic fluids of practical interest have low susceptibilities and as a result the decrease in χ increases the parameters $M_1(I)$, $M_1(E)$, and M_3, which are essentially destabilizing. These effects reinforce the destabilizing effect of buoyancy. Therefore, for small values of χ it is reasonable enough to discount oscillatory convection. However, following Murgai and Khosla (1962), the principle of exchange of stability is shown to be valid for all values of χ (see Appendix). In conclusion, oscillatory convection is ruled out for this system.

The present analysis contains six nondimensional parameters $M_1(E)$, $M_1(I)$, Ra_E, Ra_I, M_3, and χ. It is very difficult to study simultaneous coupling effects for all six parameters. Although we have computed the critical eigenvalues by taking all these parameters into consideration, to understand the physics of the problem we have presented in Figs. 1-5 only those cases in which at least two parameters are set to zero. For completeness of the problem the critical Ra_I obtained for different values of $M_1(I)$, in the presence of other four parameters, are graphically represented in Fig. 6. This reveals that as the internal magnetic number increases, the internal Rayleigh number decreases in analogy with the effect of the external magnetic number $M_1(E)$. We thus infer that the critical Rayleigh number is smaller with magnetization than without, and qualitatively this suggests that at comparable supercritical Rayleigh numbers the convection will be enhanced with magnetization. In the presence of both external temperature gradient and internal heat source (i.e., $\Delta T = Q \neq 0$), computations have also been carried out to see the effect of various parameters of the present problem on Ra_E and Ra_I and we found that their qualitative behavior is similar to that discussed above.

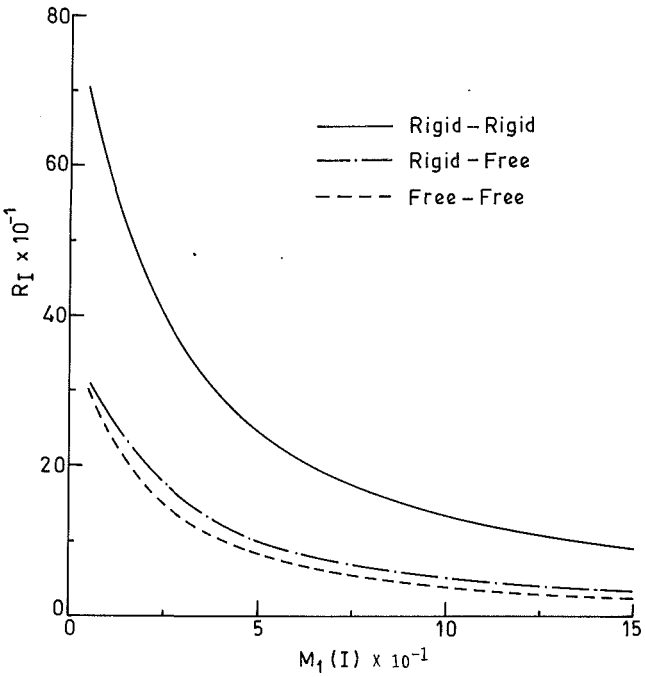

Fig. 6 Ra_I versus $M_1(I)$ for $M_1(E) = 50$, $\mathrm{Ra}_E = 5$, $\chi =$ $M_3 = 1.0$

We also conclude that the rigid-rigid boundary combination is the most stable configuration, compared to rigid-free and free-free, in all the situations considered in the paper analogous to the usual viscous fluid case.

Acknowledgments

This work is supported by the UGC (India) under the DSA Programme. One of us (G.N.S.) is grateful to the UGC for awarding a Senior Research Fellowship under the DSA Programme. We thank the referees for their comments, which improved the paper considerably.

References

Bashtovoi, V. G., and Berkovskii, B. M., 1973, "Thermomechanics of Ferromagnetic Fluids," *Magnitnaya Gidrodinamika*, No. 3, pp. 3-14.

Berkovskii, B. M., and Bashtovoi, B. G., 1971, "Gravitational Convection in a Ferromagnetic Liquid," *Magnitnaya Gidrodinamika*, No. 2, pp. 24-28.

Chandrasekhar, S., 1961, *Hydrodynamic and Hydromagnetic Stability*, Dover Publications, New York.

Finlayson, B. A., 1970, "Convective Instability of Ferromagnetic Fluids," *J. Fluid Mech.*, Vol. 40, Part 4, pp. 753-767.

Finlayson, B. A., 1972, *The Method of Weighted Residuals and Variational Principles*, Academic Press, New York.

Gasser, R. D., and Kazimi, M. S., 1976, "Onset of Convection in a Porous Medium With Internal Heat Generation," ASME JOURNAL OF HEAT TRANSFER, Vol. 98, pp. 49-54.

Gotoh, K., and Yamada, M., 1982, "Thermal Convection in a Horizontal Layer of Magnetic Fluids," *Journal of Phys. Soc. Japan*, Vol. 51, No. 9, pp. 3042-3048.

Lalas, D. P., and Carmi, S., 1971, "Thermoconvective Stability of Ferrofluids," *Phys. Fluids*, Vol. 14, pp. 436-438.

Murgai, M. P., and Khosla, P. K., 1962, "A Study of the Combined Effect of Thermal Radiative Transfer and a Magnetic Field on the Gravitational Convection of an Ionized Fluid," *J. Fluid Mech.*, Vol. 14, Part 3, pp. 433-451.

Papell, S. S., 1965, "Low Viscosity Magnetic Fluid Obtained by the Colloidal Suspension of Magnetic Particles," U.S. Patent No. 3, 215, 572.

Roberts, P. H., 1967, "Convection in Horizontal Layers With Internal Heat Generation—Theory," *J. Fluid Mech.*, Vol. 30, Part 1, pp. 33-49.

Rosensweig, R. E., and Kaiser, R., 1967, "Study of Ferromagnetic Liquid—Phase I," NASA CR-91684, p. 238.

Rosensweig, R. E., 1985, *Ferrohydrodynamics*, Cambridge University Press, Cambridge, United Kingdom.

Rudraiah, N., Veerappa, B., and Balachandra Rao, S., 1982, "Convection in a Fluid-Saturated Porous Layer With Nonuniform Temperature Gradient," *Int. J. Heat Mass Transfer*, Vol. 25, No. 8, pp. 1147-1156.

Rudraiah, N., and Chandna, O. P., 1985, "Effects of Coriolis Force and Non-uniform Temperature Gradient on the Rayleigh-Bénard Convection," *Can. J. Phys.*, Vol. 64, No. 1, pp. 90-99.

Somerton, C. W., and Catton, I., 1982, "On the Thermal Instability of Superposed Porous and Fluid Layers," ASME JOURNAL OF HEAT TRANSFER, Vol. 104, pp. 160-165.

Sparrow, E. M., Goldstein, R. J., and Jonson, V. K., 1964, "Thermal Instability in a Horizontal Fluid Layer: Effect of Boundary Conditions and Nonlinear Temperature Profile," *J. Fluid Mech.*, Vol. 18, pp. 513-528.

APPENDIX

Principle of Exchange of Stabilities

We now prove that the principle of exchange of stabilities is valid for all χ. The time-dependent equations of the system under consideration are

$$[(D^2-a^2)^2-\frac{\sigma_i}{\mathrm{Pr}}(D^2-a^2)]W_i-[M_1(E)+1+M_1(I)z]a^2T_i + a^2[M_1(E)+M_1(I)z]D\phi_i=0 \quad \text{(A1)}$$

$$\sigma_iT_i-(D^2-a^2)T_i+[\mathrm{Ra}_E+\mathrm{Ra}_Iz]W_i=0 \quad \text{(A2)}$$

$$D^2\phi_i-a^2M_3\phi_i-DT_i=0 \quad \text{(A3)}$$

where (W_i, W_j) and (ϕ_i, ϕ_j) are the eigenvalues of W and ϕ, respectively, corresponding to σ_i and σ_j.

Operating $\sigma_i-(D^2-a^2)$ on equations (A1) and (A3), eliminating T_i, multiplying the resultant equations by W_j and ϕ_j, respectively, and performing the integration by parts with respect to z over the range $-\frac{1}{2}\le z\le\frac{1}{2}$, we obtain

$$\sigma_i(1+1/\mathrm{Pr})I_1+I_2+\sigma_i^2I_3/Pr - a^2\mathrm{Ra}_E[M_1(E)+1]<W_jW_i> - a^2[\mathrm{Ra}_I\{M_1(E)+1\} + \mathrm{Ra}_EM_1(I)]\langle zW_jW_i\rangle - a^2\mathrm{Ra}_IM_1(I)\langle z^2W_jW_i\rangle + \sigma_ia^2M_1(E)\langle W_jD\phi_i\rangle + \sigma_ia^2M_1(I)\langle zW_jD\phi_i\rangle - a^2M_1(E)\langle W_j(D^2-a^2)D\phi_i\rangle - a^2M_1(I)\langle zW_j(D^2-a^2)D\phi_i\rangle - 2a^4M_1(I)M_3\langle W_j\phi_i\rangle=0 \quad \text{(A4)}$$

where

$$I_1=\langle D^2W_jD^2W_i\rangle+2a^2\langle DW_jDW_i\rangle+a^4\langle W_jW_i\rangle$$

$$I_2=\langle D^3W_jD^3W_i\rangle+3a^2\langle D^2W_jD^2W_i\rangle + 3a^4\langle DW_jDW_i\rangle+a^6\langle W_jW_i\rangle$$

$$I_3=\langle DW_jDW_i\rangle+a^2\langle W_jW_i\rangle$$

$$\sigma_i\langle\phi_j(D^2-a^2M_3)\phi_i\rangle-\langle\phi_j(D^2-a^2)(D^2-a^2M^3)\phi_i\rangle + \mathrm{Ra}_E\langle D\phi_jW_i\rangle+\mathrm{Ra}_I\langle zD\phi_jW_i\rangle=0 \quad \text{(A5)}$$

Interchanging i and j in W and ϕ

$$\sigma_i\langle\phi_i(D^2-a^2M_3)\phi_j\rangle-\langle\phi_i(D^2-a^2)(D^2-a^2M_3)\phi_j\rangle + \mathrm{Ra}_E\langle W_jD\phi_i\rangle+\mathrm{Ra}_I\langle zW_jD\phi_i\rangle=0 \quad \text{(A6)}$$

Substitute for $\langle zW_jD\phi_i\rangle$ from equation (A6) in (A4) to get

$$\sigma_i(1+1/\mathrm{Pr})I_1+I_2+\sigma_i^2I_3/\mathrm{Pr} - a^2\mathrm{Ra}_E[M_1(E)+1]\langle W_j\mathrm{W}_i\rangle - a^2[\mathrm{Ra}_I\{M_1(E)+1\} + \mathrm{Ra}_EM_1(I)]\langle zW_jW_i\rangle - a^2\mathrm{Ra}_IM_1(I)\langle z^2W_jW_i\rangle + \sigma_ia^2M_1(E)\langle W_jD\phi_i\rangle + a^2(M_1(I)/\mathrm{Ra}_I)[\sigma_i\langle\phi_i(D^2-a^2)(D^2-a^2M_3)\phi_j\rangle + \sigma_i^2\langle\phi_i(D^2-a^2M_3)\phi_j\rangle - \sigma_i\mathrm{Ra}_E\langle W_jD\phi_i\rangle - a^2M_1(E)\langle W_j(D^2-a^2)D\phi_i\rangle - a^2M_1(I)\langle zW_j(D^2-a^2)D\phi_i\rangle - 2a^4M_1(I)\mathrm{M}_3\langle W_j\phi_i\rangle=0 \quad \text{(A7)}$$

A complex value of σ will be associated with complex values of W and ϕ, as will their respective complex conjugates $(\bar{\sigma}, \bar{W}, \bar{\phi})$, which will satisfy the same equations and boundary conditions. Now we take (σ_i, W_i, ϕ_i) as (σ, W, ϕ) and (σ_j, W_j, ϕ_j) as $(\bar{\sigma}, \bar{W}, \bar{\phi})$, respectively. We change σ_i to σ_j in equation (A7) and subtract it from (A7) to get

$$\mathrm{Im}(\sigma)[(1+1/\mathrm{Pr})I_1+2\mathrm{Re}(\sigma)I_3/\mathrm{Pr}+2\mathrm{Re}(\sigma)a^2M_1(I)I_4/\mathrm{Ra}_I + 2\mathrm{Re}(\sigma)a^3M_1(I)I_5/\mathrm{Ra}_I(1+\chi)+a^5M_1(I)M_3I_5/\mathrm{Ra}_I(1+\chi) + a^2M_1(I)/\mathrm{Ra}_I\{I_5+I_6+aI_7/(1+\chi)\}]=0 \quad \text{(A8)}$$

where

$$I_4 = \langle D\phi_jD\phi_i\rangle + a^2M_3\langle\phi_j\phi_i\rangle$$
$$I_5 = \phi_i(\tfrac{1}{2})\phi_j(\tfrac{1}{2})+\phi_i(-\tfrac{1}{2})\phi_j(-\tfrac{1}{2})$$
$$I_6 = \langle D^2\phi_jD\phi_i\rangle + a^2(M_3+1)\langle D\phi_jD\phi_i\rangle + a^4M_3\langle\phi_j\phi_i\rangle$$
$$I_7 = \phi_i(\tfrac{1}{2})DT_j(\tfrac{1}{2})+\phi_j(-\tfrac{1}{2})DT_j(-\tfrac{1}{2})$$

We note that all the terms in equation (A8) are positive except I_7. However, the numerical computation of I_7 turns out to be positive for all possible trial functions. Hence the principle of exchange of stabilities is valid for all χ.

Parametric Study of Mixed Convection in a Porous Medium Between Vertical Concentric Cylinders

N. J. Kwendakwema[1]
Graduate Assistant.

R. F. Boehm[2]
Professor.
Fellow ASME

Department of Mechanical Engineering,
University of Utah,
Salt Lake City, UT 84112

A numerical study has been performed to evaluate mixed convection heat transfer in a porous medium between two vertical concentric cylinders for a constant-temperature outer and an insulated inner boundary conditions. In modeling the flow in the bed a finite difference technique was utilized to represent the governing equations with appropriate boundary layer assumptions. The effects of flow inertia, variable porosity and properties, and the Brinkman friction were all taken into account. The model simulated the condition where water was the fluid flowing through the porous material. In all flow simulations the Darcy law condition was obeyed, i.e., the Reynolds number based on the particle diameter was less than unity. Results obtained include radial and axial velocity and temperature profiles in the bed. The dependence of local Nusselt number on the axial distance for several Reynolds numbers was also obtained. Correlations of the average Nusselt number against the Grashof, Peclet, and Darcy numbers were obtained for various radius ratios. Comparisons of the heat transfer predictions to data and calculations of others for special situations showed excellent agreement.

Introduction

Studies of convective heat transfer in enclosures filled with saturated porous media have been prompted by such diverse engineering problems as heat transfer in geothermal energy systems, storage of radioactive nuclear waste materials, separation processes in chemical industries, transpiration cooling, pollutant dispersion in aquifers, and thermal enhanced oil recovery methods, to name a few.

This simulation related to the feasibility of extracting energy from the liquid magma region located near the earth's surface. The flow of water through a packed bed is related to the expected flow conditions in the solidified and fractured magma. It is anticipated that the cold water would flow from the top through a center pipe and then up through the annulus, picking up heat from the hot magma. Based on the experimental data obtained by Dunn (1983), Hickox and Dunn (1985) estimated the effective heat transfer coefficient to be at least an order of magnitude greater for this configuration than for the system where the cold water from the top is pumped to the bottom through the annulus and the heated fluid forced up through the center pipe. The heat transfer process in this arrangement would be mixed involving both natural and forced convection.

According to Vanover and Kulacki (1987), it appears that studies of mixed convection in porous media started with Combarnous and Bia (1971) when they considered the effect of mean flow on the onset of stability in a porous layer bounded by two parallel isothermal surfaces. Homsy and Sherwood (1976) later discussed the instabilities of a saturated porous medium heated from below with a flow parallel to the gravity vector. Similarity solutions have been employed by Cheng (1977a) when he also established criteria for free and mixed convection about horizontal flat plates in porous media. In this study he found the governing parameter to be $Ra/(Pe)^{1.5}$. When the value of this parameter is between 0 and 0.16, forced convection is dominant, between 0.16 and 5 mixed convection dominates, and greater than 15, free convection is dominant. Cheng (1977b) studied the problem of mixed convection about inclined surfaces in a porous medium on the basis of boundary-layer approximations. In this study he found that the parameter governing mixed convection from inclined surfaces in porous media is Gr/Re. The numerical solutions he obtained for mixed convection from an isothermal vertical flat plate showed that for Gr/Re less than 0.15 forced convection was dominant, between 0.15 and 16 mixed flow prevailed, and greater than 16, free convection was dominant.

Other studies of mixed convection in porous media include those by Haajizadeh and Tien (1984) who investigated both analytically and numerically mixed convection in a horizontal porous channel with emphasis on the effects of channel aspect ratio. Joshi and Gebhart (1985) studied mixed convection in porous media adjacent to a vertical uniform heat flux surface, while Chandrasekhara and Namboodiri (1985) determined the influence of variable permeability on mixed convection about inclined surfaces in porous media. Ranganathan and Viskanta (1984) used a finite difference numerical scheme to study combined free and forced convection boundary layer flow in a porous medium near a vertical wall. The results of their model showed that the inertial and viscous effects have a significant influence on the velocity profiles and heat transfer rate at the surface.

Little has been reported about mixed convection in an annulus. Vanover and Kulacki (1987) presented experimental results of mixed convection in a horizontal porous annulus. Their thermal boundary conditions were a constant heat flux inner cylinder and an isothermal outer cylinder. Parang and Keyhani (1986) studied mixed convection in a vertical porous annulus with constant heat flux boundaries at both the inner and outer radii. Of most pertinence to the present work are the experimental and numerical studies of mixed convection in a vertical annular geometry recently reported by Clarksean et al. (1988, 1990). In those studies the outer wall was isothermal and the inner wall was adiabatic, similar to the situation reported here. Results for only one radius ratio were reported. They presented

[1]Present address: Faculty of Engineering, University of Zambia.

[2]Present address: Mechanical Engineering Department, University of Nevada—Las Vegas.

Contributed by the Heat Transfer Division for publication in the JOURNAL OF HEAT TRANSFER. Manuscript received by the Heat Transfer Division May 19, 1988; revision received April 2, 1990. Keywords: Mixed Convection, Porous Media.

information about temperature distributions within the bed and estimated some heat transfer coefficients for a range of Pe numbers at essentially a constant value of Ra. Using a general approach to the problem, they showed that a boundary layer flow resulted.

The purpose of this work is to study mixed convection numerically in a vertical annulus filled with a saturated porous medium for various radius ratios. The system analyzed here and shown in Fig. 1 is as follows: The outer wall is maintained at a constant temperature and the inner wall is assumed adiabatic. Additional assumptions included that the top and bottom boundaries are insulated, and a slug inlet flow is imposed from the bottom. These conditions were selected because of their relevance to the conditions found in geothermal energy extraction from a magma source. To investigate the effects of the heated outer wall boundary condition on the temperature field, the local and average Nusselt numbers were calculated for various values of the ratio of the Peclet number to the Rayleigh number. To determine the effect of radius ratio on the average Nusselt number, the outer radius was assumed constant while the inner radius was varied.

Governing Equations

The governing partial differential equations for continuity, momentum, and energy for an isotropic, homogeneous, fluid-filled porous medium have been established by Wooding (1957). For steady-state, axisymmetric cylindrical geometry, and assuming a boundary layer form, these equations become:

Continuity

$$\frac{\partial u}{\partial z}+\frac{v}{r}+\frac{\partial v}{\partial r}=0 \tag{1}$$

Axial momentum

$$\rho\left[v\frac{\partial u}{\partial r}+u\frac{\partial u}{\partial z}\right]=-\frac{\partial p}{\partial z}-\rho(T)g-\frac{\mu(T)}{K(r)}u+\frac{1}{r}\frac{\partial}{\partial r}\left[r\mu(T)\frac{\partial u}{\partial r}\right] \tag{2}$$

Energy

$$v\frac{\partial T}{\partial r}+u\frac{\partial T}{\partial z}=\frac{k_e}{\rho C_{pf}}\frac{1}{r}\frac{\partial}{\partial r}\left[r\frac{\partial T}{\partial r}\right] \tag{3}$$

Equation of state

$$\rho=\rho_r(1-\beta[T-T_r]) \tag{4}$$

$K(r)$ in the momentum equation is the variable permeability of the packed bed. Although its functional relationship with the radius cannot be measured directly, it can be inferred from the variation of the porosity, which has been approximated by Vortmeyer and Schuster (1983) to be an exponential function dependent on the outer and inner bed radius and the particle diameter.

The dynamic viscosity variations with temperature can be taken to be

$$\overline{\mu}=\overline{\mu}_r+(\overline{\mu}_w-\overline{\mu}_r)\exp\{-C'(T-T_w)\}$$

and

$$\mu=\mu_r+(\mu_w-\mu_r)\exp\{-C(T-T_w)\} \tag{5}$$

The boundary conditions are

$$u=u,\quad v=0,\quad p=p_o,\quad T=T_o,\quad \text{for } r_i<r<r_o, \text{ and } z=0$$

$$u=0,\quad v=0,\quad \partial T/\partial r=0,\quad \text{for } r=r_i, \text{ and } z=0$$

$$u=0,\quad v=0,\quad T=T_o,\quad \text{for } r=r_o, \text{ and } z>0$$

For the solution of all the variables one further equation is necessary in order to solve for p, the pressure drop. Thus a further continuity requirement of constant mass flow through the annulus is introduced

$$\pi(r_o-r_i)\rho_o u_o=\int_{r_i}^{r_o}2\pi r\rho u\,dr \tag{6}$$

Using the definitions given in the nomenclature and the ones given below in equation (7), equations (1)–(3) and (6) were nondimensionalized to yield equations (8)–(11)

$$\begin{aligned} C_1&=C\Delta T & C_2&=C'\Delta T\\ EV&=\overline{\mu}_r/\mu_r & TF&=(\mu_w-\mu_r)/\mu_r\\ TE&=(\overline{\mu}_w-\overline{\mu}_r)/\mu_r \end{aligned} \tag{7}$$

$$\frac{\partial U}{\partial Z}+\frac{V}{R}+\frac{\partial V}{\partial R}=0 \tag{8}$$

Nomenclature

C_p = specific heat at constant pressure
C, C' = constants in equation (5)
C_1, C_2 = constants defined in equation (7)
d = particle diameter
D = annular gap width $=r_o-r_i$
Da = Darcy number $=K/D^2$
EV = constant defined in equation (7)
g = gravitational constant
G = D^3g/ν_r^2
Gr = $G\beta\Delta T$ = Grashof number
h = heat transfer coefficient
k_e = effective thermal conductivity of the porous bed
K = bed permeability
L = height of annulus
Nu = Nusselt number based upon (T_w-T_{mean}) and D
Nu′ = Nusselt number based upon (T_w-T_o) and bed height
$\overline{\text{Nu}}$, $\overline{\text{Nu}}'$ = average Nusselt numbers over height of bed
p = pressure
P = dimensionless pressure $=p/\rho_r\mu_r^2$
Pe = Peclet number $=\nu D/\alpha$
Pr_e = Prandtl number $=\mu_r C_p/k_e$
r = radial coordinate, measured from centerline
r_i = dimensional inner radius
r_o = dimensional outer radius
R = dimensionless radial distance $=r/D$
R_i = dimensionless inner radius $=r_i/D$
R_o = dimensionless outer radius $=r_o/D$
Ra = Rayleigh number $=G\beta\Delta T$ Pr_e Da
Re_d = Reynolds number based on particle diameter $=u_o d/\nu_r$
Re_o = Reynolds number based on the gap width $=u_o D/\nu_r$
T = temperature
T_m = mean bed temperature at a constant elevation
T_o = fluid temperature at inlet to the bed
T_w = bed outer wall temperature (assumed constant here)
T' = dimensionless temperature $(T-T_o)/(T_w-T_o)$
TF = constant defined in equation (7)
T_r = reference temperature $=T_o$
u = axial velocity
U = dimensionless axial velocity $=u/u_o$
v = radial velocity
V = dimensionless radial velocity $=vD/\nu_r$
z = vertical coordinate measured from the bottom
Z = dimensionless z coordinate $=z/(\text{Re}_o D)$
α = thermal diffusivity
β = volumetric expansion coefficient
ϵ = porosity
μ_r = dynamic viscosity
ρ = density
ρ_r = reference density

$$V\frac{\partial U}{\partial R}+U\frac{\partial U}{\partial Z}=-\frac{\partial P}{\partial Z}-\frac{G}{\mathrm{Re}_o}+\frac{\mathrm{Gr}T'}{\mathrm{Re}_o}$$
$$-\frac{U}{\mathrm{Da}}-\frac{U}{\mathrm{Da}}\exp(-C_1\{T'-T'_w\})$$
$$+EV\left(\frac{1}{R}\frac{\partial U}{\partial R}+\frac{\partial^2 U}{\partial R^2}\right)+TF\exp(-C_2\{T'-T'_w\})$$
$$+EV\left(\frac{1}{R}\frac{\partial U}{\partial R}+\frac{\partial^2 U}{\partial R^2}-C_2\frac{\partial T'}{\partial R}\frac{\partial U}{\partial R}\right) \quad (9)$$

$$V\frac{\partial T'}{\partial R}+U\frac{\partial T'}{\partial Z}=\frac{1}{\mathrm{Pr}_e}\left(\frac{1}{R}\frac{\partial T'}{\partial R}+\frac{\partial^2 T'}{\partial R^2}\right) \quad (10)$$

$$\frac{R_o^2-R_i^2}{2}=\int_{R_i}^{R_o} UR\,dR \quad (11)$$

The entry conditions are

$U=1, \quad V=0, \quad P=P_o, \quad T'=T_o$, for $Z=0$ and $R_i<R<R_o$

The inner wall conditions are

$U=0, \quad V=0, \quad \partial T'/\partial R=0, \quad$ for $R=R_i, \quad Z>0$

The outer wall conditions are

$U=0, \quad V=0, \quad T'=T'_w=\text{const}, \quad R=R_o, \quad Z>0.$

Equations (8)–(11) were then transformed into finite-difference equations following the difference representations made by Bodoia and Osterle (1961). The finite difference equations were solved using the procedure described below and also by Collins (1971) and Ledebrink (1977). Essentially the diffusion terms in the energy and momentum equations were represented by a central-difference scheme, while the advection terms in the energy equation were represented by an upwind scheme (Patankar, 1980).

Examination of the momentum and energy equations (9) and (10) shows them to be coupled and nonlinear. The coupling of the equations is necessary since with combined convection systems the hydrodynamic flow behavior is dependent on the thermal field distribution (Sherwin and Wallis, 1970). The equations have a nonlinear form because certain terms include products of two unknowns. These equations have been linearized in the finite difference form by assuming for one of the unknowns that its value at the forward radial position is approximately equal to that at the previous radial position.

The temperature equation was written for each radial position at the first axial step from entry, and the known coefficients and the right-hand sides were evaluated. This gave $M-1$ equations for the $M-1$ (M being number of radial subdivisions) unknown temperatures, and the solution for this system is easily obtained.

All the other equations were similarly written, the coefficients evaluated, and a solution for the unknown axial and radial velocity and pressure profiles follows. Where necessary, temperature data from the first solution were used in the coefficients. This procedure was then repeated for the next axial step, the input for it being partly given by output data from the first step. Hence, output data for the entire desired axial distance could be obtained.

Heat transfer from the outer surface can be correlated by the Nusselt number based on the difference between the heated wall temperature and the bulk mean temperature of the fluid and the gap width as follows:

$$\mathrm{Nu}=h\,D/k_e \quad (12)$$

where

$$h=\frac{k_e(\partial T/\partial r)_{r=r_o}}{(T_w-T_m)} \quad (13)$$

The average Nusselt number can be determined by point integration over the length of the geometry and can be expressed as

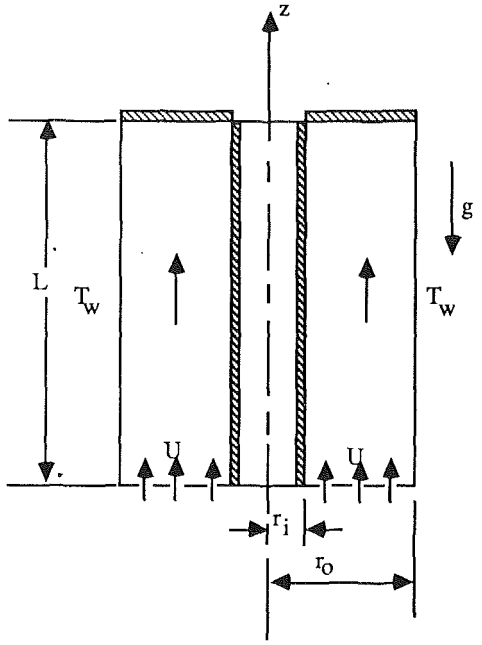

Fig. 1 Geometry of the problem

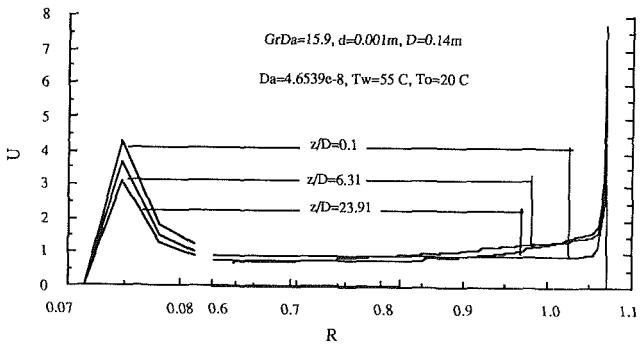

Fig. 2 Axial velocity variation with radial distance; note that detailed information near each wall, only, is shown

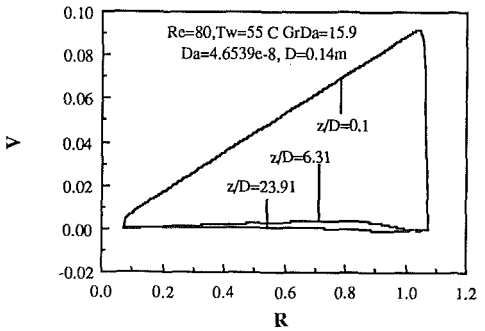

Fig. 3 Radial velocity variation with the radial distance for three vertical locations

$$\overline{\mathrm{Nu}}=\frac{1}{z}\int_0^z \mathrm{Nu}\,dz \quad (14)$$

In the solution process, a study was made of the effect of grid size on the end results. A grid size was used that was felt to be a good compromise between necessary accuracy and efficiency of performing the solution.

Results and Discussion

The results presented here were simulated assuming water as the heat transfer fluid at a constant inlet temperature of

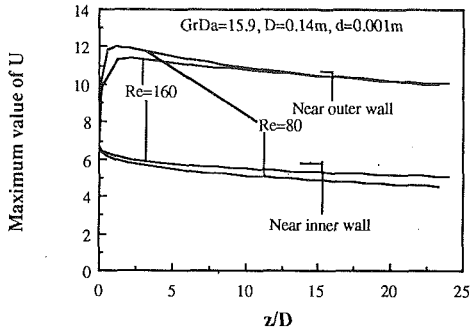

Fig. 4 Effect of Reynolds number on the vertical variation of the maximum velocity near the heated outer wall

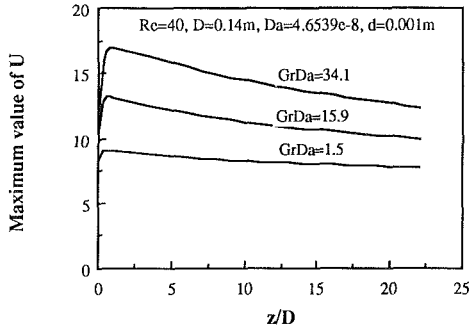

Fig. 5 Effect of GrDa on the vertical variation of the maximum velocity near the heated outer wall

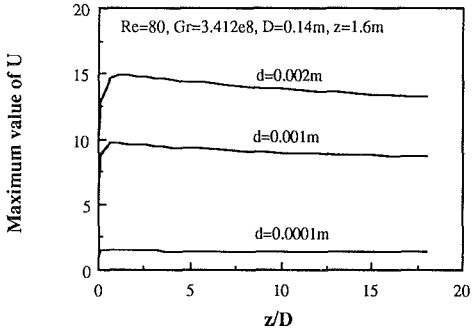

Fig. 6 Effect of particle diameter on the vertical variation of the maximum velocity near the heated outer wall

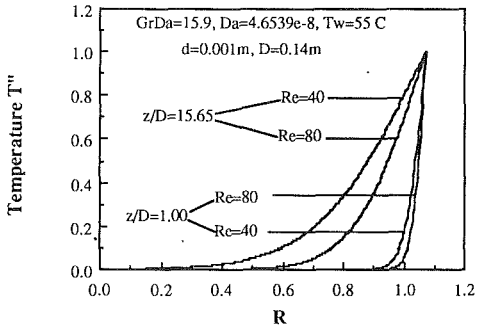

Fig. 7 Effect of Reynolds number and axial location on the radial temperature profiles

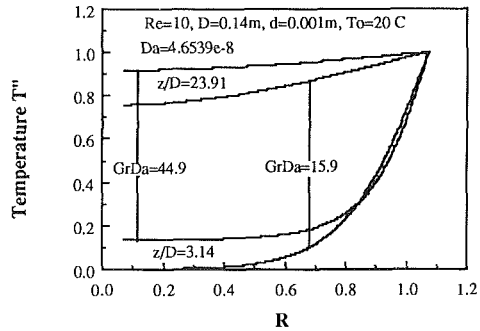

Fig. 8 Effect of GrDa on the radial temperature profiles

20°C. The inlet water temperature and the reference temperature were chosen to be the same in all the analyses, while outer wall radius was maintained constant at 0.15 m. Effective thermal conductivity of the porous bed was also assumed constant at 0.43 W/mK.

In the first portion of the analysis, the parameters were set such that the inner radius was 0.01 m and the particle diameter was 0.001 m, giving a radius ratio of 15. These parameters were chosen because they were similar to systems of interest to us. Other values were chosen also to show the effects of geometry. The results are presented and discussed separately for velocity and temperature profiles and heat transfer.

Velocity Profiles. An understanding of the velocity profiles within the bed is necessary in convection studies because of the anticipated influence the velocities have on the heat transfer. Not all velocity profiles obtained in the heat transfer analysis will be discussed; however, their influence on the heat transfer coefficients obtained will be inferred without explicitly referring to all of them.

Two-dimensional axial and radial velocity profiles are shown in Figs. 2 and 3, respectively, for several vertical positions in the bed to illustrate the general patterns for constant wall temperature conditions and radius ratio of 15. From this plot it can be seen that the velocities are generally higher near both the inner and outer walls with those near the latter being higher. Higher velocities near the solid boundary are due to higher porosity near the wall. The velocity has to go to zero at the walls to satisfy the no-slip condition. In between the two boundaries the velocity is relatively flat due to a constant porosity away from both walls.

Very high velocity near the heated wall occurs as a result of buoyancy due to high temperatures at the heated wall. Figure 4 illustrates the effect of varying Reynolds number on the maximum velocities near the outer wall for a given GrDa. It is shown in this figure that the lower the Reynolds number the higher the velocities. Intuitively it is expected that for similar bed conditions, higher Reynolds numbers should produce higher velocities in the forced convection case only. However, for aided-flow mixed convection, this is not true because as Collins (1971) pointed out, the natural convection aids the main flow. Figure 5 shows the influence of the GrDa number on the velocities near the outer (heated) wall: the higher the GrDa number, the higher the velocities. A similar effect is demonstrated in Fig. 6, where Gr has been held constant while the Darcy number has been varied by changing particle diameter.

Comparing the velocities near the heated wall in Figs. 4–6, it is seen that the peak velocity in Fig. 4 moves higher in the bed with increasing Reynolds number, while in Figs. 5 and 6, the peak velocity occurs higher in the bed for higher GrDa. It would thus be concluded that the developing region lengthens with both GrDa and Reynolds number.

Temperature Profiles. Temperature profiles are important in demonstrating the extent to which the energy supplied at the wall penetrates into the bed. Comparison of temperature profiles for a Reynolds number of 40 for $1.5 < \mathrm{GrDa} < 34.1$ showed no significant difference between them. This would thus imply that for $\mathrm{GrDa}/\mathrm{Re}_o < 1$ the effect of natural convection is quite minimal compared to forced convection indicated by Re_o. However, varying Reynolds number over the

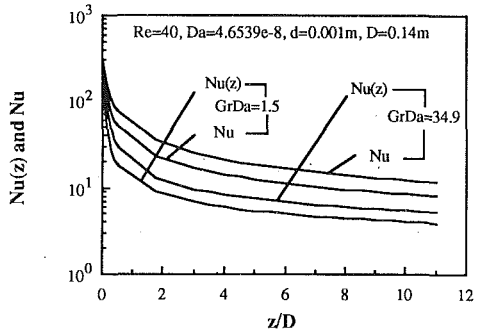

Fig. 9 Effect of GrDa on the local and average Nusselt numbers

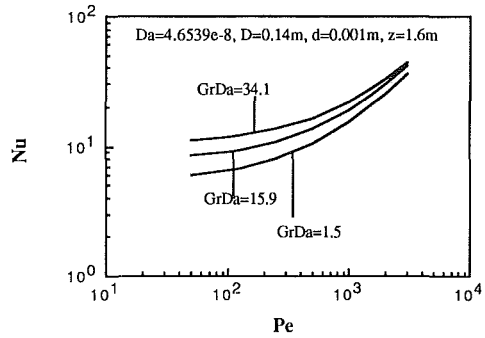

Fig. 10 Effects of GrDa and Pe on the average Nusselt number

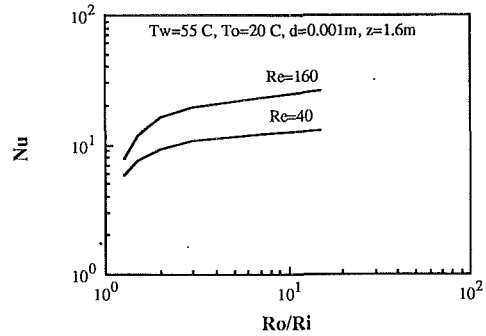

Fig. 11 Effect of radius ratio and Reynolds number on the Nusselt number

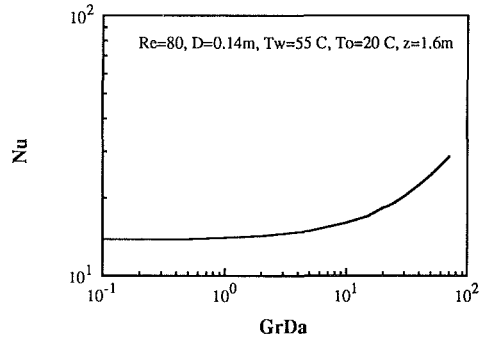

Fig. 12 Effect of particle diameter on Nusselt number

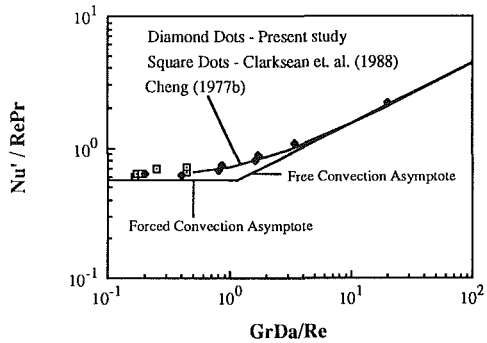

Fig. 13 Comparison of heat transfer results between those of a vertical flat plate and a vertical annular region of $R_o/R_i = 15$ in porous media

same range of GrDa given above shows a significant effect on the temperature profiles produced in the bed, as illustrated in Fig. 7. This figure shows that the higher the Reynolds number the steeper and closer to the heated wall the temperature profiles are for the same constant wall temperature. This suggests that most of the energy is convected away faster for higher Reynolds number and thus very little penetration of the heat into the bed is found. It should also be mentioned that the ratio Re/GrDa in this case is larger than 1 but less than 10 for both sets of curves. In Fig. 8 the effect of Gr/Da on the temperature profiles is shown. The figure shows that the higher the GrDa number the higher the temperatures on the same location in the bed. In both these sets of curves, the ratio Re/GrDa is less than one. The profiles are generally flat into the bed from the heated wall except for a very small section very close to the heated wall. This is a striking difference in pattern from those in Fig. 7.

Effect of Wall Temperature on Heat Transfer Coefficient. To determine the effect of outer wall temperature on both local and average Nusselt numbers, simulations were run for various heated wall temperatures and Reynolds numbers, holding particle diameter constant at 0.001 m. In Fig. 9 are shown results of both local and average Nusselt number plotted against axial distance for two values of GrDa, while Fig. 10 shows the variation of the average Nusselt number with the Peclet number for three different heated wall temperature conditions.

From Fig. 9, it is observed that both local and average Nusselt numbers increase with increasing GrDa number, which in this case corresponds to increasing wall temperature since the Darcy number is held constant. Both local and average Nusselt numbers, however, decrease with axial distance. This is because the largest temperature gradient between the heated wall and the incoming fluid occurs at the inlet and as a result the highest heat transfer occurs at the bottom of the bed. As the fluid moves up into the bed, the mean fluid temperature increases, thus decreasing the temperature gradient. From the expression of the Nusselt number one would expect that the increasing mean fluid temperature would reduce the temperature difference between the wall temperature and the mean fluid temperature, resulting in a higher Nusselt number. However, the temperature gradient drops much faster than the denominator $(T_w - T_m)$, thus effectively reducing the Nusselt number.

Plotting average Nusselt number against Peclet number for various values of GrDa shows a general increase in average Nusselt number with increasing Peclet number, as seen in Fig. 10. A close examination of Fig. 10, however, shows that two critical Peclet numbers exist: one above which variation of GrDa does not seem to affect the average Nusselt number, and the other below which reducing Peclet number does not affect the average Nusselt number. In this particular instance at a Peclet number of about 80 and below, reducing Peclet number has no significant effect on average Nusselt number. This is the region where natural convection is the dominant mode of heat transfer. Thus, the only difference between the three curves is attributed to temperature difference. As the Peclet number increases, forced convection becomes larger and eventually increases the heat transfer coefficients; thus, above about a Peclet number of 2000, the three curves tend to get closer to each other, indicating a minimal natural convection effect. It is anticipated that a much higher Peclet numbers the three

curves will collapse into one, signifying a purely forced convection effect.

Effect of Radius Ratio on the Heat Transfer Coefficient. It is expected that the geometry will have some effect on the heat transfer due to the dependence of the Peclet and Grashof numbers on the gap between two concentric cylinders.

To determine the effect of radius ratio on heat transfer, the outer wall temperature and particle diameter were kept constant at 55°C and 0.001 m, respectively. Based on the bed length of 1.6 m, the inner radius of the bed was varied from 0.01 m to 0.12 m while the outer radius was kept constant at 0.15 m.

Figure 11 shows the plot of average Nusselt number against radius ratio R_o/R_i. The heat transfer coefficient drops quite sharply with radius ratio of less than about 3 for both Reynolds numbers. Again, the figure shows that higher Reynolds number produces higher heat transfer. It would appear therefore that the flow is essentially a boundary layer flow for $R_o/R_i > 3$. This shows that everything affecting the heat transfer in the bed happens in the region very close to the heated wall. Thus the center pipe would influence the results very little if the radius ratio is large.

Effect of Particle Diameter on the Average Nusselt Number. The next analysis was to determine the effect of particle diameter on the average heat transfer coefficient in the bed. To accomplish this, inner and outer radii were held constant at 0.01 and 0.15 m, respectively. Outer wall temperature and Reynolds number were also held constant at 55°C and 80, respectively. Particle diameter was then varied from 0.0001 to 0.002 m.

In Fig. 12 is shown the variation of average Nusselt number with GrDa number. Effectively this is a variation with Darcy number, since Gr is held constant.

Finally, it is of interest to fit a correlation to some of the data found here and to compare results from the present study to appropriate situations in previous studies. Data found here for average heat transfer coefficients for R_o/R_i equal to 15 and a variety of Da and Gr values are shown in Fig. 13. Note that the Nusselt number is defined differently for these comparisons than was done previously. When a regression curve is fitted to the present data shown in Fig. 13, an expression of the form shown below is found:

$$\frac{\mathrm{Nu}'}{(\mathrm{RePr}_e)^{1/2}} = 0.613\ (\mathrm{GrDa})^{0.131} \tag{15}$$

A correlation coefficient of 0.99 over the range $0.1 < \mathrm{GrDa}/\mathrm{Re} < 20$ results.

Also shown in Fig. 13 are experimental data reported by Clarksean et al. (1988) for conditions similar to those analyzed here. Generally good agreement is shown.

The heat transfer situation in the annulus is in the boundary layer regime for the cases reported in Fig. 13. That is, the temperature increase in the fluid due to heating by the outside wall has not penetrated to the inner wall of the annulus by the time the fluid exits the annulus. Hence, results found here for these situations can be compared approximately to the vertical flat plate mixed convection results given by Cheng (1977b). (Earlier in this paper it has been shown that over a radius ratio of 3, there is no significant effect of the radius on the heat transfer.) It must be noted that Gr in Cheng's case is equal to GrDa in this study. Figure 13 shows this comparison indicating a very good agreement between the two results.

From Fig. 13 the following subdivisions are observed:

$$\mathrm{GrDa} < 0.1 \quad \text{forced convection} \tag{16a}$$

$$0.1 < \mathrm{GrDa}/\mathrm{Re} < 10 \quad \text{mixed convection} \tag{16b}$$

$$16 < \mathrm{GrDa}/\mathrm{Re} \quad \text{free convection} \tag{16c}$$

Conclusions

Variations of the Grashof, Darcy, and Reynolds numbers and their impact on the velocities, temperatures, and heat transfer in an aided-flow constant temperature outer wall porous annulus have been investigated. Along with these the effect of the radius ratio on the heat transfer has been studied. From these investigations, the following conclusions can be drawn:

1 The axial velocities near the heated wall are enhanced by natural convection in aiding flows.

2 Increasing the Reynolds number increases the heat transfer in the bed.

3 Criteria for which mixed, forced, and natural convection are the dominant modes of heat transfer have been established.

4 Heat transfer increases with radius ratio for radius ratio less than 3. Above this ratio the increase in heat transfer with radius ratio is minimal.

5 The effect of the particle size has been found to have a profound effect on the average Nusselt number. The larger the particle diameter the higher the heat transfer in the bed for a given geometry.

6 Very good agreement was shown between the results found here and the experimental results for a similar heat transfer situation.

7 A good agreement was also obtained between the results for aiding flow over a vertical flat plate in porous media and those for in a porous annulus of radius ratio 15.

Acknowledgments

This work was partially supported by Sandia National Laboratories and the Institute for International Education. Computational assistance from the San Diego Supercomputer Center is appreciated.

References

Bodoia, J. R., and Osterle, J. F., 1961, "Finite Difference Analysis of Plane Poiseuille and Couette Flow Developments," *Applied Scientific Research*, Sec. A, Vol. 10, pp. 165–276.

Chandrasekhara, B. C., and Namboodiri, P. M. S., 1985, "Influence of Variable Permeability on Combined Free and Forced Convection About Inclined Surfaces in Porous Media," *Int. J. Heat Mass Transfer*, Vol. 28, pp. 199–206.

Cheng, P., 1977a, "Similarity Solutions for Mixed Convection From Horizontal Impermeable Surfaces in Saturated Porous Media," *Int. J. Heat Mass Transfer*, Vol. 20, pp. 893–898.

Cheng, P., 1977b, "Combined Free and Forced Convection Flow About Inclined Surfaces in Porous Media," *Int. J. Heat Mass Transfer*, Vol. 20, pp. 807–814.

Clarksean, R., Kwendakwema, N., and Boehm, R., 1988, "A Study of Mixed Convection in a Porous Medium Between Vertical Concentric Cylinders," *Proceedings of the ASME 1988 National Heat Transfer Conference*, Vol. 2, pp. 339–344.

Clarksean, R., Golightly, R., and Boehm, R., 1990, "An Experimental and Numerical Investigation of Mixed Convection in a Porous Medium Between Vertical Concentric Cylinders," *Heat Transfer 1990,* Vol. 2, pp. 477–482.

Collins, M. W., 1971, "Combined Convection in Vertical Tubes," in: *Heat and Mass Transfer by Combined Forced and Natural Convection*, I Mech E, London, pp. 17–25.

Combarnous, M. A., and Bia, P., 1971, "Combined Free and Forced Convection in Porous Media," *Society of Petroleum Engineering Journal*, Vol. 11, pp. 399–405.

Dunn, J. C., 1983, "Energy Extraction From Crustal Magma Bodies," *ASME/JSME Thermal Engineering Joint Conference Proceedings*, Vol. 2, pp. 93–100.

Haajizadeh, M., and Tien, C. L., 1984, "Combined Natural and Forced Convection in a Horizontal Porous Channel," *Int. J. Heat Mass Transfer*, Vol. 27, pp. 799–813.

Hickox, C. E., and Dunn, J. C., 1985, "Preliminary Consideration for the Extraction of Thermal Energy From Magma," presented at the International Symposium on Geothermal Energy, Kailua-Kona, HI, Aug.

Homsy, G. M., and Sherwood, A. E., 1976, "Convective Instabilities in Porous Media With Through Flow," *American Institute of Chemical Engineers Journal*, Vol. 27, pp. 168–174.

Joshi, Y., and Gebhart, B., 1985, "Mixed Convection in Porous Media Adjacent to a Vertical Uniform Heat Flux Surface," *Int. J. Heat Mass Transfer*, Vol. 28, pp. 1783–1786.

Ledebrink, F. W., 1977, "Uberlagerung von Freier und Erzwungener Konvection in Kugelschuttungen bei Kleinen Flussigkeitsdurchsatzen," Doctor-Ingenieur genehmigte Dissertation, Universitat Berlin, Germany.

Parang, M., and Keyhani, M., 1986, "Boundary Effects in Laminar Mixed Convection Through an Annular Porous Medium," presented at the AIAA/ASME 4th Thermophysics and Heat Transfer Conference, Boston, MA, June 2-4.

Patankar, S. V., 1980, *Numerical Heat Transfer and Fluid Flow*, Hemisphere Publishing, Washington, DC.

Ranganathan, P., and Viskanta, R., 1984, "Mixed Convection Boundary-Layer Flow Along a Vertical Surface in a Porous Medium," *Numerical Heat Transfer*, Vol. 7, pp. 305-317.

Sherwin, K., and Wallis, J. D., 1970, "A Theoretical Study of Combined Natural and Forced Laminar Convection for Developing Flow Down Vertical Annuli," *Proceedings Fourth International Heat Transfer Conference*, Paris-Versailles, Paper No. NC3.9.

Vanover, D., and Kulacki, F., 1987, "Experimental Study of Mixed Convection in a Horizontal Porous Annulus," presented at the 1987 ASME Winter Annual Meeting, Boston, MA.

Vortmeyer, D., and Schuster, J., 1983, "Evaluation of Steady Flow Profiles in Rectangular and Circular Packed Beds by a Variational Method," *Chem. Eng. Sci.*, Vol. 38, pp. 1691-1699.

Wooding, R. A., 1957, "Steady State Free Convection of Liquid in a Saturated Permeable Medium," *J. Fluid Mechanics*, Vol. 2, pp. 273-285.

Unsteady Thermosolutal Transport Phenomena Due to Opposed Buoyancy Forces in Shallow Enclosures

H. D. Jiang

S. Ostrach

Y. Kamotani

Department of Mechanical and Aerospace Engineering, Case Western Reserve University, Cleveland, OH 44106

Thermosolutal convection driven by opposed thermal and solutal buoyancy forces is experimentally investigated, by employing an electrochemical system in a low aspect ratio enclosure. In certain parametric ranges, it is observed that both the current and the temperature fluctuate. Criteria associated with the solutal Grashof number, and buoyancy and aspect ratios have been correlated to classify the characteristics of mass and heat transfer processes and various flow regimes, and a new length scale is suggested. The unsteady transport phenomena are found to depend on the Lewis number, Grashof number, and buoyancy and aspect ratios.

1 Introduction

The importance of understanding convective influences on transport processes in various areas of sciences and engineering applications has drawn great attention to the experimental study of thermosolutal convection in shallow enclosures with horizontal temperature and concentration gradients. The solutal and thermal buoyancy forces may be initiated in three different ways for such a study. First, both concentration and temperature differences are simultaneously imposed on the two vertical end walls. Second, the solutal system is activated until it reaches steady state and then thermal convection is added into the system. The third approach requires that the concentration gradients be created only after thermal convection in the enclosure reaches steady state. When the diffusivity ratio, Le, which is referred to as the Lewis number, differs greatly from unity, the manner in which the two buoyancy forces are initially imposed has great influence on the flow structure and the nature of the transport processes. Most of the early studies have focused on the situation in which solutally stratified fluid was heated from the sides. The resulting layered flow structures were reported by Thorpe et al. (1969) and Chen and Turner (1980) in enclosures.

Since then a great deal of attention has been given to the third approach, because it somewhat simulates the horizontal Bridgman crystal growth process. By using an electrochemical system, copper–sulfate acid solution ($H_2SO_4 + CuSO_4 + H_2O$), a series of experimental investigations has been reported (Kamotani et al., 1985; Jiang et al., 1985, 1988a, 1988b, 1988c; Wang and Chuang, 1986; Ostrach et al.,1987). In those experiments the thermal and solutal buoyancy forces were imposed in either opposing or augmenting senses. It was found that the flow field undergoes a transition from multilayer flow to secondary cell flow patterns depending on the buoyancy ratio N. In certain ranges of the aspect ratio, and thermal and solutal Grashof number, electrical potential fluctuation was reported for the opposing cases. Jiang et al. (1988c) recently suggested criteria involving a modified solutal Grashof number and the buoyancy ratio to classify the multilayer, secondary cell, and mixed flow regimes.

It has been recognized that the potential fluctuations repeatedly observed for opposing cases are directly associated with an unsteady flow in the solutal boundary layer generated by the secondary cell flow. Because these unsteady characteristics of thermosolutal flows could be important in understanding crystallographic imperfections during the growth of the crystals, detailed information on unsteady transport phenomena in the thermosolutal system and their relation with the unsteady secondary cell flow are presented herein.

2 Experimental Design and Test Procedure

For the present experimental investigation, an electrochemical system similar to the one used by Jiang et al. (1985) is employed. The test cell is a horizontal low aspect ratio rectangular enclosure consisting of four insulating plexiglass plates and two copper plates (both thermally and electrically conductive). The width is 8.2 cm and the height is variable so that a range of aspect ratios can be covered. The depth of the enclosure is relatively large (15.5 cm) to ensure that the flows are two dimensional. A sketch of the test cell with the system coordinates is presented in Fig. 1, along with the orientation of the thermal and solutal buoyancy forces. In this figure, δ_s and δ_t represent the thicknesses of the solutal and thermal boundary layers, respectively. The thermal buoyancy force opposes the solutal one in the boundary layers. The vertical copper plates with double water passages are connected to two

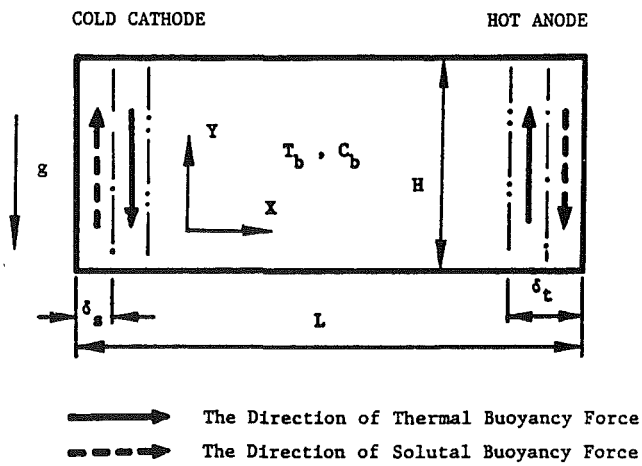

Fig. 1 Sketch of test enclosure and orientations of thermal and solutal buoyancy forces

Contributed by the Heat Transfer Division for publication in the JOURNAL OF HEAT TRANSFER. Manuscript received by the Heat Transfer Division March 9, 1989; revision received April 2, 1990. Keywords: Double Diffusion Systems, Flow Transition, Natural Convection.

constant-temperature baths (Lauda NBSHT) maintained at different temperatures (with an accuracy of $\pm 0.1^\circ$ C around the desired temperature) to generate horizontal temperature gradients. The temperature nonuniformity over the entire copper plates was measured and found to be less than ± 2 percent of the temperature difference between the hot and cold walls. Temperatures are measured by thermocouples that have accuracies of $\pm 0.1^\circ$C.

The concepts of mass transfer associated with the limiting current measurement and related techniques are reviewed by Selman and Tobias (1978). The limiting current is measured potentiostatically by a potentiostat (Princeton Applied Research 173). When current fluctuations occur, the limiting current is determined by its average value. Those values have an accuracy of 5–8 percent error. Since the total potential drop across the test section between the cathode and the anode consists not only of surface overpotentials at the electrode but also an ohmic overpotential in the bulk solution, a reference electrode is required to determine the cathodic limiting current. The details of the electrical equipment have been given by Jiang et al. (1988a). The test fluid is a copper-sulfate acid solution whose physical properties are well known (Wilke et al., 1953; Fenech and Tobias, 1960). It is carefully prepared following normal methods of chemical experiments with accuracies of ± 5 percent in H_2SO_4 and ± 2 percent in $CuSO_4$. The migration of cupric ions in the electric field is eliminated by adding sulfuric acid to the solution and thus transport of the cupric ions is controlled only by diffusion and convection. The addition of the supporting electrolyte to the solution also generates the concentration gradients of the inert ions near the electrodes, which affects the density variation. The approximation developed by Wilke et al. (1953) was used in the present study to evaluate the volumetric coefficient of solutal expansion in solutal Grashof number Gr_s. $\Delta C = 2C_b$ is used in calculating Gr_s and its justification was given elsewhere (Ostrach et al., 1987).

From a general scaling analysis (Ostrach, 1980) the following dimensionless parameters are shown to be important to the transport phenomena in shallow enclosures with horizontal temperature and concentration gradients: buoyancy ratio N, solutal Grashof number Gr_s, Schmidt number Sc, Prandtl number Pr, and geometric aspect ratio A. In a thermosolutal system, if its thermal diffusivity is very different from the solutal diffusivity, the fluid near the solid vertical boundary consists of two subregions, thermally dominant and solutally dominant regions, which are referred to as the thermal and solutal boundary layers, respectively. The ratio of thickness of these two layers is indicated by Lewis number Le. The ranges of the parameters to be covered in the present experiments are as follows: Le = 400 to 425, $-N$ = 2.8 to 102 and ∞ (pure solutal convection), A = 0.13 to 0.5, C_b = 0.05 M to 0.16 M (mole/liter), $\Delta T = 1^\circ$C to 56°C, Pr = 7, Sc = 2801 to 2977, $Gr_t = 5.7\times 10^3$ to 3.3×10^6, and $Gr_s = 1.1\times 10^5$ to 1.8×10^7.

In order to gain complete knowledge of the flow patterns and associated physical phenomena, the following is the general experimental procedure. For a fixed aspect ratio A, a particular concentration C_b of bulk solution (corresponding to the solutal Grashof number Gr_s) is chosen and the temperature difference across the entire test cell is changed from small to large, which is equivalent to changing $|N|$ from large to small. Additional bulk concentrations are run again, varying the temperature difference to effect changes in N. The effect of dendrite deposition on the cathode for the present configuration has been evaluated by Jiang et al. (1985). For this reason, the duration of each run is restricted to not more than 4 hours. Electrochemical cells are prepared in the same way as described by Jiang et al. (1988a).

3 Results and Discussion

3.1 Flow Regimes. In the present experiments, the solutal Rayleigh number Ra_s ranges from 10^8 to 10^{10} and thus near the vertical walls thin solutal boundary layers are expected. Their thicknesses are inversely proportional to the 1/4 power

Nomenclature

$A = H/L$ = aspect ratio
C_b = bulk concentration of $CuSo_4$ in working solution, g-mole/cm^3
$\Delta C = 2\,C_b$ = concentration difference between electrodes, g-mole/cm^3
D = solutal diffusivity, cm^2/s
g = gravitational acceleration, cm/s^2
$Gr_t = \beta\Delta T g H^3/\nu^2$ = thermal Grashof number
$Gr_s = \bar{\beta}\Delta C g H^3/\nu^2$ solutal Grashof number
$Gr_s^* = Gr_s/A^2$ = modified solutal Grashof number
H = height of enclosure, cm
I_L = total limiting current, mA
I_F = rms of fluctuating part of current, mA
$\hat{I}$ = current fluctuation intensity, percent
L = length of enclosure, cm
Le = Sc/Pr = α/D = Lewis number
L_R = characteristic length of suggested by experimental results, cm
$N = \bar{\beta}\Delta C/\Delta T$ = buoyancy ratio
N_C = criterion of N to distinguish mixed flow regime from secondary flow regime
N_{CL}, N_{CU} = lower and upper bounds of N to distinguish steady current region from unsteady current region
N_S = criterion of N to distinguish mixed flow regime from multilayer flow regime
Pr = ν/α = Prandtl number
$Ra_s = Sc\cdot Gr_s$ = solutal Rayleigh number
$Ra_t = Pr\cdot Gr_t$ = thermal Rayleigh number
$Sc = \nu/D$ = Schmidt number
T = temperature, °C
T_c = cold wall temperature, °C
T_h = hot wall temperature, °C
$\Delta T = T_h - T_c$ = temperature difference between electrodes, °C
X = coordinate normal to electrode surface
Y = coordinate parallel to electrode surface
α = thermal diffusivity, cm^2/s
$\bar{\beta} = \dfrac{\rho_b - \rho_i}{\rho_i}\dfrac{1}{C_b}$ = volumetric coefficient of solutal expansion, cm^3/g-mole
β = volumetric coefficient of thermal expansion, 1/°C
δ_t = thickness of vertical thermal boundary layer, cm
δ_s = thickness of vertical solutal boundary layer, cm
ν = kinematic viscosity, cm^2/s
ρ = density, g/cm^3

Superscripts

$+$ = anode
$-$ = cathode
b = bulk solution
i = electrode interface

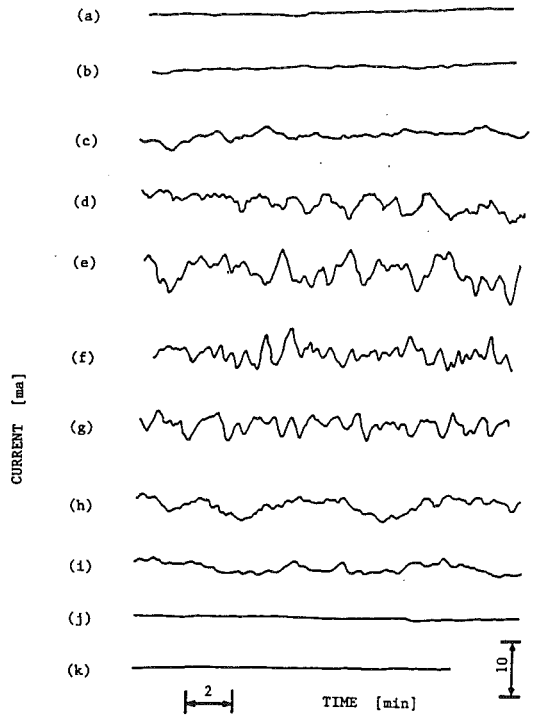

Fig. 2 Influence of buoyancy ratio N on the current variations for $A = 0.5$ and $Gr_s = 9.6 \times 10^6$ with (*a*) $N = 22.4$, (*b*) $N_{CU} = 18.4$, (*c*) $N = 15.3$, (*d*) $N = 13.1$, (*e*) $N = 10.2$, (*f*) $N = 9.2$, (*g*) $N = 8.3$, (*h*) $N = 6.0$, (*i*) $N = 5.0$, (*j*) $N_{CL} = 4.6$, (*k*) $N = 3.7$

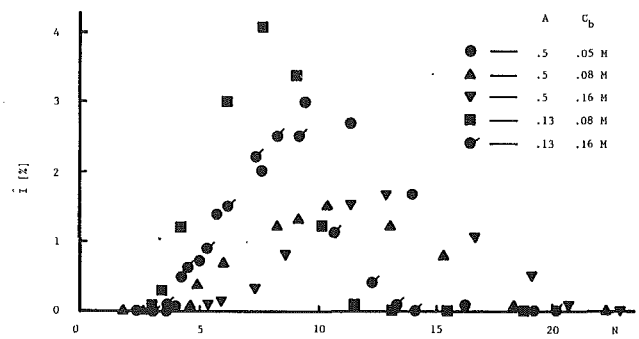

Fig. 3 Influence of buoyancy ratio N on the current fluctuation intensities $\hat{I}$

of Ra_s and are on the order of 0.1–0.2 mm. Like most aqueous electrochemical systems, the copper sulfate and sulfuric acid system used herein has a very large Le (about 400), which indicates that the thermal boundary layers, if such exist, are much larger than those of the solutal boundary layers. Since $N<0$ (opposing cases) in the present study, N represents the absolute value of N in the following discussion for simplicity. By using flow visualization techniques, both the multilayers and secondary cell flow structures were carefully observed and measured by Jiang et al. (1988c). In order to classify the flow regimes, two special values of N, N_S, and N_C were introduced. N_S represents the value for which the secondary flow cells just appear, while N_C denotes the situation in which the multilayer flow pattern just disappears. By using N_S and N_C, three flow regimes can be identified: (*i*) a multilayer flow regime with $N \geq N_S$, (*ii*) a secondary flow regime with $N \leq N_C$, and (*iii*) a mixed flow regime with $N_C < N < N_S$. The measured values of N_S and N_C were correlated respectively by the following formulae (Jiang et al., 1988c):

$$N_S = 0.39 Gr_s^{1/4} A^{-1/2} \tag{1}$$

and

$$N_C = 0.13 Gr_s^{1/4} A^{-1/2} \tag{2}$$

Shadowgraph pictures, with corresponding sketches, of the typical flow patterns in the three flow regimes have been presented by Jiang et al. (1988c).

3.2 Unsteady Mass Transfer Rate. For a constant A and Gr_s, when the thermal Grashof number Gr_t is increased, it is found that the total limiting current I_L undergoes a steady–unsteady–steady process, as demonstrated in Fig. 2, which shows the current variations with time for the various values of N. Based on the result, two particular values of N can be defined, N_{CU} and N_{CL}, so as to distinguish the steady current region from the fluctuating current region. The values of N_{CU} and N_{CL} represent the upper and lower bounds for the current transition from steady to fluctuating states, respectively. N_{CU} are represented by case (*b*) in Fig. 2 whereas N_{CL} are represented by case (*j*). For the cases with either $N \geq N_{CU}$ or $N \leq N_{CL}$, steady mass transfer rates are observed, as shown by cases (*a*), (*b*) (*j*), and (*k*) in Fig. 2. Otherwise ($N_{CU} > N > N_{CL}$), the limiting current fluctuates, as shown by cases (*c*)–(*i*). In order to quantify the fluctuation level, the average value and rms of the fluctuating current are measured.

For the purpose of comparison of the data measured under the various conditions, the following dimensionless variable, $\hat{I}$, which is referred to as "current fluctuation intensity," is defined:

$$\hat{I} = \frac{I_F}{I_L} \times 100 \text{ (percent)} \tag{4}$$

where I_L is the average total limiting current measured across the cathode and the anode, and I_F is the rms fluctuation level. Since the current is proportional to the mass transfer rate, $\hat{I}$ indicates the extent of unsteadiness of the mass transfer.

The values $\hat{I}$ measured under various conditions are plotted in Fig. 3. For each combination of A and Gr_s an $\hat{I}$–N curve is obtained. There exist two zero values of $\hat{I}$ for each curve at $N = N_{CL}$ (smaller) and $N = N_{CU}$ (larger). When N is decreased from N_{CU} to N_{CL}, the current fluctuation intensity $\hat{I}$ first increases, passes through a maximum ($\hat{I}_{max}$) and then gradually decreases. Generally, for moderately low A ($=0.5$) cases, the current fluctuations occur over wider ranges of N while $\hat{I}$ is relatively weak. For those cases with very low A ($=0.13$), the $\hat{I}$–N curves become narrower and taller. This indicates that the current fluctuations are relatively easier to be suppressed in the $A = 0.13$ cases than in the $A = 0.5$ cases, but the current fluctuation intensity, once it occurs, is stronger in the former cases than in the latter ones. The N_{CU} and N_{CL} were determined in many runs covering various A, Gr_s, and N. From these data it is found that the current fluctuations are affected not only by N but also by Gr_s and A. The N_{CU} was correlated by Jiang et al. (1988a) as follows:

$$N_{CU} = 0.25 Gr_s^{1/4} A^{-2/5} \tag{4}$$

whereas the data of N_{CL} were well fitted by the following formula:

$$N_{CL} = 0.06 Gr_s^{1/4} A^{-0.45} \tag{5}$$

From equations (1), (2), (4), and (5), it is noted that those particular values of N (N_S, N_C, N_{CU}, and N_{CL}) are all proportional to the 1/4 power of the solutal Grashof number Gr_s and inversely proportional to A^n in which n is equal to 0.5, 0.5, 0.4, and 0.45 for N_S, N_C, N_{CU}, and N_{CL}, respectively. If an average value 0.5 of n is used, the following general correlation is obtained:

$$N_i = C_i (Gr_s^*)^{1/4} \tag{6}$$

where C_i is a constant and Gr_s is a modified solutal Grashof number, defined as

$$\mathrm{Gr}_s^* = \mathrm{Gr}_s A^{-2} = \frac{\bar{\beta} g \Delta C (HL^2)}{\nu^2} \tag{7}$$

Equation (7) seems to suggest the appropriate length scale L_R for the present thermosolutal system, which can be defined as follows:

$$L_R = H^{1/3} L^{2/3} \tag{8}$$

This result indicates that two-dimensional thermosolutal convection with opposing buoyancy forces in shallow enclosures should be scaled by both the geometric length L and height H of the enclosure in any meaningful scaling analysis.

When N is either greater than N_{CU} or less than N_{CL}, a very steady current reading is recorded. For the former case, the solutal buoyancy dominates the flow field and solutal convective flow inside the inner solutal layer is steady and laminar in nature (Jiang et al., 1988c). In the latter situation, it is surprising to find that no current fluctuation is observed at all, even though a vigorous secondary cell flow exists near the vertical electrodes (Jiang et al., 1988c). This indicates that the current fluctuations can only be found when the secondary cell flow induces unsteady solutal boundary layers. In other words, unsteady flow generated by the secondary cells in the far field plays no role in the unsteady mass transfer process across the solid boundary. The effect of the unsteady solutal layer on the unsteady mass transfer process is directly attributed to the unsteady secondary cell flow generated by a thermosolutal instability (Jiang et al., 1988c).

It is interesting to note that the maximum current fluctuation occurs at a value of N very close to N_C. Jiang et al. (1988c) reported that within the secondary cell flow regime, the flow near the cold cathode consists of two portions, an upper steady and a lower unsteady region, distinguished by a stagnation line. When N is very close to N_C, the lower unsteady region covers the entire cathode surface and the whole solutal boundary layer becomes unsteady. Therefore, the fluctuation intensity $\tilde{I}$ reaches its maximum value at $N \cong N_C$. Based on this observation, the range of $N_{CU} > N > N_{CL}$ can be divided into two subregions, the region where $N_{CU} > N > N_C$ (within the mixed flow regime) and the region where $N_C \geq N > N_{CL}$ (within the secondary cell flow regime), which are classified as regions III and IV, respectively, in the later discussion. The unsteady portion of the solutal boundary layer is reduced when N is different from N_C. As a result, the current (mass flux) fluctuation diminishes and eventually disappears. It should be especially pointed out that when the lower unsteady region is reduced to about 15 percent of the electrode height, which corresponds to the cases with $N = N_{CL}$, the current fluctuation completely disappears (Jiang et al., 1988b). The observed values of N_{CL} from the present experiments are within a range of 3 to 4. This indicates that even though the solutal buoyancy is about four times stronger than the thermal buoyancy, the flow inside the major portion of the solutal boundary layer reverses its direction and becomes steady. Therefore, no variations of total average current are observed and the mass transfer process is dominated mainly by thermal convection.

Although the current fluctuates with time, the fluctuating patterns and the average amplitudes are invariant with time (Jiang et al., 1988a). Timewise variations of the local mass transfer in the turbulent regime are observed by Lloyd et al. (1972). An electrochemical system similar to the present one is used in their experiments with different cell configurations. The typical current fluctuation period and amplitude are 2 s and 0.1 mV (the shunt signal in millivolt) for vertical wall cases, and 30 s and 2 mV for inclined plate cases (45 deg to the gravitational direction). Two different current fluctuation modes are identified in Fig. 2, an "active mode" with higher frequency and lower amplitude, and a "quiescent mode" with lower frequency and higher amplitude. The typical current fluctuation periods and amplitudes are 10 to 15 s and 0.5 and 1 mA for the active modes, and 1 to 5 min and about 5 mA for the quiescent modes. Apparently, the fluctuation periods measured in the present system are much larger than that measured in the vertical wall configuration. This suggests that a shear instability does not play a dominant role in producing the unsteady thermosolutal convection observed herein.

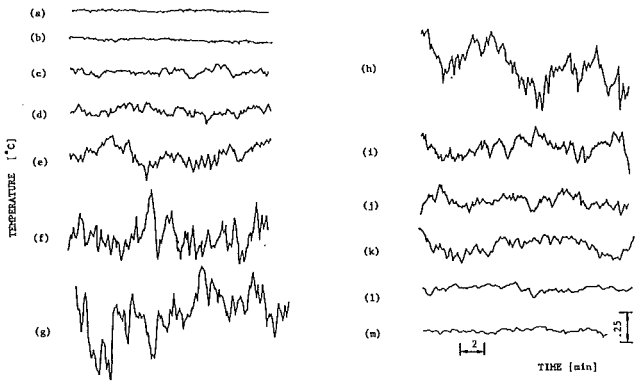

Fig 4 Influence of buoyancy ratio N on the temperature variations measured at midheight and 2 mm from the cathode surface for $A = 0.5$ with (*a*) $N = 102$, $\mathrm{Gr}_s = 1.7 \times 10^5$, (*b*) $N = 28.1$, $\mathrm{Gr}_s = 6.0 \times 10^6$; and for $A = 0.5$, $\mathrm{Gr}_s = 9.6 \times 10^6$ with (*c*) $N = 22.4$, (*d*) $N_{CU} = 18.4$, (*e*) $N = 13.1$, (*f*) $N = 11.5$, (*g*) $N_e = 10.2$, (*h*) $N = 9.2$, (*i*) $N = 8.3$, (*j*) $N = 6.0$, (*k*) $N = 5.0$, (*l*) $N_{CL} = 4.6$, (*m*) $= 3.7$

It has been reported by Kamotani et al. (1985) and Ostrach et al. (1987) that mass transfer rate is profoundly influenced by the countercurrent flow in opposing cases. The dimensionless mass transfer rate, Sherwood number Sh, first decreases as N is reduced, passes through a minimum, and then increases. The minimum current is carefully determined at the various parametric conditions and will be presented subsequently.

3.3 Unsteady Temperature Variations. In the present study, the temperature field near the end regions is measured by a thin thermocouple probe to gain further understanding of thermosolutal convection studied herein. To avoid disturbing the solutal and thermal boundary layers whose thicknesses are estimated to be on the order of 0.1 mm and 1 mm, respectively, the probe is positioned 2 mm away from the cathode surface. In a series of preliminary runs, the best vertical measuring position is determined. It is observed that for the cases within the secondary cell flow regime, the maximum amplitude of temperature fluctuations occurs in the vicinity of the midheight position of the cathode wall (Jiang et al., 1988a). Therefore, the vertical position of the measuring probe is chosen to be the midheight.

For a fixed A and Gr_s, the influence of the buoyancy ratio N upon the temperature field is shown in Fig. 4. In the multilayer flow regime ($N \geq N_S$), very steady temperature readings are recorded, as shown by cases (*a*) and (*b*). When $N_S > N \geq N_{CU}$, within the mixed flow regime, weak temperature fluctuations associated with the weak secondary cell flow are detected, represented by cases (*c*) and (*d*), while the current reading is still quite steady, as shown in cases (*a*) and (*b*) in Fig. 2. When N falls into the range of $N_{CU} > N > N_C$ (within the mixed flow regime), the secondary cell flow becomes fairly strong and, thereby, more vigorous fluctuations can be identified from cases (*e*)–(*g*), and the corresponding current fluctuations are also expected to be stronger (cases (*c*)–(*e*) in Fig. 2). At $N \cong N_C$, where the flow changes from the mixed flow regime to the secondary cell flow regime, the amplitude of the current fluctuation attains its maximum value as discussed above. Meanwhile, the temperature fluctuations also reach their maximum value when $N \cong N_C$ as shown by cases (*g*) and (*h*) in Fig. 4. When N is reduced from N_C to N_{CL}, as discussed in the last

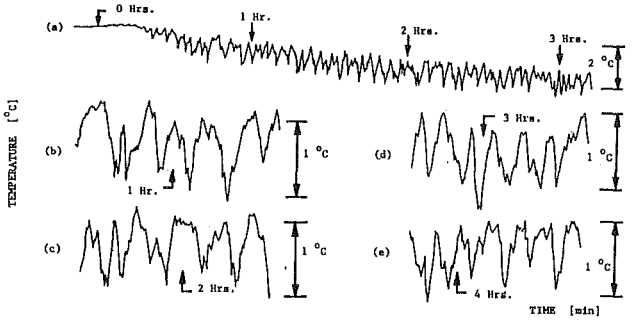

Fig. 5 Temperature fluctuations measured at midheight and 2 mm from the cathode surface, and measured at various times for $A = 0.13$, $Gr_S = 1.7 \times 10^5$, and $N = 6.1$

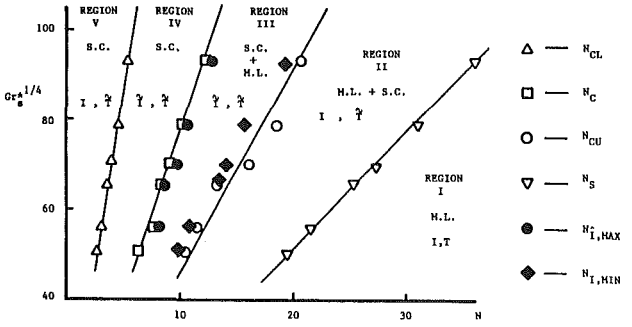

Fig. 6 Relation between the flow regimes and the fluctuations of temperature and current (including the minimum mass transfer rate I_{min} and the maximum current fluctuation intensity $\hat{I}_{max}$) in the ($Gr_s^{*1/4}$, N) plane

section, the current fluctuation intensity $\hat{I}$ falls from its maximum value $\hat{I}_{max}$ to zero, and the temperature fluctuations near the cathode wall follow a similar trend, as indicated by cases (*h*)–(*l*) in Fig. 4. However, it should be noted that when N is equal to N_{CL}, or even less than N_{CL}, the weak temperature fluctuations are still observable, as shown by cases (*l*) and (*m*), even though the current fluctuations disappear as indicated by cases (*j*) and (*k*) in Fig. 2. Such differences between the temperature and current fluctuations can be explained as follows. The current fluctuations are a boundary-layer phenomenon, which is only related to the unsteady solutal boundary layer, while the temperature fluctuations reflect the local unsteady flow field, which may occur either near the wall or elsewhere in the test cell, provided unsteady flow exists. When $N \leq N_{CL}$, the secondary flow cell is stretched and pushed away from the cathode surface, as reported by Jiang et al. (1988a). As a result, the effect of the unsteady secondary cell flow is weakened only near the surface, but it is enhanced in the far field. This indicates that inside the test enclosure, the temperature fluctuations can always be detected in the location where the unsteady secondary cell flow passes over the probe, regardless of whether the current fluctuates or not. Figure 5 shows timewise variations of temperature measured at midheight and 2 mm away from the cathode wall for the case with $A = .13$, $Gr_s = 1.7 \times 10^5$, $N = 6.1$, which is a typical run in the secondary cell flow regime. It is noticed that even though the local temperature fluctuates continuously with time, its average value stays at a constant level after about 1.5 hr, as shown by Fig. 5(*a*), whereas the average value of the fluctuating amplitude becomes constant after about 1 h, as indicated by Figs. 5(*b–e*). This reveals that the secondary cell flow is a process locally unsteady and globally steady when a global flow steady state is reached.

3.4 Flow Classification. From the discussion in the previous sections, it is obvious that thermosolutal convection in shallow enclosures is a very complex process. A summary of the transport phenomena studied here is presented next. In order to provide an overall view of the process, the information of the flow patterns reported by Jiang et al. (1988c) is also included. By using equation (6), the correlation formulae (1), (2), (4), and (5) are all plotted in Fig. 6 with two other important observed quantities, the minimum mass transfer rate (current) I_{min} and the maximum current fluctuation intensity $\hat{I}_{max}$. In this figure, I, and T represent the steady current and temperature while $\tilde{I}$ and $\tilde{T}$ indicate fluctuating current and temperature, respectively. M.L. and S.C. are the abbreviated forms of the multilayer and secondary cell flow, whereas M.L. + S.C. represents the mixed flow regime. Four solid lines represented by N_S, N_C, N_{CU}, and N_{CL} divided the flow field into three regimes with five regions. Region I ($N \geq N_S$), that is, the multilayer flow regime, has been discussed by Jiang et al. (1988c). Both T (temperature) and I (current) are steady in this region, while the convection flow near the cold cathode is laminar and bidirectional. Region II, represented by $N_S > N \geq N_{CU}$, occupies part of the mixed flow regime and was discussed by Jiang et al. (1988c). In this region, I is steady but T is not. Near the vertical end walls, the flow is steady and bidirectional while at the end region, weak secondary cell flow occurs. Region III includes the rest of the mixed flow regime ($N_{CU} > N > N_C$). Near the end walls the flow field consists of two parts: the steady region and the unsteady region; in both the flow is bidirectional. Fairly strong secondary flow cells are observed near the end walls. In this region, both T and I are fluctuating. Region IV is part of the secondary flow regime, identified by $N_C \geq N > N_{CL}$, and the related discussion can be found in Jiang et al. (1988c). Both T and I are fluctuating within that region. The flow field near the end walls consists of two parts: the steady region in which the flow is unidirectional and the unsteady region in which the flow is bidirectional. When $N \leq N_{CL}$, region V is defined. In this region very strong secondary cell flow was found. The major portion of the cathode is covered by a unidirectional steady flow. Therefore, the current is steady even though temperature fluctuations in the far field are still observed.

4 Conclusions

Criteria associated with the solutal Grashof number and aspect and buoyancy ratios have been identified to characterize the mass transfer processes (current). The current becomes unsteady in certain parametric ranges, which are generated by unsteady solutal boundary layers, while steady currents occur when the secondary cell flow is either absent and very weak or very strong. The maximum current fluctuations are obtained when the flow changes from the mixed flow regime to the secondary cell flow regime. The minimum mass transfer rates are observed right before unsteady solutal boundary layers occur. Unsteady secondary cell flow causes local temperature fluctuations near the end walls so that the heat transfer appears to be an unsteady process. Even though the solutal buoyancy is about four times stronger than the thermal buoyancy, the flow structures and the corresponding mass transfer rates are found to be mainly dominated by the thermal convection. The unsteady transport phenomena associated with the thermosolutal instability depend on the Lewis number, Grashof number, and buoyancy and aspect ratios, rather than on critical solutal and thermal Rayleigh number.

Acknowledgments

The support for this study from the National Science Foundation, under Grant No. MEA 84-01883, is gratefully acknowledged.

References

Chen, C. F., and Turner, J. S., 1980, "Crystallization in a Double-Diffusive System," *Journal of Geophysical Research*, Vol. 85, B5, pp. 2573–2593.

Fenech, E. J., and Tobias, C. W., 1960, "Mass Transfer by Free Convection at Horizontal Electrodes," *Electrochemica Acta*, Vol. 2, pp. 311–325.

Jiang, H. D., Kamotani, Y., and Ostrach, S., 1985, "Experimental Study of Natural Convective Heat and Mass Transfer in a Low Aspect Ratio Enclosure," M.S. Thesis, Case Western Reserve University, Cleveland, OH, FTAS/TR 85-178, Jan.

Jiang, H. D., Ostrach, S., and Kamotani, Y., 1988a, "Thermosolutal Convection With Opposed Buoyancy Forces in Shallow Enclosures," Ph.D. Dissertation, Case Western Reserve University, Cleveland, OH, FTAS/TR87-192, Jan.

Jiang, H. D., Ostrach, S., and Kamotani, Y., 1988b, "Thermosolutal Convection With Opposed Buoyancy Forces in Shallow Enclosures," ASME HTD-Vol. 99, pp. 53–66.

Jiang, H. D., Ostrach, S., and Kamotani, Y., 1988c, "Thermosolutal Convection Flow Regimes With Opposed Buoyancy Forces in Shallow Enclosures," *Physiochemical Hydrodynamics*, B. G. Levich Memorial Issue, Vol. 10, pp. 599–613.

Kamotani, Y., Wang, L. W., and Ostrach, S., and Jiang, H. D., 1985, "Experimental Study of Natural Convection in Shallow Enclosures With Horizontal Temperature and Concentration Gradients," *International Journal of Heat and Mass Transfer*, Vol. 28, pp. 165–173.

Lloyd, J. R., and Sparrow, E. M., and Eckert, E. R. G., 1972, "Laminar, Transition and Turbulent Natural Convection Adjacent to Inclined and Vertical Surfaces," *International Journal of Heat and Mass Transfer*, Vol. 15, pp. 457–473.

Ostrach, S., 1980, "Natural Convection With Combined Driving Forces," *PhysicoChemical Hydrodynamics*, Vol. 1, pp. 233–247.

Ostrach, S., Jiang, H. D., and Kamotani, Y., 1987, "Thermosolutal Convection in Shallow Enclosures," in: *Proceedings of the 1987 ASME/JSME Thermal Engineering Joint Conference*, Vol. 2, P. J. Marto and I. Tanasawa, eds., pp. 159–168.

Selman, J. R., and Tobias, C. W., 1978, "Limiting-Current Mass-Transfer Measurements," *Advances in Chemical Engineering*, Drew et al. eds., Vol. 10, Academic Press, New York, pp. 211–319.

Thorpe, S. A., Hutt, P. K., and Soulsby, R., 1969, "The Effect of Horizontal Gradients on Thermohaline Convection," *Journal of Fluid Mechanics*, Vol. 38, part 2, pp. 375–400.

Wang, L. W., and Chuang, P. C., 1986, "Flow Patterns of Natural Convection in Enclosures With Horizontal Temperature and Concentration Gradients," *Heat Transfer 1986*, Vol. 4, C. L. Tien, V. P. Carey, and J. K. Ferrell, eds., Hemisphere Publishing, Washington, D.C., pp. 1477–1482.

Wilke, C. R., Eisenberg, M., and Tobias, C. W., 1953, "Correlation of Limiting Currents Under Free Convection Conditions," *Journal of Electrochemical Society*, Vol. 100, pp. 513–523.

Natural Convection in Binary Gases Due to Horizontal Thermal and Solutal Gradients

J. A. Weaver

R. Viskanta

Heat Transfer Laboratory,
School of Mechanical Engineering,
Purdue University,
West Lafayette, IN 47907

The influence of augmenting and opposing thermal and solutal buoyancy forces on natural convection of binary gases due to horizontal temperature and concentration gradients is examined through comparison of smoke flow visualization and measured temperature and concentration distributions with numerical predictions. The observed flow at the cold wall was unsteady for opposing body forces. The same basic flow structure was observed, but the unsteady flow intensifies as the opposing solutal buoyancy force increases as compared to the thermal buoyancy force. Comparison of predicted and measured temperatures and concentrations is fair overall, but the steady-state analytical model fails to predict the unsteady flow and heat and mass transport for opposing body forces.

Introduction

With the growing number of technological applications involving multicomponent systems and the need for better control of such processes, natural convection due to combined thermal and solutal body forces has received increasingly more attention. In particular, the growth of crystals has spurred considerable interest (Rosenberger, 1980; Ostrach, 1983). Other applications include vapor deposition of thin films, drying processes, and building technology, although the Grashof numbers vary by several orders of magnitude between these applications. A general discussion of a wide range of buoyancy-induced transport phenomena is given by Gebhart et al. (1988).

Ostrach (1980) has reviewed the work on natural convection due to combined thermal and solutal driving forces. With both temperature and concentration gradients present to drive the flow, an increased number of transport configurations is possible with the gradients parallel or perpendicular and the body forces augmenting or opposing each other. A greater portion of the review of existing work dealt with free convection from vertical surfaces. Discussion of internal flow in enclosures concerned fluids with a large Prandtl number (liquids) and no mention was made of studies that utilized gases as the test fluid. Since the review paper by Ostrach (1980), several experimental (Kamotani et al., 1985; Lee et al., 1986, 1988; Wang and Chen, 1987; Jiang et al., 1988) and numerical (Benard et al., 1989; Han and Kuehn, 1989) investigations have been reported concerning natural convection in liquids due to thermal and solutal gradients.

The greatest portion of the more pertinent literature concerning binary gases has been analytical–numerical investigations, which examine natural convection due to horizontal temperature and concentration gradients (Greenwell et al., 1981; Jhaveri et al., 1981; Jhaveri and Rosenberger, 1982; Markham and Rosenberger, 1984; Ranganathan and Viskanta, 1986; Lai and Ramsey, 1987; Wee et al., 1989). Little experimental work has been done concerning natural convection in binary gases. Some studies related to crystal growth from the vapor have been reported (Schonherr, 1978; Chandra and Wiedemeier, 1982). In crystal growth systems, detailed measurements are difficult due to high temperature, pressures different from ambient, and corrosive environments. An investigation with application to pressure distillation has been published (Hu and El-Wakil, 1974). The system consisted of an enclosure with a fluid film flowing down the hot and cold end wall of the test cell. Temperature and concentration measurements were made with a thermocouple probe and Mach-Zehnder interferometer. Agreement between predicted and measured concentration distributions was good. The significant discrepancy between the predicted and measured temperatures was attributed to condensation of liquid on and conduction along the thermocouple probe.

There exists a lack of knowledge concerning natural convection of binary gases in cavities. In particular, there has been little experimental work. Although numerical analyses are useful, whether the analysis accurately describes the physical phenomena can only be ascertained by comparison with experimental findings. This study presents results for both augmenting and opposing body forces for natural convection due to horizontal temperature and concentration gradients, and predictions based on a mathematical model are compared with the measurements.

Experimental Methods

Consider a cavity with impermeable top, bottom (Lexan), and side (optical glass) walls where species A is introduced into and removed from the cavity at the hot and cold walls, respectively (Fig. 1). Species B is noncondensable and does not react with species A. The cold end wall is a copper heat exchanger with eight thermocouples epoxied flush with the sur-

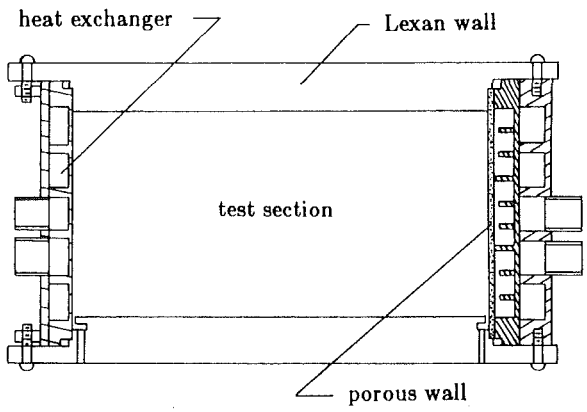

Fig. 1 Cross-sectional view of the test cell and end walls

Contributed by the Heat Transfer Division for publication in the JOURNAL OF HEAT TRANSFER. Manuscript received by the Heat Transfer Division February 2, 1990; revision received July 1, 1990. Keywords: Flow Visualization, Measurement Techniques, Natural Convection.

face of the heat exchanger introduced from the back side. The porous end wall (hot wall) is constructed as follows. Fins are machined into a block of copper and the resulting void is the reservoir in which the test fluid will reside. Soldered to the back of the copper reservoir is a brass block with channels machined into it. The brass block is used as a heat exchanger to control the temperature of the test fluid. Three separate horizontal reservoirs are used to supply liquid through a single, stainless steel porous sheet. The flow from each reservoir can be varied to achieve a nearly uniform liquid layer on the surface of the porous sheet adjacent to the test section. Thermocouples placed in each liquid reservoir from the back side are used to measure the fluid temperature which is taken to be the wall temperature. Excess liquid from the hot and cold walls is removed through the bottom connecting wall (Fig. 1).

The height and length of the cavity are each 5.5 cm for an aspect ratio of 1. The width was arbitrarily chosen to be 15 cm as a compromise between keeping the test section to a manageable size and both obtaining a sufficient number of interference fringes and insuring that the phenomenon at the midplane was as nearly two-dimensional in nature as possible.

Diagnostics. To obtain quantitative information (i.e., determine both the temperature and concentration fields) using a Mach-Zehnder interferometer, more than a single interferogram is needed, because there are two unknowns, concentration and temperature. The temperature or concentration field must be determined separately and these results can be used in conjunction with the interference fringe patterns to determine the other field (Hauf and Grigull, 1970; Goldstein, 1976; Weaver, 1989).

The temperature distribution was measured by three thermocouple probes introduced through the bottom connecting wall of the test cavity (Lexan wall) through brass Swagelok fittings. The probes are made from 1.588 mm o.d. (0.2 mm wall thickness) stainless steel tubing with a 0.5 cm right angle extension at the end (for the middle probe, the extension was aligned with the centerline of the steel tubing). Copper-constantan (Type-T) thermocouple wire of 0.076 mm diameter was threaded through the tube with the thermocouple bead epoxied 0.5 mm out from the end of the Lexan extension.

A general compensation for the temperature measurement error would be difficult due to the different flow conditions the probe realizes as it is traversed across the test cell. However, an estimate of this error was determined accounting for radiation effects and a linear variation in the gas temperature. For example, a gas temperature gradient of approximately 10 K/cm yields a 1.6 K difference between the thermocouple bead and local gas temperature.

The temperature measurements are taken at steady state. The temperature at each location was monitored until the temperature was invariant. A representative time constant is about 0.7 s, but this does not account for the conduction from the bead, which yields a larger effective time constant. Temperature fluctuations could not be resolved due to the data acquisition system and probe used. Concentrations are also average values. Density variations are averaged along the direction of the test beam and no density fluctuations could be detected with the interferometer. The sensitivity of the concentration measurements on the measured temperature and fringe shift is as follows for a methanol/helium system (run mh1). With a 25 percent difference (5 K), in measured temperature, the evaluated concentration differs by about 3.6 percent. Furthermore, a change in the measured fringe shift of 0.5 would alter the concentration by about 7.0 percent.

Flow Visualization. The flow pattern is visualized by injecting cigar smoke into the test cavity. The smoke is generated in a separate container with a small portion removed for use. Since the smoke is produced with air, some foreign gases are introduced into the cavity with the smoke. Approximately 2 percent by volume of smoke is introduced into the test cavity. The flow pattern is revealed by passing a thin plane of light through the test section and recording the pattern on photographic film. Typical exposure times were 5 to 6 s at f/5.6 with 400 ASA speed black and white film (Kodak, Tmax Professional) in a Nikon FG camera with a 35–200 zoom/macro Tokina lens. Assuming the smoke has the molecular weight of air, 2 percent by volume of smoke would decrease the buoyancy (parameter) by about 10 percent for a methanol-helium system where the mass fraction of methanol is less than 0.5 (10 percent by volume of smoke decreases the buoyancy by about 20 percent).

Procedure. Various test materials were employed. The water is once distilled and the alcohol is reagent quality, 200 proof. All of the gases were at least 99.99 percent pure. Different buoyancy parameters N^* can be achieved since the molecular weight varies approximately by a factor of ten between these gases. The mixture properties are determined using the Gibbs–Dalton law and the kinetic theory of gases at low density. The thermophysical and optical properties of all of these materials are tabulated elsewhere (Weaver, 1989).

Nomenclature

c_p = specific heat at constant pressure of binary mixture
C_{wv} = $(1-\omega_C)/(\omega_H-\omega_C)$
D_{AB} = binary mass diffusion coefficient
Gr = Grashof number = $g\beta_T(T_H-T_C)H^3/\nu_r^2$
H = test cavity height
J = dimensionless mass flux = $jH/[\rho_r D_{ABr}(\omega_H-\omega_C)]$
k = thermal conductivity of binary mixture
L = test cavity length
M = molecular weight
M^* = molecular weight ratio = M_A/M_B
N^*, N = buoyancy parameter = $(\rho_C-\rho_H)/[\rho_r\beta_T(T_H-T_C)]$ and $\beta_C(\omega_H-\omega_C)/[\beta_T(T_H-T_C)]$, respectively
P = dimensionless pressure
Pr = Prandtl number = ν_r/α_r
Sc = Schmidt number = ν_r/D_{ABr}
T = temperature
u, w = dimensionless velocity in the ξ and ζ directions, respectively; reference velocity is $(\nu_r/H)\mathrm{Gr}^{0.5}$
x, z = coordinate direction along the length and height of the test cell, respectively
α = thermal diffusivity = $k/\rho c_p$
β_C, β_T = solutal and thermal coefficient of volumetric expansion, respectively
ζ, ξ = dimensionless directions z/H and x/H, respectively; see Fig. 2
θ = dimensionless temperature = $(T-T_C)/(T_H-T_C)$
ν = kinematic viscosity of binary mixture
ρ = density of binary mixture
ϕ = normalized mass fraction = $(\omega_A-\omega_C)/(\omega_H-\omega_C)$
ω = mass fraction
ω_H, ω_C = mass fraction of species A at the hot and cold walls, respectively

Subscripts

A = species A
B = species B
C = cold wall
H = hot wall
r = reference value, evaluated at $(T_H+T_C)/2$ and/or $(\omega_H+\omega_C)/2$

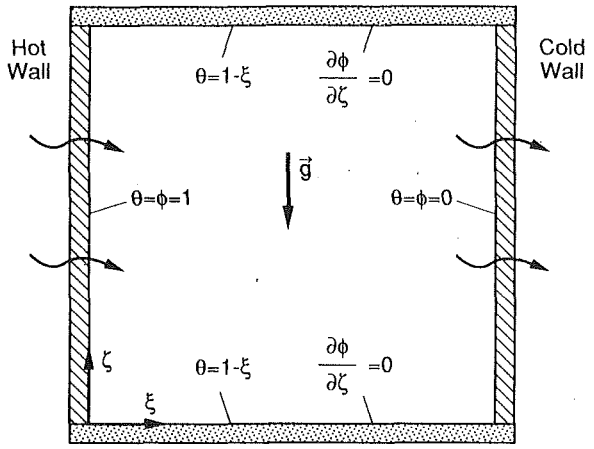

Fig. 2 Physical and mathematical model for natural convection in binary gases with horizontal temperature and solutal gradients

The test cell is assembled and covered with foam insulation. A constant temperature bath is connected to each heat exchanger to obtain the desired hot and cold wall temperatures. Before the constant temperature baths are turned on, the interferometer is adjusted to the desired initial setting. During the time allowed to reach thermal steady state (six hours), the test cavity is filled with the carrier gas (species B) by purging the cavity for one minute, allowing some time for the mixing of the new and old gases, then repeating until the test cell has been purged five times. From observation of the smoke removed while purging the test cavity, this should be sufficient to eliminate all but trace amounts of any initial gas in the cavity.

A guard heater (2.54×5.08 cm, Minco Thermofoil, Minneapolis, MN) was used to prevent condensation of species A (liquid vapor) onto the optical glass windows. The guard heater is switched on only part of the time. Visualization of the flow is performed during separate experimental runs. In this manner, the contamination from the smoke is not present during quantitative measurements. The experimental methodology is discussed elsewhere (Weaver, 1989).

Analysis

Consider a rectangular cavity with a mass flux of species A into the cavity at the hot wall (due to evaporation of a liquid) and out of the cavity at the cold wall (condensation of species A) as shown in Fig. 2. The condensation of species A on the top and bottom connecting wall and the small velocity associated with the excess liquid runoff on the hot and cold walls was neglected in the analysis. Also, the hot wall was not completely wetted (from about $\xi=0.85$ or 0.9 to 1.0) due to the position of the inlet to the top reservoir. This is also neglected in the analysis. For mathematical modeling, the system is assumed to be at steady state with no heat generation, viscous dissipation, chemical reactions, or thermal radiation. The thermophysical properties are assumed constant except in the buoyancy term (Boussinesq approximation) and conjugate effects are neglected. The conservation equations of mass, momentum, energy, and species (Bird et al., 1960) in dimensionless form are follows:

Continuity

$$\frac{\partial u}{\partial \xi}+\frac{\partial w}{\partial \zeta}=0 \tag{1}$$

ξ momentum

$$\frac{\partial}{\partial \xi}(u\,u)+\frac{\partial}{\partial \zeta}(w\,u)=-\frac{\partial P}{\partial \xi}+\frac{1}{\mathrm{Gr}^{1/2}}\left(\frac{\partial^2 u}{\partial \xi^2}+\frac{\partial^2 u}{\partial \zeta^2}\right) \tag{2}$$

ζ momentum

$$\frac{\partial}{\partial \xi}(u\,w)+\frac{\partial}{\partial \zeta}(w\,w)=-\frac{\partial P}{\partial \zeta}+\frac{1}{\mathrm{Gr}^{1/2}}\left(\frac{\partial^2 w}{\partial \xi^2}+\frac{\partial^2 w}{\partial \zeta^2}\right)+(\theta-0.5)+N(\phi-0.5) \tag{3}$$

Energy

$$\frac{\partial}{\partial \xi}(u\,\theta)+\frac{\partial}{\partial \zeta}(w\,\theta)=\frac{1}{\mathrm{PrGr}^{1/2}}\left(\frac{\partial^2 \theta}{\partial \xi^2}+\frac{\partial^2 \theta}{\partial \zeta^2}\right) \tag{4}$$

Species A

$$\frac{\partial}{\partial \xi}(u\,\phi)+\frac{\partial}{\partial \zeta}(w\,\phi)=\frac{1}{\mathrm{ScGr}^{1/2}}\left(\frac{\partial^2 \phi}{\partial \xi^2}+\frac{\partial^2 \phi}{\partial \zeta^2}\right) \tag{5}$$

The top and bottom connecting walls are not included in the analysis (conjugate effects) as a first approximation. A linear temperature distribution (perfectly conducting walls) is arbitrarily imposed as the boundary condition at the top and bottom of the cavity. This is a better approximation for the conjugate effect of the top and bottom walls as compared to an adiabatic boundary condition for a Lexan wall and most of the gases examined in this work. Hence, the dimensionless boundary conditions for temperature are

$$\theta(0,\zeta)=1,\quad \theta(A_\xi,\zeta)=0 \tag{6}$$

$$\theta=1-\xi \quad \text{at } \zeta=0 \text{ and } 1 \tag{7}$$

The dimensionless boundary conditions for species A are

$$\phi(0,\zeta)=1,\quad \phi(A_\xi,\zeta)=0 \tag{8}$$

$$\frac{\partial \phi}{\partial \zeta}=0 \quad \text{at } \zeta=0 \text{ and } 1 \tag{9}$$

The vertical hot and cold walls are assumed isothermal and the saturation concentration is determined using T_H and T_C.

The velocity boundary conditions at the impermeable walls are written in terms of dimensionless variables as

$$w(0,\zeta)=w(A_\xi,\zeta)=u(\xi,0)=w(\xi,0)=u(\xi,1)=w(\xi,1)=0 \tag{10}$$

At the end walls where mass transfer occurs, the dimensionless boundary conditions for the normal velocity component are:

$$u(0,\zeta)=\frac{1}{(C_{wv}-1)}\frac{1}{\mathrm{ScGr}^{1/2}}J_{A\xi}\bigg|_{\xi=0} \tag{11}$$

$$u(A_\xi,\zeta)=\frac{1}{C_{wv}}\frac{1}{\mathrm{ScGr}^{1/2}}J_{A\xi}\bigg|_{\xi=A_\xi} \tag{12}$$

which are not known a priori.

The value of N used to obtain the numerical simulations was taken as N^*-1. The buoyancy parameter N^* is derived from nondimensionalizing the z-momentum equation and not making the Boussinesq approximation (Weaver, 1989). Taking the average of the buoyancy force at the hot and cold walls using N^* yields $N=N^*-1$. This value (N^*-1) is taken as a better approximation to the buoyancy force. At small values of N (N^*), there is little difference between N and N^*-1. At larger values of N (N^*), there is a significant difference.

The governing conservation equations and associated boundary conditions are solved using the SIMPLER algorithm (Patankar, 1980). A nonuniform grid was employed for the finite-difference mesh. The nodes are packed at the walls. The solution is taken to be converged when overall energy and mass balances at walls that depend on unknown concentration and temperature gradients are achieved, and the dependent field variables do not change between consecutive iterations.

To gain confidence in the methodology, the computer program was used to solve for single-component natural convection in a square cavity. Agreement between a benchmark solution (de Vahl Davis, 1983) and the values predicted from

Table 1 Experiments performed involving horizontal temperature and solutal gradients

Run	Species A	Species B	T_H (°C)	T_C (°C)	ω_H	ω_C	N	N^*	Gr	Pr	Sc	M^*	C_{wv}
wa5	Water	Argon	44.8	24.9	0.045	0.014	0.55	1.56	5.91×10^5	0.85	0.50	0.45	32.4
wa6	Water	Argon	44.6	24.8	0.044	0.014	0.55	1.55	5.88×10^5	0.85	0.50	0.45	32.9
en11	Ethanol	Nitrogen	49.8	35.2	0.40	0.21	−1.85	−0.86	9.27×10^5	0.79	0.65	1.65	4.10
en12	Ethanol	Nitrogen	49.8	35.2	0.40	0.21	−1.85	−0.86	9.27×10^5	0.79	0.65	1.65	4.10
en13	Ethanol	Nitrogen	49.8	35.0	0.40	0.21	−1.85	−0.85	9.31×10^5	0.79	0.65	1.65	4.09
mh1	Methanol	Helium	20.1	0.3	0.54	0.25	−5.56	−4.74	4.00×10^4	0.52	1.06	8.01	2.56
mh2	Methanol	Helium	20.1	0.4	0.54	0.26	−5.57	−4.75	3.97×10^4	0.52	1.06	8.01	2.59
mh3	Methanol	Helium	44.5	25.2	0.86	0.62	−9.42	−9.23	1.87×10^5	0.44	0.40	8.01	1.60

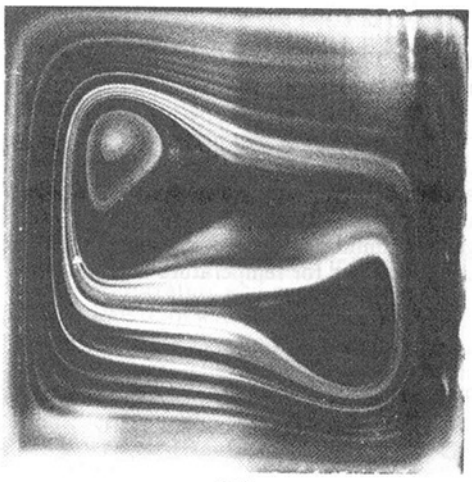

(a)

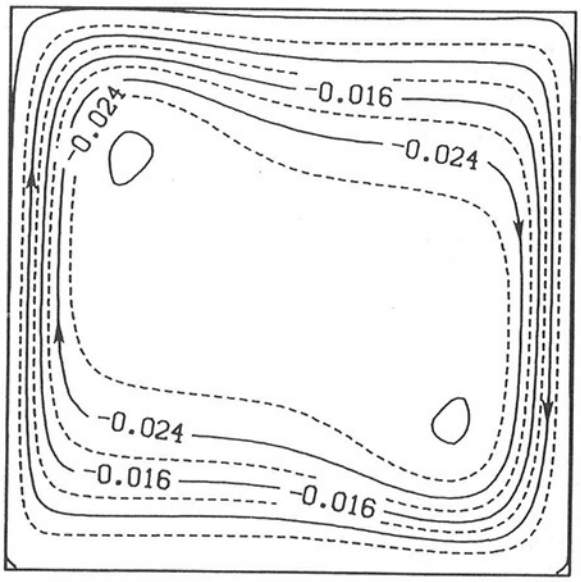

(b)

Fig. 3 Comparison of: (*a*) smoke flow visualization (run wa6: $Gr = 5.88\times10^5$, $N^* = 1.55$) and (*b*) predicted streamlines (run wa5: $Gr = 5.91\times10^5$, $N^* = 1.55$) for augmenting buoyancy forces

the program used in this work for u_{max}, w_{max}, $\overline{Nu}_H$, and $Nu_{H,max}$ is within 3 percent for a Rayleigh number of 1×10^4, 1×10^5, and 1×10^6. In addition, the grid independence of the results using a finite-difference method is of concern. The w velocity, temperature, and concentration distributions at $\zeta = 0.5$ were compared for natural convection in a binary gas using grids of 35×35, 45×45, and 55×55 nodes. There is little difference in any of the dependent variable distributions. The 55×55 node grid was used in this study, because the large number of nodes yield a better estimate of the dependent variable gradients, which helps convergence. Further details can be found elsewhere (Weaver, 1989).

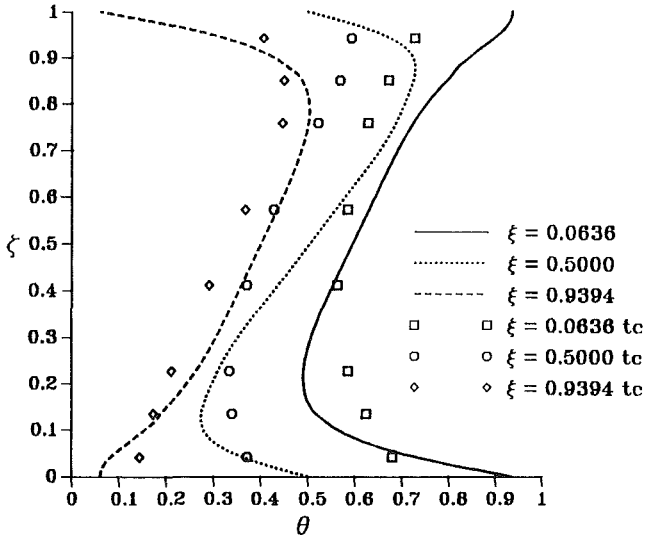

Fig. 4 Comparisons of the measured and predicted temperatures for augmenting buoyancy forces (run wa5: $Gr = 5.91\times10^5$, $N^* = 1.55$)

Results and Discussion

Table 1 lists the experiments performed and the corresponding dimensionless parameters. The designation for the experimental runs signifies species A by the first letter, species B by the second letter (*a, e, h, m, n,* and *w* are argon, ethanol, helium, methanol, nitrogen, and water, respectively), and the number is used to denote the different experiments for the same binary gas combinations.

Augmenting Flow. For water vapor (species A) and argon (species B) as the binary gas in case wa5, the solutal buoyancy force augments the thermal buoyancy force. The flow visualization (case wa6) is compared with predicted streamlines (case wa5) in Fig. 3. No separate numerical simulation was made for run wa6, since the experimental conditions were very close to those of run wa5. Since the mass flux at the wall is small for the water vapor/argon system in this case [large value of C_{WV}, equation (11)], the smoke flow pattern and predicted streamlines are in good agreement, and are very similar to that for natural convection in a single component gas (de Vahl Davis, 1983). As the mass flux at the wall increases, the influx (blowing) at the hot wall and outflux (suction) at the cold wall result in a decrease and increase, respectively, of the velocity, temperature, and concentration gradients.

A comparison between the measured and predicted temperature distributions is given in Fig. 4. Some discrepancy exists at $\zeta = 0.5$ and 0.9394. The temperature data were taken 45 minutes after the liquid was introduced into the cavity. This is ample time for the transient due to introduction of species A into the test cell to dissipate. Since the binary and single

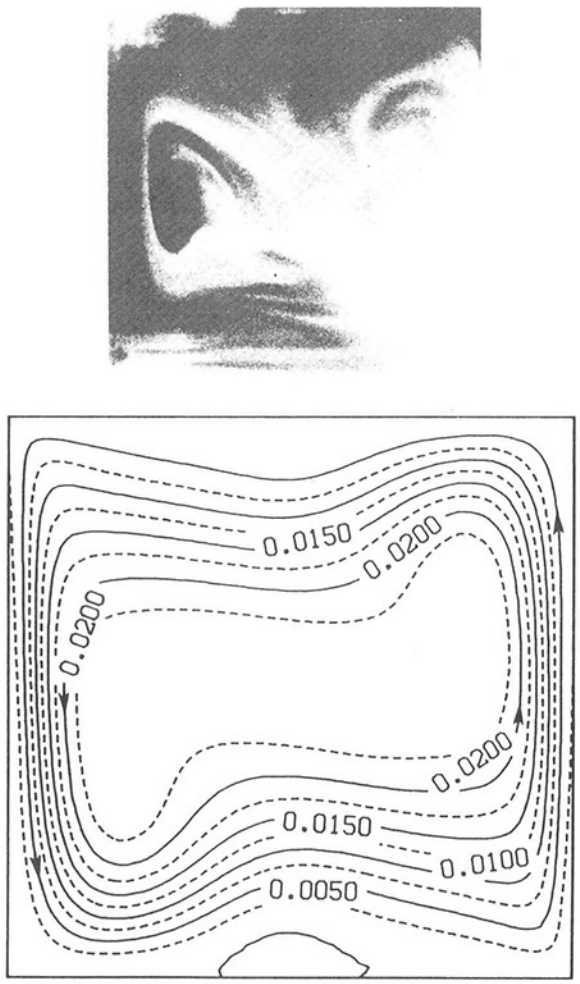

Fig. 5 Comparison of: (*a*) smoke flow visualization (run en13: $Gr = 9.31 \times 10^5$, $N^* = -0.85$) and (*b*) predicted streamlines (run en11: $Gr = 9.27 \times 10^5$, $N^* = -0.86$) for opposing buoyancy forces

component flow fields are very similar, the transient time between the two flow fields is relatively short. Only a small part of the discrepancy is attributed to the measurement error associated with the thermocouple probe (Weaver, 1989). In addition, the error at the hot wall ($\xi = 0.0636$) is attributed, in part, to the orientation between the flow field and thermocouple probe. The flow at the thermocouple bead is perturbed from passing around the shaft of the probe where the probe enters the cavity at the bottom wall. A similar trend is observed at $\xi = 0.9394$ (cold wall) when the probes enter the cavity through the top wall. These trends lend some credence to the proposed cause. Furthermore, some discrepancy is due to the heat input from the guard heater on the optical glass end walls. No concentration measurements could be made with the interferometer, because of the characteristics of an argon and water vapor system.

Opposing Flow

Ethanol–Nitrogen ($N^* = -0.856$). With $N^* < 0$, the solutal buoyancy force is dominant and opposes the thermal buoyancy force. Thus, the flow is down the hot wall and up the cold wall (Fig. 5). Interestingly, two small recirculation cells are predicted at $\xi = 0.5$ on the top and bottom connecting walls (Fig. 5*b*). These recirculation cells are attributed to the buoyancy force and are discussed elsewhere (Weaver, 1989). For the other two experiments to be discussed, recirculation cells at the top and bottom walls are not predicted.

The smoke flow visualization (run en13, Fig. 5*a*) exhibits a

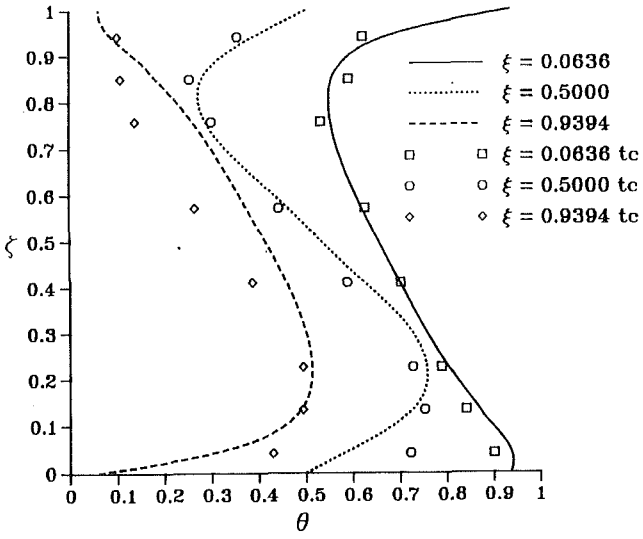

Fig. 6 Comparisons of the measured and predicted temperatures for opposing buoyancy forces (run en11: $Gr = 9.27 \times 10^5$, $N^* = -0.86$)

region near the cold wall where no streamlines are evident. This is due to the flow being unsteady near the cold wall. Photographs of smoke flow patterns (run en12) taken in succession revealed unsteady flow (Weaver, 1989). To record this unsteady flow, the photographs were taken with 3200 ASA black and white film (Kodak Tmax Professional) to reduce the exposure time (about 1 s). Fluid at the top of the cold wall breaking away from the main circulation cell and moving down is entrained by the flow up the cold wall and results in laminar mixing. A faster lens (Nikon 85 mm, f/2) was used during run en13, but the pictures obtained did not illustrate the flow at the cold wall as well as those from run en12 (attributed to the amount of smoke used). This unsteady flow cannot be predicted by the present steady-state mathematical model. Experiments in a binary liquid system ($Pr = 7$, $Sc = 2100$) due to horizontal temperature and concentration gradients (Kamotani et al., 1985; Wang and Chen, 1987; Jiang et al., 1988) exhibit an unsteady flow at the hot and cold vertical walls of a shallow enclosure under certain conditions. The thickness of the thermal and solutal boundary layers for a liquid system is quite different from that for a system of binary gases, but the observation of an unsteady flow in the liquid system is supportive of the present work.

Unstable flows in binary systems are discussed briefly by Gebhart et al. (1988). Opposing or aiding buoyancy forces and different thicknesses for the temperature and species boundary layers are cited as factors influencing the disturbances of external natural convection flows in binary systems. Furthermore, the suction or blowing at the wall present in this problem is relevant. From the limited results presented, an augmenting buoyancy force stabilizes the flow and an opposing buoyancy force destabilizes the flow when the species boundary layer is both thinner and thicker than the thermal boundary layer. However, they did not report any experiments for comparison and an explanation was not given.

A quantitative comparison of the measured and predicted temperature distributions is illustrated in Fig. 6. No concentration distribution measurements were possible, because the condensation of ethanol on the inside of the optical windows could not be eliminated. Good agreement exists between the predicted and measured temperatures, except between $\zeta = 0.4$ to 0.8 at $\xi = 0.9394$ (cold wall). This is attributed to the unsteady flow, which transports cold fluid from the top of the cold wall down adjacent to the flow that is up along the cold wall. The temperature data were taken about one hour after species A was introduced into the cavity and without using the

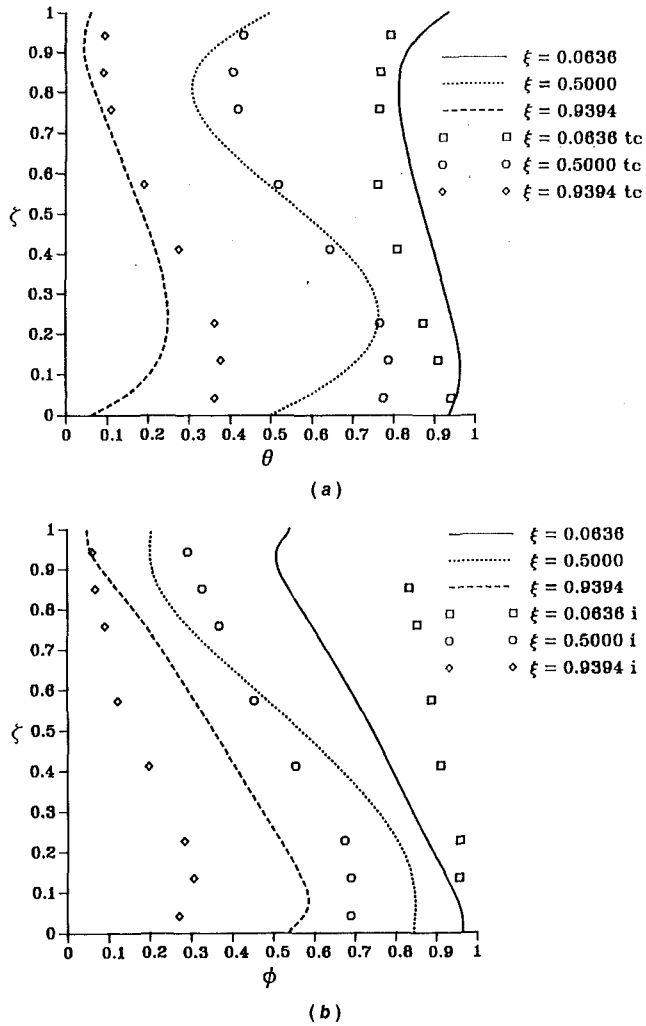

Fig. 7 Comparisons of the measured and predicted temperatures (*a*) and concentrations (*b*) for opposing buoyancy forces (run mh1: $Gr = 4 \times 10^4$, $N^* = -4.74$)

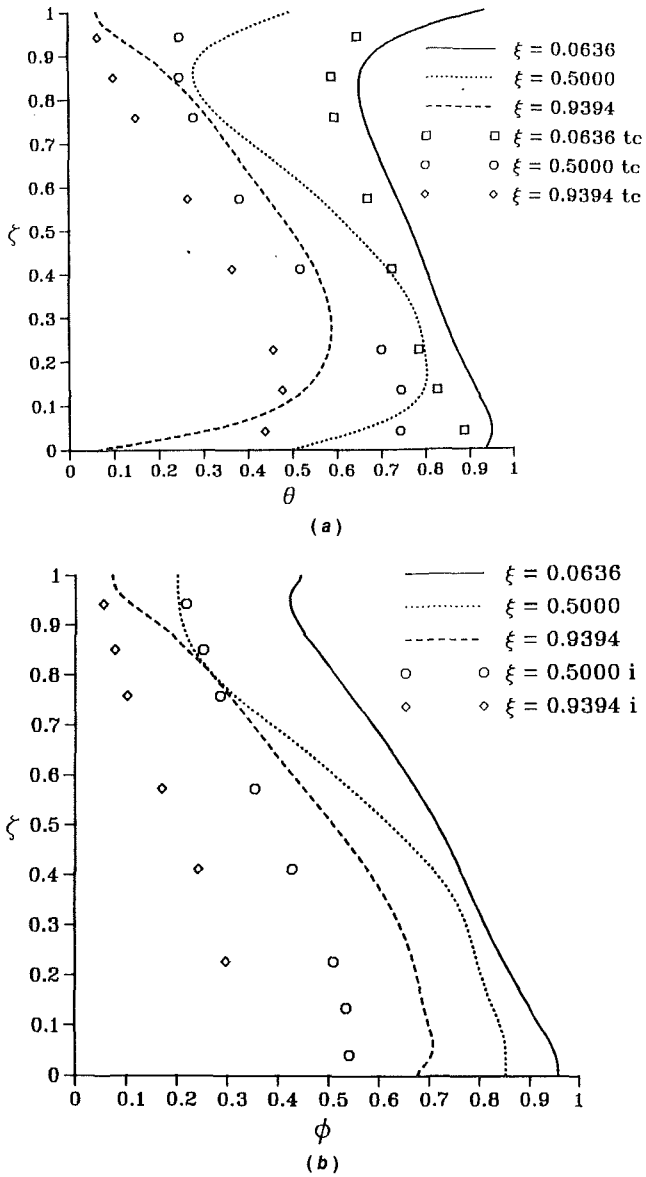

Fig. 8 Comparisons of the measured and predicted temperatures (*a*) and concentrations (*b*) for opposing buoyancy forces (run mh3: $Gr = 1.87 \times 10^5$, $N^* = -9.23$)

guard heaters to eliminate condensation from the optical windows. Part of the discrepancy between data and predictions at the connecting walls is attributed to conjugate effects (Weaver, 1989; Kim and Viskanta, 1984).

Methanol-Helium ($N^* = -4.739$ *and* -9.230). No successful pictures of the smoke flow patterns were obtained for run mh2. Unsteady flow similar to that observed in run en12 was also present in run mh2, but with more intense mixing. With the stronger circulation, the unsteadiness at the cold wall occurred over a shorter time, resulting in photographs with no clear definition.

A comparison of the measured and predicted temperature and concentration distributions are given in Fig. 7. The measured temperature distributions in Fig. 7(*a*) illustrate the effect of the mass flux at the vertical walls on the temperature field. The temperature gradient normal to the cold wall (due to the suction effect of the mass outflux) is considerably larger than that at the hot wall (due to the blowing effect of the mass influx). A similar trend is noted in the measured concentration distributions (Fig. 7*b*). This trend is not as noticeable in Fig. 6 ($N^* = -0.856$), because the mass flux at the vertical walls is smaller. The measured and predicted temperature gradients at $\zeta = 0$ and 1 do not compare well because the walls are not perfectly conducting as assumed in the analysis. Since concentration measurements depend on the temperature measurements, it would be expected that the comparison between predictions and data for the concentration field would be similar to the temperature field. However, fair agreement between the predicted and measured data is seen for the temperature field, but the predicted concentration distributions compare poorly with the measured concentration data. Although the general trends are similar, the concentration gradients normal to the hot and cold wall are overpredicted. The concentration field is more linear (as shown by both predictions and measurements) than the temperature field (Figs. 7 and 8). Some error is present because the interferometer averages along the direction of the test beam and due to the limited number of fringes. However, an additional error is due to the isothermal optical windows. For example at the cold wall, the glass plate contracts, which results in a negative fringe shift from the initial condition. The fringe shift due to the binary gas (using the cold wall as the reference) is positive in this case. Therefore, the concentration determined is less than the actual value. Also, part of the discrepancy is attributed to the unsteady flow in the cavity. The guard heater was not used during the temperature measurements, and the data were taken about one hour after species A was introduced into the cavity.

With an increase in the solutal body force, the unsteady flow observed at the cold wall is intensified, but with the same basic

flow structure as shown for run en12. Due to the higher velocity of the fluid motion, no good quality photographs could be taken. The unsteady flow transports cold fluid from the top of the cold wall down adjacent to the upward moving fluid. This results in the cooler temperatures as compared to predictions (Fig. 8*a*). Concentration data at the hot wall and near the bottom of the cold wall could not be obtained due to condensation of methanol on the inside of the optical windows that could not be eliminated. There is considerable discrepancy between the measurements and predictions at $\xi = 0.5$ and 0.9394 (centerline and cold wall) for the concentration field (Fig. 8*b*). The increase in the buoyancy parameter results in enhanced circulation and heat and mass fluxes at the hot and cold walls.

When viewing the comparisons between data and predictions, one should be careful not to attribute greater accuracy to either the experimental data or numerical predictions over the other. Errors and approximations exist with both. The intent is to report two-dimensional spatial measurements of the temperature and concentration fields and the comparison with a respective analytical model.

Conclusions

For aiding flow ($N^* > 0$), the predicted streamlines and flow visualization results compare well. Because the flow is unsteady for opposing flow ($N^* < 0$), agreement between predicted streamlines (obtained from a mathematical model that assumes steady flow) and the smoke flow patterns is poor. The comparison between predicted and measured temperatures for $N^* = -0.856$ is quite good except at the upper portion of the cold wall ($\xi = 0.9394$), which is attributed to the unsteady flow. As $|N^*|$ increases (larger negative values), the unsteady flow becomes more intense, and the agreement between predicted and measured temperature distributions deteriorates. The normal concentration gradient at the vertical walls is overpredicted, whereas for the temperature field, the gradient normal to the vertical walls compares more favorably (in particular at the hot wall).

Further experiments using improved diagnostics to make simultaneous concentration, temperature, and velocity measurements are needed. The steady-state mathematical model cannot predict the temperature and concentration fields due to an unsteady flow. Furthermore, understanding of the conjugate, three-dimensional, variable thermophysical property, species interdiffusion, Soret and Dufour effects on the natural convection transport phenomena in binary gases is incomplete (Weaver, 1989; Bergman and Srinivasan, 1989).

Acknowledgments

One author (J. A. W.) is grateful for the financial support provided by a NASA Graduate Researchers Fellowship under Grant No. NGT-50207. In addition, the authors would like to thank Professor S. Ramadhyani for providing the numerical algorithm and the many helpful discussions. Computational facilities were provided by the Purdue University Computing Center.

References

Benard, C., Gobin, D., and Thevenin, J., 1989, "Thermosolutal Natural Convection in a Rectangular Enclosure: Numerical Results," *Heat Transfer in Convective Flows,* ASME HTD-Vol. 107, pp. 249–254.

Bergman, T. L., and Srinivasan, R., 1989, "Numerical Simulation of Soret-Induced Double Diffusion in an Initially Uniform Concentration Binary Liquid," *International Journal of Heat and Mass Transfer,* Vol. 32, pp. 679–687.

Bird, R. B., Stewart, W. E., and Lightfoot, E. N., 1960, *Transport Phenomena,* Wiley, New York.

Chandra, D., and Wiedemeier, H., 1982, "Chemical Vapor Transport and Thermal Behavior of the GeSe–GeI_4 System for Different Inclinations With Respect to the Gravity Vector; Comparison With Theoretical and Microgravity Data," *Journal of Crystal Growth,* Vol. 57, pp. 159–176.

de Vahl Davis, G., 1983, "Natural Convection of Air in a Square Cavity: A Bench Mark Numerical Solution," *International Journal for Numerical Methods in Fluids,* Vol. 3, pp. 249–264.

Gebhart, B., Jaluria, Y., Mahajan, R. L., and Sammakia, B., 1988, *Buoyancy-Induced Flow and Transport,* Hemisphere, New York.

Goldstein, R. J., 1976, "Optical Measurement of Temperature," *Measurements in Heat Transfer,* E. R. G. Eckert and R. J. Goldstein, eds., Hemisphere Publishing, Washington, DC, pp. 241–294.

Greenwell, D. W., Markham, B. L., and Rosenberger, F., 1981, "Numerical Modeling of Diffusive Physical Vapor Transport in Cylindrical Ampoules," *Journal of Crystal Growth,* Vol. 51, pp. 413–425.

Hauf, W., and Grigull, U., 1970, "Optical Methods in Heat Transfer," *Advances in Heat Transfer,* J. P. Hartnett and T. F. Irvine, eds., Academic Press, New York, Vol. 6, pp. 134–366.

Han, H., and Kuehn, T. H., 1989, "A Numerical Simulation of Double Diffusive Natural Convection in a Vertical Rectangular Enclosure," *Heat Transfer in Convective Flows,* ASME HTD-Vol. 107, pp. 149–154.

Hu, C. Y., and El-Wakil, M. M., 1974, "Simultaneous Heat and Mass Transfer in a Rectangular Cavity," *Proceedings of the Fifth International Heat Transfer Conference,* Vol. 5, pp. 24–28.

Jhaveri, B. S., Markham, B. L., and Rosenberger, F., 1981, "On Singular Boundary Conditions in Mass Transfer Across Rectangular Enclosures," *Chemical Engineering Communications,* Vol. 13, pp. 65–75.

Jhaveri, B. S., and Rosenberger, F., 1982, "Expansive Convection in Vapor Transport Across Horizontal Rectangular Enclosures," *Journal of Crystal Growth,* Vol. 57, pp. 57–64.

Jiang, H. D., Ostrach, S., and Kamotani, Y., 1988, "Thermosolutal Convection With Opposed Buoyancy Forces in Shallow Enclosures," *Natural Convection in Enclosures—1988,* R. S. Figliola and P. G. Simpkins, eds., ASME HTD-Vol. 99, pp. 53–66.

Kamotani, Y., Wang, L. W., Ostrach, S., and Jiang, H. D., 1985, "Experimental Study of Natural Convection in Shallow Enclosures With Horizontal Temperature and Concentration Gradients," *International Journal of Heat and Mass Transfer,* Vol. 28, pp. 165–173.

Kim, D. M., and Viskanta, R., 1984, "Study of the Effects of Wall Conductance on Natural Convection in Differently Oriented Square Cavities," *Journal of Fluid Mechanics,* Vol. 144, pp. 153–176.

Lai, W. T., and Ramsey, J. W., 1987, "Natural Heat and Mass Transfer in a Rectangular Enclosure," *Natural Circulation,* J. H. Kim and Y. H. Hassan, eds., ASME HTD-Vol. 92, pp. 361–372.

Lee, J., Hyun, M. T., and Kim, K. W., 1988, "Natural Convection in Confined Fluids With Combined Horizontal Temperature and Concentration Gradients," *International Journal of Heat and Mass Transfer,* Vol. 31, pp. 1969–1977.

Lee, J., Kim, G. W., and Hyun, M. T., 1986, "Natural Convection in Confined Fluids With Combined Driving Forces," *Proceedings of the Korea–USA Heat Transfer Seminar,* Seoul, Korea, Oct. 16–22, pp. 500–519.

Markham, B. L., and Rosenberger, F., 1984, "Diffusive-Convective Vapor Transport Across Horizontal and Inclined Rectangular Enclosures," *Journal of Crystal Growth,* Vol. 67, pp. 241–254.

Ostrach, S., 1980, "Natural Convection With Combined Driving Forces," *PhysicoChemical Hydrodynamics,* Vol. 1, pp. 233–247.

Ostrach, S., 1983, "Fluids Mechanics in Crystal Growth—The 1982 Freeman Scholar Lecture," ASME *Journal of Fluids Engineering,* Vol. 105, pp. 5–20.

Patankar, S. V., 1980, *Numerical Heat Transfer and Fluid Flow,* Hemisphere Publishing Corporation, Washington, DC.

Ranganathan, P., and Viskanta, R., 1988, "Natural Convection in a Square Cavity Due to Combined Driving Forces," *Numerical Heat Transfer,* Vol. 14, pp. 35–59.

Rosenberger, F., 1980, "Fluid Dynamics in Crystal Growth From Vapors," *PhysicoChemical Hydrodynamics,* Vol. 1, pp. 3–26.

Schonherr, E., 1978, "Measurements of Growth Parameters During the Crystal Growth From the Vapor in Closed Ampoules," *Journal of Crystal Growth,* Vol. 44, pp. 604–608.

Wang, L. W., and Chen, J. J., 1987, "Flow Patterns of Thermosolutal Convection in Low Aspect Ratio Enclosures," *Experimental Heat Transfer,* Vol. 1, pp. 197–204.

Weaver, J. A., 1989, "Natural Convection in Binary Gases With Simultaneous Heat and Mass Transfer Across a Cavity," PhD Thesis, Purdue University, West Lafayette, IN.

Wee, H. K., Keey, R. B., and Cunningham, M. J., 1989, "Heat and Moisture Transfer by Natural Convection in a Rectangular Cavity," *International Journal of Heat and Mass Transfer,* Vol. 32, pp. 1765–1778.

Transient Double Diffusion in a Fluid Layer Extending Over a Permeable Substrate

M. Kazmierczak
Department of Mechanical, Industrial, and Nuclear Engineering, University of Cincinnati, Cincinnati, OH 45221-0072

D. Poulikakos
Department of Mechanical Engineering, University of Illinois at Chicago, Chicago, IL 60680

The problem of transient double diffusion in a composite layer is studied numerically. The composite layer consists of a fluid region extending over a fluid-saturated permeable substrate. Initially, the fluid in the system is motionless, isothermal, and stably stratified with a linear salt distribution. A constant uniform heat flux is then suddenly applied to the bottom wall of the system. The resulting coupled flow, temperature, and concentration fields as they evolve in time are obtained numerically. The flow in the fluid region was determined by solving the complete form of the two-dimensional laminar governing equations subjected to the usual Boussinesq approximations. The flow in the porous region was modeled using the general flow model, which includes both the effects of macroscopic shear (Brinkman effect) and flow inertia (Forchheimer effect). Interesting results were obtained and are presented in a systematic manner so as to document the effect of changing the important system parameters, which include the height of the permeable substrate, its permeability, and the ratio of the thermal to the solutal Rayleigh number. It was found that these parameters had a major impact on the system behavior and their effects are thoroughly discussed.

Introduction

This paper investigates transient double diffusion in a composite layer. The system consists of a horizontal fluid layer overlaying a permeable substrate. The system initially is stably stratified by a linear species concentration distribution and is heated from below. The buoyancy forces that arise from the opposing temperature and concentration gradients may induce double diffusive motion.

The aim of this study is to determine the impact that the porous substrate has on the double diffusion phenomenon in the composite system. Clearly, the two limiting bounds of the composite system are the single fluid layer, which is obtained when the thickness of the porous substrate diminishes, and the fully porous layer that corresponds to the case when the permeable substrate completely fills the system.

With regard to the first extreme (double diffusion in classical fluids), there exists a significant body of literature in terms of stability analyses (Baines and Gill, 1969; Nield, 1967) experimental investigations (Turner, 1968; Poplawsky et al., 1981; Lewis et al., 1982), one-dimensional modeling (Bergman et al., 1982, 1985), and more recently two-dimensional finite difference numerical simulations (Ungan and Bergman, 1987; Kazmierczak and Poulikakos, 1990). The effect of nonuniform bottom heating was also examined in two timely studies (Bergman and Ungan, 1986; Neilson and Incropera, 1987).

The number of studies published pertaining to the study of the second kind of system (double diffusion in fluid-saturated porous medium) is much lower. Early workers (Nield, 1968; Rubin, 1973) performed linear stability analyses to study the onset of thermohaline convection in a horizontal porous layer. The results published in these last two cited references were based on the Darcy flow model; hence, they are relevant to well-packed, low-permeability porous media. More recently, Poulikakos (1986) studied the stability of the flow in a sparsely packed porous medium (modeled using the Brinkman-extended momentum equations) for a porous layer containing linear opposing gradients of heat and salt having stress-free horizontal boundaries held at a fixed temperature and concentration. His results showed that five parameters (Ra, Ra_s, Le, Pr, Da) are now required to describe the stability boundaries completely.

An experimental study on the effect of a stable salinity gradient on the onset of convection in a porous layer heated from below was reported by Chen and Murray (1985). In their experiments, the onset of convection was detected by a heat flux sensor and by the temperature distribution in the porous medium. The onset was marked by a dramatic increase in the slope of the heat flux curve. Approximately three hours after the onset of convection, the flow pattern consisted of three-dimensional cells filling the entire enclosure. No diffusive layering, as is common in the corresponding fluid layer system, was reported above the critical ΔT.

Double diffusion convection in systems containing both a fluid and a porous region is more complex than either limiting case previously discussed and is the focus of this present investigation. To the best of the authors' knowledge, the only available published research on double diffusion in composite systems is the work of Chen and Chen (1988) and Kazmierczak and Poulikakos (1989).

Chen and Chen (1988) investigated the problem of the onset of salt finger convection in a porous layer of constant porosity underlying a fluid, using linear stability analysis. In this study of salt finger convection, the temperature gradient was stabilizing and the salt gradient was destabilizing. The results showed that for a fixed thermal Rayleigh number there exists a critical depth ratio $\hat{d}$ (the ratio of the fluid layer depth to the porous layer depth), below which the critical porous salinity Rayleigh number decreases with increasing $\hat{d}$ and above which the critical porous salinity Rayleigh number increases with increasing $\hat{d}$. This fact they explained in terms of the resulting flow pattern that changed from strong convection in the porous region to convection primarily in the fluid region. Stability analysis was not performed for the "diffusive" (destabilizing temperature gradient and stabilizing salt gradient) regime.

Related to the present problem was the recent work of Kazmierczak and Poulikakos (1989). This diffusive double diffusion study considered the same composite system geometry

Contributed by the Heat Transfer Division for publication in the JOURNAL OF HEAT TRANSFER. Manuscript received by the Heat Transfer Division May 22, 1989; revision received February 27, 1990. Keywords: Double Diffusion Systems, Porous Media, Transient and Unsteady Heat Transfer.

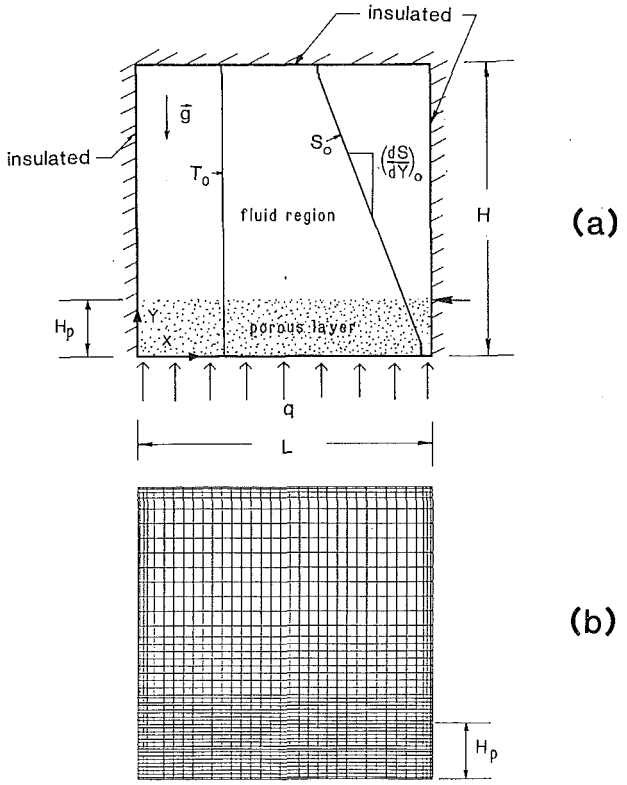

Fig. 1 System of interest: (*a*) composite layer, a horizontal fluid layer extending over a porous substrate; (*b*) computational mesh for $h_p = 0.2$

as the present investigation but examined the problem experimentally and at higher values of salinity and thermal Rayleigh numbers. The porous substrate was made from 5-mm spherical glass beads and the study considered three different porous bed heights. The results of the experiments showed that the presence of the porous layer caused large delays in the initiation of fluid motion in the system and elevated the temperature of the bottom wall. Increasing the porous bed height further accentuated the time delays and in some cases inhibited the flow altogether. Kazmierczak and Poulikakos (1989) found that if convection is initiated, the flow will likely appear first above the porous substrate in the fluid region. Depending on the system parameters, the flow may penetrate into the porous bed. Wherever convection occurred, it caused thorough mixing, resulting in uniform regions of temperature and concentration.

From the standpoint of applications, this study is directly related to geophysical fluid dynamics (the onset of thermohaline convection in shallow coastal waters and in lakes), to thermal energy storage in solar ponds, and, less directly, to alloy solidification where a mixed-phase region consisting of a fluid and dendrites and behaving like a fluid-saturated porous layer separates the solid from the liquid regions (Fisher, 1981). The interaction of the buoyancy-driven flow in the mixed-phase region and the fluid region affects the heat and mass transfer process and consequently the solidification rate and possibly the structure of the resulting solid.

Mathematical Formulation

A schematic representation of the system under investigation is shown in Fig. 1(*a*). The composite layer consists of a horizontal porous bed situated underneath a horizontal fluid layer. The fluid-saturated porous substrate is considered homogeneous and isotropic and its height is denoted by H_p. The two layers are in direct contact with each other. There are no partitions or barriers separating the two layers, i.e., the fluid saturating the bottom porous layer is free to flow into the upper fluid layer and vice versa. This complete system is enclosed by four solid walls. The top horizontal wall and the two side walls are well insulated. Initially, the fluid throughout the system is at rest, isothermal, and contains a stabilizing salt gradient. The species concentration decreases linearly as the distance from the bottom wall increases. Suddenly, at time

Nomenclature

A = aspect ratio $= H/L$
c_p = specific heat at constant pressure
C = dimensionless species concentration
d = diameter of packed spheres in porous matrix
D = mass diffusivity
Da = Darcy number $= K/H^2$
f = dummy variable
F = inertial flow coefficient, equation (12)
g = gravitational acceleration
H = vertical height of the system
h_p = dimensionless height of porous layer $= H_p/H$
H_p = height of porous layer
k = thermal conductivity
K = permeability of porous medium
L = horizontal length of the system
Le = Lewis number $= \alpha/D$
m = number of horizontal grid lines
n = number of vertical grid lines
Pr = Prandtl number $= \nu/\alpha$
q = heat transfer rate per unit area
R = conductivity ratio $= k_{\text{eff}}/k$
Ra = thermal Rayleigh number $= g\beta_t q H^4/k\alpha\nu$
Ra_s = solutal Rayleigh number $= g\beta_s (dS/dY)_0 H^4/\alpha\nu$
S = species concentration
t = time
T = temperature
u = dimensionless horizontal velocity component
U = horizontal velocity component
v = dimensionless vertical velocity component
V = vertical velocity component
x = dimensionless horizontal Cartesian coordinate
X = horizontal Cartesian coordinate
y = dimensionless vertical Cartesian coordinate
Y = vertical Cartesian coordinate
α = thermal diffusivity $= k/\rho c_p$
β_t = coefficient of thermal expansion
β_s = coefficient of concentration expansion
γ = viscosity ratio $= \mu_{\text{eff}}/\mu$
ϵ = porosity of packed porous bed
η = mass diffusivity ratio $= D_{\text{eff}}/D$
θ = dimensionless temperature
λ = prescribed error
μ = viscosity
ν = kinematic viscosity $= \mu/\rho$
ρ = fluid density
σ = heat capacity ratio of the porous medium, equation (13)
τ = dimensionless time
χ = ratio of thermal Rayleigh number to solutal Rayleigh number $= \text{Ra}/\text{Ra}_s$
Ψ = dimensionless stream function
ω = dimensionless vorticity

Subscripts

b = bottom wall
b_o = bottom wall at initial condition
eff = effective
f = fluid
i, j = nodal location
o = initial reference condition
p = porous
s = solid
t_o = top wall at initial condition

Superscripts

r = iteration number
$\bar{}$ = denoting an average quantity over x

$t=0$, the stably stratified system is heated from below with a constant heat flux.

The resulting transient behavior of the system just described is obtained by numerical simulation of the pertinent governing equations. To describe the transport of fluid, energy, and species in the composite system, two sets of conservation equations are needed: one for the fluid region and a second for the porous region. The flow in both regions in this analysis is treated as two dimensional. The thermophysical properties of both the fluid and the fluid-saturated porous medium are treated as constant everywhere except for the density in the buoyancy force term in the momentum equations. There, according to the Boussinesq approximation, the density is assumed to be a linear function of temperature and species concentration. Note that this approximation is the customary practice adopted in the literature for dealing with problems of this type (Ungan and Bergman, 1987; Han and Keuhn, 1989) and holds for systems with small temperature and concentration differences (Gebhart et al., 1988).

The flow in the fluid region is taken to be laminar and the flow in the porous region is modeled using a general non-Darcian model. The general porous model (Cheng, 1979) adopted for use in this study takes into account both the effects of friction caused by macroscopic shear and flow inertia by including the Brinkman and Forchheimer terms in the porous region momentum equations, respectively. It has been shown (Lauriat and Prasad, 1987; Prasad and Tuntomo, 1987; Bejan and Poulikakos, 1984; Poulikakos and Renken, 1987) that both these effects may be significant and therefore should be included. Furthermore, Brinkman's extension is necessary to satisfy the continuity of velocity and viscous stresses at the porous/fluid interface. It also allows the no-slip boundary condition at the solid walls in the porous region to apply. With reference to the energy equation in the porous region, it is assumed that the fluid and the porous matrix are in local thermal equilibrium. Finally, cross diffusion phenomena (Soret and Dufour effects) in both regions are neglected. With the foregoing comments in mind, the two dimensionless sets (the dimensional equations are not shown for brevity) of governing equations specific to each region are:

Porous Region $(0 \le y < H_p)$

$$\omega_p = -\nabla^2 \Psi_p \tag{1}$$

$$0 = -(\mathrm{Pr}/\mathrm{Da})\omega_p + \gamma \mathrm{Pr}\,\nabla^2 \omega_p - (F/\sqrt{\mathrm{Da}})\,|v_p|\,\omega_p - (F/\sqrt{\mathrm{Da}})[u_p(\partial|v_p|/\partial y) - v_p(\partial|v_p|/\partial x)] + \mathrm{RaPr}(\partial\theta_p/\partial x) - \mathrm{Ra}_s\mathrm{Pr}(\partial C_p/\partial x) \tag{2}$$

$$\sigma(\partial\theta_p/\partial\tau) + u_p(\partial\theta_p/\partial x) + v_p(\partial\theta_p/\partial y) = R\nabla^2\theta_p \tag{3}$$

$$\epsilon(\partial C_p/\partial\tau) + u_p(\partial C_p/\partial x) + v_p(\partial C_p/\partial y) = (\eta/\mathrm{Le})\nabla^2 C_p \tag{4}$$

Fluid region $(h_p < y \le 1)$

$$\omega_f = -\nabla^2 \Psi_f \tag{5}$$

$$\partial\omega_f/\partial\tau + u_f(\partial\omega_f/\partial x) + v_f(\partial\omega_f/\partial y) = \mathrm{Pr}\,\nabla^2\omega_f + \mathrm{RaPr}(\partial\theta_f/\partial x) - \mathrm{Ra}_s\mathrm{Pr}(\partial C_f/\partial x) \tag{6}$$

$$\partial\theta_f/\partial\tau = u_f(\partial\theta_f/\partial x) + v_f(\partial\theta_f/\partial y) = \nabla^2\theta_f \tag{7}$$

$$\partial C_f/\partial\tau + u_f(\partial C_f/\partial x) + v_f(\partial C_f/\partial y) = (1/\mathrm{Le})\nabla^2\theta_f \tag{8}$$

All symbols have been defined in the nomenclature. The nondimensionalization was carried out using the following dimensionless variables:

$$x = X/H; \quad y = Y/H; \quad u = U/(\alpha/H); \quad v = V/(\alpha/H);$$
$$C = -(S - S_{t_o})/(H(dS/dY)_o;$$
$$\theta = (T - T_o)/(qH/k); \quad \tau = t/(H^2/\alpha) \tag{9}$$

In addition, the dimensionless stream function Ψ and vorticity ω were introduced

$$u = \partial\Psi/\partial y; \quad v = -\partial\Psi/\partial x; \quad \omega = -\nabla^2\Psi \tag{10}$$

The fluid region governing equations are straightforward and no discussion is necessary. With regard to the porous region governing equations it should be noted that there is no time-dependent term in the porous region vorticity equation. Preliminary simulations performed both with and without the time-dependent term produced identical results. Thus, for the present problem, we found the transient term to be negligible, at least over the parametric domain investigated. The values of certain variables that appear in the porous region governing equations depend on the type of porous matrix. For example, for a matrix consisting of randomly packed spheres of diameter d the porosity ϵ typically varies between 38–40 percent. In addition, the values of the permeability K ($\mathrm{Da} = K/H^2$) and the inertia coefficient F can be determined from the following relations (Ergun, 1952):

$$K = d^2\epsilon^3/[175(1-\epsilon)^2] \tag{11}$$

$$F = (1.75/\sqrt{175})\epsilon^{-3/2} \tag{12}$$

The heat capacity ratio σ of the porous medium is defined as

$$\sigma = (\epsilon(\rho c_p)_f + (1-\epsilon)(\rho c_p)_s)/(\rho c_p)_f \tag{13}$$

where $(\rho c_p)_f$ and $(\rho c_p)_s$ are the heat capacities of the fluid and solid matrix, respectively.

Next, the initial boundary conditions for the system shown in Fig. 1(*a*) must be specified. Initially, the system is motionless, isothermal, and contains a species concentration distribution that decreases linearly with distance from the bottom wall.

Initial Conditions $(\tau = 0)$

$$u_p = v_p = \Psi_p = \omega_p = 0; \ \theta_p = 0; \ C_p = 1 - y, \text{ for } 0 < y < h_p \text{ and } 0 \le x \le 1/A$$
$$u_f = v_f = \Psi_f = \omega_f = 0; \ \theta_f = 0; \ C_f = 1 - y, \text{ for } h_p < y < 1 \text{ and } 0 \le x \le 1/A \tag{14}$$

Boundary Conditions $(\tau \ge 0)$

$$u_p = v_p = \Psi_p = 0; \ -1 = R(\partial\theta_p/\partial y); \ (\partial C_p/\partial y) = 0, \text{ at } y = 0 \text{ and } 0 \le x \le 1/A$$
$$u_f = v_f = \Psi_f = 0; \ (\partial\theta_f/\partial y) = (\partial C_f/\partial y) = 0, \text{ at } y = 1 \text{ and } 0 \le x \le 1/A$$
$$u_p = v_p = \Psi_p = 0; \ (\partial\theta_p/\partial x) = (\partial C_p/\partial x) = 0, \text{ at } x = 0, \ 1/A, \text{ and } 0 \le y < h_p$$
$$u_f = v_f = \Psi_f = 0; \ (\partial\theta_f/\partial x) = (\partial C_f/\partial x) = 0, \text{ at } x = 0, \ 1/A, \text{ and } h_p < y \le 1 \tag{15}$$

The above boundary conditions, equation (15), represent the fact that the walls of the system are solid, they generate no species, and all are adiabatic except for the bottom wall of the system at which a constant heat flux is applied. It is worth clarifying at this point that since we imposed the zero species flux condition at the upper and lower horizontal walls, the initial linear concentration profile is, to be more precise, "almost" linear (i.e., linear everywhere except near the top and bottom walls). Moreover, it should be stated that this "nearly linear" species distribution used in the computations more realistically describes actual experimental conditions. Finally, we note that the no-slip boundary conditions applies along all walls in the system including the walls in the lower porous region. This was only possible by including the Brinkman shear stress term in the momentum equation for the porous region.

The last issue to be discussed in this section is that of matching conditions at the porous/fluid interface. The porous layer governing equations (1)–(4) and the fluid layer governing equa-

tions (5)–(8) are strongly coupled at the permeable porous/fluid interface by the following conditions:

Matching conditions ($y = h_p$)

$$\theta_p = \theta_f \tag{16a}$$
$$R(\partial\theta p/\partial y) = \partial\theta_f/\partial y \tag{16b}$$
$$C_p = C_f \tag{16c}$$
$$\eta(\partial C_p/\partial y) = \partial C_f/\partial y \tag{16d}$$
$$v_p = v_f \tag{16e}$$
$$\gamma(\partial v_p/\partial y) = \partial v_f/\partial y \tag{16f}$$
$$u_p = u_f \tag{16g}$$
$$\gamma(\partial v_p/\partial x + \partial u_p/\partial y) = \partial v_f/\partial x + \partial u_f/\partial y \tag{16h}$$

The first four of the above conditions, equations (16*a*)–(16*d*), represent the continuity of temperature, heat flux, species, and species flux, respectively. The next four conditions, equations (16*e*)–(16*h*), pertain to the velocity field and represent the continuity of normal velocity, normal stress, horizontal velocity, and shear stress, respectively. At this point the mathematical formulation of the problem (governing equations, initial conditions, boundary conditions, and matching conditions) is complete.

During the nondimensionalization process the following ten dimensionless groups appeared:

$$\mathrm{Ra},\ \mathrm{Ra}_s,\ \mathrm{Pr},\ \mathrm{Le},\ \mathrm{Da},\ R,\ \gamma,\ \eta,\ A,\ h_p$$

The first four dimensionless parameters, the thermal Rayleigh number Ra, the solutal Rayleigh number Ra_s, the Prandtl number Pr, and the Lewis number Le depend on the fluid properties alone. Note that both Rayleigh numbers are defined based on the total height of the enclosure H and that the thermal Rayleigh number is proportional to the strength of the destabilizing bottom heat flux, whereas the solutal Rayleigh number represents the opposing initial stabilizing concentration gradient. The combined effect of the two is often represented by a single parameter, χ, the stability ratio. The next parameter, Da, is the Darcy number. The Darcy number represents the (dimensionless) permeability of the porous matrix. The smaller the value of Da, the greater the resistance to flow in the porous bed. Note that in this study the system Darcy number is reported. It is based on the total enclosure height that extends over both the porous and fluid regions. The porous layer Darcy number is considerably larger and can be easily determined since the height of the porous substrate is known. The next three parameters, R, γ, and η, are all ratios of an effective transport property (thermal conductivity, viscosity, and mass diffusivity, respectively) of the fluid-saturated porous medium to that of the fluid alone. Because of the large number of parameters involved it was necessary to hold these ratios constant to make it possible to focus our attention on the "main" parameters of the problem. In the present study, we set the values of these groups equal to unity (i.e., $R = \gamma = \eta = 1$). It has been shown by Lungren (1972) and Neale and Nader (1974) that under certain situations setting $\mu_{\mathrm{eff}} = \mu$ provides good agreement with experimental data. Note that $R \approx 1$ for highly permeable porous media or if the conductivity of the solid is fairly close to that of the saturating fluid, such as in saturated soils or in the case of porous matrices composed of glass beads and water. Finally, it is reasonable to assume that the diffusivity of the species is not affected appreciably by the presence of the porous matrix ($D_{\mathrm{eff}} = D$). The last two remaining groups are geometric parameters that characterize the overall shape of the enclosure, namely, the aspect ratio A and the dimensionless height h_p of the permeable bed.

In addition to what was discussed above, three other parameters of the problem were held constant throughout this study

$$\mathrm{Pr} = 7,\ \mathrm{Le} = 100,\ A = 1 \tag{17}$$

This was necessary in order to render the extent of the study manageable. The above values of Pr and Le are representative of a water–salt mixture. Setting the aspect ratio of unity specifies a square enclosure but it is believed that the phenomenon of interest depends weakly on A (provided that $A \leq 0(1)$) at least for early times. Thus, the results of this study can be interpreted to apply to low aspect ratio systems as well. The porous substrate is assumed to be composed of spherical beads, which sets the valve of porosity to be $\epsilon = 0.4$ and fixes the inertia flow coefficient, equation (12), to be $F = 0.52$.

Numerical Solution

The problem modeled mathematically in the last section was solved numerically using a finite difference method. The dimensionless governing equations (1)–(8) were discretized with the help of the control volume formulation (Anderson et al., 1984). The heat and mass fluxes across the boundaries of each control volume were caclulated via the power law scheme devised by Patankar (1980). The resulting system of simultaneous algebraic equations was solved using an iterative point-by-point method. For each iteration, the numerical integration started at the bottom wall and proceeded upward using the finite difference form of the porous layer equations until the grid point situated immediately below the horizontal interface $y = h_p$ was reached. Next, the interface matching conditions were used to calculate the values of the dependent variables at the interface location. Explicit algebraic relations for the quantities at the interface nodes were obtained from the discretized interface matching conditions in terms of the immediate neighboring points in both the porous region below and the fluid region above. The expression for the interface temperature was obtained using the matching conditions, equations (16*a*) and (16*b*). The expression for the species concentration at the interface was derived from equations (16*c*) and (16*d*). An expression for the interface vorticity was derived by discretizing equation (10) and accounting for all of the remaining fluid matching conditions (equations (16*e*)–(16*h*)). Continuing past the interface location, the discretized form of the fluid layer equations was used to advance the solution from the grid point located immediately above the horizontal interface up to the top wall. All interior grid points were traversed from bottom to top, in the manner just described. Next, the domain HXL was swept from left to right until all interior grid points were visited. For the nodal points located at the boundary of the enclosure, the discretized boundary conditions specified by equation (15) were applied. In addition to the above, the vorticity at the walls of the enclosure must be specified. The vorticity boundary condition, derived from the no-slip condition and given by Thom, was used (Anderson et al., 1984). Although this expression is only first-order accurate, it is widely used and it is often found to give comparable (sometimes better) results than the higher order forms without being susceptible to instabilities at high Reynolds numbers and low Darcy numbers (Lauriat and Prasad, 1987).

The iteration process was repeated at each time step until convergence was achieved. Relaxation was used to aid convergence in solving the vorticity equations although relaxation was not necessary to solve the energy, species, and stream function equations. A typical value of the relaxation parameter used in solving the vorticity equation was 0.4. At each time step the following convergence criterion applied:

$$\frac{\Sigma_{ij}|f_{i,j}^{r+1} - f_{i,j}^{r}|}{\Sigma_{i,j}|f_{i,j}^{r+1}|} < \lambda \tag{18}$$

where f stands for ω, Ψ, T, and S, r is the iteration number and λ is a prescribed error ($\lambda = 10^{-5}$ for the majority of the runs).

As the time was advanced from one time step to the next, the new solution was obtained starting with the converged

Table 1 Summary of numerical simulations

Simulation Number	Ra	Ra_s	x	h_p	Da	Le	A	Pr	Grid (mxn)
1	3×10^9	5×10^8	6	0.1	3×10^{-7}	100	1	7	42 x 36
2	3×10^9	1×10^9	3	0.1	3×10^{-7}	100	1	7	42 x 36
3	3×10^9	5×10^8	6	0.2	3×10^{-7}	100	1	7	46 x 36
4	3×10^9	1×10^9	3	0.2	3×10^{-7}	100	1	7	46 x 36
5	3×10^9	5×10^8	6	0.2	3×10^{-5}	100	1	7	46 x 36
6	3×10^9	5×10^8	6	0.35	3×10^{-7}	100	1	7	50 x 36

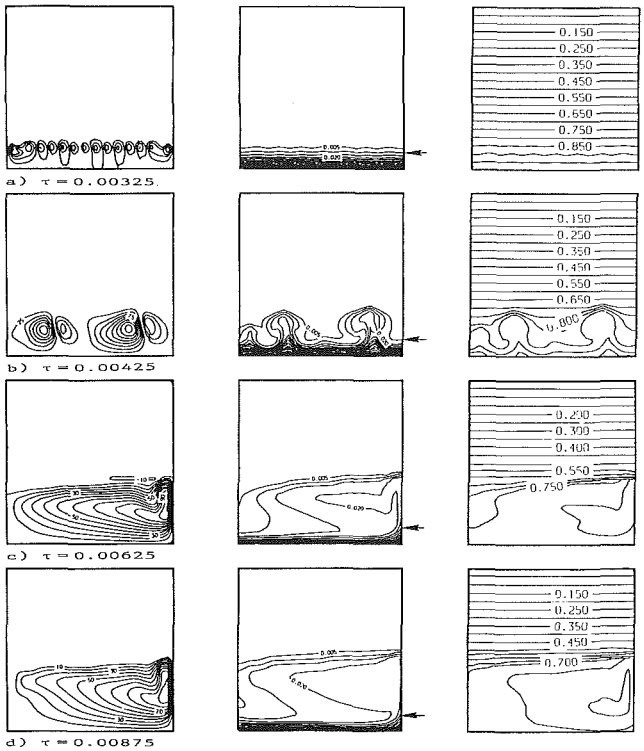

Fig. 2 Streamlines (left), isotherms (middle) and equal concentration lines (right) for Simulation 1 at characteristic times: (*a*) $\tau = 0.00325$, (*b*) $\tau = 0.00425$, (*c*) $\tau = 0.00625$, (*d*) $\tau = 0.00875$

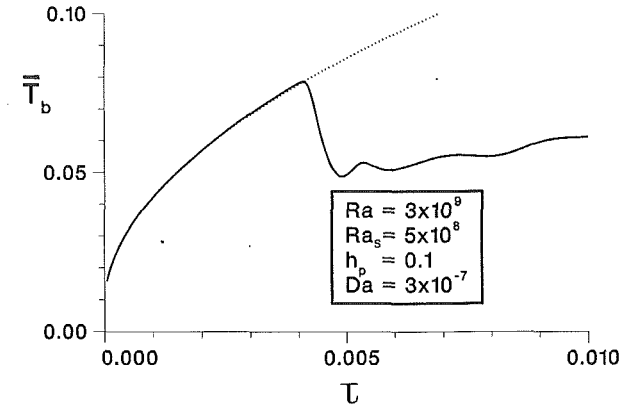

Fig. 3 Average bottom wall temperature dependence on time for Simulation 1

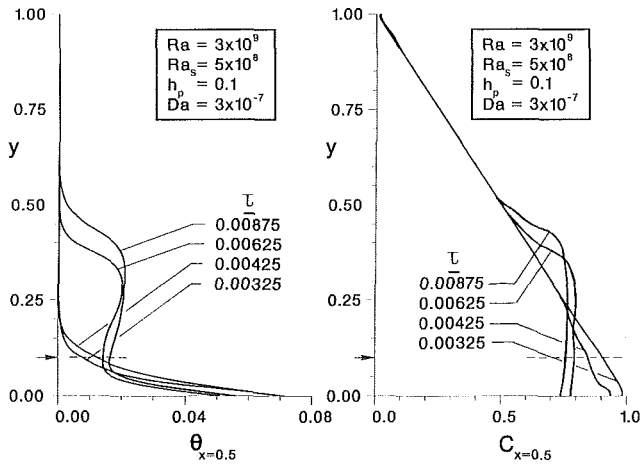

Fig. 4 Centerline profiles at selected times for Simulation 1: (*a*) temperature, (*b*) concentration

solution of the previous time step. This process was repeated, starting with the initial conditions given by equation (14), until it was terminated at a later desired time. Because of the nature of the boundary conditions, no steady-state solution exists and only the transient solution of the system is obtained. In most of the runs, the numerical simulations were terminated at approximately $\tau = 0.015$ and the typical time step size used was of the order 10^{-5}.

Since the solution must completely converge at every time step, the present problem requires a large amount of computational time (of the order of hours for a single run on an IBM 3081 mainframe computer). To minimize the cpu time without sacrificing accuracy, a nonuniform grid was employed in all the simulations performed. The grid spacing and the total number of grid points used for a given simulation depended on the height of the porous layer (h_p). The mesh shown in Fig. 1(*b*) was used in four of the simulations in which the porous layer filled the bottom 20 percent of the overall height of the enclosure. In the computational mesh shown there are $m = 46$ horizontal grid lines and $n = 36$ vertical grid lines. Note the grid is very fine in the porous and the interface regions. This was necessary to ensure that the flow initiation is accurately captured. (As shown in Fig. 1*b*, there were 16 horizontal grid lines contained within the porous layer.) Note also that the grid spacing is also very fine near the walls of the enclosure. In the upper portion of the mesh the grid spacing becomes coarser in comparison with the bottom and middle regions. This fact reduces the computer time but does not compromise the accuracy of the solution since for the time domain investigated in the study, the flow, energy, and species transport occur mainly in the lower half of the enclosure. For porous bed heights other than 20 percent, the total number and the spacing of the horizontal grid lines were adjusted accordingly to keep with the same overall grid spacing practice just described. The horizontal grid spacing did not depend on h_p.

Extensive tests were performed to check the accuracy of the numerical code. These tests are fully described by Kazmierczak (1988). First, results obtained using the present code were compared against earlier published numerical results of Patterson and Imberger (1980) for the problem of transient buoyancy-induced flow in a rectangular square enclosure filled with a viscous fluid. The horizontal walls of the enclosure were insulated and the two vertical walls isothermal. As shown by Kazmierczak (1988), the isotherms and streamlines agreed very well at the same times during the transient evolution of the problem. In the final steady state, the Nusselt number differed by only 0.21 percent when using similar grids. Next, the code was checked against the published numerical results for a problem analogous to that of Patterson and Imberger, but for an enclosure filled with a saturated porous medium (Lauriat and Prasad, 1987). The Brinkman-extended Darcy formulation

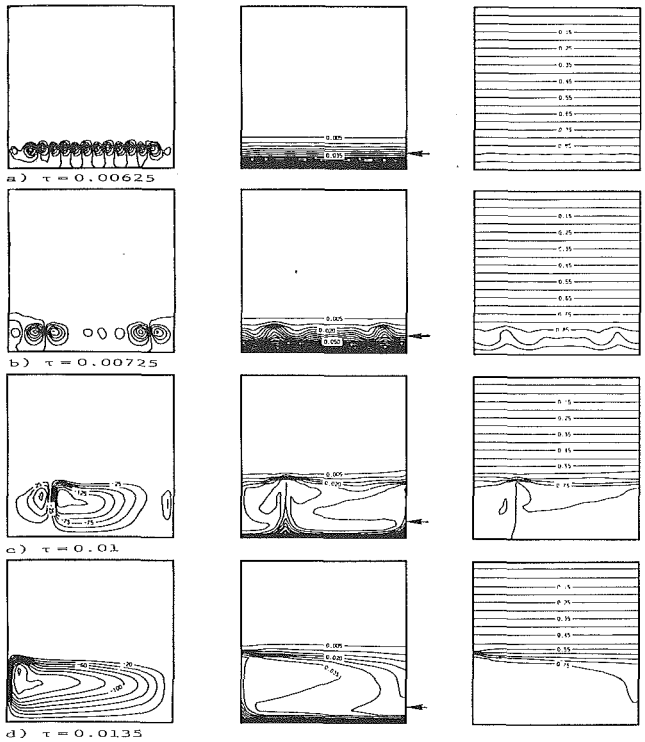

Fig. 5 Streamlines (left), isotherms (middle), and equal concentration lines (right) for Simulation 2 at characteristic times: (*a*) $\tau = 0.00625$, (*b*) $\tau = 0.00725$, (*c*) $\tau = 0.01$, (*d*) $\tau = 0.0135$

was used in this study. A comparison of the isotherms and streamlines reported by Lauriat and Prasad (1987) to those obtained using the present code again shows excellent agreement. The Nusselt number calculated for this test problem using the present code was $\mathrm{Nu} = 20.74$ as compared to $\mathrm{Nu} = 20.85$ reported by Lauriat and Prasad (1987).

The effect of the grid spacing was also tested with regard to the solution of the present problem. To exemplify, three separate sets of computations were carried out for the first simulation, but performed using different nodal meshes having 42×26, 42×36, and 42×46 grid points, respectively. Comparing the results of these test runs showed that the solution becomes grid independent when the mesh contains 42×36 nodal points or more. It is worth clarifying that this is true over the time period when the flow remains mainly in the lower half of the enclosure. All the results we report are indeed for this time period. Computations performed using the grid with the fewest number of nodal points (42×26) produced results that were different from the solution obtained with the more refined grids (42×36, 42×46). It was interesting, however, that although the predicted flow field obtained using the 42×26 grid was different, the bottom wall temperature, the time at which the flow was triggered, and the growth rate of the convective region were all very comparable to the solution with the finer mesh.

Results and Discussion

To investigate the behavior of the system, a total of six numerical experiments were performed. The values of the parameters used in each of the runs are summarized in Table 1. The simulations were carried out in a systematic fashion to determine the effect that the porous substrate had the double diffusion process. To this end, simulations were performed for three different porous bend heights ($h_p = 0.1$, 0.2, and 0.35) and for two different Darcy numbers ($\mathrm{Da} = 3 \times 10^{-7}$ and 3×10^{-5}). In addition, for two of the porous bed heights, the effect of the stability ratio χ was studied.

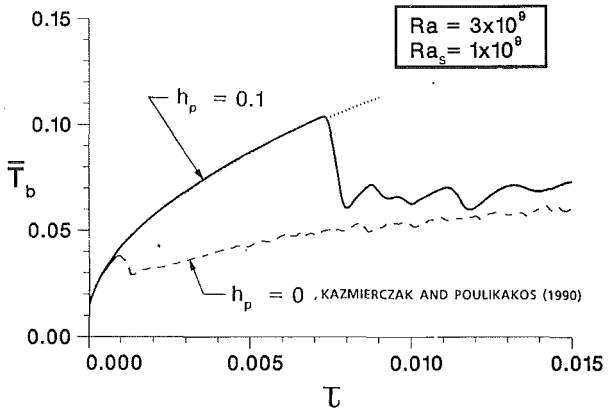

Fig. 6 Average bottom wall temperature dependence on time for Simulation 2 (solid line) and $h_p = 0$ (dashed line); comparison illustrates the effect of the porous height

Figures 2–4 report results for the simulation corresponding to the first line of Table 1. In this run the substrate is fairly thin: $h_p = 0.1$. Nevertheless, it has a major influence on the resulting solution. The stability ratio is $\chi = 6$ ($\mathrm{Ra} = 3 \times 10^9$, $\mathrm{Ra}_s = 5 \times 10^8$) and $\mathrm{Da} = 3 \times 10^{-7}$. The streamlines, isotherms, and lines of equal concentration are shown at four consecutive times in Fig. 2. In this sequence self-sustained flow first appeared at $\tau = 0.00305$. Figure 2(*a*) shows the predicted flow, temperature, and concentration fields at $\tau = 0.00325$ rather soon after the flow initiation time. Flow is initiated not at the bottom wall but at the porous/fluid interface. This flow is multicellular and penetrates partially into the porous substrate. No discernible flow occurs above the interface vicinity into the "stable" diffusive region above. This fact is also clearly revealed from the temperature and concentration fields reported at the same characteristic time. As time continues to increase cell merging occurs. At $\tau = 0.00425$ four cells exist in the system and eventually a single cell forms ($\tau = 0.00625$ and $\tau = 0.00875$). The solution was carried out up to $\tau = 0.01$ without any noticeable qualitative change in the results. The flow causes great mixing but the temperature and concentration fields remain mainly two dimensional in the fluid region at large times ($\tau = 0.00625$ and $\tau = 0.00875$). On the other hand, the temperature and concentration distributions inside the porous substrate and near the center region where the flow and the stable stagnant diffusing regions meet become rather one dimensional. At this point, it appears that the "active" (bottom) region of the system is separated from the "inactive" (top) region by a sharp double diffusive interface, which advances upward with time.

The transient response of the bottom wall temperature is shown in Fig. 3. The mean bottom wall temperature increases rapidly at first, exactly as predicted by the pure conduction solution shown by the dotted line. When the convection effect initiated at the porous/fluid interface reaches the bottom wall ($\tau \approx 0.004$) it quenches the bottom surface with cooler overlaying fluid entrained from above. After $\tau \approx 0.005$ when the flow is fully established over the entire bottom surface, the bottom wall mean temperature rises again, but this time at a much slower rate since convection aids the transport of energy away from the bottom wall to the fluid saturated substrate. The fluctuating nature of the bottom wall temperature is a direct result of the ever-changing flow structure in the system.

Figure 4 shows the centerline temperature and concentration profiles at the same characteristic times that were reported for the contours. They confirm what was discussed earlier. A strong convective mixed region forms in the system that grows progressively upward with time, separated from the upper stably stratified diffusive region above, by a diffusive type interface and bounded from below by a sharp thermal boundary layer.

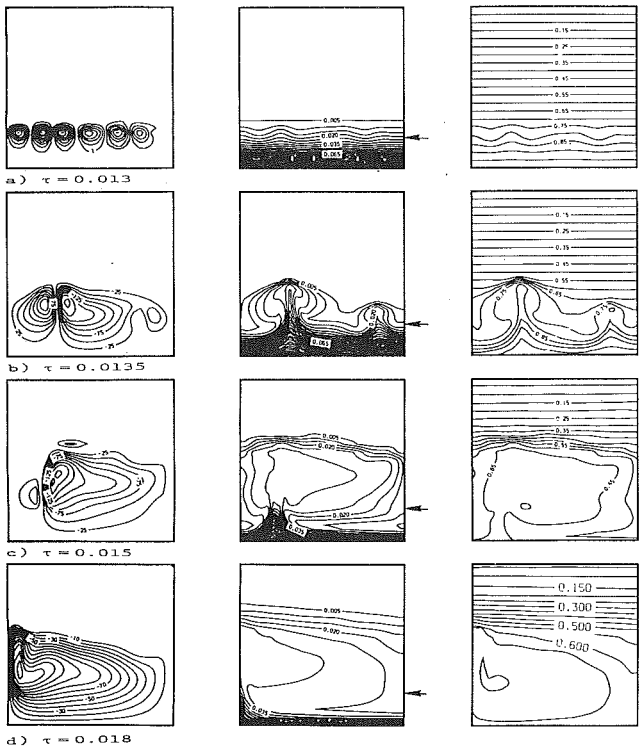

Fig. 7 Streamlines (left), isotherms (middle), and equal concentration lines (right) for Simulation 3 at characteristic times: (*a*) $\tau = 0.013$, (*b*) $\tau = 0.0135$, (*c*) $\tau = 0.015$, (*d*) $\tau = 0.018$

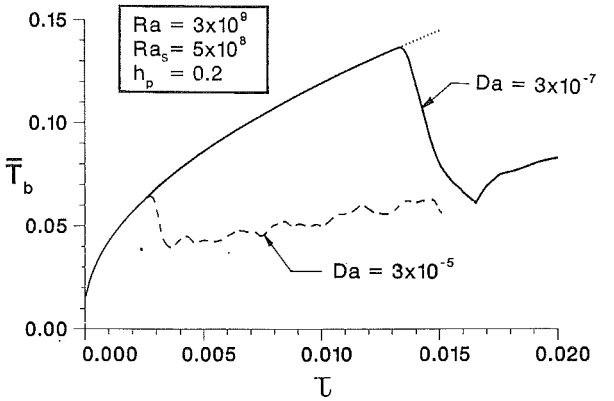

Fig. 8 Average bottom wall temperature dependence on time for Simulation 3 (solid line) and Simulation 5 (dash line); comparison illustrates the effect of Darcy number

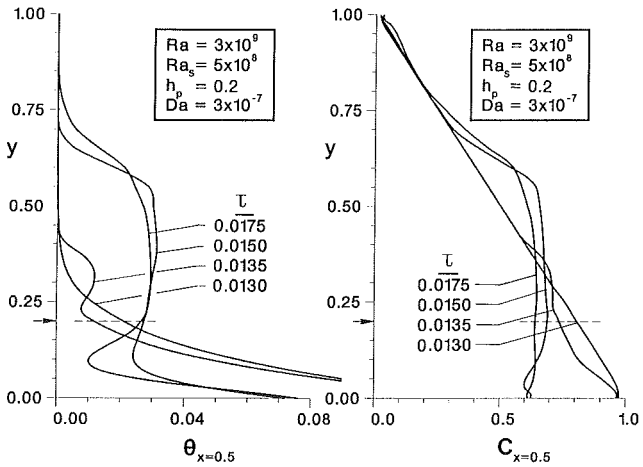

Fig. 9 Centerline profiles at selected times for Simulation 3: (*a*) temperature, (*b*) concentration

Before increasing the height of the porous layer we first document the effect of the stability ratio χ for the composite system having $h_p = 0.1$ and $\mathrm{Da} = 3 \times 10^{-7}$. In the second simulation (Table 1) the value of the stability ratio is $\chi = 3$ ($\mathrm{Ra} = 3 \times 10^9$, $\mathrm{Ra}_s = 1 \times 10^9$), half of the value of χ corresponding to Figs. 2–4. Figure 5 shows streamlines, isotherms, and lines of equal concentration at characteristic times. Once again, the flow is initiated at the porous/fluid interface in the form of a series of counterrotating cells. The time at which flow is initiated ($\tau = 0.00615$) is considerably larger than the flow initiation time of the previously discussed simulation ($\chi = 6$). The reason for this fact is that now the value of the "resistance" parameter (Ra_s) is increased (Table 1). The cells merge as time progresses to result in a single cell (Fig. 5*d*) much like in the previous simulation, with the difference that this cell rotates in the opposite direction from that of the cell in Figs. 2(*c*) and 2(*d*). The temperature and concentration fields exhibit characteristics qualitatively similar to what was discussed in connection with Fig. 2. It is worth noting that the one-dimensional nature of the sharp interface separating the stagnant region from the convecting region is more pronounced for $\chi = 3$ than $\chi = 6$.

The rise of the bottom wall temperature with time is interrupted by the cooling effect of convection, once the flow initiated at the interface penetrates effectively into the porous substrate, as shown by the solid line in Fig. 6. Thereafter, the temperature of the bottom wall fluctuates with time according to the changes of the flow field in the system. Superimposed on Fig. 6 is the predicted bottom wall temperature (dashed line) for a system with no porous layer ($h_p = 0$) taken from the earlier numerical study by Kazmierczak and Poulikakos (1990). All other parameters were identical for this run and the comparison shown in Fig. 6 clearly illustrates the delay in flow initiation and the increase in bottom wall temperature caused by the presence of a thin porous substrate. The temperature and concentration profiles at the centerline for second simulation reported in this study exhibited characteristics similar to those of the profiles in Fig. 4 and are not shown here for brevity.

Next, we examine the effect of the substrate height. The height of the porous layer in increased to $h_p = 0.2$ in the third simulation. The values of the remaining parameters are shown in the third line of Table 1 and are identical to the values of the parameters for the first simulation shown in the first line of Table 1 and discussed earlier.

Figure 7 shows streamlines, isotherms, and lines of constant concentration at characteristic times, for the above-mentioned case. Flow once again is initiated at the porous/fluid interface but at much later time ($\tau \approx 0.012$). The delay is attributed to the "insulating" effect of the porous substrate, which is twice as thick as before. The multiple counterrotating cells at the interface vicinity gradually reduce in number to two and eventually only one large cell, sweeping the bottom half of the system, exists at $\tau = 0.018$ (Fig. 7*d*). The temperature and concentration fields change from a "plume"-like structure ($\tau = 0.0135$ and $\tau = 0.015$) to a "boundary layer" structure ($\tau = 0.018$). The temperature field features two regions of sharp changes: one at the diffusive interface between the convective and the upper stagnant region, and another in the porous region near the bottom wall. The concentration fields at large times ($\tau \geq 0.015$) feature a well-mixed region with little change in concentration and a linearly stable stratified region on top of it. The two regions are separated by a sharp diffusive type interface. During most of the transient simulation the temperature and concentration fields are strongly two dimensional.

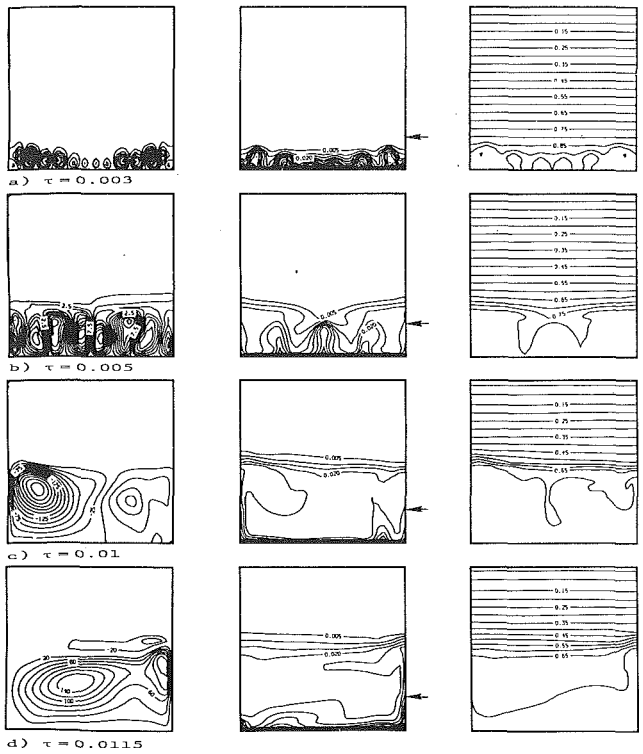

Fig. 10 Streamline (left), isotherms (middle), and equal concentration lines (right) for Simulation 5 at characteristic times: (*a*) $\tau = 0.003$, (*b*) $\tau = 0.005$, (*c*) $\tau = 0.01$, (*d*) $\tau = 0.0115$

Only at large times does the diffusive interface become weakly two dimensional.

Figure 8 shows the response of the average bottom wall temperature with time for $h_p = 0.2$. The solid line plotted in Fig. 8 corresponds to the third simulation, which we will now discuss, and the dashed line corresponds to the fifth simulation, which will be considered later. Long after the flow has been initiated in the system ($\tau = 0.012$), the temperature rise (solid line) still follows closely the prediction of a pure diffusion solution. The reason for this is the prohibitive effect the porous substrate has on the flow. Since the substrate is now rather thick ($h_p = 0.2$), it takes considerable time for the flow initiated at the porous/fluid interface gradually to penetrate through the porous bed and begin the cooling process of the bottom wall. This cooling process starts at $\tau \approx 0.0135$. As a result of this as well as because of the large delay in the flow initiation, the bottom wall temperature attains considerably higher values than what was obtained in the previous simulations.

Figure 9 shows centerline temperature and concentration profiles at various times. The temperature profiles (Fig. 9*a*) indicated a conduction process early, then convection near the porous/fluid interface, and finally two thermal boundary layers, one near the bottom wall and the other at the diffusive interface separating the convective and stagnant regions. The two thermal boundary layers are separated by an isothermal (practically) core region. The concentration profiles (Fig. 9*b*) show that the initially linear concentration distribution gradually changes to a uniform distribution at the bottom part of the system caused by the flow mixing. The upper stagnant region still contains a linear concentration distribution.

Next, maintaining the same bed height, $h_p = 0.2$, we examine the effect of the stability ratio. Following simulation 2, we halve the stability ratio to $\chi = 3$ while keeping the rest of the parameters fixed (fourth line of Table 1). In this case, decreasing the stability parameter had the effect of completely inhibiting the flow in the system. No flow was initiated in the system and the simulation terminated at $\tau = 0.015$. The conclusion drawn is that the combined resistance of the porous bed and the increased salinity gradient are responsible for the pure diffusive nature of the phenomenon within the time range examined.

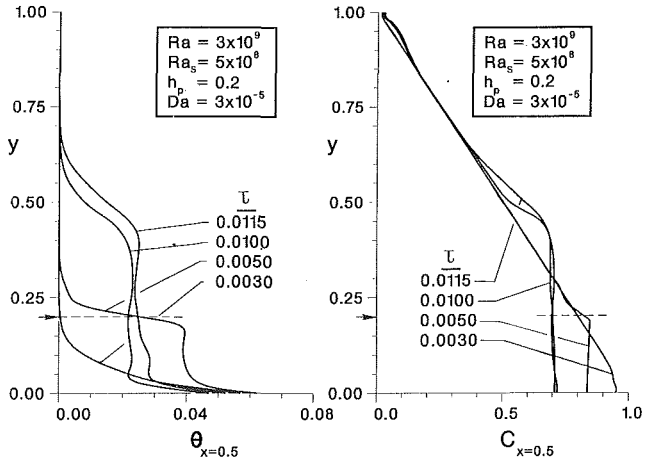

Fig. 11 Centerline profiles at selected times for Simulation 5: (*a*) temperature, (*b*) concentration

We now turn our attention to the effect of the Darcy number at the porous bed height $h_p = 0.2$. The simulation defined by the values of the parameters in the fifth line of Table 1 is identical to the simulation of the third line except that the value of Da was increased to $\mathrm{Da} = 3 \times 10^{-5}$. As shown in Fig. 10(*a*), the convection phenomenon is now initiated at the bottom wall vicinity instead of at the porous/fluid interface vicinity. This fact is readily explained if it is realized that increasing Da is equivalent to increasing the permeability of the porous bed. Therefore, the resistance to flow presented by the porous bed is reduced. As Da increases (the flow resistance in the porous matrix decreases) the composite porous/fluid system behaves more like a single fluid layer characterized by flow always starting and developing at the bottom wall (as experimentally observed by Turner (1968) and numerically predicted by Ungan and Bergman (1987) and Kazmierczak and Poulikakos (1990)). The cell merging characteristics discussed earlier are a feature of this simulation as well (Fig. 10*d*). The temperature and concentration fields change from strongly two dimensional at earlier times ($\tau = 0.003$ and $\tau = 0.005$) to weakly two dimensional at later times ($\tau = 0.001$ and $\tau = 0.001150$). The previous comments regarding the interface separating the convection bottom region from the stagnant top region apply here as well and will not be repeated for brevity.

The bottom wall temperature (dashed line of Fig. 8) feels the convective cooling early ($\tau = 0.0025$) and almost simultaneously with the appearance of flow in the system. This finding is not surprising since, as mentioned above, the flow is initiated in the bottom wall vicinity. Therefore, a result of increasing the Darcy number is that the temperature rise of the bottom wall is considerably less than what was observed in all previous simulations. A comparison demonstrating the effect of Da for $h_p = 0.2$ is shown in Fig. 8.

Figure 11 presents characteristic centerline temperature and concentration profiles. Clearly, a thin thermal boundary layer develops with time near the bottom wall. It is worth comparing Fig. 11(*a*) with the temperature profiles reported in Fig. 9(*a*) for the same bed height but having a much smaller Darcy number. We note that in the profiles having the larger Da number the temperature difference across this bottom thermal boundary layer is considerably smaller ($\Delta\theta \approx 0.02$ in Fig. 11*a* as compared to $\Delta\theta \approx 0.05$ in Fig. 9*a*). This attests to the fact of the increased strength of the flow in the porous region. A second thermal boundary layer (Fig. 11*a*) is created at the interface between the stagnant and the convective regions.

Above this thermal boundary layer the fluid is isothermal. The concentration profiles (Fig. 11*b*) show that the mixing resulting from flow yields a uniform concentration in the convection region. In the stagnant region the concentration distribution remains linear.

For the last simulation (sixth line of Table 1) the height of the porous bed was raised to $h_p = 0.35$. The Darcy number and the stability ratio are set to the same values that were used earlier in the first and the third simulations ($\mathrm{Da} = 3 \times 10^{-7}$ and $\chi = 6$). Increasing the thickness of the porous substrate had the prohibitive effect of completely preventing any convective flow from occurring. The simulation was performed up to $\tau = 0.015$. Always, the pure diffusion solution was obtained.

Before ending this section, it is necessary to discuss the results of this study in relation to the earlier experimental work on double diffusion in composite systems by Kazmierczak and Poulikakos (1989). First, it must be stated that a detailed quantitative comparison between the present numerical predictions and the experimental measurements was not possible because of the differences in the values of the Rayleigh numbers used in the two studies. The values of Ra and Ra_s used in the experiments were an order of magnitude larger than the values used in the numerical simulations. Second, it should be noted that the flow in the experiments was turbulent, not laminar. In short, the published experiments and the present numerical study investigate the same problem but over two different parametric domains. Experimentation was used to solve the problem in the higher Rayleigh number turbulent regime while the numerical simulations were based on the laminar governing equations. Together, the results of both approaches compliment each other and extend the range of the solution. A qualitative comparison between the experiments and the present numerical results shows good agreement. The same major trends and the same phenomena are revealed in both the earlier experimental study and in the present work. A summary of these important findings common to both the numerical study and the experiments is listed in the closing section.

Conclusions

This paper presented a numerical investigation of transient double diffusion in a horizontal composite system, consisting of a fluid layer extending over a porous substrate. The bottom wall of the system was heated with a constant heat flux. Initially, the system was stagnant, isothermal, and contained a linear species distribution. The detailed two-dimensional flow, temperature, and concentration fields as well as the centerline temperature and concentration profiles were reported as the system evolved over time. Also, the transient response of the bottom wall temperature was documented. Double diffusive convection was investigated for the composite system for three different bed heights and for two different values of permeabilities and system stability ratios.

The results of this study showed that the presence of the porous substrate significantly affects the system behavior. In particular, the following main conclusions were reached:

1 The porous substrate increases the bottom wall temperature and delays the onset of convection.

2 The flow in the composite system generally begins just above the interface in the fluid region. The transport in the porous layer occurs initially by diffusion and later by convection after the flow penetrates the porous substrate.

3 Increasing the Darcy number (permeability) had the effect of causing the flow to appear first near the bottom wall in the porous region.

4 Increasing the height of the porous substrate or decreasing the value of the stability ratio greatly delays the appearance of flow in the system. In some cases it completely suppresses the fluid motion. This fact results in higher bottom wall temperatures.

5 The flow initiated in the system was strongly two dimensional at all times and multicellular. As time progressed the number of cells decreased; pairs of cells merged to create single cells. The flow region grew upward with time and at late times featured regions of uniform temperature and concentration because of thorough mixing.

6 For small values of the stability ratio the temperature and concentration fields at late times are only weakly two dimensional. As χ increases the two dimensionality of the temperature and concentration fields becomes more pronounced.

7 The temperature profiles develop the following structure: A thermal boundary layer exists near the bottom wall, a thermal boundary layer exists between the convective region and the stagnant region, and a core region that is largely isothermal is present in between.

Finally, it should be noted that all the major trends and characteristics reported in the experiments by Kazmierczak and Poulikakos (1989) were also identified in the present study.

Acknowledgments

Support for this work provided by NSF through Grant No. ENG 8451144 is greatly appreciated.

References

Anderson, D. A., Tannehill, J. C., and Pletcher, R. H., 1984, *Computational Fluid Mechanics and Heat Transfer*, McGraw-Hill, New York.

Baines, P. G., and Gill, A. E., 1969, "On Thermohaline Convection With Linear Gradients," *Journal of Fluid Mechanics*, Vol. 37, pp. 289–306.

Bejan, A., and Poulikakos, D., 1984, "The Non-Darcy Region for Vertical Boundary Layers Natural Convection in a Porous Medium," *International Journal of Heat and Mass Transfer*, Vol. 27, pp. 717–722.

Bergman, T. L., Incropera, F. P., and Viskanta, R., 1982, "A Multilayer Model for Mixing Layer Development in a Double-Diffusive Thermohaline System Heated From Below," *International Journal of Heat and Mass Transfer*, Vol. 25, pp. 1411–1418.

Bergman, T. L., Incropera, F. P., and Viskanta, R., 1985, "A Differential Model for Salt-Stratified Double-Diffusive Systems Heated From Below," *International Journal of Heat and Mass Transfer*, Vol. 28, pp. 779–788.

Bergman, T. L., and Ungan, A., 1986, "Experimental and Numerical Investigation of Double-Diffusive Convection Induced by a Discrete Heat Source," *International Journal of Heat and Mass Transfer*, Vol. 29, pp. 1695–1709.

Chen, C. F., and Murray, B. T., 1985, "Double-Diffusive Convection in a Porous Medium," *Double-Diffusive Motions*, ASME FED-Vol. 24, pp. 47–55.

Chen, F., and Chen, C. F. 1988, "Onset of Finger Convection in a Horizontal Porous Layer Underlying a Fluid Layer," ASME JOURNAL OF HEAT TRANSFER, Vol. 110, pp. 403–409.

Cheng, P., 1979, "Heat Transfer in Geothermal Systems," *Advances in Heat Transfer*, Vol. 14, pp. 1–105.

Ergun, S., 1952, "Fluid Flow Through Packed Columns," *Chemical Engineering Progress*, Vol. 48, pp. 89–94.

Fisher, K. M., 1981, "Effects of Fluid Flow on the Solidification of Industrial Castings and Ingots," *Physiochemical Hydrodynamics*, Vol. 2, pp. 311–326.

Gebhart, B. J., Jaluria, Y., Mahajan, R., and Sammakia, B., 1988, *Buoyancy-Induced Flows and Transport*, Hemisphere, Washington, DC.

Han, H., and Kuehn, T., 1989, "A Numerical Simulation of Double Diffusive Natural Convection in a Vertical Rectangular Enclosure," *Heat Transfer in Convective Flows*, ASME-HTD, Vol. 107, pp. 149–154.

Kazmierczak, M. J., 1988, "Transient Double Diffusion in a Fluid Layer and a Composite Porous/Fluid Layer Heated From Below," Ph.D. Thesis, University of Illinois at Chicago, Chicago, IL.

Kazmierczak, M. J., and Poulikakos, D., 1989, "Transient Double-Diffusive Convection Experiments in a Horizontal Fluid Layer Extending Over a Bed of Spheres," *Physics of Fluids*, Vol. A1, pp. 480–489.

Kazmierczak, M. J., and Poulikakos, D., 1990, "Transient Double Diffusion in a Stably Stratified Fluid Layer Heated From Below," *International Journal of Heat and Fluid Flow*, Vol. 11, pp. 30–39.

Lauriat, G. and Prasad, V., 1987, "Natural Convection in a Vertical Porous Cavity: A Numerical Study for Brinkman-Extended Darcy Formulation," ASME JOURNAL OF HEAT TRANSFER, Vol. 109, pp. 688–696.

Lewis, W. T., Incropera, F. P., and Viskanta, R., 1982, "Interferometric Study of Stable Salinity Gradients Heated From Below or Cooled From Above," *Journal of Fluid Mechanics*, Vol. 116, pp. 411–430.

Lundgren, T. S., 1972, "Slow Flow Through Stationary Random Beds and Suspensions of Spheres," *Journal of Fluid Mechanics*, Vol. 51, pp. 1865–1874.

Neale, G., and Nader, W., 1974, "Practical Significance of Brinkman's Extension of Darcy's Law," *Canadian Journal of Chemical Engineering*, Vol. 52, pp. 475–478.

Neilson, D. G., and Incropera, F. P., 1987, "Double-Diffusive Flow and Heat Transfer for a Cylindrical Source Submerged in a Salt-Stratified Solution," *International Journal of Heat and Mass Transfer*, Vol. 30, pp. 2559–2570.

Nield, D. A., 1967, "The Thermohaline Rayleigh–Jeffreys Problem," *Journal of Fluid Mechanics*, Vol. 29, pp. 545–558.

Nield, D. A., 1968, "Onset of Thermohaline Convection in a Porous Medium," *Water Resources Research*, Vol. 4, pp. 553–560.

Patankar, S. V., 1980, *Numerical Heat Transfer and Fluid Flow*, McGraw-Hill, New York.

Patterson, J., and Imberger, J., 1980, "Unsteady Natural Convection in a Rectangular Cavity," *Journal of Fluid Mechanics*, Vol. 100, pp. 65–86.

Poplawsky, C. J., Incropera, F. P., and Viskanta, R., 1981, "Mixed Layer Development in a Double-Diffusive, Thermohaline System," ASME *Journal of Solar Energy Engineering*, Vol. 103, pp. 351–359.

Poulikakos, D., 1986, "Double Diffusive Convection in a Horizontal Sparcely Packed Porous Layer," *International Communications in Heat and Mass Transfer*, Vol. 13, pp. 587–598.

Poulikakos, D., and Renken, K., 1987, "Forced Convection in a Channel Filled With Porous Medium, Including the Effects of Flow Inertia, Variable Porosity, and Brinkman Friction," ASME JOURNAL OF HEAT TRANSFER, Vol. 109, pp. 880–888.

Prasad, V., and Tuntomo, A., 1987, "Inertia Effects on Natural Convection in a Vertical Porous Cavity," *Numerical Heat Transfer*, Vol. 11, pp. 295–320.

Rubin, H., 1973, "Effects of Nonlinear Stabilizing Salinity Profiles on Thermal Convection in a Porous Medium Layer," *Water Resources Research*, Vol. 9, pp. 211–221.

Turner, J. S., 1968, "The Behavior of a Stable Salinity Gradient Heated From Below," *Journal of Fluid Mechanics*, Vol. 33, pp. 183–200.

Ungan, A., and Bergman, T. L., 1987, "A Two-Dimensional Numerical Simulation of a Linearly-Stratified Thermohaline System Heated From Below," ASME Paper No. 87-WA/HT-19.

P. F. Peterson
Assistant Professor,
Department of Nuclear Engineering,
University of California,
Berkeley, CA 94720
Assoc. Mem. ASME

N. Elkouh[1]

K. W. Lee[2]
Visiting Researcher.

Department of Mechanical Engineering,
University of California,
Irvine, CA 92717

C. L. Tien
Department of Mechanical Engineering,
University of California,
Berkeley, CA 94720
Fellow ASME

Flow Instability and Bifurcation in Gas-Loaded Reflux Thermosyphons

In vertical gas-loaded two-phase reflux thermosyphons, the temperature and concentration gradients between the active and shut-off regions can create double-diffusive mixed convection flows. When the noncondensable gas molecular weight is greater than that of the vapor, different steady and time-dependent gas recirculation patterns develop, similar to those observed during Rayleigh–Bénard convection in vertical slots. Experimental results presented here show that bifurcations from axisymmetric to three-dimensional, then asymmetric, and finally multiple distinct gas-flow patterns occur as the Rayleigh number increases. Ultimately, a sudden transition to a large-amplitude oscillatory gas flow takes place. Detailed concentration maps and power-density spectra from point wet-bulb temperature measurements clearly chart these transitions. These results impact the design of many condensing systems where noncondensables are present.

Introduction

The vertical gas-loaded two-phase thermosyphon, illustrated schematically in Fig. 1, consists of a closed tube containing a working fluid such as water and a noncondensable gas. The device transports heat by generating vapor in the evaporator section. Film condensation occurs in the condenser section, driving forced convection flow of the vapor from the evaporator to the condenser section. Gravity then returns the liquid to the evaporator. The noncondensable gas collects at the top of the condenser, creating a region shut off to condensation. The gas-loaded thermosyphon provides an analog for several condensing systems of practical importance, including steam generators and other reactor components, which are postulated to support condensation during loss-of-coolant accidents (Hein et al., 1982), and variable-conductance heat pipes for aerospace applications (Bobco, 1987).

The temperature and concentration gradients between the shut-off and active regions of the condenser create double-diffusive mixed convection flows, recirculating and redistributing the noncondensable gas. Under steady conditions the gas flows down one side of the condenser, to be recirculated, while the vapor flows up the other and condenses at the wall (Fig. 1). This steady mixed-convection case has been studied experimentally (Peterson and Tien, 1988) and numerically (Peterson and Tien, 1990). However, in the vertical and near-vertical orientations, more complex, bifurcating, and time-dependent gas recirculatory flows can occur.

Time-dependent behavior has been observed during thermosyphon and heat pipe experiments by many investigators (Anderson et al., 1974; Kelleher, 1976; Galaktionov and Trukhanova, 1985; Kobayashi and Matsumoto, 1987). In the vertical and near-vertical orientations time dependency can begin at relatively low values of the Rayleigh number (Ra). Stability increases as the device tilts toward the horizontal, since in the horizontal orientation the gravity vector stabilizes axial stratification along the length of the condenser.

This study focuses on a near-vertical reflux thermosyphon loaded with a noncondensible gas heavier than the vapor. Vertical gas-loaded devices show many similarities with the well-documented Rayleigh–Bénard problem of flow instability and bifurcation in rectangular enclosures heated from below, which has been reviewed by Yang (1988) and discussed by Gebhart et al. (1988). High-aspect-ratio enclosures (Hele-Shaw slots) provide the closest parallels with gas-loaded thermosyphons. Both systems are characterized by the potentially unstable condition of a heavy fluid above a lighter fluid. The condensing thermosyphon system, however, possesses radically different boundary conditions. Heavy gas is buoyed upon a rising column of light vapor, a similar condition to an enclosure heated from below. Suction occurs at the condenser walls, at rates that are nonlinearly sensitive to the interface gas concentration. Given the nonlinear boundary conditions, mixed convection, and condensation in the thermosyphon, the similarities between the different time-dependent convection patterns observed here and those seen in Hele-Shaw slot experiments by Koster and Muller (1984) are remarkable. Their experiments found both single and multiple roll cells, as seen here. Hele-Shaw slots have also been studied numerically (Frick and Muller, 1983; Frick and Clever, 1982). Considerable attention has been devoted to this class of problems, with the goal of greater understanding of complex time-dependent flows and

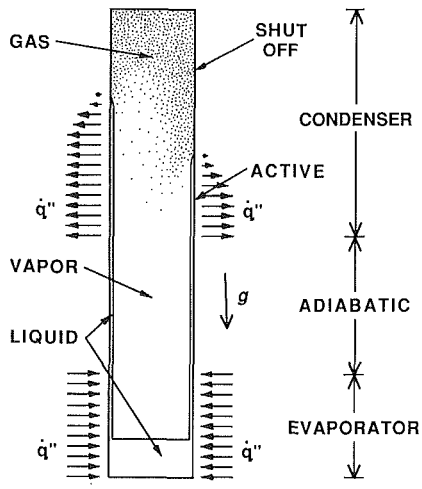

Fig. 1 Schematic of gas-loaded thermosyphon

[1]Formerly: Graduate Student, University of California at Berkeley.

[2]Permanent address: Korea Institute of Energy and Resources, Daejeon, Korea.

Contributed by the Heat Transfer Division and presented at the ASME Winter Annual Meeting, San Francisco, California, December 10–15, 1989. Manuscript received by the Heat Transfer Division January 22, 1990; revision received May 31, 1990. Keywords: Flow Instability, Heat Pipes and Thermosyphons, Natural Convection.

the onset of turbulence (Gollub and Benson, 1980; Lennie et al., 1988).

Theory

This section presents the parameters that govern bifurcation and instability in gas-loaded thermosyphons. Similarity theory permits minimization of the number of parameters required to characterize this system. In addition to thermal boundary conditions, the simpler Hele-Shaw slot convection problem requires introduction of the Rayleigh number, Prandtl number, and two aspect ratios (Chandrasekhar, 1981). For a long, cylindrical thermosyphon the only aspect ratio is associated with the location of the adiabatic section relative to the gas–vapor front. Mixed convection requires introduction of the Reynolds number. In addition, the simultaneous double-diffusive action of temperature and concentration gradients requires introduction of the Lewis number, giving a total of five parameters. The complex nonlinear boundary conditions introduce additional parameters.

A meaningful study of a system with this many degrees of freedom is difficult at best. Additional constraints on parameter variation were placed by the relatively low power inputs allowed for the experimental apparatus. Thus this study isolated the effects of the parameter of greater interest in bifurcation and instability, the Rayleigh number, and held the Reynolds, Prandtl, and Lewis numbers approximately constant. By starting from low pressure and adding gas in small quantities, Ra was changed by small increments. Increasing the quantity of noncondensable gas raised the total pressure, which increased the density difference between the active and shutoff regions, and thus the Rayleigh number.

The strength of the natural convection recirculating the gas depends on the balance of viscous forces with buoyant forces resulting from concentration and temperature gradients. Thus gas-loaded systems can be characterized by the Rayleigh number Ra, based on the density difference between the pure vapor in the evaporator and the cool gas–vapor mixture of the shutoff zone, at the cooling medium temperature T_c. Due to the importance of mass concentration on the mixture density relative to temperature, the Rayleigh number defined here uses the mass diffusivity D. This is a nonstandard formulation for Rayleigh number, but is applied here for the sake of brevity, rather than RaSc. Given the large aspect ratio, an appropriate length scale is the inner radius of the condenser tube. The Rayleigh number can then be written as

$$\mathrm{Ra}=\frac{(\rho(T_c)-\rho_v)gR^3}{\mu D}=\frac{\rho_v g R^3}{\mu D}\left\{\frac{T_v}{T_c}\left[1+x_{gc}\left(\frac{M_g}{M_v}-1\right)\right]-1\right\} \tag{1}$$

where $\rho(T_c)$ is the density of the gas–vapor mixture at the coolant temperature, ρ_v the density of the pure working fluid vapor at the saturation temperature T_v, x_{gc} the maximum gas molar fraction (at the top of the condenser), R the condenser inner radius, and M the molecular weight. The dynamic viscosity μ and the binary diffusion coefficient D are evaluated from tabular values at the average of the shut-off and active region temperatures. The average of the air and water viscosity values is used to determine the mean viscosity μ. The calculation of Ra is further simplified by treating the gas–vapor mixture as an ideal gas. This formulation of the Rayleigh number affords easy experimental evaluation, requiring only measurements of the total pressure and the cooling medium temperature.

Condensation drives the forced convection of the vapor from the evaporator to the condenser. This forced component of the flow can be characterized by the third parameter, the Reynolds number,

$$\mathrm{Re}=\frac{2\dot{q}}{\pi R h_{fg}\mu} \tag{2}$$

where $\dot{q}$ is the heat input to the evaporator, h_{fg} the latent heat of vaporization, and the characteristic velocity comes from the total heat input, $V=\dot{m}/A=\dot{q}h_{fg}/\pi R^2$. By holding the power level constant during the experiment, Re also remained relatively constant since h_{fg} and μ change by small amounts over the range of temperature and pressure encountered here.

Since this is a double-diffusive system with the recirculation of the gas driven by both temperature and concentration gradients, both the Prandtl number, quantifying the relative diffusivity of momentum and thermal energy, and the Lewis number, quantifying the relative diffusivity of mass and thermal energy, are significant

$$\mathrm{Pr}=\frac{\mu}{\rho\alpha}\qquad \mathrm{Le}=\frac{\alpha}{D} \tag{3}$$

where α is the thermal diffusivity. The Lewis number for this system was close to 0.75. This value is relatively close to unity, decreasing double-diffusive effects compared to brine and other liquid systems. However, here double-diffusive effects are also introduced by the boundary conditions.

The requirements of phase equilibrium and energy conservation at the wall introduce additional strong nonlinearity between the temperature T_i and concentration x_{gi} at the vapor–liquid interface. This introduces additional double-diffusive effects at boundaries with small to moderate concentrations of gas, since concentration gradients are steeper. Two parameters are required to characterize the nonlinear boundary conditions. The Clausius–Clapeyron equation provides a nonlinear boundary relationship between temperature T_i and concentration x_{gi} at the vapor–liquid interface

$$x_{gi}=1-\exp(T_*(1-T_r/\mathrm{T}_i)) \tag{4}$$

where T_r is a reference temperature. The parameter T_* is a property of the working fluid related to the fluid specific heat and volume through the Clausius–Clapeyron relationship. A balance between heat removed out through the condenser wall

Nomenclature

D = mass diffusivity, m^2/s
g = gravitational constant, m/s^2
h = heat transfer coefficient, kJ/m^2°C
h_{fg} = latent heat of vaporization, kJ/kg
Le = Lewis number, equation (3)
M = molecular weight, kg/kmol
P = pressure, kPa
Pr = Prandtl number, equation (3)
$\dot{q}$ = heat input to condenser, W
r = radial coordinate, m
R = thermosyphon inner radius, m
Ra = Rayleigh number, equation (1)
Re = Reynolds number, equation (2)
S = superheat parameter, equation (6)
T = absolute temperature, K
T_* = Clausius–Clapeyron constant, equation (4)
v = velocity, m/s
x = mole fraction
z = axial coordinate
α = thermal diffusivity, m^2/s
μ = dynamic viscosity, kg/m s
ρ = mass density, kg/m^3

Subscripts

c = cooling medium
db = dry bulb
g = noncondensible gas
i = liquid/vapor interface
r = reference value
s = saturation
T = total
v = vapor
wb = wet bulb

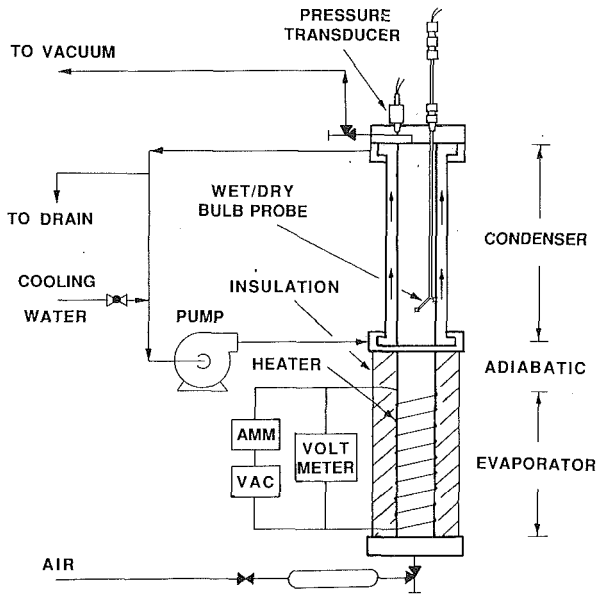

Fig. 2 Schematic of experimental apparatus

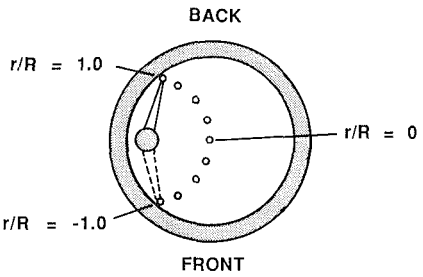

Fig. 3 Cross section of condenser, to scale, showing radial wet-bulb measurement positions

and the flux of latent heat to the gas-vapor interface gives additional nonlinear boundary relationships for the slope of x_g with the interface temperature T_i and condensation velocity v_i

$$\rho D\frac{\partial(\ln x_g)}{\partial r}=\frac{h(T_i-T_c)}{h_{fg}}=\rho v_i \tag{5}$$

where h is an overall heat transfer coefficient to the cooling medium. Nondimensionalization of this equation provides two additional parameters. Given significant thermal inertia of the pipe wall, yet another parameter would be required. Peterson and Tien (1990) give a full derivation of equations (4) and (5).

Experiment

Measurements of the distribution and temporal fluctuation of the noncondensable gas concentration are central to understanding the buoyancy-induced convective disturbances that can occur in gas-loaded devices. To provide these measurements a miniature wet-bulb concentration measurement technique was applied (Peterson and Tien, 1987). The wet-bulb probe used here consisted simply of a thermocouple embedded in a small porous sphere. The point gas concentration x_g can be found from the measured temperatures by applying Dalton's law and neglecting radiation

$$x_g=1-P_s(T_{wb})/P_T+S(T_{db}-T_{wb}) \tag{6}$$

where $P_s(T_{wb})$ is the saturation pressure at the measured wet-bulb temperature and T_{db} the dry-bulb temperature. The superheat parameter S derives from the analogy between heat and mass transfer. For this system S is less than 0.0005, so

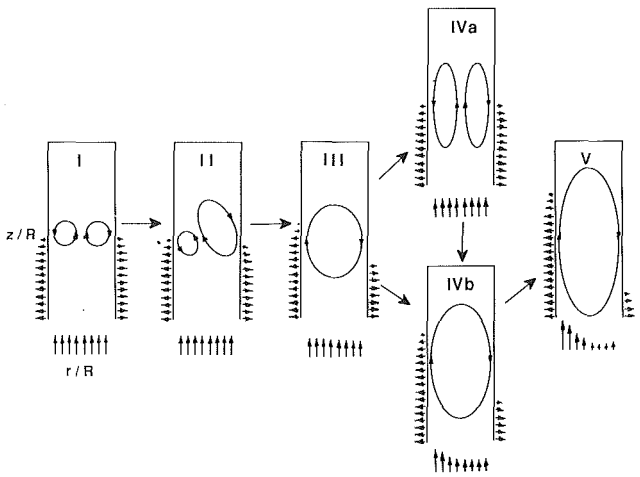

Fig. 4 Progression of gas-flow recirculation patterns in condenser section from lower to higher Rayleigh numbers; small arrows indicate vapor inflow and outflow

superheat effects could be neglected and the measurement of T_{db} was not required. A transient lumped analysis of the probe shows a characteristic time constant of under 0.1 seconds. The highest frequencies observed were below 1.0 Hz, well within the transmittance range of the probe.

Figure 2 shows a schematic of the thermosyphon experiment. Peterson and Tien (1988) provide a complete description of the experimental setup. The thermosyphon consisted of a 1.19-m-long, 41.3-mm-id., 4.76-mm-wall pyrex glass tube. Nichrome wire wound around the 0.25-m-long evaporator section supplied a constant heat load. Water circulating in the annulus between the inner and outer glass tubes cooled the 0.63-m-long condenser section. Glass fiber of 3.0-cm thickness insulated the evaporator and adiabatic sections, while 1.3-cm-thick acrylic plugs insulated the tube ends. Stainless-steel screen wrapped against the inside wall of the evaporator provided uniform wetting by the working fluid. An absolute pressure transducer monitored the system pressure, providing accuracy of ± 0.5 percent of the 101.3 kPa full-scale reading. Copper-constantan thermocouples provided temperature information with an accuracy of ± 0.3°C. The pressure measurement resulted in an absolute accuracy ranging from ± 12 percent at the lowest total pressure to ± 1.7 percent at the highest. The relative accuracy of the concentration measurements at different locations, however, was governed by the temperature measurement, ranging from 1.5 percent to 1.1 percent, since any error in the pressure measurement created a constant deviation at a given Rayleigh number. The shapes and spacing of the isoconcentration profiles given here then are governed by the higher relative accuracy, while the absolute values are governed by the lower absolute accuracy.

The miniature wet-bulb probe, a copper/constantan thermocouple embedded in a 1.5-mm ball of urethane foam, was mounted on the end of a stainless-steel tube. The finely polished tube, sealed with double O-rings and vacuum grease to allow for axial movement, was mounted offset from the tube centerline to permit gas concentration measurements in an arc from the centerline to the walls, as shown in Fig. 3.

The pressure and wet-bulb temperature analog signals were digitized and processed with a computer data acquisition system. The top of the thermosyphon tilted back 1 deg from vertical to provide a preferential orientation for any convection cells. The thermosyphon was filled with distilled water until the wet-bulb probe was immersed and wetted. The distilled water was then drained from the thermosyphon until 50 ml remained. The system was heated and a vacuum drawn, re-

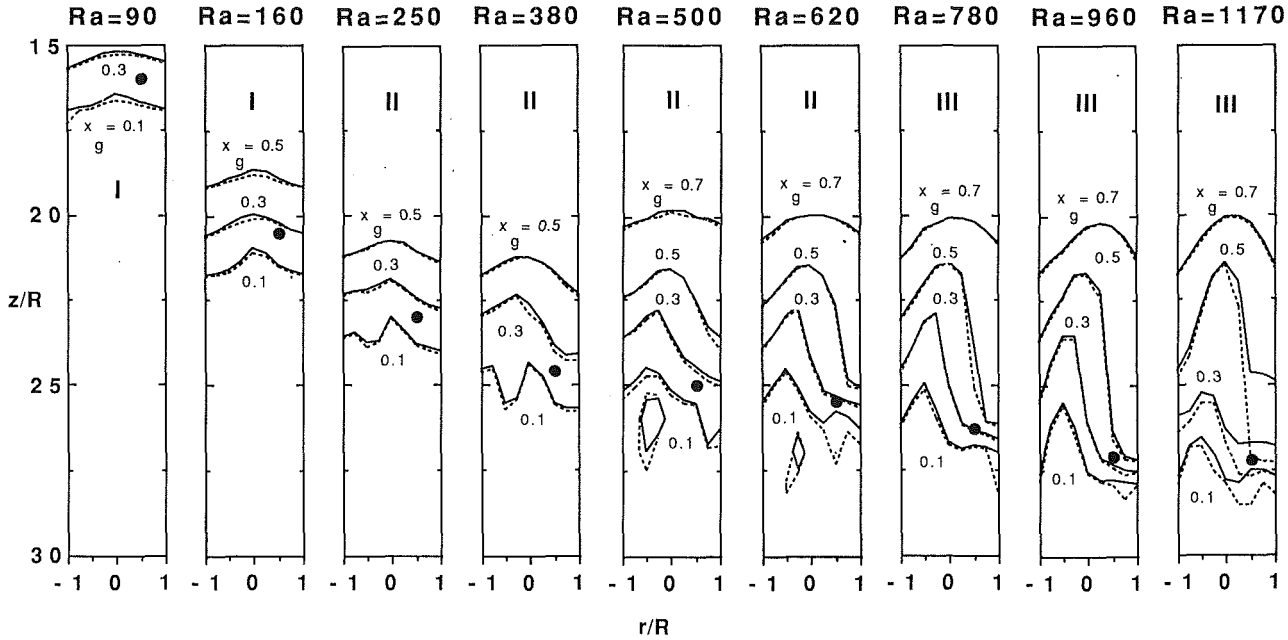

Fig. 5 Isoconcentration profiles at low Ra; dashed and solid curves denote minimum and maximum concentration measurements, respectively

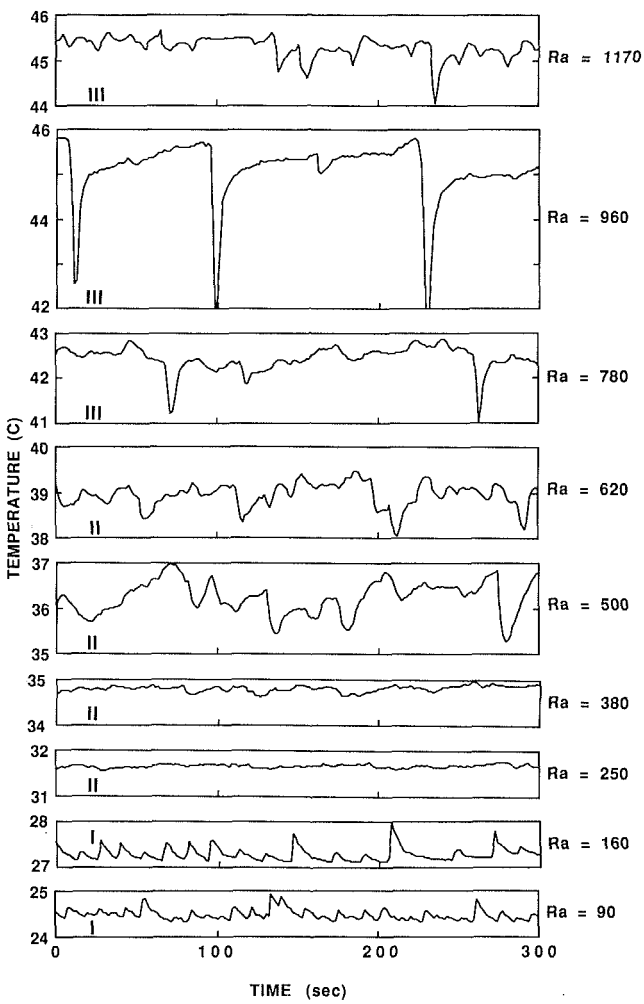

Fig. 6 Wet-bulb temperature histories at low Ra, recorded at points shown by circles in Fig. 5

Table 1 Experimental parameters

Rayleigh Number	Total Pressure (kPa)	Cooling Medium Temperature (C)	Maximum Gas Mole Fraction	Characteristic Time $(2R)^2/D$ (s)
90	3.9	17.8	0.47	2.6
160	4.8	17.6	0.58	3.1
250	5.7	17.7	0.64	3.7
380	6.8	17.8	0.70	4.3
500	7.6	17.7	0.72	4.7
620	8.4	18.1	0.72	5.2
780	9.3	18.2	0.75	5.6
960	10.2	18.3	0.78	6.1
1170	11.2	18.4	0.79	6.7
1380	12.0	18.5	0.79	7.2
1550	12.7	18.3	0.82	7.6
1800	13.6	18.4	0.83	8.0
2080	14.6	18.7	0.84	8.6
2420	15.6	17.9	0.85	8.9
7700	27.3	19.5	0.92	16.3
8500	28.6	19.2	0.92	17.0
8800	28.9	17.8	0.93	17.2
9240	29.4	17.8	0.93	17.2

moving all of the air in the system. The system was allowed to stand for 10 hours, with no measurable leakage occurring.

The evaporator heater was turned on and the power input maintained at 100 W, corresponding to a vapor Reynolds number of Re = 70. A small quantity of noncondensable gas was added to the system by opening a valve to a 7.5 cm^3 vessel containing air at ambient pressure. The thermosyphon was allowed one hour to come to its characteristic operating condition. The minimum and maximum gas concentration values were measured at nine radial locations as illustrated by Fig. 3, at axial intervals of $z/R = 1$ starting from the top of the condenser. At each measurement point the probe was allowed to equilibrate (approximately 10 seconds) and then the gas concentration was monitored until the minimum and maximum readings stabilized (approximately 30 seconds). Periodically readings were retaken at higher locations, which confirmed the quasi-steady nature of the recirculation, in that no large changes of the structures were observed. The concentration maps resulting from these measurements thus reflect the short-term fluctuations of the concentration, with no large deviations occurring over longer periods.

A detailed time history of the fluctuating wet-bulb temperature was recorded at $r/R = 0.5$ at an axial location where the

average gas concentration was approximately 0.25. This point in the gas recirculation region was observed to have the highest amplitude fluctuations. Spectral information was derived using a fast Fourier transform from the average of two-overlapping sets of 2048 wet-bulb temperature measurements, sampled at 0.5-s increments, so that the highest harmonic stayed below the Nyquist frequency. The data preparation included digital removal of the d.c. offset and filtering with a Parzen function window.

The cooling water temperature, evaporator temperature, and system pressure were also monitored. After all the desired information had been recorded, gas was added to the device. This additional gas increased the system pressure slightly, which increased the density difference between the shut-off region and the pure vapor (i.e., the evaporator), and thus slightly increased the Rayleigh number. The system was allowed 15 minutes to come to its characteristic operating condition and the measurements were repeated at the new Rayleigh number. This procedure was repeated 36 times until a Rayleigh number of 9660 was reached, and then the power was shut off and the system allowed 10 hours to equilibrate. The total pressure and equilibrium temperature were then measured (18.0 kPa, 24.6°C) to determine the final quantity of gas in the thermosyphon (9.3×10^{-6} kmol). The total pressure was monitored for another 10 hours, with no detectable change, indicating that no leakage occurred.

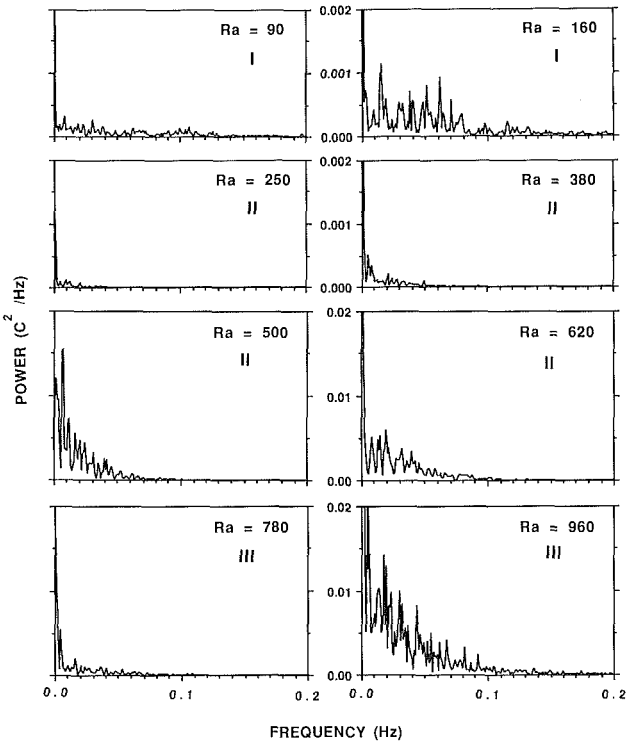

Fig. 7 Power-density spectrum at low Ra, measured at points shown by circles in Fig. 5

Results and Discussion

Figure 4 depicts schematically the gas-flow recirculation patterns observed with increasing Rayleigh number, as well as the vapor inflow and outflow. Without buoyancy effects and recirculation, the isoconcentration profiles are parabolically shaped and axisymmetric (Peterson and Tien, 1989). The gas recirculation patterns are thus inferred from the bending and distortion of the isoconcentration profiles from the axisymmetric parabolic shape. Initially axisymmetric toroidal recirculation of the gas was observed, followed by bifurcation to a three-dimensional flow structure, then a single-roll cell and other structures. The following paragraphs summarize in detail each pattern and the associated experimental results. Figures 5 and 8 provide concentration maps for the quasi-steady conditions at lower Rayleigh numbers, where concentration oscillations were relatively small. The solid and dashed curves show isoconcentration profiles interpolated from minimum and maximum concentration measurements, respectively. Table 1 presents information on the operating conditions at each Rayleigh number.

Regime I: Ra = 90—160. When the first increment of gas was added to the thermosyphon, the upper portion of the condenser from $z/R = 0$ to 15 was shut off to condensation,

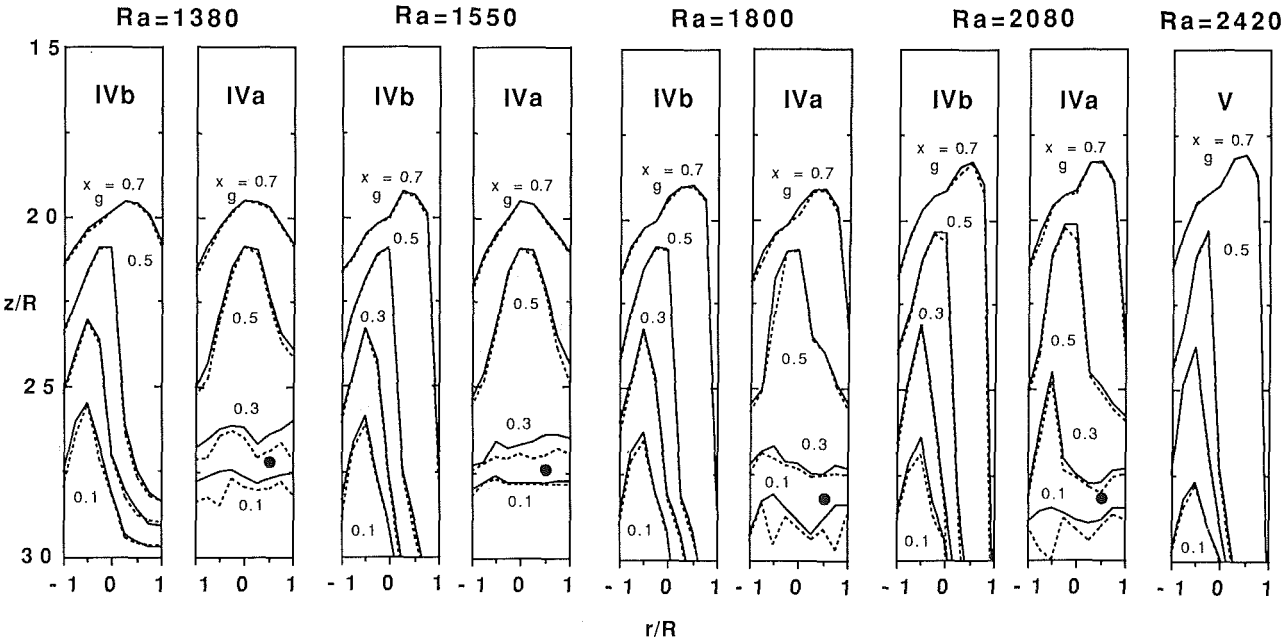

Fig. 8 Isoconcentration profiles at moderate Ra; dashed and solid curves denote minimum and maximum concentration measurements, respectively

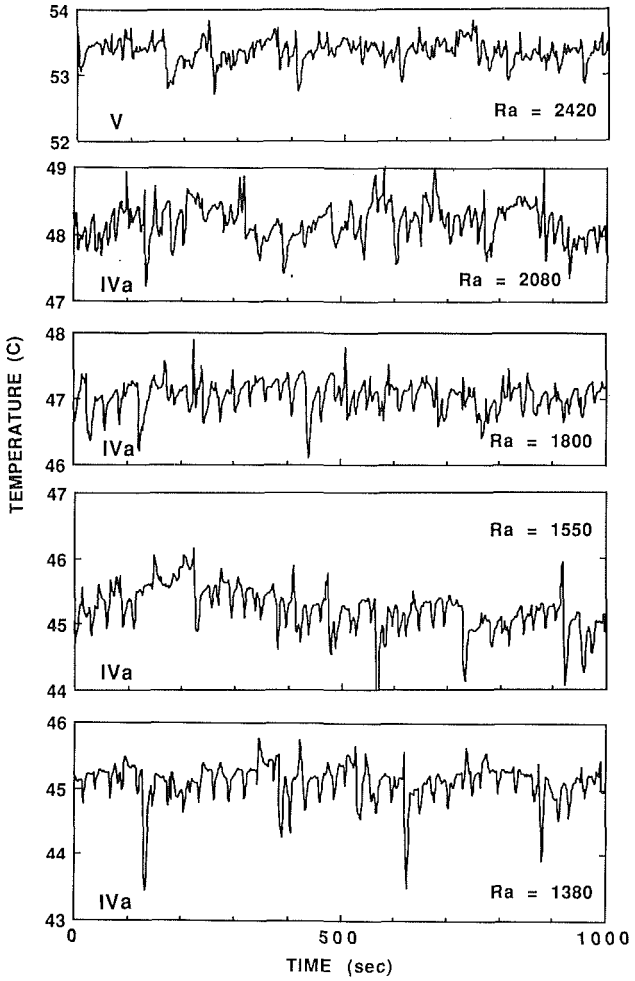

Fig. 9 Wet-bulb temperature histories at moderate Ra, recorded at points shown by circles in Fig. 8

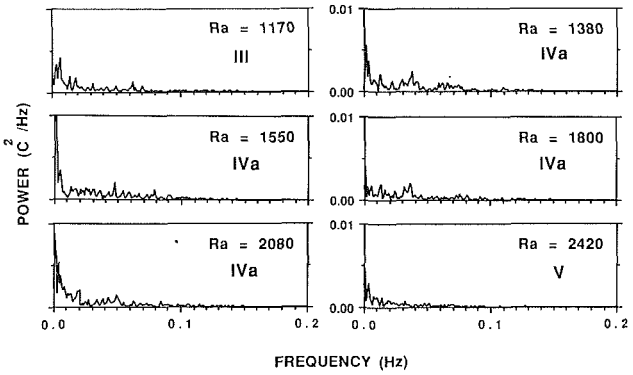

Fig. 10 Power-density spectrum at moderate Ra, measured at points shown by circles in Fig. 8

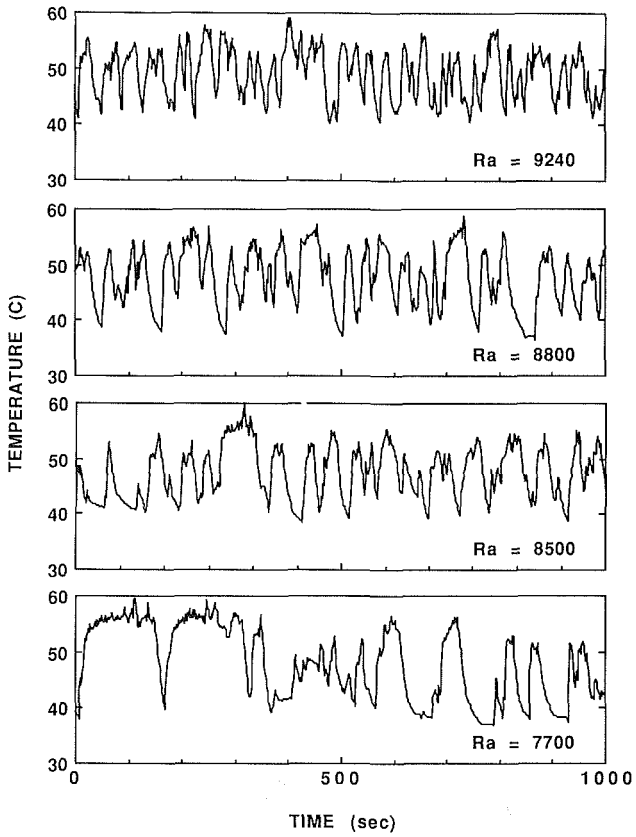

Fig. 11 Wet-bulb temperature histories at high Ra

as observed visually and by gas concentration measurement. With this small quantity of gas the maximum gas concentration in the shut-off region was $x_g = 0.47$, resulting in average Rayleigh number of Ra = 90. Figure 5 shows that the overall flow was essentially axisymmetric. Between the active and shut-off regions the lighter, decelerating vapor flowed up the centerline, as shown by the sharp peak at the center of the 0.1 isoconcentration profile. This vapor eventually diffused to the wall, and was then removed by condensation. The colder, denser gas–vapor mixture in the shut-off region flowed down along the walls, diffusing into the vapor flowing up the centerline. Thus for the very low Rayleigh numbers of regime I the gas recirculated in an axisymmetric, toroidally shaped flow, as shown schematically in Fig. 4.

Wet-bulb temperature measurements were made at 0.5-s intervals at the points indicated by circles in Fig. 5. The resulting wet-bulb time history in Fig. 6 shows that the system is slightly unstable, with the warmer vapor shooting up periodically, followed by an exponentially decaying return of the wet-bulb temperature. Similar results were found when more gas was added, increasing the Rayleigh number to Ra = 160. As seen in Table 1, this increased the maximum gas concentration in the condenser section to 0.55, and increased the instability of the flow, as shown by the temperature trace in Fig. 6. The power density spectrum information presented in Fig. 7 also reflects this trend of increasing instability.

Regime II: Ra = 250–260. When more noncondensable gas was added, increasing the Rayleigh number to Ra = 250, bifurcation to a three-dimensional asymmetric gas flow structure occurred, as indicated by the bulge in the $x_g = 0.1$ isoconcentration profile in Fig. 5. This transition stabilized the flow, as shown by the temperature trace in Fig. 6 and the power density spectrum in Fig. 7. The next addition of gas lengthened this bulge into a finger like structure. The following addition of gas raised the Rayleigh number to Ra = 500, detaching this finger and creating an island-like structure. It is important to recall that the measurements were made in an arc (Fig. 3), and thus the island seen in the isoconcentration plot is most likely the result of the probe slicing through the outside of a pocket of gas trapped against the pipe wall, below the main gas recirculation region. Creation of this pocket destabilized the gas flow, as shown by the temperature history and power density spectrum. At Ra = 620 the pocket decreased in size.

Regime III: Ra = 780–1170. At Ra = 780 the transition to a single roll cell was complete. With the 1 deg tilt of the thermosyphon, the vapor flowed up one side of the pipe and

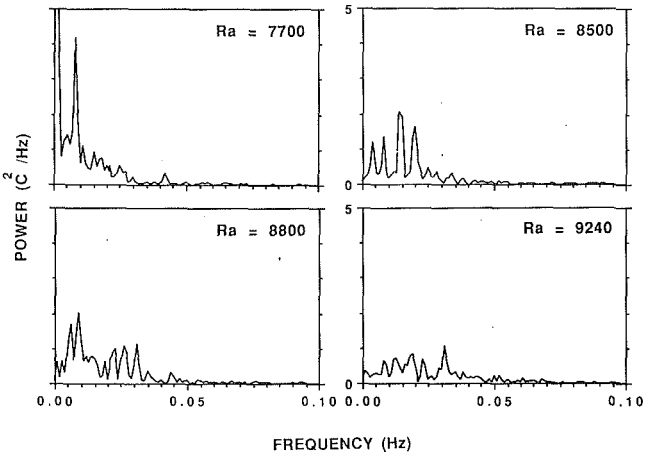

Fig. 12 Power density spectrum for the wet-bulb temperature at high Ra

condensed on the pipe wall. The roll cell became longer as the Rayleigh number increased. The temperature traces in Fig. 6 show that the gas periodically collapsed down the pipe, followed by an exponentially decaying recovery. This behavior was most prominent at Ra = 960.

Regime IV: Ra = 1380–2080. At Ra = 1380 two distinct gas flow structures were observed, as illustrated in Fig. 8. The asymmetric single-roll was quite stable (IVb), exhibiting only small fluctuations of the wet-bulb temperature. When the probe was placed in the lower right position, however, the probe disturbed the downward flowing gas, diverting some of the gas out toward the pipe centerline. This forced a rapid transition to an axisymmetric gas-flow structure (IV), also shown in Fig. 8. At this lower Rayleigh number the axisymmetric flow structure was relatively stable, persisting for as long as 40 minutes after removal of the probe before returning to the asymmetric single-roll structure. The wet-bulb temperature trace given in Fig. 9 for the axisymmetric Ra = 1380 case shows how the gas flow periodically experienced a particularly large fluctuation when an attempt to re-establish the single-roll structure occurred. The probe position in the downward flowing gas prevented re-establishment, thus maintaining the axisymmetric flow and giving the power-density spectrum presented in Fig. 10. Similar distinct axisymmetric gas flow structures persisted up to Ra = 2080, but the axisymmetric structures became increasingly unstable and degenerated more rapidly to the single-roll structure. The single-roll structure becomes longer, eventually reaching down into the adiabatic section ($z/R = 30.9$). At this point it can be argued that the aspect ratio associated with the location of the adiabatic section and the associated change of boundary conditions became important.

Regime V: Ra = 2420–7300. At Ra = 2420 the axisymmetric structure persisted for only 2 to 3 min and thus concentration plots could not be constructed. The single roll structure, as shown in Fig. 8, remained quite stable after this point, up to a relatively high value of the Rayleigh number. Concentrations measured at any point above $z/R = 27$ fluctuated by less than 2 percent. Positioning of the probe in the downward flowing gas below this point still caused instability, with a typical temperature trace for the position $z/R = 28.2$, $r/R = 0.5$ shown in Fig. 9 and power-density spectrum in Fig. 10.

Regime VI: Ra = 7700 +. When gas was added the 32nd time, giving Ra = 7700, a sudden transition to a fully unstable flow occurred. Large concentration fluctuations were observed, as well as total pressure fluctuations as high as 1.5 kPa, compared to maximum fluctuations of under 0.6 kPa at lower Rayleigh numbers. Figure 11 presents the wet-bulb temperature history for the position $z/R = 28.2$, $r/R = 0.5$. Noncondensable gas periodically began flowing down the right hand side of the pipe, causing fluctuations of the wet-bulb temperature an order of magnitude greater than at lower Ra. Figure 12 shows the power density spectrum. The strong peak at a frequency of 0.008 Hz for Ra = 7700 scales with the mass diffusion coefficient D to give length of approximately 2.5 pipe diameters. This suggests that these large fluctuations are the result of a periodic collapse from an axisymmetric gas flow structure to an asymmetric single-roll flow structure, where the single roll grows at an exponentially decaying rate governed by diffusion, as shown by the exponentially decaying drop of the wet-bulb temperature. For Ra = 7700, at some points this exponential decay of the temperature almost reaches an asymptotic limit. One potential explanation is that at a critical roll length, shear in the single-roll flow structure became too great and the roll was destroyed by a Kelvin–Helmholtz type instability in the shear layer between the falling gas and rising vapor. This instability would then have caused considerable mixing and relatively rapid re-establishment of the axisymmetric gas flow structure. At the slightly higher value Ra = 8500, the wet-bulb temperature did not decay as far before the instability occurred. However, considerable order remained in the process, with the spectral analysis of the fluctuating wet-bulb temperature showing peaks at four frequencies. Further increases in Ra caused instability to occur even earlier, creating still more rapid fluctuations, increasing noise in the spectral plots.

Summary and Conclusions

When air was added to a near-vertical (1 deg) reflux thermosyphon using water as a working fluid, a double-diffusive mixed convection flow was observed. Water vapor entered the bottom of the condenser and was removed at the walls by condensation. The air collected at the top of the condenser, riding on top of the rising column of vapor. The air circulated due to buoyancy generated by temperature and concentration gradients. Detailed measurements of the gas concentration using a miniature wet-bulb probe provided maps at the different gas flow structures present in the region between the gas and the vapor at different Ra. Unfortunately, with the apparatus used here only a highly limited range of other parameters (i.e., Re) could be explored, due to limitations on the heat input, permitting only investigation of Rayleigh number effects. At low total pressures, and thus small Rayleigh numbers, natural convection caused the gas to circulate in an axisymmetric toroidal flow, down the sides of the pipe and up the center. As the Rayleigh number was increased by adding air to the system, the torodial structure became increasingly unstable, as evidenced by periodic fluctuations of the wet-bulb temperature within the structure. At Ra = 250 the flow bifurcated to a three-dimensional structure. This bifurcation stabilized the flow, damping the fluctuations of the wet-bulb temperature. Further increases in the Rayleigh number created a pocket of gas on the pipe wall below the primary gas flow structure.

At Ra = 780 the gas flow bifurcated to a single roll cell. Beginning at Ra = 1380 distinct axisymmetric and asymmetric gas flow structures were observed. The instability of the axisymmetric structure increased with increasing Rayleigh number, with the structure collapsing to the asymmetric single roll cell. Insertion of the probe in the downward flowing gas destabilized the shear layer, returning the flow back to the axisymmetric structure. At Rayleigh numbers above 7700 a mechanism such as Kelvin–Helmholtz instability in the shear layer between the falling gas and the rising vapor destroyed the single roll structure, resulting in periodic switching between axisymmetric and asymmetric gas flows and large fluctuations of the wet-bulb temperature.

The Rayleigh–Bénard problem of natural convection in horizontal slots and rectangular enclosures provides an excellent opportunity to study bifurcation, transition, instability, and, more generally, nonlinear phenomena. The thermosyphon exhibits similar behavior that can be measured with relative ease, while introducing several new characteristics: highly nonlinear boundary conditions, forced convection flow of one species, and double diffusion. Thus the vertical two-phase thermosyphon loaded with a noncondensable gas provides an interesting extension from the simpler Rayleigh–Bénard problem. Furthermore, in design of variable-conductance heat pipes and thermosyphons, and in the evaluation of the effects of noncondensable generation and leakage in condensing systems, the distribution of the noncondensable gas has primary importance in determining condensation rates. Results presented here show that under certain conditions, bifurcating and unsteady gas recirculatory flows can occur, significantly redistributing the noncondensable gas.

References

Anderson, W. T., Edwards, D. K., Eninger, J. E., and Marcus, B. D., 1974, "Variable Conductance Heat Pipe Technology," Final Research Report, NASA CR-114750.

Bobco, R. P., 1987, "Variable Conductance Heat Pipes: A First Order Model," *Journal of Thermophysics and Heat Transfer*, Vol. 1, pp. 35–42.

Chandrasekhar, S., 1981, *Hydrodynamic and Hydromagnetic Stability*, Dover, New York.

Frick, H., and Clever, R. M., 1982, "The Influence of Side Walls on Finite-Amplitude Convection in a Layer Heated From Below," *Journal of Fluid Mechanics*, Vol. 114, pp. 467–480.

Frick, H., and Muller, U., 1983, "Oscillatory Hele-Shaw Convection," *Journal of Fluid Mechanics*, Vol. 126, pp. 521–532.

Galaktionov, V. V., and Trukhanova, L. P., 1985, "Study of the Process of Heat and Mass Transfer in the Region of the Vapor–Gas Front in a Gas-Regulable Heat Pipe," *Journal of Engineering Physics*, Vol. 48, pp. 296–300.

Gebhardt, B., Jaluria, Y., Mahajan, R. L., and Sammakia, B., 1988, *Buoyancy-Induced Flows and Transport*, Textbook Edition, Hemisphere Publishing Co., New York, pp. 699–723.

Gollub, J. P., and Benson, S. V., 1980, "Many Routes to Turbulent Convection," *Journal of Fluid Mechanics*, Vol. 100, pp. 449–470.

Hein, D., Rippel, R., and Weiss, P., 1982, "The Distribution of Gas in a U-Tube Heat Exchanger and Its Influence on the Condensation Process," *Heat Transfer 1982: Proceedings of the Seventh International Heat Transfer Conference*, Munich, Federal Republic of Germany, U. Grigull, E. Hahne, K. Stephan, and J. Straub, eds., Vol. 5, pp. 467–473, Hemisphere, Washington, DC.

Kelleher, M. D., 1976, "Effects of Gravity on Gas-Loaded Variable Conductance Heat Pipes," *Proceedings of the 2nd International Heat Pipe Conference*, Bologna, Italy, pp. 225–234.

Kobayashi, Y., and Matusumoto, T., 1987, "Vapor Condensation in the Presence of Noncondensable Gas in the Gravity Assisted Thermosyphon," *Proceedings of the Sixth International Heat Pipe Conference*, Grenoble, France, Paper No. 3.1.1.

Koster, J. N., and Muller, U., 1984, "Oscillatory Convection in Vertical Slots," *Journal of Fluid Mechanics*, Vol. 139, pp. 363–390.

Lennie, T. B., McKenzie, D. P., Moore, D. R., and Weiss, N. O., 1988, "The Breakdown of Steady Convection," *Journal of Fluid Mechanics*, Vol. 188, pp. 47–85.

Peterson, P. F., and Tien, C. L., 1987, "A Miniature Wet-Bulb Technique for Measuring Gas Concentrations in Condensing or Evaporating Systems," *Experimental Heat Transfer*, Vol. 1, pp. 1–15.

Peterson, P. F., and Tien, C. L., 1988, "Gas-Concentration Measurements and Analysis for Gas-Loaded Thermosyphons," ASME JOURNAL OF HEAT TRANSFER, Vol. 110, pp. 743–747.

Peterson, P. F., and Tien, C. L., 1989, "Numerical and Analytical Solutions for Two-Dimensional Gas Distribution in Gas-Loaded Heat Pipes," ASME JOURNAL OF HEAT TRANSFER, Vol. 111, pp. 598–604.

Peterson, P. F., and Tien, C. L., 1990, "Mixed Double-Diffusive Convection in Gas-Loaded Heat Pipes," ASME JOURNAL OF HEAT TRANSFER, Vol. 112, pp. 78–83.

Yang, K. T., 1988, "Transitions and Bifurcations in Laminar Buoyancy Flows in Confined Enclosures," ASME JOURNAL OF HEAT TRANSFER, Vol. 110, pp. 1191–1204.

Transient and Steady-State Combined Heat Transfer in Semi-Transparent Materials Subjected to a Pulse or a Step Irradiation

Tan Heping
Assistant Profeesor,
Harbin Institute of Technology,
People's Republic of China

B. Maestre

M. Lallemand
Directeur de Recherches (CNRS),

Laboratoire de Thermique,
ENSMA (URA CNRS 1403),
Poitiers Cédex, France

A numerical analysis based on the finite difference scheme and Hottel's zonal method generalized by the ray tracing method is carried out to treat the one-dimensional transient and steady-state combined radiative-conductive heat transfer in non-gray Semi-Transparent Materials (STM), especially glasses, subjected to an external pulse or a step of irradiation. Coupling problems are studied for two optical boundary conditions: opaque and vitreous interfaces with specular reflections. The influence of slab thickness, spectral properties of the STM, wavelength of the incident radiation, and diffusivity coefficient are examined. It is pointed out that the application of the laser flash method in thermal metrology may give irrelevant results if the basic heat transfer model is not able to take into account radiative-conductive coupling phenomena. The effect of semi-transparency on the steady-state temperature distribution is also examined for materials ranging from fully opaque to fully transparent.

I Introduction

The steady-state, one dimensional, radiative-conductive coupling problem in absorbing-emitting materials has received considerable attention during the past two decades. Solution techniques and results were summarized by Viskanta and Anderson (1975). In contrast, limited work has been done on the transient case (Doornink and Hering, 1972), which, for a general physical model, cannot be solved analytically, and requires numerical approaches (Siegel and Howell, 1981; Ozisik, 1973).

Recently, modeling of transient heat transfer by combined conduction-radiation-convection modes in semi-transparent materials (STM) has been presented in order to predict thermal behavior of glass at high temperature. Using Hottel's zonal method and finite difference analysis, the one-dimensional transient problem was solved for prescribed radiative-convective heat exchanges at the boundaries typically encountered in glass making (Tan, 1988; Tan and Lallemand, 1989).

This paper extends the previous problem to include: (*i*) a radiative external pulse or (*ii*) a step irradiation. The first issue is a model describing an extension to STM of the flash heating used in the determination of thermal properties of common opaque materials, and the second is a model describing thermal treatments by laser heating (annealing or tempering processes in glass). It develops the thermo-kinetics study of STM slabs, initiated by Saulnier (1980), who treated the gray body case with black boundaries. It gives an insight to thermal response of a nongray STM with vitreous reflection interfaces that are either opaque (which do not transmit radiation), or semi-transparent to infrared radiation (which transmit radiation partially in selected spectral bands). Attention is paid to incident light belonging either to the opaque spectral range or to the transparent region.

A numerical scheme is developed using a finite difference procedure to deal with the multi-reflections and angular dependency of optical properties, which are associated with Hottel's zonal method. Hottel's method, although tedious, has been chosen because of its ability to give an accurate and clear description of the various optical processes occurring in participating media as well as to take into account the medium nongray character and the nonblack properties of its interfaces.

Because of the presence of vitreous natural frontiers, spectral Extend Exchange Areas were carried out for specular multi-reflections by the ray-tracing method, which includes the fundamental features of geometric optics, in particular the total reflection phenomenon. In what follows, polarization effects and directional dependence of reflectivity, transmissivity, and emissivity factors are ignored.

In Section II the physical model and the discretized transient coupled radiative-conductive heat transfer equation are presented for various thermal and radiative boundary conditions. Section III is devoted to simulation results when a pulse of radiative flux is incident onto an STM slab. Comparisons are made between thermal responses obtained for various thicknesses, variations in absorption coefficients, and thermal diffusivity. Finally, in Section IV both transient and steady-state temperature profiles corresponding to a step irradition are discussed with reference to the spectral nature of the external radiation source.

II The Physical Model and the Discretized Energy Scheme

II.1 Physical Model. A plane parallel STM wall of emitting-absorbing (nonscattering) medium with two semi-transparent interfaces is considered (Figs. 1*a*, 1*b*, and 1*c*). The grid model used for the discretization of the simultaneous radiative, conductive, and convective heat transfer processes is also shown in Fig. 1(*a*). The STM wall is placed between two black frontiers, labeled $S_{-\infty}$ and $S_{+\infty}$, not in contact with the slab, at prescribed temperatures $T_{-\infty}$ and $T_{+\infty}$, simulating the radiative influence of the environment. It is assumed that the environmental medium is radiatively nonparticipating but may exchange heat by convection. The slab is subdivided into NM isothermal nodes labeled i ($i = 1$ and $i = \mathrm{NM}$ are associated with interfaces S_1 and S_2), which are, in the general case, either fully opaque or semi-transparent to visible and infrared radiation.

Contributed by the Heat Transfer Division for publication in the JOURNAL OF HEAT TRANSFER. Manuscript received by the Heat Transfer Division February 15, 1989; revision received April 18, 1990. Keywords: Numerical Methods, Radiation, Transient and Unsteady Transfer.

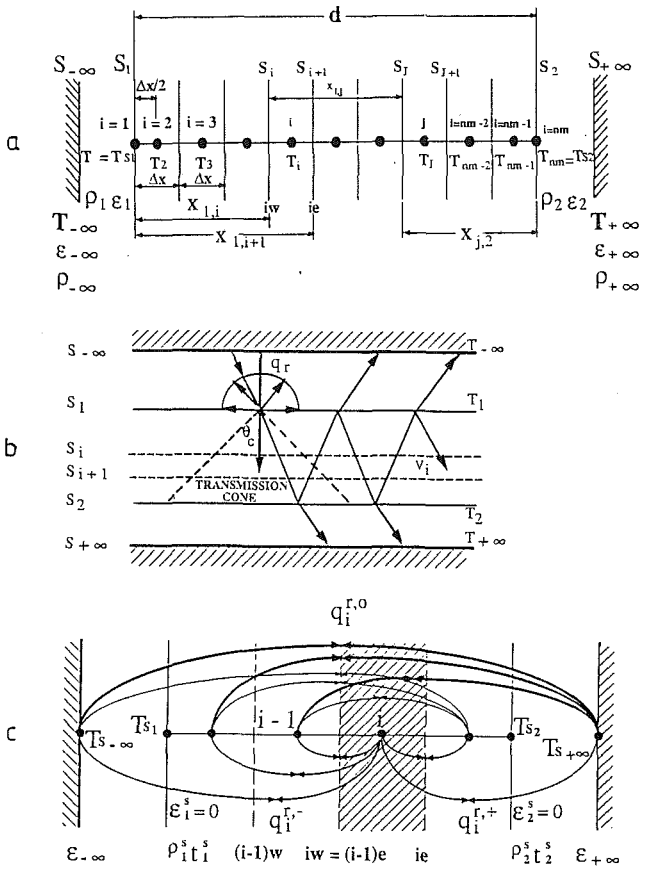

Fig. 1 *(a)* **Grid model of slab, *i*, labeled with the temperature node T_i, Δx is the thickness, and Δx_{ij} the distance between nodes *i* and *j*; *(b)* ray motion in a parallel slab of STM with semi-transparent interfaces ($t-t$), subjected to an external irradiation; (c) origin of the source term for an STM with natural semi-transparent boundaries ($t-t$); radiative interchanges between internal and external nodes are shown**

II.2 The Optical Boundary Conditions. Our objective is the modeling of thermal exchanges in semi-transparent media, especially glasses, who infrared absorption and reflection spectra are smoothly varying and may be modeled by a set of rectangular boxes (labeled k). The optical characteristics in the infrared, refractive index, reflectivity factors of interfaces, and absorption coefficient of STM slabs may conveniently be represented by four typical spectral models, labeled A, B, C, and D; Tables 1 and 2 give the spectral representations. The magnitude and variation of the optical properties in these tables are representative of typical STM materials (Hsieh and Su, 1979). Note that in Table 2, column D, for wavelengths ranging from 0.4 to 4 μm, a single band of absorption represents the semi-transparent regions whose magnitude is either 50, 100, 500, or 1500 m^{-1}. Normal spectral reflectivities are deduced from Fresnel's law when polarization effects are neglected.

In a general way energy conservation at an interface leads to the relation $t_k+\rho_k+\epsilon_k=1$ between spectral transmissivity, reflectivity, and emissivity factors. Accordingly, for an opaque boundary $\epsilon_k=1-\rho_k$ and for a semi-transparent boundary $t_k=1-\rho_k$.

The surfaces of the STM are assumed to be either coated by a medium of strong absorption index (e.g., a metallic substrate), in which case it will be called an "opaque" boundary, or in direct contact with a nonabsorbing, low refractive index dielectric medium. In this latter case it will be designated as a "semi-transparent" boundary or referred to as "natural," or for glasses with smooth interfaces, a "vitreous reflection" boundary. For natural glass there is a spectral range of nontransmission of radiation, designated as the "opacity spectral region," for which radiative energy can be exchanged externally by surface emission only.

Energy exchanges in the system under consideration are summarized as follows (see Figs. 1*b*, 1*c*):

In the semi-transparent spectral region energy is transferred simultaneously by internal radiative interchanges via multireflections and internal–external interchanges through the transmitting interface. These interchanges are interrupted by

Nomenclature

a = $\lambda_c/(\rho C_p)$ = thermal diffusivity, $m^2 s^{-1}$

$a_{k,Ti}$ = fractional spectral emissive power of spectral band k at nodal temperature Ti

Bi_1, Bi_2 = Biot number at $\xi=0$, $(h_1\delta/\lambda)$ and $\xi=1$, $(h_2\delta/\lambda)$, respectively: $\delta=d/2$

C_p = constant pressure specific heat J kg^{-1} K^{-1}

d = thickness of the slab, m

$F_k(z)$ = defined in equations (11) and (14)

Fo, Fo(Δt, Δx) = $a\Delta t/(\Delta x^2)$, the Fourier number at/d^2 or the local discretized Fourier number

h_1, h_2 = heat transfer coefficient at $\xi=0$ and $\xi=1$, respectively, $Wm^{-2}K^{-1}$

NBA = total number of spectral bands

NM = total number of nodes

N_P = $\lambda/(4d\sigma n_M^2 T_{rf}^3)$ = Planck number

$n_{k,M}$, $n_{k,rf}$ = refractive index of STM and reference, respectively, relative to the spectral band k

Op-Op = refer to two opaque boundaries

S_1, S_2 = refer to boundaries of the STM

$(S_iS_j)_k$, $(S_iV_j)_k$, $(V_iV_j)_k$ = extended exchange area relative to spectral band k

T_0 = reference temperature

T_i = nodal temperature, K

T_{rf1}, T_{rf2} = reference temperatures, K

T^* = T/T_{rf2} = dimensionless temperature

Tr-Tr = refer to two semi-transparent boundaries

t = physical time

$t_{1,k}$, $t_{2,k}$ = transmissivity of surfaces S_1 and S_2, respectively, relative to spectral band k

$t^*(d)$, $t^*(\delta)$ = dimensionless time: $t^*(d)=\text{Fo}(d)=at/(d^2)$, $t^*(\delta)=\text{Fo}(\delta)=at/(\delta^2)$, $\delta=d/2$

Δt, Δt^* = time interval and dimensionless time intervals, respectively

Table 1 Band model of the radiative properties of semi-transparent materials A and B

λ(μm)	n_k	$\rho_{k1,2}$	Spectrum A $\kappa_k(m^{-1})$	Spectrum B $\kappa_k(m^{-1})$
0.5- 2.7	1.5	0 or 0.04	10	2.5
2.7- 4.5	1.5	0 or 0.04	1000	250
4.5-40.0	2.3	0 or 0.15	10000	1250

Table 2 Band model of the radiative properties of semi-transparent materials C and D

λ(μm)	n_k*	$\rho_{k1,2}$	$t_{k1,2}$	Spectrum C $\kappa_k(m^{-1})$	Spectrum D $\kappa_k(m^{-1})$
0.4 - 2.4	1.5	0.04	0.96	50	50-1500
2.4 - 3.0	1.5	0.04	0.96	500	50-1500
3.0 - 4.0	1.5	0.04	0.96	300	50-1500
4.0 - 5.0	1.5	0.04	0.96	2500	10000
5.0 - 8.0	1.2	0.012	0	10000	10000
8.0 - 11.0	1.6	0.22	0	10000	10000
11.0 - 18.0	1.9	0.1	0	10000	10000
18.0 - 25.0	2.0	0.11	0	10000	10000
25.0 - 40.0	2.2	0.14	0	10000	10000

* Hsieh and Su (1979)

the total reflection phenomenon through a transmission cone determined by the refractive indices of the material and the environment.

In the opacity region energy is transmitted by external interchanges between the opaque emissive boundaries and the environment.

II.3 The Discretized Energy Equation Scheme. The transient one-dimensional problem of the combined conduction–radiation heat transfer in an STM slab of infinite extension subjected to an external radiation can be expressed, in dimensionless variables, for an implicit numerical scheme, as

$$T_i^{*m+1} - T_i^{*m} = \mathrm{Fo}(T_{i+1}^{*m+1} - 2T_i^{*m+1} + T_{i-1}^{*m+1}) + \mathrm{Fo}\Delta\xi\Phi_i^{*r,m+1}/N_P \quad (1)$$

Equation (1) is a well-known discretized form of the conduction equation, in which a local source term (see Fig. 1*c*) resulting from (*a*) the distant radiative interchanges between that particular node and all others, and (*b*) energy absorption of the external light beam, is added at node *i*.

II.4 The Thermal Boundary Conditions. It is assumed that a collimated square pulse flash or step flux is impinging at normal incidence on the foreface S_1 of an STM slab, with duration t_{flash}. Thus the initial boundary condition is

$$\begin{aligned} q_{\mathrm{flash}} &= \mathrm{const} \quad \text{for} \quad t \le t_{\mathrm{flash}} \\ q_{\mathrm{flash}} &= 0 \quad\quad \text{for} \quad t > t_{\mathrm{flash}} \end{aligned} \quad (2)$$

In the presence of internal conductive, radiative exchanges and external interchanges by convection and radiation between the sample and the surroundings, the conservation of energy principle leads to the general thermal boundary condition at S_1

$$q^r_{s1\to s-\infty} - \epsilon_{1,\lambda=\lambda\mathrm{flash}} q_{\mathrm{flash}} + q^{\mathrm{convection}} = q^{\mathrm{conduction}} + q^r_{s1} \quad \text{when } t \le t_{\mathrm{flash}} \quad (3a)$$

$$q^r_{s1\to s-\infty} + q^{\mathrm{convection}} = q^{\mathrm{conduction}} + q^r_{s1} \quad \text{when } t > t_{\mathrm{flash}} \quad (3b)$$

The first two terms on the left-hand side of equation (3*a*) are, respectively, the radiative flux density exchanges at the boundary S_1 with the surroundings, and the fraction of the external radiative flux of wavelength λ_{flash} absorbed by the boundary for the corresponding band of emissivity $\epsilon_{\lambda=\lambda\mathrm{flash}}$. The third term is the heat flux convected between the outside and the surface S_1, which may be expressed by means of a heat exchange coefficient. On the right-hand side of equation (3*a*) the first term is the conduction contribution expressed by

Nomenclature (cont.)

x_{ij} = distance separating node i from node j
Δx = uniform internodal distance
δ = half thickness of slab
$\epsilon_{1,k}$, $\epsilon_{2,k}$ = emissivity of surfaces S_1 and S_2, respectively, relative to spectral band k
$\epsilon_{-\infty}$, $\epsilon_{+\infty}$ = 1 = emissivity of surfaces $S_{-\infty}$ and $S_{+\infty}$, respectively
κ_k = absorption coefficient relative to spectral band k, m^{-1}
λ_c = phonic thermal conductivity, $\mathrm{Wm}^{-1}\mathrm{K}^{-1}$
λ_f = wavelength of radiant energy
λ_k = wavelength of kth spectral band
μ_c = cos θ_c; θ_c is critical angle of reflection
ξ, $\Delta\xi$ = dimensionless distance and dimensionless spatial intervals; $\xi = x/d$, $\Delta\xi = \Delta x/d$
ρ = density, kg m^{-3}
$\rho_{1,k}$, $\rho_{2,k}$ = reflectivity of surfaces S_1 and S_2, respectively, relative to spectral band k
σ = Stefan–Boltzmann constant
τ_k, $\tau_{o,k}$ = optical depth and optical thickness, respectively, relative to spectral band k
Φ^r_i = radiative source at node i
Φ^{*r}_i = $\Phi^r_i/(4\sigma n_M^2 T_{rf}^4)$ = dimensionless radiative source at node i

Superscripts

c, r, t = refer to conduction, radiation, and total, respectively
s = refer to specular reflection

Subscripts

1, 2 = refer to boundary S_1 and S_2, respectively
$-\infty$, $+\infty$ = refer to boundary $S_{-\infty}$ and $S_{+\infty}$, respectively
fl = refer to flash
$t-t$ = refer to an STM slab with two semi-transparent interfaces
$o-o$ = refer to an STM slab with two opaque boundaries

Fourier's law, and the last term is the local radiative internal flux energy at the boundary S_1. At the opposite boundary, S_2, energy balance is expressed by equation (3*b*), which is the same as equation (3*a*) with q_{flash} set equal to zero.

If the STM slab is in contact with opaque boundaries, the nondimensional form of equation (3*a*) in terms of Hottel's zonal method can be written as

$$\sum_{k=1}^{\text{NBA}} \epsilon_{1,k} n_{k,rf}^2/(4n_{k,M}^2 N_P)\{a_{k,Ts1}T_{s1}^{*4} - a_{k,Ts-\infty}T_{s-\infty}^{*4}\} + 2\text{Bi}_1(T_{s1}^* - T_{s\infty}^*) - \epsilon_{1,\lambda=\lambda\text{flash}} q_{\text{flash}}^*/N_P = q_{s1}^{*r}/N_P + 2(T_2^* - T_{s1}^*)/\Delta\xi \quad (4)$$

with

$$q_{s1}^{*r} = \sigma \sum_{k=1}^{\text{NBA}} n_{k,M}^2 \{\epsilon_{1,k}(S_1S_2)_k(a_{k,Ts2}T_{s2}^4 - a_{k,Ts1}T_{s1}^4 + \sum_{j=2}^{\text{NM-1}} \epsilon_{1,k}(S_1V_j)_k(a_{k,Tj}T_j^4 - a_{k,Ts1}T_{s1}^4)\}/(4\sigma n_M^2 T_{rf}^4) \quad (5)$$

In equations (4) and (5), the summations incorporate the total number of participating bands, NBA. When the boundaries are natural or semi-transparent, the thermal boundary conditions remain of the same form. In fact, there is no internal radiative transfer in the opacity zone and no contributions from the transparent surfaces. Also, the energy absorbed from the external source, $\epsilon_{1,\lambda\text{flash}}\, q_{\text{flash}}$, is set equal to zero if λ_{flash} belongs to the semi-transparent region, because of the null surface absorptivity in this spectral range. Furthermore, in this case, the radiative energy between internal nodes and environmental nodes $S_{-\infty}$, $S_{+\infty}$, contained in the transmission cone, is conserved when crossing the transparent interface of the two media.

II.5 The Radiative Source Term. In the more general case of semi-transparent boundaries, the radiative local source term, Φ_i^r, at the node i, in equation (1) is composed of two contributions

$$\Phi_i^r = \Phi_i^{r,\text{int}} + \Phi_i^{r,\text{ext}} \quad (6)$$

where for nonisothermal condition, $\Phi_i^{r,\text{int}}$, is the internal component, which is equal to the difference between the incoming and the outgoing radiative flux at node i, of thickness Δx, as shown in Fig 1(*b*). Thus

$$\Phi_i^{r,\text{int}} = \sigma \sum_{k=1}^{\text{NBA}} n_{k,M}^2 \{[(V_iS_{+\infty})_{k,t-t}^s(a_{k,Ts+\infty}T_{s+\infty}^4 - a_{k,Ti}T_i^4)] + [(V_iS_{-\infty})_{k,t-t}^s(a_{k,Ts-\infty}T_{s-\infty}^4 - a_{k,Ti}T_i^4)] + \sum_{j=2}^{\text{NM}-1} [(V_iV_j)_{k,t-t}^s(a_{k,Tj}T_j^4 - a_{k,Ti}T_i^4)]\} \quad (2 \le i \le \text{NM}-1) \quad (7)$$

The second component, $\Phi_i^{r,\text{ext}}$, is due to the absorption within the control volume of the transmitted external irradiation

$$\Phi_i^{r,\text{ext}} = q_{\text{flash}}\, t_{1,\lambda=\lambda\text{flash}}^s [(1 - e^{-\kappa_{\lambda=\lambda\text{flash}}\Delta x}) \cdot (e^{-\kappa_{\lambda=\lambda\text{flash}}x_{1,i}} + \rho_{2,\lambda=\lambda\text{flash}}^s\, e^{-\kappa_{\lambda=\lambda\text{flash}}(d+x_{2,i+1})})] / [1 - \rho_{1,\lambda=\lambda\text{flash}}^s\, \rho_{2,\lambda=\lambda\text{flash}}^s\, e^{-2\kappa_{\lambda=\lambda\text{flash}}d}] \quad (8)$$

Note that $\Phi_i^{r,\text{ext}} = 0$ if the wavelength of the external radiation does not belong to the spectral semi-transparent region of the medium.

The various terms $(V_iS_{-\infty})_{k,t-t}^s$, $(V_iS_{+\infty})_{k,t-t}^s$, and $(V_iV_j)_{k,t-t}^s$ in expressions (5) and (7), designate in Hottel and Sarofim's terminology (Hottel and Sarofim, 1967), the spectral Extended Exchange Area, EEA, in the presence of specular multi-reflections (superscript *s*), and for transparent interfaces (subscript $t-t$). The first two terms are associated with radiative spectral interchanges, between an internal node of volume V_i and the nodes of external environmental surfaces $S_{-\infty}$ or $S_{+\infty}$, respectively; the last term represents the EEA between two nodal volumes V_i and V_j. They may take several different mathematical forms, according to the mode of reflection, metallic or vitreous, specular or diffuse. Each of the three bracketed terms in equation (7) represents the net monochromatic energy exchange between two nodes. For example, diagrammatic representations of $(S_{-\infty}S_{+\infty})_{k,t-t}^s$, $(S_{-\infty}S_i)_{k,t-t}^s$ and $(V_iS_{-\infty})_{k,t-t}^s$ are shown in Fig. 2 for specular reflection where the various optical paths are depicted according to the optical phenomena occurring at the interface.

For transparent-transparent boundaries, it is assumed that for the rays contained in the transmission cone, the spectral transmissivity, t_k, is independent of the incident angle. For this case the EEA associated with V_i and $S_{-\infty}$ or $S_{+\infty}$ through the interface S_1 or S_2 can be written for specular reflection as (see Appendix A)

$$(V_iS_{-\infty})_{k,t-t}^s = 2t_{1,k}^s[F_k(\kappa_k x_{1,i} - F_k(\kappa_k x_{1,i+1}) + \rho_{2,k}^s F_k(\kappa_k d + \kappa_k x_{2,i+1}) - \rho_{2,k}^s F_k(\kappa_k d + \kappa_k x_{2,i})]_{\mu c}^1 \quad (9)$$

$$(V_iS_{+\infty})_{k,t-t}^s = 2t_{2,k}^s[F_k(\kappa_k x_{i+1,2}) - F_k(\kappa_k x_{i,2}) + \rho_{1,k}^s F_k(\kappa_k x_{i,1} + \kappa_k d) - \rho_{1,k}^s F_k(\kappa_k x_{i+1,1} + \kappa_k d)]_{\mu c}^1 \quad (10)$$

where the function $[F_k(z)]_{\mu c}^1$ is defined by

$$[F_k(z)]_{\mu c}^1 = \int_{\mu c}^1 (\mu e^{-z/\mu})/[1 - \rho_{1,k}^s \rho_{2,k}^s e^{-2\tau_{o,k}/\mu}]d\mu \quad (11)$$

with $\tau_{o,k} = \kappa_k d$ as the spectral optical depth for the band k. In equation (11) integration with respect to μ is carried out taking into account the existence of the critical angle θ_c of total reflection. Thus

$$\mu_c = \cos\theta_c = [1 - (n_{rf}/n_M)^2]^{1/2} \quad (12)$$

Equations (9) and (10) account for both transmission and attenuation of the rays within the transmission cone.

The detailed expressions for the EEA $(V_iV_j)_{k,t-t}^s$ have already been found by Tan and Lallemand (1989) in terms of the function $[F_k(z)]_{\mu c}^1$ (equation (11)), and of the function $[F_k(z)]_0^{\mu c}$ associated with the total reflection defined by

$$[F_k(z)]_0^{\mu c} = \int_0^{\mu c} (\mu e^{-z/\mu})/[1 - e^{-2\tau_{o,k}/\mu}]d\mu \quad (13)$$

which has the same integrant as equation (11) except than $\rho_{1,k}^s$ and $\rho_{2,k}^s$ are set equal to one.

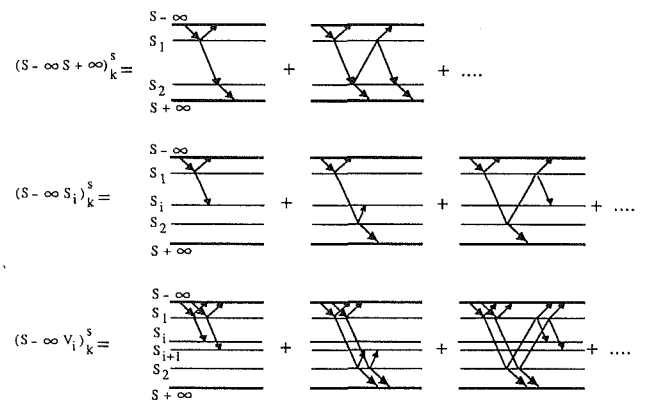

Fig. 2 Diagrammatic representation of the EEA terms $(S_{-\infty}S_{+\infty})_{k,t-t}^s$, $(S_{+\infty}S_i)_{k,t-t}^s$ and $(S_{+\infty}V_i)_{k,t-t}^s$ for vitreous reflection. $S_{+\infty}$, S_1, S_i designate environment surface, sample interface, and internal nodal surface, respectively. The various terms in the sums correspond to single transmission, transmission after two internal reflections, etc.

II.6 The Numerical Treatment. The combined conductive–radiative–convective one-dimensional problem just described with its full nonlinear feature is solved numerically. At each control volume the source term (6) is set equal to the sum of a constant term and a nonlinear function of the local nodal temperature. Furthermore radiative losses at boundaries are also of nonlinear form. A convenient numerical procedure proposed by Patankar (1980) was used to solve the problem iteratively for each time step. For more technical details of the numerical scheme the reader may refer to Tan (1988) and Tan and Lallemand (1989).

III Results of the Modeling for a Flash Irradiation

In this section, except when otherwise noted, samples initially in thermal equilibrium are heated in vacuum to an initial temperature $T_0 = 1000$ K. Thus, convective losses can be neglected. The environmental temperatures $T_{-\infty}$ and $T_{+\infty}$ are also maintained at 1000 K. At time $t = 0$ the sample is impressed by an infrared radiative pulse normal to its surface. This causes the temperature to rise and then drop when the slab returns toward thermal equilibrium due to radiative energy loss to the surroundings.

III.1 Comparison of Thermograms Obtained for an STM and an Opaque Slab With Black Boundaries. The modeling can be used to illustrate the difference in chronological thermograms of two specimens of the same thermal characteristics: One is opaque, for which internal heat transfer is due to conduction mode only, and the other is semi-transparent (Table 1, spectrum A) in which a combined mode of heat transfer evolves. Both are recovered with a nontransmitting black coating. The two materials have a thermal diffusivity $a = 6.82 \cdot 10^{-7} \mathrm{m}^2 \cdot \mathrm{s}^{-1}$, corresponding to a glass of thermal conductivity 1.5 $\mathrm{W} \cdot \mathrm{m}^{-1} \cdot \mathrm{K}^{-1}$. In this example for each specimen two thicknesses are selected: 0.5 and 1 cm. The normal incident radiant energy is a one second square pulse of 50 $\mathrm{KW} \cdot \mathrm{m}^{-2}$.

Thermal responses, $(T(t) - T_o)$, of the irradiated face and the opposite face for the two slabs are shown in Fig. 3. It is seen in Fig 3(*a*) that the temperature rise is higher for the irradiated face of the opaque material (conduction only) than for the STM slab with black boundaries (coupled radiation–conduction). This results from the fact that in the first sample, pulse energy is deposited at the boundary, while for the second sample, it is immediately transmitted throughout (the external radiative losses being of the same order in both cases). Comparison of thermograms for the 0.5 and 1 cm slabs shows little influence of the thickness in the case of the pulse side for pure conductive materials as well as for the STM.

The temperature evolution of the nonirradiated surface is illustrated in Figs. 3(*b*) and 3(*c*). For the STM material two peaks are observed in contrast to a single peak for the pure conductive material. For the former, the first peak occurs very early, while the second peak appears at a time scale corresponding to that of a poorly conductive sample. Dissimilarities between the shape of the two thermal responses, conductive (*C*) and conductive-radiative ($R + C$) are striking; temperature rise is of a higher level for the STM than for the opaque material (0.4 K) and its maximum is reached earlier, due to the enhanced transfer of energy in STM. For a given external irradiation energy, the effect of an increase in the sample thickness is to decrease the maximum of the thermograms significantly for both the STM and the opaque sample except for the first peak. The thermal responses shown in Figs. 3(*b*) and 3(*c*) indicate little difference in the tail shape of the two materials.

The presence of a discontinuity in the temperature of the irradiated surface, which coincides with the end of the pulse application, is observed in Fig. 3(*a*). In Figs 3(*b*) and 3(*c*), for the STM sample with opaque surfaces, the first peak corresponds to a direct radiative heat transfer from the hot face to the opposite face, followed by a radiative cooling of the rear face after the release of irradiation. This effect was first recognized by Saulnier (1980) by simulations of the one-dimensional coupling problem for gray walls with black boundaries.

In contrast with these results, calculations for the central node of the slabs show little difference in the thermograms for opaque and semi-transparent media.

III.2 Comparison of Thermograms for STM Slabs With Opaque or Semi-Transparent Boundaries

1 Irradiation Belonging to the Opacity Range Wavelength. Thermograms of the irradiated and nonirradiated faces corresponding to a 1-cm-thick slab of either opaque material or semi-transparent material with transparent interfaces (Table 1, spectrum A), illuminated for 1 s by a 500 $\mathrm{kW} \cdot \mathrm{m}^{-2}$ beam of wavelength in the opaque range (typically, for silicate glass it can be produced by a CO_2 laser) are represented in Figs. 4(*a*) and 4(*b*). These systems differ radiatively by the optical properties of the bulk and of the boundaries, being either fully opaque (*o-o*) with reflectivity factors, $\rho_{k1,2}$, for the three-band model, given by Table 1, or with vitreous reflection ($t - t$) with the same reflectivity spectrum.

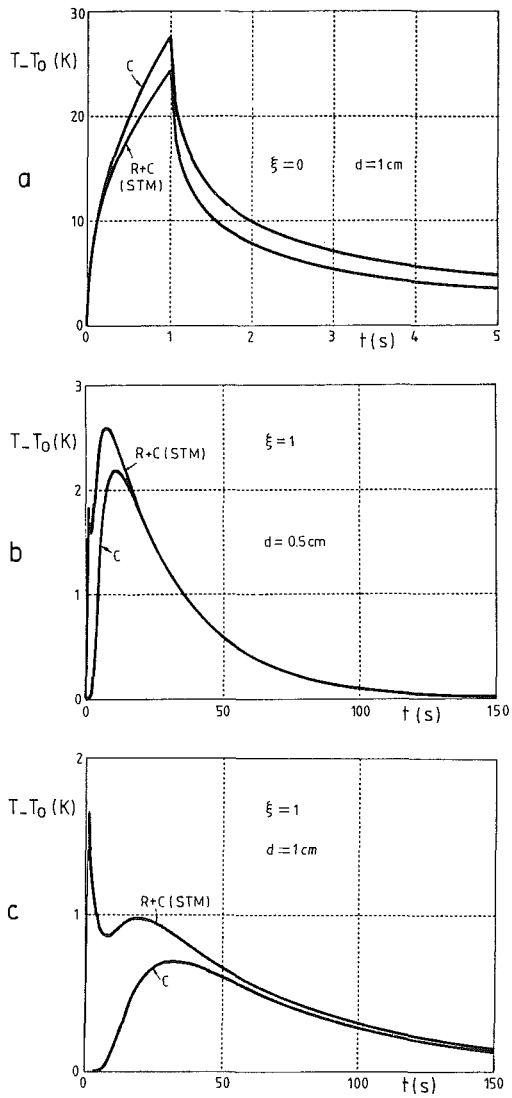

Fig. 3 Comparison of thermograms of STM with two opaque black boundaries and an opaque material of same value of thermal diffusivity irradiated by a pulse 50 $\mathrm{kW} \cdot \mathrm{m}^{-2}$ during 1 s: (*a*) irradiated face; (*b*) and (*c*) nonirradiated face for different sample thicknesses. (*C*) conduction only, ($R + C$) radiative-conductive coupling.

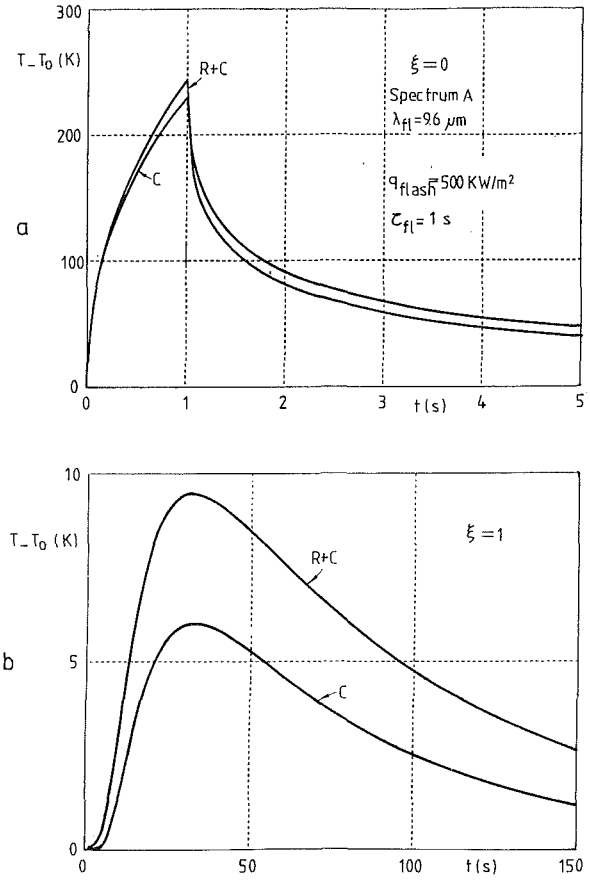

Fig. 4 Comparison of thermograms (*a*) at the fore face and (*b*) the rear face, of an opaque material and a STM of same thicknesses (1 cm), same thermal diffusivity, same reflectivity spectrum and incident radiation from the opaque spectral region, $\lambda_{flash} = 9.6$ μm; (*C*) pure conduction, (*R*+*C*) radiative-conductive coupling; energy power: 500 kW•m^{-2}, duration of pulse: 1 s

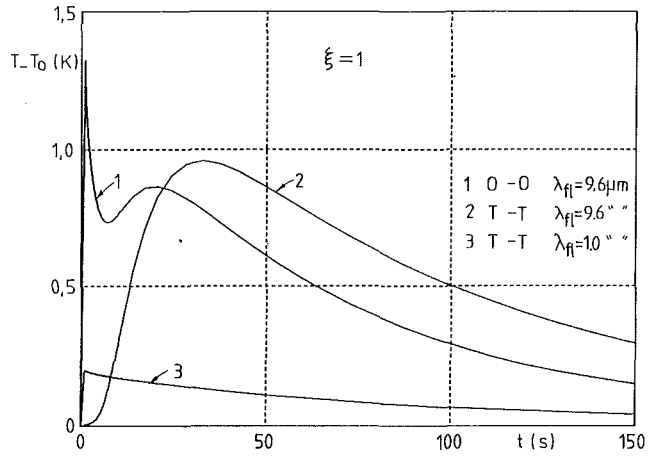

Fig. 5 Thermograms of the nonirradiated face generated by laser pulses of wavelength belonging to different spectral absorption bands of the STM and for various radiative boundary conditions; energy power: 50 kW•m^{-2}, duration of pulse: 1 s

As shown in Fig. 4(*a*), in contrast with results discussed in Section III.1, the irradiated surface reaches higher temperatures for the STM wall than for the opaque one. In fact, external radiative losses are of less importance for the conductive–radiative coupling due to the presence of the two semi-transparent poorly participating bands.

Thermograms of the rear faces are plotted in Fig. 4(*b*). They display comparable shapes for both walls, although the STM slab has a higher temperature maximum (9.5 K in place of 6.1 K), as well as a higher positive slope. Note the absence of the first peak for this STM sample. This is due to the fact that neither the semi-transparent interface nor the opaque one are able to re-emit heat by internal radiative transfer.

The thermal responses of the two STM samples, with previously mentioned radiative interface characteristics ($o-o$ and $t-t$), obtained with an irradiation source pulse in the opacity region, are presented in Fig. 5 for an energy flux of 50 kW/m^2. For the ($o-o$) boundaries sample it is observed that the position of the second peak occurs earlier than the single peak of the STM slab with ($t-t$) boundaries. This more efficient heating of the slab interior for the sample with opaque-opaque frontiers can be explained by the radiative participation of the boundaries in the semi-transparent spectral range.

2 Irradiation in the Semi-Transparent Range Wavelength. Thermal chronological response of the rear face of an STM slab with ($t-t$) boundaries heated by a laser pulse of the same energy and duration as above, but whose wavelength corresponds to the semi-transparent range of the material (typically a laser YAG radiation) is also presented in Fig. 5. For a poorly absorbing region of the glass spectrum (10 m^{-1}), the temperature rise is small compared with the previous thermograms (0.2 K instead of 0.95 K). In this case the maximum is reached at the end of the pulse. This demonstrates and quantifies the efficiency of heating an STM like glass with natural interfaces using an incident beam belonging to the opaque spectral range of the material, i.e., by a high surface absorption process, in comparison with the poor heating by radiation in the semi-transparent spectral region, which is mainly the result of energy absorption by the bulk.

III.3 Sensitivity of the Chronological Thermograms to Absorption Spectra. Another three-band model of the STM was introduced (Table 1, spectrum B) in order to test the sensitivity of the transient thermal response for different spectral properties of two slabs of the same thickness (1 cm) whose interfaces are considered black and are subjected to a 50 kW•m^{-2} energy square pulse of 1 s. The main difference in the two responses at the rear face was, at early times, a lowering of the thermogram (0.1 K) of the more opaque material, and a slight delay of its maximum.

III.4 Sensitivity of the Thermograms of an STM to Thermal Diffusivity. In order to test the thermal responses of STM walls to thermal diffusivity, a 1-cm-thick slab of spectrum A with natural semi-transparent boundaries ($t-t$) was studied for an incident radiant energy flux of wavelength in the range of the opacity region. Values of the thermal conductivity between 0.5 and 3 W•m^{-1}•K^{-1} represent the upper bound of variation range to be expected for silicate glasses when temperature effects on thermal conductivity are considered. In this case, energy loss to the environment is by radiation and convection. The convective heat transfer coefficients on the two faces, h_1 and h_2, are assumed to be 15 W•m^{-2}•K^{-1}. In Fig. 6 are displayed the different thermograms for the nonirradiated face. It is observed that the well-known behavior for opaque media is still recovered; in particular the more conducting material has the higher maximum and the faster response. Furthermore, the level of the maximum temperature is sensitive to the value of the thermal conductivity. This offers the possibility of using the response of an STM to identify the thermal diffusivity.

Differences observed in the thermal behavior of the 1.5 W•m^{-1}•K^{-1} thermal conductivity sample (i.e., between thermograms shown in Figs. 5 and 6, curve 2, with $h=0$) indicate the sensitivity of the thermograms against the convective losses.

III.5 Temperature Profiles. The temperature profiles

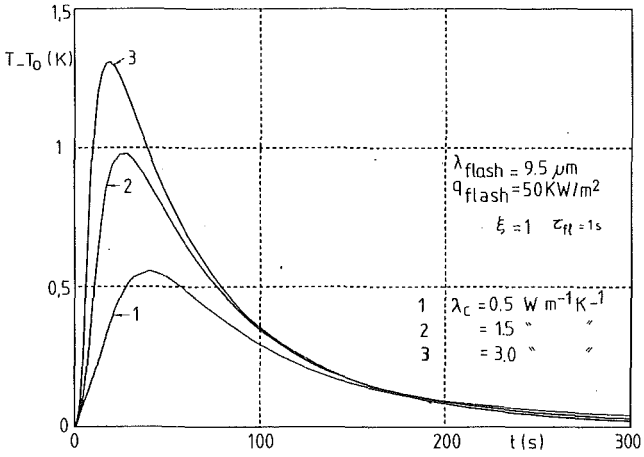

Fig. 6 Sensitivity of the thermograms to thermal diffusivity coefficients for a 1 s, 50 kW•m^{-2} square pulse (in the presence of convection) for a 1-cm-thick slab of STM with two ($t-t$) boundaries

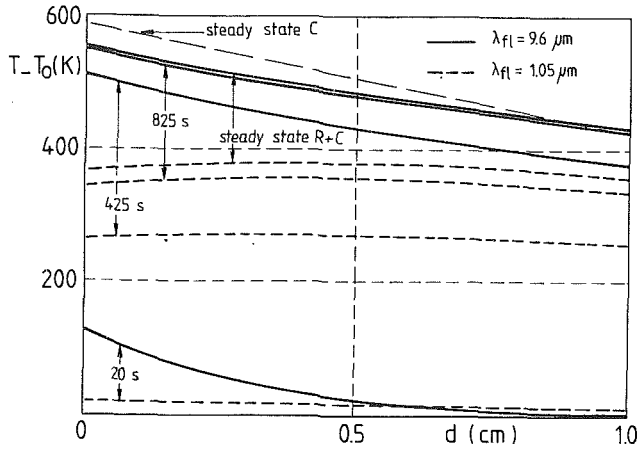

Fig. 8 Temperature profiles at various times in a 1-cm-thick slab of STM (Spectrum C) irradiated by a 1.05 μm and a 9.6 μm step of flux of 50 kW•m^{-2}: comparison with results for an opaque slab with black boundaries

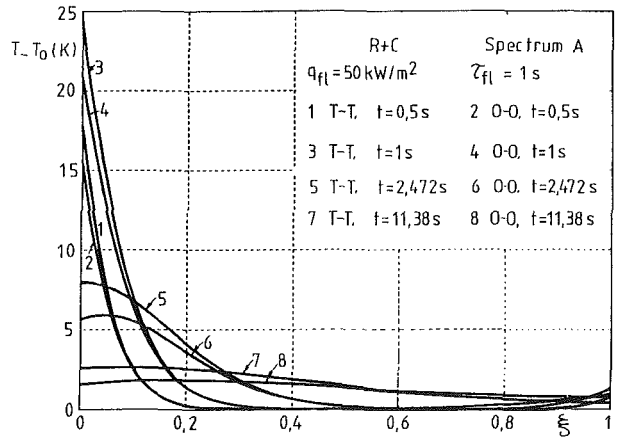

Fig. 7 Comparison of temperature profiles at various times generated by a laser square pulse of energy power 50 kW•m^{-2} during 1 s (λ_{flash} = 9.6 μm) within STM slabs with two semi-transparent frontiers ($t-t$) and two opaque boundaries ($o-o$)

generated by a square pulse of irradiation of 50 kW•m^{-2} during 1 s (of wavelength belonging to the opacity region) are reported in Fig. 7, at various times, for an STM slab of thickness 1 cm. Two radiative boundary situations are considered, one with natural interfaces and the other coated with an opaque black substance. The similarity of the isochronal temperature distributions with the opaque material case is noted. In particular at early time ($t=1$ s) the temperature decreases monotonically toward the back face. However, as previously mentioned, the ($t-t$) temperature distribution case is still found above the ($o-o$) temperature profile. Furthermore an increase of the temperature in the vicinity of the nonirradiated surface is observed for the sample fitted with opaque boundaries and, as a consequence, at intermediate times there exists a minimum in its temperature distribution.

IV Transient and Steady-State Temperature Profiles in a Slab of STM Irradiated by a Step of External Flux

A step of collimated monochromatic radiation of 50 kW•m^{-2} is used to irradiate, at normal incidence, one of the faces of an STM slab of 1 cm thickness with natural boundaries. The source wavelength is either 1.05 μm or 9.6 μm infrared radiation. The external temperature is fixed at $T_0=300$ K. Since $T_{-\infty}$ and $T_{+\infty}$ are less than internal node temperature, the STM slab releases heat by radiation by both faces, but convective losses are neglected.

IV.1 Transient Response. The optical properties of the medium are composed of nine bands (see Table 2, spectrum C).

The resulting temperature profiles are displayed in Fig. 8 at several times and compared to the pure conductive case of an opaque slab with black radiative boundaries.

For an irradiation at the wavelength of 1.05 μm (the corresponding absorption coefficient of the STM for this band is 50 m^{-1}) all temperature profiles, appear to be nearly flat. This is due to a quasi-uniform absorption in the bulk by the 50 m^{-1} band accompanied by radiative cooling at the frontier occurring in the opacity range. Results from other tests, not reported here, indicate that the STM wall becomes more and more isothermal as the absorption coefficient of the semi-transparent band decreases. In such situations the radiative-conductive heat transfer may be represented by a simplified model neglecting the internal conductive resistance.

When the slab is irradiated with a 9.6 μm incident infrared step flux, temperature profiles are very close to those of the conductive case but with a slight curvature whose concavity is of opposed sense with respect to the previous case.

In another case, not shown here, the same slab was irradiated with a step function beam originating from a black body at 969 K (corresponding to a 50 kW•m^{-2} flux). The resulting temperature profiles have been found to be similar to those obtained for the 9.6 μm irradiation but with a smaller slope. This can be explained by the fact that the major part of the incident flux is absorbed by the surface in the opacity spectral region or by the layers in the vicinity of the boundary. However, a small fraction of this energy is also absorbed by the bulk.

IV.2 Steady-State Temperature Profiles. In Fig. 9 are shown the steady-state temperature profiles for a slab of STM, which is optically characterized by a seven spectral band model (see Table 2, spectrum D), with only one band in the range of semi-transparency (0.4 μm $<\lambda<$ 4.0 μm). The influence of this band on the heat transfer, when the slab is irradiated with a 1.05 μm wavelength beam, can be examined by varying the magnitude of its absorption coefficient in the interval 50 m^{-1} $<\kappa_k<$ 1500 m^{-1}. For low values of κ_k, one observes the flat steady-state temperature profiles already described in Fig. 8. When the absorption coefficient is increased, the gradual increase of the absorbed radiative energy is accompanied by a comparable rising of the temperature profiles. For a photon mean free path greater than the slab's thickness, the energy is quasi-uniformly distributed. For a photon mean free path lower

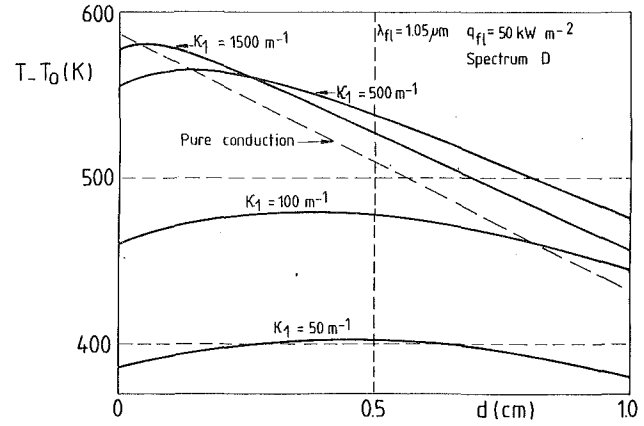

Fig. 9 Steady-state temperature profiles in a 1-cm-thick STM slab irradiated by a 1.05 μm wavelength step of flux for a (0.4–4 μm) semi-transparent band model of variable absorption coefficient (spectrum D): comparison with results for an opaque slab with black boundaries

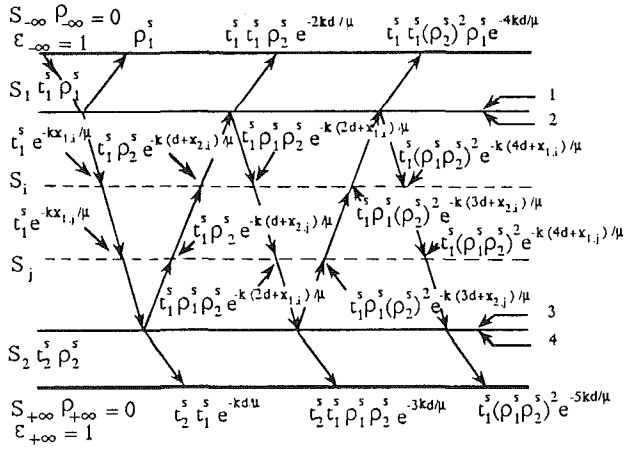

Fig. 10 Derivation of the EEA between surface and volume by ray-tracing for specular multi-reflections

than the thickness, the hot zones are closer to the impact boundary and the location of the temperature maximum is shifted toward that boundary.

V Conclusion

The present numerical analysis of the coupled conductive-radiative heat transfer in STM slabs (especially glass), illuminated by external collimated radiative pulse, enables us to simulate the temporal temperature responses of these systems in a high-temperature environment. The transient thermal behavior is found to be different for opaque and semi-transparent media due to the more complex mechanisms of dissipation. Furthermore, it depends on the nature of the absorption spectrum and on the thickness of the slab. Applications of this approach to determine the thermal diffusivity of an STM at high temperatures require precise experimental determination of the thermograms due to the extreme sensitivity of the temperature responses to convective and radiative losses. Furthermore, a three-dimensional analysis of the radiative energy interchanges of the sample device with a high thermal gradient environment is required.

Thermograms of STM slabs with natural interfaces can be generated by a laser beam operating in the long wavelength opacity range. The sensitivity of the responses against variations of the thermal diffusivity should allow experimental determination of this quantity by conventional laser pulse technique in hot glass and vitreous melts. An efficient identification algorithm for the determination of the diffusivity should first be developed.

Description of the thermal behavior of a glass slab irradiated by infrared step function has shown different internal thermal distributions depending on the spectral range of the incident radiation, ranging from a uniform temperature to one with high temperature gradients. Thus, the modeling of a coupled radiative-conductive-convective heat exchange may serve as a guide for adaptive heating or cooling processes of glass materials undergoing heat treatment.

Acknowledgments

The authors are grateful to Professor L. Jiji of City College of New York for critical reading.

References

Doornink, D. G., and Hering, R. G., 1972, "Transient Combined Conductive and Radiative Heat Transfer," ASME JOURNAL OF HEAT TRANSFER, Vol. 94, pp. 473–478.

Hottel, H. C., and Sarofim, A. F., 1967, *Radiative Transfer,* McGraw-Hill, New York.

Hsieh, C. K., and Su, K. C., 1979, "Thermal Radiative Properties of Glass From 0.32 to 206 μm," *Solar Energy,* Vol. 22, pp. 37–43.

Ozisik, M. N., 1973, *Radiative Transfer and Interaction With Conduction and Convection,* Wiley, New York.

Patankar, S. V., 1980, *Numerical Heat Transfer and Fluid Flow,* McGraw-Hill, New York.

Saulnier, J. B., 1980, "La modélisation thermique et ses applications aux transferts couplés et au contrôle actif," Thèse de Doctorat d'Etat, Université de Poitiers, France.

Siegel, R., and Howell, J. R., 1981, *Thermal Heat Transfer,* 2nd ed., McGraw-Hill, New York.

Tan, H. P., 1988, "Transfert couplé rayonnement-conduction instationnaire dans les milieux semi-transparents à frontières opaques on naturelles soumis à des conditions de température et de flux," Thèse de Doctorat, Université de Poitiers, France.

Tan, H. P., and Lallemand, M., 1988, "Transient Combined Conductive-Radiative Heat Transfer in Semi-Transparent Materials With Flux and Mixed Boundary Conditions for Semi-Transparent or Opaque Frontiers," Eurotherm Seminar, No. 1, Mons, Belgium, Mar. 7–8.

Tan, H. P., and Lallemand, M., 1989, "Transient Radiative-Conductive Heat Transfer in Flat Glasses Submitted to Temperature, Flux and Mixed Boundary Condition," *Int. J. Heat Mass Transfer,* Vol. 32, pp. 795–810.

Viskanta, R., and Anderson, E. E., 1975, "Heat Transfer in Semi-Transparent Solids," *Advances in Heat Transfer,* Academic Press, New York, Vol. 11, pp. 317–441.

APPENDIX A

Derivation of Equation (9)

The ray motion within an STM slab, which can communicate radiatively with its environment through the interfaces S_1 and S_2 when specular multi-reflections and transmission are taken into account, is represented in Figs. 1(*b*) and 10.

Since the amount of radiant energy transferred from the surface $S_{-\infty}$ to the inner space of the STM slab is contained within the transmission cone, the EEA $(S_{-\infty}S_i)^s_{k,t-t}$ associated with interchanges between $S_{-\infty}$ and S_i, by inspection of Fig. 10 is

$$(S_{-\infty}S_i)^s_{k,t-t} = 2\int_{\mu c}^{1} \mu (e^{-\kappa_k x_{1,i}/\mu} + \rho^s_{2,k} e^{-(\kappa_k d + \kappa x_{2,i}/\mu)}) / [1 - \rho^s_{1,k}\rho^s_{2,k} e^{-2\tau_{o,k}/\mu}] d\mu \quad \text{(A1)}$$

or in terms of functions $F_k(\kappa x)$, is defined by equation (11)

$$(S_{-\infty}S_i)^s_{k,t-t} = 2t^s_{1,k}[F_k(\kappa_k x_{1,i}) + \rho^s_{2,k} F_k(\kappa_k d + \kappa_k x_{2,i})]^1_{\mu c} \quad \text{(A2)}$$

The principle of energy conservation allows us to write for the EEA $(V_i S_{-\infty})^s_{k,t-t}$

$$(V_i S_{-\infty})^s_{k,t-t} = (S_{-\infty}S_i)^s_{k,t-t} - (S_{-\infty}S_{i+1})^s_{k,t-t} \quad \text{(A3)}$$

from which follows equation (9) of the main text. A similar procedure can be used for the derivation of $(V_i S_{+\infty})^s_{k,t-t}$ of equation (10) and the volume-volume terms $(V_i V_j)^s_{k,t-t}$.

Normal Spectral Emission From Nonhomogeneous Mixtures of CO_2 Gas and Al_2O_3 Particulate

D. V. Walters[1]
Research Assistant.
Mem. ASME

R. O. Buckius
Professor of Mechanical Engineering.
Fellow ASME

University of Illinois at Urbana—Champaign,
Department of Mechanical and
Industrial Engineering,
Urbana, IL 61801

Measurements of spectral, normal intensity, accounting for nongray banded emission from CO_2 gas and the influence of a highly scattering particulate, Al_2O_3, are presented. Detailed specifications of the temperatures, particle and gas properties, optical depths, and experimental uncertainties are given. The average temperatures are in the range 445 K to 600 K, pressures are approximately 1 atm, the layer depth is 0.5 cm, and particle optical depths are in the range 0 to 3. The intensity emitted from the medium is reported over a wavelength range of about 4.0 μm to 4.7 μm. Since the particle is virtually nonemitting, no continuum emission outside the 4.3 μm CO_2 band is detected. The effect of the particle is seen in the spectrally dependent and extinction coefficient dependent changes in the band structure when scattering is present. Modeling of the nonisothermal temperature distribution of the layer emerges as a critical factor in determining the magnitude of the emitted intensity. Uncertainty in the magnitude of the temperature accounts for most of the estimated uncertainty in the spectral intensity. A comparison of the experimental band intensities with values computed using a nonhomogeneous scattering model (which rigorously incorporates wide-band modeling) indicates excellent agreement for most runs.

1.0 Introduction

Considerable experimental research has been conducted on systems composed of real gases or scattering particles. Pure gas experiments (without scattering) are typically line-of-sight problems. The first gaseous emission experiments were performed with flames by Hottel and co-workers (e.g., Hottel and Sarofim, 1967; Edwards, 1976) in the 1930s. Edwards (1976) has provided a brief review of some recent gaseous radiation investigations. The pure particle systems that have been studied experimentally have typically been of the reflection/transmission type. Emission measurements are much more difficult to perform since they require high temperatures with all the associated system design problems, and they also require absolute energy measurements. Reflection/transmission energy measurements, which are relative to some prescribed energy input, are much easier to perform. Thus, the vast majority of data has been taken at room temperature and with visible light sources. Several problems exist with this type of experimental data. The extension of visible wavelength data to the infrared is often uncertain. If reflection/transmission data are collected, extracting emission information may be very difficult in any but the one-dimensional layer geometry. Even then, if nonhomogeneous conditions exist, that extraction is not valid as Kirchoff's law is inapplicable. One exception to the limited nature of the studies described above is an experiment that involves the measurement of emission from a high-temperature mixture of carbon particles in nitrogen gas (Eversole, 1984). No banded gases are present in this study and the medium is not well characterized.

There are several studies concerning rocket plume exhausts where high-temperature emission data have been taken from media of real gases and scattering particles (e.g., Konopka et al., 1980). However, such experiments, useful as they are for a given application, generally involve one or more unknown quantities, such as particle composition, particle optical properties, and exact flow field gas composition. They may also lack sufficient control to vary the fundamental system parameters in a controlled fashion. The experiment reported by Konopka et al. (1980) is deficient in not allowing detailed spectral emission information to be obtained. Skocypec et al. (1987) have investigated mixtures of real gases and scattering particulate using CO_2 and BNi-2 particles. The general behavior of the phenomena is exhibited but, unfortunately, the optical properties of this particulate are not accurately known.

There is, then, a lack of high-temperature, spectral emission data for a well-characterized medium of a real gas and scattering particles. Such a medium allows the interaction between nongray absorption and multiple scattering to be quantified. A goal of this investigation is the measurement of spectral intensity, accounting for nongray banded emission from CO_2 gas and the influence of a highly scattering particulate, Al_2O_3. An equally important goal is to present analytical predictions for this nonhomogeneous mixture using the most rigorous models currently available.

2.0 Experimental System

The experimental system consists of the same basic elements as previously reported (Skocypec et al., 1987). The presentation here will focus on the general features of the experiment and the modifications that have been made. The steady-state flow system, illustrated in Fig. 1, consists of a mixture of hot gas (CO_2 or N_2) and scattering particles (Al_2O_3) and is designed to create a reasonably one-dimensional gas–particle mixture that allows characterization of, and some degree of control over, the important system parameters. The pertinent parameters influencing the measured intensity are system temperature T, total pressure P_T, the product of absorbing gas partial pressure and path length $P_{CO_2}L$, single scattering albedo ω, phase function $P(\theta)$, extinction optical depth βL, and wall emissivity ϵ_w. Some of these variables are specified in terms of more fundamental quantities such that the basic system parameters are: T, P_T, X_{CO_2} (gaseous mole fraction), L (0.5 cm), A (test section cross-sectional area), $\dot{m}_g$ (gas mass

[1]Currently at McDonnell Aircraft Co., St. Louis, MO.

Contributed by the Heat Transfer Division for publication in the JOURNAL OF HEAT TRANSFER. Manuscript received by the Heat Transfer Division September 12, 1989; revision received March 16, 1990. Keywords: Radiation, Radiation Interactions.

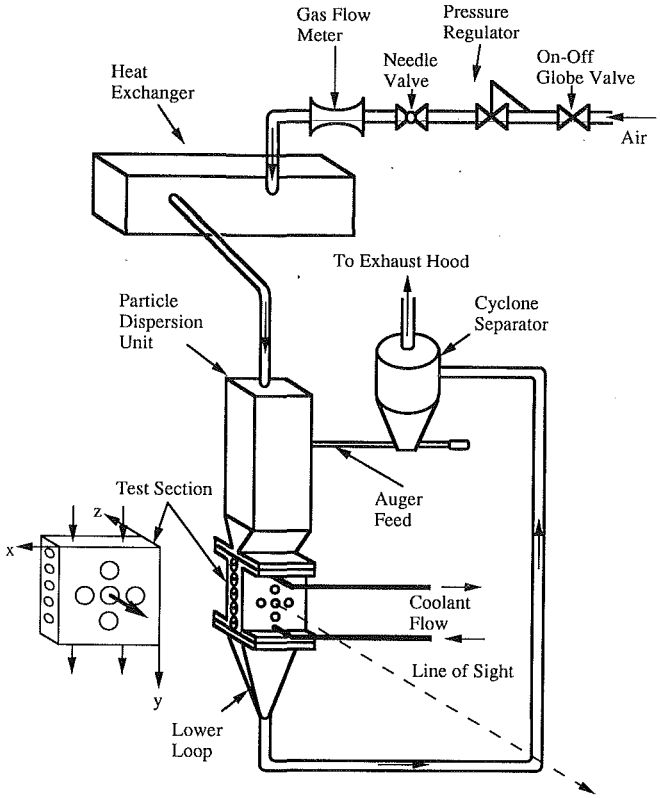

Fig. 1 Schematic of the experimental flow system

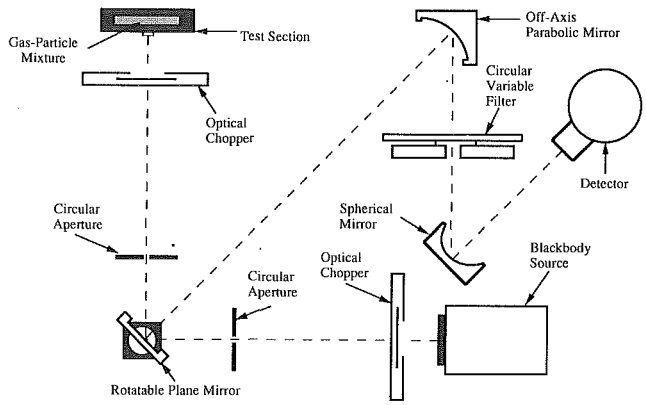

Fig. 2 Schematic of the experimental optical system

flow rate), $\dot{m}_p$ (particle mass flow rate), ρ_p (particle density), f_v (d_p) (particle size distribution), $\bar{n}$ (complex refractive index of the particle), particle shape, and ϵ_w (wall emissivity).

The gas originates from cylinders that, in general, contain a known mixture of carbon dioxide in nitrogen (known mole fraction of CO_2, X_{CO_2}). Flow from the cylinders is regulated and heated to a maximum temperature of 1061 K. The gas then enters the particle dispersion unit (PDU) where it is diverted around an interior hopper through passages between the hopper and the exterior walls. This flow path helps maintain the particles within the hopper at a temperature very near that of the gas. At the bottom of the unit, a metered flow of the particles mixes with the gas to create the desired gas–particle mixture. The particle is fed from the hopper by the rotation of a knurled stainless steel shaft that is calibrated to yield a known particle mass flow rate $\dot{m}_p$. Because of the highly flowable, abrasive nature of the particles used in this investigation, leakage of particles is a difficulty. A high-temperature, pressurized shaft housing, which applies a spring-actuated, high-temperature teflon seal, is used to reduce this leakage.

With the hot gas–particle mixture now created, the flow enters the test section (see Fig. 2) where the normal, spectral intensity is measured. The test section measures 0.5 cm in depth ($L = 0.5$ cm) and 5 cm wide, which accurately simulates a one-dimensional layer (Skocypec et al., 1987). The test section walls are cooled with a continuous flow of water. The inside walls are painted with an infrared flat black paint with a gray absorptivity of about 0.96 and typical normal emissivity

Nomenclature

a = absorption coefficient, m^{-1}
A = test section cross-sectional area, m^2
d = particle diameter, μm
d_{32} = volume to surface area average particle diameter, μm
f_v = particle volume fraction
i = intensity, $W/(m^2 \cdot sr)$
i_λ = spectral intensity, $W/(\mu m \cdot m^2 \cdot sr)$
$i_{\lambda b}$ = blackbody spectral intensity, $W/(\mu m \cdot m^2 \cdot sr)$
k = imaginary part of $\bar{n}$
L = total layer depth, cm
$\dot{m}$ = mass flow rate, kg/s
n = real part of $\bar{n}$
$\bar{n}$ = complex refractive index
$P(\theta)$ = phase function
P_T = total pressure, kPa
Q = efficiency
r = radial coordinate for cylindrical disk, cm
T = temperature, K
V = velocity, m/s
x = test section coordinate, cm
x_n = particle number density, m^{-3}
X_i = mole fraction of species i
y = test section coordinate, cm
z = test section coordinate, axial coordinate for the cylindrical disk, cm
β = extinction coefficient $= (a + \sigma)$, m^{-1}
ϵ_w = wall emissivity
θ = angle
λ = wavelength, μm
ρ = density, kg/m^3
σ = scattering coefficient, m^{-1}
ω = single scattering albedo $= \sigma/(a + \sigma)$

Subscripts

abs = absorption
ave = average
b = blackbody
c = core
cl = centerline
e = experimental value
ext = extinction
g = gas
gp = gas-particle
l = lower
max = maximum
n = normal
p = particle, predicted value
sca = scattering
u = upper
w = wall
λ = wavelength-dependent quantity
1, 2 = polarized components of the intensity

Superscripts

* = dimensionless quantity

of 0.85 ($\epsilon_{wn} = 0.85$). The radiant intensity to be measured is viewed through a CaF_2 window in a viewing port in the center of the test section.

Access to the gas-particle flow inside the system for measurement of pressure and temperature is made possible by five threaded holes located along each side of the test section (see Fig. 1). Hypodermic tubing is inserted into positioners placed in these holes and is used to encase a chromel-alumel (type K) thermocouple made of 36-gage chromel and alumel wires. The thermocouple wire is slid inside the tubing until the bead is centered in a 0.79-mm hole drilled near one end. The hole is positioned to allow the gas-particle mixture to flow over the bead while the remaining tube wall shields the bead from viewing the cold test section walls. Temperature measurement error is further reduced by the use of thin, well-insulated thermocouple wires to inhibit conduction from the bead. Test section pressure P_T is measured by using one of the side access holes as a static pressure tap.

When the gas-particle mixture leaves the test section, it enters a stainless steel pipe system. Most of the particles are removed from the flow by a cyclone separator located at the top of the pipe system. An auger transports the particles back to the PDU. Because of sealing problems around the auger shaft, a pressurized seal similar to that used on the PDU feed shaft is employed. The high temperatures necessary for this study required that the entire flow system, with the exception of the test section, be insulated with a thick layer of ceramic fiber material.

The desired measurement from this system is the normal (along the line of sight in Fig. 1) spectral intensity from the hot gas-particle medium. The optical system in Fig. 2 is therefore designed to direct energy along a path from the test section to an infrared detector. The optical path is composed of a light chopper, a 0.508-cm-dia aperture (to restrict the solid angle around the normal direction), a rotatable plane mirror, a 98 deg off-axis parabolic mirror, a circularly variable filter (CVF) (with a half-bandwidth resolution of 1.5 percent of a specific wavelength), a concave front surface spherical mirror, and the infrared detector. The CVF, which is constructed of three separate wedges, passes energy in a wavelength range of 2.5 μm to 14.5 μm. The first two wedges, those used in this investigation, cover the ranges 2.47 μm to 4.46 μm and 4.33 μm to 7.97 μm. The detector contains two semiconductor elements, a photovoltaic InSb element, which is sensitive in the wavelength range 0.5 to 5.5 μm, and a photoconductive HgCdTe element active out to 14.5 μm. The amplified detector voltage is sent to a lock-in amplifier where virtually all background radiation incident upon the detector element is filtered out. The entire path from the test section to the detector is close to 1 m in length.

The data that require collection during a typical experimental run are: test section wall temperature, test section medium temperature, laminar flow element gas temperature and pressure drop (for gas mass flow rate evaluation), test section pressure, shaft rotation rate (for particle mass flow rate evaluation), and lock-in amplifier voltage (for intensity). All thermocouples and a d-c voltage proportional to the lock-in amplifier millivolt reading are connected to a Fluke Helios intelligent computer front end, which communicates with a Macintosh SE computer.

3.0 Experiment Characterization and Calibration

Before the experimental results are presented, the experiment is characterized in terms of the mixture specification, test section measurements, and the intensity calibration. The uncertainties in these quantities are also discussed.

Mixture Specification. The gas phase is characterized by the specification of total pressure P_T, mole fraction X_{CO_2} of carbon dioxide, and gas mass flow rate $\dot{m}_g$. The pressure, as recorded by an absolute pressure transducer, is approximately 1 atm for all runs; the uncertainty in P_T is estimated as less than ± 2 percent. The mole fraction of CO_2 is unity for all runs. Since instrument grade CO_2 with a minimum purity of at least 99.999 percent is used, the uncertainty in X_{CO_2} is considered to be negligible. The uncertainty in $\dot{m}_g$ is estimated as less than ± 9 percent, based on the uncertainties in the pressure drop across the laminar flow element, upstream pressure, upstream temperature, gas dynamic viscosity, and laminar flow element calibration.

Table 1 Particle volume fractions

Size Interval, i	$d_{p,i}$ (μm)	$f_{v,i}$ [1]	$f_{n,i}$ [2]
1	3.35	0	0
2	4.70	0.018	0.5070
3	6.65	0.009	0.0895
4	9.40	0.027	0.0951
5	13.5	0.118	0.1402
6	19.	0.241	0.1027
7	26.5	0.337	0.0530
8	37.5	0.213	0.0118
9	53.	0.036	0.000707
10	75.	0	0
	$d_{32} = 20.57$	$\Sigma = 0.999$	$\Sigma = 1.000007$

1 $f_{v,i}$ = (particle volume in interval i)/(total particle volume)
2 $f_{n,i}$ = (number of particles in interval i)/(total number of particles)

The particle phase is characterized by the particle's shape, complex index of refraction $\bar{n}$, density ρ_p, size distribution $f_v(d_p)$ [$f_v(d_p)$ is the ratio of the volume of particles with diameters in a small Δd_p range about diameter d_p to the volume of all particles], and the bulk mass flow rate $\dot{m}_p$. The particle chosen for this study is a spheroidized aluminum oxide, Al_2O_3, from Union Carbide (sample name: ALO-162-1). This particle is of practical interest in rocket applications where it is an important component of many rocket exhausts. The particle is an extremely flowable, spherical powder with 99.9 percent minimum purity. Trace amounts of Cu, Fe, Si, Mg, Ti, K, Na, and Ca also exist. The excellent flowability of the particles at elevated temperatures (< 800 K) implies that no sintering occurs, as expected from data in Gitzen (1970). The particle density is 3710 kg/m^3 as measured by Union Carbide, using a stereopycnometer, which yields true powder density. Three runs were performed and all gave $\rho_p = 3710$ kg/m^3. The particle size distribution analysis was performed by Leeds and Northrupt using a Microtrac particle size analyzer. The results are given in Table 1. The volume to surface area average diameter d_{32} for the analyzed sample of Al_2O_3 is 20.57 μm. Estimating the uncertainty in the distribution is difficult, yet the uncertainty in the radiative properties for which $f_v(d_p)$ is required is expected to be most sensitive to variations in parameters such as system temperature and particle mass flow rate. Computations of the effects of an uncertainty in $f_v(d_p)$ on the radiative properties show this to be the case.

Values for the indices of refraction ($\bar{n} = n - ik$) of Al_2O_3 are plentiful, though there is some disagreement as to the value for the absorption index k. The value of the real part of the refractive index is taken to be $n = 1.64$, a value valid at $\lambda = 4.375$ μm (a wavelength in the spectral region of interest). This value is obtained by interpolating values for sapphire at $T = 300$ K as compiled by Whitson (1975). This value is reasonable considering that Makino et al. (1984) measured a value of $n \cong 1.65$ for ceramic alumina valid from 290 K to 700 K, and Dowling and Randall (1977) reported a value of $n = 1.70$ at 300 K and $n = 1.69$ at 678 K for a synthetic, pure crystal of alumina. The value taken for the complex part of the refractive index, $k = 1.385 \times 10^{-6}$, also applies at $\lambda = 4.375$ μm. Again, this value is obtained by wavelength interpolation of Whitson's compiled data at $T = 300$ K. Konopka et al.

(1983), Pluchino and Masturzo (1981), and Mularz and Yuen (1972) have discussed the difficulty in obtaining accurate values of k because of the presence of impurities (primarily carbon and metallic aluminum) in Al_2O_3 samples. The Al_2O_3 purchased from Union Carbide appears to be quite pure with no trace amounts of carbon or metallic aluminum appearing in the chemical analysis. Values of k for relatively pure, commercial Al_2O_3 at $\lambda = 4.375$ μm have also been reported by Konopka et al. (1983) ($k \cong 10^{-4}$) and Makino et al. (1984) ($k < 10^{-3}$). Although these values do not confirm the chosen value of $k = 1.385 \times 10^{-6}$ from Whitson (indicating the possible influence of contaminants), all values mentioned above are very small and imply negligible particle absorption (or a particle scattering albedo very near 1). Emission measurements presented in Figs. 4–11 confirm this by showing no detectable emission from the particle (when the wavelength regions beyond the CO_2 gas bands are considered). In summary, the value for the complex index of refraction is taken to be $\tilde{n} = 1.64 - i(1.385 \times 10^{-6})$.

The particle mass flow rate $\dot{m}_p$ is quantified by relating it to the rate of rotation of the knurled particle feed shaft. After removing the exit flow system, the calibration is performed by operating the feed shaft at a fixed rate of rotation for a given time and then weighing the amount of particles collected. The calibration was performed at room temperature for four different shaft rotation rates and for a range of gas mass flow rates from 0 to 3 g/s. This range is sufficient to encompass all gas mass flow rates and Reynolds number values used for experimental runs. The excellent flowability of the particle under all conditions resulted in particle mass flow rates with little variation from run to run. The calibrated values have a relative uncertainty of less than ±3 percent.

Test Section Measurements. The test section wall temperature and medium temperature distribution are also needed. The wall temperature T_w is monitored by thermocouples embedded in the copper walls. The variation of the temperature with wall position and with time during experimental runs is less than ±1 K. The temperature distribution $T(x, y, z)$ is quantified by first establishing that the temperature is reasonably uniform in the x and y directions under representative two-phase and pure gas flow conditions. (See Fig. 1 for a description of the x, y, z coordinate system.) Thorough temperature scans were reported by Skocypec et al. (1987), although these were performed with BNi-2 particles rather than Al_2O_3. One result of that investigation was the discovery of a slight cooling in the downstream y direction. Since the BNi-2 particles are much stronger emitters than the Al_2O_3 particles, the downstream cooling for the present study is expected to be much less. The largest temperature gradient occurs in the z direction. For this reason the test section temperature as a function of z, $T(z)$, is measured and reported for each experimental run at the center of the test section (directly behind the viewing port, along the optical line-of-sight). Including the wall temperature T_w, known at each boundary, nine temperature values are measured for the z direction $[0, L]$ ($z = 0$ is located at the viewing port). Note that the $T(z)$ scans reported in the results section are shifted by $\Delta z = 0.3$ mm due to a small misalignment of the thermocouple probe. Defining the test section core temperature as the mean of the temperatures at the three centermost z locations, a variation in the core temperature T_{cl} over the x and y directions of less than ±10 percent is reported (Skocypec et al., 1987), indicating that the system is reasonably one dimensional.

Extensive scans of the local ratio of particle volume to medium volume throughout the test section are reported (Skocypec et al., 1987) in order to characterize the uniformity of the particle loading. The medium's particle loading is believed to be homogeneous to within measurable limits (Skocypec et al., 1987). Although a different particle is being used for this investigation, the homogeneous character is accepted as applicable to the present system, noting that the Al_2O_3 and BNi-2 particles have similar shapes and similar size distributions and that the particle feed, gas flow, and gas–particle mixing systems are identical for both particles. (The effect of nonhomogeneities near the wall boundaries is investigated in the discussion of the experimental results.) Thus, the particle flow is assumed to be uniform over the cross-sectional area (x–z plane) of the test section.

Variation in particle loading in the downstream direction, due to the effects of drag and gravity on the Al_2O_3 spheres, is incorporated in analyzing the radiative properties. That is, after being fed from the PDU hopper, the particles are assumed to fall in quiescent CO_2 until they mix with the flowing CO_2 gas. Because the particle velocity at this location for particles of all diameters is very small relative to gas velocity, the particle velocity is assumed to be zero at this point. The properties of the particles at the center of the test section (behind the viewing port), which is a distance of $\Delta y = 6.013 \times 10^{-2}$ m from the point of mixing, are desired. The velocity for each particle diameter in Table 1 is computed by establishing a force balance on the particle. The gas velocity is taken as $V_g = \dot{m}_g/(\rho_g A)$, where ρ_g is the gas density from the ideal gas law and A is the cross-sectional area of the test section ($A = 2.5 \times 10^{-4}$ m^2). The velocity V_{pi} for each particle diameter d_{pi} is then obtained by integrating the force balance from the inlet to the desired y. With the particle velocities computed, the number density x_n of particles in the two-phase flow is computed as

$$x_n = \sum_i \left[\frac{\dot{m}_p f_{vi}}{\left(\frac{\pi}{6} d_{pi}^3\right) A \rho_p V_{pi}} \right] = \sum_i x_{ni} \tag{1}$$

where f_{vi} is the particle volume fraction as given in Table 1. Note that f_v refers to the Al_2O_3 size distribution, not to the volume of particles in the test section flow.

Intensity Calibration. The spectral calibration of wavelength is accomplished by matching the well-defined transmission spikes of polystyrene to specific angles (or steps) of the circularly variable filter (Skocypec et al., 1987). Once these points are known, the calibration is completed using the filter's characteristic linearity of wavelength with angle. Because a number of transmission spikes tend to occur in a very small wavelength interval, the relatively large bandwidth of the circularly variable filter tends to smooth the group of spikes into one large valley in the detected transmission curve. Thus, due to the bandpass character of the filter, the calibration point will not exactly coincide with the detected minimum of the transmission curve obtained using the circularly variable filter. This character necessitated a reinterpretation of the original calibration; the originally calibrated wavelength at each angle of the first wedge is decreased by 0.0346 μm. Since the two wedges overlap in a small spectral region, matching the predicted wavelengths on the two wedges is possible and allows a reinterpretation of the original calibration for the second wedge as well; the calibrated wavelength at each angle of the second wedge is decreased by 0.0216 μm. These changes are justified when the predicted locations of the isolated 3.419-μm and 5.143-μm transmission spikes are checked. The new calibration predicts these points to within about 0.006 μm, compared to about 0.03 μm for the unmodified calibration.

The normal spectral intensity from the test section is the

quantity desired from the optical system. This necessitates a spectral calibration of the test section line-of-sight such that millivolt values recorded at the lock-in amplifier can be directly related to normal, spectral intensity. The ideal method of calibrating the test section line-of-sight would be to place a perfectly black surface inside the test section with the surface filling the test section viewing port. By setting the surface at a specific temperature and then performing a wavelength scan, spectral millivolt values could be directly related to normal, spectral blackbody intensity at the black surface temperature. The ratio of spectral blackbody intensity to the millivolt value would then define the normal, spectral calibration factor. Because placing such a blackbody cavity inside the test section is not possible, a thin disk of known emissivity is used instead.

The calibration disk is made of copper and has a grit-blasted front surface painted with two coats of the same infrared black paint used inside the test section. The grit blasting improves paint adhesion and the diffuse nature of the surface. The back of the surface is instrumented with chromel-alumel (type K) thermocouples (Omegaclad, 1-mm-dia, inconel-600 sheath) so that the disk temperature can be monitored. The disk emissivity is obtained from the blackbody branch of the optics illustrated in Fig. 2. Note that except for the path from the blackbody to the rotatable plane mirror, the optical system is the same as that used for test section energy. In obtaining the disk emissivity, the secondary aperature (0.397-cm-dia) is necessary in the line of sight to constrict the active emitting area of the blackbody to a size that is smaller than its own aperature. In this way, if the blackbody is removed and the disk is placed in the blackbody's position, the detector views an equivalent source of energy. Finding the disk emissivity then requires heating the disk and blackbody to equal temperatures, and then placing each in the line of sight for a wavelength scan. With its emissivity known, the disk is then transferred to the test section to measure its emission in this configuration. The spectral calibration factor is then easily computed.

This calibration factor accounts for all optical influences (circularly variable filter, mirrors, apertures, detector, windows, etc.) and converts units of millivolts to intensity. The effect of the test section-side chopper is also included as long as chopper position and blade shape are retained for all intensity readings. The atmospheric transmittance from the test section to the detector is also incorporated, and changes in room humidity and temperature from day to day, for the wavelength region of concern in this investigation, are calculated to be negligible.

Disk surface reflection, uncertain surface temperature, and chopper emission present potential difficulties in determining the calibration factor for the test section emission. In any radiant emission study the possibility exists that detected power results not only from emission but also from reflection into the line of sight. This effect is minimized by the use of a high-emissivity surface, a high disk temperature (682 K) relative to the surroundings, and placement of the chopper in close proximity to the surface. The expected contribution of reflected energy to the surface radiosity is less than 0.5 percent in the wavelength region of interest in this study. Also, the chopper itself may contribute to inaccuracy in the values of the measured intensity. Since the detector-amplifier system yields a voltage reading proportional to the peak-to-peak voltage of the a-c signal coherent with the chopper frequency, the measured intensity is properly determined only when chopper radiosity is identically zero. Since the chopper is actually at room temperature and is nonblack, the detector-amplifier system yields a voltage proportional to the difference between disk and chopper blade radiosity. Since the disk temperature is much greater than the chopper blade temperature, the disk emission is appropriately measured for the wavelengths of interest in this work. Finally, although the temperature drop through the copper disk is estimated to be less than 2 K, the coating of paint on the grit-blasted front surface and the harsh high-temperature environment have adverse affects on the ability of the thermocouples to predict the front face temperature accurately. To correct for this effect, two-color pyrometry is applied to the plentiful spectral data that the wavelength scans yield to obtain more accurate values for the front surface temperature of the disk. The uncertainty in the spectral emission calibration is calculated by estimating uncertainties in the temperature and millivolt readings to yield a relative uncertainty of less than ± 14 percent, in general, and usually less than ± 6 percent.

4.0 Experimental Results

Fifteen runs (eight gas–particle runs and seven pure gas runs) were performed to obtain the emitted normal, spectral intensity in the spectral region of the 4.3-μm CO_2 band. Since the gas mole fraction is fixed at unity, the parameters varied were system temperature and particle loading (or optical depth βL). Emission in the wavelength range of about 2.5 μm to 5.5 μm is recorded. The runs involve ranges of temperature from about 450 K to 600 K and optical depth based on particle extinction from 0 to 3.

Several modifications to the raw experimental data are necessary before they are reported. As discussed above, a small misalignment of the thermocouple probe necessitates a +0.3-mm shift of the temperature distribution. In addition, a significant variation in system temperature occurs during gas–particle runs due to the effect of powder recycling. During pure gas runs, powder recycling does not occur and the average system temperature remains very stable, generally changing less than 2 K from the beginning to the end of a run. Because of the system cooling between the start of a run and the time the temperature distribution and intensity measurements are made, the temperature distribution $T(z)$ taken at the beginning of a gas–particle run overestimates the local temperature at a time later in the wavelength scan when the intensity data are collected. In fact, the data reported here constitute the final spectral values obtained during the wavelength scan. Therefore, since only the centerline temperature $T(z=L/2)=T_{cl}$ (not the entire temperature distribution) is recorded at the end of the wavelength scans, this value is used as the average test section temperature T_{ave} for gas–particle runs. Letting $T_{cl}=T_{ave}$ introduces little error since the temperature profile is very flat over the center region of the test section. It remains then to scale accurately the temperature distribution to reflect the change in the magnitude of T_{cl}. The nondimensional quantity used to do this is $T^*(z)$, defined as

$$T^*(z) = \frac{T(z)-T_w}{T_{cl}-T_w} \tag{2}$$

The gas–particle scaling distribution $T^*_{gp}(z)$ is obtained by averaging $T^*(z)$ values for runs 1, 2, 3, 4, and 6. Gas-particle runs 5, 7, and 8 are excluded from this scaling because the recording of $T(z)$ for these three runs was not repeatable. $T^*_{gp}(z)$ is plotted in Fig. 3 along with all of the discrete points used in its definition. There is some variation of the points about the scaled distribution. However, considering that the variation is partially due to small particle mass flow rate fluctuations, which will average out to some degree, $T^*_{gp}(z)$ does an excellent job of scaling the temperature profiles. The temperature distribution $T(z)$ for all gas–particle runs is then obtained by solving equation (2) for $T(z)$ with values for T_w and T_{cl} defined as described above.

The last necessary modification to the data is due to the influence of the chopper radiosity. The chopper effect is generally minimal because of the relatively large medium emission, except when the medium emittance drops to a very low

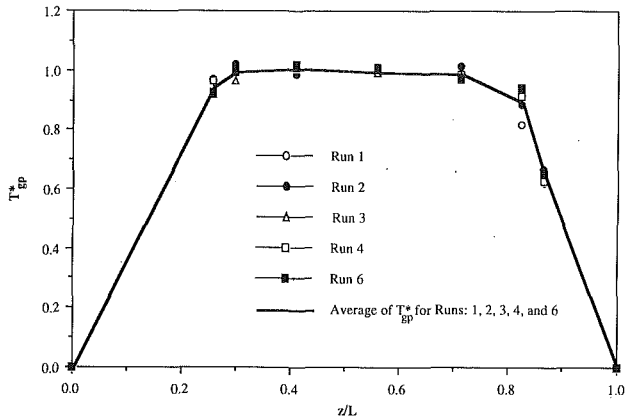

Fig. 3 Temperature distribution $T^*_{gp}(z/L)$ for scaling the gas-particle temperature profiles

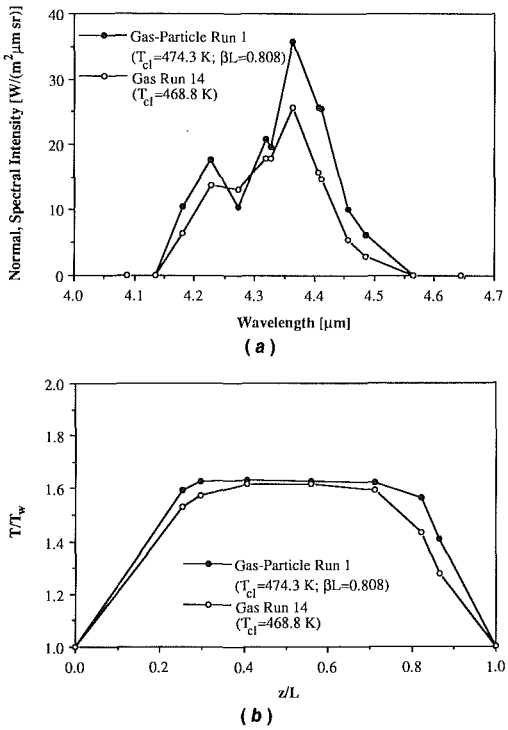

Fig. 4 (*a*) Experimentally measured normal, spectral intensity for gas-particle run 1 and gas run 14; (*b*) temperature distribution for gas-particle run 1 and gas run 14

value in the wings of the 4.3-μm CO_2 band. (Since the Al_2O_3 is virtually nonemitting, no detectable continuum emission from the particle is present outside the band.) Therefore, the effect of chopper radiosity is apparent in all nonzero intensity values. By estimating the chopper's normal emissivity and temperature and the incident room energy, corrected intensity values with the chopper's influence removed can be calculated. Large spectral intensity values near the center of the band are altered very little by this modification. Values in the band wings are affected more, especially for the low-temperature runs. The nature of the chopper influence and detection system are such that outside the gas band, measured intensity values slightly less than or approximately equal to zero are obtained. The absolute magnitude of the intensity in these cases is highly uncertain due to lock-in amplifier instability at these very low intensity values. In the experimental data to follow, measured intensity values that have this character are set to zero.

Incorporating all the above corrections, the normal, spectral intensity emitted from the test section is plotted for all

Table 2 Experimental run conditions

Run No.	T_{cl} (K)	T_{wall} (K)	P_T (kPa)	$\dot{m}_g \times 10^3$ (kg/s)	$\dot{m}_p \times 10^3$ (kg/s)	$i_{n,e}$ (W/m²/str)
1 (g-p)	474.3	291.7	102.215	2.01	5.29	6.37
2 (g-p)	481.7	291.2	103.422	1.97	5.29	6.71
3 (g-p)	488.0	291.0	103.422	1.89	7.83	7.27
4 (g-p)	446.4	292.2	99.630	0.784	7.83	4.41
5 (g-p)	512.0	294.2	101.354	1.27	7.83	7.82
6 (g-p)	509.6	292.9	102.733	1.27	5.29	9.20
7 (g-p)	598.2	295.9	106.732	2.12	5.29	21.98
8 (g-p)	482.1	294.0	99.630	1.02	7.83	7.85
9 (g)	587.9	291.2	101.354	2.28	0.	22.07
10 (g)	520.6	291.0	101.008	2.28	0.	9.75
11 (g)	500.7	291.0	101.354	2.30	0.	7.62
12 (g)	488.6	291.8	101.354	2.29	0.	6.33
13 (g)	477.9	291.8	101.354	2.30	0.	5.44
14 (g)	468.8	291.7	101.354	2.30	0.	4.74
15 (g)	447.7	291.4	101.354	2.31	0.	3.36

Experimental constants: L = 0.005 m, A = 2.5 x 10^{-4} m², ε_w = 0.85, X_{CO_2} = 1, ρ_p = 3710 kg/m³, $\bar{n}$ = 1.64 – i(1.385 x 10^{-6}) and f_v (see Table 1).

runs in Figs. 4(*a*)-11(*a*). Accompanying plots of the temperature distribution $T(z)$, scaled by the wall temperature T_w, for each run are given in Figs. 4(*b*)-11(*b*). Each plot includes gas and gas-particle runs with very similar average temperatures so that the influence of the particle is easily discernible. Table 2 details the run conditions.

The computed value in Table 2 is the normal intensity $i_{n,e}$ (the subscript e indicates the experimental value) for the 4.3 μm CO_2 gas band, which includes the spectral region from $\lambda_l = 4.088$ μm to $\lambda_u = 4.643$ μm and incorporates emission from the gas and walls. This band quantity is defined as

$$i_{n,e} = \int_{\lambda_l}^{\lambda_u} i_{\lambda n} d\lambda \tag{3}$$

As stated above, some spectral intensity values in the gas-band wings were set to zero because of radiant power detectability limits. The actual intensity at these wavelengths is well approximated by blackbody intensity at the wall temperature T_w; the quantity $i_{n,e}$ incorporates this contribution and is termed the band wing corrected normal intensity. Values of $i_{n,e}$ that are derived from a direct integration of the plotted spectral intensities (with zero values in the band wings) vary from the band wing corrected values by less than 6 percent.

5.0 Discussion of Results

The discussion of the experimental results presented in this section centers around the following issues: a description of various analytical models, the sensitivity of intensity measurements to variations in important system parameters, comparisons with chosen models, and a discussion of the phenomena.

Model Descriptions. The most comprehensive analytical models currently available are able to incorporate a nonhomogeneous scattering medium with wide-band gas contributions (Walters and Buckius, 1990b) and a nonhomogeneous, nonscattering medium with narrow-band gas contributions (Grosshandler, 1980). The scattering model applies a Monte Carlo simulation of the photon path length analysis. The solution involves solving for the emission path lengths in a conservative medium with reflecting boundaries after noting the equivalence between these paths and those from boundary incidence. This equivalence is demonstrated by first applying conservation of energy principles for boundary incidence at a transparent boundary to obtain an emission path length formulation of the medium emission. Mathematical properties of the Laplace transform are then applied to relate this boundary formulation to one obtained by considering volumetric emission. Nonhomogeneous paths for emission through the scattering medium are then defined. The wide-band model and the nonhomogeneous scaling techniques of Edwards (1976) are then applied to determine the path in-

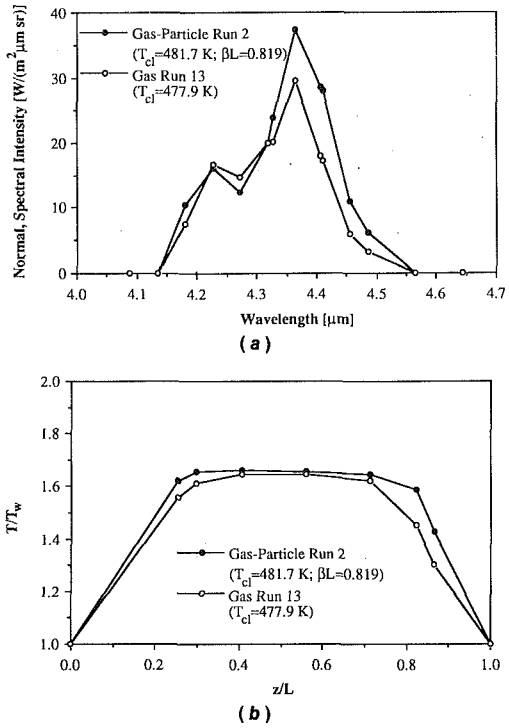

Fig. 5 (a) Experimentally measured normal, spectral intensity for gas-particle run 2 and gas run 13; (b) temperature distribution for gas-particle run 2 and gas run 13

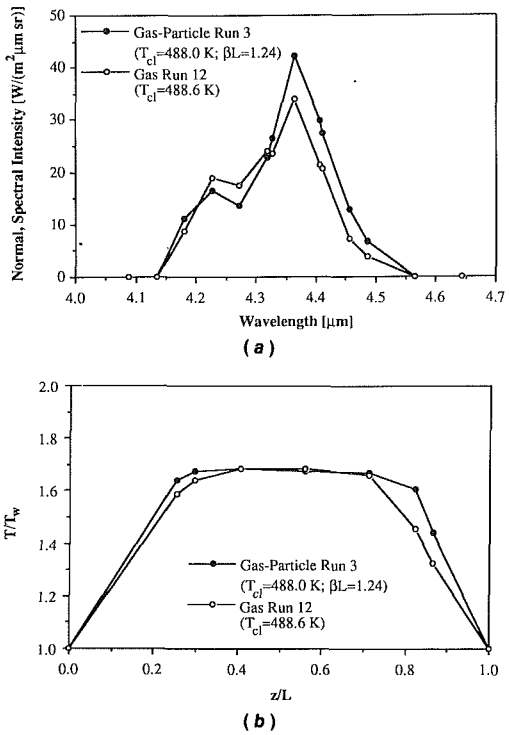

Fig. 6 (a) Experimentally measured normal, spectral intensity for gas-particle run 3 and gas run 12; (b) temperature distribution for gas-particle run 3 and gas run 12

tensity. The narrow-band gas contributions have been modeled for nonhomogeneous paths without scattering in a program called RADCAL (Grosshandler, 1980). Curtis-Godson scaling is used to quantify the nonhomogeneous concentration and temperature distributions. Thus, two analytical results are compared with the experimental data: the spectral intensity for pure gas runs (computed using RADCAL) and the wide-band intensity for all runs (calculated using the nonhomogeneous scattering code). These analytical models also provide a means to test the sensitivity of the emitted spectral intensity to various parameters to help establish the uncertainty in the experimental results.

Before the analytical results are presented, the determination of the particle properties must be detailed. The experimental measurements include the necessary quantities to permit the calculation of the radiative properties for the particulate. The required properties are the extinction coefficient β, the single scattering albedo ω, and the single scattering phase function $P(\theta)$. These properties can be determined for the Al_2O_3 particles if the index of refraction is known. As indicated in section 3.0 above, the value for the complex index of refraction is taken to be $\bar{n} = 1.64 - i(1.385 \times 10^{-6})$. With the $x_{n,i}$ defined in section 3.0, the following radiative properties are calculated:

$$a = \frac{\pi}{4} \sum_i [x_{n,i} d_{p,i}^2 Q_{\text{abs},i}] \tag{4}$$

$$\sigma = \frac{\pi}{4} \sum_i [x_{n,i} d_{p,i}^2 Q_{\text{sca},i}] \tag{5}$$

$$P(\theta) = \frac{\lambda^2}{2\pi\sigma} \sum_i [x_{n,i} (i_{l,i} + i_{2,i})] \tag{6}$$

with $\beta = a + \sigma$ and $\omega = \sigma/\beta$. The summmation over i replaces the integration over particle size necessary for a polydisperse particle. In equations (4)-(6), $Q_{\text{abs},i}$ is the absorption efficiency, $Q_{\text{sca},i}$ is the scattering efficiency, and i_1 and i_2 are the

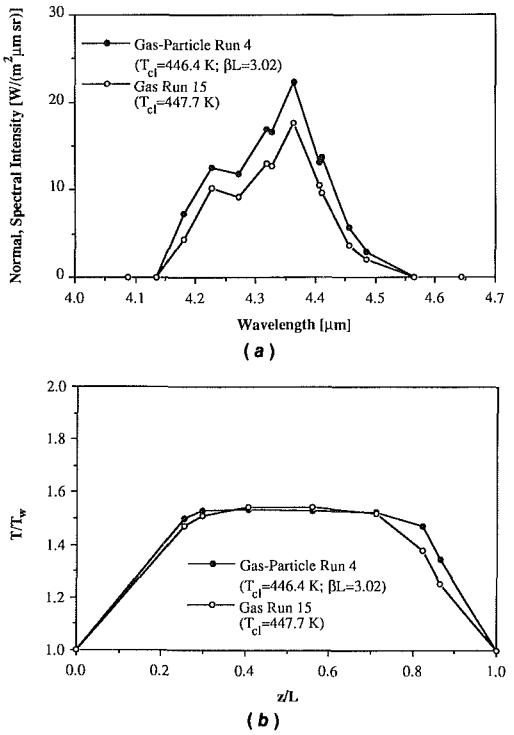

Fig. 7 (a) Experimentally measured normal, spectral intensity for gas-particle run 4 and gas run 15; (b) temperature distribution for gas-particle run 4 and gas run 15

scattering intensities for planes parallel and perpendicular to the direction of energy propagation. The extinction coefficient could alternately be expressed in terms of the extinction efficiency, $Q_{\text{ext},i}$ ($Q_{\text{ext}} = Q_{\text{abs}} + Q_{\text{sca}}$). These parameters are computed for a given particle size $d_{p,i}$ using Mie theory (Wiscombe, 1980). The validity of this modeling is confirmed by the independent scattering investigation of Menart et al.

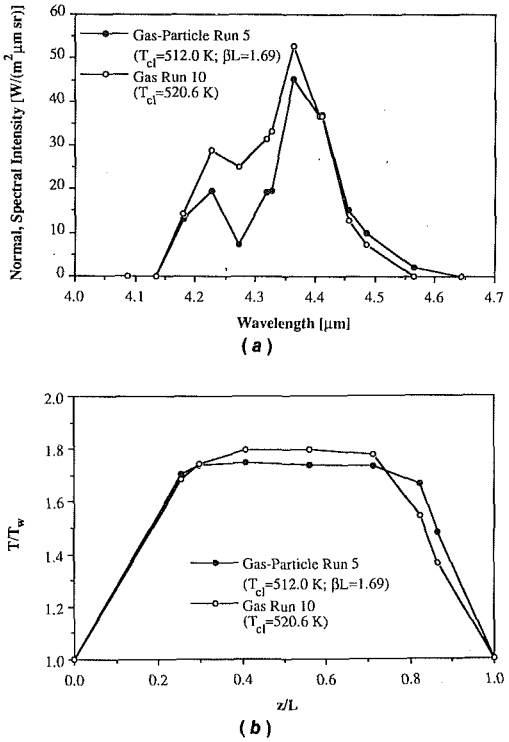

Fig. 8 (a) Experimentally measured normal, spectral intensity for gas-particle run 5 and gas run 10; (b) temperature distribution for gas-particle run 5 and gas run 10

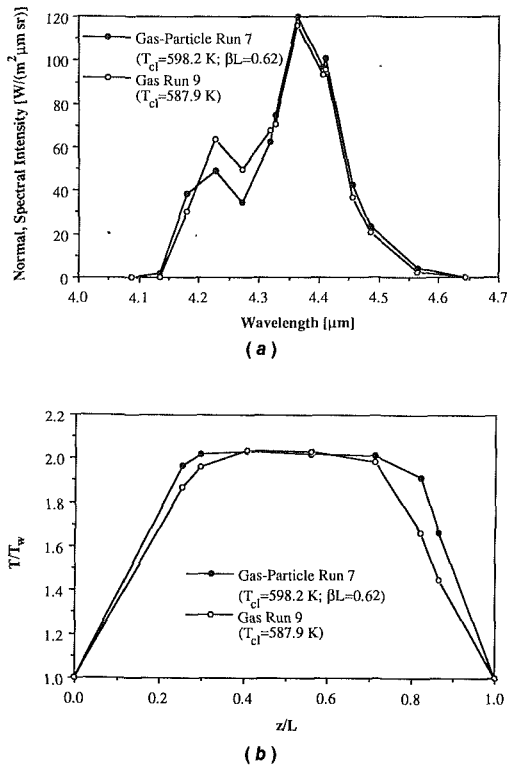

Fig. 10 (a) Experimentally measured normal, spectral intensity for gas-particle run 7 and gas run 9; (b) temperature distribution for gas-particle run 7 and gas run 9

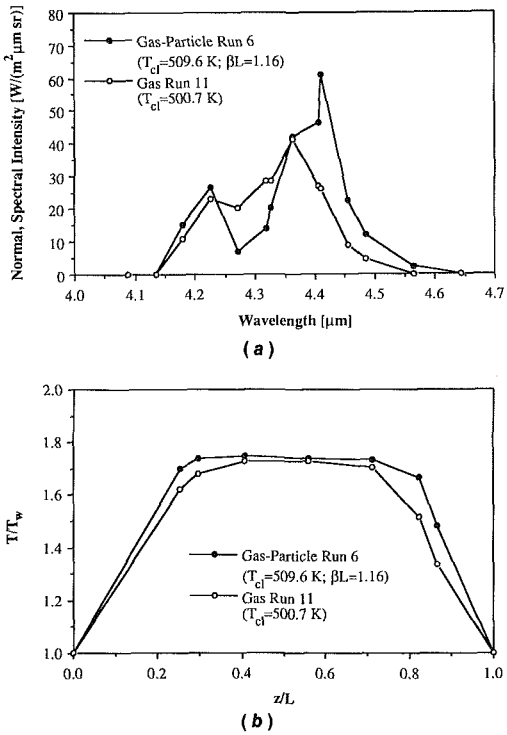

Fig. 9 (a) Experimentally measured normal, spectral intensity for gas-particle run 6 and gas run 11; (b) temperature distribution for gas-particle run 6 and gas run 11

(1989). The radiative properties β, ω, and $P(\theta)$ are reported for the same Al_2O_3 particle used in this study; reasonable agreement is found between the experimental results and the predictions of Mie theory.

Sensitivity to System Parameter Uncertainty. Using the uncertainties in the measured quantities indicated in section 3.0, the uncertainties in β, ω, and $P(\theta)$ can be determined. The uncertainty in albedo, predicted as unity for all runs, is believed to be negligible considering the confirming data of Menart et al. (1989), the data available from several references for the absorption index k for commercial alumina and sapphire, which indicate very little particle absorption, and the fact that the experimental intensity data show no detectable continuum emission from the particle outside the CO_2 gas bands. The excellent agreement that Menart et al. (1989) show between the experimentally determined phase function and the results of Mie theory for the Al_2O_3 demonstrates the accuracy of the present modeling for $P(\theta)$. The primary uncertainty is in extinction coefficient β, which is a linear function of the particle number density x_{ni}. The uncertainties in the various particle properties that Mie theory requires [$\bar{n}$ and $f_v(d_p)$] are considered insignificant, especially when compared to the uncertainty in other parameters such as temperature. The number density, in turn, is a complex function of the gas and particle properties due to the presence of the particle velocity V_p in the denominator of the equation defining x_n. For the purpose of evaluating the uncertainty in β, somewhat simplified versions of equations (1) and (5) yield the estimated uncertainty in β as a function of the estimated uncertainties in $\dot{m}_p$ (± 3 percent), P_T (± 2 percent), T_{cl} (± 10 percent), $\dot{m}_g$ (± 9 percent), and ρ_p (negligible). The resultant uncertainty in β is less than ± 14 percent.

The analytical codes discussed above are useful not just for simulating the experimental runs, but also for investigating the sensitivity of the intensity to the variation of system parameters. Using this type of approach, an experimental uncertainty in the normal, spectral intensity is estimated. The three parameters that can bias $i_{\lambda n}$ are the effects of ϵ_w (± 0.05), β (± 14 percent), and $T(z)$. The error in all other parameters is either random or negligible. Various analytical results were obtained, and they show that both ϵ_w and β in-

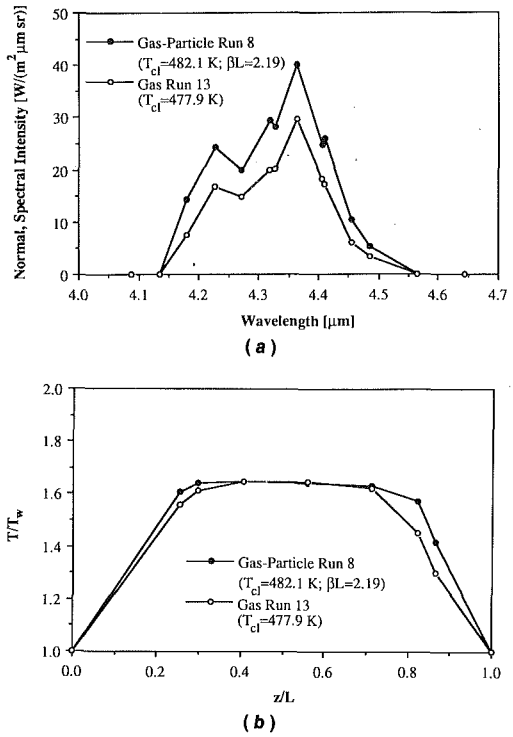

Fig. 11 (a) Experimentally measured normal, spectral intensity for gas-particle run 8 and gas run 13; (b) temperature distribution for gas-particle run 8 and gas run 13

fluence the results very little. In addition, a nonhomogeneous distribution $\beta(z)$ seems to affect the band intensity very little. To test this, experiment run 5 is assumed to have a constant value of extinction coefficient β_c between the locations $z/L=0.2$ and 0.8, which roughly define the measurement limits of the particle loading scans (Skocypec et al., 1987). A linear function is assumed between the walls and $z/L=0.2$, 0.8, with the wall value β_w specified as $\beta_w/\beta_c=0.5$ and 1.5. It is then required that

$$\beta_{\text{ave}}L=\int_0^L \beta(z)dz \tag{7}$$

where β_{ave} is the experimental extinction coefficient of run 5. This shape for $\beta(z)$ attempts to incorporate possible wall effects that are not characterizable with the present experimental system. The analytical band intensity i_n for run 5 changes by less than 1.5 percent for $\beta_w/\beta_c=0.5$ and 1.5. Although a small variation in the integrated band intensity does not necessarily mean that small variations occur in the spectral values (since cancellations can occur over the band), the extremely small extent of the variations implies that the spectral intensities probably change an insignificant amount as well.

By far the most significant parameter is the temperature $T(z)$. Recall that in section 3.0 an uncertainty in the average temperature T_{cl} of ± 10 percent, which applies for the entire test section, is used. This value probably overestimates the actual uncertainty since Al_2O_3 is nonemitting; yet, it is acceptable for calculating the uncertainty in the extinction coefficient β as it provides a conservative estimate. Furthermore, the sensitivity of the intensity to the uncertainty in β is not great. To obtain an uncertainty in temperature that is more realistic with respect to its influence on the spectral intensity, consider that the intensity is most dependent upon emission from a relatively small volume centered around the test section viewing port. Then, because the uncertainty in the centerline temperature T_{cl} is expected to be much smaller than ± 10 percent over the radiative volume of concern for Al_2O_3 particles, the actual measured temperature distribution $T(z)$ is taken to characterize the emitting medium with relatively little error. Unfortunately a variation of $T(z)$ with time occurs due to system cooling, introducing uncertainty of a temporal nature whose magnitude is expected to be much greater than that due to position in the test section. Considering the degree of temporal variation in temperature during each run, the uncertainty in T_{cl} is taken as $\Delta T_{cl}=\pm 5$ K for all runs except runs 5, 6, 7, and 8 for which $\Delta T_{cl}=\pm 10$ K applies. To estimate the effect that such a variation in T_{cl} has on $i_{\lambda n}$, RADCAL is executed for pure gas runs 9 and 15 with T_{cl} set to $T_{cl}\pm 10$ K and $T_{cl}\pm 5$ K. (The remaining parts of the temperature profiles are scaled accordingly using T_g^* and T_w.) The results indicate changes in $i_{\lambda n}$ of less than ± 12 percent for $T_{cl}\pm 5$ K and less than ± 25 percent for $T_{cl}\pm 10$ K, which is taken as the systematic uncertainty in $i_{\lambda n}$. A measurement uncertainty is estimated from uncertainties in the spectral calibration factor and the lock-in amplifier millivolt readings. Taking the overall uncertainty in the spectral intensity as the square root of the sum of the squares of the measurement and systematic errors (Benedict, 1977), the representative uncertainty in $i_{\lambda n}$ is finally obtained as less than ± 14 percent for $T_{cl}\pm 5$ K and less than ± 26 percent for $T_{cl}\pm 10$ K. These percentages apply only to wavelength regions where detectable emission exists; when the intensity is near zero in the band wings, the error in $i_{\lambda n}$ is obviously larger. Checking the differences between the analytical and experimental band intensities in Table 3, the stated uncertainties in $i_{\lambda n}$ seem reasonable. The difference for run 5 is slightly larger than desired. However, since the analytical result is sensitive to the accuracy of the wide-band model and wide-band scaling, among other modeling assumptions, the large difference cannot be completely attributed to uncertainty in the experimental data.

Observations and Comparisons. Comparing the gas and gas-particle runs, some general observations are made and the importance of the temperature distribution is noted. The peaks of the intensity curves rise with increasing T_{cl}, as expected. The spectral distributions, however, show an unusual spectral trend that cannot be explained by a temperature effect alone. If the only difference between a set of gas and gas-particle runs were the indicated shape of the temperature profile, it is expected that the intensity $i_{\lambda n}$ of the gas-particle run would be greater than that of the gas run for the entire band since the gas-particle temperature profile has a broader and more isothermal high-temperature core for a given value of T_{cl}. The gas-particle run therefore has a larger temperature at each measured point across the layer. It follows then that if scattering were not present, $i_{\lambda n}$ for the gas-particle runs would be greater than $i_{\lambda n}$ for the gas. This does not always occur, however. In most cases (runs 2, 3, 5, and 7), the introduction of the purely scattering particle seems to cause a decrease in $i_{\lambda n}$ near the band head (lower wavelength portion of the 4.3 μm CO_2 band) and an increase in the upper wavelength region of the band. This observation is also true to a lesser extent in runs 1 and 6. This behavior seems to occur only for moderate extinction optical depths (or scattering optical depths since $\omega=1$). For the two runs (4 and 8) with optical depths greater than 2 (2.2 and 3.0, respectively), the effect seems to disappear, and $i_{\lambda n}$ for the gas-particle runs is consistently higher than $i_{\lambda n}$ for the gas runs. Also evident from the emission plots is that any influence scattering may have on the emission is discernible to some degree by comparison to pure gas runs since Al_2O_3 is almost purely scattering and does not emit. Continuum particle emission would tend to obscure the effect of scattering. One anomaly in the data is the sharp rise in the intensity at the upper wavelength edge of run 6. The sudden increase bespeaks a rapid rise in system temperature, most likely due to the interruption of particle flow. The validity of upper wavelength data for run 6 is questionable as a result.

Table 3 Analytical predictions

Run No.	T_{cl} (K)	$x_n \times 10^{-3}$ (#/mm^3)	βL	τ_{HL}	$i_{n,e}$ (W/m^2/sr)	$i_{n,p}$ (W/m^2/sr)
1 (g-p)	474.3	0.533	0.808	30.87	6.37	5.98
2 (g-p)	481.7	0.541	0.819	30.73	6.71	6.63
3 (g-p)	488.0	0.823	1.24	30.30	7.27	7.38
4 (g-p)	446.4	2.072	3.02	32.18	4.41	4.25
5 (g-p)	512.0	1.136	1.69	28.03	7.82	10.36
6 (g-p)	509.6	0.783	1.16	28.60	9.20	9.85
7 (g-p)	598.2	0.403	0.62	23.87	21.98	26.19
8 (g-p)	482.1	1.484	2.19	29.47	7.85	7.06
9 (g)	587.9	0	0	25.53	22.07	20.08
10 (g)	520.6	0	0	28.70	9.75	9.55
11 (g)	500.7	0	0	29.92	7.62	7.43
12 (g)	488.6	0	0	30.65	6.33	6.37
13 (g)	477.9	0	0	31.34	5.44	5.54
14 (g)	468.8	0	0	32.02	4.74	4.84
15 (g)	447.7	0	0	33.57	3.36	3.57

The spectral comparison made between the experimental data and analytical results is performed using RADCAL, which yields normal, spectral intensity values for the pure gas runs. Since this spectral calculation is for a single line of sight, it is not possible to incorporate the effect of wall reflection into the analytical values. Instead, the walls are taken to be black at temperature T_w. Since the walls are cold with a reflectivity of only 0.15, this wall approximation is not estimated to influence $i_{\lambda n}$ significantly. The total path length for the calculation is the layer depth L. Comparisons for a number of gas runs have been performed and typical results are shown in Fig. 12. The intensity magnitudes agree quite well, although the relatively large bandwidth of the circularly variable filter averages the spectral values over a small wavelength interval. Comparative runs have been made for a constant-temperature medium, which is uniform at T_{cl}. The colder boundary layer regions have a dominant influence on the magnitude of the emitted intensity. An isothermal temperature field at T_{cl} increases the band intensity for the experimental runs by 110 percent to 175 percent, depending on the run. As mentioned above, the presence of the particle not only introduces scattering, it also flattens and broadens the high-temperature core region. This effect, if taken independent of the influence of scattering, would tend to increase the emitted spectral intensity (across the entire band) over that of a pure gas run with similar T_{cl}.

The increase in $i_{\lambda n}$ over the region of the 4.3-μm CO_2 band that is expected based solely on the particle's effect on the temperature profile is seen only for runs 4 and 8, which are characterized by the largest particle extinction optical depths. For the runs with moderate optical depths, the intensity decreases in the lower wavelength region and increases in the upper wavelength region. Reflection from the wall is not expected to be the cause of the spectral behavior since both the gas and gas-particle runs have the same wall conditions. The interaction of wall reflection and the gas-particle temperature profile is also not expected to be the cause since with all other parameters remaining equal, the introduction of wall reflection seems to increase $i_{\lambda n}$ across the gas band. The effect of P_T, on the other hand, seems partially to expain the spectral behavior. The influence of a change in P_T is tested by executing RADCAL for run 15 using P_T (actual value for the run) with a 2 percent variation. The results indicate that an increase of 2 percent in total pressure causes a decrease of about 2 percent or less in $i_{\lambda n}$ in the lower wavelength region and an increase of about 2 percent or less in the upper region. A decrease of 2 percent in the total pressure causes opposite trends. This is precisely the behavior predicted by the relative pressures for the gas and gas-particle experimental results plotted together in Figs. 4–11. What is not predicted, however, is the magnitude of the experimental spectral variation, which is much greater than 2 percent, especially in the lower wavelength region.

The effect of the particle interaction on the spectral results is investigated by simulating the increased path lengths that

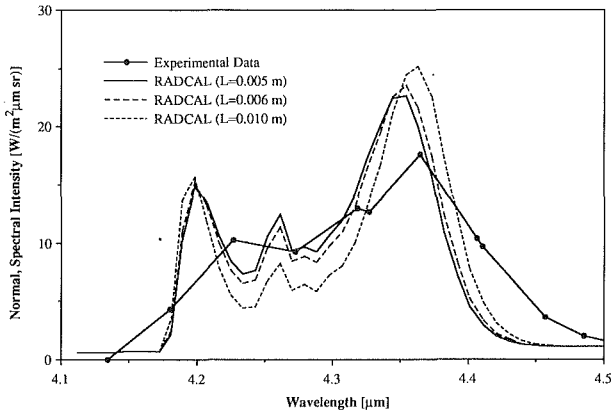

Fig. 12 Effect of path length extension on the emitted intensity for run 15

scattering introduces. Using the spectral nonscattering code, the distribution $T(z/L)$ for run 15 is expanded by increasing the layer depth L by a factor of 1.2 and 2. The spectral intensity for the path that results in each case is plotted in Fig. 12. Clearly, the increased path lengths predict the spectral behavior of the experimental runs with moderate optical depth. The large variation in $i_{\lambda n}$ shown in the plot argues in favor of scattering being the dominant mechanism for generating the complex spectral behavior. The influence of a pressure increase and path length extension are actually closely related since both have the effect of increasing the pressure-path length product of the CO_2 gas, although the path length extension is the primary cause. A preliminary check of the actual increase in the mean emission length (Walters and Buckius, 1990a), which characterizes the gas emission, shows that increases in the characteristic length by a factor of 1.3 or more are common for the gas–particle runs. Evidently, moderate scattering (βL approximately equal to or less than 2) seems to introduce a path length effect similar to that simulated with RADCAL. The highly forward scattering Al_2O_3 tends to scatter into the line of sight from slanted paths in the near forward direction, effectively expanding the layer. For larger optical depths (βL approximately equal to or greater than 2), many scattering events are introduced such that much more emission from the broader high-temperature core region can be emitted into the line of sight, helping to increase the spectral intensity across the band as occurs for runs 4 and 8.

The integrated wide-band comparison made between the experimental data and analytical results is performed using the nonhomogeneous scattering code. This Monte Carlo code is able to account for wall reflection and emission, nonisothermalities, nonhomogeneities, all particle effects, and gas emission, using wide-band modeling. The wide-band scaling technique of Edwards (1976) is used to account for nonisothermal paths. Because the application code is designed for a cylindrical geometry, the test section layer is modeled as a flat disk with radius $r_{max} = 3.54$ cm and height $z_{max} = 0.5$ cm. The diameter of the cylinder is chosen as the diagonal distance across the square test section (5 cm × 5 cm) and the height is set equal to the test section depth L. The diffuse-gray walls of the cylinder are given the temperature T_w and emissivity ϵ_w. The participating medium is assumed uniform in the r direction; in the z direction, the temperature distribution $T(z)$, measured at seven discrete points across the test section, is used. To model the thermal boundary layer near each wall, four additional temperature points are estabished within each region and defined by linear interpolation between T_w and the temperature of the nearest measurement point. Since the code handles nonhomogeneity and nonisothermality by creating a

homogeneous cell structure, the temperature field as described above is modeled as uniform cells with z boundaries established at the center point between defined temperature locations. The particle radiative properties [β, ω, and $P(\theta)$] as computed using Mie theory are assumed uniform throughout the medium.

The computed value is the normal intensity $i_{n,p}$ (subscript p for predicted) into the center ($r=0$) of the cylinder's base (the $z=0$ plane). This quantity includes the spectral region $\lambda_1=4.088$ μm to $\lambda_u=4.643$ μm (which corresponds to the range of experimental data points at the 4.3 μm CO_2 gas band) and incorporates emission from the walls and the gas. As was stated in introducing the experimental data, some spectral intensity values in the gas-band wings were set to zero because of radiant power detectability limits. Since the analytical code predicts blackbody intensity $i_{\lambda b}$ from the viewing port at these wavelengths, these experimental spectral intensities are given the value $i_{\lambda b}(T_w)$. The experimental normal intensity $i_{n,e}$, which is comparable to the analytical results, is computed by numerical integration of the spectral intensity data from $\lambda_1=4.088$ μm to $\lambda_u=4.643$ μm. A comparison of the predicted intensities $i_{n,p}$ to the experimental values is presented in Table 3; the experimental conditions are also noted. Except for runs 5 and 7, the experimental and analytical band intensity values differ by less than 11 percent. The greater differences seen for runs 5 and 7 are attributable to temperature inaccuracy due to the large temperature variations that occurred during the experimental data acquisition. Considering the complexity of the nonhomogeneous modeling, the agreement is excellent and lends considerable validity to the experimental data.

6.0 Conclusions

An experimental investigation, which yields the emitted normal, spectral intensity from a well-characterized, reasonably one-dimensional, nonisothermal layer, has been described. Experimental data are obtained for mixtures of CO_2 gas and purely scattering, spherical Al_2O_3 particles. The runs involve average temperatures in the range 445 K to 600 K, pressures of about 1 atm, a layer depth of 0.5 cm, and particle optical depths in the range 0 to 3. The normal, spectral intensity emitted from the medium is reported over a wavelength range of about 4.0 μm to 4.7 μm, which encompasses the 4.3-μm CO_2 band. Since the particle is virtually nonemitting, no continuum emission outside the band is detected. The effect of the particle is seen in the complicated spectrally dependent and extinction coefficient dependent changes in the band structure when scattering is present. Modeling of the nonisothermal temperature distribution of the layer emerges as a critical factor in determining the magnitude of the emitted intensity. Uncertainty in the magnitude of the temperature accounts for most of the estimated uncertainty in the spectral intensity. A comparison of the experimental band intensities with values computed using a nonhomogeneous scattering model (which rigorously incorporates wide-band modeling) indicates excellent agreement for most runs.

Acknowledgments

The equipment used in this investigation was purchased with support from the National Science Foundation (MEA 81-09250) and the University of Illinois.

References

Benedict, R. P., 1977, *Fundamentals of Temperature, Pressure and Flow Measurements*, 2nd ed., Wiley, New York.

Dowling, J. M., and Randall, C. M., 1977, "Infrared Emissivities of Micron-Sized Particles of C, MgO, Al_2O_3, and ZrO_2 at Elevated Temperatures," Air Force Rocket Propulsion Laboratory, AFRPL-TR-77-14.

Edwards, D. K., 1976, "Molecular Gas Band Radiation," *Advances in Heat Transfer*, T. F. Irvine and J. P. Hartnett, eds., Academic Press, New York, Vol. 12, pp. 115–193.

Eversole, J. D., 1984, "Thermal Radiation From Carbon Particles in a Heated Nitrogen Gas Flow," *Applied Optics*, Vol. 23, No. 19, pp. 3439–3443.

Gitzen, W. H., 1970, *Alumina as a Ceramic Material*, American Ceramic Society, Special Publication No. 4, Columbus, OH.

Grosshandler, W. L., 1980, "Radiative Heat Transfer in Nonhomogeneous Gases: A Simplified Approach," *Int. J. Heat Mass Transfer*, Vol. 23, pp. 1447–1458.

Hottel, H. C., and Sarofim, A. F., 1967, *Radiative Transfer*, McGraw-Hill, New York.

Konopka, W. L., Calia, V. S., Reed, R. A., and Oman, R. A., 1980, "Controlled Hot Gas/Particle Experiments for Validation of a Standardized Infrared Radiation Model," AFRPL-80-31.

Konopka, W. L., Reed, R. A., and Calia, V. S., 1983, "Measurements of Infrared Optical Properties of Al_2O_3 Rocket Particles," presented at the AIAA 18th Thermophysics Conference, Montreal, Canada; Paper No. 83-1568.

Makino, T., Kunitomo, T., Sakai, I., and Kinoshita, H., 1984, "Thermal Radiation Properties of Ceramic Materials," *Trans. JSME*, Vol. 50, No. 452, pp. 1045–1052.

Menart, J. A., Lee, H. S., and Buckius, R. O., 1989, "Experimental Determination of Radiative Properties for Scattering Particulate," *Experimental Heat Transfer*, Vol. 2, pp. 309–332.

Mularz, E. J., and Yuen, M. C., 1972, "An Experimental Investigation of Radiative Properties of Aluminum Oxide Particles," *J. Quant. Spectrosc. Radiat. Transfer*, Vol. 12, pp. 1553–1568.

Pluchino, A. B., and Masturzo, D. E., 1981, "Emissivity of Aluminum Oxide Particles in a Rocket Plume," *AIAA J.*, Vol. 19, pp. 1234–1237.

Skocypec, R. D., Walters, D. V., and Buckius, R. O., 1987, "Spectral Emission Measurements From Planar Mixtures of Gas and Particulate," ASME JOURNAL OF HEAT TRANSFER, Vol. 109, pp. 151–158.

Walters, D. V., and Buckius, R. O., 1990a, "On the Characteristic Lengths for Absorbing, Emitting, and Scattering Media," *Int. J. Heat Mass Transfer*, Vol. 33, No. 5, pp. 805–813.

Walters, D. V., and Buckius, R. O., 1990b, "Emission Calculations for Nonhomogeneous Mixtures of Real Gases and Scattering Particles," submitted for publication.

Whitson, M. E., Jr., 1975, "Handbook of the Infrared Optical Properties of Al_2O_3, Carbon, MgO, and ZrO_2," Vols. I and II, Space and Missile Systems Organization, SAMSO-75-131.

Wiscombe, W. J., 1980, "Improved Mie Scattering Algorithms," *Applied Optics*, Vol. 19, pp. 1505–1509.

Emittance of Boehmite and Alumina Films on 6061 Aluminum Alloy Between 295 and 773 K

T. G. Kollie

T. D. Radcliff

F. J. Weaver

Oak Ridge National Laboratory,
Oak Ridge, TN 37831-6092

The total hemispherical emittance of an oxide film that formed on 6061-T6 aluminum alloy parts in the Tower Shielding Reactor-II at Oak Ridge National Laboratory was measured from 295 to 773 K using an emissometer and/or a calorimeter. The emittance of this film was critically needed for heat transfer calculations in a simulated loss-of-coolant accident of the reactor. X-ray diffraction analysis identified the film as boehmite ($Al_2O_3 \cdot H_2O$), which dehydrated to alumina (Al_2O_3) upon heating above 473 K. The measured emittances for the alumina film are in excellent agreement with published values for anodized aluminum films and for bulk alumina. Published values of the emittance of boehmite could not be found for comparison, but evidence is presented that some anodization processes for aluminum yield boehmite and not alumina films.

Introduction

While upgrading the safety analysis of the Tower Shielding Reactor-II (TSR-II) at the Oak Ridge National Laboratory (ORNL), the value of the total hemispherical emittance, ϵ, between 295 K and 773 K of 6061 aluminum alloy parts was needed for radiant energy calculations in a simulated loss-of-coolant accident of the reactor. The aluminum alloy parts had hydrated oxide films over their surfaces. Because ϵ of aluminum and its alloy can be raised by a factor of 10 or more by formation of an oxide film on the surface of the metal (Touloukian and DeWitt, 1972b), a large uncertainty in the value of this property for the reactor parts existed. In addition, the hydrated oxide film is boehmite, a mineral known (Gitzen, 1970) to dehydrate above 565 K. The effect on ϵ of this decomposition was not known, and published values for ϵ of boehmite and of oxide films on aluminum above 573 K could not be found.

This paper reports the results and analysis of measurements from 295 K to 773 K of the ϵ of oxide films of 6061 aluminum alloy pipe sections taken from the TSR-II. The measurements are compared to published values for ϵ of oxide films on aluminum and aluminum alloys and for ϵ of bulk aluminum oxides.

Experimental Procedure

Specimens used in this work were sections of an ionization chamber guide tube, which had been mounted in the inlet coolant stream of the TSR-II reactor vessel. The TSR-II is a 1 MW (thermal), water-cooled, nuclear reactor that is used as an outdoor neutron source with minimal scattering effects. The guide tube was constructed of 6061-T6 aluminum alloy pipe, 66.7 mm in diameter and 3.2 mm in wall thickness. The guide tube was in service in the reactor coolant for approximately 25 years. The coolant is demineralized water at an average temperature of about 300 K (275 K to 325 K, actual) at the guide tube location. During this extended time period, a nominally 25-μm-thick, grayish film formed on the outside surface of the pipe. X-ray diffraction analysis identified the film as $Al_2O_3 \cdot H_2O$, the mineral boehmite. In this study, sections of the pipe were heated in air or vacuum to determine the effect on ϵ of the decomposition of the $Al_2O_3 \cdot H_2O$ to Al_2O_3, commonly called alumina.

Two well-established techniques were employed to measure ϵ of the oxide films on the aluminum alloy pipe. A Devices & Services (D&S) Model AE Emissometer was used (D&S, 1979) for ϵ determinations at room temperature. Measurements of ϵ as a function of temperature were performed by a calorimetric technique (McElroy and Kollie, 1962). Extensive modifications were required to the experimental apparatuses to allow measurements of the films directly on the pipe, which was a far-from-optimum shape for both techniques.

The D&S Emissometer is a comparative device requiring calibration with two materials of known ϵ. It consists of a measuring head and a digital voltmeter with a resolution of 0.001 ϵ units. The manufacturer specifies (D&S, 1979) that the output of the detector is linear with ϵ to ± 0.01 units. Kollie et al. (1989) have demonstrated that the repeatability of the technique is ± 0.008 units and that the uncertainty of the measurement is ± 0.014 units.

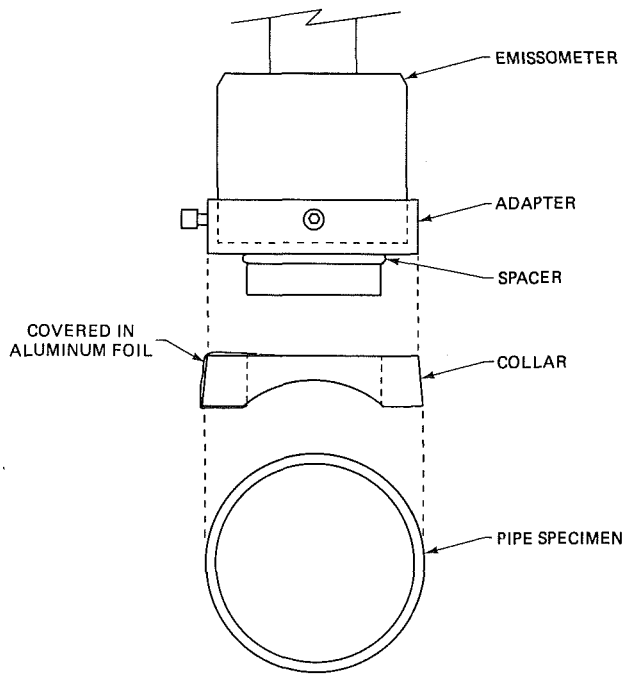

Fig. 1 Apparatus used to measure ϵ of pipe specimen with the emissometer

Contributed by the Heat Transfer Division for publication in the JOURNAL OF HEAT TRANSFER. Manuscript received by the Heat Transfer Division November 27, 1989; revision received May 15, 1990. Keywords: High-Temperature Phenomena, Radiation, Thermophysical Properties.

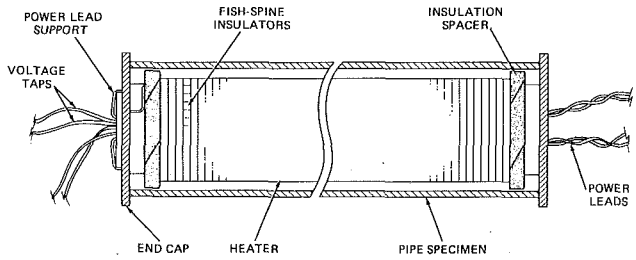

Fig. 2 Schematic of calorimeter specimen, showing details of heater

The emissometer is designed to measure on flat specimens, which are placed on a heat sink (D&S supplied) to maintain a constant specimen surface temperature during the test. Thus, measurements on the curved surfaces of the pipe required a major modification of the test method, as shown in Fig. 1 and discussed briefly by Kollie et al. (1989) and in a technical note by the manufacturer (D&S, 1981). A D&S adapter for the emissometer and a collar that matched the outside diameter of the pipe were used. The surfaces of the collar were covered with aluminum foil to minimize the heat transfer to/from the collar. Working ϵ standards were fabricated from aluminum foil ($\epsilon = 0.034$) and aluminum foil coated with a graphite film ($\epsilon = 0.803$). The first step in the modified procedure was to measure the ϵ of the working standards after placing them on the heat sink. The emissometer was then recalibrated with the standards placed directly on the pipe. Good thermal contact between the foils and the heat sink and/or pipe section was accomplished by filling the air gap between them with distilled water. Measurements of the ϵ of the films on the pipe followed. The uncertainty of these measurements is estimated to be ± 1.6 percent.

Unlike the emissometer, the calorimetric technique is an absolute method for the measurement of ϵ and is essentially the same as the ASTM standard for measurement of ϵ of metals and coated surfaces (ASTM, 1988). For this test, the specimen was a 305-mm-long section of the TSR-II pipe that was heated internally by a resistive winding inserted along its longitudinal axis. The heater was constructed of Nichrome wire, which was inserted in "fish-spine" insulators, then wound on a hollow Al_2O_3 tube. The heater was centered in the specimen by spacers (Fig. 2). After inserting the heater in the specimen, two alumina washers were used to cap the ends of the specimen.

The specimen/heater assembly was suspended from the input power electrodes by the heater leads inside a cylindrical vacuum chamber whose walls were painted with a high ϵ coating; the longitudinal axes of the specimen and chamber were parallel. The pressure in the chamber was always low enough ($< 1 \times 10^{-2}$ Pa) to ignore gaseous convection and conduction heat transfer between the specimen and chamber (ASTM, 1988). Calculation of the heat exchanged by radiation between the specimen and the chamber walls was simplified because the chamber essentially provided a blackbody enclosure for the specimen. According to ASTM C835-82 (ASTM, 1988), blackbody conditions can be assumed if for the "gray body shape factor"

$$F = \frac{1}{\frac{1}{\epsilon_s} + \left(\frac{1}{\epsilon_c} - 1\right)\frac{A_s}{A_c}} \tag{1}$$

the first term in the denominator is much larger than the second, where A_c and A_s are the radiating areas of the chamber and specimen, respectively, and ϵ_c and ϵ_s are the emittances of the chamber and specimen at absolute temperatures T_c and T_s, respectively. Because for this experiment A_c is 14.6 times larger than A_s, ϵ_c is 0.89 and ϵ_s varied between 0.55 and 0.91, the value of the second term of equation (1) was 0.0085, and the first term increased from 1.1 to 1.8 as the temperature increased.

Assuming a blackbody chamber, an energy balance between the specimen and chamber yields (Abbott, 1962)

$$VI - P = A_s \epsilon_s \sigma T_s^4 - A_s \alpha_s \sigma T_c^4 \tag{2}$$

where V is the voltage drop across the heater, σ is the Stefan-Boltzmann constant, and α_s is the absorptance of the specimen at T_s for radiation with a spectral distribution of a blackbody at T_c. The current I is calculated by Ohm's Law from measurements of the voltage drop across a standard resistor, which is in series with the specimen heater. The area A_s is the surface area of the pipe spanned by the voltage taps of the heater and is corrected for thermal expansion of the 6061 aluminum alloy, which increased A_s by 2.2 percent at 773 K.

The term P is the net power loss from the ends of the specimen by radiation from the end caps, by radiation from the hole in the end cap where the heater leads exited the top of the specimen, and by conduction through the power leads to/from the specimen. The end caps were covered with aluminum foil to reduce their radiated energy by a factor of about 20. To compensate for the small energy loss (about 2.3 percent of the input power) from the foil-covered end caps and from the hole in the end cap, a 4-mm length of both ends of the pipe specimen were covered with aluminum foil to reduce the radiation from the specimen by an amount approximately equal to this loss. Double strands of heater wire were used to reduce the temperature of the heater leads as they exited the specimen, minimizing their heat *input* into the specimen. These steps reduced P to ± 0.5 percent of VI. Thus, P can be set equal to zero, and equation (2) can be solved to yield

$$\epsilon_s = \frac{VI}{A_s \sigma \left(T_s^4 - \frac{\alpha_s}{\epsilon_s} T_c^4\right)} \tag{3}$$

As discussed elsewhere (Abbott, 1962, and McElroy and Kollie, 1962, for example), some experimentalists set α_s/ϵ_s equal to one or ignore the term $T_c^4\, \alpha_s/\epsilon_s$ altogether when $T_s \gg T_c$. In this study, values of α_s were derived by calculating ϵ_s with α_s/ϵ_s equal to one, extrapolating the computed high temperature values of ϵ_s to T_c, then recomputing ϵ_s with α_s set equal to ϵ_s at T_c. Several iterations of this process were used.

The temperature of the specimen was determined by seven, 0.13-mm-dia Type S ($Pt_{90}Rh_{10}$–Pt) thermocouples that were peened into the outer surface of the pipe. The hot junctions

Nomenclature

A_c = radiating area of the chamber
A_s = radiating area of specimen corrected for thermal expansion
F = gray body shape factor between the specimen and the chamber
I = current through specimen heater
P = net power loss from ends of specimen
T_c = absolute temperature of chamber
T_s = absolute temperature of specimen
V = voltage drop across specimen heater
α_s = absorptance of specimen at T_s for radiation from chamber wall at T_c
ϵ = emittance
ϵ_c = emittance of chamber at T_c
ϵ_s = emittance of specimen at T_s
σ = Stefan-Boltzmann constant

Table 1 Emittances of alumina and hydrated alumina films at 295 K on Type 6061 aluminum alloy measured with the emissometer and the calorimeter

Film	Film ϵ	
	Emissometer	Calorimeter
$Al_2O_3 \cdot H_2O$[a]	0.934	0.919[b]
$Al_2O_3 \cdot H_2O + Al_2O_3$[c]	0.910	
Al_2O_3[d]	0.884	
Al_2O_3[e]	0.891	0.862[b]

[a]As-received condition.
[b]Extrapolated using least-squares equations.
[c]Heat-treated at 477 K in air.
[d]Heat-treated at 755 K in air.
[e]Heated in vacuum to 775 K.

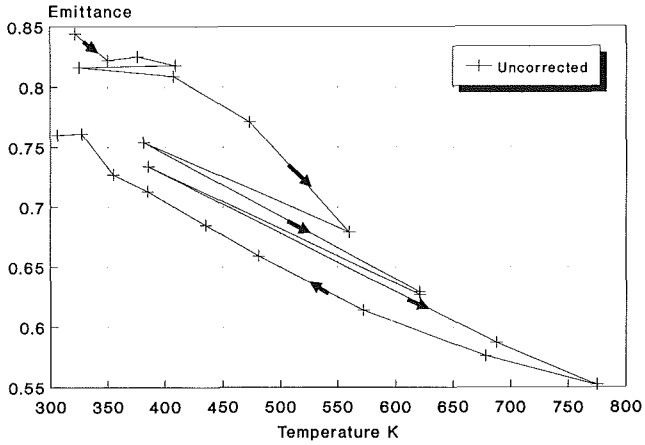

Fig. 3 Uncorrected ϵ data versus temperature obtained in calorimeter during heating of pipe specimen; the arrows show the sequence of data acquisition

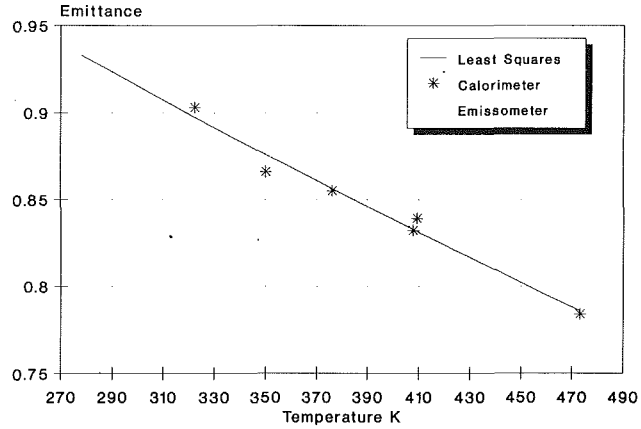

Fig. 4 The ϵ versus temperature measured on films of boehmite; least-squares fit to calorimeter data yields $\epsilon = 1.1808 - 9.75309 * 10^{-4} * T + 2.9687 * 10^{-7} * T^2$

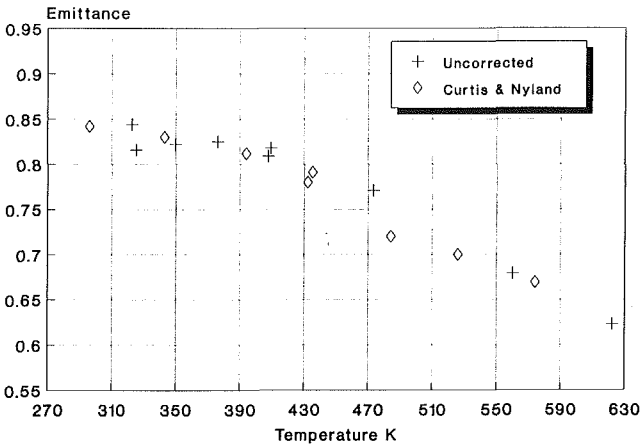

Fig. 5 Comparison of the uncorrected ϵ versus temperature measured in the calorimeter on boehmite film with the measurements of Curtis and Nyland (1965) on an anodized aluminum film

of the thermocouples were intrinsic, that is, the electrical circuit was made through the specimen. Three thermocouples were positioned at the center of the specimen but were spaced at 120 deg intervals around the circumference; two were positioned 25 mm from each end and two were 76 mm from each end. The temperatures measured by the center five thermocouples were used to compute the temperature of the specimen for use in equation (3). The temperature gradients in the specimen were quite small, however, indicating that the methods used to compensate for P were effective. The temperature of the chamber was measured by three, intrinsic junction, Type S thermocouples.

The uncertainty in ϵ_s was estimated by evaluating the errors in measurement of the terms in equation (3) and estimating the errors introduced by the assumptions made in the data analysis and derivation of this equation. This process resulted in an estimated uncertainty of ± 4.8 percent in the measurement of ϵ for the lowest temperature data point and decreased with temperature to ± 1.8 percent of the highest temperature data point.

Results, Discussion, and Conclusions

The initial experiments of this study were conducted at room temperature to determine the effects on ϵ of dehydration of the boehmite film. Several 76-mm-long sections were cut from the 6061 aluminum alloy pipe and heated in air at a uniform rate, taking 4 hours to reach 477 K or 755 K, followed by cooling overnight in the furnace to room temperature. Subsequent x-ray diffraction analyses showed that the amount of boehmite had been reduced substantially in heating to 477 K, but boehmite was not detected after the 755 K heat treatment. In addition, the x-ray diffraction pattern after the 755 K treatment is typical of a very fine crystallite size (or amorphous) film, having very broad bands rather than sharp diffraction peaks. Consequently, the structure of this film could not be identified by the x-ray analysis. It is known (ASM, 1982), however, that anodized films on aluminum and its alloys also yield x-ray diffraction patterns typical of amorphous films; yet, it is well accepted that the films are alumina.

Table 1 lists four ϵ values obtained with the emissometer for the as-received and heat-treated specimens. Complete dehydration of the boehmite in air or vacuum reduced ϵ of the film 0.050 units (5.3 percent) and 0.043 units (4.6 percent), respectively; the partial decomposition of the boehmite in air at 477 K reduced by ϵ by 0.024 units (2.6 percent). The two values of ϵ extrapolated to 295 K from higher temperature calorimetric measurements are in excellent agreement (± 1.6 percent) with the emissometer values and show a change of 0.057 units (6.2 percent) for the complete dehydration of the boehmite in vacuum.

The next set of experiments were performed in the calorimeter to determine the temperature dependence of ϵ of the films on the pipe specimen. Because the exact decomposition temperature of the boehmite film on the specimen was not known, the calorimeter specimen was heated in the vacuum chamber in stages, and the ϵ measured, as shown in Fig. 3. These data were not corrected for thermal expansion of A_s, and α_s was set equal to ϵ_s in equation (3). From these uncorrected data, however, it is apparent that partial decomposition of the boehmite began during heating between 473 and 560 K or during data acquisition at 560 K. Gitzen (1970) gives the temperature for

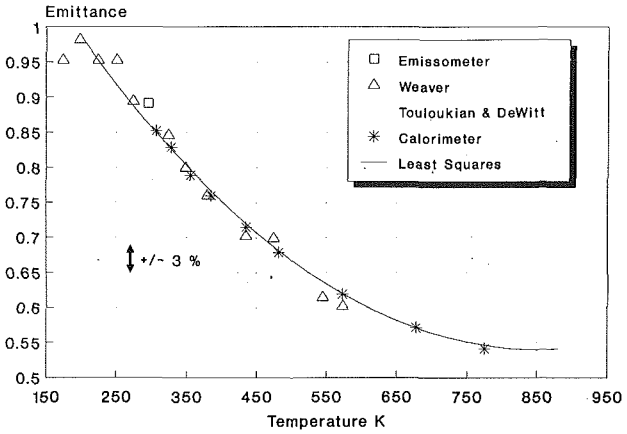

Fig. 6 Comparison of the ϵ versus temperature measured with the emissometer and with the calorimeter on dehydrated boehmite film with the measurements of Weaver (1963) on anodized alumina film and the compilation of Touloukin and DeWitt (1972a) on bulk alumina; least-squares fit to the calorimeter data yields $\epsilon = 1.30779 - 1.83452 * 10^{-3} * T + 1.0950 * 10^{-6} * T^2$; extrapolation of least-squares fit 100 deg above and below calorimeter temperature range is also shown

start of decomposition of boehmite in air as 565 K and completion of decomposition at 775 K. From the previous discussions of the data in Table 1, the start of decomposition in air for the boehmite present on the pipe specimen occurs at or below 477 K and is complete by 755 K.

Based on the foregoing, all calorimeter measurements taken before heating the specimen above 473 K were treated as a unit and attributed to boehmite. All data obtained after heating the specimen to 775 K were treated as a unit and attributed to completely dehydrated boehmite, that is, Al_2O_3. All other data points were not reported as they are attributed to partially dehydrated boehmite.

Figure 4 presents the measurements of ϵ of the boehmite film as a function of temperature determined in the calorimeter and the room temperature value of ϵ measured by the emissometer. The least-squares fit to the calorimeter data is also plotted in Fig. 4. The six calorimetric data points are within 1.1 percent of this function and the emissometer point is within 1.6 percent.

A comparison of the data in Fig. 4 with other measurements was not possible because published measurements of ϵ of boehmite could not be found. Figure 5, however, shows the calorimetric measurements of ϵ of Curtis and Nyland (1965) obtained on an anodized film on a substrate described only as "aluminum" by the authors. Their data bear a striking resemblance, both in magnitude and temperature dependence, to the uncorrected boehmite data, which also are shown in Fig. 5. In their calculation of ϵ, Curtis and Nyland assumed $\alpha_s = \epsilon_s$ in equation (3) and did not correct A_s for thermal expansion, which are the same assumptions we used to calculate the uncorrected data. Also, our T_c and that used by Curtis and Nyland were approximately the same. We hypothesize, therefore, that their anodization process, which they did not describe, included a "sealing" step typically used in industry (ASM, 1982), thereby producing a boehmite film. In addition, the data of Curtis and Nyland (not shown in Fig. 6) are in poor agreement with those on anodized aluminum presented in Fig. 6; specifically, they have a different temperature dependence, being lower near room temperature and higher above 400 K.

Figure 6 presents the measurements of ϵ of the alumina film on the 6061 aluminum alloy specimen as a function of temperature determined in the calorimeter and the room temperature value of ϵ measured by the emissometer. The least-squares fit to the calorimetric data is also plotted in Fig. 6 and is within 0.7 percent of the nine calorimetric data points. For comparison, the data of Weaver (1963) and the recommended values from Touloukian and DeWitt (1972a) are shown in Fig. 6. These vaules of ϵ are within ± 3 percent of the least-square fit to our measurements; this excellent agreement even exists for 100-deg extrapolations of the fit to both higher and lower temperatures.

The ϵ of Touloukian and DeWitt in Fig. 6 were calculated from the lower bound of their recommended values of total normal emittance of bulk alumina versus temperature. Their recommendation appears to be based heavily on the measurements of Olson and Morris (1963) on Norton RA 4213 alumina. Their total normal ϵ were corrected to the total hemispherical ϵ shown in Fig. 6 using the relationship given by Grammer and Streed (1962). That the ϵ of the film on our pipe specimen has the same magnitude and temperature dependence as bulk alumina further supports the assumption that the decomposed boehmite film is very fine-grained alumina, even though it could not be identified by x-ray diffraction.

The data of Weaver were obtained on 1199 alumina alloy (99.99 percent Al; ASM, 1979) substrates, which had been polished then anodized in sulfuric acid; the resulting alumina film thickness was 25 μm for the data shown in Fig. 6. (The thickness of the film on our pipe specimen was nominally 25 μm.) The excellent agreement of our calorimetric data with the magnitude and temperature dependence of Weaver's data is truly remarkable. In fact, the differences are essentially the scatter in the two sets of data. Such agreement is seldom observed in ϵ measurements because of the extreme sensitivity of the measurement to surface finish of the specimen, not to mention the many other experimental errors. Obviously the dehydrated boehmite film on a 6061 aluminum alloy (97.9 percent Al; ASM, 1979) has the same ϵ as an anodized film on pure aluminum.

Weaver also measured on thinner films; the ϵ of a 13-μm-thick film was the same as that of a 25-μm-thick film, indicating that a 13-μm-thick film of anodized alumina is optically thick. From his measurements, an extinction coefficient for anodized alumina films of 0.69 ± 0.06 μm^{-1} was derived.

Acknowledgments

The authors thank Dr. D. L. McElroy for his support and assistance during the course of this work. Dr. D. W. Yarbrough and Dr. R. K. Williams are thanked for their review of the manuscript. We appreciate the assistance of Mr. D. G. Morris, who fabricated and heat treated the Emissometer specimens, and Mr. O. B. Cavin, who performed the x-ray analysis of the specimens. Mrs. G. L. Burn is thanked for preparing the manuscript for publication. The research was sponsored by the Office of Nuclear Energy and the Office of Buildings and Community Systems (Building Systems Division), U.S. Department of Energy under contract No. DE-AC05-84OR21400 with Martin Marietta Energy Systems, Inc.

References

Abbott, G. L., 1962, "Total Normal and Total Hemispherical Emittance of Polished Metals," *Measurement of Thermal Radiation Properties of Solids*, NASA SP-31, pp. 293–306.

ASM, 1979, "Properties and Selection: Nonferrous Alloys and Pure Metals," *Metals Handbook*, Vol. 2, p. 45.

ASM, 1982, "Surface Cleaning, Finishing, and Coating," *Metals Handbook*, Vol. 5, pp. 585–603.

ASTM, 1988, "Standard Test Method for Total Hemispherical Emittance of Surfaces From 20 to 1400°C," ASTM Designation C 835-82 (88), *Annual Book of ASTM Standards*, Vol. 4.06, pp. 404–413.

Curtis, H. B., and Nyland, T. W., 1965, "Apparatus for Measuring Emittance and Absorptance and Results for Selected Materials," NASA TN D-2583, pp. 1–20.

D&S, 1979, *Emissometer Model AE Operating Instructions*, Devices & Services Co., Dallas, TX, pp. 1–6.

D&S, 1981, *Measurement of Emittance of Cylindrical Surfaces*, Technical Note 81-1, Devices & Services Co., Dallas, TX.

Gitzen, W. H., 1970, *Alumina As a Ceramic Material*, American Ceramic Society, Columbus, OH, pp. 1–27.

Grammer, J. R., and Streed, E. R., 1962, "Measurement of Normal and

Directional High-Temperature Total and Spectral Emittance," *Measurement of Thermal Radiation Properties of Solids*, NASA SP-31, pp. 489–498.

Kollie, T. G., Weaver, F. J., and McElroy, D. L., 1989, "Evaluation of a Commercial, Portable, Ambient Temperature Emissometer," accepted for publication in the *Rev. Sci. Instrum.* (Jan. 1990).

McElroy, D. L., and Kollie, T. G., 1962, "The Total Hemispherical Emittance of Platinum, Columbian-1% Zirconium, and Polished and Oxidized INOR-8 in the Range 100 to 1200°C," *Measurement of Thermal Radiation Properties of Solids*, NASA SP-31, pp. 365–379.

Olson, O. H., and Morris, J. C., 1963, "Determination of Emissivity and Reflectivity Data on Aircraft Structural Materials. Part III. Techniques for Measurement of Total Normal Emissivity, Normal Spectral Emissivity at 0.665 Microns, Solar Absorptivity and Presentation of Results," WADC TR 56-222, Part III, pp. 1–29.

Touloukian, Y. S., and DeWitt, D. P., 1972a, "Thermal Radiative Properties of Nonmetallic Solids," *Thermophysical Properties of Matter*, Vol. 8, Plenum, New York–Washington, pp. 141–145.

Touloukian, Y. S., and DeWitt, D. P., 1972b, "Thermal Radiative Properties of Coatings," *Thermophysical Properties of Material*, Vol. 9, Plenum, New York–Washington, pp. 1194–1201.

Weaver, J. H., 1963, *Anodized Aluminum Coatings for Temperature Control of Space Vehicles*, ASD TDR 62-918, pp. 1–29.

Development of a Flow Boiling Map for Subcooled and Saturated Flow Boiling of Different Fluids Inside Circular Tubes

S. G. Kandlikar[1]
Visiting Scientist,
Mechanical Engineering Department,
Massachusetts Institute of Technology,
Cambridge, MA 02139

The thermal behavior of a flow boiling system is represented by a flow boiling map to illustrate visually the relationships among various system parameters. An earlier flow boiling map by Collier (1981) does not include the effect of mass flux and is specific to water at low pressures. For other fluids, significant departures from the parametric trends displayed in Collier's map have been reported in the literature (e.g., Kandlikar, 1988b). In the present paper, a new flow boiling map is developed to depict the relationships among the heat transfer coefficient, quality, heat flux, and mass flux for different fluids in the subcooled and the saturated flow boiling regions. The trends observed in the experimental data and correlations for water and refrigerants are used in deriving the present map. The particular areas where further investigation is needed to validate the trends are also indicated. In the subcooled boiling region, h_{TP}/h_{lo} is plotted against x with Bo as a parameter, while in the saturated boiling region, h_{TP}/h_{lo} is plotted against x with ρ_l/ρ_g and a modified boiling number Bo as parameters. It is hoped that the map would prove to be helpful in explaining the role of different heat transfer mechanisms in flow boiling of different fluids.*

Introduction

A clear understanding of the influence of different variables on heat transfer during single-phase flow may be obtained through analytical equations and well-established empirical correlations. The insight provided by these equations and correlations proves useful not only in the design of heat transfer equipment, but also in the development and optimization of augmented surfaces and channel geometries.

Flow boiling heat transfer is more complex than single-phase heat transfer due to the interactions among the two phases and the tube wall in addition to the presence of both convective and boiling modes of heat transfer. As a result, several regions may be identified that are dominated by distinct heat transfer mechanisms. A flow boiling map provides a good way to represent the complex interrelationships among major variables in these regions.

There are three sources of information available for generating a flow boiling map. First, a number of experimental and analytical studies have been reported in the literature on the mechanism of nucleation, bubble growth, bubble departure, and heat transfer under flow boiling conditions. These fundamental studies are helpful in explaining the heat transfer characteristics of flow boiling systems. The second source of information is available through a large number of experimental investigations performed by researchers under carefully controlled conditions so as to provide much needed data to designers, and to reveal the effect of major operating variables on flow boiling heat transfer. After ascertaining the accuracy of the experimental techniques employed, these data provide a basis for establishing the parametric relationships. Finally, the third source of information is provided by generalized correlations developed from the extensive data sets for different fluids. Since the experimental conditions cannot be easily altered to generate data by varying a single variable at a time while holding other variables constant, a generalized correlation is helpful in covering these gaps. However, extreme caution needs to be exercised in the selection and use of a correlation as its overall accuracy in predicting the heat transfer coefficient may not be sufficient to reveal the correct parametric trends.

Background. Collier (1981) presented the qualitative flow boiling map shown in Fig. 1, depicting the basic relationship between the heat transfer coefficient and the quality, with the heat flux as a parameter. Positive values of quality refer to the saturated two-phase region, while negative values of quality apply to the subcooled region where the quality x is defined as

$$x=(i-i_{l,\text{sat}})/i_{lg} \tag{1}$$

Collier's map is plotted for a single value of mass flux. As will be shown later, his map is relatively specific to water at low pressures, and is representative of only approximate trends in different regions. For example, in the subcooled region, the onset of nucleate boiling is followed by a linear increase in the heat transfer coefficient with x up to $x=0$. The heat transfer coefficient in the subcooled region is defined with (T_w-T_f) as the temperature difference. The linear increase in h shown in Fig. 1 does not accurately represent the heat transfer in the subcooled boiling region. The combined effect of nucleate boiling and convective heat transfer in the partial boiling region, and the effect of net vapor generation on h in the subcooled region close to $x=0$, are also not represented in his map. In the saturated boiling region, heat transfer is initially shown to be independent of x representing the fully developed nucleate boiling. Subsequently, heat transfer is shown to be entirely by convective mode with no influence of q. Eventually the CHF condition is reached with a drastic reduction in h. The CHF is attained sooner with higher values of q. The in-

[1]Permanent address: Associate Professor, Mechanical Engineering Department, Rochester Institute of Technology, Rochester, NY 14623.

Contributed by the Heat Transfer Division and presented at the ASME Winter Annual Meeting, San Francisco, California, December 10–15, 1990. Manuscript received by the Heat Transfer Division August 4, 1989; revision received April 24, 1990. Keywords: Boiling, Evaporation, Multiphase Flows.

fluence of G on heat transfer and CHF in various regions is not included in Collier's map.

The validity of Collier's map for water and refrigerants in the saturated boiling region has been investigated by Kandlikar (1988b). The experimental data of Kenning and Cooper (1988) for water, Chawla (1967) for R-11, Jensen and Bensler (1986) for R-113, and Jallouk (1975) for R-114 were employed. The trends of a constant h_{TP} in the nucleate boiling region, and an increasing h_{TP} with x in the convective boiling region, as depicted in Collier's map, were observed to be true only for water near atmospheric pressure. For refrigerants, it was noted that the h_{TP} versus x trend in the convective boiling region was quite different from the ever-increasing trend depicted in Collier's map. A similar comparison of Collier's map with the experimental data for different fluids in the subcooled boiling region is not available in the literature.

A number of experimental investigators have represented their data in plots that depict sections of a flow boiling map. One common problem encountered while using these plots is that they are specific to the fluid employed and are generally not applicable beyond the range of conditions covered in the individual experiments. Further, they are plotted in terms of different variables, which are often dimensional.

Objective of the Present Work. The objective of the present work is to develop a flow boiling map to represent the heat transfer coefficient as a function of three major parameters: quality, heat flux, and mass flux. It is desired to present the map in terms of dimensionless parameters. Also, the entire range from the onset of nucleate boiling in the subcooled region up to a quality of 0.8 in the saturated boiling region is to be covered.

The flow boiling map will be developed using (*i*) existing experimental and analytical evidence of the heat transfer mechanisms in different regions, (*ii*), the trends predicted by generalized correlations, and (*iii*) available experimental data showing the variation of h with x and other variables.

Although it would be desirable to represent the critical heat flux and the dryout region on the map, these are beyond the scope of the present work.

Development of the Flow-Boiling Map

The final flow boiling map developed in this paper is shown in Fig. 2. It is divided into the subcooled and the saturated boiling regions. The map is applicable to vertical flow with $\mathrm{Re}_{lo} \geq 2300$, although it can be applied to horizontal flow with a high Froude number, $\mathrm{Fr}_l > 0.04$. For $\mathrm{Fr}_l < 0.04$ in horizontal tubes, the map will be able to depict only qualitative behavior

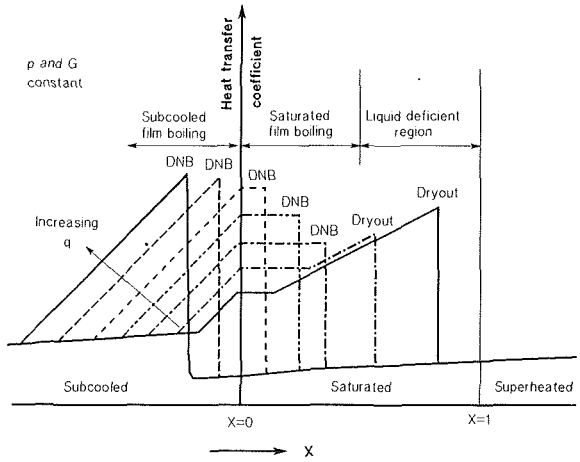

Fig. 1 Schematic of Collier's (1981) flow boiling map

since the stratification effects may modify the parametric relationships. The quantitative representation given in the saturated region may be directly applied to practical situations. In the subcooled region, only a qualitative representation is provided since specific fluid properties are needed in various equations for subcooled boiling. The development of the map along with a discussion of the heat transfer behavior in different regions is given in the following sections.

Choice of Coordinates. The functional relationship between the heat transfer coefficient and the three major system parameters (quality, heat flux, and mass flux) will be displayed in the flow boiling map.

The choice of quality as the abscissa is quite natural since it may be used as an independent variable to represent the fluid state along an evaporator tube. In the subcooled region, the liquid subcooling, $\Delta T_{\mathrm{sub}} = T_{\mathrm{sat}} - T_f$, is commonly employed in representing the onset of nucleate boiling and other subcooled boiling heat transfer mechanisms. ΔT_{sub} may be nondimensionalized in terms of x under the assumption of constant $c_{p,l}$ in the range $T_f < T < T_{\mathrm{sat}}$. Thus, x in equation (1) may be expressed as

$$x = -\Delta T_{\mathrm{sub}} c_{p,l}/i_{lg} \tag{2}$$

It may be noticed that $x<0$ corresponds to the subcooled region, while $0 \leq x \leq 1$ falls under the saturated region.

The heat transfer coefficient is usually defined on the basis of the wall to bulk fluid temperature difference. Thus,

Nomenclature

a, b = constants in equation (24)
Bo = boiling number $= q/(Gi_{lg})$
Bo* = modified boiling number $= (\mathrm{Bo}F_{fl}^{1/0.7})$
$c_{p,l}$ = specific heat of liquid, J/kg°C
D = inside diameter of tube, m
f = friction factor, given by equation (10)
f_1, f_2 = functions described by equations (10) and (38), respectively
F_{fl} = fluid-dependent parameter, given in Table 3
Fr_l = Froude number with all flow as liquid $= G^2/(\rho_l^2 gD)$
G = mass flux, kg/m²s
g = acceleration due to gravity, m/s²
h = heat transfer coefficient, W/m²°C
h_l = heat transfer coefficient with only liquid fraction flow, W/m²°C
h_{lo} = heat transfer coefficient with total flow as liquid, equation (7), W/m²°C
h_{TP} = heat transfer coefficient during two-phase flow with $T_w - T_f$ as the temperature difference, W/m²°C
h_{TP}^* = heat transfer coefficient during two-phase flow with $T_w - T_{\mathrm{sat}}$ as the temperature difference, W/m²°C
i = enthalpy, J/kg
$i_{l,\mathrm{sat}}$ = enthalpy of liquid at saturation, J/kg
i_{lg} = enthalpy of vaporization, J/kg
k = thermal conductivity, W/m°C
m, n, p = constants in equations (24)–(29)
P = pressure, Pa
Pr_l = Prandtl number of liquid $= (c_{p,l}\,\mu_l/\mathrm{k}_l)$
q = heat flux, W/m²
q_{lo} = heat flux with total flow as liquid $= h_{lo}(T_w - T_f)$, W/m²

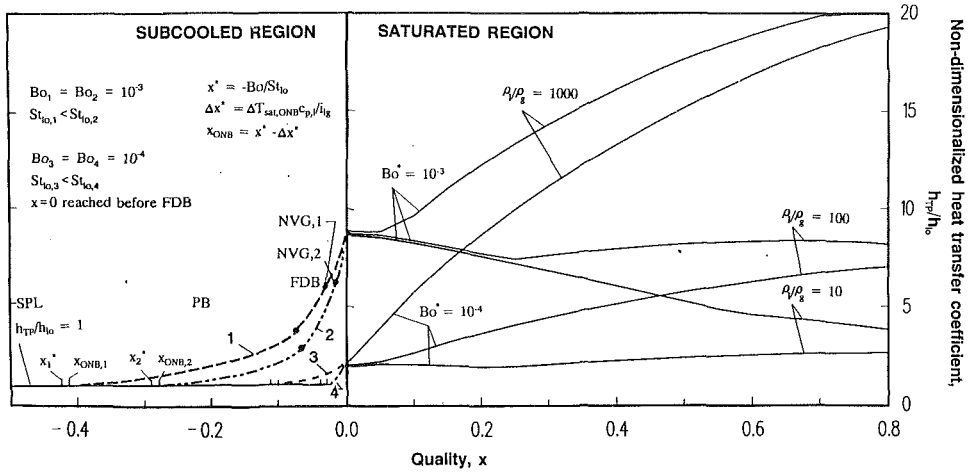

Fig. 2 Flow boiling map developed for subcooled and saturated flow boiling in circular tubes with h_{TP}/h_{lo} versus x as coordinates

$$h_{TP} = q/(T_w - T_f) = \begin{cases} q/(\Delta T_{sat} + \Delta T_{sub}) & \text{for } T_f < T_{sat} \\ q/\Delta T_{sat} & \text{for } T_f = T_{sat} \end{cases} \quad (3)$$

Another definition commonly employed in flow boiling work is based on ΔT_{sat} as the temperature difference, and is given by

$$h^*_{TP} = q/(T_w - T_{sat}) = q/\Delta T_{sat} \quad (4)$$

The two heat transfer coefficients defined by equations (3) and (4) are related in the subcooled region by

SUB:

$$h^*_{TP} = h_{TP}(1 + \Delta T_{sub}/\Delta T_{sat}) \qquad \text{for } x < 0$$

or

$$h^*_{TP} = [1/h_{TP} + x i_{lg}/(c_{p,l} q)]^{-1} \qquad \text{for } x < 0 \quad (5)$$

Alternatively,

$$h_{TP} = [1/h^*_{TP} - x i_{lg}/(c_{p,l} q)]^{-1} \qquad \text{for } x < 0 \quad (6)$$

and in the saturated region by

SAT:

$$h_{TP} = h^*_{TP} \quad \text{for } 0 \le x \le 1 \quad (7)$$

In the present flow boiling map, h_{TP} is chosen over h^*_{TP} to represent the heat transfer coefficient since it retains the physical concept of the heat transfer coefficient. It also offers certain advantages in nondimensionalizing the heat transfer coefficient, as well as in simplifying the representation of the subcooled region.

In order to represent a number of different fluids on the same map, it is essential to nondimensionalize the heat transfer coefficient. In the saturated flow boiling region, h_l, the single-phase heat transfer coefficient, with only the liquid fraction flowing in the tube, is frequently employed as a nondimensionalizing parameter. In the subcooled region, the use of h_{lo}, the single-phase heat transfer coefficient with total flow as liquid, instead of h_l is more appropriate since there is no net equilibrium vapor fraction present in the flow. Use of h_{lo} in the saturated region as well is in fact more desirable since the variation in h_{TP}/h_{lo} with x clearly represents the variation in the two-phase heat transfer coefficient, unlike h_{TP}/h_l, which is affected by the variation in h_l with x.

The ordinate of the map is therefore chosen to be h_{TP}/h_{lo}. Kandlikar (1988a, 1990a) used the Dittus-Boelter correlation for calculating h_{lo}, but later Kandlikar (1990b) showed that the Petukhov-Popov (1963) and Gnielinski (1976) correlations for h_{lo} are better able to account for the Prandtl number effect for different fluids. These correlations are therefore employed here. h_{lo} is then given by:

Petukhov-Popov (1963)

For $0.5 \le Pr \le 2000$ and $10^4 \le Re_{lo} \le 5 \times 10^6$,

Nomenclature (cont.)

Re_l = Reynolds number based on only the liquid fraction flow $= [GD(1-x)/\mu_l]$
Re_{lo} = Reynolds number based on all flow as liquid $= (GD/\mu_l)$
r_{max} = maximum cavity radius, m
T = temperature, °C
T_f = bulk mean temperature, °C
T_w = wall temperature, °C
T_{sat} = saturation temperature, °C
ΔT_{sat} = wall superheat $= (T_w - T_{sat})$, °C
ΔT_{sub} = liquid subcooling $= (T_{sat} - T_f)$, °C
ΔT = temperature difference between wall and bulk fluid $= (T_w - T_f)$, °C
x = quality
x^* = quality at the location where $T_w = T_{sat}$
ΔX^* = $= (X_{ONB} - X^*)$
μ = dynamic viscosity, kg/m s
ρ = density, kg/m^3
σ = surface tension, N/m

Subscripts

A-G = corresponding to points A-G on Fig. 4
f = bulk fluid
g = vapor
l = liquid; with only liquid fraction flow
lg = latent
lo = with total flow as liquid
ONB = onset of nucleate boiling
sat = saturated

Abbreviations

CBD = convective boiling dominant
FB = flow boiling
FDB = fully developed boiling
NBD = nucleate boiling dominant
NVG = point of net vapor generation
ONB = onset of nucleate boiling
PB = partial boiling
SAT = saturated
SPL = single-phase forced convection with liquid
SUB = subcooled

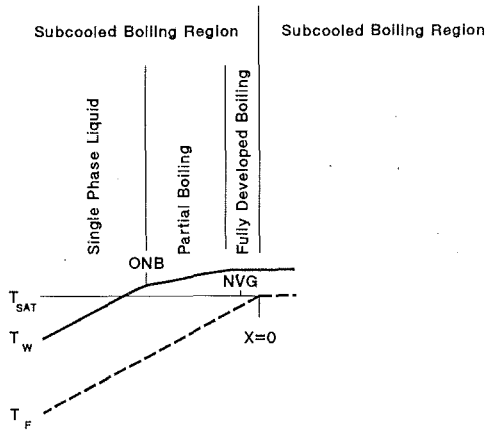

Fig. 3 A representative sketch showing the wall and fluid temperatures in the subcooled boiling

$$\mathrm{Nu}_{lo} = h_{lo}k_l/D = \mathrm{Re}_{lo}\mathrm{Pr}_l(f/2)/[1.07 + 12.7(\mathrm{Pr}^{2/3} - 1)(f/2)^{0.5}] \tag{8}$$

Gnielinski (1976)

For $0.5 \le \mathrm{Pr} \le 2000$ and $2300 \le \mathrm{Re}_{lo} < 10^4$,

$$\mathrm{Nu}_{lo} = h_{lo}k_l/D = (\mathrm{Re}_{lo} - 1000)\mathrm{Pr}_l(f/2)/[1 + 12.7(\mathrm{Pr}^{2/3} - 1)(f/2)^{0.5}] \tag{9}$$

The friction factor f in equations (8) and (9) is given by

$$f = [1.58\ \ln(\mathrm{Re}_{lo}) - 3.28]^{-2} \tag{10}$$

Based on the above discussion, h_{TP}/h_{lo} is chosen to represent the nondimensionalized heat transfer coefficient along the ordinate, and x is chosen to represent the fluid state along the abscissa.

Subcooled Region

A representative sketch showing the wall and bulk fluid temperatures in the subcooled region is shown in Fig. 3. The subregions displayed in Fig. 3 are generally of no interest in refrigerant evaporator design, but are of relevance in applications such as steam generators, nuclear reactors, and cooling systems for magnets and electronic equipments.

As a necessary condition for the onset of nucleate boiling, the wall temperature at a given location must be equal to or greater than the local saturation temperature, or $T_w \ge T_{\mathrm{sat}}$. The maximum value of ΔT_{sub} where this condition is satisfied occurs at a quality x^* and the following relations apply:

at $x = x^*$,

$$T_w = T_{\mathrm{sat}} \tag{11}$$

$$\Delta T_{\mathrm{sub}} = q/h_{lo} \tag{12}$$

Combining equations (2) and (12), x^* may be expressed as

$$x^* = -qc_{p,l}/(h_{lo}i_{lg}) = -\mathrm{Bo}/\mathrm{St}_{lo} \tag{13}$$

where Bo is the boiling number, $\mathrm{Bo} = q/(Gi_{lg})$, and St_{lo} is the Stanton number with total flow as liquid, $\mathrm{St}_{lo} = h_{lo}/(Gc_{p,l})$.

The region with $T_w < T_{\mathrm{sat}}$ lies entirely in single phase flow. The nondimensionalized heat transfer coefficient in this region is given by

$$\text{SPL:}\quad h_{TP}/h_{lo} = 1 \tag{14}$$

As T_w exceeds T_{sat}, a nonboiling region may still exist over some length since nucleation is not initiated until the onset of nucleate boiling, or ONB, is reached.

Onset of Nucleate Boiling, ONB. The wall superheat and q at ONB are governed by the superheat requirements to activate a cavity on the surface. Assuming the availability of all cavity sizes, Bergles and Rohsenow (1964) proposed that nucleation would occur when the temperature in the liquid at the interface of a hemispherical bubble attains the minimum temperature required to nucleate the cavity. This condition is reached when the liquid temperature profile near the wall is normal to the curve representing the temperature required to activate the cavity as a function of the cavity radius.

Murphy and Bergles (1972) compared the theoretical results for incipient nucleation heat flux for R-113 with and without dissolved air on copper surfaces. The equation for $\Delta T_{\mathrm{sat,ONB}}$ for pure liquids is derived as

$$\text{ONB:}\quad \Delta T_{\mathrm{sat,ONB}} = [(8\sigma q_{\mathrm{ONB}}/k_l)/(dP/dT)_{l,\mathrm{sat}})]^{1/2} \tag{15}$$

The other condition that should be satisfied at ONB is given by the single-phase forced convection relation just prior to ONB

$$q_{lo} = h_{lo}(T_w - T_f) = h_{lo}(\Delta T_{\mathrm{sat}} + \Delta T_{\mathrm{sub}}) \tag{16}$$

At ONB, q_{ONB} and q_{lo} are equal, and the solution of equations (15) and (16) yields the values of T_w and q at ONB.

The above equations may still be applied when dissolved gases are present in the liquid by calculating the T_{sat} and the slope dP/dT at the saturation condition corresponding to the mixture. Murphy and Bergles (1972) obtained satisfactory agreement with their data using equation (15) for the case of decreasing heat flux. For the case of increasing heat flux, a nucleation hysteresis was observed for R-113, which is a low surface tension fluid. For such fluids, the intitiation of nucleation is inhibited at lower wall superheats by the nonavailability of all cavity sizes due to increased wetting of the surface. With a given maximum cavity size $r_{\max}$ available on the surface, Murphy and Bergles obtained a modified equation for ONB as

$$\text{ONB},r_{\max}:\quad \Delta T_{\mathrm{sat}} = q_{\mathrm{ONB}}(r_{\max})/k_l + 2\sigma(dP/dT)^{-1}{}_{l,\mathrm{sat}}/r_{max} \tag{17}$$

Murphy and Bergles could correlate their ONB data for R-113 by employing an $r_{\max}$ of 42.7 μm. In the presence of dissolved gases, the saturation temperature and the slope of the saturation curve need to be modified as suggested by Murphy and Bergles.

From equations (2) and (16), the quality at ONB may be expressed in terms of $\Delta T_{\mathrm{sat,ONB}}$ as

$$x_{\mathrm{ONB}} = -(q/h_{lo} - \Delta T_{\mathrm{sat,ONB}})c_{p,l}/i_{lg} \tag{18}$$

Alternatively, introducing x^* from equation (13), we can write

$$x_{\mathrm{ONB}} = x^* + \Delta x^* \tag{19}$$

where Δx^* is given by

$$\Delta x^* = \Delta T_{\mathrm{sat,ONB}}c_{p,l}/i_{lg} \tag{20}$$

$\Delta T_{\mathrm{sat,ONB}}$ in equation (20) is obtained from equation (15), or if $r_{\max}$ for the particular surface is known, equation (17) may be employed.

Equations (13), (19), and (20) may be utilized in examining the effects of q and G on x at ONB. As q increases, x_{ONB} decreases since the required wall superheat to activate a cavity is attained at lower fluid temperatures. An increase in G however has an opposite effect since the single-phase heat transfer is improved and the temperature profile in the fluid near the wall becomes steeper. This causes the temperature at the top surface of a nucleating bubble to be lower, thereby delaying the nucleation until the bulk fluid temperature T_f increases. The influence of q, G, h_{lo} and the fluid properties is represented by Bo and St_{lo} as shown in Fig. 2.

For low surface tension fluids such as freons, the ONB is delayed during start-up when the heat flux is gradually increased. The improved heat transfer immediately following ONB causes T_w to reduce suddenly with a corresponding increase in the heat transfer coefficient. Since this phenomenon

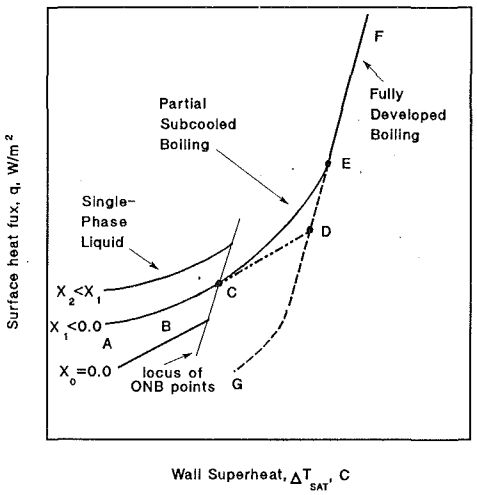

Fig. 4 A representative log-log plot of q versus ΔT_{sat} for describing the new model in the partial boiling region

is strongly dependent on the fluid and the wall conditions, it is not shown in the flow boiling map. The reader is urged to check for the temperature excursion at ONB when it is of significance in their particular application.

Partial Subcooled Boiling. Immediately following the point of ONB, an increasing number of nucleation sites become active as ΔT_{sub} is reduced, until the heat transfer is predominantly by the nucleate boiling mechanism. This region is called the partial subcooled boiling region. A number of different schemes have been proposed in the literature to predict the heat transfer in this region. For example, Bowring (1962) proposed a model that sets the limiting value of q at fully developed boiling as 1.4 times the heat flux at the intersection of the extended single-phase q versus ΔT_{sat} curve with the fully developed q versus ΔT_{sat} curve. In the partial boiling region, the single-phase contribution was assumed to be equal to $h_{lo}\Delta T_{sat}$. Another method proposed by Bergles and Rohsenow (1964) employs a superposition technique in which the fully developed boiling curve is used as an asymptotic limit for the partial boiling region. Further details of the two models may be found from Collier (1981).

A major problem while using the two models described above in the flow boiling map arises from the complexity in evaluating various terms in the correlating schemes. This difficulty is avoided in the new model developed here, which employs equation (15) proposed by Murphy and Bergles (1972) for $\Delta T_{sat,\,ONB}$, and q_{ONB} is calculated from $q_{ONB}=h_{lo}\Delta T_{ONB}$. The heat flux at FDB is calculated from the Bowring model. In the region $q_{ONB}<q<q_{FDB}$, the wall superheat is calculated from an equation derived to yield the correct limiting heat flux values at ONB and FDB, as well as provide the same slope at these two points. The details of the model and the construction of the map in the partial boiling region are described below.

Figure 4 shows a representative q versus ΔT_{sat} plot in the subcooled region. The curve ABC represents the single-phase heat transfer relation for liquid at a fixed subcooling corresponding to a quality, say x_1. Corresponding values of $q_{ONB,1}$ and $\Delta T_{sat,ONB,1}$ are calculated by solving equations (15) and (16), and ONB,1 is located at point C in Fig. 4. (Note that equation (17) should not be employed for this construction.) The fully developed boiling curve is represented by EF. Point D is then obtained at the intersection of the two curves.

The single-phase heat transfer along the curve ABCD is described by

$$q_{lo}=h_{lo}(\Delta T_{sat}+\Delta T_{sub})=h_{lo}(\Delta T_{sat}-xi_{lg}/c_{p,l}) \tag{21}$$

Equation (2) has been employed in equation (21) to express ΔT_{sub} in terms of x.

The fully developed curve is obtained from a correlation by Shah (1977). It is described later under a section on fully developed subcooled boiling, and is given by equation (32). Simultaneous solution of equations (21) and (32) for a given x_1 gives the value of $q_{D,1}$ at location D. $q_{E,1}$ is then obtained from

$$q_{E,1}=1.4q_{D,1} \tag{22}$$

Equation (22) was obtained by Forster and Greif (1959) on the basis of the experimental data covering a wide range of conditions and fluids. Bowring (1962) employed it in his model for the partial boiling region. The wall superheat $\Delta T_{sat,E}$ may be obtained from

$$\Delta T_{sat,E,1}=q_{E,1}/h_{TP,E,1} \tag{23}$$

where $h_{TP,E,1}$ in the fully developed boiling region may be obtained from equation (32). Point E can now be located on the FDB curve.

The region between C and E is identified as partial boiling region. The slope of the q versus ΔT curve varies from 1 in the single-phase region ABC to 2 in the fully developed boiling region EF. The q versus ΔT_{sat} relation in the partial boiling region may be approximated as

$$q=a+b(\Delta T_{sat})^m \tag{24}$$

where a and b are the dimensional constants corresponding to x_1, and can be obtained from the boundary conditions: $q=q_{ONB,1}$ at C where $\Delta T_{sat}=\Delta T_{sat,ONB,1}$, and $q=q_{E,1}$ at $\Delta T_{sat}=\Delta T_{sat,E,1}$ given by equation (23). The values of a and b are given by

$$b=(q_{E,1}-q_{ONB,1})/(\Delta T_{sat,E,1}-\Delta T_{sat,ONB,1}) \tag{25}$$

$$a=q_{ONB,1}-b\Delta T_{sat,ONB,1} \tag{26}$$

The exponent m in equation (24) is allowed to vary linearly from $m=1$ at $q=q_{ONB,1}$ to $m=2$ at $q=q_{E,1}$ by employing the following equation:

$$m=n+pq \tag{27}$$

The constants n and p may be calculated as

$$p=1/(q_{E,1}-q_{ONB,1}) \tag{28}$$

and

$$n=1-pq_{ONB,1} \tag{29}$$

Since a, b, and p in equations (24)–(29) are dimensional constants, a consistent set of units should be employed. Efforts to nondimensionalize these equations resulted in quite cumbersome expressions.

The construction of the partial boiling region on the flow boiling map in Fig. 2 proceeds as follows:

(*i*) Locate X_{ONB} on the map for the given conditions. Consider $x_1>x_{ONB}$.

(*ii*) Obtain $q_{D,1}$ at the intersection of the two curves given by equations (21) and (32). Obtain $q_{E,1}$ from equation (22).

(*iii*) If the imposed heat flux $q>q_{E,1}$, the point lies in or beyond the fully developed region. Partial boiling equations do not apply.

(*iv*) If $q<q_{E,1}$, the following procedure applies.

(*v*) Obtain $\Delta T_{sat,ONB,1}$ and $q_{ONB,1}$ corresponding to x_1 by solving equations (15) and (16).

(*vi*) Obtain the constants a, b, n, and p from equations (25), (26), (28), and (29).

(*vii*) Solve equations (24) and (27) to obtain $\Delta T_{sat,1}$ for the given q. $h_{TP,1}$ is then obtained from $h_{TP,1}=q/\Delta T_{sat,1}$. Knowing h_{lo}, locate $h_{TP,1}/h_{lo}$ corresponding to x_1 on the flow boiling map.

(*viii*) Consider $x_2>x_1$ and follow steps (*ii*) through (*vii*). Continue the procedure for higher values of x until the condition in step (*iii*) has been attained.

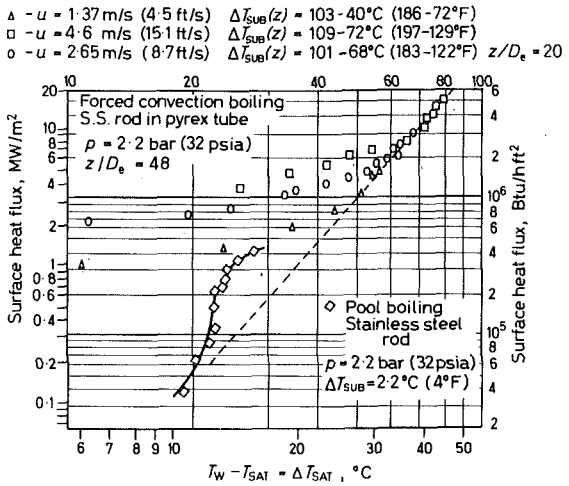

Fig. 5 Experimental results of Bergles and Rohsenow (1964) for partial and fully developed boiling, reproduced from Collier (1981) with permission

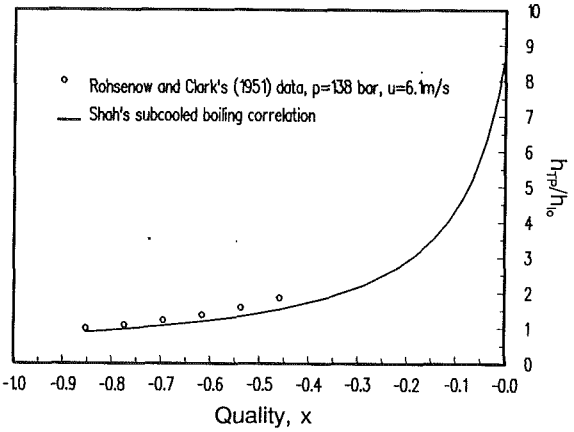

Fig. 6 Comparison of Shah's (1983) subcooled boiling correlation with Rohsenow and Clark (1951) subcooled flow boiling data for water

The procedure described above satisfies the two limiting conditions, one at the ONB and the other at the beginning of the fully developed boiling. Further, by varying the slope of the q versus ΔT_{sat} curve in the partial boiling region from 1 to 2, smooth transitions are obtained near points C and E in Fig. 4.

For some conditions with very low Bo, such as Bo_3 and Bo_4, it may be noted that the saturated liquid state may be reached before the FDB is attained. Under extreme conditions for very low values of Bo, even the ONB state may not be reached before $x=1.0$. However these situations are generally of no practical interest.

Fully Developed Subcooled Boiling, FDB. The fully developed subcooled boiling occurs as the partial boiling curve enters the region of low subcooling dominated by nucleate boiling. Bergles and Rohsenow (1964) experimentally obtained the fully developed subcooled boiling curve for flow boiling and compared it with the pool boiling curve employing the same stainless steel heater rod surface. Their results are shown in Fig. 5. It can be seen that the two curves are quite different, implying that the basic mechanism in pool boiling is altered due to the imposed flow.

A number of correlations have been proposed in the literature specifically for water; for example, the equation by Jens and Lottes (1951) is widely used. Another correlation by Bjorge et al. (1982) covers the entire range of subcooled and saturated boiling, but is not tested extensively for fluids other than water. A correlation developed by Shah (1977) is based on experimental data for water, refrigerants, alcohols, methanol, and carbon tetrachloride. Shah's correlation in the fully developed boiling region may be expressed as:

$$h^*_{TP}/h_{lo} = f_1(\mathrm{Bo}) \tag{30}$$

where $f_1(\mathrm{Bo})$ is given by

$$f_1(\mathrm{Bo}) = \begin{cases} 230\ \mathrm{Bo}^{0.5} & \text{for Bo} > 3.0\text{E-}5 \\ 1 + 46\ \mathrm{Bo}^{0.5} & \text{for Bo} \le 3.0\text{E-}5 \end{cases} \tag{31}$$

Combining equations (6), (13), and (30), h_{TP}/h_{lo} may be expressed as

$$h_{TP}/h_{lo} = [1/f_1(\mathrm{Bo}) + x/x^*]^{-1} \tag{32}$$

A comparison of Shah's correlation with the experimental data of Rohsenow and Clark (1951) shows a reasonable agreement as seen from Fig. 6.

The FDB region is plotted on the flow boiling map in Fig. 2 using equation (32). As Bo increases, the FDB region starts at lower values of x and the curve shifts higher indicating the availability of more nucleation sites similar to pool boiling heat transfer behavior with increasing heat flux.

Point of Net Vapor Generation. As the subcooled liquid in the fully developed boiling approaches the saturation state corresponding to $\Delta T_{sub}=0$ or $x=0$, a point is reached where net vapor generation occurs in the flow. The flow of the two-phase mixture from this point onward affects the nucleate boiling and the convective boiling components much the same way as in the saturated flow boiling. The fully developed nucleate boiling at some point begins to be affected by the two-phase flow, and the convective heat transfer contribution to the two-phase mixture is progressively improved with increasing x.

The point of net vapor generation is predicted from a correlation by Saha and Zuber (1974). The subcooling at this point is given by the following equation:

NVG:

$$\Delta T_{\mathrm{sub,NVG}} = \begin{cases} 0.0022\ (qD/k_l) & \text{for } \mathrm{Re}_{lo}\mathrm{Pr}_l \le 70{,}000 \\ 153.8\ q/(Gc_{pl}) & \text{for } \mathrm{Re}_{lo}\mathrm{Pr}_l > 70{,}000 \end{cases} \tag{33}$$

The quality at NVG may be obtained from equations (2) and (33) as

$$x_{\mathrm{NVG}} = \begin{cases} -0.0022\ \mathrm{Bo}\ \mathrm{Re}_{lo}\mathrm{Pr}_l & \text{for } \mathrm{Re}_{lo}\mathrm{Pr}_l \le 70{,}000 \\ -153.8\ \mathrm{Bo} & \text{for } \mathrm{Re}_{lo}\mathrm{Pr}_l > 70{,}000 \end{cases} \tag{34}$$

Based on the above criteria, the value of $\Delta T_{\mathrm{sub,NVG}}$ is calculated to be 31.9°C, and the corresponding x_{NVG} is -0.229 for the conditions of the experimental data of Rohsenow and Clark shown in Fig. 6.

In the region from the point of NVG to $x=0$, the flow effects may become important as x approaches 0. Further investigations in this area are needed to confirm the effect of NVG on the heat transfer in the subcooled boiling region. In the meantime, a linear relation between h_{TP} and x is employed with h_{TP} varying from $h_{TP,\mathrm{NVG}}$ obtained from equation (32) to $h_{TP,x=0}$ obtained from the saturated boiling correlation given by equation (35).

Saturated Boiling Region

The behavior of h_{TP} with x in the saturated region is quite complex. As Bergles (1988) notes, "In general, the prediction of heat transfer in the quality region is an elusive business that requires much more attention." The intuitive trend of increasing h_{TP} with x is observed for certain fluids, while for other fluids, a decreasing trend is noted. Further, for the same fluid, different investigators obtained different trends.

An investigation by Kandlikar (1988b) explains these differences in the observed trends. As an extension of this study, specific parameters have been identified in this paper, which enable us to predict the correct trend for a given fluid under a given set of operating conditions.

The saturated boiling region is represented on the flow boiling map in Fig. 2 for $x \geq 0$. The two heat transfer coefficients, h_{TP} and h^*_{TP}, are identical in this region since $T_f = T_{sat}$. The x range from 0.0 to 0.8 is included on the map, although it should be noted that a CHF condition may deprive the wall surface of a liquid film, thereby severely deteriorating the heat transfer. In some cases with large values of Bo, CHF is reached even in the subcooled region. Comprehensive surveys on this topic are given by Collier (1981), Rohsenow (1985), and Bergles (1988). The location of CHF depends on a number of parameters such as inlet subcooling, tube length, and pressure besides the three main parameters, x, q, and G. The reader is urged to check for the CHF condition before using the flow boiling map.

The development of the flow boiling map in the saturated boiling region is based on a correlation by Kandlikar (1988a, 1990a). The parametric trends predicted by the Kandlikar correlation and five other correlations were compared by Kandlikar (1988b) with some of the existing experimental data. It was found that the Kandlikar correlation closely represented the trends and also gave the lowest mean deviations for over 5000 data points considered. Further confirmation of the trends predicted by the Kandlikar correlation are obtained in the present study by comparing with additional data. The Kandlikar correlation (1988a, 1990a) is given by

$$h_{TP}/h_{lo} = \text{maximum of} \begin{cases} [h_{TP}/h_{lo}]_{NBD} \\ [h_{TP}/h_{lo}]_{CBD} \end{cases} \quad (35)$$

where the subscripts NBD and CBD refer to the nucleate boiling dominant and convective boiling dominant regions given by

Nucleate boiling dominant (NBD) region:

$$[h_{TP}/h_{lo}]_{NBD} = 0.6683(\rho_l/\rho_g)^{0.1} x^{0.16}(1-x)^{0.64} f_2(\mathrm{Fr}_l)$$

Convective boiling term

$$+ 1058.0\ \mathrm{Bo}^{0.7} F_{fl}(1-x)^{0.8} \quad (36)$$

Nucleate boiling term

Convective boiling dominant (CBD) region:

$$[h_{TP}/h_{lo}]_{CBD} = 1.1360\ (\rho_l/\rho_g)^{0.45} x^{0.72}(1-x)^{0.08} f_2(\mathrm{Fr}_l)$$

Convective boiling term

$$+ 667.2\ \mathrm{Bo}^{0.7} F_{fl}(1-x)^{0.8} \quad (37)$$

Nucleate boiling term

$f_2(\mathrm{Fr}_l)$ in equations (36) and (37) is given by

$$f_2(\mathrm{Fr}_l) = \begin{cases} (25\mathrm{Fr}_l)^{0.3} & \text{for } \mathrm{Fr}_l < 0.04 \text{ for horizontal tubes} \\ 1 & \text{for } \mathrm{Fr}_l > 0.04 \text{ for horizontal tubes and for vertical tubes} \end{cases} \quad (38)$$

It is suggested that in the region $x < 0.02$, h_{TP} values corresponding to $x = 0.02$ be employed. This adjustment is needed due to the form of the correlation.

F_{fl} in equations (36) and (37) is a fluid-dependent parameter, which is set equal to 1.0 for water. On the basis of a data bank consisting of over 5000 data points, Kandlikar (1988a, 1990a) obtained F_{fl} values for refrigerants R-11, R-12, R-13B1, R-22, R-113, R-114, and R-152a. Table 3 lists the values of F_{fl} for water and these seven refrigerants.

The accuracy of the experimental setup and the data reduction procedure employed in obtaining the data needs to be ascertained before using them in verifying the trends in h_{TP} versus x. Five investigations covering a wide range of parameters for water, R-12, R-22, R-113, R-114, and R-152a have been evaluated here. The results of the evaluation are presented in Tables 1 and 2.

The ranges of operating conditions of the five investigations by Jallouk (1975), Jensen and Bensler (1986), Jung et al. (1989), Kenning and Cooper (1988), and Khanpara (1986) are presented in Table 1. The data by Jung et al. and Khanpara were obtained for horizontal tubes, but since the Froude number in their experiments was high, $\mathrm{Fr}_l > 0.04$, the effect of gravity would be negligible. Table 2 gives the details of the experimental setup and data reduction procedures employed in these investigations. It may be noted that four investigators employed electrically heated stainless steel or copper tubes, while Jallouk employed a 12-mm-thick copper tube in ten sections, each individually heated with insulated nichrome wire wound around the tube. This results in a boundary condition that is probably closer to a constant wall temperature condition than a constant heat flux condition. A comparison with Jallouk's data showed that all the correlations were underpredicted consistently by about 10 percent over the entire quality range.

Another observation may be made regarding the experimental accuracy reported in Table 2. Although the investigators report an accuracy within 10 to 15 percent, larger deviations may be expected for small values of wall to fluid temperature

Table 1 Operating ranges of parameters employed by different experimental investigators

Investigator	Year	Fluid	Orientation	D, mm	p, bar	x	q, kW/m^2	G, kg/m^{2}s	Bo $\times 10^4$	N
Jallouk	1975	R-114	Vert-up	20	4.4–14.8	0.017–0.71	0.8–82.1	157–1313	0.05–24.02	347
Jensen and Bensler	1986	R-113	Vert-up	8.1	2.7–8.2	0.001–0.710	6.7–51.1	165–1523	0.035–12.65	1264
Jung et al.	1989	R-12	Hor	9.1	3.26	0.040–0.851	10–45	250–720	0.90–8.10	205
		R-22	Hor	9.1	3.95	0.071–0.868	10–45	250–720	0.66–8.33	409
		R-114	Hor	9.1	2.57	0.076–0.830	10–45	250–720	1.56–8.17	163
		R-152a	Hor	9.1	3.55	0.031–0.689	10–45	250–720	0.47–4.11	356
Kenning and Cooper	1988	Water	Vert-up	9.6	1.6–5.9	0.004–0.671	52–417	123–630	0.39–11.3	471
Khanpara	1986	R-113	Hor	8.7	3.2–3.4	0.15–0.8	17–40	248–600	NA	NA
		R-22	Hor	8.7	8.4–9.2	0.0–0.78	22–40	271–539	NA	NA

NA = data not available, h_{TP} data derived from figures.

Table 2 Details of experimental setups employed in flow boiling investigations

Investigator	Year	Fluid	Tube material	Wall thickness, mm	Heating element	$T_W - T_f$, °C	Measuring technique and accuracy						Comments	
							T_f	T_W	q	m	x	h_{TP}	Setup	Other
Jallouk	1975	R-114	Copper	12.55	Wire wrap	2.2–18.4	Thrmcpl in fluid ±0.2°C	Thrmcpl 2.78 mm from inner surface	W-h meter ±4 percent	Turbine flow meter, ±6 percent	Heat balance error ±7 percent	±10–15 percent	Entrance effect not present	Average h over 25-cm sections
Jensen and Bensler	1986	R-113	SS	0.72	Tube wall	0.6–16.1	From P_{sat}, ±0.1°C	Wall thrmcpl; accuracy not stated	Guard heater, ±1 percent	Flow meters, ±2 percent	From enthalpy balance, ±3 percent	±5 percent, higher at low $T_W - T_f$	Unheated entrance length of 527 mm	Tube wall thickness variation not stated
Jung et al.	1989	R-12	SS	0.25	Tube wall	1.9–8.4	From P_{sat}, ±0.2°C	Thrmcpl on outside stated to be from ±0.3–0.5°C, but in fact may be more accurate	±1.5 percent	Turbine flow meter	From enthalpy balance	Between 5–14 percent	Two 4-m-long test sections connected by U-tube, entrance effect not seen	Study also covered mixture refrigerants
		R-22	SS			1.5–9.4								
		R-114	SS			2.2–18.3								
		R-152a	SS			1.6–14.5								
Kenning and Cooper	1988	Water	SS	0.20	Tube wall	1.3–24.5	From P_{sat}, ±0.2°C,	Thrmcpl on outside ±0.2 percent	Volt and current, ±0.05°C	Variable area flow meters, ±3 percent	From enthalpy balance	±5 percent, higher at low $T_W - T_f$	Guard heater to reduce losses	Effect of surface treatment investigated
Khan-para	1986	R-113	Copper	0.35	Tube wall	2–4 (NA*)	From P_{sat}	Thrmcpl on outside	Volt and current ±4 percent	Rota-meter	From enthalpy balance	Guess—±10 percent (NA)	Radial guard heater	Single-phase tests done to check accuracy
		R-22	Copper	0.35	Tube wall	NA	From P_{sat}	Thrmcpl on outside	Volt and current ±4 percent	Piston-type flow meter	From enthalpy balance	Guess—±10 percent (NA)	Radial guard heater	Single-phase tests done to check accuracy

*NA = not available, h_{TP} data derived from figures.

Table 3 Fluid-dependent parameter F_{fl} in the Kandlikar correlation

Fluid	F_{fl}
Water	1.00
R-11	1.30
R-12	1.50
R-13B1	1.31
R-22	2.20
R-113	1.30
R-114	1.24
R-152a	1.10

differences. In some cases this difference is as small as 0.6°C, which is of the same order of magnitude as the accuracy of temperature difference measurements. This is suspected to be a major reason for erratic behavior in some of the data from these sources. An accurate estimation of x is desired especially in the region where h_{TP} varies strongly with x, as in the case of R-114 data at low pressures obtained by Jallouk (1975). Since x is determined from a heat balance over a long preheater section, the errors associated with the measurement of temperature, pressure, electrical power input, and the heat losses influence the determination of x.

The experimental data by Jung et al. (1989) and Khanpara (1986) were not used in the development of the Kandlikar correlation. A mean deviation of less than 20 percent was observed with R-113 and R-22 data sets by Khanpara, and R-12, R-22, R-114, and R-152a data sets by Jung et al. The trends in these data sets also agreed with those predicted by the Kandlikar correlation, as will be shown later.

To represent equation (35) on the flow boiling map in Fig. 2, three parameters are needed: ρ_l/ρ_g, Bo, and F_{fl}. A modified boiling number Bo* is introduced to include the effect of Bo and F_{fl}. Bo* is defined by

$$\text{Bo}^* = \text{Bo}F_{fl}^{1/0.7} \tag{39}$$

The variation of h_{TP}/h_{lo} with x is plotted for three values of ρ_l/ρ_g and two values of Bo* covering the ranges of parameters commonly employed in the refrigeration, power, and process industries. The influence of these parameters in various regions is discussed in the following sections.

Nucleate Boiling Dominant (NBD) Region. The nucleate boiling dominant region exists at lower values of x in the saturated boiling region in Fig. 2. Here Bo* is seen as the major influencing parameter. As Bo* increases, the contribution due to nucleate boiling increases and consequently h_{TP}/h_{lo} increases.

The trend in h_{TP}/h_{lo} versus x is also influenced by the magnitude of Bo*. At higher values of Bo*, the convective contribution is small compared to the nucleate boiling component. The primary trend of decreasing h_{TP}/h_{lo} with x associated with the nucleate boiling component is clearly seen. As ρ_l/ρ_g decreases, the convective contribution becomes less significant and the range of the nucleate boiling dominant region is extended to higher values of x. At lower values of Bo* however, the contribution due to the nucleate boiling component is not very large and the h_{TP}/h_{lo} versus x trend is influenced by the increasing trend of the convective boiling contribution with x.

The density ratio ρ_l/ρ_g affects only the convective component as seen from equations (36) and (37). Since the contribution due to the convective component at high values of Bo* is quite small in the nucleate boiling region, the effect of varying ρ_l/ρ_g from 1000 to 10 is not significant. However, at low values of Bo*, the convective contribution is quite large. Here the effect of density ratio can be clearly seen. At $\rho_l/\rho_g = 1000$, h_{TP}/h_{lo} increases with x, while at $\rho_l/\rho_g = 10$, h_{TP}/h_{lo} decreases with x.

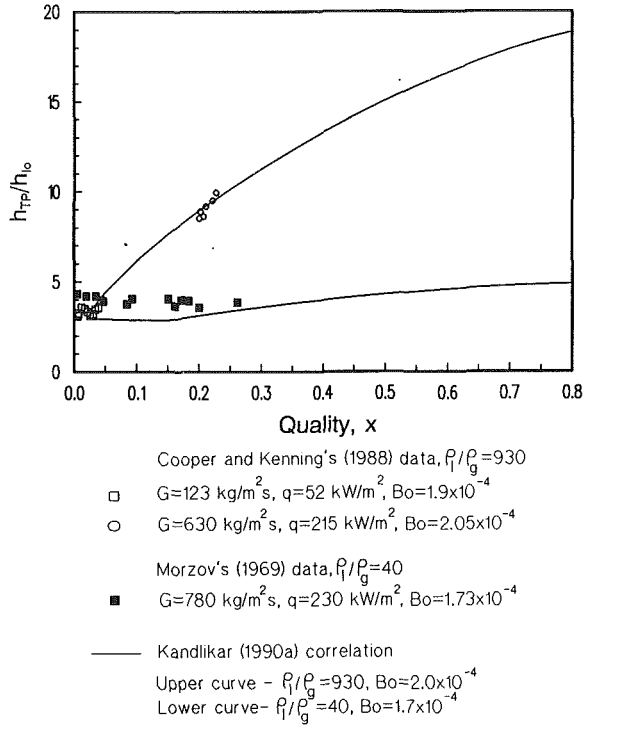

Fig. 7 Comparison of the Kandlikar (1990a) correlation with the saturated flow boiling data of Kenning and Cooper (1988) and Morzov (1961) for water

Convective Boiling Dominant (CBD) Region. In the convective boiling dominant region, the trend of h_{TP}/h_{lo} with x is strongly influenced by the trend of the convective boiling component, which depends on $(\rho_l/\rho_g)^{0.45}$ as seen from equation (37). For a given x, a higher value of (ρ_l/ρ_g) results in a larger vapor volume and a higher velocity of the two-phase mixture. The result is similar to an apparent increase in G in a single-phase flow causing the convective contribution to increase with the density ratio.

As x increases, the convective contribution increases, and with a higher density ratio, h_{TP}/h_{lo} increases rapidly with x. This trend becomes even more pronounced for lower values of Bo* where the nucleate boiling contribution is small. Increasing Bo* at a fixed value of ρ_l/ρ_g causes the h_{TP}/h_{lo} curve to become less steep due to the increasing contribution from the nucleate boiling component, which tends to decrease with increasing x.

Comparison With Trends From Experimental Data. The trends seen in the saturated boiling region of Fig. 2 may be confirmed by inspecting the experimental data for water at low and high pressures corresponding to the high and low values of ρ_l/ρ_g, respectively. Figure 7 shows the experimental data points of Kenning and Cooper (1988) corresponding to $\rho_l/\rho_g = 930$ and almost the same value of Bo. The data and the correlation both display an increasing trend in h_{TP} with x. On the same plot Morzov's (1969) data and the predicted curve from the Kandlikar correlation are also shown for approximately the same Bo but at a lower value of $\rho_l/\rho_g = 40$. Here, h_{TP} is almost independent of x. The influence of ρ_l/ρ_g is clearly seen from this comparison.

Further comparison of the h_{TP}/h_{lo} versus x trend at moderate values of ρ_l/ρ_g is carried out by employing recent data for refrigerants R-113 reported by Khanpara (1986) and for R-22 by Khanpara et al. (1986). These data sets were not employed in the development of the Kandlikar correlation. Figure 8 shows two sets of Khanpara's R-113 data at $\rho_l/\rho_g = 59.4$ and approximately the same Bo. Two observa-

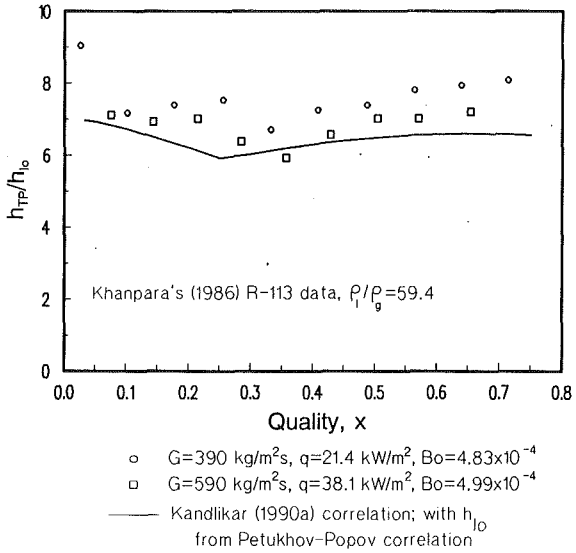

Fig. 8 Comparison of the Kandlikar (1990a) correlation with the saturated flow boiling data of Khanpara (1986) for R-113

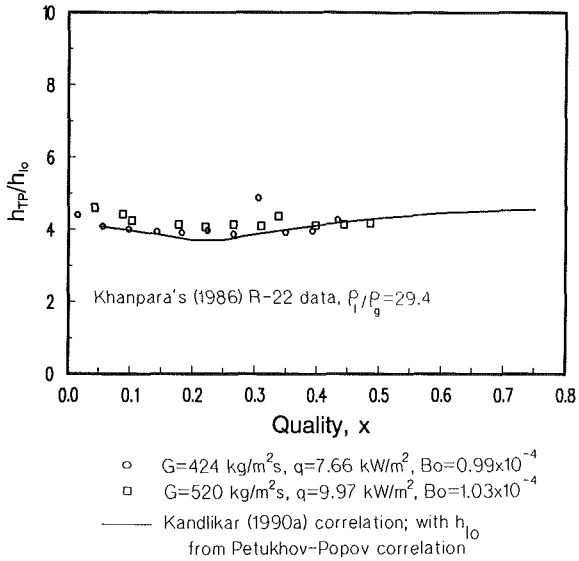

Fig. 9 Comparison of the Kandlikar (1990a) correlation with the saturated flow boiling data of Khanpara (1986) for R-22

tions may be made from this figure. Firstly, it is seen that although the two data sets shown correspond to quite different values of G, 390 and 590 kg/m^{2}s, and different values of q, 21.4 and 38.1 kW/m^2, the data points from the two data sets collapse along a single curve, thereby confirming the validity of using Bo as a parameter in the correlation. Secondly, the trend in h_{TP}/h_{lo} as seen from the data points closely follows that shown by the Kandlikar correlation. Similar trends are observed with Jensen and Bensler's (1986) data for R-113.

Figure 9 shows two sets of the experimental data points of Khanpara et al. for R-22 corresponding to $\rho_l/\rho_g = 29.4$ at approximately the same Bo. Again it can be seen that although G and q are different for the two data sets shown, they both collapse on a single curve, which follows the same trend as the Kandlikar correlation.

To confirm the decreasing trend in h_{TP}/h_{lo} versus x at low values of ρ_l/ρ_g, experimental data for R-114 by Jallouk at pressures of 3.1 and 12.0 bar are shown in Fig. 10. The density ratios ρ_l/ρ_g for R-114 at these pressures are 61.5 and 13.1, respectively. These two data sets have approximately the same

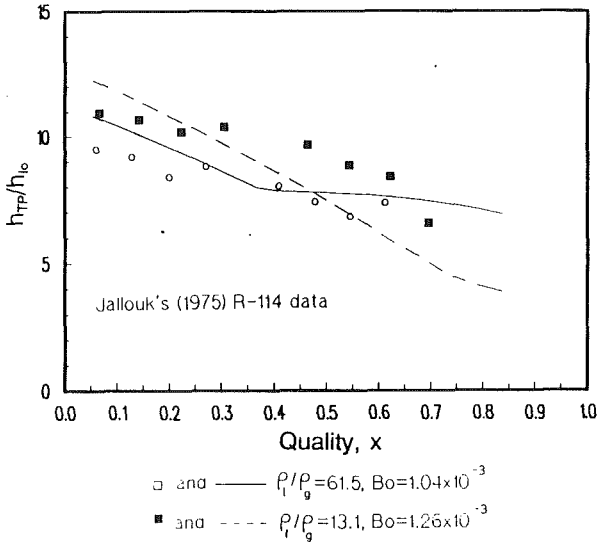

Fig. 10 Comparison of the Kandlikar (1990a) correlation with the saturated flow boiling data of Jallouk (1975) for R-114

mass flow rates and boiling numbers. Also shown in Fig. 10 are the two corresponding lines from the Kandlikar correlation. It may be seen that h_{TP}/h_{lo} decreases slightly for $\rho_l/\rho_g = 61.5$, while it decreases more rapidly for $\rho_l/\rho_g = 13.1$. This confirms the decreasing h_{TP}/h_{lo} versus x trend shown in Fig. 2 for lower values of ρ_l/ρ_g. Similar observations are made for the data sets reported by Jung et al. (1989) for R-12, R-22, R-114, and R-152a, which are within a density ratio range of 50 to 100, and conform to the respective trends depicted in Fig. 2.

Conclusions

The interrelationships between the heat transfer coefficient and other major variables during subcooled and saturated flow boiling in circular tubes are investigated. Representative correlating schemes along with some of the reliable experimental data sources on water and refrigerants have been utilized in understanding the underlying heat transfer mechanisms. The parametric behavior during flow boiling is represented in a flow boiling map, which is plotted as h_{TP}/h_{lo} versus x with the modified boiling number, Bo*, and ρ_l/ρ_g as parameters. The location of CHF is not shown on the map.

In the subcooled boiling region, the onset of nucleate boiling (ONB) and the point of net vapor generation (NVG) have been located. The heat transfer during partial boiling, fully developed subcooled boiling, and beyond the NVG point are represented on the flow-boiling map. The effects of q, G, and different fluids are represented by Bo and St_{lo}. A new model is developed to represent the heat transfer in the partial boiling region. The need for further investigation in the region between the NVG and $x = 0.0$ has been pointed out.

In the saturated flow-boiling region, the nucleate boiling and the convective boiling dominant regions are displayed. The density ratio, ρ_l/ρ_g, and Bo* are identified as the major system parameters to represent the effects due to different fluids, operating pressure, q, and G. The location of CHF is not shown on the map. It is believed that the map will prove to be useful in the design and optimization of various flow-boiling experiments, and also in understanding the underlying mechanisms while developing flow-boiling models for other geometries or for enhanced surfaces.

References

Bergles, A. E., 1988, "Fundamentals of Boiling and Evaporation," in: *Two-Phase Flow Heat Exchangers, Thermal-Hydraulic Fundamentals and Design*, S. Kakac, A. E. Bergles, and E. O. Fernandez, eds., Kluwer Academic Publishers, Dordrecht, The Netherlands, p. 166.

Bergles, A. E., and Rohsenow, W. M., 1964, "The Determination of Forced Convection Surface Boiling Heat Transfer," ASME JOURNAL OF HEAT TRANSFER, Vol. 86, pp. 365-372.

Bjorge, R. W., Hall, G. R., and Rohsenow, W. M., 1982, "Correlation of Forced Convection Boiling Heat Transfer Data," *International Journal of Heat and Mass Transfer*, Vol. 25, pp. 753-757.

Bowring, W. R., 1962, "Physical Model of Bubble Detachment and Void Volume in Subcooled Boiling," OECD Halden Reactor Project Report HPR-10.

Chawla, J. M., 1967, "Warmeubergang und Druckabdall in Waagerechten Rohren bei der Stromung von Verdampfenden Kaltemitteln," *VDI-Forschungsheft*, No. 523.

Collier, J. G., 1981, *Convective Boiling and Condensation*, McGraw-Hill, Maidenhead, United Kingdom.

Forster, E. K., and Greif, R., 1959, "Heat Transfer to a Boiling Liquid—Mechanism and Correlations," ASME JOURNAL OF HEAT TRANSFER, Vol. 81, pp. 43-53.

Gnielinski, V., 1976, "New Equations for Heat and Mass Transfer in Turbulent Pipe and Channel Flow," *International Chemical Engineer*, Vol. 16, pp. 359-368.

Jallouk, P. A., 1975, "Two-Phase Flow Pressure Drop and Heat Transfer Characteristics of Refrigerants in Vertical Tubes," Ph.D. Dissertation, University of Tennessee, Knoxville, TN.

Jens, W. H., and Lottes, P. A., 1951, "Analysis of Heat Transfer, Burnout, Pressure Drop and Density Data for High Pressure Water," U.S. AEC Report ANL-4627.

Jensen, M. K., and Bensler, H. P., 1986, "Saturated Forced-Convective Boiling Heat Transfer With Twisted-Tape Inserts," ASME JOURNAL OF HEAT TRANSFER, Vol. 108, pp. 93-99.

Jung, D. S., McLinden, M., Radermacher, R., and Didion, D., 1989, "Horizontal Flow Boiling Heat Transfer Experiments With a Mixture of R22/R114," *International Journal of Heat and Mass Transfer*, Vol. 32, pp. 131-145.

Kandlikar, S. G., 1988a, "A General Correlation for Saturated Two-Phase Flow Boiling Heat Transfer Inside Horizontal and Vertical Tubes," in: *Boiling and Condensation in Heat Transfer Equipment*, E. G. Ragi, T. M. Rudy, T. J. Rabas, and J. M. Robertson, eds., ASME HTD-Vol. 85, pp. 9-19.

Kandlikar, S. G., 1988b, "A Parametric Study of Flow Boiling Heat Transfer Inside Horizontal and Vertical Tubes," *Experimental Heat Transfer, Fluid Mechanics and Thermodynamics 1988*, R. K. Shah, E. N. Ganic, and K. T. Yang, eds., Elsevier, New York, pp. 1618-1626.

Kandlikar, S. G., 1990a, "A General Correlation for Saturated Two-Phase Flow Boiling Heat Transfer Inside Horizontal and Vertical Tubes," ASME JOURNAL OF HEAT TRANSFER, Vol. 112, pp. 219-228.

Kandlikar, S. G., 1990b, "Flow Boiling Maps for Water, R-22 and R-134a in the Saturated Region," *Heat Transfer, 1990*, Proceedings of the Ninth International Heat Transfer Conference, Jerusalem, Israel, Vol. 2, pp. 15-20.

Kenning, D. B. R., and Cooper, M. G., 1988, "Saturated Flow Boiling of Water in Vertical Tubes," *International Journal of Heat and Mass Transfer*, Vol. 31, pp. 445-458.

Khanpara, J. C., 1986, "Augmentation of In-Tube Evaporation and Condensation With Micro-fin Tubes Using Refrigerants R-113 and R-22," Ph.D. Dissertation, Iowa State University, Ames, IA.

Khanpara, J. C. Bergles, A. E., and Pate, M. B., 1986, "Augmentation of R-113 In-Tube Evaporation With Micro-fin Tubes," ASHRAE Paper PO-86-11, No. 3.

Morzov, V. G., 1969, "Heat Transfer During the Boiling of Water in Tubes," in: *Convective Heat Transfer in Two Phase and One Phase Flows*, V. M. Borishanskii and I. I. Paleev, eds., Israel Program for Scientific Translations Ltd., pp. 106-114.

Murphy, R. W., and Bergles, A. E., 1972, "Subcooled Flow Boiling of Fluorocarbons—Hysteresis and Dissolved Gas Effects on Heat Transfer," in: *Proceedings of Heat Transfer and Fluid Mechanics Institute*, Stanford University Press, Stanford, CA, pp. 400-416.

Petukhov, B. S., 1970, "Heat Transfer and Friction in Turbulent Pipe Flow With Variable Physical Properties," in: *Advances in Heat Transfer*, T. F. Irvine et al., eds., Vol. 6, pp. 503-564.

Rohsenow, W. M., and Clark, J. A., 1951, *Heat Transfer and Pressure Drop Data for High Heat Flux Densities to Water at High Subcritical Pressure*, Heat Transfer and Fluid Mechanics Institute, Stanford University Press, Stanford, CA.

Rohsenow, W. M., 1985, "Boiling," in: *Handbook of Heat Transfer*, W. M. Rohsenow, J. P. Hartnett, and E. N. Ganic, eds., McGraw-Hill, New York.

Saha, P., and Zuber, N., 1974, "Point of Net Vapor Generation and Vapor Void Fractions in Subcooled Boiling," *Proceedings of the 5th International Heat Transfer Conference*, Tokyo, Paper B4.7.

Shah, M. M., 1977, "A General Correlation for Heat Transfer During Subcooled Boiling in Pipes and Annuli," *ASHRAE Transactions*, Vol. 83, Part 1, pp. 202-215.

Variation of Superheat With Subcooling in Nucleate Pool Boiling

R. L. Judd
Department of Mechanical Engineering,
McMaster University,
Hamilton, Ontario, Canada
L8S 4L7

H. Merte, Jr.
Department of Mechanical Engineering and
Applied Mechanics,
The University of Michigan,
Ann Arbor, MI 48109

M. E. Ulucakli
Department of Mechanical Engineering,
Lafayette College,
Easton, PA 18042

An analysis is presented that explains the variation of superheat with subcooling that has been observed by a number of researchers investigating nucleate boiling heat transfer at constant heat flux. It is shown that superheat initially increases with increasing subcooling near saturated conditions because of the way in which changes in active site density and average bubble frequency with increasing subcooling affect the rate of heat removal from the heater surface by enthalpy transport and microlayer evaporation. As subcooling increases further, natural convection begins to play an increasingly important role in the heat transfer process. Ultimately, natural convection is able to accommodate the entire imposed heat flux, after which superheat decreases as subcooling increases. The success of the analysis in explaining the variation of superheat with subcooling suggests that the rate of the heat removal from the heater surface is completely determined by the mechanisms of enthalpy transport, natural convection, and microlayer evaporation.

Introduction

Numerous nucleate pool boiling heat transfer investigations conducted at constant heat flux and various levels of subcooling, established by removing heat from the pool of liquid at exactly the rate that it was produced at the boiling surface, have shown that surface superheat first increases and then decreases as subcooling increases. An extensive survey of the literature related to this topic is given by Ulucakli (1987). While the review presented below is restricted to nucleate boiling heat transfer on a plane surface, measurements of nucleate boiling heat transfer on wires and horizontal cylinders show the same effect.

Merte and Clark's (1961) study was the earliest in which the range of subcooling values was large enough to enable the effects of the variation of superheat with subcooling to be observed. Water was boiled on a chrome-plated copper surface at atmospheric pressure and various levels of gravity in the range $1 \le a/g \le 21$. At $a/g = 1$ and the lowest level of heat flux, $q/A_T = 0.062$ MW/m^2, the superheat first increased and then decreased as subcooling increased. This behavior is shown in Fig. 1, which includes the results of other studies performed at $a/g = 1$ and will be discussed below. The same type of behavior observed at this heat flux is seen in Fig. 2 at $a/g = 10$, except that the decrease in superheat with increasing subcooling is predominant. At either gravity level or higher levels of heat flux, $q/A_T = 0.138$ MW/m^2 or $q/A_T = 0.277$ MW/m^2, the superheat increased with increasing subcooling, but a maximum was not observed, presumably because it had not been possible to attain large enough levels of subcooling.

Wiebe and Judd (1971) obtained data for a system in which water was boiled on a copper surface at three different heat flux levels ($q/A_T = 0.064$ MW/m^2, 0.166 MW/m^2, and 0.333 MW/m^2) and various levels of subcooling in the range $0 \le \theta_{sub} \le 60$°C. The main objective of the study was the measurement of the liquid temperature distributions in the vicinity of the surface to determine the thermal layer thickness. The superheat/subcooling curves obtained are included in Fig. 1. In a fashion similar to that of Merte and Clark (1961), the heater surface superheat first increased and then decreased as subcooling increased. The quantitative agreement between the two sets of results is quite good, the significant difference being that Wiebe and Judd (1971) attained much higher levels of subcooling at all levels of heat flux.

Subsequently, Sultan and Judd (1978) conducted another study with the same apparatus at the same levels of heat flux and subcooling in order to investigate the interaction between bubbles forming at adjacent nucleation sites. The superheat/subcooling curves presented by Sultan and Judd (1978) differed

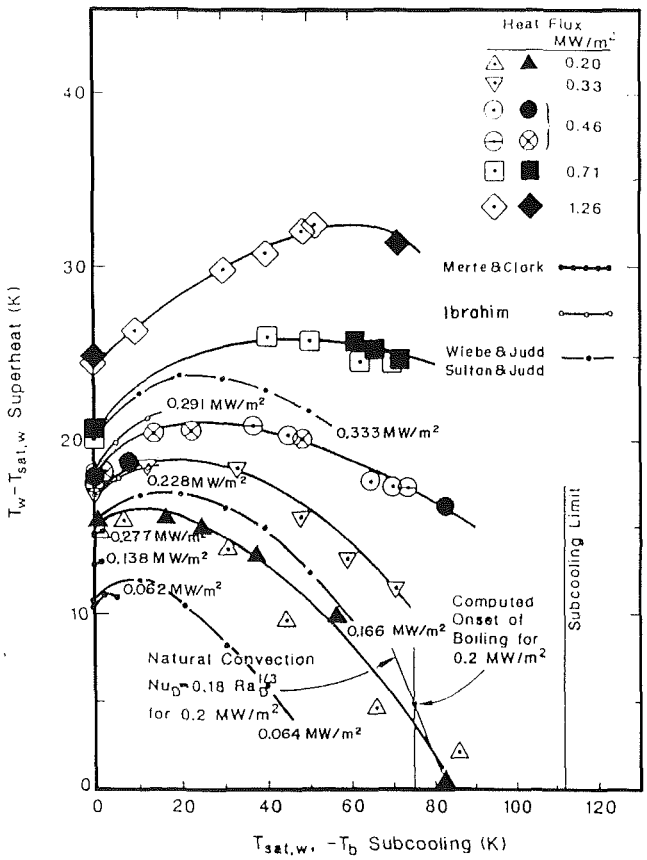

Fig. 1 Variation of superheat θ_{sup} with subcooling θ_{sub} at $a/g = 1$ for water boiling on a copper surface

Contributed by the Heat Transfer Division for publication in the JOURNAL OF HEAT TRANSFER. Manuscript received by the Heat Transfer Division September 3, 1989; revision received March 2, 1990. Keywords: Boiling, Reviews.

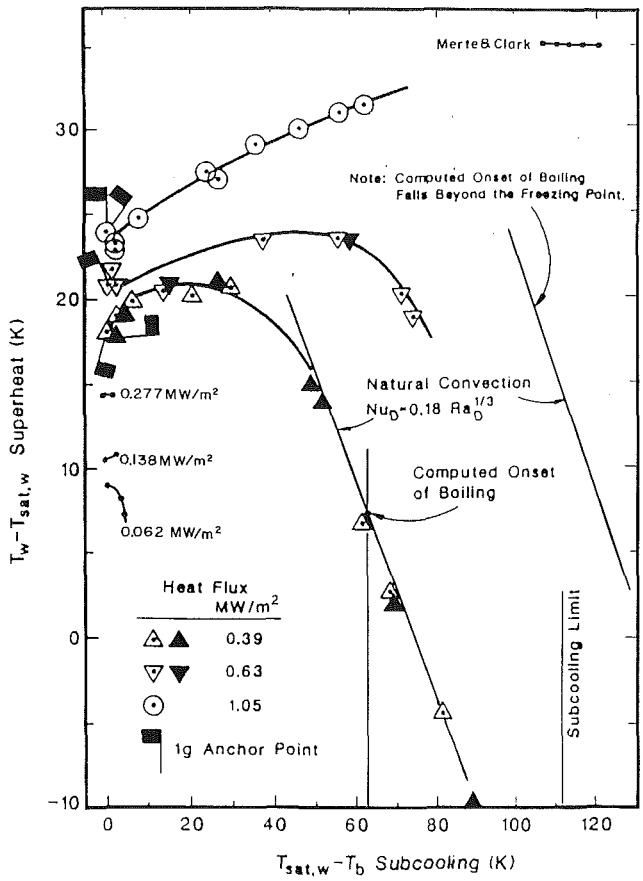

Fig. 2 Variation of superheat θ_{sup} with subcooling θ_{sub} at $a/g = 10$ for water boiling on a copper surface

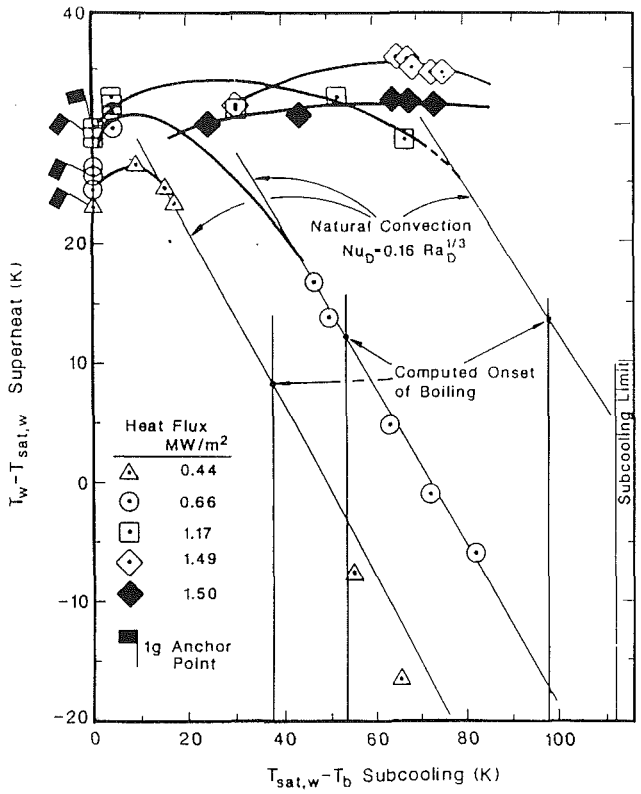

Fig. 3 Variation of superheat θ_{sup} with subcooling θ_{sub} at $a/g = 100$ for water boiling on a copper surface

little from those presented by Wiebe and Judd (1971), less than 0.5°C at any level of heat flux or subcooling.

Ibrahim and Judd (1985) conducted another study with the same apparatus at three different heat flux levels ($q/A_T = 0.166$ MW/m², 0.288 MW/m², and 0.291 MW/m²) and various levels of subcooling in the reduced range $0 \le \theta_{sub} \le 15$°C. This time the purpose of the investigation was the measurement of average bubble growth and waiting times at seven arbitrarily selected active nucleation sites on the heater surface. Data sets, comprised of growth time t_g and waiting time t_w as well as the superheat θ_{sup} corresponding to each value of subcooling θ_{sub} tested, were accumulated for each of the active nucleation sites at each of the three heat flux levels. Nearly perfect agreement was found between the measured growth time values and the predictions from a growth time model presented by Ibrahim and Judd (1985). However, the waiting time values exhibited a curious behavior that could not be explained, first increasing

Nomenclature

A = nucleation parameter = $2\sigma T_{sat}/\rho_v h_{fg}$
A_T = total heat transfer surface area
b = distance from heater surface to nucleus tip
C = specific heat
C_1 = constant = $(1+\cos\beta)/\sin\beta$
C_3 = constant = $(1+\cos\beta)$
$\bar{f}$ = bubble emission frequency
g = gravitational acceleration
h = heat transfer coefficient = $(q/A_T)/(\theta_{sup}+\theta_{sub})$
h_{fg} = latent heat of vaporization
I = integral
k = thermal conductivity
N/A_T = active site density
q/A_T = imposed heat flux
r_c = nucleation cavity radius
R_d = bubble radius at departure
t = time
t_g = bubble growth time
t_w = bubble waiting time
T = temperature
V_{ME} = volume of microlayer evaporated
z = distance from heater surface
α = thermal diffusivity
β = volumetric coefficient of expansion, contact angle
Γ = sensitivity to change in subcooling at saturated conditions
δ = thermal layer thickness
η = dimensionless distance = $1 - C_1 r_c/\delta$
θ = temperature difference $T - T_\infty$
λ_n = eigenvalue
μ = dynamic viscosity, ratio of total heat transfer per site to heat transfer by enthalpy transport
ν = kinematic viscosity, ratio of microlayer evaporation heat transfer to heat transfer by enthalpy transport
ρ = density
σ = surface tension
τ_g = dimensionless growth time = $\alpha_l t_g/\delta^2$
τ_w = dimensionless waiting time = $\alpha_l t_w/\delta^2$

Subscripts

l = liquid
sat = saturation
sub = subcooled
sup = superheated
v = vapor
w = wall

and then decreasing with increasing subcooling. The heat transfer model presented by Judd (1989) was developed for the purpose of demonstrating that this variation is consistent with theory. More will be said about the heat transfer model below because it forms the starting point for the analysis set out in this paper.

The values of superheat measured by Ibrahim and Judd (1985) are plotted in Fig. 1 versus subcooling for comparison. The superheat/subcooling curves plotted in Fig. 1 are representative of the tests that were performed at all of the seven nucleation sites at a particular level of heat flux and subcooling. The curve corresponding to $q/A_T = 0.166$ MW/m^2 cannot be distinguished from that resulting from the investigations of Wiebe and Judd (1971) and Sultan and Judd (1978). However, the curves corresponding to $q/A_T = 0.228$ MW/m^2 and $q/A_T = 0.291$ MW/m^2, which can be distinguished from the curves resulting from the investigations of these other investigators because of the differences in heat flux level, show the same behavior described earlier.

Ulucakli and Merte (1989) recently presented the results of an experiment in which water was boiled on a copper surface to which a thin stainless steel sheet was bonded, at three levels of gravity ($a/g = 1$, 10, and 100), five levels of heat flux in the range 0.19 MW/m$^2 \le q/A_T \le 1.5$ MW/m^2, and various levels of subcooling in the range $0 \le \theta_{sub} \le 89$°C. The curves representing the results of this investigation are presented in Figs. 1–3, and it can be seen that the variation of superheat with subcooling is similar to the results described previously. However, in Ulucakli and Merte's (1989) study the subcooling range was large enough that the curve representing the superheat/subcooling relationship asymptotically approached a straight line, representing the natural convection relationship, for certain combinations of gravity and heat flux. This behavior implies that boiling had been suppressed for these combinations of gravity and heat flux because natural convection was capable of completely dissipating the imposed heat flux under these conditions.

Figure 4 presents the results of a study by Judd and Merte (1970) in which trichlorotrifluoroethane (R113) was boiled on a transparent oxide-coated glass surface at three levels of gravity ($a/g = 1$, 10, and 100), five levels of heat flux ($q/A_T = 11{,}500$, 21,100, 41,600, 82,000, and 129,400 W/m^2), and various levels of subcooling in the range $0 \le \theta_{sub} \le 30$°C. The temperature of the heater surface and the temperature distribution in the adjacent liquid were measured. High-speed photography was used to determine active nucleation site density, average population density, bubble emission frequency, and bubble departure size.

The data points have been omitted in Fig. 4 for the sake of clarity. All of the trends observed in connection with the curves plotted in Figs. 1–3 are present in Fig. 4. The principal difference is that the conditions under which boiling was suppressed were attained at lower levels of gravity and heat flux, presumably because the differences in fluid properties.

Examination of the curves representing the superheat/subcooling relationship suggests that the slope approaches a constant positive value as subcooling approaches zero. The purpose of the analysis that follows is to determine whether this behavior can be predicted using an existing model for heat transfer in nucleate boiling. The adequacy of the predictions of the behavior observed will provide a measure of understanding of the basic mechanisms governing nucleate boiling heat transfer under saturated conditions.

Analysis of the Slope of the Superheat/Subcooling Curve

The heat transfer model developed by Judd (1989) to predict nucleate boiling heat flux is comprised of the mechanisms of heat transfer that occur right at the heater surface, enthalpy transport, natural convection, and microlayer evaporation. Forced convective effects that cause the energy to move into

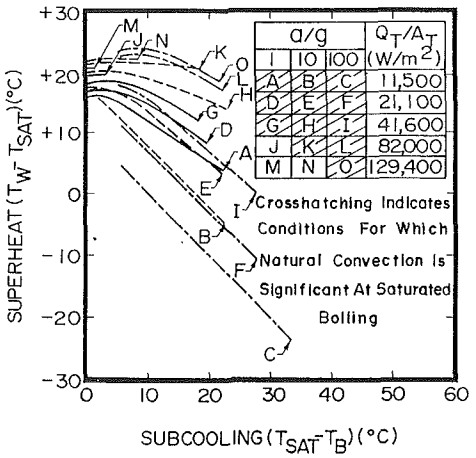

Fig. 4 Variation of superheat θ_{sup} with subcooling θ_{sub} at $a/g = 1$, 10, and 100 for R-113 boiling on glass surface

the adjacent liquid occur further out and were not included in the model. In order of appearance, the three terms in the following equation represent the heat transfer by enthalpy transport, natural convection, and microlayer evaporation, respectively

$$\frac{q}{A_T} = \left[\frac{2}{\sqrt{\pi}}\sqrt{\rho_l C_l k_l}\,\theta_w\sqrt{\bar{f}}\right] * \left(4\pi R_d^2 \frac{N}{A_T}\right) + 0.14\,k_l\left[\left(\frac{g\beta}{\nu_l^2}\right)\left(\frac{\mu_l C_l}{k_l}\right)\right]^{1/3}\theta^{4/3} * \left[1 - \left(4\pi R_d^2 \frac{N}{A_T}\right)\right] + \rho_l h_{fg} V_{ME} \frac{N}{A_T}\bar{f} \quad (1)$$

Under saturated conditions, the contribution of natural convection may be assumed to be insignificant

$$\frac{q}{A_T} = \left[\frac{2}{\sqrt{\pi}}\sqrt{\rho_l C_l k_l}\,\theta_w\sqrt{\bar{f}}\right] * \left(4\pi R_d^2 \frac{N}{A_T}\right) + \rho_l h_{fg} V_{ME} \frac{N}{A_T}\bar{f} \quad (2)$$

Equation (2) can be inverted to obtain an expression for the temperature difference $\theta_w = \theta_{sup} + \theta_{sub}$ according to

$$\theta_{sup} + \theta_{sub} = \left\{\frac{\frac{q}{A_T} - \rho_l h_{fg} V_{ME}\frac{N}{A_T}\bar{f}}{\left[\frac{2}{\sqrt{\pi}}\sqrt{\rho_l C_l k_l}\sqrt{\bar{f}}\right] * \left(4\pi R_d^2 \frac{N}{A_T}\right)}\right\} \quad (3)$$

In the course of demonstrating that the variation of waiting time t_w with subcooling θ_{sub}, as reported by Ibrahim (1983), was consistent with theory, Judd (1989) determined that the volume of the microlayer evaporated per bubble V_{ME} and the bubble departure radius R_d were nearly independent of subcooling θ_{sub} close to the saturated condition. As a consequence, the temperature difference $\theta_{sup} + \theta_{sub}$ in equation (3) is assumed to be dependent upon active site density N/A_T and average bubble frequency $\bar{f}$ only, a simplification that greatly reduces the complexity of the analysis that follows.

Differentiating the temperature difference $\theta_{sup} + \theta_{sub}$ with respect to θ_{sub} while holding V_{ME} and R_d constant yields

$$\left[1 + \frac{d\theta_{sup}}{d\theta_{sub}}\right]_{\theta_{sub}\to 0} = \mu * \Gamma(N/A_T) + (\mu + \nu) * \Gamma(\bar{f}) \quad (4)$$

where the coefficient μ is the ratio of the rate of heat transfer per nucleation site to the rate of enthalpy transport defined according to

$$\mu = -\left\{ \frac{(q/A_T)/(N/A_T)}{\left[\frac{2}{\sqrt{\pi}}\sqrt{\rho_l C_l k_l}\,\theta_w\sqrt{\bar{f}}\right] * (4\pi R_d^2)} \right\}_{\theta_{sub}\to 0} \tag{5}$$

and the coefficient ν is the ratio of the rate of heat transfer by microlayer evaporation to the rate of enthalpy transport defined according to

$$\nu = -\left\{ \frac{\rho_l h_{fg} V_{ME} \bar{f}}{\left[\frac{2}{\sqrt{\pi}}\sqrt{\rho_l C_l k_l}\,\theta_w\sqrt{\bar{f}}\right] * (4\pi R_d^2)} \right\}_{\theta_{sub}\to 0} \tag{6}$$

Because of the way in which enthalpy transport and microlayer evaporation are related through equation (2), it can be shown that $\mu = \nu - 1$. The parameters $\Gamma(N/A_T)$ and $\Gamma(\bar{f})$, defined according to

$$\Gamma(N/A) = \left[\frac{\theta_w}{(N/A_T)}\frac{\partial(N/A_T)}{\partial\theta_{\text{sub}}}\right]_{\theta_{\text{sub}}\to 0} \tag{7}$$

and

$$\Gamma(\bar{f}) = \left[\frac{1}{2}\frac{\theta_w}{\bar{f}}\frac{\partial\bar{f}}{\partial\theta_{\text{sub}}}\right]_{\theta_{\text{sub}}\to 0} \tag{8}$$

represent the sensitivities of active site density and average bubble frequency to changes in subcooling at saturated conditions, respectively.

Boiling Nucleation Theory

A relationship for nucleation site activation is required to compute $\Gamma(N/A_T)$ and $\Gamma(\bar{f})$ in equation (4). For present purposes, the Hsu (1962) nucleation theory, which is solely dependent upon diffusion effects close to the boiling surface where turbulent and convective effects are negligible, provides the most satisfactory description of the events governing nucleation site activation. This theory is predicated upon the assumption that growth of a bubble from a pre-existing vapor nucleus occurs when the temperature of the liquid surrounding the nucleus is equal to or greater than the temperature of the vapor within the nucleus, thereby upsetting the requirements for thermodynamic equilibrium. Each departing bubble was assumed to be replaced by liquid at temperature T_∞ and the liquid adjacent to the heater surface was treated as a slab of thickness $z = \delta$ in which the temperature $T_l(z, t)$ varied continually from the wall temperature T_w at $z = 0$ to the liquid temperature T_∞ at $z = \delta$. Heat was then assumed to flow from the heater surface to the liquid by diffusion, causing the temperature of the liquid in the proximity of the heater surface to increase. Ultimately, the liquid temperature distribution would achieve steady state, beyond which it would not be possible for $T_l(z, t)$ to increase any further. When the liquid temperature at a distance $b = C_1 r_c$ from the heater surface, which corresponds to the location of the tip of the nucleus, exceeded the temperature of the vapor within the nucleus T_v, the conditions for bubble growth to occur were deemed to have been satisfied.

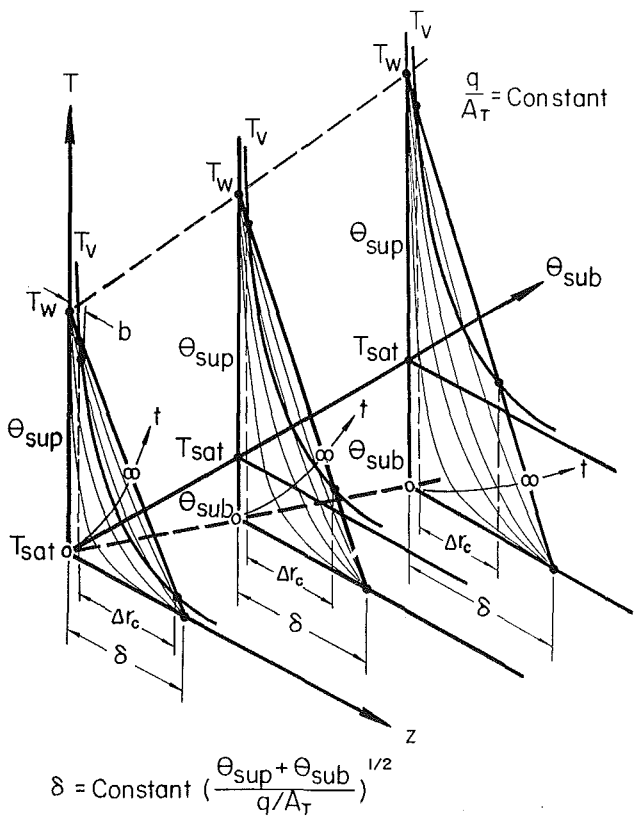

Fig. 5 Schematic representation of the concepts involved in the Hsu (1962) nucleation theory

These concepts are illustrated schematically in Fig. 5. The variation of liquid temperature $T_l(z, t)$ with distance $0 \le z \le \delta$ and time $0 \le t \le \infty$ is depicted in three diagrams, which correspond to increasing levels of subcooling θ_{sub} from left to right. In addition, a curve representing the vapor temperature T_v within a nucleus sitting at the mouth of a cavity of radius r_c has been superimposed upon each of these diagrams. The active cavity range Δr_c can be seen to be the distance between the intersections of this curve with the straight line corresponding to $T_l(z, \infty)$. For a cavity of radius r_c within this range, such that the tip of the nucleus situated in it is located b units from the heater surface, nucleation will occur when $T_l(z, t)$ exceeds T_v at a finite value of time t_w. The theory derived by Hsu (1962) was intended to predict the active cavity range under specified boiling conditions corresponding to the limits imposed by the steady temperature distribution, but it enables the waiting time between the formation of successive bubbles at a particular site within the active cavity range to be predicted as well. Both aspects of the theory will be utilized in the analysis that follows.

The analysis of temperature profiles in the vicinity of a heater surface reported by Wiebe and Judd (1971) enables the determination of the thermal layer thickness δ at various levels of imposed heat flux q/A_T, surface superheat θ_{sup}, and liquid subcooling θ_{sub}. The values of δ obtained by Wiebe and Judd (1971) agreed very closely with the results of Marcus and Dropkin (1965) and Lippert and Dougall (1968) and were correlated in a similar way by a relationship of the form $h = [(q/A_T)/(\theta_{\text{sup}} + \theta_{\text{sub}})]$. For small values of subcooling, the relationship $\delta = 0.0175 * h^{-1/2}$ represented the results very well whereas for large values of subcooling, $\delta = 1.500 * h^{-1}$ provided a more accurate correlation. The conditions close to the saturated condition are of particular interest in the analysis that follows and so the thermal layer thickness was considered to vary in accordance with the first relationship. The distance between the heater surface and the end of the straight line in Fig. 5 was determined according to the relationship $\delta = 0.0175\ [q/A_T/(\theta_{\text{sup}} + \theta_{\text{sub}})]^{-1/2}$. As can be seen in Fig. 5, the active cavity range Δr_c decreases even though the superheat layer thickness δ increases as the subcooling θ_{sub} increases.

Determination of $\Gamma(N/A_T)$

From Fig. 5, it can be seen that while δ increases as θ_{sub} increases, the range of nucleation cavity sizes capable of being activated represented as Δr_c in the illustration decreases. Ac-

cording to Hsu's (1962) nucleation theory, the extreme active cavity size values r_{cmax} and r_{cmin} are given by

$$\frac{r_{cmax}}{r_{cmin}} = \frac{\delta}{2C_1}\left\{\left(\frac{\theta_{sup}}{\theta_w}\right) \pm \left[\left(\frac{\theta_{sup}}{\theta_w}\right)^2 - 4\left(\frac{AC_3}{\delta\theta_w}\right)\right]^{1/2}\right\} \quad (9)$$

so that the range of nucleation cavities capable of being activated Δr_c can be represented by the relationship

$$(\Delta r_c) = |r_{cmax} - r_{cmin}| = \frac{\delta}{C_1}\left[\left(\frac{\theta_{sup}}{\theta_w}\right)^2 - 4\left(\frac{AC_3}{\delta\theta_w}\right)\right]^{1/2} \quad (10)$$

Partial differentiation of Δr_c with respect to θ_{sub} leads to

$$\frac{\partial(\Delta r_c)}{\partial\theta_{sub}} = \frac{1}{\theta_w}\frac{\delta}{C_1}\left\{\left(\frac{\theta_{sup}}{\theta_w}\right)^2 - 4\left(\frac{AC_3}{\delta\theta_w}\right)\right]^{1/2}\left[\frac{\theta_w}{\delta}\frac{\partial\delta}{\partial\theta_{sub}}\right] + \frac{\left(\frac{\theta_{sup}}{\theta_w}\right)^2\left[\theta_w\left(\frac{\theta_w}{\theta_{sub}}\right)\frac{\partial(\theta_{sup}/\theta_w)}{\partial\theta_{sub}}\right] + 2\left(\frac{AC_3}{\delta\theta_w}\right)\left[\frac{\theta_w}{(\delta\theta_w)}\frac{\partial(\delta\theta_w)}{\partial\theta_{sub}}\right]}{\left[\left(\frac{\theta_{sup}}{\theta_w}\right)^2 - 4\left(\frac{AC_3}{\delta\theta_w}\right)\right]^{1/2}}\right\} \quad (11)$$

where

$$\left[\frac{\theta_w}{\delta}\frac{\partial\delta}{\partial\theta_{sub}}\right] = \frac{1}{2}\left[1 + \frac{d\theta_{sup}}{d\theta_{sub}}\right]$$

$$\left[\theta_w\left(\frac{\theta_w}{\theta_{sub}}\right)\frac{\partial(\theta_{sup}/\theta_w)}{\partial\theta_{sub}}\right] = -1$$

and

$$\left[\frac{\theta_w}{(\delta\theta_w)}\frac{\partial(\delta\theta_w)}{\partial\theta_{sub}}\right] = \frac{\theta_w}{(\delta\theta_w)}\left\{\delta\left[1 + \frac{d\theta_{sup}}{d\theta_{sub}}\right] + \theta_w\frac{\partial\delta}{\partial\theta_{sub}}\right\} = \frac{3}{2}\left[1 + \frac{d\theta_{sup}}{d\theta_{sub}}\right]$$

The three equations above represent the partial derivatives of δ, (θ_{sup}/θ_w), and $(\delta\theta_w)$ with respect to θ_{sub} under saturated conditions. Accordingly, after some mathematical manipulation

$$\left[\frac{\theta_w}{(\Delta r_c)}\frac{\partial(\Delta r_c)}{\partial\theta_{sub}}\right]_{\theta_{sub}\to 0} = -\frac{1}{2}\left\{\left[\frac{2}{1-4(AC_3/\delta\theta_w)}\right] - \left[\frac{1+2(AC_3/\delta\theta_w)}{1-4(AC_3/\delta\theta_w)}\right]\left[1 + \frac{d\theta_{sup}}{d_{sub}}\right]\right\} \quad (12)$$

Assuming that the active nucleation cavities are uniformly distributed throughout the cavity size range Δr_c

$$\Gamma(N/A_T) = \left[\frac{\theta_w}{(N/A_T)}\frac{\partial(N/A_T)}{\partial\theta_{sub}}\right]_{\theta_{sub}\to 0} = -\frac{1}{2}\left\{\left[\frac{2}{1-4(AC_3/\delta\theta_w)}\right] - \left[\frac{1+2(AC_3/\delta\theta_w)}{1-4(AC_3/\delta\theta_w)}\right]\left[1 + \frac{d\theta_{sup}}{d_{sub}}\right]\right\} \quad (13)$$

Determination of $\Gamma(\bar{f})$

As stated above, Hsu's nucleation theory also permits determination of the waiting time t_w between the departure of a bubble and the formation of a subsequent bubble at a particular nucleation site of radius r_c. However, the average frequency of bubble formation over a surface based upon the contribution of all of the active nucleation sites is required in equation (4). The average bubble frequency is given by $\bar{f} = \alpha_l/\delta^2[(1/\tau)]$ where the dimensionless bubble formation period $\tau = \alpha_l t_w/\delta^2$ is the sum of the dimensionless growth time, defined according to $\tau_g = \alpha_l t_g/\delta^2$ and the dimensionless waiting time, defined according to $\tau_w = \alpha_l t_w/\delta^2$. At the saturated condition, the results obtained by Ibrahim (1983) indicate that the dimensionless growth time τ_g varies little over the range of heat flux conditions investigated so that little error would be incurred by assuming it to be constant in this analysis. However, the dimensionless waiting time τ_w varies considerably because of the wide range of potentially active nucleation cavity sizes, so that this aspect of the derivation requires attention.

The equation to be solved in order to determine the duration of the waiting time is, according to Hsu (1962)

$$\frac{\theta_{sub}}{\theta_w} + \frac{(AC_3/\delta\theta_w)}{(1-\eta)} = \eta + 2\sum_{n=1}^{\infty}\frac{(-1)^n}{\lambda_n}\exp\left[-\lambda_n^2\left(\frac{\alpha_l t_w}{\delta^2}\right)\right]\sin[\lambda_n\eta] \quad (14)$$

where $\eta = 1 - C_1 r_c/\delta$. The relationship may be inverted in order to get the dimensionless bubble formation period $\tau = \alpha_l t_w/\delta^2$

$$\left(\frac{\alpha_l t_w}{\delta^2}\right) = F\left[\left(\frac{\theta_{sub}}{\theta_w}\right), \left(\frac{AC_3}{\delta\theta_w}\right), \left(1 - \frac{C_1 r_c}{\delta^2}\right)\right] \quad (15)$$

from which average frequency can be determined according to

$$\bar{f} = \frac{1}{r_{cmax} - r_{cmin}}\int_{r_{cmin}}^{r_{cmax}}\frac{dr_c}{\alpha_l t_g/\delta^2 + F[(\theta_{sub}/\theta_w), (AC_3/\delta\theta_w), \eta]} = \frac{1}{\eta_{max} - \eta_{min}}\int_{\eta_{min}}^{\eta_{max}}\frac{d\eta}{\alpha_l t_g/\delta^2 + F[(\theta_{sub}/\theta_w), (AC_3/\delta\theta_w), \eta]} = \left(\frac{\alpha_l}{\delta^2}\right) I \quad (16)$$

Partial differentiation of $\bar{f}$ with respect to θ_{sub} leads to

$$\frac{\partial\bar{f}}{\partial\theta_{sub}} = \alpha_l\left[-\frac{2}{\delta^3}\frac{\partial\delta}{\partial\theta_{sub}}I + \frac{1}{\delta^2}\frac{\partial I}{\partial\theta_{sub}}\right] \quad (17)$$

where

$$I = I\left[\left(\frac{\theta_{sub}}{\theta_w}\right), \left(\frac{\alpha_l t_g}{\delta^2}\right), \left(\frac{AC_3}{\delta\theta_w}\right)\right]$$

so that after some further mathematical manipulation

$$\left[\frac{1}{2}\frac{\theta_w}{\bar{f}}\frac{\partial\bar{f}}{\partial\theta_{sub}}\right]_{\theta_{sub}\to 0} = -\frac{\theta_w}{\delta}\frac{\partial\delta}{\partial\theta_{sub}} + \frac{1}{2}\frac{\theta_w}{I}\frac{\partial I}{\partial\theta_{sub}} \quad (18)$$

where

$$\left[\frac{\theta_w}{\delta}\frac{\partial\delta}{\partial\theta_{sub}}\right] = \frac{1}{2}\left[1 + \frac{d\theta_{sup}}{d\theta_{sub}}\right]$$

and

$$\left[\frac{\theta_w}{I}\frac{\partial I}{\partial\theta_{sub}}\right] = \frac{1}{I}\left[\frac{\partial I}{\partial(\theta_{sub}/\theta_w)}\right] - \frac{1}{I}\left\{\left(\frac{\alpha_l t_g}{\delta^2}\right)\left[\frac{\partial I}{\partial(\alpha_l t_g/\delta^2)}\right] + \frac{3}{2}\left(\frac{AC_3}{\delta\theta_w}\right)\left[\frac{\partial I}{\partial(AC_3/\delta\theta_w)}\right]\right\}\left[1 + \frac{d\theta_{sup}}{d\theta_{sub}}\right]$$

Finally under saturated conditions, it can be shown that

$$\Gamma(\bar{f}) = \left[\frac{1}{2}\frac{\theta_w}{\bar{f}}\frac{\partial\bar{f}}{\partial\theta_{sub}}\right]_{\theta_{sub}\to 0} = \frac{1}{2}\frac{1}{I}\left[\frac{\partial I}{\partial(\theta_{sub}/\theta_w)}\right]_{\theta_{sub}\to 0} - \frac{1}{2}\left\{1 + \left(\frac{\alpha_l t_g/\delta^2}{I}\right)\left[\frac{\partial I}{\partial(\alpha_l t_g/\delta^2)}\right]_{\theta_{sub}\to 0} + \frac{3}{2}\left(\frac{AC_3/\delta\theta_w}{I}\right)\left[\frac{\partial I}{\partial(AC_3/\delta\theta_w)}\right]_{\theta_{sub}\to 0}\right\}\left[1 + \frac{d\theta_{sup}}{d\theta_{sub}}\right] \quad (19)$$

Table 1 Comparison of measured and predicted values of $[d\theta_{sup}/d\theta_{sub}]_{\theta_{sub}\to 0}$ according to Ibrahim (1983)

Heat Flux q/A_T	Predicted values	Measured values
166 kW/m^2	0.438	0.395 ± 0.029
228 kW/m^2	0.389	0.350 ± 0.026
291 kW/m^2	0.356	0.330 ± 0.023

Table 2 Comparison of measured and predicted values of $\Gamma(\bar{f})$ according to Ibrahim (1983)

Heat Flux q/A_T	Predicted values	Measured values
166 kW/m^2	-0.512	-0.490 ± 0.057
228 kW/m^2	-0.504	-0.481 ± 0.059
291 kW/m^2	-0.483	-0.476 ± 0.055

Synthesis

When the expressions for the sensitivities of active site density and average bubble frequency to changes in subcooling at saturated conditions are introduced into the relationship for the slope of the superheat/subcooling curve, the rate of change of superheat with subcooling under saturated conditions can be determined. Substitution of equation (13) for $\Gamma(N/A_T)$ and equation (19) for $\Gamma(\bar{f})$ in equation (4) leads to

$$\left[1+\frac{d\theta_{sup}}{d\theta_{sub}}\right]_{\theta_{sub}\to 0} = -\frac{\mu}{2}\left\{\left[\frac{2}{1-4(AC_3/\delta\theta_w)}\right] - \left[\frac{1+2(AC_3/\delta\theta_w)}{1-4(AC_3/\delta\theta_w)}\right]\left[1+\frac{d\theta_{sup}}{d\theta_{sub}}\right]_{\theta_{sub}\to 0}\right\} + \frac{\nu}{2}\frac{1}{I}\left[\frac{\partial I}{\partial(\theta_{sub}/\theta_w)}\right]_{\theta_{sub}\to 0} - \frac{\nu}{2}\left\{1+\left(\frac{\alpha_l t_g/\delta^2}{I}\right)\left[\frac{\partial I}{\partial(\alpha_l t_g/\delta^2)}\right]_{\theta_{sub}\to 0} + \frac{3}{2}\left(\frac{AC_3/\delta\theta_w}{I}\right)\left[\frac{\partial I}{\partial(AC_3/\delta\theta_w)}\right]_{\theta_{sub}\to 0}\right\}\left[1+\frac{d\theta_{sup}}{d\theta_{sub}}\right]_{\theta_{sub}\to 0} \tag{20}$$

A relationship to predict $\left[1+\frac{d\theta_{sup}}{d\theta_{sub}}\right]_{\theta_{sub}\to 0}$ is obtained by gathering the terms in $\left[1+\frac{d\theta_{sup}}{d\theta_{sub}}\right]_{\theta_{sub}\to 0}$ and rearranging the equation above

$$\left[1-\frac{\mu}{2}\left[\frac{1+2(AC_3/\delta\theta_w)}{1-4(AC_3/\delta\theta_w)}\right]_{\theta_{sub}\to 0} + \frac{\nu}{2}\left\{1+\left(\frac{\alpha_l t_g/\delta^2}{I}\right)\left[\frac{\partial I}{\partial(\alpha_l t_g/\delta^2)}\right]_{\theta_{sub}\to 0} + \frac{3}{2}\left(\frac{AC_3/\delta\theta_w}{I}\right)\left[\frac{\partial I}{\partial(AC_3/\delta\theta_w)}\right]_{\theta_{sub}\to 0}\right\}\right]\left[1+\frac{d\theta_{sup}}{d\theta_{sub}}\right]_{\theta_{sub}\to 0} = \left\{\frac{\mu}{2}\left[\frac{2}{1-4(AC_3/\delta\theta_w)}\right]_{\theta_{sub}\to 0} + \frac{\nu}{2}\frac{1}{I}\left[\frac{\partial I}{\partial(\theta_{sub}/\theta_w)}\right]_{\theta_{sub}\to 0}\right\} \tag{21}$$

Ibrahim's (1983) experimental results obtained at Site E for $q/A_T = 166$ kW/m^2, 228 kW/m^2, and 291 kW/m^2 were used to determine $\frac{AC_3}{\delta\theta_w}$ and $\frac{\alpha_l t_g}{\delta^2}$ as well as the terms $\left[\frac{2}{\sqrt{\pi}}\sqrt{\rho_l C_l k_l}\,\theta_w\sqrt{\bar{f}}\right] * (4\pi R_d^2)$ and $\rho_l h_{fg} V_{ME}\frac{N}{A_T}\bar{f}$ that appear in μ and ν. The theory derived by Judd (1989) was used to evaluate V_{ME} and the values of $\left[\frac{d\theta_{sup}}{d\theta_{sub}}\right]_{\theta_{sub}\to 0}$ predicted by equation (21) are presented in Table 1.

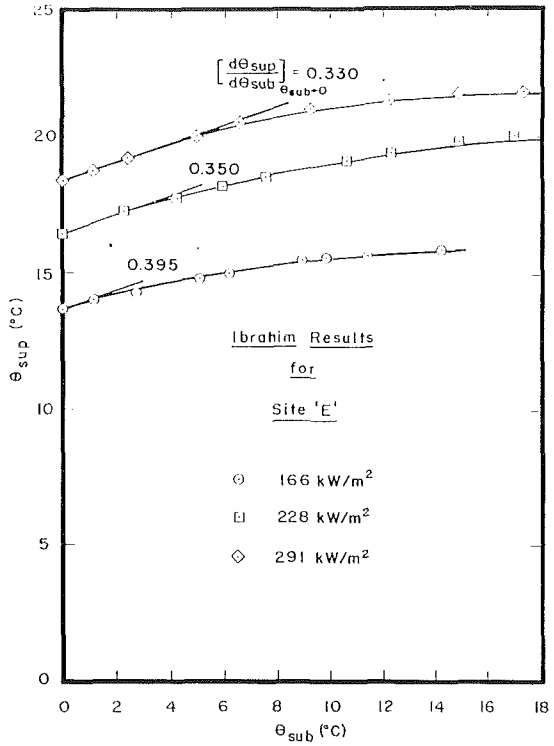

Fig. 6 Variation of superheat θ_{sup} with subcooling θ_{sub} according to Ibrahim (1983)

Table 1 also presents the corresponding values obtained from the measurements plotted in Fig. 6 along with an estimate of the precision based upon an analysis of the uncertainties associated with the measured parameters. The agreement can be observed to be quite good. Having determined $\left[\frac{d\theta_{sup}}{d\theta_{sub}}\right]$, $\Gamma(\bar{f})$ could be computed in accordance with the theory developed above. Table 2 compares the values of $\Gamma(\bar{f})$ predicted by equation (19) with the values from Fig. 7, which presents Ibrahim's (1983) experimental data for all the active nucleation sites.

Good agreement is observed here as well, thereby giving the analysis of the slope of the relationship between superheat and subcooling at saturated conditions additional credibility.

In a similar fashion, the measurements obtained by Judd and Merte (1970) were also evaluated. However, of the 15 heat flux/gravity combinations plotted in Fig. 4, natural convection was negligible enough for only the three represented by boiling curves *J*, *M*, and *N* to be tested against the predictions (less than 5 percent of the imposed heat flux). For all the others, the influence of natural convection at saturated conditions was too great, violating a key assumption of the present theory. The measured and predicted values of $\left[\frac{d\theta_{sup}}{d\theta_{sub}}\right]_{\theta_{sub}\to 0}$ are presented in Table 3 below.

The values predicted by equation (21) agree well with the values obtained from Fig. 8, indicating that the present theory applies to trichlorotrifluoroethane boiling on a glass surface at $a/g = 1$ and $a/g = 10$ as well as to water boiling on a copper surface at $a/g = 1$. The implication of this observation is that enthalpy transport and microlayer evaporation are the only mechanisms responsible for the removal of heat in nucleate boiling under saturated conditions.

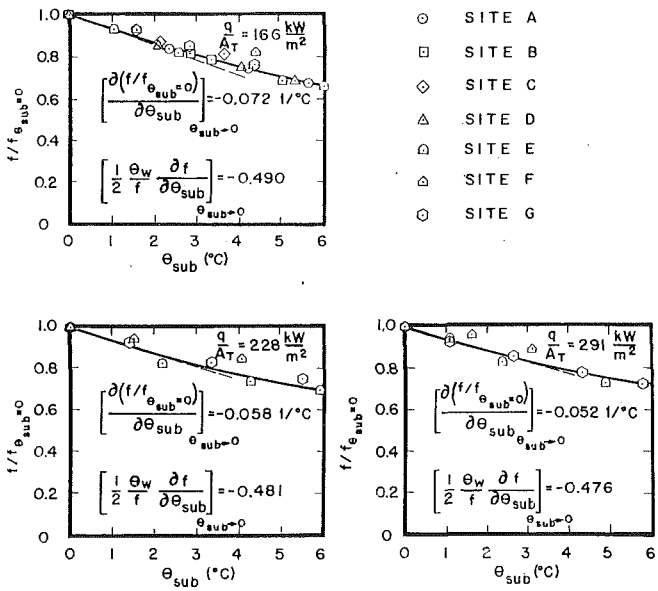

Fig. 7 Variation of bubble frequency ratio $f/f_{\theta_{sub}=0}$ with subcooling θ_{sub} according to Ibrahim (1983)

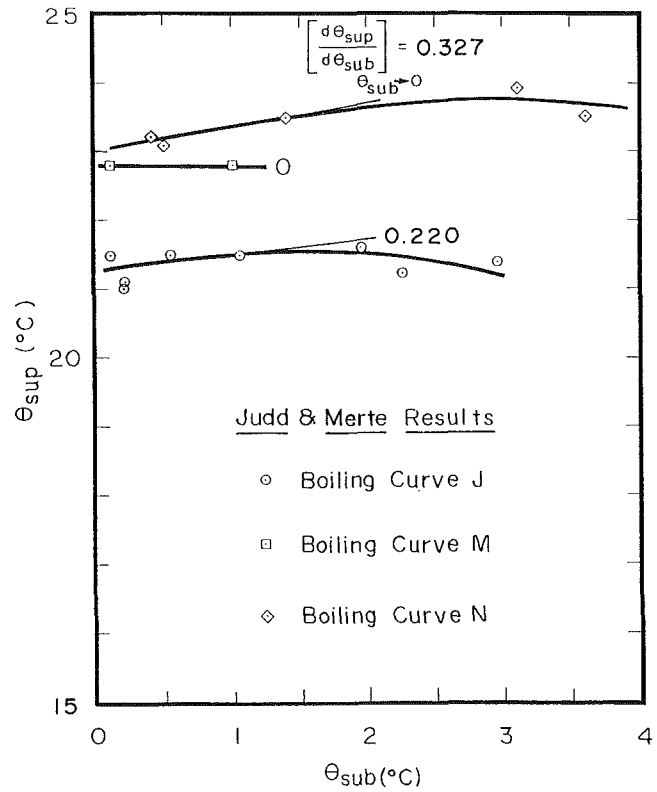

Fig. 8 Variation of superheat θ_{sup} with subcooling θ_{sub} according to Judd and Merte (1970)

The measured and predicted values of $\Gamma(\bar{f})$ and $\Gamma(N/A_T)$ are compared in Tables 4 and 5. It was only possible to compute measured values of $\Gamma(f)$ and $\Gamma(N/A_T)$ for boiling curve J because the appropriate measurements of average bubble frequency and active site density were not available for boiling curves M and N. However, reasonable agreement is seen here with respect to boiling curve J, indicating that the present theory appears to reflect the sensitivities of average bubble frequency and active site density to changes in subcooling as well the slope in the superheat/subcooling relationship at saturated conditions.

Table 3 Comparison of measured and predicted values of $[d\theta_{sup}/d\theta_{sub}]_{\theta_{sub}\to 0}$ according to Judd and Merte (1970)

Boiling curve	Predicted values	Measured values
J	0.278	0.220 ± 0.112
M	0.025	0 ± 0.100
N	0.309	0.327 ± 0.134

Table 4 Comparison of measured and predicted values of $\Gamma(f)$ according to Judd and Merte (1970)

Boiling curve	Predicted values	Measured values
J	-0.923	$-0.871 + 0.375$
M	-0.533	-
N	-0.958	-

Table 5 Comparison of measured and predicted values of $\Gamma(N/A_T)$ according to Judd and Merte (1970)

Boiling curve	Predicted values	Measured values
J	-0.355	$-0.331 + 0.168$
M	-0.492	-
N	-0.351	-

Discussion

The agreement between the predicted values of $\left[\frac{d\theta_{sup}}{d\theta_{sub}}\right]$ and those obtained from the experimental results of Ibrahim (1983) and Judd and Merte (1970) lends weight to the credibility of a heat transfer model comprised of enthalpy transport and microlayer evaporation components at the saturated condition when natural convection does not play a significant role. This agreement is consistent with the findings of Judd (1989) who demonstrated that a boiling heat transfer model comprised of enthalpy transport, natural convection, and microlayer evaporation components was capable of correlating the experimental results reported by Ibrahim (1983) for a particular active site over the entire range of subcooling values covered. It would seem that this heat transfer model is valid from $\theta_{sub} = 0$ to the value of subcooling θ_{sub} corresponding to the point at which the data plotted in Figs. 6 or 8 departs from the straight line representing the slope of the superheat/subcooling curve at saturated conditions. The fact that the point of departure increases as heat flux q/A_T increases suggests the onset of a mechanism such as natural convection, which is more significant at lower levels of heat flux.

The coefficients μ and ν were almost independent of the heat flux level q/A_T so that the slope of the superheat/subcooling curve $\left[\frac{d\theta_{sup}}{d\theta_{sub}}\right]$ was largely determined by the magnitude of $\Gamma(N/A_T)$ and $\Gamma(\bar{f})$ at saturated conditions. Both the terms $\Gamma(N/A_T)$ and $\Gamma(\bar{f})$, which in turn are dependent upon $\frac{\alpha_l t_g}{\delta^2}$ and $\frac{AC_3}{\delta\theta_w}$, were negative in the present analysis. Both μ and ν are negative by definition and equation (4) predicts that $\left[\frac{d\theta_{sup}}{d\theta_{sub}}\right]$ should be positive, in accordance with observation. It is possible for either $\Gamma(N/A_T)$ or $\Gamma(f)$ to change sign, but it is very unlikely that $\Gamma(N/A_T)$ would change sign because the range of $\frac{AC_3}{\delta\theta_w}$ values commonly encountered in nucleate boiling is such

that $\Gamma(N/A_T)$ would remain negative. This implies that an increase in subcooling would always result in a decrease in the number of active sites per unit area. However, it is possible for positive values of $\Gamma(f)$ to occur; Sultan and Judd (1978) obtained values of bubble frequency as a function of subcooling that would have yielded positive values of $\Gamma(f)$. All the same, the superheat/subcooling curve exhibited a positive slope at saturated conditions as indicated in Fig. 1, presumably because the term $\mu * \Gamma(N/A_T)$ predominated over the term $\nu * \Gamma(f)$ in equation (4).

Concluding Remarks

The analysis presented in this paper constitutes another test of the correlation advanced by Judd (1989). In order to keep the theory as simple as possible, only results corresponding to saturated boiling conditions for which the contribution of natural convection was insignificant were utilized. The procedure could be extended to the entire range of subcooling by incorporating natural convection. The theory resulting from this modified procedure would be appropriate for analyzing the maximum point in the superheat/subcooling relationship, which is easily identified in the experimental results. However, insufficient experimental data are available at this time to warrant this approach.

The slope of the superheat/subcooling relationship at saturated conditions is not fully independent of heat flux, as was assumed here. Instead, the analysis has shown that the slope is to a great extent dependent upon the change of active site density and bubble frequency with subcooling and the variation of the rate of enthalpy transport and the rate of microlayer evaporation with heat flux. However, the analysis presented in this paper explains the curious variation of superheat with subcooling that has been observed and reported upon by a number of different investigators. Initially, superheat increases with increasing subcooling at saturated conditions because of the way in which active site density and average bubble frequency respond to increasing subcooling. As subcooling increases further, natural convection, which was disregarded in the present analysis, begins to play an increasingly important role in the heat transfer process. Ultimately, a level of subcooling at which natural convection is able to accommodate the entire imposed heat flux is attained no matter what the liquid/surface combination may be, after which superheat decreases with increasing subcooling at a constant rate.

Acknowledgments

The work reported here was sponsored in part by the NASA Lewis Research Center under Grant No. NAG 3-663.

References

Hsu, Y. Y., 1962, "On the Size Range of Active Nucleation Cavities on a Heating Surface," ASME JOURNAL OF HEAT TRANSFER, Vol. 84, No. 3, pp. 207–216.

Ibrahim, E. A., 1983, "An Experimental Investigation of the Effect of Subcooling on Bubble Growth and Waiting Time in Nucleate Boiling," M. Eng. Thesis, McMaster University, Hamilton, Ontario, Canada.

Ibrahim, E. A., and Judd, R. L., 1985, "An Experimental Investigation of the Effect of Subcooling on Bubble Growth and Waiting Time in Nucleate Boiling," ASME JOURNAL OF HEAT TRANSFER, Vol. 107, No. 1, pp. 168–174.

Judd, R. L., 1989, "The Influence of Subcooling on the Frequency of Bubble Emission in Nucleate Boiling," ASME JOURNAL OF HEAT TRANSFER, Vol. 111, No. 3, pp. 747–752.

Judd, R. L., and Merte, H., Jr., 1970, "Evaluation of Nucleate Boiling Heat Flux Predictions at Varying Levels of Subcooling and Acceleration," *Int. J. Heat and Mass Transfer*, Vol. 15, No. 5, pp. 1075–1096.

Lippert, T. E., and Dougall, R. S., 1968, "A Study of the Temperature Profiles Measured in the Thermal Sublayer of Water, Freon-113, and Methyl Alcohol During Pool Boiling," ASME JOURNAL OF HEAT TRANSFER, Vol. 90, No. 3, pp. 347–352.

Marcus, B. D., and Dropkin, D., 1965, "Measured Temperature Profiles Within the Superheated Boundary Layer Above a Horizontal Surface in Saturated Nucleate Pool Boiling of Water," ASME JOURNAL OF HEAT TRANSFER, Vol. 87, No. 3, pp. 333–341.

Merte, H., Jr., and Clark, J. A., 1961, "Pool Boiling in an Accelerating System," ASME JOURNAL OF HEAT TRANSFER, Vol. 83, No. 3, pp. 234–242.

Sultan, M., and Judd, R. L., 1978, "Spatial Distribution of Active Sites and Bubble Flux Density," ASME JOURNAL OF HEAT TRANSFER, Vol. 100, No. 1, pp. 56–62.

Ulucakli, M. E., 1987, "Nucleate Pool Boiling With Increased Acceleration and Subcooling," Ph.D. Thesis, University of Michigan, Ann Arbor, MI.

Ulucakli, M. E., and Merte, H., 1990, "Nucleate Boiling With High Gravity and Large Subcooling," ASME JOURNAL OF HEAT TRANSFER, Vol. 112, No. 2, pp. 451–457.

Wiebe, J., and Judd, R. L., 1971, "Superheat Layer Thickness Measurements in Saturated and Subcooled Nucleate Boiling," ASME JOURNAL OF HEAT TRANSFER, Vol. 73, No. 4, pp. 455–461.

An Experimental Study of the Relative Effects of Transverse and Longitudinal Ribbing of the Heat Transfer Surface in Forced Convective Boiling

M. A. R. Akhanda
Department of Mechanical Engineering, Bangladesh University of Engineering and Technology (BUET), Dhaka, Bangladesh

D. D. James
Department of Mechanical Engineering, University of Manchester Institute of Science and Technology (UMIST), Manchester, United Kingdom

This work describes an experimental investigation into the effects of surface geometry variations on heat transfer performance in forced flow boiling. Ribs of rectangular cross section were machined on flat stainless steel test specimens of 1.60 mm thickness. The height of the ribs was kept constant at 0.50 mm and a number of test specimens with rib width varying from 0.50 mm to 2.0 mm and rib spacing ranging from 0.50 mm to 3.5 mm were produced. In order to maintain a constant microsurface roughness of 0.7 μm over the entire test specimen, all test surfaces were subjected to vequa-blasting after machining. Precautions were taken to ensure that aging of the heat transfer surface had been established so that the data recorded were reproducible. Experimental data are reported for water at atmospheric pressure with flow velocities of 0.20 m/s to 1.40 m/s. Inlet subcoolings were varied from 5°C to 30°C. The results for the longitudinal ribbed surfaces (LRS) were compared with those for the transverse rectangular ribbed surfaces (TRS) and both sets of data were compared with the heat transfer performance of an optimum flat roughened surface.

Introduction

Extensive studies, both experimental and theoretical, have been undertaken during the past three decades into the high heat transfer rates associated with boiling heat transfer, and this mode of heat transfer has been successfully employed in removing large quantities of heat generated in relatively small volumes. More recently, significant advances have been achieved by investigating the use of surface geometry variations to promote high-performance heat transfer characteristics with applications to heat pipe technology. Investigations involving the use of fins or extended surfaces have yielded substantial improvements in heat transfer surface performance by increasing the surface area for sustaining high film boiling temperatures at the fin base.

Information on the influence of smaller surface geometry variations—of the order of a bubble diameter at departure—on heat transfer performance in nucleate boiling is very limited. Grooves or ribs up to a few millimeters in size have been employed in heat pipe technology mainly to improve liquid transport and capillary motion; Dunn and Reay (1976) reported heat transfer data from a variety of grooved heat pipe walls and a grooved wick of an arterial-type heat pipe. Wicks such as these are employed in high-performance heat pipes for spacecraft.

Gorenflo (1966) carried out experiments on nucleate boiling from copper tubes with small circumferential fins in refrigerant R-11 at pressures above atmospheric. He compared the performance of these finned tubes with that of a smooth one and observed an improvement in the heat transfer with finned tubes. He also suggested that for finned tubes, a critical spacing of approximately twice the bubble departure diameter existed. Tubes with a fin spacing greater than and less than this value exhibited an improved heat transfer rate. Hesse (1973) compared the boiling heat transfer characteristics of R-114 from a grooved and a smooth nickel tube over a pressure range of 3 to 6 bar. At a pressure of 3 bar, heat transfer from the grooved tube was better that that for the smooth tube when both total and projected areas were considered. However, at a pressure of 6 bar the heat transfer from the grooved tube was improved only when the projected area was considered. Gogonin and Svorkova (1973) conducted experiments in nucleate boiling of refrigerant R-21 from copper and aluminum tubes provided with small trapezoidal fins. The surface roughness was stated to be the same for all tubes. However, no further finishing of the surface after machining was reported, leaving the matter of constant surface roughness in some doubt.

Joudi (1977) carried out pool boiling experiments from stainless steel ribbed surfaces to three fluids (water, refrigerant R-113, and methanol). Rib height was kept constant at 0.5 mm and clearance between ribs varied from 0.5 mm to 2.0 mm. He maintained a constant surface roughness for all specimens using a vequa-blasting technique. He used total area for evaluating heat flux and found that for an overall assessment, the flat surface having the same surface microroughness as the ribbed surfaces exhibited better heat transfer performance in fully developed boiling regime than the ribbed samples.

Webb (1981) surveyed the evolution of special surface geometries that promote high performance nucleate boiling. The effects of heating surface geometry variations (transverse rectangular ribs) on heat transfer characteristics for water in subcooled flow boiling have been investigated by Akhanda and James (1984a). They presented experimental data for forced convective boiling heat transfer from one side of the rectangular duct to an internally flowing fluid. Channel aspect ratio was maintained constant at 1.0 and inlet subcooling and flow velocity were varied. Rib height and length were kept constant at 0.5 mm and 1.0 mm, respectively and clearance between the ribs was varied from 0.50 to 3.50 mm. The surface micro-

Contributed by the Heat Transfer Division and presented at the 23rd National Heat Transfer Conference, Denver, Colorado, August 4–7, 1985. Manuscript received by the Heat Transfer Division November 3, 1988; revision received February 26, 1990. Keywords: Boiling, Finned Surfaces, Forced Convection.

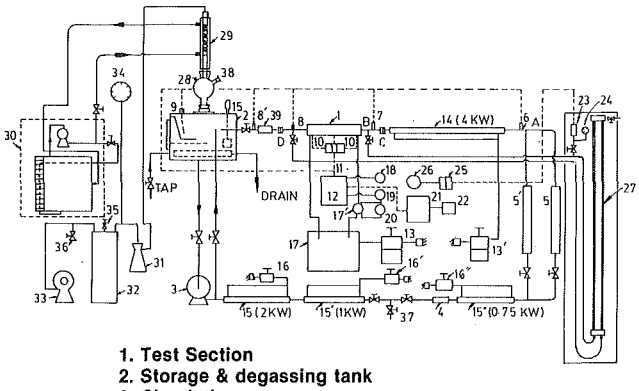

1. Test Section
2. Storage & degassing tank
3. Circulating pump
4. Strainer
5. Flow meters
6.-10. T. C. (monitor, inlet, outlet, tank, wall)
11. Junction box
12. T. C. selecting switch
13. Double variac
14. Preheater (4 kW)
15. Preheaters
16. Variac
17. Transformer (10 kVA, current)
18.-19. DVM (T.C. & volts)
20. Ammeter
21. Data logger
22. Teletype
23. Pressure transducer
24. Pressure gage
25. Bridge & amplifier
26. D.V.M. (pressure)
27. Water column manometer
28. Upper tank
29. Condenser
30. Water cooling system
31. Vapor trap
32. Vacuum reservoir chamber
33. Vacuum pump
34. Pressure gage (vacuum)
35. Needle valve
36. Air-bleed valve
37. Drain valve
38. Water inlet
39. Mixer

Fig. 1 Schematic diagram of the experimental rig

roughness for all test specimens was maintained at 0.78 μm C.L.A. using a vequa-blasting technique, thus isolating the possible effects of surface microroughness. It was found that rib spacings of less than 1.0 mm showed little improvement in heat transfer performance. Further experiments by these authors (1984b) using a similar channel geometry showed that in subcooled flow boiling an increase in surface roughness up to an average value of Ra = 0.78 μm C.L.A. improved the heat transfer. A further increase in surface roughness from Ra = 0.78 μm to Ra = 1.22 μm showed no change in the surface heat transfer performance.

Bruzzi (1969) investigated the effect of channel aspect ratio, inlet subcooling, and flow velocity on the heat transfer in an asymmetrically heated rectangular duct. More recently, Del Valle (1984) carried out subcooled flow boiling experiments employing a similar channel geometry. Channel aspect ratio was maintained constant in these tests at a value of 0.50, and the effects of specimen thickness, inlet subcooling, and flow velocity were investigated.

A review of the developments in augmented heat transfer is presented by Bergles et al. (1981) and almost without exception, investigations have been carried out either in pool boiling or in flow boiling in circular tubes with only little attention paid to isolating the effect of surface microroughness. Furthermore, where ribbing effects are investigated, only transverse ribs are considered, with no information currently available concerning the heat transfer performance of ribbed surface (either transverse or longitudinal) for boiling heat transfer from one side of a rectangular duct to an internally flowing fluid—a geometric configuration that can be usefully employed in the design of compact heat exchangers. This work was undertaken to provide such information.

Experimental Apparatus

The layout of the experimental apparatus and measuring equipment is shown in Fig. 1. It will be observed that the closed-loop system incorporates the test section, flow meters, storage and degassing tank, vacuum pump, vacuum reservoir chamber, and circulating pump. Heating of the stainless steel test surface was effected by the passage of a high a-c current (0–700 A) at low voltage (0–6 V) through the test specimen. A 10 kVA transformer regulated by a double variac was also incorporated. The total heat input to the heating surface was calculated from a knowledge of the current, which was measured by a precision ammeter through a current transformer, together with the voltage across the heating surface, which was measured with an a-c digital voltmeter (DVM). Surface temperature was measured using 17 chromel-alumel thermocouples spot-welded to the undersurface of the heated specimen, and was recorded by a data logger. Inlet and outlet bulk temperatures were measured using thermocouple probes and flow rate was measured using two rotameters in parallel. System pressure was kept constant (by controlling with vacuum pump and vacuum reservoir chamber) and measured by using a calibrated pressure transducer and a pressure gage. The difference between inlet and outlet pressures of the test section (which was very small) was measured by a water column manometer. The test section shown in Fig. 2(*a*) was 304 mm in length with a cross section of 22 mm × 22 mm. An entry length of 35 equivalent diameters and of the same cross-sectional dimen-

Nomenclature

a = channel aspect ratio
A = flat projected area of the heating surface, m^2
C_p = specific heat at constant pressure, kJ/kgK
D = equivalent diameter = $4A$/wetted perimeter, m
e = rib height, mm
g = acceleration due to gravity, m/s^2
h = heat transfer coefficient = $(q/A)/(T_w - T_{bm})$, kW/m^2K
l = rib length, mm
Nu = Nusselt number
Pr = Prandtl number
q = heat transfer rate, kW
Ra = centerline surface roughness average, μm
Re = Reynolds number
s = spacing between two ribs, mm
T = temperature
V = flow velocity, m/s
θ = angle with the direction of flow, deg
λ = latent heat of vaporization, kW/mK
μ = absolute viscosity, kg/ms
ρ = density, kg/m^3
σ = surface tension, N/m

Subscripts

B, b = bulk
bm = mean bulk
calc = calculated
expt = experimental
L = liquid
sat = saturation
sub = subcooled
v = vapor
W = wall

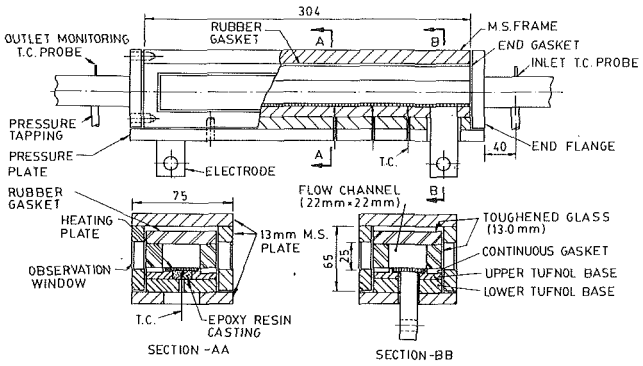

Fig. 2(*a*) Details of test section

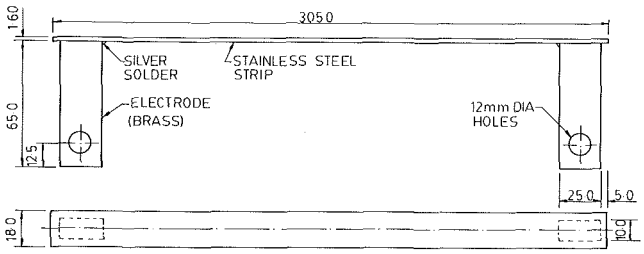

Fig. 2(*b*) Detail of flat heating plate

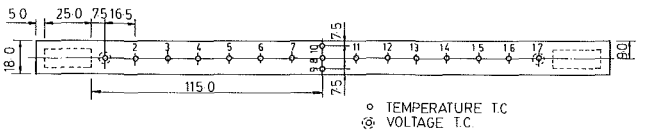

Fig. 2(c) Thermocouple positions

sions as the test section was provided. The heating surface arrangement is shown in Fig. 2(*b*) and 2(*c*).

Brass electrodes 65 mm × 25 mm × 10 mm were silver soldered 5 mm away from both ends of the test specimen. These electrodes were connected to the 10 kVA transformer by thick cables. The heating surface was attached to the upper "tufnol" (Phenolic regin—brand ASP) base by means of heat-resistant araldite 2004. A slot was machined into the upper tufnol base to receive the heating surface (specimen) so that after assembly this was flush with the base. The groove beneath the heat transfer surface was filled with a casting of epoxy resin (araldite MY750), hardener HT972, and a crack-resisting filler (mica) to strengthen the assembly. The upper tufnol base also contained a recess for a gasket on which a three-piece **U**-shaped glass channel (made of 13-mm-thick toughened glass) and the two end flanges were located. The lower tufnol base was used to reinforce the arrangement and to provide additional insulation. All components in contact with the working liquid were manufactured from materials that could adequately withstand the liquid boiling temperature and also resist corrosion. The exit section, 156 mm long, provided a smooth flow out of the test section. A mixer (helical swirl) was installed in this section to ensure that the outlet temperature was that of mixed bulk. The flow rate through the test section was controlled by adjusting as required a number of valves installed in the circuit. Four preheaters (2 kW, 1 kW, 0.75 kW, and 4 kW) were employed to control the temperature of the working fluid in the rig. A pipe strainer was used to filter out solid particles that may have found their way into the system (although much care was taken to ensure the purity and cleanliness of the working liquid prior to each run). The storage and degassing tank served as a container into which the working liquid from the test section was discharged, conditioned, and recirculated.

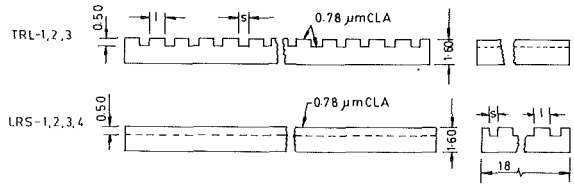

Fig. 3 Geometric variations of test surfaces

The heat transfer surfaces were manufactured from 16 S.W.G. stainless steel sheets of type EN58E (AISI304) to the following dimensions: 304 mm × 18 mm × 1.60 mm. Ribs were produced by machining the upper surfaces of these heating plates. A vequa-blasting technique was employed to obtain constant surface microroughness for all specimens. Information concerning surface geometry variations is given in Fig. 3 and dimensions are presented below:

Surface	C.L.A. surface roughness Ra, μm	Rib height *e*, mm	Rib length *l*, mm	Spacing between ribs *s*, mm
TRL-1	0.78 ± .05	0.50	0.50	0.50
TRL-2	"	0.50	1.00	0.50
TRL-3	"	0.50	2.00	0.50
LRS-1	"	0.50	1.00	0.50
LSR-2	"	0.50	1.00	1.00
LSR-3	"	0.50	1.00	1.50
LRS-4	"	0.50	1.00	3.50

It may be mentioned here that the total maximum error (uncertainties) in the measurement of heat flux was estimated to be ±4.2 percent and this was not greater than ±3 percent in case of flow measurement.

Results and Discussion

Forced convection boiling heat transfer to water from ribbed surfaces (TRL & LRS) at atmospheric pressure was experimentally investigated. Data are plotted for heat flux (q/A) from the heating surfaces versus superheat (ΔT_{sat}). Measurements were made under the following conditions and the results were compared with the existing data:

Working fluid: Distilled and deionized water.
System pressure: 1 atm.
Test section geometry: A channel of rectangular cross section having channel aspect ratio $a = 1$ and with one side (bottom horizontal wall) heated electrically.
Heating surfaces: Manufactured from stainless steel (type EN58E AISI304), Ra = 0.78 ± 0.05 μm C.L.A. Transverse rectangular ribs (TRL) of lengths 0.50 mm, 1.0 mm, and 3.0 mm. Longitudinal rectangular ribs (LRS) of spacings 0.50 mm, 1.0 mm, 1.50 mm, and 3.50 mm. Longitudinal ribs were each continuous for the entire test section.
Flow velocity: 0.20 m/s, 0.35 m/s, 0.70 m/s, 1.10 m/s, and 1.40 m/s.
Inlet subcooling: 5°C, 15°C, and 30°C.
Flow: Horizontal.
Heat flux: All the runs were made in nucleate boiling below the burnt-out heat flux.

A characteristic feature of nucleate boiling is the difficulty encountered in controlling the condition of the heat transfer surface. This is more marked in boiling than in other regimes of heat transfer and leads to poor reproducibility of results. The inconsistency and scatter of the experimental data are

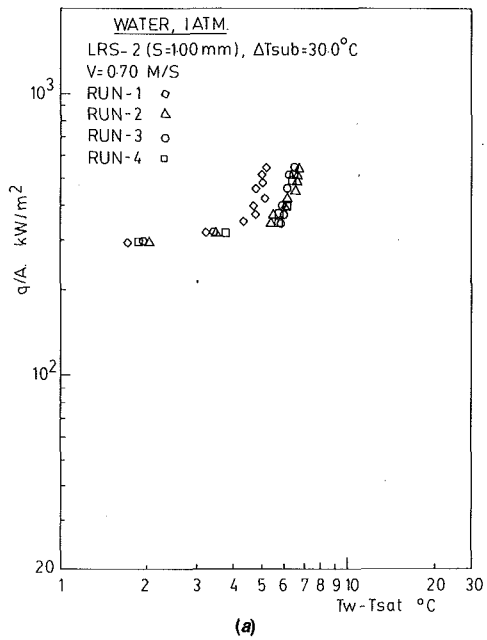

Fig. 4(*a*) Effect of order of testing and (*b*) reproducibility of data on flow boiling

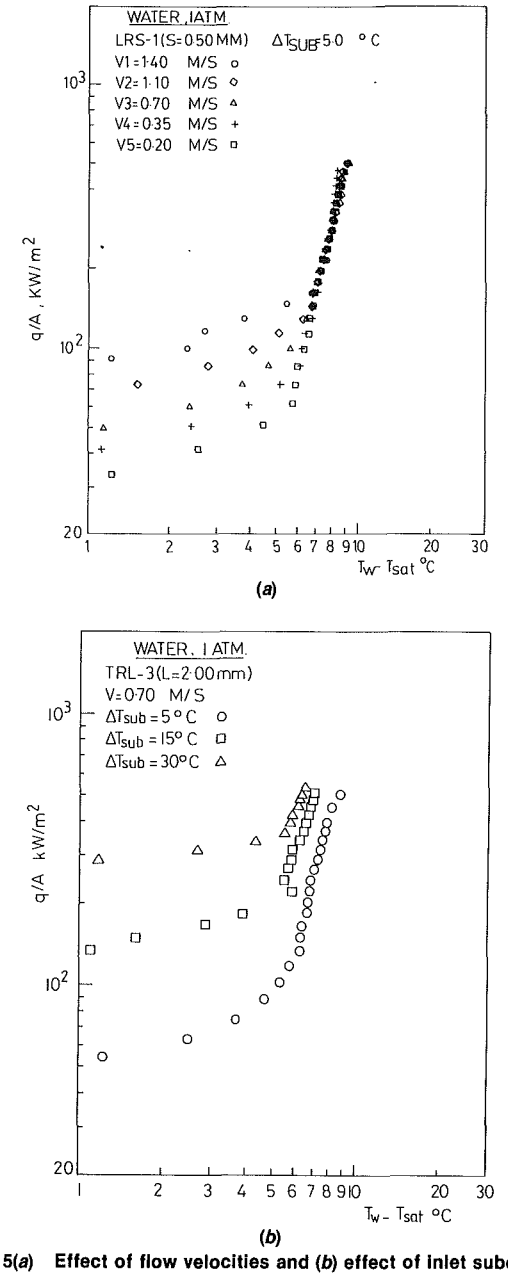

Fig. 5(*a*) Effect of flow velocities and (*b*) effect of inlet subcooling

usually attributed to "aging" of the surface on which boiling occurs. Surfaces that have been in service for long periods of time often required higher superheat temperature for a given heat flux. This is due either to the added resistance of an oxide or deposited layer or to the decrease in cavity size resulting from mild oxidation. The rates of change associated with aging generally diminish as a function of time and after a sufficiently long period has elapsed, a surface will reach a quasi-static condition and yield reproducible data. The aging effect of the boiling surface was observed experimentally with water as a working liquid. After a certain number of continuous runs, the surface shows a time-independent steady heat transfer performance as shown in Fig. 4(*a*). The reproducibility of the experimental data was also confirmed by an aged surface, as shown in Fig. 4(*b*). A similar result was also observed by Joudi (1977) in pool boiling.

Heat transfer results of the experiments with TRL and LRS surfaces in terms of heat flux (q/A), superheat temperature (ΔT_{sat}), and flow velocity (V) are shown in Figs. 5(*a*) to 6(*b*). Figure 5(*a*) is a typical plot of heat flux versus superheat for different flow velocities. It was found that when boiling took place, a pronounced increase in heat flux occurred with increasing flow velocities. As fully developed boiling was attained, the effect of velocity became negligible in comparison with the highly efficient mode of heat transfer, which operated in nucleate boiling. The effects of inlet subcoolings are shown in Fig. 5(*b*). It was found that heat flux increased with the increasing of subcooling. The effects of velocity and inlet subcooling are in good agreement with the results of Akhanda and James (1984a). Pressure drop across the short test section was also measured but no significant change was observed over the experimental range investigated.

The effects of transverse rectangular rib length on flow boiling heat transfer are shown in Fig. 6(*a*). In order that variations in boiling characteristics may be attributable solely to change of rib length, it was necessary that rib height and rib spacing should remain constant and in addition the effect of surface microroughness be isolated. Variation in surface microroughness is rarely taken into account in the analysis of flow boiling

data reported in the literature, except in the work of Joudi (1977) and Akhanda and James (1984a, 1984b). Also included for comparison are the results of a mirror polished surface and the optimum roughened surface (Ra = 0.78 μm) of Akhanda and James (1984b). It is evident from this figure that the surface (TRL-1) with rib length of 0.50 mm was the optimum heating surface in this group. The maximum improvement in heat transfer performance (compared with a mirror polished surface) was about 63 percent (at a heat flux of 500 kW/m^2) for a rib length of 0.50 mm.

The effects of spacing of longitudinal rectangular ribs on flow boiling heat transfer are shown by a typical plot in Fig. 6(*b*). As in the previous test, in order for variations in boiling characteristics to be solely attributable to change of spacing of rectangular ribs, it was necessary that rib height and rib length should remain constant and also the effect of surface microroughness be isolated. The results of a mirror polished surface and that of the optimum roughened surface of Akhanda and James (1984b) are included for comparison. It is evident from the graph that rib spacing of greater than 1.50 mm showed an increase in superheat for a given heat flux. It will be observed that a clearance between the ribs of 1.50 mm provides the optimum heat transfer performance in this group. The maximum improvement in heat transfer performance (compared with mirror polished surface) was about 55 percent at a heat flux of 500 kW/m^2 for this rib spacing.

Figures 7(*a*), 7(*b*), and 7(*c*) show the results of a comparative study of the heat transfer performance of the surface under consideration for inlet subcoolings of 5°C, 15°C, and 30°C, respectively, at a constant flow velocity of 0.70 m/s. It will be observed that for all subcoolings, the optimum transverse ribbed surface (TRS-2) of Akhanda and James (1984a) exhibits a consistently higher heat flux than that of the optimum longitudinal ribbed surface (LRS-3) for a given superheat temperature. Both surfaces show a very substantial improvement in heat transfer performance compared with the optimum

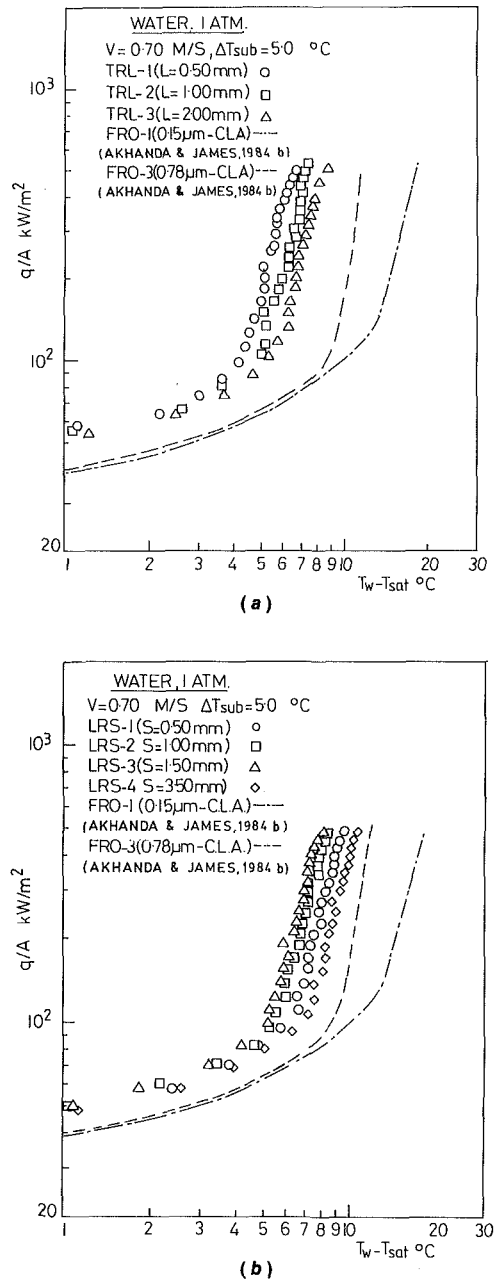

Fig. 6(*a*) Effect of rib length and (*b*) effect of rib spacing on heat flux in flow boiling

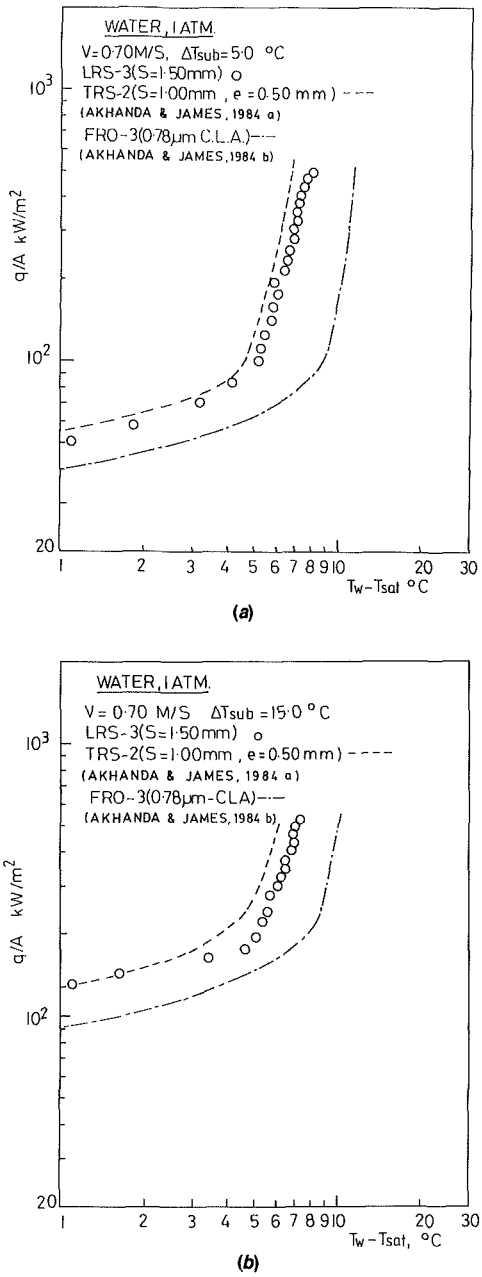

Fig. 7 Comparison of the optimum performance of test surfaces for inlet subcoolings of (*a*) 5°C, (*b*) 15°C, and (*c*) 30°C

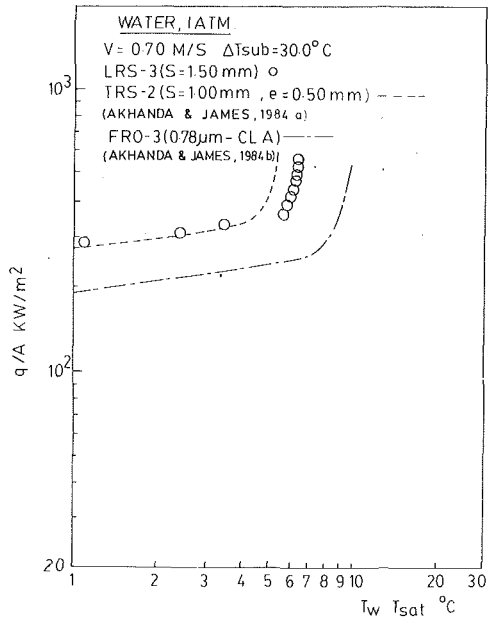

Fig. 7 (continued)

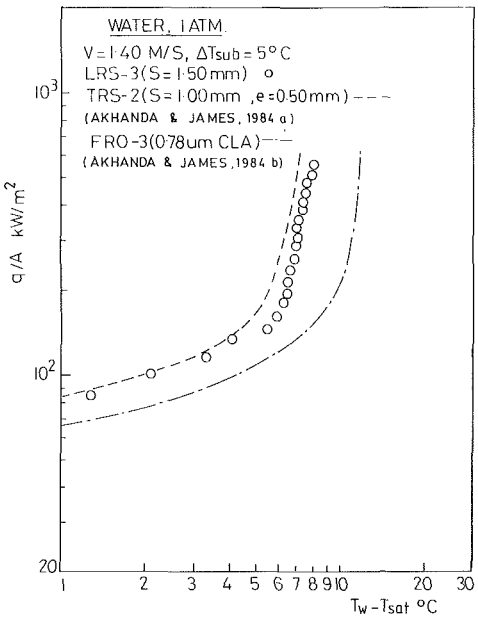

Fig. 8 Comparison of the optimum performance of test surface for a velocity of 1.4 m/s

roughened plane surface (FRO-3) of Akhanda and James (1984b) over the entire range of superheats and subcoolings investigated.

Figure 8 is a typical representation of the data recorded for the same surfaces with a flow velocity of 1.40 m/s and a subcooling of 5°C.

It will be observed that the trends exhibited are identical with those shown at lower velocities.

It is clear from the data that the optimum transverse rectangular ribbed surface (TRS-2) invariably produces a better heat transfer performance than the optimum longitudinal ribbed surface (LRS-3) and both surfaces show a substantial improvement in heat transfer performance when compared with the optimum roughened plane surface (FRO-3).

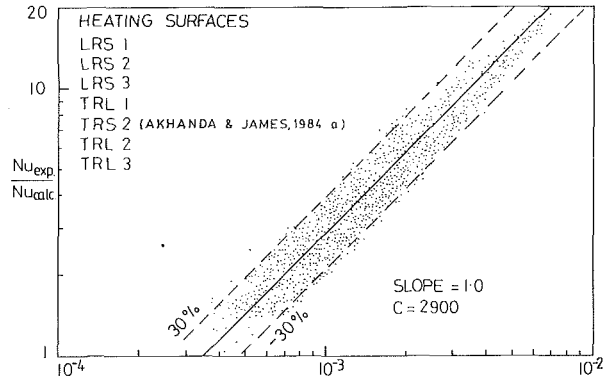

Fig. 9 Graphic representation of the correlation

The data are correlated in Fig. 9 using the following relationship:

$$\frac{\mathrm{Nu_{expt}}}{\mathrm{Nu_{calc}}} = 130.0\left(\frac{q/A}{\lambda\rho_v V}\right)^{0.73}\left(\frac{\lambda}{C_{PL}\Delta T_{\mathrm{sub}}}\right)^{0.55}$$

$$\left(\frac{\rho_v}{\rho_L}\right)^{0.7}\left(\frac{s}{\sqrt{\frac{\sigma}{g(\rho_L-\rho_v)}}}\frac{e}{l}\right)^{0.10}(1+\sin\theta)^{0.15} \qquad (1)$$

where $s \leq s_0$; s_0 is the clearance between ribs for the optimum ribbed surface.

The correlation was derived using standard procedures, and the dimensionless groups $(q/A)/(\lambda\rho_v V)$, $\lambda/C_{PL}\Delta T_{\mathrm{sub}}$, and ρ_v/ρ_L will be familiar from other established boiling heat transfer predictions.

Although the range of ρ_v/ρ_L investigated in this work was limited, its effect is well known and is, therefore, included for completeness. The dimensionless group

$$\left(\frac{s}{\sqrt{\frac{\sigma}{g(\rho_L-\rho_v)}}}\frac{e}{l}\right)$$

includes all the dimensions necessary to describe a particular geometric configuration. In addition it includes a term that is proportional to the bubble departure diameter and incorporates surface tension and buoyant forces, which are dominant in a hydrodynamic situation. The first ratio of this dimensionless group is a measure proportional to the availability of space for bubble growth between ribs, whereas the second ratio e/l is indicative of the slenderness ratio of a particular configuration. The term $(1+\sin\theta)$ accounts for the rib orientation with the direction of flow. A full development of the correlation is given by Akhanda (1985) and the single-phase Nusselt number ($\mathrm{Nu_{calc}}$) is determined from the relationship given by James (1967).

Conclusions

The following conclusions can be drawn from the investigation:

1 The aging effect of the boiling surface was observed experimentally with water as a working fluid.

2 The effects of transverse and longitudinal rectangular ribbing of the heat transfer surface were investigated experimentally.

3 An optimum transverse rectangular ribbed surface (TRS-2) was compared with the optimum longitudinal rectangular

ribbed surface (LRS-3) and it was found that the former exhibited a better heat transfer performance. Both surfaces showed a substantial improvement in heat transfer performance compared with the optimum roughened surface.

4 Experimental data were correlated to within ±30 percent by equation (1).

References

Akhanda, M. A. R., 1985, "Enhanced Heat Transfer in Flow Boiling," Ph. D. Thesis, University of Manchester Institute of Science & Technology, Manchester, United Kingdom.

Akhanda, M. A. R., and James, D. D., 1984a, "Enhanced Heat Transfer From Artificially Prepared Ribbed Surfaces in Flow Boiling," presented at the IChemE and IMechE 11th Annual Research Meeting on Heat Transfer and Catalysis and Catalytic Reaction, Bath, United Kingdom.

Akhanda, M. A. R., and James, D. D., 1984b, "Forced Convection Boiling From Roughened Surfaces," presented at the IChemE and IMechE 11th Annual Research Meeting on Heat Transfer and Catalysis and Catalytic Reaction, Bath, United Kingdom.

Bergles, A. E., Collier, J. G., Dalhaye, J. M., Hewitt, G. F., and Mayinger, F., 1981, "Augmentation of Two-Phase Heat Transfer," *Two-Phase Flow and Heat Transfer in Power and Process Industries*, Hemisphere, Washington, DC, pp. 366-382.

Bruzzi, S., 1969, "Forced Convection Boiling Heat Transfer in Rectangular Duct Heated on One Side," Ph. D. Thesis, Imperial College, University of London, United Kingdom.

Dunn, P. D., and Reay, D. A., 1976, *Heat Pipes*, Pergamon Press, New York.

Gogonin, I. I., and Sovorkova, I. N., 1973, "Heat Transfer During Boiling of Freon-21 on Finned Surfaces," *Int. Chem. Engineering*, Vol. 13, No. 4, pp. 698-701.

Gorenflo, D., 1966, "Zum Warmeubengang bei der Blasenverdamfung an Rippenrohren," Diss.-g. H. Karlsruhe, Federal Republic of Germany.

Hesse, G., 1973, "Heat Transfer in Nucleate Boiling, Maximum Heat Flux and Transition Boiling," *Int. J. Heat Mass Transfer*, Vol. 16, p. 1611.

James, D. D., 1967, "Forced Convection Heat Transfer in Ducts of Noncircular Section," Ph. D. Thesis, Imperial College, University of London, United Kingdom.

Joudi, K. A., 1977, "Surface Geometry Variations in Nucleate Pool Boiling," Ph. D. thesis, University of Manchester Institute of Science & Technology, Manchester, United Kingdom.

V. H. Del Valle, M., 1984, "Flow Boiling near Critical Heat Flux," D. Phil. Thesis, Lincoln College, University of Oxford, United Kingdom.

Webb, R. L., 1981, "The Evolution of Enhanced Surface Geometrics for Nucleate Boiling," *J. Heat Transfer Engineering*, Vol. 2, Nos. 3-4, pp. 46-67.

A. Hasan

R. P. Roy

Department of Mechanical and Aerospace Engineering, Arizona State University, Tempe, AZ 85287

S. P. Kalra

Electric Power Research Institute, Palo Alto, CA 94303

Some Measurements in Subcooled Flow Boiling of Refrigerant-113

Measurements of local vapor phase residence time fraction, liquid phase temperature, and heated wall temperature were carried out in subcooled flow boiling of Refrigerant-113 through a vertical annular channel. Data are reported for two fluid mass velocities and two pressures over a range of wall heat flux. Estimates of typical vapor bubble size and velocity are given. Some comparisons with a one-dimensional two-fluid model of subcooled boiling flow are also presented.

Introduction

Subcooled flow boiling is normally associated with the nucleate boiling mode of convective heat transfer from heated surfaces and the existence of a layer of bubbly vapor–liquid mixture adjacent to the surface. Because of the very efficient heat transfer characteristic of subcooled nucleate boiling, such flows have been the subject of numerous studies, both experimental and analytical. Experiments that have explored the basic aspects of subcooled boiling flow include those by Jiji and Clark (1964), Walmet and Staub (1969), Delhaye (1969), Dix (1971), Delhaye et al. (1973), Lung et al. (1977), and Müller-Steinhagen et al. (1986). Thermocouples (miniature and micro) and hot-film sensors operated in the constant temperature anemometer (CTA) mode are examples of devices used in these studies to measure liquid and vapor temperatures and vapor fraction distribution, respectively. Afgan et al. (1973a, 1973b) investigated the statistical aspects of temperature fluctuations in subcooled pool boiling of water by microthermocouples. Jain and Roy (1983) measured the stochastic character of chordal-average vapor fraction and wall pressure fluctuations in subcooled and saturated flow boiling of Refrigerant-113 (R-113) by means of a dual-beam x-ray system and matched piezoelectric pressure transducers, respectively.

If one scrutinizes the subcooled boiling flow models that have been proposed in recent years (e.g., Lellouche and Zolotar, 1982; Dykhuizen et al., 1986), it becomes obvious that many hypotheses and assumptions are needed to bridge crucial gaps in the understanding of subcooled boiling flow phenomena. It may be suggested that bringing forth any genuine improvement in the mechanistic modeling of subcooled boiling flow will require deeper insights into the physics of the associated phenomenon and that such insights can only be gleaned from appropriate fundamental experiments. For instance, comprehensive information is needed on the wall and phase (vapor, liquid) temperature distributions, vapor bubble size and velocity distribution, liquid velocity distribution, the distribution of residence time fraction of the phases, pressure, and turbulent heat and momentum transfer rates in the continuous (liquid) phase. It is also important that, to the extent possible, all of these measurements be carried out in the same experimental undertaking. This is our eventual goal.

R-113 was used as the working fluid in our experiments. In an earlier paper (Hasan et al., 1989) we reported on subcooled flow boiling wall heat transfer data obtained in this facility. In the present paper we first describe the techniques used to measure the local vapor phase (bubbles) residence time fraction, and the liquid and vapor phase temperatures. Results of measurements carried out in flow boiling are then presented. Estimates of vapor bubble size and velocity obtained for a typical experimental condition from high-speed movies are given next.

In order to compare the measurements in some average sense to the predictions of a one-dimensional two-fluid model of flow boiling (Dykhuizen et al., 1986), it was necessary to calculate the flow area-averaged vapor residence time fraction and the mixed-mean liquid phase temperature from the measured distributions. A few of these comparisons are reported and some shortcomings in the description of subcooled boiling flow in the model are pointed out.

Experiments

I Measurement Techniques and Their Validation in Pool Boiling

1 Vapor Bubble Detection and Residence Time Fraction Measurements. This involved the use of a cylindrical hot-film sensor operated in the CTA mode. Such a technique has been employed successfully by Delhaye (1969) and Dix (1971). Specifically, we used the TSI 1212AS-10A sensor (25-μm diameter, 250-μm length, uncoated) in conjunction with the TSI 1050 CTA. The sharpest distinction between the signals corresponding to sensor encounters with vapor bubbles and liquid occurred when nucleate boiling was established at the sensor surface. For our experiments, a sensor overheat ratio of 1.09 with respect to the local saturation temperature generally created the optimum nucleate boiling condition at the sensor surface.

A simple apparatus, the schematic of which is shown in Fig. 1, was built to validate this technique. It consisted of a pyrex glass bottle about 10 cm in diameter and 36 cm high filled to approximately 2/3 with liquid R-113. A stream of helium gas bubbles could be injected into the liquid at a desired rate through a glass tube with a 0.5-mm opening at its tip. The sensor was placed approximately 7.5 cm directly above the tube opening. The CTA output signal was routed to a data acquisition system (DATA 6000A, Analogic), an oscilloscope, and a pulse generator circuit. The pulse generator circuit, in turn, fed a trigger circuit, which operated two cameras in a synchronous fashion.

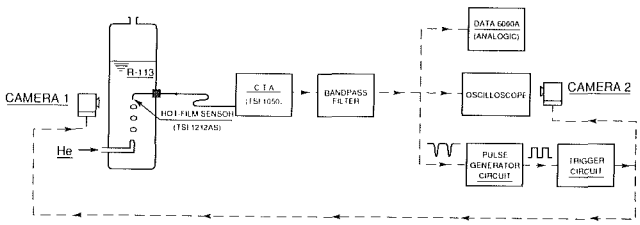

Fig. 1 Apparatus for validation of the vapor residence time fraction measurement technique

Contributed by the Heat Transfer Division for publication in the JOURNAL OF HEAT TRANSFER. Manuscript received by the Heat Transfer Division August 25, 1989; revision received May 5, 1990. Keywords: Boiling, Forced Convection, Multiphase Flows.

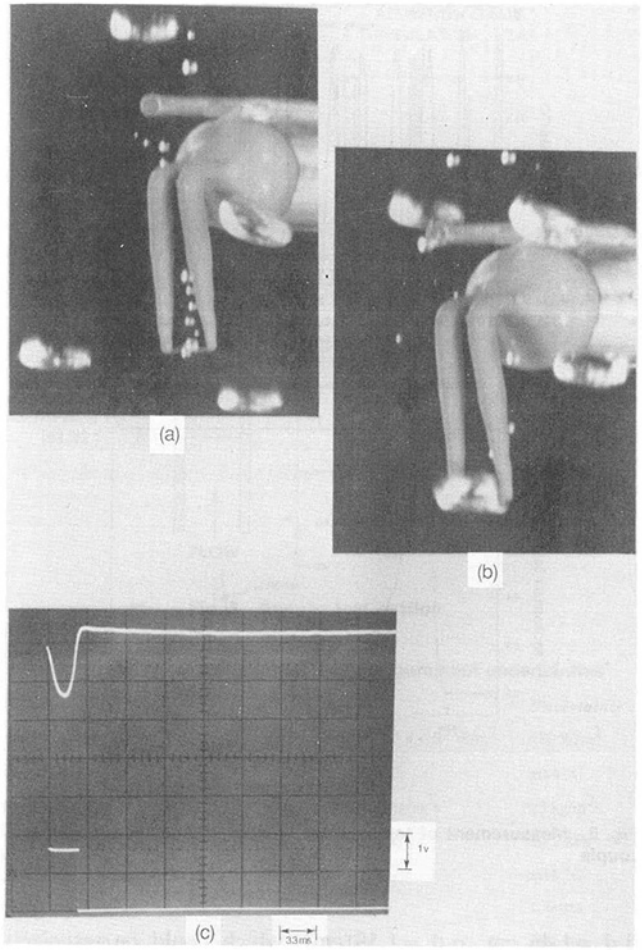

Fig. 2 Validation of the vapor residence time fraction measurement technique

Figure 2 shows three photographs: (*a*) the sensor in the nucleate boiling mode in the liquid phase; (*b*) a helium bubble encountering the sensor; and (*c*) the consequent sharp drop in the CTA output signal voltage along with the rectangular pulse generated by the pulse generator circuit as seen on the oscilloscope screen. Photographs (*b*) and (*c*) were synchronized in time. The time interval between the beginning of the sharp drop in the CTA output signal voltage and the end (i.e., its subsequent recovery to the voltage level corresponding to the state (*a*)) is a measure of the residence time of the vapor bubble, Δt_G, at the sensor location.[1] If the vapor residence time intervals are summed over a time series record of length Θ, then the vapor residence time fraction is $\Sigma\Delta t_G/\Theta$.

[1]Some uncertainty is introduced into this measure through the designation of the beginning and end points of the voltage drop. An estimate of this is given in a later section.

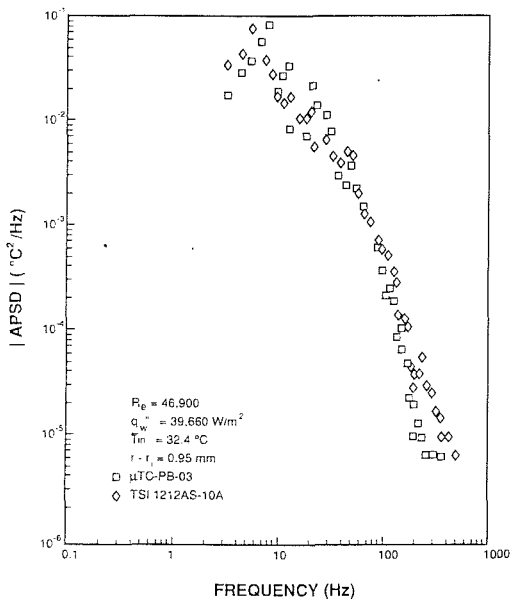

Fig. 3 APSD magnitude of temperature fluctuations in heated turbulent liquid flow as measured by two sensors

The time constant of the sensor when operated in the above-described mode was estimated to be slightly less than 1 ms.

2 Liquid and Vapor Phase Temperature Measurement. This technique utilized a specially made chromel-constant and microthermocouple (P. Beckman Co., μTC-PC-03) in which the wire elements, 18 μm in diameter, are joined together in a disk-shaped junction of 0.1-mm diameter and 2.5-μm thickness. The microthermocouple probe was installed in the measurement section in such an orientation that the main flow impinged upon the disk thickness, thereby minimizing flow disturbance. The transient response of the microthermocouple was compared to several other fast sensors including the TSI 1212AS-10A hot-film sensor operated in the constant-current mode (i.e., as a resistance thermometer in conjunction with TSI 1040). Figure 3 shows a comparison of the auto power spectral density (APSD) magnitudes of temperature fluctuations in heated turbulent single-phase liquid flow in our test section as measured by the microthermocouple and the hot-film sensor. It is apparent that these two sensors have comparable responses. Moreover, their responses were found to be significantly faster than the other sensors tested (e.g., a microthermocouple specially made by a different manufacturer, the TSI 1262 AE-10W cylindrical hot-film sensor, and 1264-BP conical hot-film sensor). The μTC-PB-03 microthermocouple was eventually selected for all fluid temperature distribution measurement in this work because of its drift-free output. Recent measurements of the transient response of the microthermocouple μTC-PB-03 to step and periodic heating by laser pulses point to a time constant of approximately

Nomenclature

A_{x-s} = flow area of test section
$\bar{D}_b$ = mean bubble diameter
G = mass velocity
h_k = enthalpy of phase k
p = pressure
p_r = partial pressure of R-113
q''_w = wall heat flux
r = radial coordinate
R^* = nondimensional radial coordinate = $(r-r_i)/(r_o-r_i)$
Re = Reynolds number
$\bar{T}$ = time-mean temperature
u_{kz} = axial velocity of phase k
u_{kr} = radial velocity of phase k
We_b = bubble Weber number
z_m = axial location of measurement plane
α_k = residence time fraction of phase k
Δt = time interval
ρ_k = density of phase k
σ = surface tension
$\langle \cdots \rangle$ = flow area average

Subscripts

bbl = bubble boundary layer
i = inner wall of annulus
in = inlet to test section
k = phase; $k=G$ for vapor, $k=L$ for liquid
o = outer wall of annulus
sat = saturation
w = heated wall

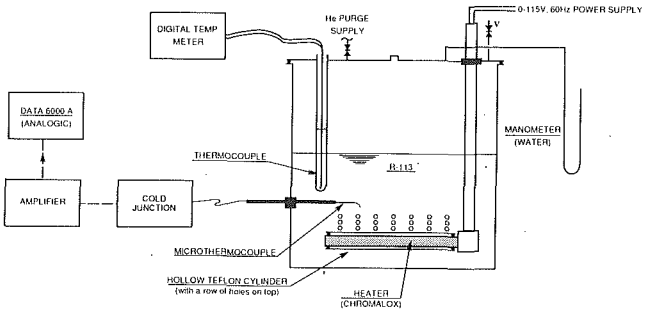

Fig. 4 Apparatus for validation of the liquid and vapor phase temperature measurement technique

7 ms in turbulent flow of liquid R-113 at comparable Reynolds numbers.

Figure 4 is schematic of the apparatus built to validate the phase(s) temperature measurement technique. A pyrex glass vessel, approximately 17 cm in diameter and 16 cm high, was equipped with a 250 W cylindrical (1.6 cm diameter, 9.5 cm long) stainless steel sheathed immersion heater installed in a horizontal configuration. The heater was shrouded with a hollow teflon cylinder, which had a row of 1 mm holes on top. This permitted a stream of vapor bubbles of reasonably large and uniform size to be released into the liquid when the heater was supplied with sufficient power to permit significant nucleate boiling at its surface. The microthermocouple could be positioned at various positions above the teflon sheath such that it was either in the path of one of the bubble streams or in an all-liquid region between two streams.

The vessel was typically half-filled with liquid R-113 prior to an experiment. The liquid was then deaerated by heating it for several hours while continuously venting the vessel to ambient. The space above the liquid was also purged of air with helium gas. A U-tube water manometer monitored any significant deviation of the vessel pressure from that of the ambient. A typical experiment consisted of gradually increasing the power to the heater by means of a variac until significant nucleate boiling occurred at the heater surface (note that the liquid in the vessel was still subcooled). Streams of vapor bubbles then emerged from the holes on the teflon cylinder, proceeding upward to the free liquid surface. Figure 5(*a*) is a time trace of a microthermocouple output signal for a situation in which the sensor was about 1.9 cm above the sheath and in the path of a stream of vapor bubbles. Each sharp rise in the signal voltage represents a bubble encounter during which the temperature rises approximately to the saturation temperature corresponding to the local pressure. Figure 5(*b*) shows the probability density function (PDF) of the signal in which two distinct peaks appear. One peak corresponds to the most probable liquid temperature and the other to the most probable vapor temperature. A distribution exists around each peak.

Two comments are pertinent here. First, the microthermocouple was clearly fast enough to distinguish between liquid and vapor temperatures in the pool boiling experiment since its time constant is considerably smaller than the typical residence times of the vapor bubbles ($\approx$30–50 ms as estimated from the time trace of Fig. 5*a*). Second, Delhaye et al. (1973) have suggested a simple method of estimating the local vapor fraction from the PDF.

This apparatus was also utilized to revalidate the hot-film sensor technique of vapor residence time fraction measurement discussed earlier in nucleate pool boiling condition.

II Measurements in Subcooled Flow Boiling. The flow boiling rig has been described in an earlier paper (Roy et al., 1988). Therefore, only a brief description of the vertical annular test section will be given here.

The inner tube of the test section was of 304 stainless steel

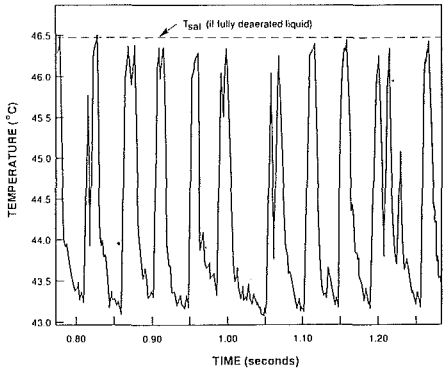

a. Time trace of microthermocouple output signal

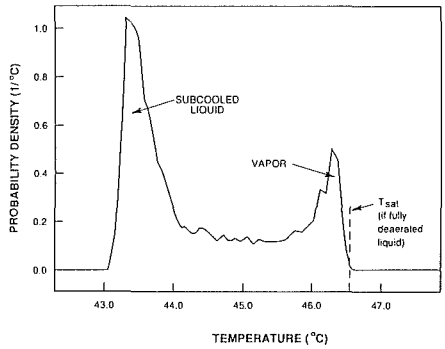

b. PDF of the signal

Fig. 5 Measurement of temperature in pool boiling by microthermocouple

(i.d. = 1.46 cm, o.d. = 1.59 cm), which could be resistively heated by direct current. The outer pipe was made of transparent pyrex glass (i.d. = 3.81 cm, o.d. = 4.70 cm) except for the measurement section, which was of 304 stainless steel, 0.495 m long, and of the same inner diameter as the pyrex pipe. The total length of the test section was 3.66 m, of which the upper 2.75 m could be heated at a maximum power of 40 kW. The lower 0.91 m served as the hydrodynamic entrance length. The heater tube was filled with aluminum oxide powder insulation. The outer pipe was insulated with 5-cm-thick jacketed fiberglass wool.

Figure 6 shows, schematically, the locations of the microthermocouple and the hot-film sensor (diametrically opposite each other) as well as of two (of a total of four) copper-constantan wall thermocouples in the measurement section. The "measurement plane," indicated in the figure, was 1.943 m downstream of the beginning of heated length. The small difference in the fluid temperature because of the axial mismatch of about 6 mm between the two sensors can be shown to be well within the experimental uncertainty associated with the fluid temperature measurement. The same holds true for the two wall thermocouples (Omega, foil thickness $\approx$ 0.01 mm, junction length $\approx$ 0.5 mm) baked on with Omegabond epoxy at diametrically opposite locations on the inner wall of the heater tube. The tube was subsequently filled with aluminum oxide powder. The tube outer wall (i.e., the annulus heated wall) temperature was calculated analytically from the measured tube inner wall value by a steady-state heat conduction analysis.

We note that both the microthermocouple and the hot-film probe were constructed with a bend in their respective stems so that in each case the sensor itself was upstream of the probe body (by about 6 mm in case of the microthermocouple and about 12 mm in the case of the hot-film probe). This minimized disturbances to the flow field at or near the sensor. Mean axial

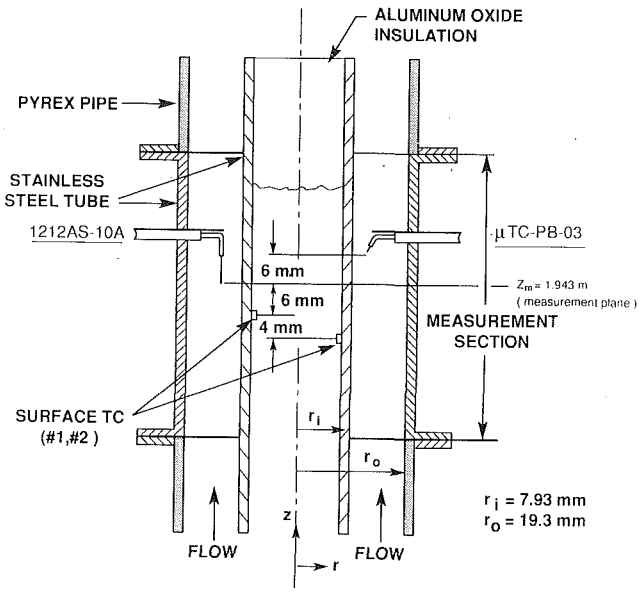

Fig. 6 Annular test section

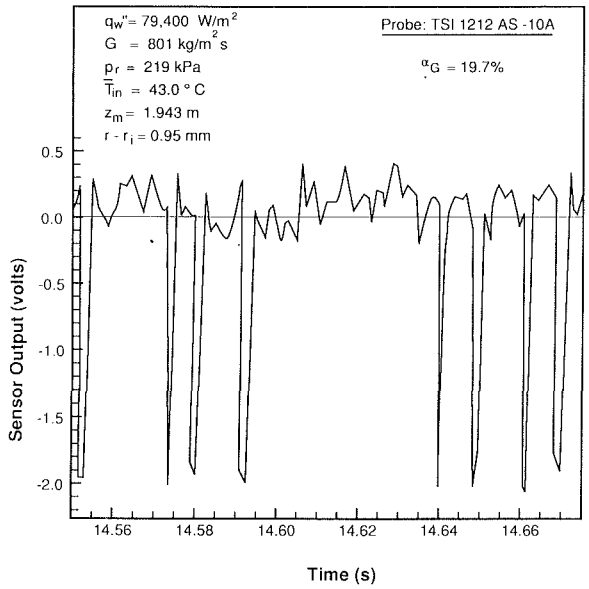

Fig. 7 A typical time race of the hot-film sensor (CTA mode) output signal in subcooled boiling flow

Table 1 Range of experiments and measurement uncertainties†

	Range	*Uncertainty*
Wall heat flux	4.2×10^4--1.4×10^5 W/m^2	±80 W/m^2
Wall temperature	60--100 °C	±0.4 °C
Mass velocity	579--801 kg/m^{2}s	±3 kg/m^{2}s
R-113 partial pressure at measurement plane	184--253 kPa	±0.7 kPa
Subcooling at testsection inlet	20--37 °C	±0.1 °C
Sensor radial traverse	0--10 mm	±30 μm
Vapor residence time fraction	0--37%	±1% for $0\% < \alpha_G < 10\%$ ± 2% for $10\% < \alpha_G < 40\%$

† The uncertainty estimates are for 95 percent confidence.

velocity and mean temperature radial profiles measured in fully developed turbulent flow of liquid R-113 in the measurement section supported this view (Hasan et al., 1989).

Table 1 shows the range of variables over which the subcooled boiling flow experiments were conducted and the associated measurement uncertainties.

1 Vapor Bubble Detection and Residence Time Fraction Measurement. Figure 7 shows a typical time trace of the output signal of the hot-film sensor operated in the CTA mode at an overheat ratio of 1.09 with respect to the local saturation temperature of R-113. The experimental condition (i.e., the wall heat flux, fluid mass velocity, local pressure, and radial location of the sensor) is given in the figure. Each sharp drop (negative "pulse") in the signal voltage of approximately 2V indicates an encounter of the sensor with a vapor bubble. The fluctuations of much smaller magnitudes (e.g., a few tenths of a volt) may be attributable to turbulence, marginal encounters with bubbles, and temperature variations in the liquid phase. The widths of the negative pulses at an *appropriate* base voltage (e.g., equal to or near zero in Fig. 7) represent the residence times of vapor bubbles at the sensor location. Three points are noteworthy here. First, the sensor length is an important parameter in that the smaller this length the more "local" the measurement. Second, it is a simple matter to obtain a count of the average number of bubbles detected by the sensor per unit time. Third, the individual bubble residence times are usually in the 2–4 ms range.

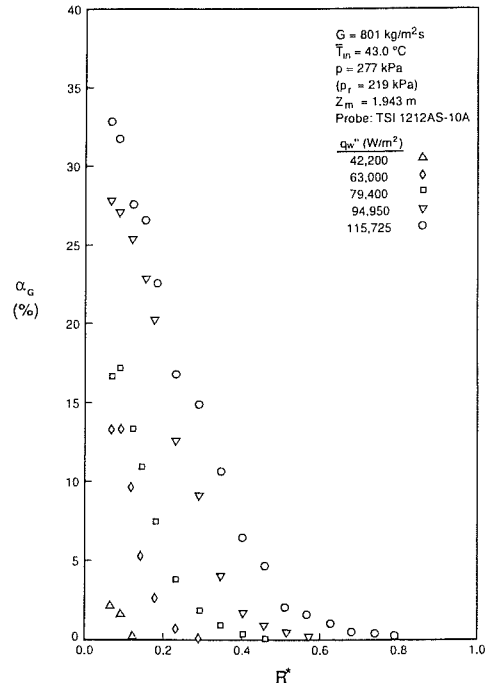

Fig. 8 Radial profiles of vapor phase residence time fraction

Base voltage values of 0.0, ±0.05, and ±0.10 were used to calculate the local residence time fractions of the vapor phase from the time series records.[2] These changes in the base voltage typically resulted in no more than ±1 percent difference in the time fractions obtained.

Figure 8 shows radial profiles of vapor phase residence time fraction at the measurement plane (m.p.) for five different wall heat fluxes and the following experimental parameters:

mass flux = 801 kg/m^{2}s
R-113 pressure at m.p. = 219 kPa
inlet temperature of liquid = 43.0°C

Figure 9 shows the vapor residence time fraction radial pro-

[2] The length of each time series record was 16.383 seconds (16,383 data points at 1 ms sampling interval).

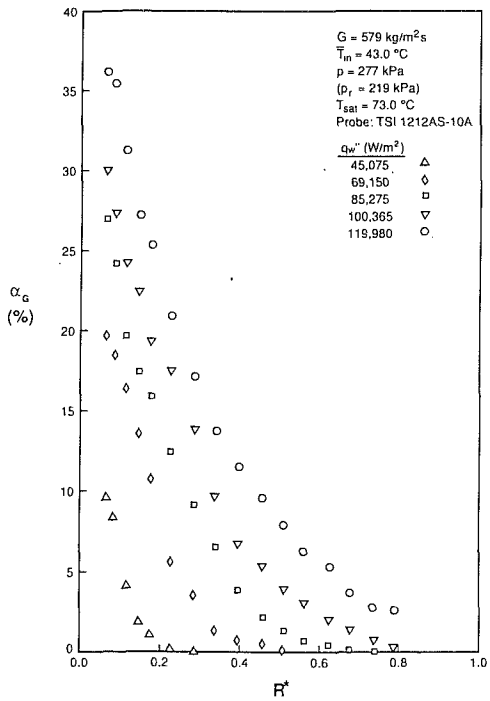

Fig. 9 Radial profiles of vapor phase residence time fraction

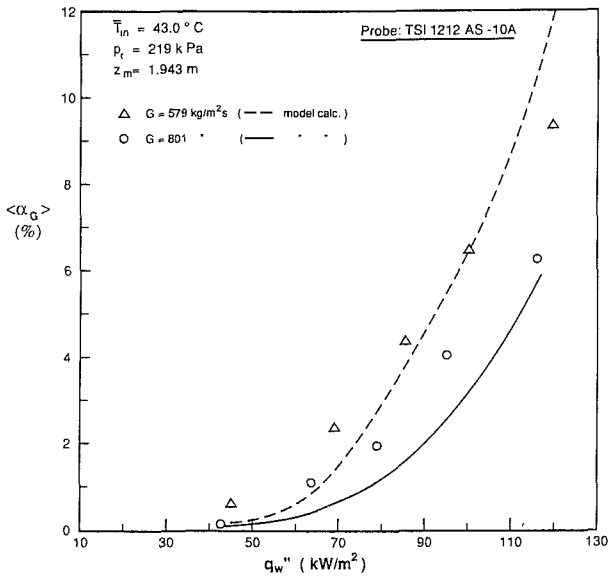

Fig. 10 Flow area-averaged vapor phase residence time fraction versus wall heat flux

files for five different wall heat fluxes and the same experimental parameter values as in the preceding case, except for the mass flux, which was now 579 kg/m²s. Profiles were also obtained for other experimental conditions but are not presented here for the sake of brevity.

Figure 10 depicts the flow area-averaged vapor residence time fraction versus the wall heat flux for these two series of experiments. The flow area-averaged value is calculated as follows:

$$\langle \alpha_G \rangle = \frac{2\int_{r_i}^{r_0} \alpha_G r \, dr}{(r_o^2 - r_i^2)} \tag{1}$$

The curves plotted on Fig. 10 are based on calculations from a one-dimensional two-fluid model of boiling flow. This model is discussed briefly in a later section.

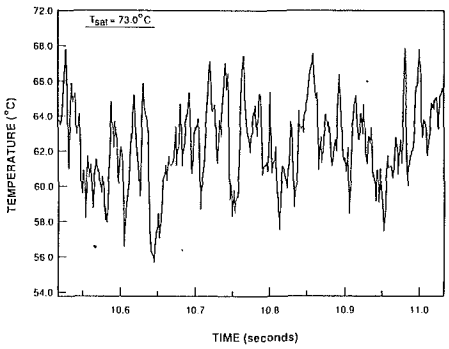

a. Time trace of microthermocouple output signal

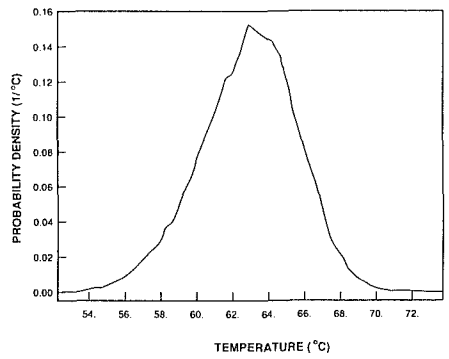

b. PDF of the signal

Fig. 11 Measurement of temperature in subcooled boiling flow by microthermocouple

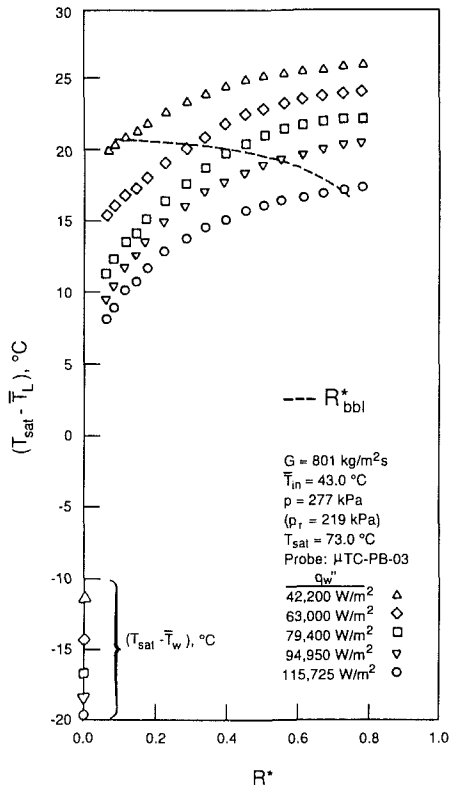

Fig. 12 Radial profiles of liquid phase subcooling

2 Liquid and Vapor Phase Temperature Measurement. Figure 11(*a*) shows a typical time trace of the microthermocouple output signal for the experimental condition of Fig. 8 at a wall heat flux of 79,400 W/m². The microther-

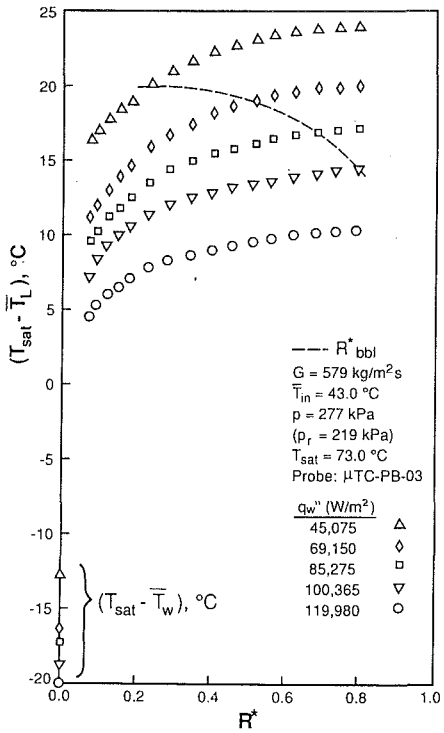

Fig. 13 Radial profiles of liquid phase subcooling

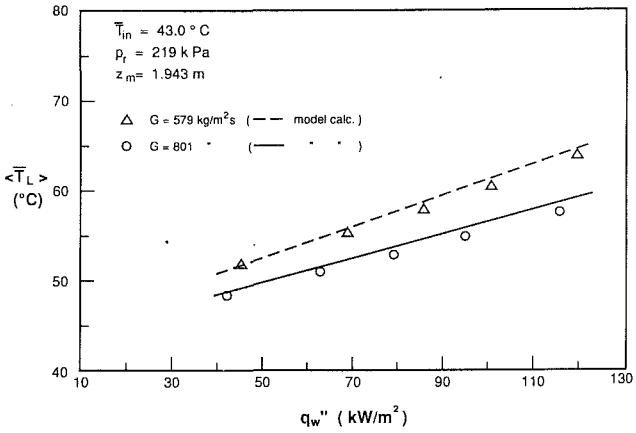

Fig. 14 Mixed-mean liquid phase temperature versus wall heat flux

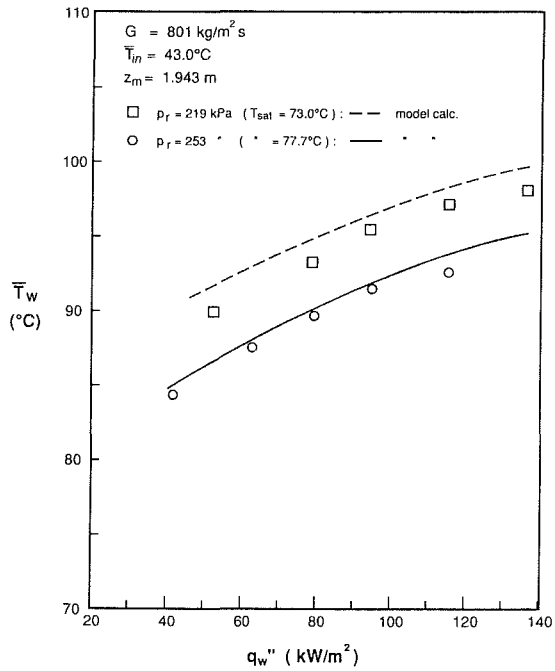

Fig. 15 Heated wall temperature versus wall heat flux

mocouple was at a distance of 0.95 mm from the heated wall. Figure 11(*b*) shows the corresponding PDF.

It is apparent from these two figures that the microthermocouple was unable to follow the rapid variations in local temperature caused by its encounters with rapidly translating small vapor bubbles (the temperature should be close to the local R-113 saturation temperature during these encounters). This is not surprising because as noted earlier the microthermocouple time constant was approximately 7 ms, whereas the residence times of the vapor bubbles were in the 2–4 ms range (see Fig. 7). This, therefore, suggests that the microthermocouple measured only the liquid phase temperature in boiling flow.

Figure 12 shows radial profiles of the mean liquid phase temperature at the measurement plane plotted as the "degree of subcooling." The experimental conditions are the same as in Fig. 8. The dotted line shown corresponds to the outer edge of the bubble boundary layer (b.b.l.) defined here as the radial location where the vapor residence time fraction is about one percent of the maximum value in the layer. Also shown in Fig. 12 are the measured wall superheats. Figure 13 shows the measured liquid phase temperature profiles and wall superheats for the experimental conditions of Fig. 9.

It can be inferred from Figs. 12 and 13 that the liquid phase was always subcooled in the time-mean sense. While small regions of saturated and/or superheated liquid may have existed in the flow especially near the heated wall, time series data as is shown in Fig. 11 indicate that such regions were none too frequent (at least within the limitations of the microthermocouple transient response).

Figure 14 shows the mixed-mean liquid phase temperature at the measurement plane versus the wall heat flux for the same two series of experiments. The mixed-mean temperature is calculated from the measured temperature profile as follows:

$$\langle \overline{T}_L \rangle = \frac{\int_{r_i}^{r_0} \alpha_L \overline{u}_{Lz} \overline{T}_L r \, dr}{\int_{r_i}^{r_0} \alpha_L \overline{u}_{Lz} \, r \, dr} \tag{2}$$

Inherent in equation (2) are the assumptions of insignificant change in liquid density and applicability of an average liquid specific heat across the flow channel. The liquid phase axial velocity distribution, $\overline{u}_{Lz}(r)$, used in the calculation was based on measurements in turbulent all-liquid flow in the same test section (Roy et al., 1986) for want of actual liquid velocity measurements in the boiling layer. Introduction of some error in the calculated mixed-mean liquid phase temperature may be anticipated because of this.

Figure 15 shows the measured heated wall temperature versus wall heat flux at two different measurement plane pressures but the same fluid mass velocity and inlet temperature.

3 Vapor Bubble Size and Velocity Determination Via High-Speed Movies. Only vapor bubbles at the outer periphery of the bubble boundary layer could be studied by this method. Even then, corrections were necessary for the effect of refraction through the liquid and the glass pipe wall. These corrections were established by immersing hollow glass spheres of various known sizes (these simulated vapor bubbles) at specific locations in a table-top replica of the test section annulus filled with liquid R-113 and determining the alterations in shape and size for each when viewed from outside.

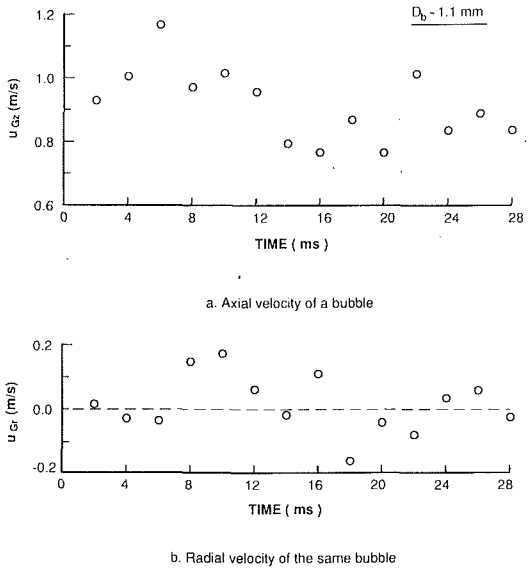

Fig. 16 Axial and radial velocities of a typical bubble during an experiment

Short sequences of high-speed movies (16-mm film; 5000 frames per second) of the flow were filmed at an axial location immediately above the measurement section.[3] The films were then projected, frame by frame, on a digitizing tabloid equipped with arrays of sensing microphones along its sides. An acoustic stylus was used to track individual vapor bubbles in each frame. Since the camera was focused on a particular r–z plane in the test section, bubbles with significant (albeit fluctuating) azimuthal velocity component moved in and out of the plane of focus. Data for only those bubbles that remained in this plane were accepted. The bubble position coordinate (in the r–z plane) data were acquired in a computer and the axial and radial velocity components of the bubble determined. An estimation of the bubble size was made as well. This procedure was repeated for several bubbles.

As an example, we consider the following experimental condition:

fluid mass velocity = 801 kg/m^{2}s
pressure at m.p. = 219 kPa
inlet temperature = 43.0°C
wall heat flux = 94,950 W/m^2

The radial profiles of the vapor phase residence time fraction and liquid subcooling for this condition are shown in Figs. 8 and 12, respectively. Figures 16(*a*) and 16(*b*) show the time behavior of the axial and radial velocity components of a typical vapor bubble at the b.b.l. edge. The mean axial velocity of this particular bubble was estimated to be about 0.9 m/s and the mean radial velocity was approximately zero. The diameter of bubbles at the b.b.l. edge ranged from 0.6 mm to 1.5 mm with the average diameter being about 1.1 mm.

Although the information obtained via this procedure was quite limited in that only bubbles at the b.b.l. edge could be studied, it was nevertheless valuable for the calculations by a two-fluid boiling flow model, which is discussed next.

Comparison With the Predictions of a One-Dimensional Two-Fluid Model

One-dimensional (the dimension being axial) models are not ideal for comparison with measurements such as reported here. This is because these models necessarily average out the distributions of field variables along the other dimensions. If the averaging procedure is carried out properly, several distribution coefficients whose values depend upon the spatial (e.g., transverse) distributions appear in the conservation equations. One is then faced with having to provide these distributions prior to carrying out computations.

Before suggesting alternatives, however, we carry out comparisons with a one-dimensional model described earlier by Roy et al. (Roy and Ho, 1982; Dykhuizen et al., 1986; Roy, 1988). In this model, given the transverse distributions of vapor residence time fraction, vapor and liquid axial velocities, and vapor and liquid enthalpies, the following averages are defined:

$$\langle \alpha_k \rangle \equiv \frac{1}{A_{x-s}} \int_{A_{x-s}} \alpha_k dA \tag{3}$$

$$\langle \bar{u}_{kz} \rangle \equiv \frac{\langle \alpha_k \bar{u}_{kz} \rangle}{\langle \alpha_k \rangle} \tag{4}$$

$$\langle \bar{h}_k \rangle \equiv \frac{\langle \alpha_k \bar{\rho}_k \bar{h}_k \bar{u}_{kz} \rangle}{\langle \alpha_k \rangle \langle \bar{\rho}_k \rangle \langle \bar{u}_{kz} \rangle} \tag{5}$$

The temperature of each phase is calculated from the corresponding enthalpy and pressure by an appropriate equation of state.

In order to be able to account for the very low vapor fraction region of subcooled boiling flow, it was necessary to eliminate the notion of the "net vapor generation point" from the original model. Instead, the vapor phase was allowed to exist immediately downstream of the onset of nucleate boiling.

Another consideration pertains to the vapor bubble size. First, if the maximum bubble diameter was established on the basis of a limiting Weber number (e.g., equal to 25; TRAC-P1A, 1979)

$$\bar{D}_{b_{\max}} = \frac{(\mathrm{We}_b)_{\mathrm{limit}} \sigma}{\bar{\rho}_L (\bar{u}_{Gz} - \bar{u}_{Lz})^2} \tag{6}$$

the calculated maximum bubble diameter at the higher heat fluxes was usually well above 2 mm. Our visual observations, on the other hand, never detected bubbles larger than 1.5 mm in diameter even at the highest vapor fractions encountered in the experiments. Therefore, an empirical upper limit of 1.5 mm was imposed on D_b. Second, we had postulated in the original model that the bubble diameter is related to the vapor fraction as

$$\bar{D}_b = A \alpha_G^{0.5} \tag{7}$$

where A is an appropriate constant. A best-estimate value of 0.0073 m was obtained for A from the experiments.

The only other relation in the original model that was modified in the wall heat transfer coefficient for subcooled nucleate flow boiling. This was reported by us in an earlier paper as the "modified Shah correlation" (Shah, 1983; Hasan et al., 1989).

No additional attempts were made to tailor the model constitutive equations so as to compare better with the data.

Calculated values of $\langle \alpha_G \rangle$, $\langle \bar{T}_L \rangle$, and $\bar{T}_w$ are plotted on Figs. 10, 14, and 15, respectively. Particularly inadequate is the comparison between the calculated and measured values of the flow area-averaged vapor residence time fraction. Given the simplistic nature of the model, this is not surprising. We add that the calculated vapor phase enthalpy and temperature were always found to be very close to the respective saturation values at the prevalent pressure.

A more appropriate model for low vapor fraction subcooled boiling flow may be based on a two-domain description of the flow field. Such an approach would, in essence, be a simplified version of the multidomain, multiphase description of vapor–liquid flow suggested by Sha and Soo (1978). In the two-domain

[3] As the measurement section was made of stainless steel, visualization of the flow could only be carried out either upstream or downstream of this section.

approach, the bubbly boiling layer will be designated as one domain and the all-liquid layer as the second domain. Formal averaging across the transverse dimension of each domain may be invoked so as to yield separate averaged conservation equations and state variables for the domains. The domains are then to be coupled at the "interface" via appropriate mass, momentum, and energy transfer relations.

Concluding Remarks

Measurements have been performed of the radial distributions of the vapor phase residence time fraction, liquid phase temperature, heated wall temperature, and local pressure in subcooled nucleate flow boiling of R-113 through a vertical annular channel. The vapor phase temperature could not be measured because of the relative sluggish response of the microthermocouple used. An effort is underway to construct a faster microthermocouple (time constant ≈ 1 ms) so that the vapor temperature may also be measured. The measurements reported here along with some others reported by us earlier (e.g., wall heat transfer coefficients) constitute important parts of the comprehensive experimental data sought to construct a mechanistic model of subcooled boiling flow.

It is apparent from the measured radial profiles of the vapor residence time faction that one-dimensional models featuring single-domain flow area-averaged equations and state variables are not particularly appropriate for describing low vapor fraction subcooled boiling flows. Our objective in this regard is to develop a two-domain model that distinguishes between the boiling layer and the all-liquid layer.

Acknowledgments

This work was supported by Electric Power Research Institute, Nuclear Division, under research project No. RP 2398.

References

Afgan, N., Jovanovic, L. J., Stefanovic, M., and Pislar, V., 1973a, "An Approach to the Analysis of Temperature Fluctuation in Two-Phase Flow," *International Journal of Heat and Mass Transfer*, Vol. 16, pp. 187–194.

Afgan, N., Stefanovic, M., Jovanovic, L. J., and Pislar, V., 1973b, "Determination of the Statistical Characteristics of Temperature Fluctuation in Pool Boiling," *International Journal of Heat and Mass Transfer*, Vol. 16, pp. 249–256.

Delhaye, J. M., 1969, "Hot-Film Anemometry in Two-Phase Flow," in: *Two-Phase Flow Instrumentation*, ASME, Eleventh National Heat Transfer Conference, pp. 58–69.

Delhaye, J. M., Semeria, R., and Flamand, J. C., 1973, "Void Fraction, Vapor and Liquid Temperatures; Local Measurements in Two-Phase Flow Using a Microthermocouple," ASME JOURNAL OF HEAT TRANSFER, Vol. 95, pp. 363–370.

Dix, G. E., 1971, "Vapor Fraction for Forced Convection With Subcooled Boiling at Low Flow Rates," General Electric Co. Report NEDO-10491.

Dykhuizen, R. C., Roy, R. P., and Kalra, S. P., 1986, "A Linear Time-Domain Two-Fluid Model Analysis of Dynamic Instability in Boiling Flow Systems" ASME JOURNAL OF HEAT TRANSFER, Vol. 108, pp. 100–108.

Hasan, A., Roy, R. P., and Kalra, S. P., 1990, "Heat Transfer Measurements in Turbulent Liquid Flow Through a Vertical Annular Channel," ASME JOURNAL OF HEAT TRANSFER, Vol. 112, pp. 247–250.

Hasan, A., Roy, R. P., and Kalra, S. P., 1990, "Experiments on Subcooled Flow Boiling Heat Transfer in a Critical Annular Channel," *International Journal of Heat and Mass Transfer*, in press.

Jain, P. K., and Roy, R. P., 1983, "Stochastic Characteristics of Vapor Fraction and Wall Pressure Fluctuations in Boiling Flow," *International Journal of Multiphase Flow*, Vol. 9, No. 5, pp. 463–489.

Jiji, L. M., and Clark, J. A., 1964, "Bubble Boundary Layer, and Temperature Profiles for Forced Convection Boiling in Channel Flow," ASME JOURNAL OF HEAT TRANSFER, Vol. 86, pp. 50–58.

Lellouche, G. S., and Zolotar, B. A., 1982, "Mechanistic Model for Predicting Two-Phase Void Fraction for Water in Vertical Tubes, Channels, and Rod Bundles," Electric Power Research Institute Report NP-2246-SR.

Lung, H., Lathseh, K., and Rampf, H., 1977, "Boiling Heat Transfer to Subcooled Water in Turbulent Annular Flow," *Heat Transfer in Boiling*, E. Hahne and U. Grigull, eds., Academic Press, New York.

Müller-Steinhagen, H., Watkinson, A. P., and Epstein, N., 1986, "Subcooled Boiling and Convective Heat Transfer to Heptane Flowing in an Annulus and Past a Coiled Wire: Part I—Experimental Results," ASME JOURNAL OF HEAT TRANSFER, Vol. 108, pp. 922–927.

Roy, R. P., and Ho, S. A., 1982, "An Unequal Velocity, Unequal Temperature Two-Fluid Description of Transient Vapor-Liquid Flow in Channels," *Nuclear Science and Engineering*, Vol. 81, No. 3, pp. 459–467.

Roy, R. P., Krishnan, V. S., and Raman, A., 1986, "Measurements in Turbulent Liquid Flow Through a Vertical Concentric Annular Channel," ASME JOURNAL OF HEAT TRANSFER, Vol. 108, No. 1, pp. 216–218.

Roy, R. P., 1988, "Stability Analysis Using Two Fluids (SAT) Code for Boiling Flow Systems," Vols. 1–4, Electric Power Research Institute Report EPRI NP-6103-CCM.

Roy, R. P., Jain, P., and Kalra, S. P., 1988, "Dynamic Instability Experiments in a Boiling Flowing System," *International Journal of Heat and Mass Transfer*, Vol. 31, No. 7, pp. 1947–1952.

Sha, W. T., and Soo, S. L., 1978, "Multidomain, Multiphase Fluid Mechanics," *International Journal of Heat and Mass Transfer*, Vol. 21, pp. 1581–1595.

Shah, M. M., 1983, "Generalized Prediction of Heat Transfer During Subcooled Boiling in Annuli," *Heat Transfer Engineering*, Vol. 4, No. 1, pp. 24–31.

"TRAC-P1A, An Advanced Best-Estimate Computer Program for PWR LOCA Analysis," 1979, Los Alamos National Laboratory Report LA-7777-MS.

Walmet, G. E., and Staub, F. W., 1969, "Pressure, Temperature, and Void Fraction Measurement in Nonequilibrium Two-Phase Flow," in: *Two-Phase Flow Instrumentation*, ASME, Eleventh National Heat Transfer Conference, pp. 89–101.

Simultaneous Fog Formation and Thermophoretic Droplet Deposition in a Turbulent Pipe Flow

M. Epstein

G. M. Hauser

Fauske & Associates, Inc.
Burr Ridge, IL 60521

Simultaneous aerosol formation by equilibrium condensation and the migration of the resulting droplets to the cold surface by thermophoresis is studied theoretically for a turbulent pipe flow. The problem is one in which a mixture of a vapor and noncondensable gas flows into a section of pipe where the pipe wall is cooled far below the dew point of the vapor. Because the temperature gradient at the pipe wall decays to zero once the gas travels far enough into the pipe, only some fraction of the droplets formed will deposit on the pipe wall. The equations of energy and diffusion suggest that turbulence leads to a discontinuity in the aerosol (fog) concentration at the boundary between the fog and clear regions. Numerical solutions are obtained for CsOH fog formation and deposition in steam flow—a particular case of current practical interest in water reactor safety. The axial and radial variations of the aerosol and vapor concentrations are displayed graphically, as are the location of the fog boundary as a function of axial distance and the efficiency of deposition as a function of the pipe wall temperature.

Introduction

It is well known that when a mixture of vapor and inert gas passes over a condenser surface and is cooled well below the dew point of the vapor component, a large fraction of the vapor mass that flows to the surface condenses at some location in the gas stream as an aerosol (or fog) rather than on the surface. The droplets formed by this vapor phase nucleation event are typically very small, of the order of 0.1 to 1.0 μm in diameter, and are not easily removed from the gas stream by natural wall deposition processes. Thus, fog formation during condensation can result in the loss of valuable or hazardous material.

The early analyses of fog formation during condensation on cold surfaces were confined to prediction of the onset of fog formation rather than to the estimation of fog density (Colburn and Edison, 1941; Johnstone et al., 1950; Rosner and Epstein, 1968). Experimental studies by Brown (1966), Hedley et al. (1966), Barron and Han (1965), and Santoro et al. (1984) have demonstrated that vapor mass collection rates on very cold surfaces are much less than predicted mass transfer rates based on vapor diffusion theory. The formation of liquid droplets or solid particles within the thermal boundary layer adjacent to the surface was believed to be the cause of the discrepancy between theory and experiment. Direct observations of fogging during vapor condensation on cold surfaces were reported by Johnstone et al. (1950) and Mori and Hijikata (1973). The problem of transient growth of a fog layer next to a cold boundary was solved by Toor (1971). An analysis of fog formation within a steady-state free convective boundary layer on a vertical surface was reported by Mori and Hijikata (1973). In these solutions the fog is in equilibrium with its vapor, and once formed either remains stationary or moves with the mass average velocity of the gas. The transport of droplets to the cold surface was neglected.

Recently, Castillo and Rosner (1989) formulated a laminar, two-phase boundary layer model in which the droplets are in local equilibrium with their parent vapor and migrate to the cold surface by the mechanism of thermophoresis. In this way a procedure was arrived at that, for the first time, allows the calculation of both the vapor and aerosol collection rates at the condenser surface, the position of the boundary between the fog and clear regions (i.e., the "fog boundary"), and the structure of the fog region between the fog boundary and the cold surface.

Our purpose here is to apply the Castillo–Rosner model to the problem of fog formation and collection in a turbulent pipe flow. This geometry involves some important qualitative differences from the boundary layer problem studied by Castillo and Rosner. First, the flow field is finite and the temperature and concentration profiles extend only over the diameter of the pipe. Thus, at any axial location the free-stream (centerline) vapor and/or fog concentrations are unknown and must be determined as part of the solution, whereas in Castillo and Rosner's case the flow field extends to infinity where the vapor concentration is specified. Second, in a turbulent flow fog droplets migrate both by diffusion and thermophoresis, a situation that leads to different fog region structure than that predicted in the laminar case. Finally, in a pipe flow the thermophoretic force vanishes once the gas travels far enough into the pipe for its temperature to equilibrate with the cold wall. In fact, far downstream the two-phase mixture will relax to thermal and concentration equilibrium with the cold wall so that a total (vapor plus condensate) collection efficiency can be associated with the pipe flow. The present formulation should prove helpful in visualizing the conditions under which appreciable reductions in collection efficiency are to be expected. Representative results for the deposition of cesium hydroxide from flowing steam are presented since this system is important to the ongoing safety reviews of the Hanford N-Reactor (Cronenberg, 1988; Hagrman, 1987).

Mathematical Model

The system to be analyzed is pictured schematically in Fig. 1. A gas containing a dilute condensable vapor flows in steady turbulent motion in a round tube. Our attention is focused on the section of pipe to the right of $x=0$. Up to this point the gas mixture possesses a fully developed turbulent velocity profile and a uniform temperature T_o greater than the dew point temperature of the vapor component. To the right of $x=0$ the wall temperature is taken to be uniform and below the dew point temperature of the vapor. The flow system for $x>0$ is

Contributed by the Heat Transfer Division for publication in the JOURNAL OF HEAT TRANSFER. Manuscript received by the Heat Transfer Division December 10, 1989; revision received June 1, 1990. Keywords: Condensation, Mass Transfer, Multiphase Flows.

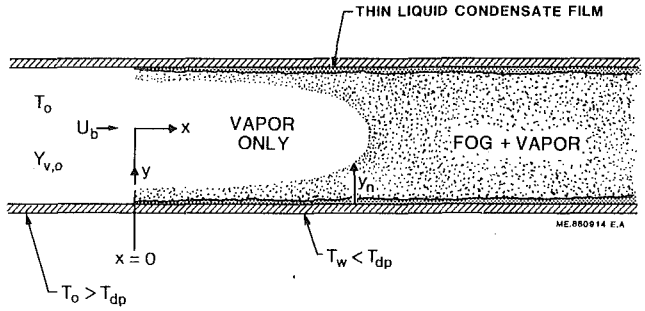

Fig. 1 Physical model of fog formation within a pipe flow and coordinates

restricted to a fluid containing three components: namely, inert gas, condensed phase (in the form of fog), and parent vapor. For an undersaturated mixture at $x = 0$, the fog boundary will be located close to the pipe wall where the temperature gradient is large. As the flow proceeds farther and farther down the pipe, the vapor state far from the pipe wall more and more closely approaches a saturated condition. Consequently the fog region thickens as x becomes large and ultimately the condensed phase fills the entire cross section of the pipe (see Fig. 1). It is desired to determine the fog and vapor concentrations and the location of the fog boundary at all positions x along the pipe.

The complete set of partial differential equations governing the combined heat, mass, and momentum transport within the pipe can be written down, and presumably, solved with the appropriate numerical technique. Rather than attempt such a numerical solution of these partial differential equations, Deissler's (1955) one-dimensional treatment of radial transport in turbulent pipe flow was adopted here and modified to incorporate fog formation. Our mathematical model for turbulent pipe flow with fog formation is defined by the following assumptions:

1 The vapor species is in equilibrium with its condensate throughout the fog region and at the pipe wall.

2 The concentration of the diffusing, condensing vapor is small enough that the mass transfer and latent heat release does not appreciably change the velocity or temperature profiles from those predicted in the absence of mass transfer and fog nucleation. Also, the fog is dilute enough so that the volume occupied by the fog droplets can be ignored.

3 All thermophysical and molecular transport properties of the gas mixture are constant, and the gas mixture is assumed to be incompressible so that its total density is constant.

4 The condensable vapor and inert gas behave as ideal gases.

5 The eddy diffusivities for momentum, heat, or mass (vapor or fog) transfer are equal.

6 The axial diffusion of heat and mass, both molecular and turbulent, is negligible compared to radial diffusion.

7 The variations across the pipe of shear stress, heat flux, and mass (vapor plus fog) flux have a negligible effect on the

Nomenclature

c_p = specific heat of binary gas mixture
d = diameter of fog particle or foreign nucleii
D = molecular diffusivity of binary gas mixture
E = vapor deposition efficiency
g = gravitational constant
k = thermal conductivity of binary gas mixture
K = dimensionless thermophoretic velocity coefficient
L = condenser pipe length
L^+ = dimensionless condenser pipe length = $u^* L/\nu$
m_w = rate of mass transfer (vapor + aerosol) toward pipe wall per unit area
M = dimensionless rate of mass transfer toward pipe wall, equation (7)
M_v = molecular weight of condensable vapor
N = concentration of foreign nucleii, particles cm^{-3}
Nu = Nusselt number for heat transfer = $2Rq_w/[k\ (T_b - T_w)]$
Nu_m = Nusselt number for mass transfer in the absence of fog = $2R\ m_w/[\rho D\ (Y_{v,b} - Y_{v,w})]$
Pr = Prandtl number = ν/α
$P_{v,eq}$ = equilibrium vapor pressure of condensable material
q_w = rate of heat transfer toward pipe wall per unit area
R = pipe radius
R^+ = dimensionless pipe radius = u^*R/ν
Re = Reynolds number = $2R\ u_b/\nu$
R_g = ideal gas constant
S = dimensionless stopping distance, equation (39)
Sc = Schmidt number = ν/D
t = time
T = temperature
T^+ = dimensionless temperature, equation (17)
T_b = bulk (radial-average) temperature at cross section of pipe
T_{dp} = dew point temperature corresponding to vapor concentration at pipe inlet
T_o = mixture temperature at pipe inlet
T_w = temperature of pipe wall
u = mixture velocity parallel to axis of pipe (x direction)
u_b = bulk (radial average) velocity at cross section of tube
u^+ = dimensionless mixture velocity = u/u^*
u_b^+ = dimensionless bulk velocity = u_b/u^*
u^* = friction velocity = $(\tau_w/\rho)^{1/2}$
x = distance measured along axis of pipe
x^+ = dimensionless axial distance = u^*x/ν
x_{fog}^+ = downstream location at which fog first appears
y = distance measured normal to and from the pipe wall
y^+ = dimensionless distance from pipe wall = u^*y/ν
y_n = distance from wall to fog boundary
y_n^+ = dimensionless location of fog boundary = u^*y_n/ν
Y_c = mass fraction of condensate
$Y_{c,b}$ = bulk (radial average) condensate mass fraction at cross section of pipe
Y_v = mass fraction of vapor
$Y_{v,b}$ = bulk (radial average) vapor mass fraction at cross section of pipe
$Y_{v,eq}$ = equilibrium mass fraction of vapor, equation (8)
Y_v^+ = normalized vapor mass fraction in the absence of fog, equation (25)
$Y_{v,o}$ = vapor mass fraction at pipe inlet
α = thermal diffusivity of binary gas mixture
ϵ = eddy diffusivity for turbulent momentum, energy, and mass transfer
μ = viscosity of gas mixture
ν = kinematic viscosity of gas mixture
ρ = density of gas mixture
ρ_p = density of condensed phase (particle or droplet)
τ_D = turbulent diffusion time constant, equation (37)
τ_{het} = time scale for heterogeneous nucleation, equation (36)
τ_w = shear stress at pipe wall

velocity, temperature, and concentration distributions. Therefore, these quantities are assumed to be constant in the radial direction (Deissler, 1955).

8 Contributions to fog droplet (or particle) transport by Brownian motion and droplet inertia are neglected. Thermophoresis and eddy diffusivity are the only important mechanisms of particle transport. It follows that thermophoresis is the only available mechanism that transports droplets to the pipe wall, as turbulence is strongly damped in the vicinity of the wall.

9 Fully developed thermal and concentration profiles are assumed to be established at the entrance of the condenser section of the pipe (i.e., $x=0$). That is, we neglect the so-called thermal entrance region, which is typically very small compared to the axial length scales of interest in practical problems.

Conservation Equations

The one-dimensional equations for the velocity, temperature, and concentration distributions in the radial direction in a pipe with turbulent flow are (see Assumption 7)

$$\tau_w = \mu(1+\epsilon/\nu)\frac{du}{dy} \tag{1}$$

$$q_w = \nu\rho c_p(1/\mathrm{Pr}+\epsilon/\nu)\frac{\mathrm{dT}}{\mathrm{dy}} \tag{2}$$

$$m_w = \rho\nu\left[\frac{K}{T}\frac{dT}{dy}\,Y_c + \frac{\epsilon}{\nu}\frac{dY_c}{dy} + (1/\mathrm{Sc}+\epsilon/\nu)\frac{dY_v}{dy}\right] \tag{3}$$

where y is the distance measured from the pipe wall in the radial direction, and τ_w, q_w, and m_w are the shear stress, heat flux, and mass flux, respectively, evaluated at the wall. The first two terms on the right-hand side of equation (3) represent the thermophoretic drift and turbulent diffusional flux of fog droplets, respectively. Here Y_c is the local mass fraction of the suspended droplets. The coefficient K is the dimensionless thermophoretic transport coefficient, which depends mainly on the Knudsen number, equal to the molecular mean free path divided by the droplet diameter. Talbot et al. (1980) proposed a semiempirical formula for K that fits the majority of available data over a wide range of Knudsen numbers. Using their formula, the value of K is found to be about 0.6 for submicron-sized droplets and decreases to 0.1 for 10-μm droplets. In the absence of fog we are left with only the last term in equation (3), the traditional sum of the molecular- and eddy-diffusivity-vapor transport terms.

Following the example of Deissler (1955), we replace u and y by their dimensionless counterparts u^+ and y^+ for turbulent flow, as given in the nomenclature, so that the governing equations become

$$\frac{du^+}{dy^+} = \frac{1}{1+\epsilon/\nu} \tag{4}$$

$$\frac{dT}{dy^+} = \frac{(T_b - T_w)\mathrm{Nu}}{2\,R^+\,\mathrm{Pr}}\cdot\frac{1}{(1/\mathrm{Pr}+\epsilon/\nu)} \tag{5}$$

$$\frac{dY_c}{dy^+} = \frac{1}{\epsilon/\nu}\left[M - \frac{K}{T}\frac{dT}{dy^+}\,Y_c - \left(\frac{1}{\mathrm{Sc}}+\frac{\epsilon}{\nu}\right)\frac{dY_{v,eq}}{dT}\frac{dT}{dy^+}\right] \tag{6}$$

where M in the above equation is the dimensionless mass flux at the wall

$$M = \frac{m_w}{\rho u^*} = \left[\frac{K}{T_w}Y_c(0) + \frac{1}{\mathrm{Sc}}\frac{dY_{v,eq}}{dT}(T_w)\right]\frac{(T_o - T_w)\ \mathrm{Nu}}{2\,R^+} \tag{7}$$

Equation (6) is written for the fog region where the vapor concentration and temperature are related by the equilibrium equation for the vapor (see Assumption 1):

$$Y_v = Y_{v,eq}(T) = \frac{P_{v,eq}(T)M_v}{\rho R_g T} \tag{8}$$

From equation (8)

$$\frac{dY_v}{dy^+} = \frac{dY_{v,eq}}{dT}\frac{dT}{dy^+} \tag{9}$$

which led to the last terms of equations (6) and (7). In the fog-free region, the concentration equation for the vapor follows directly from equation (3) with $Y_c=0$, or

$$\frac{dY_v}{dy^+} = \frac{M}{(1/\mathrm{Sc}+\epsilon/\nu)} \tag{10}$$

Note that equations (4) and (5) are valid in both the fog and fog-free regions (see Assumption 2).

To obtain solutions of equations (4)–(6) and (10), it is necessary that the variation of the eddy diffusivity ϵ with u^+ and y^+ be specified. The eddy diffusivity is given by the following equations (Deissler, 1955):

$$\frac{\epsilon}{\nu} = (0.124)^2u^+y^+\{1-\exp[-(0.124)^2u^+y^+]\}, 0\le y^+\le 26 \tag{11}$$

$$\frac{\epsilon}{\nu} = 0.36\,y^+, \quad 26 < y^+ < R^+ \tag{12}$$

In equations (4)–(6) and (10), the quantities 1, 1/Pr and 1/Sc are deleted for values of y^+ greater than 26, since molecular shear, heat transfer, and mass transfer can be neglected in the turbulent core of a pipe flow (Deissler, 1955).

Since in many cases we deal with undersaturated vapor states in the core of the pipe flow, we would expect to find a fog-free region at some distance from the wall. Hence, at each axial location in the pipe we look for a solution to the above equations in which a fog extends from the liquid condensate on the wall to some dimensionless radial distance y_n^+. The structure of the fog region ($0<y^+\le y_n^+$) is described by equations (4)–(6) and (8). Equations (4), (5), and (10) apply to the clear region defined by $y_n^+ < y^+ \le R^+$. These two regions are separated by the fog boundary at $y^+ = y_n^+$ where boundary conditions connecting the two regions must be written.

At the fog boundary between the fog and fog-free regions the following conditions must be satisfied:

$$Y_v(y_n^+) = Y_{v,eq}[T(y_n^+)] \tag{13}$$

$$\frac{K}{T(y_n^+)}\cdot\frac{dT}{dy^+}(y_n^+)\cdot Y_c(y_n^+) + \frac{\epsilon}{\nu}\frac{\mathrm{dY_c}}{\mathrm{dy^+}}(y_n^+) + \left(\frac{1}{\mathrm{Sc}}+\frac{\epsilon}{\nu}\right)\frac{dY_{v,eq}}{dy^+}(y_n^+) = \left(\frac{1}{\mathrm{Sc}}+\frac{\epsilon}{\nu}\right)\frac{dY_v}{dy^+}(y_n^+) \tag{14}$$

Equation (13) requires the continuity of Y_v, while equation (14) requires the conservation of the condensable component in both liquid and vapor forms. In addition to these conditions we assume that dY_v/dy is continuous across the fog boundary. Hence, at the fog boundary

$$\frac{dY_{v,eq}}{dy^+}\,(y_n^+) = \frac{dY_v}{dy^+}\,(y_n^+) \tag{15}$$

This continuity of vapor flux or so-called "tangency condition" has been successfully exploited in the past to define the point where fog nucleation commences within thermal boundary layers (Turkdogan, 1964; Rosner, 1967; Epstein and Rosner, 1970; Castillo and Rosner, 1989). Equation (14) then implies that the fog concentration at the boundary obeys the condition

$$\frac{K}{T(y_n^+)}\cdot\frac{dT}{dy^+}\,(y_n^+)\cdot Y_c(y_n^+) + \frac{\epsilon}{\nu}\frac{dY_c}{dy^+}\,(y_n^+) = 0 \tag{16}$$

If turbulence is not present (i.e., $\epsilon=0$) then the continuity of vapor flux or, equivalently, equation (16) demands that

$Y_c(y_n^+)=0$ and the fog concentration be continuous at the fog boundary. That is, in laminar flow the mass fraction of fog decreases with distance from the cold wall and approaches zero as the fog boundary is approached from the fog side (Castillo and Rosner, 1989). When turbulence is present, however, it can be seen from equation (16) that $Y_c(y_n^+)$ must be greater than zero. If it were not, then both $Y_c(y_n^+)$ and $dY_c/dy^+(y_n^+)$ must be zero, which would lead to the trivial but nonphysical solution that Y_c is zero everywhere in the fog region. Thus, Y_c is discontinuous at the fog boundary, because $Y_c=0$ in the clear region $y^+>y_n^+$. The discontinuity is a consequence of turbulence, which allows fog to diffuse to the boundary. By equation (16) the turbulent diffusion directed from the fog at the fog boundary is in balance with the oppositely directed thermophoretic particle drift down the temperature gradient toward the cold wall.

The most important ingredient that is needed for solving the present two-phase pipe flow problem is the radial temperature variation at various stations along the pipe. This is most conveniently obtained by introducing the dimensionless temperature

$$T^+=\frac{T-T_w}{T_b-T_w}\frac{2\,\mathrm{Pr}\,R^+}{\mathrm{Nu}} \tag{17}$$

Using this definition in equation (5) we obtain the dimensionless energy equation

$$\frac{dT^+}{dy^+}=\frac{1}{1/\mathrm{Pr}+\epsilon/\nu} \tag{18}$$

The bulk temperature T_b at any axial location is

$$T_b=\frac{2}{u_b^+R^{+2}}\int_0^{R^+}Tu^+(R^+-y^+)dy^+ \tag{19}$$

or by recasting this equation in terms of T^+

$$T_b^+=\frac{2}{u_b^+R^{+2}}\int_0^{R^+}T^+u^+(R^+-y^+)dy^+ \tag{20}$$

where u_b^+ is the dimensionless bulk velocity

$$u_b^+=\frac{2}{\mathrm{R}^{+2}}\int_0^{R^+}(\mathrm{R}^+-\mathrm{y}^+)\mathrm{u}^+\mathrm{dy}^+ \tag{21}$$

Finally, it can be shown from the definitions of the quantities involved that the Nusselt number for heat transfer and the Reynolds number are given by

$$\mathrm{Nu}=\frac{2\,\mathrm{Pr}\,R^+}{T_b^+} \tag{22}$$

$$\mathrm{Re}=2\,R^+u_b^+ \tag{23}$$

By simultaneously integrating equations (4) and (18) from $y^+=0$ to $y^+=R^+$ we can calculate T_b^+ and u_b^+ from equations (20) and (21). The values of Nu and Re for a given R^+ and Pr can then be obtained from equations (22) and (23). Actually, in any practical problem, the Reynolds number Re is known rather than the dimensionless pipe radius R^+. A value of R^+ is assumed and Nu and Re are calculated from the system comprised by equations (4), (11), (12), (18), and (20)–(23). If the calculated Re is not equal to the given value, a new R^+ is chosen and the calculations are repeated until the desired Re is obtained. The bulk temperature at various locations along the tube is given by

$$\frac{T_b-T_w}{T_o-T_w}=\exp\left[-\frac{\mathrm{Nu}\,x^+}{\mathrm{Pr}\,R^{+2}u_b^+}\right] \tag{24}$$

which is simply the solution of a heat balance equation written for an increment of pipe length x.

Suppose the mass fraction of the vapor at the entrance section, $x=0$, is low enough so that no fog forms for some distance along the pipe. Equations similar to equations (17)–(24) can be written for the vapor by defining the normalized vapor mass fraction

$$Y_v^+=\frac{Y_v-Y_{v,eq}(T_w)}{Y_{v,b}-Y_{v,eq}(T_w)}\cdot\frac{2\,\mathrm{Sc}\,R^+}{\mathrm{Nu}_m} \tag{25}$$

and letting $Y_{v,b}$, Y_v^+, $Y_{v,b}^+$, Sc and Nu_m for mass transfer replace the corresponding quantities T_b, T^+, T_b^+, Pr, and Nu for heat transfer in equations (18)–(24). In the absence of fog the radial vapor mass fraction profile is obtained by integrating (see equation (18))

$$\frac{dY_v^+}{dy^+}=\frac{1}{1/\mathrm{Sc}+\epsilon/\nu} \tag{26}$$

and the bulk vapor mass fraction at various locations along the tube is given by (see equation (24))

$$\frac{Y_{v,b}-Y_{v,eq}(T_w)}{Y_{v,o}-Y_{v,eq}(T_w)}=\exp\left[-\frac{\mathrm{Nu}_m\,x^+}{\mathrm{Sc}\,R^{+2}u_b^+}\right] \tag{27}$$

Consider the axial location that separates a fog-free pipe cross section from one in which a fog region appears adjacent to the pipe wall. At this station the fog boundary coincides with the pipe wall (i.e., $y_n^+=0$; see Johnstone et al., 1950). Combination of equations (9) and (15) gives the following condition for the intersection of the axial fog-free and fog regions:

$$\frac{dY_v}{dy^+}(0)=\frac{dY_{v,eq}}{dT}(T_w)\cdot\frac{dT}{dy^+}(0) \tag{28}$$

This expression is used to test for the onset of fog formation. Using definitions (17) and (25) and equations (18) and (26), equation (28) can be expressed in the form

$$\frac{Y_{v,b}-Y_{v,eq}(T_w)}{T_b-T_w}\cdot\frac{\mathrm{Nu}_m}{\mathrm{Nu}}=\frac{dY_{v,eq}}{dT}(T_w) \tag{29}$$

Eliminating T_b and $Y_{v,b}$ between the above equation and equations (24) and (27), respectively, we conclude that the downstream location at which fog first appears is given by

$$x_{\mathrm{fog}}^+=\frac{R^{+2}u_b^+}{\mathrm{Nu}/\mathrm{Pr}-\mathrm{Nu}_m/\mathrm{Sc}}\cdot\ln\left[\frac{\mathrm{Nu}}{\mathrm{Nu}_m}\cdot\frac{T_o-T_w}{Y_{v,o}-Y_{v,eq}(T_w)}\frac{dY_{v,eq}}{dT}(T_w)\right] \tag{30}$$

If conditions are such that the right side of equation (30) is negative, a fog zone of finite thickness will appear at the entrance to the condensation section of the pipe.

For axial distances $x^+>x_{\mathrm{fog}}^+$, equation (27) is no longer valid for the bulk vapor mass fraction profile in the axial direction. The equation for the axial variation of the bulk mass fraction of the condensable species in the presence of fog is

$$u_b\frac{d(Y_{c,b}+Y_{v,b})}{dx}=-\frac{2}{R}\left[\frac{Y_c(0)K\nu}{T_w}\frac{dT}{dy}(0)+D\frac{dY_v}{dy}(0)\right] \tag{31}$$

where

$$Y_{v,b}=\frac{2}{u_bR^{+2}}\int_0^{R^+}Y_v\,u^+(R^+-y^+)\,dy^+ \tag{32}$$

$$Y_{c,b}=\frac{2}{u_bR^{+2}}\int_0^{R^+}Y_c\,u^+(R^+-y^+)\,dy^+ \tag{33}$$

Equation (31) states that the rate of deposition of the condensable species on the pipe wall by thermophoresis and vapor diffusion is equal to the decrease of the bulk concentration of the condensable species in the pipe flow. Equation (31) rewritten in the nondimensional (y^+, x^+, u^+) coordinates is

$$u_b^+\frac{d(Y_{c,b}+Y_{v,b})}{dx^+}=-\frac{2\,M}{R^+} \tag{34}$$

Method of Solution

Our procedure to obtain the radial position of fog onset and the bulk concentrations of fog and vapor as a function of axial distance along the pipe, for given wall temperature T_w and pipe entrance conditions $Y_{v,o}$ and T_o, is as follows:

1 Given the molecular transport parameters Pr and Sc and the flow Reynolds number Re, the Nusselt numbers for heat and mass transfer, Nu and Nu_m, respectively, are determined by the method indicated following equation (23).

2 If equation (30) reveals that $x^+_{\mathrm{fog}} > 0$, fog formation at the pipe entrance is not possible and the variations of the bulk temperature and vapor mass fraction with distance are calculated with the algebraic equations (24) and (27) until $x^+ = x^+_{\mathrm{fog}}$.

3 The calculated value of $Y_{v,b}$ at $x^+ = x^+_{\mathrm{fog}}$ (or the initial value $Y_{v,o}$ if $x^+_{\mathrm{fog}} \le 0$) is assumed to represent the sum of the condensate and vapor bulk mass fractions at the axial location where condensation begins (see below).

4 A value of the condensate mass fraction at the pipe wall, $Y_c(0)$, is chosen, M is evaluated from equation (7), and the system of first-order ordinary differential equations (4), (5), (6), (9), and (10) is integrated in the radial direction, starting at the pipe wall ($y^+ = 0$) and ending at the pipe centerline ($y^+ = R^+$). Note that equations (6) and (9) are integrated until the fog boundary is reached at $y^+ = y^+_n$, as indicated by satisfying equation (16). In the fog-free core between $y^+ \approx y^+_n$ and $y^+ = R^+$, $Y_c = 0$ and equation (10) is used in place of equations (6) and (9). The bulk mass fractions $Y_{v,b}$ and $Y_{c,b}$ are calculated from equations (32) and (33).

5 The sum of the bulk mass fractions obtained in Step 4 is compared with the known total bulk mass fraction obtained from integrating the overall mass conservation equation one integration step in the axial direction. In the particular case of the onset of condensation, $Y_{v,b}$ from Step 3 represents the total bulk mass fraction with which $Y_{v,b} + Y_{c,b}$ obtained in Step 4 should be compared. If agreement is achieved, equation (34) is integrated another axial step. Otherwise a new value of $Y_c(0)$ is chosen and Step 4 is repeated.

Numerical integration in the radial direction was performed using a forward integration procedure based on the Gear (1971) method (see also Hindmarsh, 1972). The computations were run on a Micro-Vax II computer. As a partial verification of the computational procedure, results were initially obtained for turbulent pipe flow heat and mass transfer in the absence of fog formation. The results for the velocity and temperature (or concentration) profiles were in agreement with those of Deissler (1955). At first the integration of equation (34) was also performed with the GEAR method; however, the application of this method to both the radial and axial directions required considerable computer time. Accordingly, the GEAR method for the integration of equation (34) in the axial direction was replaced by the elementary Euler method. The axial length of the pipe was divided into about 150 forward steps. At each marching step, a sufficient number of radial integration iterations were carried out to ensure that the sum of the condensate and vapor bulk mass fractions agreed with that obtained from integrating the overall mass conservation equation to three significant figures. The results obtained with Euler's method were found to agree with the "all-GEAR computations" to within 1.0 percent. Exploratory runs with double the number of forward axial steps resulted in near-perfect agreement between the two methods.

It should be mentioned that in many cases equation (16) cannot be satisfied when the fog boundary coincides with the edge of the buffer layer (i.e., at $y^+ = 26$). Deissler's (1955) empirical formula for the eddy viscosity leads to discontinuities in the derivatives dT/dy^+, dY_v/dy^+, and therefore, dY_c/dy^+ at $y^+ = 26$. Thus, the particular derivations dT/dy^+ and dY_c/dy^+ required to fulfill equation (16) are often "skipped" when the solution marches across $y^+ = 26$ and the discontinuous jumps in the values of dT/dy^+ and dY_c/dy^+ occur. These discontinuous jumps, however, result in a discontinuous change in sign on the left side of equation (16), thereby indicating that the fog boundary is located at $y^+ = 26$. For conditions under which the fog boundary moves slowly inward from the wall with increasing distance along the pipe, it may remain at $y^+ = 26$ for several integration steps in the downstream direction before continuing to fill the pipe. A single continuous formula for the eddy viscosity, such as that reported by Van Driest (1956), would eliminate this nonphysical behavior and be more satisfying aesthetically. However, experience with other turbulent pipe flow problems has shown that the use of "smooth" eddy viscosity laws with continuous derivations does not alter the findings of the Deissler-type analysis in an essential way.

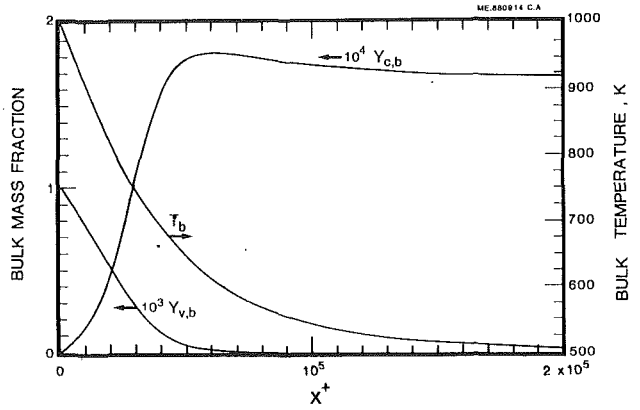

Fig. 2 Predicted axial variation of bulk temperature and CsOH bulk vapor and fog concentrations along pipe; conditions, $\mathrm{Re} = 10^4$, $Y_{v,o} = 10^{-3}$, $K = 0.6$, $L^+ = 2 \times 10^5$, $T_o = 10^3$ K, $T_w = 500$ K, $\mathrm{Sc} = 2$, $\mathrm{Pr} \approx 1$

Results and Discussion

Although, in principle, there is no limitation on most of the parameters selected for the numerical solution, there is a practical limit on the amount of numerical work that is feasible to present. As illustrations of considerable current interest in nuclear reactor safety, some results are presented here for a dilute CsOH vapor-containing flow of steam at atmospheric pressure. The Prandtl number of this binary mixture was taken to be that of steam, $\mathrm{Pr} = 1.0$, and the vapor Schmidt number was estimated to be $\mathrm{Sc} = 2.0$. The temperature dependence of the equilibrium CsOH vapor pressure is well represented by the Clausius–Clapeyron form

$$P_{v,eq}(T) = 8.3 \times 10^9 \exp\left(-\frac{1.54 \times 10^4}{T}\right)$$

This equation was used in the calculation of $Y_{v,eq}(T)$ and its derivative $dY_{v,eq}(T)/dT$ (see equation (8)). Values of the thermophoretic transport coefficient K were taken to be 0.6 and 0.2, corresponding to submicron and 1.0 μm droplets, respectively. In all the calculations the Reynolds number, temperature, and density of the steam/vapor mixture at the entrance to the condenser section, as well as the dimensionless length of the condenser section of pipe, were held fixed at $\mathrm{Re} = 10^4$, $T_o = 1000$ K, $\rho = 0.258$ kg m^{-3}, and $L^+ = 2 \times 10^5$, respectively.

Figure 2 depicts the axial variation of the bulk vapor and condensate mass fractions for $T_w = 500$ K and $Y_{v,o} = 10^{-3}$. The bulk temperature profile is also shown in Fig. 2. It can be seen that the condensate mass fraction increases rapidly at first until most of the vapor is converted into fog at $x^+ \approx 5 \times 10^4$. Further downstream the fog concentration decreases slightly with distance as a result of thermophoretic deposition on the wall. Ultimately the fog concentration levels off because the tem-

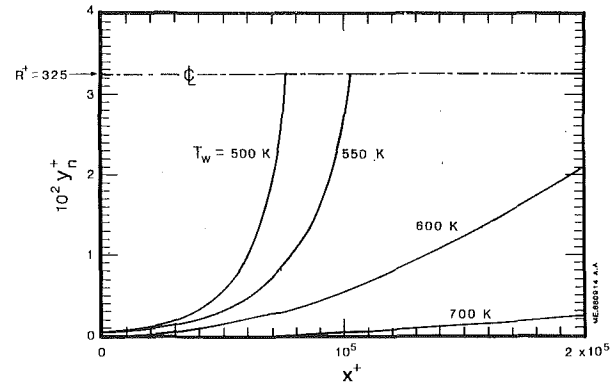

Fig. 3 Predicted axial variation of fog boundary location along pipe; conditions, $Re = 10^4$, $Y_{v,o} = 10^{-3}$, $K = 0.6$, $L^+ = 2 \times 10^5$, $T_o = 10^3$ K, $Sc = 2$, $Pr = 1$

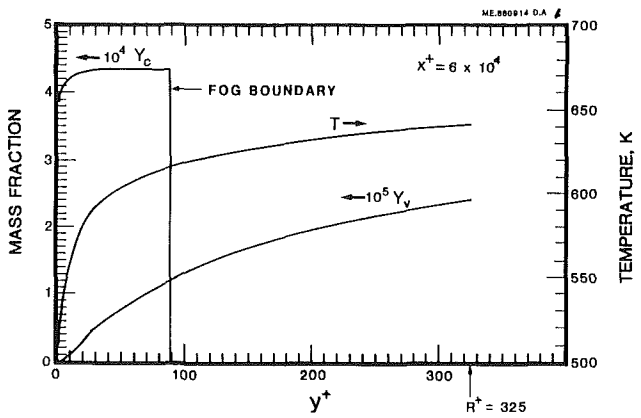

Fig. 4 Vapor and aerosol condensate mass fractions and temperature distributions at pipe axial station $x^+ = 6 \times 10^4$; conditions, see Fig. 2

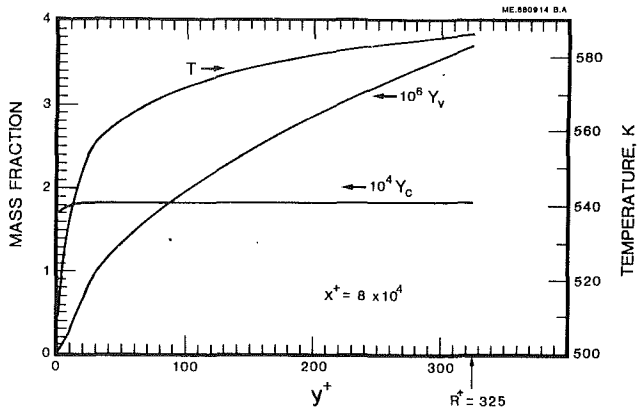

Fig. 5 Vapor and aerosol condensate mass fractions and temperature distributions at pipe axial station $x^+ = 8 \times 10^4$; conditions, see Fig. 2

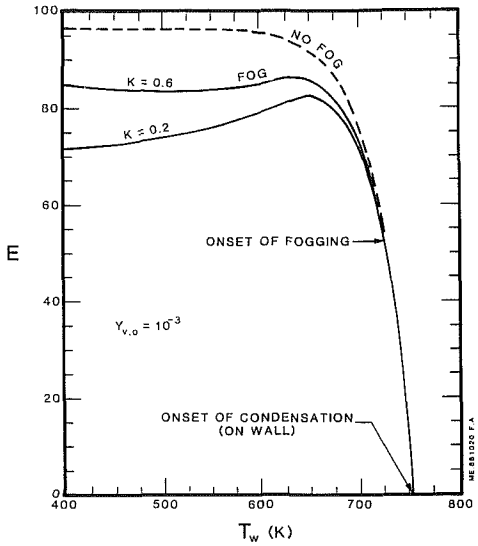

Fig. 6 CsOH vapor collection efficiency versus the wall temperature; conditions, $Re = 10^4$, $L^+ = 2 \times 10^5$, $T_o = 10^3$ K, $Sc = 2$, $Pr = 1$

perature of the two-phase mixture equilibrates with the pipe wall and thermophoretic deposition ceases. When fog formation is not taken into account, the predicted vapor mass fraction at the pipe outlet (i.e., at $x^+ = L^+ = 2 \times 10^5$) is 3.53×10^{-5}, or 3.5 percent of the initial condensable material. However, when condensation is taken into account the predicted fraction of condensable material that escapes from the pipe in percent is approximately 17.0 (see Fig. 2). This verifies our previous statement about the considerably smaller vapor collection fraction associated with fogging. Additional results relative to the collection efficiency of the cold pipe are presented below.

Figure 3 shows the shape of the fog boundary that separates the two-phase and single-phase regions for $Y_{v,o} = 10^{-3}$ and wall temperature of 500, 550 and 600 K. As expected, the fog boundary moves further downstream as the wall temperature is increased. Obviously the pipe will be fog-free when the wall temperature is sufficiently high. The value of T_w above which fog formation does not occur may be determined directly from equation (30) and is 725 K for the present example. Liquid droplets do not exist when the wall temperature exceeds this value and vapor deposition occurs only by vapor condensation at the wall (see below).

The vapor and condensate mass fraction profiles at two different axial stations are plotted in Figs. 4 and 5. There one sees how Y_c depends on the radial position in the pipe when a fog boundary is present (Fig. 4) and when fog fills the entire pipe cross section (Fig. 5).

In Fig. 6 we plot the overall vapor collection efficiency E in percent versus the wall temperature for $K = 0.2$, 0.6, and $Y_{v,o} = 10^{-3}$. The overall collection efficiency is defined as the percentage of the inlet flow of condensable vapor that is deposited on the wall in the form of aerosol and vapor over the length of the pipe-condensation section. The collection efficiency is zero for wall temperatures that exceed the dew point temperature $T_{dp} = 760$ K (for $Y_{v,o} = 10^{-3}$). By decreasing the wall temperature from T_{dp} vapor condensation on the pipe wall begins and E sharply increases until the wall temperature falls below about $T_w = 650$ K whereupon the efficiency tends to near plateau values of about 84 percent for $K = 0.6$ and 73 percent for $K = 0.2$. The dashed curve in Fig. 6 is obtained by ignoring fog formation and assuming that vapor deposition occurs only by condensation on the pipe wall. Note that small liquid droplets start to form (at the outlet of the pipe) when the wall temperature is decreased below 725 K, indicating a very narrow temperature range over which the pipe is clear of fog and vapor condensation on the pipe wall takes place (circa 725–760 K). Figure 7 shows the collection efficiency versus temperature for a larger value of the inlet vapor mass fraction of $Y_{v,o} = 10^{-2}$. We note that at low pipe wall temperatures the collection efficiencies are somewhat smaller than those predicted for $Y_{v,o} = 10^{-3}$.

Assumptions Underlying the Present Model

Most of the assumptions underlying the present theory of fog formation and droplet deposition, namely assumptions 2–7 and 9, are frequently used and accepted in the literature on two-phase flow and constant property pipe flow analysis. Thus, we will focus our attention on the validity of assumption 1 (equilibrium within the fog region) and assumption 8 (thermophoretically controlled deposition of fog droplets).

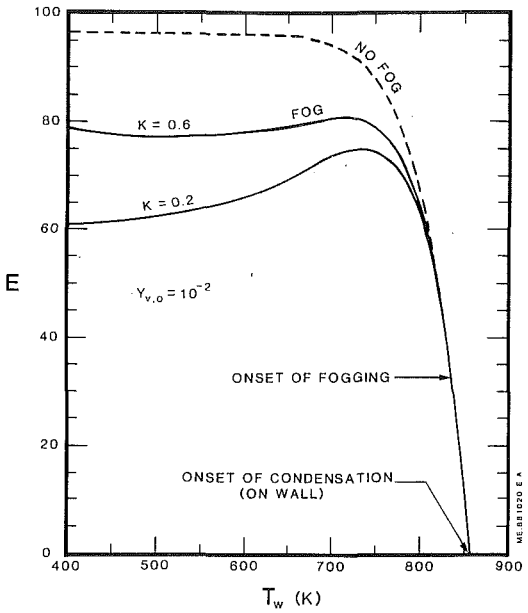

Fig. 7 CsOH vapor collection efficiency versus the wall temperature; conditions, Re = 10^4, $L^+ = 2 \times 10^5$, $T_o = 10^3$ K, Sc = 2, Pr = 1

By assuming that whenever the condensate and its vapor coexist they are in local thermodynamic equilibrium we sidestep the uncertainties associated with the kinetics of condensation. In a system free of condensation nuclei, vapor condensation does not take place when the saturation condition is first reached owing to the nucleation barrier associated with the surface free energy of forming a "nucleus" of the condensed phase. However, if active pre-existing nuclei are present, e.g., gaseous ions or "seed particles," the vapor condensation occurs under near-equilibrium conditions. In deriving a criterion for the importance of foreign nuclei we follow the approach suggested by Hidy and Friedlander (1964). They showed that the maximum relative change of vapor concentration (or mass fraction) due to foreign nuclei of diameter d is given by

$$\left(\frac{1}{Y_v}\frac{Y_v}{dt}\right)_{\max} = 2\pi dDN \tag{35}$$

where N is the concentration of foreign nuclei (in units of particles cm^{-3}). This defines a characteristic time τ_{het} for vapor depletion by heterogeneous nucleation, i.e.,

$$\tau_{het} = \frac{1}{2\pi dDN} \tag{36}$$

and we can say that heterogeneous processes are important if there is sufficient time in practice to accomplish appreciable capture of vapor by existing seed particles. In a turbulent pipe flow the characteristic vapor diffusion time is R^2/ϵ. Using the maximum value of the eddy diffusivity $\epsilon = 0.36\nu R^+$ (see equation (12)), the minimum vapor diffusion time τ_D is estimated to be

$$\tau_D = \frac{R}{0.36\, u^*} \tag{37}$$

By equating τ_{het} with τ_D we find that foreign nuclei concentrations of about

$$N \approx \frac{0.36\, u^*}{2\pi dDR} \tag{38}$$

are required to eliminate the possibility of homogeneous nucleation. Consider CsOH condensation ($D \approx 5 \times 10^{-5} m^2\, s^{-1}$ at 800 K) in a 20 m s^{-1} turbulent flow through a pipe of radius 0.026 m. From equation (38) we predict that 2.2×10^{10} nuclei m^{-3} of 1.0 μm size foreign particles is sufficient to ensure near-saturation condensation conditions. This concentration of pre-existing aerosol is equivalent to the concentration of 1.0 μm size particles measured in the atmosphere over unpolluted urban areas (Seinfeld, 1986). Based on this prediction we consider that heterogeneous nucleation is the more likely mechanism of fog formation in engineering applications and conclude that nearly saturation conditions exist within the fog zone.

To support our assumption of thermophoretically controlled deposition of fog particles, we discuss below other potential mechanisms of particle migration to the wall. Particles smaller than about 10^{-2} μm in diameter suspended in gases exhibit a Brownian motion that is sufficiently intense to contribute to the particle depostion rate. However, for the particle sizes of interest here (>0.1 μm) the particle Brownian diffusion coefficient is less than 10^{-9} $m^2\, s^{-1}$ (compared with, say, $D \approx 5 \times 10^{-5}$ $m^2\, s^{-1}$ for CsOH vapor diffusion in steam at 800 K). Thus, the particle deposition rate due to Brownian motion can be neglected.

When the flow is turbulent particles may deposit on the wall by y-directional "inertial penetration" of large particles through the laminar sublayer. The experimental data on deposition from isothermal pipe flows show that the ratio of the stopping distance based on the friction velocity to a distance approximately equivalent to the laminar sublayer is the dimensionless group that best characterizes turbulent deposition (Hanratty and McCoy, 1977). For forced turbulent pipe flow, the dimensionless stopping distance that has proved most convenient for deposition data correlation is

$$S = \frac{d^2\, u^{*2}\, \rho_p}{18\, \rho\, \nu^2} \tag{39}$$

The experimental data indicate that particles for which $S < 0.15$ follow the gas motion near the wall and do not impinge on the wall by the inertial mechanism. Returning to our example of CsOH condensation in turbulent pipe flow, we estimate $S = 0.08$ for 1.0 μm CsOH droplets. This is small enough to render turbulent (inertial) deposition negligible.

Finally, it easy to show that particle deposition by gravitational sedimentation in horizontal pipes is small compared with thermophoretic deposition by examining the inequality.

$$\frac{4}{9}\frac{g\, d^2\, \rho_p\, R\, T_w}{\nu^2\, \rho K (T_b - T_w) \mathrm{Nu}} < < 1 \tag{40}$$

The left-hand side of the above criterion is the ratio of the particle terminal velocity based on the Stokes law to the thermophoretic velocity. In the application of interest here this group is much less than unity.

Conclusions

Numerical solutions to the pipe flow equations have been obtained for problems in which trace condensable vapors are present in the gas flow and the pipe wall is cooled far below the dew point of the vapor. The distribution of condensable material in vapor and condensed form in the two-phase region was obtained for the limiting case of thermodynamic equilibrium between the vapor and its condensed phase, vapor deposition at the wall by Fick diffusion, and condensate droplets driven to the wall by thermophoresis. At present, there is no direct experimental evidence to verify the turbulent pipe-flow description given here. We might remark, however, that the Castillo-Rosner (1989) model of fog formation and thermophoretic transport in laminar boundary layers shows reasonable agreement with the experimental data of Brown (1966) and Santoro et al. (1984) on the deposition of Na_2SO_4 vapors onto cooled cylindrical tubes immersed in a combustion gas stream. Thus, the present two-phase flow/deposition rate model should provide the theoretical framework necessary for predicting the quantity of valuable or noxious material that can

pass through a cold channel. This capability should prove useful in several technologies, such as nuclear reactor safety and cooler-condenser design.

References

Barron, R. F., and Han, L. S., 1965, "Heat and Mass Transfer to a Cryosurface in Free Convection," ASME JOURNAL OF HEAT TRANSFER, Vol. 87, pp. 499–506.

Brown, T. D., 1966, "Oil Ash Deposition," *Fuel Soc. J.,* Vol. 18, pp. 28–43.

Castillo, J. L., and Rosner, D. E., 1989, "Theory of Surface Deposition From a Unary Dilute Vapor-Containing Stream Allowing for Condensation Within the Laminar Boundary Layer," *Chem. Engng. Sci.,* Vol. 44, pp. 925–937.

Colburn, A. P., and Edison, A. G., 1941, "Prevention of Fog in Cooler-Condensers," *Ind. Engng. Chemistry,* Vol. 33, pp. 457–458.

Cronenberg, A. W., 1988, "Scoping Analysis of Fission Product Behavior in the Primary Coolant System for Postulated N-Reactor Severe Accidents," Westinghouse Hanford Company Report WHC-SP-0071, Feb.

Deissler, R. G., 1955, "Analysis of Turbulent Heat Transfer, Mass Transfer and Friction in Smooth Tubes at High Prandtl and Schmidt Numbers," NACA Report 1210.

Epstein, M., and Rosner, D. E., 1970, "Enhancement of Diffusion-Limited Vaporization Rates by Condensation Within the Thermal Boundary Layer—2. Comparison of Homogeneous Nucleation Theory With the Critical Supersaturation Model," *Int. J. Heat Mass Transfer,* Vol. 13, pp. 1393–1414.

Gear, C. W., 1971, *Numerical Initial Value Problems in Ordinary Differential Equations,* Prentice Hall, Englewood Cliffs, NJ.

Hagrman, D. L., 1987, "A Scoping Study of Fission Product Transport From Failed Fuel During N-Reactor Postulated Accidents," EG&G Report EGG-SSRE-7899, Nov.

Hanratty, T. J., and McCoy, D. D., 1977, "Rate of Deposition of Droplets in Annular Two-Phase Flow," *Int. J. Multiphase Flow,* Vol. 3, pp. 319–331.

Hedley, A. B., Brown, T. D., and Shuttleworth, A., 1966, "Vanadium Pentoxide Deposition From Combustion Gases," ASME *Journal of Engineering for Power,* Vol. 88, pp. 173–178.

Hidy, G. M., and Friedlander, S. K., 1964, "Vapor Condensation in the Mixing Zone of a Jet," *AIChE J.,* Vol. 10, pp. 115–124.

Hindmarsh, A. C., 1972, "Linear Multistep Methods for Ordinary Differential Equations: Method Formulations, Stability, and the Methods of Nordsieck and Gear," Lawrence Livermore National Laboratory Report UCRL-51185, Rev. 1, Mar.

Johnstone, H. F., Kelley, M. D., and McKinley, D. L., 1950, "Fog Formation in Cooler-Condensers," *Ind. Engng. Chemistry,* Vol. 42, pp. 2298–2302.

Mori, Y., and Hijikâta, K., 1973, "Free Convective Condensation Heat Transfer With Noncondensable Gas on a Vertical Surface," *Int. J. Heat Mass Transfer,* Vol. 16, pp. 2229–2240.

Rosner, D. E., 1967, "Enhancement of Diffusion-Limited Vaporization Rates by Condensation Within the Thermal Boundary Layer—1. The Critical Supersaturation Approximation," *Int. J. Heat Mass Transfer,* Vol. 10, pp. 1267–1278.

Rosner, D. E., and Epstein, M., 1968, "Fog Formation Conditions Near Cool Surfaces," *J. Colloid Interface Sci.,* Vol. 28, pp. 60–65.

Santoro, G. J., Kohl, F. J., Stearns, C. A., Gokoglu, S. A., and Rosner, D. E., 1984, "Experimental and Theoretical Deposition Rates From Salt-Seeded Combustion Gases on a Mach 0.3 Burner Rig," NASA TP 2225.

Seinfeld, J. H., 1986, *Atmosphere Chemistry and Physics of Air Pollution,* Wiley, New York.

Talbot, L., Cheng, R. K., Schefer, A. W., and Willis, D. R., 1980, "Thermophoresis of Particles in a Heated Boundary Layer," *J. Fluid Mech.,* Vol. 101, pp. 737–758.

Toor, H. L., 1971, "Fog Formation in Boundary Value Problems," *AIChE J.,* Vol. 17, pp. 5–14.

Turkdogan, E. T., 1964, "The Theory of Enhancement of Diffusion-Limited Vaporization Rates by a Convection-Condensation Process—Part I, Theoretical," *Trans. Am. Inst. Min. Engrs.,* Vol. 230, pp. 740–749.

Van Driest, 1956, "On Turbulent Flow Near a Wall," *Journal of the Aeronautical Sciences,* Vol. 23, pp. 1007–1013.

Effect of Insoluble Surfactants in Condensation on a Moving Drop: Solutions for Intermediate Reynolds Numbers

L. J. Huang
Mem. ASME

P. S. Ayyaswamy
Fellow ASME

Department of Mechanical Engineering
and Applied Mechanics,
University of Pennsylvania,
Philadelphia, PA 19104-6315

An examination of the hydrodynamics and heat transfer associated with condensation on a moving drop in the intermediate Reynolds number regime ($Re = 0(100)$) has been carried out. The droplet is taken to be initially contaminated with an insoluble monolayer surfactant material. The drop environment is taken to consist of its own vapor and air. The ambient pressure is taken to be one atmosphere. The formulation entails a simultaneous solution of the quasi-steady elliptic partial differential equations that describe the flow field and transport in the gaseous phase, and the motion inside the liquid drop. The heat transport inside the drop is treated as a transient process. A numerical procedure based on the hybrid difference scheme has been employed. The surface tension gradient force induced by the surfactant and the shear stress from the relative motion between the droplet and its outside velocity field are evaluated. Results have been provided for the interface velocity, drag, surface vorticity, external and internal flow structure, surfactant concentration along the droplet surface, and the Nusselt and Sherwood numbers.

I Introduction

Surface-active impurities significantly lower surface tension on the interface between the gaseous and liquid phases. For a moving droplet, the impurities collect in the rear of the droplet, giving rise to surface tension gradients. These inhibit liquid circulation and increase drag, and heat and mass transport rates will be reduced. Even trace amounts of surfactant may alter the flow and transport significantly.

It is important to understand the role played by monolayer surfactants on fluid motion and transport mechanisms of droplets under condensing situations. We could then, for example, estimate the absorption of atmospheric pollutant species by condensing raindrops.

There is a large amount of published work on the effect of surfactants on fluid sphere motion; see, for example, discussions by Levich (1962), Harper (1972), Sadhal and Johnson (1983), Chang and Chung (1985), and Oguz and Sadhal (1988). In the paper by Chang and Chung (1985), the effects of insoluble monolayer surfactants on the internal circulation of a condensing drop in high Reynolds number flow have been investigated for droplet radii ranging from 100 to 1000 μm by boundary layer analyses. However, the liquid and gaseous phases have not been treated simultaneously, and wake effects have been ignored. The surfactant surface diffusivity varies from 10^{-9} to 10^{-3} m^2/s. It is found that surfactants with lower surface diffusion coefficients are more effective in weakening the strength of internal circulation.

In this paper we are concerned with condensation on a droplet contaminated with monolayer insoluble surfactants for $Re_g = O(100)$. The analysis entails a simultaneous numerical solution of the liquid and gaseous phases.

II Development of the Model

Consider the introduction of a cold, spherical water drop of radius R into a large volume of saturated steam (condensible) and air (noncondensible). Let the instantaneous translational velocity of the drop be U_∞. The total pressure p_∞ and temperature T_∞ of the saturated mixture are taken to be prescribed. The condensing droplet is assumed to be initially contaminated with a surfactant that is relatively insoluble in both phases. Since the initial temperature T_0 of the drop is lower than that

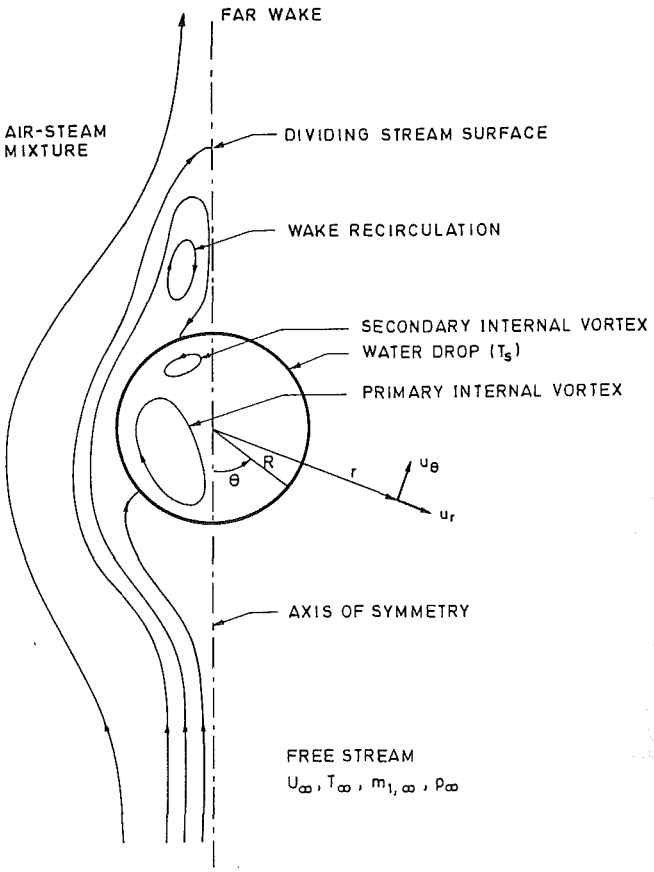

Fig. 1 Geometry and coordinate system

Contributed by the Heat Transfer Division for publication in the JOURNAL OF HEAT TRANSFER. Manuscript received by the Heat Transfer Division November 15, 1989; revision received March 29, 1990. Keywords: Condensation, Direct-Contact Heat Transfer, Sprays/Droplets.

of the saturated mixture, condensation of steam will occur on the drop surface. The shear stress at the interface will initiate liquid circulation inside the drop, as shown in Fig. 1. On the other hand, surfactants on the surface of the drop will reduce the strength of the internal circulation.

Apart from quasi-steady and other approximations made by Sundararajan and Ayyaswamy (1984), certain additional assumptions are made here. These are: (*i*) The surfactant concentration distribution on the droplet surface is at a quasi-steady state; (*ii*) the surfactant diffusion time, δ^2/D_s, where δ is the thickness of the surfactant layer and D_s is the diffusion coefficient of the surfactant, is much smaller than the time scale of the drop heating, R^2/α_l, where α_l is the thermal diffusivity of the liquid; (*iii*) the surfactant monolayer always separates the liquid and vapor phases; i.e., the condensate penetrates the surfactant monolayer immediately after it reaches the surface (Swisher, 1970; Rosen, 1978); (*iv*) the Weber number, We ($=U_\infty^2 D\rho/\sigma$), and the Eötvös number ($=g\Delta\rho D^2/\sigma$), are such that drop deformation is negligible; i.e., We <0.3 and Eo <0.4.

The surfactant induced force, $F_\sigma(\theta)$, may be evaluated on the basis of a steady convection–diffusion balance model (Levich, 1962) as follows:

Consider

$$\nabla\cdot(Y\mathbf{u}_s)-\nabla\cdot(D_s\nabla Y)=0 \tag{1}$$

where $\mathbf{u}_s$ is the surface velocity vector, Y is the surfactant surface concentration, and D_s is the coefficient of surface diffusion and assumed to be constant. For a spherical droplet, equation (1) becomes

$$\frac{\partial}{\partial\theta}(Y\,u_{l,\theta}\sin\theta)=\frac{D_s}{R}\frac{\partial}{\partial\theta}\left(\sin\theta\frac{\partial Y}{\partial\theta}\right) \tag{2}$$

Integrating equation (2) from $\theta=0$ to θ, we obtain

$$\frac{\partial Y}{\partial\theta}=\frac{RY}{D_s}u_{l,\theta} \tag{3}$$

Now, following Berg (1972), we may write

$$\frac{\partial\sigma}{\partial Y}=-\hat{R}\hat{T}_s \tag{4}$$

where σ is the surface tension, $\hat{R}$ is the universal gas constant, and $\hat{T}_s$ is the surface temperature in degrees Kelvin. With equations (3) and (4), the surface induced force may be expressed as

$$F_\sigma(\theta)=-\frac{1}{R}\frac{\partial\sigma}{\partial\theta}\bigg|_{r=R}=\frac{\hat{R}\hat{T}_s Y}{D_s}u_{l,\theta}\bigg|_{r=R} \tag{5}$$

This surfactant induced force will modify the shear stress at the drop surface.

The nondimensional equations for gaseous and liquid phases (the subscript g refers to the mixture, l to the liquid phase, 1 to the noncondensible, 2 to vapor), omitting the asterisks for convenience, are given as

$$\nabla\cdot\mathbf{u}_g = 0 \tag{6}$$

$$\mathrm{Re}_g\mathbf{u}_g\cdot\nabla\mathbf{u}_g = -\frac{1}{2}\mathrm{Re}_g\nabla p_g+2\nabla^2\mathbf{u}_g \tag{7}$$

$$\mathrm{Pe}_{g,t}\mathbf{u}_g\cdot\nabla T_g = 2\nabla^2 T_g \tag{8}$$

$$\mathrm{Pe}_{g,m}\mathbf{u}_g\cdot\nabla w_1 = 2\nabla^2 w_1 \tag{9}$$

$$\nabla\cdot\mathbf{u}_l = 0 \tag{10}$$

$$\mathrm{Re}_l\mathbf{u}_l\cdot\nabla\mathbf{u}_l = -\frac{1}{2}\mathrm{Re}_l\nabla p_l+2\nabla^2\mathbf{u}_l \tag{11}$$

$$\frac{\partial T_l}{\partial t}+\frac{\mathbf{Pe}_l}{2}\mathbf{u}_l\cdot\nabla T_l = \nabla^2 T_l \tag{12}$$

where the velocities $\mathbf{u}_g$ and $\mathbf{u}_l$ have been scaled by U_∞, the r coordinate has been scaled by R. In the above equations, the dimensionless pressures p_g^* and p_l^*, temperatures T_g and T_l mass fraction w_1, Reynolds numbers Re_g and Re_l, Peclet numbers $\mathrm{Pe}_{g,t}$, $\mathrm{Pe}_{g,m}$, Pe_l and time t^* are given by

Nomenclature

c_p = specific heat, J/kg K
D = drop diameter, m
D_{12} = binary diffusion coefficient, m^2/s
D_s = diffusion coefficient of the surfactant, m^2/s
Eo = Eötvös number $= g\Delta\rho D^2/\sigma$
F_σ = surfactant induced force
g = gravity
Ja_g = Jakcob number $= c_{pg}(T_\infty - T_0)/\lambda$
i, **j** = unit vector in the direction $\theta=\pi/2$, π
k = thermal conductivity, W/mK
Le = Lewis number $= \alpha/D_{12}$
m_1 = noncondensible mass fraction
p = pressure (scaled by $\frac{1}{2}\rho_g U_\infty^2$)
Pe = Peclet number $= U_\infty D/\alpha$, $U_\infty D/D_{12}$, or $U_\infty D/D_s$
Pr = Prandtl number $= \nu/\alpha$
q = heat flux (scaled by $\rho\alpha\lambda/R$)
r = radial coordinate (scaled by R)
R = drop radius
$\hat{R}$ = universal gas constant
$\dot{R}$ = dimensionless rate of change of drop-radius (scaled by U_∞)
Re = Reynolds number $= U_\infty D/\nu$
t = time $= \int\alpha_l dt/R^2$
T = temperature $= (T-T_\infty)/(T_0-T_\infty)$
$\hat{T}_s$ = surface temperature in degrees Kelvin
u = velocity vector (scaled by U_∞)
u_r, u_θ = velocity components (scaled by U_∞)
u_c = dimensionless condensation velocity at the drop surface (scaled by D_{12}/D)
U_0 = initial velocity of drop
U_∞ = far-stream translational velocity
w_1 = normalized noncondensible mass fraction
W = condensation parameter $= 1-m_{1,\infty}/m_{1,s}$
We = Weber number $= U_\infty^2 D\rho/\sigma$
Y = surfactant concentration (scaled by Y_0)
Y_0 = surfactant concentration at $\theta=\pi$(g-mole/m^2)
α = thermal diffusivity, m^2/s
δ = thickness of surfactant layer
ζ = vorticity (scaled by U_∞/R)
θ = polar angle
λ = latent heat
μ = dynamic viscosity
ν = kinematic viscosity
ρ = density, kg/m^3
σ = surface tension
ψ = stream function (scaled by $U_\infty R^2$)

Subscripts

c = condensation
g = gas-phase
l = liquid-phase
m = mass transfer
s = drop-surface, surfactant
t = thermal
0 = at initial time
1 = noncondensible
∞ = far-stream

Superscripts

$\bar{}$ = average
* = dimensionless quantity

$$p_g^* = \frac{p_g - p_\infty}{0.5\rho_g U_\infty^2}, \quad p_l^* = \frac{p_l - p_\infty}{0.5\rho_l U_\infty^2}, \quad T_g^* = \frac{T_g - T_\infty}{T_0 - T_\infty}, \quad T_l^* = \frac{T_l - T_\infty}{T_0 - T_\infty},$$

$$w_1^* = \frac{m_1 - m_{1,\infty}}{m_{1,0} - m_{1,\infty}}, \quad \mathrm{Re}_g = \frac{U_\infty 2R}{\upsilon_g}, \quad \mathrm{Re}_l = \frac{U_\infty 2R}{\upsilon_l},$$

$$\mathrm{Pe}_{g,t} = \frac{U_\infty 2R}{\alpha_g}, \quad \mathrm{Pe}_{g,m} = \frac{U_\infty 2R}{D_{12}}, \quad \mathrm{Pe}_l = \frac{U_\infty 2R}{\alpha_l}, \quad t^* = \int \frac{\alpha_l}{R^2} dt$$

Here, ν, α, and D_{12} denote the kinematic viscosity, thermal diffusivity, and the binary diffusion coefficient for the gaseous phase, respectively.

Initial and boundary conditions governing the condensation problem are given below. Again, we have omitted asterisks for convenience.

The initial condition:

$$T_l = 1, \text{ at } t = 0 \tag{13}$$

At the interface (r = 1):

- Continuity of tangential velocity:

$$u_{g,\theta} = u_{l,\theta} \tag{14}$$

- Continuity of shear stress:

$$\frac{\mu_g}{\mu_l}\left[r\frac{\partial}{\partial r}\left(\frac{u_{g,\theta}}{r}\right) + \frac{1}{r}\frac{\partial u_{g,r}}{\partial \theta}\right] - \left[r\frac{\partial}{\partial r}\left(\frac{\partial u_{l,\theta}}{r}\right) + \frac{1}{r}\frac{\partial u_{l,r}}{\partial \theta}\right] = \frac{\hat{T}_s \hat{R} R Y_0}{\mu_l D_s} Y u_{l,\theta} \tag{15}$$

where $Y^* = Y/Y_0$, and Y_0 is the prescribed surfactant concentration at $\theta = \pi$. The surface concentration Y can be derived by integrating equation (3) from $\theta = \theta$ to π:

$$\ln(Y) = -\frac{\mathrm{Pe}_s}{2}\int_\theta^\pi u_{l,\theta} d\theta \tag{16}$$

where

$$\mathrm{Pe}_s = \frac{2RU_\infty}{D_s}$$

- Continuity of mass flux:

$$\rho_g(u_{g,r} - \dot{R}) = \rho_l(u_{l,r} - \dot{R}) \tag{17}$$

where $\dot{R}$ is the growth rate of the drop.

- Impermeability of the noncondensible:

$$\frac{2W}{\mathrm{Pe}_{g,m}}\frac{\partial w_1}{\partial r} = \frac{u_c}{\mathrm{Pe}_{g,m}} = u_{g,r} \tag{18}$$

where u_c is the nondimensional condensation velocity and is given by $u_c = u_{g,r}/\mathrm{Pe}_{g,m}$. The parameter W referred to as the condensation parameter is given by $W = 1 - m_{1,\infty}/m_{1,s}$, and it is a function of the thermodynamic conditions p_∞, T_∞, and T_s. W varies from 0 to 1. The limit zero corresponds to a noncondensing situation and $W = 1$ to a pure vapor environment.

- Temperature continuity:

$$T_g = T_l \tag{19}$$

- Heat flow continuity:

$$Ja_g\frac{\partial T_g}{\partial r} + \frac{1}{2\mathrm{Le}_g}\left(u_c + \frac{\rho_g \bar{u}_c}{\rho_l - \rho_g}\right) = q_s \tag{20}$$

where the Jackob number Ja_g, Lewis number Le_g, and nondimensional heat flux q_s^* are

$$Ja_g = \frac{c_{pg}(T_\infty - T_0)}{\lambda}, \quad \mathrm{Le}_g = \frac{\alpha_g}{D_{12}}, \quad q_s^* = \frac{q_s R}{\rho_g \alpha_g \lambda}$$

and c_p is specific heat, and λ is latent heat of condensation. The quantity $\bar{u}_c$ is the average value of u_c and is given by

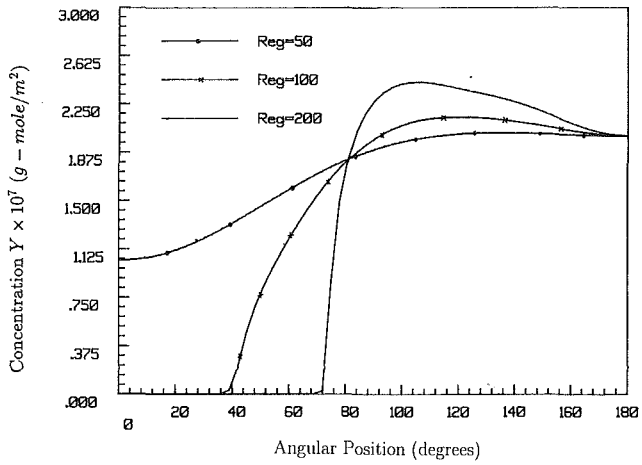

Fig. 2 Variation of surfactant concentration with θ and Re_g: $W = 0.1$, $R_0 = 0.2$ mm, $D_s = 50\mathrm{E}-07$ m²/s, $T_s = 353$ K, $p_\infty = 100$ kPa, $Y_0 = 2.0\mathrm{E}-0.7$ g-mole/m²

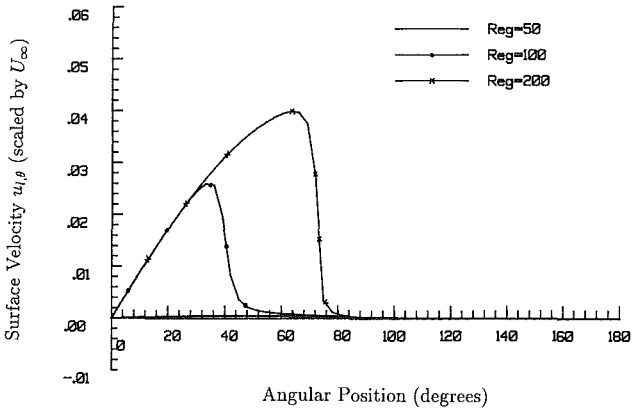

Fig. 3 Variation of surface tangential velocity u_θ with θ and Re_g: $W = 0.1$, $R_0 = 0.2$ mm, $D_s = 5.0\mathrm{E}-07$ m²/s, $T_s = 353$ K, $p_\infty = 100$ kPa, $Y_0 = 2.0\mathrm{E}-07$ g-mole/m²

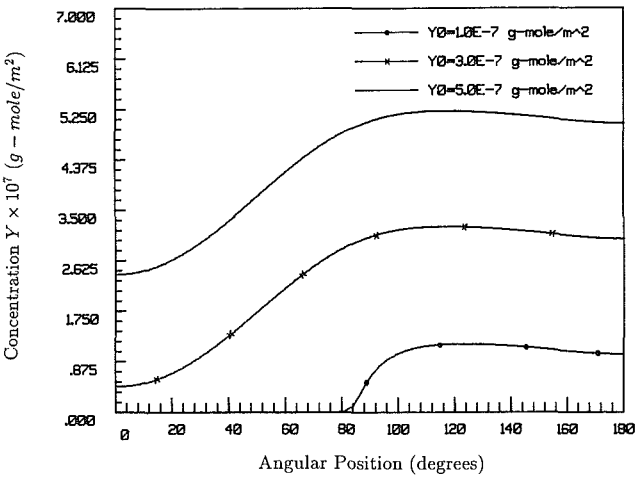

Fig. 4 Variation of surfactant concentration Y with θ and the amount of surfactant: $W = 0.1$, $R_0 = 0.2$ mm, $D_s = 5.0\mathrm{E}-07$ m²/s, $T_s = 353$ K, $p_\infty = 100$ kPa, $\mathrm{Re}_g = 100$

$$\bar{u}_c = \frac{1}{2}\int_0^\pi u_c \sin\theta \, d\theta \tag{21}$$

- Normalized mass fraction at interface:

$$w_1 = w_s \tag{22}$$

where w_s can be evaluated by using the Clapeyron equation with the assumption of local thermodynamic equilibrium.

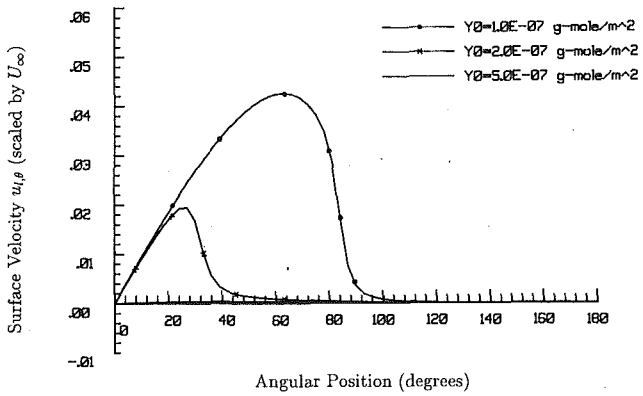

Fig. 5 Variation of surface tangential velocity $u_{l,\theta}$ with θ and the amount of surfactant: $W = 0.1$, $R_0 = 0.2$ mm, $D_s = 5.0E-07$ m^2/s, $T_s = 353$ K, $p_\infty = 100$ kPa, $Re_g = 100$

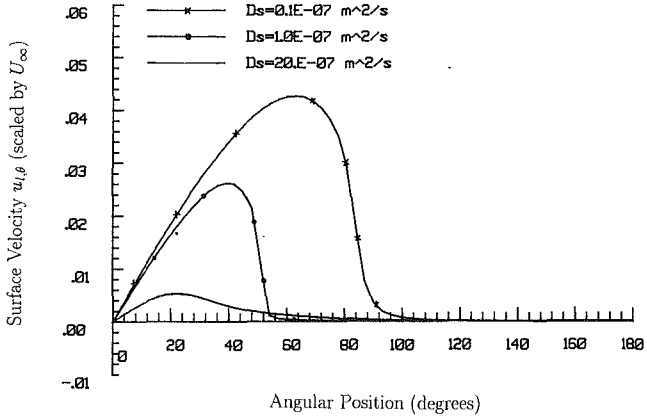

Fig. 8 Variation of surface tangential velocity $u_{l,\theta}$ with θ and D_s: $W = 0.1$, $R_0 = 0.2$ mm, $T_s = 353$ K, $p_\infty = 100$ kPa, $Y_0 = 2.0E-07$ g-mole/m^2, $Re_g = 100$

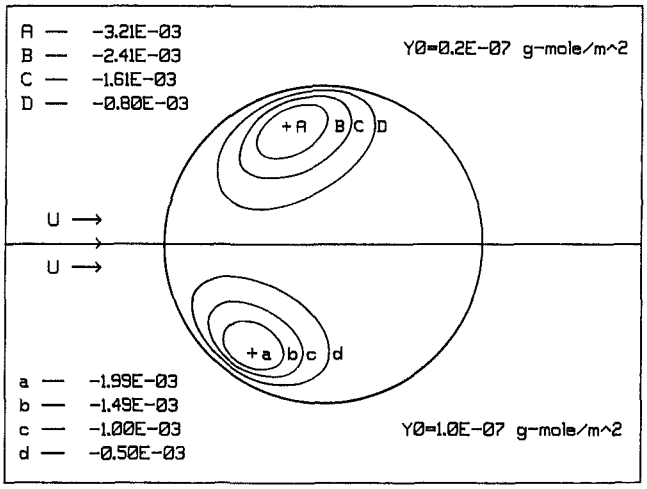

Fig. 6 Effect of the amount of surfactant on liquid circulation (stream function values are shown in key): $W = 0.1$, $R_0 = 0.2$ mm, $D_s = 5.0E-07$ m^2/s, $T_s = 353$ K, $p_\infty = 100$ kPa, $Re_g = 100$

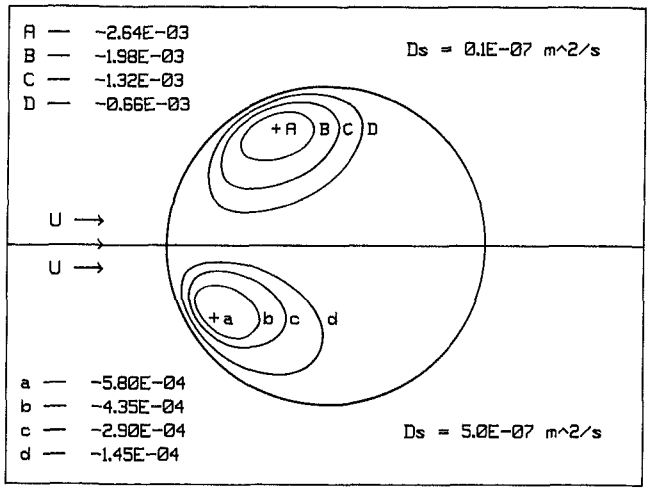

Fig. 9 Effect of D_s on liquid circulation (stream function values are shown in key): $W = 0.1$, $R_0 = 0.2$ mm, $T_s = 353$ K, $p_\infty = 100$ kPa, $Y_0 = 2.0E-07$ g-mole/m^2, $Re_g = 100$

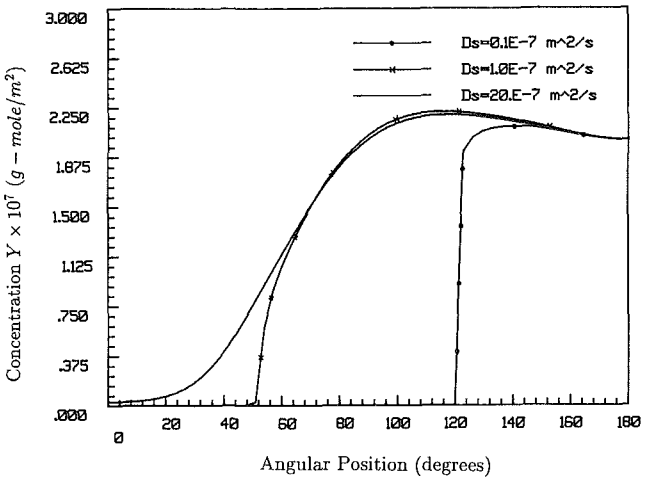

Fig. 7 Variation of surfactant concentration with θ and D_s: $W = 0.1$, $R_0 = 0.2$ mm, $T_s = 353$ K, $p_\infty = 100$ kPa, $Y_0 = 2.0E-07$ g-mole/m^2, $Re_g = 100$

Far-stream conditions ($r \to \infty$)

- Uniform velocity:

$$\mathbf{u}_g = \mathbf{j} \tag{23}$$

where $\mathbf{j}$ is the unit vector along the axis.

- Bulk mixture conditions

$$T_g = p_g = w_1 = 0 \tag{24}$$

Axisymmetric conditions at $\theta = 0$ and π:

$$u_{g,\theta} = \frac{\partial u_{g,r}}{\partial \theta} = \frac{\partial p_g}{\partial \theta} = \frac{\partial T_g}{\partial \theta} = \frac{\partial w_1}{\partial \theta} = 0 \tag{25}$$

$$u_{l,\theta} = \frac{\partial u_{l,r}}{\partial \theta} = \frac{\partial p_l}{\partial \theta} = \frac{\partial T_l}{\partial \theta} = 0 \tag{26}$$

III Solution Procedure

A numerical procedure that is based on the hybrid difference scheme will be employed. This scheme is a combination of a second-order accurate central difference scheme (CDS) and a first-order accurate upwind difference scheme (UDS). (See, for example, Sundararajan and Ayyaswamy (1984, 1985) for details.) The governing equations and boundary conditions of the problems are solved using the dimensionless stream function ψ (scaled with $U_\infty R^2$) and vorticity ζ (scaled with U_∞/R). The algebraic difference equations are solved iteratively, starting from suitable guess solutions. A successive overrelaxation procedure is used to accelerate the convergence. Computations are carried out until changes in the predicted transport quantities are less than 10^{-7} (absolute error) or less than 0.1 percent (relative error) between successive iterations. The time for a typical computer run, is on the order of 600 seconds on the Pittsburgh Supercomputer CRAY-X/MP or 1 CPU hour on the Harris computer.

IV Results and Discussion

The quasi-steady hydrodynamic and heat transfer results are

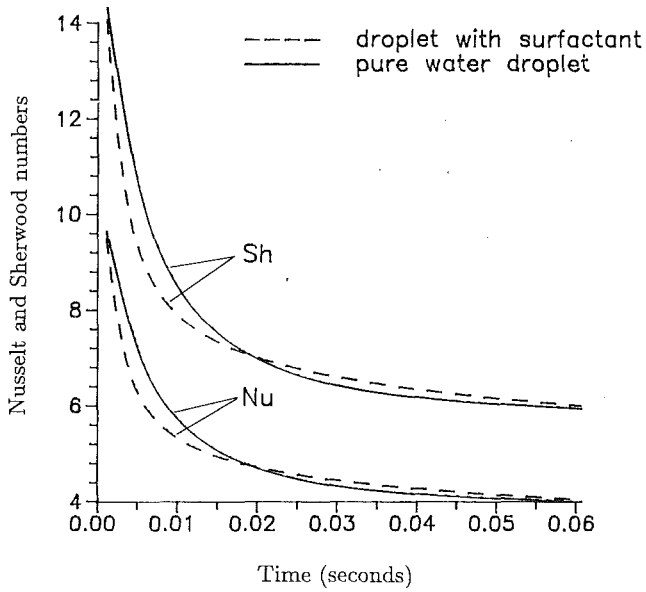

Fig. 10 Nusselt and Sherwood number time histories: $R_o = 0.2$ mm, $T_0 = 313$ K, $T_\infty = 368$ K, $p_\infty = 100$ kPa, $Y_0 = 3.0E-07$ g-mole/m^2, $Re_g = 100$, $D_s = 5.0E-07$ m^2/s

presented for various combinations of Re_g, surfactant concentration, and diffusivity of the surfactant. The effect of surfactant on the surface conditions and fluid motion inside the drop have been examined. The ambient pressure p_∞ is equal to 100 kPa, W equal to 0.1, and R_o equal to 0.2 mm.

In Fig. 2, the variations in surfactant concentration along the droplet surface for various values of Re_g have been plotted. With increasing Re_g, both the shear stress at the droplet surface and the gradient of the surfactant concentration increase. For $Re_g = 50$, the stagnant cap of surfactant film covers the entire droplet surface, while at $Re_g = 200$, it covers the surface segment from 70 deg to 180 deg. Another interesting result is the angular position of the maximum surfactant concentration. For low Re_g, the highest surface surfactant concentration is at $\theta = \pi$. With increasing Re_g, at a given W, flow separation occurs earlier; the strength of recirculation in the wake region increases, and the wake region becomes larger. As a consequence of these effects, the location of the maximum surfactant concentration moves forward. The surface velocity on the droplet decreases with decreasing Re_g. For $Re_g = 50$, the surface velocity is completely suppressed, as shown in Fig. 3.

In Figs. 4 and 5, the surfactant concentration and surface velocity along the droplet surface are plotted for varying amounts of the surfactant. As seen in Fig. 4, the surfactant concentration and the extent of surfactant coverage both increase with an increasing among of surfactant. This is as would be expected. The surface velocity correspondingly decreases (Fig. 5). The strength of the internal circulation also decreases (reduced shear stress at the surface), and the center of the vortex moves toward the front of the droplet (uneven shear stress distribution at the surface) as shown in Fig. 6.

The diffusivity of the surfactant strongly influences the surfactant concentration along the droplet surface as shown in Fig. 7. The surface coverage of the surfactant increases with increasing diffusivity of the surfactant, but the surface velocity decreases as shown in Fig. 8. Correspondingly, the strength of the internal circulation decreases and the center of vortex is again noted to move toward the front of the drop as shown in Fig. 9.

The effects of the presence of the surfactant on the transient variations in heat and mass transfer are shown in Fig. 10. Transport rates for identical ambient conditions have been evaluated for a pure droplet and a droplet with a monolayer of surfactant, and the results have been provided for comparison. Immediately upon introduction, the heat and mass transport rates are very high owing to the large thermal driving force $(T_\infty - T_s)$. A vigorous condensation accompanied by large heat release rapidly raises the surface temperature of the droplet. As a result the thermal driving force decreases and there is a corresponding steep decrease in heat and mass transfer. This observation holds true for both the drops. Beyond the early transient period, the condensation is at a much reduced level and a gradual decrease in heat transfer is noted. For otherwise identical conditions, the internal circulation in a pure drop is vigorous compared to that in a contaminated drop. A strong circulation acts as an efficient mixing mechanism, and the surface temperature of a pure drop remains relatively cold compared to that of a drop surface with surfactant coating; as a consequence, the Nu and Sh are relatively lower for a contaminated drop.

V Conclusions

The important conclusions that arise from the numerical solutions are:

1 With increasing Re_g, the gradient of the surfactant concentration on the surface increases. For low Re_g, the highest surfactant concentration is at $\theta = \pi$. With increasing Re_g, the angular location of the maximum surfactant concentration moves forward. The surface velocity on the droplet decreases with decreasing Re_g.

2 The surfactant concentration and the surfactant coverage increase with increasing amounts of the surfactant. The surface velocity and the strength of the internal circulation both decrease with increasing amount of surfactant.

3 The diffusivity of the surfactant strongly influences the surfactant concentration on the droplet surface. The covering angle of the surfactant on the surface increases with increasing diffusivity of the surface. However, the surface velocity and the strength of the internal circulation decrease.

4 The surfactant on the droplet decreases the strength of the internal circulation, and as a consequence, during early stages of the droplet lifetime Nu and Sh are relatively low for a contaminated drop.

Acknowledgments

The authors are grateful to Professor S. S. Sadhal (USC) and to a reviewer for many helpful suggestions. The numerical calculations were made by using the Pittsburgh Supercomputer under NSF Grant No. ECS-0000000/8515068. The authors are grateful for PSC services and to the NSF.

References

Berg, J. C., 1972, "Interfacial Phenomena in Fluid Phase Separation Processes," *Recent Developments in Separation Science*, Vol. 2, N. N. Li, ed., Chemical Rubber Co. Press, Cleveland, OH, pp. 1-31.

Chang, T. H., and Chung, J. N., 1985, "The Effects of Surfactants on the Motion and Transport Mechanisms of a Condensing Droplet in a High Reynolds Number Flow," *AIChE J.*, Vol. 31, pp. 1149-1156.

Clift, R., Grace, J. R., and Weber, M. E., 1978, *Bubbles, Drops, and Particles*, Academic Press, New York.

Harper, J. F., 1972, "The Motion of Bubbles and Drops Through Liquids," *Advances in Applied Mechanics*, Vol. 12, Academic Press, New York, pp. 59-129.

Levich, V. G., 1962, *Physico-Chemical Hydrodynamics*, Prentice-Hall, New Jersey.

Oguz, H. N., and Sadhal, S. S., 1988, "Effects of Soluble and Insoluble Surfactants on the Motion of Drops," *J. Fluid Mech.*, Vol. 194, pp. 563-579.

Rosen, M. J., 1978, *Surfactants and Interfacial Phenomena*, Wiley, New York.

Sadhal, S. S., and Johnson, R. E., 1983, "Stokes Flow Past Bubbles and Drops Partially Coated With Thin Films. I. Stagnant Cap of Surfactant Film—Exact Solution," *J. Fluid Mech.*, Vol. 126, pp. 237-250.

Sundararajan, T., and Ayyaswamy, P. S., 1984, "Hydrodynamics and Heat Transfer Associated With Condensation on a Moving Drop: Solutions for Intermediate Reynolds Numbers," *J. Fluid Mech.*, Vol. 149, pp. 33-58.

Sundararajan, T., and Ayyaswamy, P. S., 1985, "Numerical Evaluation of Heat and Mass Transfer to a Moving Liquid Drop Experiencing Condensation," *Numerical Heat Transfer*, Vol. 8, No. 6, pp. 689-706.

Swisher, R. D., 1970, *Surfactant Biodegradation*, Dekker, New York.

Journal of Heat Transfer

Technical Notes

This section contains shorter technical papers. These shorter papers will be subjected to the same review process as that for full papers.

Analytical Solution for Heat Conduction in a Two-Material-Layer Slab With Linearly Temperature Dependent Conductivity

K. C. Chang[1] and U. J. Payne[2]

Introduction

In many electronic components or some composite materials, the structure is made of different material layers, which have different thermal conductivities. Investigations of heat conduction, incorporated with abrupt changes of thermal conductivity, are of interest to heat transfer problems because of their importance in many engineering applications. Furthermore, when temperature variations are great or the transport properties vary rapidly with temperature, variations of the transport properties must be considered in the formulation of the problem. The governing equation of heat conduction associated with temperature-dependent thermal conductivity is nonlinear and the powerful superposition principles of the linear theory of mathematics cannot be applied to obtain analytical solutions. A number of analytical techniques used in application for solutions of nonlinear heat-conduction problems can be found in the literature (Halle, 1965; Peletier, 1970; Suzuki et al., 1977; Özisik, 1980; Tao, 1989). The previous analytical investigations, however, were mainly concerned with the heat conduction problems in a homogeneous slab (Eckert and Irving, 1971, 1977). Solutions to the corresponding problems in a composite slab are very often difficult to obtain in analytical form because of the presence of nondifferentiability at the interface and nonlinearity of the governing equations. This study attempts to obtain an exact solution of heat conduction in a two-material-layer slab in which the temperature dependency on thermal conductivity is taken into account.

Analysis

Consider a two-dimensional rectangular slab without any energy generation, constructed of two different materials, which are attached to the same material bases that are held at two constant base temperatures, respectively. The slab is convection cooled with a uniform and constant temperature and the radiant interactions with the air environment as well as the base surfaces can be overlooked if the temperatures involved are not too high. Taking the environmental temperature as the reference temperature and using the symmetry characteristics, the example problem is now schematically shown in Fig. 1. The dependence of thermal conductivity upon temperature is assumed in the linear form

$$\lambda_m = \lambda_{mo}(1+\alpha_m T) \ , \qquad m=1,\ 2 \tag{1}$$

where λ_{mo} is the thermal conductivity of material m at the reference temperature, and α_m is constant. The linear dependence form of transport property is usually applicable to quite a wide range of temperature. The heat-conduction equations can be formulated as follows:

$$\frac{\partial}{\partial x}\left[\lambda_1(T_1)\frac{\partial T_1}{\partial x}\right]+\frac{\partial}{\partial y}\left[\lambda_1(T_1)\frac{\partial T_1}{\partial y}\right]=0, \qquad 0<x<\frac{1}{2}, \quad 0<y<w \tag{2a}$$

$$\frac{\partial}{\partial x}\left[\lambda_2(T_2)\frac{\partial T_2}{\partial x}\right]+\frac{\partial}{\partial y}\left[\lambda_2(T_2)\frac{\partial T_2}{\partial y}\right]=0, \qquad \frac{1}{2}<x<1, \quad 0<y<w \tag{2b}$$

$$T_1 = T_2 \quad \text{at} \quad x=\frac{1}{2}, \quad 0<y<w \tag{2c}$$

$$\lambda_1\frac{\partial T_1}{\partial x}=\lambda_2\frac{\partial T_2}{\partial x} \quad \text{at} \quad x=\frac{1}{2}, \quad 0<y<w \tag{2d}$$

Here perfect thermal contact is assumed at the interface. The other associated boundary conditions are depicted in Fig. 1.

A new dependent variable U is defined, according to the Kirchhoff transformation, as

$$U=\int_0^T \frac{\lambda(T')}{\lambda_{mo}}\,dT' \tag{3}$$

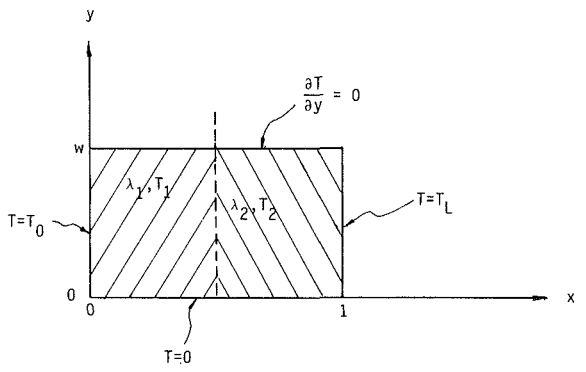

Fig. 1 Description of two-material-layer slab

[1]Associate Professor, Institute of Aeronautics and Astronautics, National Cheng-Kung University, Tainan, Taiwan; Assoc. Mem. ASME.

[2]Research Assistant, Institute of Aeronautics and Astronautics, National Cheng-Kung University, Tainan, Taiwan.

Contributed by the Heat Transfer Division for publication in the JOURNAL OF HEAT TRANSFER. Manuscript received by the Heat Transfer Division July 24, 1989; revision received April 27, 1990. Keywords: Conduction.

Then, equation (2) is transformed utilizing equation (3) and becomes

$$\frac{\partial^2 U_1}{\partial x^2} + \frac{\partial^2 U_1}{\partial y^2} = 0, \quad 0 < x < \frac{1}{2}, \quad 0 < y < w \tag{4a}$$

$$\frac{\partial^2 U_2}{\partial x^2} + \frac{\partial^2 U_2}{\partial y^2} = 0, \quad \frac{1}{2} < x < 1, \quad 0 < y < w \tag{4b}$$

The transformations of the boundary conditions give

$$U_1(0, y) = T_0 + \frac{\alpha_1}{2} T_0^2 = U_0 \tag{5a}$$

$$U_2(1, y) = T_L + \frac{\alpha_2}{2} T_L^2 = U_L \tag{5b}$$

$$U_1(x, 0) = U_2(x, 0) = 0 \tag{5c}$$

$$\frac{\partial}{\partial y} U_1(x, w) = \frac{\partial}{\partial y} U_2(x, w) = 0 \tag{5d}$$

The transformed interfacial temperatures turn out to be

$$U_m\left(\frac{1}{2}, y\right) = T_i(y) + \frac{\alpha_m}{2} T_i^2(y) = U_{im}(y), \quad m = 1, 2 \tag{6}$$

Note that $U_{m1}(1/2, y) \neq U_{m2}(1/2, y)$ since $\alpha_1 \neq \alpha_2$. The transformation of the interfacial condition, equation (2*d*), gives

$$\lambda_{10} \frac{\partial}{\partial x} U_1\left(\frac{1}{2}, y\right) = \lambda_{20} \frac{\partial}{\partial x} U_2\left(\frac{1}{2}, y\right) \tag{7}$$

The application of the method of separation of variables to the transformed linear partial differential equations and their boundary conditions yields

$$U_1(x, y) = \sum_{n=0}^{\infty} \frac{\sin \beta_n y}{\sinh \beta_n/2} \times \left\{\frac{2U_0}{w\beta_n} \sinh\left[\beta_n\left(\frac{1}{2} - x\right)\right] + (U_{i1})_n \sinh \beta_n x\right\}$$

$$\text{for } 0 \le x \le \frac{1}{2}, \quad 0 \le y \le w \tag{8a}$$

$$U_2(x, y) = \sum_{n=0}^{\infty} \frac{\sin \beta_n y}{\sinh \beta_n/2} \times \left\{(U_{i2})_n \sinh\left[\beta_n(1-x)\right] + \frac{2U_L}{w\beta_n} \sinh\left[\beta_n\left(x - \frac{1}{2}\right)\right]\right\}$$

$$\text{for } \frac{1}{2} \le x \le 1, \quad 0 \le y \le w \tag{8b}$$

where the eigenvalues are given by

$$\beta_n = \left(\frac{2n+1}{2}\right)\frac{\pi}{w}, \quad n = 0, 1, 2, \ldots \tag{9}$$

The values of $(U_{i1})_n$ and $(U_{i2})_n$ are determined by two interfacial conditions, equations (2*c*) and (7), as follows:

$$(U_{i1})_n = T_{in} + \frac{\alpha_1 w}{4} \beta_n T_{in}^2 \tag{10}$$

and

$$(U_{i2})_n = T_{in} + \frac{\alpha_2 w}{4} \beta_n T_{in}^2 \tag{11}$$

where

$$T_{in} = \frac{2}{w\beta_n(\lambda_{10}\alpha_1 + \lambda_{20}\alpha_2)} \left\{\left[(\lambda_{10} + \lambda_{20})^2 + \frac{2}{\cosh \beta_n/2}(\lambda_{10}U_0 + \lambda_{20}U_L)(\lambda_{10}\alpha_1 + \lambda_{20}\alpha_2)\right]^{1/2} - (\lambda_{10} + \lambda_{20})\right\} \tag{12}$$

If the thermal conductivities are independent of temperature, i.e., $\alpha_1 = \alpha_2 = 0$, the analytical solution can be obtained in a similar mathematical procedure without transformation and expressed as

$$T_1(x, y) = \sum_{n=0}^{\infty} \frac{\sin \beta_n y}{\sinh \beta_n/2} \times \left\{\frac{2T_0}{w\beta_n} \sinh\left[\beta_n\left(\frac{1}{2} - x\right)\right] + T_{in} \sinh \beta_n x\right\}$$

$$\text{for } 0 \le x \le \frac{1}{2}, \quad 0 \le y \le w \tag{13a}$$

$$T_2(x, y) = \sum_{n=0}^{\infty} \frac{\sin \beta_n y}{\sinh \beta_n/2} \times \left\{T_{in} \sinh\left[\beta_n(1-x)\right] + \frac{2T_L}{w\beta_n} \sinh\left[\beta_n\left(x - \frac{1}{2}\right)\right]\right\}$$

$$\text{for } \frac{1}{2} \le x \le 0, \quad 0 \le y \le w \tag{13b}$$

but T_{in} is now given in the following expression instead of equation (12):

$$T_{in} = \frac{2(\lambda_1 T_0 + \lambda_2 T_L)}{w\beta_n(\lambda_1 + \lambda_2) \cosh(\beta_n/2)} \tag{14}$$

Discussion

The exact solution is expressed in the form of Fourier series in terms of y. The precision of the analytical solution depends upon the determination of the number of terms (N) in the Fourier series to be summed up. The criterion to determine N is set as follows in the study:

$$\left|\frac{\text{the } (N+1) \text{ term}}{\sum_{i=1}^{N} \text{terms}}\right| \le 10^{-7} \tag{15}$$

For most computers, the magnitude order of machine epsilon is 10^{-7} for single precision.

The Gibbs phenomenon is an overshoot, a peculiarity of the Fourier series and other eigenfunction series at a single discontinuity. There are two step functions of y in the example problem.

$$\text{at } x = 0, \quad T = \begin{cases} 0 & y = 0 \\ T_0 & 0 < y < w \end{cases} \tag{16a}$$

and

$$\text{at } x = 1, \quad T = \begin{cases} 0 & y = 0 \\ T_L & 0 < y < w \end{cases} \tag{16b}$$

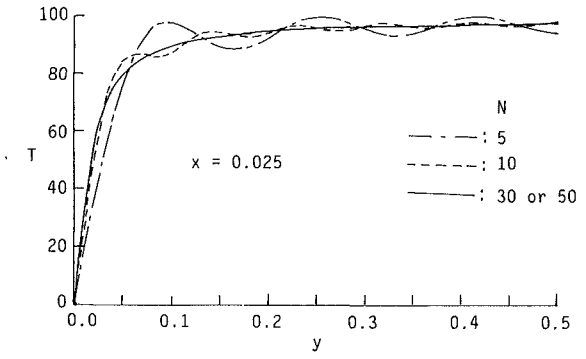

Fig. 2 Temperature profiles at $x = 0.025$ for the truncated Fourier sum of various terms

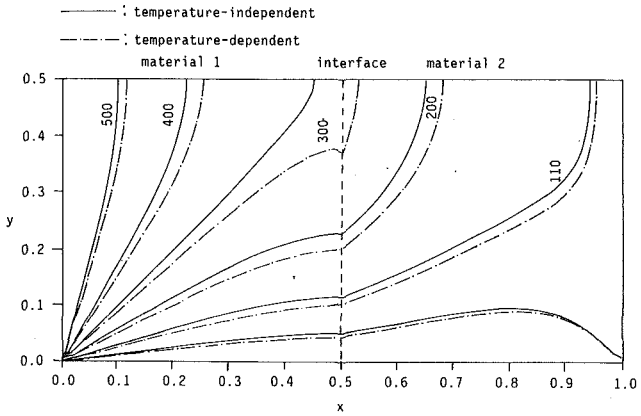

Fig. 3 Comparison of temperature contours of Test Case 1 (temperature-independent) and Test Case 2 (temperature-dependent)

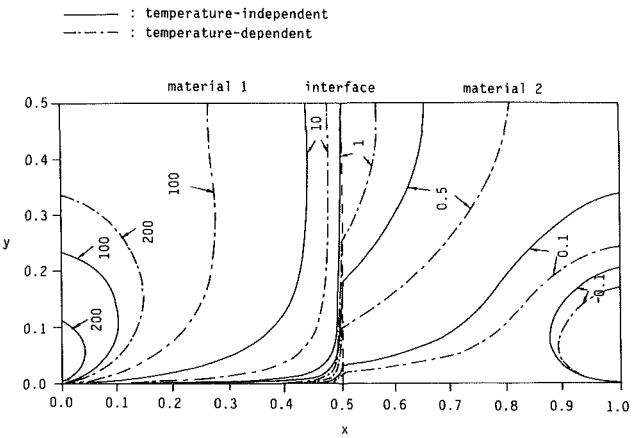

Fig. 4 Comparison of distributions of heat-flux component along x coordinate of Test Case 1 (temperature-independent) and Test Case 2 (temperature-dependent)

The inclusion of more terms (increasing N) does nothing to remove this overshoot but merely moves it closer (to some extent) to the point of discontinuity. Therefore, the overshoot due to the Gibbs phenomenon may render the solution highly unreliable, especially in the vicinity of a discontinuity. Several methods to smooth or even eliminate the Gibbs oscillations were reported in the text of Lanczos (1956) but the main drawback is that the application of these methods is always accompanied with very slow convergence. However, since our interest is not focused on the region in the vicinity of discontinuity, the remedy for Gibbs oscillations of the analytical solution is outside the scope of this study.

Figure 2 shows the temperature profiles at $x=0.025$ for the truncated sum of 5, 10, 30, and 50 terms of the Fourier series. The overshoot has been removed before N reaches 30 terms, while about 40 terms are required to satisfy the criterion of equation (15). Therefore, the analytical solutions can be reasonably regarded as free of Gibbs phenomenon except for the positions in the vicinity of discontinuity.

Two test cases were selected to show the temperature and heat-flux distributions for the test problem with and without temperature-dependent thermal conductivity. The calculation conditions are: $T_0=600$, $T_L=100$, $w=0.5$, $\lambda_{10}=0.06$, and $\lambda_{20}=0.001$.

Test Case 1: temperature-independent thermal conductivity, $\alpha_1=\alpha_2=0$

Test Case 2: temperature-dependent thermal conductivity, $\alpha_1=0.0006$ and $\alpha_2=0.00001$

Presented in Fig. 3 is the comparison of temperature contours of Test Cases 1 and 2. Since the given value of α_1 is much higher than that of α_2 (by 60 times), this given condition enhances the heat-conduction rate, particularly in the high-temperature regions, and then leads to the situation shown in Fig. 3 where the upper-left part of the test problem becomes hotter in Test Case 2 than in Test Case 1. This is also clearly seen in Fig. 4, which compares distributions of the heat-flux component along the x coordinate of Test Cases 1 and 2. The comparisons of the results, shown in Figs. 3 and 4, reveal that there do exist significant differences in the distributions of temperature and heat flux between those cases, the constant thermal conductivity and the variable one. The present method provides a unique and viable analytical tool for solutions of heat conduction problems in a composite slab.

References

Eckert, E. R. G., and Irving, T. F., 1971, *Progress in Heat and Mass Transfer*, Vol. 3, Pergamon, Oxford, United Kingdom.

Eckert, E. R. G., and Irving, T. F., 1977, *Progress in Heat and Mass Transfer*, Vol. 8, Pergamon, Oxford, United Kingdom.

Halle, H., 1965, "Exact Solution of Elementary Transient Heat Conduction Problem Involving Temperature-Dependent Properties," ASME JOURNAL OF HEAT TRANSFER, Vol. 87, pp. 420–421.

Lanczos, C., 1956, *Applied Analysis*, Chap. 4, Prentice-Hall, Englewood Cliffs, NJ.

Özişik, M. N., 1980, *Heat Conduction*, Chap. 11, Wiley, NY.

Peletier, L. A., 1970, "Asymptotic Behavior of Temperature Profiles of a Class of Nonlinear Heat Conduction Problems," *Quart J. Mech. Appl. Math.*, Vol. 23, pp. 441–447.

Suzuki, M., Matsumoto, S., and Maeda, S., 1977, "New Analytical Method for a Nonlinear Diffusion Problem," *Int. J. Heat Mass Transfer*, Vol. 20, pp. 883–889.

Tao, L. N., 1989, "The Heat Conduction Problem With Temperature-Dependent Material Properties," *Int. J. Heat Mass Transfer*, Vol. 32, pp. 487–491.

A New Criterion for Assuming Negligible Internal Thermal Resistance in Transient Heat Conduction Problem

B. P. A. Grandjean[1] and J. Thibault[1]

Nomenclature

A = surface area, m^2
$A()$ = transcendental summation term
Bi = Biot number $=hL/k$ or hR/k
Fo = Fourier number $=\alpha t/L^2$ or $\alpha t/R^2$
h = heat transfer coefficient, W/(m^2K)
J_0, J_1 = Bessel functions
k = thermal conductivity, W/m K
L = half-thickness of the infinite flat plate, m
m = geometric parameter
Pd = Predvoditelev number $=L^2/(\alpha\tau)$ or $R^2/(\alpha\tau)$
r = radial position, m
R = radius, m
t = time, s

[1]Department of Chemical Engineering, Laval University, Sainte-Foy, Québec, Canada G1K 7P4.

Contributed by the Heat Transfer Division for publication in the JOURNAL OF HEAT TRANSFER. Manuscript received by the Heat Transfer Division November 6, 1989; revision received May 21, 1990. Keywords: Conduction, Transient and Unsteady Heat Transfer.

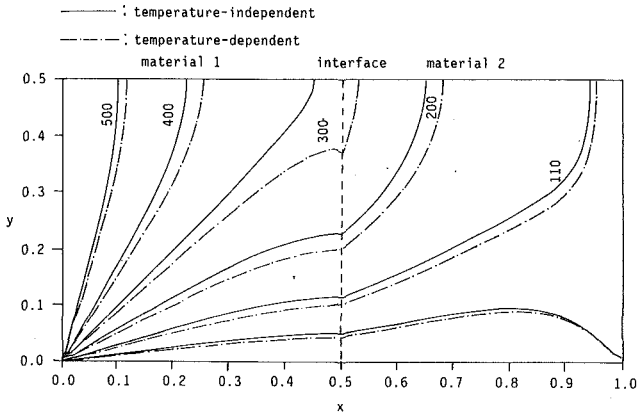

Fig. 3 Comparison of temperature contours of Test Case 1 (temperature-independent) and Test Case 2 (temperature-dependent)

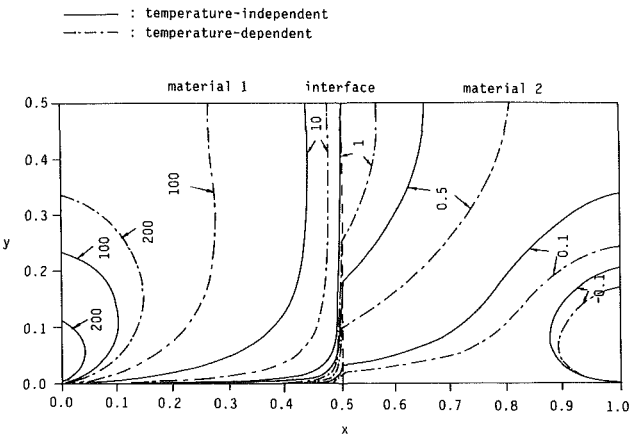

Fig. 4 Comparison of distributions of heat-flux component along x coordinate of Test Case 1 (temperature-independent) and Test Case 2 (temperature-dependent)

The inclusion of more terms (increasing N) does nothing to remove this overshoot but merely moves it closer (to some extent) to the point of discontinuity. Therefore, the overshoot due to the Gibbs phenomenon may render the solution highly unreliable, especially in the vicinity of a discontinuity. Several methods to smooth or even eliminate the Gibbs oscillations were reported in the text of Lanczos (1956) but the main drawback is that the application of these methods is always accompanied with very slow convergence. However, since our interest is not focused on the region in the vicinity of discontinuity, the remedy for Gibbs oscillations of the analytical solution is outside the scope of this study.

Figure 2 shows the temperature profiles at $x=0.025$ for the truncated sum of 5, 10, 30, and 50 terms of the Fourier series. The overshoot has been removed before N reaches 30 terms, while about 40 terms are required to satisfy the criterion of equation (15). Therefore, the analytical solutions can be reasonably regarded as free of Gibbs phenomenon except for the positions in the vicinity of discontinuity.

Two test cases were selected to show the temperature and heat-flux distributions for the test problem with and without temperature-dependent thermal conductivity. The calculation conditions are: $T_0=600$, $T_L=100$, $w=0.5$, $\lambda_{10}=0.06$, and $\lambda_{20}=0.001$.

Test Case 1: temperature-independent thermal conductivity, $\alpha_1=\alpha_2=0$

Test Case 2: temperature-dependent thermal conductivity, $\alpha_1=0.0006$ and $\alpha_2=0.00001$

Presented in Fig. 3 is the comparison of temperature contours of Test Cases 1 and 2. Since the given value of α_1 is much higher than that of α_2 (by 60 times), this given condition enhances the heat-conduction rate, particularly in the high-temperature regions, and then leads to the situation shown in Fig. 3 where the upper-left part of the test problem becomes hotter in Test Case 2 than in Test Case 1. This is also clearly seen in Fig. 4, which compares distributions of the heat-flux component along the x coordinate of Test Cases 1 and 2. The comparisons of the results, shown in Figs. 3 and 4, reveal that there do exist significant differences in the distributions of temperature and heat flux between those cases, the constant thermal conductivity and the variable one. The present method provides a unique and viable analytical tool for solutions of heat conduction problems in a composite slab.

References

Eckert, E. R. G., and Irving, T. F., 1971, *Progress in Heat and Mass Transfer*, Vol. 3, Pergamon, Oxford, United Kingdom.

Eckert, E. R. G., and Irving, T. F., 1977, *Progress in Heat and Mass Transfer*, Vol. 8, Pergamon, Oxford, United Kingdom.

Halle, H., 1965, "Exact Solution of Elementary Transient Heat Conduction Problem Involving Temperature-Dependent Properties," ASME JOURNAL OF HEAT TRANSFER, Vol. 87, pp. 420–421.

Lanczos, C., 1956, *Applied Analysis*, Chap. 4, Prentice-Hall, Englewood Cliffs, NJ.

Özişik, M. N., 1980, *Heat Conduction*, Chap. 11, Wiley, NY.

Peletier, L. A., 1970, "Asymptotic Behavior of Temperature Profiles of a Class of Nonlinear Heat Conduction Problems," *Quart J. Mech. Appl. Math.*, Vol. 23, pp. 441–447.

Suzuki, M., Matsumoto, S., and Maeda, S., 1977, "New Analytical Method for a Nonlinear Diffusion Problem," *Int. J. Heat Mass Transfer*, Vol. 20, pp. 883–889.

Tao, L. N., 1989, "The Heat Conduction Problem With Temperature-Dependent Material Properties," *Int. J. Heat Mass Transfer*, Vol. 32, pp. 487–491.

A New Criterion for Assuming Negligible Internal Thermal Resistance in Transient Heat Conduction Problem

B. P. A. Grandjean[1] and J. Thibault[1]

Nomenclature

A = surface area, m^2
$A()$ = transcendental summation term
Bi = Biot number $=hL/k$ or hR/k
Fo = Fourier number $=\alpha t/L^2$ or $\alpha t/R^2$
h = heat transfer coefficient, W/(m^2K)
J_0, J_1 = Bessel functions
k = thermal conductivity, W/m K
L = half-thickness of the infinite flat plate, m
m = geometric parameter
Pd = Predvoditelev number $=L^2/(\alpha\tau)$ or $R^2/(\alpha\tau)$
r = radial position, m
R = radius, m
t = time, s

[1]Department of Chemical Engineering, Laval University, Sainte-Foy, Québec, Canada G1K 7P4.

Contributed by the Heat Transfer Division for publication in the JOURNAL OF HEAT TRANSFER. Manuscript received by the Heat Transfer Division November 6, 1989; revision received May 21, 1990. Keywords: Conduction, Transient and Unsteady Heat Transfer.

T_0 = initial temperature, K
$T\infty$ = steady-state temperature, K
V = volume, m^3
x = distance from the center of the infinite plate, m
α = thermal diffusivity, m^2/s
β = roots of transcendental equation
θ = normalized temperature = $(T - T_0)/(T_\infty - T_0)$
ϕ = normalized position = (x/L) or (r/R)
τ = time constant, s

Subscripts

E = environment or ambient
max = maximum value
n = summation index

Introduction

Heat transfer is a science that has greatly benefited from the development of numerical methods. Solution of complex problems, such as calculation of heat exchangers and heat conduction in solids of irregular geometries that were impossible to solve analytically, can now be obtained numerically. However, in practice, heat transfer remains in many aspects a heuristic science where criteria are used to make appropriate simplifying assumptions. One of these criteria, for conduction problems that involve surface convective effects, is the upper limit of 0.1 imposed on the Biot number to assume a uniform temperature distribution throughout a solid, at any time during the transient process, when it is submitted to a change in convective boundary conditions. This assumption stipulates that the resistance to conduction within a solid is much less than the resistance to convection across the fluid boundary layer. With this assumption it is possible to solve transient conduction problems with the well-known lumped capacitance method (De Vriendt, 1982; Holman, 1981; Léontinev, 1985; Incropera and DeWitt, 1985). This value of the Biot number was obtained for the case where the surrounding fluid temperature increased as a step function. However, in most real situations, the surrounding fluid temperature will increase at a slower rate and it is reasonable to expect that the upper limit of the Biot number of 0.1 could be relaxed.

In this note analytical solutions for the temperature distribution inside three representative geometries will be derived for the case where the temperature of the surrounding fluid changes according to first-order dynamics. Results for the maximum difference between temperatures obtained with the lumped capacitance method and exact temperature solutions, as a function of the Biot number and the Predvoditelev criterion (Pd), are presented. It is shown that, indeed, the Biot number criterion for a uniform temperature assumption can be relaxed for small values of the Pd criterion.

Analysis

Consider a body that is initially at a uniform temperature T_0 and is subjected to a change in the ambient temperature T_E. It is assumed that T_E varies according to first-order dynamics expressed in normalized temperature by

$$\theta_E = 1 - e^{-(t/\tau)} = 1 - e^{-(\mathrm{Pd}\cdot\mathrm{Fo})} \tag{1}$$

Convection occurs at the surface of the body with a constant heat transfer coefficient h and it is assumed that all physical properties are invariant with time. Two situations are considered: solids of infinite thermal conductivity ($\mathrm{Bi} \ll 1$) and solids with a finite thermal conductivity. For both cases, the heat balance and the boundary conditions needed to obtain the transient temperature in the solid can be found in many textbooks and are not given here.

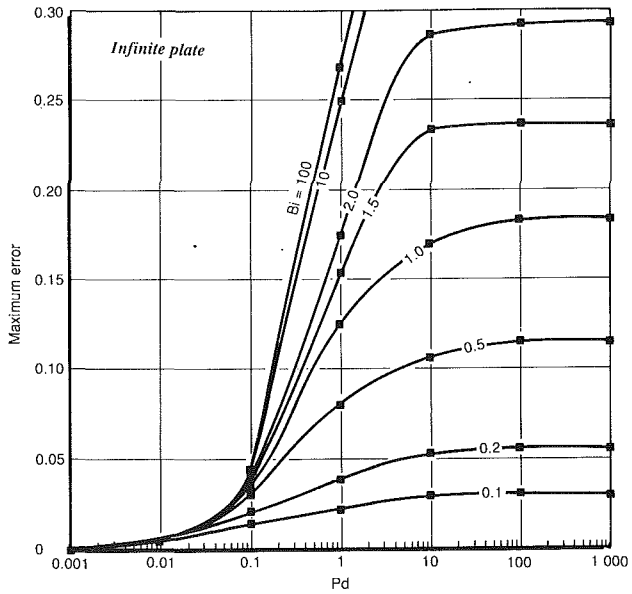

Fig. 1 Maximum temperature error between the exact temperature and the temperature calculated by the lumped capacitance method for an infinite flat plate.

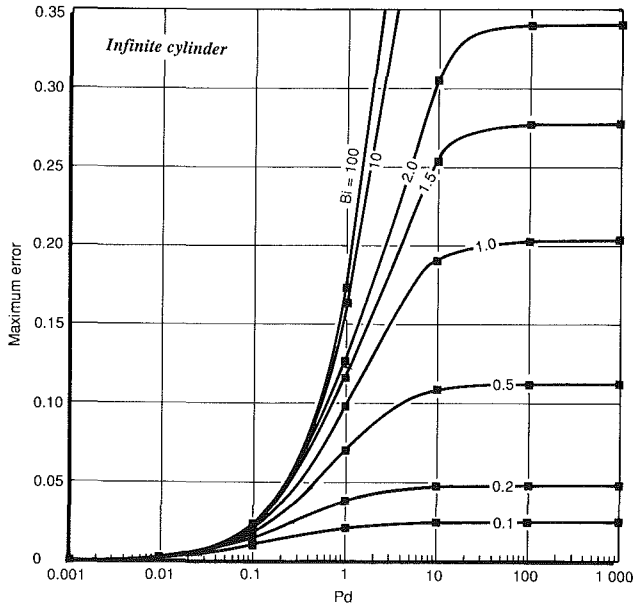

Fig. 2 Maximum temperature error between the exact temperature and the temperature calculated by the lumped capacitance method for an infinite cylinder.

Solids of Infinite Thermal Conductivity. The solution obtained with the lumped capacitance method is the following:

For $m\cdot Bi \neq Pd$

$$\theta = 1 - e^{-(m\cdot\mathrm{Bi}\cdot\mathrm{Fo})} + \frac{e^{-(\mathrm{m}\cdot\mathrm{Bi}\cdot\mathrm{Fo})}}{\left(1 - \dfrac{\mathrm{Pd}}{m\cdot\mathrm{Bi}}\right)} - \frac{e^{-(\mathrm{Fo}\cdot\mathrm{Pd})}}{\left(1 - \dfrac{\mathrm{Pd}}{m\cdot\mathrm{Bi}}\right)} \tag{2}$$

For $m\cdot Bi = Pd$

$$\theta = 1 - (1 + m\cdot\mathrm{Bi}\cdot\mathrm{Fo})e^{-(m\cdot\mathrm{Bi}\cdot\mathrm{Fo})} \tag{3}$$

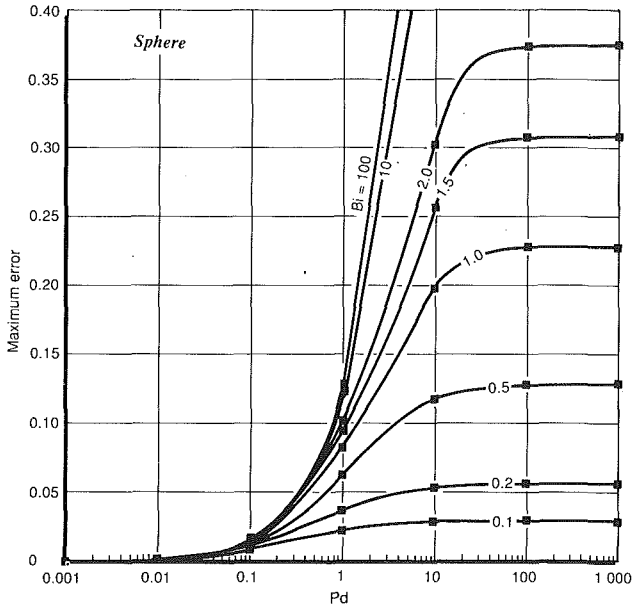

Fig. 3 Maximum temperature error between the exact temperature and the temperature calculated by the lumped capacitance method for a sphere.

The parameter m in equations (2) and (3) is the geometric factor of the solid considered. It is the factor appearing in the ratio of the volume of the body to the surface area. The three geometries considered in this study are respectively the infinite plate of thickness $2L$, the infinite cylinder of radius R, and the sphere of radius R. The values of m are equal respectively to 1, 2, and 3.

Solids With Finite Thermal Conductivity. When both convective and conductive resistances are important ($0.1 < \mathrm{Bi} < 100$), the heat balance can be solved by two methods: the Laplace transformation (Luikov, 1968) and Duhamel's superposition integral (Carslaw and Jaeger, 1959; Arpaci, 1966). The latter method gives the following compact set of equations:

$$\theta = [1 - e^{-(\mathrm{Pd}\cdot\mathrm{Fo})}] + \sum_{n=1}^{\infty} A_n(\phi) \frac{[e^{-(\mathrm{Pd}\cdot\mathrm{Fo})} - e^{-(\beta_n^2\cdot\mathrm{Fo})}]}{\left(1 - \frac{\beta_n^2}{\mathrm{Pd}}\right)} \tag{4}$$

where $A_n(\phi)$ and β_n are dependent on solid geometry.

For an infinite flat plate

$$A_n(\phi) = (-1)^{n+1} \frac{2\mathrm{Bi}\sqrt{\mathrm{Bi}^2 + \beta_n^2}}{\beta_n (\mathrm{Bi}^2 + \mathrm{Bi} + \beta_n^2)} \cos [\beta_n \phi] \tag{5a}$$

$$\beta_n \text{ is the solution of } \beta = \mathrm{Bi} \cot (\beta) \tag{5b}$$

For an infinite cylinder

$$A_n(\phi) = \frac{2J_1(\beta_n)}{\beta_n [J_0^2(\beta_n) + J_1^2(\beta_n)]} J_0(\beta_n \phi) \tag{6a}$$

$$\beta_n \text{ is the solution of } J_1(\beta) = \mathrm{Bi} J_0(\beta) \tag{6b}$$

For a sphere

$$A_n(\phi) = \frac{4\ [\sin \beta_n - \beta_n \cos \beta_n]}{2\beta_n - \sin (2\beta_n)} \cdot \frac{\sin (\beta_n \phi)}{\beta_n \phi} \tag{7a}$$

$$\beta_n \text{ is the solution of } 1 - \beta \cot (\beta) = \mathrm{Bi} \tag{7b}$$

Results and Discussion

The main objective of this note is to investigate under which conditions the lumped capacitance method is valid when the change in the surrounding temperature adopts first-order dynamics rather than the traditional step function increase. Results are reported in terms of maximum temperature differences between equations (2) or (3), where an infinite heat conductance is assumed, and equation (4) where the exact temperature profile is calculated. By virtue of the differential equation involved and the resulting parabolic profile, the maximum temperature difference will either be located at the boundary of the solid ($\phi = 1$) or on the symmetry line ($\phi = 0$). It is, therefore, sufficient to examine the time-dependent temperature at these two points to determine the maximum difference.

For a wide range of Predvoditelev and Biot numbers, the maximum temperature differences are presented in Figs. 1–3, respectively, for an infinite flat plate, an infinite cylinder, and a sphere. For all geometries considered, if the Predvoditelev number is greater than 100 (that is, corresponding to small time constants in the change of the ambient fluid temperature), the maximum error is constant and identical to the one obtained with a step change. For a Pd number of 0.1 or less and for large Biot numbers, the maximum temperature difference is always less than 4.5, 2.3, and 1.6 percent, respectively, for an infinite flat plate, an infinite cylinder, and a sphere. For a Pd number of less than 0.01, the error is negligible for all Biot numbers. The Predvoditelev number thus provides an additional criterion, along with the Biot number, to judge whether the thermal transient can be evaluated adequately with the lumped capacitance method.

This new criterion does not invalidate the Biot criterion for opting for the lumped capacitance method rather than the exact solution. The Pd criterion simply extends the range of validity of the lumped capacitance method in situations where the ambient temperature changes progressively. Figures 1–3 can also serve as charts to determine the maximum error incurred when the lumped capacitance method is used instead of the exact solution.

Conclusion

This note has presented an analysis of a transient heat conduction problem when the surface of a solid is exposed to a convective boundary condition changing according to first-order dynamics. Temperatures obtained with the exact solution for three representative geometries have been compared with the solution obtained with the lumped capacitance method.

A new criterion, the Predvoditelev number (Pd), has been suggested to help in deciding when it is safe to use the lumped capacitance method to calculate the temperature transient with sufficient accuracy. The value of 0.1 of the Biot number still remains the primary criterion to use. The Pd number simply extends the range of validity to higher Biot numbers when the change in convective boundary conditions is more gradual than a step change. It is shown that for all Biot numbers the lumped capacitance method can be safely used for Pd number of less than 0.1.

References

Arpaci, V. S., 1966, *Conduction Heat Transfer,* Addison and Wesley, New York.

Carslaw, H. S., and Jaeger, J. C., 1959, *Conduction of Heat in Solids,* Oxford University Press, United Kingdom.

De Vriendt, A. B., 1982, *La transmission de la chaleur,* Vol. 1, Gaëtan Morin Editeur, Canada.

Holman, J. P., 1981, *Heat Transfer,* McGraw-Hill, New York.

Incropera, F. P., and DeWitt, D. P., 1985, *Introduction to Heat Transfer,* Wiley, New York.

Léontinev, A., 1985, *Théorie des échanges de chaleur et de masse,* Editions MIR, Moscow, USSR.

Luikov, A. V., 1968, *Analytical Temperature Distribution,* Academic Press, New York.

Thermal Shock Formation in a Three-Dimensional Solid Around a Rapidly Moving Heat Source

D. Y. Tzou[1]

Nomenclature

c = $v/2\alpha$ = parameter used in the thermal wave equation, 1/m
C = speed of heat propagation in the solid, m/s
C_p = heat capacity, kJ/kg-K
f = transformation on the dependent variables
f_g = Green's function used in the subsonic and supersonic cases
G = Green's function for the transformed equation of f
I_n = modified Bessel function of the first kind of order n
k = thermal conductivity, W/m-K
M = v/C = thermal Mach number
q, q_i = heat flux vector and its components, W/m^2; $i=1, 2, 3$
Q = intensity of the heat source, W/m
r = transformation function for the independent variables, m
R = radial distance from the heat source, m
S = general heat source term, W/m
t = physical time, s
T = temperature, K
T_g = Green's function for the transonic case
v = speed of the moving heat source, m/s
x_i = stationary coordinates, m; $i=1, 2, 3$
α = thermal diffusivity, m^2/s
δ = Dirac delta function
η_i = position of the point heat source, m; $i=1, 2, 3$
θ = angle in the polar coordinate system, deg
θ_M = thermal shock angle, deg
ξ_i = moving coordinates with the heat source, m; $i=1, 2, 3$
ρ = mass density, kg/m^3
∇ = gradient operator, 1/m
$(\ )_{,i}$ = $\partial/\partial\xi_i$; $i=1, 2, 3$
$(\bar{\ })$ = dimensionless quantity

Introduction

The thermal shock wave studied in this work results from the accumulation of thermal energy in a *preferential* direction around a rapidly moving heat source in the solid. It is a physical phenomenon pertinent to the thermal wave model and cannot be depicted by the classical diffusion theory. In a series of recent studies made by Tzou (1989a, 1989b, 1989c, 1990a, 1990b), the formation of thermal shock waves in a two-dimensional solid with finite speed of heat propagation has been studied for both a moving heat source (Tzou, 1989a, 1989c) and a rapidly propagating crack (Tzou, 1990a, 1990b). The thermal shock formation was examined in these works via both the temperature and the flux formulations. Due to the presence of the thermal shock waves, the thermoelastic fracture pattern around the moving heat source is significantly different from that predicted by the traditional diffusion theory (Tzou, 1989b).

The present work further extends the thermal shock theory to a three-dimensional solid. The energy equation with temperature representation will be considered in the analysis. Because the effect of the finite wave speed intrinsically varies the mathematical type of the energy equation, the temperature distributions will be obtained individually in the subsonic, transonic, and supersonic ranges (Tzou, 1989a). In a similar manner to the two-dimensional problems, the hypo-variable transformations will be applied to reduce the three-dimensional energy equation to a one-dimensional equation. The Green's functions for the one-dimensional equations in the hypo-space are then sought to yield analytical expressions for temperature, which facilitates an exact description on the thermal shock formation around a rapidly moving heat source.

Under an intensified thermal irradiation through a localized area, the irreversible physical processes such as crack or yield initiation around a point heat source may occur in a much shorter time interval than that required for the diffusion behavior to be retrieved (Sih and Tzou, 1986), and consideration of the wave nature in the process of heat transport is necessary. The thermal shock formation is indeed a physical phenomenon resulting from such a consideration.

Temperature Formulation

Without loss in generality, a point heat source is assumed to move along the positive x_1 axis at a constant speed, as shown in Fig. 1. At a certain time instant, the thermal wavefront is spherical due to the finite speed of heat propagation. The energy equation with temperature representation can be written as (Tzou, 1989a)

$$\alpha\nabla^2 T-(\alpha/C^2)T_{,tt}-T_{,t}=-(Q/\rho C_p)[\delta(x_1-vt)+(\alpha/C^2)\delta_{,t}(x_1-vt)]\delta(x_2)\delta(x_3) \quad (1)$$

To an observer moving with the heat source, equation (1) can be further expressed in terms of the material coordinates ξ_i, for $i=1$, 2, and 3. Through the Galiléi transformation

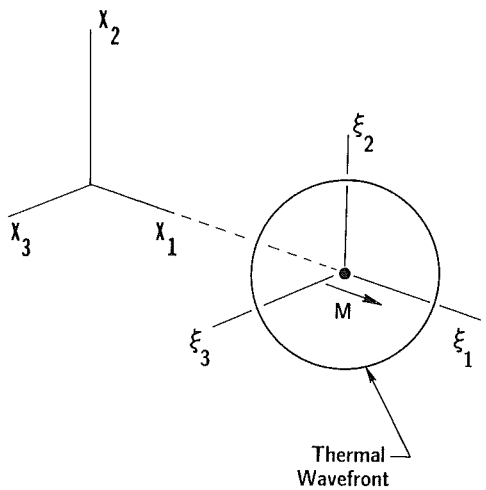

Fig. 1 Spherical thermal wavefront emanating from a moving heat source and the coordinate system

[1]Assistant Professor, Department of Mechanical Engineering, University of New Mexico, Albuquerque, NM 87131.

Contributed by the Heat Transfer Division for publication in the JOURNAL OF HEAT TRANSFER. Manuscript received by the Heat Transfer Division July 3, 1989; revision received February 5, 1990. Keywords: Conduction, Laser Processing.

$$x_1 = \xi_1 + vt, \qquad x_2 = \xi_2, \qquad x_3 = \xi_3 \tag{2}$$

Then, equation (1) can be written as

$$\alpha[(1-M^2)T_{,11} + T_{,22} + T_{,33}] + 2c\alpha T_{,1} = -(Q/\rho C_p)[\delta(\xi_1) - (M^2/2c)\delta_{,1}(\xi_1)]\delta(\xi_2)\delta(\xi_3) \tag{3}$$

where $M = v/C$ is the thermal Mach number of the moving heat source with reference to the speed of heat propagation in the solid and c a parameter defined as $v/2\alpha$.

The thermal Mach number M appears in the *highest* order differentials in equation (3) and intrinsic variation of temperature from the *subsonic* ($M<1$), *transonic* ($M=1$), to the *supersonic* ($M>1$) ranges are expected. In the sequel, therefore, the temperature distributions are to be obtained individually in the respective range of the thermal Mach number. In all cases, the physical quantities are assumed to vanish at infinity.

(a) Subsonic Case With $M<1$. Consider the hypo-variables transforming the dependent variable from $T(\xi_i)$ to $f(\xi_i)$ and the independent variables from ξ_i to r:

$T(\xi_i) = \exp[-c\xi_1/(1-M^2)]\, f(\xi_i)$ and

$$r = \sqrt{\xi_1^2/(1-M^2) + \xi_2^2 + \xi_3^2}, \text{ for } M<1 \tag{4}$$

Equation (3) can be reduced to a one-dimensional equation in the hypospace r:

$$f_{,rr} + \frac{2}{r} f_{,r} - [c^2/(1-M^2)]\, f = \exp[c\xi_1/(1-M^2)] \left\{ -(Q/\rho C_p\alpha)\delta(\xi_1) + (QM^2/2c\rho C_p\alpha)\delta_{,1}(\xi_1) \right\} \delta(\xi_2)\delta(\xi_3), \quad M<1 \tag{5}$$

In addition to the terms containing $\delta(\xi_3)$ due to the extra dimensionality, the coefficient in front of $f_{,r}$ changes from $1/r$ for the two-dimensional problem to $2/r$ in the present three-dimensional formulation. Equation (5) is governed by a generalized Bessel operator (Hildebrand, 1974) whose Green's function can be obtained as

$$f_g(r|r_\eta) = A\{\cosh[c|r-r_\eta|/(1-M^2)^{1/2}] - \sinh[c|r-r_\eta|/(1-M^2)^{1/2}]\}/c|r-r_\eta| \tag{6}$$

By noticing the integral properties of the Dirac-delta functions (Morse and Feshbach, 1953)

$$\int G[r(\xi_1, \xi_2, \xi_3)|r_\eta(\eta_1, \eta_2, \eta_3)]\delta(\eta_1)\delta(\eta_2)\delta(\eta_3)d\eta_1 d\eta_2 d\eta_3 = G[r(\xi_1, \xi_2, \xi_3)|r_\eta(0, 0, 0)]$$

$$\int G[r(\xi_1, \xi_2, \xi_3)|r_\eta(\eta_1, \eta_2, \eta_3)]\delta_{,1}(\eta_1)\delta(\eta_2)\delta(\eta_3)d\eta_1 d\eta_2 d\eta_3 = -\left\{\frac{\partial}{\partial\eta_1} G[r(\xi_1, \xi_2, \xi_3)|r_\eta(\eta_1, 0, 0)]\right\}_{\eta_1 - 0} \tag{7}$$

the solution of equation (5) for $f(r)$ can be integrated directly to give

$$f(r(\xi_i)) = (Q/\rho\alpha C_p)\{\cosh[cr/(1-M^2)^{1/2}] - \sinh[cr/(1-M^2)^{1/2}]\} \cdot [2cr(1-M^2)^{1/2} + M^2]/[2c^2r^2] \tag{8}$$

which yields, from equation (4) for the inverse transform

$$T(\xi_i)/(Q/\rho\alpha C_p) = \exp[-c\xi_1/(1-M^2)]\{\cosh[cr/(1-M^2)^{1/2}] - \sinh[cr/(1-M^2)^{1/2}]\} - [2cr(1-M^2)^{1/2} + M^2]/[2c^2r^2], \quad \text{for } M<1 \tag{9}$$

(b) Supersonic Case With $M>1$. When the heat source is moving with a speed faster than the thermal wave speed in the solid, equation (3) can be arranged in the following form:

$$\alpha[(M^2-1)T_{,11} - T_{,22} - T_{,33}] - 2c\alpha T_{,1} = (Q/\rho C_p)\{\delta(\xi_1) - (M^2/2c)\delta_{,1}(\xi_1)\}\delta(\xi_2)\delta(\xi_3) \tag{10}$$

The hypo-variable transformations in this case are

$T(\xi_i) = \exp[c\xi_1/(M^2-1)]f(\xi_i)$, and

$$r = [\xi_1^2/(M^2-1) - \xi_2^2 - \xi_3^2]^{1/2}, \text{ for } M>1 \tag{11}$$

and the corresponding equation governing the function of $f(\xi_i)$ becomes

$$f_{,rr} + \frac{2}{r} f_{,r} - [c^2/(M^2-1)]f = (Q/\rho C_p\alpha)\exp[-c\xi_1/(M^2-1)]\{\delta(\xi_1) - (M^2/2c)\delta_{,1}(\xi_1)\}\delta(\xi_2)\delta(\xi_3) \tag{12}$$

whose Green's function can be found as

$$f_g(r|r_\eta = A\{\cosh[c|r-r_\eta|/(M^2-1)^{1/2}] - \sinh[c|r-r_\eta|/(M^2-1)^{1/2}]\}/c|r-r_\eta| \tag{13}$$

By employing the same procedure as that used in the previous case, then, the temperature distribution in the supersonic range can be obtained as

$$T(\xi_i)/(Q/\rho\alpha C_p) = \exp[c\xi_1/(M^2-1)]\{\cosh[cr/(M^2-1)^{1/2}] - \sinh[cr/(M^2-1)^{1/2}]\} \cdot [2cr(2M^2-1) + M^2(M^2-1)^{1/2}]/[2c^2r^2(M^2-1)^{1/2}], \text{ for } M>1 \tag{14}$$

The applicable range of equation (14), unlike the subsonic case, is restricted to the domain of

$$\xi_1^2/(M^2-1) \geq \xi_2^2 + \xi_3^2 \tag{15}$$

such that the variable r in equation (11) is well defined. The equality in equation (15) represents a quasi-hyperboloid surface with its vertex coincident with the moving heat source at $\xi_i = 0$. On a plane with ξ_3 being a parametric constant, it represents a hyperbola with asymptotes $\xi_1^2/(M^2-1) - \xi_2^2 = 0$, which are the thermal shock surface generated in a two-dimensional solid with $\xi_3 = 0$ (Tzou, 1989a). In terms of the polar coordinates, it depicts a thermal shock wave inclining an angle of $\sin^{-1}(1/M)$ to the trailing edge of the moving heat source. By the same argument made in the previous work (Tzou, 1989a, 1989c), therefore, equation (15) represents the physical domain of the *heat-affected zone* in the three-dimensional solid within which the temperature distribution is given by equation (14). In the rest of the physical domain out of that specified by equations (15), because the thermal waves propagate at a finite speed, the material points thereby can not sense the presence of the heat source and the temperature stays at the reference value. Such a physical domain is therefore defined as the *thermally undisturbed zone*. When the thermal shock surface is approached from the site in the heat affected zone, the value of r approaches zero and the temperature represented by equation (14) approaches infinity. When the thermal shock surface is approached from the site in the thermally undisturbed zone, on the other hand, the temperature stays at the reference value and a discontinous variation of temperature across the shock surface is obvious. Note that the infinite value of temperature at the shock surface results from the mathematical singularity of the Dirac-delta functions.

(c) Transonic Case With $M=1$. As the heat source moves at the same speed as the heat propagation speed in the solid, a normal shock wave exists at $\xi_1 = 0$ according to equation (15). The heat-affected zone is confined to the domain of $\xi_1 < 0$ for a heat source moving along the positive x_1 axis. In this case, equation (10) is degenerated into a diffusion equation in the (ξ_2, ξ_3) space with ξ_1 replacing the position of the time variable:

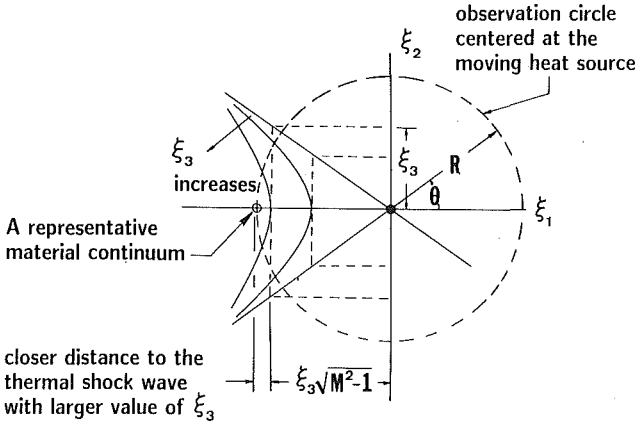

Fig. 2 The stronger influence of the temperature singularity existing at the thermal shock surface with a larger value of ξ_3 on the temperature level in a material volume on the circle for observations

$$T_{,22}+T_{,33}+2cT_{,1}=-(Q/\rho\alpha C_p)\{\delta(\xi_1) - (1/2c)\delta_{,1}(\xi_1)\}\delta(\xi_2)\delta(\xi_3) \quad (16)$$

The Green's function for equation (16) can be found as (Morse and Feshbach, 1953)

$$T_g(\xi_i|\eta_i)=[1/(4\pi c)]\exp\{c[(\xi_2-\eta_2)^2 + (\xi_3-\eta_3)^2]/2|\xi_1-\eta_1|\}/[|\xi_1-\eta_1|]^{1/2} \quad (17)$$

and the temperature distribution in the heat affected zone ($\xi_1<0$) can be integrated to give:

$$T(\xi_i)/(Q/\rho\alpha C_p)=-[1/(4\pi c)]\exp[c(\xi_2^2+\xi_3^2)/2\xi_1]\{1/\xi_1 + [c(\xi_2^2+\xi_3^2)+2\xi_1]/4c\xi_1^3\},\ \text{for } \xi_1<0 \quad (18)$$

Similar to the supersonic case with $M>1$, the temperature represented by equation (18) has a singularity at the thermal shock surface $\xi_1=0$.

Results and Discussion

In the respective range of the thermal Mach number, the temperature field induced by a moving heat source has been obtained in the subsonic range with $M<1$, equation (9), at the transonic stage with $M=1$, equation (18), and in the supersonic range with $M>1$, equation (14). Due to the accumulation of thermal energy in a preferential direction, thermal shock waves tend to form at the transonic and in the supersonic ranges with $M\geq 1$, which separate the heat-affected zone from the thermally undisturbed zone in the physical domain. The geometry of the thermal shock wave has been obtained as a quasi-hyperboloid surface represented by $\xi_1^2/(M^2-1)=\xi_2^2+\xi_3^2$. Because the thermal shock surface on the ξ_1–ξ_2 plane with ξ_3 being zero is identical to that in the two-dimensional problem, the temperature distributions are comparable with the two-dimensional results. Through the graphic representations for the temperature distributions, it is perceived that the two-dimensional analysis *overestimates* the temperature level in the heat-affected zone.

In the supersonic range the $M>1$, the near-field temperature *increases* with the distance ξ_3 away from the heat source is a salient feature in the three-dimensional analysis. This unusual trend can be observed qualitatively from equations (11) and (14). As the value of ξ_3 increases, the value of r decreases according to equation (11). Consequently, the difference of the hyper-cosine and -sine functions in equation (14) and the ratio of the bracketed quantities followed increases, which results in an increasing temperature level in the heat-affected zone. The physical interpretation for this phenomenon lies in the thermal shock formation as shown in Fig. 2. As the value of ξ_3 increases, the lengths of both the major and minor axes of the hyperbola increase. By noticing that the hyperbolic surface is indeed the thermal shock surface where the temperature approaches a large value, it reveals that the material continuum at a fixed location on the circle for observation is *closer* to the thermal shock wave with a larger value of ξ_3. As a result, the local temperature level in the heat-affected zone is higher and in terms of angle θ, the physical domain of the heat-affected zone is narrower.

Experimental verifications for the thermal shock formation in the solid are evidently needed. Along with the previous development (Tzou, 1989a, 1989b, 1989c, 1990a, 1990b), the present analysis further fulfills the physical contents of the thermal shock theory such that the potential measures for the experimental confirmation for the thermal shock phenomena could be identified.

References

Hildebrand, F. B., 1974, *Advanced Calculus for Applications*, Prentice-Hall, New York, Chap. 4, p. 155.

Morse, P. M., and Feshbach, H., 1953, *Methods of Theoretical Physics*, Vol. 1, Chap. 7, McGraw-Hill, New York, pp. 837, 857–865.

Sih, G. C., and Tzou, D. Y., 1986, "Arrest Characteristics of an Impacted Crack Dissipating Plastic Energy," *Journal of Theoretical and Applied Fracture Mechanics*, Vol. 6, pp. 29–37.

Tzou, D. Y., 1989a, "On the Thermal Shock Waves Induced by a Moving Heat Source," ASME JOURNAL OF HEAT TRANSFER, Vol. 111, pp. 232–238.

Tzou, D. Y., 1989b, "Thermoelastic Fracture Induced by the Thermal Shock Waves Around a Moving Heat Source," *Heat Transfer in Manufacturing and Materials Processing*, ASME HTD-Vol. 113, pp. 11–17.

Tzou, D. Y., 1989c, "Shock Wave Formation Around a Moving Heat Source in a Solid With Finite Speed of Heat Propagation," *International Journal of Heat and Mass Transfer*, Vol. 32, pp. 1979–1987.

Tzou, D. Y., 1990a, "Thermal Shock Waves Induced by a Moving Crack," ASME JOURNAL OF HEAT TRANSFER, Vol. 112, pp. 21–27.

Tzou, D. Y., 1990b, "Thermal Shock Waves Induced by a Moving Crack—A Heat Flux Formulation," *International Journal of Heat and Mass Transfer*, Vol. 33, pp. 877–885.

A Note on the Interface Condition in Phase Change Problems

L. J. Huang,[1,2] P. S. Ayyaswamy,[3] and I. M. Cohen[1]

Introduction

In this note the fundamental relations to be satisfied at the solid–liquid interface for phase-change problems are examined. The attention is focused on situations in which melting (or solidification) takes place at a discrete melting point temperature and, as a result, the solid and liquid phases are separated by a sharp interface. The interface condition appropriate for a general nonorthogonal curvilinear coordinate system has been developed. The result is suitable for studying various problems of practical interest where the formulation in terms of general nonorthogonal curvilinear coordinates is either required or convenient.

A specific example wherein the relationships derived in this note have proved useful is in the wire melting, ball roll-up,

[1]Department of Mechanical Engineering and Applied Mechanics, University of Pennsylvania, Philadelphia, PA 19104-6315; Mem. ASME.

[2]Present address: Harrison Division, General Motors, Lockport, NY.

[3]Department of Mechanical Engineering and Applied Mechanics, University of Pennsylvania, Philadelphia, PA 19104-6315; Fellow ASME.

Contributed by the Heat Transfer Division for publication in the JOURNAL OF HEAT TRANSFER. Manuscript received by the Heat Transfer Division September 4, 1989; revision received April 12, 1990. Keywords: Conduction, Moving Boundaries, Phase-Change Phenomena.

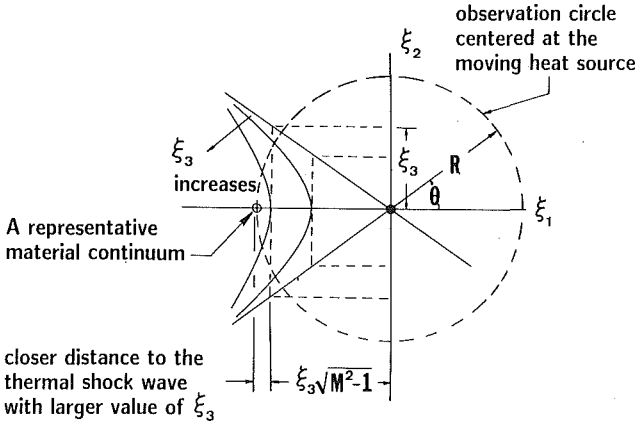

Fig. 2 The stronger influence of the temperature singularity existing at the thermal shock surface with a larger value of ξ_3 on the temperature level in a material volume on the circle for observations

$$T_{,22}+T_{,33}+2cT_{,1}=-(Q/\rho\alpha C_p)\{\delta(\xi_1) - (1/2c)\delta_{,1}(\xi_1)\}\delta(\xi_2)\delta(\xi_3) \quad (16)$$

The Green's function for equation (16) can be found as (Morse and Feshbach, 1953)

$$T_g(\xi_i|\eta_i)=[1/(4\pi c)]\exp\{c[(\xi_2-\eta_2)^2 + (\xi_3-\eta_3)^2]/2|\xi_1-\eta_1|\}/[|\xi_1-\eta_1|]^{1/2} \quad (17)$$

and the temperature distribution in the heat affected zone ($\xi_1<0$) can be integrated to give:

$$T(\xi_i)/(Q/\rho\alpha C_p)=-[1/(4\pi c)]\exp[c(\xi_2^2+\xi_3^2)/2\xi_1]\{1/\xi_1 + [c(\xi_2^2+\xi_3^2)+2\xi_1]/4c\xi_1^3\},\ \text{for } \xi_1<0 \quad (18)$$

Similar to the supersonic case with $M>1$, the temperature represented by equation (18) has a singularity at the thermal shock surface $\xi_1=0$.

Results and Discussion

In the respective range of the thermal Mach number, the temperature field induced by a moving heat source has been obtained in the subsonic range with $M<1$, equation (9), at the transonic stage with $M=1$, equation (18), and in the supersonic range with $M>1$, equation (14). Due to the accumulation of thermal energy in a preferential direction, thermal shock waves tend to form at the transonic and in the supersonic ranges with $M\geq 1$, which separate the heat-affected zone from the thermally undisturbed zone in the physical domain. The geometry of the thermal shock wave has been obtained as a quasi-hyperboloid surface represented by $\xi_1^2/(M^2-1)=\xi_2^2+\xi_3^2$. Because the thermal shock surface on the ξ_1–ξ_2 plane with ξ_3 being zero is identical to that in the two-dimensional problem, the temperature distributions are comparable with the two-dimensional results. Through the graphic representations for the temperature distributions, it is perceived that the two-dimensional analysis *overestimates* the temperature level in the heat-affected zone.

In the supersonic range the $M>1$, the near-field temperature *increases* with the distance ξ_3 away from the heat source is a salient feature in the three-dimensional analysis. This unusual trend can be observed qualitatively from equations (11) and (14). As the value of ξ_3 increases, the value of r decreases according to equation (11). Consequently, the difference of the hyper-cosine and -sine functions in equation (14) and the ratio of the bracketed quantities followed increases, which results in an increasing temperature level in the heat-affected zone. The physical interpretation for this phenomenon lies in the thermal shock formation as shown in Fig. 2. As the value of ξ_3 increases, the lengths of both the major and minor axes of the hyperbola increase. By noticing that the hyperbolic surface is indeed the thermal shock surface where the temperature approaches a large value, it reveals that the material continuum at a fixed location on the circle for observation is *closer* to the thermal shock wave with a larger value of ξ_3. As a result, the local temperature level in the heat-affected zone is higher and in terms of angle θ, the physical domain of the heat-affected zone is narrower.

Experimental verifications for the thermal shock formation in the solid are evidently needed. Along with the previous development (Tzou, 1989a, 1989b, 1989c, 1990a, 1990b), the present analysis further fulfills the physical contents of the thermal shock theory such that the potential measures for the experimental confirmation for the thermal shock phenomena could be identified.

References

Hildebrand, F. B., 1974, *Advanced Calculus for Applications*, Prentice-Hall, New York, Chap. 4, p. 155.

Morse, P. M., and Feshbach, H., 1953, *Methods of Theoretical Physics*, Vol. 1, Chap. 7, McGraw-Hill, New York, pp. 837, 857–865.

Sih, G. C., and Tzou, D. Y., 1986, "Arrest Characteristics of an Impacted Crack Dissipating Plastic Energy," *Journal of Theoretical and Applied Fracture Mechanics*, Vol. 6, pp. 29–37.

Tzou, D. Y., 1989a, "On the Thermal Shock Waves Induced by a Moving Heat Source," ASME JOURNAL OF HEAT TRANSFER, Vol. 111, pp. 232–238.

Tzou, D. Y., 1989b, "Thermoelastic Fracture Induced by the Thermal Shock Waves Around a Moving Heat Source," *Heat Transfer in Manufacturing and Materials Processing*, ASME HTD-Vol. 113, pp. 11–17.

Tzou, D. Y., 1989c, "Shock Wave Formation Around a Moving Heat Source in a Solid With Finite Speed of Heat Propagation," *International Journal of Heat and Mass Transfer*, Vol. 32, pp. 1979–1987.

Tzou, D. Y., 1990a, "Thermal Shock Waves Induced by a Moving Crack," ASME JOURNAL OF HEAT TRANSFER, Vol. 112, pp. 21–27.

Tzou, D. Y., 1990b, "Thermal Shock Waves Induced by a Moving Crack—A Heat Flux Formulation," *International Journal of Heat and Mass Transfer*, Vol. 33, pp. 877–885.

A Note on the Interface Condition in Phase Change Problems

L. J. Huang,[1,2] P. S. Ayyaswamy,[3] and I. M. Cohen[1]

Introduction

In this note the fundamental relations to be satisfied at the solid–liquid interface for phase-change problems are examined. The attention is focused on situations in which melting (or solidification) takes place at a discrete melting point temperature and, as a result, the solid and liquid phases are separated by a sharp interface. The interface condition appropriate for a general nonorthogonal curvilinear coordinate system has been developed. The result is suitable for studying various problems of practical interest where the formulation in terms of general nonorthogonal curvilinear coordinates is either required or convenient.

A specific example wherein the relationships derived in this note have proved useful is in the wire melting, ball roll-up,

[1]Department of Mechanical Engineering and Applied Mechanics, University of Pennsylvania, Philadelphia, PA 19104-6315; Mem. ASME.

[2]Present address: Harrison Division, General Motors, Lockport, NY.

[3]Department of Mechanical Engineering and Applied Mechanics, University of Pennsylvania, Philadelphia, PA 19104-6315; Fellow ASME.

Contributed by the Heat Transfer Division for publication in the JOURNAL OF HEAT TRANSFER. Manuscript received by the Heat Transfer Division September 4, 1989; revision received April 12, 1990. Keywords: Conduction, Moving Boundaries, Phase-Change Phenomena.

and subsequent solidification aspects of ball bonding in the packaging of microelectronic semiconductor chips. Depending on the material and detailed boundary conditions, we have successfully tracked phase-change interfaces of different shapes. A brief description of this example has been included in this note.

Theory

Consider a phase-change circumstance wherein the solid and liquid phases are separated by a sharp interface. Let this interface be defined by the equation

$$F(x, y, z, t)=0 \tag{1}$$

in a Cartesian system (x, y, z). The fundamental relations at such an interface should express the following facts: (*i*) The temperatures of the adjacent phases should be equal to the melting (or solidification) temperature, T_m, and (*ii*) an energy balance between conduction and latent heat must be satisfied. These conditions are

$$\left.\begin{aligned} T_s(x, y, z, t)=T_l(x, y, z, t)=T_m \qquad (2)\\ k_s\frac{\partial T_s}{\partial n}-k_l\frac{\partial T_l}{\partial n}=\rho_s\lambda v_n \qquad (3)\end{aligned}\right\} \text{ at } F(x, y, z, t)=0$$

where n denotes the normal at the interface, T, k, ρ, λ, and v_n are temperature, thermal conductivity, density, latent heat, and normal component of the velocity of the interface motion, and the subscripts s and l denote the solid and liquid phases, respectively.

In the development of analytical solutions and for numerical work, it is useful to simplify equation (3) with the aid of equation (2). This has been done in the literature for several special coordinate systems (Carslaw and Jaeger, 1959; Boley, 1964; Patel, 1968); however, a relationship that is suitable for a general nonorthogonal curvilinear coordinate system has not been developed. It is the purpose of this note to derive a suitable relation appropriate for the general case.

In view of equations (1) and (2), the following relations hold at the interface:

$$\mathbf{n}=\frac{\nabla F}{|\nabla F|}=\frac{\nabla T_i}{|\nabla T_i|}, \qquad i=s \text{ or } l \tag{4}$$

$$\frac{\partial T_i}{\partial n}=\nabla T_i\cdot\mathbf{n}=\frac{\nabla \mathrm{T}_i\cdot\nabla \mathrm{F}}{|\nabla \mathrm{F}|}, \qquad i=s \text{ or } l \tag{5}$$

$$v_n=\mathbf{v}\cdot\mathbf{n}=\frac{\mathbf{v}\cdot\nabla F}{|\nabla F|} \tag{6}$$

The total derivative of equation (1) is defined by

$$\frac{DF}{Dt}=0 \text{ on } F=0$$

or

$$-\frac{\partial F}{\partial t}=\mathbf{v}\cdot\nabla F \tag{7}$$

Substitute equation (7) into equation (6) to get

$$v_n=-\frac{\dfrac{\partial F}{\partial t}}{|\nabla F|} \tag{8}$$

With equations (5) and (8), equation (3) can be expressed in the following form:

$$k_s\nabla T_s\cdot\nabla F-k_l\nabla T_l\cdot\nabla F=-\rho_s\lambda\frac{\partial F}{\partial t} \tag{9}$$

Next, consider a completely general transformation of the form:

$$\left.\begin{aligned}\xi=\xi(x, y, z)\\ \eta=\eta(x, y, z)\\ \zeta=\zeta(x, y, z)\end{aligned}\right\} \tag{10}$$

which can be used to transform the equations from the Cartesian system (x, y, z) to the general nonorthogonal curvilinear system (ξ, η, ζ). Using the chain rule of partial differentiation, the partial derivatives become

$$\begin{bmatrix}\dfrac{\partial}{\partial x}\\ \dfrac{\partial}{\partial y}\\ \dfrac{\partial}{\partial z}\end{bmatrix}=\begin{bmatrix}\xi_x & \eta_x & \zeta_x\\ \xi_y & \eta_y & \zeta_y\\ \xi_z & \eta_z & \zeta_z\end{bmatrix}\begin{bmatrix}\dfrac{\partial}{\partial \xi}\\ \dfrac{\partial}{\partial \eta}\\ \dfrac{\partial}{\partial \zeta}\end{bmatrix} \tag{11}$$

Here the subscripts denote partial differentiation with respect to the pertinent variable. The Jacobian of the transformation is

$$\mathbf{J}=\begin{bmatrix}x_\xi & x_\eta & x_\zeta\\ y_\xi & y_\eta & y_\zeta\\ z_\xi & z_\eta & z_\zeta\end{bmatrix} \tag{12}$$

The determinant of the transformation matrix is

$$\begin{vmatrix}\xi_x & \xi_y & \xi_z\\ \eta_x & \eta_y & \eta_z\\ \zeta_x & \zeta_y & \zeta_z\end{vmatrix}=\frac{1}{\mathbf{J}}\begin{vmatrix}y_\eta z_\zeta-y_\zeta z_\eta & -(x_\eta z_\zeta-x_\zeta z_\eta) & x_\eta y_\zeta-x_\zeta y_\eta\\ -(y_\xi z_\zeta-y_\zeta z_\xi) & x_\xi z_\zeta-x_\zeta z_\xi & -(x_\xi y_\zeta-x_\zeta y_\xi)\\ y_\xi z_\eta-y_\eta z_\xi & -(x_\xi z_\eta-x_\eta z_\xi) & x_\xi y_\eta-x_\eta y_\xi\end{vmatrix} \tag{13}$$

Using equations (11) and (13), we develop the following expressions:

$$\begin{aligned}\nabla T_s\cdot\nabla F=[&a_{11}T_{s,\xi}F_\xi+a_{22}T_{s,\eta}F_\eta+a_{33}T_{s,\zeta}F_\zeta\\ &-a_{12}(T_{s,\xi}F_\eta+T_{s,\eta}F_\xi)-a_{13}(T_{s,\xi}F_\zeta+T_{s,\zeta}F_\xi)\\ &-a_{23}(T_{s,\eta}F_\zeta+T_{s,\zeta}F_\eta)]/\mathbf{J}^2\end{aligned} \tag{14}$$

and

$$\begin{aligned}\nabla T_l\cdot\nabla F=[&a_{11}T_{l,\xi}F_\xi+a_{22}T_{l,\eta}F_\eta+a_{33}T_{l,\zeta}F_\zeta\\ &-a_{12}(T_{l,\xi}F_\eta+T_{l,\eta}F_\xi)-a_{13}(T_{l,\xi}F_\zeta+T_{l,\zeta}F_\xi)\\ &-a_{23}(T_{l,\eta}F_\zeta+T_{l,\zeta}F_\eta)]/\mathbf{J}^2\end{aligned} \tag{15}$$

where

$$a_{11}=(y_\eta z_\zeta-y_\zeta z_\eta)^2+(y_\xi z_\zeta-y_\zeta z_\xi)^2+(y_\xi z_\eta-y_\eta z_\xi)^2 \tag{16}$$

$$a_{22}=(x_\eta z_\zeta-x_\zeta z_\eta)^2+(x_\xi z_\zeta-x_\zeta z_\xi)^2+(x_\xi z_\eta-x_\eta z_\xi)^2 \tag{17}$$

$$a_{33}=(x_\eta y_\zeta-x_\zeta y_\eta)^2+(x_\xi y_\zeta-x_\zeta y_\xi)^2+(x_\xi y_\eta-x_\eta y_\xi)^2 \tag{18}$$

$$a_{12}=(y_\eta z_\zeta-y_\zeta z_\eta)\,(x_\eta z_\zeta-x_\zeta z_\eta)+(y_\xi z_\zeta-y_\zeta z_\xi)\,(x_\xi z_\zeta-x_\zeta z_\xi)+(y_\xi z_\eta-y_\eta z_\xi)\,(x_\xi z_\eta-x_\eta z_\xi) \tag{19}$$

$$a_{13}=(y_\eta z_\zeta-y_\zeta z_\eta)\,(x_\eta y_\zeta-x_\zeta y_\eta)+(y_\xi z_\zeta-y_\zeta z_\xi)\,(x_\xi y_\zeta-x_\zeta y_\xi)+(y_\xi z_\eta-y_\eta z_\xi)\,(x_\xi y_\eta-x_\eta y_\xi) \tag{20}$$

$$a_{23}=(x_\eta y_\zeta-x_\zeta y_\eta)\,(x_\eta z_\zeta-x_\zeta z_\eta)+(x_\xi y_\zeta-x_\zeta y_\xi)\,(x_\xi z_\zeta-x_\zeta z_\xi)+(x_\xi y_\eta-x_\eta y_\xi)\,(x_\xi z_\eta-x_\eta z_\xi) \tag{21}$$

On the other hand, from equation (4)

$$\nabla T_s = \frac{|\nabla T_s|}{|\nabla F|}\nabla F = C_1 \nabla F \tag{22}$$

$$\nabla T_l = \frac{|\nabla T_l|}{|\nabla F|}\nabla F = C_2 \nabla F \tag{23}$$

and we get

$$T_{s,\eta} = \frac{F_\eta}{F_\xi} \cdot T_{s,\xi} \tag{24}$$

$$T_{s,\zeta} = \frac{F_\zeta}{F_\xi} \cdot T_{s,\xi} \tag{25}$$

$$T_{l,\eta} = \frac{F_\eta}{F_\xi} \cdot T_{l,\xi} \tag{26}$$

$$T_{l,\zeta} = \frac{F_\zeta}{F_\xi} \cdot T_{l,\xi} \tag{27}$$

where C_1 and C_2 are functions of (ξ, η, ζ). Substituting equations (24) and (25) into (14), and (26) and (27) into (15):

$$\nabla T_s \cdot \nabla F = T_{s,\xi} F_\xi \left[a_{11} + a_{22}\left(\frac{F_\eta}{F_\xi}\right)^2 + a_{33}\left(\frac{F_\zeta}{F_\xi}\right)^2 - 2a_{12}\frac{F_\eta}{F_\xi} - 2a_{13}\frac{F_\zeta}{F_\xi} - 2a_{23}\frac{F_\eta}{F_\xi}\frac{F_\zeta}{F_\xi}\right]/\mathbf{J}^2 \tag{28}$$

$$\nabla T_l \cdot \nabla F = T_{l,\xi} F_\xi \left[a_{11} + a_{22}\left(\frac{F_\eta}{F_\xi}\right)^2 + a_{33}\left(\frac{F_\zeta}{F_\xi}\right)^2 - 2a_{12}\frac{F_\eta}{F_\xi} - 2a_{13}\frac{F_\zeta}{F_\xi} - 2a_{23}\frac{F_\eta}{F_\xi}\frac{F_\zeta}{F_\xi}\right]/\mathbf{J}^2 \tag{29}$$

Substituting equations (28) and (29) into (9) results in the following general expression for the interface condition:

$$\frac{F_\xi}{\mathbf{J}^2}\left[a_{11} + a_{22}\left(\frac{F_\eta}{F_\xi}\right)^2 + a_{33}\left(\frac{F_\zeta}{F_\xi}\right)^2 - 2a_{12}\frac{F_\eta}{F_\xi} - 2a_{13}\frac{F_\zeta}{F_\xi} - 2a_{23}\frac{F_\eta}{F_\xi}\frac{F_\zeta}{F_\xi}\right]\cdot\left[k_s\frac{\partial T_s}{\partial \xi} - k_l\frac{\partial T_l}{\partial \xi}\right] = -\rho_s \lambda \frac{\partial F}{\partial t} \tag{30}$$

If $F(\xi, \eta, \zeta, t) = \xi - \Gamma(\eta, \zeta, t) = 0$, equation (30) reduces to the following form:

$$\left[a_{11} + a_{22}\left(\frac{\partial \Gamma}{\partial \eta}\right)^2 + a_{33}\left(\frac{\partial \Gamma}{\partial \zeta}\right)^2 + 2a_{12}\frac{\partial \Gamma}{\partial \eta} + 2a_{13}\frac{\partial \Gamma}{\partial \zeta} - 2a_{23}\frac{\partial \Gamma}{\partial \eta}\frac{\partial \Gamma}{\partial \zeta}\right]\cdot\left[k_s\frac{\partial T_s}{\partial \xi} - k_l\frac{\partial T_l}{\partial \xi}\right] = \mathbf{J}^2\rho_s \lambda \frac{\partial \Gamma}{\partial t} \tag{31}$$

For the Cartesian system (x, y, z), $F(x, y, z, t) = x - \Gamma(y, z, t) = 0$, and the Jacobian $\mathbf{J}$ (12) and the coefficients (16) to (21) become:

$$\left.\begin{aligned} a_{11} = a_{22} = a_{33} = 1 \\ a_{12} = a_{13} = a_{23} = 0 \\ \mathbf{J}^2 = 1 \end{aligned}\right] \tag{32}$$

Now equation (31) can be rewritten as

$$\left[1 + \left(\frac{\partial \Gamma}{\partial y}\right)^2 + \left(\frac{\partial \Gamma}{\partial z}\right)^2\right]\cdot\left[k_s\frac{\partial T_s}{\partial x} - k_l\frac{\partial T_l}{\partial x}\right] = \rho_s \lambda \frac{\partial \Gamma}{\partial t} \tag{33}$$

Equation (33) is already available in the published literature (Sikarskie and Boley, 1965; Ozisik, 1980).

Illustrative Example

In the ball-wedge bonding process that is employed in semiconductor chip assembly and packaging, a wire is heated from the bottom by an electric arc beyond melting temperature. As the wire melts, surface tension causes the liquid to form a ball. When the heating is terminated, the ball cools and solidifies, whereupon the bond head of the machine presses the ball onto the bond pad on the chip to make a ball bond. It is important to make "good" balls in order to guarantee good and secure bonding. We have developed a numerical model of this melting/solidification process (Huang et al., 1989). We have simultaneously tracked phase-change interfaces of different shapes that arise in this problem by successfully employing equation (31). Details are available from Huang (1989).

Briefly, the energy equations for solid and liquid phases in the ball are

$$\frac{\partial T_l}{\partial t} = \alpha_l \nabla^2 T_l \tag{34}$$

$$\frac{\partial T_s}{\partial t} = \alpha_s \nabla^2 T_s \tag{35}$$

subject to coupled conductive, convective, and radiative boundary conditions on the outer surface of the ball. The

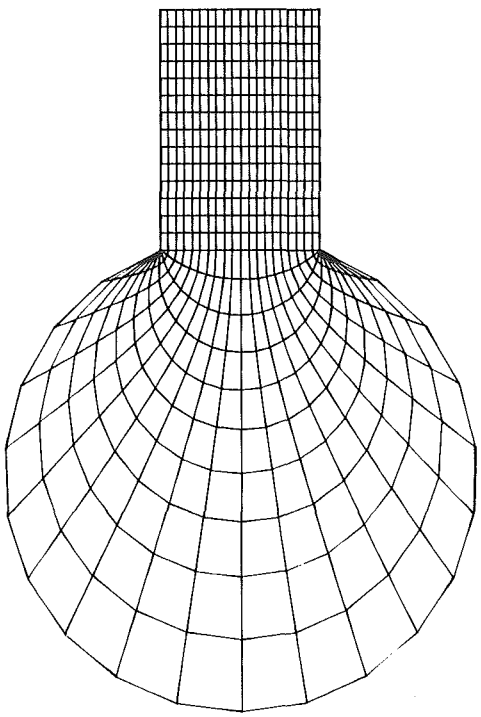

Fig. 1 Physical domain for body-fitted coordinate system

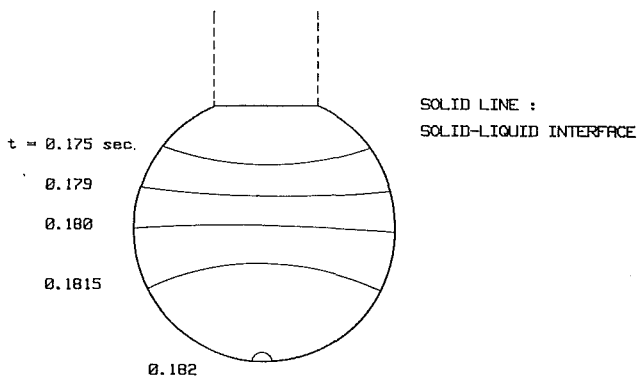

Fig. 2 Evolution of the solid-liquid interface location; $R_w = 0.25$ mm, $T_\infty = 300$ K, aluminum wire

movement of the solid–liquid interface is governed by equations (2) and (3).

The above mathematical formulation is solved by the ADI method using the body-fitted coordinate system. Figure 1 shows the general nonorthogonal curvilinear coordinate system for the physical domain. The body contour has been generated using the minimum energy principle (Huang, 1989). The corresponding computational domain is a rectangular, uniformly spaced grid in (ξ, η). Figure 2 shows how the solidification front progresses with time and has been generated using equation (31) to describe the interface movement.

Acknowledgments

This work was supported by the Ben Franklin Technology Center of Southeastern Pennsylvania under Ben Franklin Partnership grant No. 07.510RU, by the International Society for Hybrid Microelectronics Educational Foundation under grant No. 88-13, and by the National Science Foundation under grant No. DMC 8709537. We gratefully acknowledge the help received from the Pittsburgh Supercomputing Center.

References

Boley, B. A., 1964, "The Analysis of Problems of Heat Conduction and Melting," *Proceedings of the Third Symposium on Naval Structural Mechanics*, Pergamon Press, New York, pp. 260–315.

Carslaw, H. S., and Jaeger, J. C., 1959, *Conduction of Heat in Solids*, Clarendon Press, Oxford, United Kingdom.

Huang, L. J., 1989, "Fundamental Problems in Heat Transfer and Fluid Mechanics of Phase Change Processes with Liquid Drops," Ph.D. Dissertation, MEAM Dept., University of Pennsylvania, Chap. 4.

Huang, L. J., Ayyaswamy, P. S., and Cohen, I. M., *1989*, "Numerical Simulation of the Ball Formation Process in Wire Bonding Apparatus," *Proc. of NSF 15th Conference on Production Research and Technology*, Berkeley, CA, pp. 637–645.

Ozisik, M. N., 1980, *Heat Conduction*, Wiley, New York.

Patel, P. D., 1968, "Interface Conditions in Heat Conduction Problems With Change of Phase," *AIAA J.*, Vol. 6, p. 2454.

Sikarskie, D. L., and Boley, B. A., 1965, "The Solution of a Class of Two-Dimensional Melting and Solidification Problems," *Int. J. Solids Structures*, Vol. 1, pp. 207–234.

Treatment of Transverse and Longitudinal Heat Conduction in Regenerators

F. E. Romie[1]

Nomenclature

A_x = total conduction area, m^2
$A_{xa,b}$ = conduction areas in rotary regenerator = $A_{xa} + A_{xb} = A_x$, m^2
C = per-unit-mass capacitance of matrix, J/(kgK)
d = density of matrix material, kg/m^3
$(hA)_{a,b}$ = thermal conductances, W/K
k = thermal conductivity of matrix material, W/(mK)
$t_{a,b}$ = flow periods, s
t_t = time for one revolution = $t_a + t_b$, s
$(wc)_{a,b}$ = capacitance rates of gases, W/K
WC = capacitance of entire matrix, J/K
Λ_a = $(hA)_a/(wc)_a$

Subscripts

a = assigned such that C^* (Table 1) is not greater than unity

[1]Palos Verdes Estates, CA 90274.

Contributed by the Heat Transfer Division for publication in the JOURNAL OF HEAT TRANSFER. Manuscript received by the Heat Transfer Division December 12, 1989; revision received July 7, 1990. Keywords: Heat Exchangers, Thermal Energy Storage, Transient and Unsteady Heat Transfer.

Introduction

Regenerators in steady-state periodic operation are usually analyzed using the following idealizations: (1) The thermal conductances, $(hA)_{a,b}$, gas capacitance rates, $(wc)_{a,b}$, and matrix thermal capacitance, WC, are uniform and constant. (2) No heat is conducted in the matrix in the direction of gas flows (zero longitudinal heat conduction). (3) No resistance is offered in the matrix material to heat conduction in the direction normal to gas flow (zero resistance to transverse heat conduction). (4) The thermal capacitances of the contained gases are negligibly small compared to the thermal capacitance of the containing matrix. Under these conditions the thermal effectiveness, ϵ, of the counterflow regenerator is expressible in terms of four parameters

$$\epsilon = \epsilon(Ntu,\ C^*,\ C^*_{rr},\ (hA)^*) \tag{1}$$

The four parameters are defined in Table 1 for both rotary and single stationary regenerators. For stationary regenerators the magnitude of the heat transferred between the gas and matrix during a flow period is necessarily the same for both flow periods and is $Q = \epsilon\ (wct)_a\ (\tau_{hin} - \tau_{cin})$ in which τ_{hin} and τ_{cin} are constant inlet temperatures of the hot and cold gases. For rotary regenerators the heat rate is $q = \epsilon(wc)_a\ (\tau_{hin} - \tau_{cin})$.

Tables of ϵ in terms of the four parameters are given by many sources, for example, Lambertson (1958), Bahnke and Howard (1964), Kays and London (1984), and Romie (1990). Methods of computing the thermal effectiveness are described by, for example, Hill and Willmott (1987) and Romie and Baclic (1988).

In this note the effects on thermal effectiveness of longitudinal conduction and finite resistance to transverse heat conduction are expressed in terms of two factors, G_L and G_T. The product $G_T Ntu$ replaces Ntu in equation (1) to give the thermal effectiveness with finite resistance to transverse conduction.

Table 1 Parameter definitions

	Stationary	Rotary
Ntu	$\frac{\Lambda_a}{1+hA^*}$	$\frac{\Lambda_a}{1+hA^*}$
C^*	$\frac{(wct)_a}{(wct)_b}$	$\frac{(wc)_a}{(wc)_b}$
C^*_{rr}[1]	$\frac{(wct)_a}{WC}$	$\frac{(wc)_a t_t}{WC}$
hA^*	$\frac{(hAt)_a}{(hAt)_b}$	$\frac{(hA)_a}{(hA)_b}$
λ	$\frac{kA_x}{L(wc)_a}\left(\frac{t_a+t_b}{t_a}\right)$	$\frac{kA_x}{L(wc)_a}$
A^*_x	$\frac{t_a}{t_b}$	$\frac{A_{xa}}{A_{xb}}$

[1]C^*_{rr} is the reciprocal of the often-used C^*_r.

movement of the solid–liquid interface is governed by equations (2) and (3).

The above mathematical formulation is solved by the ADI method using the body-fitted coordinate system. Figure 1 shows the general nonorthogonal curvilinear coordinate system for the physical domain. The body contour has been generated using the minimum energy principle (Huang, 1989). The corresponding computational domain is a rectangular, uniformly spaced grid in (ξ, η). Figure 2 shows how the solidification front progresses with time and has been generated using equation (31) to describe the interface movement.

Acknowledgments

This work was supported by the Ben Franklin Technology Center of Southeastern Pennsylvania under Ben Franklin Partnership grant No. 07.510RU, by the International Society for Hybrid Microelectronics Educational Foundation under grant No. 88-13, and by the National Science Foundation under grant No. DMC 8709537. We gratefully acknowledge the help received from the Pittsburgh Supercomputing Center.

References

Boley, B. A., 1964, "The Analysis of Problems of Heat Conduction and Melting," *Proceedings of the Third Symposium on Naval Structural Mechanics*, Pergamon Press, New York, pp. 260–315.

Carslaw, H. S., and Jaeger, J. C., 1959, *Conduction of Heat in Solids*, Clarendon Press, Oxford, United Kingdom.

Huang, L. J., 1989, "Fundamental Problems in Heat Transfer and Fluid Mechanics of Phase Change Processes with Liquid Drops," Ph.D. Dissertation, MEAM Dept., University of Pennsylvania, Chap. 4.

Huang, L. J., Ayyaswamy, P. S., and Cohen, I. M., *1989*, "Numerical Simulation of the Ball Formation Process in Wire Bonding Apparatus," *Proc. of NSF 15th Conference on Production Research and Technology*, Berkeley, CA, pp. 637–645.

Ozisik, M. N., 1980, *Heat Conduction*, Wiley, New York.

Patel, P. D., 1968, "Interface Conditions in Heat Conduction Problems With Change of Phase," *AIAA J.*, Vol. 6, p. 2454.

Sikarskie, D. L., and Boley, B. A., 1965, "The Solution of a Class of Two-Dimensional Melting and Solidification Problems," *Int. J. Solids Structures*, Vol. 1, pp. 207–234.

Treatment of Transverse and Longitudinal Heat Conduction in Regenerators

F. E. Romie[1]

Nomenclature

A_x = total conduction area, m^2
$A_{xa,b}$ = conduction areas in rotary regenerator = $A_{xa} + A_{xb} = A_x$, m^2
C = per-unit-mass capacitance of matrix, J/(kgK)
d = density of matrix material, kg/m^3
$(hA)_{a,b}$ = thermal conductances, W/K
k = thermal conductivity of matrix material, W/(mK)
$t_{a,b}$ = flow periods, s
t_t = time for one revolution = $t_a + t_b$, s
$(wc)_{a,b}$ = capacitance rates of gases, W/K
WC = capacitance of entire matrix, J/K
Λ_a = $(hA)_a/(wc)_a$

Subscripts

a = assigned such that C^* (Table 1) is not greater than unity

[1]Palos Verdes Estates, CA 90274.

Contributed by the Heat Transfer Division for publication in the JOURNAL OF HEAT TRANSFER. Manuscript received by the Heat Transfer Division December 12, 1989; revision received July 7, 1990. Keywords: Heat Exchangers, Thermal Energy Storage, Transient and Unsteady Heat Transfer.

Introduction

Regenerators in steady-state periodic operation are usually analyzed using the following idealizations: (1) The thermal conductances, $(hA)_{a,b}$, gas capacitance rates, $(wc)_{a,b}$, and matrix thermal capacitance, WC, are uniform and constant. (2) No heat is conducted in the matrix in the direction of gas flows (zero longitudinal heat conduction). (3) No resistance is offered in the matrix material to heat conduction in the direction normal to gas flow (zero resistance to transverse heat conduction). (4) The thermal capacitances of the contained gases are negligibly small compared to the thermal capacitance of the containing matrix. Under these conditions the thermal effectiveness, ϵ, of the counterflow regenerator is expressible in terms of four parameters

$$\epsilon = \epsilon(Ntu,\ C^*,\ C^*_{rr},\ (hA)^*) \tag{1}$$

The four parameters are defined in Table 1 for both rotary and single stationary regenerators. For stationary regenerators the magnitude of the heat transferred between the gas and matrix during a flow period is necessarily the same for both flow periods and is $Q = \epsilon\ (wct)_a\ (\tau_{hin} - \tau_{cin})$ in which τ_{hin} and τ_{cin} are constant inlet temperatures of the hot and cold gases. For rotary regenerators the heat rate is $q = \epsilon(wc)_a\ (\tau_{hin} - \tau_{cin})$.

Tables of ϵ in terms of the four parameters are given by many sources, for example, Lambertson (1958), Bahnke and Howard (1964), Kays and London (1984), and Romie (1990). Methods of computing the thermal effectiveness are described by, for example, Hill and Willmott (1987) and Romie and Baclic (1988).

In this note the effects on thermal effectiveness of longitudinal conduction and finite resistance to transverse heat conduction are expressed in terms of two factors, G_L and G_T. The product $G_T Ntu$ replaces Ntu in equation (1) to give the thermal effectiveness with finite resistance to transverse conduction.

Table 1 Parameter definitions

	Stationary	Rotary
Ntu	$\frac{\Lambda_a}{1+hA^*}$	$\frac{\Lambda_a}{1+hA^*}$
C^*	$\frac{(wct)_a}{(wct)_b}$	$\frac{(wc)_a}{(wc)_b}$
C^*_{rr}[1]	$\frac{(wct)_a}{WC}$	$\frac{(wc)_a t_t}{WC}$
hA^*	$\frac{(hAt)_a}{(hAt)_b}$	$\frac{(hA)_a}{(hA)_b}$
λ	$\frac{kA_x}{L(wc)_a}\left(\frac{t_a+t_b}{t_a}\right)$	$\frac{kA_x}{L(wc)_a}$
A^*_x	$\frac{t_a}{t_b}$	$\frac{A_{xa}}{A_{xb}}$

[1]C^*_{rr} is the reciprocal of the often-used C^*_r.

Similarly the product $G_L Ntu$ gives the effectiveness with longitudinal conduction.

The size of a regenerator, particularly the flow length, is closely proportional to Ntu. Thus the factors G_L and G_T give an immediate indication of the importance of conduction effects. For example, if G_L is 0.8, then, to achieve a specified effectiveness, the regenerator must be roughly 1/0.8 or 25 percent larger than would be the case with zero longitudinal conduction.

Transverse Conduction

The effect of transverse conduction is approximated by finding a single internal resistance R (per unit heat transfer area) that best represents the distributed internal resistance of the individual elements forming the regenerator matrix. According to Hausen (1983), $R = \psi\delta/k$ in which δ is the half-thickness of a slab element exposed on both surfaces to the gas, or the radius of solid cylindrical or spherical elements. The function ψ has the same form for the three element shapes. (For notational simplification, ψ is defined as twice the value of ϕ used by Hausen.)

$$\psi = \frac{1}{K_1} - \frac{1}{K_2}\left(\frac{1}{F_a} + \frac{1}{F_b}\right) + \left(\frac{1}{F_a} + \frac{1}{F_b}\right)\sum_{n=1}^{\infty} \frac{2}{\beta_m^4}\left(\frac{e^{-\beta_n^2 F_a} + e^{-\beta_n^2 F_b} - 2e^{-\beta_n^2 (F_a + F_b)}}{1 - e^{-\beta_n^2 (F_a + F_b)}}\right) \quad (2)$$

For slabs, cylinders, and spheres, respectively, $K_1 = 3, 4, 5$, $K_2 = 45, 96, 175$, and β_n are successive nonzero positive zeroes of $\sin(\beta) = 0$, $J_1(\beta) = 0$, $\tan(\beta) - \beta = 0$. (Hausen also gives simple empirical equations to compute ϕ for the three element shapes.)

The parameters F_a and F_b are Fourier numbers, $(k/Cd)t_{a,b}/\delta^2$. The matrix thermal capacitance per unit heat transfer area, WC/A, is $C\,\delta\,d/K$ with $K = 1$, 2, or 3 for slab, cylindrical, or spherical elements. Thus, using the parameter definitions in Table 1, $F_a = Ntu\, C_{rr}^*(1 + hA^*)/(KBi_a)$, $F_b = F_a/(hA^* Bi_b/Bi_a)$ and

$$\frac{1}{F_a} + \frac{1}{F_b} = \frac{K\, Bi_a}{C_{rr}^* Ntu B} \quad (3)$$

with $B = (1 + hA^*)/(1 + hA^* Bi_b/Bi_a)$. The parameters $Bi_{a,b}$ are Biot numbers, $h_{a,b}\delta/k$. Hausen simplified calculations with negligible error by using the harmonic mean of F_a and F_b under the summation sign: $F_a = F_b = 2C_{rr}^* NtuB/(KBi_a)$.

The effective per-unit-area thermal resistance, $1/\bar{h}_{a,b}$, for transfer of heat between the gas and element is taken to be the sum of R and the per-unit-area convective resistance $1/h_{a,b}$; $1/\bar{h}_{a,b} = R + 1/h_{a,b}$. Thus

$$\frac{\bar{h}_{a,b}}{h_{a,b}} = \frac{1}{1 + \psi\, Bi_{a,b}} \quad (4)$$

The factor G_T is the quotient of Ntu formed using $\bar{h}_a$ and $\bar{h}_b$ divided by Ntu formed using, as usual, h_a and h_b.

$$G_T = \frac{1}{1 + \psi\, Bi_a}\left[\frac{1 + hA^*}{1 + hA^*\left(\frac{1 + \psi Bi_b}{1 + \psi\, Bi_a}\right)}\right] \quad (5)$$

The parameter hA^* has a dual role: It is used in evaluating Ntu and is an independent parameter in equation (1). The effectiveness is only slightly dependent on hA^* as an independent parameter and thus the moderate change in hA^* due to consideration of transverse conduction can be ignored in its role as an independent parameter.

For the special case in which $Bi_a = Bi_b = Bi$ (equivalently, $h_a = h_b$) both the bracketed term in equation (5) and B in equation (3) are unity. In this case the preceding equations

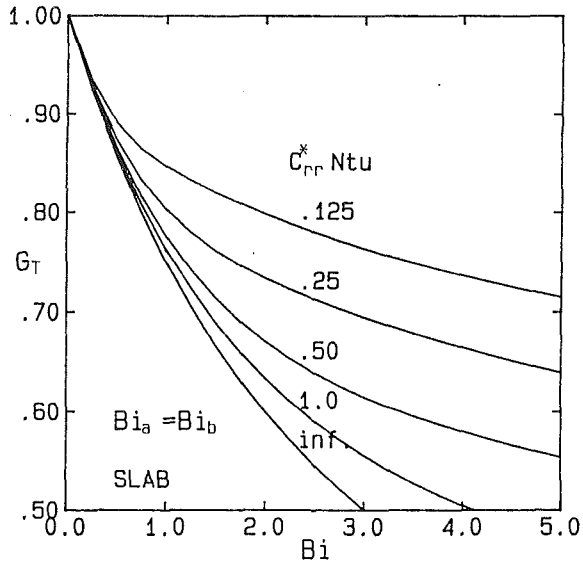

Fig. 1 G_T for slab elements

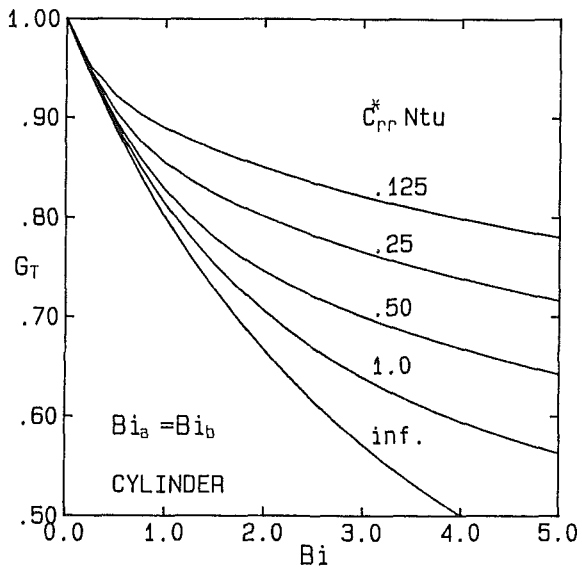

Fig. 2 G_T for cylindrical elements

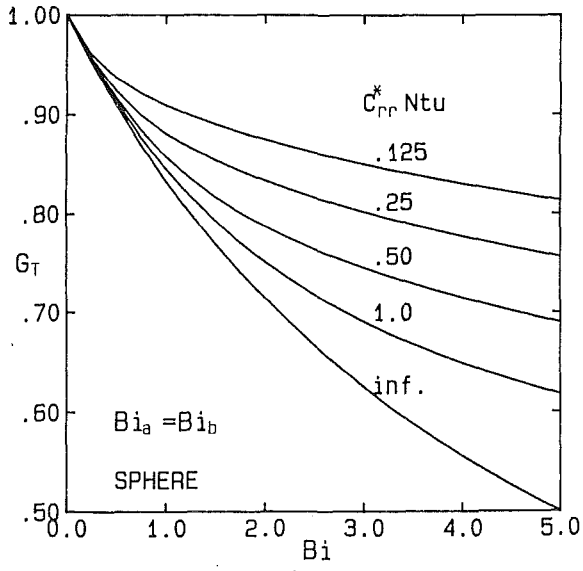

Fig. 3 G_T for spherical elements

show that $G_T = G_T(Bi, C_{rr}^* Ntu)$. Figures 1, 2, and 3 show this relationship for matrices constructed using slabs, cylinders, or spheres. For $C_{rr}^* Ntu$ large, G_T equals $1/(1 + Bi/K_1)$. This equality is seen also to apply when $Bi \lesssim 0.2$ and $C_{rr}^* Ntu \geq 1/8$.

Heggs et al. (1980) used finite difference methods to compute the thermal effectiveness, ϵ_H, for symmetric (C^*, $hA^* = 1$) regenerators with transverse conduction. Their results, which apply to the three element shapes with $Bi = 1, 2, 3, 4$, and 5, can be used to find the percent error, 100 $(\epsilon(G_T)/\epsilon_H - 1)$, in which $\epsilon(G_T)$ is the effectiveness computed using the G_T method. For $Ntu = 25$ and $C_{rr}^* = 0.02$ the maximum error is -0.3 percent. For $Ntu = 20$ and $C_{rr}^* = 0.5$ the maximum error is -0.2 percent but with $Ntu = 2.5$ and $C_{rr}^* = 1.0$ it is $+3.3$ percent. The latter error is for the slab with $Bi = 5$. The error decreases linearly with Bi to zero at $Bi = 1$. (Bi will rarely exceed unity in practice.) These errors are based on tabulated data presented by Heggs et al., but the remainder of their work is presented in graphic form. Errors due to the approximate nature of the G_T method cannot be distinguished from errors incurred in reading the graphs.

Longitudinal Conduction

For longitudinal conduction the conduction path is assumed continuous along the flow length, L, of the regenerator and to have a uniform total cross-sectional area A_x. The factor G_L is derived from an analysis of axial conduction in counterflow recuperators by Hahnemann (1948) whose closed form solution for recuperator effectiveness, E, is reproduced by Bahnke and Howard (1964). The solution is quite long and is not repeated in this note but will be represented as

$$E = E(Ntu, C^*, hA^*, \lambda) \tag{6}$$

The parameter λ is defined in Table 1. The factor G_L will be shown to be applicable to regenerators even though it is derived from recuperator analysis.

The factor G_L is found using the expression for counterflow recuperator effectiveness with Ntu replaced by $G_L Ntu$

$$E = \frac{1 - e^{-G_L Ntu(1-C^*)}}{1 - C^* e^{-G_L Ntu(1-C^*)}}, \qquad C^* < 1 \tag{7}$$

from which

$$G_L = \frac{1}{Ntu(1-C^*)} \log\left(\frac{1 - C^* E}{1 - E}\right), \qquad C^* < 1 \tag{8}$$

For $C^* = 1$, $E = G_L Ntu/(1 + G_L Ntu)$ and

$$G_L = E/(Ntu(1-E)), \qquad C^* = 1 \tag{9}$$

For the symmetric (C^*, $hA^* = 1$) recuperator Hahnemann's equation for E reduces to a simple form

$$E = 1 - 1/[1 + Ntu - (1 - \tanh(b)/b) Ntu^3/b^2] \tag{10}$$

with $b = Ntu\ [1 + 1/(\lambda Ntu)]^{1/2}$. Using $E = G_L Ntu/(1 + G_L Ntu)$ gives

$$G_L = 1 - (1 - \tanh(b)/b)\,(Ntu/b)^2, \qquad C^*, \quad hA^* = 1 \tag{11}$$

Figure 4 shows G_L as a function of the product λNtu for several values of Ntu. The curves are for $hA^* = 1$ and $C^* = 0.9$ and 1. The same curves are obtained using $hA^* = 0.5$, thus indicating that G_L is a very weak function of hA^*.

Bahnke and Howard used finite difference methods to find the counterflow regenerator effectiveness, ϵ_{BH}, with longitudinal conduction; $\epsilon_{BH}(Ntu, C^*, C_{rr}^*, hA^*, \lambda, A_x^*)$. They found the influence of A_x^* (defined in Table 1) to be negligibly small and equated A_x^* to hA^*. ($A_x^* = hA^*$ if $h_a = h_b$.) Their values for ϵ_{BH} are stated to have four place accuracy and thus the percent error, 100 $(\epsilon(G_L)/\epsilon_{BH} - 1)$, attributable to the G_L method can be determined.

For $Ntu = 1$ to 100, $C^* = 0.9$ to 1, $C_{rr}^* = 0$ to 0.5, $hA^* = 0.25$ to 1, and $\lambda = 0.01$ to 0.32 the maximum error was found to be $+0.59$ percent and occurred with $\lambda = 0.32$. For $\lambda = 0.16$ and 0.04 the maximum errors are $+0.27$ percent and $+0.09$ percent. These errors do not include results obtained with $G_L < 0.5$. However G_L (or G_T) less than 0.5 represents a very large adverse effect of heat conduction and will be avoided if feasible.

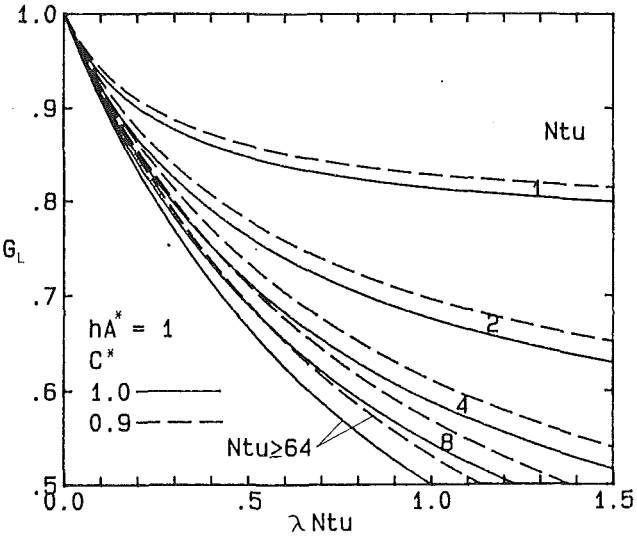

Fig. 4 G_L for longitudinal conduction

References

Bahnke, G. D., and Howard, C. P., 1964, "The Effect of Longitudinal Heat Conduction on Periodic-Flow Heat Exchanger Performance," ASME *Journal of Engineering for Power*, Vol. 86, pp. 105–119.

Hahnemann, H. W., 1948, "Approximate Calculation of Thermal Ratios in Heat Exchangers Including Heat Conduction in Direction of Flow," National Gas Turbine Establishment Memorandum No. M36.

Hausen, H., 1983, *Heat Transfer in Counterflow, Parallel Flow and Cross Flow*, McGraw-Hill, New York, pp. 310–350.

Heggs, P. J., Bansal, L. S., Bond, R. S., and Vazakas, V., 1980, "Thermal Regenerator Design Charts Including Intraconduction Effects," *Transactions of Industrial Chemical Engineering*, Vol. 58, pp. 265–270.

Hill, A., and Willmott, A. J., 1987, "A Robust Method for Regenerative Heat Exchanger Calculations," *International Journal of Heat and Mass Transfer*, Vol. 30, pp. 241–249.

Kays, W. M., and London, A. L., 1984, *Compact Heat Exchangers*, 3rd ed., McGraw-Hill, New York, pp. 57–62.

Lambertson, T. J., 1958, "Performance Factors of a Periodic-Flow Heat Exchanger," *Transactions of the ASME*, Vol. 80, pp. 586–592.

Romie, F. E., 1990, "A Table of Regenerator Effectiveness," ASME JOURNAL OF HEAT TRANSFER, Vol. 112, pp. 497–499.

Romie, F. E., and Baclic, B. S., 1988, "Methods for Rapid Calculation of the Operation of Asymmetric Counterflow Regenerators," ASME JOURNAL OF HEAT TRANSFER, Vol. 110, pp. 785–788.

Convection in the Cavity Between Two Rollers: the Effect of Thermal Boundary Conditions

P. A. Litsek,[1] Z. Zhang,[2] and A. Bejan[2,3]

Introduction

In this study we examine the convective cooling provided

[1]Promon Engenharia, Praia do Flamengo 154, Rio De Janeiro, RJ 22210 Brazil.

[2]Department of Mechanical Engineering and Materials Science, Duke University, Durham, NC 27706.

[3]J. A. Jones Professor of Mechanical Engineering; Fellow ASME.

Contributed by the Heat Transfer Division for publication in the JOURNAL OF HEAT TRANSFER. Manuscript received by the Heat Transfer Division November 3, 1989; revision received July 2, 1990. Keywords: Enclosure Flows, Forced Convection, Rotating Flows.

show that $G_T = G_T(Bi, C_{rr}^* Ntu)$. Figures 1, 2, and 3 show this relationship for matrices constructed using slabs, cylinders, or spheres. For $C_{rr}^* Ntu$ large, G_T equals $1/(1 + Bi/K_1)$. This equality is seen also to apply when $Bi \lesssim 0.2$ and $C_{rr}^* Ntu \geq 1/8$.

Heggs et al. (1980) used finite difference methods to compute the thermal effectiveness, ϵ_H, for symmetric (C^*, $hA^* = 1$) regenerators with transverse conduction. Their results, which apply to the three element shapes with $Bi = 1, 2, 3, 4$, and 5, can be used to find the percent error, 100 $(\epsilon(G_T)/\epsilon_H - 1)$, in which $\epsilon(G_T)$ is the effectiveness computed using the G_T method. For $Ntu = 25$ and $C_{rr}^* = 0.02$ the maximum error is -0.3 percent. For $Ntu = 20$ and $C_{rr}^* = 0.5$ the maximum error is -0.2 percent but with $Ntu = 2.5$ and $C_{rr}^* = 1.0$ it is $+3.3$ percent. The latter error is for the slab with $Bi = 5$. The error decreases linearly with Bi to zero at $Bi = 1$. (Bi will rarely exceed unity in practice.) These errors are based on tabulated data presented by Heggs et al., but the remainder of their work is presented in graphic form. Errors due to the approximate nature of the G_T method cannot be distinguished from errors incurred in reading the graphs.

Longitudinal Conduction

For longitudinal conduction the conduction path is assumed continuous along the flow length, L, of the regenerator and to have a uniform total cross-sectional area A_x. The factor G_L is derived from an analysis of axial conduction in counterflow recuperators by Hahnemann (1948) whose closed form solution for recuperator effectiveness, E, is reproduced by Bahnke and Howard (1964). The solution is quite long and is not repeated in this note but will be represented as

$$E = E(Ntu, C^*, hA^*, \lambda) \tag{6}$$

The parameter λ is defined in Table 1. The factor G_L will be shown to be applicable to regenerators even though it is derived from recuperator analysis.

The factor G_L is found using the expression for counterflow recuperator effectiveness with Ntu replaced by $G_L Ntu$

$$E = \frac{1 - e^{-G_L Ntu(1-C^*)}}{1 - C^* e^{-G_L Ntu(1-C^*)}}, \qquad C^* < 1 \tag{7}$$

from which

$$G_L = \frac{1}{Ntu(1-C^*)} \log\left(\frac{1 - C^* E}{1 - E}\right), \qquad C^* < 1 \tag{8}$$

For $C^* = 1$, $E = G_L Ntu/(1 + G_L Ntu)$ and

$$G_L = E/(Ntu(1-E)), \qquad C^* = 1 \tag{9}$$

For the symmetric (C^*, $hA^* = 1$) recuperator Hahnemann's equation for E reduces to a simple form

$$E = 1 - 1/[1 + Ntu - (1 - \tanh(b)/b) Ntu^3/b^2] \tag{10}$$

with $b = Ntu\ [1 + 1/(\lambda Ntu)]^{1/2}$. Using $E = G_L Ntu/(1 + G_L Ntu)$ gives

$$G_L = 1 - (1 - \tanh(b)/b)\,(Ntu/b)^2, \qquad C^*, \quad hA^* = 1 \tag{11}$$

Figure 4 shows G_L as a function of the product λNtu for several values of Ntu. The curves are for $hA^* = 1$ and $C^* = 0.9$ and 1. The same curves are obtained using $hA^* = 0.5$, thus indicating that G_L is a very weak function of hA^*.

Bahnke and Howard used finite difference methods to find the counterflow regenerator effectiveness, ϵ_{BH}, with longitudinal conduction; $\epsilon_{BH}(Ntu, C^*, C_{rr}^*, hA^*, \lambda, A_x^*)$. They found the influence of A_x^* (defined in Table 1) to be negligibly small and equated A_x^* to hA^*. ($A_x^* = hA^*$ if $h_a = h_b$.) Their values for ϵ_{BH} are stated to have four place accuracy and thus the percent error, 100 $(\epsilon(G_L)/\epsilon_{BH} - 1)$, attributable to the G_L method can be determined.

For $Ntu = 1$ to 100, $C^* = 0.9$ to 1, $C_{rr}^* = 0$ to 0.5, $hA^* = 0.25$ to 1, and $\lambda = 0.01$ to 0.32 the maximum error was found to be $+0.59$ percent and occurred with $\lambda = 0.32$. For $\lambda = 0.16$ and 0.04 the maximum errors are $+0.27$ percent and $+0.09$ percent. These errors do not include results obtained with $G_L < 0.5$. However G_L (or G_T) less than 0.5 represents a very large adverse effect of heat conduction and will be avoided if feasible.

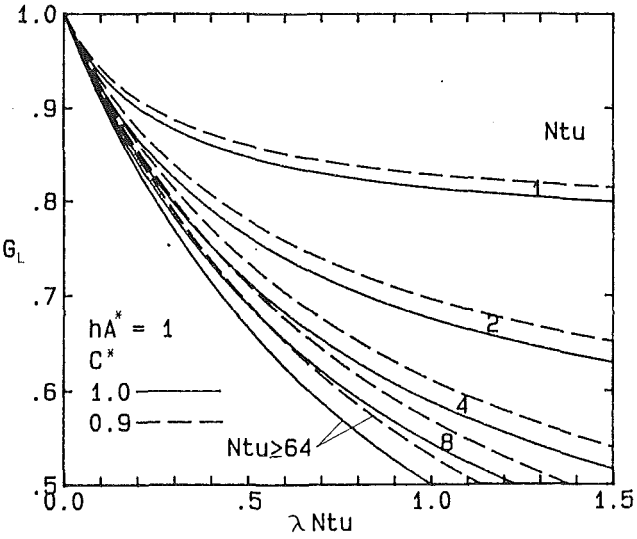

Fig. 4 G_L for longitudinal conduction

References

Bahnke, G. D., and Howard, C. P., 1964, "The Effect of Longitudinal Heat Conduction on Periodic-Flow Heat Exchanger Performance," ASME *Journal of Engineering for Power*, Vol. 86, pp. 105–119.

Hahnemann, H. W., 1948, "Approximate Calculation of Thermal Ratios in Heat Exchangers Including Heat Conduction in Direction of Flow," National Gas Turbine Establishment Memorandum No. M36.

Hausen, H., 1983, *Heat Transfer in Counterflow, Parallel Flow and Cross Flow*, McGraw-Hill, New York, pp. 310–350.

Heggs, P. J., Bansal, L. S., Bond, R. S., and Vazakas, V., 1980, "Thermal Regenerator Design Charts Including Intraconduction Effects," *Transactions of Industrial Chemical Engineering*, Vol. 58, pp. 265–270.

Hill, A., and Willmott, A. J., 1987, "A Robust Method for Regenerative Heat Exchanger Calculations," *International Journal of Heat and Mass Transfer*, Vol. 30, pp. 241–249.

Kays, W. M., and London, A. L., 1984, *Compact Heat Exchangers*, 3rd ed., McGraw-Hill, New York, pp. 57–62.

Lambertson, T. J., 1958, "Performance Factors of a Periodic-Flow Heat Exchanger," *Transactions of the ASME*, Vol. 80, pp. 586–592.

Romie, F. E., 1990, "A Table of Regenerator Effectiveness," ASME JOURNAL OF HEAT TRANSFER, Vol. 112, pp. 497–499.

Romie, F. E., and Baclic, B. S., 1988, "Methods for Rapid Calculation of the Operation of Asymmetric Counterflow Regenerators," ASME JOURNAL OF HEAT TRANSFER, Vol. 110, pp. 785–788.

Convection in the Cavity Between Two Rollers: the Effect of Thermal Boundary Conditions

P. A. Litsek,[1] Z. Zhang,[2] and A. Bejan[2,3]

Introduction

In this study we examine the convective cooling provided

[1]Promon Engenharia, Praia do Flamengo 154, Rio De Janeiro, RJ 22210 Brazil.

[2]Department of Mechanical Engineering and Materials Science, Duke University, Durham, NC 27706.

[3]J. A. Jones Professor of Mechanical Engineering; Fellow ASME.

Contributed by the Heat Transfer Division for publication in the JOURNAL OF HEAT TRANSFER. Manuscript received by the Heat Transfer Division November 3, 1989; revision received July 2, 1990. Keywords: Enclosure Flows, Forced Convection, Rotating Flows.

by fluid trapped in the cavity between two consecutive rollers in a roller bearing. Previous studies of roller bearing heat transfer characteristics have dealt almost exclusively with the generation and partition of heat transfer at the point of rolling contact (e.g., Schneider et al., 1977; Yuen, 1985). In order to calculate the steady-state temperature of the roller, however, the designer must know not only the rolling-contact heat input received by the roller but also the convection cooling effect of the surrounding fluid. Until recently, this lateral convection cooling effect was modeled by assuming a certain (constant) heat transfer coefficient h at the roller surface, and then calculating the steady-state temperature distribution around the roller (e.g., Gecim and Winer, 1984, 1986).

In real life, the convection heat transfer through the cavity fluid is coupled to conduction processes that take place in the peripheral regions of the four moving walls. The assumption of a certain set of thermal boundary conditions around the cavity becomes necessary when, for the sake of simplicity, cavity flow and heat transfer are singled out for investigation. The need to assume thermal boundary conditions arises also in the reverse case, when conduction in the moving walls is being studied separately, i.e., decoupled from convection in the surrounding fluid (e.g., Gecim and Winer, 1984, 1986).

Details of the fluid flow and heat transfer inside the hourglass-shaped cavity were analyzed for the first time in the first part of the present study (Litsek and Bejan, 1990). That work was based on an overly simplified model in which the heat flux from the roller to the cavity fluid was assumed uniform over the roller surface. Furthermore, the temperature of both runners was assumed uniform and equal to the ambient temperature.

Reviewers of the first paper recommended that we continue this work by relying on alternative thermal boundary conditions at the interfaces between rollers and cavity fluid, and between runners and cavity fluid. The present note is the result of this recommendation. Two new models are described in Figs. 1 and 2. In both figures, the rollers rotate with a constant angular velocity ω, and the runners move to the right and left with a roller peripheral speed $U=\omega R$. The geometry of the hourglass shaped cavity is described fully by the roller radius R and the distance L between the centers of two consecutive rollers.

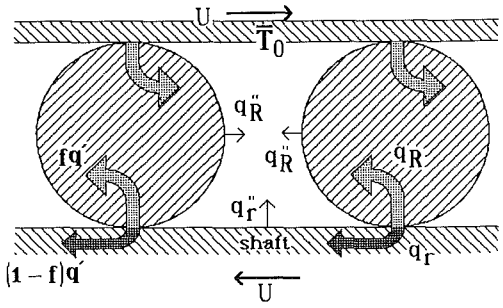

Fig. 1 Rollers and shaft with constant heat flux

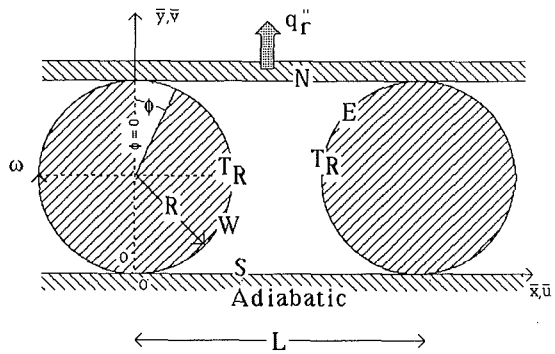

Fig. 2 Isothermal rollers and adiabatic shaft

The mathematical formulation and numerical method are described in detail in the companion paper (Litsek and Bejan, 1990); therefore, they will not be repeated here. In short, the cavity fluid is modeled as Newtonian with constant properties. The Navier–Stokes and energy equations also contain the time-derivative terms. In the limit where the volumetric effect of viscous heat generation in the fluid is negligible, the dimensionless groups that govern the flow and heat transfer are the geometric ratio L/R, and the Reynolds and Prandtl numbers, $\mathrm{Re} = UR/\nu$ and $\mathrm{Pr} = \nu/\alpha$. The Pr effect was documented in the earlier paper; therefore Pr was set equal to 1 in all the numerical runs conducted in this study.

Steady-state solutions were obtained by marching in time from an initial condition where the cavity fluid is motionless and isothermal. The equations and boundary conditions were transformed from the hourglass-shaped domain of Fig. 1 to a square computational domain, which was covered with a uniform grid. The grid size (39×39) was determined based on accuracy tests conducted at the highest Reynolds number ($\mathrm{Re}=400$). These tests were reported in the companion paper, along with an additional test of whether the results represent true steady-state solutions. For the calculated flow pattern, the maximum acceptable difference between the current solution and the solution at the preceding iteration (the iteration error) was less than 10^{-4}. The acceptable iteration error for the temperature field solution was less than 10^{-6}. This numerical code was tested also against the classical solution for the flow driven by the lid in a square cavity, and the agreement was excellent.

Rollers and Shaft With Uniform Heat Flux (Fig.1)

The new model of Fig. 1 accounts for the partition of heat generation at the points of rolling contact. Let q' [W/m] represent the rate of heat generation at a single point of rolling contact, expressed per unit length in the direction perpendicular to the plane of Fig. 1. A fraction (f) of this heating effect is absorbed superficially (under the surface) by the roller, fq', and later rejected to the cavity fluid

$$fq' = \pi R q''_R \tag{1}$$

The right roller in Fig. 1 rejects this heat transfer rate through the east side of the hourglass-shaped cavity. The heat flux q''_R is assumed uniform over the roller surface touched by cavity fluid.

The remaining portion of the rolling-contact heating effect, $(1-f)q'$, is transmitted to the runner. In the case of the lower runner, which accounts for the shaft, this heat transfer rate is rejected to the cavity fluid in the direction of lower temperatures

$$(1-f)q' = \mathrm{L}q''_r \tag{2}$$

The lower-runner heat flux q''_r is also uniformly distributed.

The role of eventual heat sink is played by the upper roller, the temperature of which is assumed uniform and equal to the ambient temperature $\bar{T}_0$. The conservation of energy requires that in the steady state the surface of the upper roller (the north side of the cavity) is crossed by the sum of the heat inputs to the cavity fluid; namely, $fq' + fq' + (1-f)q' = (1+f)q'$.

The effects of both Re and f on the roller surface temperature are displayed in the upper frame of Fig. 3, by calculating the average temperature difference $(\bar{T}_{R,\mathrm{avg}} - \bar{T}_0)$, and constructing the overall Nusselt number

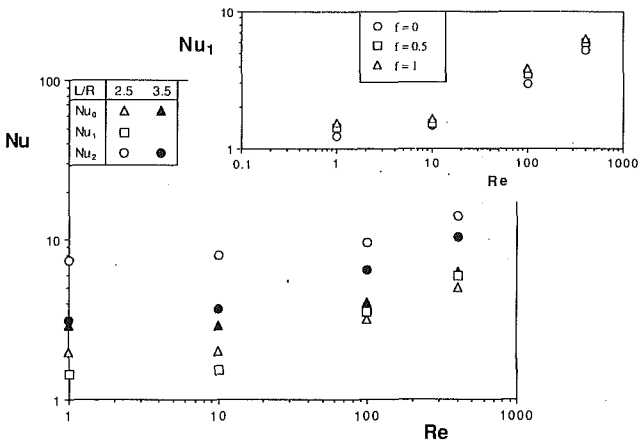

Fig. 3 The effect of thermal boundary conditions on the overall Nusselt number across the cavity

$$\mathrm{Nu}_1 = \frac{(1+f)q'}{k\left(\overline{\mathrm{T}}_{R,avg} - \overline{\mathrm{T}}_0\right)} \tag{3}$$

The numerator in this definition is the total rate of heat transfer into the cavity fluid. The upper graph in Fig. 3 shows that the Nusselt number increases appreciably when the Reynolds number becomes greater than approximately 10. This effect was also brought to light by the simpler model used in the companion to this study (Litsek and Bejan, 1990). New in the present case is the effect of the point-heating partition parameter f, which turns out to be quite small in the entire f range 0–1.

Isothermal Rollers and Adiabatic Shaft (Fig. 2)

In the second new model, (Fig. 2), it is assumed that the roller rotates fast enough so that its temperature is practically constant around the circumference, T_R. The surface of the lower runner (the shaft) is assumed adiabatic, as a model for a shaft that is long in the direction normal to Fig. 2, i.e., a shaft that cannot conduct away a significant portion of the heat generated in the rolling contact regions. Finally, the heat flux across the wetted surface of the upper runner is assumed uniform, q_r''.

It is worth noting that in this model the use of runner "flux" conditions is recommended by the numerical method or, more specifically, by the search for numerical solutions that do not depend on the fineness of the grid. Had we continued to model the upper runner as isothermal, as done in Fig. 1, the temperature at each point of rolling contact would have been double valued ($\overline{T}_R, \overline{T}_0$), and the calculated heat flux through the wedge-shaped corner of the cavity would have increased significantly with each increase in the fineness of the corner grid.

The effects of both L/R and Re on the heat transfer rate are shown in the lower part of Fig. 3 by means of the second overall Nusselt number

$$\mathrm{Nu}_2 = \frac{q_r'' L}{k\left(\overline{T}_{R,\mathrm{avg}} - \overline{T}_{N,\mathrm{avg}}\right)} \tag{4}$$

in which $(\overline{T}_{R,\mathrm{avg}} - \overline{T}_{N,\mathrm{avg}})$ is the average temperature difference between the roller surface and the upper (north) boundary. The Nusselt number Nu_2 increases appreciably as the Reynolds number exceeds 10. This increase is more pronounced when the geometric ratio L/R is large.

Conclusion

It is useful to take another look at the heat transfer conclusions generated by these two new models, and to recognize the important similarities between them, as well as between the new conclusions and the conclusions of the companion to this study (Litsek and Bejan, 1990). We accomplish this by looking at the lower part of Fig. 3, which shows the "Nusselt number" results produced by all three models. In each model the Nusselt number is a dimensionless way of expressing the inverse of the average temperature difference that is established across the fluid cavity.

In the first part of this study (Litsek and Bejan, 1990), the Nusselt number Nu_0 was based on the roller heat flux $q_R'' R$ (assumed uniform) and the average temperature difference between the roller surface and the runner surface ($\overline{T}_0$, uniform)

$$\mathrm{Nu}_0 = \frac{q_R'' R}{k\left(\overline{T}_{R,\mathrm{avg}} - \overline{T}_0\right)} \tag{5}$$

These data are represented by triangles in the lower frame of Fig. 3. The data obtained using the two new models (Nu_1, Nu_2) are represented respectively by squares and circles.

In spite of the significant changes in boundary conditions from one model to the next, the calculated overall Nusselt numbers Nu_0, Nu_1, and Nu_2 cover the same general area. In all three models, the cavity heat transfer mechanism is dominated by conduction at Reynolds numbers smaller than approximately 10, where it is practically independent of Re. At Reynolds numbers greater than 10, all three models show that the heat transfer rate is dominated by convection. The two new models constructed in this paper (Figs. 1, 2) reinforce the conclusion that in the convection regime the overall Nusselt number increases as $\mathrm{Re}^{1/2}$, in accordance with laminar forced-convection boundary layer theory.

For engineering design calculations, it may be sufficient to assume a constant heat transfer coefficient h at the roller surface (as done by Gecim and Winer, 1984, 1986). The contribution of this study is that the order of magnitude of the assumed h can be estimated by reading Fig. 3.

Acknowledgments

This work was supported by the National Science Foundation through Grant No. CBT-8711369. The numerical work was conducted using the Cornell National Supercomputer Facility, a resource of the Center for Theory and Simulation in Science and Engineering (Cornell Theory Center), which receives major funding from the National Science Foundation and IBM Corporation, with additional support from New York State and members of the Corporate Research Institute.

References

Gecim, B., and Winer, W. O., 1984, "Steady Temperature in a Rotating Cylinder Subject to Surface Heating and Convective Cooling," ASME *Journal of Tribology*, Vol. 106, pp. 120–127.

Gecim, B., and Winer, W. O., 1986, "Steady Temperatures in a Rotating Cylinder—Some Variations in the Geometry and Thermal Boundary Conditions," ASME *Journal of Tribology*, Vol. 108, pp. 446–454.

Litsek, P. A., and Bejan, A., 1990, "Convection in the Cavity Formed Between Two Cylindrical Rollers," ASME JOURNAL OF HEAT TRANSFER, Vol. 112, pp. 625–631.

Schneider, G. E., Strong, A. B., and Yovanovich, M. M., 1977, "Transient Thermal Response of Two Bodies Communicating Through a Small Circular Contact Area," *International Journal of Heat and Mass Transfer*, Vol. 20, pp. 301–308.

Yuen, W.Y.D., 1985, "On the Heat Transfer of a Moving Composite Strip Compressed by Two Rotating Cylinders," ASME JOURNAL OF HEAT TRANSFER, Vol. 107, pp. 541–548.

Non-Darcy Mixed Convection Along a Vertical Wall in a Saturated Porous Medium

F. C. Lai[1] and F. A. Kulacki[1]

Nomenclature

b = coefficient in Forchheimer's equation, m^{-1}
C = coefficient of thermal dispersion, $1/7 \le C \le 1/3$
d = mean particle diameter or pore diameter, m^{-1}
Fo = Forchheimer number = $(Kb/d)(\alpha/\nu)$
f = dimensionless stream function
g = acceleration due to gravity, m/s^2
h = local heat transfer coefficient, W/m^2-K
K = permeability, m^2
k_e = effective thermal conductivity of the saturated porous medium, W/m-K
Nu = local Nusselt number = hx/k_e
Pe = Peclet number = $U_\infty x/\alpha$
Pe_d = Peclet number based on the pore diameter = $U_\infty d/\alpha$
Ra = Rayleigh number = $Kg\beta|T_w - T_\infty|x/\nu\alpha$
Ra_d = Rayleigh number based on the pore diameter = $Kg\beta|T_w - T_\infty|d/\nu\alpha$
T = temperature, K
u, v = volume-averaged velocity in x and y direction, m/s
U_∞ = free-stream velocity, m/s
α_e = effective thermal diffusivity, m^2/s
β = coefficient of thermal expansion, K^{-1}
η = similarity variable
θ = dimensionless temperature = $(T - T_\infty)/(T_w - T_\infty)$
ν = kinematic viscosity, m^2/s
ψ = stream function

Subscripts

mx = mixed convection
nc = natural convection
w = condition at wall
∞ = condition at infinity

Introduction

In most of the previous studies of either natural or mixed convection, the boundary-layer formulation of Darcy's law and the energy equation were used. However, the inertial effect is expected to become very significant when the pore Reynolds number is large. This is especially true for the case of either the high Rayleigh number regime or for high-porosity media. In spite of its importance in many applications, the non-Darcy flow effect has not received much attention.

Plumb and Huenefeld (1981) and Vasantha et al. (1986) have reported on non-Darcy natural convection for different geometries in saturated porous media by employing Ergun's model (1952). By using the same model, Lai and Kulacki (1987) have studied non-Darcy mixed convection over a horizontal impermeable surface, with results including the non-Darcy natural convection as a limiting case. Both boundary and inertial effects have been considered by Vafai and Tien (1980) for the case of forced convection over a horizontal plate. Ranganathan and Viskanta (1984) have also considered these effects on mixed convection along a vertical surface in a porous medium. However, these previous studies of the non-Darcy heat transfer have not considered the effects of thermal dispersion. As pointed out by Cheng (1981), Plumb (1983), and Hong et al. (1987), thermal dispersion effects may become very important when flow inertia is prevalent. Kvernvold and Tyvand (1980) have also shown that a better agreement between the theoretical prediction and experimental data could be obtained if the thermal dispersion effects were taken into account properly.

In this note, non-Darcy flow effects, which include the inertial and thermal dispersion effects, are closely examined. Steady-state non-Darcy convection, in the form of natural, mixed, and forced convection, is considered for a heated vertical surface embedded in a saturated porous medium.

Analysis

Consider a vertical wall embedded in a saturated porous medium (Fig. 1). Having invoked the Boussinesq and boundary-layer approximations, the governing equations based on Forchheimer's formulation (1901) are given by

$$\frac{\partial^2\psi}{\partial y^2} + \frac{Kb}{\nu}\left[\frac{\partial}{\partial y}\left(\frac{\partial\psi}{\partial y}\right)^2\right] = \pm\frac{Kg\beta}{\nu}\frac{\partial T}{\partial y} \tag{1}$$

$$\frac{\partial\psi}{\partial y}\frac{\partial T}{\partial x} - \frac{\partial\psi}{\partial x}\frac{\partial T}{\partial y} = \frac{\partial}{\partial y}\left[\alpha_e\frac{\partial T}{\partial y}\right] \tag{2}$$

and the boundary conditions are

$$y = 0, \quad T = T_w, \quad v = -\frac{\partial\psi}{\partial x} = 0 \tag{3}$$

$$y \to \infty, \quad T = T_\infty, \quad u = \frac{\partial\psi}{\partial y} = 0$$

(natural convection) (4*a*)

$= U_\infty$

(mixed convection) (4*b*)

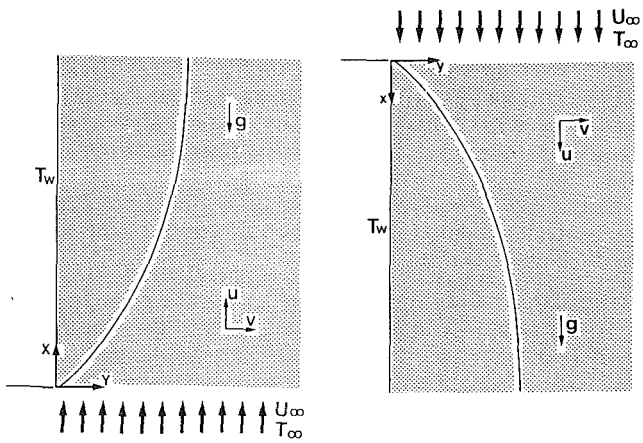

Fig. 1 Coordinate systems for a vertical wall imbedded in a saturated porous medium; (*a*) aiding flows, (*b*) opposing flows

[1]Department of Mechanical Engineering, Colorado State University, Fort Collins, CO 80523.

Contributed by the Heat Transfer Division for publication in the JOURNAL OF HEAT TRANSFER. Manuscript received by the Heat Transfer Division January 10, 1989; revision received April 16, 1990. Keywords: Mixed Convection, Porous Media.

The generalized Forchheimer formulations have been theoretically derived by Irmay (1958) and are widely adopted in the literature. The value of Forchheimer's coefficient, b, depends on the type of porous medium under investigation. As suggested by the experiments of Beavers and Sparrow (1969), this value is given by $0.074/\sqrt{K}$. The effective thermal diffusivity, α_e, is assumed to comprise α, the effective molecular diffusivity, and α', the diffusivity due to thermal dispersion. Since few data on thermal dispersion are available in the literature, thermal dispersion is usually approximated by hydrodynamic dispersion despite the fact that heat is also transported through the solid phase (Bear, 1972). Available experimental data have suggested that the longitudinal dispersion is directly proportional to the Peclet number (Bear, 1972; Whitaker, 1967). In addition, the transverse dispersion coefficient defined by equation (5) is on the order of 1/7 to 1/3 of the longitudinal value. Therefore, the thermal diffusivity due to the transverse dispersion is given by

$$\alpha' = Cud \tag{5}$$

The assumption of a constant dispersion coefficient is a first approach to the problem. A refined model on dispersion coefficient has been recently proposed by Hunt and Tien (1988); however, further fundamental experimental studies are needed for justifying its applicability.

Mixed Convection. When considering mixed convection, we designate the flow as an "aiding" flow when the buoyancy force has a component in the direction of the free-stream velocity, and likewise, as an "opposing" flow when the buoyancy component is opposite to the free-stream velocity. The suitable similarity variables for solving the non-Darcy mixed convection problem are those employed by Cheng (1977)

$$\eta = \mathrm{Pe}^{1/2} y/x, \qquad \psi = \alpha \mathrm{Pe}^{1/2} f(\eta) \tag{6}$$

After transformation, equations (1) and (2) become

$$f'' + (\mathrm{FoPe}_d)[(f')^2]' = \pm \frac{\mathrm{Ra}}{\mathrm{Pe}} \theta' \tag{7}$$

$$-\frac{1}{2} f\theta' = \theta'' + C\mathrm{Pe}_d (f''\theta' + f'\theta'') \tag{8}$$

where Pe_d is the Peclet number based on the pore diameter, Ra the modified Rayleigh number, and Fo, not to be confused with the Fourier number in heat conduction problems, is a new dimensionless number, which we tentatively name the Forchheimer number. The Forchheimer number characterizes the porous system under investigation since it represents the structure of the porous matrix, Kb/d, and the thermophysical properties of the porous medium, ν/α. The "+" sign in equation (7) denotes aiding flows and the "−" sign, opposing flow. It is important to note that the ratio of the Rayleigh number to Peclet number, Ra/Pe, is an important parameter for mixed convection and its value is independent of x, i.e.,

$$\frac{\mathrm{Ra}}{\mathrm{Pe}} = \frac{\mathrm{Ra}_d}{\mathrm{Pe}_d} \tag{9}$$

The corresponding boundary conditions are

$$\eta = 0, \quad \theta = 1, \quad f = 0 \tag{10}$$

$$\eta \to \infty, \quad \theta = 0, \quad f' = 1 \tag{11}$$

Natural Convection. With the similarity variables introduced by Cheng and Minkowycz (1977),

$$\eta = \mathrm{Ra}^{1/2} y/x, \qquad \psi = \alpha \mathrm{Ra}^{1/2} f(\eta), \tag{12}$$

the governing equations are transformed to

$$f'' + (\mathrm{FoRa}_d)[(f')^2]' = \theta' \tag{13}$$

$$-\frac{1}{2} f\theta' = \theta'' + C\mathrm{Ra}_d (f''\theta' + f'\theta'') \tag{14}$$

With boundary conditions given by

$$\eta = 0, \quad \theta = 1, \quad f = 0 \tag{15}$$

$$\eta \to \infty, \quad \theta = 0, \quad f' = 0 \tag{16}$$

Forced Convection. It is noted that the governing equations for non-Darcy forced convection can be deduced from equations (7) and (8) by simply setting Ra/Pe = 0. Therefore,

$$f'' + (\mathrm{FoPe}_d)[(f')^2]' = 0 \tag{17}$$

$$-\frac{1}{2} f\theta' = \theta'' + C\mathrm{Pe}_d (f''\theta' + f'\theta'') \tag{18}$$

Results and Discussion

The transformed ordinary differential equations, with their corresponding boundary conditions, are solved by numerical integration using the fourth-order Runge-Kutta method and by the shooting technique with a systematic guessing of $-\theta'(0)$ and $f'(0)$. To indicate the proper treatment of the problem, the solutions have been compared with those of the corresponding Darcy cases (Cheng and Minkowycz, 1977; Cheng 1977) by setting $b = C = 0$. The results are in excellent agreement.

By setting $C = 0$, thermal dispersion can be completely neglected. For mixed convection, it is noted that the dimensionless velocity and temperature profiles approach those of forced convection when $\mathrm{FoPe}_d > 10$. This indicates that the buoyancy effect diminishes as FoPe_d increases. For natural convection, it is observed that the deviation from Darcy flow becomes more significant as FoRa_d increases. For both natural convection and aiding mixed convection, one also observes that the boundary layer thickness increases as the inertial effect becomes stronger, while for opposing flows in mixed convection, the relation is just reversed.

It is interesting to point out that the solutions of equations (17) and (18) turn out to be the same as those of Darcy forced convection. For a fixed free-stream velocity, the inclusion of the inertial terms will lead only to an increase of the pressure gradient, while the heat transfer rate will remain unaffected. The result is different from that reported by Plumb (1983), for which the analysis was based on a fixed pressure gradient.

The heat transfer coefficient in terms of the Nusselt number can be expressed as

Mixed convection

$$\frac{\mathrm{Nu}}{\mathrm{Pe}^{1/2}} = [-\theta'(0)]_{mx} \tag{19}$$

Natural convection

$$\frac{\mathrm{Nu}}{\mathrm{Ra}^{1/2}} = [-\theta'(0)]_{nc} \tag{20}$$

and

Forced convection

$$\frac{\mathrm{Nu}}{\mathrm{Pe}^{1/2}} = 0.5642 \tag{21}$$

Equation (19) is plotted in Fig. 2 as a function of Ra/Pe. The limiting cases of free and forced convection are shown as asymptotes in the same figure. For comparison, the results of the corresponding Darcy flows ($\mathrm{FoPe}_d = 0$) are also included. As observed, for aiding mixed convection, the heat transfer coefficient is decreased as FoPe_d is increased while it is increased with FoPe_d for opposing flows. In addition, it shows that the results approach that for forced convection as FoPe_d becomes large, which was also observed earlier.

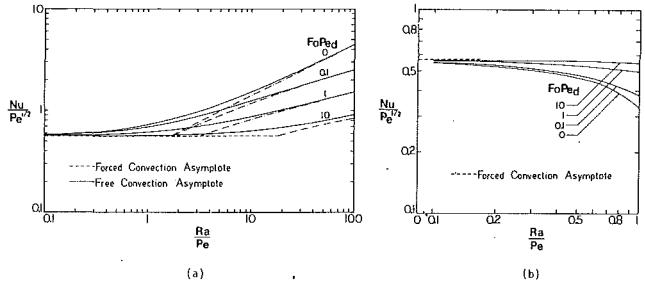

Fig. 2 Heat transfer results for non-Darcy mixed convection with dispersion effect neglected; (*a*) aiding flows, (*b*) opposing flows

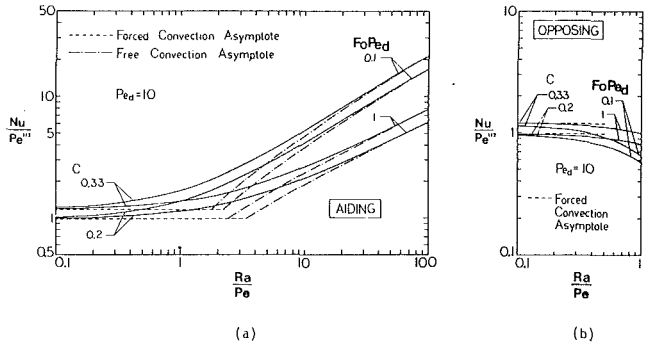

Fig. 3 Heat transfer results for non-Darcy mixed convection with dispersion effect included; for $Pe_d = 10$; (*a*) aiding flows, (*b*) opposing flows

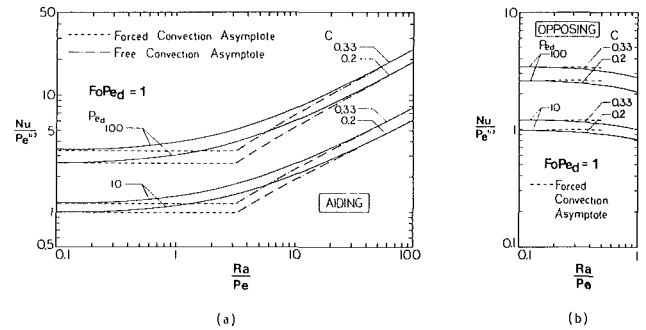

Fig. 4 Heat transfer results for non-Darcy mixed convection with dispersion effect included; for $FoPe_d = 1$; (*a*) aiding flows, (*b*) opposing flows

It is noted that the asymptotes of non-Darcy free convection are not linear, which is quite different from the Darcy case. The corresponding free convection asymptotes can be obtained by rewriting equation (19) as

$$\frac{\mathrm{Nu}}{\mathrm{Pe}^{1/2}} = \frac{\mathrm{Nu}}{\mathrm{Ra}^{1/2}}\left[\frac{\mathrm{Ra}}{\mathrm{Pe}}\right]^{1/2} = \left[\frac{\mathrm{Ra}}{\mathrm{Pe}}\right]^{1/2}[-\theta'(0)]_{nc} \tag{22}$$

and rewriting FoRa_d as

$$\mathrm{FoRa}_d = \mathrm{FoPe}_d\left[\frac{\mathrm{Ra}_d}{\mathrm{Pe}_d}\right] = \mathrm{FoPe}_d\left[\frac{\mathrm{Ra}}{\mathrm{Pe}}\right] \tag{23}$$

Therefore, for a given Ra/Pe and FoPe_d, FoRa_d is specified and $[-\theta'(0)]_{nc}$ can be solved from equations (13) and (14). The free convection asymptote is then obtained from equation (22), for each corresponding FoPe_d.

When thermal dispersion effects are taken into account, both thermal and hydrodynamic boundary layers are thicker than those with dispersion effects neglected. It is also noted that the value of $-\theta'(0)$ decreases as the dispersion coefficient, C, increases while the value of $f'(0)$ remains unaffected. In fact, it is observed that $f'(0)$ has an interesting property that it is a function of one parameter only, that is, FoRa_d for natural convection and FoPe_d for mixed convection.

When dispersion is taken into consideration, the heat transfer coefficient is expressed as

Mixed convection

$$\frac{\mathrm{Nu}}{\mathrm{Pe}^{1/2}} = [1 + C\mathrm{Pe}_d f'(0)][\theta'(0)]_{mx} \tag{24}$$

Natural convection

$$\frac{\mathrm{Nu}}{\mathrm{Ra}^{1/2}} = [1 + C\mathrm{Ra}_d f'(0)][-\theta'(0)]_{nc} \tag{25}$$

and

Forced convection

$$\frac{\mathrm{Nu}}{\mathrm{Pe}^{1/2}} = 0.5642\,(1 + C\mathrm{Pe}_d)^{1/2} \tag{26}$$

Each expression now comprises two terms: The first is the contribution from the molecular diffusion and the second is from the dispersion effect. Although the value of $-\theta'(0)$, i.e., the contribution by molecular diffusion, decreases with an increase in Ra/Pe for mixed convection and Ra_d for natural convection, the overall heat transfer is increased due to a significant contribution from dispersion.

Equation (24) is plotted in Figs. 3 and 4 as a function of Ra/Pe. The limiting cases of free and forced convection are also shown as asymptotes in these figures. As seen, for a fixed Pe_d, the heat transfer coefficient increases with FoPe_d (more specifically, Fo) for opposing flows and decreases for aiding flows (Fig. 3). For a fixed FoPe_d the heat transfer coefficient increases with Pe_d for both aiding and opposing flows (Fig. 4). In addition, these results have further revealed that the Peclet number, Pe_d, has a much pronounced effect in the asymptotic forced convection regime (Ra/Pe→0.1), as does the Forchheimer number in the asymptotic free convection regime (Ra/Pe→100), while the dispersion coefficient has played the role of amplifying the differences in the heat transfer rates. In comparison to the results for which only the inertial effect is considered, the differences are significant. Similar observations have also been reported by Plumb (1983) and Hong et al. (1987) for the case of natural convection.

The corresponding asymptotes can be obtained by a manner similar to that described earlier, except that equation (24) is modified to

$$\frac{\mathrm{Nu}}{\mathrm{Pe}^{1/2}} = \frac{\mathrm{Nu}}{\mathrm{Ra}^{1/2}}\left[\frac{\mathrm{Ra}}{\mathrm{Pe}}\right]^{1/2} = \left[\frac{\mathrm{Ra}}{\mathrm{Pe}}\right]^{1/2}$$
$$[1 + C\mathrm{Ra}_d f'(0)][-\theta'(0)]_{nc} \tag{27}$$

Conclusion

For non-Darcy mixed convection along a vertical isothermal wall in a saturated porous medium, the governing parameters are the dispersion coefficient, Forchheimer number, and Rayleigh and Peclet numbers based on the pore diameter. When considering the inertial effects alone, the heat transfer coefficient is found to be less than that for a Darcy flow in free and aiding mixed convection. However, if thermal dispersion effects are taken into consideration, the heat transfer coefficient then becomes larger than that for a Darcy case. Therefore, it can be concluded that the dispersion effect is important when the inertial effect is prevalent. When neglected, it can result in a considerable error.

Acknowledgments

The authors would like to acknowledge support from the Computer Center at the Colorado State University and the U.S. Nuclear Regulatory Commission.

References

Bear, J., 1972, *Dynamics of Fluids in Porous Media*, Elsevier Publishing Co., New York.

Beavers, G. S., and Sparrow, E. M., 1969, "Non-Darcy Flow Through Fibrous Porous Media," ASME *Journal of Applied Mechanics*, Vol. 36, pp. 711–714.

Cheng, P., 1977, "Combined Free and Forced Boundary Layer Flows About Inclined Surfaces in a Porous Medium," *International Journal of Heat and Mass Transfer*, Vol. 20, pp. 806–814.

Cheng, P., and Minkowycz, W. J., 1977, "Free Convection About a Vertical Flat Plate Imbedded in a Porous Medium With Application to Heat Transfer From a Dike," *Journal of Geophysical Research*, Vol. 82, pp. 2040–2044.

Cheng, P., 1981, "Thermal Dispersion Effects in Non-Darcian Convective Flows in a Saturated Porous Medium," *Letters in Heat and Mass Transfer*, Vol. 8, pp. 267–270.

Ergun, S., 1952, "Fluid Flow Through Packed Columns," *Chemical Engineering Progress*, Vol. 48, pp. 89–94.

Forchheimer, P., 1901, "Wasserbewegung durch Boden," *Forschtlft Ve. D. Ing.*, Vol. 45, pp. 1782–1788.

Hong, J. T., Yamada, Y., and Tien, C. L., 1987, "Effects of Non-Darcian and Nonuniform Porosity on Vertical-Plate Natural Convection in Porous Media," ASME JOURNAL OF HEAT TRANSFER, Vol. 109, pp. 356–362.

Hunt, M. L., and Tien, C. L., 1988, "Diffusion and Dispersion Regimes for Boundary-Layer Flow in a Porous Medium," *Proceedings of the 1988 National Heat Transfer Conference*, Vol. 1, pp. 635–641.

Irmay, S., 1958, "On the Theoretical Derivation of Darcy and Forchheimer Formulas," *Transactions, American Geophysical Union*, Vol. 39, pp. 702–707.

Kvernvold, O., and Tyvand, P. A., 1980, "Dispersion Effects on Thermal Convection in Porous Media," *Journal of Fluid Mechanics*, Vol. 99, pp. 673–686.

Lai, F. C., and Kulacki, F. A., 1987, "Non-Darcy Convection From Horizontal Impermeable Surfaces in Saturated Porous Medium," *International Journal of Heat and Mass Transfer*, Vol. 30, pp. 2189–2192.

Plumb, O. A., and Huenefeld, J. C., 1981, "Non-Darcy Natural Convection From Heated Surfaces in Saturated Porous Media," *International Journal of Heat and Mass Transfer*, Vol. 24, pp. 765–768.

Plumb, O. A., 1983, "The Effect of Thermal Dispersion on Heat Transfer in Packed Bed Boundary Layers," *Proceedings of 1st ASME-JSME Thermal Engineering Joint Conference*, Vol. 2, pp. 17–21.

Ranganathan, P., and Viskanta, R., 1984, "Mixed Convection Boundary-Layer Flow Along a Vertical Surface in a Porous Medium," *Numerical Heat Transfer*, Vol. 7, pp. 305–317.

Vafai, K., and Tien, C. L., 1980, "Boundary and Inertia Effects on Flow and Heat Transfer in Porous Media," *International Journal of Heat and Mass Transfer*, Vol. 24, pp. 195–203.

Vasantha, R., Pop, I., and Nath, G., 1986, "Non-Darcy Natural Convection Over a Slender Vertical Frustum of a Cone in a Saturated Porous Medium," *International Journal of Heat and Mass Transfer*, Vol. 29, pp. 153–156.

Whitaker, S., 1967, "Diffusion and Dispersion in Porous Media," *AIChE Journal*, Vol. 13, pp. 420–427.

Thermal Radiation, Convection, and Conduction in Porous Media Contained in Two-Dimensional Vertical Cavities

C. Bouallou[1] and J. F. Sacadura[2]

Nomenclature

A = enclosure aspect ratio
c = specific heat of the interstitial fluid
g = gravitational acceleration
G = incident radiation
H = width of the enclosure
K = permeability
L = height of the enclosure
n = refractive index
N = conduction to radiation parameter = $\lambda^p \Delta T \beta / n^2 \sigma T_0^4$
N_T = Tong's conduction to radiation parameter = $\lambda^p \Delta T \beta / 4n^2 \sigma T_h^4$
Nu = Nusselt number; equations (7) and (8)
q_x^r = vertical component of radiative flux
q_y^r = horizontal component of radiative flux
Ra^0 = modified Rayleigh number = $g\alpha\rho c\, \Delta T\, HK/\lambda^p \nu$
T = dimensionless temperature
$\tilde{T}$ = temperature
T_0 = mean temperature = $(T_c + T_h)/2$
u, v = vertical and horizontal components of the velocity field
x, y = vertical and horizontal coordinates
α = thermal diffusivity
β = extinction coefficient
ϵ_i = emissivity of wall i ($i = c, h$)
λ^p = thermal conductivity of the porous medium and the fluid at stagnant flow
Λ_i = $\epsilon_i/(2(2-\epsilon_i))$ ($i = c, h$)
ν = kinematic viscosity of the fluid
ρ = density of the interstitial fluid
ρ^p = density of the porous medium
σ = Stefan–Boltzmann constant
τ_0 = optical thickness
ϕ = dimensionless temperature = $\tilde{T}/T_h$
ψ = dimensionless stream function
ω = single scattering albedo

Subscripts

c = cold wall
h = hot wall

Introduction

This publication deals with the modeling of heat transfer by thermal radiation and natural convection in a fluid-saturated semitransparent porous medium contained within an inclinable two-dimensional cavity whose larger boundaries are isothermal and gray, whereas the smaller boundaries are insulated and reflecting. Applications are mainly relevant to the thermal insulation technologies, due to the wide use of high-porosity insulation in many engineering systems.

In most publications on heat transfer in cavities containing a porous medium, convection is the only mode taken into account or the radiation effects are treated through an effective conductivity (Caltagirone, 1976; Burns et al., 1977; Tong and Subramanian, 1983; Shiralkar et al., 1983; Arquis and Caltagirone, 1987; Beckermann et al., 1987). It is only lately that coupled radiation-natural convection has been considered and, in the few publications dealing with it, radiation is considered under a one-dimensional form while convection is considered under a two-dimensional (Lauriat, 1980; Uny, 1986; Tong et al., 1983). Furthermore, the two-flux radiation model has usually been employed. This process has all the shortcomings of the two-flux model and is also little adapted to the small-aspect-ratio geometries (square cavities for instance).

The model used here is entirely two-dimensional and is based on the P1 approximation for the treatment of thermal radiation in an isotropically scattering semitransparent medium. Such a model is necessary when dealing with small-aspect-ratio cavities or when the convective heat transfer is less important than the radiative transfer.

[1]Doctoral Student, Institut National des Sciences Appliquées de Lyon, France.
[2]Professor, Department of Mechanical Engineering (GMC), Institut National des Sciences Appliquées de Lyon, France.

Contributed by the Heat Transfer Division for publication in the JOURNAL OF HEAT TRANSFER. Manuscript received by the Heat Transfer Division September 28, 1989; revision received June 1, 1990. Keywords: Natural Convection, Porous Media, Radiation.

Beavers, G. S., and Sparrow, E. M., 1969, "Non-Darcy Flow Through Fibrous Porous Media," ASME *Journal of Applied Mechanics*, Vol. 36, pp. 711–714.

Cheng, P., 1977, "Combined Free and Forced Boundary Layer Flows About Inclined Surfaces in a Porous Medium," *International Journal of Heat and Mass Transfer*, Vol. 20, pp. 806–814.

Cheng, P., and Minkowycz, W. J., 1977, "Free Convection About a Vertical Flat Plate Imbedded in a Porous Medium With Application to Heat Transfer From a Dike," *Journal of Geophysical Research*, Vol. 82, pp. 2040–2044.

Cheng, P., 1981, "Thermal Dispersion Effects in Non-Darcian Convective Flows in a Saturated Porous Medium," *Letters in Heat and Mass Transfer*, Vol. 8, pp. 267–270.

Ergun, S., 1952, "Fluid Flow Through Packed Columns," *Chemical Engineering Progress*, Vol. 48, pp. 89–94.

Forchheimer, P., 1901, "Wasserbewegung durch Boden," *Forschtlft Ve. D. Ing.*, Vol. 45, pp. 1782–1788.

Hong, J. T., Yamada, Y., and Tien, C. L., 1987, "Effects of Non-Darcian and Nonuniform Porosity on Vertical-Plate Natural Convection in Porous Media," ASME JOURNAL OF HEAT TRANSFER, Vol. 109, pp. 356–362.

Hunt, M. L., and Tien, C. L., 1988, "Diffusion and Dispersion Regimes for Boundary-Layer Flow in a Porous Medium," *Proceedings of the 1988 National Heat Transfer Conference*, Vol. 1, pp. 635–641.

Irmay, S., 1958, "On the Theoretical Derivation of Darcy and Forchheimer Formulas," *Transactions, American Geophysical Union*, Vol. 39, pp. 702–707.

Kvernvold, O., and Tyvand, P. A., 1980, "Dispersion Effects on Thermal Convection in Porous Media," *Journal of Fluid Mechanics*, Vol. 99, pp. 673–686.

Lai, F. C., and Kulacki, F. A., 1987, "Non-Darcy Convection From Horizontal Impermeable Surfaces in Saturated Porous Medium," *International Journal of Heat and Mass Transfer*, Vol. 30, pp. 2189–2192.

Plumb, O. A., and Huenefeld, J. C., 1981, "Non-Darcy Natural Convection From Heated Surfaces in Saturated Porous Media," *International Journal of Heat and Mass Transfer*, Vol. 24, pp. 765–768.

Plumb, O. A., 1983, "The Effect of Thermal Dispersion on Heat Transfer in Packed Bed Boundary Layers," *Proceedings of 1st ASME-JSME Thermal Engineering Joint Conference*, Vol. 2, pp. 17–21.

Ranganathan, P., and Viskanta, R., 1984, "Mixed Convection Boundary-Layer Flow Along a Vertical Surface in a Porous Medium," *Numerical Heat Transfer*, Vol. 7, pp. 305–317.

Vafai, K., and Tien, C. L., 1980, "Boundary and Inertia Effects on Flow and Heat Transfer in Porous Media," *International Journal of Heat and Mass Transfer*, Vol. 24, pp. 195–203.

Vasantha, R., Pop, I., and Nath, G., 1986, "Non-Darcy Natural Convection Over a Slender Vertical Frustum of a Cone in a Saturated Porous Medium," *International Journal of Heat and Mass Transfer*, Vol. 29, pp. 153–156.

Whitaker, S., 1967, "Diffusion and Dispersion in Porous Media," *AIChE Journal*, Vol. 13, pp. 420–427.

N_T = Tong's conduction to radiation parameter = $\lambda^p \Delta T \beta / 4n^2 \sigma T_h^4$
Nu = Nusselt number; equations (7) and (8)
q_x^r = vertical component of radiative flux
q_y^r = horizontal component of radiative flux
Ra^0 = modified Rayleigh number = $g\alpha\rho c\ \Delta T\ HK/\lambda^p \nu$
T = dimensionless temperature
$\tilde{T}$ = temperature
T_0 = mean temperature = $(T_c + T_h)/2$
u, v = vertical and horizontal components of the velocity field
x, y = vertical and horizontal coordinates
α = thermal diffusivity
β = extinction coefficient
ϵ_i = emissivity of wall i ($i = c, h$)
λ^p = thermal conductivity of the porous medium and the fluid at stagnant flow
Λ_i = $\epsilon_i/(2(2-\epsilon_i))$ ($i = c, h$)
ν = kinematic viscosity of the fluid
ρ = density of the interstitial fluid
ρ^p = density of the porous medium
σ = Stefan–Boltzmann constant
τ_0 = optical thickness
ϕ = dimensionless temperature = $\tilde{T}/T_h$
ψ = dimensionless stream function
ω = single scattering albedo

Subscripts

c = cold wall
h = hot wall

Thermal Radiation, Convection, and Conduction in Porous Media Contained in Two-Dimensional Vertical Cavities

C. Bouallou[1] and J. F. Sacadura[2]

Nomenclature

A = enclosure aspect ratio
c = specific heat of the interstitial fluid
g = gravitational acceleration
G = incident radiation
H = width of the enclosure
K = permeability
L = height of the enclosure
n = refractive index
N = conduction to radiation parameter = $\lambda^p \Delta T \beta / n^2 \sigma T_0^4$

Introduction

This publication deals with the modeling of heat transfer by thermal radiation and natural convection in a fluid-saturated semitransparent porous medium contained within an inclinable two-dimensional cavity whose larger boundaries are isothermal and gray, whereas the smaller boundaries are insulated and reflecting. Applications are mainly relevant to the thermal insulation technologies, due to the wide use of high-porosity insulation in many engineering systems.

In most publications on heat transfer in cavities containing a porous medium, convection is the only mode taken into account or the radiation effects are treated through an effective conductivity (Caltagirone, 1976; Burns et al., 1977; Tong and Subramanian, 1983; Shiralkar et al., 1983; Arquis and Caltagirone, 1987; Beckermann et al., 1987). It is only lately that coupled radiation-natural convection has been considered and, in the few publications dealing with it, radiation is considered under a one-dimensional form while convection is considered under a two-dimensional (Lauriat, 1980; Uny, 1986; Tong et al., 1983). Furthermore, the two-flux radiation model has usually been employed. This process has all the shortcomings of the two-flux model and is also little adapted to the small-aspect-ratio geometries (square cavities for instance).

The model used here is entirely two-dimensional and is based on the P1 approximation for the treatment of thermal radiation in an isotropically scattering semitransparent medium. Such a model is necessary when dealing with small-aspect-ratio cavities or when the convective heat transfer is less important than the radiative transfer.

[1]Doctoral Student, Institut National des Sciences Appliquées de Lyon, France.
[2]Professor, Department of Mechanical Engineering (GMC), Institut National des Sciences Appliquées de Lyon, France.

Contributed by the Heat Transfer Division for publication in the JOURNAL OF HEAT TRANSFER. Manuscript received by the Heat Transfer Division September 28, 1989; revision received June 1, 1990. Keywords: Natural Convection, Porous Media, Radiation.

Hypothesis and Mathematical Modeling

The porous medium is considered as a fictitious homogeneous and isotropic medium. Consequently the following hypothesis may be introduced:

- the thermal conductivity λ^p of the porous medium is independent of the temperature for slight temperature differences;
- the variations of the densities ρ^p of the porous medium, and ρ of the interstitial fluid, caused by the change of temperature are neglected except for the term linked to gravity (Boussinesq's approximation);
- the specific heats of the fictitious medium and interstitial fluid are considered as constant.

The semitransparent porous medium is confined within a vertical rectangular cavity whose larger side walls are kept at uniform temperatures T_c and T_h, with emissivities ϵ_c and ϵ_h. The other surfaces are insulated, perfectly diffuse, and reflective. The geometry of the enclosure is the same as that adopted by Tong et al. (1983).

The study is two dimensional. The governing dimensionless equations are (Caltagirone, 1976; Bejan, 1984):

$$\frac{\partial^2\psi}{\partial x^2}+\frac{\partial^2\psi}{\partial y^2}=-\mathrm{Ra}^0\frac{\partial T}{\partial y} \tag{1}$$

$$\frac{\partial^2 T}{\partial x^2}+\frac{\partial^2 T}{\partial y^2}-u\frac{\partial T}{\partial x}-v\frac{\partial T}{\partial y}-\frac{\tau_0}{N}\left(\frac{\partial q_x^r}{\partial x}+\frac{\partial q_y^r}{\partial y}\right)=0 \tag{2}$$

$$u=\frac{\partial\psi}{\partial y};\quad v=-\frac{\partial\psi}{\partial x} \tag{3}$$

The radiative transfer equation, which is solved by the P1 method, takes the following form (Desrayaud, 1987):

$$\frac{\partial^2 G}{\partial x^2}+\frac{\partial^2 G}{\partial y^2}-3\tau_0^2(1-\omega)G=-12\tau_0^2(1-\omega)\phi^4 \tag{4}$$

$$q_x^r=-\frac{1}{3\tau_0}\frac{\partial G}{\partial x};\quad q_y^r=-\frac{1}{3\tau_0}\frac{\partial G}{\partial y} \tag{5}$$

The boundary conditions are

$$T(x,0)=+0.5;\ \psi(x,0)=0;\ \frac{\partial G}{\partial Y}(x,0);=3\Lambda_h\,\tau_0(G-4)$$

$$T(x,1)=-0.5;\ \psi(x,1)=0;\ \frac{\partial G}{\partial y}(x,1)=-3\Lambda_c\tau_0(G-4\phi_c^4) \tag{6a}$$

$$\text{where } \Lambda_i=\epsilon_i/(2(2-\epsilon_i)),\quad i=c,\ h$$

$$\text{for } 0\le x\le A$$

$$\frac{\partial T}{\partial x}(0,y)=0;\quad \psi(0,y)=0;\quad \frac{\partial G}{\partial x}(0,y)=0 \tag{6b}$$

$$\frac{\partial T}{\partial x}(A,y)=0;\quad \psi(A,y)=0;\quad \frac{\partial G}{\partial x}(A,y)=0$$

$$\text{for } 0\le y\le 1$$

The nondimensional heat transfer across the enclosure is given by an average Nusselt number defined as

$$\mathrm{Nu}\,(y)=\frac{1}{A}\int_0^A\left\{-\frac{\partial T}{\partial y}+vT-\frac{1}{3N}\frac{\partial G}{\partial y}\right\}dx \tag{7}$$

The global Nusselt number is defined by

$$\mathrm{Nu}=\int_0^1 \mathrm{Nu}\,(y)\,dy \tag{8}$$

Method of Solution

The medium is discretized by a rectangular grid. The stream function is obtained by solving Poisson's equations numerically using a central finite difference scheme with an initial temperature field specified by $T(x, y) = 0.5 - y$. The velocity field appearing in the energy equation is deduced from the stream function. Then the incident radiation for the given temperature field is computed. This leads to the components of the radiant flux and its divergence. The latter enters as a source term in the energy equation, which is solved using the A.D.I. method giving the solution for the next iteration. The calculations are repeated until the convergence criterion

$$\max_{\substack{1\le i\le im\\ 1\le j\le jm}}\left|\frac{T_{i,j}^n-T_{i,j}^{n-1}}{T_{i,j}^n}\right|\le 5\times 10^{-6}$$

is satisfied.

T_{ij}^n is the temperature at iteration n and at point (i, j).

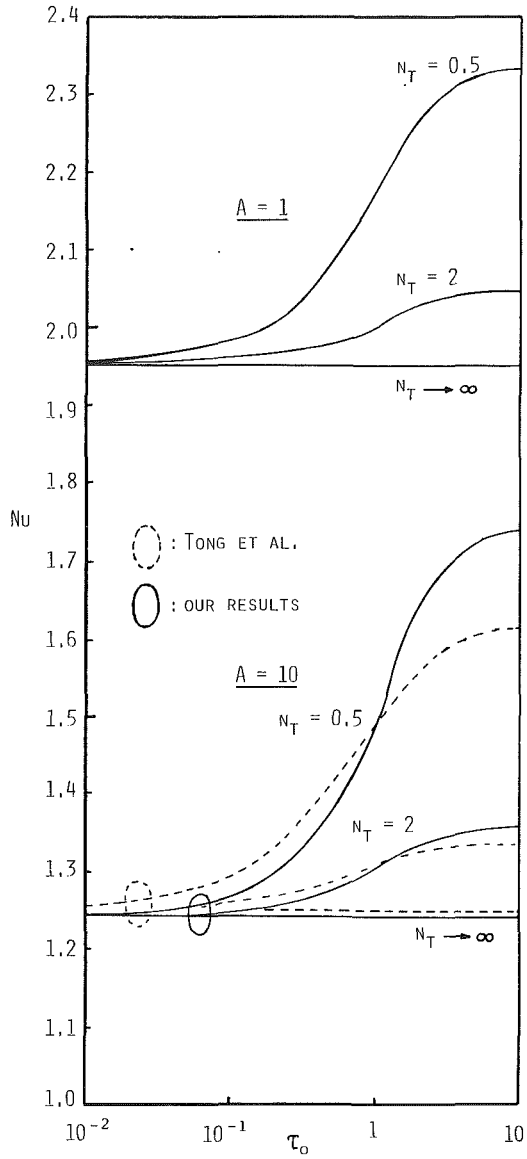

Fig. 1 Influence of conduction to radiation parameter and optical thickness on the total heat transfer (Nusselt number), for small and large aspect ratios (ω = 0.5; $\epsilon_c = \epsilon_h$ = 1; ϕ_c = 0.5; Ra^0 = 50)

Results and Discussion

The global Nusselt number values obtained using 33 × 21, 33 × 41, and 33 × 61 grids were compared for the same

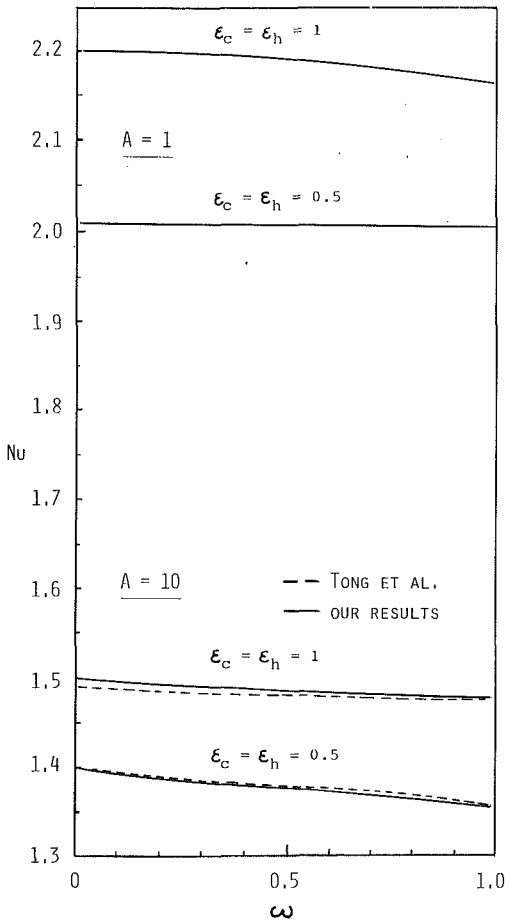

Fig. 2 Influence of ϵ_c, ϵ_h, and ω on Nu, for small and large aspect ratios ($\tau_0 = 1$; $\phi_c = 0.5$; $Ra^0 = 50$; $N_T = 0.5$).

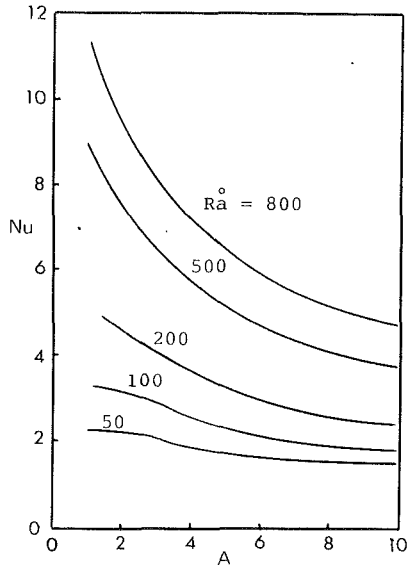

Fig. 3 Variation of the total Nusselt number with the aspect ratio for different Ra^0 values ($\tau_0 = 1$; $\omega = 0.5$; $\epsilon_c = \epsilon_h = 1$; $\phi_c = 0.5$; $N_T = 0.5$)

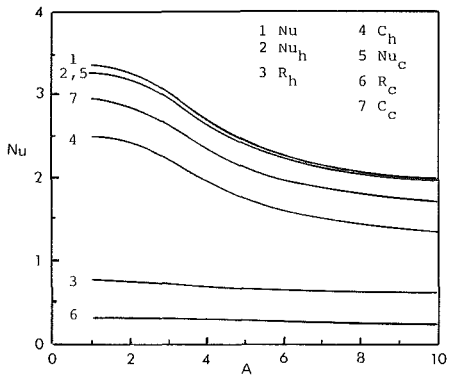

Fig. 4 Effect of aspect ratio on: the total heat transfer across the enclosure (Nu); the total heat transfer at the hot (Nu_h) and cold (Nu_c) walls; the radiative (R_h, R_c) and conductive (C_h, C_c) contributions to the total heat transfer at the walls ($\tau_0 = 5$; $\omega = 0.5$; $\epsilon_c = \epsilon_h = 1$; $\phi_c = 0.5$; $N_T = 0.5$; $Ra^0 = 100$)

convergence criteria. The maximum difference was found to be 0.33 percent between the first and the second grids and 0.1 percent between the second and the third grids. Then the 33 × 41 grid, which is reasonably precise and less expensive, has been adopted.

Figure 1 shows the variation of the global Nusselt number with the conduction/radiation parameter and the optical thickness τ_0. The results are presented for an aspect ratio $A = 10$ in order to make a comparison with Tong's results, and also for a small aspect ratio $A = 1$ corresponding to the present problem.

The conduction/radiation parameter used is the same as that of Tong:

$$N_t = \lambda^p \Delta T \beta / 4n^2 \sigma T_h^4$$

The results, for $A = 10$, seem to be in a reasonably good agreement with those of Tong when the optical thickness is moderate and the radiation is not dominant.

To analyze the observed difference for $\tau_0 > 2$ and small N_T values, it should be noted that:

- the P1 method used here is rather accurate in the optically thick limit but the radiative heat flux is slightly overpredicted. This has been reported by Yücel and Bayazitoglu (1983) using the P3 approximation as a reference method;
- the two-flux model used by Tong underpredicts the radiative heat flux. This has been shown by Bouallou (1989), who compared this model, in the case of radiative equilibrium, with the discrete oridinates method as a reference.

So the use of the two-dimensional P1 approximation appears to yield satisfactory results. It makes also possible to alleviate some numerical problems arising with the two-flux model for large optical thicknesses.

It may be also observed from Fig. 1 that the global heat flux can be affected in the same way either by increasing the optical thickness or by decreasing the coupling parameter. The increase in Nusselt number is rapid for $\tau_0 < 5$. Similar effects are observed for square cavities ($A = 1$).

The influence of wall emissivities ϵ_c, ϵ_h and of the single scattering albedo ω on the global heat transfer was examined using the same parameters for $N_T = 0.5$ and $\tau_0 = 1$. The results are given in Fig. 2. They are in good agreement with those of Tong.

The influence of isotropic scattering is consistent with the usual results: When the albedo increases, the absorption in the medium decreases and the interaction between radiation and natural convection becomes less important. The use of black surfaces ($\epsilon_c = \epsilon_h = 1$) brings about a noticeable increase of the global heat transfer, especially for the small aspect ratio values.

The influence of the aspect ratio of the modified Rayleigh number Ra^0 on the global heat transfer is shown in Fig. 3.

The Ra^0 is increased from 50 up to 800 (the high values are just used to examine the model behavior, but they do not correspond to a real situation for a porous medium). The

Nusselt number decreases rapidly for $A < 5$, especially for large Ra^0 values. Beyond this value, the decrease becomes less, which suggests that the Nusselt number could reach an asymptotic value for a large aspect ratio. In such a case, the vertical component of the radiant flux may be neglected. This would justify the use of a one-dimensional radiative model for $A > 5$ even though the temperature distribution remains essentially two dimensional.

Finally, Fig. 4 shows the respective contributions of conduction and radiation at the hot and cold walls, as well as the global Nusselt number, versus the aspect-ratio values.

Conclusion

To our knowledge, this work is the first attempt to present a completely two-dimensional model dealing with the coupled radiation-convection heat transfer through a fluid-saturated semitransparent porous medium contained in a rectangular enclosure.

An advantage of this model is the possibility to deal with cavities of small aspect ratio.

The study of inclinable cavities will be considered in the near future.

References

Arquis, E., and Caltagirone, J. P., 1987, "Interacting Convection Between Fluid and Open Porous Layers," presented at the ASME Winter Annual Meeting, Boston, MA, Dec. 13–18.

Bejan, A., 1984, *Convection Heat Transfer*, Wiley, NY.

Beckermann, C., Ramadhyani, S., and Viskanta, R., 1987, "Natural Convection Flow and Heat Transfer Between a Fluid Layer and a Porous Layer Inside a Rectangular Enclosure," ASME JOURNAL OF HEAT TRANSFER, Vol. 109, pp. 363–370.

Bouallou, C., 1989, "Modélisation bidimensionnelle des transferts couplés rayonnement-convection naturelle dans les milieux semi-transparents," Thèse de Doctorat, INSA de Lyon, No. 89 ISAL, France.

Burns, P. J., Chow, L. C., and Tien, C. L., 1977, "Convection in a Vertical Slot Filled With a Porous Insulation," *Int. J. Heat Mass Transfer*, Vol. 20, pp. 919–926.

Caltagirone, J. P., 1976, "Instabilités Thermoconvectives en milieu poreux," Thèse de Doctorat d'Etat, Université Pierre et Marie Curie, Paris VI, France.

Desrayaud, G., 1987, "Analyse de stabilité linéaire dans un milieu semi-transparent," Thése de Doctorat d'Etat, Université Pierre et Marie Curie, Paris VI, France.

Lauriat, G., 1980, "A Numerical Study of a Thermal Insulation Enclosure: Influence of the Radiative Transfer," *Natural Convection in Enclosures*, ASME HTD-Vol. 8, pp. 63–71.

Shiralkar, G. S., Haajizadeh, M., and Tien, C. L., 1983, "Numerical Study of High Rayleigh Number Convection in a Vertical Porous Enclosure," *Numerical Heat Transfer*, Vol. 6, pp. 223–234.

Tong, T. W., and Subramanian, E., 1983, "Natural Convection in Rectangular Enclosures Partially Filled With a Porous Medium," *ASME/JSME Thermal Engineering Joint Conf.*, Vol. 1, pp. 331–338.

Tong, T. W., Birkebak, R. C., and Enoch, I. E., 1983, "Thermal Radiation, Convection and Conduction in Porous Media Contained in Vertical Enclosures," ASME JOURNAL OF HEAT TRANSFER, Vol. 105, pp. 414–418.

Uny, G., 1986, "Modélisation du transfert couplé rayonnement-convection au sein de matériaux poreux et identification de leurs propriétés radiatives. Application aux laines de verre," Thèse de Doctorat, INSA - Lyon, France.

Yücel, A., and Bayazitoglu, Y., 1983, "PN Approximation for Radiative Heat Transfer in a Nongray Medium," *AIAA J.*, Vol. 21, No. 8, pp. 1191–1203.

Analytical Solution for Boundary Heat Fluxes From a Radiating Rectangular Medium

R. Siegel[1]

Nomenclature

A_R = aspect ratio of rectangular region = d/b

a = absorption coefficient of radiating medium

B_0 = optical length of short side of rectangle = ab

b = length of short side of rectangle

d = length of long side of rectangle

K_0, K_1 = modified Bessel functions of orders zero and one

Q = heat emission rate from entire rectangle to cold black boundaries

q_l, q_s = local heat fluxes along long and short boundaries of rectangle (for square q_l, $q_s = q$)

R_1, R_2 = dimensionless distances defined in equations (1)

S_n = integral function defined in equations (2)

T_b = absolute temperature of cold boundaries

T_m = uniform absolute temperature of radiating medium

t = integration variable in S_n, equation (2*b*)

u, v = quantities used in integration by parts

X, Y = dimensionless coordinates = x/b, y/b

X', Y' = coordinate variables in integrations

x, y, z = rectangular coordinates (see Fig. 1)

β = argument of S_n, equations (2)

ϵ_{ut} = emittance of entire rectangle at uniform temperature

θ = integration variable for S_n, equation (2*a*)

ξ = dummy integration variable

Introduction

The analysis of radiative heat flow from multidimensional emitting and absorbing media is difficult because of the integrations needed to account for radiation from all parts of the medium to each local volume element. With more powerful computers, it is reasonable to obtain results for some situations by direct numerical integration. This can be done by using discrete ordinates, as did Fiveland (1984) and Truelove (1987); finite elements (Razzaque et al., 1983); or by use of available integration subroutines (Siegel, 1989). A convenient case for testing numerical accuracy is the local radiation to cold black boundaries by a two-dimensional rectangular region filled with a gray emitting medium. For this situation, it was shown by Shah (1979) that it is possible to partially integrate the radiative equations analytically, yielding what was called an "exact" solution. This was used for comparisons by Fiveland (1984) with discrete ordinate solutions.

The solution by Shah (1979) is given as a double integration of the modified Bessel function of order zero. However, as discussed by Yuen and Wong (1983), it is convenient in two-dimensional radiation solutions to use an integral function (called S_n) that is analogous to the exponential integral function that appears in plane-layer solutions. The purpose of this note is to show that the "exact" solution for a rectangular region radiating to cold black walls can be very conveniently derived, and expressed in a simple form, by use of the S_n functions.

[1]National Aeronautics and Space Administration, Lewis Research Center, Cleveland, OH 44135; Fellow ASME.

Contributed by the Heat Transfer Division for publication in the JOURNAL OF HEAT TRANSFER. Manuscript received by the Heat Transfer Division November 27, 1989; revision received March 22, 1990. Keywords: Furnaces and Combustors, Radiation.

Nusselt number decreases rapidly for $A < 5$, especially for large Ra^0 values. Beyond this value, the decrease becomes less, which suggests that the Nusselt number could reach an asymptotic value for a large aspect ratio. In such a case, the vertical component of the radiant flux may be neglected. This would justify the use of a one-dimensional radiative model for $A > 5$ even though the temperature distribution remains essentially two dimensional.

Finally, Fig. 4 shows the respective contributions of conduction and radiation at the hot and cold walls, as well as the global Nusselt number, versus the aspect-ratio values.

Conclusion

To our knowledge, this work is the first attempt to present a completely two-dimensional model dealing with the coupled radiation-convection heat transfer through a fluid-saturated semitransparent porous medium contained in a rectangular enclosure.

An advantage of this model is the possibility to deal with cavities of small aspect ratio.

The study of inclinable cavities will be considered in the near future.

References

Arquis, E., and Caltagirone, J. P., 1987, "Interacting Convection Between Fluid and Open Porous Layers," presented at the ASME Winter Annual Meeting, Boston, MA, Dec. 13–18.

Bejan, A., 1984, *Convection Heat Transfer*, Wiley, NY.

Beckermann, C., Ramadhyani, S., and Viskanta, R., 1987, "Natural Convection Flow and Heat Transfer Between a Fluid Layer and a Porous Layer Inside a Rectangular Enclosure," ASME JOURNAL OF HEAT TRANSFER, Vol. 109, pp. 363–370.

Bouallou, C., 1989, "Modélisation bidimensionnelle des transferts couplés rayonnement-convection naturelle dans les milieux semi-transparents," Thèse de Doctorat, INSA de Lyon, No. 89 ISAL, France.

Burns, P. J., Chow, L. C., and Tien, C. L., 1977, "Convection in a Vertical Slot Filled With a Porous Insulation," *Int. J. Heat Mass Transfer*, Vol. 20, pp. 919–926.

Caltagirone, J. P., 1976, "Instabilités Thermoconvectives en milieu poreux," Thèse de Doctorat d'Etat, Université Pierre et Marie Curie, Paris VI, France.

Desrayaud, G., 1987, "Analyse de stabilité linéaire dans un milieu semi-transparent," Thése de Doctorat d'Etat, Université Pierre et Marie Curie, Paris VI, France.

Lauriat, G., 1980, "A Numerical Study of a Thermal Insulation Enclosure: Influence of the Radiative Transfer," *Natural Convection in Enclosures*, ASME HTD-Vol. 8, pp. 63–71.

Shiralkar, G. S., Haajizadeh, M., and Tien, C. L., 1983, "Numerical Study of High Rayleigh Number Convection in a Vertical Porous Enclosure," *Numerical Heat Transfer*, Vol. 6, pp. 223–234.

Tong, T. W., and Subramanian, E., 1983, "Natural Convection in Rectangular Enclosures Partially Filled With a Porous Medium," *ASME/JSME Thermal Engineering Joint Conf.*, Vol. 1, pp. 331–338.

Tong, T. W., Birkebak, R. C., and Enoch, I. E., 1983, "Thermal Radiation, Convection and Conduction in Porous Media Contained in Vertical Enclosures," ASME JOURNAL OF HEAT TRANSFER, Vol. 105, pp. 414–418.

Uny, G., 1986, "Modélisation du transfert couplé rayonnement-convection au sein de matériaux poreux et identification de leurs propriétés radiatives. Application aux laines de verre," Thèse de Doctorat, INSA - Lyon, France.

Yücel, A., and Bayazitoglu, Y., 1983, "PN Approximation for Radiative Heat Transfer in a Nongray Medium," *AIAA J.*, Vol. 21, No. 8, pp. 1191–1203.

Analytical Solution for Boundary Heat Fluxes From a Radiating Rectangular Medium

R. Siegel[1]

Nomenclature

A_R = aspect ratio of rectangular region = d/b

a = absorption coefficient of radiating medium

B_0 = optical length of short side of rectangle = ab

b = length of short side of rectangle

d = length of long side of rectangle

K_0, K_1 = modified Bessel functions of orders zero and one

Q = heat emission rate from entire rectangle to cold black boundaries

q_l, q_s = local heat fluxes along long and short boundaries of rectangle (for square q_l, $q_s = q$)

R_1, R_2 = dimensionless distances defined in equations (1)

S_n = integral function defined in equations (2)

T_b = absolute temperature of cold boundaries

T_m = uniform absolute temperature of radiating medium

t = integration variable in S_n, equation (2*b*)

u, v = quantities used in integration by parts

X, Y = dimensionless coordinates = x/b, y/b

X', Y' = coordinate variables in integrations

x, y, z = rectangular coordinates (see Fig. 1)

β = argument of S_n, equations (2)

ϵ_{ut} = emittance of entire rectangle at uniform temperature

θ = integration variable for S_n, equation (2*a*)

ξ = dummy integration variable

Introduction

The analysis of radiative heat flow from multidimensional emitting and absorbing media is difficult because of the integrations needed to account for radiation from all parts of the medium to each local volume element. With more powerful computers, it is reasonable to obtain results for some situations by direct numerical integration. This can be done by using discrete ordinates, as did Fiveland (1984) and Truelove (1987); finite elements (Razzaque et al., 1983); or by use of available integration subroutines (Siegel, 1989). A convenient case for testing numerical accuracy is the local radiation to cold black boundaries by a two-dimensional rectangular region filled with a gray emitting medium. For this situation, it was shown by Shah (1979) that it is possible to partially integrate the radiative equations analytically, yielding what was called an "exact" solution. This was used for comparisons by Fiveland (1984) with discrete ordinate solutions.

The solution by Shah (1979) is given as a double integration of the modified Bessel function of order zero. However, as discussed by Yuen and Wong (1983), it is convenient in two-dimensional radiation solutions to use an integral function (called S_n) that is analogous to the exponential integral function that appears in plane-layer solutions. The purpose of this note is to show that the "exact" solution for a rectangular region radiating to cold black walls can be very conveniently derived, and expressed in a simple form, by use of the S_n functions.

[1]National Aeronautics and Space Administration, Lewis Research Center, Cleveland, OH 44135; Fellow ASME.

Contributed by the Heat Transfer Division for publication in the JOURNAL OF HEAT TRANSFER. Manuscript received by the Heat Transfer Division November 27, 1989; revision received March 22, 1990. Keywords: Furnaces and Combustors, Radiation.

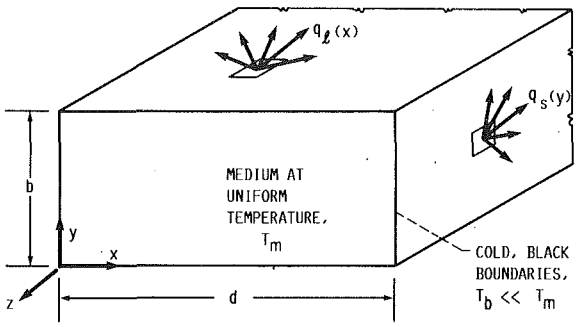

Fig. 1 Geometry of radiating medium at uniform temperature with cold, black boundaries

The integration for part of the solution can then be carried one step further than did Shah (1979). The resulting final expression is very convenient to evaluate and can be readily examined with regard to limiting cases.

Tables of local boundary heat fluxes are presented and discussed for various aspect ratios and optical thicknesses of the rectangular region. The overall emittance is also obtained by integrating the heat fluxes around the boundary. If the walls are not cold, but are black and are all at the same uniform temperature T_b, the same dimensionless heat flux values can be used with T_m^4 replaced by $T_m^4 - T_b^4$.

Analysis

The rectangular region in Fig. 1 is filled with a gray emitting, absorbing medium at a uniform temperature T_m. The bounding walls are black and at low temperature ($T_b << T_m$), and do not radiate significant energy. It is desired to find the distribution along the walls of the energy flux radiated by the medium to the walls. Conduction and convection are assumed small compared with radiation. The geometry is long in the z direction, so that the behavior is two dimensional. From Siegel (1989), the local heat fluxes absorbed at the black walls are given by

$$\frac{q_l(x)}{\sigma T_m^4} = B_0 \int_{X'=0}^{A_R} \int_{Y'=0}^{1} S_2(B_0 R_2) \frac{1-Y'}{R_2^2}\, dX'\, dY' \qquad (1a)$$

$$\frac{q_s(y)}{\sigma T_m^4} = B_0 \int_{X'=0}^{A_R} \int_{Y'=0}^{1} S_2(B_0 R_1) \frac{A_R - X'}{R_1^2}\, dX'\, dY' \qquad (1b)$$

where

$$R_1^2 = (A_R - X')^2 + (Y - Y')^2$$

$$R_2^2 = (X - X')^2 + (1 - Y')^2$$

The S_2 is one of a class of S_n functions given by Yuen and Wong (1983) that arise in two-dimensional radiative transfer. They can be evaluated by numerical integration of the expression

$$S_n(\beta) = \frac{2}{\pi} \int_0^{\pi/2} e^{-\beta/\cos\theta} \cos^{n-1}\theta\, d\theta \qquad \beta \geq 0;\ n = 0, 1, 2, \ldots \qquad (2a)$$

Another form for S_n that will be used in the analysis is

$$S_n(\beta) = \frac{2}{\pi} \int_{t=1}^{\infty} \frac{e^{-\beta t}}{t^n (t^2-1)^{1/2}}\, dt \qquad (2b)$$

To obtain a much more convenient form for equations (1), a few transformations will be made. Equation (1a) will be used, and the evaluation of equation (1b) follows in an identical way. From the definition of R_2, differentiation with respect to Y' gives $dY' = -R_2 dR_2/(1-Y')$. This is substituted into equation (1a), and the optical length of R_2 is defined as $\xi = B_0 R_2$. The result is

Table 1 Local values of $q_\ell(x)/\sigma T_m^4$ and $q_s(y)/\sigma T_m^4$ along the boundary for a rectangular region at uniform temperature

(a) $q_\ell(x)/\sigma T_m^4$ values:

	B_0 = 0.2			B_0 = 0.5			B_0 = 1.0			B_0 = 2.0		
	A_R			A_R			A_R			A_R		
x/b	1	2	4	1	2	4	1	2	4	1	2	4
.000	.123	.139	.146	.248	.271	.278	.369	.387	.390	.462	.470	.470
.025	.134	.153	.160	.280	.303	.310	.426	.446	.449	.561	.569	.569
.050	.145	.162	.169	.300	.325	.332	.462	.483	.486	.618	.626	.627
.100	.158	.177	.184	.330	.357	.364	.512	.536	.540	.694	.704	.704
.200	.175	.197	.206	.368	.401	.410	.575	.605	.610	.779	.794	.794
.300	.186	.212	.221	.391	.431	.441	.611	.650	.655	.824	.844	.845
.400	.192	.222	.233	.403	.453	.464	.630	.680	.686	.846	.875	.876
.500	.193	.230	.242	.407	.468	.481	.636	.701	.708	.853	.895	.896
.600		.236	.249		.479	.494		.715	.724		.907	.910
.700		.240	.255		.487	.504		.726	.737		.916	.919
.800		.243	.259		.493	.513		.732	.746		.921	.925
.900		.245	.263		.496	.519		.736	.753		.924	.929
1.000		.245	.266		.497	.524		.737	.758		.924	.932
1.200			.271			.532			.766			.936
1.400			.274			.537			.770			.938
1.600			.276			.540			.773			.938
2.000			.278			.542			.775			.939

(b) $q_s(y)/\sigma T_m^4$ values:

y/b												
.000	.123	.172	.211	.248	.318	.353	.369	.426	.441	.462	.485	.487
.025	.134	.186	.225	.280	.350	.385	.426	.485	.500	.561	.585	.586
.050	.145	.195	.234	.300	.372	.407	.462	.521	.537	.618	.642	.644
.100	.158	.210	.249	.330	.403	.439	.512	.574	.590	.694	.719	.721
.200	.175	.229	.269	.368	.445	.481	.575	.641	.656	.779	.807	.809
.300	.186	.241	.281	.391	.470	.507	.611	.679	.695	.824	.852	.855
.400	.192	.247	.288	.403	.484	.521	.630	.699	.716	.846	.876	.878
.500	.193	.250	.290	.407	.488	.525	.636	.706	.722	.853	.883	.885

(a) $q_\ell(x)/\sigma T_m^4$ values:

	B_0 = 4			B_0 = 7			B_0 = 10			B_0 = 15		
	A_R			A_R			A_R			A_R		
x/b	1	2	4	1	2	4	1	2	4	1	2	4
.000	.496	.497	.497	.500	.500	.500	.500	.500	.500	.500	.500	.500
.025	.655	.656	.656	.721	.721	.721	.767	.767	.767	.823	.823	.823
.050	.734	.735	.735	.813	.813	.813	.862	.862	.862	.912	.912	.912
.100	.827	.828	.828	.904	.904	.904	.942	.942	.942	.974	.974	.974
.200	.914	.916	.916	.969	.969	.969	.987	.987	.987	.997	.997	.997
.300	.950	.954	.954	.988	.989	.989	.997	.997	.997	1.000	1.000	1.000
.400	.966	.973	.973	.995	.996	.996	.999	.999	.999	1.000	1.000	1.000
.500	.971	.982	.982	.996	.998	.998	.999	1.000	1.000	1.000	1.000	1.000
.600		.988	.988		.999	.999		1.000	1.000		1.000	1.000
.700		.990	.991		1.000	1.000		1.000	1.000		1.000	1.000
.800		.992	.992		1.000	1.000		1.000	1.000		1.000	1.000
.900		.993	.993		1.000	1.000		1.000	1.000		1.000	1.000
1.000		.993	.994		1.000	1.000		1.000	1.000		1.000	1.000
1.200			.994			1.000			1.000			1.000
1.400			.994			1.000			1.000			1.000
1.600			.994			1.000			1.000			1.000
2.000			.994			1.000			1.000			1.000

(b) $q_s(y)/\sigma T_m^4$ values:

y/b												
.000	.496	.499	.499	.500	.500	.500	.500	.500	.500	.500	.500	.500
.025	.655	.658	.658	.721	.721	.721	.767	.767	.767	.823	.823	.823
.050	.734	.737	.737	.813	.813	.813	.862	.862	.862	.912	.912	.912
.100	.827	.830	.830	.904	.904	.904	.942	.942	.942	.974	.974	.974
.200	.914	.917	.917	.969	.969	.969	.987	.987	.987	.997	.997	.997
.300	.950	.954	.954	.988	.989	.989	.997	.997	.997	1.000	1.000	1.000
.400	.966	.970	.970	.995	.995	.995	.999	.999	.999	1.000	1.000	1.000
.500	.971	.974	.974	.996	.997	.997	.999	.999	.999	1.000	1.000	1.000

$$\frac{q_l(X)}{\sigma T_m^4} = -B_0 \int_{X'=0}^{A_R} \int_{\xi=B_0|X-X'|}^{B_0[(X-X')^2+1]^{1/2}} \frac{S_2(\xi)}{\xi}\, d\xi\, dX' \quad (3)$$

The $S_2(\xi)/\xi$ will now be placed in another form.

Using equation (2*b*),

$$\frac{S_2(\xi)}{\xi} = \frac{2}{\pi} \int_{t=1}^{\infty} u\, dv \quad (4)$$

where $u = e^{-\xi t}/\xi$ and $dv = dt/t^2(t^2-1)^{1/2}$. Then $du = -e^{-\xi t}dt$ and $v = (t^2-1)^{1/2}/t$. Since uv vanishes at both of the limits $t=1$ and ∞, integration by parts gives

$$\frac{S_2(\xi)}{\xi} = \frac{2}{\pi} \int_{t=1}^{\infty} e^{-\xi t} \frac{(t^2-1)^{1/2}}{t}\, dt$$

$$= \frac{2}{\pi} \int_{t=1}^{\infty} \frac{te^{-\xi t}}{(t^2-1)^{1/2}}\, dt - \frac{2}{\pi} \int_{t=1}^{\infty} \frac{e^{-\xi t}}{t(t^2-1)^{1/2}}\, dt \quad (5)$$

The first integral on the right-hand side is a form of $K_1(\xi)$, the modified Bessel function of order 1. The second integral is $(\pi/2)S_1(\xi)$. Hence,

$$\frac{S_2(\xi)}{\xi} = \frac{2}{\pi} K_1(\xi) - S_1(\xi) \quad (6)$$

The following relations can now be used (Yuen and Wong, 1983):

$$\int S_1(\xi)d\xi = -S_2(\xi) \text{ and } \frac{2}{\pi}\int K_1(\xi)d\xi = -\frac{2}{\pi} K_0(\xi) = -S_0(\xi)$$

Equation (1*a*) then becomes the single integral

$$\frac{q_l(X)}{\sigma T_m^4} = B_0 \int_{X'=0}^{A_R} \{S_0(B_0|X-X'|) - S_2(B_0|X-X'|)$$

$$- S_0(B_0[(X-X')^2+1]^{1/2})$$

$$+ S_2(B_0[(X-X')^2+1]^{1/2}\}dX' \quad (7)$$

By using a change of variable, $\eta = B_0|X-X'|$, the first two terms on the right-hand side can be integrated into S_1 and S_3 functions. Using $S_1(0)=1$ and $S_3(0)=1/2$, the final form for the boundary heat flux along the long side then becomes

$$\frac{q_l(X)}{\sigma T_m^4} = 1 - S_1(B_0X) + S_3(B_0X)$$

$$- S_1[B_0(A_R - X)] + S_3[B_0(A_R - X)]$$

$$- B_0 \int_{X'=0}^{A_R} \{S_0(B_0[(X-X')^2+1]^{1/2})$$

$$- S_2(B_0[(X-X')^2+1]^{1/2})\}dX' \quad (8a)$$

Table 2 Values of overall emittance $\epsilon_m = Q/2(b+d)\sigma T_m^4$ for rectangle at uniform temperature

B_0	A_R		
	1	2	4
.2	.175	.223	.256
.5	.367	.446	.495
1.0	.571	.657	.708
2.0	.768	.833	.875
4.0	.891	.925	.952
7.0	.939	.958	.975
10.0	.958	.972	.983
15.0	.972	.981	.989

By the same procedure, the local heat flux along the short side is

$$\frac{q_s(Y)}{\sigma T_m^4} = 1 - S_1(B_0Y) + S_3(B_0Y)$$

$$- S_1[B_0(1-Y)] + S_3[B_0(1-Y)]$$

$$- B_0 \int_{Y'=0}^{1} \{S_0(B_0[A_R^2 + (Y-Y')^2]^{1/2})$$

$$- S_2(B_0[A_R^2 + (Y-Y')^2]^{1/2})\}dY' \quad (8b)$$

At the corner of the rectangle $q_l(0) \neq q_s(0)$ unless $A_R = 1$. However as B_0 becomes large, $q_l(0)$ and $q_s(0)$ approach the same constant value. From equation (8*a*), at the corner

$$\frac{q_l(0)}{\sigma T_m^4} = 1 - S_1(0) + S_3(0) - S_1(B_0A_R) + S_3(B_0A_R)$$

$$- B_0 \int_{X'=0}^{A_R} \{S_0(B_0[X'^2+1]^{1/2}) - S_2(B_0[X'^2+1]^{1/2})\}dX' \quad (9)$$

For large B_0, all the S_n with B_0 in the argument become very small. Then since $S_1(0)=1$ and $S_3(0)=1/2$, the limit at the corner for large B_0 is $q_l(0)/\sigma T_m^4 = 1/2$. The same limit applies for q_s at a corner.

The local q_l and q_s values were evaluated numerically for three aspect ratios, $A_R = 1$, 2, 4, and eight optical lengths of the short side, $B_0 = 0.2$, 0.5, 1, 2, 4, 7, 10, 15. A computer computation package was used that employs Romberg integration. The S_n values agreed with those in Yuen and Wong (1983) to six significant figures. The S_n integrations took so little time that the S_0 and S_2 in the integrands were evaluated from equation (2*a*) as required, rather than using interpolation tables of S_n values.

The local heat flux values were integrated over the boundaries to obtain the overall heat radiated to the black walls

$$Q = 2\int_0^d q_l(x)dx + 2\int_0^b q_s(y)dy$$

In dimensionless form, this yields the overall emittance of the rectangle as

$$\epsilon_m = \frac{Q}{2(b+d)\sigma T_m^4} = \frac{1}{1+A_R}\left[\int_0^{A_R} \frac{q_l(X)}{\sigma T_m^4}\, dX + \int_0^1 \frac{q_s(Y)}{\sigma T_m^4}\, dY\right] \quad (10)$$

This was evaluated numerically by Simpson's rule using the q_l and q_s values from equations (8*a*) and (8*b*), and results are in Table 2.

An approximation can be obtained by noting that, for large B_0, the integral terms in equations (8*a*) and (8*b*) become small. The remaining terms can then be integrated analytically to yield (note that $S_4(0) = 4/3\pi$),

$$\epsilon_m \approx 1 - \frac{2}{B_0(A_R+1)}\left[\frac{4}{3\pi} - S_2(B_0) + S_4(B_0) - S_2(B_0A_R) + S_4(B_0A_R)\right] \quad (11)$$

The results from the approximate equation (11) are always larger than those in Table 2 from equation (10). For $B_0 \geq 10$ the agreement is within three significant figures, and for $B_0 = 4$, the results agree within 1/2 percent. For $B_0 = 2$ the error increases to about 4 percent, so equation (11) is not recommended for B_0 values less than about 4.

Results and Discussion

The local heat fluxes as obtained from equations (8*a*) and

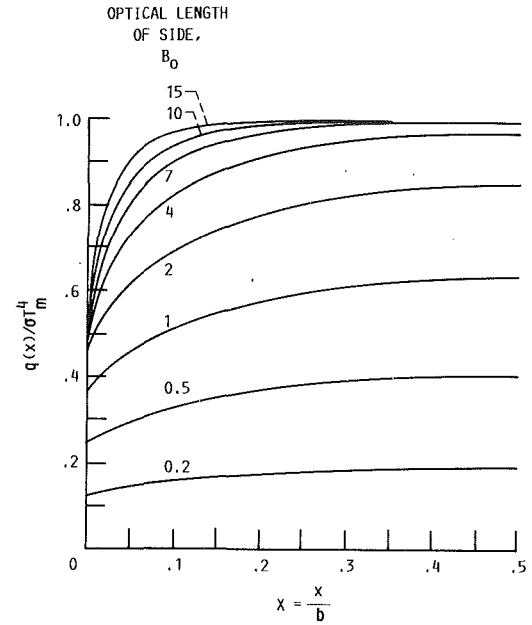

Fig. 2 Local heat flux along boundary for square region, as a function of optical length of side

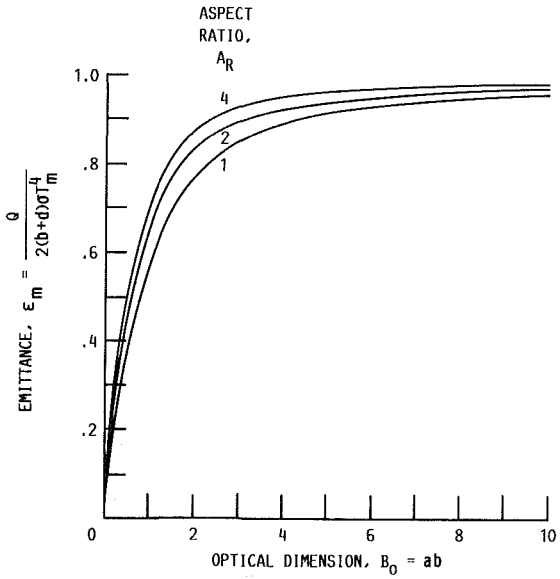

Fig. 3 Overall emittance of rectangular region as a function of aspect ratio and optical density

(8*b*) are given in Table 1 as a function of the aspect ratio and optical thickness of the rectangular region. The boundary fluxes for a square region along one-half of one side are plotted in Fig. 2. The dimensionless fluxes (local emittances) are relatively small for an optically thin region and increase as B_0 is increased. As shown in the analysis, a value of one-half is reached at the corner as B_0 becomes larger than about 6. Away from the corner, the values approach unity for large B_0 (blackbody emission), as would be expected for an optically thick region away from other boundaries. As B_0 becomes large, the change in heat flux becomes very rapid near the corner.

For B_0 greater than about 6, each corner region becomes an isolated nonblack volume, and for $A_R = 2$ and 4, the flux variation moving away from the corner is the same along both the long and short sides (for $A_R = 1$ results are, of course, always symmetric about the corner).

The overall emittances are given in Table 2 and Fig. 3. The values are not a strong function of aspect ratio. Starting from $B_0 = 0$, there is a rapid increase in ϵ_m with optical thickness. For $B_0 > 3$, the rate of increase diminishes rapidly, and the curves rise very gradually toward unity. The approximation for ϵ_m in equation (11) can be conveniently used for $B_0 \geq 4$ with 1/2 percent accuracy or better.

Now consider the situation where the boundary is not cold, but is black and all at uniform temperature T_b. The same dimensionless heat flux and emittance values apply, but T_m^4 is replaced by $T_m^4 - T_b^4$. The heat flux is then the net energy absorbed by the wall.

References

Fiveland, W. A., 1984, "Discrete-Ordinates Solutions of the Radiative Transport Equation for Rectangular Enclosures," ASME JOURNAL OF HEAT TRANSFER, Vol. 106, pp. 699–706.

Razzaque, M. M., Klein, D. E., and Howell, J. R., 1983, "Finite Element Solution of Radiative Heat Transfer in a Two-Dimensional Rectangular Enclosure With Gray Participating Media," ASME JOURNAL OF HEAT TRANSFER, Vol. 105, pp. 933–936.

Shah, N., 1979, "New Method of Computation for the Radiation Heat Transfer in Combustion Chambers," Ph.D. Thesis, Department of Mechanical Engineering, Imperial College of Science and Technology, University of London, United Kingdom.

Siegel, R., 1989, "Some Aspects of Transient Cooling of a Radiating Rectangular Medium," *International Journal of Heat and Mass Transfer*, Vol. 32, pp. 1955–1966.

Truelove, J. S., 1987, "Discrete-Ordinate Solutions of the Radiation Transport Equation," ASME JOURNAL OF HEAT TRANSFER, Vol. 109, pp. 1048–1051.

Yuen, W. W., and Wong, L. W., 1983, "Numerical Computation of an Important Integral Function in Two-Dimensional Radiative Transfer," *Journal of Quantitative Spectroscopy and Radiative Transfer*, Vol. 29, pp. 145–149.

Predicting the Pool Fire Vortex Shedding Frequency

A. Bejan[1]

Nomenclature

C = dimensionless factor, equation (2)
D = diameter or width of pool fire base, m
f = vortex shedding frequency, s^{-1}
g = gravitational acceleration, m/s^2
g' = effective gravitational acceleration, equation (4), m/s^2
P = pressure, N/m^2
R = ideal gas constant, kJ/kg•K
t = period of vortex shedding, s
T = temperature, K
v = vertical velocity scale, m/s
λ_B = buckling wavelength, m
ν = kinematic viscosity, m^2/s
ρ_{fire} = density of fire plume fluid, kg/m^3
ρ_∞ = density of ambient air, kg/m^3

Experimental Observations

It seems that the most talked-about session at the 1989 ASME Winter Annual Meeting was the open forum titled "Some Unanswered Questions in Fluid Mechanics" (Trefethen and Panton, 1989). The interest in this session was stimulated not

[1]J. A. Jones Professor of Mechanical Engineering, Department of Mechanical Engineering and Materials Science, Duke University, Durham, NC 27706; Fellow ASME.

Contributed by the Heat Transfer Division for publication in the JOURNAL OF HEAT TRANSFER. Manuscript received by the Heat Transfer Division January 5, 1990; revision received June 6, 1990. Keywords: Fire/Flames, Natural Convection, Turbulence.

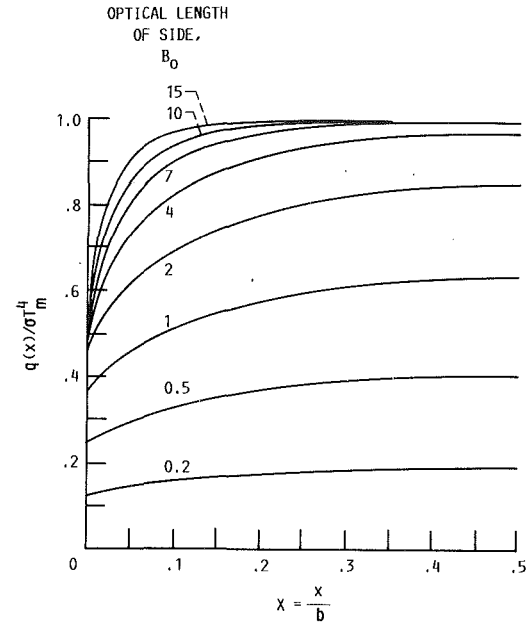

Fig. 2 Local heat flux along boundary for square region, as a function of optical length of side

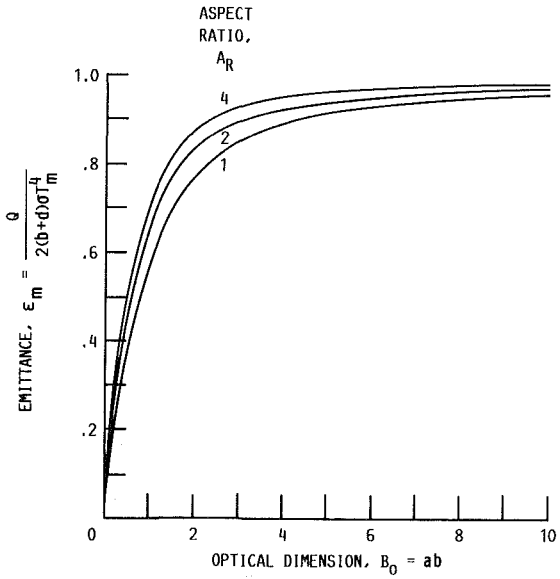

Fig. 3 Overall emittance of rectangular region as a function of aspect ratio and optical density

(8*b*) are given in Table 1 as a function of the aspect ratio and optical thickness of the rectangular region. The boundary fluxes for a square region along one-half of one side are plotted in Fig. 2. The dimensionless fluxes (local emittances) are relatively small for an optically thin region and increase as B_0 is increased. As shown in the analysis, a value of one-half is reached at the corner as B_0 becomes larger than about 6. Away from the corner, the values approach unity for large B_0 (blackbody emission), as would be expected for an optically thick region away from other boundaries. As B_0 becomes large, the change in heat flux becomes very rapid near the corner.

For B_0 greater than about 6, each corner region becomes an isolated nonblack volume, and for $A_R = 2$ and 4, the flux variation moving away from the corner is the same along both the long and short sides (for $A_R = 1$ results are, of course, always symmetric about the corner).

The overall emittances are given in Table 2 and Fig. 3. The values are not a strong function of aspect ratio. Starting from $B_0 = 0$, there is a rapid increase in ϵ_m with optical thickness. For $B_0 > 3$, the rate of increase diminishes rapidly, and the curves rise very gradually toward unity. The approximation for ϵ_m in equation (11) can be conveniently used for $B_0 \geq 4$ with 1/2 percent accuracy or better.

Now consider the situation where the boundary is not cold, but is black and all at uniform temperature T_b. The same dimensionless heat flux and emittance values apply, but T_m^4 is replaced by $T_m^4 - T_b^4$. The heat flux is then the net energy absorbed by the wall.

References

Fiveland, W. A., 1984, "Discrete-Ordinates Solutions of the Radiative Transport Equation for Rectangular Enclosures," ASME JOURNAL OF HEAT TRANSFER, Vol. 106, pp. 699–706.

Razzaque, M. M., Klein, D. E., and Howell, J. R., 1983, "Finite Element Solution of Radiative Heat Transfer in a Two-Dimensional Rectangular Enclosure With Gray Participating Media," ASME JOURNAL OF HEAT TRANSFER, Vol. 105, pp. 933–936.

Shah, N., 1979, "New Method of Computation for the Radiation Heat Transfer in Combustion Chambers," Ph.D. Thesis, Department of Mechanical Engineering, Imperial College of Science and Technology, University of London, United Kingdom.

Siegel, R., 1989, "Some Aspects of Transient Cooling of a Radiating Rectangular Medium," *International Journal of Heat and Mass Transfer*, Vol. 32, pp. 1955–1966.

Truelove, J. S., 1987, "Discrete-Ordinate Solutions of the Radiation Transport Equation," ASME JOURNAL OF HEAT TRANSFER, Vol. 109, pp. 1048–1051.

Yuen, W. W., and Wong, L. W., 1983, "Numerical Computation of an Important Integral Function in Two-Dimensional Radiative Transfer," *Journal of Quantitative Spectroscopy and Radiative Transfer*, Vol. 29, pp. 145–149.

Predicting the Pool Fire Vortex Shedding Frequency

A. Bejan[1]

Nomenclature

- C = dimensionless factor, equation (2)
- D = diameter or width of pool fire base, m
- f = vortex shedding frequency, s^{-1}
- g = gravitational acceleration, m/s^2
- g' = effective gravitational acceleration, equation (4), m/s^2
- P = pressure, N/m^2
- R = ideal gas constant, kJ/kg•K
- t = period of vortex shedding, s
- T = temperature, K
- v = vertical velocity scale, m/s
- λ_B = buckling wavelength, m
- ν = kinematic viscosity, m^2/s
- ρ_{fire} = density of fire plume fluid, kg/m^3
- ρ_∞ = density of ambient air, kg/m^3

Experimental Observations

It seems that the most talked-about session at the 1989 ASME Winter Annual Meeting was the open forum titled "Some Unanswered Questions in Fluid Mechanics" (Trefethen and Panton, 1989). The interest in this session was stimulated not

[1]J. A. Jones Professor of Mechanical Engineering, Department of Mechanical Engineering and Materials Science, Duke University, Durham, NC 27706; Fellow ASME.

Contributed by the Heat Transfer Division for publication in the JOURNAL OF HEAT TRANSFER. Manuscript received by the Heat Transfer Division January 5, 1990; revision received June 6, 1990. Keywords: Fire/Flames, Natural Convection, Turbulence.

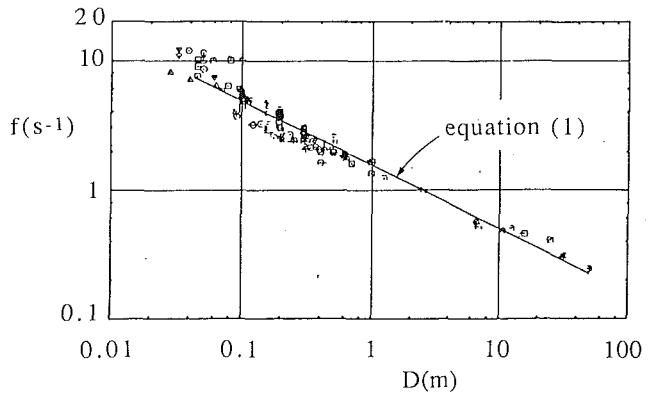

Fig. 1 Measured shedding frequencies as a function of pool base width. Data are for liquids (ethanol, methanol, JP4, oils, gasoline, kerosene, acetone, heptane, hexane, pentane), solids (PMMA, polyurethane, wood), and gases (natural gas, propane) (Pagni, 1989)

only by the excitement of facing the questions identified by its 33 contributors, but also by the fact that most of these "fluid mechanics" questions are pivotal also in the field of heat transfer. Indeed, on the first day of the Winter Annual Meeting, several participants to the "Panel on Directions and Issues in Heat Transfer: An Agenda" argued that the identification and facing of "unanswered questions" is essential to the process of intellectually revitalizing the field of heat transfer.

In this note, I want to contribute to this process by facing one of the unanswered questions of the 1989 Winter Annual Meeting, namely Professor P. J. Pagni's question on "Pool Vortex Shedding Frequencies" (Pagni, 1989). With reference to Fig. 1, he pointed out that "it has been known for twenty years (e.g., McCamy, 1956; Byram and Nelson, 1970; Portscht, 1975; Sibulkin and Hanson, 1975; Detriche and Lanore, 1980; Cox and Chitty, 1980) that fires pulsate with a regular frequency, releasing large annular vortices (coherent structures) from their bases. What is not known is why

$$f^2 \cong \frac{2.3\text{m/s}^2}{D} \tag{1}$$

describes the shedding frequency of pool-flame oscillation over more than three orders of magnitude of the flame base diameter, from 0.03 to 60 m?"

The data displayed in Fig. 1 represent a wide variety of fuels, and fire pool (base) shapes, from circular to rectangular. The alignment of the (f, D) data along the line represented by equation (1) is remarkable.

Theory

Equation (1) can be anticipated based on the buckling theory of inviscid streams (e.g., Bejan, 1984). The older applications of this theory have been reviewed recently by Bejan (1987, 1989) and Gore et al. (1990). According to this theory, a stream that is not penetrated transversally by viscous diffusion will buckle (meander) sinusoidally with a unique wavelength λ_B, which is a multiple of the local stream thickness D,

$$\frac{\lambda_B}{D} = C \tag{2}$$

The theoretical proportionality constant is $C \cong 1.6$ for a stream with round cross section, and $C \cong 1.8$ for one with two-dimensional (flat) cross section.

Consider now the fire plume rising above the base of width D in Fig. 2, and *assume* that the plume thickness (of order D itself) is large enough so that the stream is not penetrated horizontally by viscous diffusion (i.e., it is "inviscid"). We will re-examine this assumption in the next section. In an inviscid plume, the vertical flow is ruled by a balance between

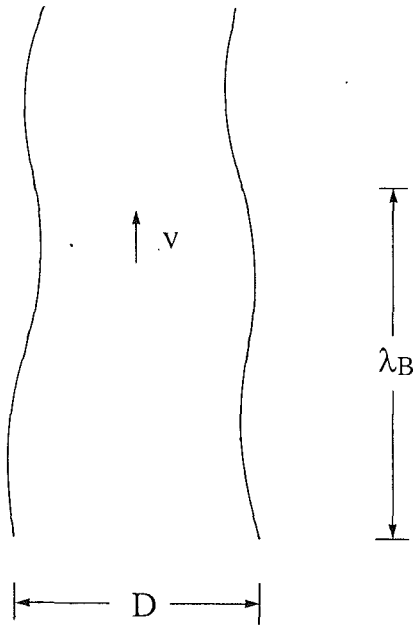

Fig. 2 Length scales of the buckled fire plume

buoyancy and inertia. At a height corresponding to the wavelength of the buckled shape, the vertical velocity scale is the same as the known Gallilean velocity

$$v \cong (2g'\lambda_B)^{1/2} \tag{3}$$

where

$$g' = \frac{\rho_\infty - \rho_{\text{fire}}}{\rho_\infty} g \tag{4}$$

and ρ_∞ is the density of the surrounding atmosphere. The effective gravitational acceleration g' is nearly the same as g, because $\rho_\infty \gg \rho_{\text{fire}}$ (recall that $\rho = P/RT$, P = const, $\rho_\infty \sim$ 300 K, and $\rho_{\text{fire}} \sim$ 1000–2000 K); therefore

$$g' \cong g \tag{5}$$

The symmetry of the shear flow about the fire-ambient interface suggests that if the plume velocity is v and the ambient velocity is zero, the interface (meander) velocity is approximately $v/2$. This means that the meander of the length λ_B rises along the plume with the velocity $v/2$. The period of the swaying motion of the λ_B-tall section of the fire plume is

$$t \cong \frac{\lambda_B}{v/2} \tag{6}$$

From the point of view of the observer on the ground, t is also the period of the fire vortex shedding process. The frequency of this pulsating motion is

$$f = \frac{1}{t} \cong \frac{v/2}{\lambda_B} \tag{7}$$

or, after squaring and using equations (2), (3), and (5)

$$f^2 \cong \frac{g/(2C)}{D} \tag{8}$$

This theoretical trend agrees already with the trend of the empirical correlation (1). It also agrees *quantitatively*, for if we substitute $g = 9.81$ m/s^2, we obtain

$$f^2 \cong \frac{3.1\ \text{m/s}^2}{D} \text{ (round plume)} \tag{9}$$

$$f^2 \cong \frac{2.7\ \text{m/s}^2}{D} \text{ (two-dimensional plume)} \tag{10}$$

The better than 16-percent agreement between these theoretical f values and the empirical f value provided by equation (1) is remarkable, in view of the approximate character of the scale analysis on which equations (8) and (9) are based. Furthermore, the 7-percent discrepancy between the f values calculated with equations (9) and (10) explains some of the scatter that is visible in the data of Fig. 1. This scatter can be attributed in part to the different shapes of the pool fires whose pulsating frequencies have been plotted in this figure.

Conclusion

The observed vortex shedding frequency of pool fires is anticipated very well by the buckling theory of inviscid streams. The empirical information collected in Fig. 1 and equation (1) adds to the growing list of physical observations that supports this theory (Bejan, 1987, 1989; Gore et al., 1990).

It remains to clarify when the fire plume is thick enough to be modeled as inviscid. According to the same buckling theory, the plume is not penetrated by viscous diffusion when the order of magnitude of the "local Reynolds number" is greater than 10^2 (e.g., Bejan, 1984, p. 213):

$$\frac{vD}{\nu} > 10^2 \tag{11}$$

When this inequality (transition criterion) holds, the plume buckles and becomes turbulent. The vertical velocity scale can be calculated as in the preceding section, by using equations (2), (3), and (5). The kinematic viscosity ν can be approximated in terms of the viscosity of air at atmospheric pressure and a temperature of order 1000°C. And, if we use $C \cong 1.7$ as an average value of the geometric constant of the buckled plume, the inequality (11) assumes the dimensional form

$$D > 0.02 \text{ m} \tag{12}$$

This order of magnitude threshold for the size of the flame base agrees very well with Pagni's observation that vortex shedding occurs when D exceeds 0.03 m [see the quotation under equation (1), and the leftmost data in Fig. 1]. It also suggests that vortex shedding can be observed in pool fires with base diameters even larger than 60 m, i.e., to the right of the data of Fig. 1.

In conclusion, the accumulated observations on vortex shedding in small pool fires provide additional support for the turbulence (meandering) transition criterion (11), and for the buckling theory from which that criterion was derived.

References

Bejan, A., 1984, *Convection Heat Transfer*, Wiley, New York, Chap. 6.

Bejan, A., 1987, "Buckling Flows: A New Frontier in Fluid Mechanics," *Annual Review of Numerical Fluid Mechanics and Heat Transfer*, Vol. 1, Hemisphere, Washington, DC, Chap. 5.

Bejan, A., 1989, "Buckling Flows: Exploring the Origins and Structure of Turbulence," *Mechanical Engineering*, Vol. 111, No. 11, pp. 70–74.

Byram, G. M., and Nelson, R. M., 1970, "The Modeling of Pulsating Fires," *Fire Technology*, Vol. 6, pp. 102–110.

Cox, G., and Chitty, R., 1980, "A Study of the Deterministic Properties of Unbounded Fire Plumes," *Combustion and Flame*, Vol. 39, pp. 191–209.

Detriche, P., and Lanore, J. C., 1980, "An Acoustic Study of Pulsation Characteristics of Fires," *Fire Technology*, Vol. 16, pp. 204–211.

Gore, R. A., Crowe, T. C., and Bejan, A., 1990, "The Geometric Similarity of Laminar Sections of Boundary Layer-Type Flows," *Int. Comm. Heat Mass Transfer*, Vol. 17, pp. 465–475.

McCamy, C. S., 1956, "A Five-Band Recording Spectroradiometer," *J. of RES. at NBS*, Research Paper No. 2678, pp. 293–299.

Pagni, P. J., 1989, "Pool Vortex Shedding Frequencies," in ASME Paper No. 89-WA/FE-5, L. M. Trefethen and R. L. Panton, "Some Unanswered Questions in Fluid Mechanics," p. 26.

Portscht, R., 1975, "Studies on Characteristic Fluctuation of the Flame Radiation Emitted by Fires," *Comb. Sci. Tech.*, Vol. 10, pp. 73–84.

Sibulkin, M., and Hanson, A. G., 1975, "Experimental Study of Flame Spreading Over a Horizontal Fuel Surface," *Comb. Sci. Tech.*, Vol. 10, pp. 85–92.

Trefethen, L. M., and Panton, R. L., 1989, "Some Unanswered Questions in Fluid Mechanics," ASME Paper No. 89-WA/FE-5.

A Simple Correlation for the Minimum Film Boiling Temperature

S. Olek,[1] Y. Zvirin,[2] and E. Elias[3]

Numerous correlations for the minimum film boiling temperature have been published, but none have been shown to apply to a great variety of liquids. For example, Berenson's (1961) correlation, which served as a basis for the other correlations, e.g., Iloeje et al. (1975) or Henry (1973), was criticized by Baumeister (see discussion on p. 89 of Henry, 1973) who argued that it does not work for water, liquid metals, Freons, and cryogens. Based on the behavior of liquid droplets coming into contact with a hot surface, Olek et al. (1988) proposed that the rewetting temperature corresponds to very small liquid–solid contact angles. A relation by Adamson (1973) between the contact angle and the temperature was then used to determine the rewetting temperature for water on several polymeric surfaces.

Adamson observed that the results he obtained for the temperature corresponding to a zero contact angle often lie in quite a narrow range around the geometric mean, T_{GM}, of the normal boiling point, T_s, and the critical temperature of the liquid, T_c.

Adamson's suggestion, together with our argument about the fact that the rewetting temperature corresponds to small contact angles, led us to examine whether Adamson's proposal can be used as a simple correlation for the minimum film boiling temperature. Table 1 shows a comparison between T_{GM} and experimental data for either the minimum film boiling temperature, T_{MFB}, or the Leidenfrost temperature, T_{Leid}, when experimental values for T_{MFB} are not available. This comparison is carried out for 17 liquids of different nature: organic, inorganic, cryogenic, and liquid metals. Except for two cases, the comparison is made for liquids at atmospheric pressure. The experimental results for T_{MFB} of potassium display a large scatter. For this liquid, T_{GM} is within the range of T_{MFB} (or T_{Leid}).

From Table 1 it can be realized that the simple correlation suggested here for the minimum film boiling temperature applies for a wide range of liquids. It should be mentioned that, so far, this correlation has no theoretical basis. The limitations of a correlation that takes into account only two thermodynamic properties of the liquid and does not account for the surface properties, hydrodynamics of the problem (e.g., Yilmaz and Westwater, 1980) and geometry (e.g., Lin and Westwater, 1982) are obvious. On the other hand, the success of the correlation suggests that T_{MFB} may primarily be determined by the thermodynamic properties. The latter can serve at least to find a first approximation for the minimum film boiling temperature.

[1]Research and Development Division, Israel Electric Corporation Ltd., Haifa 31000, Israel.

[2]Department of Mechanical Engineering, Technion, Haifa, Israel.

[3]Department of Nuclear Engineering, Technion, Haifa, Israel.

Contributed by the Heat Transfer Division for publication in the JOURNAL OF HEAT TRANSFER. Manuscript received by the Heat Transfer Division August 17, 1989; revision received February 5, 1990. Keywords: Boiling, Evaporation, Multiphase Flows.

The better than 16-percent agreement between these theoretical f values and the empirical f value provided by equation (1) is remarkable, in view of the approximate character of the scale analysis on which equations (8) and (9) are based. Furthermore, the 7-percent discrepancy between the f values calculated with equations (9) and (10) explains some of the scatter that is visible in the data of Fig. 1. This scatter can be attributed in part to the different shapes of the pool fires whose pulsating frequencies have been plotted in this figure.

Conclusion

The observed vortex shedding frequency of pool fires is anticipated very well by the buckling theory of inviscid streams. The empirical information collected in Fig. 1 and equation (1) adds to the growing list of physical observations that supports this theory (Bejan, 1987, 1989; Gore et al., 1990).

It remains to clarify when the fire plume is thick enough to be modeled as inviscid. According to the same buckling theory, the plume is not penetrated by viscous diffusion when the order of magnitude of the "local Reynolds number" is greater than 10^2 (e.g., Bejan, 1984, p. 213):

$$\frac{vD}{\nu} > 10^2 \tag{11}$$

When this inequality (transition criterion) holds, the plume buckles and becomes turbulent. The vertical velocity scale can be calculated as in the preceding section, by using equations (2), (3), and (5). The kinematic viscosity ν can be approximated in terms of the viscosity of air at atmospheric pressure and a temperature of order 1000°C. And, if we use $C \cong 1.7$ as an average value of the geometric constant of the buckled plume, the inequality (11) assumes the dimensional form

$$D > 0.02 \text{ m} \tag{12}$$

This order of magnitude threshold for the size of the flame base agrees very well with Pagni's observation that vortex shedding occurs when D exceeds 0.03 m [see the quotation under equation (1), and the leftmost data in Fig. 1]. It also suggests that vortex shedding can be observed in pool fires with base diameters even larger than 60 m, i.e., to the right of the data of Fig. 1.

In conclusion, the accumulated observations on vortex shedding in small pool fires provide additional support for the turbulence (meandering) transition criterion (11), and for the buckling theory from which that criterion was derived.

References

Bejan, A., 1984, *Convection Heat Transfer*, Wiley, New York, Chap. 6.

Bejan, A., 1987, "Buckling Flows: A New Frontier in Fluid Mechanics," *Annual Review of Numerical Fluid Mechanics and Heat Transfer*, Vol. 1, Hemisphere, Washington, DC, Chap. 5.

Bejan, A., 1989, "Buckling Flows: Exploring the Origins and Structure of Turbulence," *Mechanical Engineering*, Vol. 111, No. 11, pp. 70–74.

Byram, G. M., and Nelson, R. M., 1970, "The Modeling of Pulsating Fires," *Fire Technology*, Vol. 6, pp. 102–110.

Cox, G., and Chitty, R., 1980, "A Study of the Deterministic Properties of Unbounded Fire Plumes," *Combustion and Flame*, Vol. 39, pp. 191–209.

Detriche, P., and Lanore, J. C., 1980, "An Acoustic Study of Pulsation Characteristics of Fires," *Fire Technology*, Vol. 16, pp. 204–211.

Gore, R. A., Crowe, T. C., and Bejan, A., 1990, "The Geometric Similarity of Laminar Sections of Boundary Layer-Type Flows," *Int. Comm. Heat Mass Transfer*, Vol. 17, pp. 465–475.

McCamy, C. S., 1956, "A Five-Band Recording Spectroradiometer," *J. of RES. at NBS*, Research Paper No. 2678, pp. 293–299.

Pagni, P. J., 1989, "Pool Vortex Shedding Frequencies," in ASME Paper No. 89-WA/FE-5, L. M. Trefethen and R. L. Panton, "Some Unanswered Questions in Fluid Mechanics," p. 26.

Portscht, R., 1975, "Studies on Characteristic Fluctuation of the Flame Radiation Emitted by Fires," *Comb. Sci. Tech.*, Vol. 10, pp. 73–84.

Sibulkin, M., and Hanson, A. G., 1975, "Experimental Study of Flame Spreading Over a Horizontal Fuel Surface," *Comb. Sci. Tech.*, Vol. 10, pp. 85–92.

Trefethen, L. M., and Panton, R. L., 1989, "Some Unanswered Questions in Fluid Mechanics," ASME Paper No. 89-WA/FE-5.

A Simple Correlation for the Minimum Film Boiling Temperature

S. Olek,[1] Y. Zvirin,[2] and E. Elias[3]

Numerous correlations for the minimum film boiling temperature have been published, but none have been shown to apply to a great variety of liquids. For example, Berenson's (1961) correlation, which served as a basis for the other correlations, e.g., Iloeje et al. (1975) or Henry (1973), was criticized by Baumeister (see discussion on p. 89 of Henry, 1973) who argued that it does not work for water, liquid metals, Freons, and cryogens. Based on the behavior of liquid droplets coming into contact with a hot surface, Olek et al. (1988) proposed that the rewetting temperature corresponds to very small liquid–solid contact angles. A relation by Adamson (1973) between the contact angle and the temperature was then used to determine the rewetting temperature for water on several polymeric surfaces.

Adamson observed that the results he obtained for the temperature corresponding to a zero contact angle often lie in quite a narrow range around the geometric mean, T_{GM}, of the normal boiling point, T_s, and the critical temperature of the liquid, T_c.

Adamson's suggestion, together with our argument about the fact that the rewetting temperature corresponds to small contact angles, led us to examine whether Adamson's proposal can be used as a simple correlation for the minimum film boiling temperature. Table 1 shows a comparison between T_{GM} and experimental data for either the minimum film boiling temperature, T_{MFB}, or the Leidenfrost temperature, T_{Leid}, when experimental values for T_{MFB} are not available. This comparison is carried out for 17 liquids of different nature: organic, inorganic, cryogenic, and liquid metals. Except for two cases, the comparison is made for liquids at atmospheric pressure. The experimental results for T_{MFB} of potassium display a large scatter. For this liquid, T_{GM} is within the range of T_{MFB} (or T_{Leid}).

From Table 1 it can be realized that the simple correlation suggested here for the minimum film boiling temperature applies for a wide range of liquids. It should be mentioned that, so far, this correlation has no theoretical basis. The limitations of a correlation that takes into account only two thermodynamic properties of the liquid and does not account for the surface properties, hydrodynamics of the problem (e.g., Yilmaz and Westwater, 1980) and geometry (e.g., Lin and Westwater, 1982) are obvious. On the other hand, the success of the correlation suggests that T_{MFB} may primarily be determined by the thermodynamic properties. The latter can serve at least to find a first approximation for the minimum film boiling temperature.

[1]Research and Development Division, Israel Electric Corporation Ltd., Haifa 31000, Israel.

[2]Department of Mechanical Engineering, Technion, Haifa, Israel.

[3]Department of Nuclear Engineering, Technion, Haifa, Israel.

Contributed by the Heat Transfer Division for publication in the JOURNAL OF HEAT TRANSFER. Manuscript received by the Heat Transfer Division August 17, 1989; revision received February 5, 1990. Keywords: Boiling, Evaporation, Multiphase Flows.

Table 1 A comparison between T_{GM} and experimental values of T_{MFB} (or T_{Leid})

Liquid	T_s K	T_c K	T_{GM} K	T_{MFB} K	Source for T_{MFB} or T_{Leid}
Water	373.2	647.4	491.5	508.2	Henry (1973), Table 1
Carbon tetrachloride	350.0	556.4	441.3	435.0	Baumeister and Simon (1973), Table 2
Ethane	185	306	238	233	Westwater et al. (1989).
Etanol	351.7	516.2	426.0	428.0	Baumeister and Simon (1973), Table 2
Benzene	353.3	562.7	445.8	461.5	Capone and Park Jr. (1979), Fig. 3
n-Pentane	309.2	469.6	381.0	378.6	Henry (1973), Table 1
Metanol	338.2	512.5	416.3	408.2	Dhuga and Winterton (1985), Fig. 8
Freon-11	297.0	471.2	374.1	374.8	Henry (1973), Table 2
Freon-12*	317.6	385.2	349.8	357.2	Groeneveld and Gardiner (1978), Fig. 2
Freon-22	195	293	239	235	Westwater et al. (1989).
Freon-113	320.8	487.3	395.4	399.0	Baumeister and Simon (1973), Table 2
Freon-114**	309.2	418.9	359.9	361.1	Hesse (1973), Table 1
Freon-116	232	369	293	298	Westwater et al. (1989).
Nitrogen	77.4	126.2	98.8	94.0	Baumeister and Simon (1973), Table 2
Helium	4.3	5.3	4.7	4.5	Baumeister and Simon (1973), Table 2
Sodium	1156.2	2503.2	1701.2	1683.2	Henry (1973), Table 2
Potassium	1033.2	2073.2	1463.6	1271.0	Henry (1973), Table 2
				1588.2	Baumeister and Simon (1973), Table 2

* The values are for a pressure of 10.7 bars.
** The values are for a pressure of 3 bars.

T_{MFB} of Potassium display a large scatter. T_{GM} for this case is within the range of T_{MFB} (or T_{Leid}) for this liquid.

From Table 1 it can be realized that the simple correlation suggested here for the minimum film boiling temperature applies for a wide range of liquids. It should be mentioned that, so far, this correlation has no theoretical basis. The limitations of a correlation which takes into account only two thermodynamical properties of the liquid and does not account for the surface properties, hydrodynamics of the problem (e.g. Yilmaz and Westwater (1980)) and geometry (e.g. Lin and Westwater (1982)) are obvious. On the other hand, the success of the correlation suggests that T_{MFB} may primarily be determined by the thermodynamical properties. The latter can serve at least to find a first approximation for the minimum film boiling temperature.

Acknowledgments

We thank one of the reviewers for his comments, especially adding the data for ethane, Freon-22, and Freon-116.

References

Adamson, A. W., 1973, "Potential Distortion Model for Contact Angle and Spreading II. Temperature Dependence Effects," *Journal of Colloid and Interface Science*, Vol. 44, pp. 273–281.

Baumeister, K. J., and Simon, F. F., 1973, "Leidenfrost Temperature—Its Correlation for Liquid Metals, Cryogenics, Hydrocarbons and Water," ASME JOURNAL OF HEAT TRANSFER, Vol. 95, pp. 166–173.

Berenson, P. J., 1961, "On Transition Boiling Heat Transfer From a Horizontal Surface," ASME JOURNAL OF HEAT TRANSFER, Vol. 83, pp. 351–358.

Capone, G. J., and Park, E. L., Jr., 1979, "Film Boiling of Freon 113, Normal Pentane, Cyclopentane and Benzene From Cylindrical Surfaces at Moderate Pressures," *International Journal of Heat and Mass Transfer*, Vol. 28, pp. 121–129.

Dhuga, D. S., and Winterton, R. H. S., 1985, "Measurement of Surface Contact in Transition Boiling," *International Journal of Heat and Mass Transfer*, Vol. 28, pp. 1869–1880.

Groeneveld, D. C., and Gardiner, S. R. M., 1978, "A Method for Obtaining Flow Film Boiling Data for Subcooled Water," *International Journal of Heat and Mass Transfer*, Vol. 21, pp. 664–665.

Henry, R. E., 1973, "A Generalized Correlation for the Minimum Point in Film Boiling," presented at the ASME/AIChE 14th National Heat Transfer Conference, Atlanta, GA.

Hesse, G., 1973, "Heat Transfer in Nucleate Boiling, Maximum Heat Flux and Transition Boiling," *International Journal of Heat and Mass Transfer*, Vol. 16, pp. 1611–1627.

Iloeje, O. C., Plummer, D. N., Rohsenow, W. M., and Griffith, P., 1975, "An Investigation of the Collapse and Surface Rewet in Film Boiling in Forced Vertical Flow," ASME JOURNAL OF HEAT TRANSFER, Vol. 97, pp. 166–172.

Lin, D. Y. T., and Westwater, W. J., 1982, "Effects of Metal Thermal Properties on Boiling Curves Obtained by the Quenching Method," *Proceedings, 7th International Heat Transfer Conference*, U. Grigull et al., eds., Hemisphere Publishing Corp., Washington, DC, Vol. 4, pp. 155–160.

Olek, S., Zvirin, Y., and Elias, E., 1988, "The Relation Between the Rewetting Temperature and the Liquid-Solid Contact Angle," *International Journal of Heat and Mass Transfer*, Vol. 31, pp. 898–902.

Westwater, W. J., Zinn, J. C., and Brodbeck, K. J., 1989, "Correlation of Pool Boiling Curves for the Homologous Group: Freon," ASME JOURNAL OF HEAT TRANSFER, Vol. 111, pp. 204–207.

Yilmaz, S., and Westwater, W. J., 1980, "Effect of Velocity on Heat Transfer to Boiling Freon-113," ASME JOURNAL OF HEAT TRANSFER, Vol. 102, pp. 26–31.

Critical Heat Flux and Heat Transfer Transition for Subcooled Flow Boiling

R. D. Boyd, Sr.[1]

Nomenclature

CHF = critical heat flux, W/cm^2
D = inside diameter of coolant channel, cm
G = mass velocity, Mg/m^{2}s
h = local (axial) heat transfer coefficient for subcooled flow boiling, W/cm^{2}K
L = heated length of the coolant channel, cm
p_{exit} = exit pressure of coolant, MPa
Q = net thermal power generation, kW
Q_2 = thermal power generation necessary to cause saturated liquid conditions at the exit of the coolant channel, kW
T_{in} = inlet bulk temperature, °C
z = axial coordinate, cm
θ = angular coordinate ($\theta = 0$ deg on top of the coolant channel)

Introduction

The emphasis in the engineering development of fusion reactor components has been on material development. If high heat fluxes are to be accommodated with the present emphasis, low-pressure thermal data will be needed for: (1) both high CHF and L/D, (2) local heat transfer coefficients, and (3) single-sided heating. The technical literature (Boyd, 1985; Collier, 1981) shows that: (1) Abundant data exist below CHF = 0.1 kW/cm^2 for all L/D, and below 0.5 kW/cm^2 for $L/D < 150.0$ and $D < 1.0$ cm, (2) a moderate data base exists above 2.0 kW/cm^2 for $L/D < 35.0$ and $D < 0.5$ cm, (3) a sparse but growing data base exists above 2.0 kW/cm^2 for $35.0 < L/D < 100.0$ and $D < 0.5$ cm, and (4) a sparse but growing data base exists above 0.8 kW/cm^2 for $L/D > 40.0$ and $D > 0.5$ cm. The objectives of this experiment were to: (1) expand the CHF data base near 4.0 kW/cm^2 and L/D near 100.0 (near-term application), (2) add low-pressure quantitative data to our existing knowledge of the qualitative influence of p_{exit} on CHF, and (3) provide thermal data in a region applicable to high heat flux components for assessing existing and evolving CHF and local heat transfer coefficient correlations (long-term).

Experimental Description

Steady-state subcooled water flow boiling experiments were carried out in a uniformly heated horizontal circular channel with an exit pressure of 1.66 MPa. The smooth zirconium–copper test section had a tube diameter of 0.3 cm, and

[1]Department of Mechanical Engineering, Prairie View A&M University, Prairie View, TX 77446.

Contributed by the Heat Transfer Division for publication in the JOURNAL OF HEAT TRANSFER. Manuscript received by the Heat Transfer Division April 3, 1989; revision received February 28, 1990. Keywords: Flow Instability, Forced Convection, Multiphase Flows.

Table 1 A comparison between T_{GM} and experimental values of T_{MFB} (or T_{Leid})

Liquid	T_s K	T_c K	T_{GM} K	T_{MFB} K	Source for T_{MFB} or T_{Leid}
Water	373.2	647.4	491.5	508.2	Henry (1973), Table 1
Carbon tetrachloride	350.0	556.4	441.3	435.0	Baumeister and Simon (1973), Table 2
Ethane	185	306	238	233	Westwater et al. (1989).
Etanol	351.7	516.2	426.0	428.0	Baumeister and Simon (1973), Table 2
Benzene	353.3	562.7	445.8	461.5	Capone and Park Jr. (1979), Fig. 3
n-Pentane	309.2	469.6	381.0	378.6	Henry (1973), Table 1
Metanol	338.2	512.5	416.3	408.2	Dhuga and Winterton (1985), Fig. 8
Freon-11	297.0	471.2	374.1	374.8	Henry (1973), Table 2
Freon-12*	317.6	385.2	349.8	357.2	Groeneveld and Gardiner (1978), Fig. 2
Freon-22	195	293	239	235	Westwater et al. (1989).
Freon-113	320.8	487.3	395.4	399.0	Baumeister and Simon (1973), Table 2
Freon-114**	309.2	418.9	359.9	361.1	Hesse (1973), Table 1
Freon-116	232	369	293	298	Westwater et al. (1989).
Nitrogen	77.4	126.2	98.8	94.0	Baumeister and Simon (1973), Table 2
Helium	4.3	5.3	4.7	4.5	Baumeister and Simon (1973), Table 2
Sodium	1156.2	2503.2	1701.2	1683.2	Henry (1973), Table 2
Potassium	1033.2	2073.2	1463.6	1271.0	Henry (1973), Table 2
				1588.2	Baumeister and Simon (1973), Table 2

* The values are for a pressure of 10.7 bars.
** The values are for a pressure of 3 bars.

T_{MFB} of Potassium display a large scatter. T_{GM} for this case is within the range of T_{MFB} (or T_{Leid}) for this liquid.
From Table 1 it can be realized that the simple correlation suggested here for the minimum film boiling temperature applies for a wide range of liquids. It should be mentioned that, so far, this correlation has no theoretical basis. The limitations of a correlation which takes into account only two thermodynamical properties of the liquid and does not account for the surface properties, hydrodynamics of the problem (e.g. Yilmaz and Westwater (1980)) and geometry (e.g. Lin and Westwater (1982)) are obvious. On the other hand, the success of the correlation suggests that T_{MFB} may primarily be determined by the thermodynamical properties. The latter can serve at least to find a first approximation for the minimum film boiling temperature.

Acknowledgments

We thank one of the reviewers for his comments, especially adding the data for ethane, Freon-22, and Freon-116.

References

Adamson, A. W., 1973, "Potential Distortion Model for Contact Angle and Spreading II. Temperature Dependence Effects," *Journal of Colloid and Interface Science*, Vol. 44, pp. 273–281.

Baumeister, K. J., and Simon, F. F., 1973, "Leidenfrost Temperature—Its Correlation for Liquid Metals, Cryogenics, Hydrocarbons and Water," ASME JOURNAL OF HEAT TRANSFER, Vol. 95, pp. 166–173.

Berenson, P. J., 1961, "On Transition Boiling Heat Transfer From a Horizontal Surface," ASME JOURNAL OF HEAT TRANSFER, Vol. 83, pp. 351–358.

Capone, G. J., and Park, E. L., Jr., 1979, "Film Boiling of Freon 113, Normal Pentane, Cyclopentane and Benzene From Cylindrical Surfaces at Moderate Pressures," *International Journal of Heat and Mass Transfer*, Vol. 28, pp. 121–129.

Dhuga, D. S., and Winterton, R. H. S., 1985, "Measurement of Surface Contact in Transition Boiling," *International Journal of Heat and Mass Transfer*, Vol. 28, pp. 1869–1880.

Groeneveld, D. C., and Gardiner, S. R. M., 1978, "A Method for Obtaining Flow Film Boiling Data for Subcooled Water," *International Journal of Heat and Mass Transfer*, Vol. 21, pp. 664–665.

Henry, R. E., 1973, "A Generalized Correlation for the Minimum Point in Film Boiling," presented at the ASME/AIChE 14th National Heat Transfer Conference, Atlanta, GA.

Hesse, G., 1973, "Heat Transfer in Nucleate Boiling, Maximum Heat Flux and Transition Boiling," *International Journal of Heat and Mass Transfer*, Vol. 16, pp. 1611–1627.

Iloeje, O. C., Plummer, D. N., Rohsenow, W. M., and Griffith, P., 1975, "An Investigation of the Collapse and Surface Rewet in Film Boiling in Forced Vertical Flow," ASME JOURNAL OF HEAT TRANSFER, Vol. 97, pp. 166–172.

Lin, D. Y. T., and Westwater, W. J., 1982, "Effects of Metal Thermal Properties on Boiling Curves Obtained by the Quenching Method," *Proceedings, 7th International Heat Transfer Conference*, U. Grigull et al., eds., Hemisphere Publishing Corp., Washington, DC, Vol. 4, pp. 155–160.

Olek, S., Zvirin, Y., and Elias, E., 1988, "The Relation Between the Rewetting Temperature and the Liquid-Solid Contact Angle," *International Journal of Heat and Mass Transfer*, Vol. 31, pp. 898–902.

Westwater, W. J., Zinn, J. C., and Brodbeck, K. J., 1989, "Correlation of Pool Boiling Curves for the Homologous Group: Freon," ASME JOURNAL OF HEAT TRANSFER, Vol. 111, pp. 204–207.

Yilmaz, S., and Westwater, W. J., 1980, "Effect of Velocity on Heat Transfer to Boiling Freon-113," ASME JOURNAL OF HEAT TRANSFER, Vol. 102, pp. 26–31.

Critical Heat Flux and Heat Transfer Transition for Subcooled Flow Boiling

R. D. Boyd, Sr.[1]

Nomenclature

CHF = critical heat flux, W/cm^2
D = inside diameter of coolant channel, cm
G = mass velocity, Mg/m^{2}s
h = local (axial) heat transfer coefficient for subcooled flow boiling, W/cm^{2}K
L = heated length of the coolant channel, cm
p_{exit} = exit pressure of coolant, MPa
Q = net thermal power generation, kW
Q_2 = thermal power generation necessary to cause saturated liquid conditions at the exit of the coolant channel, kW
T_{in} = inlet bulk temperature, °C
z = axial coordinate, cm
θ = angular coordinate ($\theta = 0$ deg on top of the coolant channel)

Introduction

The emphasis in the engineering development of fusion reactor components has been on material development. If high heat fluxes are to be accommodated with the present emphasis, low-pressure thermal data will be needed for: (1) both high CHF and L/D, (2) local heat transfer coefficients, and (3) single-sided heating. The technical literature (Boyd, 1985; Collier, 1981) shows that: (1) Abundant data exist below CHF = 0.1 kW/cm^2 for all L/D, and below 0.5 kW/cm^2 for $L/D < 150.0$ and $D < 1.0$ cm, (2) a moderate data base exists above 2.0 kW/cm^2 for $L/D < 35.0$ and $D < 0.5$ cm, (3) a sparse but growing data base exists above 2.0 kW/cm^2 for $35.0 < L/D < 100.0$ and $D < 0.5$ cm, and (4) a sparse but growing data base exists above 0.8 kW/cm^2 for $L/D > 40.0$ and $D > 0.5$ cm. The objectives of this experiment were to: (1) expand the CHF data base near 4.0 kW/cm^2 and L/D near 100.0 (near-term application), (2) add low-pressure quantitative data to our existing knowledge of the qualitative influence of p_{exit} on CHF, and (3) provide thermal data in a region applicable to high heat flux components for assessing existing and evolving CHF and local heat transfer coefficient correlations (long-term).

Experimental Description

Steady-state subcooled water flow boiling experiments were carried out in a uniformly heated horizontal circular channel with an exit pressure of 1.66 MPa. The smooth zirconium–copper test section had a tube diameter of 0.3 cm, and

[1]Department of Mechanical Engineering, Prairie View A&M University, Prairie View, TX 77446.

Contributed by the Heat Transfer Division for publication in the JOURNAL OF HEAT TRANSFER. Manuscript received by the Heat Transfer Division April 3, 1989; revision received February 28, 1990. Keywords: Flow Instability, Forced Convection, Multiphase Flows.

a heated L/D of 96.6. T_{in} was 20.0°C. The L/D was more than three times that for most data in the literature for CHF near 4.0 kW/cm^2. A 250.0 kW (25 V, 10^4 A, d-c) transformer was used as the energy source. The experimental apparatus and procedure have been described previously by Boyd et al. (1987).

Local (axial) wall temperatures were measured on the outside surface of each test section using 0.51-mm-dia type-K thermocouples at three locations for $\theta = 0$ deg (i.e., on top of the test section and at $z = 0.317$, 14.586, and 28.655 cm). In a few cases, a fourth thermocouple was mounted on the bottom ($\theta = 180$ deg) of the test section and at $z = 28.655$ cm to assess the significance of both circumferential temperature variations and test section orientation. The thermocouples were electrically isolated from the test section with high temperature cement.

The accuracy of the CHF was not only a function of the accuracy to which basic flow parameters (i.e., p_{exit}, G, etc.) were held constant, but it was also closely dependent on the accuracy of: (1) the current and voltage measurements, and (2) the control parameter's step size as CHF was approached. The CHF was approached by controlling the current flow through the test section. This current, which also flowed through a precision shunt resistor, was measured to within 0.067 percent. The corresponding test section voltage drop was measured to within 0.5 percent. As CHF was approached, the current increment was kept to within 2 percent of the previous current level. After linearizing the nonlinear equation describing the contributions to the uncertainty of CHF, it was found that current step size had the greatest effect on the uncertainty. Other contributions included 0.5 percent due to voltage, 0.002 percent due to the temperature dependence of the shunt resistance, and 0.01 percent due to current. A CHF search procedure was developed and followed so as to keep the uncertainty due to current step size at or below 2 percent. These contributions resulted in an apparent CHF uncertainty slightly greater than 2.5 percent. However, there was a slight voltage spike as CHF was approached. Rather than using the spiked voltage value to compute CHF, the measured current was used to extrapolate the voltage over the small increment to the voltage corresponding to the maximum recorded current. Since the extrapolated voltage increment was less than 1.3 percent, the overall uncertainty in the CHF was estimated to be less than 4.0 percent.

Results

Critical Heat Flux. The measured CHF was compared with both previous data at a lower pressure (Boyd, 1988) and Gambill's (1963) correlation. Figure 1 indicates that as p_{exit} increased from 0.77 to 1.66 MPa, the CHF increased at all mass velocity levels. However, the extent of the enhancement initially increased with G but later decreased. More specifically, the effect of increasing p_{exit} was to increase CHF progressively from 2.0 to 19.0 percent, as the mass velocity varied from 4.4 to 25.0 Mg/m^{2}s. However, the percentage increase in CHF dropped to 10.0 percent as G increased above 25.0 Mg/m^{2}s. Below 25.0 Mg/m^{2}s, the relationship between CHF and G was linear. The effect of increasing the exit pressure was to increase the slope of this relationship. Further, Fig. 1 shows that only a slight enhancement in CHF resulted for G near 4.0 Mg/m^{2}s. Nevertheless, *for the relatively large value of L/D* and the low exit pressure, the measured CHFs are higher than any previous values for *smooth tube* axial (i.e., nonswirl) flow. This includes the previous work by Gambill et al. (1958, 1961), who measured CHF for smooth tubes as high as 5500 W/cm^2 but for $L/D < 22.0$. They had one data point for $L/D = 88.4$ (CHF = 3969 W/cm^2). Although significantly higher CHF (< 17,700 W/cm^2) was measured for tangential-slot vortex flow, their L/D was < 3.0.

In all cases, Fig. 2 shows that the CHF occurred at Q/Q_2 between 0.55 and 0.7. In most cases, it occurred at $Q/Q_2 = 0.6$. The implication is that at least two subcooled flow regimes (see Fig. 2) were spanned by the data. The dimen-

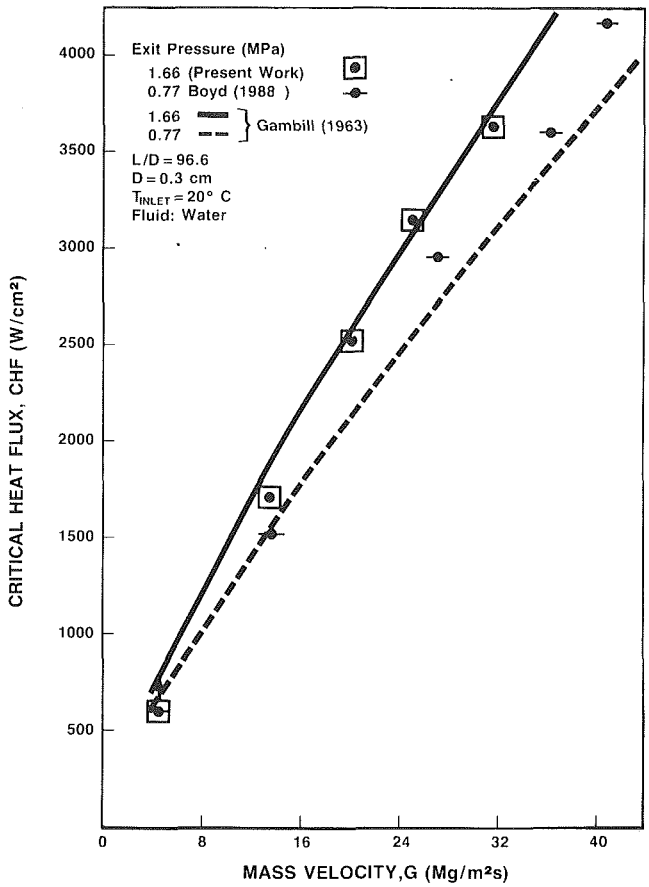

Fig. 1 Measured subcooled flow boiling CHF as a function of mass velocity

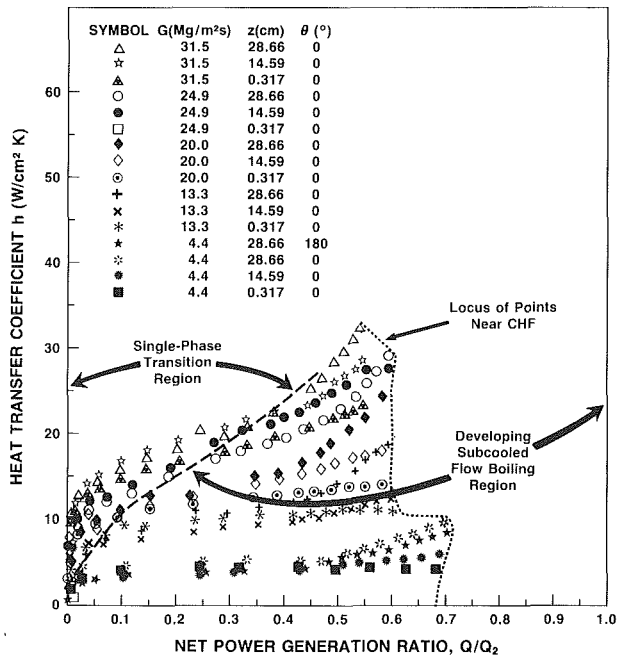

Fig. 2 Subcooled flow boiling heat transfer coefficient map for water flow through uniformly heated copper tubes with the following conditions: $D = 0.3$ cm, $L/D = 96.6$, $p_{exit} = 1.66$ MPa, and $T_{in} = 20.0$°C

sionless parameter Q/Q_2 was selected for the abscissa to emphasize that subcooled boiling occurred in all cases. This choice has proved to be illuminating. For example, for G and CHF varying by almost an order of magnitude, the CHF for all cases occurred over a small range of Q/Q_2. This suggests that if the existing CHF data are to be unified, future CHF correlations must include Q/Q_2 as a fundamental parameter.

Most CHF correlations have limited applicability beyond the range for which they were developed. For example, Boyd (1987) compared correlations by Merilo, Bowring, and Katto with data for $p_{exit} = 1.6$ MPa, $L/D = 115.6$, and $T_{in} = 21.0°C$. The results showed that all correlations predicted CHF substantially above the data. In a previous technical assessment, Boyd et al. (1985) suggested that Gambill's correlation might apply for subcooled flows with both high CHF and L/D. However, only sparse data existed at that time. Figure 1 shows reasonable agreement between his correlation and the present data. The correlation underpredicted the lower-pressure CHF ($p_{exit} = 0.77$ MPa) by increasing amounts as G increased. Recently, Weisman (1988) obtained good agreement with this latter set of data.

Local (Axial) Heat Transfer Transition. For $G < 5.0$ Mg/m^{2}s, the change in temperature across the copper test section (0.105 cm) was significant. This change was accounted for in the present work (e.g., see Boyd et al., 1987).

Figure 2 shows the variations of h as a function of Q/Q_2, G, and z. The effects of increases in G (and exit subcooling) on the heat transfer are also clearly shown. For an increase in G from 4.4 to 31.5 Mg/m^{2}s (or an increase in the exit subcooling from approximately 53.0 to 82.0°C), h at the exit of the coolant channel increased by more than a factor of three (from 10.0 to 32.0 W/cm^{2}K). At upstream locations, this increase was more pronounced. At a given value of Q/Q_2, the axial variation in h initially increased with G. However, as subcooled boiling occurred over a greater portion of the flow channel, these variations were reduced. Nevertheless, substantial variations (50.0 percent) in h existed as CHF was approached.

Figure 2 can be used to trace both the transition from single-phase regime to subcooled flow boiling regime, and the migration of the localized boiling front from the downstream end of the channel as Q was increased. The boundary shown on the left side of the figure corresponds to the condition of negligible axial variation in h. The transition from single-phase to two-phase flow was most noticeable when considering the change of the gradient of h with respect to Q/Q_2. In the single-phase region, h was inversely related to z. However, as boiling ensued, a reversal in the single-phase trend occurred. The onset of developing flow boiling was characterized by an increase in the slope of a given curve. The point of this increase shifted to higher Q/Q_2 as G and z decreased. Prior to the onset of this developing flow, h was essentially constant over most of the channel. However, as Q/Q_2 was increased, h increased substantially at the exit.

Exit Pressure Influence. With respect to p_{exit}, the present experiment represents an additional data point toward the identification of the condition corresponding to optimum subcooled flow boiling CHF and heat transfer for the given conditions. Doubling the exit pressure enhanced the CHF, but for the most part reduced the local (axial) heat transfer at a given Q. However, an apparent enhancement in h occurred if comparisons are made at the same Q/Q_2. This enhancement rarely exceeded 16.0 percent. Although the axial variation in h does not appear to be greatly changed with p_{exit}, the onset of developing subcooled boiling occurred at lower Q/Q_2. Further, the inside wall temperature in the boiling regime increased for a given Q and G. Although Q_2 increased with p_{exit}, other changes in the flow structure may be contributing to these trends. Finally, little or no effect in the pressure drop resulted when p_{exit} was changed.

Conclusions

Although previous summaries (e.g., Collier, 1981) contain valuable trends and some quantitative data, there is still a lack of highly subcooled CHF data and correlations for cases involving both high CHF and L/D. Gambill's correlation adequately predicted the CHF data at 1.66 MPa, but underpredicted CHF at 0.77 MPa for $G > 14.0$ Mg/m^{2}s. The h and CHF data: (1) provided a means of tracing both the transition from single-phase flow to subcooled flow boiling and the migration of the boiling front along the channel, (2) added to the presently sparse data base, and (3) will aid in assessing both theoretical and phenomenological models.

References

Boyd, R. D., 1985, "Subcooled Flow Boiling Critical Heat Flux (CHF) and Its Application to Fusion Energy Components. Parts I and II," *Fusion Technology*, Vol. 7(1), pp. 7–52.

Boyd, R. D., et al., 1985, "Technical Assessment of Thermal-Hydraulics for High Heat Flux Fusion Components," SAND84-0159, Sandia National Laboratories, Albuquerque, NM.

Boyd, R. D., et al., 1987, "Experimental Flow Boiling for High Heat Flux Applications," *Heat Transfer in High Technology and Power Engineering*, W.-J. Yang and Y. Mori., eds., Hemisphere Publishing Corporation, New York.

Boyd, R. D., 1988, "Subcooled Water Flow Boiling Experiments Under Uniform High Heat Flux Conditions," *Fusion Technology*, Vol. 13(1), pp. 131–142.

Collier, J. G., 1981, *Convective Boiling and Condensation*, McGraw-Hill, New York.

Gambill, W. R., and Greene, N. D., 1958, "Boiling Burnout With Water in Vortex Flow," *Chemical Engineering Progress*, Vol. 54, pp. 68–76.

Gambill, W. R., et al., 1961, "Heat Transfer, Burnout, and Pressure Drop for Water in Swirl Flow Through Tubes With Internal Twisted Tapes," *Chemical Engineering Progress*, Symposium Series No. 32, Vol. 57, pp. 127–137.

Gambill, W. R., 1963, "Generalized Prediction of Burnout Heat Flux for Flowing, Subcooled, Wetting Liquids," *AIChE Series*, Vol. 59, pp. 71–87.

Weisman, J., 1988, "Comments on Subcooled Water Flow Boiling Experiments Under Uniform High Heat Flux Conditions," *Fusion Technology*, Vol. 14, p. 1418.

Film Boiling Heat Transfer to Large Superheats From a Horizontal Flat Surface

M. R. Duignan,[1] G. A. Greene,[2] and T. F. Irvine, Jr.[3]

Nomenclature

c_p = specific heat at constant pressure
D = characteristic dimension of the heat transfer surface
g = acceleration of gravity
h = heat transfer coefficient
h_{fg} = latent heat
k = thermal conductivity
q = heat flux
T = temperature

[1]Westinghouse Savannah River Company, Savannah River Laboratory, Aiken, SC 29802.

[2]Brookhaven National Laboratory, Department of Nuclear Energy, Upton, NY 11973-5000.

[3]State University of New York at Stony Brook, Department of Mechanical Engineering, Stony Brook, NY 11794-1603.

Contributed by the Heat Transfer Division for publication in the JOURNAL OF HEAT TRANSFER. Manuscript received by the Heat Transfer Division October 19, 1989; revision received June 12, 1990. Keywords: Boiling, High-Temperature Phenomena, Phase-Change Phenomena.

sionless parameter Q/Q_2 was selected for the abscissa to emphasize that subcooled boiling occurred in all cases. This choice has proved to be illuminating. For example, for G and CHF varying by almost an order of magnitude, the CHF for all cases occurred over a small range of Q/Q_2. This suggests that if the existing CHF data are to be unified, future CHF correlations must include Q/Q_2 as a fundamental parameter.

Most CHF correlations have limited applicability beyond the range for which they were developed. For example, Boyd (1987) compared correlations by Merilo, Bowring, and Katto with data for $p_{exit} = 1.6$ MPa, $L/D = 115.6$, and $T_{in} = 21.0°C$. The results showed that all correlations predicted CHF substantially above the data. In a previous technical assessment, Boyd et al. (1985) suggested that Gambill's correlation might apply for subcooled flows with both high CHF and L/D. However, only sparse data existed at that time. Figure 1 shows reasonable agreement between his correlation and the present data. The correlation underpredicted the lower-pressure CHF ($p_{exit} = 0.77$ MPa) by increasing amounts as G increased. Recently, Weisman (1988) obtained good agreement with this latter set of data.

Local (Axial) Heat Transfer Transition. For $G < 5.0$ Mg/m^{2}s, the change in temperature across the copper test section (0.105 cm) was significant. This change was accounted for in the present work (e.g., see Boyd et al., 1987).

Figure 2 shows the variations of h as a function of Q/Q_2, G, and z. The effects of increases in G (and exit subcooling) on the heat transfer are also clearly shown. For an increase in G from 4.4 to 31.5 Mg/m^{2}s (or an increase in the exit subcooling from approximately 53.0 to 82.0°C), h at the exit of the coolant channel increased by more than a factor of three (from 10.0 to 32.0 W/cm^{2}K). At upstream locations, this increase was more pronounced. At a given value of Q/Q_2, the axial variation in h initially increased with G. However, as subcooled boiling occurred over a greater portion of the flow channel, these variations were reduced. Nevertheless, substantial variations (50.0 percent) in h existed as CHF was approached.

Figure 2 can be used to trace both the transition from single-phase regime to subcooled flow boiling regime, and the migration of the localized boiling front from the downstream end of the channel as Q was increased. The boundary shown on the left side of the figure corresponds to the condition of negligible axial variation in h. The transition from single-phase to two-phase flow was most noticeable when considering the change of the gradient of h with respect to Q/Q_2. In the single-phase region, h was inversely related to z. However, as boiling ensued, a reversal in the single-phase trend occurred. The onset of developing flow boiling was characterized by an increase in the slope of a given curve. The point of this increase shifted to higher Q/Q_2 as G and z decreased. Prior to the onset of this developing flow, h was essentially constant over most of the channel. However, as Q/Q_2 was increased, h increased substantially at the exit.

Exit Pressure Influence. With respect to p_{exit}, the present experiment represents an additional data point toward the identification of the condition corresponding to optimum subcooled flow boiling CHF and heat transfer for the given conditions. Doubling the exit pressure enhanced the CHF, but for the most part reduced the local (axial) heat transfer at a given Q. However, an apparent enhancement in h occurred if comparisons are made at the same Q/Q_2. This enhancement rarely exceeded 16.0 percent. Although the axial variation in h does not appear to be greatly changed with p_{exit}, the onset of developing subcooled boiling occurred at lower Q/Q_2. Further, the inside wall temperature in the boiling regime increased for a given Q and G. Although Q_2 increased with p_{exit}, other changes in the flow structure may be contributing to these trends. Finally, little or no effect in the pressure drop resulted when p_{exit} was changed.

Conclusions

Although previous summaries (e.g., Collier, 1981) contain valuable trends and some quantitative data, there is still a lack of highly subcooled CHF data and correlations for cases involving both high CHF and L/D. Gambill's correlation adequately predicted the CHF data at 1.66 MPa, but underpredicted CHF at 0.77 MPa for $G > 14.0$ Mg/m^{2}s. The h and CHF data: (1) provided a means of tracing both the transition from single-phase flow to subcooled flow boiling and the migration of the boiling front along the channel, (2) added to the presently sparse data base, and (3) will aid in assessing both theoretical and phenomenological models.

References

Boyd, R. D., 1985, "Subcooled Flow Boiling Critical Heat Flux (CHF) and Its Application to Fusion Energy Components. Parts I and II," *Fusion Technology*, Vol. 7(1), pp. 7–52.

Boyd, R. D., et al., 1985, "Technical Assessment of Thermal-Hydraulics for High Heat Flux Fusion Components," SAND84-0159, Sandia National Laboratories, Albuquerque, NM.

Boyd, R. D., et al., 1987, "Experimental Flow Boiling for High Heat Flux Applications," *Heat Transfer in High Technology and Power Engineering*, W.-J. Yang and Y. Mori., eds., Hemisphere Publishing Corporation, New York.

Boyd, R. D., 1988, "Subcooled Water Flow Boiling Experiments Under Uniform High Heat Flux Conditions," *Fusion Technology*, Vol. 13(1), pp. 131–142.

Collier, J. G., 1981, *Convective Boiling and Condensation*, McGraw-Hill, New York.

Gambill, W. R., and Greene, N. D., 1958, "Boiling Burnout With Water in Vortex Flow," *Chemical Engineering Progress*, Vol. 54, pp. 68–76.

Gambill, W. R., et al., 1961, "Heat Transfer, Burnout, and Pressure Drop for Water in Swirl Flow Through Tubes With Internal Twisted Tapes," *Chemical Engineering Progress*, Symposium Series No. 32, Vol. 57, pp. 127–137.

Gambill, W. R., 1963, "Generalized Prediction of Burnout Heat Flux for Flowing, Subcooled, Wetting Liquids," *AIChE Series*, Vol. 59, pp. 71–87.

Weisman, J., 1988, "Comments on Subcooled Water Flow Boiling Experiments Under Uniform High Heat Flux Conditions," *Fusion Technology*, Vol. 14, p. 1418.

Film Boiling Heat Transfer to Large Superheats From a Horizontal Flat Surface

M. R. Duignan,[1] G. A. Greene,[2] and T. F. Irvine, Jr.[3]

Nomenclature

c_p = specific heat at constant pressure
D = characteristic dimension of the heat transfer surface
g = acceleration of gravity
h = heat transfer coefficient
h_{fg} = latent heat
k = thermal conductivity
q = heat flux
T = temperature

[1]Westinghouse Savannah River Company, Savannah River Laboratory, Aiken, SC 29802.

[2]Brookhaven National Laboratory, Department of Nuclear Energy, Upton, NY 11973-5000.

[3]State University of New York at Stony Brook, Department of Mechanical Engineering, Stony Brook, NY 11794-1603.

Contributed by the Heat Transfer Division for publication in the JOURNAL OF HEAT TRANSFER. Manuscript received by the Heat Transfer Division October 19, 1989; revision received June 12, 1990. Keywords: Boiling, High-Temperature Phenomena, Phase-Change Phenomena.

ΔT_{SAT} = $T_{SURF} - T_{SAT}$
ϵ = total normal surface emittance
λ = Taylor wavelength
μ = dynamic viscosity
σ = surface tension
σ_{SB} = Stefan–Boltzmann constant

Subscripts

d = most dangerous
f = physical property determined at the vapor film temperature, $(T_{SURF} + T_{SAT})/2$
FB = film boiling
ℓ = physical property determined at the liquid saturation temperature
min = minimum
SAT = saturation
SURF = heat transfer surface

Introduction

In 1961 Berenson published his theory of film boiling heat transfer. That theory applies to film boiling of a liquid at its saturation temperature and atmospheric pressure over a flat horizontal surface and predicts the surface heat flux from knowledge of the surface superheat. The model was developed for the hydrodynamic conditions (e.g., bubble size, location, and release frequency) that exist at the minimum film boiling (MFB) point, the superheat where transition boiling ends and film boiling begins. The surface superheat (i.e., the difference between the temperature of the heat transfer surface and the saturated liquid, ΔT_{SAT}) at the MFB point, ΔT_{min}, is a function of the test fluid and the pressure. For water at atmospheric pressure, Hosler and Westwater (1962) observed $\Delta T_{min} \sim 158$ K and Nishikawa et al. (1966) observed $\Delta T_{min} \sim 110$ K.

On comparing his experimental data of surface heat flux versus surface superheat for *n*-pentane and carbon tetrachloride to his model, Berenson (1960) concluded that the data and the film boiling theory agreed within ±10 percent. Moreover, he stated that while his model was developed for, and only experimentally verified near, the MFB point, it "... probably applies to temperature differences as high as (~ 550 K) for some fluids." It appears that the validity of this statement is still left unchecked since film boiling data on large flat horizontal surfaces are scarce.

The Berenson film boiling experiment has been repeated by others (e.g., Nishikawa et al., 1965; Ramilison and Lienhard, 1978) for several fluids but only for surface superheats near the MFB point. For water, Hosler and Westwater (1962) and Yilmaz et al. (1976) made film boiling heat transfer measurements from a 200 mm × 200 mm flat horizontal plate, but the maximum surface superheat used by the latter was only 320 K. Conversely, large surface temperature measurements (to 600 K) were made by Greene and Irvine (1986) of quasi-steady-state film boiling of Freon-11 on confined pools of liquid metals. They found the Berenson model to be accurate over their measured temperature range after correcting for thermal radiation.

A recent investigation (Duignan, 1989) reported steady-state measurements of film boiling heat transfer from a flat horizontal circular surface (D = 101.6 mm) to an overlying pool of water at saturation and atmospheric pressure. Measurements were made from near the MFB point to a superheat of approximately 570 K. These data substantiate that the Berenson model is applicable at temperatures larger than previously observed, as long as a correction is applied to account for the effect of thermal radiation to the overall heat transfer. The objective of this work is to show quantitatively the validity of the Berenson film boiling model at surface superheats well above the MFB to approximately 600 K.

Film Boiling Model Corrected for Radiation

For the hydrodynamic conditions near the MFB point, Berenson (1961) developed the following heat transfer model:

$$q_{FB} = h_{FB}(T_{SURF} - T_{SAT}) = h_{FB}\Delta T_{SAT} \quad (1)$$

where

$$h_{FB} = 0.425[k_f^3 g\rho_f \times (\rho_\ell - \rho_f) h'_{fg}/(\mu_f \Delta T_{SAT}[\sigma/(g(\rho_\ell - \rho_f))]^{1/2})]^{1/4} \quad (2)$$

and

$$h'_{fg} = h_{fg}(1 + 0.5c_{p_f}\Delta T_{SAT}/h_{fg}) = \text{modified latent heat} \quad (3)$$

Equation (2) was based on the heat transfer model developed by Bromley (1950) and incorporates the hydrodynamic wave instability theory of Taylor (1950) with the properties of the vapor film determined at the mean film temperature (i.e., $(T_{SURF} + T_{SAT})/2$) and at atmospheric pressure. Near the MFB point, thermal radiation does not contribute significantly to the total film boiling heat flux; therefore, Berenson did not address that problem. However, Bromley (1950) took his heat transfer surfaces (carbon black tubes) to large surface temperatures at which thermal radiation could not be neglected. He developed the following model to include thermal radiation:

$$q = (q_{FB}^4/q)^{1/3} + q_{RADIATION} \quad (4)$$

He further suggested that heat transfer by thermal radiation could be determined by using a parallel plate model, i.e.,

$$q_{RADIATION} = \sigma_{SB}[1/\epsilon_{SURF} + 1/\epsilon_\ell - 1]^{-1}(T_{SURF}^4 - T_{SAT}^4) \quad (5)$$

An analysis by Sparrow (1964) determined equation (4) and (5) to accurately represent the contribution of radiation to the film boiling heat transfer. With respect to the radiative participation of water vapor in the vapor film, he concluded that the emissivity of steam at atmospheric pressure (less than 0.01) on the heat transfer is completely negligible because of the thin vapor film typical of film boiling (~ 0.25 to 0.50 mm).

In summary, equation (4) can be used to determine the total heat transfer for film boiling from a flat horizontal surface to an overlying liquid pool at its saturation temperature, which would include the effect of radiation.

Experimental Apparatus and Procedure

The experimental apparatus shown in Fig.1 and used in the present investigation consisted of a polished heat transfer plate made of 304 stainless steel that was 6.35 mm thick. Over the plate was mounted a 101.6-mm inside diameter clear quartz tube, approximately 250 mm in height. The tube was secured at its top and insulated at the bottom from the heat transfer surface by a 0.4-mm-high gasket. The plate was heated by a flexible high-watt-density electric heater, which was pressed against the heat transfer plate from below by a supporting plate, also made of 304 stainless steel. To measure the temperature and the heat flux at the surface of the heat transfer plate, seven micro thermocouples were used. Three of the thermocouples were installed within 0.75 mm of the surface; the other four thermocouples together with two near the surface were used to calculate the heat flux through the stainless steel plate. As an independent check on the heat flux, the vapor flux of water leaving the boiling chamber was measured by condensing the steam.

After initiating film boiling in the boiling chamber of the apparatus, the entire system was left operating until a steady-state condition was achieved. Steady state was determined when the temperatures of all of the heat transfer plate thermocouples did not vary with time. The height of the water pool was maintained at 100 mm or higher for all measurements. Further details of the experimental apparatus and procedure can be found from Duignan (1989), but an important fact should be pointed out concerning the size of the heat transfer surface.

Kesselring et al. (1967) showed that when the smallest hor-

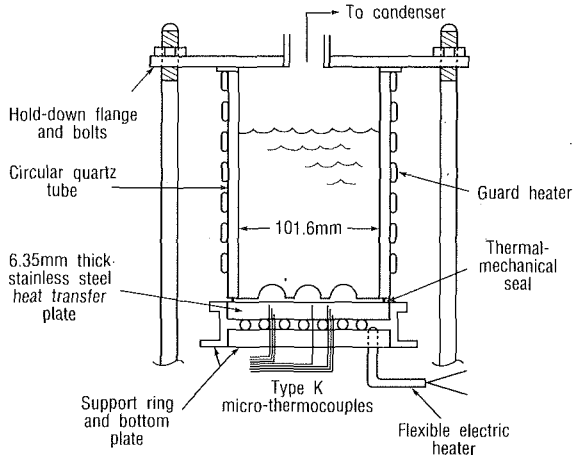

Fig 1 Experimental apparatus

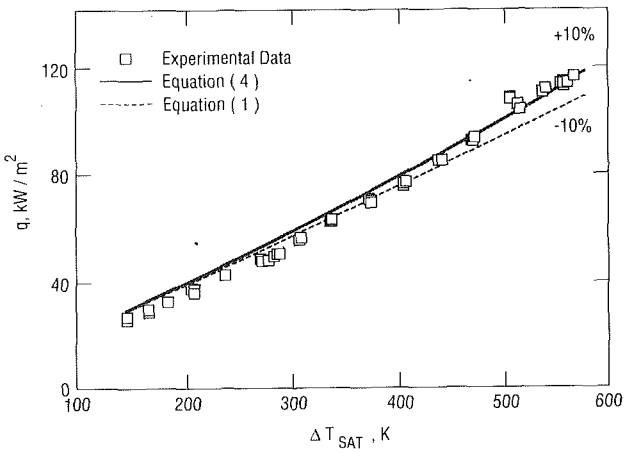

Fig 2 Stable film boiling of water over a flat horizontal surface.

izontal dimension of a flat heat transfer surface is less than approximately $2\lambda_d$, the film boiling heat transfer becomes a function of the surface geometry, similar to that experienced when changing the diameter of a tube heater (Lienhard and Wong, 1964). The dimension λ_d is the length of a wave at the vapor–liquid interface created by the vapor bubbles, and the subscript d refers to the "most dangerous" wavelength, a term coined by Bellman and Pennington (1954) to indicate the wavelength whose amplitude grows most rapidly. Klimenko (1981) also noted the importance of the size of the heat transfer surface and proposed that when the surface dimension D is greater than $2.8\lambda_d$, the surface is considered "large" and any further increase in size will not affect the heat transfer. The current study used a circular flat surface with a diameter of 101.6 mm. Since λ_d is equal to 27.2 mm for water (at the surface superheats of concern) the surface is considered to be large by both criteria.

Results and Discussion

Figure 2 shows a comparison of the experimental heat transfer data to the film boiling model by Berenson (1961). Duignan (1989) gives a complete list of those data. Two curves for the model are shown to illustrate the results of using only equation (1), and also when the effect of radiation is considered, equation (4) (a ± 10 percent region on the heat flux as calculated with equation (4) is indicated on the figure). Near the smallest measured surface superheat ($\Delta T_{SAT} = 143$ K) radiation contributes less than 1 percent of the total heat transfer, but at the largest superheat ($\Delta T_{SAT} = 567$ K) the radiation contribution is more than 7 percent of the total. To include the contribution of radiation to the heat flux by using equation (4), the total emittances of the water and the stainless steel had to be estimated. Sources for these radiative properties are cited by Duignan (1989); for the vapor–liquid interface of water, ϵ_ℓ was assumed to remain constant at 0.96. The emittance of the heat transfer plate was assumed to be that of a polished surface and a function of temperature. At the smallest surface superheat $\epsilon_{SURF} \sim 0.11$ and at the largest $\epsilon_{SURF} \sim 0.27$.

As previously stated, the experimentally measured heat fluxes were obtained by two separate methods: conduction through the heat transfer plate and condensation of the water vapor leaving the boiling chamber. Over the entire range where both measurements were made, the two heat flux values at the same surface superheat differed on the average by approximately 8 percent. The data shown in Fig. 2 are the result of averaging both heat flux measurements at each surface superheat. At the smaller surface superheats, the data fall below the Berenson prediction by slightly more than 10 percent but the comparison becomes increasingly better with increasing surface temperature. The average difference between the data and the Berenson model (including the radiation correction) over the range of surface superheats (i.e., 143 K $\leq \Delta T_{SAT} \leq$ 567 K) is less than 7 percent.

As Berenson hypothesized in 1961, equation (1) predicts the heat flux of film boiling to surface superheats of 567 K, which is within the ± 10 percent he observed at small superheats. To obtain the heat flux more accurately at large superheats equation (4) should be used to include the contribution of thermal radiation. These statements are probably applicable for fluids other than water (e.g., Greene and Irvine, 1986, for Freon 11) and for surface superheats above 570 K, but they still remain to be verified.

Acknowledgments

This work was performed under the auspices of the U.S. Nuclear Regulatory Commission.

References

Bellman, R., and Pennington, R. H., 1954, "Effects of Surface Tension and Viscosity on Taylor Instability," *Q. J. Appl. Math.*, Vol. 12, pp. 151–162.

Berenson, P. J., 1960, "On Transition Boiling Heat Transfer From a Horizontal Surface," Ph.D. Thesis, Dept. Mech. Eng., Massachusetts Institute of Technology, Cambridge, MA.

Berenson, P.J., 1961, "Film-Boiling Heat Transfer From a Horizontal Surface,"ASME JOURNAL OF HEAT TRANSFER, Vol. 83, pp. 351–358.

Bromley, L.A., 1950, "Heat Transfer in Stable Film Boiling," *Chem. Eng. Prog.*, Vol. 46, No. 5, pp. 221–227.

Duignan, M.R., 1989, "Enhanced Convective and Film Boiling Heat Transfer by Surface Gas Injection," Ph.D. Thesis, Dept. Mech. Eng., State University of York at Stony Brook.

Greene, G.A., and Irvine, T.F., Jr., 1986, "Film Boiling of R-11 on Liquid Metal Surfaces," *Proceedings, 8th International Heat Transfer Conference*, C.L. Tien et al., eds., Hemisphere Publishing Corp., Washington, DC, Vol. 4, pp. 2049-2054.

Hosler, E. R., and Westwater, J.W., 1962, "Film Boiling on a Horizontal Plate," *ARS Journal*, Vol. 32, No. 4, pp. 553–558.

Kesselring, R.C., Rosche, P.H., and Bankoff, S.G., 1967, "Transition and Film Boiling from Horizontal Strips," *AIChE Journal*, Vol. 13, No. 4, pp. 669–675.

Klimenko, V.V., 1981, "Film Boiling on a Horizontal Plate—New Correlation," *Int. J. Heat Mass Transfer*, Vol. 24, No. 1, pp. 69–79.

Lienhard, J.H., and Wong, P.T.Y., 1964, "The Dominant Unstable Wavelength and Minimum Heat Flux During Film Boiling on a Horizontal Cylinder," ASME JOURNAL OF HEAT TRANSFER, Vol. 86, pp. 220–226.

Nishikawa, K., Hasegawa, S., Iwabuchi, T., and Miyabara, Y., 1965, "Characteristics of Transition Boiling on the Horizontal Plate," *Technol. Reports Kyushu Univ.*, Vol. 38, pp. 306–310.

Nishikawa, K., Hasegawa, S., Kitayama, N., and Sakamoto, T., 1966, "The Effect of Heating Surface Conditions on the Transition Boiling—The Investigation of Transition Boiling (2nd Report)," *Technol. Reports Kyushu Univ.*, Vol. 38, pp. 399–404.

Ramilison, J.M., and Lienhard, J.H., 1987, "Transition Boiling Heat Transfer and the Film Transition Regime," ASME JOURNAL OF HEAT TRANSFER, Vol. 109, pp. 746–752.

Sparrow, E.M., 1964, "The Effect of Radiation on Film Boiling Heat Transfer," *Int. J. Heat Mass Transfer*, Vol. 7, No. 2, pp. 229–238.

Taylor, G.I., 1950, "The Instability of Liquid Surfaces When Accelerated in a Direction Perpendicular to Their Plane," *Proc. Roy. Soc. London*, Vol. 201, Series A, pp. 192–196.

Yilmaz, B.S., Clarke, S.F., and Westwater, J.W., 1976, "Heat Transfer From Water in Film Boiling to an Upper Layer of Paraffinic Hydrocarbon," ASME Paper No. 76-HT-24.

Flashing Two-Phase Flow Including the Effects of Noncondensible Gases

J. C. Leung[1] and M. Epstein[1]

Nomenclature

a, b = constants in Antoine equation, equation (5)
C_p = specific heat at constant pressure
$\bar{C}_p$ = mixture specific heat
G = mass velocity or flux
G^* = normalized mass velocity
h = specific enthalpy
M_i = molecular weight of phase i
P = total pressure
P_i = partial pressure of phase i
R = gas constant
T = temperature
u = linear velocity
v = specific volume
x = quality
x_i = mass fraction of phase i
y_{go} = inlet gas mole fraction in vapor phase
α_o = stagnation inlet void fraction
β = gas-to-vapor pressure ratio
ω = parameter defined by equation (15)

Subscripts

a = refers to ambient pressure
c = critical or choked
g = gas
l = liquid
o = stagnation (inlet) condition
s = saturated liquid condition
v = vapor
vl = difference between vapor and liquid properties

Introduction

The theoretical treatment of two-phase compressible flow through nozzles dates back to the work of Tangren et al. (1949) and Starkman et al. (1964) where classical homogeneous equilibrium flow models were presented for the nonflashing flow case and the flashing flow case, respectively. These reference models were recast recently in the form of simple correlations characterized by only a few dimensionless physical parameters (Leung, 1986; Leung and Epstein, 1990). To the authors' knowledge, the case of flashing two-phase flow in the presence of noncondensible gases has not been treated in the literature. This case can be viewed as a hybrid flow between the flashing regime and the nonflashing regime. This type of flow is often encountered at metering devices in chemical processing and in relief valve sizing applications where both condensible (flashing) component and noncondensible component co-exist. An example would be to consider the pressure relief situation of a hydrogenation reaction mixture containing gaseous hydrogen and an organic solution at elevated pressure. For the extreme case of an inlet subcooled liquid under an imposed gas pressure in the reservoir, the effect of the gas partial pressure is known to have a significant effect in augmenting the flow and can be readily quantified (Leung and Grolmes, 1988). The purpose of this paper is to present an exact solution method for this flashing liquid/gas mixture as well as an approximate analytical solution adequate for most engineering applications. The latter will be shown to yield the correct limiting solutions for the nonflashing (liquid/gas) flow case, the flashing (liquid/vapor) flow case and also the subcooled liquid inlet flow case. The proposed analytical solution has an added attribute in clearly identifying the key dimensionless variables relevant to this flow process. Before we develop the analytical solution, we first consider the governing flow equations and their numerical solution.

Theoretical Formulation and Numerical Solution

In accordance with the above-referenced treatments on compressible two-phase flow, the following assumptions are made in the current modeling: (1) There are no mass, heat, or momentum losses from the flow to the nozzle walls; (2) there is no slip between the phases (a homogeneous flow assumption); (3) the flashing process is in thermodynamic equilibrium; (4) the gas and condensible vapor behave as ideal gases and the gas is insoluble in the liquid phase; and (5) the liquid is considered incompressible. Although these assumptions may be physically unrealistic in certain applications, this simple model should serve as a useful instructional tool and as a reference model against which more complex models, such as those incorporating slip and nonequilibrium effect, can be compared. Moreover, for vent sizing applications, this model will yield the lowest flow rate and hence a more conservative design.

Using the above assumptions, the conservation equations governing the homogeneous flow of a flashing liquid–gas mixture are

$$G = u/v \tag{1}$$

$$v\,dP + u\,du = 0 \tag{2}$$

$$h_o = h + \frac{1}{2}u^2 \tag{3}$$

where $h = x_g h_g + x_v h_v + x_l h_l$ and $v = x_g v_g + x_l v_l = x_v v_v + x_l v_l$ are the mixture enthalpy and mixture specific volume, respectively. It is noted that the sum of the mass fractions should add up to unity, i.e., $x_g + x_v + x_l = 1.0$ and that the gas mass fraction x_g remains unchanged in the flow process ($dx_g = 0$). The mixture specific volume formula follows from the ideal gas behavior according to Dalton's law of partial pressures:

$$P = P_g + P_v \tag{4}$$

where $P_g v_g = RT/M_g$ and $P_v v_v = RT/M_v$. The condition for thermodynamic equilibrium to exist between the vapor and the liquid phases requires its partial pressure to fall on the saturation line,

$$P_v = \exp(a - b/T) \tag{5}$$

where in this simple form of representation, a and b are the so-called Antoine constants.

Substituting the following ideal gas and incompressible liquid relations for specific enthalpies into the differential form of equation (3):

$$dh_g = C_{pg}dT; \quad dh_v = C_{pv}dT; \quad dh_l = C_{pl}dT + v_l dP_l \tag{6}$$

we arrive at

$$\bar{C}_p dT + h_{vl}dx_v = x_v v_v dP \tag{7}$$

where $\bar{C}_p \equiv x_g C_{pg} + x_v C_{pv} + x_l C_{pl}$. The vapor and gas mass fractions are related to their own partial pressures via

[1]Fauske & Associates, Inc., Burr Ridge, IL 60521.

Contributed by the Heat Transfer Division for publication in the JOURNAL OF HEAT TRANSFER. Manuscript received by the Heat Transfer Division August 17, 1989; revision received March 6, 1990. Keywords: Modeling and Scaling, Multiphase Flows.

$$\frac{x_v}{x_g} = \frac{M_v}{M_g} \cdot \frac{P_v}{P_g} \tag{8}$$

Substituting the above equation into equation (4) and differentiating the result yields

$$dP = (1+\beta)dP_v - \frac{\beta}{x_v} P_v \, dx_v \tag{9}$$

where $\beta = (x_g/x_v)\ (M_v/M_g) = P_g/P_v$. Substituting equation (9) into (7) and making use of the Clapeyron relation, $dP_v/dT = h_{vl}/v_{vl}T$, we obtain

$$\frac{dx_v}{dT} = \frac{(1+\beta)x_v v_v \dfrac{h_{vl}}{v_{vl}T} - \bar{C}_p}{h_{vl} + \beta\, v_v P_v} \tag{10}$$

Equation (10) can be combined with equation (9) to yield the final expression for dx_v/dP

$$\frac{dx_v}{dP} = \frac{(1+\beta)x_v v_v \left(\dfrac{h_{vl}}{v_{vl}T}\right) - \bar{C}_p}{(1+\beta)\left(\dfrac{h_{vl}^2}{v_{vl}T}\right) + \dfrac{\beta}{x_v} P_v \, \bar{C}_p} \tag{11}$$

This equation is to be solved simultaneously with the differential momentum equation, equation (2), in the form of $du/dP = -v/u$. Starting at the stagnation upstream conditions, equations (2) and (11) can be numerically integrated in the "direction" of decreasing pressure. The critical or choked flow condition is reached when G (i.e., u/v) is found to attain a maximum value. The corresponding pressure is said to be the critical or choked pressure.

Approximate Analytical Solution

An approximate solution can be obtained by making use of two approximate equations of state (EOS) for two-phase mixtures in the mass velocity expression [from integrating equation (2)],

$$G = \left(-2\int_{P_o}^{P} v dP\right)^{1/2} / v \tag{12}$$

Substituting for P the sum of the partial pressures P_g and P_v, the integral in equation (12) becomes

$$\int_{P_o}^{P} v\, dP = \int_{P_{go}}^{P_g} v\, dP_g + \int_{P_{vo}}^{P_v} v\, dP_v \tag{13}$$

For the second integral on the right-hand side of equation (13), we make use of the EOS for describing a flashing vapor/liquid mixture (Leung, 1986)

$$\frac{v}{v_o} = \omega\left[\frac{P_{vo}}{P_v} - 1\right] + 1 \tag{14}$$

where the parameter ω is given by the following stagnation properties (Leung, 1986):

$$\omega = \frac{x_o v_{vlo}}{v_o} + \frac{C_p T_o P_{vo}}{v_o}\left(\frac{v_{vlo}}{h_{vlo}}\right)^2 \approx \alpha_o + (1-\alpha_o)\frac{C_p T_o P_{vo}}{v_l}\left[\frac{v_{vlo}}{h_{vlo}}\right]^2 \tag{15}$$

Thus this ω parameter is made up of two entirely separable terms: The first reflects the compressibility of the mixture due to the existing void fraction α_o and the second reflects the compressibility due to flashing or phase change upon depressurization. But for nonflashing flow mixtures, the second term vanishes and ω reduces simply to α_o, i.e.,

$$\frac{v}{v_o} = \alpha_o\left[\frac{P_{go}}{P_g} - 1\right] + 1 \tag{16}$$

This EOS is then used in the first integral on the right-hand side of equation (13). It is noted that ω and α_o have been found to be the key correlating parameters in flashing flow (Leung, 1986) and in nonflashing flow (Leung and Epstein, 1990), respectively. The principal assumptions made in arriving at EOS (14) and (16) are an isenthalpic expansion process and an isothermal expansion process, respectively. Upon substitution and integration, equation (12) yields

$$G^* = \left\{2\left[-\alpha_o y_{go} \ln\frac{P_g}{P_{go}} + (1-\alpha_o)y_{go}\left(1-\frac{P_g}{P_{go}}\right) - \omega(1-y_{go})\ln\frac{P_v}{P_{vo}} + (1-\omega)(1-y_{go})\left(1-\frac{P_v}{P_{vo}}\right)\right]\right\}^{1/2} \Bigg/ \left(\omega\left(\frac{P_{vo}}{P_v} - 1\right) + 1\right) \tag{17}$$

where $G^* \equiv G/\sqrt{P_o/v_o}$ is the so-called normalized mass velocity and $y_{go} \equiv P_{go}/P_o$ is the inlet gas mole fraction in the vapor phase. Equation (17) provides a general expression for the two-phase mass flux. For given inlet conditions (i.e., P_o, T_o, α_o, ω, y_{go}) an additional expressionn relating the two partial pressures, P_v and P_g, is needed before equation (17) can be solved for G^*. This relationship is obtained by combining equations (14) and (16) to yield

$$\alpha_o\left(\frac{P_{go}}{P_g} - 1\right) = \omega\left(\frac{P_{vo}}{P_v} - 1\right) \tag{18}$$

This result states that during the expansion process the two pressure ratios, P_g/P_{go} and P_v/P_{vo}, are solely governed by the ratio (α_o/ω), which is a measure of the relative "compressibility" of the nonflashing component to the flashing component. For low void-fraction two-phase flow with correspondingly small (α_o/ω) ratio, equation (18) indicates that P_g/P_{go} will decay much faster than P_v/P_{vo} during the initial expansion. Their decay rates are equal only at $\alpha_o = 1.0$, the all-vapor/gas inlet condition.

Examination of equation (17) shows that as the downstream pressure is reduced, the mass velocity reaches a maximum at

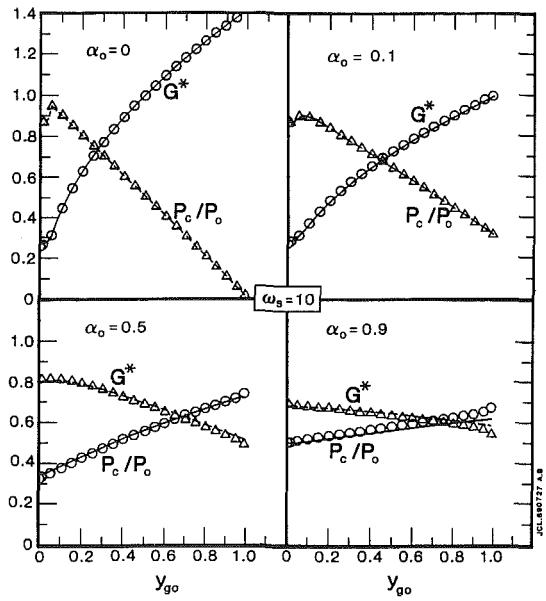

Fig. 1 Comparison of approximate analytical solutions (lines) against exact numerical integrations (symbols)

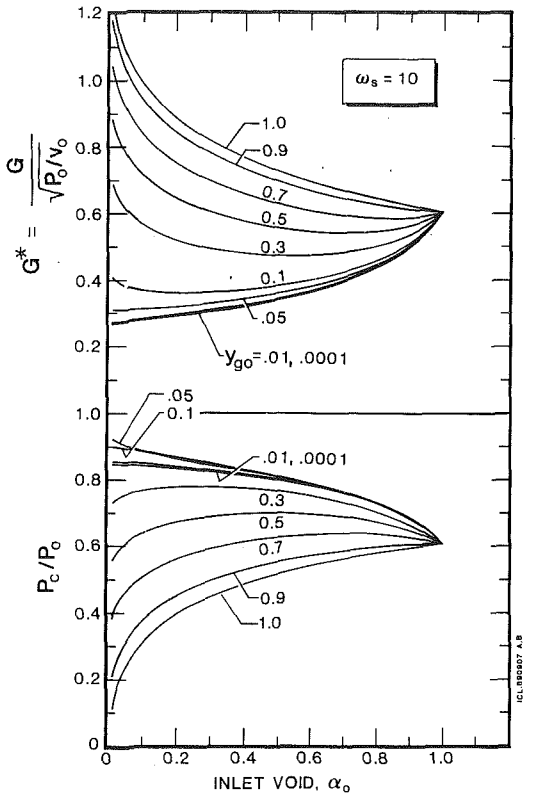

Fig. 2 Normalized mass velocity and critical pressure ratio versus inlet void fraction

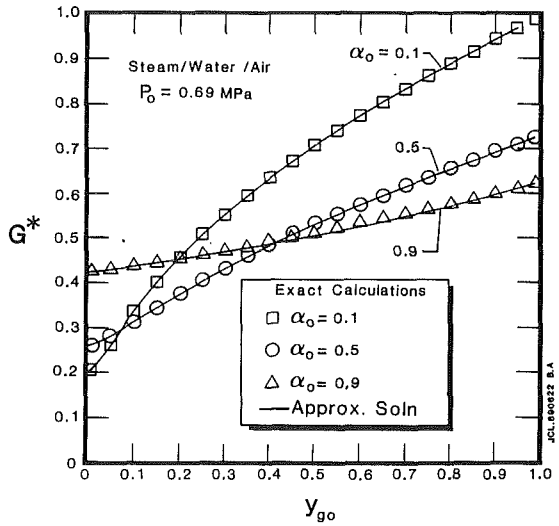

Fig. 3 G* calculations as a function of y_{go} at constant upstream pressure

the so-called choking condition. To find this maximum flow condition, one can compute the derivative dG/dP from equation (17) and set it equal to zero. An equivalent but more straightforward approach is to evaluate the following local condition governing choking:

$$G^2 = \frac{-1}{\left(\frac{dv}{dP}\right)} = \frac{-1}{\left(\frac{dv}{dP_g}\right)} + \frac{-1}{\left(\frac{dv}{dP_v}\right)} \tag{19}$$

where strictly speaking the derivatives are to be evaluated along an isentropic path. For the present approximate treatment, these derivatives are simply evaluated in accordance with the assumed EOS (14) and (16). The result in normalized form is given by

$$G^* = \left[\frac{y_{go}}{\alpha_o}\left(\frac{P_g}{P_{go}}\right)^2 + \frac{(1-y_{go})}{\omega}\left(\frac{P_v}{P_{vo}}\right)^2\right]^{1/2} \tag{20}$$

Thus the final expression governing the choking condition is obtained by equating equations (17) and (20), yielding

$$\begin{aligned} &-\alpha_o y_{go} \ln\frac{P_g}{P_{go}} + (1-\alpha_o) y_{go}\left(1-\frac{P_g}{P_{go}}\right) \\ &-\omega(1-y_{go})\ln\frac{P_v}{P_{vo}} + (1-\omega)(1-y_{go})\left(1-\frac{P_v}{P_{vo}}\right) \\ &= \frac{1}{2}\left[\frac{y_{go}}{\alpha_o}\left(\frac{P_g}{P_{go}}\right)^2 + \frac{(1-y_{go})}{\omega}\left(\frac{P_v}{P_{vo}}\right)^2\right] \\ &\left[\omega\left(\frac{P_{vo}}{P_v}-1\right)+1\right]^2 \end{aligned} \tag{21}$$

This is a transcendental equation for either P_g/P_{go} or P_v/P_{vo} as it is to be solved simultaneously with equation (18) for these "critical" pressure ratios. Once these ratios are found, the overall critical pressure ratio is given by

$$\frac{P_c}{P_o} = y_{go}\frac{P_g}{P_{go}} + (1-y_{go})\frac{P_v}{P_{vo}} \tag{22}$$

In the case where the ambient pressure P_a is higher than the choking exit pressure P_c, then equation (18) is solved for P_g/P_{go} and P_v/P_{vo} subject to the obvious condition that P_g and P_v add up to P_a. Equation (17) is then used to yield the unchoked mass flux.

Results and Comparisons

The validity of the approximate solutions can be tested by comparing the results against the exact solutions based on numerical integration of equations (2) and (11). Here we chose an example utilizing typical steam/water/air properties with $M_v = 18$, $M_g = 29$, $v_l = 0.001$ m^3/kg, $C_v = 2017$ J/kg K, $C_g = 1088$, $C_l = 4184$, $a = 4795$, $b = 24.37$, and $T_o = 485$ K. As is evident from equation (15), the key variable in describing the flashing process, ω, is simply a function of α_o and T_o only, since the other properties P_{vo}, v_{vlo}, h_{vlo}, and v_l are all uniquely defined by T_o. In this particular illustration, T_o was chosen to yield an all-liquid saturated ($\alpha_o = 0$) value for ω of 10, hereafter designated as ω_s. In other words, ω_s is simply the value of the coefficient that multiplies $(1-\alpha_o)$ in equation (15). At a given α_o, comparison between the exact and approximate solutions can be made with y_{go} ranging from 0 (pure flashing flow regime) to 1.0 (nonflashing two-phase flow regime). As shown in Fig. 1, the results for G^* and P_c/P_o at four different α_o values clearly demonstrate the accuracy of the approximate solutions. It is notable that at the limit of $\alpha_o = 0$ (absence of both vapor and gas at the inlet), both results are in perfect agreement with the choked flow solutions for subcooled liquid inlet conditions (Leung and Grolmes, 1988); this observation is reassuring. It is further noted that the approximate solutions reduce exactly in equation form to the flashing flow solutions at $y_{go} = 0$ (Leung, 1986) and to the nonflashing flow solutions based on the isothermal approximation at $y_{go} = 1$ (Leung and Epstein, 1990). Note also that the solutions presented in Fig. 1 are equally valid for other mixtures with $\omega_s = 10$.

It is instructive also to illustrate how G^* and P_c/P_o depend on α_o at various y_{go} (or P_{go}/P_o) as shown in Fig. 2. Again, at a fixed inlet temperature yielding $\omega_s = 10$, this figure displays the shape of the G^* versus α_o curves and the P_c/P_o versus α_o

curves for the entire range of y_{go} values. At all-vapor or gas inlet conditions, i.e., $\alpha_o = 1.0$, the solution as expected converges to the isothermal gas flow result for all y_{go} values.

Finally, Fig. 3 illustrates the sensitivity of G (or G^*) to y_{go} (or the gas partial pressure) for the steam/water/air example at a fixed inlet pressure of 0.69 MPa. As expected, the effect of the entrained gas is much more pronounced at lower inlet void fraction. For the indicated inlet void fractions, the approximate solutions closely duplicate the exact results. Although not shown in Fig. 3, the all-liquid inlet flow case ($\alpha_o = 0$) is in perfect agreement with the subcooled liquid choked flow results (Leung and Grolmes, 1988).

References

Leung, J. C., 1986, "A Generalized Correlation for One-Component Homogeneous Equilibrium Flashing Choked Flow," *AIChE J.*, Vol. 32(10), p. 1743.

Leung, J. C., and Grolmes, M. A., 1988, "A Generalized Correlation for Flashing Choked Flow of Initially Subcooled Liquid," *AIChE J.*, Vol. 34(4), p. 688.

Leung, J. C., and Epstein, M., 1990, "A Generalized Correlation for Two-Phase Non-flashing Homogeneous Choked Flow," ASME JOURNAL OF HEAT TRANSFER, Vol. 112(2), p. 528.

Starkman, E. S., Schrock, V. E., Neusen, K. F., and Maneely, D. J., 1964, "Expansion of a Very Low Quality Two-Phase Fluid Through a Convergent-Divergent Nozzle," ASME *Journal of Basic Engineering*, Vol. 86(2), p. 247.

Tangren, R. F., Dodge, C. H., and Seifert, H. S., 1949, "Compressibility Effects in Two-Phase Flow," *J. of Applied Physics*, Vol. 20(7), p. 637.

Effect of Pressure on the Micro-explosion of Water/Oil Emulsion Droplets Over a Hot Plate

P. Cho,[1] C. K. Law,[2] and M. Mizomoto[3]

1 Introduction

Since the original suggestion and preliminary observation by Ivanov and Nefedov (1965) that water/oil emulsion droplets undergoing combustion can spontaneously explode and thereby promote almost instant gasification of the droplets, much experimental (Dryer, 1977; Chandra and Avedisian, 1987; Lasheras et al., 1980; Mizomoto et al., 1983, 1986; Wang and Law, 1985) and theoretical (Law, 1977) advances have been made regarding this phenomenon, which has been termed micro-explosion or secondary atomization. Specifically, Dryer (1977) clarified that this micro-explosion is caused by the homogeneous nucleation of the superheated water micro-droplets embedded within the hot emulsion droplet, and Lasheras et al. (1980) demonstrated that micro-explosion of a freely falling droplet is indeed possible and that the concept of superheating of the water microdroplet is correct. Furthermore, Law (1977) formulated a model for emulsion droplet gasification, and postulated that the potential for micro-explosion should be enhanced with increasing system pressure. Wang and Law (1985) subsequently demonstrated that freely falling droplets do micro-explode earlier during their lifetime when the system pressure is increased, up to five atmospheres, which is the highest pressure investigated.

The purpose of the present investigation is experimentally to study the micro-explosion behavior of water/oil emulsion droplets over a hot plate in general, and the effect of pressure on this droplet/plate system in particular. The technological relevance of this study stems from the interest in direct-injection high-compression-ratio engines because droplet/wall interaction is believed to be an important process within these engines, and because water/oil emulsion is most suitable for application with the heavier oils used by them. From the fundamental viewpoint it is not clear a priori that insights gained from results of freely falling droplets can be readily applied to the present system. This is because droplet gasification behavior over a hot plate (commonly known as the Leidenfrost phenomenon) is a nonmonotonic one. Specifically, for a droplet originally in contact with the plate, with increasing plate temperature the droplet lifetime will first decrease, then increase rapidly as the droplet attempts to levitate itself by its outgasing vapor, and finally decrease gradually when it is in the totally levitated mode. Furthermore, a change in pressure not only will shift the transition plate temperatures for the different gasification modes, but it can also conceivably alter the nucleation mode of the superheated water microdroplets depending on whether the emulsion droplet is in physical contact with the plate.

2 Experimental Methodology

The high-pressure combustion chamber, 12.7 cm i.d. by 15.2 cm, is designed for a maximum pressure of 10 atm. The hot plate is a stainless steel disk, 7.62 cm in diameter and 1.33 cm thick, which has a shallow spherial indentation in the center of the upper surface to confine the freely moving droplet. Heating of the plate is achieved by a heating coil concentrically arranged below the plate. The plate temperature is determined from linear extrapolation of measurements made by two thermocouples placed 0.127 cm and 0.38 cm below the lowest point of the indentation.

After the desired plate temperature and chamber pressure are established, a single droplet is introduced onto the hot plate by using a high-precision hypodermic needle. The possible occurrence of droplet micro-explosion is noted. After each run the plate surface is cleaned to remove any particulate residue, which can inhibit the droplet motion as well as induce heterogeneous nucleation within the droplet.

The emulsions are prepared from distilled water and commercial grade n-paraffins with purity ranging from 97 to 99+ percent. Emulsion stability is achieved by using a mixture of Span 80 and Tween 80 with an HBL number of 5.3. The surfactant content of 2 percent by volume is found to be adequate to provide stability. The size of the water micro-droplets is of the order of 1 μm.

3 Results and Discussions

For consistence, for all runs the plate temperature was maintained at 600°C such that under atmospheric pressure droplets of all fuels were in the levitated gasification mode. The initial droplet size was maintained at 1.9 mm. We shall also reserve the term "micro-explosion" for the most violent disruption in which the droplet is instantly pulverized. Less violent disruptions are referred to as fragmentation.

The results of six liquid fuels tested with 10, 20, and 30 percent water content in a nitrogen environment at one atmosphere are summarized in Fig. 1. The results show that increase in water content increases the potential of droplet disruption, and that increase in the fuel boiling point inten-

[1]Department of Mechanical Engineering and Engineering Mechanics, Michigan Technological University, Houghton, MI 49931.

[2]Department of Mechanical and Aerospace Engineering, Princeton University, Princeton, NJ 08544.

[3]Department of Mechanical Engineering, Keio University, Yokohama, Japan.

Contributed by the Heat Transfer Division for publication in the JOURNAL OF HEAT TRANSFER. Manuscript received by the Heat Transfer Division April 18, 1988; revision received April 10, 1990. Keywords: Combustion, Evaporation, Sprays/Droplets.

curves for the entire range of y_{go} values. At all-vapor or gas inlet conditions, i.e., $\alpha_o = 1.0$, the solution as expected converges to the isothermal gas flow result for all y_{go} values.

Finally, Fig. 3 illustrates the sensitivity of G (or G^*) to y_{go} (or the gas partial pressure) for the steam/water/air example at a fixed inlet pressure of 0.69 MPa. As expected, the effect of the entrained gas is much more pronounced at lower inlet void fraction. For the indicated inlet void fractions, the approximate solutions closely duplicate the exact results. Although not shown in Fig. 3, the all-liquid inlet flow case ($\alpha_o = 0$) is in perfect agreement with the subcooled liquid choked flow results (Leung and Grolmes, 1988).

References

Leung, J. C., 1986, "A Generalized Correlation for One-Component Homogeneous Equilibrium Flashing Choked Flow," *AIChE J.*, Vol. 32(10), p. 1743.

Leung, J. C., and Grolmes, M. A., 1988, "A Generalized Correlation for Flashing Choked Flow of Initially Subcooled Liquid," *AIChE J.*, Vol. 34(4), p. 688.

Leung, J. C., and Epstein, M., 1990, "A Generalized Correlation for Two-Phase Non-flashing Homogeneous Choked Flow," ASME JOURNAL OF HEAT TRANSFER, Vol. 112(2), p. 528.

Starkman, E. S., Schrock, V. E., Neusen, K. F., and Maneely, D. J., 1964, "Expansion of a Very Low Quality Two-Phase Fluid Through a Convergent-Divergent Nozzle," ASME *Journal of Basic Engineering*, Vol. 86(2), p. 247.

Tangren, R. F., Dodge, C. H., and Seifert, H. S., 1949, "Compressibility Effects in Two-Phase Flow," *J. of Applied Physics*, Vol. 20(7), p. 637.

Effect of Pressure on the Micro-explosion of Water/Oil Emulsion Droplets Over a Hot Plate

P. Cho,[1] C. K. Law,[2] and M. Mizomoto[3]

1 Introduction

Since the original suggestion and preliminary observation by Ivanov and Nefedov (1965) that water/oil emulsion droplets undergoing combustion can spontaneously explode and thereby promote almost instant gasification of the droplets, much experimental (Dryer, 1977; Chandra and Avedisian, 1987; Lasheras et al., 1980; Mizomoto et al., 1983, 1986; Wang and Law, 1985) and theoretical (Law, 1977) advances have been made regarding this phenomenon, which has been termed micro-explosion or secondary atomization. Specifically, Dryer (1977) clarified that this micro-explosion is caused by the homogeneous nucleation of the superheated water micro-droplets embedded within the hot emulsion droplet, and Lasheras et al. (1980) demonstrated that micro-explosion of a freely falling droplet is indeed possible and that the concept of superheating of the water microdroplet is correct. Furthermore, Law (1977) formulated a model for emulsion droplet gasification, and postulated that the potential for micro-explosion should be enhanced with increasing system pressure. Wang and Law (1985) subsequently demonstrated that freely falling droplets do micro-explode earlier during their lifetime when the system pressure is increased, up to five atmospheres, which is the highest pressure investigated.

The purpose of the present investigation is experimentally to study the micro-explosion behavior of water/oil emulsion droplets over a hot plate in general, and the effect of pressure on this droplet/plate system in particular. The technological relevance of this study stems from the interest in direct-injection high-compression-ratio engines because droplet/wall interaction is believed to be an important process within these engines, and because water/oil emulsion is most suitable for application with the heavier oils used by them. From the fundamental viewpoint it is not clear a priori that insights gained from results of freely falling droplets can be readily applied to the present system. This is because droplet gasification behavior over a hot plate (commonly known as the Leidenfrost phenomenon) is a nonmonotonic one. Specifically, for a droplet originally in contact with the plate, with increasing plate temperature the droplet lifetime will first decrease, then increase rapidly as the droplet attempts to levitate itself by its outgasing vapor, and finally decrease gradually when it is in the totally levitated mode. Furthermore, a change in pressure not only will shift the transition plate temperatures for the different gasification modes, but it can also conceivably alter the nucleation mode of the superheated water microdroplets depending on whether the emulsion droplet is in physical contact with the plate.

2 Experimental Methodology

The high-pressure combustion chamber, 12.7 cm i.d. by 15.2 cm, is designed for a maximum pressure of 10 atm. The hot plate is a stainless steel disk, 7.62 cm in diameter and 1.33 cm thick, which has a shallow spherial indentation in the center of the upper surface to confine the freely moving droplet. Heating of the plate is achieved by a heating coil concentrically arranged below the plate. The plate temperature is determined from linear extrapolation of measurements made by two thermocouples placed 0.127 cm and 0.38 cm below the lowest point of the indentation.

After the desired plate temperature and chamber pressure are established, a single droplet is introduced onto the hot plate by using a high-precision hypodermic needle. The possible occurrence of droplet micro-explosion is noted. After each run the plate surface is cleaned to remove any particulate residue, which can inhibit the droplet motion as well as induce heterogeneous nucleation within the droplet.

The emulsions are prepared from distilled water and commercial grade *n*-paraffins with purity ranging from 97 to 99+ percent. Emulsion stability is achieved by using a mixture of Span 80 and Tween 80 with an HBL number of 5.3. The surfactant content of 2 percent by volume is found to be adequate to provide stability. The size of the water micro-droplets is of the order of 1 μm.

3 Results and Discussions

For consistence, for all runs the plate temperature was maintained at 600°C such that under atmospheric pressure droplets of all fuels were in the levitated gasification mode. The initial droplet size was maintained at 1.9 mm. We shall also reserve the term "micro-explosion" for the most violent disruption in which the droplet is instantly pulverized. Less violent disruptions are referred to as fragmentation.

The results of six liquid fuels tested with 10, 20, and 30 percent water content in a nitrogen environment at one atmosphere are summarized in Fig. 1. The results show that increase in water content increases the potential of droplet disruption, and that increase in the fuel boiling point inten-

[1]Department of Mechanical Engineering and Engineering Mechanics, Michigan Technological University, Houghton, MI 49931.

[2]Department of Mechanical and Aerospace Engineering, Princeton University, Princeton, NJ 08544.

[3]Department of Mechanical Engineering, Keio University, Yokohama, Japan.

Contributed by the Heat Transfer Division for publication in the JOURNAL OF HEAT TRANSFER. Manuscript received by the Heat Transfer Division April 18, 1988; revision received April 10, 1990. Keywords: Combustion, Evaporation, Sprays/Droplets.

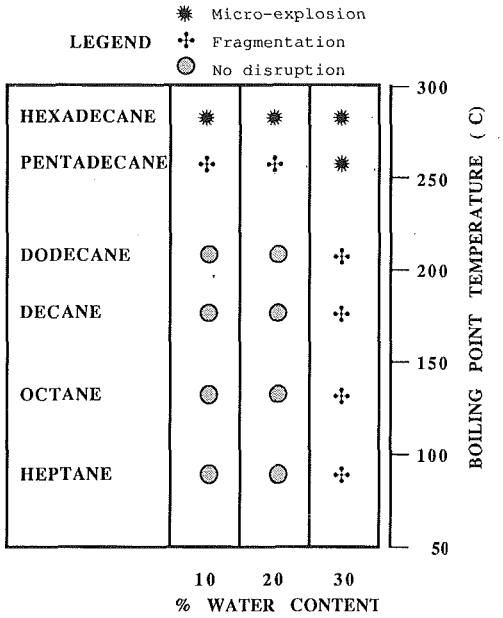

Fig. 1 Intensity of micro-explosion at one atmosphere; fuels are tabulated according to their normal boiling temperatures

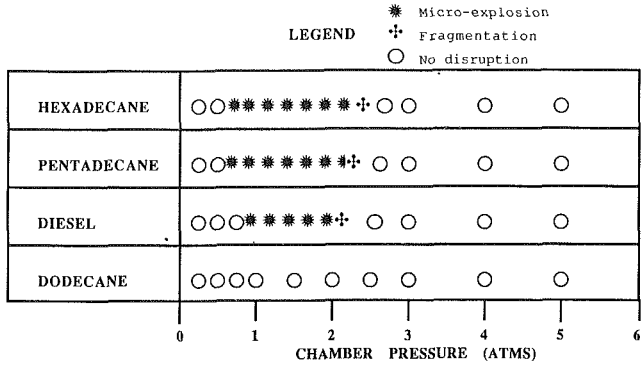

Fig. 2 Range of micro-explosion in nitrogen atmosphere; all fuels are emulsified with 20 percent water by volume

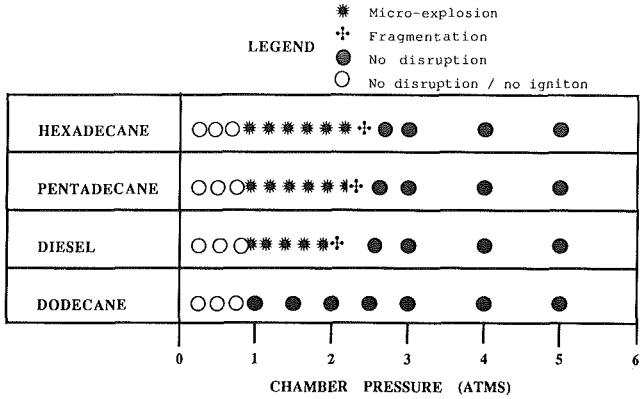

Fig. 3 Range of micro-explosion in air atmosphere; all fuels are emulsified with 20 percent water by volume

sifies the disruption. These observations are consistent with the criteria set forth by Law (1981) and by Avedisian and Sullivan (1984), and are also in agreement with the experimental observation of Lasheras et al. (1980). Visually, a heptane droplet with 10 and 20 percent water quietly vaporizes without disruption. However, with 30 percent water content it weakly breaks up into a number of smaller droplets toward the end of its lifetime. Similar behavior is observed with octane and decane. A change in the intensity of disruption is apparent from the 30 percent water-in-dodecane droplets, which fragment rather rapidly. Definitive change from fragmentation to micro-explosion takes place with 30 percent water-in-pentadecane. All emulsions of hexadecane micro-explode. The quiescent evaporation period preceding micro-explosion is also reduced to one to two seconds. Also, the emulsions became clear before micro-exploding. The reason for clearing may be due to the dissolution of water into fuel and/or the coalescence of internal water micro-droplets (Avedisian and Fatehi, 1988).

To investigate the effect of pressure, 20 percent emulsions prepared from dodecane, pentadecane, hexadecane, and diesel oil were tested for both reduced and elevated atmospheric pressures. Testing conducted at high pressures is not only difficult but also time consuming because the tarlike residue and soot that settle on the surface of the plate necessitate thorough cleaning after each test.

Figures 2 and 3, respectively, summarize the droplet disruption modes for pure vaporization in a nitrogen environment and burning in the air environment. These results clearly demonstrate that droplet disruption occurs within a specific pressure range such that increases or decreases in pressure from this range tend to inhibit disruption, and that there is not much difference between the results of vaporization and combustion.

The inhibition of droplet disruption in the low-pressure regime is likely caused by the mechanism postulated by Law (1977). That is, with decreasing pressure the liquid boiling point and thereby the droplet temperature are reduced, while the limit of superheat of water remains practically unaffected. Consequently the water microdroplets cannot easily attain the temperature needed for homogeneous nucleation.

The mechanism responsible for the inhibition in the high-pressure regime is less clear. It is contrary to the freely falling droplet results of Wang and Law (1985). It may also be noted that in all our experiments droplet disruption was terminated while the droplet was still levitated. Thus inhibition of disruption is not caused by direct physical contact between the droplet and the plate. One mechanical that has been suggested to have an adverse effect on droplet disruption with increasing pressure is the suppression of the vapor bubble expansion dynamics at high pressures (Lasheras et al., 1984). In particular, experimental studies on the effects of ambient pressure on evaporation of pure liquid droplets at the superheat limits (Avedisian, 1987; Frost and Sturtevant, 1987) have shown that the dynamic instability that drives micro-explosion at atmospheric pressure is suppressed at higher pressures. Other mechanisms for the suppression of micro-explosion at high pressures include the dissolution of permanent gases into the droplet, thereby elevating the limit of superheat, and enhanced buoyancy and thus internal motion, which promotes preferential vaporization (Law et al., 1980).

In summary, we have experimentally investigated the disruption of water/oil droplets over a hot plate, and found that there exists an optimum pressure range over which droplet disruption occurs.

Acknowledgments

This research was supported by the Army Research Office under the technical management of Dr. David Mann.

References

Avedisian, C. T., and Sullivan, J. R., 1984, "A Generalized Corresponding States Methods for Predicting the Limits of Superheat of Mixtures: Application to the Normal Alcohols," *Chemical Engineering Science*, Vol. 39, pp. 1033–1041.

Avedisian, C. T., 1987, "An Experimental Study of High-Pressure Bubble Growth Within Multicomponent Liquid Droplets Levitated in a Flowing Stream of Another Immiscible Liquid," *Proc. R. Soc. Lond. A*, Vol. 409, pp. 271–285.

Avedisian, C. T., and Fatehi, M., 1988, "An Experimental Study of the Leidenfrost Evaporation Characteristics of Emulsified Liquid Droplets," *Int. J. Heat Mass Transfer*, Vol. 31, No. 8, pp. 1587–1603.

Chandra, S., and Avedisian, C. T., 1987, "Experiments on Film Evaporation and Combustion of Binary Linear Droplet Arrays at a Hot Surface," ASME Paper No. 87-HT-54.

Dryer, F. L., 1977, "Water Addition to Practical Combustion Systems—Concepts and Applications," *Sixteenth Symposium (International) on Combustion*, The Combustion Institute, pp. 279–295.

Frost, D., and Sturtevant, B., 1987, "Effects of Ambient Pressure on the Instability of a Liquid Boiling Explosively at the Superheat Limit," ASME JOURNAL OF HEAT TRANSFER, Vol. 108, pp. 418–424.

Ivanov, V. M., and Nefedov, P. I., 1965, "Experimental Investigation of the Combustion Process of Natural and Emulsified Liquid Fuels," NASA TT, F-258, pp. 35–45.

Lasheras, J. C., Fernandez-Pello, A. C., and Dryer, F. L., 1980, "Experimental Observations on the Disruptive Combustion of Free Droplets of Multicomponent Fuels," *Combustion Science and Technology*, Vol. 22, pp. 195–209.

Lasheras, J. C., Yap, L. T., and Dryer, F. L., 1984, "Effect of the Ambient Pressure on the Explosive Burning of Emulsified and Multicomponent Fuel Droplets," *Twentieth Symposium (International) on Combustion*, The Combustion Institute, pp. 1761–1772.

Law, C. K., 1977, "A Model for the Combustion of Oil/Water Emulsion Droplets," *Combustion Science and Technology*, Vol. 17, pp. 29–38.

Law, C. K., Lee, C. H., and Srinivasan, N., 1980, "Combustion Characteristics of Water-in-Oil Emulsion Droplets," *Combustion Science and Technology*, Vol. 37, pp. 125–143.

Law, C. K., 1981, "Comments," *Eighteenth Symposium (International) on Combustion*, The Combustion Institute, p. 359.

Mizomoto, M., Ikai, S., and Morita, A., 1983, "Evaporation and Ignition of a Fuel Droplet on a Hot Surface," *Combustion and Flame*, Vol. 51, pp. 95–104.

Mizomoto, M., Masuda, I., and Ikai, S., 1986, "Combustion of a Coal-Oil Mixture Droplet on a Hot Surface," *Combustion and Flame*, Vol. 63, pp. 289–301.

Wang, C. H., and Law, C. K., 1985, "Microexplosion of Fuel Droplets Under High Pressure," *Combustion and Flame*, Vol. 59, pp. 53–62.

Thermal Conductivity of Selected Superconducting Materials

L. S. Fletcher,[1,4] G. P. Peterson,[2,4] and R. Schaup[3,4]

Introduction

The potential for High Temperature Superconductor (HTS) materials has expanded dramatically as critical temperatures have approached the liquid nitrogen temperature range. HTS materials may be used for more efficient generation and transmission of electrical power, magnetically levitated systems, electronic switching devices, and radiation shielding. HTS-based electronics could lead to faster, more powerful computers and medical diagnostic facilities. The continued development and commercialization of HTS-based materials, however, will depend upon a more thorough characterization of these materials, including their thermophysical properties.

Over the past several years there has been a significant increase in the critical temperature of superconducting materials. Initially, the niobium-titanium materials exhibited superconducting characteristics at liquid helium temperatures. Then, the copper-oxide-based superconducting materials containing the rare earth elements lanthanum and yttrium exhibited superconducting characteristics at liquid nitrogen temperatures. More recently, the development of copper oxide superconducting materials containing bismuth and thallium has resulted in materials with critical temperatures in the range of 100 K.

Increasing emphasis on the development of HTS-based devices suggests the need for a better understanding of their heat transfer characteristics. Therefore, knowledge of the thermal conductivity of superconductor materials, as well as the associated carrier materials, is essential. One class of HTS materials that has become increasingly important is the yttrium-barium-copper-oxide compounds; however, only limited information is available concerning the thermal characteristics of such compounds. This lack of knowledge concerning the characteristics of these materials may limit their usefulness. Therefore, an experimental investigation was conducted to determine the thermal conductivity of selected yttrium- and bismuth-based copper oxide superconducting materials.

Literature Review

There have been numerous heat transfer studies of the niobium-based materials, especially at liquid helium temperatures (Schmidt, 1979), and knowledge of the thermophysical properties provides a basis for understanding both their structure and their characteristics. The more recently developed rare earth materials, such as the yttrium-barium-copper-oxides (YBaCuO) have not received the attention of the earlier materials. Further, the structure and mechanical characteristics of these materials are not well understood, and few studies of the thermophysical properties have been conducted.

Jezowski et al. (1987) investigated the thermal conductivity and electrical resistivity of single-phase orthorhombic YBaCuO samples in the superconducting and normal states. The authors concluded that YBaCuO exhibited a metallic-like conductivity behavior over the temperature range of 5 to 320 K. The heat capacities of LaSrCuO and YBaCuO were measured for a temperature range of 1.5 to 40 K by Collocott et al. (1987). In addition, the thermal expansion characteristics of LaSrCuO were measured for a temperature range of 2 to 80 K. The measured values of thermal expansion at room temperature were reported to be similar to those of many ceramic oxides. Freeman et al. (1987) investigated the thermal conductivity of YBaCuO over the temperature range of 0.1 to 7 K and reported that both the magnitude and temperature dependence were similar to those of insulating sintered ceramic materials.

Morelli et al. (1987) measured the thermal conductivity of a YBaCuO material over a temperature range of 15 to 140 K. Results indicated that the thermal conductivity was not strongly temperature dependent above the transition temperature and that virtually all of the heat conduction in the system was due to phonon transport. The electrical resistivity, thermal conductivity, and specific heat of a series of HTS compounds were measured by Heremans et al. (1988). The materials included yttrium, europium, gadolinium, dysprosium, and erbium. The heat capacity measurements were made on a differential scanning calorimeter (DSC) in the temperature range of 240 to 490 K. The thermal conductivity was observed to be nearly constant above the critical temperature, with a rather significant increase as the temperature was reduced below the critical temperature. Based on an evaluation of the experimental results, it was concluded that the heat transport was predominantly due to lattice vibrations.

Kirk et al. (1989) reported measurements of the thermal conductivity of hot-pressed, sintered YBaCuO over the temperature range 0.055 to 300 K. The authors reported that the thermal conductivity displayed noticeable anisotropic behavior at high temperatures. This characteristic was observed to be dependent upon the direction of the hot-pressing fabrication, which affected the orientation of the crystallites in the heat

[1]Dietz Professor of Mechanical Engineering, Fellow ASME.
[2]Professor of Mechanical Engineering, Mem. ASME.
[3]Graduate Research Assistant.
[4]Department of Mechanical Engineering, Texas A&M University, College Station, TX 77843-3123.

Contributed by the Heat Transfer Division and presented at the ASME Winter Annual Meeting, San Francisco, California, December 10–15, 1989. Manuscript received by the Heat Transfer Division January 22, 1990; revision received June 12, 1990. Keywords: Conduction, Cryogenics, Thermophysical Properties.

Avedisian, C. T., and Fatehi, M., 1988, "An Experimental Study of the Leidenfrost Evaporation Characteristics of Emulsified Liquid Droplets," *Int. J. Heat Mass Transfer*, Vol. 31, No. 8, pp. 1587–1603.

Chandra, S., and Avedisian, C. T., 1987, "Experiments on Film Evaporation and Combustion of Binary Linear Droplet Arrays at a Hot Surface," ASME Paper No. 87-HT-54.

Dryer, F. L., 1977, "Water Addition to Practical Combustion Systems—Concepts and Applications," *Sixteenth Symposium (International) on Combustion*, The Combustion Institute, pp. 279–295.

Frost, D., and Sturtevant, B., 1987, "Effects of Ambient Pressure on the Instability of a Liquid Boiling Explosively at the Superheat Limit," ASME JOURNAL OF HEAT TRANSFER, Vol. 108, pp. 418–424.

Ivanov, V. M., and Nefedov, P. I., 1965, "Experimental Investigation of the Combustion Process of Natural and Emulsified Liquid Fuels," NASA TT, F-258, pp. 35–45.

Lasheras, J. C., Fernandez-Pello, A. C., and Dryer, F. L., 1980, "Experimental Observations on the Disruptive Combustion of Free Droplets of Multicomponent Fuels," *Combustion Science and Technology*, Vol. 22, pp. 195–209.

Lasheras, J. C., Yap, L. T., and Dryer, F. L., 1984, "Effect of the Ambient Pressure on the Explosive Burning of Emulsified and Multicomponent Fuel Droplets," *Twentieth Symposium (International) on Combustion*, The Combustion Institute, pp. 1761–1772.

Law, C. K., 1977, "A Model for the Combustion of Oil/Water Emulsion Droplets," *Combustion Science and Technology*, Vol. 17, pp. 29–38.

Law, C. K., Lee, C. H., and Srinivasan, N., 1980, "Combustion Characteristics of Water-in-Oil Emulsion Droplets," *Combustion Science and Technology*, Vol. 37, pp. 125–143.

Law, C. K., 1981, "Comments," *Eighteenth Symposium (International) on Combustion*, The Combustion Institute, p. 359.

Mizomoto, M., Ikai, S., and Morita, A., 1983, "Evaporation and Ignition of a Fuel Droplet on a Hot Surface," *Combustion and Flame*, Vol. 51, pp. 95–104.

Mizomoto, M., Masuda, I., and Ikai, S., 1986, "Combustion of a Coal-Oil Mixture Droplet on a Hot Surface," *Combustion and Flame*, Vol. 63, pp. 289–301.

Wang, C. H., and Law, C. K., 1985, "Microexplosion of Fuel Droplets Under High Pressure," *Combustion and Flame*, Vol. 59, pp. 53–62.

Thermal Conductivity of Selected Superconducting Materials

L. S. Fletcher,[1,4] G. P. Peterson,[2,4] and R. Schaup[3,4]

Introduction

The potential for High Temperature Superconductor (HTS) materials has expanded dramatically as critical temperatures have approached the liquid nitrogen temperature range. HTS materials may be used for more efficient generation and transmission of electrical power, magnetically levitated systems, electronic switching devices, and radiation shielding. HTS-based electronics could lead to faster, more powerful computers and medical diagnostic facilities. The continued development and commercialization of HTS-based materials, however, will depend upon a more thorough characterization of these materials, including their thermophysical properties.

Over the past several years there has been a significant increase in the critical temperature of superconducting materials. Initially, the niobium-titanium materials exhibited superconducting characteristics at liquid helium temperatures. Then, the copper-oxide-based superconducting materials containing the rare earth elements lanthanum and yttrium exhibited superconducting characteristics at liquid nitrogen temperatures. More recently, the development of copper oxide superconducting materials containing bismuth and thallium has resulted in materials with critical temperatures in the range of 100 K.

Increasing emphasis on the development of HTS-based devices suggests the need for a better understanding of their heat transfer characteristics. Therefore, knowledge of the thermal conductivity of superconductor materials, as well as the associated carrier materials, is essential. One class of HTS materials that has become increasingly important is the yttrium-barium-copper-oxide compounds; however, only limited information is available concerning the thermal characteristics of such compounds. This lack of knowledge concerning the characteristics of these materials may limit their usefulness. Therefore, an experimental investigation was conducted to determine the thermal conductivity of selected yttrium- and bismuth-based copper oxide superconducting materials.

Literature Review

There have been numerous heat transfer studies of the niobium-based materials, especially at liquid helium temperatures (Schmidt, 1979), and knowledge of the thermophysical properties provides a basis for understanding both their structure and their characteristics. The more recently developed rare earth materials, such as the yttrium-barium-copper-oxides (YBaCuO) have not received the attention of the earlier materials. Further, the structure and mechanical characteristics of these materials are not well understood, and few studies of the thermophysical properties have been conducted.

Jezowski et al. (1987) investigated the thermal conductivity and electrical resistivity of single-phase orthorhombic YBaCuO samples in the superconducting and normal states. The authors concluded that YBaCuO exhibited a metallic-like conductivity behavior over the temperature range of 5 to 320 K. The heat capacities of LaSrCuO and YBaCuO were measured for a temperature range of 1.5 to 40 K by Collocott et al. (1987). In addition, the thermal expansion characteristics of LaSrCuO were measured for a temperature range of 2 to 80 K. The measured values of thermal expansion at room temperature were reported to be similar to those of many ceramic oxides. Freeman et al. (1987) investigated the thermal conductivity of YBaCuO over the temperature range of 0.1 to 7 K and reported that both the magnitude and temperature dependence were similar to those of insulating sintered ceramic materials.

Morelli et al. (1987) measured the thermal conductivity of a YBaCuO material over a temperature range of 15 to 140 K. Results indicated that the thermal conductivity was not strongly temperature dependent above the transition temperature and that virtually all of the heat conduction in the system was due to phonon transport. The electrical resistivity, thermal conductivity, and specific heat of a series of HTS compounds were measured by Heremans et al. (1988). The materials included yttrium, europium, gadolinium, dysprosium, and erbium. The heat capacity measurements were made on a differential scanning calorimeter (DSC) in the temperature range of 240 to 490 K. The thermal conductivity was observed to be nearly constant above the critical temperature, with a rather significant increase as the temperature was reduced below the critical temperature. Based on an evaluation of the experimental results, it was concluded that the heat transport was predominantly due to lattice vibrations.

Kirk et al. (1989) reported measurements of the thermal conductivity of hot-pressed, sintered YBaCuO over the temperature range 0.055 to 300 K. The authors reported that the thermal conductivity displayed noticeable anisotropic behavior at high temperatures. This characteristic was observed to be dependent upon the direction of the hot-pressing fabrication, which affected the orientation of the crystallites in the heat

[1]Dietz Professor of Mechanical Engineering, Fellow ASME.
[2]Professor of Mechanical Engineering, Mem. ASME.
[3]Graduate Research Assistant.
[4]Department of Mechanical Engineering, Texas A&M University, College Station, TX 77843-3123.

Contributed by the Heat Transfer Division and presented at the ASME Winter Annual Meeting, San Francisco, California, December 10–15, 1989. Manuscript received by the Heat Transfer Division January 22, 1990; revision received June 12, 1990. Keywords: Conduction, Cryogenics, Thermophysical Properties.

flux direction. At temperatures between 100 K and 270 K, the thermal conductivity was observed to be nearly constant.

The effect of lead on the stability of the bismuth-superconductors was reviewed by Escudero et al. (1989). They found that lead promoted electron transfer, improved thermal conductivity, and resulted in onset temperatures that were slightly higher than those of compounds without lead. Further, the introduction of lead increased the bonding strength of the material.

Experimental Program

The present experimental investigation utilized a standard, cut-bar thermal-conductivity facility modified for operation at cryogenic temperatures and housed in a vacuum system capable of obtaining vacuum levels of less than 10^{-2} Torr.

Experimental Facility. The experimental facility used in this investigation incorporated two heat-flux meters composed of Stainless Steel 304 cylinders, 25.4 mm in diameter and 76.2 mm long, stacked to form a vertical test column. The superconducting material samples were inserted between these two heat flux meters, which were instrumented with chromel/alumel thermocouples inserted in #54 drilled holes 12.7 mm deep. The thermocouples were cemented into the holes with a metal-filled epoxy and wrapped around the heat-flux meters to enhance the accuracy of the thermal measurements.

The facility was fully instrumented with temperature controllers and an overtemperature control. The heat sink was designed to utilize either fluid from a constant temperature bath or liquid nitrogen for lower temperature investigations. The liquid nitrogen cooling system was arranged so the liquid nitrogen could flow through the heat sink and exhaust to the atmosphere. In order to assure the accuracy of the thermal-conductivity measurements, the test column was calibrated using an electrolytic-iron reference standard obtained from the National Bureau of Standards (NIST).

The heat flux through the test specimens and electrolytic iron was calculated from the known thermal conductivity of the electrolytic iron and the measured temperature gradients. This heat flux was then used to determine the thermal conductivity of the stainless steel heat flux meters. In order to extend the temperature range of the test column, one Aluminum 6061-T6 heat flux meter and one Stainless Steel 304 heat-flux meter were used and calibrated in the same manner. The aluminum heat-flux meter reduced the overall thermal resistance of the test column, thus providing a lower sample temperature range.

Superconducting Material Preparation. Both hot and cold-pressed techniques have previously been used to prepare high-temperature superconductors (Pandey et al., 1988). Generally, cold-pressed materials result in lower densities (usually 50–60 percent below the theoretical values), do not withstand thermal cycling very well, and are subject to damage by environmental influences. Hot-pressed materials provide a high-quality, single-phase ceramic of orthorhombic structure. In addition, hot-pressed samples provide a well-defined superconducting phase transition at the critical temperature, with improved reproducibility at elevated levels of excitation, increased ability to withstand thermal cycling, and higher current-carrying capability. For this investigation, two different materials, hot-pressed bismuth-lead-strontium-calcium-copper-oxide and hot-pressed yttrium-barium-copper-oxide were used.

The materials were prepared by thoroughly mixing the ingredients in a ball-mill and then reacting the mixture in air at approximately 1200 K in a clean purity-grade alumina crucible. The solid-lump material formed after reaction was ground to a fine powder and rereacted at approximately 1250 K in an oxygen atmosphere for several subsequent heating and cooling cycles to drive off the remaining carbon-dioxide. The proper composition of the resulting material was checked by x-ray diffraction and found suitable for use in processing dense polycrystalline samples and for epitaxial deposition of superconducting films on substrates, as well as for growth of bulk single crystals. For this investigation, the hot-pressed material was pressed to a maximum of 69 MPa, while the temperature was raised to a maximum temperature of approximately 925 K. The material was sintered and annealed, as reported by Pandey et al. (1988), resulting in single-phase polycrystalline samples. Selected properties are shown in Table 1.

Table 1 Physical properties of superconducting materials

Physical Property	YBaCuO	BiPbSrCaCuO
Critical Temperature, T_c[K]	91.6[a]	110[a]
Density, ρ $\left[\frac{g}{cm^3}\right]$	4.79[a]	4.38[a]
Electrical Resistivity, ρ [Ωm]	2.0×10^{-5} [at 100 K][a]	3.8×10^{-5} [at 120K][b]
Critical Current Density, I_c $\left[\frac{A}{cm^2}\right]$	18.5×10^{3} [c]	—
Volume Specific Heat, C_v $\left[\frac{J}{cm^3K}\right]$	1.178 [at 90K][d]	—
Thermal Expansion, α $\left[\frac{cm}{cmK}\right]$	1.44×10^{-5} [e]	—

[a](Pandey et al., 1988)

[b](Hashimoto et al., 1988b)

[c](Salama et al., 1989)

[d](Junod et al., 1988)

[e](Hashimoto et al., 1988a)

Experimental Procedure. For all tests, the interfaces between the test material and test specimen were filled with a contact-enhancement grease. The column load was kept under pressure by a spring-loaded screw in the support system. To reduce heat flux to the support system, an insulator was placed between the heater and the screw. The cooling system was turned on when a vacuum level of 10^{-2} Torr had been achieved. The time required to cool the test column to a steady temperature was approximately 45 minutes. To gain a one-dimensional heat flux through the test column, the heater was turned on, and the temperature set point was increased in equal increments. The temperature at the center of the superconducting material was recorded along with the heat flux and temperature gradients in the test specimens.

This procedure assumed that the contact resistance at the interfaces between the sample and heat-flux meters had been minimized by the use of a heat-sink compound and was negligible when compared to the temperature drop through the sample. The uncertainty of the thermal-conductivity data was evaluated in terms of the error contributions of each component and ranged from 3.2 to 3.6 percent (Shenck, 1961).

Results and Discussion

Thermal conductivity data were obtained for both yttrium- and bismuth-based superconducting materials parallel to the pressing direction over temperature ranges of 120 K to 290 K and 320 to 360 K, respectively. As illustrated in Fig. 1, the measured thermal conductivities are relatively invariant with temperature over the temperature ranges investigated.

Because of the similarities between ceramic oxides and superconducting materials, data previously obtained for several types of ceramic oxides are also illustrated in Fig. 1. It is interesting to note that for the range of temperatures shown, the thermal conductivities for all the ceramic oxides except beryllium oxide are lower than the measured thermal conductivity of the superconducting materials.

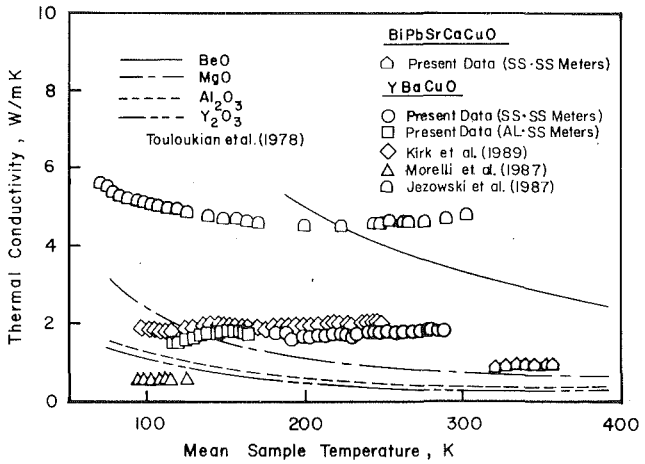

Fig. 1 Thermal conductivity as a function of temperature for YBaCuO and BiPbSrCaCuO superconducting materials compared with the thermal conductivity of several ceramic oxides

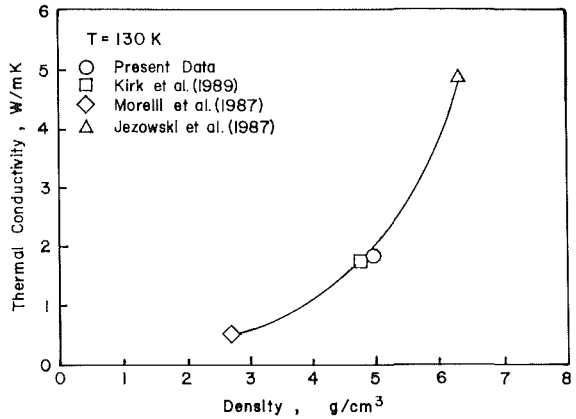

Fig. 2 The effect of density on the thermal conductivity of YBaCuO at constant temperature

The experimental measurements of Kirk et al. (1989), Jezowski et al. (1987), and Morelli et al. (1987) are also shown in Fig. 1 for comparison. The experimental results obtained by Kirk et al. are almost identical to those obtained in the present investigation, while those of Jezowski are more than twice the magnitude of the present measurements and show a slight decrease with respect to increasing temperature. The data of Morelli et al., however, are an order of magnitude smaller than the present results. This variation in the thermal conductivity appears to be due to the effect of density. As illustrated in Fig. 2, there is a substantial increase in thermal conductivity with density for the same superconducting material. The present experimental results compare most favorably with the work of Kirk et al. (1989). The similar results are believed to be due to the similarity in the densities, i.e., the density of the material used by Kirk et al. was 5.00 ± 0.05 g/cm^3, and that of the present material was 4.90 ± 0.05 g/cm^3. Although the experimental measurement techniques were different, the difference between the data obtained by Kirk et al. and the present data is on the order of 8 percent over the temperature range investigated.

Conclusions and Recommendations

An experimental investigation of the thermal conductivity of yttrium- and bismuth-based superconducting materials was conducted. Data were obtained for the yttrium-based material over a temperature range of 120 K to 290 K and the bismuth-based material over a temperature range of 320 to 360 K. These results compare favorably with published data for similar density materials. The thermal conductivities of the two materials exhibit almost no dependence on temperature over the range tested, and the bismuth-based material demonstrated a lower thermal conductivity than the yttrium-based material. The superconducting material fabrication method was found to have a significant effect on the overall thermal properties of each material.

Acknowledgments

The authors would like to acknowledge the assistance of Professor R. K. Pandey of the Electrical Engineering Department at Texas A&M University and the Texas Higher Education Coordinating Board Advanced Technology Program.

References

Collocott, S. J., White, G. K., Dou, S. X., and Williams, R. K., 1987, "Thermal Properties of the High-T_c Superconductors $La_{1.85}Sr_{0.15}CuO_4$ and $YBa_2Cu_3O_7$," *Physical Review B*, Vol. 36, No. 10, pp. 5684–5685.

Escudero, R., Chavira, E., and Rios-Jara, D., 1989, "Isolation of the 110 K Superconducting Phase of Bi–Pb–Sr–Ca–Cu–O Compounds," *Appl. Phys. Lett.*, Vol. 54, No. 16, pp. 1576–1578.

Freeman, J. J., Friedman, W. T. A., Ginsberg, D. M., Chen, J., and Zangvil, A., 1987, "Low-Temperature Thermal Conductivity of $YBa_2Cu_3O_{7-\delta}$," *Physical Review B*, Vol. 36, No. 16, pp. 8786–8787.

Hashimoto, T., Fueki, K., Kishi, A., Azumi, T., and Koinuma, H., 1988a, "Thermal Expansion Coefficients of High-T_c Superconductors," *Japanese J. Applied Physics*, Vol. 27, No. 2, pp. L214–L216.

Hashimoto, T., Kosaka, T., Yoshida, Y., Fueki, K., and Koinuma, H., 1988b, "Superconductivity and Substrate Interaction of Screen-Printed Bi–Sr–Ca–Cu–O Films," *Japanese J. Applied Physics*, Vol. 27, No. 3, pp. L348–L386.

Heremans, J., Morelli, D. T., Smith, G. W., and Strite, S. C., III., 1988, "Thermal and Electronic Properties of Rare-Earth $Ba_2Cu_3O_x$ Superconductors," *Physical Review B*, Vol. 37, No. 4, pp. 1604–1610.

Jezowski, A., Mucha, J., Rogacki, K., Horyn, R., Bukowski, Z., Horobiowski, M., Rafalowicz, J., Stepien-Damm, J., Sulkowski, C., Trojnar, E., Zaleski, A. J., and Klamut, J., 1987, "Thermal Conductivity and Electrical Resistivity of the High-T_c Superconductor $YBa_2Cu_3O_{9-\delta}$," *Physics Letters A*, Vol. 122, No. 8, pp. 431–433.

Junod, A., Bezinge, A., Eckert, D., Graf, T., and Muller, J., 1988, "Specific Heat Magnetic Susceptibility and Superconductivity of $YBa_2Cu_3O_{7-\delta}$ Doped With Iron," *Physica C.*, Vol. 152, pp. 495–504.

Kirk, W. P., Kobiela, P. S., Tsumura, R. N., and Pandey, R. K., 1989 "Thermal Conductivity of Hot-Pressed 123 YBCO Superconducting Oxides: Anisotropic Behavior at High and Very Low Temperatures," *Ferroelectrics*, Vol. 92, pp. 151–157.

Morelli, D. T., Heremans, J., and Swets, D. E., 1987, "Thermal Conductivity of Superconductive Y–Ba–Cu–O," *Physical Review B*, Vol. 36, No. 7, pp. 3917–3919.

Pandey, R. K., Gilbert, G. R., Kirk, W. R., Kobiela, P. S., Clearfield, A., and Squattrito, P. J., 1988, "Processing of Single-Phase Ceramic 1–2–3 YBaCu-Oxide Superconductor by Hot Pressing," *J. Superconductivity*, Vol. 1, No. 1, pp. 45–52.

Salama, K., Selvamanickam, V., Gao, L., and Sun, K., 1989, "High Current Density in Bulk $YBa_2Cu_3O_x$ Superconductor," *Appl. Phys. Lett.*, Vol. 54, No. 23, pp. 2352–2354.

Schmidt, C., 1979, "Simple Method to Measure the Thermal Conductivity of Technical Superconductors, e.g., NbTi," *Rev. Sci. Instruments*, Vol. 50, No. 4, pp. 454–457.

Shenck, H., Jr., 1961, *Theories of Engineering Experimentation*, McGraw-Hill, New York.

Touloukian, Y. S., Powell, R. W., Ho, C. Y., and Klemans, P. G., 1970, *Thermal Conductivity-Non-Metallic Solids, Vol. 2, Thermophysical Properties of Matter*, TPRC Data Series, IFI/Plenum Data Corporation.